Progress in Optical Science and Photonics
Series Editor: Javid Atai

Boris A. Malomed *Editor*

Spontaneous Symmetry Breaking, Self-Trapping, and Josephson Oscillations

Springer

Progress in Optical Science and Photonics

Series Editor

Javid Atai

For further volumes:
http://www.springer.com/series/10091

The purpose of the series Progress in Optical Science and Photonics is to provide a forum to disseminate the latest research findings in various areas of Optics and its applications. The intended audience is physicists, electrical and electronic engineers, applied mathematicians, and advanced graduate students.

Boris A. Malomed
Editor

Spontaneous Symmetry Breaking, Self-Trapping, and Josephson Oscillations

Springer

Editor
Boris A. Malomed
Department of Physical Electronics
Faculty of Engineering
Tel Aviv University
Ramat Aviv
Israel

ISBN 978-3-642-21206-2 ISBN 978-3-642-21207-9 (eBook)
DOI 10.1007/978-3-642-21207-9
Springer Heidelberg New York Dordrecht London

Library of Congress Control Number: 2013936952

Printed on acid-free paper

Springer is part of Springer Science+Business Media (www.springer.com)

Preface

A Brief Overview of Historical Origins of the Theme

Properties of collective excitations in physical systems are determined, in generic situations, by the interplay of a few fundamental ingredients: spatial dimension, external potential acting on the physical fields or wave functions, the number of independent components of the relevant fields (i.e., one may naturally categorize the systems as single-component *scalar* and multi-component *vectorial* ones), and nonlinear self-interactions of the fields. In particular, the shape of the external potentials determines the system's symmetry, two most ubiquitous types of which correspond to periodic lattice potentials and double-well potentials (DWPs) with the symmetry between the wells.

It is commonly known that the ground state in quantum mechanics exactly follows the symmetry of the underlying potential, while excited states may realize other representations of the same symmetry [1]. In particular, the wave function of the ground state of a particle trapped in the one-dimensional DWP potential is even, with respect to the double-well structure, while the first excited state has the opposite parity, being odd. Similarly, the wave function corresponding to the state at the bottom of the lowest Bloch band induced by the periodic potential features the same periodicity.

While the quantum-mechanical Schrödinger equation is linear for the single particle, the description of rarefied gases formed by quantum bosonic particles (i.e., Bose–Einstein condensates, BECs) is provided by the Gross–Pitaevskii equation (GPE), which, in the mean-field approximation, takes into account effects of collisions between the particles through an effective cubic term, added to the Schrödinger equation for the single-particle wave function [2, 27]. The cubic term, which corresponds to repulsive or attractive forces between the colliding particles, gives rise, respectively, to the self-defocusing (SDF), alias self-repulsion, or self-focusing (SF), i.e., self-attraction, of the wave function. A similar model, based on the nonlinear Schrödinger equation (NLSE) with the cubic term accounting for the effective SF or SDF, describes the propagation of the amplitude of electromagnetic waves in nonlinear optical media [3].

As well as their linear counterparts, the GPE and NLSE include external potentials, which often feature the DWP symmetry. However, the symmetry of the ground state in models with the SF nonlinearity (i.e., the state minimizing the energy at a fixed number of particles in the bosonic gas, or fixed total power of the optical beam—in either case, this is represented by a fixed norm of the respective wave function) follows the symmetry of the underlying potential structure only in the weakly nonlinear regime. A generic effect which occurs with the increase of the norm is *spontaneous symmetry breaking* (SSB). In its simplest manifestation, the SSB implies that the probability to find the particle in one well of the DWP structure is larger than in the other. This, incidentally, implies that another commonly known principle of quantum mechanics, according to which the ground state cannot be degenerate, is no longer valid in the nonlinear models: obviously, the SSB which takes place in the presence of the DWP gives rise to a degenerate pair of two mutually symmetric ground states, with the maximum of the wave function pinned to either potential well.

It should be stressed that the same system admits a symmetric state coexisting with the asymmetric ones, but, above the SSB point, the symmetric wave function no longer represents the ground state, being, in fact, unstable against small symmetry-breaking perturbations. Accordingly, in the course of the spontaneous transition from the unstable symmetric state to a stable asymmetric one, the choice between the two mutually degenerate asymmetric states is determined by random perturbations, which "push" the system with the SF nonlinearity to build the maximum of the wave function in the left or right potential well.

In systems with the SDF nonlinearity, the ground state remains symmetric and stable. In this case, the SSB manifests itself in the form of the spontaneous breaking of the *antisymmetry* of the first excited state (the spatially odd one, which has exactly one zero of the wave function, at the central point, in the one-dimensional setting). The state with the spontaneously broken antisymmetry also features a zero, which may be shifted from the central position.

To the best of my knowledge, the concept of the SSB in nonlinear systems of the NLSE type was first formulated in 1979 by Davies [4], although in a rather abstract form, using a "very mathematical" language. In that work, a nonlinear extension of the Schrödinger equation for a pair of quantum particles, interacting via a three-dimensional isotropic potential, was introduced, and the SSB was predicted in terms of the breaking of the rotational symmetry of the ground state.

Another early work, which predicted the SSB in a relatively simple form, dealt with the *self-trapping model*, which is based on a system of linearly coupled ordinary differential equations (ODEs) with SF cubic terms [5]. This model finds applications to some types of molecular dynamics. In fact, it was work [5] which had made the research community aware of the SSB concept, and helped to initiate a broad work on this topic.

Another important article which studied in detail the SSB in a physically relevant model described by an ODE system addressed the propagation of CW (continuous-wave) optical beams in dual-core nonlinear optical fibers (alias *nonlinear directional couplers*) [6]. In a scaled form, the corresponding system of equations is

$$
\begin{aligned}
i\frac{du_1}{dz} + f\left(|u_1|^2\right)u_1 + \kappa u_2 = 0, \\
i\frac{du_2}{dz} + f\left(|u_2|^2\right)u_2 + \kappa u_1 = 0,
\end{aligned}
\tag{1}
$$

where u_1 and u_2 are the CW amplitudes in the two cores ("CW" implies, in this case, that the amplitudes do not depend on the temporal variable), z is the propagation distance, κ the coefficient of the linear coupling between the two cores, due to the mutual penetration of evanescent fields from each core into the parallel one, and $f\left(|u_{1,2}|^2\right)$ is a function of the intensity which accounts for the intrinsic nonlinearity of each core. The study of SSB *bifurcations*, which occur with the increase of the intensity of the symmetric mode ($u_1 = u_2$), has demonstrated that, in the simplest case of the Kerr SF nonlinearity, which corresponds to $f(u^2) = |u|^2$ (in an appropriately normalized form), the symmetry-breaking bifurcation is of the simplest *supercritical*, alias *forward*, type [7], which destabilizes the symmetric state and, simultaneously, gives rise to a pair of stable asymmetric states, with $|u_1|^2 \neq |u_2|^2$. The latter states are mutually symmetric, i.e., one is obtained from the other by the interchange, $u_1 \rightleftarrows u_2$. On the other hand, the saturable nonlinearity, in the form of $f\left(|u|^2\right) = |u|^2/\left(I_0 + |u|^2\right)$, where I_0 is a positive constant (the nonlinearity of this type can be induced by dopants added to the material of the dual-core fiber) gives rise to a *subcritical*, alias *backward*, symmetry-breaking bifurcation. In that case, the branches of asymmetric states, which originate at the point of the destabilization of the symmetric mode, originally go backward (in terms of the total power, $|u_1|^2 + |u_2|^2$), as unstable solutions, and then turn forward, getting stable precisely at the turning point. This scenario implies that the pair of stable asymmetric states actually emerge *subcritically*, at a value of the total power smaller than that at which the symmetric mode loses its stability. In terms of statistical physics, the super- and subcritical bifurcations may be identified as symmetry-breaking phase transitions of the second and first kinds, respectively.

The next essential step in the studies of the SSB phenomenology in dual-core nonlinear optical fibers and similar systems was the consideration of the fields depending on the temporal variable, τ. In that case, assuming the anomalous sign of the group-velocity dispersion in the fiber, Eq. (1) are replaced by linearly coupled partial differential equations (PDEs), in the form of a system of NLSEs, which is usually considered with the Kerr nonlinearity:

$$
\begin{aligned}
i\frac{\partial u_1}{\partial z} + \frac{1}{2}\frac{\partial^2 u_1}{\partial \tau^2} + f\left(|u_1|^2\right)u_1 + \kappa u_2 = 0, \\
i\frac{\partial u_2}{\partial z} + \frac{1}{2}\frac{\partial^2 u_2}{\partial \tau^2} + f\left(|u_2|^2\right)u_2 + \kappa u_1 = 0.
\end{aligned}
\tag{2}
$$

The same system, but with τ replaced by transverse coordinate x, models the spatial-domain evolution of time-independent electromagnetic fields in a dual-core nonlinear planar waveguide.

A commonly known fact is that uncoupled NLSEs give rise to solitons (temporal or spatial solitary waves, in the temporal or spatial domain, respectively) [3]. Accordingly, the SSB bifurcation may destabilize obvious symmetric soliton solutions of system (2),

$$u_1 = u_2 = \eta \ \mathrm{sech}\ (\eta\tau) \exp\left(\left(\frac{1}{2}\eta^2 + \kappa\right)z\right) \tag{3}$$

(here η is an arbitrary amplitude of the soliton), replacing them by nontrivial asymmetric two-component soliton modes. The point of the onset of the symmetry-breaking instability of the symmetric solitons with the increase of the soliton's peak power, η^2, was found in an exact analytical form, as $\eta^2_{\mathrm{crit}} = 4/3$, in Ref. [8]. The resulting transition to asymmetric solitons was first predicted, in an approximate analytical form, by means of the variational approximation, in Refs. [9] and [10]. Afterward, it was found that, on the contrary to the supercritical bifurcation of the CW states in system (1) with the Kerr nonlinearity, the symmetry-breaking bifurcation of the solitons in system (2) is subcritical [11, 12].

An independent line of the studies of the SSB originated from the consideration of models of atomic BECs trapped in potential landscapes of the DWP type. The scaled form of the corresponding GPE for the single-particle wave function, $\psi(x,t)$, is

$$i\frac{\partial\psi}{\partial t} = -\frac{1}{2}\frac{\partial^2\psi_1}{\partial x^2} + \sigma|\psi|^2\psi + U(x)\psi, \tag{4}$$

where $\sigma = +1$ and -1 for the repulsive and attractive collision-induced nonlinearity, respectively, and the DWP can be taken, e.g., as

$$U(x) = U_0\left(x^2 - a^2\right)^2, \tag{5}$$

where U_0 and a^2 are positive constants. It is relevant to mention that the connection between the equation in the form of PDE (4) and a simpler ODE system (1) (with z replaced by time t) can be established by means of the *tight-binding approximation* [13], replacing $\psi(x,t)$ by a linear superposition of two stationary wave functions, ϕ, corresponding to states trapped separately in the two potential wells, with centers at points $x = \pm a$:

$$\psi(x,t) = u_1(t)\phi(x-a) + u_2\phi(x+a). \tag{6}$$

The analysis of the SSB in BEC and quantum models based on Eq. (4) and similar models was initiated in Refs. [14] and [15]. Most typically, the BEC nonlinearity is self-repulsive, which, as mentioned above, gives rise to the spontaneous breaking of the antisymmetry of the odd states, with $\psi(-x) = -\psi(x)$. Further, the GPE can

be extended by adding an extra spatial coordinate, on which the DWP potential does not depend, i.e., one arrives at a two-dimensional GPE with a *double-trough potential*. In such a setting, the self-attractive nonlinearity (which, although being less typical in BEC, is possible too) gives rise to matter-wave solitons, which may self-trap in the free direction [16]. Accordingly, symmetric solitons are possible in the double-trough potential, which are replaced, via the subcritical bifurcation, by stable asymmetric solitons, provided that the number of particles in the BEC (which determines the effective strength of the intrinsic nonlinearity) exceeds a certain critical number [17].

The above discussion was dealing with static symmetric and asymmetric modes supported by various nonlinear systems. The consideration of dynamical regimes, most typically in the form of oscillations of the norm of the wave function between two wells of the DWP structure, i.e., as a matter of fact, between the two mutually degenerate asymmetric states existing above the critical values of the effective strength of the nonlinearity, has been developed too. Following the analogy with well-known Josephson oscillations of the wave function of superconducting electrons in tunnel junctions, formed by bulk superconductors separated by a narrow dielectric layer [18] (note that topological solitons, in the form of quanta of trapped magnetic flux, are well-known in long Josephson junctions of this type [19]), the possibility of similar oscillations in *bosonic Josephson junctions* was predicted [20]. The simplest model of the Josephson oscillations in bosonic systems is based on the dynamical version of Eq. (1), which was derived from the full GPE by means of the tight-binding approximation relying upon expansion (6).

As is the case with many other general topics, especially those in the area of nonlinear science, the variety of theoretically predicted results concerning the SSB phenomenology by far exceeds the number of experimental works. Nevertheless, some experimental manifestations of the SSB have been observed in a clear form. In particular, the self-trapping of a macroscopically asymmetric state of the atomic condensate of ^{87}Rb atoms with repulsive interactions between them, loaded into the DWP, as well as Josephson oscillations in that setting, were reported in Ref. [21]. On the other hand, the SSB of laser beams coupled into an effective transverse DWP created in the SF photorefractive medium has been explicitly demonstrated in Ref. [22]. Still another result of an experimentally observed SSB effect in nonlinear optics is the spontaneously established asymmetric regime of operation of a symmetric pair of coupled lasers [23]. More recently, symmetry breaking was experimentally demonstrated in a plasmonic coupler [24], although in the latter case the effect was not spontaneous, being induced by a structural element of the system.

Survey of Chapters in the Present Volume

Studies of SSB effects, self-trapping, and Josephson oscillations in very diverse nonlinear systems have been subjects of a great number of publications, chiefly theoretical ones. These general topics have seen a great deal of development in

many directions. Despite the obvious imbalance between the theoretical and experimental works, the topics call for a comprehensive review article, or even a book, which, as a matter of fact, is still missing. The present volume partly compensates this omission in the literature, offering a collection of 28 chapters which cover many (although definitely not all) aspects of the general themes named in the title of the volume, as well as related topics (even if symmetry breaking, self-trapping, or Josephson junctions are not mentioned in titles of particular chapters, some of these research items are considered in all of them). Most of the chapters are written as semi-review articles, giving an adequate presentation of the respective topics, and also offering references for further reading.

The chapters are briefly surveyed below under rubrics corresponding to different types of physics which are considered in them. It is worthy to note that, quite naturally, not all important branches of the field are covered by particular chapters. In particular, the SSB occurs too in a class of systems with symmetric *pseudopotentials* (rather than usual potential structures), which are induced by appropriate spatial modulations of the local nonlinearity strength. Models of this type were comprehensively reviewed in Ref. [25]. A more specific topic is the SSB of discrete solitons in parallel-coupled dual-core nonlinear lattices [26].

Nonlinear Optics and Plasmonics

This topical section is the largest one in the volume, including 14 chapters, see the list following below. It is relevant to stress that one of the chapters, "Spontaneous Formation and Switching of Optical Patterns in Semiconductor Microcavities", by J. Scheuer and M. Orenstein, includes a vast experimental material. Two chapters, viz., "Defect Modes, Fano Resonances and Embedded States in Magnetic Metamaterials", by M. I. Molina, and "Sub-Wavelength Plasmonic Solitons in 1D and 2D Arrays of Coupled Metallic Nanowires", by F. Ye, D. Mihalache, and N. C. Panoiu, deal not with optics proper, but rather with plasmonics and metamaterials, which are new directions in studies of the propagation of electromagnetic fields in artificially built media. It is relevant to note that chapters "Frequency and Phase Locking of Laser Cavity Solitons", by T. Ackemann, Y. Noblet, P. V. Paulau, C. McIntyre, P. Colet, W. J. Firth,and G.-L. Oppo, "Guided Modes and Symmetry Breaking Supported by Localized Gain", by Y. V. Kartashov, V. V. Konotop, V. A. Vysloukh, and D. A. Zezyulin, and "Pattern Formation Under a Localized Gain", by A. A. Nepomnyashchy, are dealing with dissipative models of nonlinear optics, while chapter "Spatial Solitons in Parity-Time-Symmetric Photonic Lattices: Recent Theoretical Results", by Y.-J. He and B. A. Malomed, presents a short review of solitons in $\mathcal{PT}$-symmetric nonlinear models, which are intermediate between conservative systems and usual dissipative ones.

(1) Nonlinear Dynamics of Bloch wave packets in honeycomb lattices, by M. J. Ablowitz and Y. Zhu.

(2) Light self-localization and power-dependent steering in anisotropic dielectrics: Spatial solitons in uniaxial nematic liquid crystals, by A. Alberucci and G. Assanto.
(3) Frequency and phase locking of laser cavity solitons, by T. Ackemann, Y. Noblet, P. V. Paulau, C. McIntyre, P. Colet, W. J. Firth, and G.-L. Oppo.
(4) Light-induced breaking of symmetry in photonic crystal waveguides with nonlinear defects as a key for all-optical switching circuits, by E. Bulgakov, A. Sadreev, and K. N. Pichugin.
(5) Spatial solitons in parity-time-symmetric photonic lattices: Recent theoretical results, by Y.-J. He and B. A. Malomed.
(6) Spontaneous symmetry breaking of pinned modes in nonlinear gratings with an embedded pair of defects, by I. V. Kabakova, I. Uddin, J. Jeyaratnam, C. M. de Sterke, and B. A. Malomed.
(7) Guided modes and symmetry breaking supported by localized gain, by Y. V. Kartashov, V. V. Konotop, V. A. Vysloukh, and D. A. Zezyulin.
(8) Analytical solitary wave solutions of a nonlinear Kronig–Penney model for photonic structures consisting of linear and nonlinear layers, by Y. Kominis and K. Hizanidis.
(9) Trapping polarization of light in nonlinear optical fibers: An ideal Raman polarizer, by V. V. Kozlov, J. Nuño, J. D. Ania-Castañón, and S. Wabnitz.
(10) Studies of existence and stability of circularly polarized few-cycle solitons beyond the slowly varying envelope approximation, by H. Leblond, D. Mihalache, and H. Triki.
(11) Defect modes, Fano resonances, and embedded states in magnetic metamaterials, by M. I. Molina.
(12) Pattern formation under a localized gain, by A. A. Nepomnyashchy.
(13) Spontaneous formation and switching of optical patterns in semiconductor microcavities, by J. Scheuer and M. Orenstein.
(14) Sub-wavelength plasmonic solitons in 1D and 2D arrays of coupled metallic nanowires, by F. Ye, D. Mihalache, and N. C. Panoiu.

Bose–Einstein Condensates

The second largest topical section, which includes nine chapters, is dealing with BEC and related subjects, such as bosonic Josephson junctions. In addition to atomic quantum gases, condensates of quasiparticles (polaritons) are considered too, in chapter "Symmetry-breaking effects for polariton condensates in double-well potentials", by A. S. Rodrigues, P. G. Kevrekidis, J. Cuevas, R. Carretero-Gonzalez, and D. J. Frantzeskakis. It is relevant to mention that chapter "Classical dynamics of a two-species Bose-Einstein condensate in the presence of nonlinear maser processes", by B. M. Rodriguez-Lara and R.-K. Lee, is dealing with a situation which combines problems in the fields of both BEC and optics.

(1) From coherent modes to turbulence and granulation of trapped gases, by V. S. Bagnato and V. I. Yukalov.
(2) Bright solitary matter waves: Formation, stability, and interactions, by T. P. Billam, A. L. Marchant, S. L. Cornish, S. A. Gardiner, and N. G. Parker.
(3) Temporal quantum fluctuations in the fringe-visibility of atom interferometers with interacting Bose–Einstein condensate, by D. Cohen and A. Vardi.
(4) Temperature effects on the quantum coherence of bosonic Josephson junctions, by B. Julía-Díaz, J. Martorell, and A. Polls.
(5) Multiple fluxon analogues and dark solitons in linearly coupled Bose–Einstein condensates, by M. I. Qadir, H. Susanto, and P. C. Matthews.
(6) Symmetry-breaking effects for polariton condensates in double-well potentials, by A. S. Rodrigues, P. G. Kevrekidis, J. Cuevas, R. Carretero-González, and D. J. Frantzeskakis.
(7) Classical dynamics of a two-species Bose–Einstein condensate in the presence of nonlinear maser processes, by B. M. Rodríguez-Lara and R.-K. Lee.
(8) Existence, stability, and nonlinear dynamics of vortices and vortex clusters in anisotropic Bose–Einstein condensates, by J. Stockhofe, P. G. Kevrekidis, and P. Schmelcher.
(9) Josephson tunneling of excited states in a double-well potential, by H. Susanto and J. Cuevas.

General Models of Nonlinear Symmetric Systems

Two chapters deal with general aspects of the symmetry breaking in models of nonlinear systems, which are based on discrete and continual equations of the NLSE type. One chapter is dealing with dissipative dynamics, and the other one reports results for a conservative model:

(1) Solitons in a parametrically driven damped discrete nonlinear Schrödinger equation, by M. Syafwan, H. Susanto, and S. M. Cox.
(2) Conditions and stability analysis for saddle-node bifurcations of solitary waves in generalized nonlinear Schrödinger equations, by J. Yang.

Josephson Junctions in Superconductivity

One chapter addresses the area in which the Josephson junctions had been first predicted and created, namely, traditional low-temperature superconductivity:

(1) Escape time of Josephson junctions for signal detection, by P. Addesso, G. Filatrella, and V. Pierro.

Micromechanical Systems

A separate chapter is dealing with a physical setting different from those considered in other chapters, namely, dynamics of nonlinear micromechanical elements:

(1) Symmetry breaking criteria in electrostatically loaded bistable curved/pre-buckled micro beams, by L. Medina, R. Gilat and S. Krylov.

Acknowledgments

As the editor of the volume, I would like to thank all the contributing authors for their work on drafting and, in case that was necessary, revising their chapters. I also thank Javid Atai of the University of Sydney (Australia) who had originally suggested me to formulate a topic of a volume for the Springer series on *Progress in Optical Sciences and Photonics*, and be its editor. Finally, thanks are due to members of the Springer's staff for their valuable help provided in the course of my editorial work on the volume: Dr. Christoph Baumann, Tanja Jaeger, and Umashankar Gayathri.

On a more private note, being a coauthor of two chapters included into this volume, I would like to thank my collaborators for their excellent work on these chapters. They are Irina Kabakova, I. Uddin, J. Jeyaratnam, and C. Martijn de Sterke at the University of Sydney, and Ying-Ji He at the Guangdong Polytechnic Normal University (Guangzhou, China).

Boris A. Malomed

References

1. D. Landau, E.M. Lifshitz, *Quantum Mechanics*, (Nauka Publishers, Moscow, 1974)
2. F. Dalfovo, S. Giorgini, L.P. Pitaevskii, S. Stringari, Theory of Bose-Einstein condensation in trapped gases, Rev. Mod. Phys. **71**, 463–512 (1999)
3. Y.S. Kivshar, G.P. Agrawal, *Optical Solitons*: *From Fibers to Photonic Crystals* (Academic Press, San Diego, 2003)
4. E.B. Davies, Symmetry breaking in a non-linear Schrödinger equation. Commun. Math. Phys. **64**, 191–210 (1979)

5. J.C. Eilbeck, P.S. Lomdahl, A.C. Scott, The discrete self-trapping equation. Physica D **16**, 318–338 (1985)
6. A.W. Snyder, D.J. Mitchell, L. Poladian, D.R. Rowland, Y. Chen, Physics of nonlinear fiber couplers. J. Opt. Soc. Am. B **8**, 2101–2118 (1991)
7. G. Iooss, D.D. Joseph, *Elementary Stability Bifurcation Theory* (Springer, New York, 1980)
8. E.M. Wright, G.I. Stegeman, S. Wabnitz, Solitary-wave decay and symmetry-breaking instabilities in two-mode fibers. Phys. Rev. A **40**, 4455–4466 (1989)
9. C. Paré and M. Flłorjańczyk, Approximate model of soliton dynamics in all-optical couplers. Phys. Rev. A **41**, 6287–6295 (1990)
10. A.I. Maimistov, Propagation of a light pulse in nonlinear tunnel-coupled optical waveguides. Kvant. Elektron. **18**, 758–761 (1991). Sov. J. Quantum Electron. **21**, 687–690 (1991)
11. N. Akhmediev, A. Ankiewicz, Novel soliton states and bifurcation phenomena in nonlinear fiber couplers. Phys. Rev. Lett. **70**, 2395–2398 (1993)
12. B.A. Malomed, I. Skinner, P.L. Chu, G.D. Peng, Symmetric and asymmetric solitons in twin-core nonlinear optical fibers. Phys. Rev. E **53**, 4084 (1996)
13. G.L. Alfimov, P.G. Kevrekidis, V.V. Konotop, M. Salerno, Wannier functions analysis of the nonlinear Schrödinger equation with a periodic potential. Phys. Rev. E **66**, 046608 (2002)
14. G.J. Milburn, J. Corney, E.M. Wright, D.F. Walls, Quantum dynamics of an atomic Bose–Einstein condensate in a double-well potential. Phys. Rev. A **55**, 4318–4324 (1997)
15. A. Smerzi, S. Fantoni, S. Giovanazzi, S.R. Shenoy, Quantum coherent atomic tunneling between two trapped Bose–Einstein condensates. Phys. Rev. Lett. **79**, 4950–4953 (1997)
16. V.M. Pérez-García, H. Michinel, H. Herrero, Bose–Einstein solitons in highly asymmetric traps. Phys. Rev. A **57**, 3837–3842 (1998)
17. M. Matuszewski, B.A. Malomed, M. Trippenbach, Spontaneous symmetry breaking of solitons trapped in a double-channel potential. Phys. Rev. A **75**, 063621 (2007)
18. G. Schön and A.D. Zaikin, Quantum coherent effects, phase transitions, and the dissipative dynamics of ultra small tunnel junctions. Phys. Rep. **198**, 237–412 (1990)
19. A.V. Ustinov, Solitons in Josephson junctions. Physica D **123**, 315–329 (1998)
20. S. Raghavan, A. Smerzi, S. Fantoni, S.R. Shenoy, Coherent oscillations between two weakly coupled Bose–Einstein condensates: Josephson effects, π oscillations, and macroscopic quantum self-trapping. Phys. Rev. A **59**, 620–633 (1999)
21. M. Albiez, R. Gati, J. Fölling, S. Hunsmann, M. Cristiani, and M.K. Oberthaler, Direct observation of tunneling and nonlinear self-trapping in a single bosonic Josephson junction. Phys. Rev. Lett. **95**, 010402 (2005)
22. P.G. Kevrekidis, Z. Chen, B.A. Malomed, D.J. Frantzeskakis, M.I. Weinstein, Spontaneous symmetry breaking in photonic lattices: Theory and experiment. Phys. Lett. A **340**, 275–280 (2005)
23. T. Heil, I. Fischer, W. Elsässer, J. Mulet, C.R. Mirasso, Chaos synchronization and spontaneous symmetry-breaking in symmetrically delay-coupled semiconductor lasers. Phys. Rev. Lett. **86**, 795–798 (2000)
24. A. Christ, O.J.F. Martin, Y. Ekinci, N.A. Gippius, S.G. Tikhodeev, Symmetry breaking in a plasmonic metamaterial at optical wavelength. Nano Lett. **8**, 2171–2175 (2008)
25. Y.V. Kartashov, B.A. Malomed, L. Torner, Solitons in nonlinear lattices. Rev. Mod. Phys. **83**, 247–306 (2011)
26. G. Herring, P.G. Kevrekidis, B.A. Malomed, R. Carretero-González, D.J. Frantzeskakis, Symmetry breaking in linearly coupled dynamical lattices. Phys. Rev. E **76**, 066606 (2007)
27. H.T.C. Stoof, K.B. Gubbels, D.B.M. Dickersheid, *Ultracold Quantum Fields* (Springer, Dordrecht, 2009)

Contents

Nonlinear Dynamics of Bloch Wave Packets in Honeycomb Lattices 1
Mark J. Ablowitz and Yi Zhu

Light Self-Localization and Power-Dependent Steering in Anisotropic Dielectrics: Spatial Solitons in Uniaxial Nematic Liquid Crystals 27
Alessandro Alberucci and Gaetano Assanto

Frequency and Phase Locking of Laser Cavity Solitons 49
T. Ackemann, Y. Noblet, P. V. Paulau, C. McIntyre, P. Colet, W. J. Firth and G.-L. Oppo

Light-Induced Breaking of Symmetry in Photonic Crystal Waveguides with Nonlinear Defects as a Key for All-Optical Switching Circuits 89
Evgeny Bulgakov, Almas Sadreev and Konstantin N. Pichugin

Spatial Solitons in Parity-Time-Symmetric Photonic Lattices: Recent Theoretical Results 125
Ying-Ji He and Boris A. Malomed

Spontaneous Symmetry Breaking of Pinned Modes in Nonlinear Gratings with an Embedded Pair of Defects 149
I. V. Kabakova, I. Uddin, J. Jeyaratnam, C. M. de Sterke and B. A. Malomed

Guided Modes and Symmetry Breaking Supported by Localized Gain 167
Yaroslav V. Kartashov, Vladimir V. Konotop, Victor A. Vysloukh and Dmitry A. Zezyulin

Analytical Solitary Wave Solutions of a Nonlinear Kronig-Penney Model for Photonic Structures Consisting of Linear and Nonlinear Layers 201
Yannis Kominis and Kyriakos Hizanidis

Trapping Polarization of Light in Nonlinear Optical Fibers: An Ideal Raman Polarizer 227
Victor V. Kozlov, Javier Nuño, Juan Diego Ania-Castañón and Stefan Wabnitz

Studies of Existence and Stability of Circularly Polarized Few-Cycle Solitons Beyond the Slowly-Varying Envelope Approximation 247
Hervé Leblond, Dumitru Mihalache and Houria Triki

Defect Modes, Fano Resonances and Embedded States in Magnetic Metamaterials 277
M. I. Molina

Pattern Formation Under a Localized Gain 309
Alexander A. Nepomnyashchy

Spontaneous Formation and Switching of Optical Patterns in Semiconductor Microcavities 321
Jacob Scheuer and Meir Orenstein

Sub-Wavelength Plasmonic Solitons in 1D and 2D Arrays of Coupled Metallic Nanowires 357
F. Ye, D. Mihalache and N. C. Panoiu

From Coherent Modes to Turbulence and Granulation of Trapped Gases 377
V. S. Bagnato and V. I. Yukalov

Bright Solitary Matter Waves: Formation, Stability and Interactions 403
T. P. Billam, A. L. Marchant, S. L. Cornish, S. A. Gardiner and N. G. Parker

Temporal Quantum Fluctuations in the Fringe-Visibility of Atom Interferometers with Interacting Bose–Einstein Condensate 457
Doron Cohen and Amichay Vardi

Temperature Effects on the Quantum Coherence of Bosonic Josephson Junctions 473
B. Juliá-Díaz, J. Martorell and A. Polls

Multiple Fluxon Analogues and Dark Solitons in Linearly Coupled Bose–Einstein Condensates 485
M. I. Qadir, H. Susanto and P. C. Matthews

Symmetry-Breaking Effects for Polariton Condensates in Double-Well Potentials 509
A. S. Rodrigues, P. G. Kevrekidis, J. Cuevas, R. Carretero-González and D. J. Frantzeskakis

Classical Dynamics of a Two-species Bose–Einstein Condensate in the Presence of Nonlinear Maser Processes 531
B. M. Rodríguez-Lara and R.-K. Lee

Existence, Stability and Nonlinear Dynamics of Vortices and Vortex Clusters in Anisotropic Bose–Einstein Condensates 543
J. Stockhofe, P. G. Kevrekidis and P. Schmelcher

Josephson Tunneling of Excited States in a Double-Well Potential . . . 583
H. Susanto and J. Cuevas

Solitons in a Parametrically Driven Damped Discrete Nonlinear Schrödinger Equation 601
M. Syafwan, H. Susanto and S. M. Cox

Conditions and Stability Analysis for Saddle-Node Bifurcations of Solitary Waves in Generalized Nonlinear Schrödinger Equations 639
Jianke Yang

Escape Time of Josephson Junctions for Signal Detection 657
P. Addesso, G. Filatrella and V. Pierro

Symmetry Breaking Criteria in Electrostatically Loaded Bistable Curved/Prebuckled Micro Beams 679
Lior Medina, Rivka Gilat and Slava Krylov

Erratum to: Escape Time of Josephson Junctions for Signal Detection 707
P. Addesso, G. Filatrella and V. Pierro

Nonlinear Dynamics of Bloch Wave Packets in Honeycomb Lattices

Mark J. Ablowitz and Yi Zhu

Abstract Nonlinear waves in deformed optical honeycomb lattices are investigated. Discrete couple mode equations are used to find higher order continuous nonlinear Dirac systems which are employed to describe key underlying phenomena. For weak deformation and nonlinearity the wave propagation is circular–ellliptical. At strong nonlinearity the diffraction pattern becomes triangular in structure which is traced to appropriate nonequal energy propagation in momentum space. At suitably large deformation the dispersion structure can have nearby Dirac points or small gaps. The effective dynamics of the wave packets is described by two maximally balanced nonlocal nonlinear Schrödinger type equations.

1 Introduction

Wave propagation in honeycomb lattices has attracted considerable interest in physics and applied mathematics. One of the main reasons to understand these lattices and their behavior is due to the recent fabrication of the new material graphene and its success in numerous applications [1]. Many of the important properties associated with graphene come from the two-dimensional honeycomb

M. J. Ablowitz
Department of Applied Mathematics, University of Colorado, 526 UCB,
Boulder, CO 80309-0526, USA

Y. Zhu (✉)
Zhou Pei-Yuan Center for Applied Mathematics, Tsinghua University,
Beijing 100084, China
e-mail: yizhu@tsinghua.edu.cn

Progress Optical Sci., Photonics (2013): 1–26
DOI: 10.1007/10091_2012_27

Published Online: 30 January 2013

arrangement of its atoms which has major effect on how the associated matter waves propagate. More specifically, the spectrum of the Schrödinger operator with a honeycomb lattice exhibits conical structure in the neighborhood where two dispersion branches touch; these locations are referred as Dirac points. In the vicinity of the Dirac points, the dispersion relation locally forms a double-cone, referred as a Dirac cone. This special geometric structure gives rise to two independent Bloch wave envelopes or packets. In other words the conical dispersion relation admits the propagation of massless Fermions. Interestingly important and novel phenomena are related to these unusual electronic excitations; e.g., anomalous integer quantum Hall effect, Klein tunneling, enhanced conductivity etc. [1–3]. Other fields where honeycomb lattices play important roles include electromagnetic waves propagating in photonic crystals with a honeycomb background [4] and ultra cold atoms trapped in optic induced honeycomb lattices [5, 6].

On the other hand even though electromagnetic waves which are classical waves obey Maxwell equations, the propagation of light in a paraxial photonic crystal can be described by a lattice nonlinear Schrödinger (NLS) Eq. (1), see for example, [7]. In order to stablize the lattice, for instance, in optically induced crystals, the lattice intensity is often much higher than the intensities of the propagation waves [8–10]. This setup leads to the strong potential or so-called tight-binding limit. In this context, coupled-mode theory provides an approximate model for the wave packets which are represented as discrete evolution equations [11]. In the case when the simple background lattice is square or rectangular the governing Bloch envelope equation can often be reduced to a discrete nonlinear Schrödinger equation; this generally corresponds to single band approximations [12, 13]. But when the background lattice is not simple, such as a honeycomb-hexagonal lattice, one finds that the fundamental governing Bloch envelope equation satisfies a discrete nonlinear Dirac system which describes the wave dynamics associated with the Dirac cone [14–16]. From a mathematical point of view these problems have certain common features; in particular wave envelopes associated with Bloch modes and the associated nonlinearity are centrally important in the analytical description.

The study of the interplay between periodicity and nonlinearity leads to important mathematical questions. Periodicity relates to the band structure of the dispersion relation and Bloch waves which are similar in spirit to plane waves in Fourier analysis. In many cases the nonlinearity induces pure self phase modulation. But nonlinearity can also couple waves between different Fourier modes or Bloch bands. In simple lattices Bloch envelopes can lead to interesting localized structures which propagate in the gap regimes of the spectrum; they are sometimes referred to as gap solitons. Associated with such gaps in the spectrum many different types of propagating localized waves have been found; examples include but are not limited to dipole solitons, vortex solitons and soliton trains [8–10, 17–23]. As in the simple lattice case honeycomb lattices can also admit gap solitons [4, 12]. These solitons are often considered theoretically as bifurcations from the Bloch-band edges into the band gaps [24–26]. Similarly solitons can sometimes be found in near periodic and complex media cases [27–29].

Wave propagation in honeycomb lattices when the potential is strong (the tight-binding limit) was first considered by Wallace in 1947 [30]; this work paved the way for researchers to begin to understand the theoretical underpinnings of the linear wave propagation in honeycomb lattices. The first experimental fabrication of the material graphene was carried out by Geim and Novoselov [1, 2]. Inspired by the success of graphene, honeycomb structures have been studied in many fields. In optics, gap solitons were studied in honeycomb lattices [4, 12] and conical diffraction in honeycomb lattice was observed in [4, 31]. They experimentally demonstrated conical diffraction and gap solitons in honeycomb lattices. Theoretically speaking, wave dynamics associated with the Dirac points in honeycomb lattices has recently been considered. Ablowitz and Zhu found a general discrete envelope Dirac wave system in the tight-binding limit and studied the associated nonlinear dynamics, including conical and triangular diffraction of the optical wave field [14, 15, 32]. In the context of Bose-Einstein condensation, Haddad and Carr studied nonlinear atomic waves propagating in honeycomb optical lattices [16] in the tight binding limit. Haldane and Raghu studied linear propagation of electromagnetic waves in the full Maxwell equations [33, 34]; Ablowitz and Zhu analyzed the wave propagation in the shallow potential and weak nonlinear limits [35]. Wave dynamics in $\mathcal{PT}$-symmetric honeycomb lattices were studied in [36, 37] and symmetry breaking and wave dynamics in deformed honeycomb lattices were studied in [31, 32, 38, 39]. Fefferman and Weinstein rigorously proved the existence of Dirac points for a perfect honeycomb lattice in a generic regime and obtained the first order approximation in the neighborhood of Dirac cones [40].

As indicated above, one of the key features of honeycomb lattices is the existence of the Dirac cones and the associated envelope wave dynamics. This paper addresses the novel aspects of the nonlinear propagation of wave packets near the Dirac cone in two-dimensional (2-D) honeycomb lattices. The outline of this paper is as follows. In Sects. 2–3 the fundamentals of periodic optical and honeycomb lattices are discussed. In Sect. 4 the discrete nonlinear Dirac system is derived; we include a deformation parameter ρ. Depending on the size of ρ in Sect. 5 we explain that one might or might not have Dirac points. The continuum limit of the discrete system associated with the special points is studied in Sect. 6; here we obtain the nonlinear Dirac equation and discuss the associated conical dynamics. In Sect. 7 we show the symmetry breaking of the conical dynamics due to the nonlinearity which also requires the higher order dispersive terms to describe the dynamics. We then study deformed honeycomb lattices in Sect. 8. The effect of nonlinearity on the wave propagation in the various deformation regions is explored in the remaining parts of the paper. Novel nonlinear wave equations are derived in the two different regimes: (i) where there are two neighboring Dirac points (ii) no Dirac points. We find asymptotically valid equations to be nonlocal NLS equations which we refer to as NLS Kadomtsev–Petviashvili (KP) type equations—or NLSKP type equations; i.e., they are analogs of nonlocal KP equations which arise in water waves [41].

2 2-D Optical Periodic Lattices

As mentioned earlier, electromagnetic waves propagating in an inhomogeneous Kerr nonlinear medium can often be described by a two-dimensional nonlinear Schrödinger Eq. (7); this equation written in dimensionless form is given by

$$i\psi_z + \nabla^2\psi - \delta V(\mathbf{r})\psi + \sigma|\psi|^2\psi = 0. \tag{1}$$

Here $\mathbf{r} = (r_1, r_2)$ is the transverse coordinate; z is the propagation direction; the potential, $V(\mathbf{r})$ is a real periodic function which represents the transverse variation of the refractive index, and δ represents its order of magnitude; σ is the nonlinear coefficient which is positive for focusing nonlinearity and negative for defocusing nonlinearity. In Bose–Einstein condensation this equation is usually called the Gross–Pitaevskii (GP) equation. In this context it describes the wave propagation associated with the ultra cold atoms trapped in a periodic lattice [5].

The geometric distribution of local minima of the potentials, also called sites, determines the main features of the periodic potential. These sites are the positions of the potential wells. In optics, they have increased refractive index the electromagnetic field is attracted to the sites. A 2-D periodic function has two periods along two different directions which we call primitive lattice vectors. Let $\Gamma \simeq \mathbb{Z}^2$ denote a two-dimensional lattice generated through the basis $\{\mathbf{v}_1, \mathbf{v}_2\}$, i.e.,

$$\Gamma = \{m\mathbf{v}_1 + n\mathbf{v}_2 : \quad m, n \in \mathbb{Z}\}.$$

The primitive unit cell Ω is defined as

$$\Omega = \{q_1\mathbf{v}_1 + q_2\mathbf{v}_2 : q_j \in [0, 1)\}.$$

The primitive cell Ω is the fundamental tile of a tessellation of the plane associated with the lattice Γ, i.e., $\mathbb{R}^2 = \bigcup_{\mathbf{v}\in\Gamma}(\Omega + \mathbf{v})$.

For simple 2-D lattices, there is only one site (local minimum) per cell. All sites can be generated by a starting point with two discrete translational symmetries, i.e., two periods $\mathbf{v}_1$ and $\mathbf{v}_2$. Interactions between two sites are the same as the interactions between two cells. Typical examples are square lattices and triangular lattices. In so-called non-simple lattices, there are multiple sites per cell. In addition to periodicity, extra freedoms are needed to identify the distributions of the sites. They are the inner freedoms which, for instance, describe the distances between sites in the same cell or depths of the sites. All sites are identical under translational symmetries in simple lattices while non-simple lattices contain at least two different types of sites. A honeycomb lattice is such a structure. It has two sites per cell. The inner parameters (distance between two sites and depths of each site) play very important roles. The dual lattice Γ' is spanned by the dual basis vectors $\mathbf{k}_1$ and $\mathbf{k}_2$ where $\mathbf{k}_m \cdot \mathbf{v}_n = 2\pi\delta_{mn}$. Namely $\Gamma' = \{m\mathbf{k}_1 + n\mathbf{k}_2 : \quad m, n \in \mathbb{Z}\}$.The primitive dual unit cell Ω' is defined

$$\Omega' = \left\{ q_1\mathbf{k}_1 + q_2\mathbf{k}_2 : q_j \in [-\frac{1}{2}, \frac{1}{2}) \right\}.$$

This is also called the Brillouin zone. It is noted that Brillouin zone has other representations but all representations are the same due to the periodicity [42].

3 Honeycomb Lattices and Bloch Theory

A honeycomb lattice is a special 2-D lattice. Its unit cell is equivalent to a hexagon under discrete translational symmetries and all sites (local minima of the continuous periodic potential) are located at the vertices of this hexagon. Note that only two of these six vertices are independent under discrete translational symmetries. It also should be noted that a triangular lattice has a hexagonal structure as well but it has only one independent starting site which is located at the center. A triangular lattice only has one site per cell and all sites are identical.

By considering the site distribution, a honeycomb lattice is composed of two triangular sublattices. Namely there are two initial points $\mathbf{A} \in \Omega$ and $\mathbf{B} \in \Omega$, where $\mathbf{A} \neq \mathbf{B}$; then the two sublattices are

$$\Gamma_{\mathbf{A}} = \mathbf{A} + \Gamma; \qquad \Gamma_{\mathbf{B}} = \mathbf{B} + \Gamma$$

A honeycomb lattice is the union of the two sublattices, i.e.,

$$\Gamma_{\mathbf{H}} = \Gamma_{\mathbf{A}} \cup \Gamma_{\mathbf{B}}.$$

A honeycomb lattice and corresponding indices used herein are displayed in Fig. 1; we note that in the strong potential limit which we will consider there are coefficients ρ and ρ_0 that arise in the dispersion structure of the linear lattice; they are usually termed nearest neighbor hopping energies. In this paper we take $\rho_0 = 1$. The filled black dots are $\mathbf{A}$ lattice points and the circles are $\mathbf{B}$ lattice points. We see that an $\mathbf{A}$ lattice point $\mathbf{A_p} \in \Gamma_{\mathbf{A}}$ has three nearest neighbors that are all $\mathbf{B}$ lattice points: $\mathbf{B_p}, \mathbf{B_{p-v_1}}$ and $\mathbf{B_{p-v_2}}$; a $\mathbf{B}$ lattice point has three nearest neighbors that are all $\mathbf{A}$ lattice points: $\mathbf{A_p}, \mathbf{A_{p+v_1}}$ and $\mathbf{A_{p+v_2}}$.

Here we choose the following characteristic vectors of the honeycomb lattice

$$\mathbf{v}_1 = l\left(\frac{\sqrt{3}}{2}, \frac{1}{2}\right), \qquad \mathbf{v}_2 = l\left(\frac{\sqrt{3}}{2}, -\frac{1}{2}\right),$$
$$\mathbf{k}_1 = \frac{4\pi}{l\sqrt{3}}\left(\frac{1}{2}, \frac{\sqrt{3}}{2}\right), \qquad \mathbf{k}_2 = \frac{4\pi}{l\sqrt{3}}\left(\frac{1}{2}, -\frac{\sqrt{3}}{2}\right),$$

where l is the lattice constant.

If the wave intensity $|\psi(z, \mathbf{r})|$ is infinitesimal, the nonlinear term can be omitted and we get a linear Schrödinger equation with a periodic potential. Certain key

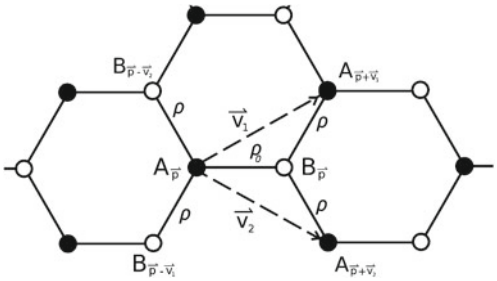

Fig. 1 A honeycomb lattice is composed of two triangular sublattices, $\Gamma_{\mathbf{A}}$ (*dots*) and $\Gamma_{\mathbf{B}}$ (*circles*), generated by $\mathbf{v}_1$ and $\mathbf{v}_2$ from different starting points. ρ and ρ_0 are coefficients associated with the dispersion structure of the linear lattice; they are usually termed nearest neighbor hopping energies; here we take $\rho_0 = 1$

solutions are obtained by considering $\psi(z, \mathbf{r}) = \varphi(\mathbf{r})e^{-i\mu z}$, where μ is constant. Then we obtain a linear eigenvalue problem

$$\left(-\nabla^2 + \delta V(\mathbf{r})\right)\varphi = \mu\varphi. \tag{2}$$

According to Bloch's theorem [43], the eigenfunction of the the eigenvalue problem (2), called the Bloch mode or the Bloch wave, has the $\mathbf{k}$-dependent form

$$\varphi(\mathbf{r}; \mathbf{k}) = e^{i\mathbf{k}\cdot\mathbf{r}}u(\mathbf{r}; \mathbf{k}) \tag{3}$$

where $u(\mathbf{r}; \mathbf{k})$ has the same periodicity as the potential $V(\mathbf{r})$ for any $\mathbf{k}$, i.e., $u(\mathbf{r} + \mathbf{v}; \mathbf{k}) = u(\mathbf{r}; \mathbf{k})$ for $\mathbf{v} \in \Gamma$. The eigenvalue $\mu = \mu(\mathbf{k})$ is referred to the dispersion relation.

Since the Bloch mode φ is usually not periodic in $\mathbf{r}$, it is more convenient to study $u(\mathbf{r}; \mathbf{k})$ (instead of $\varphi(\mathbf{r}; \mathbf{k})$) where $u(\mathbf{r}; \mathbf{k}) \in L^2_{per}(\Omega)$. The following eigenvalue problem arises

$$\mathcal{H}_{\mathbf{k}}u^{(n)}(\mathbf{r}; \mathbf{k}) = \mu^{(n)}(\mathbf{k})u^{(n)}(\mathbf{r}; \mathbf{k}), n \geq 1 \tag{4}$$

where the operator $\mathcal{H}_{\mathbf{k}}$ is defined as

$$\mathcal{H}_{\mathbf{k}} = -\nabla^2 - 2i\mathbf{k}\cdot\nabla + |\mathbf{k}|^2 + \delta V(\mathbf{r}). \tag{5}$$

The spectrum of the operator $\mathcal{H}_{\mathbf{k}}$ is discrete [43], i.e.,

$$\sigma(\mathcal{H}_{\mathbf{k}}) = \bigcup_{n\geq 1} \mu^{(n)}(\mathbf{k}),$$

and they can be ordered as

$$\mu^{(1)}(\mathbf{k}) \leq \mu^{(2)}(\mathbf{k}) \leq \mu^{(3)}(\mathbf{k}) \leq \cdots.$$

$\mu^{(n)}(\mathbf{k})$ is continuous as a function of $\mathbf{k}$ and due to the gauge invariance $\mu^{(n)}(\mathbf{k})$ is periodic. As $\mathbf{k}$ varies in the Brillouin zone Ω', $\mu^{(n)}(\mathbf{k})$ sweep out a closed interval

which is called the nth, $n = 1, 2, 3...$ band of the dispersion relation. In the literature, a dispersion band is often referred as the entire continuous region which supports bounded Bloch modes, i.e., the whole interval between two adjacent regions where bounded Bloch modes are not allowed. In this context, a dispersion band can have multiple branches. Generally, the lowest band in the tight-binding limit is usually simple and well-separated from higher bands. However, due to the underlying symmetries honeycomb lattices may have degenerate ground states.

If the eigenvalue problem (2) can be solved completely, i.e., the dispersion relation $\mu(\mathbf{k})$ and associated Bloch waves can be constructed, the general linear problem can then be solved by a Bloch decomposition; this is due to the completeness of the Bloch waves in $L^2(\mathbb{R}^2)$; furthermore each Bloch mode propagates independently. However, it is usually not possible to construct the dispersion relation and associated Bloch waves analytically. Hence numerical and asymptotic approximations are usually used. There are various numerical schemes that can be used to solve this eigenvalue problem; e.g., finite differences and spectral methods are often utilized [44]. On the other hand, asymptotic approximations require some asymptotic limits. Two typical limits are $\delta \ll 1$ and $\delta \gg 1$ where the former case is sometimes referred as the low contrast limit (or shallow potential) and the latter case high contrast limit, or more often, tight-binding limit. If $\delta \ll 1$, direct perturbation theory of the eigenvalue problem can be carried out and $u(\mathbf{r}; \mathbf{k})$ can be obtained. The dispersion relation is obtained via solvability conditions; see [13] for example. If $\delta \gg 1$, an orbital approximation can be employed. In this case, the Bloch waves are localized around the wells and can be approximated by appropriate superposition of the orbitals. From the orbital approximation one can find the dispersion relation.

4 Nonlinear Discrete Dynamics

In the tight-binding limit ($\delta \gg 1$), the Bloch waves are localized around the sites and their main properties are determined from the potential in the vicinities of the wells. We introduce two single-well potentials $W_A(\mathbf{r})$ and $W_B(\mathbf{r})$ which approach $\max\{V(\mathbf{r}) : \mathbf{r} \in \Omega\}$ rapidly as $|\mathbf{r}| \to \infty$ and coincide with $V(\mathbf{r})$ in the vicinities of $\mathbf{A}$ and $\mathbf{B}$ respectively.

The orbitals ϕ_A and ϕ_B are defined as the eigenfunctions of the one-well potentials; namely,

$$\left(-\nabla^2 + \delta W_j(\mathbf{r})\right)\phi_j(\mathbf{r}) = E_j\phi_j(\mathbf{r}) \quad j = A, B \tag{6}$$

where E_j are the orbital energies. For simplicity, we let $W_A(\mathbf{r}) = W_B(\mathbf{r} - \mathbf{d})$ where $\mathbf{d}$ is the shift vector from $\mathbf{A}$ site to the $\mathbf{B}$ site in the same cell, then $E_A = E_B = E$. It is noted that the eigenvalue problem can have multiple discrete eigenvalues. We are only interested in the ground (or lowest) state which in turn gives the lowest band of the dispersion relation and determines the associated dynamics of the

honeycomb lattice. For these single-well potentials $W_A(\mathbf{r})$, the ground state is simple and the orbital energy E is well-separated from the excited energies on the order of $O(\sqrt{\delta})$ (cf. [45] and references therein).

Then the Bloch waves associated with the lowest band can be approximated by

$$\varphi(\mathbf{r};\mathbf{k}) = \sum_{\mathbf{v}} (\alpha(\mathbf{k})\phi_A(\mathbf{r}-\mathbf{v}) + \beta(\mathbf{k})\phi_B(\mathbf{r}-\mathbf{v}))e^{i\mathbf{k}\cdot\mathbf{v}}, \tag{7}$$

where $\alpha(\mathbf{k})$ and $\beta(\mathbf{k})$ are determined later by the original eigenvalue problem (2).

Substituting the above expression into eigenvalue problem (2) leads to a matrix eigenvalue problem where $(\alpha(\mathbf{k}), \beta(\mathbf{k}))$ is the eigenvector. The orbital approximation converts the eigenvalue problem of a differential operator to an eigenvalue problem of a 2×2 matrix. Since the discrete envelope equation, which will be obtained later in this section, inherits the dispersion relation of the eigenvalue problem (4) in the tight-binding limit, the direct derivation of the dispersion relation is omitted here. We explain later how to get the discrete dispersion relation in the following section where the full dispersion relation is given—see Eqs. (17)–(18a, b). Additional details can be found in [15].

The aim of this section is to understand the key equations which govern the dynamics of the wave packets associated with the lowest band. It turns out that the dispersion relation are exactly related to the linear part of the governing equation of the wave packets. The set $\{(\phi_A(\mathbf{r}-\mathbf{v}), \phi_B(\mathbf{r}-\mathbf{v}))\}_{\mathbf{v}\in\Gamma}$ can approximate the wave packets associated with the lowest band in the sense that

$$\psi(\mathbf{r}) = \sum_{\mathbf{v}} (A_{\mathbf{v}}\phi_A(\mathbf{r}-\mathbf{v}) + B_{\mathbf{v}}\phi_B(\mathbf{r}-\mathbf{v})). \tag{8}$$

In other words, $\{(A_{\mathbf{v}}, B_{\mathbf{v}})\}_{\mathbf{v}\in\Gamma} \in l^2(\Gamma)$ is a natural representation of the continuous $L^2(\mathbb{R}^2)$ envelope associated with the lowest band and $\{(\phi_A(\mathbf{r}-\mathbf{v}), \phi_B(\mathbf{r}-\mathbf{v}))\}_{\mathbf{v}\in\Gamma}$ plays the role of a basis. This decomposition is sometimes referred as coupled mode theory [11].

The above decomposition (8) is similar to a Wannier decomposition (see for example [46]). But orbitals and Wannier functions are not the same. Wannier functions are the Fourier coefficients of the Bloch modes $\varphi(\mathbf{r};\mathbf{k})$ which are periodic functions in $\mathbf{k}$. Hence they are only defined in periodic lattices. On the other hand in the tight-binding limit orbitals are natural approximations to eigenfunctions associated with complicated potentials and this is not necessarily limited to periodic potentials. The definition of the orbital is straightforward and leads to physical insight and intuition. In simple lattices, orbitals can be used as the approximations to the Wannier functions; but in many cases Wannier functions can be employed directly. However, in non-simple lattices, Wannier functions are difficult to construct and their interactions are complicated.

Substituting the above wave packet approximation (8) into the lattice NLS Eq. (1) implies

$$\sum_{\mathbf{v}}\left(i\frac{dA_{\mathbf{v}}}{dz}+A_{\mathbf{v}}\delta(V(\mathbf{r})-W_A(\mathbf{r}-\mathbf{v}))\right)\phi_A(\mathbf{r}-\mathbf{v})$$
$$+\sum_{\mathbf{v}}\left(i\frac{dB_{\mathbf{v}}}{dZ}+B_{\mathbf{v}}\delta(V(\mathbf{r})-W_B(\mathbf{r}-\mathbf{v})\right)\phi_B(\mathbf{r}-\mathbf{v})$$
$$+\sigma\left(\sum_{\mathbf{v}}(A_{\mathbf{v}}\phi_A(\mathbf{r}-\mathbf{v})+B_{\mathbf{v}}\phi_A(\mathbf{r}-\mathbf{v}))\right)^2$$
$$\times\left(\sum_{\mathbf{v}}(A_{\mathbf{v}}\phi_A(\mathbf{r}-\mathbf{v})+B_{\mathbf{v}}\phi_B(\mathbf{r}-\mathbf{v}))\right)^*=0. \tag{9}$$

Multiplying both sides by $\phi_A(\mathbf{r}-\mathbf{p})$ and $\phi_B(\mathbf{r}-\mathbf{p})$ respectively and integrating lead to (only nearest neighbor interaction terms are kept)

$$i\frac{dA_{\mathbf{p}}}{dz}+c_0A_{\mathbf{p}}+(\tau\mathcal{L}^-)B_{\mathbf{p}}+\sigma g|A_{\mathbf{p}}|^2A_{\mathbf{p}}=0,$$
$$i\frac{dB_{\mathbf{p}}}{dz}+c_0B_{\mathbf{p}}+(\tau\mathcal{L}^+)A_{\mathbf{p}}+\sigma g|B_{\mathbf{p}}|^2B_{\mathbf{p}}=0,$$

where $c_0=\int\phi_A(\mathbf{r})\delta(V(\mathbf{r})-W_A(\mathbf{r}))\phi_A d\mathbf{r}$, $\tau=\int\phi_A(\mathbf{r})\delta(V(\mathbf{r})-W_A(\mathbf{r}-\mathbf{v}))\phi_A(\mathbf{r})d\mathbf{r}$, $g=\int\phi_A^4 d\mathbf{r}$,

$$\mathcal{L}^-B_{\mathbf{p}}=B_{\mathbf{p}}+\rho_1B_{\mathbf{p}-\mathbf{v}_1}+\rho_2B_{\mathbf{p}-\mathbf{v}_2}, \tag{10}$$

$$\mathcal{L}^+A_{\mathbf{p}}=A_{\mathbf{p}}+\rho_1A_{\mathbf{p}+\mathbf{v}_1}+\rho_2A_{\mathbf{p}+\mathbf{v}_2}, \tag{11}$$

and $\rho_j=\frac{1}{\tau}\int\phi_A(\mathbf{r})\delta(V(\mathbf{r})-W_A(\mathbf{r}))\phi_A(\mathbf{r}-\mathbf{v}_j)d\mathbf{r}$, $j=1,2$. Here c_0 represents the correction to the orbital energy due to the difference between the orbital potentials and the lattice potentials, τ is the magnitude of the nearest neighbor hopping energy while ρ_1 and ρ_2 represent the inequality of the three nearest neighbor hopping energies. This inequality measures the deformation of the honeycomb lattice. If $\rho_1=\rho_2=1$, the honeycomb lattice is undeformed. The deformation is induced by the inequality of distances of any given site to its three nearest neighbors. It can also be induced by other reasons, for example, local doping to change the depth of wells and so on. For simplicity, we take $\rho_1=\rho_2$. More detailed calculations of these parameters can be found in [15].

Rewriting the discrete system, we have the following rescaled couple-mode equation

$$i\frac{dA_{\mathbf{p}}}{dz}+\mathcal{L}^-B_{\mathbf{p}}+\sigma|A_{\mathbf{p}}|^2A_{\mathbf{p}}=0, \tag{12}$$

$$i\frac{dB_{\mathbf{p}}}{dz}+\mathcal{L}^+A_{\mathbf{p}}+\sigma|B_{\mathbf{p}}|^2B_{\mathbf{p}}=0. \tag{13}$$

It governs the evolution of Bloch waves associated with the lowest band. This coupled mode equation is different from the 2-D discrete NLS equation associated with simple lattices. A significant difference is that this couple mode equation contains two equations which come from the non-equivalence of **A** and **B** sites. This coupled mode equation governs the dynamics of the wave packets associated with the whole lowest band.

If an envelope is associated with a specific wave number **k**, then it can be conveniently represented by

$$\psi(\mathbf{r}) \approx \sum_{\mathbf{p}\in\Gamma} \big(a_{\mathbf{p}}\phi_A(\mathbf{r}-\mathbf{p}) + b_{\mathbf{p}}\phi_B(\mathbf{r}-\mathbf{p})\big)e^{i\mathbf{k}\cdot\mathbf{p}}.$$

A single-mode equation is then obtained. For completeness we also give the equations of the discrete envelope in terms of the variables $\{(a_{\mathbf{p}}(z), b_{\mathbf{p}}(z))\}_{\mathbf{p}\in\Gamma}$ (see [15])

$$i\frac{da_{\mathbf{p}}}{dz} + \mathcal{L}_{\mathbf{k}}^{-} b_{\mathbf{p}} + \sigma|a_{\mathbf{p}}|^2 a_{\mathbf{p}} = 0, \tag{14a}$$

$$i\frac{db_{\mathbf{p}}}{dz} + \mathcal{L}_{\mathbf{k}}^{+} a_{\mathbf{p}} + \sigma|b_{\mathbf{p}}|^2 b_{\mathbf{p}} = 0, \tag{14b}$$

where

$$\mathcal{L}_{\mathbf{k}}^{-} b_{\mathbf{p}} = b_{\mathbf{p}} + \rho b_{\mathbf{p}-\mathbf{v}_1} e^{-i\mathbf{k}\cdot\mathbf{v}_1} + \rho b_{\mathbf{p}-\mathbf{v}_2} e^{-i\mathbf{k}\cdot\mathbf{v}_2},$$
$$\mathcal{L}_{\mathbf{k}}^{+} a_{\mathbf{p}} = a_{\mathbf{p}} + \rho a_{\mathbf{p}+\mathbf{v}_1} e^{i\mathbf{k}\cdot\mathbf{v}_1} + \rho a_{\mathbf{p}+\mathbf{v}_2} e^{i\mathbf{k}\cdot\mathbf{v}_2}.$$

It is noted that the single-mode Eq. (14a, b) can be obtained from Eq. (12) by changing $(A_{\mathbf{p}}, B_{\mathbf{p}})$ to $(a_{\mathbf{p}}e^{i\mathbf{k}\cdot\mathbf{p}}, b_{\mathbf{p}}e^{i\mathbf{k}\cdot\mathbf{p}})$. This is due to the linear properties of the coupled mode equation which will be discussed in the next section. It should also be noted that the above discrete approach can be extended beyond the tight binding limit. If the potential intensity δ is not sufficiently large, the nearest neighbor interaction approximation may not be adequate. In such cases additional sites should be included in order to get more accurate approximations. A rigorous discussion for the validity of the orbital approximation can be found in [45].

5 Linear Properties

Neglecting the nonlinear terms in (12), the linear equation can be solved by using a discrete Fourier transform, i.e.,

$$\hat{A}(\mathbf{k}; z) = \sum_{\mathbf{v}\in\Gamma} A_{\mathbf{v}} e^{-i\mathbf{k}\cdot\mathbf{v}}, \quad A_{\mathbf{v}} = \frac{1}{|\Omega'|}\int_{\Omega'} \hat{A}(\mathbf{k}) e^{i\mathbf{k}\cdot\mathbf{v}} d\mathbf{k},$$

where $|\Omega'|$ is the area of Ω'.

Similar to what is indicated above, substituting the Fourier mode $\{(\hat{A}(\mathbf{k}), \hat{B}(\mathbf{k}))e^{-i\omega z+i\mathbf{k}\cdot\mathbf{v}}\}_{\mathbf{v}\in\Gamma}$ into the linear discrete evolution problem associated with Eq. (12) leads to

$$\begin{pmatrix} \omega & \gamma(\mathbf{k}) \\ \gamma^*(\mathbf{k}) & \omega \end{pmatrix} \begin{pmatrix} \hat{A}(\mathbf{k}) \\ \hat{B}(\mathbf{k}) \end{pmatrix} = \begin{pmatrix} 0 \\ 0 \end{pmatrix}, \tag{15}$$

where $\gamma(\mathbf{k}) = 1 + \rho e^{-i\mathbf{k}\cdot\mathbf{v}_1} + \rho e^{-i\mathbf{k}\cdot\mathbf{v}_2}$. Unlike the continuous Fourier transform, in the discrete Fourier transform $\mathbf{k}$ only takes values in Ω' as opposed to all of $\mathbb{R}^2$. Existence of nontrivial solutions leads to the dispersion relation $\omega(\mathbf{k})$ which is only defined in the Brillouin zone Ω'; In other words, the dispersion relation $\omega(\mathbf{k})$ is continuous and periodic with two periods $\mathbf{k}_1$ and $\mathbf{k}_2$ in $\mathbb{R}^2$. This dispersion relation $\omega(\mathbf{k})$ approximates the original dispersion relation $\mu(\mathbf{k})$ apart from scalings; namely,

$$\mu(\mathbf{k}) = E + c_0 + \tau\omega(\mathbf{k}) \tag{16}$$

where we recall that E is the orbital energy which is mainly determined by the potential in the vicinity of a site; c_0 is the correction to the orbital energy which is from the difference between the lattice potential and the approximating orbital potential; as indicated above τ is the magnitude of the nearest neighbor hopping energy which represents the strength of the interactions between sites; $\omega(\mathbf{k})$ is the effective dispersion relation. The corresponding Bloch modes can then be constructed from Eq. (7) where $(\alpha(\mathbf{k}), \beta(\mathbf{k}))$ are the eigenvectors of (15). Hence the coupled mode equation inherits the dispersion relation of the original lattice NLS equation. In our case, existence of nontrivial solutions to (15) leads

$$\omega_\pm(\mathbf{k}) = \pm\left|1 + \rho e^{-i\mathbf{k}\cdot\mathbf{v}_1} + \rho e^{-i\mathbf{k}\cdot\mathbf{v}_2}\right|. \tag{17}$$

We see that the dispersion relation has two branches: $\omega_+(\mathbf{k}) = -\omega_-(\mathbf{k})$. The two branches may or may not intersect with each other depending on the value of ρ. Let $\mathbf{K}_* = \mathbf{K}_*(\rho) \in \Omega'$ denote the special point(s) in the Brillouin zone such that $\omega_+(\mathbf{K}_*) = \min_{\mathbf{k}\in\Omega'}\omega_+(\mathbf{k})$, and, $\omega_-(\mathbf{K}_*) = \max_{\mathbf{k}\in\Omega'}\omega_-(\mathbf{k})$. The values, $(\mathbf{K}_*, \omega_\pm(\mathbf{K}_*))$ are the closest values of the two branches if there is a gap between them. If the two branches intersect, $\omega_+(\mathbf{K}_*) = \omega_-(\mathbf{K}_*) = 0$ and $(\mathbf{K}_*, \omega_\pm(\mathbf{K}_*))$ are the intersection points.

Calling $\beta = 2\rho - 1$, a direct calculation shows that

1. If $\beta > 0$, the two branches touch each other at two different points which are referred as the Dirac points. Namely, $\mathbf{K}_*$ has two values in entire the Brillouin zone Ω': $\mathbf{K}_* = \pm\mathbf{K} = \pm\frac{2}{l}\left(0, \pi - \arccos(\frac{1}{2\rho})\right)$. Near the $\mathbf{K}$ point, the dispersion relation has the leading expansion $\omega_\pm(\mathbf{K}+\mathbf{q}) \sim \pm\sqrt{q_1^2 + (\beta^2+2\beta)q_2^2}$ where $\mathbf{q} = (q_1, q_2)$ and $|\mathbf{q}| \ll 1$ which forms a local elliptic cone.

2. If $\beta = 0$, the two branches touch each other at one point. In this critical case, the two Dirac points actually merge into one due to the underlying periodicity of $\mathbf{k} \in \mathbb{R}^2$. Namely, $\mathbf{K} \to \frac{2}{l}(0, \pi) = \frac{1}{2}(\mathbf{k}_1 - \mathbf{k}_2)$ as $\rho \to \frac{1}{2}$, and both $\frac{1}{2}(\mathbf{k}_1 - \mathbf{k}_2)$ and $-\frac{1}{2}(\mathbf{k}_1 - \mathbf{k}_2)$ are equivalent to $\frac{1}{2}(-\mathbf{k}_1 - \mathbf{k}_2) \in \Omega'$ due to the periodicity. Near the intersection point $\mathbf{K}_*$, the dispersion relation has the leading expansion $\omega_\pm(\mathbf{K}_* + \mathbf{q}) \sim \pm |q_1|$ where $\mathbf{q} = (q_1, q_2)$ and $|\mathbf{q}| \ll 1$ which is the degeneration of the above ellipse to local crossing of planes.
3. If $\beta < 0$, the two branches separate from each other and there exists a gap between the two branches. The only closest point is $\mathbf{K}_* = \frac{1}{2}(-\mathbf{k}_1 - \mathbf{k}_2) = (\frac{4\pi}{l\sqrt{3}}, 0)$. Near $\mathbf{K}_*$ points, the dispersion relation has the leading expansion $\omega_\pm(\mathbf{K}_* + \mathbf{q}) \sim \pm \sqrt{\beta^2 + (1+\beta)^2 q_1^2}$ where $\mathbf{q} = (q_1, q_2)$ and $|\mathbf{q}| \ll 1$ which has the structure of a hyperboloid. The gap width is $2|\beta|$.

6 Conical Dirac Dynamics

In many applications, the dynamics of an envelope associated with a specific value of $\mathbf{k}$ is of interest. Then the Eq. (14a, b) are more convenient to use. From these equations we can derive a continuous system which is more convenient to study instead of the differential-difference equation.

The discrete envelope can be considered as the continuous envelope evaluated at the lattice points, i.e., $a_{\mathbf{p}}(z) = a(\mathbf{r} = \mathbf{p}, z)$ and $b_{\mathbf{p}}(z) = b(\mathbf{r} = \mathbf{p}, z)$; here the continuous transverse variable associated with the lattice is $\mathbf{r} = (r_1, r_2)$. In this application the envelopes are assumed to depend only on the long-wave variables and the amplitudes are assumed small. Accordingly, we define, $(a(\mathbf{r}, z), b(\mathbf{r}, z)) = \sqrt{v}(\tilde{a}(\mathbf{x}, \tilde{z}), \tilde{b}(\mathbf{x}, \tilde{z}))$ where the transverse variable is given by $\mathbf{x} = (x_1, x_2) = \mathbf{r}/L$, the propagation variable is $\tilde{z} = vz$, $v = \frac{\sqrt{3}\, l}{2L} \ll 1$, where the lattice size is l and the envelope scale L is much greater than l, i.e., $\frac{l}{L} \ll 1$. For simplicity, we drop the tildes on the top of a, b and z.

Here we are interested in the effective dynamics associated with the special point(s) $\mathbf{K}_*$. It turns out that if the initial envelope is associated with a value $\mathbf{k}$ which is far away from $\mathbf{K}_*$, then the continuous dynamics reduces to an effective nonlinear Schrödinger equation in a moving frame [15]. One can find effective NLS equations associated for simple bands; the lowest bands of most simple lattices also yield effective NLS equations. At $\mathbf{K}_*$, as β changes from positive to negative values, both the geometric structure of the dispersion relation and the associated effective wave dynamics change dramatically. We investigate some of the important cases next.

We first consider the case $\beta > 0$. As indicated above, the two branches touch each other at the Dirac points: $\mathbf{K}$ and $-\mathbf{K}$. Here we only consider the effective

dynamics associated with $\mathbf{K}$; the analysis for $-\mathbf{K}$ is similar. At $\mathbf{k} = \mathbf{K}$, $\omega_\pm = 0$ and by direct calculation we have

$$\rho e^{-i\mathbf{K}\cdot\mathbf{v}_1} + \rho e^{-i\mathbf{K}\cdot\mathbf{v}_2} = -1, \qquad \rho e^{-i\mathbf{K}\cdot\mathbf{v}_1} - \rho e^{-i\mathbf{K}\cdot\mathbf{v}_2} = -i\sqrt{4\rho^2 - 1}.$$

Calling $\zeta = \sqrt{4\rho^2 - 1} = \sqrt{\beta^2 + 2\beta}$ and using Taylor expansion, and evaluating at $\mathbf{k} = \mathbf{K}$, we have

$$\mathcal{L}_{\mathbf{K}}^{-} b_{\mathbf{p}} \sim v^{3/2}\left[(\partial_{x_1} + i\frac{\zeta}{\sqrt{3}}\partial_{x_2}) - \frac{v}{2}\left(\partial_{x_1}^2 + \frac{1}{3}\partial_{x_2}^2 + 2i\frac{\zeta}{\sqrt{3}}\partial_{x_1}\partial_{x_2}\right) + \frac{v^2}{6}\left(\partial_{x_1}^3 + \frac{1}{3\sqrt{3}}\partial_{x_2}^3 + \partial_{x_1}\partial_{x_2}^2 + \sqrt{3}i\zeta\partial_{x_1}^2\partial_{x_2}\right)\right] b + \cdots$$

and

$$\mathcal{L}_{\mathbf{K}}^{+} a_{\mathbf{p}} \sim v^{3/2}\left[(-\partial_{x_1} + i\frac{\zeta}{\sqrt{3}}\partial_{x_2}) - \frac{v}{2}\left(\partial_{x_1}^2 + \frac{1}{3}\partial_{x_2}^2 - 2i\frac{\zeta}{\sqrt{3}}\partial_{x_1}\partial_{x_2}\right) - \frac{v^2}{6}\left(\partial_{x_1}^3 + \frac{1}{3\sqrt{3}}\partial_{x_2}^3 + \partial_{x_1}\partial_{x_2}^2 - \sqrt{3}i\zeta\partial_{x_1}^2\partial_{x_2}\right)\right] a + \cdots$$

If $\beta = O(1)$, i.e., $\zeta = O(1)$, then only taking the leading order term, we immediately obtain the so-called nonlinear Dirac equation

$$i\partial_z a + \left(\partial_{x_1} + i\frac{\zeta}{\sqrt{3}}\partial_{x_2}\right) b + \sigma|a|^2 a = 0; \tag{18a}$$

$$i\partial_z b + \left(-\partial_{x_1} + i\frac{\zeta}{\sqrt{3}}\partial_{x_2}\right) a + \sigma|b|^2 b = 0. \tag{18b}$$

The above nonlinear Dirac equation describes the evolution of the wave packet in the vicinity of the Dirac points. It is seen that the linear dispersion relation of Eq. (18a, b) reveals the leading order expansion of the effective dispersion relation which is a double cone. Namely, $\omega_\pm(\mathbf{q}) = \pm\sqrt{q_1^2 + \frac{\zeta^2}{3}q_2^2}$. A typical phenomenon associated with this equation is the conical diffraction. It says a localized input evolves into expending rings and a cone forms in the direction of propagation in the crystal. Typical conical diffraction is illustrated in Fig. 2. The top panel shows the evolution of an initial Gaussian envelope at the Dirac point $\mathbf{K}$ and then at two different propagating distances. If the lattice is not deformed, i.e., $\rho = 1$, then $\zeta = \sqrt{4\rho^2 - 1} = \sqrt{3}$ and circular ring structures are obtained. Figure 2 shows a comparison between the circular conical diffraction in the NLS Eq. (1) and the approximate nonliner Dirac equation (18a, b). The initial condition for the NLS equation is a weak and wide Gaussion envelope multiplied by a Bloch wave associated with the Dirac point $\mathbf{K}$. The initial condition for the nonlinear Dirac equation (18a, b) is $a(z = 0) = e^{-x_1^2 - x_2^2}$ and $b(z = 0) = 0$.

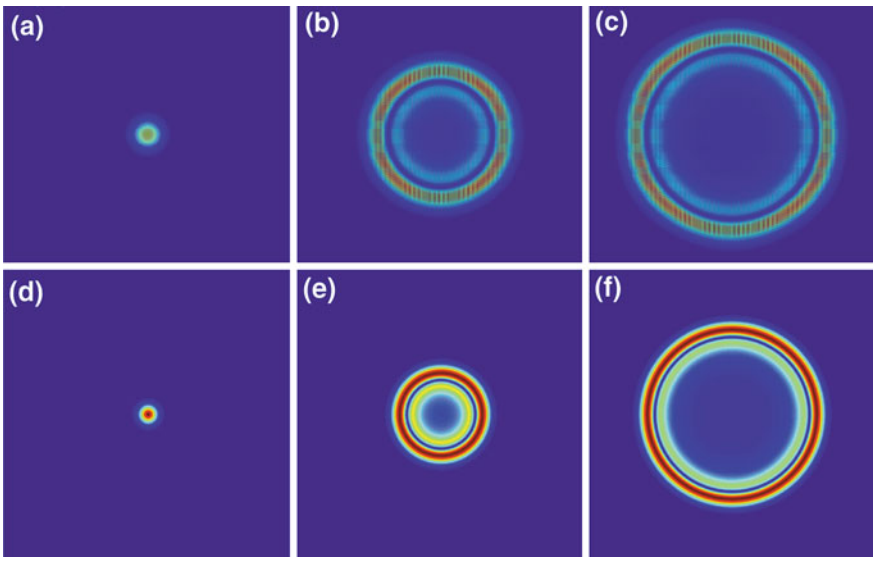

Fig. 2 Wave intensities initially a localized pulse (Gaussian) and subsequently at two successive propagating distances. *Top panel*: simulations of the lattice NLS equation (1). *Bottom panel*: simulations of the nonlinear Dirac equation (18a, b)

7 Symmetry Breaking and Nonlinear Transitions

Conical diffraction is a consequence of the behavior associated with a dispersion relation that has conical crossings. In principle it can be either linear and nonlinear; but as we will see with strong nonlinearity the conical behavior is modified. Next we analyze higher order dispersive effects and nonlinear transitions. It is found that the Dirac dynamics breaks down in the lattice NLS equation if the nonlinearity is strong [38]. As nonlinearity increases, the circular rings deform and become triangular. Figure 3 shows the evolution patterns for different nonlinear coefficients. It is noted that changing the value of σ is equivalent to changing the magnitude of the input.

Defining the operators $\mathcal{L}_0 = \begin{pmatrix} 0 & \partial_{x_1} + i\zeta\partial_{x_2} \\ -\partial_{x_1} + i\zeta\partial_{x_2} & 0 \end{pmatrix}$ and $\mathcal{L}_1 = \begin{pmatrix} 0 & \Delta_+ \\ \Delta_- & 0 \end{pmatrix}$, where $\Delta_\pm = \partial_{x_1}^2 + \frac{1}{3}\partial_{x_2}^2 \pm \frac{2}{\sqrt{3}} i\zeta\partial_{x_1}\partial_{x_2}$, we can write the higher order nonlinear Dirac equation in the following vector form

$$i\partial_z U + \mathcal{L}_0 U - \frac{v}{2}\mathcal{L}_1 U + N(U)U = 0 \tag{19}$$

where $U = (a, b)^T$ and the nonlinear operator is given by $N(U) = \begin{pmatrix} |a|^2 & 0 \\ 0 & |b|^2 \end{pmatrix}$.

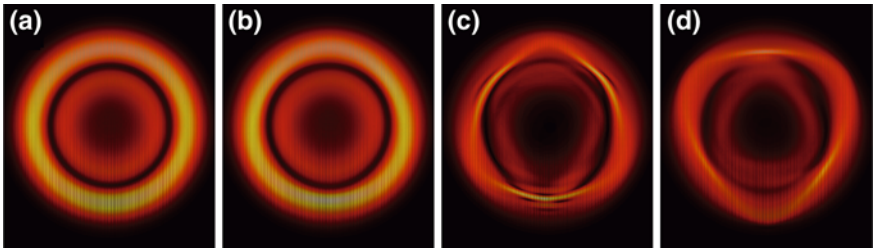

Fig. 3 Evolution patterns of the NLS equation (1) with nonlinear coefficient σ being: **a** 0; **b** 1; **c** 5; (**d**) −5. Here $v = 0.1$ and the evolution distance is $z = 50$ and $\delta = 100$ which is in the tight-binding regime

We first study the linear case. Define the Fourier transform $\mathcal{F}(F) = \hat{F} = \int F(\mathbf{x}) e^{-i\mathbf{q}\cdot\mathbf{r}} d\mathbf{x}$ and inverse Fourier transform $\mathcal{F}^{-1}(F) = \frac{1}{4\pi^2}\int F(\mathbf{q}) e^{i\mathbf{q}\cdot\mathbf{x}} d\mathbf{q}$. Note that $\mathbf{x} = (x_1, x_2)^T$ is the envelope coordinate, $\mathbf{q} = (q_1, q_2)^T$ is the wave number associated with the envelope, and from the above definitions the scales are different from $\mathbf{r}$ and $\mathbf{k}$ in the original lattice NLS Eq. (1).

Letting $\mathcal{L} = \mathcal{L}_0 - \frac{v}{2}\mathcal{L}_1$. Since $\mathcal{L}$ is a linear differential operator with constant coefficients, $\mathcal{F}(\mathcal{L}U) = \hat{\mathcal{L}}\hat{U}$ where $\hat{\mathcal{L}}$ is a 2×2 $\mathbf{k}$ $\mathbf{q}$-dependent matrix which has the form

$$\hat{\mathcal{L}} = \begin{pmatrix} 0 & iq_1 - q_2 \\ -iq_1 - q_2 & 0 \end{pmatrix} - \frac{1}{2}v \begin{pmatrix} 0 & -q_1^2 - \frac{1}{3}q_2^2 - \frac{2}{\sqrt{3}}i\zeta q_1 q_2 \\ -q_1^2 - \frac{1}{3}q_2^2 + \frac{2}{\sqrt{3}}i\zeta q_1 q_2 & 0 \end{pmatrix}.$$

We see that $\hat{\mathcal{L}}$ is a Hermitian matrix. In $\mathbf{q}$ space, the linear initial value problem becomes

$$i\hat{U}_z + \hat{\mathcal{L}}\hat{U} = 0, \hat{U}(z = 0) = \hat{U}_0.$$

Then we have

$$\hat{U}(z) = e^{i\hat{\mathcal{L}}z}\hat{U}_0.$$

$\hat{\mathcal{L}}$ has two eigenvalues $\omega_\pm(\mathbf{q}) = \pm q + O(v)$ which correspond to the two branches of the dispersion relation. The two branches intersect each other at the single point $\mathbf{q} = \mathbf{0}$. Note that at the degenerate point $\mathbf{q} = \mathbf{0}$, the multiplicity is two and for any $\mathbf{q}$ there are two linearly independent eigenvectors $\Phi_\pm$ which are normalized to be $\Phi_m^\dagger \Phi_n = \delta_{mn}$ where $m, n = +, -$. Hereafter, the superscript $\dagger$ means the complex conjugate with a transpose.

Then $\hat{\mathcal{L}} = (\Phi_+, \Phi_-)\Lambda(\Phi_+, \Phi_-)^\dagger$ where $\Lambda = \mathrm{diag}(\omega_1, \omega_2)$. Thus

$$\hat{U}(z) = (\Phi_+, \Phi_-)e^{i\Lambda z}(\Phi_+, \Phi_-)^\dagger \hat{U}_0$$

or rewriting

$$(\Phi_+, \Phi_-)^\dagger \hat{U}(z) = \mathrm{diag}(e^{i\omega_+ z}, e^{i\omega_- z})(\Phi_+, \Phi_-)^\dagger \hat{U}_0. \tag{20}$$

If we call $\hat{p}_\pm(z) = \Phi_\pm^\dagger \hat{U}(z)$, then $\hat{p}_\pm(z)$ represents the projection of $\hat{U}$ onto the $\pm$ branch in $\mathbf{q}$ space. From (20), we immediately obtain that

$$\hat{p}_\pm(z) = e^{i\omega_\pm z} p_\pm(z=0). \tag{21}$$

In addition we denote $\epsilon_\pm = \frac{1}{(2\pi)^2}\int |\hat{p}_\pm|^2 d\mathbf{k}$ which represents the energy associated with $\pm$ branch. From (21), we know that $\epsilon_\pm(z) = \epsilon_\pm(z=0)$. There is no energy exchange between two branches in the linear evolution.

Since (Φ_+, Φ_-) is unitary, the total energy of the system is given by

$$\begin{aligned}\epsilon(z) &= \int |U(\mathbf{r}, z)|^2 d\mathbf{r} = \frac{1}{(2\pi)^2}\int |\hat{U}(z)|^2 d\mathbf{k} = \frac{1}{(2\pi)^2}\int |(\Phi_+, \Phi_-)^\dagger \hat{U}|^2 d\mathbf{k} \\ &= \frac{1}{(2\pi)^2}\int |(\hat{p}_+, \hat{p}_-)^\dagger|^2 d\mathbf{k} = \epsilon_+(z) + \epsilon_-(z)\end{aligned}$$

where we have used Parseval's theorem.

The above analysis shows that: (i) the linear propagation can be decomposed into upper and lower components and each component evolves independently; (ii) the magnitudes of the projections of each branch remain the same under propagation—see Eq. (21).

We first focus on the combination of the higher order effects and nonlinearity without deformations. We take $\zeta = \sqrt{3}$ in the remainder of this section. The linear Dirac dynamics is essentially a 2-D wave equation after eliminating b and keeping a only or vice verse and it is a weakly dispersive system. Letting $q = |\mathbf{q}|$ and $\theta = \arctan(\frac{q_2}{q_1})$, then the dispersion relation has the form

$$\omega_\pm(q, \theta) = \pm q + O(v)$$

and the group velocities for $\mathbf{q} \neq \mathbf{0}$ are $\frac{\partial \omega_\pm}{\partial q} = \pm 1 + O(v)$, $\frac{\partial \omega_\pm}{\partial \theta} = 0 + O(v)$. Two eigenvectors have the form

$$\Phi_+ = \frac{1}{\sqrt{2}}\begin{pmatrix} e^{-i\frac{\theta}{2}} \\ ie^{i\frac{\theta}{2}} \end{pmatrix} + O(v), \quad \Phi_- = \frac{1}{\sqrt{2}}\begin{pmatrix} e^{-i\frac{\theta}{2}} \\ -ie^{i\frac{\theta}{2}} \end{pmatrix} + O(v).$$

Then to leading order, an initial localized input (e.g., a Gaussian spot) evolves into radially spreading rings. Along any specific angle θ, the field behaves like a traveling wave with unit velocity since the group velocity along θ direction is zero. The conical diffraction then ensues. Further, due to the preservation of the mass one expects that the intensity decays at the order of $O(\frac{1}{z})$. These conclusions can be deduced from long-time asymptotic methods.

Next we turn to the nonlinear and higher order dispersive effects. When higher order terms ($O(v)$ terms) are included, the dispersion relation is approximated by

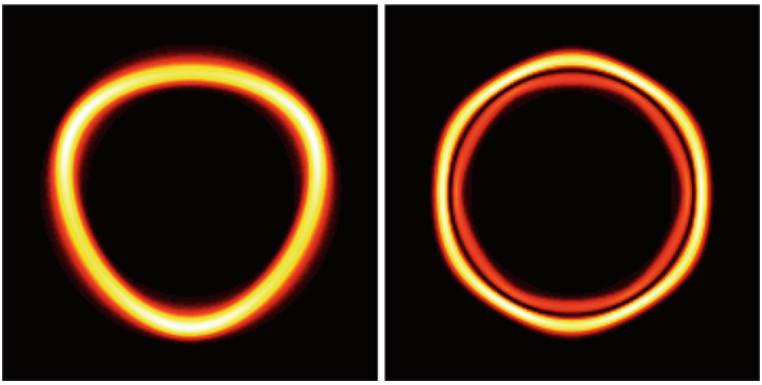

Fig. 4 Triangular and hexagonal patterns in the linear evolution of the HONLD Eq. (19). Here we take $v = 0.2$ to show higher order linear propagations

$$\omega_{\pm}(q,\theta) = \pm q(1 - \frac{v}{6} q \sin(3\theta)) + O(v^2) \tag{22}$$

we see that there is a three-fold symmetry. The dispersion $\omega_+(\mathbf{q})$ has three steepest descent directions and $\omega_-(\mathbf{q})$ has three orthogonal steepest descent directions. Each admits the so-called 'triangular warping'. If the initial condition is specified completely in one branch, the linear wave remains in that branch since there is no branch transition in the linear problem. In such a case a triangular pattern results. If initial condition is evenly distributed into the two branches, the patten is the superposition of two triangular patterns which evolves into a hexagonal shape. Figure 4 triangular and hexagonal patterns due to different initial conditions where $a(z=0) = e^{-x_1^2 - x_2^2}$ is a unit Gaussian and the choice of $b(z=0)$ for the left triangular figure is such that $\hat{p}_-(z=0) = 0$ and for the right hexagonal figure is $b(z=0) = 0$ which ensures $\hat{p}_-(z=0) = \hat{p}_+(z=0)$; i.e we take equal strength in both components. Here we choose $v = 0.2$ which corresponds to the strength of the higher order effects.

Nonlinearity brings two major effects. The first one is to couple the upper and lower branches together and the second one is to broaden $\hat{p}_{\pm}(z)$ in $\mathbf{q}$ space under propagation. Next we give some brief discussion on this matter. We first describe some numerical results for the HONLD equation. In the numerical simulations here, the initial input is always taken to be $a(x,y,0) = e^{-x^2-y^2}, b(x,y) = 0$ which ensures the two branches are initially evenly distributed. Figure 5 shows the evolution of such an input in the HONLD Eq. (19) for different σ. It is seen that a conical diffraction pattern changes into a triangular-like pattern as nonlinearity increases. This is consistent with Fig. 3. These results show that when the nonlinearity is significant the HONLD equation is needed in order to describe the envelope dynamics.

HONLD Eq. (19) is the single-mode equation which asymptotically describes the dynamics of the envelope associated with the Dirac point. Since the

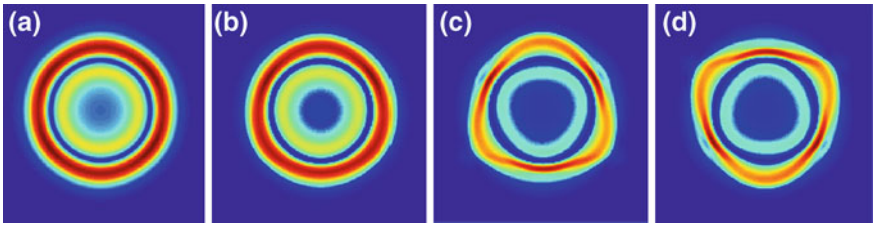

Fig. 5 Evolution patterns in the HONLD equation (19) with σ equal **a** 0; **b** 1; **c** 5, **d** -5. Here $v = 0.1$ and the evolution distance is $z = 5$

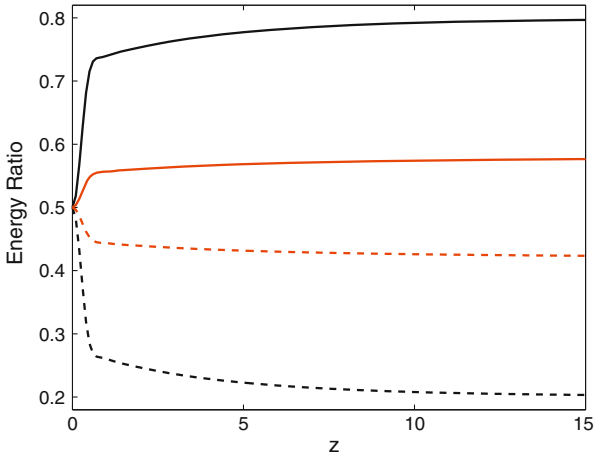

Fig. 6 The percentages of the energy in the two branches. The *black curves* are for $\sigma = 5$ and *red curves* for $\sigma = 1$; *dashed lines* for the lower branch and *solid lines* for the upper branch

nonlinearity is found to couple the two branches we plot the energy ratios of the two branches—see Fig. 6. It is seen that one branch is enhanced and the other is weakened. It is also seen that modifications to the energy ratios occur rapidly at the beginning and gradually saturates so that the percentages of the two branches tend to constant values. We reiterate that this occurs when the initial branches are taken to have the same energies.

Meanwhile, the projections $\hat{p_{\pm}}(z)$ also change under propagation. Figure 7 displays the changes of the projection $\hat{p}_+$ under propagation. It is seen that the energy spreads in $\mathbf{q}$ space. Since triangular warping increases as $|\mathbf{q}|$ increases, triangular diffraction become more noticeable. In order words, triangular warping breaks the radial symmetry of the circularly conical dispersion relation. This symmetry breaking is amplified when the nonlinearity is included.

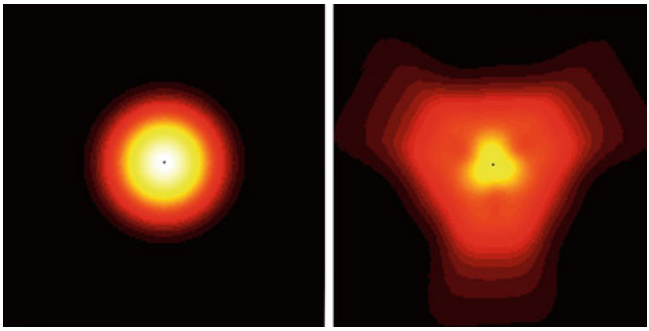

Fig. 7 The magnitude of the projection $\hat{p}_+(z)$ in the nonlinear evolution at $z = 0$ (*left*) and $z = 5$ (*right*). Here $\sigma = 5$

8 Effective Dynamics for Deformation Lattices

In applications, the honeycomb lattices are often not perfect. Deformations occur for many reasons such as local doping and uniform strains to the lattice. In such cases $\zeta \neq \sqrt{3}$ and $\beta \neq 1$. If the lattice is deformed slightly the diffraction is modified so that the circular rings now become elliptical in structure. Figure 8 shows such a deformation with elliptical conical diffraction. It is also noted that the energy is centralized to the x_1 direction of the ellipse. This is traced to the fact that $\frac{\partial \omega}{\partial \theta} \neq 0$ when $\zeta \neq \sqrt{3}$. Two steepest descent directions are $\theta = 0, \pi$. So the field is attracted to the horizontal axis.

However, in some cases, the deformation can be large enough so that the deformation parameter β becomes small enough to become comparable to the long wave parameter v. Then the dynamics changes considerably. When $|\beta| \ll 1$, the leading order equations is nearly a one-dimensional wave equation. In this case, instead of splitting to expanding rings, the localized input separates into two traveling waves.

Figure 9 displays such straight line diffraction patterns which are the simulations of the continuous equations of the coupled mode Eq. (14a, b) in two cases. The initial conditions are $a(z = 0) = x_1 e^{-x_1^2 - x_2^2}, b(z = 0) = 0$. This initial input ensures the regularity of the nonlocal equations we will derive later [47]. We see that the evolutions are degenerated into nearly straight line diffraction with some additional parabolic structures.

This section is devoted to understanding the effective dynamics along the moving frames. There are two small parameters noting: β and v. If they are comparable, various interesting maximally balanced equations and associated phenomena arise. We only illustrate a special balance $|\beta| = O(v^2)$ which has two subcases: $\beta > 0$ when the two branches still touch each other and $\beta < 0$ when a gap just opens.

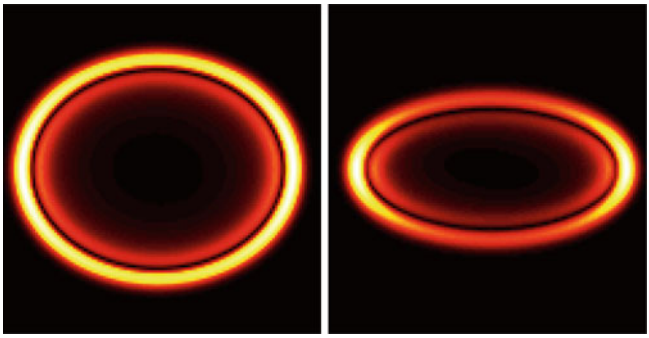

Fig. 8 Elliptical diffractions of the nonlinear Dirac equation (18a, b). *Left*: $\zeta = \frac{4\sqrt{3}}{5}$. *Right*: $\zeta = \frac{\sqrt{3}}{2}$

8.1 Before Separation

For simplicity, we introduce the variables $x = x_1, y = \frac{x_2}{\sqrt{3}}$. We then convert continuous system to a second order system which are linearly decoupled. Keeping terms up to $O(v^2)$ leads to

$$\partial_z^2 a - \partial_x^2 a + v^2 \mathcal{T}_{x,y} a + \sigma\Big[-i\partial_z(|a|^2 a) + \partial_x(|b|^2 b)\Big] = 0 \tag{23a}$$

$$\partial_z^2 b - \partial_x^2 b + v^2 \mathcal{T}_{x,y} b + \sigma\Big[-i\partial_z(|b|^2 b) - \partial_x(|a|^2 a)\Big] = 0 \tag{23b}$$

where

$$\mathcal{T}_{x,y} = -\alpha_1^2 \partial_y^2 + i\alpha_1(\partial_x^2 \partial_y - \partial_y^3) - \frac{1}{12}\left(\partial_x^4 + 6\partial_x^2\partial_y^2 - 3\partial_y^4 + 4\partial_x\partial_y^3\right)$$

and $\alpha_1 = \frac{\zeta}{v}$ which we assume is $O(1)$. Note that we only consider the case with weak nonlinearity, i.e., $|(a, b)| = O(v)$, some higher order terms in the nonlinear terms can be neglected in the above equation.

Accordingly, we introduce a slow time scale, $Z = v^2 z$ and we express a and b as

$$a = v(a_0(z, x, y, Z) + v^2 a_1(z, x, y, Z) + \cdots),$$
$$b = v(b_0(z, x, y, Z) + v^2 b_1(z, x, y, Z) \cdots)$$

where a_0 and b_0 satisfy the leading order equations and the dependence on z can be understood via the leading order equations while the dependence on Z will be given by the effective dynamics. Note that the only small parameter is v^2.

Define two moving frames, i.e., $\xi = x - z$ and $\eta = x + z$; hence a_0 and b_0 have the form

$$a_0 = F(\xi, y, Z) + G(\eta, y, Z)$$
$$b_0 = \tilde{F}(\xi, y, Z) + \tilde{G}(\eta, y, Z).$$

Furthermore, from the leading order equation we can easily get

Fig. 9 Diffraction patterns for large deformations. *Top*: $\beta = 0.005$ *Bottom*: $\beta = -0.01$. Here $v = 0.1$

$$\partial_\xi(-iF + \tilde{F}) = 0, \quad \partial_\eta(iG + \tilde{G}) = 0.$$

Hence for decaying functions: $\tilde{F} = iF$ and $\tilde{G} = -iG$.

At order $O(v^2)$, we have the equation

$$2\partial_\xi\partial_\eta a_1 = \mathcal{T}_{\xi,y}F + \mathcal{T}_{\eta,y}G + \left(-2\partial_\xi\partial_Z F + 2\partial_\eta\partial_Z G\right) + \sigma\Big[2i\partial_\xi(|F|^2F + 2|G|^2F + G^2F^*) - 2i\partial_\eta(|G|^2G + 2|F|^2G + F^2G^*)\Big];$$

When we integrate a_1, secular terms arise from the pieces that are functions of ξ or η alone, not both. Removal of secular terms at order $O(v^2)$ leads to the following maximally balanced nonlocal nonlinear equation for the right moving component

$$\partial_\xi\partial_Z F - \frac{1}{2}\mathcal{T}_{\xi,y}F - \sigma i\partial_\xi(|F|^2F) = 0, \tag{24}$$

and similarly the left moving component equation is

$$\partial_\eta\partial_Z G + \frac{1}{2}\mathcal{T}_{\eta,y}G - \sigma i\partial_\eta(|G|^2G) = 0.$$

We see that the above equations have a special nonlocal structure. The is reminiscent of the non-locality of the 2-D KP equation [41]. These equations are a two-dimensional NLS analog of the KP equation. We refer to them as NLSKP type equations. They describe the additional evolution structures along the moving frames. The simulation given in Fig. 10 shows the evolution given the initial data $F(\xi, y, Z = 0) = \xi e^{-\xi^2 - y^2}$, $\sigma = +1$. The additional structure obtained from the NLSKP Eq. (24) is consistent with Fig. 9; i.e. it is consistent with a blowup of the local structure depicted in Fig. 9.

8.2 After Separation

When $\beta < 0$, there is a gap between two dispersion branches. The edges to this gap for both branches are reached at $\mathbf{K}_* = -\frac{1}{2}\mathbf{k}_1 - \frac{1}{2}\mathbf{k}_2$. The width of the band gap is

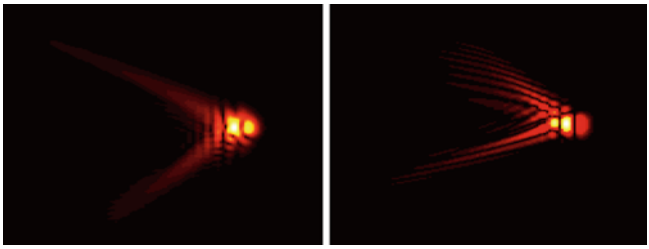

Fig. 10 Numerical simulations of NLSKP equations. *Left*: Eq. (24). *Right*: Eq. (26). Here $\sigma = +1$ and $\alpha_1 = \alpha_2 = 1$

$2|\beta|$. We then study the effective dynamics close to the edge; more specifically we study the case that $|\beta| = O(v^2)$ with $\alpha_2 = \frac{|\beta|}{v^2} = O(1)$.

It is noted that the continuous expansion changes when the gap is open. It is similar to the above case, so we omit the details. Taking the continuous limit from the discrete system (14a, b), making use of the relation: $\rho e^{-i\mathbf{K}_*\cdot\mathbf{v}_1} = \rho e^{-i\mathbf{K}_*\cdot\mathbf{v}_2} = -\rho$, keeping terms up to v^2 and rescaling the variables $x = x_1, y = x_2/\sqrt{3}$, we obtain the continuous equations

$$i\partial_z a + (1 - \alpha_2 v^2)\mathcal{F}_1 b + \alpha_2 v b + \sigma|a|^2 a = 0; \tag{25a}$$

$$i\partial_z b + (1 - \alpha_2 v^2)\mathcal{F}_2 a + \alpha_2 v a + \sigma|b|^2 b = 0; \tag{25b}$$

where

$$\mathcal{F}_1 = \partial_x - \frac{v}{2}(\partial_x^2 + \partial_y^2) + \frac{v^2}{6}\left(\partial_x^3 + \partial_y^3 + 3\partial_x\partial_y^2\right)$$
$$\mathcal{F}_2 = -\partial_x - \frac{v}{2}(\partial_x^2 + \partial_y^2) - \frac{v^2}{6}\left(\partial_x^3 + \partial_y^3 + 3\partial_x\partial_y^2\right).$$

As before we convert the above equations to a second order system which is of the form

$$\partial_z^2 a - \partial_x^2 a + v^2\mathcal{F}_{x,y}a + \sigma\left[-i\partial_t(|a|^2 a) + \partial_x(|b|^2 b)\right] = 0$$
$$\partial_z^2 b - \partial_x^2 b v^2\mathcal{F}_{x,y}b + \sigma\left[-i\partial_t(|b|^2 b) + \partial_x(|a|^2 a)\right] = 0,$$

where the operator

$$\mathcal{F}_{x,y} = \alpha_2^2 - \alpha_2(\partial_x^2 + \partial_y^2) - \frac{1}{12}\left(\partial_x^4 + 6\partial_x^2\partial_y^2 - 3\partial_y^4 + 4\partial_x\partial_y^3\right)$$

and we recall $\alpha_2 = \frac{|\beta|}{v^2}$ is $O(1)$.

Then we express a and b as

$$a = v(a_0(\xi, \eta, y, Z) + v^2 a_1(\xi, \eta, y, Z) + \cdots),$$
$$b = v(b_0(\xi, \eta, y, Z) + v^2 b_1(\xi, \eta, y, Z) + \cdots),$$

where a_0 and b_0 satisfy the leading order equations.

As above, a similar calculation shows that

$$a_0 = F(\xi, y, Z) + G(\eta, y, Z), \quad b_0 = iF(\xi, y, Z) - iG(\eta, y, Z).$$

At order $O(v^2)$, we have

$$2\partial_\xi\partial_\eta a_1 = \mathcal{F}_{\xi,y}F + \mathcal{F}_{\eta,y}G + \left(-2\partial_\xi\partial_Z F + 2\partial_\eta\partial_Z G\right) + \sigma\Big[2i\partial_\xi(|F|^2F + 2|G|^2F + G^2F^*) - 2i\partial_\eta(|G|^2G + 2|F|^2G + F^2G^*)\Big];$$

$\mathcal{F}_{\xi,y}$ and $\mathcal{F}_{\eta,y}$ are obtained from $\mathcal{F}_{x,y}$ by changing x to ξ and η respectively.

Removal of secular terms at order v^2 leads to two maximally balanced equations which govern the leading order dynamics of the right and left moving components; the equation for F is

$$\partial_\xi\partial_Z F - \frac{1}{2}\mathcal{F}_{\xi,y}F - \sigma i\partial_\xi(|F|^2F) = 0, \tag{26}$$

and the equation for G is

$$\partial_\eta\partial_Z G + \frac{1}{2}\mathcal{F}_{\eta,y}G - \sigma i\partial_\eta(|G|^2G) = 0.$$

These nonlocal equations are also NLSKP-type, though slightly different from those found the preceding subsection. In Fig. 10 we show a typical numerical result. We see similarity to the preceding case –see Eq. (24)—but with more of a focusing effect which is ascribed to our now being in the gap region.

9 Conclusion

Wave propagation in honeycomb lattices has attracted keen interest in many disciplines. This paper discusses nonlinear waves in honeycomb lattices and in particular nonlinear optical wave propagation are studied in deformed honeycomb lattices. Discrete coupled mode equations were obtained via an orbital approximation. These equations describe the lowest band of the linear dispersion relation of the original lattice NLS equation. Depending on the deformation, the dispersion relation may or may not admit conical crossings. In undeformed lattices, there are two Dirac cones. The associated envelope dynamics is obtained by taking the continuum limit of the couple mode equations near the Dirac points. This results in a higher order nonlinear Dirac equation. Utilizing this equation, both linear and nonlinear propagation of the envelope wave packets near Dirac points are analyzed. The leading order effect is a circular conical diffraction while the next order correction modifies the circular structure into hexagonal structure in the linear problem and triangular diffraction when nonlinearity is included. In general higher

order linear effects become noticeable even when v is very small. We see that nonlinearity expands the energy distribution in momentum space. In addition, nonlinearity also induces the coupling of two branches. Depending on the sign of the nonlinearity, one branch is enhanced while the other is weakened. Triangular diffraction is obtained even when initial condition is evenly distributed between the two branches.

When the deformation is small, the evolution pattern is changed moderately: circular conical diffraction becomes elliptical. However, when the deformation is large, the two branches may separate from each other and conical crossings in the dispersion relation disappear. In this regime a localized input splits into two moving nearly straight line components propagating in 'left and right' going directions. The effective dynamics of the wave packets associated with the Dirac point (before separation) or edge point (after separation) is described by into two maximally balanced nonlocal NLS equations termed here as: NLSKP type equations.

Acknowledgments Mark J. Ablowitz was partially supported by the U.S. Air Force Office of Scientific Research, under grant FA9550-12-0207 and by NSF under grants DMS-0905779, CHE 1125935. Yi Zhu was partially supported by the NSFC under grant 11204155.

References

1. K.S. Novoselov, A.K. Geim, S.V. Morozov, D. Jiang, Y. Zhang, S.V. Dubonos, I.V. Grigorieva, A.A. Firsov, Electric field effect in atomically thin carbon films. Science **306**, 666–669 (2004)
2. K.S. Novoselov, A.K. Geim, S.V. Morozov, D. Jiang, M.I. Katsnelson, I.V. Grigorieva, S.V. Dubonos, A.A. Firsov, Two-dimensional gas of massless Dirac fermions in graphene. Nature **438**, 197–200 (2005)
3. N.M.R. Peres, K.S. Novoselov, A.H. Castro Neto, F. Guinea, A.K. Geim, The electronic properties of graphene. Rev. Modern Phys. **81**, 109 (2009)
4. O. Peleg, G. Bartal, B. Freedman, O. Manela, M. Segev, D.N. Christodoulides, Conical diffraction and gap solitons in honeycomb photonic lattices. Phys. Rev. Lett. **98**, 103901 (2007)
5. O. Morsch, M. Oberthaler, Dynamics of bose-einstein condensates in optical lattices. Rev. Mod. Phys. **1**, 179–215 (2006)
6. S.L. Zhu, B. Wang, L.M Duan, Simulation and detection of Dirac fermions with cold atoms in an optical lattice. Phys. Rev. Lett. **98**, 260402 (2007)
7. Y.S. Kivshar, P. Agrawal Govind, *Optical Solitons: From Fibers to Photonic Crystals* (Academic press, San Diego, 2003)
8. M.I. Carvalho, S.R. Singh, D.N. Christodoulides, Vector interactions of steady-state planar solitons in biased photorefractive media. Opt. Lett. **20**, 2177–2179 (1995)
9. M. Segev, N.K. Efremidis, J.W. Fleisher, T. Carmon, D.N. Christodoulides, Observation of discrete solitons in optically induced real time waveguide arrays. Phys. Rev. Lett. **90**, 023902 (2003)
10. N.K Efremidis, J.W. Fleisher, M. Segev, D.N. Christodoulides, Observation of two-dimensional discrete solitons in optically induced nonlinear photonic lattices. Nature **422**, 147 (2003)

11. D.N. Christodoulides, R.J. Joseph, Discrete self-focusing in nonlinear arrays of coupled waveguides. Opt. Lett. **13**, 794–796 (1988)
12. P.G. Kevrekidis, B.A. Malomed, Y.B. Gaididei, Solitons in triangular and honeycomb dynamical lattices with the cubic nonlinearity. Phys. Rev. E **66**, 016609 (2002)
13. M.J. Ablowitz, Y. Zhu, Unified description of the dynamics of wave envelopes in two-dimensional simple periodic lattices. Stud. Appl. Math. (to appear)
14. M. Ablowitz, S. Nixon, Y. Zhu, Conical diffraction in honeycomb lattices. Phys. Rev. A **79**, 053830 (2009)
15. M.J. Ablowitz, Y. Zhu, Evolution of bloch-mode envelopes in two-dimensional generalized honeycomb lattices. Phys. Rev. A **82**, 013840 (2010)
16. L.H. Haddad, L.C. Carr, The nonlinear Dirac equation in bose-einstein condensates: foundation and symmetries. Physica D **238**, 1413–1421 (2009)
17. A.B. Aceves, B. Costantini, C. De Angelis, Two-dimensional gap solitons in a nonlinear periodic slab waveguide. J. Opt. Soc. Am. B **12**, 1475–1479 (1995)
18. J.K. Yang, I. Makasyuk, A. Bezryadina, Z. Chen, Dipole solitons in optically induced two-dimensional photonic lattices. Opt. Lett. **29**, 1662–1664 (2004)
19. D.N. Neshev, T.J. Alexander, E.A. Ostrovskaya, Y.S. Kivshar, I. Martin, H. Makasyuk, Z.G. Chen, Observation of discrete vortex solitons in optically induced photonic lattices. Phys. Rev. Lett. **92**, 123903 (2004)
20. X. Wang, Z. Chen, J. Wang, J. Yang, Observation of in-band lattice solitons. Phys. Rev. Lett. **99**, 243901 (2007)
21. R. Driben, I.M. Merhasin, B.V. Gisin, B.A. Malomed, Finite-band solitons in the kronig-penney model with the cubic-quintic nonlinearity. Phys. Rev. E **71**, 016613 (2005)
22. E.A. Ostrovskaya, Y.S. Kivshar, Photonic crystals for matter waves: Bose-einstein condensates in optical lattices. Opt. Exp. **12**, 19–29 (2004)
23. H. Sakaguchi, B.A. Malomed, Two-dimensional loosely and tightly bound solitons in optical lattices and inverted traps. J. Phys. B: At. Mol. Opt. Phys. **37**, 2225–2239 (2004)
24. F.W. Wise, Y.-F. Chen, K. Beckwitt, B.A. Malomed, Criteria for the experimental observation of multidimensional optical solitons in saturable media. Phys. Rev. E **70**, 046610 (2004)
25. Z. Shi, J. Yang, Solitary waves bifurcated from bloch-band edges in two-dimesional periodic media. Phys. Rev. E **75**, 056602 (2007)
26. B. Ilan, M.I. Weinstein, Band-edge solitons, nonlinear schrödinger / gross-pitaevskii equations and effective media. SIAM Multiscale Model. Simul. **8**, 1055–1101 (2010)
27. M.J. Ablowitz, B. Ilan, E. Schonbrun, R. Piestun, Solitons in two-dimensional lattices possessing defects, dislocations, and quasicrystal structures. Phys. Rev. E **74**, 035601(R) (2006)
28. B. Freedman, G. Bartal, M. Segev, R. Lifshitz, D.N. Christodoulides, J.W. Fleischer, Wave and defect dynamics in nonlinear photonic quasicrystals. Nature **440**, 1166–1169 (2006)
29. H. Sakaguchi, B.A. Malomed, Gap solitons in quasiperiodic optical lattices. Phys. Rev. E **74**, 026601 (2006)
30. P.R Wallace, The band theory of graphite. Phys. Rev. **71**, 622 (1947)
31. O. Bahat-Treidel, O. Peleg, M. Segev, Symmetry breaking in honeycomb photonic lattices. Opt. Lett. **33**, 2251–2253 (2008)
32. M.J. Ablowitz, Y. Zhu, Nonlinear diffraction in photonic graphene. Opt. Lett. **36**, 3762–3764 (2011)
33. F.D.M. Haldane, S. Raghu, Possible realization of directional optical waveguides in photonic crystals with broken time-reversal symmetry. Phys. Rev. Lett. **100**, 013904 (2008)
34. S. Raghu, F.D.M. Haldane, Analogs of quantum hall effect edge states in photonic crystals. Phys. Rev. A **78**, 033834 (2008)
35. M.J. Ablowitz, Y. Zhu, Nonlinear waves in shallow honeycomb lattices. SIAM J. Appl. Math. **72**, 240–260 (2012)
36. O. Bahat-Triedel, A. Szameit, M. Rechtsman, M. Segev, $\mathcal{PT}$-symmetry in honeycomb photonic lattices. Phys. Rev. A **84**, 021806(R) (2011)

37. H. Ramezani, T. Kottos, V. Kovanis, D.N. Christodoulides, Exceptional-point dynamics in photonic honeycomb lattices with $\mathcal{PT}$ symmetry. Phys. Rev. A **85**, 013818 (2012)
38. O. Bahat-Treidel, O. Peleg, M. Segev, H. Buljan, Breakdown of Dirac dynamics in honeycomb lattices due to nonlinear interactions. Phys. Rev. A **82**, 013830 (2010)
39. O. Bahat-Treidel, O. Peleg, M. Grobman, N. Shapira, M. Segev, T. Pereg-Barnea, Klein tunneling in deformed honeycomb lattices. Phys. Rev. Lett. **104**, 063901 (2010)
40. C.L. Fefferman, M. Weinstein, Honeycomb lattice potentials and Dirac points. J. Amer. Math. Soc. **25**, 1169–1220 (2012)
41. M.J. Ablowitz, *Nonlinear Dispersive Waves: Asymptotic Analysis and Solitons* (Cambridge University Press, New York, 2011)
42. N.W. Ashcroft, N.D. Mermin, *Solid State Physics* (Brooks Cole, Brooks, 1978)
43. M. Reed, B. Simon, *Methods of Mathematical Physics IV: Analysisi of operators* (Acdemic Press, New York, 1978)
44. J. Yang, *Nonlinear Waves in Integrable and Nonintegrable Systems* (Society for Industrial and Applied Mathematics, Philadelphia, 2010)
45. M.J. Ablowitz, C.W. Curtis, Y. Zhu, On tight binding approximations in optical lattices. Stud. Appl. Math. **129**, 366–388 (2012)
46. G.L. Alfimov, P.G. Kevrekidis, V.V. Konotop, M. Salerno, Wannier functions analysis of the nonlinear schröinger equation with a periodic potential. Phys. Rev. E, **66**, 046608 (2002)
47. M.J. Ablowitz, J. Villarroel, On the Kadomtsev-Petviashili equation and associated constrints. Stud. Appl. Math. **85**, 195–213 (1991)

Light Self-Localization and Power-Dependent Steering in Anisotropic Dielectrics: Spatial Solitons in Uniaxial Nematic Liquid Crystals

Alessandro Alberucci and Gaetano Assanto

Abstract We discuss nonlinear propagation of light beams in anisotropic media, addressing the role of nonlocality and nonlinearity in power-dependent beam self-steering. With specific reference to spatial solitons in positive uniaxial nematic liquid crystals (i.e. nematicons), we describe soliton self-acceleration through reorientational response and nonlinear walk-off.

1 Introduction

Since the invention of laser by Maiman in 1960 [1] and the consequent availability of intense coherent light sources, nonlinear optics has been widely investigated [2, 3] and several phenomena have been demonstrated: frequency generation, stimulated scattering, wave-mixing, self-action, electromagnetic-induced transparency, etcetera. We focus hereby on beam self-focusing [4]: as the refractive index depends on light intensity via the Kerr effect, a bell-shaped wavepacket is able to define an index well which, in turn, acts on the confinement of the beam itself. When nonlinear trapping balances diffractive spreading, a spatial soliton is generated [5–7].[1] Self-focusing in anisotropic dielectrics has not been studied as in-depth as in isotropic media, despite the fact that light propagation in anisotropic media encompasses peculiar properties such as double and conical refraction,

[1] In this work we will use the terms soliton and solitary waves interchangeably, even though in mathematical physics they can refer to distinct wave entities.

A. Alberucci (✉) · G. Assanto
Nonlinear Optics and OptoElectronics Lab (NooEL), University "Roma Tre", Via della Vasca Navale 84 00146 Rome, Italy
e-mail: alberucc@uniroma3.it

G. Assanto
e-mail: assanto@uniroma3.it

Progress Optical Sci., Photonics (2013): 27–47
DOI: 10.1007/10091_2012_23

Published Online: 17 January 2013

nonspecular reflection, etc. [8]. Anisotropic materials are employed in optical signal processing to realize basic components, such as waveplates, polarizers, beam splitters, spin-to-orbital angular momenta converters, displays, modulators and so on. Therefore, it appears quite natural to investigate how light self-traps in the presence of optical anisotropy, with specific attention to inherently anisotropic nonlinear mechanisms: spatial solitons have been observed e.g. in photorefractive media [9], parametric crystals [10–12] and liquid crystals [13–15].

In this chapter we describe spatial self-focusing of light in anisotropic media, emphasizing the interplay between birefringence and nonlinearity, and the appearance of effects unavailable in isotropic materials, such as self-steering due to nonlinear changes in walk-off. In isotropic media, self-steering of individual solitons was predicted in conjunction with asymmetric beams [16] or transverse phase modulation [17], through the nonlinear tunnelling of a linear barrier [18, 19], the asymmetric interaction with boundaries in the absence [20] or in the presence [21] of a linear trapping potential. In photorefractive crystals soliton self-steering was demonstrated via the asymmetric diffusion of photogenerated charges [22], in quadratic parametric media through mutual dragging of fundamental and second harmonic field components [12], in liquid crystals owing to the interaction with a linear trapping potential [23] or finite boundaries [24]. Recently, self-acceleration of linear as well as nonlinear Airy beams has been investigated and reported [25–29].

In the next sections, following a general discussion, we will focus on nematic liquid crystals, a highly nonlinear and highly birefringent uniaxial. The theoretical ideas discussed in this chapter were tested with several experiments in nematic liquid crystals: an excellent good agreement was found, both on soliton properties and on walk-off dependence with power [30]. Finally, for the sake of conciseness, we limit our discussion to the propagation of individual nematicons. However, the results presented in this chapter can be extended to the case of interacting nematicons as in Ref. [31].

2 Nonlinear Light Propagation in Anisotropic Media

In this section, starting from Maxwell's equations in complete vectorial form, we show how it is possible to model nonlinear light propagation in uniaxials using a single (scalar) equation. Such an equation is able to describe nonlinear phenomena occurring uniquely to anisotropic media, including power-dependent beam self-steering via nonlinear changes in walk-off.

2.1 Equations for the Optical Field

Let us consider a uniaxial medium with a dielectric tensor of the form $\boldsymbol{\epsilon} = \left[\epsilon_{xx}, 0, 0; 0, \epsilon_{yy}, \epsilon_{yz}; 0, \epsilon_{zy}, \epsilon_{zz}\right]$, that is, an optic axis lying in the plane yz. The dielectric tensor $\boldsymbol{\epsilon}^L$ accounts only for the linear polarizability of the medium: we

explicitly write the nonlinear polarization $\boldsymbol{P}^{NL}$ by defining $\boldsymbol{D} = \boldsymbol{\epsilon} \cdot \boldsymbol{E} + \boldsymbol{P}^{NL}$. For the sake of simplicity we limit ourselves to the (1 + 1)D case, i.e. we set $\partial_x = 0$. The previous assumptions guarantee the independence of extraordinary and ordinary components, avoiding energy exchange between the two waves and related effects. The Maxwell's equations for the extraordinary component in the harmonic regime (pulsation ω) take the form [32]

$$\left(\partial_z + \frac{\epsilon_{yz}}{\epsilon_{zz}}\partial_y\right) H_x = j\omega\left[n_e^2 \epsilon_0 E_y - \frac{\epsilon_{yz}}{\epsilon_{zz}} P_z^{NL} + P_y^{NL}\right], \tag{1a}$$

$$\left(\partial_z + \frac{\epsilon_{yz}}{\epsilon_{zz}}\partial_y\right) E_y = \frac{j}{\omega \epsilon_{zz}} \partial_y^2 H_x + j\omega\mu_0 H_x - \frac{\partial_y P_z^{NL}}{\epsilon_{zz}}, \tag{1b}$$

$$E_z = -\frac{\epsilon_{yz}}{\epsilon_{zz}} E_y + \frac{j}{\omega \epsilon_{zz}} \partial_y H_x - \frac{P_z^{NL}}{\epsilon_{zz}}, \tag{1c}$$

where we neglected the spatial derivatives of $\boldsymbol{\epsilon}^L$ and set $n_e^2 = \left(\epsilon_{yy} - \epsilon_{yz}^2/\epsilon_{zz}\right)/\epsilon_0$. Equations (1a–1c) are quite general and hold valid even for an inhomogeneous dielectric tensor $\boldsymbol{\epsilon}$, for any nonlinearity and in the non-paraxial limit. To analyze the physical meaning of Eqs. (1a–1c), we note that the quantity $\epsilon_{yz}/\epsilon_{zz}$ correspond to the walk-off angle δ of a plane wave with wavevector parallel to $\hat{z}$ ($\boldsymbol{k} \uparrow\uparrow \hat{z}$). If we take the walk-off to be uniform in space, we can introduce the new reference system $y' = y - \tan\delta\, z$ and $z' = z$. We also define the unit vectors $\hat{t} = \cos\delta\, \hat{y} - \sin\delta\, \hat{z}$ and $\hat{s} = \cos\delta\, \hat{z} + \sin\delta\, \hat{y}$, parallel to the electric field and the Poynting vector, respectively. Thus, light propagation can be modeled by the scalar equation [32]

$$\begin{aligned} &\partial_{z'}^2 H_x - 2\partial_{z'}(\ln n_e)\left[\partial_{z'} H_x + \frac{j\omega}{\cos\delta} P_t^{NL}\right] + D\partial_{y'}^2 H_x \\ &+ k_0^2 n_e^2 H_x - \frac{j\omega}{\cos\delta}\left[\partial_{z'} P_t^{NL} - D\cos\delta\, \partial_{y'} P_z^{NL}\right] = 0, \end{aligned} \tag{2}$$

where k_0 is the vacuum wavevector and $D = \epsilon_0 n_e^2/\epsilon_{zz}$. The magnetic field H_x completely describes the electromagnetic wave, with electric field components given by $E_t = \frac{\partial_{z'} H_x}{j\omega\epsilon_0 n_e^2 \cos\delta} - \frac{j\sin\delta}{\omega\epsilon_{zz}}\partial_{y'} H_x - \frac{P_t^{NL}}{\epsilon_0 n_e^2 \cos^2\delta} + \frac{\sin\delta}{\epsilon_{zz}} P_z^{NL}$ and $E_s = \frac{j\cos\delta}{\omega\epsilon_{zz}}\partial_{y'} H_x - \frac{\cos\delta}{\epsilon_{zz}} P_z^{NL}$.

Let us first consider the application of Eq. (2) to the simplest case of a homogenous uniaxial. Equation (2) provides $\partial_{z'}^2 H_x + D\partial_{y'}^2 H_x + k_0^2 n_e^2 H_x = 0$, i.e. the walk-off angle of beams with center wavevector $\boldsymbol{k} = k_0\hat{z}$ is δ, even in the non-paraxial regime [33]. For beams paraxial along z, Eq. (2) becomes the classical paraxial Helmholtz equation, but with a diffraction coefficient D determined by the orientation of the optic axis. The latter suggests to enforce the paraxial approximation in the moving frame $y'z'$.

We now turn to shape-preserving solutions of Eq. (2), i.e., solitary waves, propagating with a walk-off δ in geometries retaining their transverse distribution along z', i.e., with $\partial_{z'} n_e = 0$. Accordingly, we set $H_x = u(y')e^{-jk_0(n_0+n_{NL})z'}$, with n_0 and n_{NL} the linear and the nonlinear contributions to the effective index, respectively; similarly, we define $\boldsymbol{p}^{NL}$ from $\boldsymbol{P}^{NL}$. Equation (2) thus gives [32, 34]

$$\begin{aligned} &- k_0^2\left(n_{NL}^2 + 2n_0 n_{NL}\right)u + D\partial_{y'}^2 u + k_0^2 \Delta n_e^2 u \\ &- \frac{k_0^2 c(n_0 + n_{NL})}{\cos\delta} p_t^{NL} + jk_0 cD\partial_{y'} p_z^{NL} = 0, \end{aligned} \tag{3}$$

where $\Delta n_e^2 = n_e^2 - n_0^2$ accounts for a linear index well, when present. For a generic solution u of Eq. (3) we can compute the corresponding Poynting vector $\mathbf{S}$ as [34]

$$\begin{aligned} \boldsymbol{S} = \frac{1}{2}\Bigg[\hat{s}\Bigg(&\frac{n_0 + n_{NL}}{n_e^2 \cos\delta} Z_0 |u|^2 + \frac{j\sin\delta}{\omega\epsilon_{zz}} u^* \partial_{y'} u + \frac{p_t^{NL} u^*}{\epsilon_0 n_e^2 \cos\delta} \\ &- \frac{\sin\delta\, p_z^{NL} u^*}{\epsilon_{zz}}\Bigg) + \hat{t}\left(\frac{j\cos\delta}{\omega\epsilon_{zz}} u^* \partial_{y'} u - \frac{\cos\delta}{\epsilon_{zz}} u^* p_z^{NL}\right)\Bigg], \end{aligned} \tag{4}$$

being Z_0 the vacuum impedance.

Equation (3), coupled with an expression for the nonlinear polarization, yields the profile of solitary waves in uniaxials, generally accounting for large anisotropy, large (i.e., non-perturbative) nonlinear effects and beam non-paraxiality. According to Eq. (3), the phase of u does not vary on a generic plane $z' =$ constant if p_t^{NL} is real (i.e., in phase with u) and p_z^{NL} is purely imaginary (i.e., shifted by 90° with respect to u). The term proportional to p_t^{NL} is responsible for light self-trapping, with the nonlinear index well depending on the optical field according to the specific nonlinearity. In the case of asymmetric nonlinearities [20, 35], p_t^{NL} can induce distortions on the phase front of u, corresponding to a sideway motion of input beams with phase fronts normal to $\hat{z}$. The term proportional to p_z^{NL} can be also responsible for soliton self-steering via nonlinear changes in walk-off, as we will show in the following section.

Finally, we stress that generalizations to the full (2 + 1)D case are easily accomplished if we neglect the field components E_x, H_y and H_z; the changes in Eq. (2) mainly consist in the addition of the second derivatives along x [36].

2.2 Soliton Self-Steering

For an arbitrary nonlinear polarization, we expect the beam walk-off to vary with power P owing to the changes in the medium polarization with respect to the linear case. Let us begin discussing which nonlinear response would conserve the walk-off constant to its linear value. We use the superscript *ov* to indicate the overall

properties of the dielectric, i.e. both linear and nonlinear contributions. For the walk-off we then have $\delta^{ov} = \arctan\left(\epsilon^{ov}_{yz}/\epsilon^{ov}_{zz}\right)$: by setting $\boldsymbol{\epsilon}^{ov} = \boldsymbol{\epsilon} + \boldsymbol{\chi}^{NL}$, at the first order we get $\delta^{ov} = \delta$ if the equivalence

$$\frac{\chi^{NL}_{yz}}{\chi^{NL}_{zz}} = \tan\delta \tag{5}$$

is satisfied. In deriving Eq. (5) we assumed $\boldsymbol{\chi}^{NL}$ purely real: for the sake of simplicity we will retain this hypothesis hereafter. The condition (5) seems to rely on physical grounds, as in order to conserve the direction of propagation of the photons, the dipoles induced by the external field have to keep oscillating in the same (linear) direction.

We now validate condition (5) using the mathematical tools developed in the previous section. From Eqs. (3) and (4) we find that the phase front of u conserves its shape for increasing P if $\mathrm{Re}\left(p^{NL}_z/\epsilon^{ov}_{zz}\right) = 0$. It is then straightforward to obtain the condition (5), confirming the intuitive result.

Whenever condition (5) is not satisfied, the nonlinear eigenvalue problem of Eq. (3) is solved by a complex u. The appearance of a tilted phase on the soliton indicates a variation in walk-off, i.e. an angle change between the wavevector—no longer aligned to $\hat{z}$ due to the nonlinear polarization—and the Poynting vector along $\hat{s}$.

To prove the latter statement, we assume a local Kerr-like nonlinearity with $\boldsymbol{P}^{NL} = \epsilon_0 n_2\left(|E_t|^2 + |E_s|^2\right)\boldsymbol{E}$. Since the nonlinearity is symmetric, p^{NL}_t acts only on the beam waist. We get $p^{NL}_z \propto |u|^2 u$ if $E_s \ll E_t$; in addition $\partial_{y'} p^{NL}_z \propto \left(u^2\partial_{y'}u^* + 2|u|^2\partial_{y'}u\right)$, where the star stands for complex conjugate. Substituting back into Eq. (3), the imaginary terms can be dropped with the substitution $u(y') = v(y')\exp\left(j\xi_0 y'\right)$, thus ensuring that v is purely real. The quantity ξ_0 represents the variation in walk-off with respect to the unperturbed value δ [32].

To conclude this section we stress that, when the condition (5) is not satisfied, nonlinear changes in walk-off take place, even at low powers. In homogeneous media (i.e., $\Delta n^2_e = 0$) we expect distinct behaviors in the perturbative and in the highly nonlinear regimes, respectively, depending on the size the excitation [37]. For small input powers the beam evolves in the perturbative regime, that is, the nonlinear polarization is small with respect to the linear polarization. The observable role of the nonlinearity is to change the beam waist via self-focusing, whereas changes in walk-off are negligible as $\boldsymbol{P}^{NL}$ is much smaller than $\boldsymbol{\epsilon}\cdot\boldsymbol{E}$. When the nonlinear and linear polarizations becomes comparable, the walk-off becomes a function on the beam power P, yielding a measurable power-dependent beam trajectory [38].

3 Highly Nonlocal Case

An important case is the high nonlocality, i.e., the case of uniaxials with nonlinear polarization extending much beyond the beam profile [39]. High nonlocal responses are usually related to diffusion, comprising charge diffusion in photorefractive materials [40], heat transfer in thermo-optic media [41] and elastic interactions in liquid crystals [42].

In these dielectrics the mathematical description of solitons is based on the well-known quantum harmonic oscillator [43]. For example, supposing $\boldsymbol{P}^{NL} = [V_0(P) + V_2(P)y'^2]u\hat{t}$ and small nonlinear deflections, Eq. (3) provides

$$\left(2n_0 n_{NL} + \frac{cn_0 V_0}{\cos\delta} - \frac{DV_0^2 c^2 \sin^2\delta}{4}\right)v = \frac{D}{k_0^2}\partial_{y'}^2 v - \frac{cn_0}{\cos\delta}V_2 y'^2 v, \tag{6}$$

with a phase-front tilt given by $\xi_0 = \frac{k_0 V_0 c \sin\delta}{2}$, thus depending only on the peak of $\boldsymbol{P}^{NL}$. Equation (6) can be solved once a specific nonlinear mechanism is invoked, so that a the dependence of V_0 and V_2 on the soliton power P can be derived. The nonlinear eigenvalue problem stated by Eq. (6) governs nonlocal solitons in uniaxial media, accounting also for nonlinear variations in walk-off. Solitons are Hermite-Gauss functions, with waist depending on P via V_2 [43]. The illustrated approach fails for large nonlinear effects, when neither the dependence of D and δ on power P can be neglected, nor the nonlinear polarization in the relationship between electric and magnetic fields. The arbitrarily nonlinear case needs be treated with reference to a specific response. In the following of the chapter we will focus on the reorientational nonlinearity in nematic liquid crystals, which has lately stimulated a good deal of attention [15].

3.1 Reorientational Nonlinearity in Nematic Liquid Crystals

Liquid crystals are phases of matter characterized by properties of both solids and liquids. In the nematic phase the organic molecules are randomly located on a macroscopic scale, but in average they are oriented in the same direction due to strong mutual interactions (Fig. 1) [44].

Macroscopically, nematic liquid crystals (NLC) behave as uniaxial crystals, with the optic axis parallel to the molecular director $\hat{n}$ defined as the preferential alignment of the molecules (Fig. 1). We name $n_\parallel$ and $n_\perp$ the refractive indices experienced by light polarized parallel and normal to the director, respectively (Fig. 1) and introduce the optical anisotropy $\epsilon_a = \epsilon_0\left(n_\parallel^2 - n_\perp^2\right)$. The director distribution varies from point to point, thus NLC can in general be modelled as inhomogeneous birefringent media; defining θ as the angle between $\hat{n}$ and wavevector $\boldsymbol{k}//\hat{z}$, the elements of $\boldsymbol{\epsilon}$ are $\epsilon_{lk}(\theta) = n_\perp^2\delta_{lk} + \epsilon_a n_l n_k$ $(l,k = x,y,z)$,

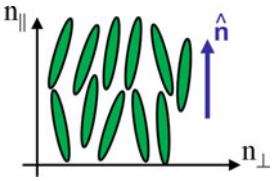

Fig. 1 Molecule distribution (*green ellipses*) in liquid crystals in the nematic phase; the molecular director and the principal axes are indicated, as well

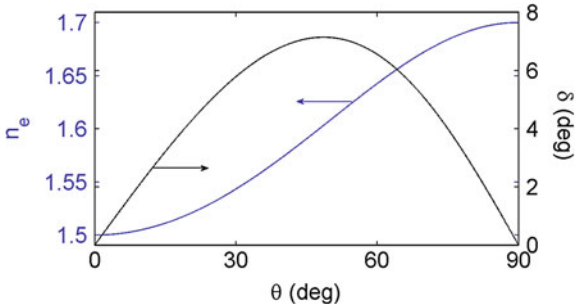

Fig. 2 Extraordinary refractive index n_e and walk-off δ versus θ. Here we took $n_\perp = 1.5$, $n_\parallel = 1.7$

where $n_l = \hat{n} \cdot \hat{l}$ and δ_{lk} is the Kronecker delta. We recall that $n_e(\theta) = \left(\frac{\cos^2\theta}{n_\perp^2} + \frac{\sin^2\theta}{n_\parallel^2}\right)^{-1/2}$ and $\delta(\theta) = \arctan\left[\frac{\epsilon_a \sin(2\theta)}{\epsilon_a + 2\epsilon_0 n_\perp^2 + \epsilon_a \cos(2\theta)}\right]$; n_e and δ are graphed in Fig. 2 for a typical NLC (e.g. E7). When subjected to external electric fields, the NLC director undergoes a torque as the induced molecular dipoles tend to align with the field lines (see Fig. 3).

The electric torque is counteracted by an elastic torque due to the microscopic intermolecular forces. The director distribution in equilibrium can be found by minimizing the total free energy [44].

Since electric fields are able to rotate the director (i.e. the optic axis), they can strongly modify the optical properties of the uniaxial NLC [45]. When the electric fields are at low frequency, i.e. they stem from the application of an external voltage, a strong electro-optic effect characterizes the NLC, a phenomenon widely employed in flat display technology. When the electric fields are associated with light waves, a strong Kerr-like response takes place with a resulting self-focusing [13, 46]. In either cases, NLC possess a very large polarizability, making them ideal candidates for external control on light wave propagation [47].

Mathematically, if we assume that the NLC molecules rotate in the plane yz exclusively under the action of an optical field, the director distribution can be calculated by solving the Euler-Lagrange equation

$$K\nabla^2\theta + \frac{\boldsymbol{\epsilon}_a}{4}\left[\sin(2\theta)\left(|E_x|^2 - |E_z|^2\right) + 2\cos(2\theta)\mathrm{Re}\left(E_x E_z^*\right)\right] = 0, \qquad (7)$$

where K is the scalar Frank elastic constant [44, 45]. To identify the various contributions to θ, we write $\theta = \theta_0(x, y, z) + \psi(x, y, z)$, with θ_0 the director

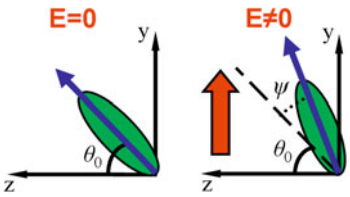

Fig. 3 Effect of an external electric field $\boldsymbol{E}$ (*red arrow*) polarized along y on molecular orientation in a positive uniaxial NLC (i.e., $\epsilon_a > 0$). In the absence of perturbation (*left*) the molecular director is at an angle θ_0 with $\hat{z}$. When an intense electric field $\boldsymbol{E}$ is present (*right*), the molecule tends to rotate and align the induced dipole (parallel to $\hat{n}$) with $\boldsymbol{E}$, with a net change ψ in θ

orientation in the absence of illumination and ψ its nonlinear optical perturbation (see Fig. 3). Noteworthy, Eq. (7) establishes a nonlinear relationship between the intensity and the perturbation of the director angle. Equation (7) permits the evaluation of the width w_ψ of the angular perturbation ψ; the magnitude of the nonlocality can be determined by the ratio between the beam waist w in intensity (defined as the square root of the second-order centered momentum) and w_ψ. In fact, the spatial extent of ψ is determined by the Green function of the linearized version of Eq. (7) (corresponding to a Poisson-like equation), in turn fixed by the boundary conditions [30]. If the beam is narrower than any linear dimension of the sample, the width w_ψ depends on the shortest side of the cell which confines the NLC.

Equation (7) has to be solved in conjunction with Maxwell's equations. At variance with the notation introduced to derive Eq. (2), we now indicate with $\boldsymbol{\epsilon}$ the overall dielectric tensor, including the power-dependent contributions (depending on ψ). Since ψ and θ_0 can be comparable under experimental conditions, the latter choice helps simplifying the description of beam evolution. Therefore, in the highly nonlocal limit paraxial light beams propagating along $\hat{z}$ obey the generalized anisotropic NLSE [30]

$$2jk_0 n_b\left(\frac{\partial A}{\partial z}+\tan\delta_b\frac{\partial A}{\partial y}\right)+D\frac{\partial^2 A}{\partial y^2}+\frac{\partial^2 A}{\partial x^2}+k_0^2\Delta n_e^2 A=0, \tag{8}$$

with A the slowly varying envelope of H_x and subscript b indicating values on the beam axis (i.e. peak intensity). The term $\Delta n_e^2 = n_e^2(\theta) - n_b^2$ accounts for index inhomogeneities, of both linear (given by θ_0) and nonlinear (given by ψ) origins, respectively. We stress that the nonlinear index well is computed via Eq. (7), the latter determining the relationships between the optical intensity $|A|^2$ and the optical perturbation ψ. Analogously, the trajectory dependence on nonlinear walk-off variations is modelled by $\delta_b(z)$ and its dynamics with the evolution coordinate z is governed by Eq. (7) [38].

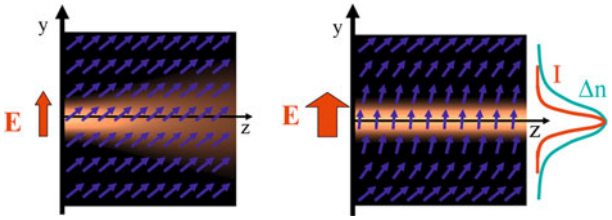

Fig. 4 Propagation of single-hump beams in NLC. When reorientation is negligible (*left*), the beam diffracts linearly. For high enough powers, the director distribution is perturbed and self-focusing takes place; when diffraction and self-focusing counterbalance one another (*right*) a profile invariant nematicon is generated

4 Basic Physics of Nematicons

Nematicons can be modelled by the system of Eqs. (7–8). The physics of nematicon formation through reorientation is sketched in Fig. 4. Hereafter, we will assume positive NLC, i.e., $\epsilon_a > 0$ in the optical spectrum.[2] In the following, unless specified otherwise, we will assume a homogeneous director distribution in the absence of light, i.e., θ_0 independent from spatial coordinates. A finite beam in the extraordinary polarization is launched into the NLC. At small power, the torque is weak and no appreciable director reorientation occurs: the beam undergoes diffractive spreading. At high power, the beam induces molecular reorientation and, in turn, a focusing increase in refractive index n_e. When the latter lens-like effect due to ψ compensates diffraction, a bright solitary wave is obtained [15]. In general, solitary waves in NLC undergo periodic oscillations in waist and peak intensity, i.e., they breathe [43, 48]; profile-invariant nematicons [49] will be dealt with in Sect. 5, breathers in Sect. 6. In the remaining of this section we describe perturbative and highly nonlinear regimes of nematicon propagation [37] for both breathing and steady nematicons.

4.1 Perturbative Regime

The nonlinear perturbative regime is characterized by the condition $\psi \ll \theta_0$, i.e., the optical perturbation is small with respect to the distribution of the director angle at rest. In this regime the light beam is able to self-write a photonic potential [given by Δn_e^2 in Eq. (8)] strong enough to affect the beam via self-focusing. The self-induced index well is due to the inhomogeneous nonlinear polarization.

[2] Nematicons could propagate even in negative uniaxial NLC, the only difference being the sign of the torque. To our knowledge, no experimental observation was reported in this case.

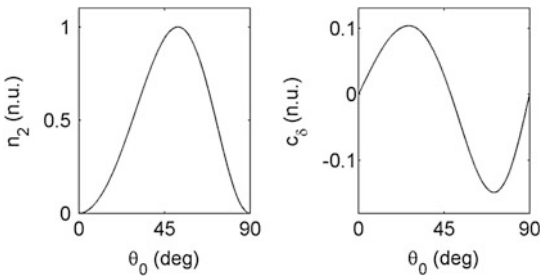

Fig. 5 Calculated n_2 (*left*) and c_δ (*right*) versus θ_0 for $n_\parallel = 1.7$ and $n_\perp = 1.5$

The beam trajectory, fully determined by the walk-off,[3] is not appreciably modified as compared with the linear response.

When solving Eq. (7), θ in the trigonometric functions can be replaced by θ_0 without significant error. After setting $\delta_0 = \delta(\theta_0)$ and $\gamma = \epsilon_a/(4K)$, the reorientational equation takes the form of a linear Poisson equation, i.e. $\nabla^2\psi + \gamma|E_t|^2 \sin[2(\theta_0 - \delta_0)] = 0$, the solution of which is given by $\psi(x, y, z) = n_2(\theta_0)g(x, y, z)$, with g the convolution between $|E_t|^2$ and the Green function G. Thus, the shape of the nonlinear photonic potential relates to the Green function G in the highly nonlocal limit. In the latter limit the nonlocality is fixed by G, i.e. it depends on the geometry of the NLC cell. The depth of the light-induced index well depends on the effective nonlocal Kerr coefficient [30]

$$n_2(\theta_0) = 2\gamma \sin[2(\theta_0 - \delta_0)] n_e^2(\theta_0) \tan\delta_0, \tag{9}$$

which is only a function of the initial angle θ_0, the refractive index $n_\perp$ and the anisotropy ϵ_a.

A similar approach leads to the walk-off change. After defining $c_\delta = d\delta_b/dP$, we can express it as [38]

$$c_\delta(\theta_0) = \frac{\sin[2(\theta_0 - \delta_0)]}{1 + \tan^2\delta_0} \frac{d\delta_0}{d\theta_0}. \tag{10}$$

Calculated n_2 and c_δ are plotted in Fig. 5 for a standard NLC (E7). Self-focusing, ruled by n_2, is maximum for $\theta_0 \approx \pi/4$ where the light torque is maximum, zero for $\theta_0 = 0$ (Freedericksz threshold) and $\theta_0 = \pi/2$ (no torque). The function c_δ depends on the interplay between the field-dipole torque and the derivative of δ with respect to θ. The net results is that self-steering is zero for $\theta_0 \approx \pi/4$, whereas it is positive for $0 < \theta_0 < \pi/4$ and negative for $\pi/4 < \theta < \pi/2$; c_δ is zero in $\theta_0 = 0$ and $\theta_0 = \pi/2$ owing to the lack of reorientation at those angles. Noteworthy, the perturbative regime is limited by the size of c_δ: the larger c_δ is for a given θ_0, the sooner the highly nonlinear regime needs to be considered.

[3] Hereby we ignore wavevector deflections associated with asymmetric boundary conditions.

4.2 Highly Nonlinear Regime

When the power is large enough, the approximation $\theta \approx \theta_0$ is no longer valid and the nematicon trajectory depends on power via variations of δ_b. The linearization of Eq. (7) becomes inaccurate as the nonlinear response takes a saturating character, with nonlinear effects drastically reducing for angles θ_b approaching $\pi/2$. It is important to underline that the nonlocality, in the highly nonlocal limit, is not affected by saturation. In fact, from the reorientational equation we can write (the vector $\boldsymbol{r}_b$ follows the nematicon trajectory) [38]

$$\psi(x, y, z, P) \approx \frac{2Z_0\gamma}{n_b \cos^2 \delta_b} G(\boldsymbol{r}_b) \int_0^P \sin\{2[\theta_0 + \psi_b - \delta_b]\} dP. \tag{11}$$

Equation (11) is not valid by the beam peak due to the divergence of G; from the accessible soliton model, in this region ψ has a parabolic profile with curvature stemming from the conditions of continuity and derivability of ψ. Despite these limitations, we see that saturation affects the amplitude of the perturbation ψ_b [from Eq. (11)] but not its profile.

5 Profile-Preserving Nematicons

The system of Eqs. (7–8) models light self-focusing in NLC. First, we look for solitary waves when the NLC is homogeneous in the absence of a beam (i.e., θ_0 has the same value everywhere), using the ansatz $\psi = \psi_s(x, y - \tan\delta_b z)$ and $A = A_s(x, y - \tan\delta_b z) \exp(jk_0 n_{NL} z)$, with δ_b a constant depending on input power. At variance with Sect. 3, we now fix the phase-front (planes normal to $\hat{z}$) and let the director free to rotate in the plane yz, such rotation leading to a varying walk-off. We have to solve the nonlinear eigenvalue problem

$$2n_{NL} n_b k_0^2 A_s = \frac{\partial^2 A_s}{\partial x^2} + D\frac{\partial^2 A_s}{\partial y^2} + k_0^2 \Delta n_e^2 A_s, \tag{12}$$

$$\left(1 + \tan^2 \delta_b\right) \frac{\partial^2 \psi_s}{\partial y^2} + \frac{\partial^2 \psi_s}{\partial x^2} + \kappa^2 \gamma \sin\left[2(\theta_0 + \psi_b - \delta_b)\right] |A_s|^2 = 0, \tag{13}$$

with $\kappa = Z_0/(n_b \cos\delta_b)$. The solution of the two coupled equations (12–13) for a given input power consists in the profiles ψ_s and A_s, with the scalar δ_b which determines the soliton trajectory along propagation. Here we focus on lowest-order bright solitons, i.e., bell-shaped solutions. We consider planar cells, i.e. a slab of NLC infinitely extended along y and z, but with finite thickness L along x (the cell mid-plane is chosen in $x = 0$). To avoid repulsive effects due to the boundaries (where molecules are anchored), we restrict to beams propagating in the mid-plane

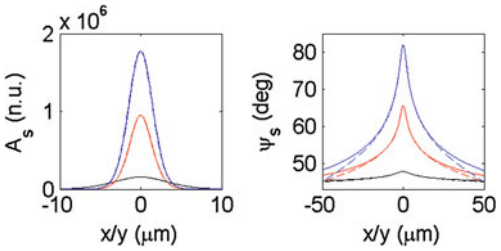

Fig. 6 Transverse profile of A_s (*left*) and ψ_s (*right*). $\theta_0 = \pi/4$ when the input powers are $P = 1.8$ mW (*bottom black lines*), 12 mW (*middle red lines*) and 47 mW (*top blue lines*). *Dashed* and *solid lines* correspond to profiles versus x and y, respectively

$x = 0$ [24]. In this case, taking the peak of the intensity profile in $y = \tan\delta_b z$, it is $\delta_b = \delta(\theta_b)$.

We solved numerically the system (12–13) using typical experimental conditions, setting $n_\parallel = 1.7$, $n_\perp = 1.5$ (indices corresponding to the NLC E7 in the near infrared), $L = 100\,\mu$m and $\lambda = 1064$ nm (both L and λ will be kept constant in the following). The computed A_s and ψ_s are graphed in Fig. 6. For every excitation, ψ_s is affected by the boundaries in the tails of the distribution, with a cylindrically symmetric curvature around the beam center. Away from the beam, ψ_s closely follows the Green function for the Poisson equation in the given geometry, confirming that w_ψ is nearly equal to L. The corresponding profiles A_s are symmetric for waists w small compared to L, with transverse shape closely resembling a Gaussian function, in agreement with the accessible soliton theory [43]. Small anisotropies arise only for large waists or small powers, when the confinement is weaker. These results demonstrate that the asymmetry stemming from D is negligible for typical anisotropies ϵ_a.

Due to the nonlocal and saturating character of Eq. (13), we expect that nematicon properties versus power strongly depend on the rest orientation of the director. Numerical results, plotted in Fig. 7 versus the initial director angle θ_0 and input power P, confirm the prediction. Clearly, the peak in reorientation θ_b always increases with P, but with a rate proportional to the light-dipole torque: in fact, the density of the isolines in Fig. 7 is higher for θ_b close to $\pi/4$, the latter corresponding to the maximum torque according to Eq. (13). It is also apparent that saturation of the nonlinearity versus P begins at lower excitations for larger θ_0. The behavior of θ_b and the dependence of n_e from θ (see Fig. 2) imply a monotonic growth of n_{NL} versus P, therefore ensuring nematicon stability on the basis of the Vakhitov-Kolokolov criterion [7]. The walk-off experienced by the nematicon depends on θ_b as in Fig. 2. Since the walk-off is maximum for θ_b close to $\pi/4$ (see Fig. 2),[4] in Fig. 7 (middle panel) the locus of maximum walk-off is a quasi-straight line starting from $(P = 0\,\text{mW}, \theta_0 = 45^\circ)$ and ending in $(P = 16\,\text{mW}, \theta_0 = 15^\circ)$. Below (above) the straight line the walk-off increases (decreases), in agreement with the behavior of c_δ in Fig. 2. Hence, the walk-off δ_b versus P has a local

[4] This is true for the given anisotropy; see [50] for a complete discussion on the role played by the anisotropy ϵ_a on nematicon properties.

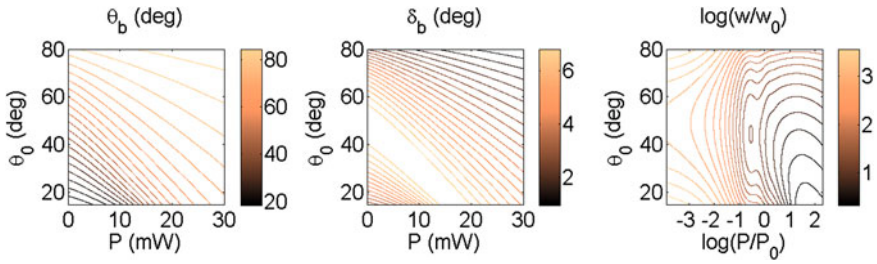

Fig. 7 Contour plots of θ_b (*left*) and the corresponding δ_b (*middle*) versus nematicon power P and the initial director orientation θ_0. *Right* Contour plots of $\log(w/w_0)$ versus $\log(P/P_0)$ and θ_0; here $P_0 = 5$ mW and $w_0 = 1\,\mu$m

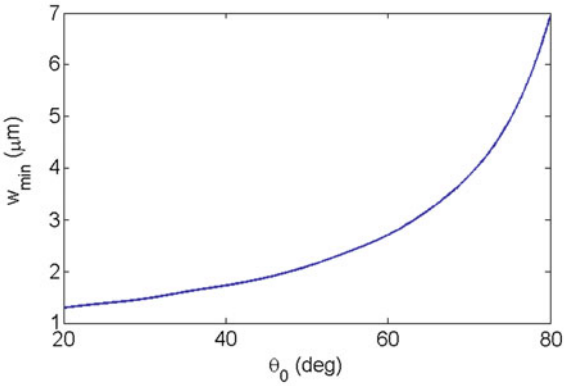

Fig. 8 Minimum nematicon waist calculated for each θ_0. For small θ_0 the waist tends to the minimum set by the wavelength

maximum for $\theta_0 < \pi/4$, whereas for larger θ_0 the Poynting vector monotonically relaxes towards $\mathbf{k}//\hat{z}$ for increasing P [49].

Another important quantity is the nematicon waist w: in Fig. 7 we can see that the nematicon size is symmetric with respect to $\theta_0 \approx \pi/4$ for powers up to 5 mW, as expected based on the plot of $n_2(\theta_0)$ (Fig. 2), whereas for larger excitations the plot develops a strong asymmetry. This is connected with the transition from perturbative to highly nonlinear regimes, as detailed in Sect. 4.2. Figure 8 graphs the minimum soliton waist (versus input power) for each fixed θ_0: the highly nonlinear regime breaks the symmetry around $\theta_0 \approx \pi/4$.

6 Breathing Nematicons

In Sect. 5 we discussed profile-preserving nematicons and their properties. As well known, the family of self-trapped waves in highly nonlocal media comprises breathing solitons, i.e., self-localized structures undergoing periodic oscillation in

waist, in full analogy with linear propagation in a parabolic index well. In fact, the existence curve for invariant nematicons is of the form $P = \text{const} \times w^{-2}$ [43, 48]: parameter pairs $w-$P not satisfying the existence relation give rise to breathing solitons, widening or narrowing by the input region for parameters below or above the existence curve in the plane $P-$w, respectively.

We analyze breathing solutions studying light propagation when Gaussian beams with various waists and powers are launched into NLC. This strictly relates to typical experimental conditions, when TEM_{00} laser beams are coupled into an NLC sample.

6.1 Simplified (1 + 1)D Model

The numerical simulations of the system of Eqs. (7–8) require considerable computer effort. A substantial simplification can be achieved with the ansatz $\psi(x,y,z) = \psi_{2D}(y,z)\cos\left(\frac{\pi x}{L}\right)$, providing [30]

$$2jk_0 n_b\left(\frac{\partial A}{\partial z} + \tan\delta_b \frac{\partial A}{\partial y}\right) + D\frac{\partial^2 A}{\partial y^2} + k_0^2 \Delta n_e^2 A = 0, \tag{14}$$

$$\nabla_{yz}^2 \psi_{2D} - \left(\frac{\pi}{L}\right)^2 \psi_{2D} + \kappa^2 \gamma \sin[2(\theta_0 + \psi_{2D} - \delta_b)]|A|^2 = 0. \tag{15}$$

Equations (14–15) govern light beam propagation in the mid-plane $x = 0$ when neglecting the dynamics across x, i.e., they form a (1 + 1)D model. Noticeably, Eq. (15) is a Yukawa equation with a screening term given by L, i.e. the nonlocality is correctly accounted for. Equation (15) includes nonlocal effects along $\hat{z}$ by retaining the term $\partial_z^2 \psi_{2D}$, previously neglected in most of the models on nematicons [42, 51–53]. In the (1 + 1)D approximation, the beam power in Eqs. (14–15) is underestimated with respect to the full 3D case; otherwise stated, light self-localization can be obtained at powers much lower than in a 3D analysis [30].

The inclusion of the elastic forces along z permits to correctly model important effects: self-steering due to nonlinear changes in walk-off, the smoothing action of nonlocality along z, the attenuation due to the unavoidable scattering losses. Concerning self-steering, the solution of the reorientational equation (15) does not need the *a priori* knowledge of the nematicon propagation angle, which varies with power as demonstrated in Sect. 5. The averaging/smoothing along z plays an important role in the computation of the waist since, according to a model local along z, the curvature of the nonlinear index well should be proportional to the intensity peak [48]; the effect would be a fast z-varying nonlinear photonic potential, which is unphysical. Finally, when propagating in NLC, light undergoes scattering losses due to the size of the molecules [45] (of the order of $0.5\,\text{cm}^{-1}$ in the infrared region), with a consequent change in the strength of the nonlinear response and, in turn, a non negligible $\partial_z^2 \psi$.

6.2 Lossless Limit

In this subsection we show numerical solutions of the system (14–15) when a Gaussian beam of the form $A(y, z = 0) = \sqrt{4Z_0P/(\kappa^2\pi n_b w_{in}^2)}\exp\left(-y^2/w_{in}^2\right)$ is launched in a planar homogeneous NLC cell. In the simulations we kept the input waist w_{in} fixed to 5 μm. The numerical code is based on a Crank-Nicolson beam propagation method and standard relaxation algorithms for the computation of light propagation and director distribution, respectively. Consistent combined solutions are pursued by alternatively launching the two numerical procedures until convergence is achieved.

Figure 9a–f shows the beam evolution in the plane yz for three input powers and $\theta_0 = \pi/4$, the latter maximizing self-focusing. The size of the numerical grid in the y-direction was much larger than $2L$ in order to avoid spurious effects from the boundaries. The thickness L was 100 μm and the wavelength 1064 nm: both these values were kept constant. At the input ($z = 0$) and output sections ($z = 1.5$ mm) we assumed strong anchoring by imposing $\theta = \theta_0$.

In the linear regime ($P = 50\,\mu$W) the beam diffracts while propagating at the linear walk-off angle δ_0, with a Rayleigh distance $L_R = \pi n_e(\theta_0)w_{in}^2/(D\lambda)$ [50] (see Fig. 9a). As power increases, self-focusing counteracts diffraction, reducing the spreading as compared with the linear case. For further increase in power, the waist versus z begins to decrease, i.e., a breathing nematicon is formed (see Fig. 9b). As excitation keeps increasing, both the period and the amplitude of the breathing diminish (Fig. 9c), reaching a quasi-stationary behavior versus z for

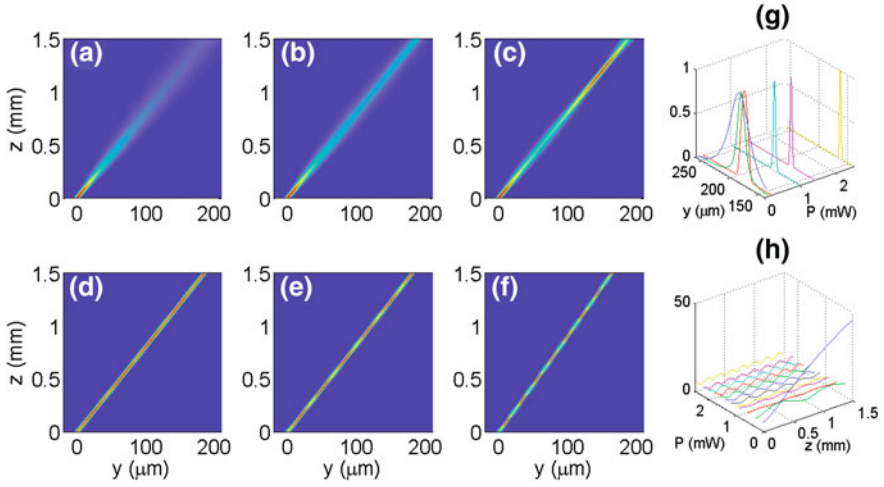

Fig. 9 Nematicon evolution in yz for $P = 50\,\mu$W (**a**), 100 μW (**b**), 200 μW (**c**), 1 mW (**d**), 1.4 mW (**e**) and 2.5 mW (**f**). **g** Beam profile computed at the output section $z = 1.5$ mm versus y for the same set of powers used in **a**–**f**; the fields are normalized with respect to their own peak value. **h** Nematicon waist (in microns) versus z and P

$P = 1$ mW (Fig. 9d). Up to this excitation the walk-off is nearly unperturbed, as seen in the output field profile in Fig. 9g. Consistently with the results in Sect. 5, the variations in beam profile along z are minimized for a power depending on θ_0, corresponding to the profile invariant nematicon for the waist w_{in}. Note that a truly stationary nematicon can never be obtained as we launched a Gaussian beam, not matching the exact nematicon solution (Sect. 5). For still higher powers (Fig. 9e–f) the waist resumes oscillating with period and amplitude monotonically growing versus excitation P. The trend in waist is summarized in Fig. 9h. We pinpoint that, in the initial stage of propagation, the beam widens (narrows) if the input power is smaller (larger) than the stationary value, respectively, due to the interplay of self-focusing and diffractive spreading. At all powers nematicons propagate in a straight line, in a direction corresponding to the power-dependent walk-off. In particular, the walk-off in the considered range of powers and for the given θ_0 reduces, as visible by the shift of the beam output profile versus y, see Fig. 9g.

The profiles of the corresponding reorientation angle θ are shown in Fig. 10a–f. The perturbation follows the beam profile, with the peaks of the field and of ψ perfectly overlapping (i.e. no deflections due to gradients in the refractive index well). Figure 10g shows θ_b versus z: the oscillations in reorientation are strongly damped by the nonlocality along z and the nematicon breathing remains almost periodic, at variance with local models predicting strongly aperiodic oscillations at high powers [54]. Finally, Fig. 10 graphs the transverse profile of ψ: the shape is consistent with the full 3D model (Sect. 5), confirming that the (1 + 1)D model encompasses the correct amount of nonlocality.

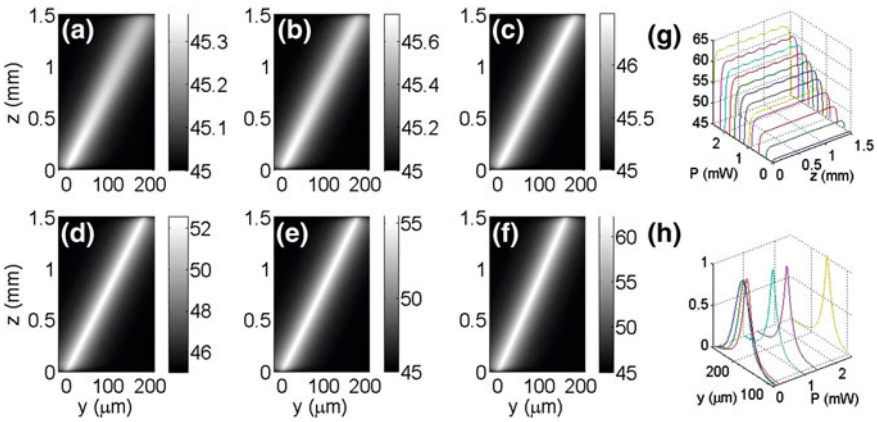

Fig. 10 Distribution of θ (measured in degrees) in the plane yz for $P = 50\,\mu$W (**a**), 100 μW (**b**), 200 μW (**c**), 1 mW (**d**), 1.4 mW (**e**) and 2.5 mW (**f**), respectively. **g** Maximum director orientation θ_b (in degrees) versus z for various powers P. **h** Transverse profile of ψ in the section $z = 1.45$ mm versus y for the same set of powers used in **a**–**f**; the functions are normalized to their own peak value

6.3 Lossy Case

We now turn our attention to the more realistic case of a medium with scattering losses, accounted for in Eq. (14). As shown in Ref. [30], the inclusion of losses in the theoretical description of nematicons is essential in order to accurately describe the experimental results. We assume an attenuation coefficient $\alpha \approx 5\,\mathrm{cm}^{-1}$ (power drops as $\exp(-2\alpha z)$); such value is realistic with reference to near-infrared scattering in the NLC E7. Typical beam profiles and corresponding distribution of the director orientation are plotted in Fig. 11 for $w_{in} = 5\,\mu\mathrm{m}$.

In the linear regime (Fig. 11a) the beam diffracts as the nonlinear index well is negligible (Fig. 11d), with its power decreases in propagation. As power increases (Fig. 11a, e) the beam self-confines, even if its average amplitude attenuates with z. The beam trajectory bends because the amount of self-steering varies along z owing to power attenuation and the consequent drop in field-dipole torque. The sign of the curvature depends on the rest angle θ_0 via the coefficient c_δ [Eq. (10)], as confirmed by a direct comparison between panels (e) and (f) of Fig. 11. It can also been appreciated how self-confinement is much stronger for $\theta_0 = 50°$ than for $\theta_0 = 10°$ [see Eq. (9)], resulting in a more gradual reduction of the maximum perturbation ψ_b thanks to the stronger localization. When the power in a given section is too low, diffraction prevails over self-focusing. For the same reason, for large enough z the nematicon walk-off is the linear value δ_0, regardless the excitation. Summarizing, the losses make the beam evolution more involved due to the continuous variation of local power versus z.

Figure 12 plots the beam waist versus z for various excitations and θ_0. With respect to the case of no losses (Fig. 9), breathing is in general aperiodic due to the

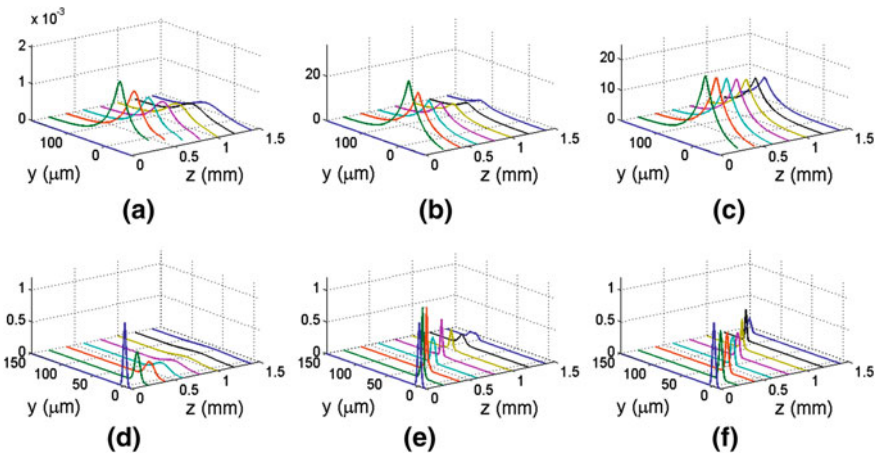

Fig. 11 **a–c** Perturbation ψ (measured in degrees) and **d–f** beam intensity profile $|A|^2$ (normalized to the peak at the input) in the plane yz, for $P = 1\,\mu\mathrm{W}$ and $\theta_0 = 10°$ (**a**, **d**), $P = 5$ mW and $\theta_0 = 10°$ (**b**, **e**), $P = 5$ mW and $\theta_0 = 50°$ (**c**, **f**), respectively

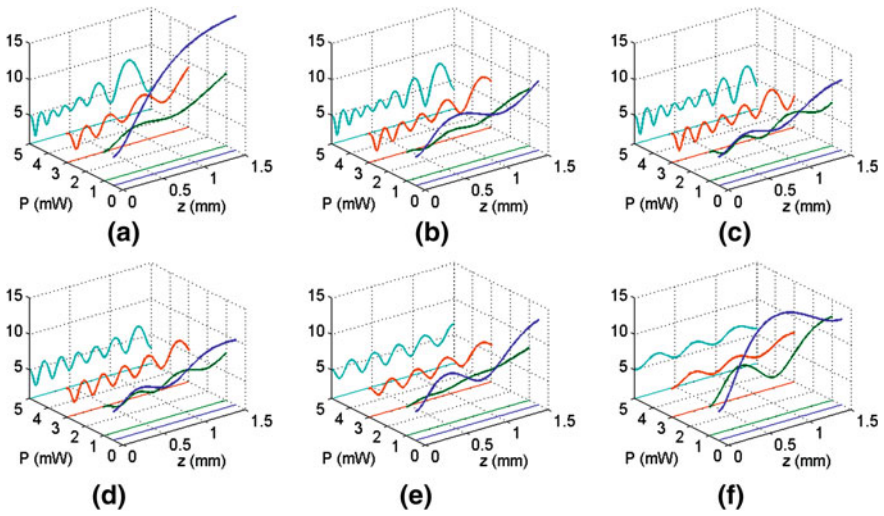

Fig. 12 Nematicon waist versus z for $\theta_0 = 20°$ (**a**), 30° (**b**), 40° (**c**), 50° (**d**), 60° (**e**) and 70° (**f**). Here the input powers are 0.5, 1, 3 and 5 mW, from *navy blue* to *light blue*, respectively

dynamics stemming from a continuous transition between lossless solutions at each power versus propagation distance. Self-trapping is stronger for θ_0 close to $\pi/4$, in agreement with Eq. (9). The results for initial angles θ_0 equally distant from $\pi/4$ show comparable nematicon properties at low powers, whereas at high powers a strong discrepancy appears as the system evolves from the perturbative to the highly nonlinear regimes.

Figure 13 shows power-dependent changes in nematicon trajectory $\Delta y_b = y_b(z,P) - z\tan\delta_0$, with $y_b(z) \equiv \int y|A|^2 dy / \int |A|^2 dy$. Δy_b follows Eq. (10) and approaches a constant value for large propagation distances, i.e., when ψ_b goes to zero. Interestingly, the variations of Δy_b are monotonic with power except for $\theta_0 = 30°$ and $\theta_0 = 40°$. In these latter cases the system is in the highly nonlinear regime as the reorientation is large enough to reach $\theta_b = 45°$, where $d\delta/d\theta$ changes sign.

To conclude, Fig. 14a plots the breathing period Ω versus θ_0 for $P = 0.8$ mW. Due to the breathing aperiodicity, we approximate $\Omega/4$ with the distance of the waist first maximum from the input. In agreement with the theory, the larger n_2 the shorter Ω is. To quantify self-trapping for fixed θ_0 and P we introduce the average waist $\overline{w} = (1/L_z)\int_0^{L_z} w(z')dz'$ with $L_z = 1.5$ mm. Figure 14b shows the computed $\overline{w}$. At small excitations $\overline{w}$ varies with θ_0 owing to the different diffraction D, the latter larger (smaller) for θ_0 closer to $\pi/2$ (0) [50]. Up to $P = 1.5$ mW, the plot is nearly symmetric with respect to $\theta_0 = \pi/4$ as the system is in the perturbative regime. For larger powers, self-trapping becomes much stronger for small θ_0 due to saturation close to $\pi/2$.

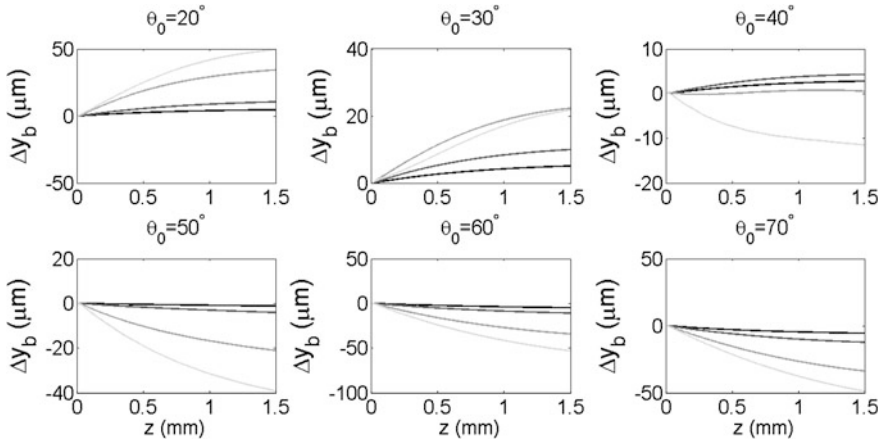

Fig. 13 Nonlinear changes in nematicon trajectory Δy_b with respect to the linear case for various θ_0. The input powers are 0.5, 1, 3 and 5 mW, from the *darkest* to the *lightest line*, respectively

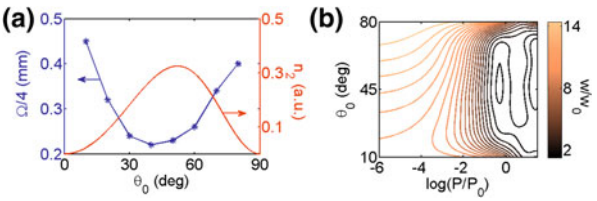

Fig. 14 **a** $\Omega/4$ versus θ_0 for $P = 0.8$ mW; n_2 versus θ_0 is also plotted for a direct comparison. **b** Normalized average waist $\overline{w}/w_{in}$ versus $\log(P/P_0)$ and θ_0. Here $P_0 = 1$ mW and $w_{in} = 5\,\mu$m

7 Conclusions

We discussed light self-trapping in nonlinear uniaxials. We demonstrated that spatial solitons in general self-steer as power changes, owing to a power-dependence in walk-off; the latter is clearly more appreciable in the highly nonlinear regime. We specialized the study to the case of reorientational nonlinearity in nematic liquid crystals featured by a high nonlinearity: hence, they are ideal candidates for investigating highly-nonlinear effects. We showed that nematic liquid crystals exhibit a nonlocal response to a degree determined by the confinement geometry. In typical experimental conditions where the sample is much larger than the beam profile, light propagates according to the highly nonlocal limit. We discussed and derived expressions of both profile-invariant and breathing nematicons, in the perturbative and highly nonlinear regimes, respectively, detailing their behavior in terms of waist and trajectory versus input beam and sample parameters. Finally, we demonstrated that nematicon trajectories evolve from straight to bent owing to scattering losses, the latter responsible for decay in nonlinear response versus propagation.

The results presented in this work demonstrate how, in anisotropic media, parity symmetry is broken as photon properties depend on their spin (i.e., field polarization); in particular, symmetry breaking depends on excitation in the highly nonlinear regime.

References

1. T.H. Maiman, Nature **187**, 493 (1960)
2. Y.R. Shen, *The Principle of Nonlinear Optics* (Wiley, New York, 2002)
3. G.I. Stegeman, R.A. Stegeman, *Nonlinear Optics* (Wiley, New York, 2012)
4. P.L. Kelley, Phys. Rev. Lett. **15**(26), 1005 (1965)
5. R.Y. Chiao, E. Garmire, C.H. Townes, Phys. Rev. Lett. **13**(15), 479 (1964)
6. G.I. Stegeman, M. Segev, Science **286**(5444), 1518 (1999)
7. Y.S. Kivshar, G.P. Agrawal, *Optical Solitons* (Academic, San Diego, 2003)
8. A. Yariv, P. Yeh (eds.), *Optical Waves in Crystals: Propagation and Control of Laser Radiation* (Wiley, Hoboken, 2003)
9. G.C. Duree, J.L. Shultz, G.J. Salamo, M. Segev, A. Yariv, B. Crosignani, P. Di Porto, E.J. Sharp, R.R. Neurgaonkar, Phys. Rev. Lett. **71**(4), 533 (1993)
10. W.E. Torruellas, Z. Wang, D.J. Hagan, E.W. Van Stryland, G.I. Stegeman, L. Torner, C.R. Menyuk, Phys. Rev. Lett. **74**(25), 5036 (1995)
11. R. Schiek, Y. Baek, G.I. Stegeman, Phys. Rev. E **53**, 1138 (1996)
12. W.E. Torruellas, G. Assanto, B.L. Lawrence, R.A. Fuerst, G.I. Stegeman, Appl. Phys. Lett. **68**(11), 1449 (1996)
13. E. Braun, L.P. Faucheux, A. Libchaber, Phys. Rev. A **48**(1), 611 (1993)
14. G. Assanto, A. Fratalocchi, M. Peccianti, Opt. Express **15**(8), 5248 (2007)
15. M. Peccianti, G. Assanto, Phys. Rep. **516**, 147 (2012)
16. A.E. Kaplan, JETP Letters **9**, 33 (1969)
17. A.T. Ryan, G.P. Agrawal, Opt. Lett. **18**, 1795 (1993)
18. A. Barak, O. Peleg, C. Stucchio, A. Soffer, M. Segev, Phys. Rev. Lett. **100**(15), 153901 (2008)
19. A. Barak, O. Peleg, A. Soffer, M. Segev, Opt. Lett. **33**(16), 1798 (2008)
20. B. Alfassi, C. Rotschild, O. Manela, M. Segev, D.N. Christodoulides, Opt. Lett. **32**, 154 (2006)
21. F. Ye, Y.V. Kartashov, B. Hu, L. Torner, Opt. Lett. **34**(17), 2658 (2009)
22. J. Petter, C. Weilnau, C. Denz, A. Stepken, F. Kaiser, Opt. Commun. **170**, 291 (1999)
23. M. Peccianti, A. Dyadyusha, M. Kaczmarek, G. Assanto, Phys. Rev. Lett. **101**(15), 153902 (2008)
24. A. Alberucci, M. Peccianti, G. Assanto, Opt. Lett. **32**(19), 2795 (2007)
25. G.A. Siviloglou, J. Broky, A. Dogariu, D.N. Christodoulides, Phys. Rev. Lett. **99**, 213901 (2007)
26. S. Jia, J. Lee, J.W. Fleischer, G.A. Siviloglou, D.N. Christodoulides, Phys. Rev. Lett. **104**, 253904 (2010)
27. I. Kaminer, M. Segev, D.N. Christodoulides, Phys. Rev. Lett. **106**, 213903 (2011)
28. P. Zhang, Y. Hu, D. Cannan, A. Salandrino, T. Li, R. Morandotti, X. Zhang, Z. Chen, Opt. Lett. **37**(14), 2820 (2012)
29. I. Kaminer, R. Bekenstein, J. Nemirovsky, M. Segev, Phys. Rev. Lett. **108**, 163901 (2012)
30. A. Alberucci, A. Piccardi, M. Peccianti, M. Kaczmarek, G. Assanto, Phys. Rev. A **82**(2), 023806 (2010)
31. M. Kwasny, A. Piccardi, A. Alberucci, M. Peccianti, M. Kaczmarek, M.A. Karpierz, G. Assanto, Opt. Lett. **36**(13), 2566 (2011)

32. A. Alberucci, G. Assanto, Opt. Lett. **36**(2), 193 (2011)
33. A. Alberucci, G. Assanto, Opt. Lett. **36**(3), 334 (2011)
34. A. Alberucci, G. Assanto, Phys. Rev. A **83**, 033822 (2011)
35. D.N. Christodoulides, T.H. Coskun, Opt. Lett. **21**(16), 1220 (1996)
36. A. Piccardi, A. Alberucci, G. Assanto, Phys. Rev. Lett. **104**, 213904 (2010)
37. A. Piccardi, A. Alberucci, G. Assanto, Mol. Cryst. Liq. Cryst. **549**(1), 1 (2011)
38. A. Piccardi, A. Alberucci, G. Assanto, J. Opt. Soc. Am. B **27**, 2398 (2010)
39. O. Bang, W. Krolikowski, J. Wyller, J.J. Rasmussen, Phys. Rev. E **66**, 046619 (2002)
40. W. Krolikowski, B. Luther-Davies, C. Denz, J. Quantum Electron. **39**, 3 (2003)
41. C. Rotschild, B. Alfassi, O. Cohen, M. Segev, Nat. Phys. **2**, 769 (2006)
42. C. Conti, M. Peccianti, G. Assanto, Phys. Rev. Lett. **91**, 073901 (2003)
43. A.W. Snyder, D.J. Mitchell, Science **276**, 1538 (1997)
44. F. Simoni, *Nonlinear Optical Properties of Liquid Crystals* (World Scientific, Singapore, 1997)
45. I.C. Khoo, *Liquid Crystals: Physical Properties and Nonlinear Optical Phenomena* (Wiley, New York, 1995)
46. M. Peccianti, A.D. Rossi, G. Assanto, A. De Luca, C. Umeton, I.C. Khoo, Appl. Phys. Lett. **77**(1), 7 (2000)
47. I.C. Khoo, Phys. Rep. **471**, 221 (2009)
48. C. Conti, M. Peccianti, G. Assanto, Phys. Rev. Lett. **92**, 113902 (2004)
49. A. Alberucci, G. Assanto, Opt. Lett. **35**(15), 2520 (2010)
50. A. Piccardi, M. Trotta, M. Kwasny, A. Alberucci, R. Asquini, M. Karpierz, A. D'Alessandro, G. Assanto, Appl. Phys. B **104**(4), 805 (2011)
51. C. Conti, M. Peccianti, G. Assanto, Phys. Rev. E **72**, 066614 (2005)
52. S. Ouyang, Q. Guo, W. Hu, Phys. Rev. E **74**(3), 036622 (2006)
53. G. Assanto, A.A. Minzoni, N.F. Smyth, J. Nonlinear Opt. Phys. Mat. **18**, 657 (2009)
54. A. Alberucci, G. Assanto, J. Nonlinear Opt. Phys. Mat. **16**(3), 295 (2007)

Frequency and Phase Locking of Laser Cavity Solitons

T. Ackemann, Y. Noblet, P. V. Paulau, C. McIntyre, P. Colet, W. J. Firth and G. -L. Oppo

Abstract Self-localized states or dissipative solitons have the freedom of translation in systems with a homogeneous background. When compared to cavity solitons in coherently driven nonlinear optical systems, laser cavity solitons have the additional freedom of the optical phase. We explore the consequences of this additional Goldstone mode and analyze experimentally and numerically frequency and phase locking of laser cavity solitons in a vertical-cavity surface-emitting laser with

T. Ackemann (✉) · Y. Noblet · C. McIntyre ·
W. J. Firth · G.-L. Oppo
SUPA and Department of Physics, University of Strathclyde,
Glasgow, Scotland, G4 0NG, UK
e-mail: thorsten.ackemann@strath.ac.uk

Y. Noblet
e-mail: yoann.noblet@strath.ac.uk

C. McIntyre
e-mail: craig.mcintyre@strath.ac.uk

W. J. Firth
e-mail: willie@phys.strath.ac.uk

G.-L. Oppo
e-mail: g.l.oppo@strath.ac.uk

P. V. Paulau
TU Berlin, Institut für Theoretische Physik, Hardenbergstr.
36, Sekr EW 7-1, 10623 Berlin, Deutschland
e-mail: pavel.paulau@tu-berlin.de

P. Colet
IFISC, (CSIC-UIB), Campus Universitat Illes Balears,
E-07071 Palma de Mallorca, Spain
e-mail: pere@ifisc.uib-csic.es

Progress Optical Sci., Photonics (2013): 49–87
DOI: 10.1007/10091_2012_16

Published Online: 18 September 2012

frequency-selective feedback. Due to growth-related variations of the cavity resonance, the translational symmetry is usually broken in real devices. Pinning to different defects means that separate laser cavity solitons have different frequencies and are mutually incoherent. If two solitons are close to each other, however, their interaction leads to synchronization due to phase and frequency locking with strong similarities to the Adler-scenario of coupled oscillators.

1 Introduction

Lasers are a prominent example for self-sustained nonlinear oscillators. The phase of the oscillation of the electromagnetic field is not determined but results from the spontaneous breaking of the time symmetry present for cw pumping. Hence, the phase is a Goldstone mode of the dynamics and couples easily to perturbations, such as, for example, spontaneous emission. As a result of the induced 'phase diffusion' [1], a laser has a finite linewidth (Schalow–Townes limit) and the mutual coherence between two independent lasers will be limited even if they have the same center frequency. Hence a lot of attention has been given to the phenomena of *frequency and phase locking*, by which coupled lasers can synchronize their frequency and phases to achieve coherent emission [2–5]. Laser synchronization is just a special example of synchronization dynamics of coupled oscillators, which is of high importance in all fields of Nonlinear Science [6, 7], the earliest example being the famous observation made by Christiaan Huygens on two pendulum clocks. A very well known biological example involving a large number of oscillators is the synchronized flashing of fireflies [6, 7].

In photonics, frequency and phase locking has particular relevance for laser injection [8, 9] and in laser arrays where it can establish coherence between individual emitters even in the presence of disorder [10–12], i.e. an unintentional variation of the frequencies of the free-running emitters forming the array. Phase-locking of disorder-induced localized modes was observed in microchip lasers [13]. Synchronization of chaotic lasers has promises for secure communication [14–17].

One other object of fundamental importance in different areas of Nonlinear Science is the soliton [18–20], i.e. a nonlinearly self-localized state in one or more dimensions in a conservative or dissipative system. As a self-localized state it can exist anywhere in a translationally invariant system. Hence, laser solitons [21, 22] have the freedom of translation in an ideally homogeneous system typical of solitary waves as well as the freedom to choose the oscillation phase typical of lasers. Both are Goldstone modes of the dynamics. Their interplay involves aspects of synchronization dynamics and of soliton interaction. Dissipative solitons in coherently driven optical systems [23] (Fig. 1a)—i.e. without the phase degree of freedom—display a peculiar interaction behavior with a set of bound states with different, discrete distances between constituents [24–27], which is also typical of many non-optical systems [28], and is related to modulated tails of the solitons.

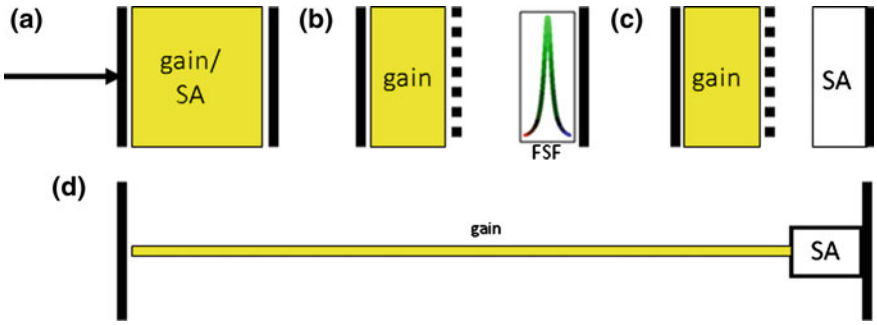

Fig. 1 Optical schemes displaying dissipative solitons. Panels **a**–**c** illustrate different schemes for spatial solitons where the gain cavity is short to achieve a high Fresnel number or aspect ratio (ideally single longitudinal mode, for simplicity and the validity of an uniform field approximation), whereas scheme **d** illustrates a scheme for temporal solitons as, e.g., a fiber laser, where the cavity is long and highly multi-longitudinal mode. *SA* saturable absorber, *FSF* frequency selective feedback, *thick black lines*: cavity mirrors, *dashed lines*: partial reflectors (in scheme **c** the partial reflector is not mandatory but present in many experimental realizations). In panel **a**, illustrating an amplifier (or a driven passive cavity), the phase symmetry is broken due to an external coherent field

Propagation solitons in conservative system like the Nonlinear Schrödinger equation show phase-sensitive interaction behavior (attraction for zero relative phase, repulsion for π relative phase) [18]. In the present case of a soliton laser, phase and location are both dynamical variables.

As a consequence of synchronization and interaction, phase-locked bound states with well defined phases and distances of the constituent laser solitons have been predicted to form in simple model systems like the cubic-quintic Ginzburg–Landau equation (CQGLE) [29–36]. These works concentrate on one-dimensional dissipative solitons being motivated by temporal solitons in mode-locked lasers (Fig. 1d). Indeed corresponding bound states were observed experimentally in fiber lasers [26, 37–39]. A recent review of these phenomena is in [40].

Until recently the spatial case had been addressed only theoretically in lasers with saturable absorbers (LSA) (Fig. 1c) [21, 41, 42]. Early experiments on solitons in LSA using dyes and photorefractives as gain medium were limited to one soliton due to specific cavity geometries [43–45]. Later investigations in a photorefractive oscillator found multiple spatial laser solitons but did not investigate the interaction and phase properties [46]. Recently, there has been strong progress in the realization of spatial laser solitons in semiconductor-based microresonators with frequency-selective feedback [47–52] and saturable absorption [42, 53–56]. In these systems, a broad transverse area (transverse indicates the plane orthogonal to the cavity axis) is pumped in a marginally stable plano-planar cavity. Emission does not take place over the whole aperture but on filaments which are much smaller than the pumped aperture. These filaments are dissipative solitons. We will refer to them as laser cavity solitons (LCS) and to the device as a cavity soliton laser (CSL). Recent reviews are in [57, 58].

LCS represent small coherent emitters, i.e. microlasers [47, 49]. Spatially separated LCS are usually found to be incoherent in experiments [49, 59]. This is due to uncontrolled fluctuations in the expitaxial growth process, which cause a variation of resonance conditions across the pumped aperture of the device. Since translation is a Goldstone mode of a soliton, it will couple to all spatially inhomogeneous perturbations and the soliton will move until it reaches a local extremum of the perturbation, where the gradient vanishes [60, 61]. This leads first to a pinning of the solitons at certain positions generally referred as either traps or defects. This was investigated in detail in coherently driven semiconductor microcavities [62, 63] (Fig. 1a). More recently, frequency-selective feedback (Fig. 1b) to a laser device was shown to provide simple means for mapping these variations [64].

Background defects in lasers not only fix LCS position but also induce a shift in the LCS natural frequency. Recently it was shown that this diversity in natural frequencies among LCS pinned by defects is a critical ingredient in the description of their interaction and synchronization in real systems, leading to a scenario quite different from the CQGLE on a homogenous background [65]. Reference [65]—which we review and extend here—presents experimental and theoretical evidence that the interaction of spatial LCS in real lasers is governed by the archetypal Adler locking mechanism [66]. The Adler locking mechanism has relevance in biological clocks, chemical reactions, mechanical and electrical oscillators [6]. In optics frequency locking of the Adler type was first observed in lasers with injected signals [9] with more recent generalizations to coupled lasers [4], the spatio-temporal domain [67], quantum dot lasers [68] and frequency without phase locking [69].

We note that for temporal LCS, such as those arising in fiber lasers [26, 37, 38] and driven fiber cavities [70, 71], the effects of longitudinal inhomogeneities are washed out by the propagation dynamics along the cavity axis (see Fig. 1d). Thus every soliton sees the same material characteristics [72]. Hence, theoretical studies considering the interaction of identical LCS arising on a homogeneous background seem to be suitable for temporal LCS, but are not adequate to describe the dynamics of coupled spatial LCS. Temporal solitons would be affected by copropagating inhomogeneities [73, 74] which can be induced by modulating laser parameters [75–78]. These regular parameter modulations were shown to have a substantial effect on the phase-locked bound states but do not induce frequency detunings between solitons when these are assembling at the minima of the potential. Hence the relevance of frequency and phase locking and the Adler scenario was not addressed in these works.

The organization of this book chapter is as follow. In the next section, Sect. 2, we introduce the experimental system, a vertical-cavity surface-emitting laser (VCSEL) coupled to a volume Bragg grating (VBG) as a frequency-selective element (Fig. 1b). We review basic features and observations in this system and then provide evidence and a detailed analysis of frequency and phase locking. From a dynamical point of view, VCSELS can be considered as Class B lasers characterized by the fact that the dynamics can be described in terms of the

complex optical field and population inversion while the material dielectric polarization can be adiabatically eliminated. For a theoretical and numerical description of the system, we discuss in Sect. 3 a class B-laser model [52]. This model is simplified afterwards to a complex equation for the optical field alone, which is a Ginzburg–Landau equation with an additional linear filter (GLE-F) [79, 80] and provides the simplest framework to understand the observed dynamics. In Sect. 4 we study first the interaction of LCS on a homogeneous background in the GLE-F and find a close correspondence to the results predicted by the CQGLE. We will see that some of the LCS interaction properties on a homogeneous background are significantly modified in the class-B model that works for more realistic parameters. Then, in Sect. 5, we investigate the case of LCS interaction in the presence of inhomogeneities, describe the resulting Adler-synchronization for both models and compare the results to experiments. Section 6 provides then a final discussion and outlook.

2 Laser Cavity Solitons and Their Interactions in VCSELs with Feedback

2.1 Devices and Experimental Setup

A vertical-cavity surface-emitting laser (VCSEL) is a semiconductor laser in which the emission is in the direction of the epitaxial growth (see Fig. 2a). The VCSEL used for this experiment is similar to the ones described in more detail in [49, 81–83]. Three InGaAs quantum wells are serving as gain medium leading to emission in the 980 nm range. The quantum wells are surrounded by passive AlGaAs spacer layers with a total thickness of one wavelength. The cavity is closed by high reflectivity distributed Bragg reflectors (DBR) with 33 layers AlGaAs/GaAs on the top side (p-contact) and 22 layers on the bottom side (n-contact). The emission takes place through the n-doped Bragg reflector and through the transparent substrate. In this so-called bottom-emitting geometry a reasonable uniformity of carrier injection can be achieved over fairly large apertures [81, 82]. A 200 μm diameter circular oxide aperture provides optical and current guiding. This active diameter is much larger than the effective cavity length of about 1.2 μm. As a result, the VCSEL has a large Fresnel number allowing for the formation of many transverse cavity modes of fairly high order.

The laser has an emission wavelength around 975 nm at room temperature. Frequency-selective feedback is provided by an external volume Bragg grating (VBG). The VBG has a reflection peak at $\lambda_g = 981.1$ nm with a reflection bandwidth of 0.2 nm full-width half-maximum (FWHM). The VCSEL is tuned in temperature up to 70 °C so that the emission wavelength approaches the reflection peak of the VBG. At such a high temperature the free running laser has an infinite threshold and lasing only occurs because of the feedback from the VBG.

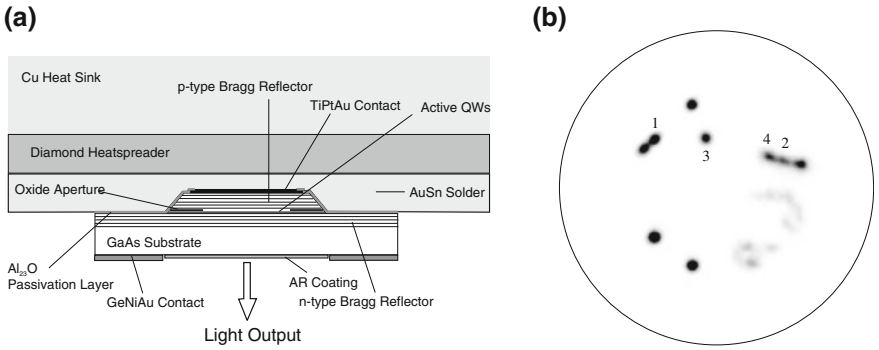

Fig. 2 **a** Schematic diagram of VCSEL layer structure (from [84]). **b** Near field image of the VCSEL aperture taken at 396 mA showing the relative position and numbering of a few solitons. Output VCSEL images, like all in the following, are in a linear gray scale with black denoting high intensity

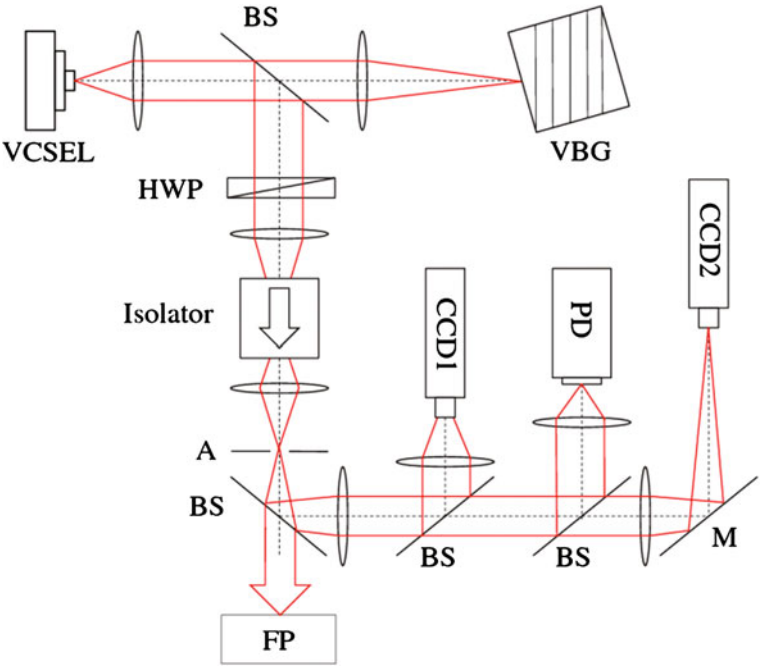

Fig. 3 Experimental setup. *VCSEL* Vertical-cavity surface-emitting laser, *BS* Beam splitter, *VBG* Volume Bragg grating, *HWP* Half wave plate, *A* Aperture, *M* Mirror, *PD* Photo diode, *CCD1* CCD camera in near field image plane of VCSEL, *CCD2* CCD camera in far field image plane of VCSEL, *FP* Fabry–Perot

A schematic diagram of the experimental setup is illustrated in Fig. 3. The VCSEL is coupled to the VBG via a self-imaging external cavity. Every point of the VCSEL is imaged at the same spatial position after each round trip therefore maintaining the high Fresnel number of the VCSEL cavity and ensuring local feedback compatible with self-localization.

The VCSEL is collimated by $f_1 = 8$ mm focal length plano-convex aspheric lens. The second lens is a $f_2 = 50$ mm focal length plano-convex lens and is used to focus the light onto the VBG. This telescope setup gives a 6.25:1 magnification factor onto the VBG. This cavity has a round trip frequency of 1.23 GHz which corresponds to a round trip time of 0.81 ns. The light is coupled out of the cavity using a glass plate (beam splitter with a front uncoated facet and a back anti-reflection coated facet). The reflection is relying on Fresnel reflection and therefore is polarization dependent. The reflectivity is on the order of 10 % for s-polarized light and 1 % for p-polarized light.

An optical isolator is used to prevent reflection from the detection system to pass into the external cavity. There are two charge-coupled-device (CCD) cameras used for detection, one is used to produce images of the VCSEL emission in the gain region (near field) and the other camera produces images of the Fourier plane of the gain region (far field). The optical spectrum is recorded with a scanning Fabry–Perot interferometer (FP). It has free spectral range (FSR) of 10 GHz and a maximal Finesse of 80. There is also a photodiode which measures the total laser power.

As it will be discussed in more detail in the following, the precise alignment of the VBG is very important. It is controlled by fine adjustment screws. The tilt β (see Fig. 4) in the horizontal direction can be fine-adjusted by a piezo-electric transducer (PZT), which is stabilized against drift by a servo-loop controlled by a strain gauge. A computer-controlled voltage U applied to the PZT leads to a tilt of $\delta\beta/\delta U = 2.1 \times 10^{-5}/\mathrm{V}$, a change of the external cavity length at a rate of $\delta L/\delta U = 0.628\,\mu\mathrm{m/V}$, and a change of the resonance frequency in the external cavity by $\delta\nu/\delta U = 1.576$ GHz/V. Perhaps even more importantly for what follows, there is also a differential shift for two LCS. If their distance projected onto a plane orthogonal to the rotation axis is Δx, this shift is

$$\Delta\nu = \Delta x \frac{2\nu_{FSR} \sin\beta}{\lambda}, \tag{1}$$

where ν_{FSR} is the free spectral range of the external cavity and λ the operating wavelength of the VCSEL. The change of the ray angle after returning to the VCSEL (corrected for the magnification of the telescope) is $\theta = \beta$ M.

The adjustment of the self-imaging condition is described in detail in [85]. The distance between the VCSEL and the collimating lens can be adjusted for best collimation, while the distance between the focusing lens and the VBG is selected by adjusting the images of the VCSEL emission at high current for maximum sharpness of the aperture. For the distance between the two lenses there is no simple alignment criterion, hence it needs to be set from the lens specifications

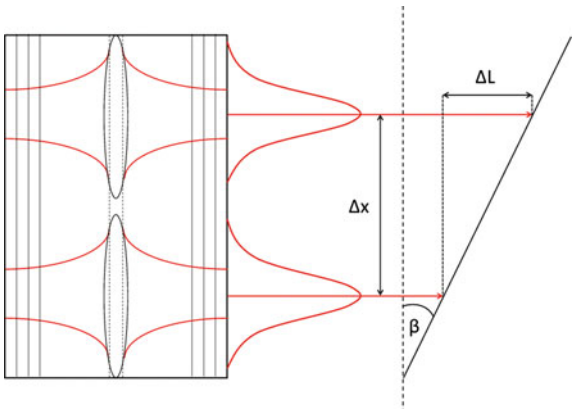

Fig. 4 Scheme of VCSEL cavity carrying two LCS with feedback from a tilted VBG. The tilt angle β of the VBG controls the mutual detuning of the two LCS (see text for details). The pivot point is much further away from the optical axis in reality (about 30 mm)

taking the dispersion data of the lenses into account. Then it can be checked by measuring dispersion curves of the off-axis states above threshold [85]. After optimization we estimate to be within ± 0.2 mm of the self-imaging condition with a reasonable depth of focus [85].

2.2 Basic Properties of Laser Cavity Solitons

When increasing the VCSEL input current, LCS appear at specific spatial locations. The first lasing emission occurs at currents of about 360–380 mA, depending on the exact temperature and alignment of the VBG. Figure 2b shows a typical near field intensity distribution slightly above threshold. There are several distinct spots of emission, which are approximately circularly symmetric and approximately equal in amplitude and shape. These are the LCS. The size of a LCS is about 5–7 μm ($1/e^2$-radius). The far field has also a single-lobe, well-behaved profile with a width of a few 10 s of mrad [49], i.e. the LCS have a high spatial coherence. The emission is also temporally coherent with a typical linewidth of about 6 MHz when operating on a single longitudinal mode of the external cavity [49], quite a typical value for grating-controlled lasers on millisecond and second time scales. Hence each LCS is a coherent emitter, a *micro-laser*. We will discuss the mutual coherence of LCS below. For increasing current, a soliton typically splits into a compound state with two humps, and then possibly three or four, followed by disordered extended states. Evidence for these states, stemming from the LCS with the lowest threshold, is visible in the lower right part of the aperture in Fig. 2b. Details on the LCS and pattern evolution beyond threshold can be found in [49, 85].

The appearance of each LCS is abrupt and we observe hysteresis when the current is ramped up and down, i.e., each LCS shows bistability. Figure 5 illustrates this phenomena for two sample LCS shown in the corresponding inset. The

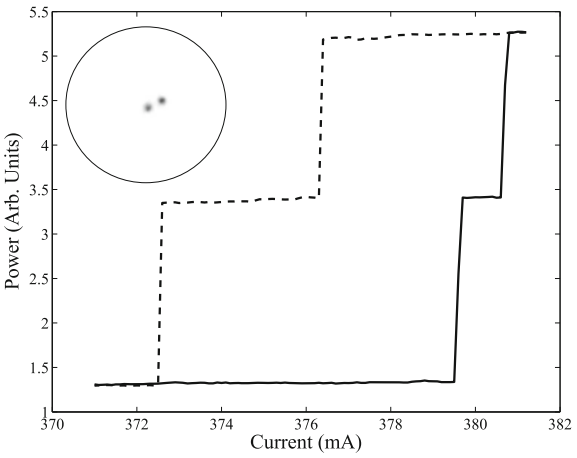

Fig. 5 Light-current (LI) curve for two sample LCS (shown in inset). The *solid line* refers to increasing current and the *dashed line* to decreasing current. Measurements taken at 0.1 mA intervals at a rate of 1 mA per second to avoid thermal hysteresis

right one switches on abruptly at about 379.5 mA, the left one only slightly later at about 381 mA. If the current is decreased again, the latter survives till about 376 mA, the former till 372.5 mA. In between 376 and 379.5 mA the two LCS are simultaneously and individually bistable, i.e. they can be independently switched on and off by an external writing pulse [47–49]. This represent a 2-bit memory, which is interesting for optical information processing when extended to more channels that can provide the potential for massive parallelism in broad-area VCSELs. The details of this hysteresis loops are different for different LCS and also depend on alignment. Typically switch-on occurs to the single-humped fundamental LCS as demonstrated in Fig. 5. Corresponding scenarios are described in [47–49, 86], but a direct transition to multi-humped and ring-shaped states is also possible for, e.g., solitons 1 and 2. The experiments described later in Sect. 2.3 are performed at a bias current at which two fundamental, single-humped LCS are individually bistable.

The mechanism for the bistability is the following [48, 85, 87, 88]. Initially, the longitudinal resonance of the cavity is blue-detuned to (at higher frequency than) the grating frequency (the reflection peak of the grating). Hence there is a frequency gap, in which no linear state exists. The gain is below the value where lasing without the help of the feedback from the grating is possible. Increasing the current leads to an increase of Ohmic dissipation and hence to a temperature rise in the laser structure. This results in an increase of the refractive index and hence in a red-shift of the cavity resonance. This shift is around 0.0035 nm/mA. Let's assume now a fluctuation leading to an increase in output power. Due to stimulated emission, the carrier density is decreased and this increases the refractive index due to phase-amplitude coupling in semiconductors, described phenomenologically by Henry's alpha-factor [89]. This red-shifts the cavity resonance and hence the detuning between VCSEL and VBG decreases. As a result, the feedback strength increases and the intensity will increase ever further leading to positive feedback. At a certain critical detuning, the positive feedback is strong enough to

cause an abrupt switch-on of the laser. After switch-on, the laser can self-sustain the condition of the near-resonance between the (shifted) cavity resonance and the VBG in the high-amplitude emission state due to the continuous depletion of carriers and the resulting refractive index shift even if the current is reduced again, resulting in a bistable situation. Bistability due to shifts of cavity resonances is usually referred to as dispersive optical bistability [90].

In a spatially extended system, the whole aperture might switch to the high-amplitude state, but it turns out that this state is unstable, or at least that there is the coexisting possibility of localized emission, the LCS [51, 52]. An intuitive mechanism to understand the drive for localization is self-lensing, as indicated in Fig. 4. A self-induced lens can render the marginally stable plano-planar resonator locally stable and lead to a self-induced nonlinear mode, the LCS [25, 91]. It is important to realize that under our typical operating conditions the main effect of the change of the control parameter 'current' (see e.g. Fig. 5) is the change of the detuning condition and not the gain change. This is further evidenced by the fact that a decrease of the ambient temperature of the VCSEL leads to an increase in threshold current. Since the gain at constant current increases in a semiconductor with decreasing temperature, this indicates that the main function of the increased current is to provide the larger detuning shift required at lower temperature. The system with feedback by a normal mirror lases already at about 180 mA [85], demonstrating that ample gain is available.

The reason for the difference in threshold for the different solitons as well as for the preference of certain locations lies in growth irregularities of the semiconductor material. If the cavity resonance of the VCSEL is spatially varying, the linear gap between the grating frequency and the cavity resonance is changing in space and a minimum value of the detuning for switch-on is met at different locations at different injection currents. Hence the lasing will start first at the most 'reddish' location with the smallest gap. With increasing currents more locations reach the critical detuning value and additional LCS switch on, whereas the LCS formed originally may give way to high-order compound states and extended, off-axis lasing states [64, 85]. Typical length scales of disorder are about 10 μm and they span some tens of GHz [64] in line with the results from other devices in the literature [63, 92, 93]. A simple calculation shows that a monolayer variation of $\Delta L \approx 0.3$ nm corresponds to a frequency variation of $\Delta\nu \approx 76$ GHz. Similar results are obtained with more accurate models of the multi-layer stacks forming a VCSEL [94, 95]. Since the cavity linewidth of a low-loss VCSEL is about 0.1 nm or 30 GHz (depending on the actual free-carrier and scattering losses), this explains the extreme sensitivity of the feedback light distribution to disorder.

As explained in the introduction, LCS will couple to parameter variations and drift [60, 61] until they either disappear from the system or reach a point in which all first order perturbations, i.e. gradients, vanish at a local extremum of the 'landscape' imposed by the variations. These preferred locations are the ones where we find LCS in Fig. 2b. We will refer to them as traps or defects. This disordered 'landscape' is frozen after the growth process of the semiconductor structure although some minor external influence on the position of the LCS is

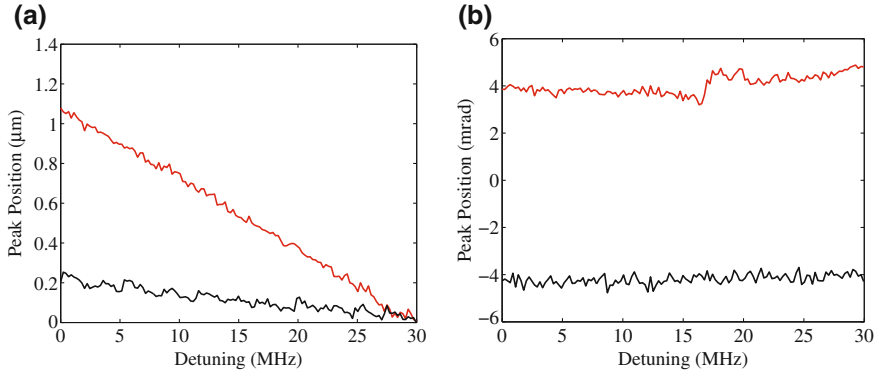

Fig. 6 **a** (Color online) Peak position of the near field profile as a function of the tilt angle for LCS 1 (*red curve*, *gray* in print) and 2 (*black curve*); **b** Peak position of the far field profile as a function of the tilt angle. The curves are averaged over two runs and most of the undulations are likely to stem from measurement noise, although a deterministic contribution due to small-scale disorder within the trap cannot be ruled out. The zero of the y-axis in panel **b** is set at the center of the two individual angular centres of the far fields of LCS 1 and 2. For a better comparison with the results presented below the horizontal axis is scaled in the change of differential detuning between the two LCS in the external cavity as obtained from Eq. (1). The total tilt is 0.15 mrad

possible by alignment changes in the external cavity. In particular, a tilt of the VBG induces a tilt of the wavefront of the returning beam, which should lead to continuous drift of the LCS in a homogeneous system. For a LCS in a trap, the tilt shifts the position where the potential minimum of the combined perturbation (frozen disorder plus tilt) lies and hence the LCS shifts to a new equilibrium position (see [49] for images). As the quantitative analysis in Fig. 6a shows, this shift is quite small. It should be noted also that the tilt is minute, about 0.15 mrad total, leading to a change of ray angle at the VCSEL smaller than 1 mrad, much smaller than, e.g., the angular width of a LCS. The shift within the trap is also different for different solitons, which is expected for a disordered system because the curvature of the potential should vary randomly from trap to trap. At some critical tilt angle (larger than typically achievable with the PZT), the LCS disappears. The expectation is that the potential minimum disappears for a critical tilt and the LCS unpins and starts to drift. A corresponding transition between drifting and pinned patterns was found in [96]. In our system, an experimental investigation of the unpinning phenomenon requires simultaneous spatial and temporal resolution and has not been undertaken, yet.

In conclusion, bistable emission spots with high temporal and spatial coherence emerge at the threshold of a VCSEL with frequency-selective feedback. Although their position is affected by the disordered landscape due to the variations of the cavity resonance, these spots maintain rotational symmetry and a common spatial shape and width, i.e. their shape seems to be dominated by the nonlinear process. Theoretical results discussed below confirm the existence of self-localized LCS for realistic parameter values. Hence these spots are identified as LCS. The spatial

fluctuation of the cavity resonance condition, however, pins LCS to certain locations and leads to a dispersion of thresholds and operating frequencies. Each of these LCS is a coherent emitter but they are mutually incoherent due to the spatial disorder of the background [49, 59, 65].

2.3 Phase Locking of Laser Cavity Solitons Via Change of Current

Investigation of LCS interactions were done on pairs of different LCS. We report here results on LCS with a separation distance of 49 (LCS 3 and 4) and 79 μm (LCS 1 and 2). The qualitative features of the observations are robust, but the details can vary a fair amount as one would expect since parameters are affected by spatial disorder. We stress that we are only looking at LCS in different traps. The coherence properties of compound, high-order states of LCS in the same trap are a separate issue and more detailed investigation are needed in our system. For the LSA some results are in [59, 86].

Two spatially separated LCS are typically incoherent. Then their combined far field is the incoherent sum of the intensity distributions of the two solitons. Under certain conditions (explained in detail below), this changes drastically and a pronounced fringe pattern is visible across the far field intensity profile (Fig. 7c, d). Its wavevector is parallel to the connection line between the two solitons, i.e. the fringes are orthogonal to it. This far-field fringe pattern is stable for longer than the exposure time of the CCD (20 ms), typically it can be observed for minutes to hours, once achieved. This evidences phase-coherence between the two LCS over time spans orders of magnitude higher than the intrinsic dynamics (nanoseconds) and also higher than typical time scales of technical noise (microseconds to seconds). A cut through the fringe pattern is taken across the center of the far field intensity. Then a Gaussian profile modulated by a sine-wave is fitted to this cut,

$$y = y_0 + A \exp\left[\frac{-(\theta - \theta_0)^2}{2w^2}\right]\left[\frac{1 + M\sin(F(\theta - \theta_0) + P)}{1 + M}\right]. \tag{2}$$

Here y_0 is the offset, A is the amplitude, θ_0 is the peak center, w is the width, M is the modulation depth or fringe visibility, F is the frequency of the sine modulation and P its phase.

Figure 7a, b show the locking behavior of LCS 1 and 2 during an upward scan of the current. The dominant features of the spectra in Fig. 7b are multi-frequency emission and the common red-shift of all modes due to the Ohmic heating discussed earlier. This shift is about 0.44 GHz/mA, about half the value of the free-running laser. This is expected because the grating stabilizes the emission frequency [85, 87]. At low current the LCS emit on two or three different external cavity modes

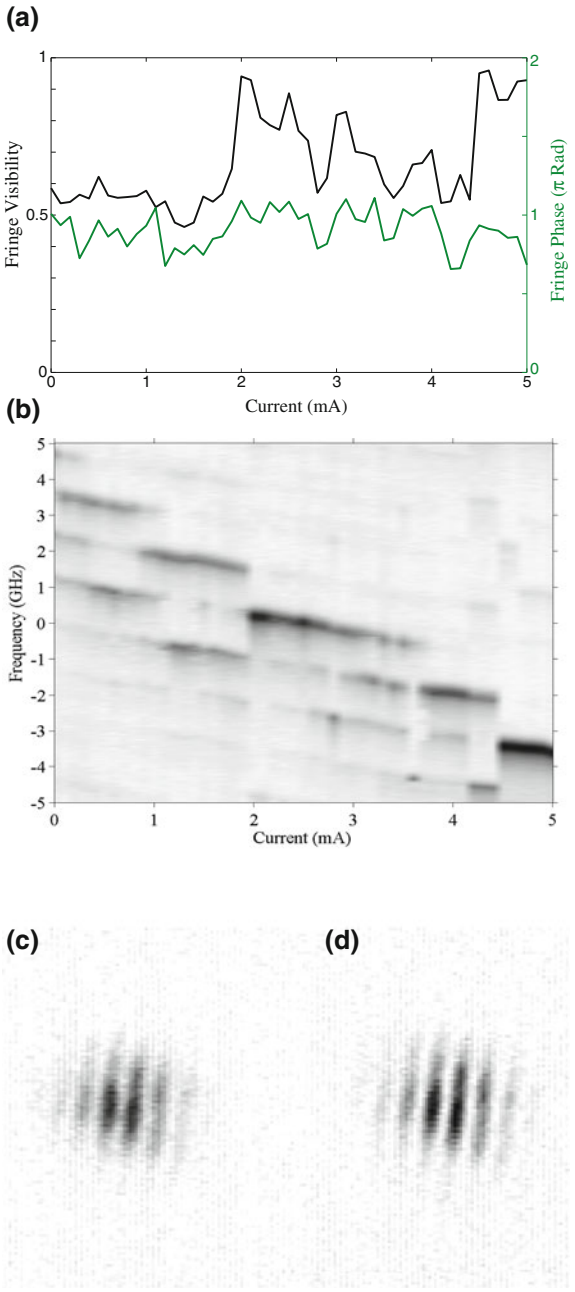

Fig. 7 **a** (Color online) Fringe visibility (*black*) and fringe phase (*green curves*, *gray* in print) as a function of current for LCS 1 and 2, 79 μm apart. The zero of the current scale corresponds to a current of 380 mA. The fringe visibility and phase are obtained from a fit of far field profiles to Eq. (2). **b** Evolution of frequencies; the frequency distribution is obtained from the optical spectra recorded by a Fabry–Perot with a FSR of 10 GHz. The frequency separation between side modes corresponds to the free spectral range of the external cavity (1.23 GHz). In these measurements, the Finesse is only 25 due to misalignment (frequency resolution 400 MHz). **c** Far field intensity distribution at 380 mA corresponding to a fringe visibility of 0.55. **d** Far field intensity distribution at 385.5 mA corresponding to a fringe visibility of 0.95. Other parameter: Temperature 69 °C

which corresponds to a fringe visibility close to 0.5. This indicates that the LCS operate on different external cavity modes but share side-bands, i.e. each LCS is not single-mode. Then, as the current is increased, the fringe visibility increases

abruptly to reach up to 0.95. At this point, only one spectral line is strongly dominant and both LCS occupy the same external cavity mode and are then strongly frequency and phase locked. Increasing the current further leads to a jump of one LCS to an adjacent external cavity mode inducing a drop in fringe visibility back to 0.5. A similar scenario with a transition to nearly complete locking occurs at the end and high visibility is reached again. Beyond this point, a third LCS switches on in the detection area thus complicating the interpretation of the results.

From the Fourier theorems, a field distribution shifted by a distance a in the near field acquires a phase-shift of $\exp(ik_{\perp}a)$ in far field. Hence a, the separation of the interference source (here the LCS) in near field and the fringe period $\Delta\theta = 2\pi/F$ are related by

$$a = \frac{\lambda}{\Delta\theta}. \tag{3}$$

For a far field fringe spacing of 12.6 mrad obtained from the fit one obtains a near field separation of 77.8 μm which agrees very well with the measured LCS separation of 79 μm thus confirming that the interference comes from the two interacting LCS.

From Fig. 7a it is apparent that the fringe phase fluctuates around a value smaller than π. As we will discuss below, a locking phase of π is typical for two coupled oscillators without detuning while a non-zero detuning changes the locking phase away from π. The current induced heating is a global parameter and hence it should not change the detuning condition between the two LCS in the VCSEL cavity, in line with the fact that the locking phase is not varying by much. The operating frequency of the solitons, however, is a compromise between the VCSEL cavity resonance and the external cavity resonance leading to a transcendent equation for the operating frequency [97] (see (A.3) of [87] for a VCSEL with FSF). With an initial, position dependent offset, a global shift of the VCSEL resonance conditions can result in a change of relative stability and frequency of the modes of the coupled cavity system (e.g. a destabilization of an external cavity mode for one LCS but not for the other), leading to the possibility of a non-synchronous evolution of soliton frequencies and locking or unlocking. In addition, there might be small local variations either in gain or cavity resonance because the current induced temperature shift is only nominally homogeneous. These considerations indicate that the global parameter 'current' is not a good handle to investigate the locking behavior, but one should look for a 'local knob'.

2.4 Phase and Frequency Locking of Laser Cavity Solitons Via Change of Feedback Phase

Since it is experimentally difficult to change the detuning of two LCS by locally changing the properties of the VCSEL itself, the PZT is used to minutely tilt the

VBG of the external cavity with respect to the optical axis (Fig. 4). As indicated by Eq. (1) this induces a difference in external cavity length ΔL for the two solitons therefore leading to a difference of feedback phase and detuning in the external cavity. It is then possible to adjust the frequency difference (i.e. the detuning) between two LCS. Indeed, the locking discussed in the previous section was achieved by aligning the VBG such that a high fringe visibility was obtained for some current (2 or 4.5 mA). This follows the procedure used to control the detuning of coupled solid-state lasers, see [4, 5], but with the additional complication of coupled cavity effects due to the high reflectivity of the VCSEL outcoupling mirror, whereas the gain chip in the solid-state lasers is typically anti-reflection coated.

As indicated before, the tilts are actually quite small and it turns out that the soliton profiles are essentially unaffected. The width of the near field is constant within 0.3 μm (variation ≤ 5 % of a single soliton width) and the width of the far field profiles to within 1.5 mrad (6 % of a single soliton width). When tilting the VBG both near and far field profiles of the LCS are not affected while the positions are. As discussed in conjunction with Fig. 6, the positions and beam pointing of the LCS change slightly in the trap, but the changes are small and the differential changes are even smaller. Hence, it seems reasonable to assume that the dominant effect of the tilt is indeed the change of differential feedback phase.

When tilting the VBG a region of phase and frequency locking appears as illustrated in Fig. 8a, c by a range of high fringe visibility in the far field. This region of high fringe visibility can last for seconds to hours depending on parameters. It confirms that locking is a robust feature once achieved by a fine alignment of the VBG. We note that the choice to start the x-axis displaying the detuning parameter with zero is arbitrary. If one considers the locking-dynamics, it would be reasonable to expect that the zero lies at the center of the locking region. However, as the fringe phase is only approximately symmetric with respect to the center of the locking range and the details of the underlying dynamics are unknown, the position of the zero is somewhat ill-defined and no adjustments were made. Such cautious choice comes at the expense of a slightly awkward labelling: whereas the real detuning decreases in the left half (roughly) of the figure and increases in the right half, the detuning parameter chosen increases all along the x-axis. As qualitatively apparent from Fig. 8c, the fringes shift with detuning within the locking region (within a fringe visibility higher than 0.5), i.e. the locking phase changes. The quantitative analysis in Fig. 8a indicates that this variation is nearly linear over most of the range. The width of the locking range is close to π. If the direction of the scan of the tilt is reversed (see green dashed line in panel a) the locking phase shadows the one obtained in the up-scan, i.e. there is no discernible hysteresis. As we will discuss in the theoretical sections, these features are fingerprints of the Adler locking. The noise of the fringe phase is considerably smaller in the region corresponding to complete locking than in the partially locked regions. For even larger tilts (not achievable with the PZT), the two LCS are completely unlocked and their phases random. Modulations depths of about 5 % are due to noise in the images.

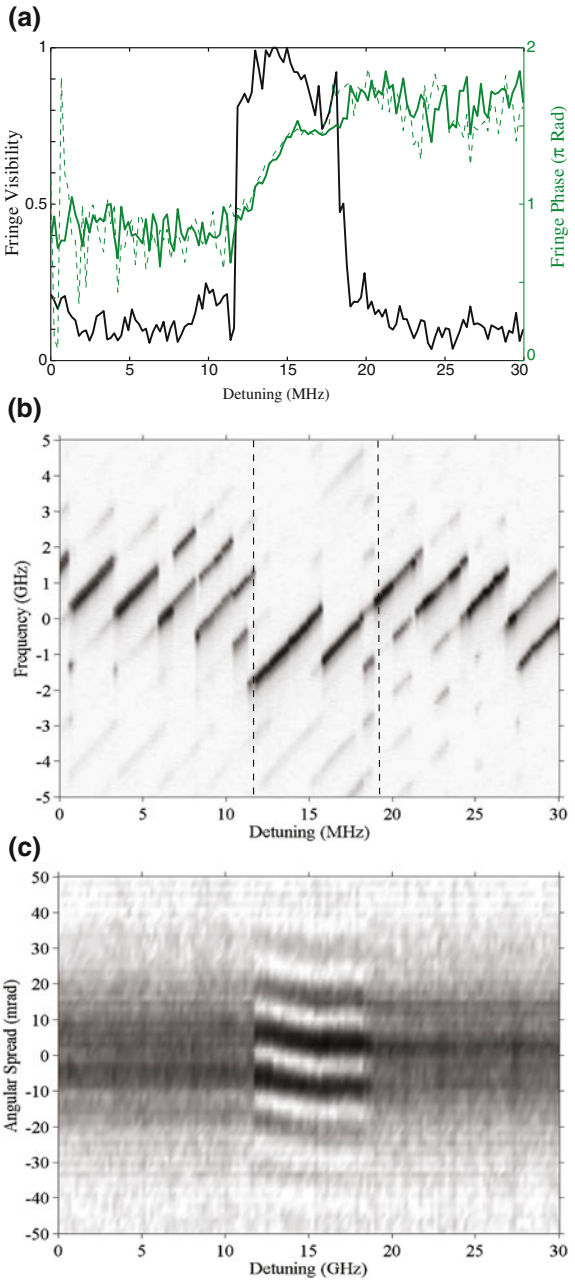

Fig. 8 **a** (Color online) Fringe visibility (*black*) and fringe phase (*green curves*, *gray* in print) as a function of the tilt angle that changes the difference between the feedback phases for LCS 1 and 2, 79 μm apart. This difference is converted to a frequency scale by multiplying it by the free spectral range of the external cavity thus providing the change of the relative detuning between the two LCS in the external cavity. The zero of this detuning scale is arbitrary. The *solid* and *dashed green curves* are obtained for scanning the tilt back and forth. **b** Evolution of frequencies, the frequency distribution is obtained from the optical spectra recorded by the FP (Finesse 80). **c** Cut through far field intensity distribution orthogonal to fringe orientation. Other parameters: Temperature 69 °C, current $I = 373$ mA

The transitions to and from frequency and phase locking are rather abrupt and one might expect hysteresis at their onset. Due to the mechanical scanning, there is some jitter of the transition point. Hence only one sweep is shown in Fig. 8a and we are currently not in a position to investigate possible hysteresis systematically.

Panel b of Fig. 8 illustrates the evolution of the frequencies of LCS in optical spectra. The first obvious feature is that all spectral lines are shifted due to the tilt of the VBG. The Finesse of the FP is 80, hence the frequency resolution is only about 130 MHz. This means that the differential frequency shift of the two LCS cannot be resolved (it is in total about 30 MHz), but only inferred from its indirect effect via stabilization and destabilization of external cavity modes and the resulting possibility of locking and unlocking. When comparing panel b to panels a and c one observes that when the fringe visibility is high, the two LCS operate on a single frequency (region within dashed lines in panel b).

There is a jump in the common operation frequency of the LCS by one FSR slightly after 15 GHz, where the fringe visibility is nearly maintained. It drops from 0.9–1 to 0.8–0.9. This indicates that the two LCS do a common mode jump retaining phase and frequency locking, though at this point there is a change of behavior in the phase evolution (green solid line in Fig. 8a); it becomes essentially flat.

Outside the locking region the two LCS operate on two different external cavity modes (with a frequency separation of 1.23 GHz between two adjacent modes). In this region the fringe visibility is rather low (below 0.25) and the locking is very weak. Some residual coupling via side-modes is probably responsible for this residual partial locking. As indicated, for higher tilts, the visibility drops to a background given by noise on the order of 5 % or less.

Although the transition from locking to unlocking seems to be accompanied by a transition between a one-frequency to a two-frequency spectrum, there are other regions in which the spectrum appears to be predominantly single-humped (possibly with weak side-modes) but with low fringe visibility. A close inspection however shows that the spectral line is wider there than in the central locking range, by around 45–55 % in the region between 2 and 6 MHz detuning, and by 27 % in the region at 19.5–20.5 MHz (close to the locking range). This indicates that the two LCS are operating close in frequency so that the difference cannot be resolved within the limited resolution of the FP (about 130 MHz). There is a third region around 26 MHz, where the spectral line seems to be slightly, but not significantly broader, and we conjecture that the frequency difference is below the resolution there.

The basic features of the scenario described for LCS 1 and 2 (79 μm apart) are also typical for other distances and other pairs of LCS. Fig. 9 shows phase and frequency locking for LCS 3 and 4, which are 49 μm apart. In this case we observe a far field fringe spacing of 19.1 mrad which corresponds to a near field separation of 51.3 μm. It again agrees well with the measured LCS separation of 49 μm. Again, there is a region of nearly complete locking with a high fringe visibility. The phase (within the locking region) is centred around π and varies linearly with the detuning from 0.6π to 1.4π (green curve in panel a, see also panel c). The locking-unlocking transition is accompanied by a transition between a single-frequency and a two-frequency regime. Around a detuning of 4 MHz, the transition leads to a single locked state with a visibility of 0.7 dominated by a single mode, although weak side-modes are still present in the spectrum, the latter disappearing with a further increase of the visibility to the 0.9 level. As in Fig. 8b, the

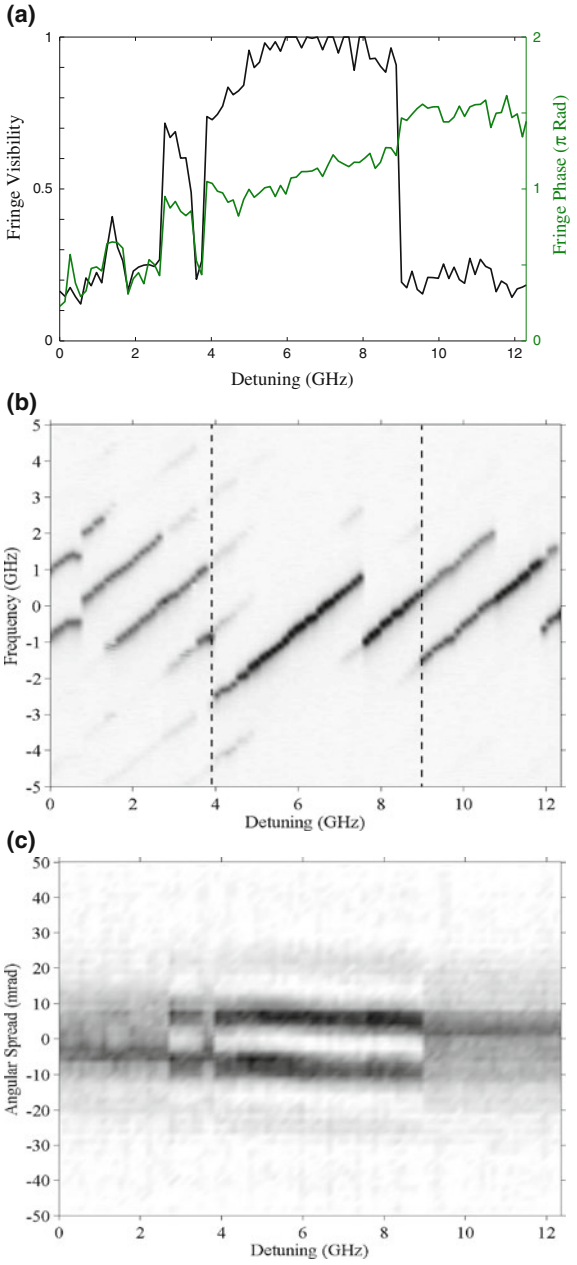

Fig. 9 **a** (Color online) Fringe visibility (*black*) and fringe phase (*green curve*, *gray* in print) as a function of the tilt angle that changes the difference between the feedback phases for LCS 3 and 4, 49 μm apart. The zero of this detuning scale is arbitrary. **b** Evolution of frequencies, the frequency distribution is obtained from the optical spectra recorded by the FP (Finesse 80). **c** Cut through far field intensity distribution orthogonal to fringe orientation. Other parameters: Temperature 69 °C, current $I = 387$ mA

LCS perform a common mode-hop within the locking region (around 7.5 MHz detuning), but remain locked. In contrast to the previous case, the phase evolution is not perturbed, i.e. the phase continues to grow approximately linearly. This

might be related to the fact that the visibility remains above the 0.9 level, i.e. remains higher than in Fig. 8a.

Before the main locking region, there are already small regions (around 1.5 and 3 GHz) in which partial locking takes place. An extrapolation of the phase in the main locking region seems to match qualitatively the phase values obtained in these regions. There are also some ranges of non-monotonous behavior of the phase (a decrease with increasing detuning) in the partial locking regions around 3 and 4 GHz. The significance of these observations is not clear at the present stage of investigations.

In summary, we have obtained a variety of different dynamical behaviors for LCS pairs with different distances ranging from 30 to 80 μm. They all share the common feature of a region of nearly complete locking in which the phase is evolving approximately linearly with detuning. The locking is dominantly anti-phase (π locking phase) and the locking phase varies by nearly π over the locking range. We will argue in the next sections that these observations are a manifestation of the Adler-scenario. The observed variations in dynamics are expected since important parameters are associated to background disorder that cannot be controlled by the operator.

3 Theoretical Description

3.1 The Semiconductor Class-B Model

Since the pioneering work of Lang and Kobayashi [97] a good deal of attention has been paid to the modelling of feedback effects on the dynamics of semiconductor lasers (see for example [98]). Most of the work has been done however by neglecting the spatial degrees of freedom in the transverse direction. Transverse-space dependence is critical for LCS and it should be included in any model that describes the set-up discussed in the previous section. Following [52] the dynamical evolution of the intra–VCSEL optical field E and carrier density N of a VCSEL with frequency-selective feedback can be modelled by the following system of coupled partial differential equations and mapping:

$$\partial_t E = -(1 + i\theta)E + i\nabla^2 E + \sigma(1 - i\alpha)(N - 1)E + \frac{2\sqrt{T_1}}{(T_1 + T_2)}F \tag{4}$$

$$\partial_t N = -\gamma\Big[N - J + |E|^2(N - 1) + D\nabla^2 N\Big] \tag{5}$$

$$F(t) = e^{-i\delta\tau_f}\hat{G}(t - \tau_f/2)\left\{-\sqrt{1 - T_1}F(t - \tau_f) + \sqrt{T_1}E(t - \tau_f)\right\} \tag{6}$$

In Eq. (4), θ is the detuning of the VCSEL cavity with respect to the carrier reference frequency, σ is a coupling constant, α is the linewidth enhancement

factor, and T_1 and T_2 are the transmittivities of the VCSEL mirrors. Note that light propagation in the external cavity is considered here without approximations typical of the Lang–Kobayashi approximation (see also [99]). This allows for the consideration of large feedback reflectivities without incurring in unphysical results (see more details in [52]).

In Eq. (5), J is the injection current normalized to the value at transparency. Time is scaled to the VCSEL cavity lifetime, and γ is the ratio of the cavity lifetime to the carrier response time in the VCSEL. The term $D\nabla^2 N$ describes carrier diffusion but is omitted in what follows. A similar description for field and carriers dynamics was used to model an amplifier CS [23, 100]. Here, the holding field of the amplifier model is replaced by the feedback field F due to the external Bragg reflector. Space is normalized to the square root of the diffraction parameter. For a low-loss VCSEL, where losses are dominated by the outcoupling, the time scale is of the order of 10 ps, while the spatial scale is around 4 μm (see also [100]). Since losses due to scattering and background absorption are difficult to quantify we have restricted the analysis to these values of the physical scales.

In Eq. (6), δ is the external cavity carrier field detuning, τ_f the external round–trip time (see [52] for a detailed description of the external cavity). The operator $\hat{G}$ describes the frequency–selective operation of the Bragg reflector on the field envelope and is taken to be

$$\hat{G}(t)\ \{h(t)\}\ = \frac{r_g}{2\zeta} \int_{t-2\zeta}^{t} e^{i\Omega_g (t'-t)}\ h(t')\ dt', \tag{7}$$

where Ω_g is the grating central frequency relative to the reference (carrier) frequency (shifted to zero in the following), ζ the inverse of the filter bandwidth and r_g the overall reflection coefficient. Note that this description neglects the transverse wavevector dependence of the reflector response. Transverse effects of free–space propagation (i.e. diffraction) in the external cavity are also disregarded, since in the experimental setup the VCSEL output coupler is imaged directly onto the Bragg reflector as described in the previous section.

Equations (4)–(6) have traveling wave solutions as discussed in [52]. It turns out that there are two relevant sets of modes. One set is grouped around the grating frequency and the other around the solitary VCSEL lasing frequency, with a frequency gap in between. The former modes owe their existence to the strong feedback provided by the grating at frequencies close to its central frequency and as a result, have the lowest thresholds. The latter modes exist where the feedback is small and so can be termed VCSEL modes. The frequency gap between grating–determined and VCSEL modes depends on the detuning between VCSEL and grating, as well as on other system parameters.

Under suitable operating conditions it is possible to create a threshold gap between the highest–threshold grating mode and the lowest–threshold VCSEL mode [52]. As a result, a range of currents opens up where the grating–determined modes exist (i.e. the system can lase) but where the laser off state is also stable (i.e.

the system can also not lase). In this region of bistability between lasing and non–lasing states it is possible to observe LCS. Numerically one finds that the LCS can be either single– or multi–frequency, depending on system parameters, in 2D as well as 1D [52].

Spatial inhomogeneities, such as those associated to uncontrolled fluctuations in the VCSEL growth process, can be introduced in the model by considering spatial dependence on the model parameters. In particular one can consider in Eq. (4) a spatially dependent detuning, that is $\theta = \theta(x)$ for a 1D system and $\theta = \theta(x, y)$ for a 2D one.

3.2 The Simplifed Ginzburg–Landau Model

In this work we are primarily interested in single-frequency laser solutions, in particular solitons. For such solutions the carrier dynamics can be eliminated, reducing the model to a nonlinear equation for $E(x, t)$, coupled to a linear equation for the feedback field F. As discussed in [52] and in more detail in [79] these equations have a structure corresponding to the matching of a nonlinear 'soliton' response to a linear 'spectral' response. The latter contains all the gain/loss and phase dependence arising from the delay, grating and mirror properties, while the former describes the effects of current (gain, saturation) and of diffraction. The matching of these responses is associated with the intersection of corresponding curves in a complex plane (C in Fig. 10) describing net gain and phase shift [79]. As illustrated in Fig. 10, the soliton curve is typically rather smooth, originating in a point whose location depends smoothly on current. The spectral curve can be highly structured, especially in the case of delayed feedback as is clear when one considers that each external cavity mode must correspond to a different intersection between the soliton line and the spectral curve [52]. Figure 10 shows an example.

It is instructive to investigate the simplest scenario of LCS, which we can obtain by setting aside complications such as delay and high-order nonlinearity. Doing so will also enable us to compare and contrast other models of dissipative soliton interaction, such as those based on generic models such as the cubic-quintic complex Ginzburg–Landau equation (CQGLE) and systems of CGLE [30, 101, 102]. If we eliminate delay and replace the feedback grating with a Lorentzian-response filter, the spectral response curve is broadly similar to the envelope of that in Fig. 10. It is intersected only twice by the soliton line in relevant cases, corresponding to two single-frequency soliton solutions. One (of lower amplitude) is always unstable, while the other may be stable.

A simple model based on this scenario, which captures the basic features of a semiconductor laser with feedback, consists of a cubic complex Ginzburg–Landau equation (CGLE3) linearly coupled to an additional linear filter equation [80, 103]

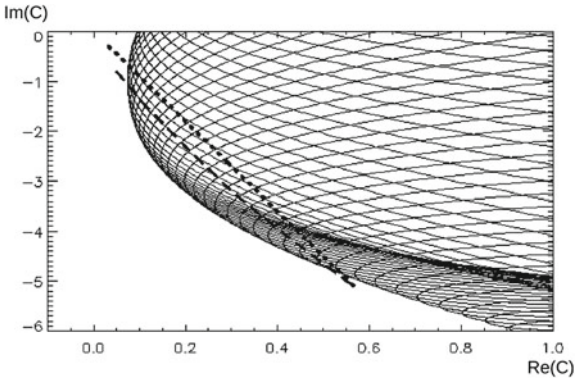

Fig. 10 Spectral curve for the coupled–cavity system showing the soliton line (*dashed*) and the plane–wave threshold (*dotted line*). After [52]

$$\begin{aligned}\frac{\partial E}{\partial t} &= g_0 E + g_2|E|^2 E + \tilde{D}\frac{\partial^2}{\partial x^2}E + F + in(x)E,\\ \frac{\partial F}{\partial t} &= -\lambda F + \tilde{\sigma}E.\end{aligned} \tag{8}$$

Here, $E(x,t)$ is the intra-cavity field (we consider only the 1D case), g_0 describes linear gain and detuning, g_2 nonlinear gain saturation and frequency shifts (the ratio $\mathrm{Im}(g_2)/\mathrm{Re}(g_2)$ corresponds to the α-factor of semiconductor lasers discussed above). The spatial coupling parameter $\tilde{D}$ represents diffusion and/or diffraction depending on its phase: we will set $\tilde{D} = -i$ corresponding to pure diffraction. $F(x,t)$ is the feedback field, $\tilde{\sigma}$ the feedback strength and λ the bandwidth of the feedback. Finally, $n(x)$ describes spatial variations of the linear detuning due to local variations in the optical length of the cavity, as discussed in Sect. 2. The time and space coordinates (t,x) are scaled to 1 ns and 40 µm, respectively, i.e. the normalized scalings cannot be compared directly between the class-B and the CGLE-F model, but they refer to similar physical scales, after the scalings are undone.

For $n(x) = 0$, Eq. (8) has an analytical soliton solution of chirped-sech type [79, 103, 104]:

$$E = E_{max}[cosh(Kx)]^{-1-i\beta}e^{i\phi}e^{i\omega t} \tag{9}$$

where the amplitude E_{max}, the inverse width K, the chirp β and the frequency ω are expressed through system parameters. ϕ is an arbitrary phase, indicating the phase invariance of the system. The field amplitude decays exponentially in the wings of the soliton (see Fig. 11a below for a particular example). The full width at half maximum of the intensity profile of the soliton is $2x_0$, where $cosh^2(Kx_0) = 2$, i.e. $x_0 \sim 0.88/K$. The crucial difference between the dissipative soliton (9) and an analogous conservative soliton is the nonzero value of β leading to the dependence of the phase on x as illustrated in Fig. 11a. Far from the center, the phase changes linearly with distance and hence repeats with a period of $P = 2\pi/(K\beta)$. Hence only with a moderate to large absolute value of chirp will the soliton phase change

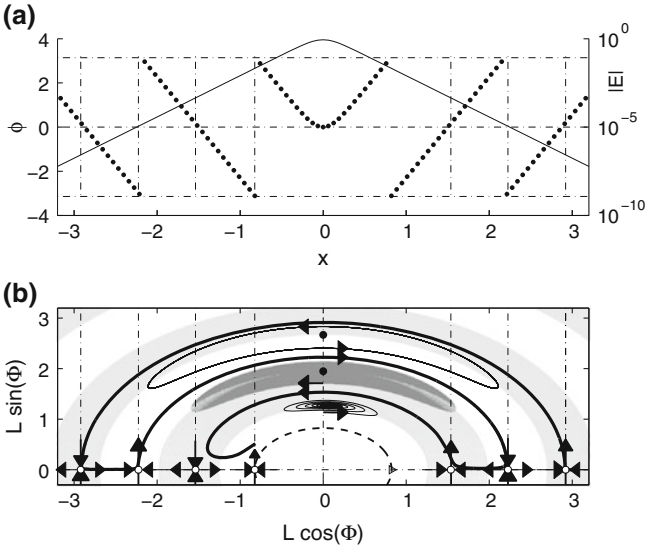

Fig. 11 **a** Profile of the soliton field (9) for the parameters listed in the text. *Dots* show the phase (left vertical axis); solid line shows the amplitude distribution (right vertical axis, semi-logarithmic scale). **b** 'interaction plane' of two LCS. The *arrows* indicate the direction of motion of the system along any trajectory. The *dark-gray* shaded region is a dense spiral. *Black dots* near $\Phi = \pi/2$ are foci, while the *open dots* (along $\Phi = 0$ and $\Phi = \pi$) are saddle points. The *vertical dash-dotted* lines link subplots **a** and **b**, and confirm that the saddles have the same spatial period as the phase of an isolated soliton. The *shading* is explained in the text

significantly within the soliton width x_0. Recall that an NLSE soliton has flat phase, i.e. zero chirp: broadly speaking, the chirp increases with the ratio of nonlinear gain to nonlinear dispersion.

4 Theoretical Results: Homogeneous Systems

4.1 Ginzburg–Landau Model

In this subsection and in Sect. 5.1 we consider the pairwise interaction of solitons found in the model (8). We adopt throughout the parameter values of $g_0 = (-4, 28)$, $g_2 = (-96, -48)$, $\lambda = 2.71$, $\tilde{\sigma} = 162.6$ (see [80]). These parameters imply a rather small value (0.5), of the alpha-factor, so chosen in order to enhance the soliton chirp, thus making the interaction stronger and easier to model.

We consider first the ideal case with translational invariance ($n(x) = 0$), where a single soliton has two free parameters, location and phase. We chose a superposition of two solutions of type (9), with the maximum of the left soliton at x_1, and the maximum of the right soliton at $x_2 > x_1$ as initial conditions for the evolution. We also chose the initial phases ϕ_1 and ϕ_2. The two LCS will mutually

interact by providing a perturbation to each other. The interaction can indeed be understood as if each solitons is placed in a potential created by the other, considered as the 'driver'. This means that the field profile of a solitary soliton can be considered as the 'driving potential (and field)' (see Fig. 11a).

The integration of model (8) can be visualized nicely in the 'interaction plane', introduced in [30] and spanned by polar coordinates $L = |x_2 - x_1|$ and $\Phi = \phi_2 - \phi_1$. The temporal evolution on the interaction plane with different initial values of L and Φ is presented in Fig. 11b, which depicts key trajectories. It is characterized by a series of foci at $\Phi \approx \pi/2$ corresponding to moving bound states, and two series of saddles with $\Phi = 0$ and $\Phi = \pi$ representing stationary bound states. The stable and unstable manifolds of the saddles coincide with the Goldstone modes of the single soliton. The horizontal manifolds correspond to the soliton translation mode, while the vertical manifolds to that of the local phase. Note that neighboring saddles have opposite stability properties with respect to phase and translation. The light-gray (white) shading in Fig. 11b shows the regions where the active tangential components are directed counterclockwise (clockwise) in the upper half-plane (the sense of rotation is inverted in the lower half-plane that is not shown). It is clear that the location of the saddles is strongly determined by the chirped phase of the individual solitons, which leads to intensity oscillations in their mutual interference profile [29, 34]. We will see how the linewidth enhancement factor α affects the chirped phase and consequently the LCS interaction in Sect. 4.2. Note that in driven systems without phase symmetry the amplitude already oscillates in the tail of the single soliton as it decays, providing direct means for the formation of bound states at discrete separations [24, 25, 27].

The interaction phase space diagram of our cubic system with filter looks qualitatively similar to that of the cubic-quintic complex Ginzburg–Landau equation [34, 36]. We can conclude that this kind of weak-interaction scenario is qualitatively independent from the mechanism of soliton stabilization (quintic nonlinearity or linear filter), although details as soliton width and interaction strength are affected by the details of the nonlinearity quantitatively, of course. This is maybe not surprising since the weak-interaction scenario is dominated by the spatial region in the middle between the solitons where the intensities of both LCS are rather small.

As the principal structure of the interaction plane has been described before [34, 36], we do not go into more detail but mention the deviations of the foci points from $\pm\pi/2$ (see, in particular, the innermost focus in Fig. 11b). It appears that the foci are slightly shifted from $\phi = \pi/2$ (asymptotically approaching $\pi/2$ for $L \to \infty$), while the exact $\pi/2$ would correspond to fixed points of center type, rather than attracting foci [41]. In summary when the soliton phase is strongly chirped, the dynamics in the interaction plane consists of sets of trajectories which spiral (sometimes very slowly if L is large) into one of a series of foci, each corresponding to a two-soliton bound state which moves transversely. These spirals are bounded by a semi-annulus consisting of a set of four heteroclinic trajectories separate linking adjacent pairs of $(0, \pi)$ saddles. This picture loses validity for very small values of L, when the description as a pair of separate,

weakly-interacting, solitons becomes problematic and soliton merging takes place [105] (see also the discussion in the following subsection).

For increasing absolute value of the imaginary part of g_2 (increasing α-factor of the semiconductor laser) the phase profile of the solitons becomes flatter and the saddles move to higher distances in the interaction plane. The chosen value of g_2 here corresponds to $\alpha = 0.5$, which is smaller than the experimentally relevant value ($\alpha \approx$2–9) but allows for an effective utilization of the interaction plane.

4.2 Semiconductor Class-B Model

As in the case of the Ginzburg–Landau model described above, the semiconductor class-B model (4)–(6) plus (7) does not contain any optical injection, i.e. it is not an externally driven system. The LCS are then free to choose their own frequency and phase. As such, each LCS can take on a different phase from its neighbouring LCS. We examine here the interaction between two LCS with an initial phase difference at a fixed value while increasing the initial spearation distance. In order to be closer to the experimental realization we use two separate values of the linewidth enhancement factor: $\alpha = 5.0$ and $\alpha = 9.0$. Other parameter values are: $\zeta = 1$, $\gamma = 0.01$, $T_1 = 0.008$, $T_2 = 0.0002$, $\tau_f = 0.05$ ns, $r_g = 0.9$ and $\sigma = 0.9$. For $\alpha = 9.0$ LCS are found for $J = 1.63$, $\theta = 1.0$ and $\delta = 0.0$ while for $\alpha = 5.0$ LCS are found for $J = 1.61$, $\theta = 1.0$ and $\delta = 2.0$. We note that since the reflection of the grating is large ($r_g = 0.9$) and the return times are relatively short, Lang–Kobayashi models cannot be applied here since they would produce spurious solutions with no physical meaning [52]. Model (4)–(7) does not contain Lang–Kobayashi approximations and carefully describes configurations close to the experimental realizations of high feedback reflectivities.

Figure 12 displays the single LCS profiles of amplitude and phase for the two parameter cases corresponding to $\alpha = 9.0$ and $\alpha = 5.0$. It is clear when comparing these figures with Fig. 11a that the LCS phase profiles greatly depend on the linewidth enhancement factor α. In the phase profile of the LCS in the Ginzburg–Landau model with $\alpha = 0.5$, the range of phase variation within the width over which the LCS is above the noise floor was larger than 9π. In the semiconductor class-B models with α factors ten times larger, the total phase variation over which the LCS is above the noise floor is instead just above π. The much smaller chirp of the LCS has important consequences on the position and dynamical relevance of the saddle points in the interaction $(Lcos(\Phi), Lsin(\Phi))$ plane (see Fig. 11b). By linearly fitting the phase profiles of the LCS we have estimated the position of the closest saddle points with growing distances L (taking the results of Fig. 11 as a guidance). In physical units the saddles are expected to be around $L = 108\,\mu$m and $L = 117\,\mu$m for $\alpha = 9.0$ and $\alpha = 5.0$, respectively, i.e. more than ten times the FWHM size of the LCS.

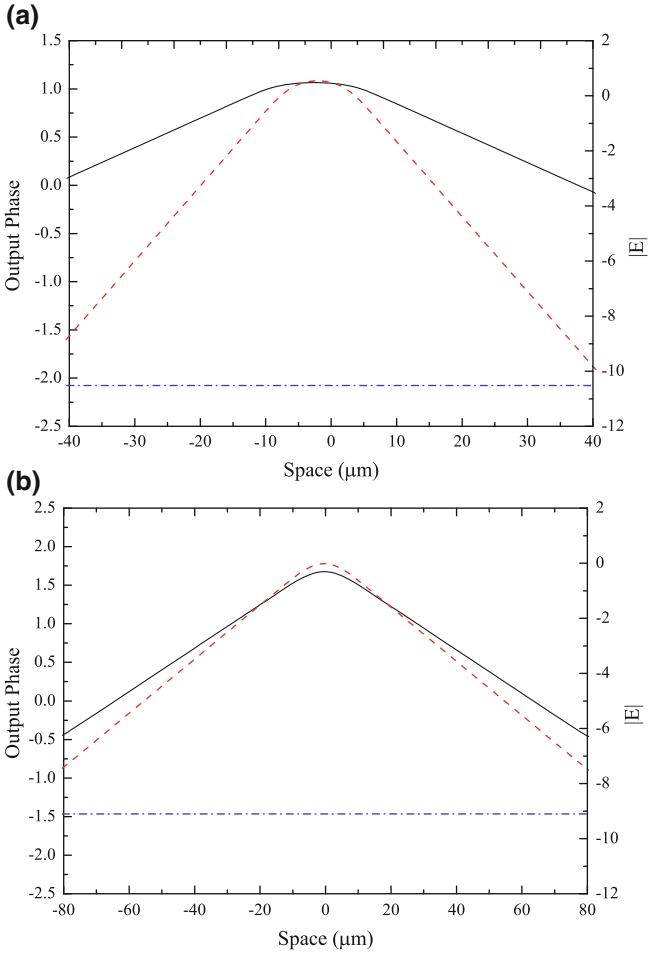

Fig. 12 (Color online) **a** The phase (*solid line*) and log of the amplitude (*dashed line*) of a LCS for $\alpha = 9.0$. **b** The phase (*solid line*) and log of the amplitude (*dashed line*) for a LCS with $\alpha = 5.0$. The *blue dashed-dotted line* corresponds to the noise floor

Numerical simulations of the interaction of two closely placed LCS on a homogeneous background have been performed. Figure 13 shows the temporal evolution of the laser intensity for the process of merging of two LCS when the initial distance of the LCS is 18.8 μm for $\alpha = 9$. The two peaks oscillate out of phase while approaching each other before merging takes place. Merging of interacting spatial solitons is intrinsically related to their dissipative nature and has been described at length in the case of VCSELs with optical injection in [105]. The phase difference between the LCS first rotates and then becomes ill-defined when one of the two LCS disappears.

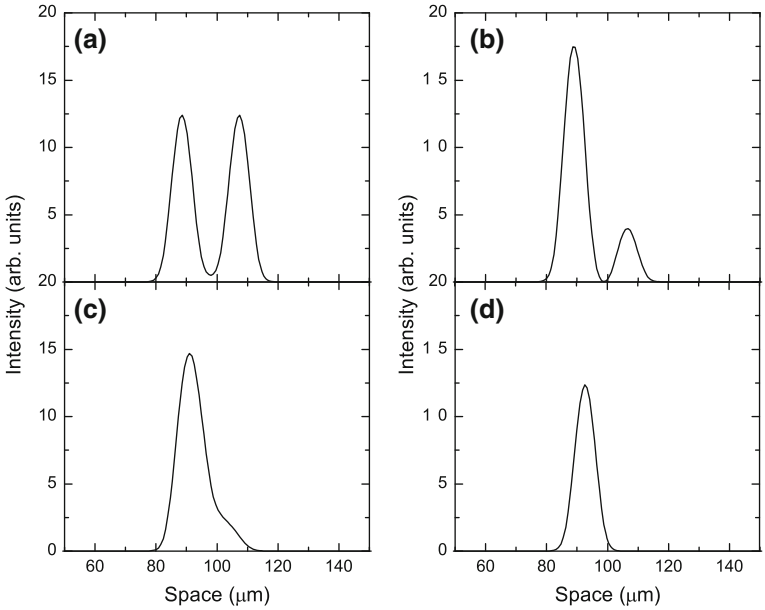

Fig. 13 Time evolution of the intensity of two interacting LCS for an initial distance of 18.8 μm and $\alpha = 9$ for the class-B VCSEL model with FSF. **a** $t = 0$ ns, **b** $t = 1.2$ ns, **c** $t = 1.8$ ns and **d** $t = 6$ ns. Parameter values are specified in the text

We have then increased the initial separation distances L of the LCS to 27 μm for $\alpha = 9.0$ and to 50 μm for $\alpha = 5.0$. These distances are above the critical values below which LCS merging is observed. Figure 14 shows the time evolution on the interaction plane $(Lcos(\Phi), Lsin(\Phi))$ of simulations starting at $\Phi = \pm 0.1\pi$.

One first observes a quick resetting of the LCS phase difference to the value of $\Phi = \pi$ followed by a very slow progressive separation of the two LCS. The tip of the *solid line* after phase resetting and along the horizontal axis of Fig. 14 corresponds to the final LCS distance after long extended simulations (90 μs). This means that the dashed line on the horizontal axis corresponds to regions where the LCS are almost incapable to interact. The situation is similar to what has been observed in numerical simulations for LCS in semiconductor lasers with saturable absorbers and large initial separation distances between the solitons [42]. In our case the LCS reach a distance larger than five soliton diameters at which they do not feel each other any longer. More importantly, the slowly decaying phase profile implies that interacting LCS at physical values of the α factor cannot reach the saddle points that re-direct the phase difference evolution towards the foci at $\Phi = \pi/2$ in the Ginzburg–Landau model of Sect. 4.1.

One cannot refer to the two LCS at the end of the simulations of the semiconductor class-B model of Fig. 14 as 'locked' although the phase difference Φ is π, since the LCS are not interacting any longer. Moreover, defects in the growth of the semiconductor material pin LCS to given spatial positions. For these reasons we

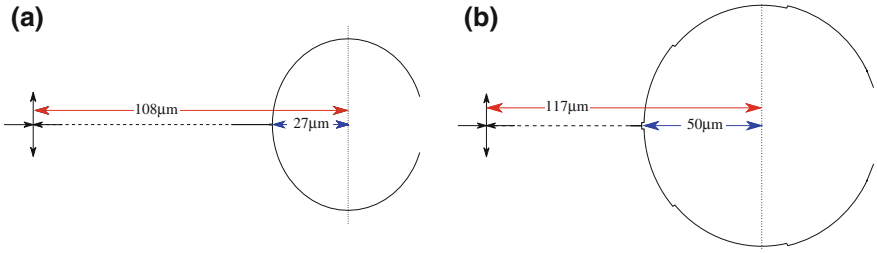

Fig. 14 The interaction plane $(Lcos(\Phi), Lsin(\Phi))$ showing a numerically calculated trajectory and the estimated location of the anticipated closest saddle for **a** $\alpha = 9.0$ and **b** $\alpha = 5.0$. The origin of the plane is in the center of the circle

decided that is was important to study locking of LCS when pinned in material defects as described in details in Sect. 5.

5 Theoretical Results: Inhomogeneous Systems and Adler-Locking

5.1 Ginzburg–Landau Model

We turn now to address the case of practical importance in which the interaction is between solitons trapped by defects. We break the translational invariance by imposing a pinning potential, $n(x)$, which is localized, being zero everywhere except in the intervals $x_j - \frac{W}{2} < x < x_j + \frac{W}{2}$ with $j = 1, 2$, where it is given by

$$n(x) = \frac{n_j}{2}\left[sin\left(-\frac{\pi}{2} + \frac{2\pi(x - x_j)}{W}\right) - 1\right]. \tag{10}$$

This potential is a smooth function, as shown for example in Fig. 16 by a gray line. The width W of each trap is chosen close to the width at half maximum of the LCS. The trap separation $L_t = |x_2 - x_1|$ is obviously an important parameter. We consider the practically-relevant initial condition where there is one soliton in each trap. In terms of the unperturbed (L, Φ) phase space diagram we are interested in trajectories emanating from (L_t, Φ_0), where Φ_0 is arbitrary.

We consider first the symmetric case of two identical traps with $n_1 = n_2 = n_0$, and examine the changes in the interaction plane trajectories as n_0 is increased. Since translation is a neutral mode of the unperturbed system, any attractive potential is able to trap an isolated LCS. Two solitons in identical, weak, traps will still interact, and the strength and sign of their interaction depend strongly on the separation L_t of their respective traps. As mentioned above, almost all trajectories in the trap-free case are attracted to one of the the foci in Fig. 11b for the considered values of g_2, in accordance with the literature [30, 31, 34]. The

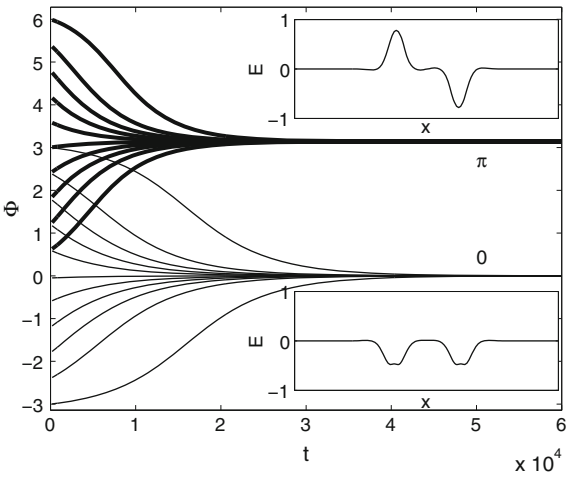

Fig. 15 Dynamics of the phase difference Φ for different initial values for $L_t = 1.9$ (*upper*, *bold lines*) and for $L_t = 2.1$ (*lower*, *thin lines*). The insets show the instantaneous real part distribution of the corresponding final states

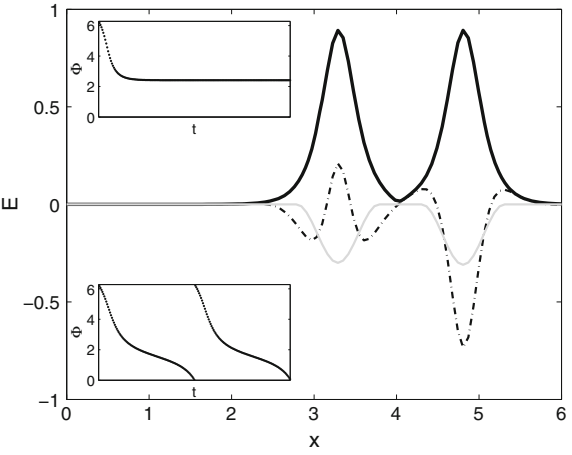

Fig. 16 The *bold line* is the spatial profile of amplitude of two coupled and synchronized solitons, the *dash dotted line* is the corresponding instantaneous real part profile. The *grey line* is the profile of the trapping potential with $n_1 = 3.0$ and $n_2 = 3.1$ ($n(x)/10$ is plotted). The insets show the dynamics of Φ. The *top* one is for $L_t = 1.581$, and displays synchronization. The *bottom* one is for $L_t = 1.644$—the LCS do not synchronize

corresponding bound states move with a *finite* speed, and so these states are not destroyed by infinitesimal perturbations, but only by those of finite amplitude. Since almost all trajectories in the interaction plane are attracted to a focus for $n_0 = 0$, they will still do so in the presence of infinitesimal perturbations. Trajectories starting close enough to a L-unstable saddle will however be modified by infinitesimal perturbations because the unstable eigenvalue becomes vanishingly small close enough to such a saddle. We can therefore expect that such saddles become stable nodes when L_t is close enough to the saddle separation. Such a node corresponds to the two solitons being phase-locked, either in-phase or out-of-phase, depending on L_t. The basin of attraction of each new node will be infinitesimal for an infinitesimal perturbation, but grows with n_0. Note that the

L-stable saddles of the homogeneous system are all Φ-unstable, and will remain so under perturbation.

For finite n_0, the solitons will phase-lock over a finite range of L_t around the saddle-separation. These trap-induced nodes will become the dominant attractors once n_0 is large enough to destroy the $\pi/2$ foci thus implying that the solitons remain locked for all times. For strongly-trapped solitons the interaction plane dynamics collapses onto the circle $L = L_t$, and the phase difference Φ is attracted to either 0 or π, depending on L_t but independent of Φ_0.

Due to the decrease of interaction strength with distance L, the outermost foci and saddles are affected first. For $n_0 = 3.0$ (still an order of magnitude smaller than $\mathrm{Im}(g_0) = 28$), the depth of the trap is large enough to prevent drift and to keep the solitons at fixed positions for $L_t > 1.25$, i.e. outside the central white region in Fig. 11b. At the same time, the perturbation by $n(x)$ is still small enough that the shape of the solitons deviates only slightly from (9) within the trap. Within each of the colored bands (light-gray or white) in Fig. 11b the locking phase is that of the saddle lying in that band, which is phase-stable in the unperturbed problem. This is illustrated in Fig. 15, where the anti-phase state is selected for $L_t = 1.9$ but the in-phase one for $L_t = 2.1$.

Since the trapped soliton pairs have a pure phase dynamics, we can attempt to describe the system by an Adler equation [66], the archetypical equation describing synchronization between coupled oscillators. For our case it can be written in the form

$$\frac{d\Phi}{dt} = \Delta\omega - \varepsilon \sin(\Phi)\,, \tag{11}$$

where $\Delta\omega$ is the trap-detuning (which is zero for $n_1 = n_2$), and ε is a coupling constant. In-phase and anti-phase solutions are selected for $\Delta\omega = 0$, depending on the sign of the coupling. For positive ε the stable final state is $\Phi = 0$, for negative ε it is $\Phi = \pi$. It is obvious from the above results that the distance between traps affects both the magnitude and sign of the coupling in our system. Corresponding terms appear in the perturbation analysis of the cubic-quintic Ginzburg–Landau equation [34]. The survival of the (slightly modified) $\pi/2$-states for weak perturbations, followed by a transition to in- or anti-phase locking was also observed numerically for the CQGLE with regular modulations [76, 78].

In- and anti-phase synchronization are the only possibilities in the Adler equation for $\Delta\omega = 0$, corresponding to the ideal situation of identical traps with $n_1 = n_2$. The pinning potential of real systems is however the result of the growth process of the semiconductor material and the traps are not identical. Then we model this fact by introducing a difference in the trap depths (gray line in Fig. 16). This difference leads to the crucial consequence that the natural frequencies of the two LCS are unequal, and so $\Delta\omega$ is finite in the Adler equation. For states with negligible interaction (large L_t), the phase difference evolves as a linear function of time, $\Phi = \Delta\omega t$. Decreasing L_t the coupling increases and the dynamics of Φ starts to deviate from a linear change (see Fig. 16 bottom inset). For small enough L_t,

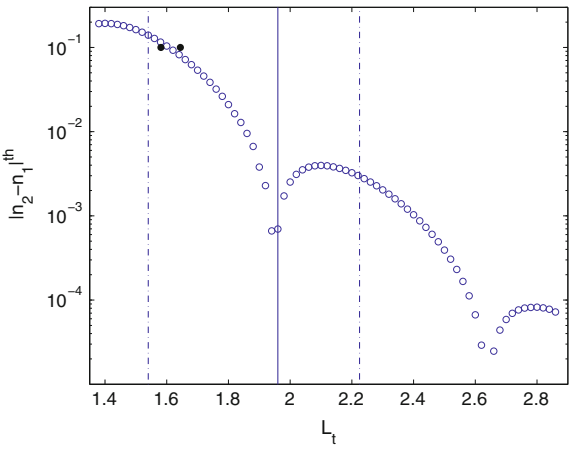

Fig. 17 Critical difference in trap depths for unlocking of LCS versus distance L_t between traps (*open circles*). The two *filled circles* correspond to the data of Fig. 16, which straddle the critical curve. The *vertical line* at $L_t \approx 2$ corresponds to the LCS separation in one of the focus states in the unperturbed problem, which appears linked to a local minimum of the locking range. The two *dash-dot vertical lines* correspond to the adjacent saddles

there is frequency and phase locking (see Fig. 16 top inset). One can see that the system is synchronized now to a phase-locked state (Fig. 16 main panel) with a locking phase which is neither 0 or π.

For a single soliton in a shallow trap direct numerical integration demonstrates that its frequency depends linearly on the depth of the trap. Hence, for each value of n_1 and n_2, we can calculate the frequencies ω_1 and ω_2 which the LCS would have in the absence of neighbors. We have studied the synchronization dynamics for different detunings $\Delta\omega$ for various choices $n_2 \neq n_1$, and found very good agreement with that predicted by the Adler equation (11) (see Fig. 18, for a plot). The stable steady state of the system (11) gives the simple expression $\sin^{-1}(\Delta\omega/\varepsilon)$ for the locked value of Φ. Locking obviously becomes impossible for $|\Delta\omega| > |\varepsilon|$, and we can use this limit to compute the coupling constant ε as a function of trap separation L_t. We find that the interaction strength has an oscillatory component superimposed on the expected decay with increasing trap separation, which we can attribute to the saddle distribution in the unperturbed problem, see Fig. 11. This is illustrated in Fig. 17.

One can interpret the findings in Figs. 11 and 17 in the way that the coupling coefficient ε has an (exponentially) damped oscillatory behavior with inter-soliton distance L_t. In particular this implies that the coupling becomes zero at some distances (at the boundaries between the ring-shaped regions in Fig. 11, where the direction of phase flow in the phase direction changes), at least in leading orders, and the tendency to locking is very weak. It also explains, at least qualitatively, why the points of strongest locking are shifted away from the center of the ring-shaped regions in Fig. 11: The coupling strength is defined by the maximum of the product of the exponential decay and the oscillatory component and hence occurs at smaller distances than the maximum of the oscillation, which determines the ring structures. The decay of coupling strength is related to the diminishing overlap between the soliton tails with increasing distance, the oscillatory

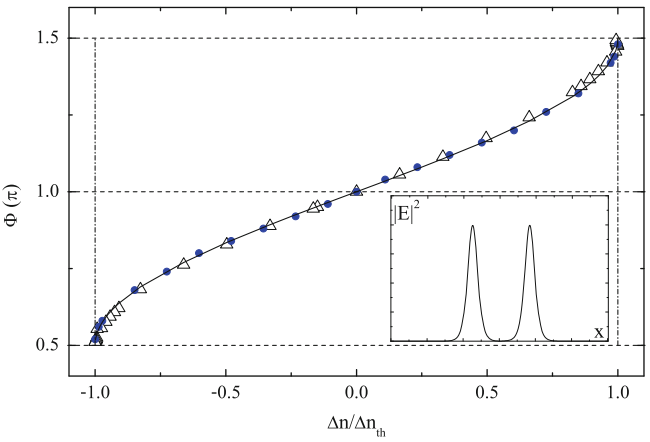

Fig. 18 (Color online) Locked phase differences Φ of pinned LCS versus the potential depth difference $\Delta n = n_1 - n_2$ from integration of the semiconductor class-B model (*triangles*, LCS separation of 4 soliton widths) and Ginzburg–Landau model (*blue circles*, $|x_2 - x_1| = 1.5$). The *solid line* refers to the Adler equation (11) for negative ε. The inset shows the near-field profile of the $|E|^2$ of two interacting LCS. Such profile changes very little across the Adler locking region. From [65]

component to the change of interference conditions due to chirp. One can also reinterpret the sequence of phase-stable and phase-unstable saddles at $\Phi = 0, \pi$ in Fig. 11 as being due to an Adler-type phase selection for zero detuning and an oscillatory sign of the coupling coefficient ε. Indeed, for the LSA and the CQGLE Adler-type equations for the relative phase with an interaction coefficient showing an exponentially damped oscillatory behavior with distance were derived in [34, 41], but with additional terms due to the translational Goldstone mode. Of course, the damped oscillatory behavior of the phase-coupling coefficient with inter-soliton distance in the Adler equation is related to a corresponding behavior of the overall interaction strength between solitons with inter-soliton distance as described first in [29] and then explored in many of the references given in the introduction.

Taking into account the L_t dependence by scaling $\Delta\omega$ by ε, the Adler equation predicts a universal *arcsin* dependence of the locking phase on the trap-detuning. We find just such a dependence for a broad range of parameters. An example is shown in Fig. 18 for $L_t = 1.5$, where analogous data for the semiconductor class-B model shows exactly the same Adler signature as discussed in the following section.

Before ending this section, we mention that two LCS in two traps of different depths (or widths) are obviously not entirely equivalent but for the parameters considered the differences are negligible as shown by the profiles in Fig. 16. The same holds for the class-B case discussed below. In the experiment there are actually noticeable variations in width and amplitude between different LCS, although still small, as evidenced in Fig. 5 (see also the text in Sect. 2.2 and [49]).

5.2 Semiconductor Class-B Model

The locking of LCS pinned to background defects as observed experimentally in the VCSEL with frequency-selective feedback in Sect. 2 and in the simulations of the Ginzburg–Landau model in Sect. 5.1 is a universal phenomenon and has been found in the semiconductor class-B model of Eqs. (4)–(7) too. In order to simulate the presence of the pinning defects, we have modified the field equation to

$$\partial_t E = -(1+i\theta)E + i\frac{\partial^2}{\partial x^2}E + \sigma(1-i\alpha)(N-1)E + in(x)E + \frac{2\sqrt{T_1}}{(T_1+T_2)}F, \quad (12)$$

where the feedback field is still given by Eq. (6) and the trapping potential $n(x)$ is equal to zero everywhere except in the two intervals $x_j - W < x < x_j + W$ where $n(x) = n_j$ with $j = 1, 2$. The homogeneous case is recovered when $n_1 = n_2 = 0$. The pinning potential is now a step function of x and the width $2W$ of the defects is chosen to be around twice the width at half maximum of the LCS. As in the Ginzburg–Landau case, differences between the defects are described by the depths n_1 and n_2 of the pinning potential. For n_j different from zero, the presence of the pinning potential breaks the translational invariance of each LCS. Small variations of n_j from zero lead to small changes in the soliton frequency ω without modifying its stability properties.

If two trapped defects are close enough in space, the LCS interaction locks their phase difference to values that depend on $\Delta n = n_1 - n_2$ until the potential depth difference is too large to maintain strong interaction. When compared to the case without defects (see Sect. 4.2) the evolution of the phase difference Φ between the trapped LCS contains now only a fast relaxation to well determined stationary values that depend on Δn and consequently on the frequency difference between the two LCS. The triangles in Fig. 18 show the stationary phase difference Φ from numerical simulations of Eq. (12) and (5)–(7) when changing the depth of one of the trap while keeping the second one fixed to the value of -0.1 while the distance between the centres of the traps is kept fixed at $|x_2 - x_1| = 31\,\mu\text{m}$. LCS phase locking takes place for $|\Delta n| < \Delta n_{tr}$. This locking phenomenon is universal for LCS pinned by defects and the blue circles in Fig. 18 corresponds to numerical simulations of the Ginzburg–Landau model of Sect. 18 under very different conditions of operation. The solid line in Fig. 18 shows an excellent agreement of the Adler equation (11) predictions with the numerical results of both the Ginzburg–Landau and the semiconductor class-B models for two interacting LCS trapped by defects.

In the locked state, LCS have a fixed phase difference and the same frequency. This is demonstrated in Fig. 19a where the optical spectra for two values of Δn inside the locked region are shown, which correspond to $\Delta n/\Delta n_{th} = 0$ and 0.99, respectively. Within the locked region, the spectra of the two LCS overlap exactly indicating a strong interaction. There is a progressive shift of the locked frequency while scanning the Adler region. This matches qualitatively the experimental results in Figs. 8 and 9, though the absolute value is much lower. This is not

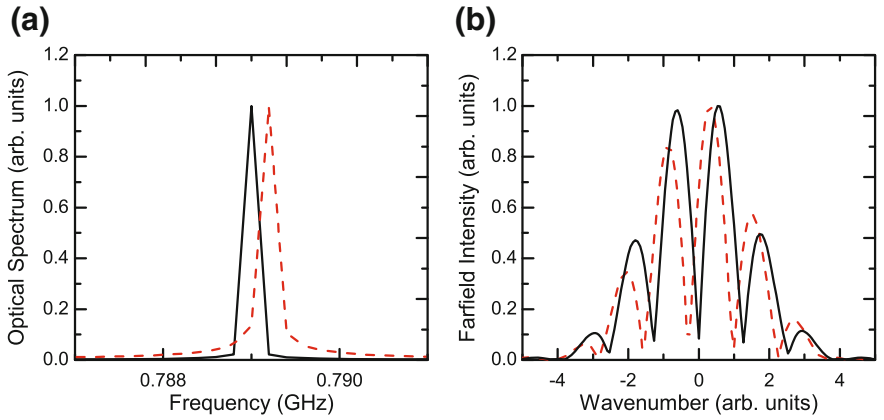

Fig. 19 Optical spectra for a time window of 5 μs (**a**) and far field fringes averaged over 2 μs (**b**), for $\Delta n/\Delta n_{th} = 0$ (*solid lines* in **a** and **b**) and 0.99 (*dashed lines* in **a** and **b**). In **a** each line contains the overlap of the spectra of both LCS. Simulations of the semiconductor class-B model

surprising, because the technique used to change detuning in the experiment is different.

Figure 19b displays the corresponding far field images. Interference fringes between the two locked solitons are clearly visible. A progressive change of the LCS phase difference Φ (from π at $\Delta n/\Delta n_{th} = 0$ to around 1.5π at $\Delta n/\ \Delta n_{th} = 0.99$) is reflected in the change in the symmetry of the fringe pattern. All these features of the LCS locked states are confirmed in the Ginzburg–Landau model and, more importantly, in the experiments on VCSELs with frequency-selective feedback presented in Sect. 2.

Both optical spectrum and far-field fringes change greatly as soon as one moves outside of the locking range as shown in Fig. 20 for $\Delta n/\Delta n_{th} = 2$ and 5. The spectra of the two LCS are now clearly separated although a partial overlap of some of the peaks is still present due to the non-uniform evolution of the relative phase. Such feature affects the far-field image, too, where some interference maxima are still visible although progressively disappearing with increasing Δn. For very large difference of the defect minima, the fringe visibility disappears completely, as expected for two LCS with large frequency separation.

The Adler locked state between LCS is a robust feature independent of initial conditions such as initial phases, frequencies and sequential order of creation of the two LCS. Once the locked state is attained, one of the two LCS can be switched off by a short, localized perturbation to the carrier density at its location. Hence, LCS retain their solitonic properties in the phase-locked state in the sense that they are still individually bistable and optically controllable.

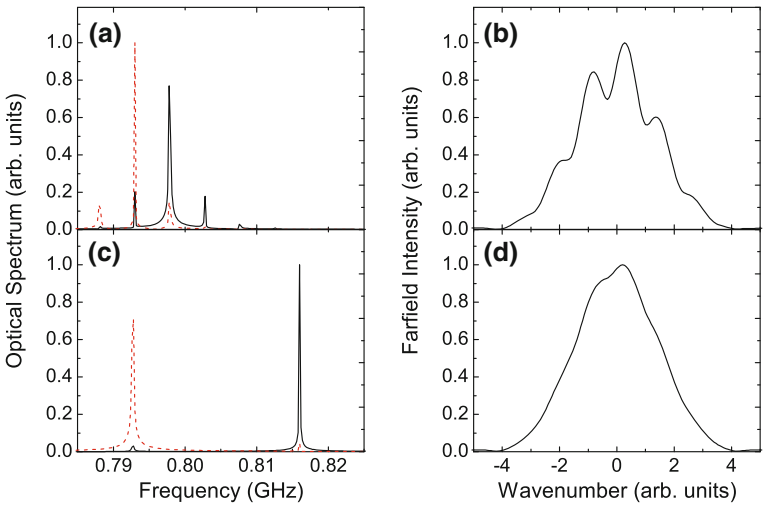

Fig. 20 Optical spectra for a time window of 5 μs **a–c** and far field fringes averaged over 2 μs **b–d**, for $\Delta n/\Delta n_{th} = 2$ (**a–b**) and 5 (**c–d**). In **a** and **c** the *solid* and *dashed lines* correspond to the spectra of each LCS

6 Conclusions

Lasers are oscillators of very high-frequency electromagnetic radiation amplified via stimulated emission in a cavity. Thus, it is not surprising that coupled lasers lock their phases and frequencies in a way similar to oscillators as demonstrated in the seventies through injection locking [9]. Indeed phase and frequency locking of master-slave lasers is almost as old as the laser itself [2]. In the nineties, coupling between adjacent laser elements in arrays also resulted in phase locking typical of coupled oscillators [4].

Here we have demonstrated that locked laser beams can be contained in the same semiconductor laser device in the form of coupled spatial solitons. The specific configuration of choice is that of a VCSEL with frequency-selective feedback provided by a volume Bragg grating. Such systems has been shown to sustain localized structures in the form of bright LCS corresponding to narrow intensity peaks of coherent light on a dark background [47–49]. In principle, well separated LCS are independent micro-laser beams that can be individually addressed and removed thus forming an optical memory. Theoretically, the interaction of two phase-chirped LCS should lead to a phase locked state with a frequency difference close to $\pi/2$ in a way similar to what is observed in temporal-longitudinal systems [40]. The reality of VCSELs with frequency-selective feedbacks is however quite different from this scenario. First, realistic values of the linewidth enhancement factor α strongly reduce the LCS phase chirp making it impossible to observe the $\pi/2$ locking even on homogeneous backgrounds.

Secondly and more importantly, LCS in real systems are pinned to local defects that are due to the growth process of the semiconductor material. We have shown that the pinning process has two fundamental effects on a single LCS: to break the translational symmetry and to modify its frequency. When these effects are taken into consideration, the picture of the interaction of pinned LCS changes drastically from that of cavity solitons in temporal-longitudinal systems. We demonstrated both experimentally and theoretically that two trapped LCS in VCSELs with frequency-selective feedback display Adler synchronization leading to phase and frequency locking.

We expect similar considerations to apply to solitons in LSA and non-semiconductor systems with phase symmetry such as photorefractive oscillators. Moreover our study uses a continuous model, but synchronization is between discrete entities, the solitons. As such, we have provided a bridge between spatially extended media and coupled, predefined oscillators. Furthermore we note that the LCS are quite peculiar micro-lasers since they are self-localized and bistable so that new interesting dynamics beyond the standard Adler scenario is expected from these properties.

We plan to extend the study of interaction of pinned LCS from two to multiple elements as well as considering their pinning into externally induced regularly and irregularly arranged traps. This can be based on codes already developed for 2D dynamical simulations and stability analysis of single soliton solutions in the CGLE-F as well as class-B models [52, 80, 106]. In view of the random detuning conditions due to the disorder, it can be anticipated that it is impossible, or at least difficult, to achieve locking of more than two LCS by a single, global control parameter (as the VBG tilt). Although we occasionally observed phase-locking of three solitons [107], it would be useful to have control on the local values of the detuning, in addition to the global one used in this work. Previous investigations established that the hysteresis loop of LCS can be shifted to some extent independently by local injection of an external beam [108]. The external beam generates or depletes carriers (depending on wavelength), the refractive index changes and this causes a shift of the cavity resonance (there might be a thermal effect in addition) and finally of switching thresholds. Although not investigated in [108], we expect the change of switching thresholds to be accompanied by a change in frequency. This would open up the intriguing possibility of shaping the disorder dynamically via an external beam structured with a spatial light modulator.

Acknowledgments P.V.P. acknowledges support from SFB 910; C.M., and Y.N. from EPSRC DTA; P.C. from MICINN and Feder (FIS2007-60327, FISICOS, TEC2009-14101, DeCoDicA). Y.N. and C.M. were supported by EPSRC DTA/DTG grants. We are grateful to A. G. Vladimirov for useful discussions, R. Jäger (Ulm Photonics) for the devices and N. Radwell for fruitful collaboration in the initial phases of the work. Phase locking of LCS was first described in his thesis [107].

References

1. H. Haken, Zeitschrift fur Physik **181**, 96 (1964)
2. J.W. Crowe, W.E. Ahearn, IEEE J. Quantum Electron. **4**, 169 (1968)
3. Z. Jiang, M. McCall, J. Mod. Opt. **39**, 159 (1992)
4. L. Fabiny, P. Colet, R. Roy, D. Lenstra, Phys. Rev. A **47**, 4287 (1993)
5. M. Möller, B. Forsmann, W. Lange, Chaos, Solitons & Fractals **10**, 825 (1999)
6. A. Pikovsky, M. Rosenblum, J. Kurths, *Synchronization—A Universal Concept in Nonlinear Sciences, Cambridge Nonlinear Science Series*, vol. 12 (Cambridge University Press, Cambridge, 2001)
7. S. Strogatz, I. Steward, Sci. Am. **269**, 102 (1993)
8. R.H. Pantell, Proc. IEEE **53**, 474 (1965)
9. C.J. Buczek, R.J. Freiberg, M.L. Skolnick, Proc. IEEE **61**, 1411 (1973)
10. J.J. Raftery, A.C. Lehman, A.J. Danner, P.O. Leisher, A.V. Giannopoulos, K.D. Choquette, Appl. Phys. Lett. **89**, 081119 (2006)
11. L.D.A. Lundeberg, G.P. Lousberg, D.L. Boiko, E. Kapon, Appl. Phys. Lett. **90**, 021103 (2007)
12. H. Pier, E. Kapon, Opt. Lett. **22**, 546 (1997)
13. K. Otsuka, Y. Miyasaka, T. Narita, S.C. Chu, C.C. Lin, J.Y. Ko, Phys. Rev. Lett. **97**, 213901 (2006)
14. P. Colet, R. Roy, Opt. Lett. **19**, 2056 (1994)
15. G. Van Wiggeren, R. Roy, Science **20**, 1198 (1998)
16. J. Goedgebuer, L. Larger, H. Porte, Phys. Rev. Lett. **80**, 2249 (1998)
17. A. Argyris, D. Syvridis, L. Larger, V. Annovazzi-Lodi, P. Colet, I. Fischer, J. Garcia-Ojalvo, C.R. Mirasso, L. Pesquera, A. Shore, Nature **437**, 343 (2005)
18. G.I. Stegeman, M. Segev, Science **286**, 1518 (1999)
19. N. Akhmediev, A. Ankiewicz, *Dissipative Solitons, Lecture Notes in Physics*, vol. 661 (Springer, Berlin, 2005)
20. N. Akhmediev, A. Ankiewicz, *Dissipative Solitons: From Optics to Biology and Medicine: Lecture Notes in Physics*, vol. 751 (Springer, Berlin, 2008)
21. N.N. Rosanov, *Spatial hysteresis and optical patterns. Springer Series in Synergetics* (Springer, Berlin, 2002)
22. K. Staliunas, V. Sánchez-Morcillo, *Transverse Patterns, Springer Tracts in Modern Physics*, vol. 183 (Springer, Berlin, 2003)
23. S. Barland, J.R. Tredicce, M. Brambilla, L.A. Lugiato, S. Balle, M. Giudici, T. Maggipinto, L. Spinelli, G. Tissoni, T. Knödel, M. Miller, R. Jäger, Nature **419**, 699 (2002)
24. N.N. Rosanov, G.V. Khodova, J. Opt. Soc. Am. B **7**, 1057 (1990)
25. B. Schäpers, M. Feldmann, T. Ackemann, W. Lange, Phys. Rev. Lett. **85**, 748 (2000)
26. D.Y. Tang, W.S. Man, H.Y. Tam, P.D. Drummond, Phys. Rev. A **64**, 033814 (2001)
27. P.L. Ramazza, E. Benkler, U. Bortolozzo, S. Boccaletti, S. Ducci, F.T. Arecchi, Phys. Rev. E **65**, 066204 (2002)
28. C.P. Schenk, P. Schütz, M. Bode, H.G. Purwins, Phys. Rev. E **57**, 6480 (1998)
29. B.A. Malomed, Phys. Rev. A **44**, 6954 (1991)
30. N. Akhmediev, A. Ankiewicz, J.M. Soto-Crespo, Phys. Rev. Lett. **79**, 4047 (1997)
31. V.V. Afanasjev, B.A. Malomed, P.L. Chu, Phys. Rev. E **56**, 6020 (1997)
32. N. Akhmediev, F. Zen, P. Chu, Opt. Commun. **201**, 217 (2002)
33. H. Leblond, A. Komarov, M. Salhi, A. Haboucha, F. Sanchez, J. Opt. A **8**, 319326 (2006)
34. D. Turaev, A.G. Vladimirov, S. Zelik, Phys. Rev. E **75**, 045601(R) (2007)
35. J.M. Soto-Crespo, P. Grelu, N. Akhmediev, N. Devine, Phys. Rev. E **75**, 016613 (2007)
36. A. Zavyalov, R. Iliew, O. Egorov, F. Lederer, Phys. Rev. A **79**, 053841 (2009)
37. P. Grelu, F. Belhache, F. Gutty, J.M. Soto-Crespo, Opt. Lett. **27**, 966 (2002)
38. J.M. Soto-Crespo, N. Akhmediev, P. Grelu, F. Belhache, Opt. Lett. **28**, 1757 (2003)
39. D.Y. Tang, B. Zhao, L.M. Zhao, H.Y. Tam, Phys. Rev. A **64**, 016616 (2005)

40. P. Grelu, N. Akhmediev, Nat. Phot. **6**, 84 (2012)
41. A.G. Vladimirov, G.V. Khodova, N.N. Rosanov, Phys. Rev. E **63**, 056607 (2001)
42. H. Vahed, R. Kheradmand, H. Tajalli, G. Tissoni, L.A. Lugiato, F. Prati, Phys. Rev. A **84**, 063814 (2011)
43. V.Y. Bazhenov, V.B. Taranenko, M.V. Vasnetsov, Proc. SPIE **1806**, 14 (1992)
44. M. Saffman, D. Montgomery, D.Z. Anderson, Opt. Lett. **19**, 518 (1994)
45. V.B. Taranenko, K. Staliunas, C.O. Weiss, Phys. Rev. A **56**, 1582 (1997)
46. G. Slekys, K. Staliunas, C.O. Weiss, Opt. Commun. **149**, 113 (1998)
47. Y. Tanguy, T. Ackemann, W.J. Firth, R. Jäger, Phys. Rev. Lett. **100**, 013907 (2008)
48. Y. Tanguy, N. Radwell, T. Ackemann, R. Jäger, Phys. Rev. A **78**, 023810 (2008)
49. N. Radwell, T. Ackemann, IEEE J. Quantum Electron. **45**, 1388 (2009)
50. P.V. Paulau, A.J. Scroggie, A. Naumenko, T. Ackemann, N.A. Loiko, W.J. Firth, Phys. Rev. E **75**, 056208 (2007)
51. P.V. Paulau, D. Gomila, T. Ackemann, N.A. Loiko, W.J. Firth, Phys. Rev. E **78**, 016212 (2008)
52. A.J. Scroggie, W.J. Firth, G.L. Oppo, Phys. Rev. A **80**, 013829 (2009)
53. P. Genevet, S. Barland, M. Giudici, J.R. Tredicce, Phys. Rev. Lett. **101**, 123905 (2008)
54. T. Elsass, K. Gauthron, G. Beaudoin, I. Sagnes, R. Kuszelewicz, S. Barbay, Appl. Phys. B **98**, 327 (2010)
55. M. Bache, F. Prati, G. Tissoni, R. Kheradmand, L.A. Lugiato, I. Protsenko, M. Brambilla, Appl. Phys. B **81**, 913 (2005)
56. L. Columbo, L. Gil, P. Genevet, Eur. Phys. J. D **59**, 97107 (2010)
57. T. Ackemann, G.L. Oppo, W.J. Firth, Adv. Atom. Mol. Opt. Phys. **57**, 323 (2009)
58. S. Barbay, R. Kuszelewicz, J.R. Tredicce, Adv. Opt. Tech. **2011**, 628761 (2011)
59. P. Genevet, M. Turconi, S. Barland, M. Giudici, J.R. Tredicce, Eur. Phys. J. D **59**, 109 (2010)
60. N.N. Rosanov, Proc. SPIE **1840**, 130 (1991)
61. W.J. Firth, A.J. Scroggie, Phys. Rev. Lett. **76**, 1623 (1996)
62. F. Pedaci, S. Barland, E. Caboche, P. Genevet, M. Giudici, J.R. Tredicce, T. Ackemann, A.J. Scroggie, W.J. Firth, G.L. Oppo, G. Tissoni, R. Jäger, Appl. Phys. Lett. **92**, 011101 (2008)
63. F. Pedaci, G. Tissoni, S. Barland, M. Giudici, J.R. Tredicce, Appl. Phys. Lett. **93**, 111104 (2008)
64. T. Ackemann, N. Radwell, Y. Noblet, R. Jäger, Opt. Lett. **37**, 1079 (2012)
65. P.V. Paulau, C. McIntyre, Y. Noblet, N. Radwell, W.J. Firth, P. Colet, T. Ackemann, G.L. Oppo, Phys. Rev. Lett. **108**, 213904 (2012)
66. R. Adler, Proc. IRE **34**, 351 (1946)
67. P. Coullet, D. Daboussy, J.R. Tredicce, Phys. Rev. E **58**, 5347 (1998)
68. D. Goulding, S.P. Hegarty, O. Rasskazov, S. Melnik, M. Hartnett, G. Greene, J.G. McInerney, D. Rachinskii, G. Huyet, Phys. Rev. Lett. **98**, 153903 (2007)
69. J. Thévenin, M. Romanelli, M. Vallet, M. Brunel, T. Erneux, Phys. Rev. Lett. **107**, 104101 (2011)
70. A. Schwache, F. Mitschke, Phys. Rev. E **55**, 7720 (1997)
71. F. Leo, S. Coen, P. Kockaert, S.P. Gorza, P. Emplit, M. Haelterman, Nat. Phot. **4**, 471 (2010)
72. W.J. Firth, Nat. Phot. **4**, 415 (2010)
73. A. Shipulin, G. Onishchukov, B.A. Malomed, J. Opt. Soc. Am. B **14**, 3393 (1197)
74. B.A. Malomed, A. Shipulin, Opt. Commun. **162**, 140 (2009)
75. W.W. Hsiang, C.Y. Lin, Y. Lai, Opt. Lett. **31**, 1627 (2006)
76. W. Chang, N. Akhmediev, S. Wabnitz, Phys. Rev. A **80**, 013815 (2009)
77. W. Chang, N. Akhmediev, S. Wabnitz, M. Taki, J. Opt. Soc. Am. B **26**, 2204 (2009)
78. Y.J. He, B.A. Malomed, D. Mihalache, B. Liu, H.C. Huang, H. Yang, H.Z. Wang, Opt. Lett. **34**, 2976 (2009)
79. W.J. Firth, P.V. Paulau, Eur. Phys. J. D **59**, 13 (2010)

80. P.V. Paulau, D. Gomila, P. Colet, B.A. Malomed, W.J. Firth, Phys. Rev. E **84**, 036213 (2011)
81. M. Grabherr, R. Jäger, M. Miller, C. Thalmaier, J. Herlein, K.J. Ebeling, IEEE Photon. Technol. Lett. **10**, 1061 (1998)
82. M. Grabherr, M. Miller, R. Jäger, R. Michalzik, U. Martin, H.J. Unold, K.J. Ebeling, IEEE J. Sel. Top. Quantum Electron. **5**, 495 (1999)
83. M. Schulz-Ruhtenberg, Y. Tanguy, K.F. Huang, R. Jäger, T. Ackemann, J. Phys. D Appl Phys. **42**, 055101 (2009)
84. T. Ackemann, S. Barland, M. Cara, S. Balle, J.R. Tredicce, R. Jäger, P.M. Grabherr, M. Miller, K.J. Ebeling, J. Opt. B Quantum Semiclass. Opt. **2**, 406 (2000)
85. Y. Noblet, T. Ackemann, Phys. Rev. A **85**, 05381 (2012)
86. P. Genevet, S. Barland, M. Giudici, J.R. Tredicce, Phys. Rev. Lett. **104**, 223902 (2010)
87. A. Naumenko, N.A. Loiko, M. Sondermann, K.F. Jentsch, T. Ackemann, Opt. Commun. **259**, 823 (2006)
88. A.V. Naumenko, N.A. Loiko, T. Ackemann, Phys. Rev. A **76**, 023802 (2007)
89. C.H. Henry, IEEE J. Quantum Electron. **18**, 259 (1982)
90. L.A. Lugiato, Progress in Optics XXI pp. 70–216 (1984)
91. R. Neubecker, T. Tschudi, J. Mod. Opt. **41**, 885 (1994)
92. R. Kuszelewicz, I. Ganne, I. Sagnes, G. Slekys, Phys. Rev. Lett. **84**, 6006 (2000)
93. D. Sanvitto, D.N. Krizhanovskii, D.M. Whittaker, S. Ceccarelli, M.S. Skolnick , J.S. Roberts, Phys. Rev. B **73**, 241308(R) (2006)
94. J.P. Weber, K. Malloy, S. Wang, IEEE Photon. Tech. Lett. **2**, 162 (1990)
95. J.L. Oudar, R. Kuszelewicz, B.G. Sfez, J.C. Michel, R. Planel, Opt. Quantum Elect. **24**, S193 (1992)
96. J.P. Seipenbusch, T. Ackemann, B. Schäpers, B. Berge, W. Lange, Phys. Rev. A **56**, R4401 (1997)
97. R. Lang, K. Kobayashi, IEEE J. Quantum Electron. **16**, 347 (1980)
98. D.M. Kane, K.A. Shore, *Unlocking Dynamical Diversity: Optical Feedback Effects on Semiconductor Lasers* (Wiley, New York, 2005)
99. M. Giudici, S. Balle, T. Ackemann, S. Barland, J.R. Tredicce, J. Opt. Soc. Am. B **16**, 2114 (1999)
100. L. Spinelli, G. Tissoni, M. Brambilla, F. Prati, L.A. Lugiato, Phys. Rev. A **58**, 2542 (1998)
101. J. Atai, B.A. Malomed, Phys. Rev. E **54**, 4371 (1996)
102. H. Sakaguchi, B.A. Malomed, Physica D **154**, 229 (2001)
103. J. Atai, B.A. Malomed, Phys. Lett. A **246**, 412 (1998)
104. N.R. Pereira, L. Stenflo, Phys. Fluids **20**, 1733 (1998)
105. C. McIntyre, A.M. Yao, G.L. Oppo, F. Prati, G. Tissoni, Phys. Rev. A **81**, 013838 (2010)
106. P.V. Paulau, D. Gomila, P. Colet, N.A. Loiko, N.N. Rosanov, T. Ackemann, W.J. Firth, Opt. Exp. **18**, 8859 (2010)
107. N. Radwell, Characteristics of a Cavity Soliton Laser Based on a VCSEL with Frequency Selective Feedback. Ph.D. thesis, University of Strathclyde, 2010
108. N. Radwell, P. Rose, C. Cleff, C. Denz, T. Ackemann, Opt. Exp. **18**, 23121 (2010)

Light-Induced Breaking of Symmetry in Photonic Crystal Waveguides with Nonlinear Defects as a Key for All-Optical Switching Circuits

Evgeny Bulgakov, Almas Sadreev and Konstantin N. Pichugin

Abstract We consider light transmission in 2D photonic crystal waveguide coupled with two identical nonlinear defects positioned symmetrically aside the waveguide. We show that with growth of injected light power there is a breaking of symmetry by two ways. In the first way the symmetry is broken because of different light intensities at the defects. In the second way the intensities at the defects are equaled but phases of complex amplitudes are different. That results in a vortical power flow between the defects similar to the DC Josephson effect if the input power over the waveguide is applied and the defects are coupled. As application of these phenomena we consider the symmetry breaking for the light transmission in a T-shaped photonic waveguide with two nonlinear defects. We demonstrate as this phenomenon can be explored for all-optical switching of light transmission from the left output waveguide to the right one by application of input pulses. Finally we consider the symmetry breaking in the waveguide coupled with single defect presented however by two dipole modes.

1 Introduction

Symmetry breaking in a nonlinear quantum system is a fundamental effect caused by the interplay of nonlinearity with linear potential which defines the symmetry. It is commonly known that the ground state in one-dimensional linear quantum mechanics is nodeless and follows the symmetry of the potential. However the self-attractive nonlinearity in the nonlinear Schrödinger equation breaks the

E. Bulgakov · A. Sadreev (✉) · K. N. Pichugin
Kirensky Institute of Physics, Krasnoyarsk, Russia 660036
e-mail: almas@tnp.krasn.ru

Progress Optical Sci., Photonics (2013): 89–124
DOI: 10.1007/10091_2012_1

Published Online: 19 February 2012

symmetry of the ground state, replacing it by a new asymmetric state minimizing the system's energy. For example, the nonlinear Schrödinger equation in double-well potential reveals asymmetric ground state with variation of normalization of the state [1, 2]. The phenomenon of the spontaneous symmetry breaking in analogy with the double-well potential are realized in a nonlinear dual-core directional fiber [3–5]. Spontaneous symmetry breaking was demonstrated recently by Brazhnyi and Malomed in a linear discrete chain (Schrödinger lattice) with two nonlinear sites [6]. They have shown as analytically as well as numerically the existence of symmetric, anti-symmetric, and non-symmetric eigenmodes with eigen-frequencies below the propagation band of the chain, and that a variation of the population of modes can give rise to a bifurcation form one to another mode. The system has direct relation to photonic crystal (PhC) waveguides with two in-channel nonlinear cavities where the population of the cavities might be governed by external source of the light.

Indeed, the phenomenon of symmetry breaking is studied in the nonlinear optics with injection of input power with the establishment of one or more asymmetric states which no longer preserve the symmetry properties of the original state [7–11]. In particular Maes et al. [12, 13] considered the symmetry breaking for the nonlinear cavities aligned along the waveguide, that is a Fabry-Pérot architecture close to the system considered in Ref. [9]. That system is symmetric relative to the mirror of the transport axis if equal power is injected on both sides of the coupled cavities. The symmetry breaking was found also for the case of many coupled nonlinear optical cavities in ring-like architecture [14, 15]. In the Sect. 2 we write the equations of motion for the nonlinear optical cavities coupled with PhC waveguides by using an analogy of the two-dimensional PhC with quantum mechanics [16]. As for an application we consider three simple PhC systems which undergo the symmetry breaking phenomena for variation of the light frequency or the input power. The first simplest system is two identical nonlinear defects positioned symmetrically aside a linear waveguide (Sect. 3). Each defect is presented by single monopole mode. We show two types of the symmetry breaking [17, 18]. In the first type the symmetry is broken because of different light intensities at the defects. In the second type of the symmetry breaking the intensities at the cavities are equal but phases of complex amplitudes are different. That results in a vortical power flow between the defects similar to the DC Josephson effect if the input power over the waveguide is applied, and the defects are coupled.

In Sect. 4 we consider as the phenomenon of the symmetry breaking can be explored for so called all-optical switching [19–22] by use of the T-shaped photonic waveguide with two identical nonlinear cavities positioned symmetrically. That system combines two systems. The first one is the Fabry-Pérot interferometer (FPI) consisting of two nonlinear off-channel cavities aligned along the linear waveguide considered in Refs. [12, 13, 23]. As was shown in Ref. [23] there is a discrete set of the a self-induced bound (localized) states in continuum (BSC) which are the standing waves between off-channel cavities. In the second system two nonlinear cavities are aligned perpendicular to the input waveguide. As was said above there is the anti-bonding BSC which was recently observed

experimentally in PhC [24]. Here we show that both types of the bound states might be important for the breaking of symmetry. All these phenomena agree well with computations based on an expansion of the electromagnetic field into optimally adapted photonic Wannier functions in two-dimensional PhC [25, 26].

Finally, in Sect. 5 we consider the single nonlinear defect with two dipole eigen-modes which belong to the propagation band of the PhC linear waveguide (Sect. 3). We demonstrate the symmetry breaking provided that the system is excited with equal powers from both sides similar to that Maes et al. has shown in the system of two coupled nonlinear cavities [12, 13].

Finally, we note that the Sects. 2–4 mostly review the papers [17, 18, 27] which were published in 2011 for preparation of the present article article while Sect. 5 is reports new results.

2 Basic Equations

The light propagation in linear PhC is described by the Maxwell equations

$$\begin{aligned} \nabla \times \vec{E} &= -\frac{\partial \vec{H}}{\partial t} \\ \nabla \times \vec{H} &= \frac{\partial \vec{D}}{\partial t}, \\ \vec{D}(\vec{r},t) &= \epsilon_0(\vec{r})\vec{E}(\vec{r},t). \end{aligned} \tag{1}$$

We take the light velocity to be equal to unit. However if there are defects with instantaneous Kerr nonlinearity, the displacement electric vector interior to the defects has a nonlinear contribution $\vec{D}(\vec{r},t) = \epsilon_0(\vec{r})\vec{E}(\vec{r},t) + \chi^{(3)}[\vec{E}(\vec{r},t)]^2\vec{E}(\vec{r},t)$ [28]. A substitution of the electric field in the form $[\vec{E}(\vec{r},t) = \frac{1}{2}[\vec{E}(\vec{r})e^{i\omega t} + \vec{E}^*(\vec{r})e^{-i\omega t}]$ into Eq. (1) and neglect by highly oscillating terms such as $e^{2i\omega}$ allows us to write the Maxwell equations in the same form as Eq. (1) with

$$\epsilon(\vec{r}) = \epsilon_0(\vec{r}) + \chi^{(3)}(\omega)|E(\vec{r})|^2. \tag{2}$$

We took into account that in what follows we consider the 2D PhC with arrays of infinitely long dielectric rods as shown in Fig. 1a in which the electric field is directed along the rods while the magnetic field is directed perpendicular to the rods (in the plane of Fig. 1a).

There is a remarkable analogy of electrodynamics in dielectric media with quantum mechanics [16, 29]. In particular, if the nonlinear contribution to the dielectric constant is small we can use the well-known methods of quantum mechanical perturbation theory. Let $|\psi\rangle = \begin{pmatrix} \vec{E} \\ \vec{H} \end{pmatrix}$ be the electromagnetic state in the PhC. Then the Maxwell equations (1) can be written as the Schrödinger equation $i|\dot{\psi}\rangle = \widehat{H}|\psi\rangle$ indeed with the Hamiltonian [16, 29, 30]

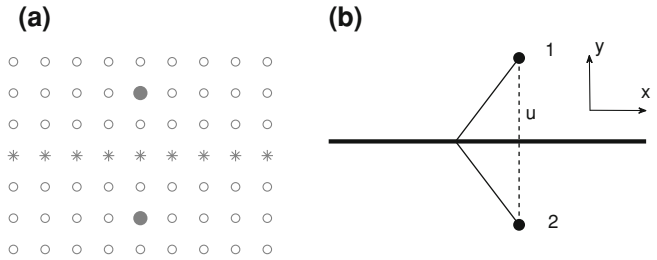

Fig. 1 **a** Two defect rods made from a Kerr media marked by *filled circles* are inserted into the *square lattice* PhC of dielectric rods with the lattice constant $a = 0.5\,\mu\text{m}$, the cylindrical dielectric rods have radius $0.18a$ and dielectric constant $\epsilon_0 = 11.56$. The 1D waveguide is formed by substitution of linear chain of rods by the rods with dielectric constant $\epsilon_W + \epsilon_0$ marked by stars. **b** Schematic system consisting of a waveguide aside coupled with two single-mode cavities. The cavities are coupled to each other via u

$$\widehat{H} = \begin{pmatrix} 0 & \frac{i}{\epsilon(\vec{r})}\nabla\times \\ -i\nabla\times & 0 \end{pmatrix}. \tag{3}$$

Because of the perturbation of the dielectric constant (2) the Hamiltonian can be presented as $\widehat{H} = \widehat{H}_0 + \widehat{V}$ where

$$\widehat{H}_0 = \begin{pmatrix} 0 & \frac{i}{\epsilon_0(\vec{r})}\nabla\times \\ -i\nabla\times & 0 \end{pmatrix}, \quad \widehat{V} = \begin{pmatrix} 0 & i\delta\left(\frac{1}{\epsilon(\vec{r})}\right)\nabla\times \\ 0 & 0 \end{pmatrix}, \tag{4}$$

and

$$\delta\left(\frac{1}{\epsilon(\vec{r})}\right) = \frac{1}{\epsilon(\vec{r})} - \frac{1}{\epsilon_0(\vec{r})}. \tag{5}$$

Let us introduce (following, for example, Refs. [30, 31]) the following inner product for the unperturbed system:

$$\langle\psi|\psi'\rangle = \frac{1}{2}\int [\epsilon_0(\vec{r})\vec{E}^*\vec{E}' + \vec{H}^*\vec{H}']d^3\vec{r}. \tag{6}$$

which obeys the following normalization and orthogonality conditions for the bound eigen-states of the unperturbed Hamiltonian $\widehat{H}_0|\psi_m\rangle = \omega_m|\psi_m\rangle$

$$\langle\psi_n|\psi_{n'}\rangle = \frac{1}{2}\int [\epsilon_0(\vec{r})\vec{E}_n^*\vec{E}_{n'} + \vec{H}_n^*\vec{H}_{n'}]d^3\vec{r} = \int \epsilon_0(\vec{r})\vec{E}_n^*\vec{E}_{n'}d^3\vec{r} = \delta_{nn'}. \tag{7}$$

Then the matrix elements for the perturbation calculated by use of these eigen-states are

$$\langle m|V|n\rangle = \frac{\omega_n}{2}\int d^3\vec{r}\epsilon_0^2(\vec{r})\delta\left(\frac{1}{\epsilon(\vec{r})}\right)\vec{E}_m^*(\vec{r})\vec{E}_n(\vec{r}). \tag{8}$$

One can see that the matrix (8) is not Hermitian as was noted in Ref. [30]. The origin is that the unperturbed states obey the inner product (6) with the dielectric constant $\epsilon_0(\vec{r})$ while the eigen-states of the full Hamiltonian $\widehat{H}_0 + \widehat{V}$ obey the inner product with a different dielectric constant $\epsilon(\vec{r})$. Respectively, the Hamiltonian $\widehat{H}$ is non-Hermitian with the inner product (7).

In order to avoid this problem we must use the inner product which is not tied to a specific choice of the dielectric constant. One way, given in Ref. [16], is by using only the magnetic field for the state. Another way is to absorb the dielectric constant in the scalar product by a new function as $\vec{F} = \sqrt{\epsilon(\vec{r})}\vec{E}$. Then the inner product becomes

$$\langle\psi|\psi'\rangle = \frac{1}{2}\int [\vec{F}^*\vec{F}' + \vec{H}^*\vec{H}']d^3\vec{r}. \tag{9}$$

The value $\langle\psi|\psi\rangle = \frac{1}{2}\int[\epsilon(\vec{r})|\vec{E}|^2 + |\vec{H}|^2]d^3\vec{r}$ is proportional to the energy of EM field which is important for the derivation of the forthcoming coupled mode theory (CMT) equations. That technique changes the Maxwell equations as follows:

$$\begin{aligned} \nabla \times \frac{\vec{F}}{\sqrt{\epsilon(\vec{r})}} &= -\dot{\vec{H}} \\ \frac{1}{\sqrt{\epsilon(\vec{r})}}\nabla \times \vec{H} &= \dot{\vec{F}}. \end{aligned} \tag{10}$$

The Hamiltonian takes the following form

$$\begin{aligned} \widehat{H}_0 &= \begin{pmatrix} 0 & \frac{i}{\sqrt{\epsilon_0(\vec{r})}}\nabla\times \\ -i\nabla \times \frac{1}{\sqrt{\epsilon_0(\vec{r})}} & 0 \end{pmatrix}, \\ \widehat{V} &= \begin{pmatrix} 0 & i\delta\left(\frac{1}{\sqrt{\epsilon(\vec{r})}}\right)\nabla\times \\ -i\nabla \times \delta\left(\frac{1}{\sqrt{\epsilon(\vec{r})}}\right) & 0 \end{pmatrix}. \end{aligned} \tag{11}$$

Now the eigen-states of the full Hamiltonian can be expanded over the eigen-states $|m\rangle = \begin{pmatrix} \vec{F}_m \\ \vec{H}_m \end{pmatrix}$ of the unperturbed Hamiltonian $\widehat{H}_0$ where

$$\begin{aligned} \nabla \times \frac{\vec{F}_m}{\sqrt{\epsilon_0(\vec{r})}} &= i\omega_m\vec{H}_m \\ \nabla \times \vec{H}_m &= -i\omega_m\sqrt{\epsilon_0(\vec{r})}\vec{F}_m. \end{aligned} \tag{12}$$

Then we obtain from (8)

$$\langle m|V|n\rangle = \frac{(\omega_m + \omega_n)}{2}\int d^3\vec{r}\epsilon_0^{3/2}(\vec{r})\delta\left(\frac{1}{\sqrt{\epsilon(\vec{r})}}\right)E_m^*(\vec{r})E_n(\vec{r}). \tag{13}$$

One can see that the full Hamiltonian is Hermitian now.

If the nonlinear defect rods are thin enough, the dielectric constant (2) can be rewritten as follows

$$\epsilon_j(\mathbf{x}) = \left(\epsilon_0 + \frac{3}{4}\chi^{(3)}(\omega)|E(\mathbf{x})|^2\right)\sum_j \theta(\mathbf{x}-\mathbf{x}_j). \tag{14}$$

Here j enumerates the defects, $\theta = 1$ inside the defect rod and $\theta = 0$ outside. As was shown for the simple square lattice 2D PhC from thin GaAs dielectric rods [26] the resonance spectra in the PhC waveguide are located in a rather narrow frequency domain. Therefore, we neglect the frequency dependence in the nonlinear susceptibility $\chi^{(3)}(\omega)$ in the following. Assuming that the nonlinear contribution in Eq. (14) is small compared to ϵ_0 we obtain for the matrix elements (13) per unit length of the defect rods

$$\langle m|V|n\rangle \approx -\frac{3}{16\epsilon_0^{3/2}}\chi^{(3)}(\omega_m+\omega_n)\sum_j\int_{\sigma_j} d^2\mathbf{x}|E(\mathbf{x})|^2 E_m(\mathbf{x})^* E_n(\mathbf{x}). \tag{15}$$

In order to find electric fields at the defects we must constitute a way to excite the defect modes. Here we consider that the EM field propagates from the left along the linear single-channel waveguide, interacts with the nonlinear defects, reflects back and transmits to the right. Then the transmission process can be described by the CMT stationary equations [32–35]

$$\left[\omega - \sum_n(\omega_m\delta_{mn} + V_{mn} + i\Gamma_n)\right]A_m = i\sqrt{\Gamma_m}E_{in}. \tag{16}$$

These CMT equations, in fact, are the Lippmann–Schwinger equation [36, 37]

$$(\omega - \widehat{H}_{eff})\Psi = i\widehat{W}E_{in}. \tag{17}$$

where the complex matrix $\widehat{H}_{eff}$ equals

$$\widehat{H}_{eff} = \widehat{H}_0 + \widehat{V} - i\widehat{W}\,\widehat{W}^+, \tag{18}$$

the columns of the matrix $\widehat{W}$ consists of coupling constants of the m-th eigenmode with the p-th injecting wave $\sqrt{\Gamma_{mp}}$, and the column Ψ consists of the mode amplitudes A_m. The solution Ψ is given by inverse of the matrix $\omega - \widehat{H}_{eff}$ where the matrix elements of the effective Hamiltonian $\widehat{H}_{eff}$ in turn depend on the mode amplitudes A_m. In order to write the equations of self-consistency for the amplitudes at the defects we expand the electric field at the j-th defect over eigenmodes $E(\mathbf{x}_j) = \sum_m A_m\psi_m(\mathbf{x}_j)$. That defines the equations of self-consistency after substitution into Eq. (16).

Finally, we present the transmission amplitude in the framework of the CMT [33, 34]

$$t = E_{in} - \widehat{W}^+\Psi. \tag{19}$$

3 Linear Optical Waveguide Coupled with Two Nonlinear Off-Channel Cavities Aligned Symmetrically

Two identical nonlinear defects positioned symmetrically relative to the single linear waveguide is one of the simplest systems in which the breaking of symmetry occurs [17, 18]. The system can easily be realized in 2D PhC as shown in Fig. 1a. The system is symmetric relative to the inversion of the y axis, as shown in Fig. 1b, and thereby supplements the system in which two nonlinear cavities are aligned along the waveguide considered by Maes et al. [12, 13]. That system is symmetric relative to the inversion of the x axis if equal power is injected on both sides of the waveguide.

Let each defect supports a localized non degenerate monopole solution for the TM mode only, which has the electric field component parallel to the infinitely long rods [16, 26]. Other solutions, (dipole, quadrupole, etc.) are assumed to be extended in the photonic crystal for the appropriate cavity radius and the dielectric constant [26, 38] and are thereby excluded from the consideration. Therefore, we have a two-level description for $\hat{H}_0$ with the eigen-frequencies

$$\omega_{s,a} = \omega_0 \pm u \tag{20}$$

where u is the coupling constant u. We denote the corresponding even (bonding) and odd (anti-bonding) eigen-modes as $\psi_{s,a}(\mathbf{x})$. Both modes for specific PhC are shown in Fig. 2. We pay attention that the frequency of the bonding (nodeless) mode is higher than the frequency of the anti-bonding mode with one nodal line.

Next, we assume that the EM wave which propagates along the waveguide obeys the symmetry of the total system. Therefore the wave might be only symmetrical relative to $y \to -y$ or anti-symmetrical. Respectively, the symmetric wave could excite only the bonding mode while the anti-bonding mode would remain as a hidden mode. Other words, the anti-bonding mode is the bound state in symmetrical continuum [36]. The same refers to the case of the anti-symmetric wave and the defect bonding mode. Therefore, for the linear case one can see the only resonance dip at ω_s, if the symmetric wave propagates along the waveguide. However due to the nonlinearity the light transmission acquires much more rich behavior because of spontaneous breaking of symmetry.

Substituting two eigen-functions $\psi_{s,a}(\mathbf{x})$ into Eq. (15) and considering a radius of the defect rods are very thin compared to the characteristic scale of wave function we obtain

$$\langle m|V|n\rangle \approx -\frac{3}{16}\sigma\chi^{(3)}(\omega_m + \omega_n)\sum_{j=1,2}|E(\mathbf{x}_j)|^2\psi_m(\mathbf{x}_j)^*\psi_n(\mathbf{x}_j), \tag{21}$$

where σ is the cross-section of the defects. Finally, we obtain from Eq. (21)

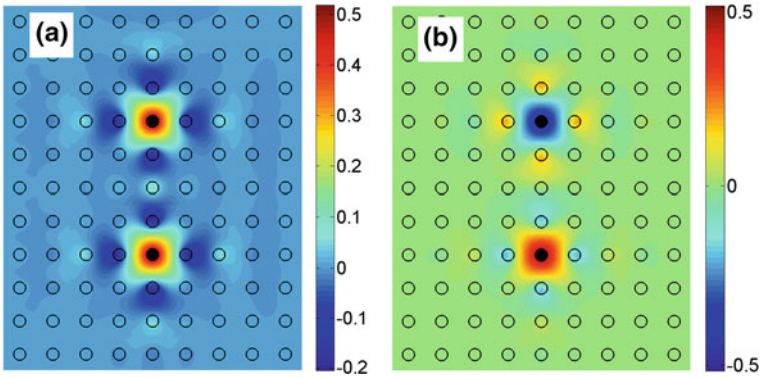

Fig. 2 **a** Bonding (even) mode and **b** anti-bonding (odd) mode of two overlapped linear defects in the 2D PhC. The defects have the same radius as the radius of rest rods but different dielectric constant $\epsilon_0 = 3$. The frequency of the isolated defect equals 0.3593 in terms of a value $2\pi c/a$. For the case of two overlapped defects shown here the frequency is split to be equal 0.3603 (bonding) and 0.3584 (anti-bonding)

$$\widehat{V} = \lambda \begin{pmatrix} \omega_s \phi_s^2 (I_1 + I_2) & \omega_0 \phi_s \phi_a (I_1 - I_2) \\ \omega_0 \phi_s \phi_a (I_1 - I_2) & \omega_a \phi_a^2 (I_1 + I_2) \end{pmatrix} \tag{22}$$

where $\phi_s = \psi_s(\mathbf{x}_1)\sqrt{\sigma} = \psi_s(\mathbf{x}_2)\sqrt{\sigma}$, $\phi_a = \psi_a(\mathbf{x}_1)\sqrt{\sigma} = -\psi_a(\mathbf{x}_2)\sqrt{\sigma}$, $\mathbf{x}_1$ and $\mathbf{x}_2$ are the positions of the defects in the two-dimensional PhC, and $I_j = |E(\mathbf{x}_j)|^2$, $j = 1, 2$ are the intensities of the electric field at the nonlinear defects, $\lambda = -\frac{3}{4}\chi^{(3)}$.

In order to find electric fields at the defects we must constitute a way to excite the defect modes. Here we consider that the EM field propagates from the left along the waveguide, interacts with the nonlinear defects, reflects back, and transmits to the right. Then the transmission process can be described by the CMT stationary equations [32–34] for the bonding mode amplitude A_s and the anti-bonding amplitude A_a

$$\begin{aligned} &[\omega - \omega_s - \lambda\omega_s\phi_s^2(I_1 + I_2) + i\Gamma]A_s - \lambda\omega_0\phi_s\phi_a(I_1 - I_2)A_a = i\sqrt{\Gamma}E_{in}, \\ &-\lambda\omega_0\phi_s\phi_a(I_1 - I_2)A_s + [\omega - \omega_a - \lambda\omega_a\phi_a^2(I_1 + I_2)]A_a = 0, \end{aligned} \tag{23}$$

where only the bonding mode is coupled with the waveguide because of the symmetry. The equivalent model is shown in Fig. 1b.

The amplitudes A_s and A_a are given by inverse of the matrix given in the right hand of Eq. (23) whose matrix elements in turn depend on the intensities I_1, I_2. In order to write the equations of self-consistency for the intensities at the defects $I_j, j = 1, 2$ we expand the electric field $E(\mathbf{x})$ at the thin j-th defect over eigen-modes $\phi_s(\mathbf{x})$ as $E(\mathbf{x}_j) = \sum_{m=s,a} A_m \phi_m(\mathbf{x}_j)$. The expansion can be specified as follows

$$E_1 = E(\mathbf{x}_1) = \phi_s A_s + \phi_a A_a, \quad E_2 = E(\mathbf{x}_2) = \phi_s A_s - \phi_a A_a \tag{24}$$

where symmetry properties of the eigen modes $\phi_m(\mathbf{x})$ were taken into account. Respectively,

$$I_1 = |\phi_s A_s + \phi_a A_a|^2, \quad I_2 = |\phi_s A_s - \phi_a A_a|^2 \tag{25}$$

which defines the equations of self-consistency after substitution into Eq. (23). In general they are rather cumbersome. Let us, first, consider the more simple case of the isolated defects so that the overlapping u can be neglected. Then the values of the eigen-functions at the defects are equal $\phi_s = \phi_a$. Even in that simplified case the solution of Eq. (23) has cardinal features different from the case of the single nonlinear defect considered in Refs. [39–46]. These features are the result of the mutual interference of wave flows reflected by the nonlinear defects. If $det(\widehat{H}_{eff} - \omega) \neq 0$ the amplitudes of the mode excitement for the transmission can be easily found from Eq. (23) as follows

$$\begin{aligned} A_s &= \frac{i\sqrt{\Gamma}E_{in}[\omega - \omega_0(1 + 2\lambda I)]}{(\omega - \omega_0(1 + 2\lambda I))^2 - \omega_0^2\Delta^2 + i\Gamma(\omega - \omega_0(1 + 2\lambda I))}, \\ A_a &= \frac{i\sqrt{\Gamma}E_{in}\omega_0\Delta}{(\omega - \omega_0(1 + 2\lambda I))^2 - \omega_0^2\Delta^2 + i\Gamma(\omega - \omega_0(1 + 2\lambda I))}, \end{aligned} \tag{26}$$

where the values $I = (I_1 + I_2)/2, \Delta = \lambda(I_1 - I_2)$ in turn depend on the mode amplitudes according to (25). Substituting these solutions into Eq. (25) we obtain the following nonlinear equations of self-consistency

$$\begin{aligned} I_1 &= \frac{\Gamma E_{in}^2[\omega - \omega_0(1 + 2\lambda I_2)]^2}{[\omega - \omega_0(1 + 2\lambda I_1)]^2[\omega - \omega_0(1 + 2\lambda I_2)]^2 + \Gamma^2[\omega - \omega_0(1 + 2\lambda I)]^2}, \\ I_2 &= \frac{\Gamma E_{in}^2[\omega - \omega_0(1 + 2\lambda I_1)]^2}{[\omega - \omega_0(1 + 2\lambda I_1)]^2[\omega - \omega_0(1 + 2\lambda I_2)]^2 + \Gamma^2[\omega - \omega_0(1 + 2\lambda I)]^2}. \end{aligned} \tag{27}$$

The solution of these equations gives the steady state for the transmission in the waveguide coupled with two nonlinear defects. Finally, we write from Eq. (19) equation for the transmission amplitude:

$$t = E_{in} - \sqrt{\Gamma}A_s. \tag{28}$$

The odd amplitude A_a does not contribute into the transmission amplitude because of the symmetry. In the forthcoming CMT calculations we fix the parameters of the CMT model as follows: $\omega_0 = 1, \Gamma = 0.01, \lambda = -0.01$. We consider the case of isolated defects $u = 0, \phi_s = \phi_a = 1$ and the case of coupled defects with $u = 0.01, \phi_s = 1, \phi_a = 1.1$. Rigorously speaking these values u and ϕ_s, ϕ_a correlate with each other. However, in our model case, we disregard this correlation.

3.1 Symmetry Preserving Solution

We start with the solution $E_1 = E_2$ that preserves the symmetry. In this case the incident wave excites only the symmetric even mode A_s

$$A_s = \frac{i\sqrt{\Gamma}E_{in}}{\omega - \omega_0(1 + 2\lambda I) + i\Gamma} \tag{29}$$

as follows from Eq. (26) with the only resonance frequency $\omega_0(1 + 2\lambda I)$ and the width 2Γ. The self-consistency equation for the symmetry preserving solution $I = I_1 = I_2$ simplifies

$$I[(\omega - \omega_0(1 + 2\lambda I))^2 + \Gamma^2] = \Gamma E_{in}^2. \tag{30}$$

That coincides with the equation of self-consistency for the single off-channel nonlinear defect obtained in Ref. [41]. The solution of this cubic nonlinear equation is shown in Fig. 3 by dashed blue lines. The frequency behavior of the intensities inherits the linear case, as shown in the inset. With growth of the input power the resonance frequency shifts to the left because of the nonlinear contribution $2\lambda I$ as seen from Eq. (29).

The frequency behavior of mode excitations $|A_s|, |A_a|$ is shown in Fig. 4 by blue dashed lines. As seen from Fig. 4a A_s has a resonance peak. Respectively, the transmission $T = |t|^2/E_{in}^2$ has a resonance dip at the frequency $\omega_0(1 + 2\lambda I) = \omega_0(1 + 2\lambda E_{in}^2/\Gamma)$ as shown in Fig. 5a by the dashed line. The last equality follows from Eq. (30).

3.2 Symmetry Breaking Solution

For the transmission through the nonlinear symmetric media the symmetry might be broken [7–15]. Numerical solution of Eq. (23), indeed, reveals the solution with $I_1 > I_2$, i.e., the nonlinearity gives rise to a breaking of the symmetry below (above) the critical frequency ω_c for $\lambda < 0$ ($\lambda > 0$). The symmetry breaking solution is shown in Fig. 3 by solid lines for I_1 and dash-dotted lines for I_2. There is also the solution that differs from the former in that $E_1 \leftrightarrow E_2$. If the solutions are stable, a choice of the solution happens incidentally, as it does for a phase transition of the second order in cooperative systems. As shown in Fig. 6, a value $I_1 - I_2$ or the odd mode amplitude A_a, indeed, might serve as the order parameter that characterizes the symmetry breaking.

It is surprising that there is the frequency at which the intensity at one of the nonlinear defects turns to zero as shown in Fig. 3. According to Eq. (27) that occurs at the frequency

$$\omega_{dip} = \omega_0(1 + 8\lambda E_{in}^2/\Gamma). \tag{31}$$

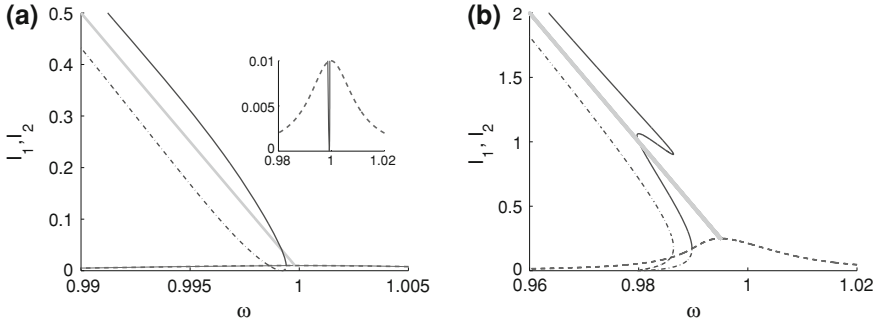

Fig. 3 Frequency behavior of the intensities at the isolated defects $u = 0$. **a** $E_{in} = 0.01$, **b** $E_{in} = 0.05$. Here and in the forthcoming figures *dashed blue line* shows the symmetry preserving solution. *Solid* and *dash-dotted red lines* show the symmetry breaking solutions which has different intensities at the defects I_1 and I_2. *Gray thick solid line* shows a new phase symmetry breaking solution at which $det(\omega - \widehat{H}_{eff}) = 0$

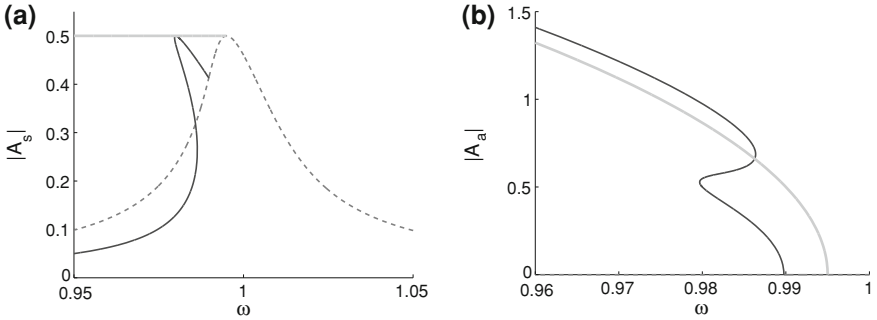

Fig. 4 Frequency behavior of (**a**) the bonding amplitude $|A_s|$ and (**b**) the anti-bonding amplitude $|A_a|$ of the model shown in Fig. 1b for $u = 0, E_{in} = 0.05$

At this frequency we have $A_s = A_a = E_1/2 = E_{in}/\sqrt{\Gamma}$ in accordance with Eqs. (26) and (24). By substituting this equality into Eq. (19) we immediately obtain that the frequency (31) defines the position of resonance dip for the symmetry breaking solution. As will be shown, that result of full extinction of one of the nonlinear defects is observed in the PhC system as well (Fig. 13b).

In Fig. 4a and b we show the frequency dependence of the even and odd mode amplitudes $|A_s|$ and $|A_a|$ respectively for $E_{in} = 0.05$. One can see that, first, the incident wave begins to excite the odd mode below ω_c for $\lambda < 0$, and, second, $|A_s|$ and $|A_a|$ show the bistability. The even mode A_s displays a resonance peak (solid line) with the resonance width twice less than the resonance width of the peak for the symmetry preserving solution (dashed line). Correspondingly, the transmission in Fig. 5 demonstrates a narrow dip for the symmetry breaking solution. In order to understand that phenomenon let us consider the resonance poles of the even and odd amplitudes given by zeros of the denominators in Eq. (26)

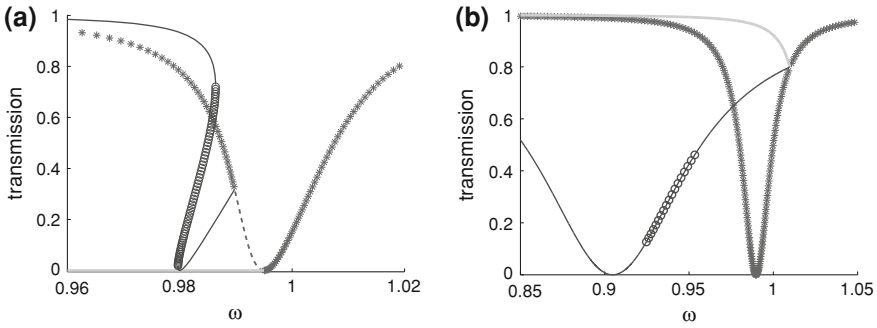

Fig. 5 Frequency behavior of the transmission for the isolated defects for (**a**) $E_{in} = 0.05$ and (**b**) for the coupled defects for $E_{in} = 0.01$. *Stars* and *open circles* show stable domains of the solutions

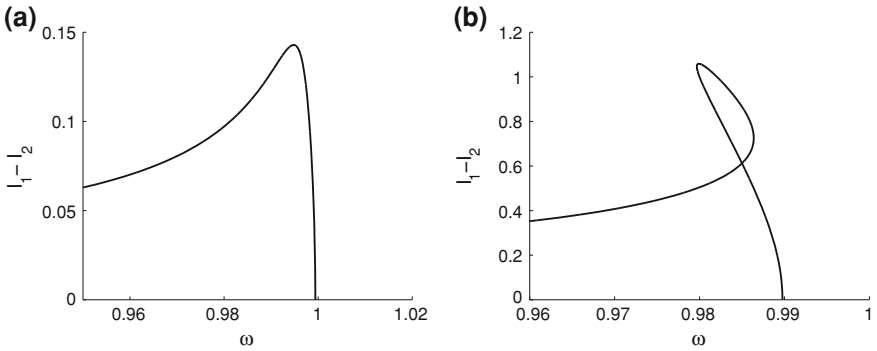

Fig. 6 The difference between the intensities at the defects for $u = 0$: **a** $E_{in} = 0.01$ and **b** $E_{in} = 0.05$. Only the symmetry breaking solution is shown

$$z_{1,2} = \omega_0(1 + 2\lambda I) - \frac{i\Gamma}{2} \pm \sqrt{\omega_0^2\Delta^2 - \frac{\Gamma^2}{4}}. \tag{32}$$

For the solution with $\Delta = 0$ we had the only resonance pole with the resonance half width Γ. As Fig. 6 shows there is the frequency domain roughly between 0.98 and 0.99 where $\omega_0\Delta > \Gamma/2$ and where the resonance half-width is twice less than Γ according to formula (32). Therefore, in this frequency domain we can expect the resonance dip to be twice narrower compared to the symmetry preserving solution with $\Delta = 0$.

The lesser the width of resonance, the more unstable the resonance [16]. One can thereby see that the bistability of the symmetry breaking solution is more profound in comparison to the symmetry preserving solution. The resonance peak in $|A_s|$ for the symmetry breaking solution terminates at that frequency where the odd mode amplitude $|A_a|$ arises as seen from Fig. 4b. Close to this frequency

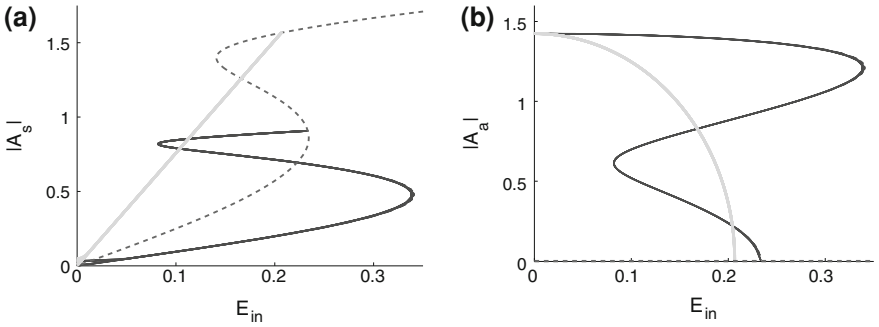

Fig. 7 Amplitudes (**a**) $|A_s|$ and (**b**) $|A_a|$ as a function of the incident wave amplitude E_{in} for the coupled defects with the parameters $\omega = 0.95, u = 0.01, \phi_s = 1, \phi_a = 1.1$

the amplitude A_a has a square root behavior typical for the order parameter in phase transition of the second order. The dependence of A_a on the amplitude of the incident wave demonstrates the same behavior (see below Fig. 7b).

3.3 Phase Symmetry Breaking Solution

At last, there is the solution that has equal intensities at the defects but nevertheless a symmetry is broken because of phases of the complex amplitudes E_1 and E_2. This solution refers to the special case of Eq. (23) when the determinant of the matrix $\omega - \widehat{H}_{eff}$ equals zero, (i.e., the inverse of matrix does not exist). It occurs at

$$I_1 = I_2 = I, \quad \omega = \omega_a(1 + 2\lambda\phi_a^2 I). \tag{33}$$

Then the solution of Eq. (23) for the even mode amplitude A_s is

$$A_s = \frac{E_{in}}{\sqrt{\Gamma}}, \tag{34}$$

while A_a is undetermined yet.

Let us take for a while, the defects to be linear. Then the second equation in (33) shrinks to the isolated point $\omega = \omega_a$. As given by the CMT equations (23) and as seen from Fig. 1 this odd mode has zero overlapping with the waveguide and Eq. (33) thereby defines the bound state in continuum (BSC) [36, 47–51]. The solution of the Eq. (23) $\begin{pmatrix} A_s \\ A_a \end{pmatrix}$ with A_s given by Eq. (34) and arbitrary A_a is therefore a superposition of the transport solution and the BSC.

For the nonlinear defects the situation changes dramatically. First, there is the whole frequency region $\omega \geq \omega_a$ for $\lambda > 0$ or $\omega \leq \omega_a$ for $\lambda < 0$ where $det(\omega - \widehat{H}_{eff}) = 0$ as seen from Eq. (33). Equation (33) thereby defines the BSC with eigen frequency in whole region as dependent on the BSC intensity. Second,

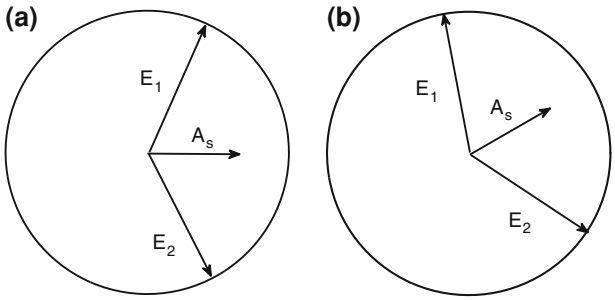

Fig. 8 Graphic solutions of (**a**) Eqs. (35) and (**b**) (39), respectively. Radius of circle is $\sqrt{I}$

the BSC can not be independently superposed to the transport solution for the nonlinear case. The BSC begins to couple with the incident wave and can not be defined as the bound state if $E_{in} \neq 0$.

(1) Let the defects be isolated; (i.e. $u = 0, \phi_s = \phi_a = 1$. On the one hand, we obtain from Eq. (34)

$$A_s = \frac{E_1 + E_2}{2} = E_{in}/\sqrt{\Gamma}, \tag{35}$$

according to Eq. (24). That is the bonding mode amplitude is constant over the frequency as shown in Fig. 4a by the gray thick solid line. On the other hand, Eq. (33) directly shows that the intensities at the defects do not depend on E_{in},

$$I = \frac{\omega - \omega_0}{2\lambda}. \tag{36}$$

Since $|E_1| = |E_2| = \sqrt{I}$ the only way to satisfy Eqs. (35) and (36) is to consider that the amplitudes at the defects are $E_1 = \sqrt{I}\exp(i\theta), E_2 = \sqrt{I}\exp(-i\theta)$. That is illustrated in Fig. 8a. With the use of Eqs. (35) and (36), we obtain

$$\cos^2\theta = \frac{2\lambda E_{in}^2}{\Gamma(\omega - \omega_0)}. \tag{37}$$

For $E_{in} \to 0$ we have the following limits: $\theta \to \pi/2, E_1 \to i\sqrt{I}, E_2 \to -i\sqrt{I}, E_1 + E_2 \to 0$ as seen from Eq. (37). As soon as $E_{in} \neq 0$ the defects amplitudes are seized to oscillate in fully anti-symmetric way as shown in Fig. 8a. We emphasize that phase difference 2θ has nontrivial behavior if the defects are nonlinear ($\lambda \neq 0$) and the incident wave is applied ($E_{in} \neq 0$) as follows from Eq. (37). For the symmetry preserving solution $\theta = 0$ (dashed line in Fig. 9), for the symmetry breaking solution $2\theta = 0$ or π (solid line in Fig. 9) while for the present solution the phase difference 2θ behaves as an order parameter (gray thick dashed line in Fig. 9) similar to A_a shown in Figs. 4b or 7b. We define the present solution of the CMT equations (23) with

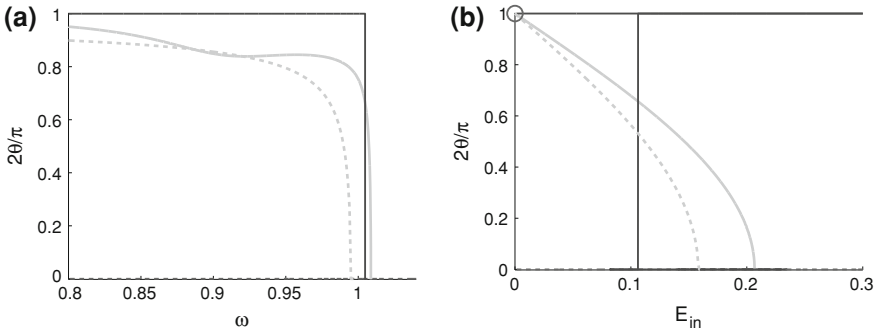

Fig. 9 Difference between phases of the amplitudes E_1 and E_2 for $u = 0.01$ as a function of (**a**) the frequency for $E_{in} = 0.05$ and (**b**) the amplitude of the incident wave for $\omega = 0.95$. *Dashed blue line* shows the symmetry preserving solution, *solid red line* shows the symmetry breaking solution, and *gray lines* show the phase symmetry breaking solution, $u = 0$ *dashed* and $u = 0.01$ *solid*. The BSC point is shown by *open bold circle*

the zero determinant $det(\omega - H_{eff}) = 0$ as the phase symmetry breaking solution. It exists for $\omega \leq \omega_0 + 2\lambda E_{in}^2/\Gamma$ for $\lambda < 0$. Knowledge of the phase θ allows us now to find the anti-bonding amplitude

$$A_a = (E_1 - E_2)/2 = i\sqrt{I}\sin\theta. \tag{38}$$

The frequency behavior of the even and odd amplitudes $|A_s|, |A_a|$ are shown in Figs. 4b and 7b. Finally, by substituting Eq. (35) into Eq. (28) we obtain $t = 0$ for the phase symmetry breaking solution as shown in Fig. 5a by gray thick dashed line.

(2) 1a the coupling between the defects u is rather small compared to the coupling between the waveguide and defects $\sqrt{\Gamma}$. Nevertheless, an account of the coupling between the defects has a principal importance as will be seen below. As was given earlier, the parameters of the coupled defects are specified as follows $u = 0.01, \phi_s = 1, \phi_a = 1.1$.

A substitution of Eq. (33) into Eq. (34) gives

$$A_s = \frac{\omega_0 + u}{\omega_0(1-\alpha) + u(1+\alpha)} \cdot \frac{\sqrt{\Gamma}E_{in}}{\omega - \omega_r + i\Gamma_r} = \frac{A_{s0}}{\omega - \omega_r + i\Gamma_r} \tag{39}$$

where

$$\omega_r = \frac{(1-\alpha)\omega_s\omega_a}{\omega_0(1-\alpha) + u(1+\alpha)}, \tag{40}$$

$$\Gamma_r = \Gamma\frac{\omega_a}{\omega_0(1-\alpha) + u(1+\alpha)}, \tag{41}$$

$$A_{s0} = \frac{\sqrt{\Gamma} E_{in} \omega_a}{\omega_0(1-\alpha) + u(1+\alpha)} \tag{42}$$

$\alpha = \phi_s^2/\phi_a^2$. Therefore for the coupled defects the amplitude A_s acquires typical Bright–Wigner resonance behavior in which the nonlinearity is excluded. Respectively, a substitution of the solution (39) into Eq. (28) immediately results in the transmission having the resonance dip at the frequency ω_r with the half width Γ_r which depends on ratio α and u. That result is shown in Fig. 5b by the gray thick line. If $u \to 0, \phi_a \to \phi_s, \alpha \to 1$ the frequency of the resonance dip goes away, and $\Gamma_r \to \infty$; that is, the resonance at the phase symmetry breaking solution disappears, and the corresponding transmission tends to zero as seen from Fig. 5a.

Equation (33) fixes intensity at the defects

$$I = \frac{\omega - \omega_a}{2\lambda \phi_a^2 \omega_a} \tag{43}$$

which is similar to the former case given by Eq. (36). On the other hand, we have according to Eq. (24) $E_1 + E_2 = A_s/2\phi_s$ where A_s is given by Eq. (39). A graphic illustration of the solution of this equation with modules of $E_j, j = 1, 2$ fixed by Eq. (43), is shown in Fig. 8b. By presenting $E_1 = \sqrt{I}\exp(i(\beta + \theta))$ and $E_2 = \sqrt{I}\exp(i(\beta - \theta))$ we obtain from Eq. (39)

$$\begin{aligned} \cos^2\theta &= \frac{\lambda \Gamma_r \omega_a \omega_r E_{in}^2}{2\alpha(1-\alpha)\omega_s(\omega - \omega_a)[(\omega - \omega_r)^2 + \Gamma_r^2]}, \\ \tan\beta &= \frac{\omega - \omega_r}{\Gamma_r}. \end{aligned} \tag{44}$$

The behavior of the phase difference 2θ on the frequency or the incident wave amplitude E_{in} for $u = 0.01$ is shown in Fig. 9.

However, the most remarkable feature of the phase symmetry breaking solution for $u \neq 0$ is related in a current circulated between the defects. When the phase difference 2θ exists between two quantum dots (QD) or superconductors, connected by a weak link, a tunneling or Josephson current $J = J_0 \sin 2\theta$ will flow between them. The value of the current J_0 is proportional to the coupling constant between QDs or superconductors [52]. In order to explicitly write the expression for a current flowing between defects we use the Green function approach developed in Refs. [39, 40, 42, 53] for the 2D PhC of dielectric rods with the dielectric constant ϵ_0. The PhC holds the 1D cavity (waveguide) and two 0D defects (nonlinear cavity rods) as shown in Fig. 1a. Then the dielectric constant of full system $\epsilon(\mathbf{x})$ is a sum of periodic perfect PC and cavity-induced terms $\epsilon(\mathbf{x}) = \epsilon_{PC}(\mathbf{x}) + \delta\epsilon(\mathbf{x}|E)$, where $\delta\epsilon(\mathbf{x}|E) = \epsilon_W(\mathbf{x}) + \epsilon_d(\mathbf{x}|E)$ is contributed by the waveguide and the two nonlinear defects:

$$\epsilon_d(\mathbf{x}|E) = \epsilon_W \sum_{n=-\infty}^{\infty} \theta(\mathbf{x} - \mathbf{x}_n) + \sum_{j=1,2} \epsilon_j. \tag{45}$$

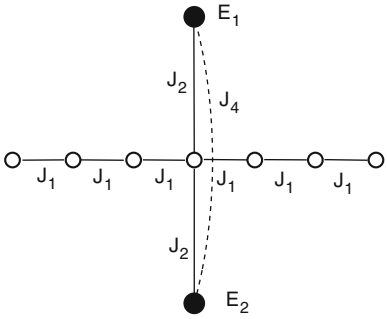

Fig. 10 Tight-binding version of the PhC system shown in Fig. 1a: J_2 couples the chain and the defects and J_4 connects the defects to each other

Here $\theta = 1$ inside the cavity rod and $\theta = 0$ outside, and the nonlinear contributions ϵ_j are given by Eq. (14). Then the TM electric field directed along the rods of the PhC $E(\mathbf{x}, t) = E(\mathbf{x})e^{i\omega t}$ is satisfied the integral equation

$$E(\mathbf{x}) = \frac{\omega^2}{c^2} \int d^2\mathbf{y} G(\mathbf{x}, \mathbf{y}|\omega)\delta\epsilon(\mathbf{y}|E)E(\mathbf{y}) \tag{46}$$

where $G(\mathbf{x}, \mathbf{y}|\omega)$ is the Green function of the ideal 2D PC of the rods which was calculated in Ref. [53] for the square lattice PhC. If the radius of the defects rods is sufficiently small in comparison to the wavelength of the EM wave, we can write Eq. (46) as the discrete nonlinear equation [42, 53]

$$E_{\mathbf{n}} = \sum_{\mathbf{m}} J_{\mathbf{n}-\mathbf{m}}(\omega)\delta\epsilon_{\mathbf{m}}E_{\mathbf{m}} \tag{47}$$

where $J_{\mathbf{n}-\mathbf{m}}(\omega) = \sigma\frac{\omega^2}{c^2}G(\mathbf{x}_{\mathbf{n}}, \mathbf{x}_{\mathbf{m}}|\omega)$, σ is the cross-section of the rods, and **n, m** runs over sites of the defects (marked by stars and filled circles in Fig. 1a).

We use the nearest-neighbor approximation and write (47) as the tight-binding linear chain coupled with two nonlinear defects

$$\begin{aligned} \left[\frac{1}{\epsilon_W} - J_0(\omega)\right]E_n &= J_1(E_{n+1} + E_{n-1}) + \delta_{n,0}\frac{J_2}{\epsilon_W}(\delta\epsilon_1 E_1 + \delta\epsilon_2 E_2), \\ [1 - \delta\epsilon_1 J_0(\omega)]E_1 &= J_2\epsilon_W E_0 + J_4\delta\epsilon_2 E_2, \\ [1 - \delta\epsilon_2 J_0(\omega)]E_2 &= J_2\epsilon_W E_0 + J_4\delta\epsilon_1 E_1. \end{aligned} \tag{48}$$

The model is shown in Fig. 10 and consists of a linear infinitely long tight-binding chain presented by amplitudes E_n whose spectrum is given by dispersion equation $J_0(\omega) = \frac{1}{\epsilon_W} - 2J_1\cos k$, and two nonlinear defects presented by amplitudes ϕ_1, ϕ_2. The coupling J_2 connects the defects and the chain and the coupling J_4 connects the defects.

By multiplying Eq. (48) by $E_0^* = t^*$ and subtracting the complex conjugated terms one can obtain the value of the power flow current flowing between the chain at the "0"-th site and the defects enumerated as $j = 1, 2$ as follows

$$j_{0\to 1,2} = \epsilon_W J_2 Im(tE_{1,2}^*). \tag{49}$$

Similar manipulations with the cavity's amplitudes give the current between the defects

$$j_{1\to 2} = J_4\delta\epsilon Im(E_1E_2^*) = J_4\delta\epsilon I\sin(2\theta). \tag{50}$$

It follows also that the current from the "−1"-th site to the "0"-th site of the chain coincide with the current from the "0"-th site to the "1"-th one. Therefore the currents (49) and (50) coincide also in accordance to the Kirchhoff rule. Thus, the input power induces vortical current between the waveguide and defects via the couplings J_2 and J_4. The current is excited by the incident wave provided the defects are nonlinear. Thus, our analysis shows that the symmetry can be broken not only because of different intensities at the defects but also by a circulating current between the defects although the intensities at the defects are equal. This model result of the Josephson like current between the defects with different phase is reflected in computations of the Poynting vector in the PhC structure as will be shown below.

3.4 Stability of Solutions

Furthermore, we studied stability of different solutions by standard methods given for example in Ref. [31]. The stability of the solution can be found from the temporal CMT equations

$$\begin{aligned} i\dot{a}_s &= [\omega_s + \lambda\omega_s\phi_s^2(I_1+I_2) - i\Gamma]a_s + \lambda\omega_0\phi_s\phi_a(I_1-I_2)a_a + \sqrt{\Gamma}E_{in}e^{-i\omega t}, \\ i\dot{a}_a &= \lambda\omega_0\phi_s\phi_a(I_1-I_2)a_s + [\omega_a + \lambda\omega_a\phi_a^2(I_1+I_2)]a_a. \end{aligned} \tag{51}$$

By presenting $a_s(t) = (A_s + \xi_s(t))e^{-i\omega t}, a_a(t) = (A_a + \xi_a(t))e^{-i\omega t}$ with A_s, A_a as the steady state obeying the stationary CMT equations (23) and $|\xi_s(t)| \ll |A_s|, |\xi_a(t)| \ll |A_a|$ we obtain the linearized time-dependent equations for complex ξ_s, ξ_a

$$\begin{pmatrix} Re(\dot{\xi}_s) \\ Im(\dot{\xi}_s) \\ Re(\dot{\xi}_a) \\ Im(\dot{\xi}_a) \end{pmatrix} = \widehat{L}\begin{pmatrix} Re(\xi_s) \\ Im(\xi_s) \\ Re(\xi_a) \\ Im(\xi_a) \end{pmatrix}. \tag{52}$$

Their stability is determined by eigen values of the matrix $\widehat{L}$ which is time independent. The results of our calculation of stability are presented in Fig. 5 which shows that the stability of the phase symmetry breaking solution appears if only the defects are coupled and $\phi_s \neq \phi_a$. We collected the results of stability of all three solutions in Fig. 11 in the form of phase diagrams in plane of the incident wave amplitude and the frequency. One can see that the phase symmetry breaking solution is stable in some small area of the phase diagram.

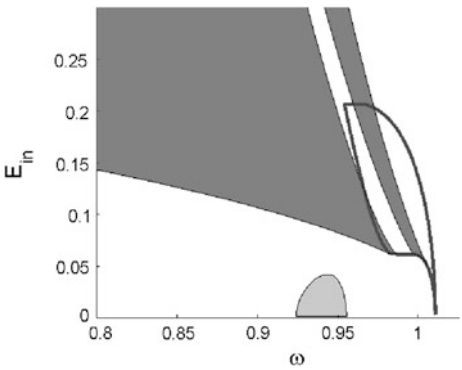

Fig. 11 Regions of stability of the solution. The symmetry preserving solution is stable everywhere except interior of the closed region shown by *solid blue line*. The stability of the symmetry breaking solution is shown by *red*, while the phase symmetry breaking solution is shown by *gray*. The parameters are $u = 0.01$, $\omega_0 = 1$, $\Gamma = 0.01$, $\lambda = -0.01$, $\phi_s = 1$, $\phi_a = 1.1$

3.5 Numerical Calculations in Photonic Crystal

We numerically solve the Maxwell equations (1) for the TM mode in the PhC with defect nonlinear rods by expansion of electromagnetic field over maximally localized photonic Wannier functions [25, 26, 36]. The square lattice 2D PhC has the same parameters as given earlier [see Fig. 1a]. For the case of isolated linear defects with the same radius as the radius of host rods and the dielectric constant $\epsilon_d = 3$ their eigen frequency $\omega_0 = 0.3593$ in terms of $2\pi c/a$. Overlapping of the defect's monopole modes gives rise to splitting of this frequency $\omega_s = 0.3603, \omega_a = 0.3584$ as numerical computation of Eq. (1) gives. Respectively we obtain that the value of coupling $u = -0.001$. The corresponding bonding and anti-bonding modes for the nearest distance a between defects were found in Refs. [54, 55]. For more distance $4a$ they are shown in Fig. 2. By the normalization condition (7) the heights of the amplitude modes at the defects equal $\phi_s = 0.5569, \phi_a = 0.6179$. Let us evaluate the dimensionless nonlinearity constant λ. We take in numerical calculations the incident power per length of order 100 mW/a which corresponds to the incident intensity $I_0 = 100\,\mathrm{mW/a^2}$. For chosen PhC lattice with period $a = 0.5\,\mu\mathrm{m}$ we obtain that the incident intensity equals $0.04\,\mathrm{GW/cm^2}$. With the use of $\epsilon = \epsilon_0 + 2\sqrt{\epsilon_0} n_2 I_0$ we obtain

$$\lambda \approx 2\sqrt{\epsilon_0}\omega'(\epsilon_0) n_2 I_0, \tag{53}$$

where the value ω' is the rate of change of the eigen frequency of the defect with the dielectric constant ϵ. That rate was calculated for example in Refs. [16, 26]. We take the linear and nonlinear refractive indexes of the defect rods to be, respectively, $n_0 = \sqrt{\epsilon_0} = \sqrt{3}, n_2 = 2 \times 10^{-12}\mathrm{cm^2}/W$ and $\omega' = -0.01 \times 2\pi c/a$. By substituting all of these estimates into (53) we obtain $\lambda \sim -2 \times 10^{-5}$ provided that the frequency is given in terms of $2\pi c/a$. Finally, we estimate the coupling of the defect mode with the propagation mode of the PhC waveguide $\sqrt{\Gamma}$. There are many ways to calculate Γ using for example Refs. [31, 56, 57]. In the present paper we estimated Γ numerically by using the following approach. We took the

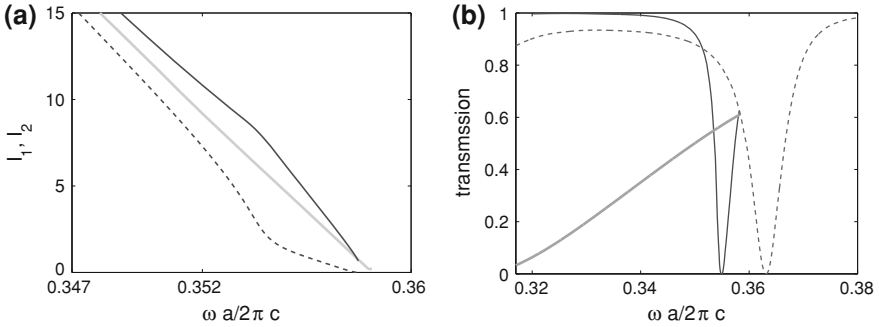

Fig. 12 Self-consistent solution for (**a**) the intensities of the EM field at the nonlinear defects and (**b**) transmission spectra in the PhC structure in the PhC structure shown in Fig. 1. The parameters of the PhC and defects are given in Fig. 2. The input power per length equals $100\,\mathrm{mW/a}$. $n_2 = 2 \times 10^{-12}\mathrm{cm}^2/W$, $\lambda = -0.009$

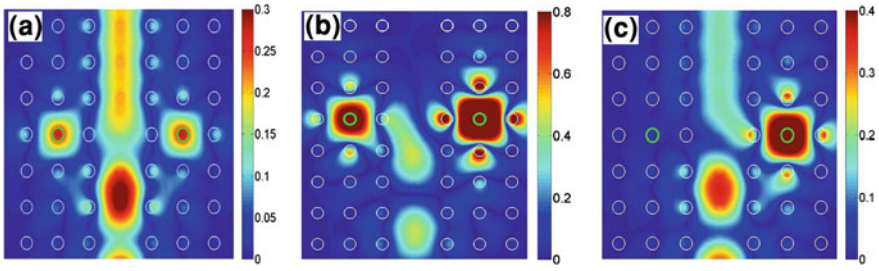

Fig. 13 Absolute value of the EM field solution for (**a**) the symmetry preserving solution $\omega a/2\pi c = 0.355$, (**b**) and (**c**) the symmetry breaking solution for $\omega a/2\pi c = 0.355$ and $\omega a/2\pi c = 0.358$ respectively. The EM wave incidents at the left of the waveguide

single linear defect aside the PC waveguide as shown in Fig. 1a, and calculated the transmission spectra. By the resonance width of the spectra we evaluated $\Gamma = 0.00185$.

The self-consistent solutions are presented in the form of the intensities in Fig. 12a, which are similar to the CMT results shown in Fig. 3a. Also, one can see three solutions in the transmission shown in Fig. 12b, as was found in the CMT model for the transmission shown in Fig. 5. Figure 13 shows the EM field (the absolute value of the electric field) for the symmetry preserving solution (a) and for the symmetry breaking solution (b) and (c). In the latter case one can see that the field is strongly different at bottom and top. Moreover Figs. 3 and 12 show that there is a frequency at which the intensity of the EM field might be zero at the bottom defect. Indeed, Fig. 13c demonstrates this case.

In agreement with the model consideration Fig. 14 shows that current flows (the Poynting's vector patterns) are strongly different for the different solutions. For the symmetry preserving solution we have laminar current flow over the

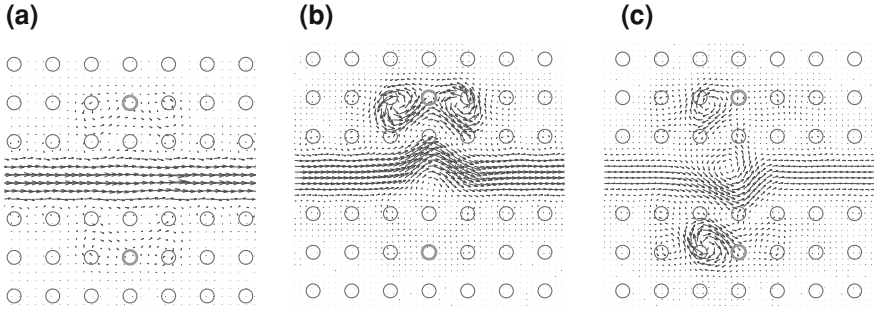

Fig. 14 Current flows for the symmetry preserving solution which inherits linear case (**a**), the symmetry breaking solution (**b**), and (**c**) the phase symmetry breaking one at $a\omega/2\pi c = 0.35$. *Bold open circles* mark the nonlinear defects

waveguide with excitation of two current vortices around each defect. The laminar flow over the waveguide and the vortical flows around defects are well separated. The whole current pattern is symmetrical relative to the symmetry transformation $y \to -y$. The picture has a similarity with ballistic electron transport in waveguide coupled with off-channel quantum dot [58]. For the case of the symmetry breaking solution there is a current vortex inside the waveguide complemented by two vortices near each defect, as shown in Fig. 14b. The circulation in vortical flow around the upper defect is opposite to the circulation around the bottom defect. The vortical flow in the waveguide and the vortical flows around the defects are well separated for both solutions. In the third case (c) for the phase symmetry breaking solution one can see the current vortex in the waveguide and single vortices around the defects are mixed. Nevertheless because of the continuity equation in the space beyond of the nonlinear defects $\nabla \overrightarrow{j}(x, y) = 0$ the vortical flows around the defects and in the waveguide can not cross.

4 The T-Shape Waveguide Coupled with Two Nonlinear Defects

One of the most ambitious goals in nonlinear optics is the design of an all-optical computer that will overcome the operation speeds in conventional (electronic) computers. Vital in this respect is the design of basic components such as all-optical routing switches and logic gates. It is believed that future integrated photonic circuits for ultra fast all-optical signal processing require different types of nonlinear functional elements such as switches, memory and logic devices. Therefore, both physics and designs of such all-optical devices have attracted significant research efforts during the last two decades, and most of these studies utilize the concepts of optical switching and bistability. One of the simplest bistable optical devices which can be built-up in photonic integrated circuits is a single cavity coupled with optical waveguide or waveguides [16, 59].

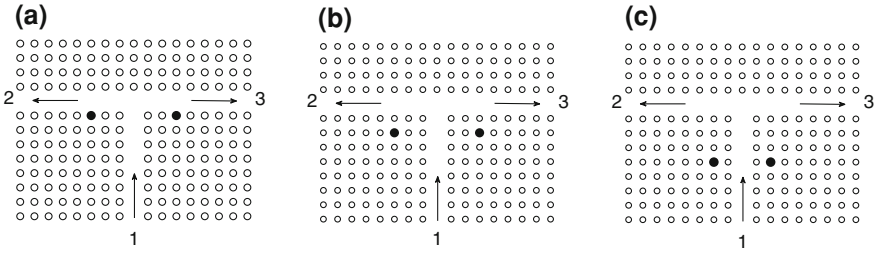

Fig. 15 T-shaped waveguide with two nonlinear defect rods. The cases (**a**)–(**c**) differ by the positions of the nonlinear defects

The concept of the all-optical switching is based on a discontinuous transition between the symmetry breaking solutions by a small change of the input [20]. Many of these devices employ a configuration of two parallel coupled nonlinear waveguides [19, 21, 60–62]. Recently Maes et al. demonstrated the all-optical switching in the system of two nonlinear micro-cavities aligned along the waveguide [12] by the use of pulses of injected light. In the present section we use similar approach to demonstrate the all-switching effects in the T-shaped waveguide coupled with two nonlinear micro-cavities [27, 63]. The PhC structure of the T-shaped waveguide shown in Fig. 15 differs from the structures considered before in Sects. 2 and 3 a mechanism for the all-optical switching is mainly based on the symmetry breaking solutions.

We consider the PhC shown in Fig. 15 with the same parameters as given in Sect. 3: the lattice constant $a = 0.5\,\mu m$, the cylindrical dielectric rods have radius $0.18a$ and dielectric constant $\epsilon = 11.56$. We substitute two defect rods of the same radius as shown in Fig. 15 made from an instantaneous Kerr media with the nonlinear refractive index $n = n_0 + n_2 I_0$ where $n_0 = \sqrt{3}$ and $n_2 = 2\times 10^{-12}\mathrm{cm}^2/\mathrm{W}$. The corresponding equivalent configuration of the T-shaped waveguide with two nonlinear defects is presented in Fig. 16.

We start with the position of the defect rods shown in Fig. 15a which have strong coupling with the output waveguides 2 and 3, and negligibly weak coupling with the input waveguide 1. We consider a light given by the amplitude S_{1+} is incident into the waveguide 1 and outputs into all three terminals as shown schematically in Fig. 16. The outgoing amplitudes are labelled as S_{1-}, S_{2-} and S_{3-}. Each nonlinear optical cavity is assumed to be given by single mode amplitudes $A_j, j = 1, 2$ and coupled with the guides 2, 3 via the coupling constant γ shown in Fig. 16 by dotted lines and with the guide 1 via the coupling constant Γ.

We consider that the defects are not coupled. Therefore the eigen frequencies of the system of the defects equal the monopole eigen frequencies of the isolated defects $\omega_j = \omega_0 + \lambda|A_j|^2, j = 1, 2$ shifted because of the Kerr effect. Then the Eq. (16) will take the following form

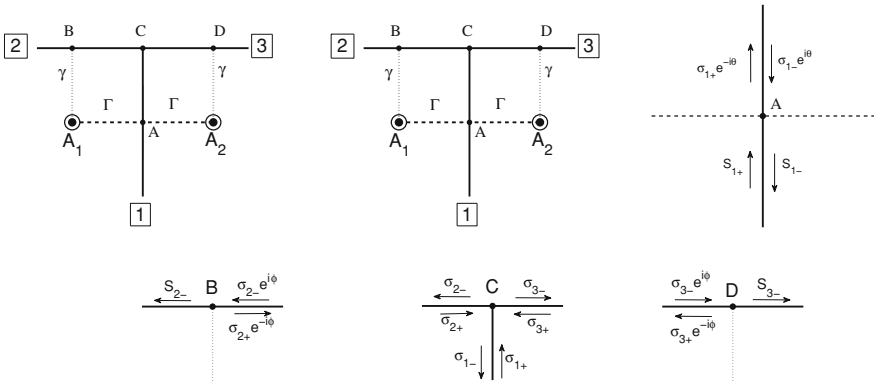

Fig. 16 CMT model of the T-shape photonic crystal waveguide coupled with two nonlinear defects shown by *filled bold circles*. The defects are coupled with input waveguide 1 via the constant Γ shown by *dashed lines* and with the output waveguides 2,3 via the constant γ shown by *dotted line*. Separately each connection is shown with corresponding light amplitudes

$$\begin{aligned}(\omega-\omega_0-\lambda|A_1|^2+i\gamma+i\Gamma)A_1+i\Gamma A_2 &= i\sqrt{\Gamma}(S_{1+}+\sigma_{1-}e^{i\theta})+i\sqrt{\gamma}\sigma_{2-}e^{i\phi}\\ (\omega-\omega_2-\lambda|A_2|^2+i\gamma+i\Gamma)A_2+i\Gamma A_1 &= i\sqrt{\Gamma}(S_{1+}+i\sigma_{1-}e^{i\theta})+i\sqrt{\gamma}\sigma_{3-}e^{i\phi}\end{aligned} \tag{54}$$

Here phases θ and ϕ as shown in Fig. 16 are the optical lengths through which light goes between the connections. These CMT equations are to be complemented by the equations for light amplitudes at each connection A, B, and D

$$\begin{aligned}\sigma_{1+}e^{-i\theta} &= S_{1+}-\sqrt{\Gamma}(A_1+A_2)\\ S_{1-} &= \sigma_{1-}e^{i\theta}-\sqrt{\Gamma}(A_1+A_2)\\ S_{2-} &= \sigma_{2-}e^{i\phi}-\sqrt{\gamma}A_1\\ S_{3-} &= \sigma_{3-}e^{i\phi}-\sqrt{\gamma}A_2.\\ \sigma_{2+}e^{-i\phi} &= -\sqrt{\gamma}A_1.\\ \sigma_{3+}e^{-i\phi} &= -\sqrt{\gamma}A_2.\end{aligned} \tag{55}$$

The T-connection at the C point connects ingoing and outgoing amplitudes by the S-matrix as follows

$$\begin{pmatrix}\sigma_{1-}\\ \sigma_{2-}\\ \sigma_{3-}\end{pmatrix}=\begin{pmatrix}a & b & b\\ b & c & d\\ b & d & c\end{pmatrix}\begin{pmatrix}\sigma_{1+}\\ \sigma_{2+}\\ \sigma_{3+}\end{pmatrix}. \tag{56}$$

In particular, the solution of the Maxwell equations for the T-shaped waveguide without defects gives the matrix elements of the S-matrix (56) $a=-0.3547+0.308i, b=0.6+0.173i, c=-0.4319+0.2271i, d=-0.568+0.2225i$ at $\omega a/2\pi c=0.35$. Equations (54–56) form a full system of equations for 11

Table 1 Parameter sets of the CMT for PhC T-shaped waveguide shown in Fig. 15

Type of structure in Fig. 15	(a)	(b)	(c)
Γ (in terms of $a/2\pi c$)	0.0002	0.0002	0.00189
γ (in terms of $a/2\pi c$)	0.03093	0.00189	0.00002
ω_0 (in terms of $a/2\pi c$)	0.3609	0.365	0.3596

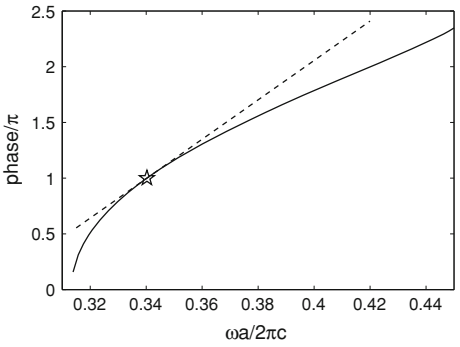

Fig. 17 Frequency behavior of the optical length (phase) shown by *solid line* for the linear PhC waveguide which is fabricated by removing one row of dielectric rods. The parameters of the PhC are listed in figure caption of Fig. 1. The BSC point is marked by *star*

amplitudes $A_1, A_2, \sigma_{1+}, \sigma_{1-}, \sigma_{2+}, \sigma_{2-}, \sigma_{3+}, \sigma_{3-}, S_{1-}, S_{2-}, S_{3-}$. Substituting $S_{1+} = E_{in}e^{i\omega t}$, $A_{1,2} = A_{1,2}e^{-i\omega t}$ we obtain after some algebra the following stationary CMT equations

$$(\omega - H_{eff})\begin{pmatrix} A_1 \\ A_2 \end{pmatrix} = iE_{in}F\begin{pmatrix} 1 \\ 1 \end{pmatrix}, \tag{57}$$

where

$$H_{eff} = \begin{pmatrix} \omega_1 - iG & -iH \\ -iH & \omega_2 - iG \end{pmatrix}, \tag{58}$$

$$\begin{aligned} G &= \gamma + \Gamma(1 + ae^{2i\theta}) + \gamma de^{2i\phi} + \sqrt{\gamma\Gamma}(b + c)e^{i\theta + i\phi}, \\ H &= \Gamma + \sqrt{\gamma\Gamma}(b + c)e^{i\theta + i\phi} + \Gamma ae^{2i\theta} + \gamma de^{2i\phi}, \\ F &= \sqrt{\Gamma}(1 + ae^{2i\theta}) + \sqrt{\gamma}be^{i(\theta+\phi)}. \end{aligned} \tag{59}$$

We can calculate all parameters which are necessary in Eqs. (57–59). For the light transmission in the linear single-channel waveguide coupled with the single linear off-channel defect positioned at different positions we able to extract the coupling constant of the cavity with PhC waveguide Γ and the eigen frequency of monopole mode ω_0. The results are collected in Table 1. The limiting case of the T-shaped waveguide with $\Gamma = 0$ is considered in Ref. [27] with results qualitatively close to those shown in Fig. 18. Here we find the solutions with the

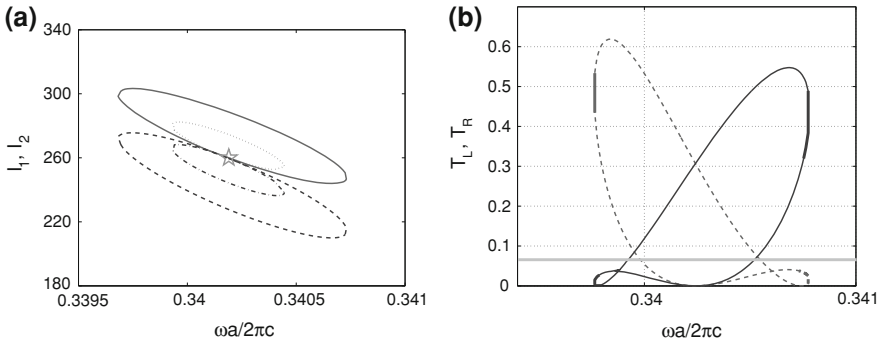

Fig. 18 **a** Frequency behavior of light intensities at the defect rods given in terms of W/a^2 in the PhC T-shaped waveguide shown in Fig. 15a. *Dotted blue* and *dash-dotted red lines* correspond to the input power equal to $0.48\,W/a^2$, *solid blue* and *dashed red lines* do to $1.92\,W/a^2$. Only those solution for intensities is shown which breaks the symmetry. The BSC point is shown by *blue star*. **b** The frequency dependence of the transmissions to the *left* T_L (*blue dashed lines*) and to the right T_R (*red solid lines*). The *thicker lines* show the domains of stability. *Gray thick line* shows the equal transmissions for the symmetry preserving solution

substitution of concrete parameters listed in Table 1 and present the output light transmission to the left and to the right waveguides. We start with the case shown in Fig. 15a.

Moreover we present real dispersion curve $\omega(k)$ calculated for the linear PhC waveguide to find as the optical length given by the phase θ or ϕ depends on the frequency ω. This curve is shown in Fig. 17 by solid curve for the parameters of PhC given in Fig. 1. In the vicinity of the BSC frequency $\omega_c a/2\pi c = 0.3402$ we approximate the dispersion curve as linear to obtain

$$\frac{phase}{\pi} = 1 + \frac{17.68(\omega - \omega_c)a}{2\pi c}. \tag{60}$$

parameters for the phases.

After substitution of the parameters listed in Table 1 for the case shown in Fig. 15a and material parameters given in the beginning of this section into Eq. (61) we calculated the solution of Eq. (61) for the light intensities of the nonlinear defects $I_j = c|A_j|^2/8\pi$ in terms of W/a^2 for broken mirror symmetry with the input power $I_0 = 0.48\,W/a^2$. That choice of the input power gives according to Eq. (53) $\lambda = -1.3 \times 10^{-3}$. The results of computation are presented in Fig. 18. The case of the T-shaped structure shown in Fig. 15a has an analogy with the Fabry-Pérot interferometer (FPI) comprising two off-channel nonlinear cavities. As was shown in Ref. [23] there is a series of the self-induced BSCs which are the standing waves between the off-channel cavities. It was shown that the BSCs exist for any distance between the off-channel defect rods because of their nonlinearity [23] however for the limit of $S_{1+} \to 0$ (vanishing input power).

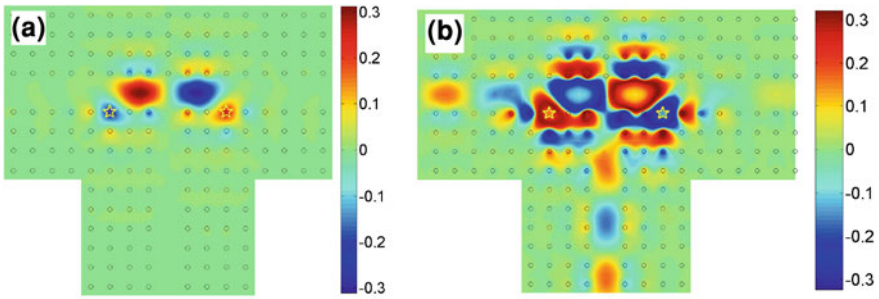

Fig. 19 Solutions of Maxwell equations for the case shown in Fig. 15a which demonstrate (**a**) the anti-symmetric FPI BSC (standing wave between nonlinear off-channel defects marked by *stars*) with frequency $\omega_c a/2\pi c = 0.3402$ for zero input power $P = 0$ and (**b**) as because of nonlinearity this anti-symmetric BSC mixes with the symmetric incident EM wave to give rise to the symmetry breaking for $P = 1.94\,\mathrm{W/a}$. *Yellow stars* mark defect rods

Similar BSC solutions are expected to exist in the present case of the T-shaped waveguide coupled with two off-channel cavities shown in Fig. 15a. However these solutions must be the standing waves with nodes at the point of connection of the waveguides. Therefore in the present case the BSCs are the anti-symmetric standing waves. Figure 19 shows one of these waves in the T-shaped waveguide with two nonlinear defect rods with the eigen frequency $\omega_c a/2\pi c = 0.3402$ which satisfies the condition $3k(\omega_c)a = \pi$. Figure 18a demonstrates the solution for the light intensities of the cavities $I_j = c|E_j|^2/8\pi$, $j = 1, 2$ with broken mirror symmetry where E_j are the amplitudes of the electric field in thin defect rods for two values of input power. The solution converges to the BSC point marked by the star if the input power limits to zero. At this point the symmetry is restored. For the linear case the BSC shown in Fig. 19a has zero coupling with the symmetric EM wave which inputs in the waveguide 1. However as was considered in Sect. 2 nonlinearity gives rise to the important effect of the excitation of BSC by the transmitted wave as shown in Fig. 19b. As a result the total solution lacks the mirror symmetry of the PhC structure shown in Fig. 15a. That is one of the scenarios of the symmetry breaking, respectively for the input power $P \neq 0$ the light transmission from the input waveguide 1 to the left waveguide 2 differs from the transmission and to the right waveguide 3 as seen from Fig. 18b. Moreover the difference $T_L - T_R$ crucially depends on the frequency in the vicinity of the BSC point. Note, that Maes et al. [12] have already reported the symmetry breaking in the FPI. In order for the FPI with two off-channel nonlinear cavities to have the mirror symmetry equal input power must be applied to both sides of the FPI [12]. In our case of the T-shaped waveguide this symmetry is achieved by application of the input power via the additional waveguide positioned at the center of the FPI.

As seen from Fig. 18b the system of two nonlinear cavities close to the waveguide (see Fig. 15a) has extremely small frequency domains of the stability

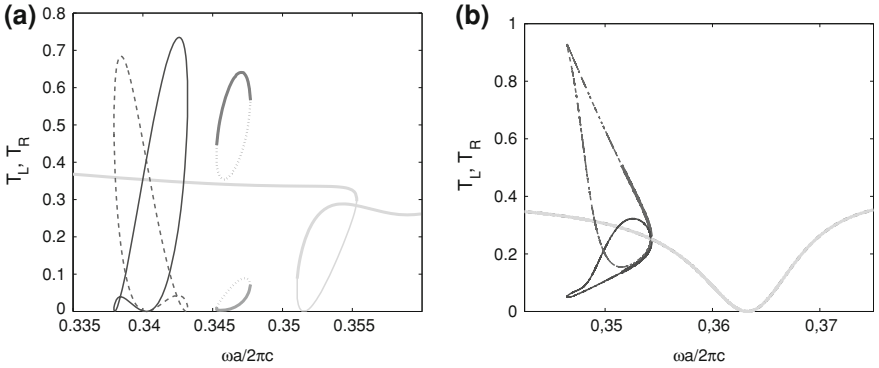

Fig. 20 Frequency behavior of the transmissions T_L and T_R in the PhC T-shaped waveguide shown in (**a**) Fig. 15b for the input power $P = 5.57\,\mathrm{W/a}$ and (**b**) Fig. 15c for $P = 0.48\,\mathrm{W/a}$. The symmetric solution is shown by *solid gray line* which inherits the linear case. The symmetry breaking solution is shown by *solid blue* and *red lines*. The next symmetry breaking solution because of a bistability of the transmission in each output waveguides is shown by *dotted brown* and *green lines*. The *thicker lines* show the domains of stability of the symmetry breaking solution

for the symmetry breaking solution. In Fig. 20a we show that with change of position of defect rods in the T-shaped PhC waveguide additional branch of a loop shape for the symmetry breaking solution appears which has sufficient domains of stability of the symmetry breaking solutions. The loops shown by dotted lines in Fig. 20 are the result of individual instability that arises for transmission in the left or right waveguide coupled with the left or right nonlinear off-channel cavity [27]. With further moving away of the nonlinear optical cavities from the output waveguide (see configuration in Fig. 15c) the system becomes close to the that considered in Refs. [17, 18]. Then the anti-symmetric standing wave additional loops in the transmission disappear Bistability of the light transmission in the PhC waveguide coupled with nonlinear optical cavity crucially depends on the coupling: the smaller a coupling the less input power is needed for bistability [16]. For case (a) in Fig. 15 the coupling is rather large to observe bistability in the transmission. However case (b) has the sufficiently smaller coupling as one can see from Table 1. As a result case in Fig. 15b gives rise to additional loops as shown in Fig. 21 for larger input power $5.57\mathrm{W/a}$. Figure 21 shows the wave function for the symmetry preserving solution (a) and the symmetry breaking solutions (b–d). Cases (b) and (c) differ by the frequency but correspond to the same defect configuration shown in Fig. 15b. The case corresponds to the configuration shown in Fig. 15c. One can see from Fig. 21 that for the symmetric solution the transmission excites the cavities weakly, while for the symmetry breaking solution the defects are strongly excited because of mixing the injecting symmetrical wave with the anti-symmetric FPI BSC. Figure 21c shows that for the frequency in the loop domain $\omega a/2\pi c = 0.3442$ the first nonlinear cavity is excited much more than the second one that is correlated with the outputs. However for the nonlinear

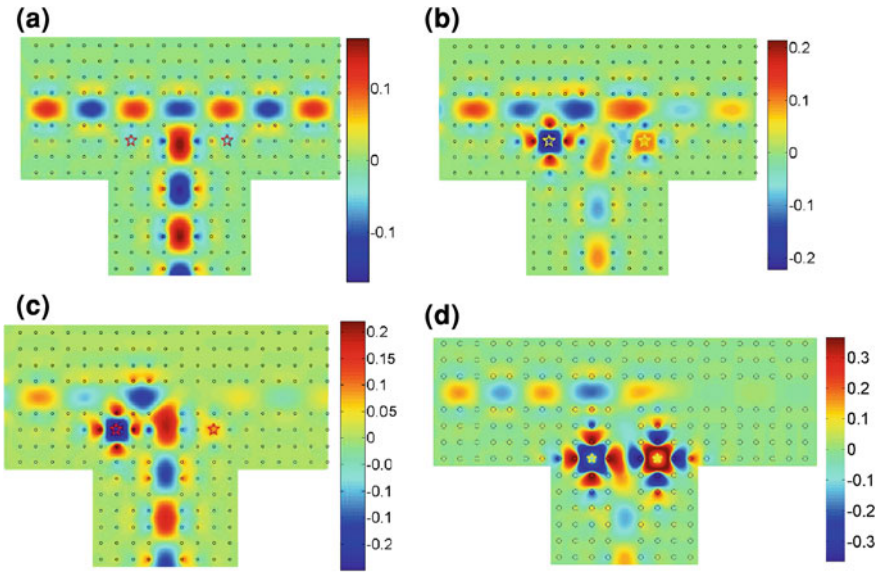

Fig. 21 The EM field solution in a scale $real(E_z)\exp(-|E_z|)$ for (**a**) the symmetry preserving solution for $\omega a/2\pi c = 0.3442$, (**b**) the symmetry breaking solution caused by the BSC for $\omega a/2\pi c = 0.3388$, and (**c**) the for $\omega a/2\pi c = 0.3442$. Light with power $P = 5.57\mathrm{W}/\mathrm{a}$ is incident into the 1 waveguide and scatters to the *left* and *right waveguides* 2 and 3. **d** The symmetry breaking solution for $P = 0.48\,W/a, \omega a/2\pi c = 0.3505$ and the configuration shown in Fig. 15c. *Yellow stars* mark defect rods

defects far from the output waveguides, they are excited almost equally as shown in Fig. 21d.

The T-shaped waveguide coupled with two nonlinear cavities shown in Fig. 15 is remarkable in that it allows the limit to the FPI [case (a)] with the FPI BSC in the form of the standing waves between two off-channel defects [23] as well as the limit to case (c) in Fig. 15 with the BSC in the form of the anti-bonding defect's state. Patterns of such anti-bonding BSC in PhC linear waveguide coupled with two cavities positioned perpendicular to the waveguide are shown in Fig. 2. The nonlinearity gives rise to mixing the anti-bonding BSC with the wave transmitted over waveguide 1. For the linear defect rods this state would be the perfect BSC. For the nonlinear cavities mixing this anti-bonding BSC with symmetric input light leads to the breaking of the mirror symmetry to give rise to the breaking of symmetry in the input waveguide. Then for the evolution of this structure to the T-shaped case can expect different outputs to the right and to the left. Indeed, in spite of the small difference of the defect intensities presented in Fig. 20a the transmissions T_L and T_R demonstrate vast difference including the case of almost perfect blocking of the transmission to the left.

These results are extremely important for the switching of the output power from the left waveguide to the right one. In order to switch the system from one

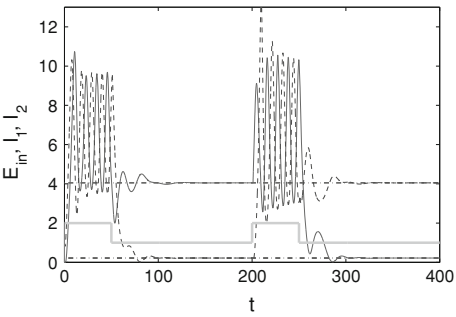

Fig. 22 The time dependence of the amplitudes of the light amplitudes $|A_1|, |A_2|$ in the cavities (*solid and dashed* respectively) which follow the impulses of the input amplitude E_{in} (*gray*). We take the cavities oscillate in non symmetric way: $A_1 = 0, A_2 = 1$

asymmetric state to the other we following Refs. [12, 14] apply pulses of the input power injected into the waveguide 1. The direct numerical solution of the temporal CMT equation

$$\begin{aligned} i\dot{A_1} &= (\omega_1 - i\gamma)A_1 + i\sqrt{\gamma}\sigma_{2-}e^{i\phi} \\ i\dot{A_2} &= (\omega_2 - i\gamma)A_2 + i\sqrt{\gamma}\sigma_{3-}e^{i\phi} \end{aligned} \tag{61}$$

with $S_{1+}(t) = E_{in}(t)e^{-i\omega t}$ is shown in Fig. 22 which demonstrates the switching effect. The stepwise time behavior of amplitude $E_{in}(t)$ is shown by gray line. One can see that after the first impulse of the input amplitude the oscillations of the cavity amplitude relax onto the stable stationary solutions with broken symmetry. Moreover after each next impulse the state of the system transmits from one asymmetric state to the other as was observed by Maes et al. [12].

5 Dipole Modes of the Single Nonlinear Defect Coupled with Waveguide

If to present the defect by the single monopole mode $E_s(\mathbf{x})$ we obtain from Eq. (16)

$$[\omega - \omega_s - \lambda|A_s|^2 - i\Gamma_s]A_s = i\sqrt{\Gamma_s}E_{in}, \tag{62}$$

$$t = E_{in} - \sqrt{\Gamma_s}A_s, \tag{63}$$

where $\lambda = -\frac{3}{4}\sigma\chi^{(3)}(\omega_s)E_s((\mathbf{x}_d)^2$. That model has attracted interest over the past two decades because of analytical treatment and its generality for description of bistability phenomena [16, 39–46]. However the monopole eigen-function presents only the trivial identical symmetry transformation. Respectively there is no room for the breaking of symmetry.

In this respect the system becomes nontrivial if we include two eigen dipole modes $E_1(\mathbf{x})$ and $E_2(\mathbf{x})$ of the defect rod with the eigen-frequencies ω_1 and ω_2.

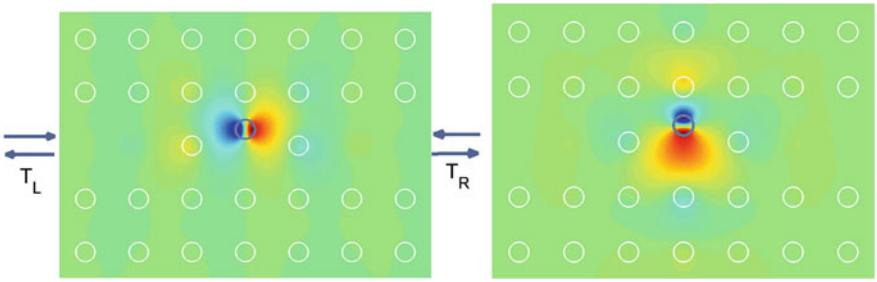

Fig. 23 Two defect dipole eigen-modes with the eigen frequencies $\omega_1 = 0.3578$ and $\omega_2 = 0.3616\ \pi a/c$ in the two-dimensional square lattice PhC consisted of the GaAs dielectric rods with radius $0.18a$ and dielectric constant $\epsilon = 11.56$ where $a = 0.5\ \mu m$ is the lattice unit. These rods are shown by *black open circles*. The defect shown by *open gray circle* has the same radius $0.18a$ and $\epsilon_0 = 30$. Its center is positioned at $x_d = 0, y_d = 0.3a$

The modes are shown in Fig. 23. Respectively, the electric field at the thin defects can be expanded over these dipole modes $E(\mathbf{x}_d) = A_1 E_1(\mathbf{x}_d) + A_2 E_2(\mathbf{x}_d)$ only. Substituting that expansion into Eq. (15) we obtain that Eq. (16) will take the following form

$$\begin{aligned}
&[\omega - \omega_1 - \lambda_{11}|A_1|^2 - \lambda_{12}|A_2|^2 + i\Gamma_1]A_1 - 2\lambda_{12} Re(A_1^* A_2)A_2 = i\sqrt{\Gamma_1}(S_1^+ - S_2^+),\\
&-2\lambda_{12} Re(A_1^* A_2 + [\omega - \omega_1 - \lambda_{22}|A_2|^2 - \lambda_{12}|A_1|^2 + i\Gamma_2]A_2 = i\sqrt{\Gamma_2}(S_1^+ + S_2^+),
\end{aligned} \tag{64}$$

where $S_{1,2}^+$ are the amplitudes of light injected simultaneously into both sides of the waveguide. Here with accordance to Eq. (13) we have

$$\lambda_{mn} = \frac{3}{16\epsilon^{3/2}}\chi^{(3)}(\omega_m + \omega_n)Q_{mn}, \quad Q_{mn} = \int E_m^2(\mathbf{x})E_n^2(\mathbf{x})d^2\mathbf{x} \tag{65}$$

Moreover we have taken into account the symmetry relations for the coupling constants of the dipole modes with the waveguide solutions [64]. As seen from Fig. 23 the first dipole mode has the coupling with the left and the right ingoing waves opposite signs while the second dipole mode has the same coupling with these waves. Therefore the coupling matrix in Eq. (17) equals

$$W = \begin{pmatrix} \sqrt{\Gamma_1} & -\sqrt{\Gamma_1} \\ \sqrt{\Gamma_2} & \sqrt{\Gamma_2} \end{pmatrix}. \tag{66}$$

Moreover Eq. (64) must be complemented by equation for the transmission amplitude

$$\begin{aligned}
t_{LR} &= S_1^+ - i\sqrt{\Gamma_1}A_1 + i\sqrt{\Gamma_2}A_2,\\
t_{RL} &= S_2^+ - i\sqrt{\Gamma_1}A_1 + i\sqrt{\Gamma_2}A_2.
\end{aligned} \tag{67}$$

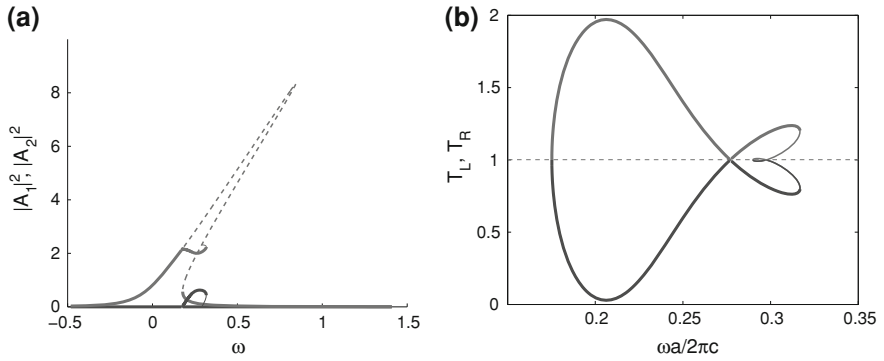

Fig. 24 Frequency behavior of (**a**) intensities of dipole modes and (**b**) transmissions from the *right* to the *left* $T_L = |t_{RL}|^2$ and from the *left* to the *right* $T_R = |t_{LR}|^2$ for light injection $S^+_{1,2} = 0.025$ onto both sides of the waveguide. In (**a**) *dashed blue lines* show the intensity of even dipole mode, while *red lines* show the intensity of odd dipole mode. The model parameters are listed in the text. In (**b**) *dashed blue line* shows the symmetry preserving solution while *solid lines* do the symmetry breaking solution. The *red solid line* shows T_R, *blue solid line* does T_L. In both subplots the *thicker lines* mark stable solutions

Figure 24 shows the self-consistent solutions of Eq. (64) after substitution of the following model parameters $\omega_1 = 0, \omega_2 = 0.01, \lambda_{11} = \lambda_{22} = 0.1, \lambda_{12} = 0.05, \Gamma_1 = 0.1, \Gamma_2 = 0.03$. One can see that for the symmetry preserving branch the first even dipole mode is excited with frequency behavior typical for the single nonlinear mode described by Eq. (35) while the second odd dipole mode is not excited because of symmetry. Respectively, the transmission probability to both sides of the waveguide equals 1/2 because of normalization condition for the intensity of input light and unitarity of the S-matrix $|S_1|^2 + |S_2|^2 + |t_{LR}|^2 + |t_{RL}|^2 = 1$. However there is also the symmetry breaking branch in some narrow frequency domain. Respectively, that branch gives rise to an asymmetry in the light outputs. Moreover there is a frequency at which the right (left) output is blocked almost perfectly.

Also we consider the phenomenon of the symmetry breaking based on the parameters calculated in the 2D square lattice PhC with parameters given earlier. The results for the eigen frequencies are collected in Fig. 23 caption where the parameters of the PhC are given too. The coupling constants are the following $\Gamma_1 = 0.00075, \Gamma_2 = 0.00025$ in terms of $2\pi c/a$. In order to enhance the coupling constants we substituted two additional linear rods nearby the nonlinear defect rod as shown in Fig. 23. Let us evaluate the nonlinearity constants λ_{mn}. With use $\epsilon_d = \epsilon_0 + 2\sqrt{\epsilon_0} n_2 I_0, n_2 \approx \frac{2\pi\chi^{(3)}}{n_0}$ we obtain from (65)

$$\lambda_{mn} = -\frac{3\pi}{8}\sqrt{\epsilon_0} n_2 I_0 \int E_m^2(\mathbf{x}) E_n^2(\mathbf{x}) d^2\mathbf{x}. \tag{68}$$

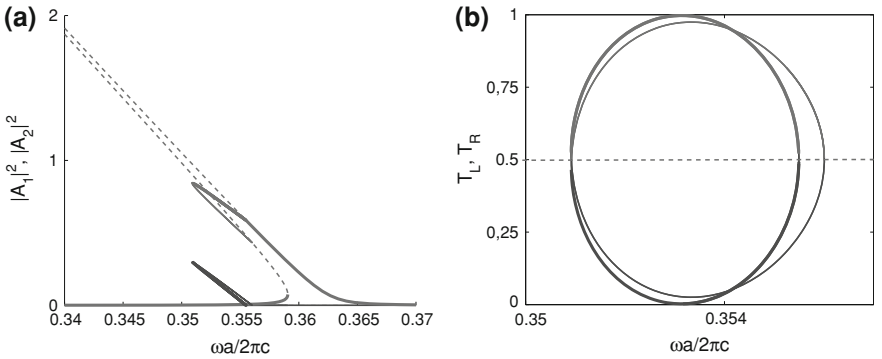

Fig. 25 Frequency behavior of (**a**) intensities of dipole modes and (**b**) transmissions to the *left* and to the *right* after substitution of the parameters $\Gamma_1 = 0.00075$, $\Gamma_2 = 0.00025$ in terms of $2\pi c/a$ which corresponds to the real 2D PhC for $S_{1,2} = 0.015$. In (**a**) *dashed/solid blue lines* show the intensity of even dipole mode for the symmetry preserving/symmetry breaking solution, *solid red lines* show the intensity of the odd dipole mode amplitude for the symmetry breaking solution. In (**b**) *dashed blue line* shows the symmetry preserving solution while *solid lines* do the symmetry breaking solution. The *red solid line* shows T_R, *blue solid line* does T_L. In both subplots the *thicker lines* mark stable solutions

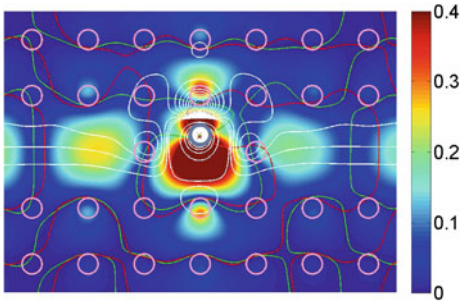

Fig. 26 EM field solution for the symmetry breaking solution caused by excitation of the odd dipole mode $\omega a/2\pi c = 0.369$. *Gray thick open circle* marks the nonlinear defect rod. *White solid lines* mark the Poynting vector energy flows (streamlines)

We take the linear and nonlinear refractive indexes of the defect rods are, respectively, $n_0 = \sqrt{\epsilon_0} = \sqrt{3}$, $I_0 = 1.8$ W/a, $n_2 = 2 \times 10^{-12}\,\mathrm{cm}^2/\mathrm{W}$ [65, 66]. Moreover substituting the dipole modes into integrals in Eq. (68) we obtain $Q_{11} = 0.0123, Q_{22} = 0.0114, Q_{12} = 0.0037$. Results of solution of the self-consistency equations for two complex amplitudes A_1 and A_2 are presented in Fig. 25a. Correspondingly from Eq. (67) we obtain the transmission coefficients shown in Fig. 25b. Finally, Fig. 26 shows the solution of the Maxwell equation in the form of the electric field directed along the rods of the 2D PhC for the symmetry breaking solution. The streamlines in Fig. 26 demonstrate a formation of two optical vortices, one around the defect rod cavity, and the second one near by. The streamlines are the lines along which the Poynting vector energy flows [67, 68].

6 Summary and Conclusions

By solution of the Maxwell equations complemented by solution of the CMT equations we have demonstrated the symmetry breaking in the system of two nonlinear defects coupled with waveguide through which a light is injected. The defects are aligned symmetrically relative to the waveguide as shown in Fig. 1, so there is the mirror symmetry relative to the waveguide axis. The thin dielectric rods made from Kerr media are defect rod cavities which presented by the eigen monopole mode whose eigen frequency belongs to the propagation band of the waveguide. We assume that other eigen modes are beyond the band, and therefore have no coupling with the injected light with accuracy of evanescent modes.

That simplest system is remarkable in that it reveals as nonlinearity gives rise to the breaking of symmetry. Indeed, let us take temporarily the defects are linear. If the coupled defects were isolated, it would have only two eigen-modes, bonding (even) and anti-bonding (odd) with corresponding eigen frequencies (20). The modes are shown in Fig. 2. For light propagating over the waveguide we take that the input wave possesses by the mirror symmetry. Then the light can excite only the bonding mode A_s to give rise typical resonance dip at the symmetrical eigen frequency ω_s while the anti-bonding mode A_a would remain hidden for the propagating light as shown in Fig. 13a. Obviously, that mode is the simplest case of the bound state in continuum [17, 24, 69, 70]. That state can be superposed to the scattering function with coefficient determined by a way to excite the anti-bonding mode [49]. However the principle of linear superposition is not valid for the nonlinear case. Therefore the nonlinearity gives rise to interaction of the scattering state with the anti-bonding mode, i.e., to the interaction of the symmetric propagating light with the anti-bonding mode. That obviously breaks the mirror symmetry as explicitly shown in Figs. 13b, c, 19b, 21b–d, and 26. Obviously, the mixing gives total state which is nor symmetrical neither anti symmetrical, breaking the mirror symmetry, similar to results obtained in Ref. [1, 2]. However the symmetry can be broken not only because of different light intensities but also because of different phases of light oscillations at the cavities to provoke the Josephson like current between cavities [18]. For the light transmission in two-dimensional PhC the Poynting power vector is an analog of the Josephson currrent, which is shown in Fig. 14c. It is clear that for the light transmission in PhC waveguide there is the energy flow over the waveguide. As Fig. 14a shows the flow is mostly laminar for the symmetry breaking solution. However if the mirror symmetry is broken, the Poynting vector pattern might be rather complicated as shown in Fig. 14b and c. One can see that laminar current flow over the waveguide induces two vortices around the defects which obey the mirror symmetry. As the symmetry has broken the vortex in the waveguide appears which is well separated from the defect vortices. Although the mirror symmetry relative to circulation of currents in defect vortices is broken, however, the symmetry is remained relative to absolute value of current flows. At last, for the phase symmetry breaking solution still there is symmetry in absolute value of

current, but all vortices are exchanging by current flows as seen from Fig. 14c. The case of the isolated nonlinear defect rod cavity with two dipole eigen-modes demonstrates similar effect as shown in Fig. 26.

The T-shaped waveguide coupled with two symmetrically positioned nonlinear defects as shown in Fig. 15 can be considered as a combination of the previous system and the Fabry-Pérot interferometer (FPI) consisted of two nonlinear off-channel cavities aligned along the waveguide considered in Refs. [12, 13, 23]. As was shown in Ref. [23] there is a discrete set of the a self-induced bound states in continuum (BSC) which are standing waves between off-channel cavities which are to be anti-symmetric in order to elucidate an escape to the input waveguide 1. As dependent on position of the nonlinear defects shown consequently in Fig. 15 the system goes from the FPI (case a) to the system considered in Sect. 2 (case c). In the case (a) the nonlinearity couples the FPI BSC shown in Fig. 19 with the incident wave which is symmetrical relative to the inversion left to right. As the result the mirror symmetry is broken as shown for real PhC in Figs. 19b and 21b–d to give rise to strong asymmetry of light outputs to the left and to the right. We demonstrate as these phenomena can be explored for all-optical switching of light transmission from the left output waveguide to the right one by application input pulses (see Fig. 22).

In Sect. 5 we show that breaking of symmetry might occur even for the single nonlinear defect positioned in the linear single-channel waveguide provided that the defect is presented by two dipole modes. That model embraces two dipole eigen-modes of the defect rod cavity while in the former models each defect rod cavity was presented by the only monopole eigen-mode. Therefore the model realizes the nonlinear Fano-Anderson model [70].

Acknowledgments AS is grateful to Boris Malomed for fruitful and helpful discussions. The work is partially supported by RFBR grant 12-02-00483.

References

1. E.A. Ostrovskaya, Y.S. Kivshar, M. Lisak, B. Hall, F. Cattani, D. Anderson, Phys. Rev. A **61**, 031601 (2000)
2. R.D. Agosta, B.A. Malomed, C. Presilla, Phys. Lett. A **275**, 424 (2000)
3. N. Akhmediev, A. Ankiewicz, Phys. Rev. Lett. **70**, 2395 (1993)
4. R. Tasgal, B.A. Malomed, Physica Scripta **60**, 418 (1999)
5. A. Gubeskys, B.A. Malomed, Eur. Phys. J. D **28**, 283 (2004)
6. V.A. Brazhnyi, B.A. Malomed, Phys. Rev. A **83**, 053844 (2011)
7. M. Haelterman, P. Mandel, Opt. Lett. **15**, 1412 (1990)
8. T. Peschel, U. Peschel, F. Lederer, Phys. Rev. A **50**, 5153 (1994)
9. I.V. Babushkin, Yu.A. Logvin, N.A. Loĭko, Quant. Electron. **28**, 104 (1998)
10. J.P. Torres, J. Boyce, R.Y. Chiao, Phys. Rev. Lett. **83**, 4293 (1999)
11. L. Longchambon, N. Treps, T. Coudreau, J. Laurat, C. Fabre, Opt. Lett. **30**, 284 (2005)
12. B. Maes, M. Soljaćić, J.D. Joannopoulos, P. Bienstman, R. Baets, S-P. Gorza, M. Haelterman, Opt. Express **14**, 10678 (2006)
13. B. Maes, P. Bienstman, R. Baets, Opt. Express **16**, 3069 (2008)

14. K. Otsuka, K. Ikeda, Opt. Lett. **12**, 599 (1987)
15. K. Huybrechts, G. Morthier, B. Maes, J. Opt. Soc. Am. B **27**, 708 (2010)
16. J. Joannopoulos, S.G Johnson, J.N. Winn, R.D. Meade, *Photonic Crystals: Molding the Flow of Light* (Princeton University Press, Princeton, 2008)
17. E.N. Bulgakov, K.N. Pichugin, A.F. Sadreev, Phys. Rev. B **83**, 045109 (2011)
18. E.N. Bulgakov, K.N. Pichugin, A.F. Sadreev, J. Phys. Condens. Mat. **23**, 065304 (2011)
19. S.M. Jensen, The nonlinear coherent coupler. IEEE J. Quantum Electron. **QE-18**, 1580 (1982)
20. A.A. Maĭer, Sov. J. Quantum Electron. **12**, 1940 (1982)
21. S.R. Friberg, Y. Silberberg, M.K. Oliver, M.J. Andrejco, M.A. Saifi, P.W. Smith, Appl. Phys. Lett. **52**, 1135 (1987)
22. H.M. Gibbs, *Optical Bistability: Controlling Light with Light* (Academic, New York, 1985)
23. E.N. Bulgakov, A.F. Sadreev, Phys. Rev. B **81**, 115128 (2010)
24. Y. Plotnik, O. Peleg, F. Dreisow, M. Heinrich, S. Nolte, A. Szameit, M. Segev, Phys. Rev. Lett. **107**, 183901 (2011)
25. N. Marzari, D. Vanderbilt, Phys. Rev. B **56**, 12847 (1997)
26. K. Busch, S.F. Mingaleev, A. Garcia-Martin, M. Schillinger, D. Hermann, J. Phys. Cond. Mat. **15**, R1233 (2003)
27. E.N. Bulgakov, A.F. Sadreev, J. Phys. Cond. Mat. **23**, 315303 (2011)
28. J. Bravo-Abad, S. Fan, S.G. Johnson, J.D. Joannopoulos, M. Soljaĉić, J. Lightwave Technol. **25**, 2539 (2007)
29. M. Skorobogatiy, J. Yang, *Fundamentals of Photonic Crystal Guiding* (University Press, Cambridge, 2009)
30. J.N. Winn, S. Fan, J.D. Joannopoulos, E.P. Ippen, Phys. Rev. B **59**, 1551 (1999)
31. A.R. Cowan, J.F. Young, Phys. Rev. E **68**, 046606 (2003)
32. H.A. Haus, *Waves and Fields in Optoelectronics* (Prentice-Hall, NY, 1984)
33. C. Manolatou, M.J. Khan, S. Fan, P.R. Villeneuve, H.A. Haus, J.D. Joannopoulos, IEEE J. Quantum Electron. **35**, 1322 (1999)
34. S. Fan, W. Suh, J.D. Joannopoulos, J. Opt. Soc. Am. A **20**, 569 (2003)
35. W. Suh, Z. Wang, S. Fan, IEEE J. of Quantum Electron. **40**, 1511 (2004)
36. E.N. Bulgakov, A.F. Sadreev, Phys. Rev. B **78**, 075105 (2008)
37. S. Fan, P.R. Villeneuve, J.D. Joannopoulos, M.J. Khan, C. Manolatou, H.A. Haus, Phys. Rev. B **59**, 15–882 (1999)
38. P.R. Villeneuve, S. Fan, J.D. Joannopoulos, Phys. Rev. B **54**, 7837 (1996)
39. A.R. McGurn, Chaos **13**, 754 (2003)
40. A.R. McGurn, J. Phys. Condens. Matter **16**, S5243 (2004)
41. A.E. Miroshnichenko, S.F. Mingaleev, S. Flach, Yu.S. Kivshar, Phys. Rev. E **71**, 036626 (2005)
42. A.E. Miroshnichenko, Yu.S. Kivshar, Phys. Rev. E **72**, 056611 (2005)
43. S.F. Mingaleev, A.E. Miroshnichenko, Yu.S. Kivshar, K. Busch, Phys. Rev. E **74**, 046603 (2006)
44. S. Longhi, Phys. Rev. B **75**, 184306 (2007)
45. A.E. Miroshnichenko, Yu. Kivshar, C. Etrich, T. Pertsch, R. Iliew, F. Lederer, Phys. Rev. A **79**, 013809 (2009)
46. A.E. Miroshnichenko, Phys. Rev. E **79**, 026611 (2009)
47. J. von Neumann, E. Wigner, Phys. Z. **30**, 465 (1929)
48. A.Z. Devdariani, V.N. Ostrovsky, Yu.N. Sebyakin, Sov. Phys. JETP **44**, 477 (1976)
49. H. Friedrich, D. Wintgen, Phys. Rev. A **32**, 3231 (1985)
50. E.N. Bulgakov, K.N. Pichugin, A.F. Sadreev, I. Rotter, JETP Lett. **84**, 508 (2006)
51. A.F. Sadreev, E.N. Bulgakov, K.N. Pichugin, I. Rotter, T.V. Babushkina, in *Quantum Dots, Research, Technology and Applications*, ed. by R.W. Knoss (Nova Sciencers Publ. Hauppauge, NY, 2008), pp. 547–577
52. D.R. Tilley, J. Tilley, *Superfluidity and Superconductivity* (Van Nostrand Reinhold Co, NY, 1974)

53. S.F. Mingaleev, Yu.S. Kivshar, R.A. Sammut, Phys. Rev. E **62**, 5777 (2000)
54. S.F. Mingaleev, A.E. Miroshnichenko, Y.S. Kivshar, Opt. Express **15**, 12380 (2007)
55. S.F. Mingaleev, A.E. Miroshnichenko, Y.S. Kivshar, Opt. Express **16**, 11647 (2008)
56. D. Michaelis, U. Peschel, C. Wächter, A. Bräuer, Phys. Rev. E **68**, 065601R (2003)
57. G. Lecamp, J.P. Hugonin, P. Lalanne, Opt. Express **15**, 11042 (2007)
58. P. Exner, P. Šeba, A.F. Sadreev, P. Středa, P. Feher, Phys. Rev. Lett. **80**, 1710 (1998)
59. G.S. McDonald, W.J. Firth, J. Mod. Opt. **37**, 613 (1990)
60. Y. Chen, A.W. Snyder, D.N. Payne, IEEE J. Quantum Electron. **28**, 239 (1992)
61. N. Boumaza, T. Benouaz, A. Chikhaoui, A. Cheknane, Int. J. Phys. Sci. **4**, 505 (2009)
62. V. Grigoriev, F. Biancalana, Opt. Lett. **36**, 2131 (2011)
63. E.N. Bulgakov, A.F. Sadreev, Phys. Rev. B **84**, 155304 (2011)
64. S.G. Johnson, C. Manolatou, S. Fan, P. R. Villeneuve, J.D. Joannopoulos, H.A. Haus, Opt. Lett. **23**, 1855 (1998)
65. D. Milam, Appl. Opt. **37**, 546 (1998)
66. G. Boudebs, K. Fedus, J. Appl. Phys. **105**, 103106 (2009)
67. R.V. Waterhouse, D. Feit, J. Acoust. Soc. Am. **80**, 681 (1986)
68. K.-F. Berggren, A.F. Sadreev, A.A. Starikov, Phys. Rev. E **66**, 016218 (2002)
69. de M.L.L. Guevara, F. Claro, P.A. Orellana, Phys. Rev. B **67**, 195335 (2003)
70. E.N. Bulgakov, A.F. Sadreev, Phys. Rev. B **80**, 115308 (2009)

Spatial Solitons in Parity-Time-Symmetric Photonic Lattices: Recent Theoretical Results

Ying-Ji He and Boris A. Malomed

1 Introduction

In 1998, seminal work [1] had demonstrated that non-Hermitian Hamiltonians ($\hat{H}^{\dagger} \neq \hat{H}$) can give rise to entirely real eigenvalue spectra (thus being appropriate for physical applications), provided that they obey the condition of the parity-time (PT) symmetry, i.e., $\hat{H}(-\mathbf{r}) = \hat{H}^{\dagger}(\mathbf{r})$. This condition implies that the Hermitian and anti-Hermitian parts of the Hamiltonian are spatially even and odd, respectively. Such a Hamiltonian usually features spontaneous breaking of the PT-symmetry at a critical value of the coefficient accounting for its anti-Hermitian part. Above the critical point, the spectrum is no longer completely real [2–6].

More recently, it was proposed [6–13] and demonstrated experimentally [14, 15] that PT-symmetric can be implemented in optics, see also review [16]. This possibility relies upon the fact that the propagation of optical waves obeys the same Schrödinger equation as the evolution of the wave function in quantum mechanics, while the spatially odd anti-Hermitian part of the corresponding Hamiltonian may be represented by symmetrically placed and mutually balanced gain and loss elements, which are represented by an imaginary part of the effective potential in the corresponding propagation equation.

In most cases, the PT-symmetric setting is built in the form of a periodic structure in the optical medium, i.e., as a complex photonic lattice (PL), with

Y.-J. He (✉)
School of Electronics and Information, Guangdong Polytechnic Normal University, Guangzhou 510665, China
e-mail: heyingji8@126.com

B. A. Malomed
Department of Physical Electronics, School of Electrical Engineering, Faculty of Engineering, Tel Aviv University, 69978 Tel Aviv, Israel
e-mail: malomed@post.tau.ac.il

Progress Optical Sci., Photonics (2013): 125–148
DOI: 10.1007/10091_2012_24

Published Online: 1 January 2013

spatially even and odd real and imaginary parts, respectively. The use of such lattices makes it possible to demonstrate a number of interesting features, such as double refraction, power oscillations, nonreciprocal diffraction patterns, etc.

Further, both one-dimensional (1D) and two-dimensional (2D) *PT*-symmetric linear PLs can be created in Kerr-nonlinear media [8, 9, 12, 13, 16], which naturally opens the way to the creation of *PT*-symmetric optical solitons. In the framework of this topic, interactions of spatial solitons in *PT*-symmetric periodic complex-valued potentials with defect of the PL have been studied in Refs. [17, 18]. Another variety of defects is represented by a domain wall in a chain of *PT*-symmetric dimers, with the orientation of dimers inverted at a particular site. Scattering of propagating waves ion the domain wall was investigated in Ref. [19]. Solitons in *PT*-symmetric complex-valued periodic PLs, whose real part is represented by a superlattice potential, were investigated in Ref. [20]. Stable 1D and 2D bright spatial solitons in defocusing Kerr media with *PT*-symmetric potentials have been found too [21]. Also, it was demonstrated that gray solitons in *PT*-symmetric potentials can be stable [22]. The analysis of the stability of solitons in *PT*-symmetric lattices has revealed that both 1D and 2D solitons have their stability regions [23]. Dark solitons and vortices in *PT*-symmetric systems combined with defocusing nonlinearities were constructed in Ref. [24].

The model of a *PT*-symmetric nonlinear optical coupler was introduced in Ref. [25], as a system of linearly coupled cores, with the intrinsic self-focusing Kerr nonlinearity and mutually balanced gain and loss introduced in them. Families of analytical *PT*-symmetric and antisymmetric solitons were found, and their stability investigated by a combination of analytical and numerical methods. Soon afterwards, a similar analysis was independently reported in Ref. [26], and optical modes in *PT*-symmetric double-channel waveguides were also considered in Ref. [27]. Oscillatory localized modes (breathers) in the *PT*-symmetric nonlinear couplers were recently investigated in Refs. [28] and [29]. In the latter work, it was shown that stability of both high- and low-frequency breathers is determined by a single combination of its amplitude and the gain-loss coefficient of the coupled waveguides. A special case of the *PT*-supersymmetric coupler, with equal the gain and loss coefficients in the two cores equal to the constant of the inter-core linear coupling, was introduced in Ref. [30], where it was demonstrate that solitons, which are unstable in this system, can be stabilized by means of periodic "management", in the form of the periodic synchronous reversal of the sigh of all these three coefficients.

Nonlinear modes in finite-dimensional *PT*-symmetric systems, based on coupled waveguides, were studied in Ref. [31]. It was shown that the transformations among the *PT*-symmetric systems by rearrangements of waveguiding arrays carrying the balanced gain and loss do not affect their real linear spectra, while nonlinear features of such *PT*-symmetric systems undergo significant changes.

Recently, it was demonstrated that stable solitons may exists in localized *PT*-symmetric potential embedded into an optical medium with quadratic (alias second-harmonic-generating) optical medium [32], in addition to many results reported in other works for the cubic (Kerr) nonlinearity.

Bragg gap solitons in *PT*-symmetric lattices with competing optical nonlinearities of the cubic-quintic type have been investigated in recent work [33]. Various families of solitons, including multi-stable ones, with even and odd symmetries, were found in both the semi-infinite and the first finite bandgaps [34].

Recently, solitons in *PT*-symmetric potentials with nonlocal nonlinearities were also investigated [35–37]. The nonlocality can significantly affect the structure and stability of *PT*-symmetric lattice solitons [35]. Defect solitons in *PT*-symmetric potentials with nonlocal nonlinearity were investigated in recent work [36]. It was shown that, for positive and zero defects, fundamental and dipole solitons may be stable in the semi-infinite gap, and in the first finite bandgap, respectively. A recent study of solitons in *PT*-symmetric potentials with a spatially modulated nonlocal nonlinearity [37] revealed the existence of stable and unstable solitons in low-power and high-power regions, respectively. Unstable solitons spontaneously jump from the original site (channel) to the next one, and can continue this model of the motion into adjacent channels [37].

In addition to solitons in uniform PLs, it is natural to consider surface solitons in truncated lattice. Surface solitons cannot be stable in the truncation of *PT*-symmetric complex-valued potentials, because such semi-infinite potentials break the *PT* symmetry of the complex-valued potentials, and do not support the formation of stationary states at the edge of the potential profile. However, surface solitons, that may form at the edge of truncated conservative periodic lattices (without the gain and loss) were theoretically studied and subsequently observed in 1D and 2D settings, in various optical media [38–43], and stationary states may exist near the edge of the truncated potential if gain also acts at the edge [44]. Recently, it was demonstrated that truncated periodic complex potentials (involving the truncation of *PT*-symmetric complex-valued potentials) with homogeneous losses can support stable surface solitons in both focusing and defocusing media [45].

The study of solitons in nonlinear PLs, with the linear potential replaced by or combined with a spatially periodic modulation of the local strength of the nonlinearity, has recently attracted a lot of attention [46]. It should be mentioned that *PT*-symmetric nonlinear PLs can support stable discrete solitons [46]. A series of works dealing with *PT*-symmetric nonlinear lattices in various physical settings have been recently published [47–49]. The existence of localized modes, including multipole solitons, supported by *PT*-symmetric nonlinear lattices was reported in this context [47]. Such *PT*-symmetric nonlinear PLs can be implemented by means of a proper periodic modulation of nonlinear gain and losses, in specially engineered nonlinear optical waveguides. Further, solitons in purely *PT*-symmetric nonlinear lattices were studied too [47, 50, 51].

Also investigated were solitons in mixed linear-nonlinear lattices [52]. In particular, the competition between linear and nonlinear lattices in contexts of matter waves in Bose–Einstein condensates was the subject of Ref. [53]. Solitons in mixed *PT*-symmetric linear-nonlinear lattices have been investigated too [54]. It was found that the combination of *PT*-symmetric linear and nonlinear lattices can stabilize solitons, with parameters of the periodic lattice potential playing a significant

role in controlling the extent of the stability domains [54, 55]. In addition, the existence and stability of defect gap solitons in real linear periodic PLs with *PT*-symmetric nonlinear optical potentials was reported in Ref. [55]. For uniform real periodic PLs including positive defects, the fundamental solitons exist in the semi-infinite gaps, where they are stable in wide regions. For negative defects, solitons can exist in the semi-infinite gap and in the first finite bandgap [56].

In this chapter, we present an outline of basic theoretical results obtained for lattice solitons which can be supported by various types of *PT*-symmetric optical potentials. The most general model for the spatial beam propagation in *PT*-symmetric periodic PLs with the Kerr nonlinearity is described in Sect. 2. Then, in Sect. 3 we review the simplest case of the lattice solitons in 1D Kerr media in *PT*-symmetric periodic PLs. In Sect. 4, the existence of dark solitons and vortices in *PT*-symmetric nonlinear media is analyzed. The existence and stability of lattice solitons in *PT*-symmetric mixed linear-nonlinear PLs in self-focusing Kerr media is briefly discussed in Sect. 5. Finally, solitons in *PT*-symmetric PLs combined with spatially periodic modulation of the Kerr and nonlocal nonlinearities is briefly overviewed in Sect. 6.

2 The General Model

The spatial beam propagation in *PT*-symmetric periodic PLs with the Kerr optical nonlinearity obeys the following normalized 1D nonlinear Schrödinger (NLS) equation:

$$i\frac{\partial q}{\partial z}+\frac{1}{2}\frac{\partial^2 q}{\partial x^2}+[v(x)+iw(x)]q\pm|q|^2q=0, \tag{1}$$

where i is the imaginary unit, q is the complex field amplitude, and z and x are the normalized longitudinal coordinate and transverse coordinate, respectively. Note that $v(x)$ and $w(x)$ are even and odd functions of transverse spatial coordinate x, respectively. The nonlinear terms, $\pm|q|^2q$ correspond, severally, to the self-focusing self-defocusing media. Stationary solutions of Eq. (1) are searched for as $q(x,z) = f(x)\exp(i\mu z)$, where μ is a real propagation constant, and complex-valued function $f(x)$ satisfies the following nonlinear differential equation:

$$\frac{1}{2}\frac{d^2f}{dx^2}+[v(x)+iw(x)]f+|f|^2f=\mu f. \tag{2}$$

By substituting $f(x) = h(x) + ie(x)$ in Eq. (2), the following coupled nonlinear differential equations are derived for real functions h and e:

$$\frac{1}{2}h_{xx}+vh-we+e^2h+h^3=\mu h, \tag{3a}$$

$$\frac{1}{2}e_{xx} + ve + wh + h^2 e + e^3 = \mu e. \tag{3b}$$

The linear stability of stationary soliton solutions is analyzed by adding small perturbations $g(x)$ and $t(x)$ to the stationary soliton solution:

$$q(x,z) = \exp(i\mu z)\{f(x) + [g(x) - t(x)]\exp(\delta z) + [g(x) + t(x)]^* \exp(\delta^* z)\},$$

where δ is the instability growth rate and the asterisk stands for the complex conjugate. Substituting this expression into Eq. (1) and linearizing it, the following coupled equations are derived:

$$\begin{cases} \delta g = -i\left\{\dfrac{d^2 t}{dx^2} - \mu t + vt - iwg + 2\left[|f|^2 t - \dfrac{1}{4}\left(f^2 - f^{*2}\right)g - \dfrac{1}{4}\left(f^2 + f^{*2}\right)t\right]\right\}, \\ \delta t = -i\left\{\dfrac{d^2 g}{dx^2} - \mu g + vg - iwt + 2\left[|f|^2 g + \dfrac{1}{4}\left(f^2 + f^{*2}\right)g + \dfrac{1}{4}\left(f^2 - f^{*2}\right)t\right]\right\}. \end{cases} \tag{4}$$

Coupled equations (4) can be numerically solved by means of the matrix eigenvalue method. If there exists at least a single eigenvalues with $\mathrm{Re}(\delta) > 0$, the solitons are linearly unstable, otherwise they are stable.

The linear version of nonlinear Eq. (2) is

$$\frac{1}{2}\frac{d^2 f}{dx^2} + [v(x) + iw(x)]f = \mu f. \tag{5}$$

According to the Bloch theorem, eigenfunctions of Eq. (5) can be constructed in the form of $f = F_k \exp(ikx)$, where k is the Bloch wave number, and F_k is a periodic function with the same period as functions $v(x)$ and $w(x)$. Substituting the Bloch solution in Eq. (5), the following eigenvalue equation is obtained,

$$\left(\frac{d^2}{dx^2} + 2ik\frac{d}{dx} - k^2\right)F_k + [v(x) + iw(x)]F_k = \mu F_k. \tag{6}$$

Finally, the basic characteristic of the soliton is its total power, $P = \int_{-\infty}^{+\infty} |f|^2 dx$.

3 Optical Solitons in PT-Symmetric Periodic Potentials

Following Ref. [8], we here consider for simple lattice model, with

$$v(x) = v_0 \cos^2(x),\ w(x) = w_0 \sin(2x). \tag{7}$$

In this section, $v_0 = 1$ is fixed. Corresponding to such a potential, purely real spectral bands exist in the range of $0 \le w_0 < 1/2$. Figure 1 shows the associated

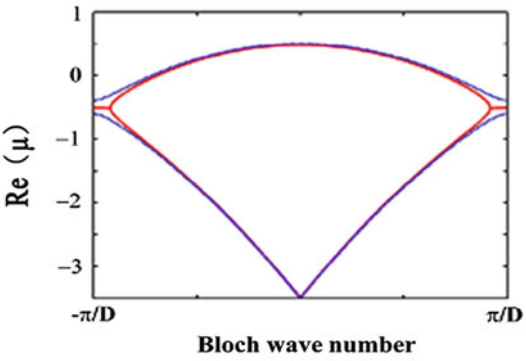

Fig. 1 The bandstructure for the *PT* potential. (7) with $w_0 = 0.45$ (*dotted line*), and $w_0 = 0.6$ (*solid line*), as per Ref. [8]

band structure for various values of potential parameter w_0. With the increase of w_0, the bandgap becomes narrower and closes completely at the critical point, $w_0 = 1/2$. For $w_0 < 1/2$, families of soliton solutions with real eigenvalues, located within the semi-infinite gap, were constructed numerically. A typical profile of such a soliton is shown in Fig. 2a.

Next, the stability of these solutions was addressed, given that these complex structures involve strong loss and gain. In general, the instability growth rate tends to increase with w_0. In addition, narrower self-trapped waves are more stable, as the nonlinearity tends to further enhance the index guiding. Accordingly, the beam becomes confined and propagates undistorted with the increase of the power, thus forming a stable lattice soliton. Figure 2b shows the propagation dynamics of such a soliton (for $w_0 = 0.45$ and $\mu = 1.57$). The corresponding transverse power flow is plotted in Fig. 2c. As seen in the latter panel, the direction of the flow from gain to loss regions varies across the lattice. More specifically, it is positive (from left to right) in waveguiding channels, and becomes negative (from right to left) in the space between the channels. This may be anticipated, as the power transport is always directed from gain to loss domains.

For the 2D case, the bandgap structure corresponding to the periodic potential with

$$v(x, y) = \cos^2(x) + \cos^2(y), \; w(x, y) = w_0[\sin(2x) + \sin(2y)] \tag{8}$$

is depicted in Fig. 3a for $w_0 = 0.3$. Note that the *PT*-symmetry-breaking critical value of the coefficient in front of the imaginary part of 2D potential (8) is identical to that for the 1D potential, i.e., $w_0 = 0.5$. Above this point, the first two bands merge together forming an oval, a double-valued surface attached to a 2D membrane of complex eigenvalues. A 2D *PT*-symmetric soliton with eigenvalue belonging to the semi-infinite gap is shown in Fig. 3b. At low intensities, the nonlinearity is not strong enough, hence this beam asymmetrically diffracts in the complex lattice, as shown in Fig. 3c. However, if the power is high enough, the nonlinear wave propagates as a stable soliton. To further understand the internal structure of these self-trapped states, the corresponding transverse power flow

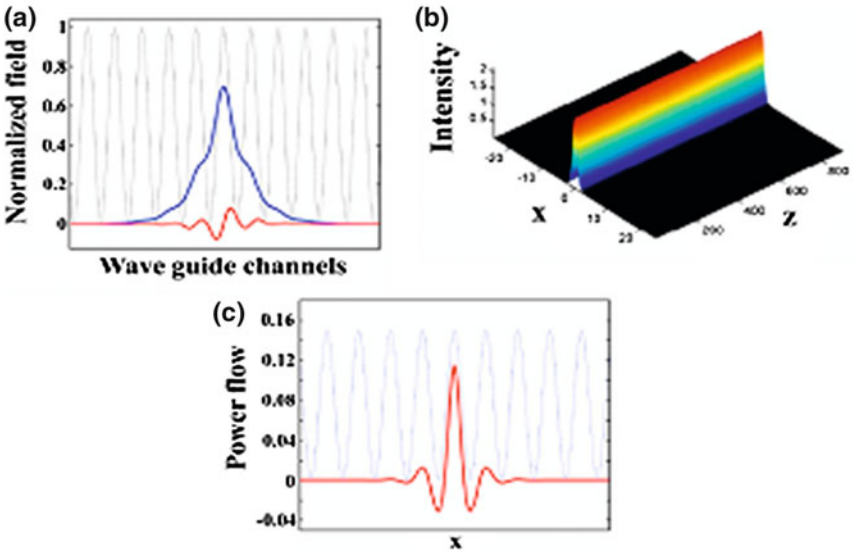

Fig. 2 **a** The soliton field profile in the *PT* lattice (7) with $w_0 = 0.45$. The real and imaginary parts are shown by the *blue* and *red lines*, respectively, for $\mu = 0.7$. **b** The stable propagation of a *PT* lattice soliton with eigenvalue $\mu = 1.57$. **c** The transverse power flow (*solid line*) of the soliton in (**a**) across the lattice. The *dotted line* represents the real part of the lattice potential in panels (**a**) and (**c**). The results were reported in Ref. [8]

vector is depicted in Fig. 3d, which again implies the energy exchange among the gain or loss domains.

4 Dark Solitons and Vortices in PT-Symmetric Nonlinear Self-Defocusing Media: From Spontaneous Symmetry Breaking to Nonlinear PT Phase Transitions

4.1 One-Dimensional Dark Solitons

In Ref. [24], Eq. (1) was considered for the self-defocusing medium, with a real parabolic potential of strength Ω,

$$v(x) = (1/2)\Omega x^2, \tag{9}$$

which models the transverse distribution of the refractive index (or the external trap in Bose–Einstein condensates), while the imaginary part $w(x)$ is assumed to be an odd localized function of spatial width $\ll \Omega^{-1}$, viz.,

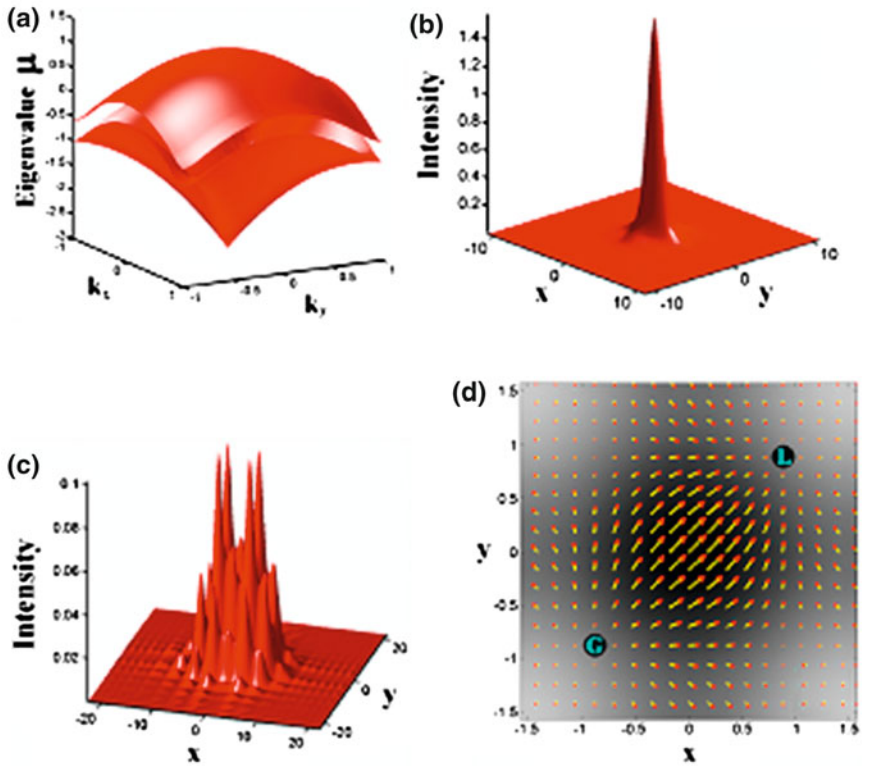

Fig. 3 **a** The band structure of 2D *PT*-symmetric potential (8) with $w_0 = 0.3$. **b** The intensity profile of a *PT* soliton with the propagation eigenvalues $\mu = 1.3$. **c** The linear diffraction pattern generated by the low-power single-channel excitation (the formal soliton input with $\mu = 1.3$). **d** The transverse power flow of this *PT* soliton solution within one cell where the dark area of the background represents the waveguide area. Positions, at which the gain and loss attain the maximum, are indicated by points G and L, respectively. The results are represented as per Ref. [8]

$$w(x) = \varepsilon x \exp\left(-x^2/2\right)\cdot \tag{10}$$

The solution is factorized into the background part, q_b, and the soliton proper, $q(x,t)$, using the product ansatz,

$$\psi(x) = q_b(x)q(x,t), \tag{11}$$

where function $q(x,t)$ assumes—in the absence of the imaginary potential ($\varepsilon = 0$)—a hyperbolic tangent profile. Then, the following perturbed NLS equation is derived:

$$i\partial_t q + \frac{1}{2}\partial_x^2 q + q\left(1 - |q|^2\right) = q - 2p(q), \tag{12}$$

where perturbation $p(q)$ is $p(q) = \left(1 - |q|^2\right)q(v + 2w^2) + q_x\left[\frac{1}{2}v_x - 2(w - i)\int w dx\right]$.

Equation (12) possesses a dark soliton solution of the form

$$q(x,t) = \cos\varphi \tanh\xi + i\sin\varphi, \tag{13}$$

where $\xi \equiv \cos\varphi[x - x_0(t)]$ with φ and $x_0(t) = (\sin\varphi)t$ representing the soliton's phase angle and central coordinate, respectively. The evolution of these parameters is governed by the following equations:

$$\frac{dx_0}{dt} = \sin\varphi(t), \tag{14}$$

$$\frac{d\varphi}{dt} = -\frac{1}{2}\frac{\partial v(x_0)}{\partial x_0} - \int_{-\infty}^{+\infty} \mathrm{sech}^4(\xi)\left[\tanh(\xi)\left(\int w dx\right)^2 + w\int w dx\right]dx. \tag{15}$$

To examine the stability of the equilibrium at $x_0 = 0$, the Taylor expansion of Eq. (15) can be used, as the leading order:

$$\frac{d^2x_0}{dt^2} = -\omega_{\mathrm{osc}}^2 x_0, \quad \omega_{\mathrm{osc}}^2 \approx \left(\frac{\Omega}{\sqrt{2}}\right)^2 - \frac{6}{5}\varepsilon^2. \tag{16}$$

Equation (16) implies that, if amplitude ε of $w(x)$ is less than a critical value, $\varepsilon_{\mathrm{cr}}^{(1)} = \sqrt{5/12}\Omega$, then the soliton performs oscillations in the effective potential with frequency ω_{osc}. Such a case is demonstrated in the bottom panel of Fig. 4, where a dark soliton oscillating around the trap's center is shown for $\varepsilon = 0.04 < \varepsilon_{\mathrm{cr}}^{(1)}$. The numerically found trajectory, obtained by direct numerical integration of Eq. (1), is compared with the analytical result given by Eq. (16) [the dashed (white) line]. Excellent agreement is observed between the analytical and numerical results. On the other hand, Eq. (16) predicts that the soliton becomes unstable at $\varepsilon > \varepsilon_{\mathrm{cr}}^{(1)}$.

4.2 Two-Dimensional Generalizations

Next, the case of a 2D *PT*-symmetric potential with a real parabolic part and an odd imaginary one,

$$v(x,y) = (1/2)\Omega^2\left(x^2 + y^2\right), \quad w(x,y) = \varepsilon(x + y)\exp\left[-\left(x^2 + y^2\right)/4\right], \tag{17}$$

is considered, following Ref. [24]. The bifurcation of nonlinear structures emerging in this 2D setting follows a similar, but more complex, pattern than in the corresponding 1D setting. Figure 5a depicts the full bifurcation scenario for solutions bearing no vortices [the Thomas–Fermi (TF) background states], one to

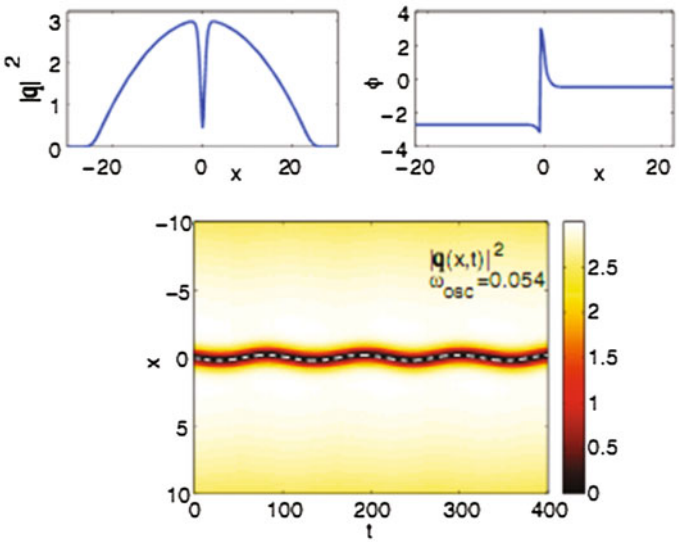

Fig. 4 *Top*: The density (*left*) and phase (*right*) of a single stationary dark-soliton state in the 1D model with the real and imaginary parts of the PT-symmetric potential given by Eqs. (9) and (10), respectively. Parameters are $\mu = 3$, $\Omega = 3$, and $\varepsilon = 0.3$. *Bottom*: A contour plot showing small-amplitude oscillations of a dark soliton. The *dashed* (*white*) *line* depicts the corresponding analytical prediction. Parameters are as in the *top panel*, but with $\varepsilon = 0.04$. The results were reported in Ref. [24]

six vortices, and a dark soliton stripe. Dipole modes, built as bound states of vortices with opposite charges (hence, the net topological charge is zero) are represented by the top-right red curve. At the first critical point the dipole branch is destabilized through a spontaneous symmetry-breaking bifurcation (the dipole is stable between $\varepsilon = 0$ and this critical point). As this branch is followed (from top to bottom in the figure), a series of bifurcations occur where the existing vortices are drawn to the periphery of the cloud, and a dip in the center deepens, leading to emergence of a new vortex pair (i.e., a higher excited state). In this manner, the branches with even number of vortices are all connected. As more and more vortex pairs emerge, the cloud "saturates" and can no longer fit in new vortex pairs, finally colliding with a dark soliton stripe (see the lower blue branch in Fig. 5a). This overall bifurcating structure with even vortex numbers is depicted in Fig. 5a, with the corresponding density and phase profiles shown in the series of panels of Fig. 5b.

As for the bifurcation scenario with odd numbers of vortices, the first excited state bearing a single vortex at the origin (for $\varepsilon = 0$) is stable at small values of ε, while it again sustains a spontaneous symmetry-breaking bifurcation at larger ε. As ε increases, the vortex moves toward the periphery of the cloud and a dip at the center of the cloud deepens until a vortex pair emerges from it. This scenario connects the single-vortex branch with an asymmetric three-vortex ($+ - +$ vortex

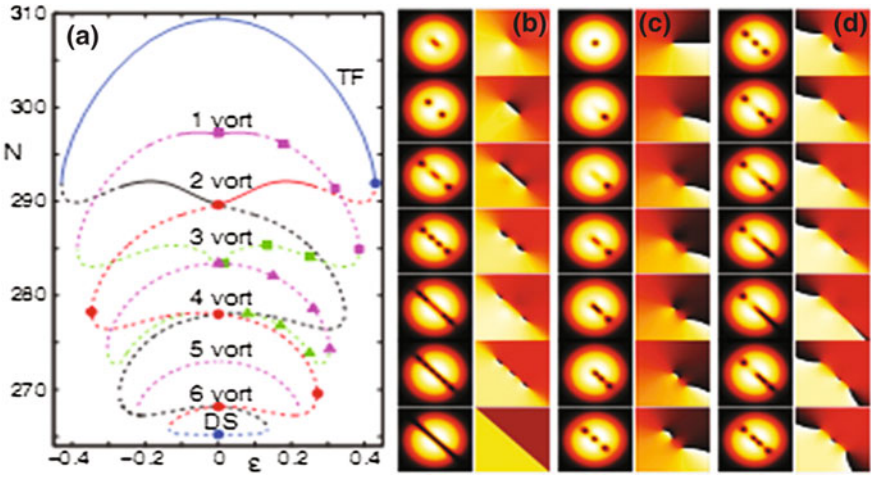

Fig. 5 Results for the 2D *PT*-symmetric model corresponding to the complex potential (17), reported in Ref. [24]. **a** The bifurcation diagram for the 2D stationary nonlinear (vortex and dark-soliton stripe) states. Stable (unstable) branches are depicted by *solid* (*dashed*) *lines*. **b** Series of density (*left*) and phase (*right*) configurations along the branch with an even number of vortices, corresponding to circles in panel (**a**) (from *top* to *bottom*). **c** Same as (**b**) for the branch starting with one vortex and connecting with the three-vortex state corresponding to the squares in panel (**a**) (from *top* to *bottom*). **d** Same as (**b**), for the branch starting from three symmetric vortices and ending with the four-vortex state corresponding to triangles in panel (**a**) (from *top* to *bottom*). Parameters are $\mu = 2$ and $\Omega = 2$. The size of the displayed domains is $[-10.5, 10.5] \times [-10.5, 10.5]$

tripole) branch, as shown by the top (magenta and green) lines in panel 5a, and the series of snapshots in panels 5c. It is evident from the figure that the asymmetric three-vortex branch eventually connects with the symmetric state at $\varepsilon \to 0$. A similar bifurcation occurs with the symmetric three-vortex branch, which becomes asymmetric with a deepening dip at the center, where a vortex pair emerges (at the same moment when a vortex is lost at the periphery), connecting in this way with the four-vortex branch (see series of snapshots in panels 5d).

5 Soliton in PT-Symmetric Mixed Linear-Nonlinear PLs

For the *PT*-symmetric mixed linear-nonlinear PL structure introduced in Ref. [53], Eq. (1) for the spatial beam propagation is

$$i\frac{\partial q}{\partial z} + \frac{\partial^2 q}{\partial x^2} + [v(x) + iw(x)]q + [v_1(x) + iw_1(x)]q|q|^2 = 0. \tag{18}$$

In this section, three typical cases of different *PT*-symmetric periodic mixed linear-nonlinear PLs are considered.

5.1 The PT-Symmetric Linear Lattice Potential Different from its PT-Symmetric Nonlinear Counterpart

Following Ref. [54], the *PT*-symmetric linear-lattice profile is taken as in Eq. (7), whereas the *PT*-symmetric nonlinear-lattice modulation in Eq. (18) is defined as

$$v_1(x) = v_1 \cos(2x), \quad w_1(x) = -w_1 \sin(2x). \tag{19}$$

For this choice of the two jointly acting linear and nonlinear lattice potentials, the real parts, signs of the imaginary parts, and amplitudes of the modulation profiles may be totally different.

First, parameters of the *PT*-symmetric linear lattice are fixed as $v_0 = 4$ and $w_0 = 0.8$, to investigate effects of the *PT*-symmetric nonlinear lattice on the soliton propagation. Dependences of soliton power P on propagation constant μ are shown in Fig. 6a–c, for three sets of the nonlinear PL parameters, $v_1 = 0.1$ and $w_1 = 0.1$, $v_1 = 0.5$ and $w_1 = 0.5$, and $v_1 = 1$ and $w_1 = 1$, respectively. From Fig. 6, one sees that the soliton power increases with the decrease of amplitudes v_1 and w_1 of the nonlinearity modulation. This can be explained as follows. In the case of the self-focusing Kerr nonlinearity, if the depth of the nonlinear lattice increases, the corresponding self-focusing effect exerted on the optical beam, which is determined by $[1 + v_1(x)]|q|^2 q$, and the associated effect of the nonlinear gain effect, coming from the imaginary part of the nonlinear lattice potential, become stronger. In addition, for a given depth of the nonlinear lattice, a higher peak power of solitons will cause a much stronger self-focusing of the optical beam. If the combination of the self-focusing and nonlinear-gain effects is stronger than a certain critical value, the lattice solitons will collapse. Therefore, the existence of solitons in this specific situation requires that their peak powers must decrease with the increase of the depth of the nonlinear lattice, in order to avoid the destruction of the solitons in the course of the propagation due to the very strong self-focusing effect. Note that if only the depth of the dissipative part of the nonlinearity modulation increases, the soliton power decreases, i.e., the effect of the imaginary (dissipative) part of the nonlinearity modulation on the soliton power is smaller than that induced by the real part of the nonlinearity modulation.

Typical results of simulations of the evolution of the lattice solitons are shown in Fig. 7, where both the soliton field profiles and their development in the course of the propagation were plotted. Stable soliton regions are: $2.7 \leq \mu \leq 3.4$ for $v_1 = 0.1$ and $w_1 = 0.1$, $2.7 \leq \mu \leq 3.2$ for $v_1 = 0.5$ and $w_1 = 0.5$, and $2.7 \leq \mu \leq 3.0$ for $v_1 = 1$ and $w_1 = 1$. These results clearly show that lattice solitons may be stabilized only in the low-power range, and that the stable soliton domain narrows with the growth of amplitudes v_1 and w_1 of the nonlinear lattice.

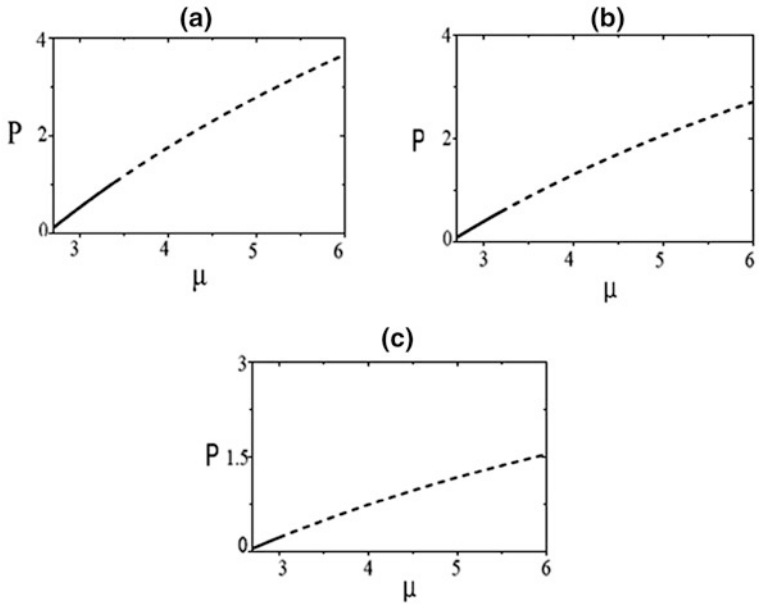

Fig. 6 Power P versus propagation constant μ for $v_0 = 4$ and $w_0 = 0.8$ and **a** $v_1 = 0.1$ and $w_1 = 0.1$, **b** $v_1 = 0.5$ and $w_1 = 0.5$, and **c** $v_1 = 1$ and $w_1 = 1$, in the 1D *PT*-symmetric model with the mixed linear-nonlinear model, defined according to Eqs. (7) and (19), as per Ref. [54]. Here and in similar figures below, the stable and unstable branches are plotted by *solid* and *dashed curves*, respectively

5.2 The PT-Symmetric Linear Lattice Potential Identical to the PT-Symmetric Nonlinear Lattice Potential

In what follows, the special case when identical *PT*-symmetric lattice potentials for both linear and nonlinear PLs is considered, as per Ref. [54], taking the linear modulation profiles as in Eq. (7), and the identical profiles for the nonlinear modulation, $v_1(x) = v(x)$ and $w_1(x) = w(x)$.

To illustrate effects of the amplitudes of the real and imaginary parts of the linear and nonlinear modulation profiles on the soliton propagation, three typical sets of parameters are displayed in Fig. 8: (i) $v_0 = 4$ and $w_0 = 0.8$; (ii) $v_0 = 3$ and $w_0 = 0.8$; (iii) $v_0 = 4$ and $w_0 = 0.6$. The corresponding dependences of total power P on propagation constant μ are shown. The stability domains are found to be $2.7 \leq \mu \leq 3.5$, $1.9 \leq \mu \leq 3.0$, and $2.7 \leq \mu \leq 4.5$, for the above sets of parameters (i), (ii), and (iii), respectively. These results clearly show that solitons may be stable, again, only in the low-power regime, and that the stability region increases with the decrease of amplitudes of the imaginary parts of the modulation profiles. Also, the stability region shifts towards lower values of μ with the decrease of the modulation amplitude of the real parts of the PL potentials.

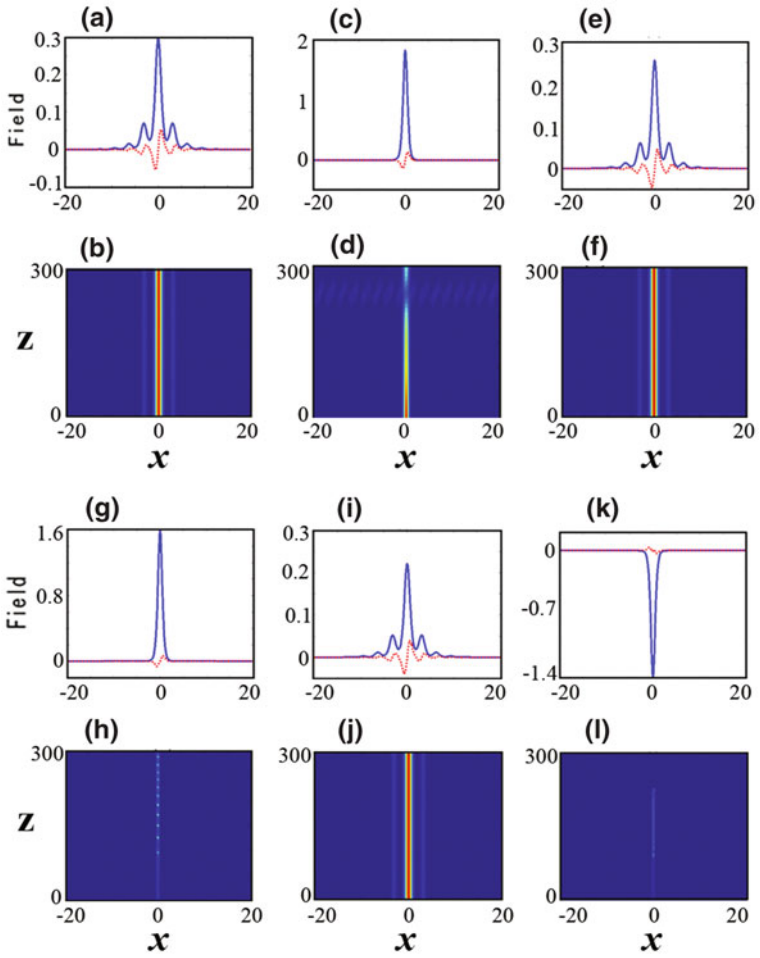

Fig. 7 Soliton profiles in the same model as represented in Fig. 6, for $v_0 = 4$, $w_0 = 0.8$, and $\mu = 2.7$, as per Ref. [54]. Stable evolution of the solitons is displayed for: **a**, **b** $v_1 = 0.1$ and $w_1 = 0.1$; **e**, **f** $v_1 = 0.5$ and $w_1 = 0.5$; **i**, **j** $v_1 = 1$ and $w_1 = 1$. Unstable evolution is displayed for $\mu = 5$: **c**, **d** $v_1 = 0.1$ and $w_1 = 0.1$; **g**, **h** $v_1 = 0.5$ and $w_1 = 0.5$; **k**, **l** $v_1 = 1$ and $w_1 = 1$

5.3 *Defect Gap Solitons in Real Linear Lattices Combined with the PT-Symmetric Nonlinear Potentials*

Here, the linear lattice in Eq. (18) is defined by its real part,

$$v = v_0 \cos^2(x)\left[1 + \varepsilon \exp\left(-x^8/128\right)\right] \tag{20}$$

in the absence of the imaginary part, $w = 0$. It represents the PL of depth v_0 (here, we fix $v_0 = 6$), which contains a single defect of depth ε. This real linear potential

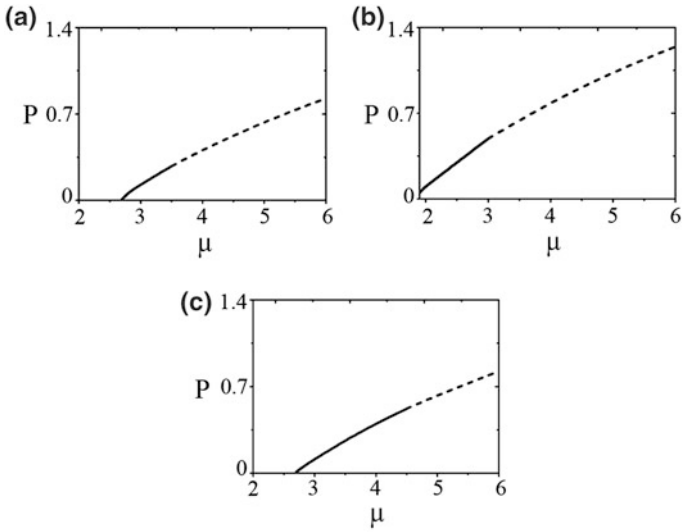

Fig. 8 Power P versus μ for **a** $v_0 = 4$ and $w_0 = 0.8$; **b** $v_0 = 3$ and $w_0 = 0.8$; **c** $v_0 = 4$ and $w_0 = 0.6$, in the model with the identical modulation profiles of the linear and nonlinear profiles, taken as in Eq. (7), as per Ref. [54]

is combined with the *PT*-symmetric nonlinear one, which is taken as per Eq. (19) with $v_1 = 1$ and w_1 replaced by $-w_0$. Profiles of the real linear lattice with the defect are shown in Fig. 9a, c and d, respectively. The respective band structure diagram is shown in Fig. 9b. In the present case, the semi-infinite gap is $\mu \geq 3.94$ and the first finite band gap is $0.84 \leq \mu \leq 3.73$.

For the positive defect with $\varepsilon = 0.5$ and $w_0 = 0.4$, solitons exist only in the semi-infinite gap, Fig. 10a showing the corresponding power diagram. Solitons are stable in a wide region. For $\mu = 9$ (point A in Fig. 10a), a stable soliton profile is shown in Fig. 10b, and Fig. 10d shows the corresponding propagation. Figure 10c shows the profile of another stable soliton for $\mu = 7.0$ (point B in Fig. 10a), whose propagation is displayed in Fig. 10e.

For the negative defect with $\varepsilon = -0.5$ and $w_0 = 0.4$, Fig. 11a shows the soliton's power versus propagation constant μ. In this case, the solitons exist in the semi-infinite gap and the first finite bandgap as well. In the semi-infinite gap, the solitons are stable in a wide region, but cannot be stable in the region $3.94 \leq \mu \leq 4.19$ near the Bloch band, as follows from the picture for $\mathrm{Re}(\delta)$ shown in Fig. 11b. Figure 11c, e show profiles and propagation of a stable soliton for $\mu = 6.0$. Figure 11d, f present the profile and propagation of an unstable soliton for $\mu = 4.15$.

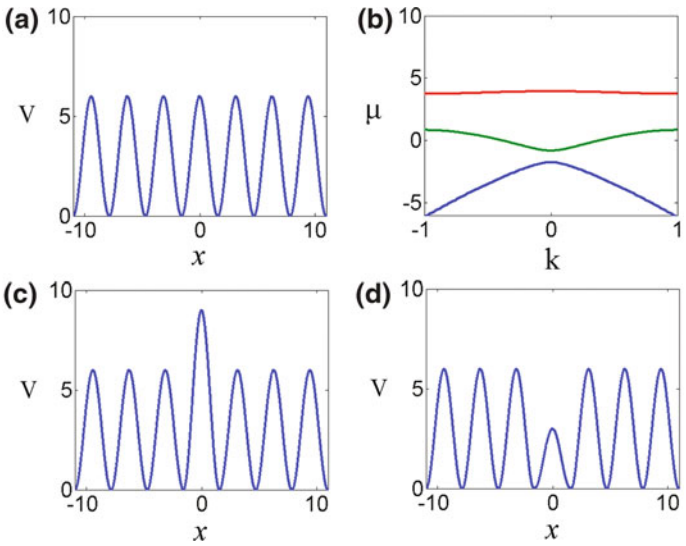

Fig. 9 **a** The uniform real linear PL. **b** The corresponding band structure. **c** The PL with a positive defect ($\varepsilon = 0.5$). **d** The PL with a negative defect ($\varepsilon = -0.5$). The results were reported in Ref. [56] for the linear potential (20) with $v_0 = 6$

6 Solitons in PT-Symmetric Periodic Linear Potentials with Spatially Modulated Nonlinearity

6.1 The Periodic Modulation of the Kerr Nonlinearity

The beam propagation in the *PT*-symmetric linear PLs, combined with a modulation of the nonlinearity (without nonlinear gain and loss, unlike the models based on Eq. (18) considered above) obeys the following normalized 1D nonlinear Schrödinger equation [51]:

$$i\frac{\partial q}{\partial z} + \frac{1}{2}\frac{\partial^2 q}{\partial x^2} + [v(x) + iw(x)]q + [1 - N(x)]|q|^2 q = 0, \tag{21}$$

where the *PT*-symmetric periodic linear potential us again taken in the form of Eq. (7), and the nonlinearity-modulation function is chosen as

$$N(x) = p\cos^2(x/T), \tag{22}$$

where p is the amplitude of the modulation of the nonlinear refractive index, and T is the corresponding period.

For $v_0 = 4$ and $w_0 = 0.8$, the *PT*-symmetric complex-valued PL (7) and the corresponding band structure are displayed in Fig. 12a, b, respectively. The results for power P versus μ, and for $\mathrm{Re}(\delta)$ versus μ, obtained by means of numerical

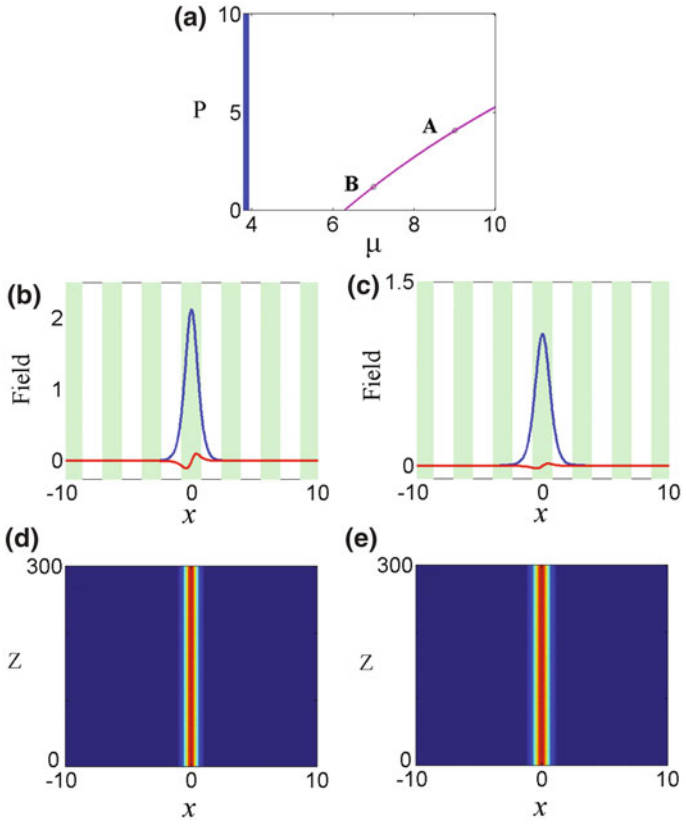

Fig. 10 Results obtained in Ref. [56] for the model combing the real linear potential (20) with $\varepsilon = 0.5$ (a positive defect), $v_0 = 6$, and the *PT*-symmetric nonlinearity modulation as in Eq. (19) with $v_1 = 1$ and $w_1 = -0.4$. **a** The power diagram. **b** The profile of a soliton and **d** its propagation for $\mu = 9$ (point A in panel (**a**)). **c** The profile of a soliton and **e** its propagation for $\mu = 7$ (point B in panel (**a**))

methods for the soliton family, are shown in Fig. 13 for different depths P of the nonlinearity-modulation function (22). Figure 13 shows that for, $v_0 = 4$ and $w_0 = 0.8$, the solitons exist in the semi-infinite gap and are stable in the low-power regime. Moreover, the picture of $\mathrm{Re}(\delta)$ shown in Fig. 13b, d, f demonstrate that the stable range of the soliton propagation $[\mathrm{Re}(\delta) = 0]$ expands with the decrease of depth P of the nonlinearity-modulation function $N(x)$.

Typical examples of stable and unstable solitons propagation for different depths P are presented in Fig. 14. This figure demonstrates that, in the low-power regime, the solitons exhibit have a multi-peak structure and stable propagation, while in the high-power regime, the solitons feature a single peak and unstable evolution.

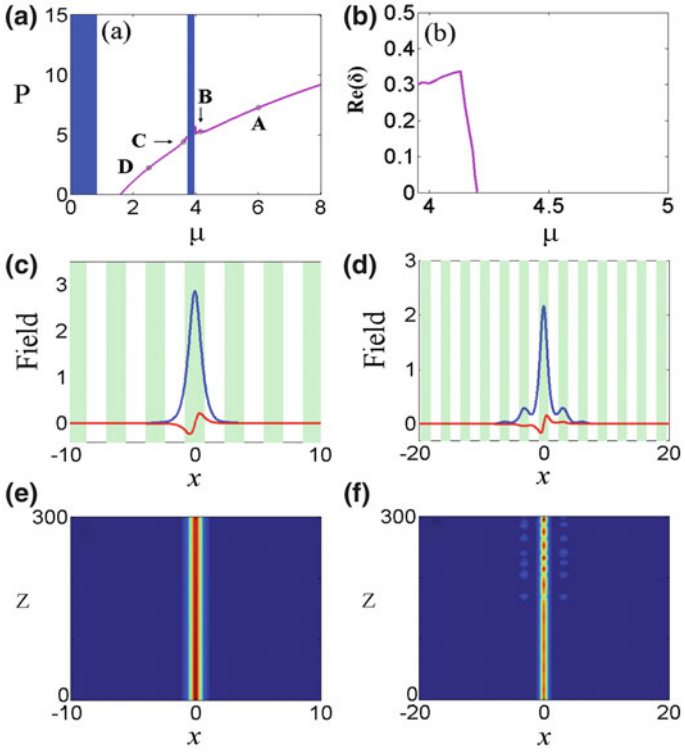

Fig. 11 The same as in Fig. 10, but for the linear lattice with a negative defect, $\varepsilon = -0.5$. **a** The power diagram for the solitons. **b** The instability growth rates of the soliton solutions, $\mathrm{Re}(\delta)$, versus propagation constant μ. **c** The profile of a soliton and **e** its propagation for $\mu = 6.0$ (point A in panel (**a**)). **d** The profile of a soliton and **f** the corresponding propagation for $\mu = 4.15$ (point B in panel (**a**)). The results were reported in Ref. [56]

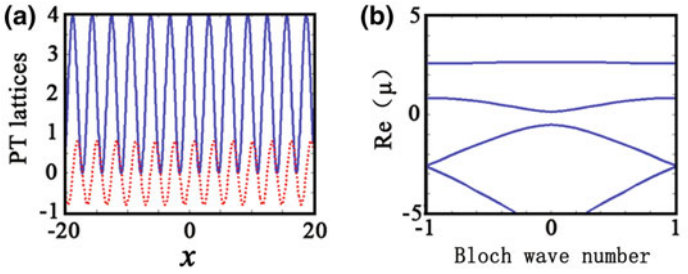

Fig. 12 **a** The *PT*-symmetric complex-valued periodic lattice potential (7) (real part: the *solid curve*, imaginary part: the *dashed curve*) with $v_0 = 4$ and $w_0 = 0.8$. **b** The corresponding bandgap structure of (**a**), as per Ref. [51]

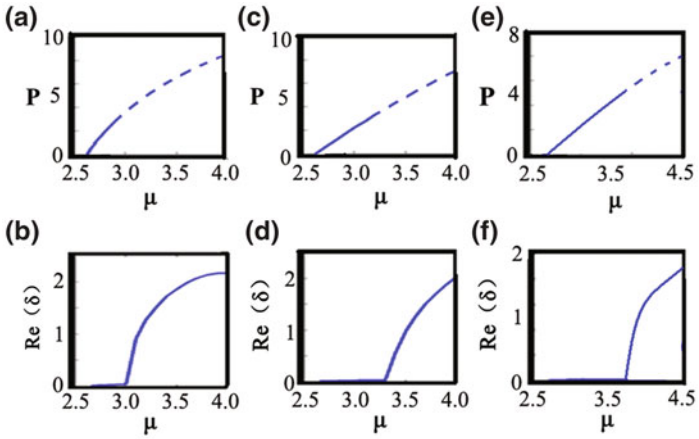

Fig. 13 The total power and Re(δ) (the instability growth rate) versus μ, for the soliton family in the model based on Eqs. (21) and (22), with the *PT*-symmetric potential taken as in Eq. (7) with $v_0 = 4$ and $w_0 = 8$. The corresponding parameters of the nonlinearity modulation in Eq. (22) are $p = 1.2$ in (**a**, **b**), $p = 1$ in (**c**, **d**), and $p = 0.8$ in (**e**, **f**). The results were reported in Ref. [51]

6.2 Spatially Modulated Nonlocal Nonlinearity

A 1D model including the *PT*-symmetric linear PL and spatial modulation of nonlocal nonlinearity was put forward in Ref. [37], in the form of the following equation:

$$i\frac{\partial q}{\partial z} + \frac{1}{2}\frac{\partial^2 q}{\partial x^2} + (V + iW)q + [1 + f(x)]q \int_{-\infty}^{+\infty} g(x-\lambda)|q(\lambda)|^2 d\lambda = 0, \tag{23}$$

with

$$g(x) = 1\Big/\left(2d^{\frac{1}{2}}\right)\exp\left(-|x|\Big/d^{\frac{1}{2}}\right). \tag{24}$$

where d is the range of the uniform nonlocality. When $d \to 0$, the nonlinearity in Eq. (23) becomes linear. Here, the *PT*-symmetric periodic potential and the function accounting for the periodic modulation of the nonlocal nonlinearity are taken as

$$V(x) = 4\cos(2x),\ W(x) = w_0 \sin(2x),\ \text{and}\, f(x) = k\cos^2(2x), \tag{25}$$

cf. Eq. (7).

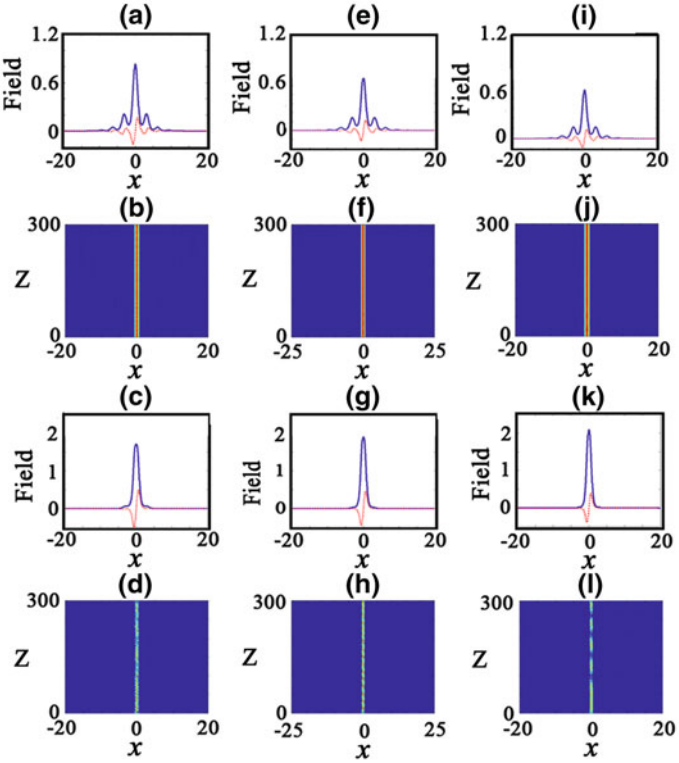

Fig. 14 Soliton profiles in the same model which is represented by Figs. 12 and 13 (real part: the *solid curves*, imaginary part: the *dashed curves*), and the corresponding soliton-propagation pictures. With $p = 1.2$ in Eq. (22), a stable case is shown in (**a**, **b**) for $\mu = 2.7$, and unstable one is shown in (**c**, **d**) for $\mu = 3.1$. With $p = 1$, stable and unstable cases are shown, respectively, in (**e**, **f**) for $\mu = 2.7$, and in (**g**, **h**) for $\mu = 3.5$. With for $p = 0.8$, stable and unstable examples are presented in (**i**, **j**) for $\mu = 2.7$, and in (**k**, **l**) for $\mu = 4.0$, respectively. Other parameters and the nonlinear modulation function are the same as in Fig. 13. The results were reported in Ref. [51]

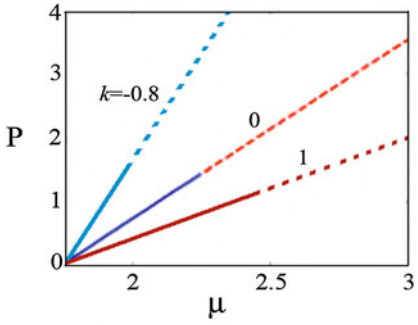

Fig. 15 Power P versus propagation constant μ at different values of k for the soliton family, found in Ref. [37] in the model based on Eqs. (23), (24), and (25), with $d = 1$ and $w_0 = 2$

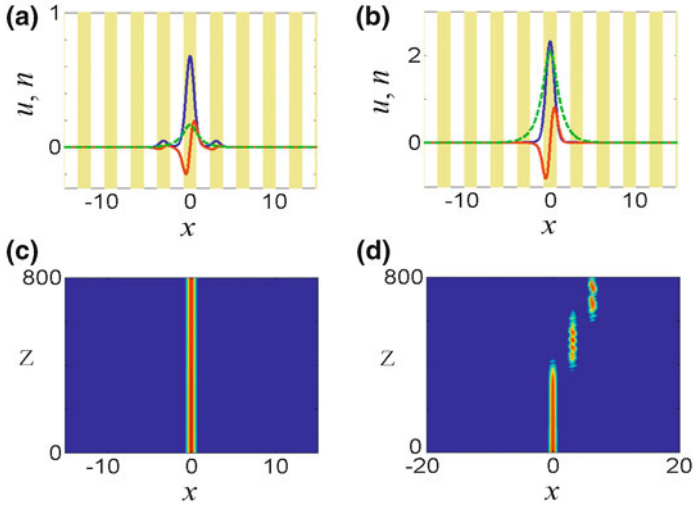

Fig. 16 Soliton profiles (the *blue* and *red lines* stand for the real and imaginary parts, respectively, and the *green dashed line* is the refractive index profile), and the simulated evolution of the soliton, in the same model as presented in Fig. 15, for $\mu = 1.8$ (**a**, **c**), and $\mu = 2.5$ (**b**, **d**). The other parameters are $d = 1$, $w_0 = 2$, and $k = -0.8$. The results were reported in Ref. [37]

Soliton solutions of Eq. (23) are looked for in the usual form, $q = u(x)\exp(i\mu z)$, here μ is a real propagation constant and $u(x)$ is a complex function. The refractive index distribution induced by the nonlocality in this model can be written as $n = \int_{-\infty}^{+\infty} g(x-\lambda)|q(\lambda)|^2 d\lambda$.

First, by setting d = 1 and $w_0 = 2$ and varying the strength of the modulated nonlocality, k, solitons can be found in the semi-infinite gap. They are stable in the low-power region but unstable at higher powers. Figure 15 shows the power diagram for $k = -0.8$, $k = 0$ (which corresponds to the unmodulated nonlinearity in Eq. (23)), and $k = 1$. These results indicate that the stability region for the solitons expands with the growth of k. Further, typical examples of stable and unstable solitons are presented in Fig. 16. Stable and unstable examples for $k = -0.8$ are shown in Fig. 16a, c and b, d, respectively.

Figure 16d shows that unstable solitons may jump into adjacent channels in the course of the propagation. This effect of the transverse motion is more pronounced for smaller k. The effects arise from the interplay of the modulation of the nonlocal nonlinearity and the *PT*-symmetric potentials. Moreover, it is seen in Fig. 17 that the stability domain becomes narrower with the increase of the w_0 and d.

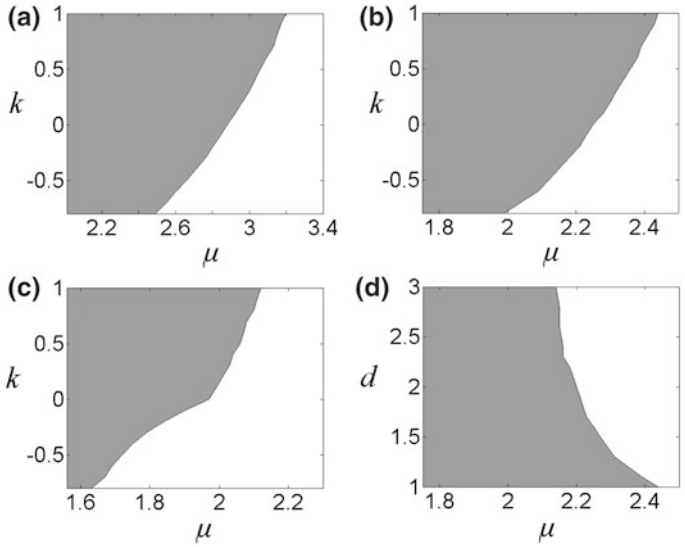

Fig. 17 Stability domains (*gray*) in the plane of (μ, k), produced in Ref. [37] in the same model which is presented in Figs. 15 and 16, for: **a** $w_0 = 1.2$, **b** $w_0 = 2$, and **c** $w_0 = 2.4$, while $d = 1$. **d** The stability domain in the plane of (μ, d) for $w_0 = 2$ and $k = 1$

7 Conclusions

In this chapter, we have presented a review of recent results concerning the spatial solitons dynamics in parity-time- (*PT*-) symmetric potentials in optical media with one- and two-dimensional photonic lattices (PLs). The following basic findings were included.

(1) Firstly, the landmark result that stable propagation of 1D and 2D solitons is possible in such *PT*-symmetric synthetic periodic potentials.
(2) Dark solitons and vortices, supported by the defocusing nonlinearity combined with the *PT*-symmetric potential, were described concisely. Spontaneous generation of complex multi-soliton and multi-vortex patterns can be controlled by varying the strength of the *PT*-symmetric potential.
(3) The existence and stability of lattice solitons in *PT*-symmetric mixed linear-nonlinear PLs in Kerr-linear media were overviewed. It is concluded that the parameters of the linear lattice potential play a significant role in controlling the size of stability domains for the solitons. In addition, effect of defects in such potentials on the soliton propagation was considered. It was found that positive defects can expand the existence domain of the stable modes, while the negative defects reduce it.
(4) Finally, we have briefly summarized the soliton dynamics in the *PT*-symmetric potential in the medium with the spatially modulated local or nonlocal cubic

nonlinearity. The depth of the spatial modulation of the nonlinearity and the range of the nonlocality can profoundly affect the stability of solitons.

These results suggest new possibilities for experimental and theoretical studies of the dynamics in more complex *PT*-symmetric potentials and in higher-dimensional settings. A challenging direction for further studies is to consider similar possibilities in 3D models. On the other hand, it may also be interesting to study solitons in *PT*-symmetric potentials combined with the quadratic (rather than cubic) nonlinearity.

Acknowledgments This work was supported by the National Natural Science Foundation of China (Grant No. 11174061) and the Guangdong Province Natural Science Foundation of China (Grant No. S2011010005471).

References

1. C.M. Bender, S. Boettcher, Phys. Rev. Lett. **80**, 5243 (1998)
2. Z. Ahmed, Phys. Lett. A **282**, 343 (2001)
3. C.M. Bender, D.C. Brody, H. Jones, Phys. Rev. Lett. **89**, 270401 (2002)
4. C.M. Bender, D.C. Brody, H. Jones, Am. J. Phys. **71**, 1095 (2003)
5. C.M. Bender, D.C. Brody, H.F. Jones, B.K. Meister, Phys. Rev. Lett. **98**, 040403 (2007)
6. A. Ruschhaupt, F. Delgado, J.G. Muga, Phys. A **38**, L171 (2005)
7. R. El-Ganainy, K.G. Makris, D.N. Christodoulides, Z.H. Musslimani, Opt. Lett. **32**, 2632 (2007)
8. Z.H. Musslimani, K.G. Makris, R. El-Ganainy, D.N. Christodoulides, Phys. Rev. Lett. **100**, 030402 (2008)
9. K.G. Makris, R.D. El-Ganainy, N. Christodoulides, Z.H. Musslimani, Phys. Rev. Lett. **100**, 103904 (2008)
10. S. Klaiman, U. Günther, N. Moiseyev, Phys. Rev. Lett. **101**, 080402 (2008)
11. S. Longhi, Phys. Rev. Lett. **103**, 123601 (2009)
12. K.G. Makris, R. El-Ganainy, D.N. Christodoulides, Z.H. Musslimani, Phys. Rev. A **81**, 063807 (2010)
13. O. Bendix, R. Fleischmann, T. Kottos, B. Shapiro, Phys. Rev. Lett. **103**, 030402 (2009)
14. A. Guo, G.J. Salamo, D. Duchesne, R. Morandotti, M. Volatier-Ravat, V. Aimez, G.A. Siviloglou, D.N. Christodoulides, Phys. Rev. Lett. **103**, 093902 (2009)
15. C.E. Rüter, K.G. Makris, R. El-Ganainy, D.N. Christodoulides, M. Segev, D. Kip, Nat. Phys. **6**, 192 (2010)
16. K.G. Makris, R. El-Ganainy, D.N. Christodoulides, Z.H. Musslimani, Int. J. Theor. Phys. **50**, 1019 (2011)
17. H. Wang, J. Wang, Opt. Express **19**, 4030 (2011)
18. K. Zhou, Z. Guo, J. Wang, S. Liu, Opt. Lett. **35**, 2928 (2010)
19. S.V. Suchkov, S.V. Dmitriev, B.A. Malomed, Y.S. Kivshar, Phys. Rev. A **85**, 033835 (2012)
20. X. Zhu, H. Wang, L.-X. Zheng, H. Li, Y.-J. He, Opt. Lett. **36**, 2680 (2011)
21. Z. Shi, X. Jiang, X. Zhu, H. Li, Phys. Rev. A **84**, 053855 (2011)
22. H. Li, Z. Shi, X. Jiang, X. Zhu, Opt. Lett. **36**, 3290 (2011)
23. S. Nixon, L. Ge, J. Yang, Phys. Rev. A **85**, 023822 (2012)
24. V. Achilleos, P.G. Kevrekidis, D.J. Frantzeskakis, R. Carretero-González, Phys. Rev. A **86**, 013808 (2012)
25. R. Driben, B.A. Malomed, Opt. Lett. **36**, 4323 (2011)

26. N.V. Alexeeva, I.V. Barashenkov, A.A. Sukhorukov, Y.S. Kivshar, Phys. Rev. **85**, 063837 (2012)
27. L. Chen, R. Li, N. Yang, D. Chen, L. Li, Proc. Romanian Acad. A **13**, 46 (2012)
28. R. Driben, B.A. Malomed, Europhys. Lett. **99**, 54001 (2012)
29. I.V. Barashenkov, S.V. Suchkov, A.A. Sukhorukov, S.V. Dmitriev, Y.S. Kivshar, Phys. Rev. A **86**, 053809 (2012)
30. R. Driben, B.A. Malomed, Europhys. Lett. **96**, 51001 (2011)
31. D.A. Zezyulin, V.V. Konotop, Phys. Rev. Lett. **108**, 213906 (2012)
32. F.C. Moreira, F. K. Abdullaev, V.V. Konotop, A.V. Yulin, Phys. Rev. A **86**, 053815 (2012)
33. S. Liu, C. Ma, Y. Zhang, K. Lu, Opt. Commun. **285**, 1934 (2012)
34. C. Li, H. Liu, L. Dong, Opt. Express **20**, 16823 (2012)
35. H. Li, X. Jiang, X. Zhu, Z. Shi, Phys. Rev. A **86**, 023840 (2012)
36. S. Hu, X. Ma, D. Lu, Y. Zheng, W. Hu, Phys. Rev. A **85**, 043826 (2012)
37. C. Yin, Y. He, H. Li, J. Xie, Opt. Express **20**, 19355 (2012)
38. D. Mihalache et al., Phys. Scr. **29**, 269 (1984)
39. V.K. Fedyanin, D. Mihalache, Z. Phys. B **47**, 167 (1982)
40. D. Mihalache, M. Bertolotti, C. Sibilia, Prog. Opt. **27**, 229 (1989)
41. Y.V. Kartashov, V.A. Vysloukh, D. Mihalache, L. Torner, Opt. Lett. **31**, 2329 (2006)
42. D. Mihalache, D. Mazilu, F. Lederer, Y.S. Kivshar, Opt. Lett. **32**, 3173 (2007)
43. F. Lederer, G.I. Stegeman, D.N. Christodoulides, G. Assanto, M. Segev, Y. Silberberg, Phys. Rep. **463**, 1 (2008)
44. Y.V. Kartashov, V.V. Konotop, V.A. Vysloukh, Europhys. Lett. **91**, 34003 (2010)
45. Y. He, D. Mihalache, X. Zhu, L. Guo, Y.V. Kartashov, Opt. Lett. **37**, 2526 (2012)
46. Y.V. Kartashov, B.A. Malomed, L. Torner, Rev. Mod. Phys. **83**, 247 (2011)
47. F.K. Abdullaev, Y.V. Kartashov, V.V. Konotop, D.A. Zezyulin, Phys. Rev. A **83**, 041805 (2011)
48. A.E. Miroshnichenko, B.A. Malomed, Y.S. Kivshar, Phys. Rev. A **84**, 012123 (2011)
49. S.V. Suchkov, B.A. Malomed, S.V. Dmitriev, Y.S. Kivshar, Phys. Rev. E **84**, 046609 (2011)
50. D.A. Zezyulin, Y.V. Kartashov, V.V. Konotop, Europhys. Lett. **96**, 64003 (2011)
51. Y. He, X. Zhu, D. Mihalache, J. Liu, Z. Chen, Opt. Commun. **285**, 3320 (2012)
52. H. Sakaguchi, B.A. Malomed, Phys. Rev. A **81**, 013624 (2010)
53. Y.V. Bludov, V.V. Konotop, Phys. Rev. A **74**, 043616 (2006)
54. Y. He, X. Zhu, D. Mihalache, J. Liu, Z. Chen, Phys. Rev. A **85**, 013831 (2012)
55. Y. He, D. Mihalache, Rom. Rep. Phys. **64**, 1243 (2012)
56. H. Wang, W. He, L. Zheng, X. Zhu, H. Li, Y. He, J. Phys. B At. Mol. Opt. Phys. **45**, 245501 (2012)

Spontaneous Symmetry Breaking of Pinned Modes in Nonlinear Gratings with an Embedded Pair of Defects

I. V. Kabakova, I. Uddin, J. Jeyaratnam, C. M. de Sterke and B. A. Malomed

Abstract We consider spontaneous symmetry breaking (SSB) in nonlinear periodic structures with two embedded identical defects. We focus on Bragg grating (BGs) in which the defects are formed by local phase shifts. The defects are positioned relatively close to each other, so as to allow the light to couple between them. At low optical energies, i.e., in the linear regime, this system supports two symmetric eigenstates, which have identical intensity distributions but different frequencies. At higher energies, the lower-frequency state becomes unstable against symmetry-breaking perturbations, and the light gets predominantly trapped by one of the defects, leading to an asymmetric field distribution. We analyze the SSB effect for different coupling strengths and conclude that, quite naturally, the symmetry-breaking energy threshold increases with the strength. The symmetric state is stable below the SSB threshold, while the emerging asymmetric mode is stable above the threshold.

1 Introduction

Spontaneous symmetry breaking (SSB) is a general phenomenon in modern nonlinear physics. Its manifestations can be found in a variety of settings, including classical and quantum mechanics [1, 2], dual-core optical waveguides with the intrinsic Kerr [3–9] and quadratic [10] nonlinearities, dual-core Bragg gratings

I. V. Kabakova (✉) · I. Uddin · J. Jeyaratnam · C. M. d. Sterke
Center for Ultrahigh-bandwidth Devices for Optical Systems (CUDOS) and Institute of Photonics and Optical Sciences (IPOS), School of Physics, University of Sydney, Sydney, NSW 2006, Australia
e-mail: kabakova@physics.usyd.edu.au

B. A. Malomed
Department of Physical Electronics, School of Electrical Engineering, Tel Aviv University, 69978 Tel Aviv, Israel

Progress Optical Sci., Photonics (2013): 149–165
DOI: 10.1007/10091_2012_22

Published Online: 14 December 2012

(BGs) [11], various nonlinear discrete systems [12–16], and other settings in nonlinear optics [17–26] and plasmonics [27–31]. Further, SSB effects were studied in detail in quantum field theory [32–35], Bose–Einstein condensates (BECs) [22, 36–40] (specifically, in BEC [41–53] and degenerate Bose–Fermi mixtures [54, 55] trapped in double-well potentials), spin waves in ferromagnets [56], and in other physical systems. The symmetry-breaking phenomena occur in situations described by symmetric Hamiltonians, which are expected to support symmetric and anti-symmetric eigenstates. However, in the presence of nonlinearity the (anti)symmetry can be broken and asymmetric states become favorable, realizing an energy minimum (the ground state of the system). In addition to SSB in ordinary Hamiltonian systems, the spontaneous breaking of parity-time ($\mathcal{PT}$) symmetry was predicted in models described by $\mathcal{PT}$-symmetric models, with spatially separated mutually balanced gain and loss [57–59] added to the conservative part.

The propagation of optical [60–67] and plasmon [68, 69] waves in nonlinear media is a tremendous area of research, which gives rise to a great variety of fundamental effects and offers a myriad of potential applications to classical and quantum telecommunications, lasers, all-optical data processing, etc. Recently, there have been several experimental demonstrations of SSB in Kerr-nonlinear media using two-component optical solitons [17] and optically induced photonic latices [18]. A major application envisioned in these studies is the all-optical steering and switching of laser beams. In particular, a nonlinear device which would implement switching and flip-flop operations was proposed by a number of authors [19–21]. It is built of two coupled micro-cavities embedded into a two-dimensional (2D) photonic crystal (as similar 2D configuration for the trapped BEC was introduced in [53]). Similar effects of the SSB between two mutually symmetric trapping elements inserted into a uniform matrix can be achieved in 1D periodic structures, which are much easier to fabricate and straightforward to model, using coupled-mode theory [15, 16, 22, 51, 52]. In particular, a pair of repulsive local defects embedded into a nonlinear fiber BG may form an effective *cavity* trapping gap solitons [70]. A generalization in the form of a *triplet* of local defects embedded into the nonlinear BG was considered too [71].

In this chapter we discuss SSB in a 1D model of light propagation in a dielectric medium combining the Kerr nonlinearity and a simple periodic structure in the form of a BG. To be definite, we consider a *shallow* grating, which means that the local variations of the refractive index are much smaller than the average value of the index, $\Delta n \ll \bar{n}$. Such gratings can be written in optical fibers or waveguides by exploiting the photosensitivity of germanosilicate glasses in the ultraviolet range [72–74], or by other processes [75]. In this way, long gratings, which can be several centimeters long, carrying as many as $\sim 100{,}000$ periods, can be written.

Solitons in the Kerr-nonlinear fiber BG were predicted as exact analytical solutions [76, 77], and further analysis has demonstrated that, roughly speaking, half of this soliton family is stable [78–80]. While the theoretical analysis predicts that the BG solitons (also frequently called gap solitons) may exist as quiescent pulses trapped in the grating, in the experiment such solitons were created as moving ones [81, 82].

To implement a symmetric two-component system based on the 1D grating, we here introduce a model with two identical embedded defects, in the form of local phase shifts of the grating. Each defect creates a trapped state with an exponentially decaying field distribution around it (the localized mode attached to the single defect may be realized as a pinned soliton [83]). If the two defects are located close to each other, the light can leak from one defect to another, resulting in their coupling.

To analyze the possibility of SSB in this system, we first consider its linear version, which is valid for low intensity of light. In this case, there are two eigenmodes with different frequencies, which can be found in an analytical form. The two modes feature field distributions in which the energy is split evenly between the two defects, but which differ in their phases. When the intensity increases, the frequencies of the modes shift at the same rate, due to the action of the Kerr nonlinearity, and the intensity distributions remain largely unchanged, until the intensity attains a threshold at which the SSB bifurcation occurs and one of the symmetric mode becomes unstable, similar to the situation considered in Refs. [51, 52] and [22]. Above the threshold, the stable solution demonstrates an asymmetric field distribution, with most of the energy captured by one of the defects. We show that the strength of the coupling between the defects determines the energy threshold for the SSB: the stronger the coupling (i.e., the closer the defects to each other), the larger the energy required for the bifurcation to occur.

This chapter is structured as follows: in Sect. 2 we briefly revisit coupled-mode theory of BGs and discuss steady-state linear solutions for the BG with one and two local defects. Section 3 provides a short description of numerical methods used for solving nonlinear coupled mode equations in steady-state and dynamic regimes. In Sect. 4 we present results of our analysis, including the stability of the trapped states. A short discussion about implication of the results for all-optical switching completes the chapter.

2 The Model

2.1 The Coupled-Mode Theory

The propagation of light in a shallow 1D periodic medium is conventionally described using coupled mode theory [84], which represents the total optical field as a superposition of two modes, which are linearly coupled through Bragg scattering in the periodic medium. In the usual BG, these are forward- and backward-traveling modes.

Thus, we assume that the refractive index of the waveguide can be written as

$$n(z) = \bar{n} + \Delta n \cos\left(\frac{2\pi z}{\Lambda} - \varphi\right). \tag{1}$$

where $\bar{n}$ is the average refractive index, Δn the modulation amplitude, Λ the period and φ the phase of the grating. The coupling between the forward and backward propagating modes arises from the partial reflections from the grating induced by the periodic modulation of the refractive index. At the Bragg wavelength, $\lambda_B = 2\bar{n}\Lambda$, all partial reflections occur in-phase, resulting in constructive interference. For a narrow interval of incident wavelengths $\Delta\lambda$ around λ_B, the grating acts as a reflector, providing for the strongest linear coupling between the forward- and backward-traveling modes.

The coupled-mode equations (CMEs) can be derived as described by Marcuse [84]. These equations link the complex amplitudes of the forward, $E_+(z,t)$, and the backward, $E_-(z,t)$, traveling components of the total electric field at frequency ω, so that

$$\mathrm{E}(z,t) = \left[E_+(z,t)\mathrm{e}^{+i\beta z} + E_-(z,t)\mathrm{e}^{-i\beta z}\right]e^{-i\omega t} + \text{c.c.}, \tag{2}$$

where c.c. stands for the complex conjugate. We now take the propagation constant $\beta = \pi/\Lambda$ corresponding to the Bragg resonance, and ω to be the associated frequency. In the Kerr medium, described by the effective refractive index, $n(z,I) = n(z) + n_2 I(z)$ where n_2 is the Kerr coefficient and I intensity of the electromagnetic waves, the nonlinear CMEs [85] are

$$\begin{aligned} i\frac{\partial E_+}{\partial z} + \frac{i}{v}\frac{\partial E_+}{\partial t} + \kappa E_- e^{-i\varphi} + \Gamma|E_+|^2 E_+ + 2\Gamma|E_-|^2 E_+ = 0, \\ -i\frac{\partial E_-}{\partial z} + \frac{i}{v}\frac{\partial E_-}{\partial t} + \kappa E_+ e^{+i\varphi} + \Gamma|E_-|^2 E_- + 2\Gamma|E_+|^2 E_- = 0. \end{aligned} \tag{3}$$

where v is the group velocity at the Bragg frequency in the waveguide in the absence of the grating. The terms involving the coupling coefficient,

$$\kappa = \frac{\pi}{\lambda_B}\Delta n,$$

represent the grating. Further, $\Gamma = 4\pi n_2/\lambda Z_0$ is the nonlinearity coefficient, $Z_0 = 377\ \Omega$ is the characteristic free-space impedance, and the total electric field is related to the field intensity by $I = 2\bar{n}|\mathrm{E}|^2/Z_0$, assuming the field is in the form of Eq. (2).

At low intensities, where the nonlinear effects are negligible, the uniform BG, with constant κ, gives rise to the photonic bandgap at [85]

$$-\kappa \le \delta \le +\kappa, \tag{4}$$

in terms of the detuning from the Bragg frequency,

$$\delta = (\bar{n}/c)(\omega - \omega_B). \tag{5}$$

Equations (3) are the CME system, which forms a basis for the analysis reported in this chapter below. We will now discuss stationary solutions of these equations.

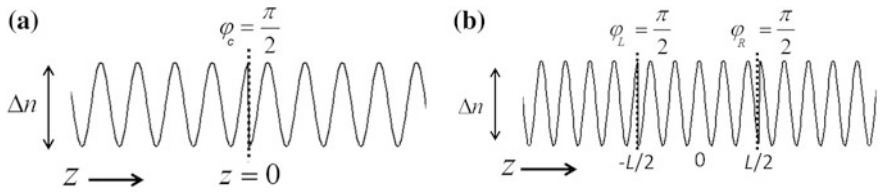

Fig. 1 Schematic of the refractive-index grating with **a** one $\pi/2$ defect placed at $z = 0$, and **b** two $\pi/2$ defects at $z = \pm L/2$

2.2 Linear Solutions for the Single Defect

We first consider gratings with a single defect placed at $z = 0$, as shown in Fig. 1a. It is modeled by a jump of the phase in Eq. (1) between values $\varphi_I \neq \varphi_{II}$ at $z<0$ and $z > 0$:

$$\varphi_c = \frac{1}{2}(\varphi_{II} - \varphi_I) \tag{6}$$

We here address solutions for the linear BG ($\Gamma = 0$), with the $e^{-iv\delta t}$ time dependence, where detuning δ is defined as per Eq. (5). By demanding the field of the trapped mode to decay as $|z| \to \infty$, which can only occur for frequencies in the photonic bandgap (4), and by requiring $E_\pm$ to be continuous, we construct the solution for the localized mode pinned to the defect which consists of an resonant frequency and an associated electric field. The resonant frequency is expressed in the angle ψ where

$$e^{i\psi} = \frac{\delta + i\alpha}{\kappa}, \tag{7}$$

where $\alpha = \sqrt{\kappa^2 - \delta^2}$. The implication of Eq. (7) is that the solution exists at the single value of the detuning,

$$\delta = \kappa \cos \varphi_c \tag{8}$$

Note that Eq. (7) automatically satisfies the consistency condition, $\left|e^{i\psi}\right| \equiv 1$, inside of the photonic bandgap (4). The associated state can be written as

$$\begin{aligned} \begin{pmatrix} E_+(z) \\ E_-(z) \end{pmatrix} &= \begin{pmatrix} 1 \\ -e^{i\psi} e^{i\varphi_I} \end{pmatrix} e^{\alpha z}, \text{ for } z<0 \\ \begin{pmatrix} E_+(z) \\ E_-(z) \end{pmatrix} &= \begin{pmatrix} 1 \\ -e^{-i\psi} e^{i\varphi_{II}} \end{pmatrix} e^{-\alpha z}, \text{ for } z > 0. \end{aligned} \tag{9}$$

Here we are particularly interested in the case of $\varphi_c = \pi/2$, for which Eq. (8) yields $\delta = 0$, i.e., the defect state is placed at the center of the bandgap.

2.3 Linear Solutions for the Double Defect

We now consider gratings with two identical defects placed at $z = \pm L/2$, as shown in Fig. 1b, which corresponds to the following phase distribution in Eq. (1):

$$\varphi = \begin{cases} \varphi_I, & z < -L/2, \\ \varphi_{II}, & -L/2 < z < L/2, \\ \varphi_{III}, & z > L/2. \end{cases}$$

As in Sect. 2.2, we aim to find solutions which are continuous at $z = \pm L/2$ and exponentially decay as $|z| \to \infty$. After a simple analysis, this results in the condition

$$\frac{\sin(\psi - \varphi_L)\sin(\psi - \varphi_R)}{\sin\varphi_L \qquad \sin\varphi_R} = \exp\left(-2\kappa L \sin\psi\right), \tag{10}$$

where ψ is the phase defined by Eq. (7), and

$$\varphi_L \equiv \frac{1}{2}(\varphi_{II} - \varphi_I), \ \varphi_R \equiv \frac{1}{2}(\varphi_{III} - \varphi_{II}). \tag{11}$$

The associated state can be written as

$$\begin{aligned} &z < -L/2: \\ &\begin{pmatrix} E_+(z) \\ E_-(z) \end{pmatrix} = \left(1 + e^{-i\psi}\frac{\sin(\psi - \varphi_L)}{\sin\varphi_L}\right)\begin{pmatrix} 1 \\ -e^{i\psi}e^{i\varphi_I} \end{pmatrix} e^{\alpha(z+L)}, \\ &-L/2 < z < +L/2: \\ &\begin{pmatrix} E_+(z) \\ E_-(z) \end{pmatrix} = \frac{\sin(\psi - \varphi_L)}{\sin\varphi_L}\begin{pmatrix} 1 \\ -e^{i\psi}e^{i\varphi_{II}} \end{pmatrix} e^{\alpha(z+L)-i\psi} + \\ &\begin{pmatrix} 1 \\ -e^{-i\psi}e^{i\varphi_{II}} \end{pmatrix} e^{-\alpha z} \\ &z > L/2: \\ &\begin{pmatrix} E_+(z) \\ E_-(z) \end{pmatrix} = \left(1 + e^{-i\psi}e^{2\alpha L}\frac{\sin(\psi - \varphi_L)}{\sin\varphi_L}\right)\begin{pmatrix} 1 \\ -e^{-i\psi}e^{i\varphi_{III}} \end{pmatrix} e^{-\alpha z}. \end{aligned} \tag{12}$$

In the limit of a very large spacing between the defects, i.e., $\kappa L \gg 1$, the exponential factor in Eq. (10) vanishes, and this condition amount to its counterpart (7) for the isolated defects. In the general case, Eq. (10) is a transcendental equation which should be solved numerically.

Here we only consider the case of $\varphi_L = \varphi_R = \pi/2$, reducing Eq. (10) to

$$\delta = \pm\kappa \exp\left(-2\kappa L \sin\psi\right), \tag{13}$$

leading to the two solutions with detunings $(\pm|\delta|)$ which are located symmetrically around the center of the bandgap ($\delta = 0$). Equation (13) is still transcendental, as the

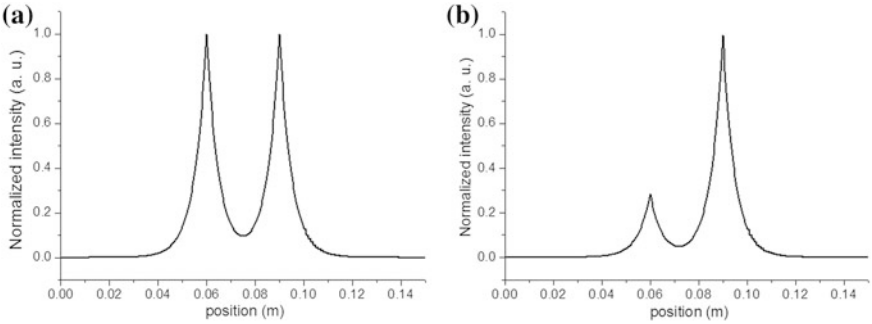

Fig. 2 **a** Symmetric and **b** asymmetric eigenstates of the nonlinear stationary problem. The total length of the grating is $l = 15$ cm, the coupling coefficient $\kappa = 100\ \mathrm{m}^{-1}$ and the separation between two $\pi/2$ defects is $L = 3$ cm. The intensity for each distribution is normalized to its maximum

parameter ψ depends on δ via Eq. (7). When the spacing between the defects increases, the splitting between the eigenvalues of δ in Eq. (13) decreases, as expected in analogy with the properties of double-well potentials in quantum mechanics. Note that κL is the single parameter which determines the strength of the coupling between the defects. It can be shown, though we do not do it here, that the intensity distributions of the two solutions, corresponding to the upper and lowers signs in Eq. (13), are identical, while their phases differ. An example of the intensity distribution is displayed in Fig. 2a.

3 Methods for Solving the Nonlinear Problem

In the previous section we found solutions for the linear BG with a single defect or a symmetric pair of coupled defects. These solutions are valid in most situations that involve low to moderate optical powers. For gratings written in silica fibers, which has a positive Kerr coefficient ($n_2 = 2.7 \times 10^{-20}\ \mathrm{m}^2/\mathrm{W}$), the nonlinearity starts to play a significant role at kilowatt power levels [82]. The increase of the effective refractive index due to the nonlinear correction is equivalent to a longer optical path in the medium for a high-intensity pulse, compared to its low-intensity counterpart at the same wavelength. Briefly speaking, an approximate relationship $\Delta\lambda/\lambda \approx \Delta n/n$ holds, hence the nonlinearity manifests itself by a shift of the Bragg resonances towards longer wavelengths, i.e., lower frequencies. To find the exact shift of the resonance for a given optical energy, nonlinear CMEs (3) need to be solved. These equations are difficult to solve analytically, especially for gratings with multiple phase-shift defects (an analytical solution for a trapped gap soliton is available in the framework of the nonlinear CME system with a single attractive defect [83]). Therefore, solutions should be obtained in a numerical form, as discussed below.

3.1 Solving the Steady-State Nonlinear Problem

We are looking for the stationary solutions of the time-independent nonlinear CMEs for the grating with a pair of defects. This can be done by solving the stationary version of Eq. (3), produced by the substitution of the $e^{-iv\delta t}$ time dependence. For the numerical solution we chose the 4th-order Runge–Kutta algorithm, due to its accuracy.

In the stationary regime without a driving source, no energy flow must exist inside the grating. Therefore, far from the defects the total electric field should approach zero. However, to start the integration we need to introduce some non-zero value to at least one of the field amplitudes at the grating's boundary. To this end, we apply the boundary conditions at the end of the grating, $z = l$:

$$\begin{aligned} E_+(l,\delta) &= A_0, \\ E_-(l,\delta) &= -A_0\left(\frac{\delta + i\alpha}{\kappa}\right), \end{aligned} \tag{14}$$

where amplitude A_0 is sufficiently small to fall into the linear limit, i.e., $\Gamma|A_0|^2 \ll \kappa$. We integrate the steady-state nonlinear CMEs from the end of the grating $(z = l)$ towards its beginning $(z = 0)$. By setting boundary fields as in Eq. (14) we ensure no energy flow at $z = l$, i.e., $|E_+(l)|^2 - |E_-(l)|^2 = 0$. With Eq. (14), the transmission and reflection coefficients of the grating cannot be defined in the usual way [86], as we have $E_-(l) \neq 0$. The valid eigenstates, however, can be found (which is the objective of the present analysis) by tracking amplitudes (E_+, E_-) at $z = 0$ and choosing those solutions for which $I(0) \equiv |E_+(0)|^2 + |E_-(0)|^2 \to 0$.

3.2 Solving the Time-Dependent Nonlinear Problem

After the stationary solutions of the nonlinear problem have been found, they need to be tested for the stability against perturbations. This can be studied numerically by monitoring the evolution of a particular perturbed solution in time. A small noise added to the solution can show if the latter is stable, remaining unchanged over a substantial period of time, or breaks down. To solve time-dependent Eq. (3), we used a versatile numerical procedure developed earlier by de Sterke et al. [86]. It was shown that Eq. (3) posses linear characteristics, and, by means of an appropriate coordinate transformation, they can be brought into the form of a set of coupled ordinary differential equations. The latter can be integrated along the characteristics by using a variety of algorithms, e.g., the 4th-order collocation method. More details of this integration technique can be found in [86]. We utilize it for our time-dependent numerical calculations presented in Sect. 4.2.

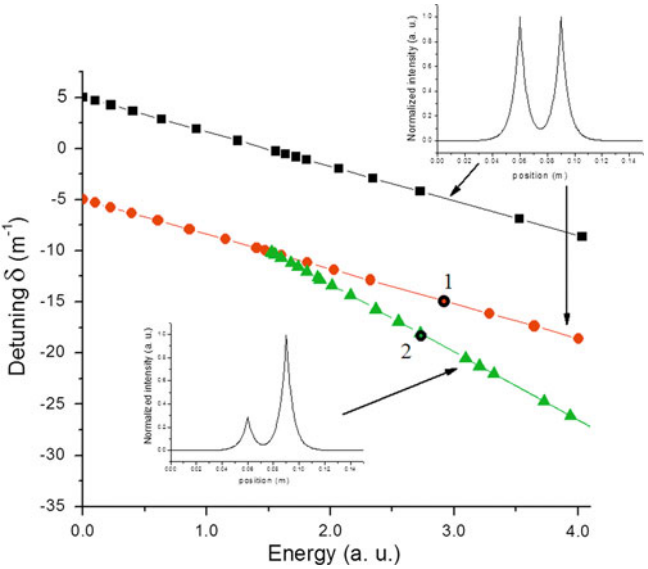

Fig. 3 Map of resonances for the nonlinear grating with $\kappa L = 3$. *Square* and *circular markers* represent symmetric eigenstates, whereas *triangular markers* show asymmetric ones, which occur at energies above the threshold, $\varepsilon_{\text{th}} = 1.5$

4 Results of the Numerical Analysis

4.1 Eigenstates of the Nonlinear Grating with a Pair of Coupled Defects

We use the method described in Sect. 3.1 to solve the stationary version of Eq. (3) for a 15 cm long grating with the coupling coefficient $\kappa = 100\ \text{m}^{-1}$. The grating incorporates a pair of $\pi/2$ defects positioned around its center and separated by distance L. Varying L, we can control the strength of the coupling between the defects. If L is small, viz., $\kappa L \ll 3$, the defects are strongly coupled. This means that the field localized around one of the defects decays on a spatial scale essentially larger than L, hence it covers the second defect too.

Figure 2a, b shows two distinctly different modes, symmetric and asymmetric ones, found for different energies inside the grating with separation $L = 0.2l \equiv 3$ cm between the two defects. These modes are normalized to their maxima, for convenience. The map of the trapped modes versus the energy in the grating is shown in Fig. 3, the energy inside the grating being defined as

$$\varepsilon = \int_0^l |E_+(z)|^2 + |E_+(z)|^2 dz. \tag{15}$$

To characterize the degree of asymmetry in the symmetry-breaking eigenmodes, we introduce the parameter

$$\Omega = \frac{I_R - I_L}{I_R + I_L}, \tag{16}$$

where $I_{R,L}$ are the intensities at positions of the left- and right-hand defects. Obviously, the symmetric eigenstates have $\Omega = 0$.

As mentioned earlier, two different eigenstates are found at low energies, in agreement with analysis in Sect. 2.3 The frequencies of these eigenstates are symmetrically positioned around the Bragg frequency [$\delta = 0$, see Eq. (10)], and the eigenstates feature identical intensity distributions [as in Fig. 2a], but differ in the phase. The intensity distribution has two equal peaks at positions of the defects, reflecting the symmetry of the grating. Only this solution can be found at low to moderate optical energies trapped inside the grating.

Figure 2b shows an asymmetric solution that has been found at energies above the threshold, $\varepsilon_{th} = 1.5$ (it corresponds to the branch labeled with "2" in Fig. 3). The branch of the asymmetric eigenstates splits off from the low-frequency (symmetric) one at $\varepsilon = \varepsilon_{th}$. For the solution shown in Fig. 2b most of light is captured by the right-hand defect. Of course, there also exists its left-hand counterpart (specular image) with the maximum localization at the left-hand defect. It is worth noticing that we did not find any asymmetric states corresponding to the higher-frequency trapped modes [i.e., the nonlinear extension of the eigenmodes corresponding to the upper sign in Eq. (13)]. This suggests that the SSB does not occur for them, an analytic proof of which can also be made.

The energy threshold, ε_{th}, at which the SSB takes place strongly depends on separation L between the defects, and on the coupling coefficient, κ. The larger the product κL, the faster the fields decay away from the defects and the weaker is the coupling between the defects. Therefore, less energy is required to break the coupling and to localize the field chiefly at one of the defects, due to the Kerr nonlinearity. Figure 4 shows the map of the bound states for two gratings, with $\kappa L = 3$ and $\kappa L = 2$ respectively. It is clearly seen that the grating with a smaller product $(\kappa L = 2)$ has a substantially larger bifurcation threshold.

Next, in Fig. 5 we plot the asymmetry parameter, Ω [see Eq. (16)], for all the eigenstates that have been found above. Black and red symbols correspond, respectively, to the gratings with $\kappa L = 3$ and $\kappa L = 2$. The curves in Fig. 5 demonstrate the familiar supercritical pitchfork bifurcation [87], for both gratings. Similar symmetry-breaking bifurcations were found in many other nonlinear double-well, dual-core, and double-defect systems [10, 11, 15, 16, 18, 22–26], [41–55]. As mentioned before, the bifurcation point for the grating with $\kappa L = 2$ is located at a higher energy.

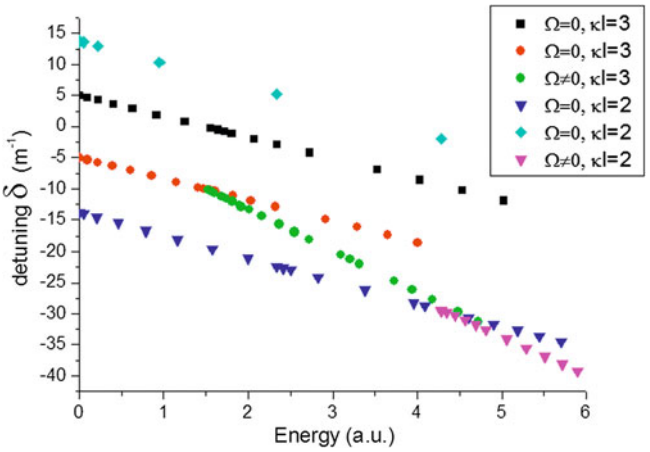

Fig. 4 The map of the trapped modes for two gratings with $\kappa L = 3$ and $\kappa L = 2$. Parameter Ω [see Eq. (16)] represents asymmetry of the solution, so that $\Omega = 0$ corresponds to the symmetric solution, and $\Omega \neq 0$ to an asymmetric one

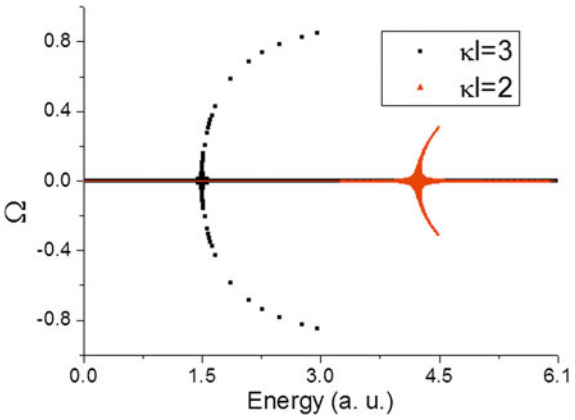

Fig. 5 The evolution of the eigenstate's asymmetry (Ω) with the energy for the gratings with $\kappa L = 3$ (*black markers*) and $\kappa L = 2$ (the *red solid curve*)

4.2 Stability of Nonlinear Solutions

The stability of the modes displayed in Figs. 3 and 4 was studied by means of the numerical algorithm briefly described in Sect. 3.2 Initial condition for the field were taken as the steady-state numerical solutions presented in Fig. 2a, b. In the course of the simulated evolution, the solutions are perturbed by the noise induced by the numerical truncation. This weak perturbation is sufficient to cause a breakdown of unstable eigenstates.

We have thus found that, below the threshold value, ε_{th}, of energy (15), both the lower- and higher-frequency eigenstates [the ones corresponding to the two signs in Eq. (13)] are stable, maintaining their shapes in the course of long simulations.

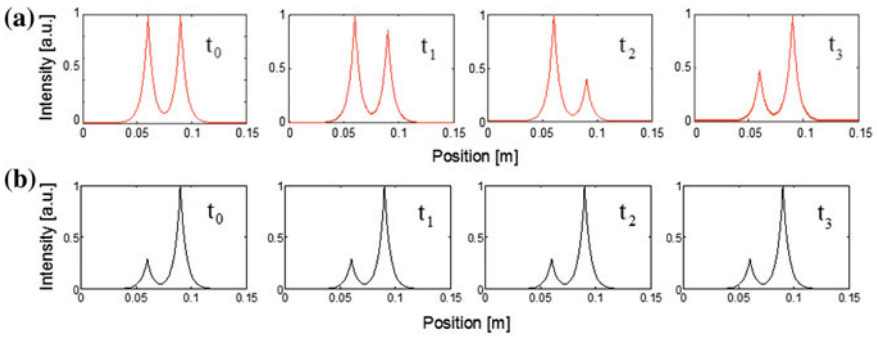

Fig. 6 The time evolution of the eigenstates labeled by 1 and 2 in Fig. 3: **a** a symmetric mode, **b** an asymmetric one. The intensity distribution are normalized to their maxima

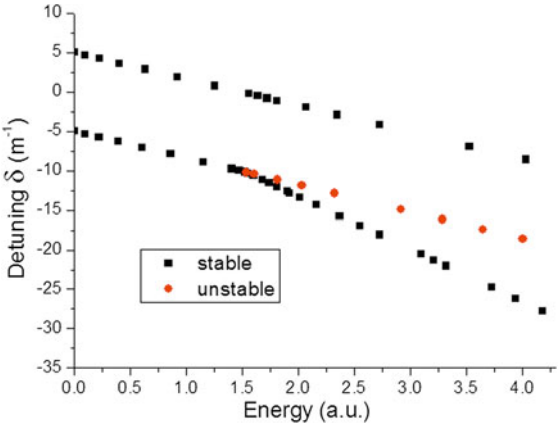

Fig. 7 The stability diagram for a grating with $\kappa L = 3$

Above the threshold, the lower-frequency branch splits, as discussed above, into two sub-branches corresponding to the symmetric and asymmetric solutions. Figure 6a, b summarizes results of the stability analysis, and display the time evolution of the two arbitrary chosen eigenstates, which are labeled by 1 and 2 in Fig. 3, belonging to each of the sub-branches above the threshold.

It is clearly observed in Fig. 6a that the symmetric solution is destabilized by a symmetry-breaking perturbations by time $t = t_1$. Although the SSB is obvious in this case, the field does not relax to a stationary asymmetric mode, but rather performs oscillations between the two defects, similar to Josephson oscillations, which are well known in *bosonic junctions* studied in BEC [41–45]. The oscillations give rise to leakage of the field, and eventually [on a time scale essentially longer than that shown in Fig. 6a], all of the energy escapes.

On the other hand, the asymmetric mode is clearly stable in Fig. 6b. Testing the solutions for gratings with different values of κL, we have concluded that the stability diagram for each grating is similar to that shown in Fig. 7: all the states below the threshold are stable, whereas above it the lower-frequency symmetric

state becomes unstable, while the asymmetric modes emerge as stable ones. On the other hand, the higher-frequency branch does not undergo any bifurcation and is completely stable.

5 Implications for Light Switching

We have demonstrated how the symmetry of the light distribution in a 1D periodic structure with the embedded pair of defects can be manipulated through the nonlinear light-matter interaction, depending on the strength of the coupling between the defects. Since the field distribution is drastically changed by the SSB, it can be employed for all-optical switching. For example, one can implement an optical switch with two states, i.e., "on" or "off", which are encoded into the ratio of the peak intensity at the two defects, via parameter Ω, see Eq. (16). Such a switch flips its state at the SSB point. However, it may not be easy to realize such a practical device, because it is impossible to measure the intensity distribution inside the grating without destroying it.

This problem can be overcome if surface gratings are used. However, they cannot be described by the "shallow grating" model, as the refractive-index contrast between the dielectric material and air is ~ 1. This fact may strongly affect the dynamics in the nonlinear regime, and has to be studied separately, cf. [88]. Discrete arrays with embedded defects may provide a better experimental implementation for the switching device based on the SSB principle, as they admit straightforward access to measuring the power of localized states [89].

Thus, the study presented in this chapter provides a clear illustration of the SSB phenomenon in periodic media with the cubic nonlinearity. Further studies are necessary to transform these fundamental effects into practically usable photonic devices.

References

1. J.C. Eilbeck, P.S. Lomdahl, A.C. Scott, The discrete self-trapping equation. Physica D **16**, 318–338 (1985)
2. C. Yannouleas, U. Landman, Group theoretical analysis of symmetry breaking in two-dimensional quantum dots. Phys. Rev. B **68**, 035325 (2003)
3. E.M. Wright, G.I. Stegeman, S. Wabnitz, Solitary-wave decay and symmetry-breaking instabilities in 2-mode fibers. Phys. Rev. A **40**, 4455–4466 (1989)
4. C. Pare, M. Florjańczyk, Approximate model of soliton dynamics in all-optical couplers. Phys. Rev. A **41**, 6287–6295 (1990)
5. A.W. Snyder, D.J. Mitchell, L. Poladian, D.R. Rowland, Y. Chen, Physics of nonlinear fiber couplers. J. Opt. Soc. Am. B **8**, 2102–2118 (1991)
6. A.I. Maimistov, On the light-pulse propagation in nonlinear tunnel-coupled optical waveguides. Kvantovaya Elektronika **18**, 758–761 (1991)

7. P.L. Chu, B.A. Malomed, G.D. Peng, Soliton switching and propagation in nonlinear fiber couplers: analytical results. J. Opt. Soc. Am. B **10**, 1379–1385 (1993)
8. N. Akhmediev, A. Ankiewicz, Novel soliton states and bifurcation phenomena in nonlinear fiber couplers. Phys. Rev. Lett. **70**, 2395–2398 (1993)
9. B.A. Malomed, I. Skinner, P.L. Chu, G.D. Peng, Symmetric and asymmetric solitons in twin-core nonlinear optical fibers. Phys. Rev. E **53**, 4084–4091 (1996)
10. W.C.K. Mak, B.A. Malomed, P.L. Chu, Soliton coupling in waveguide with quadratic nonlinearity. Phys. Rev. E **55**, 6134–6140 (1997)
11. W.C.K. Mak, B.A. Malomed, P.L. Chu, Solitary waves in coupled nonlinear waveguides with Bragg gratings. J. Opt. Soc. Am. B **15**, 1685–1692 (1998)
12. R. Morandotti, U. Peschel, J.S. Aitchison, H.S. Eisenberg, Y. Silberberg, Experimental observation of linear and nonlinear optical Bloch oscillations. Phys. Rev. Lett. **83**, 4756–4759 (1999)
13. G. Herring, P.G. Kevrekidis, B.A. Malomed, R. Carretero-González, D.J. Frantzeskakis, Symmetry breaking in linearly coupled dynamical lattices. Phys. Rev. E **76**, 066606 (2007)
14. Lj. Hadžievski, G. Gligorić, A. Maluckov, B.A. Malomed, Interface solitons in one-dimensional locally coupled lattice systems. Phys. Rev. A **82**, 033806 (2010)
15. V.A. Brazhnyi, B.A. Malomed, Spontaneous symmetry breaking in Schrödinger lattices with two nonlinear sites. Phys. Rev. A **83**, 053844 (2011)
16. V.A. Brazhnyi, B.A. Malomed, Symmetric and asymmetric localized modes in linear lattices with an embedded pair of $\chi^{(2)}$-nonlinear sites. Phys. Rev. A **86**, 013610 (2012)
17. C. Cambournac, T. Sylvestre, H. Maillotte, B. Vanderlinden, P. Kockaert, Ph. Emplit, M. Haelterman, Symmetry-breaking instability of multimode vector solitons. Phys. Rev. Lett. **89**, 083901 (2002)
18. P.G. Kevrekidis, Z. Chen, B.A. Malomed, D.J. Frantzeskakis, M.I. Weinstein, Spontaneous symmetry breaking in photonics lattices: theory and experiment. Phys. Lett. A **340**, 275–280 (2005)
19. B. Maes, M. Soljacic, J.D. Joannopoulos, P. Bienstman, R. Baets, S.P. Gorza, M. Haelterman, Switching through symmetry breaking in coupled nonlinear micro-cavities. Opt. Express **14**, 10678 (2006)
20. B. Maes, P. Bienstman, R. Baets, Symmetry breaking with coupled Fano resonances. Opt. Express **16**, 3069–3076 (2008)
21. K. Huybrechts, G. Morthier, B. Maes, Symmetry breaking in networks of nonlinear cavities. J. Opt. Soc. Am. B **27**, 708–713 (2010)
22. N. Dror, B.A. Malomed, Solitons supported by localized nonlinearities in periodic media. Phys. Rev. A **83**, 033828 (2011)
23. E. Bulgakov, K. Pichugin, A. Sadreev, Light induced Josephson like current between two coupled nonlinear cavities coupled with a symmetrically positioned photonic crystal waveguide. J. Phys. Condens. Matter **23**, 065304 (2011)
24. E. Bulgakov, K. Pichugin, A. Sadreev, Symmetry breaking for transmission in a photonic waveguide coupled with two off-channel nonlinear defects. Phys. Rev. B **83**, 045109 (2011)
25. E. Bulgakov, A. Sadreev, Symmetry breaking in a T-shaped photonic waveguide coupled with two identical nonlinear cavities. Phys. Rev. B **84**, 155304 (2011)
26. E.N. Bulgakov, A.F. Sadreev, Symmetry breaking in photonic crystal waveguide coupled with the dipole modes of a nonlinear optical cavity. J. Opt. Soc. Am. B **29**, 2924–2928 (2012)
27. A. Christ, O.J.F. Martin, Y. Ekinci, N.A. Gippius, S.G. Tikhodeev, Symmetry breaking in a plasmonic metamaterial at optical wavelength. Nano Lett. **8**, 2171–2175 (2008)
28. A.R. Davoyan, I.V. Shadrivov, Y.S. Kivshar, Nonlinear plasmonic slot waveguides. Opt. Express **16**, 21209–21214 (2008)
29. Y. Gorodetski, N. Shitrit, I. Bretner, V. Kleiner, E. Hasman, Observation of optical spin symmetry breaking in nanoapertures. Nano Lett. **9**, 3016–3019 (2009)

30. B. Luk'yanchuk, N.I. Zheludev, S.A. Maier, N.J. Halas, P. Nordlander, H. Giessen, C.T. Chong, The Fano resonance in plasmonic nanostructures and metamaterials. Nat. Mater. **9**, 707–715 (2010)
31. K. Aydin, M. Imogen, H.A. Atwater, Symmetry breaking and strong coupling in planar optical metamaterials. Opt. Express **18**, 13407–13417 (2010)
32. J.M. Blairon, R. Brout, F. Englert, J. Greensite, Chiral symmetry-breaking in the action formulation of lattice gauge theory. Nucl. Phys. **180**, 439–457 (1981)
33. R. Brout, A brief course in spontaneous symmetry breaking. I. The paleolitic age, arXiv:hep-th /0203096
34. F. Englert, A brief course in spontaneous symmetry breaking. II. Modern times: the BEH mechanism, arXiv:hep-th /0203097
35. R. Brout, F. Englert, Spontaneous broken symmetry. Comptes Rendue Phys. **8**, 973–985 (2007)
36. B.D. Esry, C.H. Greene, Spontaneous spatial symmetry breaking in two-component Bose–Einstein condensates. Phys. Rev. A **59**, 1457–1460 (1999)
37. B. Wu, Q. Niu, Landau and dynamical instabilities of the superflow of Bose–Einstein condensates in optical lattices. Phys. Rev. A **64**, 061603 (2001)
38. D. Snoke, Spontaneous Bose coherence of excitons and polaritons. Science **298**, 1368 (2002)
39. L.E. Sadler, J.M. Higbie, S.R. Leslie, M. Vengalattore, D.M. Stamper-Kurn, Spontaneous symmetry breaking in a quenched ferromagnetic spinor Bose–Einstein condensate. Nature **443**, 312–315 (2006)
40. E.J. Mueller, T.L. Ho, M. Ueda, G. Baym, Fragmentation of Bose–Einstein condensates. Phys. Rev. A **74**, 033612 (2006)
41. M.W. Jack, M.J. Collett, D.F. Walls, Coherent quantum tunneling between two Bose–Einstein condensates. Phys. Rev. A **54**, R4625–R4628 (1996)
42. J. Ruostekoski, D.F. Walls, Bose–Einstein condensate in a double-well potential as an open quantum system. Phys. Rev. A **58**, R50–R53 (1998)
43. M. Albiez, R. Gati, J. Folling, S. Hunsmann, M. Cristiani, M.K. Oberthaler, Direct observation of tunneling and nonlinear self-trapping in a single bosonic Josephson junction. Phys. Rev. Lett. **95**, 010402 (2005)
44. L.C. Qian, M.L. Wall, S.L. Zhang, Z.W. Zhou, H. Pu, Bose–Einstein condensates on a ring with periodic scattering length: spontaneous symmetry breaking and entanglement. Phys. Rev. A **77**, 013611 (2008)
45. B. Xiong, J.B. Gong, H. Pu, W.Z. Bao, B.W. Li, Symmetry breaking and self-trapping of a dipolar Bose–Einstein condensate in a double-well potential. Phys. Rev. A **79**, 013626 (2009)
46. M. Matuszewski, B.A. Malomed, M. Trippenbach, Spontaneous symmetry breaking of solitons trapped in a double-channel potential. Phys. Rev. A **75**, 063621 (2007)
47. A. Gubeskys, B.A. Malomed, Symmetric and asymmetric solitons in linearly coupled Bose–Einstein condensates trapped in optical lattices. Phys. Rev. A **75**, 063602 (2007)
48. A. Gubeskys, B.A. Malomed, Spontaneous soliton symmetry breaking in two-dimensional coupled Bose–Einstein condensates supported by optical lattices. Phys. Rev. A **76**, 043623 (2007)
49. M. Trippenbach, E. Infeld, J. Gocalek, M. Matuszewski, M. Oberthaler, B.A. Malomed, Spontaneous symmetry breaking of gap solitons in double-well traps. Phys. Rev. A **78**, 013603 (2008)
50. N.V. Hung, M. Trippenbach, B.A. Malomed, Symmetric and asymmetric solitons trapped in H-shaped potentials. Phys. Rev. A **84**, 053618 (2011)
51. T. Mayteevarunyoo, B.A. Malomed, G. Dong, Spontaneous symmetry breaking in a nonlinear double-well structure. Phys. Rev. A **78**, 053601 (2008)
52. X.-F. Zhou, S.-L. Zhang, Z.-W. Zhou, B.A. Malomed, H. Pu, Bose–Einstein condensation on a ring-shaped trap with nonlinear double-well potential. Phys. Rev. A **85**, 023603 (2012)
53. T. Mayteevarunyoo, B.A. Malomed, A. Reoksabutr, Spontaneous symmetry breaking of photonic and matter waves in two-dimensional pseudopotentials. J. Mod. Opt. **58**, 1977–1989 (2011)

54. S.K. Adhikari, B.A. Malomed, L. Salasnich, F. Toigo, Spontaneous symmetry breaking of Bose–Fermi mixtures in double-well potentials. Phys. Rev. A **81**, 053630 (2010)
55. P.-T. Qi, W.-S. Duan, Tunneling dynamics and phase transition of a Bose–Fermi mixture in a double well. Phys. Rev. A **84**, 033627 (2011)
56. S.O. Demokritov, A.A. Serga, B. Hillebrands, M.P. Kostylev, B.A. Kalinikos, Experimental observation of symmetry-breaking nonlinear modes in an active ring. Nature **426**, 159–162 (2003)
57. A.E. Miroshnichenko, B.A. Malomed, Y.S. Kivshar, Nonlinearly PT-symmetric systems: spontaneous symmetry breaking and transmission resonances. Phys. Rev. A **84**, 012123 (2011)
58. R. Driben, B.A. Malomed, Stability of solitons in parity-time-symmetric couplers. Opt. Lett. **36**, 4323–4325 (2011)
59. N.V. Alexeeva, I.V. Barashenkov, A.A. Sukhorukov, Y.S. Kivshar, Optical solitons in PT - symmetric nonlinear couplers with gain and loss. Phys. Rev. A **85**, 063837 (2012)
60. A.C. Newell, J.V. Moloney, *Nonlinear Optics* (Addison-Wesley, Redwood City, 1992)
61. A. Hasegawa, M. Matsumoto, *Optical Solitons in Fibers* (Springer, Berlin, 2003)
62. B.A. Malomed, *Soliton Management in Periodic Systems* (Springer, New York, 2006)
63. G.P. Agrawal, *Nonlinear Fiber Optics* (Academic Press, San Diego, 2007)
64. C. Denz, S. Flach, Y.S. Kivshar (eds.) *Nonlinearities in Periodic Structures and Metamaterials*, (Springer, Heidelberg, 2010)
65. F. Lederer, G.I. Stegeman, D.N. Christodoulides, G. Assanto, M. Segev, Y. Silberberg, Discrete solitons in optics. Phys. Rep. **463**, 1–126 (2008)
66. Y.V. Kartashov, V.A. Vysloukh, L. Torner, Soliton shape and mobility control in optical lattices. Progr. Opt. **52**, 63–148 (2009)
67. Y.V. Kartashov, B.A. Malomed, L. Torner, Solitons in nonlinear lattices. Rev. Mod. Phys. **83**, 247–306 (2011)
68. P. Berini, Long-range surface plasmon polaritons. Adv. Opt. Phot. **1**, 484–588 (2009)
69. M. Kauranen, A.V. Zayats, Nonlinear plasmonics. Nat. Phot. **6**, 737–748 (2012)
70. P.Y.P. Chen, B.A. Malomed, P.L. Chu, Trapping Bragg solitons by a pair of defects. Phys. Rev. E **71**, 066601 (2005)
71. P.Y.P. Chen, B.A. Malomed, P.L. Chu, Interaction of solitons with complex defects in Bragg gratings. Phys. Lett. A **372**, 327–332 (2008)
72. D.P. Hand, P.St.J. Russell, Photoinduced refractive index changes in germanosilicate fibers. Opt. Lett. **15**, 102–104 (1990)
73. K.O. Hill, Y. Fujii, D.C. Johnson, B.S. Kawasaki, Photosensitivity in optical fiber waveguides: application to reflection filter fabrication. Appl. Phys. Lett. **32**, 647 (1978)
74. R. Kashyap, *Fiber Bragg Gratings* (Academic Press, San Diego, 1999)
75. K.M. Davis, K. Miura, N. Sugimoto, K. Hirao, Writing waveguides in glass with a femtosecond laser. Opt. Lett. **21**, 1729–1731 (1996)
76. D.N. Christodoulides, R.I. Joseph, Slow Bragg solitons in nonlinear periodic structures. Phys. Rev. Lett. **62**, 1746–1749 (1989)
77. A.B. Aceves, S. Wabnitz, Self-induced transparency solitons in nonlinear refractive periodic media. Phys. Lett. A **141**, 37–42 (1989)
78. B.A. Malomed, R.S. Tasgal, Vibration modes of a gap soliton in a nonlinear optical medium. Phys. Rev. E **49**, 5787–5796 (1994)
79. I.V. Barashenkov, D.E. Pelinovsky, E.V. Zemlyanaya, Vibrations and oscillatory instabilities of gap solitons. Phys. Rev. Lett. **80**, 5117–5120 (1998)
80. A. De Rossi, C. Conti, S. Trillo, Stability, multistability, and wobbling of optical gap solitons. Phys. Rev. Lett. **81**, 85–88 (1998)
81. B.J. Eggleton, R.E. Slusher, C.M. de Sterke, P.A. Krug, J.E. Sipe, Bragg grating solitons. Phys. Rev. Lett. **76**, 1627–1630 (1996)
82. J.T. Mok, C.M. de Sterke, I.C.M. Littler, B.J. Eggleton, Dispersionless slow light using gap soliton. Nat. Phys. **2**, 775–780 (2006)

83. W.C.K. Mak, B.A. Malomed, P.L. Chu, Interaction of a soliton with a local defect in a fiber Bragg grating. J. Opt. Soc. Am. B **20**, 725–735 (2003)
84. D. Marcuse, *Theory of Dielectric Optical Waveguides* (Academic Press, New York, 1991)
85. C.M. de Sterke, J.E. Sipe, Gap solitons, in *Progress in Optics XXXIII*, ed. by E. Wolf (Elsevier Science, Amsterdam, 1994)
86. C.M. de Sterke, K.R. Jackson, B.D. Robert, Nonlinear coupled mode equations on a finite interval: a numerical procedure. J. Opt. Soc. Am. B **8**, 403–412 (1991)
87. G. Iooss, D.D. Joseph, *Elementary Stability Bifurcation Theory* (Springer, New York, 1980)
88. T. Iizuka, C.M. de Sterke, Phys. Rev. E **61**, 4491–4499 (2000)
89. D. Mandelik, R. Morandotti, J.S. Aitchison, Y. Silberberg, Gap solitons in waveguide arrays. Phys. Rev. Lett. **92**, 093904 (2004)

Guided Modes and Symmetry Breaking Supported by Localized Gain

Yaroslav V. Kartashov, Vladimir V. Konotop, Victor A. Vysloukh and Dmitry A. Zezyulin

Abstract We review numerous physical phenomena which occur in one- and two-dimensional nonlinear media in the presence of localized gain-defects, and which recently attracted considerable attention. In particular, we discuss stable localized modes in media with linear and nonlinear dissipation; breathers which can be excited in the presence of more than one localized gain channels; vortices. We address the phenomenon of the symmetry breaking in one- and two-dimensional media, resulting in emergence of stable nonsymmetric modes, and analyze possibilities of guiding and switching of waves with help of guiding channels.

Y. V. Kartashov (✉)
ICFO-Institut de Ciencies Fotoniques, Universitat Politecnica de Catalunya,
Mediterranean Technology Park, 08860 Castelldefels (Barcelona), Spain
e-mail: yaroslav.kartashov@icfo.es

Y. V. Kartashov
Institute of Spectroscopy, Russian Academy of Sciences,
Moscow Region, Troitsk 142190, Russia

V. V. Konotop
Centro de Física Teórica e Computacional and Departamento de Física,
Faculdade de Ciéncias, Universidade de Lisboa, Avenida Professor
Gama Pinto 2, Lisboa 1649-003, Portugal
e-mail: vvkonotop@fc.ul.pt

V. A. Vysloukh
Departamento de Fisica y Matematicas, Universidad de las Americas -Puebla,
Santa Catarina Martir, 72820 Puebla, Mexico
e-mail: victora.vysloukh@udlap.mx

D. A. Zezyulin
Centro de Física Teórica e Computacional, Faculdade de Ciências, Universidade de Lisboa,
Avenida Professor Gama Pinto 2, Lisboa 1649-003, Portugal
e-mail: zezyulin@cii.fc.ul.pt

Progress Optical Sci., Photonics (2013): 167–200
DOI: 10.1007/10091_2012_4

Published Online: 24 June 2012

1 Introduction

Dissipative solitons appear in various systems and physical settings, including optics, hydrodynamics, plasmas, and plasmonics, to name just a few. Optical dissipative solitons belong to a special class of self-sustained nonlinear excitations that, on the one hand, exist due to the mutual balance between nonlinearity and diffraction (or dispersion) and, on the other hand, due to the balance between gain and dissipation acting in the system [2, 3, 48]. Due to this double balance the dissipative solitons usually do not exist as families, parameterized solely by the propagation constant, as it occurs in conservative settings [30]. Instead, all parameters of dissipative solitons are usually uniquely determined by the amount of gain and losses acting in the system. Stability is a fundamental issue for such solitons, because losses in the medium must be compensated by gain. The classical stable dissipative soliton is the attractor of the system, i.e. it can be excited from the relatively broad spectrum of initial conditions (known as a basin of attraction).

Dissipative solitons may form in a variety of settings, including systems governed by the cubic-quintic Ginzburg-Landau equation [2, 3, 11, 12, 39, 43, 46, 47, 50, 51, 59] laser amplifiers with saturable gain and absorption [15, 48, 49], driven nonlinear optical cavities [9, 16, 18, 35, 55], medium with narrow "hot spots" [61] etc. The experimental observation of dissipative solitons was reported, for example, in semiconductor microcavities [6, 58] and electrically pumped semiconductor amplifiers [62]. Since uniform linear gain usually destabilizes any localized wavepacket by making the background around it unstable, stable dissipative solitons were obtained mostly in systems with nonlinear gain acting in a combination with stabilizing linear and higher-order nonlinear absorption (as it occurs in conventional complex cubic-quintic Ginzburg-Landau equation). It is relevant to mention that dissipative solitons also can be stabilized in a dual-core system with only cubic nonlinearity, where the stability of the zero background is provided by the additional linearly coupled lossy subsystem [5, 40].

However, the instability of the background that is unavoidable in the system with uniform gain [19] can be suppressed if the gain acts only in a limited spatial domain. Such spatially localized gain, when combined with suitable linear or nonlinear absorption, may result in the formation of stable one- and two-dimensional dissipative solitons. The effect of spatially localized gain was analyzed first for the existence and interaction of gap solitons in shallow fiber Bragg gratings with uniform background linear losses [36], for interaction of optical pulses in an one-dimensional, resonant photonic crystal with the defect produced by a coherent pump [42], and for dynamic emission of conservative moving lattice solitons from the domain with gain [22]. The modification of complex Ginzburg-Landau equation with background linear and nonlinear losses and gain acting in only one spatial point or in finite, but narrow domain was introduced in [52]. The competition between localized gain and losses in this system was shown to lead to the formation of stable cusp-like solitons in delta-shaped gain landscapes or breathers in gain landscapes of finite width. The modification of this model to the case of

delta-shaped Kerr nonlinearity and nonlinear losses was suggested in [60]. We also notice that spatially inhomogeneous gain can be realized not only in optics, but also in the field of matter waves. The nonlinear eigenstates of complex periodic and parabolic external potentials were obtained in [1, 65, 66].

It turns out that even in the case of delta-shaped gain landscapes the resulting dissipative solitons are characterized by the complex internal energy flows that are usually directed from the domain with gain into domain with losses and that dramatically impact the soliton's intensity distribution and its localization. Therefore, not only the strength of the gain, but also the very shape of the gain landscape should strongly affect the properties of solitons in such systems as we will show below. Among the most striking phenomena which can be observed in the presence of localized gain we mention the possibility of symmetry breaking in localized gain landscapes, as well as the existence and stability of multidimensional fundamental and more complex vortex soliton states.

In this chapter we will present an overview of our results on dissipative solitons supported by localized gain landscapes in both one- and two-dimensional settings in focusing and defocusing media with (or without) nonlinear two-photon absorption. In particular, we will show that a localized gain imprinted in the material with background losses and defocusing nonlinearity can support stable one-dimensional solitons not only for particular value of linear gain (as it occurs in conventional gain guiding), but for a broad range of gain coefficients [67]. Among the unique properties of this system is the possibility of formation of localized states with negative propagation constants. We will show that the symmetry breaking can occur even in systems with bell-shaped gain landscapes and focusing nonlinearity that start supporting highly asymmetric solitons for sufficiently high gain levels, where symmetric states become unstable [28]. When placed into a lattice created by periodic modulation of linear refractive index [25], the localized gain supports dissipative lattice solitons whose localization and stability properties are dictated by the location of propagation constant depending on the values of gain and losses in the band-gap spectrum of the conservative lattice, by analogy with conservative lattice solitons (for recent reviews on optical lattice solitons see [23, 33]). Dissipative surface solitons may form when gain is concentrated in the near-surface channel of truncated one-dimensional periodic lattice [24]. Like their conservative counterparts introduced in [37] and observed in both one- and two-dimensional geometries [56, 57, 63], the dissipative surface lattice solitons exist above the threshold energy flow and require certain minimal gain for their existence. Notice that dissipative surface solitons were studied before only in the truncated discrete systems governed by Ginzburg–Landau equation with uniform nonlinear gain [44].

An especially interesting problem is the possibility of stabilization of multidimensional solitons due to the interplay between the localized gain and two-photon absorption. We will show that such an interplay can stabilize even two-dimensional solitons [27] in cubic nonlinear media where conservative solitons suffer from collapse [7]. Notice that such two-dimensional solitons may also experience symmetry breaking resulting in the transformation of radially

symmetric solitons into stable elliptical states supported by the system despite the fact that all its parameters are either uniform or radially symmetric. The impact of localized gain on multidimensional solitons was also considered in planar waveguide arrays where spatially inhomogeneous electric pumping can be used to route solitons along predetermined trajectories [64]. Spatially localized gain allows for excitation of not only simplest fundamental solitons, but also vortex solitons. Vortex solitons, being higher-order excited states of the system are prone to azimuthal modulational instabilities [14]. However, the interplay between gain and two-photon absorption in ring-like gain landscapes renders vortex solitons completely stable [34]. Moreover, if the gain landscape is azimuthally modulated, the necklace-like vortex states may form that can carry only specific topological charges dictated by the topology of gain landscape (the effect is somehow analogous to restrictions on topological charges arising in lattices produced by refractive index modulation [17, 20, 32, 38, 45]). Finally, localized gain implemented in selected channels of periodic conservative lattice supports vortex lattice solitons emerging from different gaps of lattice spectrum that will be discussed below [26]. The coincidence of the discrete rotational symmetries of the gain landscape and refractive index distribution is a necessary condition for excitation of such vortex solitons, which otherwise transform into stable dissipative multipoles. Finally, one should stress that while this chapter focuses on the impact of spatially inhomogeneous gain on various dissipative solitons, the transversally inhomogeneous losses also may dramatically affect the symmetries and stability of available solitons. One such example was reported very recently in the frames of the model governed by Ginzburg–Landau equation with radially inhomogeneous linear losses [54].

2 Localized Gain in One-Dimensional Problems

2.1 Some General Comments

We start by considering the one-dimensional (1D) model

$$iq_\xi = -\frac{1}{2}q_{\eta\eta} - i[\gamma_0 - \gamma(\eta)]q + (\sigma - i\alpha)|q|^2 q, \tag{1}$$

where $\sigma = 1$ ($\sigma = -1$) corresponds to defocusing (focusing) nonlinearity, $\gamma(\eta)$ describes a localized gain concentrated in the domain (or domains) having a characteristic width d; γ_0 and α denote linear and nonlinear dissipation respectively.

We mention that from the experimental point of view Eq. (1) can be used to describe the nonlinear response of semiconductor materials where soliton formation occurs for wavelengths below half the band-gap and the two-photon absorption dominates [29]. Such semiconductor materials are used for fabrication of optical amplifiers with high optical gain [10].

In the typical optical applications (we bear in mind through the whole Chapter) the dimensionless variables are defined as $\eta = x/x_0$ and $\xi = z/L_{dif}$, where x_0 is the characteristic transverse beam width, $L_{dif} = kx_0^2$ is the diffraction length, $k = 2\pi n_0/\lambda$, λ is the wavenumber, and n_0 is the unperturbed refractive index. For the linear gain coefficient one has $p_i = L_{dif}/L_{gain}$, $L_{nl} = n_0/kn_2I_0$ is the nonlinear self-action length, I_0 is the characteristic intensity, and L_{gain} is the amplification length. Finally, for the coefficient of nonlinear losses we have $\alpha = L_{dif}/L_{loss}$, where $L_{loss} = 1/\alpha_2 I_0$ characterizes the length of two-photon absorption.

Now we focus on stationary spatially localized solutions which can be written down as follows

$$q(\xi,\eta) = e^{ib\xi}w(\eta), \quad w(\eta) = w_r(\eta) + iw_i(\eta) = e^{i\theta(\eta)}u(\eta) \tag{2}$$

with $u(\eta) \geq 0$ and $\theta(\eta)$ being real functions. Localized solutions obey zero boundary conditions $\lim_{|\eta|\to\infty}|q(\xi,\eta)| = \lim_{|\eta|\to\infty} u(\eta) = 0$. The constant b will be referred to as the propagation constant. It is straightforward to show that for the stationary mode Eq. (1) can be rewritten either in the complex form

$$\frac{1}{2}w_{\eta\eta} - bw + i[\gamma_0 - \gamma(\eta)]w - (\sigma - i\alpha)|w|^2 w = 0, \tag{3}$$

or in the form of the system

$$\frac{1}{2}u_{\eta\eta} - bu - \sigma u^3 - \frac{j^2}{u^3} = 0, \quad \frac{1}{2}j_\eta + [\gamma_0 - \gamma(\eta)]u^2 + \alpha u^4 = 0. \tag{4}$$

where we have introduced the current density $j(\eta) \equiv \theta_\eta u^2$.

Throughout this Chapter the localized gain will be presented in the form $\gamma(\eta) = p_i G(\eta)$, where $p_i > 1$ characterizes the gain strength (amplitude), while $G(\eta)$ describes the gain profile and is considered normalized to a fixed constant of order one.

The second of Eqs. (4) allows one to obtain the condition of balance between the dissipation and gain. It reads

$$\gamma_0 U = \int \gamma(\eta)u^2 d\eta - \alpha \int u^4\, d\eta \tag{5}$$

where we have introduced the energy flow

$$U = \int u^2\, d\eta \tag{6}$$

The equations of balance between the nonlinearity and diffraction

$$bU = -\frac{1}{2}\int |w_\eta|^2 d\eta - \sigma \int |w|^4 d\eta = -\frac{1}{2}\int u_\eta^2 d\eta - \int \frac{j^2}{u^2} d\eta + \int u^4 d\eta \tag{7}$$

are obtained from the first of Eqs. (4).

2.2 Localized Gain and Linear Dissipation

The first problem we address, is the case where only linear dissipation is present, i.e. $\alpha = 0$. Without loss of generality we rescale the background dissipation to the unity value, i.e. set $\gamma_0 = 1$, and consider the situation where $\max_\eta \gamma(\eta) > 1$. In order to establish the domain of possible variation of the propagation constant b, we consider the limit $\eta \to \infty$ and focus on the exponentially decaying solutions, i.e. we assume $u \sim Ce^{-\mu\eta}$, where C and μ are positive constants. From the second of Eqs. (4) it readily follows that in this limit $j \sim C^2 e^{-2\mu\eta}/\mu$. This suggests that in the first of Eqs. (4) the term σu^3 can be neglected in the limit $\eta \to \infty$, while substituting the asymptotic values of u and j in the terms which are left we obtain $b = \mu^2/2 - 1/\mu^2$. It follows from this formula that the propagation constant for localized solutions can be either positive or negative even if the nonlinearity is focusing (contrary to what happens in uniform conservative systems or in dissipative systems [25–27, 31]). If $b \to +\infty$ then $\mu \to +\infty$ while if $b \to -\infty$ then $\mu \to +0$. Respectively, there must exist localized modes with $\mu > 0$ even at $b = 0$ while the spatial delocalization occurs in the limit $b \to -\infty$.

According to (7), for zero propagation constant the mode should decay with the exponent $\mu = 2^{1/4}$, i.e. $|w_\eta|^2 \not\equiv 0$. Hence for $b = 0$ Eq. (7) can be satisfied only in the focusing medium (i.e. at $\sigma = -1$). Thus the linear limit of the problem (i.e. $U \to 0$) corresponds to a localized mode with $b = b^{(0)} < 0$ [indeed, in this case $\int |w|^4 d\eta / U \leq \max |w|^2 \to 0$ and can be neglected in (7)]. In the defocusing medium exponentially localized solutions exist only if $b < b^{(0)}$ while in the focusing medium dissipative solitons can exist with both positive and negative propagation constants, i.e. at $b > b^{(0)}$.

We start with the case of the gain localized in one spatial domain, setting $G(\eta) = e^{-\eta^2/d^2}$ and $p_i > 1$. By fixing the width of the gain landscape d and changing p_i we obtain the dependencies $b(p_i)$ and $U(p_i)$, which are depicted in Fig. 1a, b for $d = 1/\sqrt{2}$. These dependencies bifurcate from the linear limit corresponding to $U = 0$ and to $b^{(0)} \approx -0.61$. The very fact of existence of localized linear modes with $b = b^{(0)}$ in inhomogeneous gain landscapes is known as the gain-guiding effect (see e.g. [53]). In the linear case the guiding occurs for a particular value of $p_i = p_i^{(0)} \approx 1.98$. Focusing nonlinearity diminishes gain at which localization occurs, while in a defocusing medium a higher gain is required for localization (Fig. 1). In Fig. 1c we also show an example of a nonlinear mode. Increase of the gain results in decrease of U in the focusing medium, that is also accompanied by the expansion of the soliton. In the defocusing medium the growth of p_i results in increase of the energy flow and progressive expansion of the soliton outwards the gain domain. Solitons are exponentially localized in both focusing and defocusing media, as predicted by the analysis of (4), which also shows that the current results in effective renormalization of the propagation constant. Physical understanding of the exponential localization in the defocusing

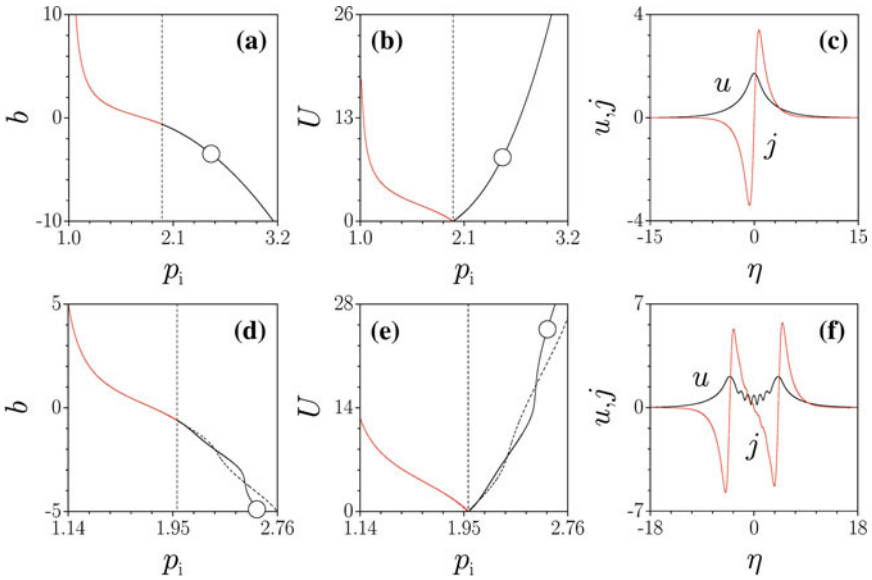

Fig. 1 Propagation constant (**a**) and energy flow (**b**) *vs* p_i for solitons supported by single gain channel. *Red and black curves* correspond to focusing and defocusing media. The solitons are stable in the decocusing medium and are stable in the focusing medium. *Vertical dashed line* indicates p_i value corresponding to the linear limit. (**c**) Profile of a stable soliton (c) and current density in defocusing medium at $p_i = 2.5$ corresponding to the *circles* in (**a**) and (**b**). (**d**) and (**e**) The same as (**a**) and (**b**) but for two gain channels; while the solitons are unstable in the focusing medium, they can be either stable or unstable in the focusing medium. (**f**) Profile of a stable soliton and current density in defocusing medium at $p_i = 2.6$.

medium, comes also form the observation that the current results in the effective self-focusing of the beam, what stems form the negative sign in front of j^2/u^3 [see the first of Eqs. (4)].

Linear stability analysis (confirmed by the direct propagation) indicates that the solitons in the focusing medium are unstable while in the defocusing medium they are attractors and can be excited with a variety of inputs, ranging from noisy to localized patterns. This difference in the stability can be understood from Eqs. (4). The solution represents a flow outwards the "source" (i.e. the gain domain). The defocusing nonlinearity enhances the outflow from the high intensity region thus contributing to the stability, while the focusing medium enhances the field concentration in the gain domain, what stimulates further growth of the peak amplitude.

Next we study the case of the gain landscape with two maxima at $\eta = \pm\eta_0$ considering $G(\eta) = e^{-(\eta-\eta_0)^2/d^2} + e^{-(\eta+\eta_0)^2/d^2}$. Here one also can obtain modes both for focusing and defocusing media. In Fig. 1d, e we present the branches of symmetric (even) and antisymmetric (odd) modes for $d = 1/\sqrt{2}$. Both types of solutions bifurcate from the linear limit. The values of parameters p_i and b at

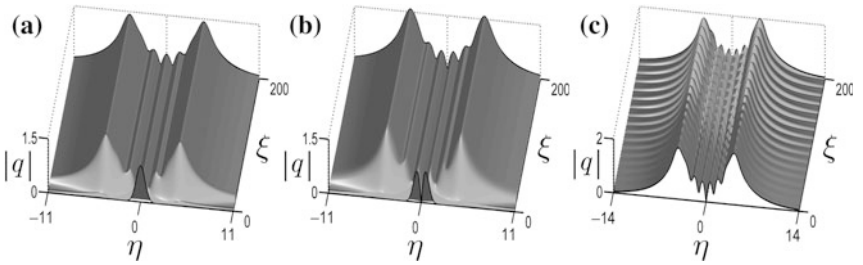

Fig. 2 Excitation of a stable symmetric (**a**) and antisymmetric (**b**) solitons by symmetric and antisymmetric input beams in the system with two gain channels for $p_i = 2.391$. **c** Excitation of a breather at $p_i = 2.61$ starting with the unstable antisymmetric soliton

which bifurcations take place are very close ($b_s^{(0)} \approx -0.61, p_{i,s}^{(0)} \approx 1.99$ for symmetric, and $b_a^{(0)} \approx -0.60, p_{i,a}^{(0)} \approx 1.98$ for antisymmetric solitons). Closely to the linear limit and in the focusing medium the $U(p_i)$ curves for the symmetric and antisymmetric solitons are almost indistinguishable, while in the defocusing medium their energy flows may differ considerably.

Linear stability analysis reveals multiple alternating stability and instability domains (in p_i) for both symmetric and antisymmetric modes. A remarkable fact is that stable symmetric and antisymmetric modes can co-exist at the same parameters of the system. By considering dynamical excitation of the modes discussed above we found that for certain values of p_i even input beams evolve into the symmetric stationary mode while odd input beams evolve into the antisymmetric mode, see panels (a) and (b) of Fig. 2. When one of the modes is unstable it usually evolves into a stable mode or into *pulsating mode* (dissipative breather). An example of such behavior is shown in Fig. 2c where perturbed unstable antisymmetric mode transforms into the pulsating soliton.

2.3 Guiding the Dissipative Modes

Stable nonlinear modes reported above represent attractors with large basins. This fact allows one to guide stable modes by designing the shape of localized gain channels in a desirable manner.

As a first example we consider a gain channel which at some propagation distance, say $\xi = \tilde{\xi}$, branches out into two new channels. This situation is described by gain function

$$\gamma(\eta, \xi) = p_i \begin{cases} 1 - \tanh^2[\sqrt{2}\eta], & \text{if } 0 \le \xi < \tilde{\xi}; \\ 1 - \tanh^2[\sqrt{2}(\eta - \eta_0)] \tanh^2[\sqrt{2}(\eta + \eta_0)], & \text{if } \xi > \tilde{\xi}. \end{cases} \quad (8)$$

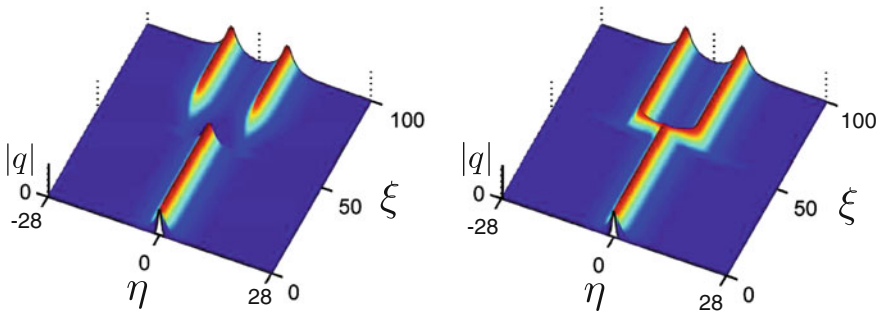

Fig. 3 Propagation of the initial profile $q(\eta, 0) = 1.18e^{-2\eta^2}$ for abrupt gain switching from single-channel to two-channel (*left panel*) and for switching with finite velocity $\ell = 2$ (*right panel*). Other parameters: $p_i = 2.2, \eta_0 = 7, \tilde{\xi} = 50$

In this example at $\xi = \tilde{\xi}$ the "switch" between single channel and two channels is abrupt. Corresponding solution $q(\eta, \xi)$ is illustrated on the left panel of Fig. 3. A symmetric input initial profile rapidly evolves to the nonlinear mode since the latter is an attractor. Right after the switching point the peak amplitude and energy of the solution abruptly decrease. But for some larger ξ the solution evolves to a symmetric mode for the two-channels system.

As another example let us consider a situation when the switching from the single-channel gain to the two-channel one occurs smoothly over the transition region of the length ℓ. In other words, for $\xi > \tilde{\xi}$ the distance-dependent localized gain reads

$$\gamma(\eta, \xi) = p_i \left\{ 1 - \tanh^2 \left[\sqrt{2} \left(\eta - \eta_0 \tanh \left(\frac{\xi - \tilde{\xi}}{\ell} \right) \right) \right] \times \tanh^2 \left[\sqrt{2} \left(\eta + \eta_0 \tanh \left(\frac{\xi - \tilde{\xi}}{\ell} \right) \right) \right] \right\}, \tag{9}$$

i.e. the switching is performed along a tanh-shaped trajectory. Results are shown on the right panel of Fig. 3. We note that for the case of finite switching region a slightly shorter propagation distance is required for the final two-hump profile to be established.

The splitting of the beams reported above, was based on the fact that each of the solutions is an attractor and can be excited starting with rather broad range of the initial conditions. This also means that the described procedure can be easily extended either to splitting of one beam in a several (more than two) ones, or on the subsequent splitting of the new born beams in several ones. The inverse procedure, where several guided beams are "collected" into a single one can be also easily implemented.

2.4 Symmetry Breaking in a Medium with Nonlinear Losses

In addition to standard constraints imposed by the balance between the dissipation and gain (5), a localized gain introduces a new spatial scale—the width of the gain domain. This suggests a possibility of existence of more sophisticated structures than the simplest symmetric and/or anti-symmetric dissipative solitons, considered above. One of such phenomena is the symmetry breaking. It is considered in this section, following [28], within the framework of the model (1) with $\sigma = -1$ and $\gamma_0 = 0$. It will be assumed that the gain landscape contains an integer number n of periods of $\cos^2 \eta$. This allows us to write down

$$G(\eta) = \begin{cases} \cos^2(\Omega\eta), & \text{for } |\eta| \le \eta_n = n\pi/(2\Omega) \\ 0 & \text{otherwise} \end{cases} \tag{10}$$

More specifically, in this subsection we set $\Omega = 1$ and vary p_i, α and n. Eqs. (4) can be written now in the form:

$$bu = \frac{u_{\eta\eta}}{2} + u^3 - \frac{j^2}{2u^3}, \quad j_\eta = 2p_i G(\eta)u^2 - 2\alpha u^4, \tag{11}$$

and the decaying asymptotics imply that $u \sim e^{-\sqrt{2b}|\eta|}$ and $j \sim e^{-4\sqrt{2b}|\eta|}$.

Let us now use scaling arguments to argue that in the limit of large amplification $p_i \to \infty$ there can exist more than one stationary state. Assuming that the solution amplitude $\mathscr{A} = \max\{u\}$ grows and the width ℓ decreases, Eq. (5) with $\gamma_0 = 0$ suggests the scaling $\mathscr{A} \sim 1/\ell \sim \sqrt{p_i/\alpha}$. This allows us to deduce the estimate $U \approx (\alpha/p_i) \int u^4 d\eta \sim \sqrt{p_i/\alpha}$, valid subject to the assumption that the soliton maximum is placed exactly at $\eta = 0$ where the pump has the maximal value, i.e. valid for a symmetric mode. On the other hand assuming the solution wide enough, i.e. $\ell \gg \eta_0 = \pi$, we obtain the estimates $p_i \sim \alpha \mathscr{A}^2 \ell$ and $U \sim \mathscr{A}^2 \ell$, i.e. $U \sim p_i/\alpha$. Now we are restricted neither by the position of the maximum of the mode, nor by the symmetry of its shape. Moreover, in the corresponding solution, the diffraction term $u_{\eta\eta} \sim \mathscr{A}/\ell^2$ cannot be compensated by the Kerr nonlinearity $u^3 \sim \mathscr{A}^3$ alone, and the role of the current distribution, i.e. of j^2/u^3, becomes crucial. The major influence of the current occurs not at the origin but at some intermediate point η_* defined by the condition $j_\eta(\eta_*) = 0$. Thus if a solution with the suggested scaling exists, it should have asymmetric shape, with the maximum located in the vicinity of the point η_*.

The above prediction of symmetric and asymmetric modes is confirmed in simulations [Fig. 4]. We observe that while the growth of zero background is suppressed at large η, the light concentrates inside the amplifying channels. Strictly speaking this feature is typical for symmetric modes. A maximum of an asymmetric mode is shifted from the gain peak and the width of the mode grows with p_i, according to the estimates presented above. This broadening of the soliton leads to the situation where an appreciable part of the light energy concentrates outside the gain channel for large p_i.

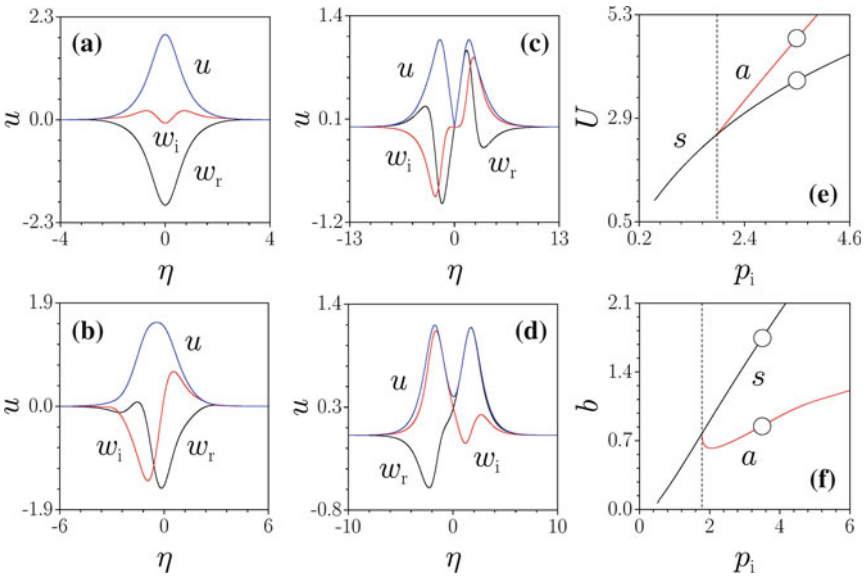

Fig. 4 Profiles of unstable symmetric (**a**) and stable asymmetric (**b**) one-hump solitons at $n = 1$, $p_i = 3.5, \alpha = 1.2$ and profiles of unstable symmetric (**c**) and stable asymmetric (**d**) two-hump solitons at $n = 2$, $p_i = 2.5, \alpha = 1.8$. The energy flow (**e**) and propagation constant (**f**) versus p_i for symmetric "s" and asymmetric "a" families of one-hump solitons at $n = 1, \alpha = 1.2$. *Vertical dashed lines* in (**e**) and (**f**) indicate the borders of stability domains $p_i = p_i^{cr}$ for symmetric modes. Asymmetric solitons addressed in the panels (**e**) and (**f**) are stable. The profiles in panels (**a**) and (**b**) correspond to circles in panels (**e**) and (**f**)

The existence of asymmetric states in a system where gain landscape is symmetric and all other parameters are uniform, i.e. the *symmetry breaking*, is an unexpected result. Indeed, unlike in conservative systems, the understanding of the phenomenon cannot be related to the energetic arguments. Our system also does not allow for reduction to a simpler discrete model, as this happens, say, in the case of a double-well potential. Moreover, in our case the symmetry breaking occurs even for a single gain channel in contrast to conservative systems (where at least two potential minima are required).

We performed numerical study of the entire branches of the solutions and studied their stability [Fig. 4]. In Fig. 4e, f for $n = 1$ we observe two branches of the solutions, one of them corresponding to the symmetric solitons, and another one, bifurcating form the symmetric branch at certain value $p_i = p_i^{cr}$, that corresponds to the asymmetric solutions (having smaller amplitudes and larger widths as compared to the symmetric ones). The dependences $U(p_i)$ and $b(p_i)$ for both branches well reproduce the estimates presented above. The linear stability analysis of the modes is performed by plugging in the perturbed field $q = \left(w + ve^{i\delta\xi}\right)e^{ib\xi}$ into Eq. (1) with $\gamma_0 = 0$ and performing linearization around w. For odd numbers of amplifying channels, exactly at the bifurcation point p_i^{cr}

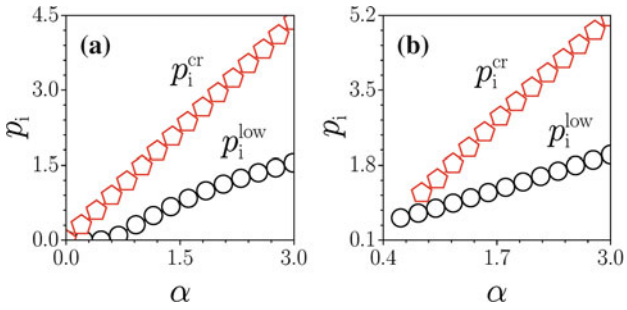

Fig. 5 The domain of existence ($p_i \geq p_i^{low}$) and stability domain ($p_i^{cr} \geq p_i \geq p_i^{low}$) for one-hump (**a**) and three-hump (**b**) solitons on the plane (α, p_i)

the branch of symmetric solutions looses its stability, while the stable asymmetric branch emerges. Since the asymmetric modes appear in pairs (corresponding to the left and right shifts of the maximum outwards the origin) at the point where the symmetric mode becomes unstable we deal with the pitchfork bifurcation.

For small p_i symmetric solitons broaden dramatically and may expand far beyond the region with gain. Increase of p_i results in growth of the peak amplitude and progressive localization of the soliton inside the amplifying domains. For small values of α the symmetric one-hump solitons can be found even for $p_i \to 0$, for moderate and high values of α such solitons exist only above certain minimal value of gain coefficient p_i^{low} [see Fig. 5a].

For even n the symmetric modes appear unstable in the whole domain of existence, and the only stable modes are asymmetric ones. In this case the dependencies $U(p_i)$ for symmetric and asymmetric modes do not overlap and no bifurcations occur. Except for stability, other properties of modes supported by even and odd number of amplifying channels are similar.

In dissipative multi-hump solitons both real and imaginary parts of the field w_r and w_i change their signs in neighboring channels with gain, while the field amplitude u is nonzero even in the regions between the channels [see Fig. 4c, d]. Indeed, let us assume that at some point $\tilde{\eta}$ the field is zero, i.e. $u(\tilde{\eta}) = 0$. Since $u(\eta)$ is nonnegative, in the vicinity of $\tilde{\eta}$ we have: $u(\eta) = \mathcal{O}((\eta - \tilde{\eta})^2)$ and $j_\eta = \mathcal{O}((\eta - \tilde{\eta})^4)$. Expanding $u(\eta)$ and $j(\eta)$ in the Taylor series in the vicinity of $\tilde{\eta}$, from Eqs. (11) we find subsequently that all the expansion coefficients are zero, what means that if u becomes zero at some point, then $u(\eta) \equiv 0$ and $j(\eta) \equiv 0$.

The critical gain, at which the bifurcation of asymmetric mode from symmetric branch occurs, increases almost linearly with α, so that the domain of stability of symmetric solitons $p_i^{cr} \geq p_i \geq p_i^{low}$ expands with α (Fig. 5a). The stability domain of symmetric three-hump soliton expands almost linearly with increase of α (Fig. 5b).

With increase of the number of the gain channels the picture becomes even richer. When the number of channels is odd, the number of asymmetric modes that can be stable all together for fixed p_i and α values increases. This feature indicates on the presence of several stable attractors (multistability) in multichannel

landscapes. The critical value of the gain coefficient (i.e. the bifurcation point) p_i^{cr} also grows with n, reaching however certain saturation value. In particular, for $\alpha = 1.5$ this value is about 2.59 and it is reached already at $n = 7$.

3 Localized Gain and Nonlinear Dissipation with Lattice

Now, following [25] we turn to the existence and stability of dissipative defect modes in periodic optical lattices. The problem is described by the NLS equation

$$iq_\xi = -\frac{1}{2}q_{\eta\eta} - R(\eta)q + i\gamma(\eta)q + (\sigma - i\alpha)|q|^2 q, \tag{12}$$

where $R(\eta)$ is a periodic function with the period a, *i.e.* $R(\eta) = R(\eta + a)$. In this section we concentrate on the gain which is nonzero only in a finite domain. More specifically we choose

$$\gamma(\eta) \equiv 0 \quad \text{for } |\eta| > a/2. \tag{13}$$

Now Eqs. (4) should be rewritten as

$$bu = \frac{u_{\eta\eta}}{2} - \frac{j^2}{2u^3} - \sigma u^3 + Ru, \quad j_\eta = 2\gamma u^2 - 2\alpha u^4 \tag{14}$$

The propagation constant of an exponentially localized mode must belong to a gap in the spectrum of the periodic "potential" $R(\eta)$, i.e. to an empty domain in Fig. 6a. Indeed, let us consider the limit $\eta \to \infty$. From the second of Eqs. (14) and (13) it follows that $j = 2\alpha \int_\eta^\infty w^4 d\eta$ for $\eta > \eta_0$. Thus (i) there exists an energy flow outwards the impurity, $j > 0$, and (ii) the following relation (obtained using l'Hôpital's rule) $\lim_{\eta\to\infty} j/u^2 = -\alpha \lim_{\eta\to\infty} u^3/u_\eta$ holds. For localized modes with a finite energy flow U, i.e. with u^2 decaying more rapidly than $1/\eta$, one obtains that the above mentioned limit is zero as long as u_η does not acquire zero values [indeed, in this case $u^3/u_\eta = -1/(2u^{-2})_\eta = o(\eta^{-1})$]. Otherwise, if u_η changes sign at large η, one also verifies that the established condition $j > 0$ can hold only if the above mentioned limit is zero. Hence, j^2/u^3 decays faster than u and can be neglected at $\eta \to \infty$ and b satisfies the Hill equation

$$b\tilde{u} = \frac{1}{2}\tilde{u}_{\eta\eta} + R(\eta)\tilde{u}. \tag{15}$$

Thus, to guarantee the decaying asymptotic of the mode b must belong to a gap of the lattice spectrum. We emphasize the importance of the sufficiently fast decay of the coefficient of linear dissipation.

For numerical study of the modes, we chose $R(\eta) = p_r \cos^2(2\eta)$ to model the lattice, whose spectrum is shown in Fig. 6a and assume that $\gamma(\eta) \propto R(\eta)$ on one or several periods of $R(\eta)$. For instance, if amplification is realized only in one

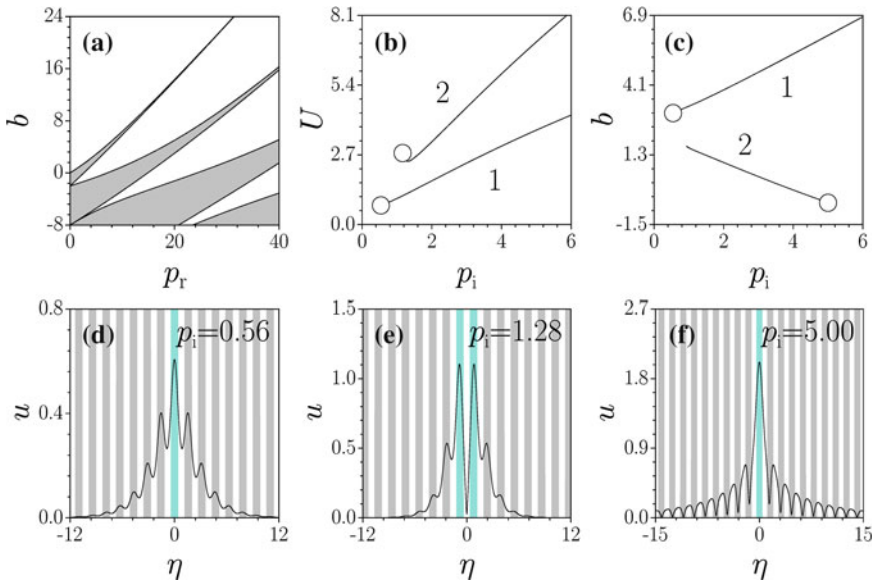

Fig. 6 (**a**) Band spectrum of $R(\eta)$. *Gray* (*white*) regions indicate the allowed bands (*gaps*). (**b**) Energy flow vs gain parameter for the one-hump (*curve 1*) and two-hump (*curve 2*) modes in focusing medium. (**c**) Propagation constant vs gain parameter for one-hump modes in focusing (*curve 1*) and defocusing (*curve 2*) media. Circles in (**b**) and (**c**) correspond to modes shown in panels (**d–f**). In all cases $\alpha = 1$ and $p_r = 5$. All shown modes are stable

period, then $\gamma(\eta) = p_i \cos^2(2\eta)$ for $|\eta| \le a/2 = \pi/4$ and $\gamma \equiv 0$ for $|\eta| > a/2$. Further we set $p_r = 5$ and vary p_i and α.

When the propagation constant belongs to the semi-infinite gap (i.e. lies above all gray domains in Fig. 6a), the defect modes can be obtained in focusing medium only. The emerging branches of the modes are shown in Fig. 6b, while examples of their profiles are presented in the lower row of the figure. Now b is determined by the gain/loss as shown in Fig. 6c. Notice that depending on whether the gain is applied to one or to two channels the attractor is a one-hump [panels (d) and (f)] or a two-hump [panel (e)] mode.

For b in the first finite gap we have found the stable defect modes in the defocusing medium. The dependence $b(p_i)$ for such modes is shown in Fig. 6c, and an example of the profile of such mode is given in the panel (f).

Like in the conservative case, when the propagation constant approaches a gap edge the defect modes extend far beyond the lattice channels where amplification is applied, exhibiting pronounced shape oscillations which approach properly normalized Bloch states $\tilde{w}$ bordering the respective gap edge. At fixed α in a focusing medium increase of the gain p_i results in progressive increase of the mode peak intensity and in gradual contraction of light into the amplifying channel (Fig. 6d). In defocusing medium the peak amplitude also grows with p_i but the modes possess strongest localization at intermediate values of p_i and may extend

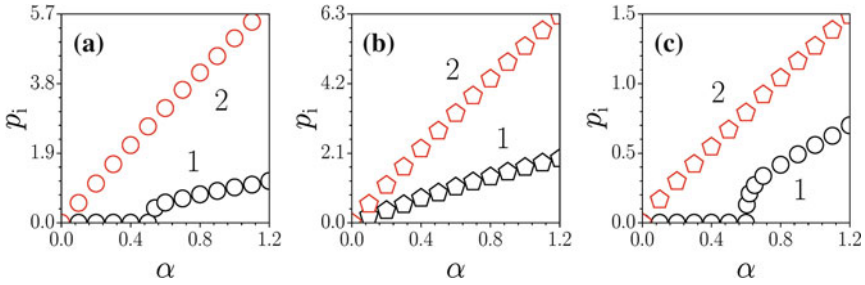

Fig. 7 Domains of existence for stable one-hump and two-hump modes (boundaries denoted by *circles* and *pentagons*, respectively) in defocusing (**a**, **b**) and focusing (**c**) media. In the defocusing medium either one-hump (**a**) or two-hump (**b**) modes modes exist between the *curves 1* and *2*. In the focusing medium one-hump and two-hump modes exist above the *curves 1* and *2*, respectively

dramatically across the lattice when the gain intensity becomes too high (Fig. 6f). The energy flow U monotonically grows with p_i (Fig. 6b). For sufficiently small and moderate nonlinear losses one-hump modes exist even at $p_i \to 0$ in both focusing and defocusing media. In this limit the b value approaches the band-edge, the amplitude of the mode becomes small and its width grows dramatically. The nonlinear losses diminish as well, and the balance between gain and losses requires the linear gain to go to zero.

Higher-order modes possess energy flow threshold for their existence (curve 2 in Fig. 6b). Increase of p_i results in monotonic growth of b in focusing medium accompanying mode contraction (Fig. 6c, curve 1) and decrease of b in defocusing medium resulting in mode expansion across the lattice when b reaches the lower edge of the gap at sufficiently large p_i (Fig. 6c, curve 2).

The domains of existence of dissipative lattice modes on the plane (α, p_i) are shown in Fig. 7. In the focusing medium one-hump modes exist for all values of p_i above curve 1 in Fig. 7c, while two-hump modes are found for p_i values above curve 2 (the minimal value of p_i necessary for existence of two-hump modes grows almost linearly with α). The situation is more complicated in defocusing medium where one-hump (Fig. 7a) and two-hump (Fig. 7b) modes exist only in a finite domain of p_i between curves 1 and 2. The presence of upper limit for the linear gain is connected with delocalization of high-power modes whose propagation constants approach lower edge of first finite gap with increase of p_i.

4 Gain at a Surface

Now we turn to the impact of non-conservative surfaces on the existence and properties of the localized modes. More specifically, following Ref. [24] we address the properties of truly stationary dissipative solitons forming at the edge

of semi-infinite lattice and existing due to the balance between localized gain in a near-surface lattice channel and strong two-photon absorption in a cubic medium. The model describing such modes reads

$$iq_\xi = -\frac{1}{2}q_{\eta\eta} - [R(\eta) - i\gamma(\eta)]q + (\sigma - i\alpha)|q|^2 q, \tag{16}$$

where

$$R(\eta) = \begin{cases} p_r \sin^2(2\eta) & \text{for } \eta > 0 \\ 0 & \text{for } \eta \le 0 \end{cases} \tag{17}$$

with p_r being the depth of the lattice. We suppose that the localized gain, whose profile is described by the function $\gamma(\eta)$, is realized in the vicinity of a near-surface lattice channel. In the simplest case we consider $\gamma(\eta)$ exactly coinciding with $R(\eta)$ in the first channel of the lattice [c.f. (10)] i.e. $\gamma(\eta) = p_i \sin^2(2\eta)$ in the first channel $\gamma(\eta) \equiv 0$ otherwise.

Exponentially localized modes in periodic media [4] and conservative surface modes [21, 37, 56] emerge when the propagation constant b falls into one of the gaps of spectrum of periodic guiding structure. It turns out that this is also true in the case of dissipative surface solitons. To prove this, we rewrite Eq. (16) in terms of the real functions $u(\eta)$ and $v(\eta) \equiv \theta_\eta$:

$$u_{\eta\eta} - 2bu - v^2 u - 2\sigma u^3 + 2Ru = 0, \quad (vu^2)_\eta - 2\gamma u^2 + 2\alpha u^4 = 0 \tag{18}$$

and consider first the limit $\eta \to -\infty$. Since in this limit $R \equiv 0$, one finds the explicit asymptotics

$$u = A_- e^{\sqrt{2b}\eta} + \sigma A_-^3 e^{3\sqrt{2b}\eta}/(8b) + \mathcal{O}(e^{5\sqrt{2b}\eta}) \tag{19a}$$

$$v = -\alpha A_-^2 e^{2\sqrt{2b}\eta}/(2\sqrt{2b}) + \mathcal{O}(e^{4\sqrt{2b}\eta}) \tag{19b}$$

where A_- is a real constant. The first consequence of the obtained asymptotics is that localized solutions exist only in domains outside the linear spectrum, i.e. at $b > 0$. The second conclusion is that in the asymptotic region $v^2 u \sim \exp(5\sqrt{2b}\eta)$, i.e. decays faster than u^3. Thus, at $\eta \to -\infty$ the solution $q(\eta, \xi)$ exponentially approaches the standard stationary NLS soliton.

Similar, but more sophisticated, analysis can be performed for the limit $\eta \to \infty$, where the linear lattice is present. One still can prove that $v^2 u$ decays faster than u^3, and thus the leading order for the field amplitude is given by the Floquet theorem: $u = A_+ \exp(-\mu\eta) P_n(\eta)$ where $P_n(\eta)$ is $\pi/2$ or π periodic function, μ is the Floquet exponent which is determined by the detuning of the propagation constant from the band-edge towards the n-th stop gap (the lower and upper boundary of n-th gap will be designated by b_n^- and b_n^+, respectively, the number of the first finite gap is set to be $n = 1$, while the semi-infinite gap is denoted by $n = 0$), and A_+ is the normalization constant (see e.g. [4] for more details).

Thus, for the existence of a localized surface mode one has to require that the propagation constant simultaneously lies beyond the allowed band of the linear spectrum of the uniform medium and belongs to a gap of the periodic structure. The respective domains will be termed total gaps (to distinguish them form the own gaps of the lattice). For example, for the case of $p_r = 5$, studied below in details, there are only two total gaps: the semi-infinite total gap $b \in (2.875, \infty)$ and the total finite gap $(0, 1.840)$ while the lattice gaps, are given by $(2.875, \infty)$, $(-0.645, 1.840)$, etc. i.e. $b_0^- = 2.875, b_1^+ = 1.840, b_1^- = -0.645$ etc. (notice that the band-gap structure of our lattice is identical to the one shown in Fig. 6a where b must be substituted by $b + p_r$.)

The established constrains on b, impose limitations on the possibility of the excitation of the surface modes. The mismatch between the boundaries of the gaps in the left and right hand structures implies the existence of a threshold of the energy flow U_{cut}. Indeed let us consider a mode with b belonging to the total semi-infinite gap and approaching b_0^-, i.e. $0 < b - b_0^- \ll 1$. Considering $\eta > 0$, we observe that when $b \to b_0^-$ the maximum of the amplitude u tends to zero: $u_{\max} \to 0$ (see e.g. [13]). On the other hand, considering (4) at $\eta < 0$ as an ODE defining the shape of the soliton, the smallness of u means that the terms $v^2 u$ in Eqs. (18) can be neglected and the asymptotic behavior is described by the conservative NLS equation, i.e. by (19a). Since, b does not go to zero (due to finite value of b_0^-), also the nonlinear term u^3 can be neglected and the field behavior is described by the linear equation $u_{\eta\eta} = 2bu$. Thus the function u must be exponentially decaying, what for the linear ODE at hand is possible only if $u_\eta(0) = \sqrt{2b}u(0)$. This is an extra condition, in addition to the continuity of q and q_η, which must be satisfied at the boundary, i.e. at $\eta = 0$. In a general situation this is impossible with only two available constants A_+ and A_-, which are determined by the total energy U and by the properties of the linear lattice at $\eta > 0$. In other words, by assuming that the amplitude of the mode can go to zero we have arrived at a contradiction. Thus, there exists a minimal threshold value of $u_{\max}$ above which surface modes can exist.

Typical profiles of dissipative surface solitons in a focusing medium are shown in Fig. 8d. For low values of p_i the surface solitons expand considerably into the lattice region and acquire shape reminiscent to shape of Bloch state bordering the respective gap edge. We notice that solitons may also form in the near-surface lattice channel even when the gain is displaced by a distance η_s with respect to the first maximum of the lattice. The energy flow of surface solitons first decreases with η_s, and then increases when shift approaches maximal value beyond which surface soliton can not form in the first lattice channel (Fig. 8b). The maximal possible shift of gain landscape quickly increases with p_i and saturates already at $p_i = 3$ (see Fig. 8c). Remarkably, surface solitons may form not only when gain profile is shifted into the depth of the lattice (positive η_s), but also when gain is shifted into uniform medium (negative η_s). When shift η_s becomes sufficiently large solitons may form in second, third, etc, channels of the lattice.

In the case of defocusing medium localized gain can support dissipative gap solitons featuring characteristic oscillating tails (inside the lattice, see Fig. 8e, f).

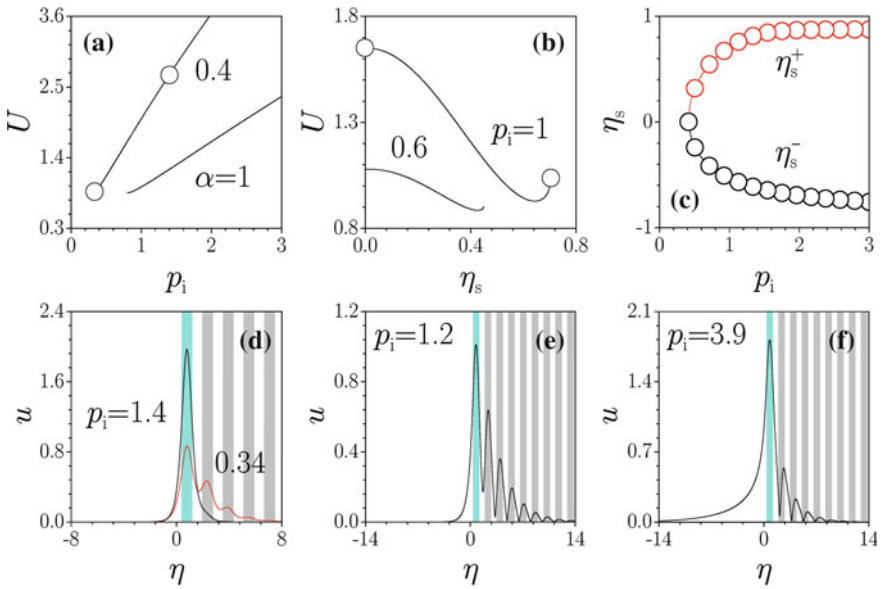

Fig. 8 (**a**) Energy flow of surface soliton vs p_i in focusing medium. *Circles* correspond to solitons in (**d**). (**b**) Energy flow of surface soliton in focusing medium vs η_s at $\alpha = 0.5$. (**c**) Maximal positive (η_s^+) and negative (η_s^-) shifts of amplifying domain with respect to $R(\eta)$ at which surface solitons still exist vs p_i at $\alpha = 0.5$. (**e**) and (**f**) show profiles of gap surface solitons in defocusing medium at $\alpha = 1$. All shown modes are stable

The propagation constant of such solitons falls into the finite total gap, $b \in (0, b_1^+)$ and decreases with p_i. Like their counterparts in focusing medium, now the solitons emerging from the finite total gap exist above the minimal value of gain coefficient p_i^{low}. However, due to finiteness of the gap, there exists also the upper limit for the linear gain p_i^{upp} at which b reaches zero value, i.e. dissipative gap solitons can be found for $p_i^{low} \le p \le p_i^{upp}$. Respectively, the energy flow takes on the values from the finite interval, where it is the increasing function of p_i. When $p_i \to p_i^{low}$ gap surface solitons expand dramatically into lattice region (Fig. 8e), but remain well localized inside uniform medium in accordance with the asymptotics (19). The best overall localization is achieved for intermediate p_i values. When b approaches zero (respectively p_i approaches p_i^{upp}) the gap surface solitons again become poorly localized due to appearance of long tails in the uniform medium (see Fig. 8f). The domains of existence of dissipative surface solitons in both focusing and defocusing media on the (α, p_i)-plane are shown in Fig. 9. Minimal gain p_i^{low} required for the existence of solitons in uniform medium, as well as the width $p_i^{upp} - p_i^{low}$ of the band of gain coefficients where solitons exist in defocusing medium, increase with nonlinear losses α.

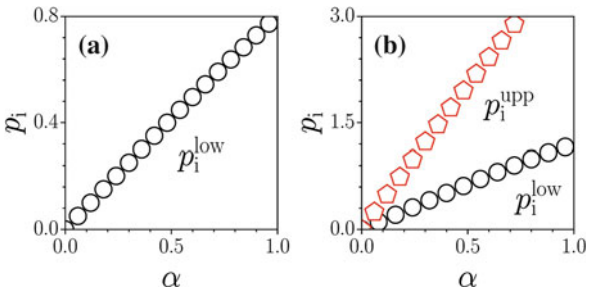

Fig. 9 Domains of existence of surface solitons in focusing (**a**) and defocusing (**b**) media. In the focusing medium surface solitons exist for all p_i exceeding lower value p_i^{low}, while in defocusing medium surface solitons exist between lower p_i^{low} and upper p_i^{upp} values of gain coefficient

Finally, we analyzed stability of obtained soliton solutions and verified that they are exceptionally robust and can withstand even strong shape deformations almost in the entire existence domain (we considered the lowest branches only).

5 Symmetry Breaking in Homogeneous Two-Dimensional Media

In the above sections we have considered several types of dissipative solitons supported by the localized gain in 1D systems. It turns out that a localized source in the presence of nonlinear losses allows one to obtain stable dissipative solitons also in a 2D dissipative NLS equation. Following [27], we consider the model

$$iq_\xi = -\frac{1}{2}\nabla^2 q + i\gamma(r)q - |q|^2 q - i\alpha|q|^2 q, \tag{20}$$

where $\mathbf{r} = (\eta, \zeta)$ is a vector in the transverse plane, $\nabla \equiv (\partial/\partial\eta, \partial/\partial\zeta)$, the localized gain $\gamma(r)$ is a real decaying function of $r = |\mathbf{r}|$, and other notation are identical to ones, used above for 1D settings. It will be convenient to represent $\gamma \equiv p_i f(r)$, where p_i is the gain coefficient and $f(r)$ is a real decaying function with $\max\{f(r)\} = f(0) = 1$.

Solutions of Eq. (20) predicting dissipative solitons are searched in the form

$$q = w(\mathbf{r})e^{ib\xi}, \quad w(\mathbf{r}) = w_r + iw_i = u(\mathbf{r})e^{i\theta(\mathbf{r})}, \tag{21}$$

where, as well as in the 1D case, b is the propagation constant. Now Eqs. (4) are replaced by

$$-2bu + \nabla^2 u - u\mathbf{v}^2 + 2u^3 = 0, \quad \nabla\cdot(u^2\mathbf{v}) + 2\gamma(r)u^2 - 2\alpha u^4 = 0, \tag{22}$$

where $\mathbf{v} = \nabla\theta$. We are interested in the localized solutions with zero asymptotics: $u, |\mathbf{v}| \to 0$ at $r \to \infty$.

First of all we observe that by properly choosing the gain one can construct an exact solution of Eqs. (22). To this end we notice that for $\mathbf{v} = 0$ the first of Eqs. (22) has the well known radially symmetric Townes soliton solution, which we denote as $w_T(r)$. Then, in order to support the existence of the dissipative Townes soliton, the gain must be chosen in the form $\gamma_T(r) = \alpha w_T^2(r)$. This also leads us to the conclusion that for any $\gamma(r) \neq \gamma_T(r)$ dissipative solitons with a trivial phase do not exist.

When $\mathbf{v}$ is not necessarily zero, stationary localized solutions exist only for $b > 0$; what follows from the limit $r \to \infty$, where one can neglect both nonlinear terms (i.e. $\mathbf{v}^2$ and u^3) in Eqs. (22). From (20) one readily obtains the equation for the balance between conservative terms

$$bU + \frac{1}{2}\int |\nabla w|^2 d\mathbf{r} = \int |w|^4 d\mathbf{r}, \quad U = \int u^2 d\mathbf{r} \tag{23}$$

On the other hand, the balance between gain and dissipation is expressed by

$$\int \gamma(r)|w|^2 d\mathbf{r} = \alpha \int |w|^4 d\mathbf{r}. \tag{24}$$

This condition imposes restrictions on the range of variation of b. Indeed, from Eqs. (24) and (23), combined with the estimate $\int \gamma u^2 d\mathbf{r} \leq p_i U$, we obtain $\int |\nabla w|^2 d\mathbf{r} \leq (p_i/\alpha - b)U$. Hence $b \in (0, p_i/\alpha)$.

We consider the simplest Gaussian gain profile $\gamma(r) = p_i e^{-r^2/d^2}$. Typical shapes of the simplest radially symmetric dissipative solitons obtained with the relaxation method are shown in Fig. 10a. For a given α, the soliton parameters (including b) are dictated by the gain coefficient. When p_i is sufficiently small the solitons are broad. The field can expand far beyond the spatial region where the gain is realized due to the energy flow outward the amplifying domain. Growth of p_i is accompanied by progressively increasing localization. For $\alpha \gtrsim 2$ with increase of p_i the soliton shape takes on the form of a narrow peak superimposed on broader beam (Fig. 10a).

The energy flow U of a dissipative soliton is a nonmonotonic function of the gain coefficient p_i (Fig. 10b). For small and moderate nonlinear losses the initial decrease of U is followed by its growth, and then again replaced by decrease as p_i increases. In the cutoff point p_i^{co} the tangential line to $U(p)$ is vertical, but the value $U^{co} = U(p_i^{co})$ remains finite. We notice that it is possible to find the second branch of solutions vanishing in the same point (p_i^{co}, U^{co}) for which energy flow increases with p_i in the vicinity of cutoff, i.e. in (p_i^{co}, U^{co}) two soliton families smoothly join, rather than one family terminates. However, this second branch is unstable as the linear stability analysis predicts. The character of $U(p_i)$ dependence changes dramatically when α is sufficiently large (c.f. the curves with $\alpha = 1.4$ with ones with $\alpha = 1.6$ and $\alpha = 1.9$ in Fig. 10b). In this case U grows with p_i everywhere except for a region close to the cutoff. Interestingly, this change in the behavior of $U(p_i)$ accompanies the tendency for development of a narrow peak in the center of soliton. The propagation constant b increases monotonically with p_i

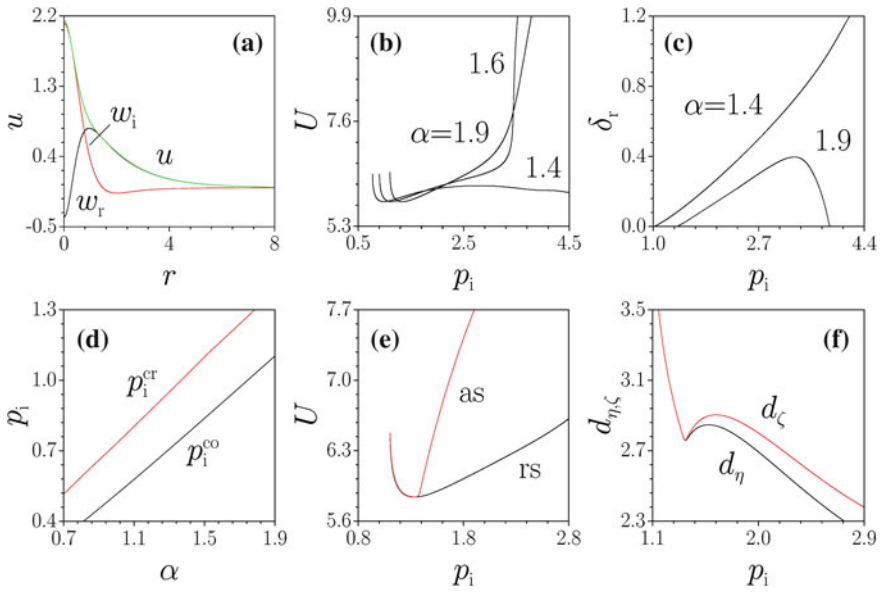

Fig. 10 (**a**) Profile of stable radially symmetric dissipative solitons at $p_i = 4, \alpha = 1.9$. Real, imaginary parts of the field, and field modulus are shown with *black*, *red*, and *green lines*, respectively. Energy flow (**b**) and real part of perturbation growth rate (**c**) of radially symmetric solitons vs p_i. (**d**) The domain of stability on the plane (α, p_i). (**e**) Bifurcation of asymmetric soliton family from symmetric one at $\alpha = 1.9$. (**f**) $d_{\eta,\zeta}$ vs p_i for asymmetric soliton family. In all cases $d = 1.5$

for small and moderate values of α, but when α approaches 2 the dependence $b(p_i)$ becomes nonmonotonic. At a fixed width of the amplifying domain, p_i^{co} grows almost linearly with increase of nonlinear losses (Fig. 10d). Meantime, p_i^{co} diminishes with increase of d, so that at $d \to \infty$ we naturally recover the case of medium with uniform gain where solitons can be found for any p_i.

The stabilization of 2D solitons means that for the respective initial conditions the localized gain does not induce collapse, which is arrested by the nonlinear dissipation. On the other hand the spatial localization of gain prevents growth of the background noise in domains outside amplifying channel. This is in contrast to the case of Kerr medium with uniform gain and two-photon absorption where solitons are unstable even in 1D geometries [41]. These facts have been numerically verified by the linear stability analysis with the ansatz $q = [w + v_1 e^{\delta\xi + in\varphi} + v_2^* e^{\delta^*\xi - in\varphi}]$, where n is an integer azimuthal index. Solution of the respective linearized equations reveals a surprising result: the most destructive perturbations correspond to $n = 1$, rather than to $n = 0$. The typical dependencies of real part of perturbation growth rate δ_r on p_i for $n = 1$ are shown in Fig. 10c. For small and moderate nonlinear losses δ_r vanishes for any n when $p_i^{co} < p_i < p_i^{cr}$, where p_i^{cr} is some critical value. Thus the dissipative solitons are linearly stable in the region adjacent to the cutoff p_i^{co}. The stability domain slowly expands with increase of α (Fig. 10d) and broadens

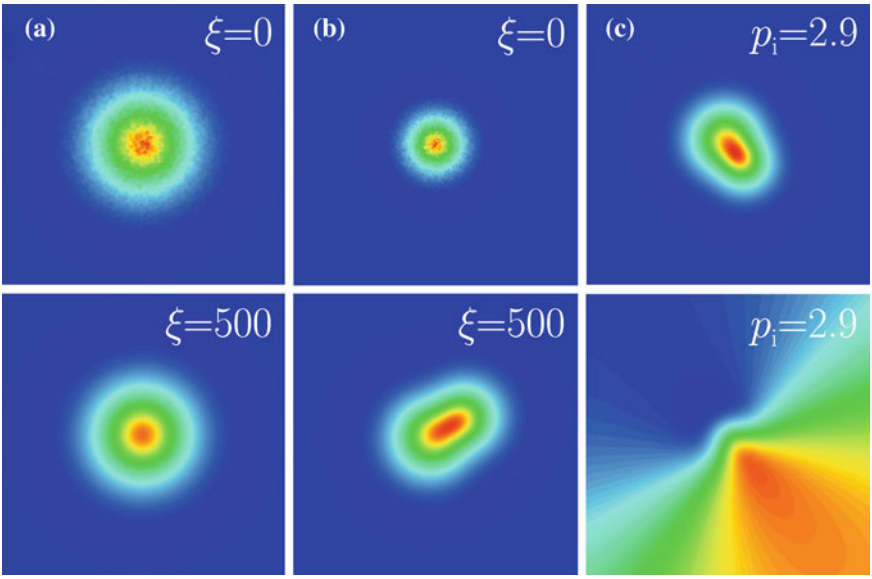

Fig. 11 Stable propagation of radially-symmetric solitons at (**a**) $p_i = 0.8, \alpha = 1.2$, and (**b**) transformation of unstable radially-symmetric soliton into asymmetric stable state at $p_i = 2.0, \alpha = 1.2$. (**c**) Field modulus (*top*) and phase (*bottom*) distributions in stable asymmetric dissipative soliton at $p_i = 2.9$ and $\alpha = 1.9$. In all cases $d = 1.5$

considerably with decrease of the width d of amplifying domain. At small and moderate α inside the instability domain δ_r increases monotonically with p_i, but for sufficiently high nonlinear losses the character of this dependence changes (Fig. 10d) and another stability domain appears also at high p_i values. This stability domain is limited since with further increase of p_i the perturbations with $n = 2$ become destructive. Results of linear stability analysis are supported by direct propagation of perturbed radially-symmetric dissipative solitons. Stable propagation of a relatively broad soliton taken from stability domain adjacent to p_i^{co} is shown in Fig. 11a.

Surprisingly, the development of instability for perturbed unstable radially symmetric solitons results in their transformation into strongly asymmetric non-rotating dissipative soliton whose center is slightly displaced from the origin towards the periphery of amplifying domain (Fig. 11b). Such states can be excited with Gaussian beams too, i.e. they are attractors with large basin. The energy flow and propagation constant of the asymmetric soliton remain the same as long as $p_i, d,$ and α are fixed and only the beam orientation changes for different inputs and noise realizations. Thus the medium with localized gain and nonlinear losses can support strongly asymmetric dissipative solitons despite the fact that all parameters in the system are either uniform (diffraction, nonlinearity, and losses) or radially symmetric (gain). The asymmetric solitons are characterized by a specific phase distribution (Fig. 11c) that is asymmetric along longer axis of the beam and symmetric along its shorter axis.

Using a method of direct propagation we obtained the entire family of asymmetric solitons. The dependencies of energy flow and integral widths

$$d_\eta = 2\left(\frac{1}{U}\int \eta^2|q|^2 d\mathbf{r}\right)^{1/2}, \quad d_\zeta = 2\left(\frac{1}{U}\int \zeta^2|q|^2 d\mathbf{r}\right)^{1/2} \tag{25}$$

on p_i are shown in Fig. 10e, f, respectively. The family of asymmetric solitons bifurcates from the family of radially symmetric solitons with increase of p_i. The bifurcation occurs exactly in the point p_i^{cr} where the radially symmetric solitons become unstable. With increase of p_i the asymmetry of soliton shape increases. The obtained asymmetric solitons propagate stably in the presence of small-scale input noise.

6 Radially Symmetric, Rotating, and Azimuthally Modulated Vortex Solitons Supported by Localized Gain

Vortex solitons are self-sustained excitations carrying a nonzero angular momentum and topological phase singularities [14]. In uniform focusing local media, vortex solitons exhibit ring-like profiles, a property that makes them prone to azimuthal modulation instabilities. Such instability can be suppressed in dissipative media by various mechanisms. Stable vortex solitons have been found in laser amplifiers with saturable gain and absorption and in systems described by the complex cubic-quintic Ginzburg-Landau equation.

In this section, we present a rich variety of stable vortex solitons and vortex complexes existing in media with suitably shaped gain landscapes, cubic nonlinearity, and two-photon absorption. Following [26], we consider a model

$$iq_\xi = -\frac{1}{2}\nabla^2 q + R(\mathbf{r})q + i\gamma(\mathbf{r})q + (\sigma - i\alpha)|q|^2 q, \tag{26}$$

which is a generalization of the model (20). In the latter equation $R(\mathbf{r})$ stands for possible refractive index modulation, $\gamma(\mathbf{r})$ is not required to be necessarily radially symmetric, and other notations are as defined above.

6.1 Vortex Solitons in the Square Photonic Lattices with Amplifying Channels

Now we show that stable vortex solitons in focusing and even defocusing Kerr media with imprinted refractive index periodicity (an optical lattice) can be supported by properly engineered localized gain landscapes. More specifically we consider the infinite harmonic lattice of the form:

$$R(\mathbf{r}) = -p_r \cos^2(\pi\eta/a)\cos^2(\pi\zeta/a) \tag{27}$$

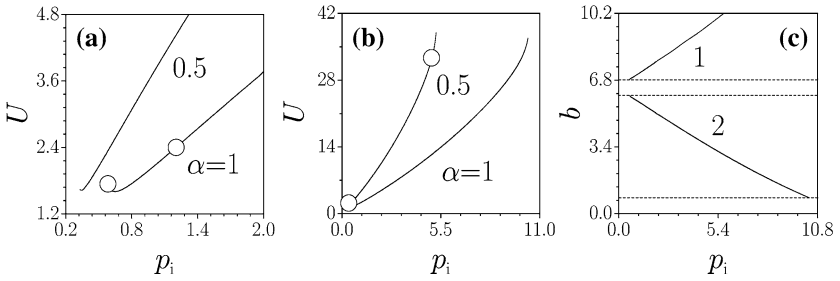

Fig. 12 Energy flow of off-site dissipative vortex solitons versus p_i in focusing (**a**) and defocusing (**b**) media. Points marked by circles correspond to solitons shown in Figs. 13 (**a–d**). (**c**) Propagation constant versus p_i for solitons in focusing (*curve 1*) and defocusing (*curve 2*) media at $\alpha = 1$. *Dashed lines* indicate gap edges. All solitons, which belong to the curves shown in panels (**a–c**), are stable

characterized by its depth p_r, and the spatial period a. The gain term appears as superposition of a few amplifying channels: $\gamma(\mathbf{r}) = p_i \sum_{\mathbf{a}_j} R_0(\mathbf{r} + \mathbf{a}_j)$, where $R_0(\mathbf{r}) \equiv R(\mathbf{r})$ inside the single period $0 < \eta, \zeta < a$ and vanishes outside it; the lattice vectors in the (η, ζ)-plane are introduced as $\mathbf{a}_1 = (a, 0), \mathbf{a}_2 = (0, a)$, and p_i is the gain parameter.

Using the ansatz (21) in Eq. (26), in the presence of the optical lattice we rewrite the equations of the balance between the gain and dissipation, as well as between diffraction and nonlinearity in the form [c.f. (23) and (24)]

$$2Ub = \int \left[-\sigma |w|^4 - 2\mathbf{r} \cdot \mathbf{v}\mathcal{D} - |w|^2 \nabla \cdot \mathbf{r} R(\mathbf{r}) \right] d\mathbf{r} \tag{28}$$

$$2Ub = \int \left(-2\sigma |w|^4 - 2R|w|^2 - |\nabla w|^2 \right) d\mathbf{r} \tag{29}$$

where $\mathscr{D}(\mathbf{r}) \equiv \alpha |w|^4 - \gamma(\mathbf{r}) |w|^2$. From the diffraction-nonlinearity balance (29) one can expect that the simplest vortex solitons in a focusing medium will form in the semi-infinite gap of the lattice spectrum, while in a defocusing medium, such solutions will emerge only in finite gaps, provided that the lattice is deep enough and at least one finite gap exists.

In computer simulations we used $p_r = 16$ and $a = \pi/2$, which guarantee the existence of the first finite gap. Then the branch of vortex solitons in a focusing medium may emerge from the semi-infinite gap $b > 6.81$, while the propagation constant should belong to the finite gap $(0.811, 6.029)$ in a defocusing medium (Fig. 12c).

Examples of the vortex soliton profiles are shown in Fig. 13. The numerical simulations were performed by the direct propagation method with the input beam carrying the unit topological charge: $q|_{\xi=0} = Ar \exp(-r^2/r_0^2) \exp(i\varphi)$, where parameters A and r_0 describe the input beam amplitude and width. The beams were

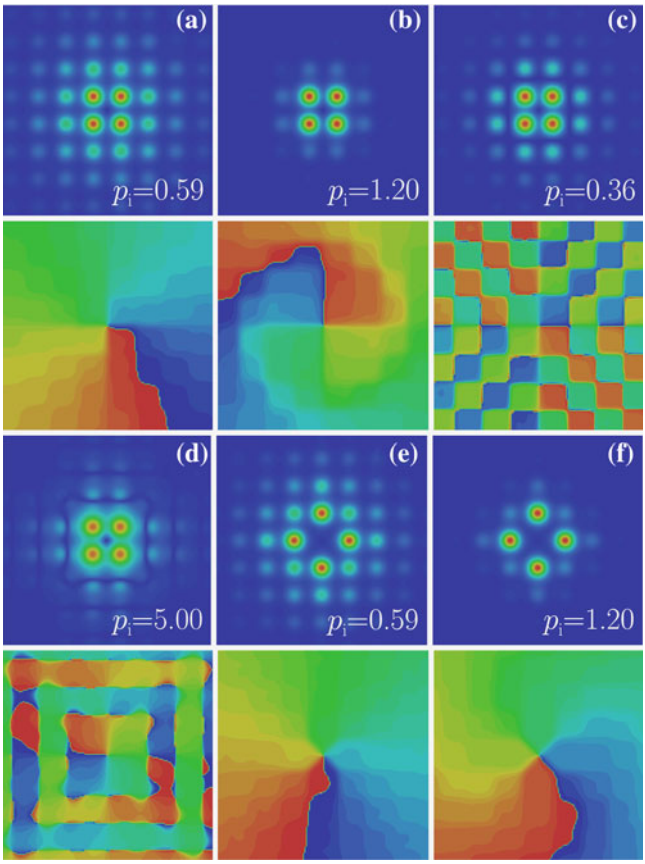

Fig. 13 Profiles of stable off-site vortex solitons in focusing medium at $\alpha = 1$ (**a**) and (**b**), and in defocusing medium at $\alpha = 0.5$ (**c**) and (**d**). (**e**), (**f**): Profiles of stable on-site vortex solitons in focusing medium at $\alpha = 0.1$. *Top panels* show field modulus, while bottom panels show phase distribution. The values of gain coefficient are indicated on the plots

propagated up to the huge distance ($\xi = 10^3$), ensuring that the obtained vortex solitons are stable. We explored a large domain of the input beam parameters resulting, however, in the same output profile. Thus, the output beam is an attractor with a large basin. The stability was additionally tested by propagating the obtained solitons in the presence of small input random perturbations.

Upon selection of the gain profile we supposed that there exist four gain channels described by a square-like gain landscape:

$$\gamma_1(\eta, \zeta) = R_0(\mathbf{r}) + R_0(\mathbf{r} + \mathbf{a}_1) + R_0(\mathbf{r} + \mathbf{a}_2) + R_0(\mathbf{r} + \mathbf{a}_1 + \mathbf{a}_2) \qquad (30)$$

since it favors formation of the off-site vortex solitons (Fig. 13a–d), or by

$$\gamma_2(\eta, \zeta) = R_0(\mathbf{r}) + R_0(\mathbf{r} + \mathbf{a}_1 + \mathbf{a}_2) + R_0(\mathbf{r} + \mathbf{a}_1 - \mathbf{a}_2) + R_0(\mathbf{r} + 2\mathbf{a}_1) \qquad (31)$$

since such cross-like configuration is favorable for the formation of the on-site vortices (Fig. 13e, f). In all the cases, the field maxima coincide with the local maxima of the gain and vortex solitons feature four pronounced bright spots.

For both focusing and defocusing media, there exist cutoff values of the energy flow, below which stable dissipative vortex solitons do not exist (Fig. 12a, b). In a focusing medium, increasing gain results in monotonic growth of the peak amplitude of a vortex soliton and its contraction to the four amplifying lattice sites (Fig. 13a, b). With growth of p_i the propagation constant shifts deeper into the semi-infinite gap. In contrast, for gap vortex solitons in a defocusing medium, increasing p_i results in diminishing of the propagation constant (Fig. 12c). Gap vortex solitons display the strongest localization for the intermediate p_i values b located in the middle of the gap; panels (c) and (d) in Fig. 13. In very deep lattices, the shape of the gap vortex approaches four well-localized bright spots with proper phase distribution imprinted on the top of them, while in shallow lattices, the vortex always extends considerably across the lattice. Expectably, the domain of existence of stable vortex solitons expands remarkably with growth of p_r. Notice, that if a topological charge of the input beam is bigger than one, the same gain landscape results in excitation of stable multipole solitons. If the gain distribution does not fit the lattice symmetry (for instance, only three channels are amplifying) any input also results in excitation of a multipole soliton occupying three lattice sites (see [26] for details).

6.2 Radially-Symmetric Vortex Solitons

In the setting discussed previously the presence of the optical lattice (or refractive index modulation) is essential for the formation of stable vortex states. Now, following [34], we consider the case in which stable vortices emerge in the absence of refractive index modulation, i.e. when $R(\eta, \zeta) = 0$. First we address vortex solitons supported by a single amplifying ring $\gamma(r) = p_i \exp[-(r - r_c)^2/d^2]$, where d and r_c are the ring width and radius, respectively. Nonlinearity is supposed to be focusing ($\sigma = -1$). In computer simulations we set $r_c = 5.25, d = 1.75$, and search for the spinning vortex solitons of the form $q = w(\mathbf{r}) \exp[i(b\xi + m\varphi)]$. A first important result, which was revealed in computer simulations, is that Eq. (26) does admit solutions in the form of stable radially symmetric vortex solitons, which means that the competition between localized ring-like gain and nonlinear losses results in simultaneous suppression of collapse and azimuthal modulation instabilities. We found that vortex solitons with charges at least up to $m = 6$ can be excited in ring-like gain landscapes, although vortices with high charges require higher gain levels for their formation. Typical shapes of stable symmetric vortex solitons with different topological charges ($m = 1, 2, 3$) are shown in Fig. 14.

The propagation constant, as well as all other soliton parameters, are determined by the gain and nonlinear loss coefficients p_i and α. Interestingly, for fixed values of p_i and α, stable vortex solitons with different charges can coexist (Fig. 14), but the

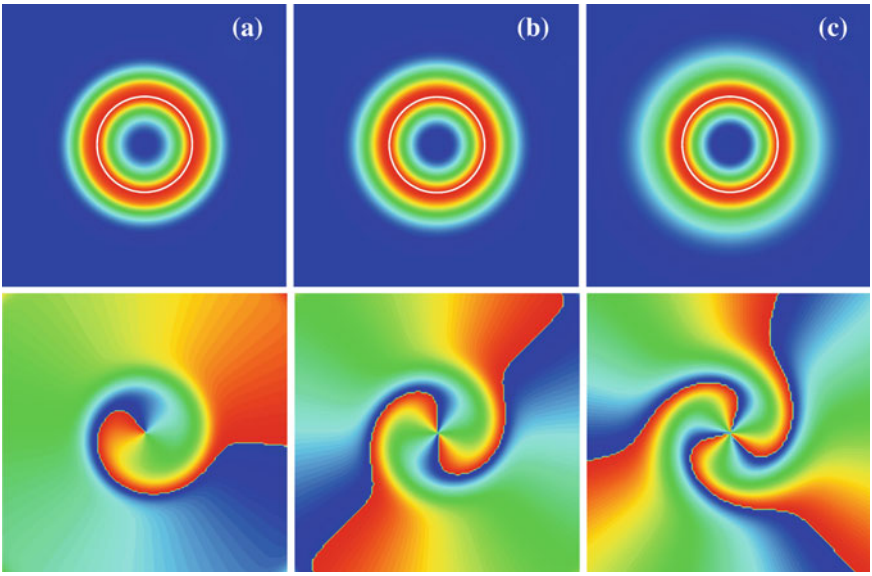

Fig. 14 Field modulus (*top*) and phase distribution (*bottom*) for stable vortex solitons with (**a**) $m = 1$, (**b**) $m = 2$, and (**c**) $m = 3$ at $\alpha = 2, p_i = 3$. *White circles* indicate maximum of gain ring

ones with higher topological charges are somewhat broader. The dependencies of the steady-state energy flow U and the ξ-component of the angular momentum $L = \int\int_{-\infty}^{\infty} \mathrm{Im}\left[\eta q^* \frac{\partial q}{\partial \zeta} + \zeta q^* \frac{\partial q}{\partial \eta}\right] d\eta d\zeta$ on the gain parameter are shown in Fig. 15a. Both U and L are monotonically growing functions of p_i and in the considered case of radial symmetry one has the simple relation: $L = mU$. At fixed p_i the energy flow only slightly increases with growth of topological charge. One finds that below a threshold p_i value, symmetric vortex solitons become unstable (the dependencies $U(p_i)$ and $L(p_i)$ terminate in the corresponding points in Fig. 15a). Notice that the threshold value of gain coefficient increases with growth of α, at least for $\alpha > 1.5$ (Fig. 15b) and diminishes with growth of the radius and the width of the amplifying ring. Expectably, the vortices with higher topological charges require higher gain levels for their stabilization, and the threshold gain of vortex with $m = 3$ increases with α much faster than the threshold gain for vortex with $m = 1$.

6.3 Rotating Vortex Structures

Besides radially symmetric vortex solitons, ring-like gain landscapes can support a rich variety of nonconventional rotating vortex states [8]. In all such states, the phase singularities are embedded in a single vortex core and perform persistent rotation around the center of the gain ring. Illustrative examples of the simplest

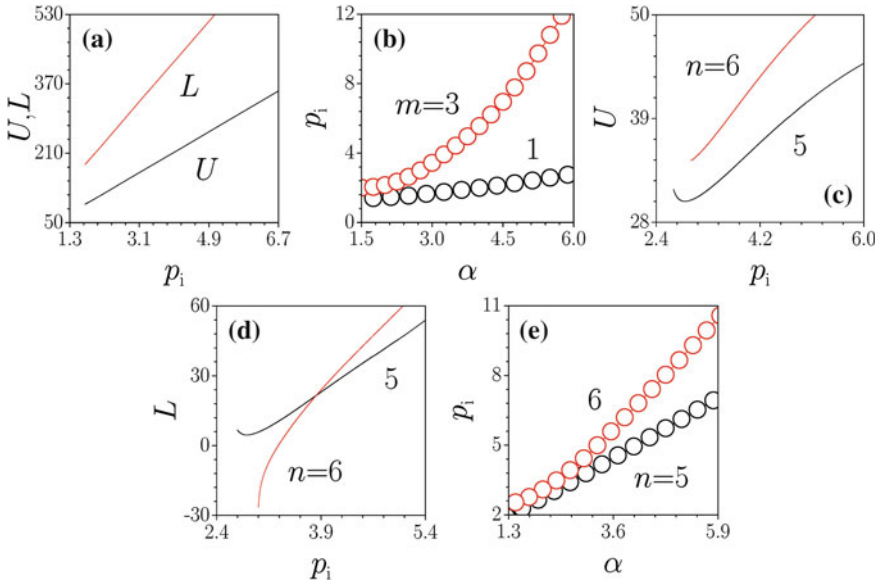

Fig. 15 (**a**) Energy flow and angular momentum of $m = 2$ vortex soliton supported by ring-like gain landscape versus gain parameter at $\alpha = 2$. (**b**) Minimal gain required for existence of stable ring-like vortex solitons with $m = 1$ and $m = 3$ vs α. Energy flow (**c**) and angular momentum (**d**) of azimuthally modulated vortex solitons with $m = 2$ versus gain parameter at $\alpha = 2$. **e** Minimal gain required for existence of stable azimuthally modulated vortex solitons with $m = 2$ vs α. All solitons, which belong to the curves shown in panels (**a**), (**c**) and (**d**), are stable

rotating structures with one, two, or three phase singularities are presented in Fig. 16. Notice that all such states emerge from the ring input beams, carrying singularities with winding numbers $m = 1, 2, 3$, but under the condition that their centers are strongly displaced from the center of the amplifying ring. All rotating vortex solutions exhibit azimuthal modulation of the intensity distributions, in spite of the radial symmetry of the gain landscape. The depth of this modulation depends on the magnitude of the gain parameter p_i. We observed that, as a rule, the azimuthal modulation is most pronounced in the center of the existence domain (in terms of p_i) and decreases when approaching the upper boundary of this domain. The diminishing of the azimuthal modulation is usually accompanied by a decrease of separation between the phase singularities nested in the vortex core. Expectably, the phase singularities in the simplest rotating vortex complex are located symmetrically with respect to the propagation axis, but we found that vortex states with an asymmetric arrangement of the singularities might be generated, too.

The existence domains of the rotating vortex solitons with two and three phase singularities are presented in Fig. 17. These domains were calculated using the small-step variations of the gain parameter until either transformation into radially symmetric vortex states (this scenario is typical for high p_i values) or the

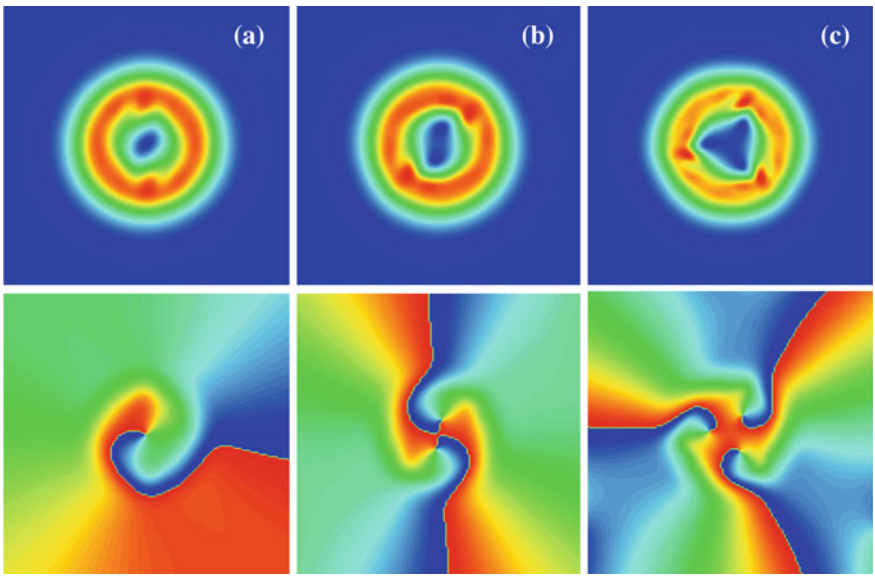

Fig. 16 Field modulus (*top*) and phase distributions (*bottom*) for stable rotating vortex solitons having (**a**) one phase singularity at $p_i = 1.7$, (**b**) two singularities at $p_i = 2.0$, and (**c**) three singularities at $p_i = 2.8$. In all cases $\alpha = 2.0$

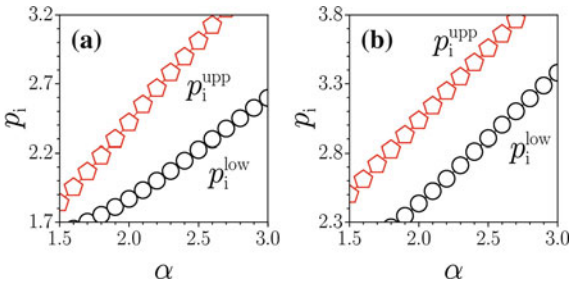

Fig. 17 Domains of existence of stable rotating vortex solitons with (**a**) two and (**b**) three singularities on the plane (α, p_i)

development of instabilities is achieved. Therefore, the domains shown in Fig. 17 correspond to the parameter range, where the rotating vortex complexes are stable. For a fixed strength of the two-photon absorption, the stable rotating vortex solitons exist inside a limited range of values of the gain coefficient $p_i^{low} \leq p_i \leq p_i^{upp}$ and the growth of α shifts this domain to higher gain values. According to our observations, higher gain values allow generation of more complex rotating vortex structures with larger number of singularities, although, for instance, the existence domains for solitons with two and three singularities may overlap slightly. Notice, that the domains of existence of rotating vortices may overlap with that of radially symmetric states, i.e. several stable attractors coexist for the same set of parameters clearly indicating on the multistability phenomena.

6.4 Necklace Vortex States in the Azimuthally Modulated Gain Landscapes

The available new phenomena become even richer if the gain landscape is azimuthally modulated [34]. In order to illustrate this we set

$$\gamma = p_i \sum_{k=1}^{n} \exp[-(\eta - r_c \cos\varphi_k)^2/d^2 - (\zeta - r_c \sin\varphi_k)^2/d^2], \tag{32}$$

where $\varphi_k = 2\pi(k-1)/n$. Such gain landscape consists of n amplifying Gaussian channels of the width $d = 1.0$ arranged into a necklace structure of the radius $r_c = 0.7n$. We found that such gain landscapes support stable vortex solitons, which are strongly azimuthally modulated (typical shapes are depicted in Fig. 18).

Importantly, the azimuthal modulation of the gain landscape imposes restrictions on the maximal charge of the stable vortex structures. This means that gain landscapes with certain discrete rotational symmetry affect the topology of the dissipative vortices, somehow mimicking how optical lattices determine the topology of vortex solitons (Fig. 13). The comprehensive simulations that we performed, using a variety of inputs, lead to the conclusion that an azimuthally modulated gain landscape with n amplifying channels can support vortex solitons with topological charges $\mathrm{m} \leq \mathrm{int}[(\mathrm{n}-1)/2]$, where the function int(x) stands for the integer part of the argument. Thus, landscapes with $n = 3, 4$ support vortex solitons with charge $m = 1$, landscapes with $n = 5, 6$ support vortex solitons with $m = 1, 2$, while for $n = 7, 8$ one gets $m = 1, 2, 3$, etc. The minimal number of amplifying channels that can support azimuthally modulated vortex solitons is $n = 3$. At low amplification level, the azimuthally modulated vortex solitons are extended and the light field penetrates considerably into the absorbing domain; the bright spots in such low-amplitude vortices are symmetric (see Fig. 18a, c, e. However, with growth of p_i the symmetry breaking occurs, with individual bright spots in the vortex profile becoming asymmetric. This happens because at high amplification level, a branch of asymmetric solitons bifurcates from the branch of symmetric states even in a single gain channel, making individual fragments unstable to perturbations with the unit azimuthal index. In this case the maxima of bright spots shift from the centers of the amplifying channels, while the spots experience considerable reorientation with respect to the axes connecting the centers of the amplifying channels and the center of the entire structure at $\eta, \zeta = 0$ (see Fig. 18b, d, f). Therefore, azimuthally modulated gain landscapes can support stable vortex solitons with multi-hump intensity profiles, which are composed of highly asymmetric fragments. Notice, that the asymmetry becomes more pronounced with increasing gain.

Interestingly, not all vortex structures whose charges satisfy the above mentioned charge rule are stable. We found that vortices with highest charges can be stable, while vortices with lowest charges are usually unstable. Thus, for modulation indices $n = 3, 4$ the only existing vortex with $m = 1$ can be stable. For

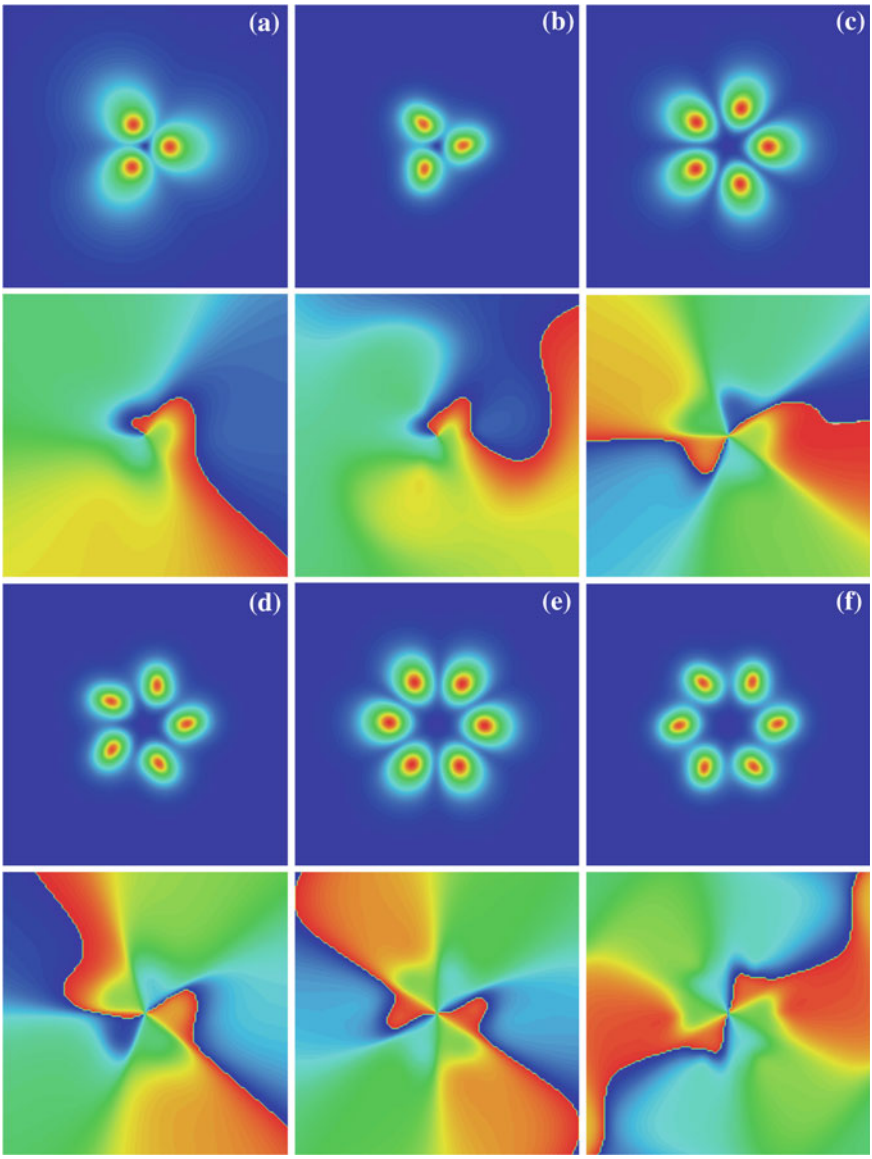

Fig. 18 Field modulus (*top*) and phase distribution (*bottom*) for stable vortex solitons with (**a**), (**b**) $n = 3, m = 1$, (**c**), (**d**) $n = 5, m = 2$, and (**e**), (**f**) $n = 6, m = 2$. Panels (**a**), (**c**), (**e**) correspond to $p_i = 3.2$, while panels (**b**), (**d**), (**f**) correspond to $p_i = 5.5$. In all cases $\alpha = 2$

$n = 5, 6$ the vortex with $m = 2$ can be stable, but vortex with $m = 1$ was unstable for all parameters that we considered. A typical dependence of the angular momentum L on gain parameter p_i is shown in Fig. 15d. Interestingly, for $n = 6$ the angular momentum, which monotonically decreases with decrease of p_i, may

change its sign. This occurs due to the symmetry breaking, when the local energy flows, circulating inside of each asymmetric bright spot, start contributing to the global angular momentum. Stable azimuthally modulated vortex structures exist above the threshold gain level Fig. 15e, and the minimal gain, required for their existence, rapidly increases with growth of the nonlinear losses.

7 Conclusions and Perspectives

To conclude, in this Chapter we have presented a variety of stable spatially localized nonlinear modes (we also call then dissipative solitons), which can exist in nonlinear media and can be supported by a localized gain. Among such objects we mention one- and two-dimensional solitons, vortex solitons, surface modes, dissipative breathers, and localized lattice solitons and vortices.

The localized gain introduces two important physical factors in the problem. First, it requires satisfying the balance between the gain and dissipation (what is typical to the known situation with the dissipative solitons in continuum medium). Second, a localized gain introduces a new spatial scale in the problem, which in particular appears to be responsible for possibility of observing the phenomenon of the symmetry breaking in such systems, either in one or in two-dimensional settings.

The results reported in the present chapter illustrate that either increasing the number of localized impurities or increasing the dimensionality of the problem results in qualitatively new phenomena. This suggests one of the lines for further studies. In particular, we mention such problems as solutions (attractors) in systems with multiple localized hot spots and in a limit with gain lattices; focusing of light in Kerr media with localized gain; the existence of localized modes in three-dimensional media with localized gain; possibility of obtaining stable rotating asymmetric fundamental solitons in two-dimensional setting. Above we have considered only solutions decaying at the infinity. The presented theory can also be further extended by including into consideration stationary solutions obeying different boundary conditions, like modes (or currents) on a nonzero background. Finally, one can consider more sophisticated systems involving both localized gain and localized dissipation.

From the point of view of practical applications the reported models besides the nonlinear optics of active media, can be highly relevant to the theory of Bose–Einstein condensate of quasi-particles, like exciton-polaritons, magnons or photons. In optics, dissipative solitons supported by the localized gain can be used for several practical purposes, including guiding beams, splinting an input beam in a series of beams with desired properties, etc.

Acknowledgements DAZ acknowledges the grant SFRH/BPD/64835/2009 (FCT, Portugal). DAZ and VVK were supported by the FCT under the grant PEst-OE/FIS/UI0618/2011.

References

1. F.Kh. Abdullaev, V.V. Konotop, M. Salerno, A.V. Yulin, Phys. Rev. E **82**, 056606 (2010)
2. N. Akhmediev, A. Ankiewicz (ed.), *Dissipative Solitons*. Lecture Notes in Physics, vol. 661 (Springer, Berlin Heidelberg, 2005)
3. N. Akhmediev, A. Ankiewicz (ed.), *Dissipative Solitons: From Optics to Biology and Medicine*, Lecture Notes in Physics, vol. 751 (Springer, Berlin, 2008)
4. G.L. Alfimov, V.V. Konotop, M. Salerno, Europhys. Lett. **58**, 7 (2002)
5. J. Atai, B.A. Malomed, Phys. Rev. E **54**, 4371 (1996)
6. S. Barland, J.R. Tredicce, M. Brambilla, L.A. Lugiato, S. Balle, M. Giudici, T. Maggipinto, L. Spinelli, G. Tissoni, T. Knodl, M. Miller, R. Jager, Nature **419**, 699 (2002)
7. L. Berge, Phys. Rep. **303**, 260 (1998)
8. O.V. Borovkova, V.E. Lobanov, Y.V. Kartashov, L. Torner, Opt. Lett. **36**, 1936 (2011)
9. M. Brambilla, L.A. Lugiato, F. Prati, L. Spinelli, W.J. Firth, Phys. Rev. Lett. **79**, 2042 (1997)
10. M.J. Connelly, *Semiconductor Optical Amplifiers* (Springer, Berlin, 2002)
11. L.-C. Crasovan, B.A. Malomed, D. Mihalache, Phys. Rev. E **63**, 016605 (2000)
12. M.C. Cross, P.C. Hohenberg, Rev. Mod. Phys. **65**
13. H.A. Cruz, V.A. Brazhnyi, V.V. Konotop, M. Salerno, Physica D **238**, 1372 (2009)
14. A.S. Desyatnikov, Y.S. Kivshar, L. Torner, Prog. Opt. **47**, 291 (2005)
15. S.V. Fedorov, N.N. Rosanov, A.N. Shatsev, N.A. Veretenov, A.G. Vladimirov, IEEE J. Quantum Electron. **39**, 197 (2003)
16. W. Firth, O. Weiss, Opt. Photonic News **13**, 55 (2002)
17. J.W. Fleischer, G. Bartal, O. Cohen, O. Manela, M. Segev, J. Hudock, D.N. Christodoulides, Phys. Rev. Lett. **92**, 123904 (2004)
18. D. Gomila, A.J. Scroggie, W.J. Firth, Physica D **227**, 70 (2007)
19. L.M. Hocking, K. Stewartson, Proc. R. Soc. London, Ser. A **326**, 289 (1972)
20. Y.V. Kartashov, A. Ferrando, A.A. Egorov, L. Torner, Phys. Rev. Lett. **95**, 123902 (2005)
21. Y.V. Kartashov, V.A. Vysloukh, L. Torner, Phys. Rev. Lett. **96**, 073901 (2006)
22. Y.V. Kartashov, V.A. Vysloukh, L. Torner, Opt. Lett. **32**, 2061 (2007)
23. Y.V. Kartashov, V.A. Vysloukh, L. Torner, Prog. Opt. **52**, 63 (2009)
24. Y.V. Kartashov, V.V. Konotop, V.A. Vysloukh, Europhys. Lett. **91**, 34003 (2010)
25. Y.V. Kartashov, V.V. Konotop, V.A. Vysloukh, L. Torner, Opt. Lett. **35**, 1638 (2010)
26. Y.V. Kartashov, V.V. Konotop, V.A. Vysloukh, L. Torner, Opt. Lett. **35**, 3177 (2010)
27. Y.V. Kartashov, V.V. Konotop, V.A. Vysloukh, Opt. Lett. **36**, 82 (2011)
28. Y.V. Kartashov, V.V. Konotop, V.A. Vysloukh, Phys. Rev. A **83**, 041806(R) (2011)
29. O. Katz, Y. Lahini, Y. Silberberg, Opt. Lett. **33**, 2830 (2008)
30. Y.S. Kivshar & G.P. Agrawal, *Optical Solitons: From Fibers to Photonic Crystals* (Academic Press, London, 2003)
31. C.-K. Lam, B.A. Malomed, K.W. Chow, P.K.A. Wai, Eur. Phys. J. **173**, 233 (2009)
32. H. Leblond, B.A. Malomed, D. Mihalache, Phys. Rev. A **80**, 033835 (2009)
33. F. Lederer, G.I. Stegeman, D.N. Christodoulides, G. Assanto, M. Segev, Y. Silberberg, Phys. Rep. **463**, 1 (2008)
34. V.E. Lobanov, Y.V. Kartashov, V.A. Vysloukh, L. Torner, Opt. Lett. **36**, 85 (2011)
35. L. Lugiato, R. Lefever, Phys. Rev. Lett. **58**, 2209 (1987)
36. W.C.K. Mak, B.A. Malomed, P.L. Chu, Phys. Rev. E **67**, 026608 (2003)
37. K.G. Makris, S. Suntsov, D.N. Christodoulides, G.I. Stegeman, A. Hache, Opt. Lett. **30**, 2466 (2005)
38. B.A. Malomed, P.G. Kevrekidis, Phys. Rev. E **64**, 026601 (2001)
39. B.A. Malomed, A.A. Nepomnyashchy, Phys. Rev. A **42**, 6009 (1990)
40. B.A. Malomed, H.G. Winful, Phys. Rev. E **53**, 5365 (1996)
41. B.A. Malomed, M. Gölles, I.M. Uzunov, F. Lederer, Phys. Scr. **55**, 73 (1997)
42. I.V. Melnikov, J.S. Aitchison, Appl. Phys. Lett. **87**, 201111 (2005)

43. D. Mihalache, D. Mazilu, F. Lederer, Y.V. Kartashov, L.-C. Crasovan, L. Torner, B.A. Malomed, Phys. Rev. Lett. **97**, 073904 (2006)
44. D. Mihalache, D. Mazilu, F. Lederer, Y.S. Kivshar, Phys. Rev. A **77**, 043828 (2008)
45. D.N. Neshev, T.J. Alexander, E.A. Ostrovskaya, Y.S. Kivshar, H. Martin, I. Makasyuk, Z. Chen, Phys. Rev. Lett. **92**, 123903 (2004)
46. C. Paré, L. Gagnon, P.A. Bélanger, Opt. Commun. **74**, 228 (1989)
47. V. Petviashvili, A. Sergeev, DAN SSSR **276**, 1380 (1984)
48. N.N. Rosanov, *Spatial Hysteresis and Optical Patterns* (Springer, Berlin, 2010)
49. N.N. Rosanov, S.V. Fedorov, A.N. Shatsev, Phys. Rev. Lett. **95**, 053903 (2005)
50. W. van Saarloos, P.C. Hohenberg, Phys. Rev. Lett. **64**, 749 (1990)
51. W. van Saarloos, P.C. Hohenberg, Physica D **56**, 303 (1992)
52. H. Sakaguchi, B.A. Malomed, Phys. Rev. E **72**, 046610 (2005)
53. A.E. Siegman, J. Opt. Soc. Am. A **20**, 1617 (2003)
54. V. Skarka, N.B. Aleksic, H. Leblond, B.A. Malomed, D. Mihalache, Phys. Rev. Lett. **105**, 213901 (2010)
55. K. Staliunas, O. Egorov, Y.S. Kivshar, F. Lederer, Phys. Rev. Lett. **101**, 153903 (2008)
56. S. Suntsov, K.G. Makris, D.N. Christodoulides, G.I. Stegeman, A. Haché, R. Morandotti, H. Yang, G. Salamo, M. Sorel, Phys. Rev. Lett. **96**, 063901 (2006)
57. A. Szameit, Y.V. Kartashov, F. Dreisow, T. Pertsch, S. Nolte, A. Tünnermann, L. Torner, Phys. Rev. Lett. **98**, 173903 (2007)
58. V.B. Taranenko, I. Ganne, R.J. Kuszelewicz, C.O. Weiss, Phys. Rev. A **61**, 063818 (2000)
59. O. Thual, S. Fauve, J. Phys. **49**, 1829 (1988)
60. C.H. Tsang, B.A. Malomed, C.-K. Lam, K.W. Chow, Eur. Phys. J. D **59**, 81 (2010)
61. C.H. Tsang, B.A. Malomed, K.W. Chow, Phys. Rev. E **84**, 066609 (2011)
62. E.A. Ultanir, G.I. Stegeman, D. Michaelis, Ch.H. Lange, F. Lederer, Phys. Rev. Lett. **90**, 253903 (2003)
63. X. Wang A. Bezryadina, Z. Chen, K.G. Makris, D.N. Christodoulides, G.I. Stegeman, Phys. Rev. Lett. **98**, 123903 (2007)
64. M.O. Williams, C.W. McGrath, J.N. Kutz, Opt. Express **18**, 11671 (2010)
65. D.A. Zezyulin, G.L. Alfimov, V.V. Konotop, Phys. Rev. A **81**, 013606 (2010)
66. D.A. Zezyulin, V.V. Konotop, G.L. Alfimov, Phys. Rev. E **82**, 056213 (2010)
67. D.A. Zezyulin, Y.V. Kartashov, V.V. Konotop, Opt. Lett. **36**, 1200 (2011)

Analytical Solitary Wave Solutions of a Nonlinear Kronig-Penney Model for Photonic Structures Consisting of Linear and Nonlinear Layers

Yannis Kominis and Kyriakos Hizanidis

Abstract In this chapter we review some recent results for the construction of analytical solutions for a class of systems consisting of interlaced linear and nonlinear parts. Periodic waveguide arrays as well as structures consisting of semi-infinite waveguide arrays and their interfaces have been studied, while the method presented here can be applied to even larger classes of systems including combinations of parts of waveguide arrays, homogeneous parts and defects as well as different types of nonlinearities. The method utilizes the phase space description of the system for the construction of analytical solutions. Such solutions can serve as starting points for the exploration of even larger classes of solutions and systems with the utilization of perturbation methods. Moreover, the method provides physical intuition for the formation of solitary waves in such structures.

1 Introduction

Periodic photonic structures fabricated in nonlinear dielectric media became recently a subject of major importance for photonic applications. Such structures are very promising for applications in integrated photonic devices, such as multiport beam coupling, steering and switching. Therefore, the study of self-trapped, spatially localized modes in periodic optical structures, consisting of arrays of nonlinear optical waveguides, has been a field of continuously increasing research interest from both the experimental and the theoretical point of view [1–6]. These

Y. Kominis (✉) · K. Hizanidis
School of Electrical and Computer Engineering,
National Technical University of Athens, 15773 Zographou, Greece
e-mail: gkomin@central.ntua.gr

Progress Optical Sci., Photonics (2013): 201–226
DOI: 10.1007/10091_2012_6

Published Online: 27 July 2012

modes have the form of gap solitons inside the photonic gaps of the periodic structure and result from the dynamical balancing between the nonlinearity and the diffraction. In contrast to the case of homogeneous structures, where the corresponding models can be integrable and soliton propagation occurs, periodically inhomogeneous systems are typically nonintegrable. This fact excludes the possibility of pure soliton existence (in the strict mathematical sense, this prerequisites complete integrability), but also gives rise to the potentiality of existence of a plethora of solitary waves which do not have a counterpart in the homogeneous cases. Although, these structures are not solitons, they can exhibit a quite robust behavior under propagation, a property that considerably facilitates their experimental observation.

The transverse inhomogeneity of a photonic structure results in breaking of the translational invariance. Thus, the existence of traveling waves is generally not ensured, while wave localization can take place in specific positions with respect to the underlying structure. Depending on the complexity of the structure, the position and stability of a solitary wave may additionally depend on wave's power and width [7–10]. The relative soliton immobility in inhomogeneous structures has led to an extensive study of the existence and the stability of stationary wave solutions in a variety of configurations. On the other hand, it is well known that solitary waves can travel, without significant radiation emission, across an inhomogeneous structure under certain conditions for which the effective potential seen by the wave is weak. Therefore solitary wave dynamics emerges as a field of open research problems. [5, 10–13].

From the theoretical point of view, in order to study these structures, a variety of models and different approaches has been considered, including: the tight-binding approximation, based on the assumption of weakly coupled waveguides and leading to a Discrete Nonlinear Schrödinger Equation (D-NLSE) [14], and the coupled-mode theory, based on the assumption of strong coupling and resulting to a set of coupled equations governing the forward and backward wave propagation [15]. On the basis of these approaches the existence of various solitary wave modes has been shown, and their propagation has been studied [1–6]. However, both methods are strongly restricted to specific limits of the configuration parameter range [16]. In order to overcome these restrictions and study the solitary wave formation in a unified model, the original NLSE, with periodically varying coefficients, modeling the waveguide array structure, has to be considered:

$$i\frac{\partial\psi}{\partial z}+\frac{\partial^2\psi}{\partial x^2}+\epsilon(x)\psi+g(x,|\psi|^2)\psi=0 \tag{1}$$

where z, x and ψ are the normalized propagation distance, transverse dimension and electric field, respectively. When x is normalized to X_0, z is normalized to $Z_0=4\pi n_0 X_0^2/\lambda$ and u is normalized to $U_0=\lambda/(2\pi X_0\sqrt{n_0 n_2})$, where λ is the wavelength and n_0, n_2 are the linear and nonlinear refractive index coefficients. A normalized propagation distance $z_{max}=100$, corresponds to an actual propagation length of $10.7-24.3$ mm, for the case of a nonlinear material of AlGaAs

type, and $22.3 - 50\,\text{mm}$ for the case of $LiNbO_3$, when the transverse coordinate is normalized to $X_0 = 2 - 3\,\mu\text{m}$. The periodic transverse variation of the linear refractive index is given by $\epsilon(x)$, while the spatial and intensity dependence of the nonlinear refractive index is provided through $g(x, |\psi|^2)$. This improved model has been studied in cases where the periodic transverse inhomogeneity is related either to the linear [3, 17–20] or the nonlinear refractive index [21] while the transverse profile of the inhomogeneity has been assumed to have the form of the so-called Dirac comb. Within this approach the linear band structure of the model has been shown and localized modes with various symmetries have been provided. However, it is obvious that a Dirac comb description of the spatial dependence of the nonlinearity, can render only qualitative results and is far from being generic and adequate for describing realistic configurations.

In this work, we review some recent analytical results for the case of a realistic model described by Eq. (1) with piecewise-constant coefficients [22–30], namely a nonlinear Kronig-Penney type of model [31]. This model is more general than the aforementioned ones, which are contained as limiting cases of the model in hand. More specifically, we consider a large variety of photonic structures consisting of interlaced linear and nonlinear layers which can be either self-focusing or self-defocusing, while the geometry of the structures can be either infinite periodic, as in the case of a periodic waveguide array, or semi-infinite periodic, as in the cases of interfaces between waveguide arrays and homogeneous linear or nonlinear media as well as between two dissimilar waveguide arrays. More complex geometries consisting of linear/nonlinear, self-focusing/defocusing and homogeneous/periodic parts and defects can also be considered in the same context. Although we focus on cases of Kerr-type of nonlinearity, other types of nonlinearities can also be treated under the same approach. On the other hand, the method presented in this work applies directly to the closely related field of Bose–Einstein condensates loaded in optical lattices [32–34] for cases of both attractive and repulsive interatomic interactions, since the underlying models are identical.

A phase space method is employed for the construction of analytical solitary wave solutions supported by the aforementioned photonic structures. The method provides physical insight on the formation of spatially localized waves. The various classes of solutions are obtained under quite generic conditions and include symmetric, anti-symmetric and asymmetric forms corresponding to bright, dark and anti-dark solitary waves as well as solitary waves with semi-infinite periodic pedestal for the cases of semi-infinite periodic structures. It is worth mentioning that knowledge of analytical solutions is extremely rare for inhomogeneous nonlinear wave models and can serve as the basis for further investigations of the configurations considered in this work as well similar ones, either in the context of analytical perturbation methods or numerical continuation methods.

2 Phase Space Method for the Construction of Analytical Solutions

The stationary wave solutions of Eq. (1) have the form

$$\psi(x,z) = u(x;\beta)e^{i\beta z}, \tag{2}$$

and satisfy the nonlinear ordinary differential equation

$$\frac{d^2u}{dx^2} + [\epsilon(x) - \beta]u + g(x,u^2)u = 0 \tag{3}$$

where β is the propagation constant and $u(x;\beta)$ is the real transverse wave profile. Equation (3) describes a nonautonomous nonlinear dynamical system (with the spatial variable x playing the role of time) which is in general nonintegrable.

The complexity of the dynamical system is evident, even in the limiting case where the transverse variation of the linear and nonlinear refractive index is considered as a small perturbation to an autonomous system with constant coefficients, corresponding to the mean values of $\epsilon(x)$ and $g(x,u^2)$. The explicit dependence of a dynamical system on the evolution variable (time or space) results in an additional dimension in the phase space of the system (extended phase space). In most cases this explicit dependence leads to chaotic dynamics. Indeed, even within the class of integrable Hamiltonian systems, it is well known that small nonautonomous perturbations lead, in general, to nonintegrability and irregular dynamics. Perturbative approaches, on the other hand, allow for the investigation of the relation between the dynamics of the autonomous integrable system and the nonautonomous perturbed system. The Poincare-Birkhoff theorem as well as Melnikov's theory for periodic orbits [35] predict that when certain resonance conditions between the unperturbed system and the time-dependent perturbation are satisfied, a finite discrete family of periodic solutions persist under perturbation. Additionally, Melnikov's theory for homoclinic/heteroclinic orbits [35] relates the existence of an unperturbed homoclinic/heteroclinic orbit to fixed points with the persistence of a discrete number of orbits homoclinic/heteroclinic to periodic orbits and predicts the formation of homoclinic/heteroclinic tangles and the presence of chaos, resulting in a complex transverse profile for the stationary solitary wave.

The case of a nonlinear Kronig-Penney model for photonic structures consisting of linear and nonlinear layers corresponds to Eq. (3) with $\epsilon(x)$ and $g(x,u^2)$ being piecewise constant with $g(x,u^2)$ equal to zero in the linear layers of the structure. This system belongs to a class of nonautonomous dynamical systems consisting of an autonomous nonlinear system and an autonomous linear periodic system, each acting alone at different intervals. It has been shown that under certain conditions for the lengths of the linear intervals, the behavior of the nonautonomous piecewise linear system is closely connected with the dynamics of its nonlinear autonomous component. In particular, it has been proved that, under certain

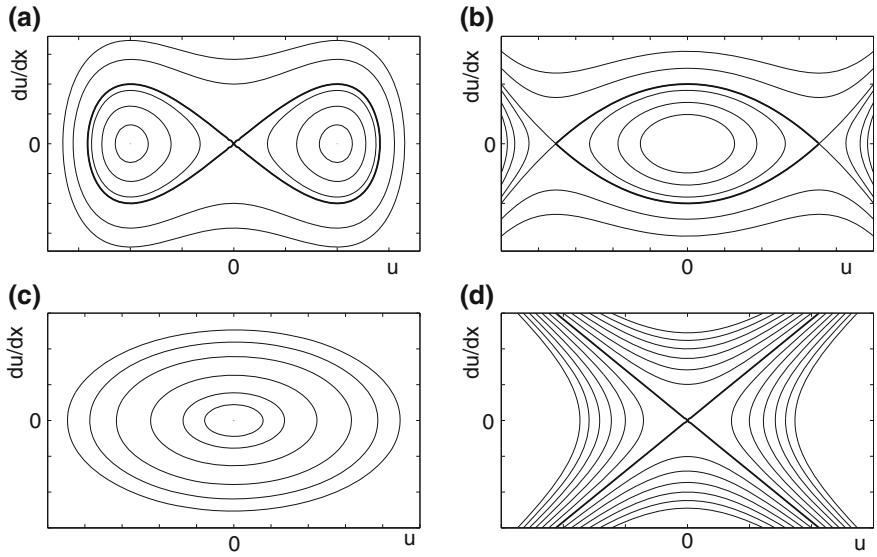

Fig. 1 Phase space for each part of the system Eq. (4): **a** nonlinear part with $N(u^2) = 2u^2$ for $\beta > \epsilon_N$, **b** nonlinear part with $N(u^2) = -2u^2$ for $\beta < \epsilon_N$, **c** linear part for $\beta < \epsilon_L$ and, **d** linear part for $\beta > \epsilon_N$

conditions, a Poincare surface of section of the nonautonomous system is identical to the phase space of the autonomous nonlinear system. This result applies to a general class of dynamical systems including dissipative, integrable and nonintegrable Hamiltonian systems. [36]

In each part of the photonic structure the wave profile is described by the following equations:

$$\begin{aligned} \frac{d^2u}{dx^2} + \big(\epsilon_{N,i} - \beta\big)u + N(u^2)u = 0, x \in X_{N,i}, (i = 1, 2, \ldots) \\ \frac{d^2u}{dx^2} + \big(\epsilon_{L,i} - \beta\big)u = 0, x \in X_{L,j}, (j = 1, 2, \ldots) \end{aligned} \tag{4}$$

where $\epsilon_{N,i}$ and $\epsilon_{L,j}$ are the values of the linear refractive index in the nonlinear $(X_{N,i})$ and linear $(X_{L,j})$ layers, respectively, and $N(u^2)$ is the nonlinearity function. Although the overall system is nonautonomous, in each part of the structure the wave formation is described by an autonomous system. The form of the respective phase spaces depend on the sign of the nonlinearity as well as on the propagation constant β and are shown in Fig. 1. The stationary solutions of the system of Eq. (4) can be provided by composing solutions of these two systems, which have matched conditions for u and its derivative, at the boundaries between different layers. For specific values of the propagation constants β these conditions can be fulfilled simultaneously and analytical solutions can be obtained. In the following

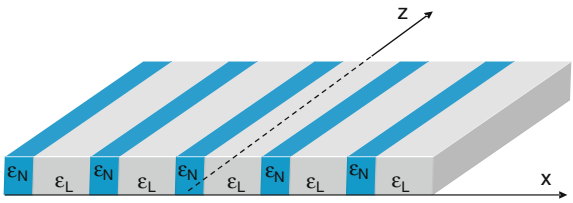

Fig. 2 Geometry of the periodic structure consisting of linear (ϵ_L) and nonlinear (ϵ_N) layers

sections, we demonstrate the application of this method on three basic examples of photonic structures having fundamental importance.

3 Waveguide Arrays with Self-Focusing Nonlinearity

We consider the case of an infinite periodic photonic structure consisting of linear and nonlinear self-focusing layers as shown in Fig. 2 [23]. The linear and the nonlinear refractive index are given by

$$\left[\epsilon(x), g(x,u^2)\right] = \begin{cases} [\epsilon_N, N(u^2)], & x \in U_N \\ [\epsilon_L, 0], & x \in U_L \end{cases} \tag{5}$$

where $U_N = \bigcup_k [kT - N/2, kT + N/2)$, $U_L = \bigcup_k [kT + N/2, (k+1)T - N/2)$, L and N are the lengths of the linear and the nonlinear layers, respectively, and $T = L + N$ is the spatial period of the structure.

3.1 Model and Analytical Solutions

In each part of the photonic structure the wave profile is described by the following equations:

$$\begin{aligned} \frac{d^2u}{dx^2} + (\epsilon_N - \beta)u + N(u^2)u = 0,\ x \in U_N \\ \frac{d^2u}{dx^2} + (\epsilon_L - \beta)u = 0,\ x \in U_L \end{aligned} \tag{6}$$

The stationary solutions of the system of Eq. (6) can be provided by composing solutions of these two systems, which have matched conditions for u and its derivative, at the interfaces. Furthermore, we assume that the propagation constant β is such that:

1. The linear system has periodic (sinusoidal) solutions [phase space as in Fig. 1c].

2. The nonlinear system has a homoclinic orbit, tending to the origin for $x \to \pm\infty$ and being symmetric with respect to the origin [phase space as in Fig. 1a].

For a propagation constant corresponding to the case where an integer number of half-periods of the solution of the linear system is contained in the linear part of length L, i.e.

$$\beta_n = \epsilon_L - \left(\frac{n\pi}{L}\right)^2, n = 1, 2, \ldots \tag{7}$$

the continuity conditions are met simultaneously in all boundaries: any solution of Eq. (6) starting from a point of the homoclinic orbit inside the nonlinear part at some x, returns to the homoclinic orbit after evolving in the linear part and subsequently evolves again according to the homoclinic orbit. Thus, the solution approaches the origin asymptotically as $x \to +\infty$, moving on the homoclinic orbit but interrupted periodically due to the linear part of the structure. The same argument holds for the evolution of the stationary solution as $x \to -\infty$. These arguments are illustrated in Fig. 3, where the phase space representation of the homoclinic orbit and the phase space of the linear system have been superimposed. The branches of solutions are shown to coincide with parts of the (nonlinear) homoclinic orbit and parts of the (linear) periodic ellipsoid orbits. Several properties and symmetries of the solutions can be derived from their phase space representation: for odd n (Fig. 3a), the solutions lie in both branches of the homoclinic orbit so that u has an alternating sign between neighboring nonlinear layers, while modes with constant sign of u, lying exclusively in one branch, are obtained for even n (Fig. 3b). Following the same arguments, not only asymptotic (solitary) solutions, but also nonlinear periodic stationary solutions can be generated. In fact, for $\beta = \beta_n$ the entire Poincare surface of section (including both asymptotic and periodic orbits) of the system (6) as defined stroboscopically (with respect to x) is identical to the phase space of the nonlinear system, while for $\beta \neq \beta_n$ the Poincare surface of section appears chaotic. [36] This abrupt change of the phase space topology for the specific values of β, has a form of a *global bifurcation*. More specifically, for the asymptotic solutions, β_n are values for which a complete homoclinic tangency occurs, resulting in an infinite set of solutions, each one starting from a different point of the homoclinic orbit; for $\beta \neq \beta_n$ it is expected that the stable and unstable manifolds intersect transversely [35] and only some of these solutions, corresponding to intersection points, persist.

The solitary wave stationary solutions corresponding to β_n can be given analytically in the following form

$$u(x; \beta_n, x_0) = \begin{cases} (-1)^{nk} v(x - kL; \beta_n, x_0) & x \in U_N \\ a_k \sin(\sqrt{\epsilon_l - \beta_n} x + \phi_k) & x \in U_L \end{cases} \tag{8}$$

where $v(x; \beta, x_0)$ is the homoclinic solution of the nonlinear system (4) and (a_k, ϕ_k) are directly obtained from the continuity conditions of u and its derivative at the interfaces. The homoclinic solution, in general, is given by

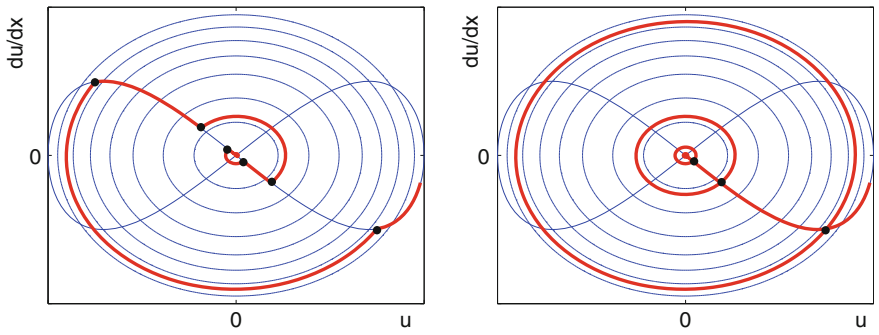

Fig. 3 Phase space construction of asymptotic (solitary) solutions of Eq. (6) for n, odd (*left*), and n, even (*right*). *Black dots* depict transition at the boundary between a linear and a nonlinear layer

$$x - x_0 = \pm \int_{v_m}^{v} \frac{dv'}{\sqrt{(\beta - \epsilon_n)v'^2 - F(v')}} \tag{9}$$

with F being defined by $dF/du = 2N(u^2)u$, and v_m is the nonzero root of the denominator in the integrand, corresponding to the extreme value of the solution, which is placed at x_0.

3.2 Results and Discussion

Although the method, presented in the previous section, applies in a general class of nonlinearities, for illustrative purposes, in the following we consider the case of a Kerr-type self-focusing nonlinearity, $N(u^2) = 2u^2$. In this case, the second assumption of the existence of a homoclinic orbit results in the condition

$$\beta_n > \epsilon_N \tag{10}$$

and the homoclinic solution is $v(x; \beta, x_0) = \pm\sqrt{\beta - \epsilon_N}$ sech $(\sqrt{\beta - \epsilon_N}(x - x_0))$. As it can be seen from Eqs. (7) and (10) the conditions for existence of the aforementioned solutions are quite generic: solutions of the form of Eq. (8) exist for a positive linear refractive index difference $\Delta\epsilon \equiv \epsilon_L - \epsilon_N$, and for discrete values of the propagation constant.

In general, the geometry of the structure is crucial for both the existence and the form of the localized modes. The number of modes for a given $\Delta\epsilon$ depends on the length (L) of the linear part of the periodic structure: for increasing L, the number and the density of the modes $\beta_n \in (\epsilon_N, \epsilon_L)$, also increase. Each value β_n is located inside a finite band gap, of the spectral band structure of the linearized system associated to (1), which corresponds to a resonant Bragg-type reflection from the periodic structure. On the other hand, the length N of the nonlinear layer

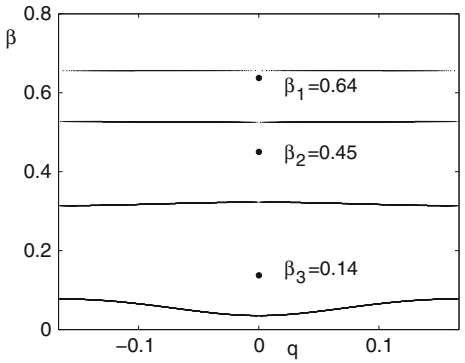

Fig. 4 Band structure of the linearized system (propagation constant β versus Bloch wavenumber q) for a photonic structure having $L = 4\pi$, $N = 2\pi$, $\epsilon_N = 0$ and $\Delta\epsilon = 0.7$. *Black dots* depict the location of the analytically obtained localized modes for $n = 1, 2, 3$

determines the spatial width of the solution, since for large N the solutions are strongly localized in the nonlinear layer, and only small side-lobes appear in the neighboring linear layers.

As an example, we consider the case of a linear refractive index difference $\Delta\epsilon = 0.7$, where we have set $\epsilon_N = 0$, without loss of generality, since a nonzero ϵ_N results only in a shift in the values of β_n, as obtained from Eqs. (7) and (10). The length of the linear and nonlinear layers are $L = 4\pi$ and $N = 2\pi$, respectively. According to the existence conditions [Eqs. (7) and (10)], for this parameter set, three families of solutions, corresponding to $n = 1, 2, 3$, are found. The location of β_n in the band structure of the linear system is illustrated in Fig. 4, where it is shown that each β_n is representative for a finite gap. Each family of localized solutions, corresponding to β_n, is parameterized by the location of the maximum of the homoclinic part of the solution in the nonlinear layer, $x_0 \in [-N/2, N/2]$. Due to symmetry of the structure with respect to $x = 0$, we can restrict our analysis to solutions with $x_0 \in [0, N/2]$. In Fig. 5, we show the profiles of several stationary localized solutions, corresponding to $n = 1, 2, 3$ and $x_0 = 0, N/4, N/2$. The mode number n, determines the number of nodes of the solution in the linear parts of the structure, as well as the constancy (n, even) or the alternation (n, odd) of the sign of u in the nonlinear parts. On the other hand, x_0 determines the symmetry of the solutions. Thus, for $x_0 = 0$, we have modes which are symmetric with respect to the center of the nonlinear layer (Fig. 5, top row), while for $x_0 = N/2$, the modes can be either symmetric (n, even) or antisymmetric (n, odd), with respect to the center of the linear layer (Fig. 5, bottom row). For $x_0 \neq 0, N/2$, we can have a general class of asymmetric localized modes (Fig. 5, middle row).

The evolution of several characteristic localized modes, obtained analytically with the aforementioned method, is depicted in Fig. 6. The propagation has been simulated using the standard beam propagation method for the numerical solution of Eq. (1). In all numerical simulations, a random noise of the order of 10^{-2} (with respect to the maximum of the stationary solution) has been superimposed to the solution. It is shown that modes corresponding to $n = 2, 3$ are quite robust under propagation, while for $n = 1$ the mode corresponding to $x_0 = N/2$, is unstable. This kind of instability is typical for gap solitons in lattices and periodic media and

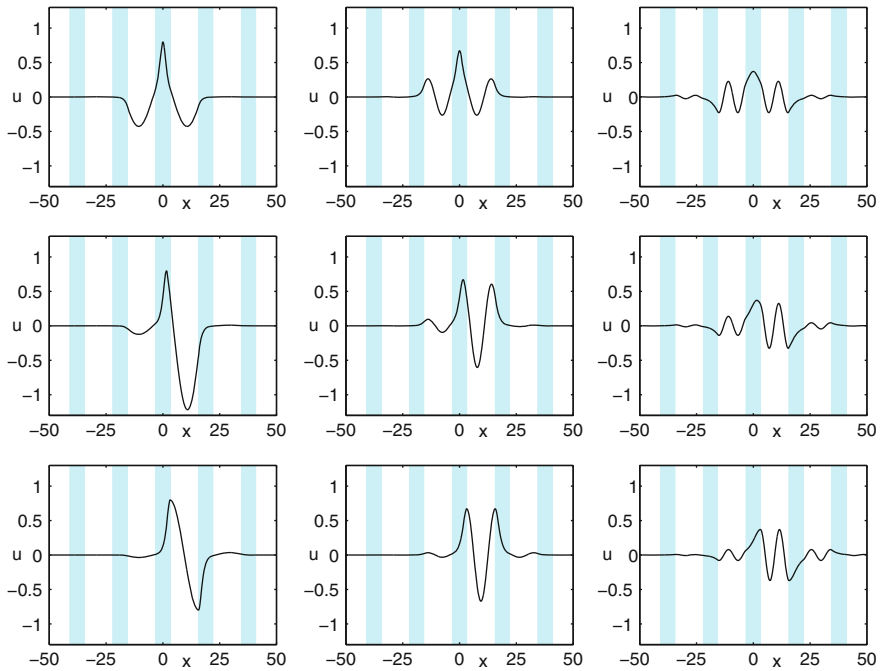

Fig. 5 Analytically obtained profiles of solitary wave solutions, for $n = 1, 2, 3$ (*left to right*). Shaded areas correspond to nonlinear layers. The first and third row depict solutions having a symmetry with respect to the center of the nonlinear $(x_0 = 0)$ and the linear $(x_0 = N/2)$ layer, respectively. The *middle row* depicts asymmetric solutions $(x_0 = N/4)$. All parameters are the same as in Fig. 4. The solution depicted in *first column*, *third row* is unstable as shown in Fig. 6

occurs when β is large enough so that an internal (discrete) mode [37] of the linear spectrum of the solution crosses into a linear transmission band (shown in Fig. 4) and resonates with the linear Bloch waves. Such instabilities can trigger various types of spatial dynamics including the symmetry breaking and oscillatory instabilities, as well as mode transformation scenarios according to which an unstable localized mode evolves (transforms) to a stable one. [38] However, it is worth mentioning that in experimental configurations, even if some kind of instability occurs, the laminar propagation distance in several cases is much larger than the actual length of the device (as for the aforementioned case of an AlGaAs type of nonlinear material). This fact is quite promising for potential applications.

Finally, it is useful to locate the analytically obtained solutions in the low dimensional space of specific conserved quantities. The energy Q and Hamiltonian H functionals

$$Q = \int_{-\infty}^{+\infty} |\psi|^2 dx \tag{11}$$

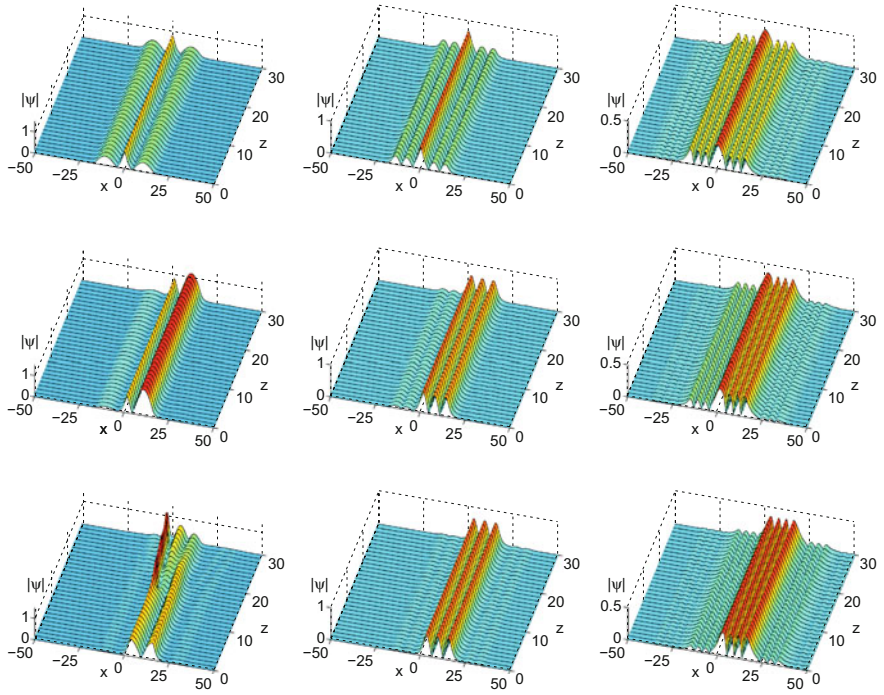

Fig. 6 Propagation of solitary wave solutions shown in Fig. 5. The solutions correspond to $n = 1, 2, 3$ (*left to right*) and $x_0 = 0, N/4, N/2$ (*top to bottom*)

$$H = \int_{-\infty}^{+\infty} \left(|\psi_x|^2 - \epsilon(x)|\psi|^2 - g(x, |\psi|^2) \frac{|\psi|^2}{2} \right) dx \tag{12}$$

are calculated for each family of solutions as shown in Fig. 7a. The representation (projection) of the families of solutions in the Hamiltonian-Energy plane is depicted in Fig. 7b, and can be used for providing an overview of the analytically obtained solutions. It is shown that, solutions having the same β_n and different x_0 lie on the same straight line with slope $dH/dQ = -\beta_n$, in accordance with Ref. [38].

4 Waveguide Arrays with Self-Defocusing Nonlinearity

In this section, we utilize the same approach in order to provide analytical solutions of (1) for the case of waveguide arrays as those shown in Fig. 2, but with a self-defocusing nonlinearity (corresponding to repulsive interatomic interactions for the case of Bose-Einstein condensates). These solutions correspond to localized excitations on a finite periodic background, having the form of dark and anti-dark solitary waves. [24, 39, 40]

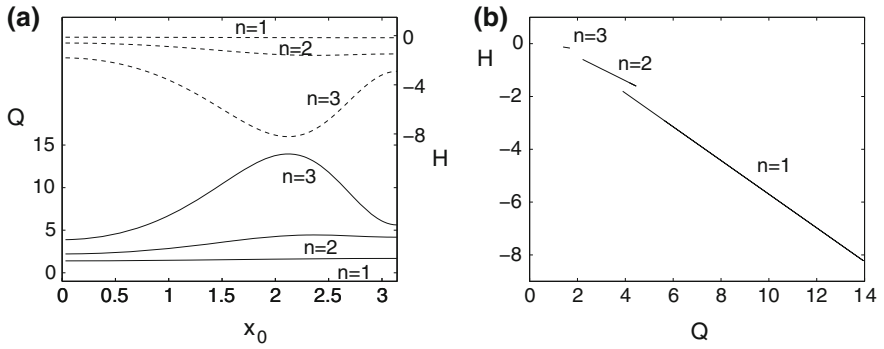

Fig. 7 **a** Energy Q (*solid lines*) and Hamiltonian H (*dashed lines*) versus x_0. **b** Hamiltonian versus energy diagram. All parameters are the same as in Fig. 4

4.1 Model and Analytical Solutions

The stationary solutions of Eq. (1) having the form $\psi(x,z) = u(x;\beta)e^{i\beta z}$, satisfy the nonlinear ordinary differential Eq. (6) with $N(u^2) = -2u^2$, where the minus sign corresponds to as self-defocusing nonlinearity.

We assume that the propagation constant β is such that:

1. The linear system has periodic (sinusoidal) solutions, i.e. $\beta < \epsilon_L$ (phase space as in Fig. 1c).
2. The nonlinear system has a heteroclinic orbit $v(x;\beta,x_0) = \pm\sqrt{(\epsilon_N - \beta)/2}\tanh(\sqrt{(\epsilon_N - \beta)/2}(x - x_0))$, connecting the saddle points $(u, du/dx) = (\pm\sqrt{(\epsilon_N - \beta)/2}, 0)$, i.e. $\beta < \epsilon_N$ [phase space as in Fig. 1b].

For a propagation constant corresponding to the case where an integer number of half-periods of the solution of the linear system is contained in the linear part of length L, i.e.

$$\beta_n = \epsilon_L - \left(\frac{n\pi}{L}\right)^2, n = 1, 2, \ldots \tag{13}$$

any solution of Eq. (6), starting from a point of the heteroclinic orbit inside the nonlinear part at some x, returns to the heteroclinic orbit after evolving in the linear part; subsequently, it evolves again according to the heteroclinic orbit. Thus, the solution tends asymptotically to the saddle points for $x \to \pm\infty$. The representation of the composite solutions in the phase space of the system (u, u_x) is depicted in Fig. 8, for the case of an odd (even) n where the solution lays on both (one of the) heteroclinic branches. The localized stationary solutions corresponding to β_n can be given analytically in the following form

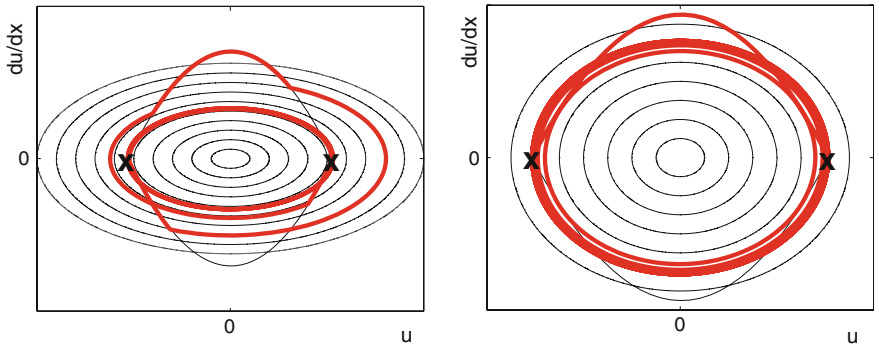

Fig. 8 Phase space representation of the stationary solutions (*thick line*) for the case of n, odd (*left*), and n, even (*right*). The phase space of the linear system (*elliptic curves*) and the heteroclinic orbit connecting the saddle points (X) of the nonlinear system, are shown

$$u(x;\beta_n,x_0)=\begin{cases}(-1)^{nk}\sqrt{\frac{\epsilon_N-\beta_n}{2}}\tanh\left(\sqrt{\frac{\epsilon_N-\beta_n}{2}}(x-x_0-kL)\right), x\in U_N\\ a_k\sin(\sqrt{\epsilon_L-\beta_n}x+\phi_k), x\in U_L\end{cases} \tag{14}$$

where (a_k,ϕ_k) are directly obtained from the continuity conditions of u and its derivative at the interfaces. It is worth mentioning that, in contrast to the case of a self-focusing nonlinearity, studied in the previous section, for the present case and for any parameter set there exists an infinite number of β_ns and solutions can be found for $\epsilon_L=\epsilon_N$, as well.

For each β_n a family consisting of an infinite number of solutions parameterized by $x_0\in[-N/2,N/2]$ is obtained. Due to the symmetry of the periodic structure the analysis is restricted to solutions with $x_0\in[0,N/2]$. The solutions are symmetric or anti-symmetric with respect to the center of the nonlinear or the linear layer for $x_0=0,N/2$, respectively, while they are in general asymmetric for $x_0\neq 0,N/2$. In Fig. 9 several spatial profiles are shown for $x_0=0,N/2$ for the case of a periodic structure having $L=4\pi$ and $N=\pi$ and $\epsilon_N=0$. For a $\Delta\epsilon\equiv\epsilon_L-\epsilon_N>0$ [Fig. 9(left)], one obtains dark solitary wave profiles formed as localized dips on a finite periodic background for $n=2$. For a negative $\Delta\epsilon$, anti-dark solitary wave profiles are obtained for $n=1$ [Fig. 9(middle)], while for $n=2$ the profile changes from (slightly) dark to anti-dark when x_0 increases from zero to $N/2$ [Fig. 9(right)].

A characteristic parameter for the form of a profile is the contrast C with respect to the background. It is defined as the ratio between the maximum field value in the linear layer $x\in[N/2,N/2+L]$ to the absolute field value on a nonlinear layer for large x [i.e. the saddle point of the nonlinear system (4)]. It can be readily calculated analytically and its dependence on x_0 is shown in Fig. 10. It is shown that for the case $\Delta\epsilon=0.1$ only dark localized modes exist $(C<1)$, while for $\Delta\epsilon=-0.5$ both dark $(C<1)$ and anti-dark $(C>1)$ modes exist. Note that in both

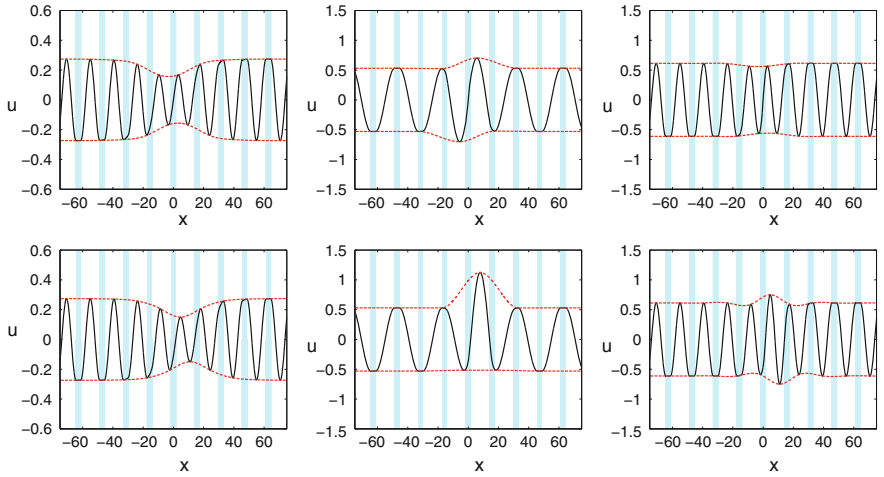

Fig. 9 Field profiles of the analytically obtained stationary solutions for a periodic structure having $L = 4\pi, N = \pi$ and $\epsilon_N = 0$. (*left column*) $\epsilon_L = 0.1$, $n = 2$, (*middle column*) $\epsilon_L = -0.5$, $n = 1$, and (*right column*) $\epsilon_L = -0.5$, $n = 2$. *First* and *second rows* correspond to $x_0 = 0, N/2$, respectively

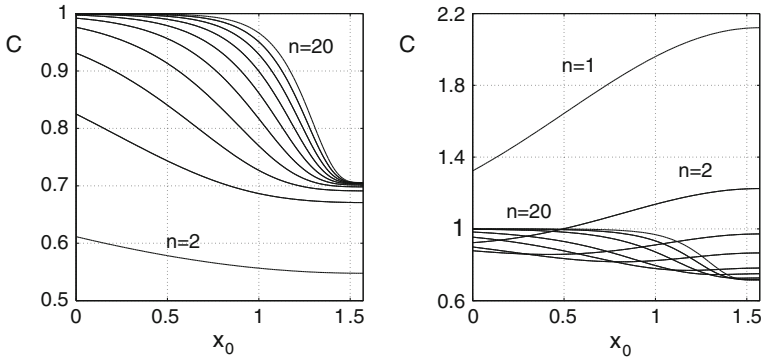

Fig. 10 Contrast versus x_0. The parameters are: $L = 4\pi$, $N = \pi$ and $\epsilon_N = 0$ and $\epsilon_L = 0.1$ (*left column*), $\epsilon_L = -0.5$ (*right column*)

configurations a dark solitary wave is formed for large n and for values of x_0 close to $N/2$, while a x_0 close to zero results to $C = 1$.

The location of the β_n corresponding to solutions (14) in the linear band structure (propagation constant β versus Bloch wavenumber q) of the system is depicted in Fig. 11 for $\Delta\epsilon = 0.1, -0.5$. The band structure has been obtained by linearizing (4) around its fixed points (saddles). It is shown that all β_n's corresponding to solutions are located inside the gaps of the band structure. For the case of $\Delta\epsilon = 0.1$, β_1 [as obtained from (13)], does not fulfill the existence condition (ii)

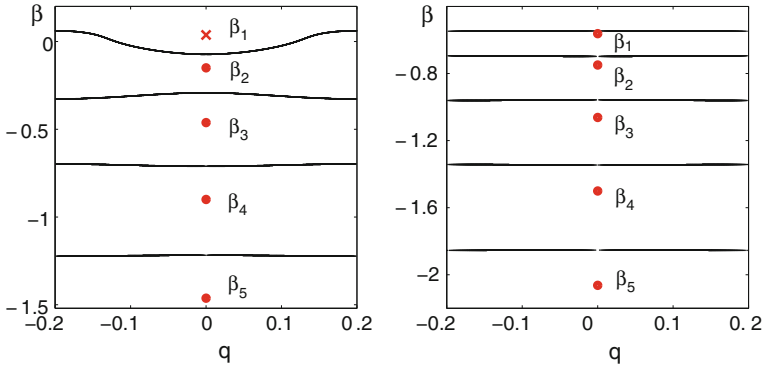

Fig. 11 Band structure (propagation constant β versus Bloch wavenumber q) and location of the propagation constants β_n of the analytically obtained stationary solutions (x: no analytical solution exists). The parameters are: $L = 4\pi$, $N = \pi$ and $\epsilon_N = 0$ and $\epsilon_L = 0.1$ (*left column*), $\epsilon_L = -0.5$ (*right column*)

$(\beta < \epsilon_N)$. It is noticeable that this value [marked as x in Fig. 11(left)] is located within the linear transmission band where, in principle, solitary waves are not expected to exist. The evolution of the stationary solutions, corresponding to Fig. 9 (first row, left) and (second row, middle), is shown in Fig. 12. The stationary solutions undergo robust evolution, which is quite promising for potential optical applications.

5 Interfaces Between Waveguide Arrays and Homogeneous Media or Dissimilar Waveguide Arrays

Surface waves appear in diverse areas of physics, chemistry, biology, and display properties that have no counterpart in the bulk [41]. Surface waves have been originally considered in the context of solid state and condensed matter physics, where a Kronig-Penney model was introduced to demonstrate the band structure of electronic states in crystals. This model has been used by Tamm [42] who showed that at a semi-infinite Kronig-Penney potential, the formation of surface states (also known as Tamm states) is possible under certain conditions, while the case of a more general one-dimensional potential was examined by Shockley [43].

In linear optics, the utilization of periodic layered media in guided wave optical applications has been a subject of theoretical and experimental investigations for a few decades. Among these studies of particular interest is the investigation of the wave guiding properties of the interface between such a periodic medium and a homogeneous medium and the formation of the surface waves. [44] In the context of nonlinear optics, the combination of nonlinearity and periodicity have allowed for overcoming the experimental limitations of the homogeneous cases, mainly

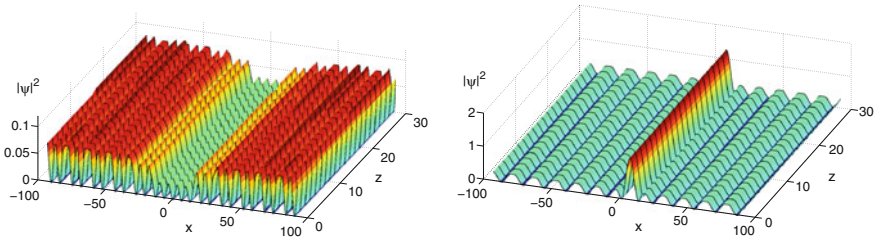

Fig. 12 Propagation of the solitary waves corresponding to Fig. 9 (*first row, left*) and Fig. 9 (*second row, middle*), from *left to right*, respectively

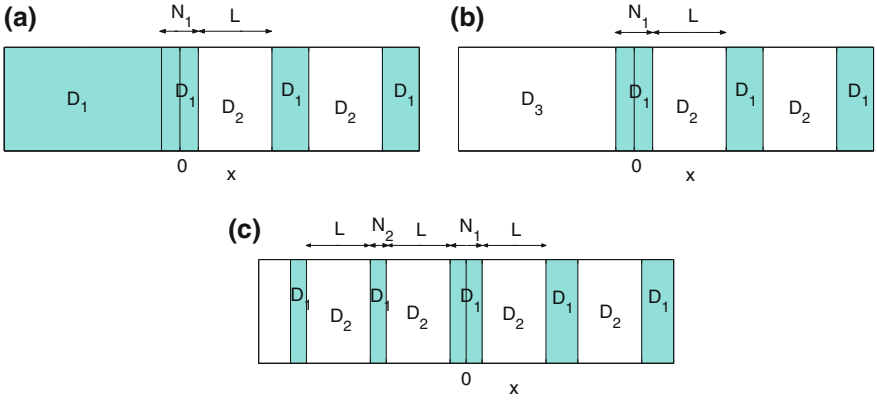

Fig. 13 Transverse profile of the photonic structure consisting of a nonlinear lattice (parts D_1 and D_2) and a homogeneous linear (**a**) or nonlinear (**b**) homogeneous medium (part D_3) as well as two dissimilar nonlinear lattices having different widths of the corresponding nonlinear parts (**c**). *Shaded areas* denote nonlinear medium while *nonshaded areas* denote linear medium

related to high power thresholds required for proper excitation. The latter resulted in the recent renewal of the interest for the study of surface waves in the interfaces of such photonic structures. The formation of surface solitons was predicted and almost directly observed in 2006 for the cases of discrete surface solitons [45–51] and surface gap solitons [52–54]. Moreover, surface lattice solitons have been theoretically predicted for the case of the heterointerface between two different semi-infinite waveguide arrays [55–57], as well as at the boundaries of two-dimensional nonlinear lattices [55, 58].

In this section we apply the phase space method for the construction of analytical solitary wave solutions located at the interface of a nonlinear (Kerr) Kronig-Penney lattice with a homogeneous linear or nonlinear medium as well as at the interface between two dissimilar nonlinear lattices. [25] We consider the case of a photonic structure consisting of two parts: either a nonlinear lattice and a homogeneous (linear or nonlinear) medium or two dissimilar nonlinear lattices having different widths of the corresponding nonlinear parts. The geometry of the configurations is shown in Fig. 13.

5.1 Model and Analytical Solutions

The stationary wave solutions are given by Eq. (3) with the functions $\epsilon(x)$ and $g(x)$ defined as follows

$$(\epsilon(x), g(x)) = \begin{cases} (\epsilon_1, 2), & x \in D_1 \\ (\epsilon_2, 0), & x \in D_2 \\ (\epsilon_3, 0), & x \in D_3 \end{cases} \tag{15}$$

In each part Eq. (3) is integrable with corresponding phase spaces such as those shown in Fig. 1. The phase space corresponding to the nonlinear part is shown in Fig. 1a, for the case $\beta > \epsilon_1$, where a homoclinic solution exist. For a linear part the phase space is shown in Fig. 1c and (d) for $\beta < \epsilon_i$ and $\beta > \epsilon_i$ ($i = 2$ or 3), respectively. The stationary solutions of (3) can be provided by composing solutions of these systems, which have matched conditions for u and its derivative, at the interfaces. Following arguments similar to those of previous sections, for a propagation constant

$$\beta_n = \epsilon_2 - \left(\frac{n\pi}{L}\right)^2, n = 1, 2, \ldots \tag{16}$$

corresponding to the case where an integer number of half-periods of the solution in the linear part (D_2) is contained in the length L, the continuity conditions are met simultaneously in all boundaries, for $x > 0$: Any solution of Eq. (3) starting from a point of the homoclinic orbit inside the nonlinear part (D_1) at some x, returns to the homoclinic orbit after evolving in the linear part (D_2) and subsequently evolves again according to the homoclinic orbit. Thus, the solution approaches the origin asymptotically as $x \to +\infty$, moving on the homoclinic orbit but interrupted periodically due to the linear part of the structure. For the case of a nonlinear homogeneous part [Fig. 13 (a)] (for simplicity we consider that the medium characteristics are identical with those of the nonlinear part of the lattice (D_1)), the solution moves on the same homocinic orbit for $x < -N_1/2$, approaching the origin as $x \to -\infty$ (Fig. 14a). The resulting solutions form a family, parameterized by the position of the maximum of the homoclinic orbit x_0, corresponding to solitary wave profiles zero asymptotic values. For the case of a linear homogeneous medium (Fig. 13b) we can distinguish two different cases depending on the value of the propagation constant β with respect to the value of the linear refractive index ϵ_3: (i) For a $\beta < \epsilon_3$ any solution (for every x_0) constructed in the aforementioned way for the lattice part of the structure meets at $x = -N_1/2$ one of the elliptical curves of the phase space shown in Fig. 1c and then evolves periodically for $x \in [-N_1/2, -\infty)$ (Fig. 14b). This family of solutions correspond to solitary wave profiles with a zero asymptotic value for $x \to +\infty$ and a finite periodic (sinusoidal) pedestal for $x \to -\infty$. (ii) For every $\beta > \epsilon_3$ there exist a solution (for a particular x_0) for which the part of the homoclinic orbit comprising the lattice part of the solution in $x \in [-N_1/2, N_1/2]$ intersects one of the straight

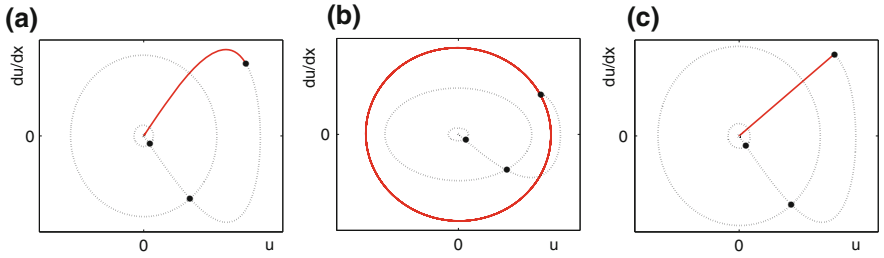

Fig. 14 Phase space representation of the constructed solutions for n even. **a** Nonlinear homogeneous part, **b** Linear homogeneous part having $\beta < \epsilon_3$, and **c** Linear homogeneous part having $\beta > \epsilon_3$. *Dotted line* denotes the solution in the lattice part and *solid line* denotes the solution in the homogeneous part. *Black dots* depict transition at the boundary between different layers

lines tending to the origin as $x \to +\infty$ of the phase space shown in Fig. 1d (this having $u > 0$, without loss of generality), at the boundary $x = -N_1/2$. This solution correspond to a solitary wave profile with zero asymptotic values [Fig. 14c]. Finally, for the case of two dissimilar lattices [Fig. 13c], the solution evolves in the the left lattice, similarly to the right lattice, tending to the origin as $x \to -\infty$. Note that in Fig. 14, the case of an even n is shown, so that the solution in the lattice part lays on a single branch of the homoclinic; in the case of n odd, the solution in the lattice part lays on both branches of the homoclinic.

In all cases, the solitary wave stationary solutions corresponding to β_n can be given analyticaly in the following form

$$u(x;\beta_n,x_0) = \begin{cases} v(x;\beta_n,x_0) & x \in D_1 \\ a_k \sin(\sqrt{\epsilon_{2,3} - \beta_n}x + \phi_k) & x \in D_2, D_3 \end{cases} \tag{17}$$

where $v(x;\beta,x_0) = \pm\sqrt{\beta - \epsilon_1}$ sech $(\sqrt{\beta - \epsilon_1}(x - x_0))$ is the homoclinic solution of the nonlinear part (D_1) of the structure (Fig. 1a), and (a_k, ϕ_k) are directly obtained from the continuity conditions of u and its derivative at the interfaces.

5.2 Results and Discussion

In the following we apply the phase space method for the construction of surface localized solutions for the case of a lattice having a linear refractive index profile with parameters $\epsilon_1 = 0$, $\epsilon_2 = 0.3$, $N_1 = 2\pi$, $L = 4\pi$. For this case the condition for the existence of the aforementioned family of solutions $(\epsilon_1 < \beta < \epsilon_2)$ are met for propagation constants β_n given by Eq. (16) for $n = 1, 2$. Each one of these values β_n is located in a different finite gap of the linear band structure of the infinite lattices, as shown in Fig. 15.

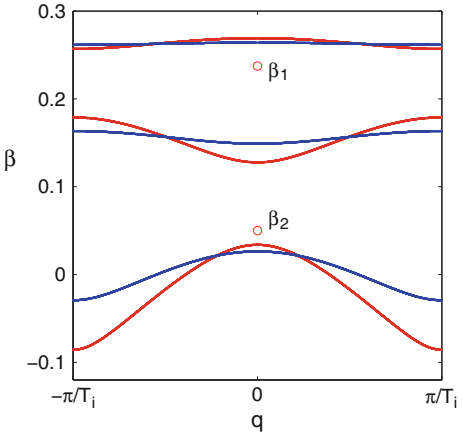

Fig. 15 Band structure of the linearized system (propagation constant β vs Bloch wave number q) for the two lattices having $\epsilon_1 = 0$, $\epsilon_2 = 0.3$, $L = 4\pi$ and $N_1 = 2\pi$ (*blue line*), $N_2 = \pi$ (*red line*). $T_i = L + N_i$, $i = 1, 2$ is the period of each lattice. *Circles* depict the location of the analytically obtained localized modes for $n = 1, 2$

5.2.1 Nonlinear Homogeneous Medium

We consider the case where the nonlinear homogeneous medium has the same material characteristics with the nonlinear part of the lattice. In this case there exist an infinite number of solutions corresponding to different x_0 for each β_n. The phase space representation of a typical solution is shown in Fig. 14a, while their profiles for some characteristic cases of x_0 are shown in Fig. 16. Solitary wave profiles can attain their maximum amplitude inside the homogeneous medium [Fig. 16(left)], in the linear part of the lattice [Fig. 5(middle)], or in the first nonlinear part of the lattice [Fig. 16(right)].

The propagation of the analytically obtained solitary wave profiles of Fig. 16 is illustrated in Fig. 17. It is shown that the solutions corresponding to $n = 1$ [Fig. 17(top)], under propagation, break in two parts: one traveling inside the homogeneous part and one which is localized close to the interface. The latter corresponds to a surface mode having different x_0 and/or β. Such mode transformations are characterized by evolution of an initial mode to a more stable mode having lower values of Hamiltonian and Energy [38] as discussed in previous section: the initial solution emits part of its energy as a wave traveling inside the homogeneous energy, in order to evolve to the new localized mode. It is remarkable that this transformation process can be quite slow [Fig. 17(top, right)], and become apparent for large propagation distances. Depending on the length of an actual experimental configuration some these cases can also be considered as robust, since the laminar propagation distance can be larger than the actual propagation length. Also, the mode transformation process itself can also be potentially useful in applications. On the other hand, as shown in Fig. 17(bottom) the solutions corresponding to $n = 2$ are remarkably stable.

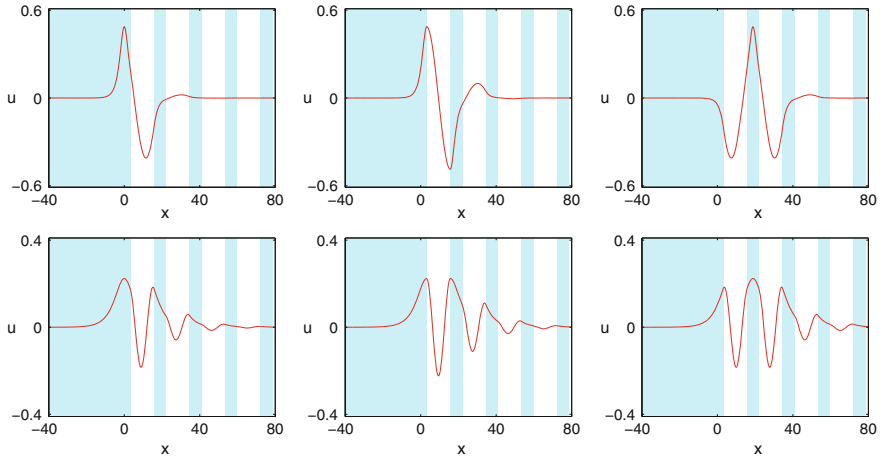

Fig. 16 Profiles of stationary surface lattice solutions for the case of a nonlinear homogeneous medium having the same material characteristics with the nonlinear part of the lattice, for $n = 1, 2$ (*top to bottom*) and $x_0 = 0, \pi, 2\pi$ (*left to right*). The solutions depicted in the *first* (*second*) *row* are unstable (stable) as shown in Fig. 17

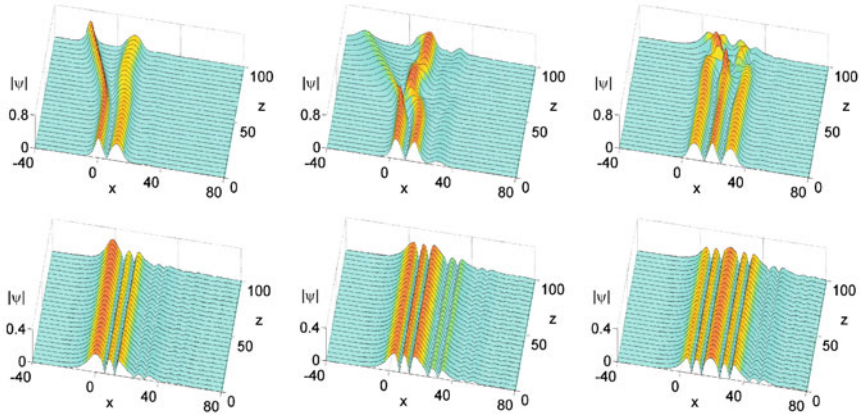

Fig. 17 Propagation of the stationary solutions shown in Fig. 16

5.2.2 Linear Homogeneous Medium

In this case we consider a homogeneous linear medium having $\epsilon_3 = 0.1$. For the formation of surface waves in the interface between the lattice and a linear homogeneous medium, we can distinguish between two qualitatively different cases:

Case $\beta < \epsilon_3$

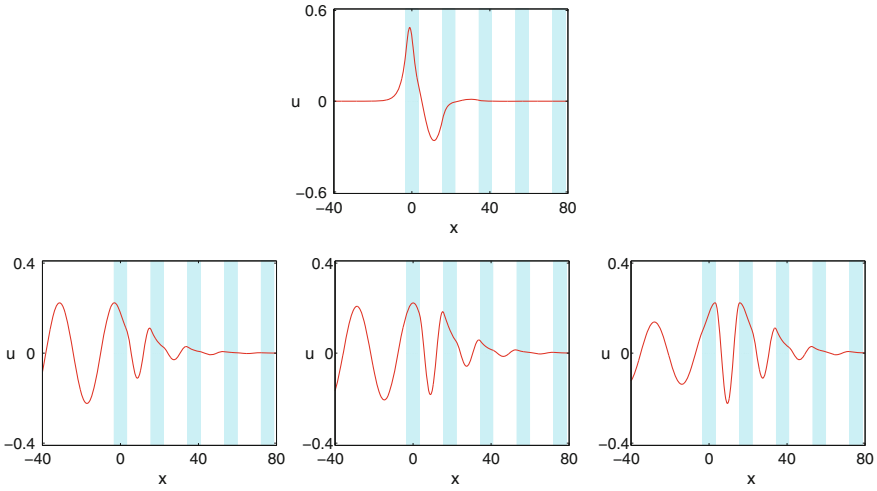

Fig. 18 Profiles of stationary surface lattice solutions for the case of a linear homogeneous medium having $\epsilon_3 = 0.1$, for $n = 1, 2$ (*top to bottom*) and $x_0 = -\pi, 0, \pi$ (*left to right*). The solutions depicted in the *first* (*second*) *row* are unstable (stable) as shown in Fig. 19

In this case, for each β_n there exist a infinite number of solutions, characterized by a different x_0. Their phase space representation has been shown in Fig. 14b and their profiles for some characteristic values of x_0 are shown in Fig. 18(bottom), corresponding to $n = 2$, for which $\beta_2 < \epsilon_3$ (for the specific values of the linear refractive indices used in our example). It is shown that for $x_0 \in [-N_1/2, N_1/2]$ the maximum of the solution is located inside the first nonlinear waveguide while the amplitude of the periodic pedestal in the linear homogeneous medium decreases as x_0 moves from the left boundary of the nonlinear part to the right. An increasing width of the nonlinear part N_1 would also results in decreasing pedestal. Also, solutions having their maxima located in other than the first nonlinear waveguide, can be constructed. Figure 19(bottom) shows a stable evolution of these stationary solutions under propagation.

Case $\beta > \epsilon_3$

In this case, for each value of β_n, there exist one solution for a particular x_0, given by

$$x_0 = \frac{1}{\sqrt{\beta - \epsilon_1}} sech^{-1}\left(\frac{\sqrt{\epsilon_3 - \epsilon_1}}{\sqrt{\beta - \epsilon_1}}\right) - \frac{N_1}{2} \tag{18}$$

The phase space representation of the solutions is shown in Fig. 14c. For our example, this case corresponds to $n = 1$. The profile of such a solution is shown in Fig. 18(top), while its propagation is illustrated in Fig. 19(top), where a large distance of laminar propagation is shown, with the part in the right slightly moving to the right for $z > 60$.

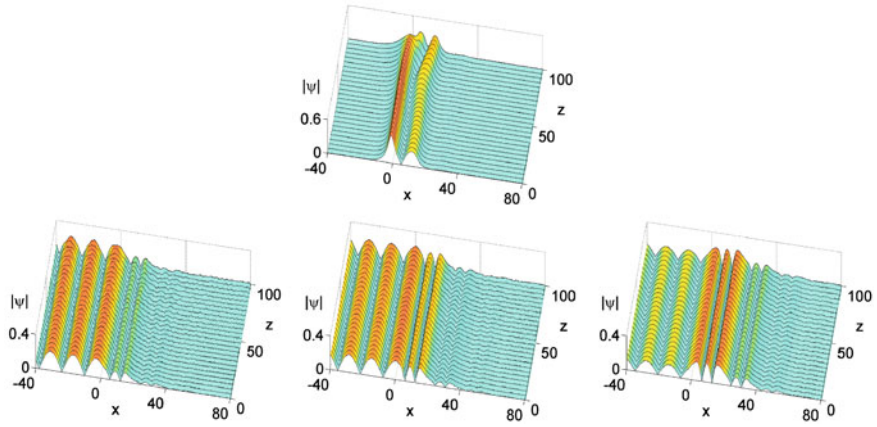

Fig. 19 Propagation of the stationary solutions shown in Fig. 18

5.2.3 Two Dissimilar Nonlinear Waveguide Arrays

We consider the configuration shown in Fig. 13c, with $N_2 = \pi$. The profiles of the analytically obtained solutions are shown in Fig. 20, for the case where the maximum of the solution is located at the center of the first nonlinear part of the right lattice $(x_0 = 0)$, at the linear part between the two lattices $(x_0 = -\pi)$ and at the center of the first nonlinear part of the left lattice $(x_0 = -3\pi/2)$. It is shown that the solitary wave is more extended inside the array with the narrower nonlinear part. The propagation of these solutions is shown in Fig. 21, with the solutions corresponding to $n = 2$ [Fig. 21(bottom)], having stable evolution under propagation. Note that the values of the propagation constants $\beta_{1,2}$ corresponding to the analytically obtained solutions are located within the finite band gaps of both lattices, as shown in Fig. 15.

6 Concluding remarks

The study of the formation and dynamics of solitary waves in photonic structures is a field of continuously increasing research interest from both theoretical and experimental point of view. The spatial inhomogeneity and nonlinearity of such structures result to unique properties of solitary wave propagation. Appropriate design can provide useful widespread technological applications in optical telecommunications, medicine and biotechnology. In accordance with numerous other cases of related physical or man-made systems, the nonlinear effects and the accompanying complexity of the wave dynamics and interactions have been recognized as effective potential mechanisms for light control. Therefore it is possible

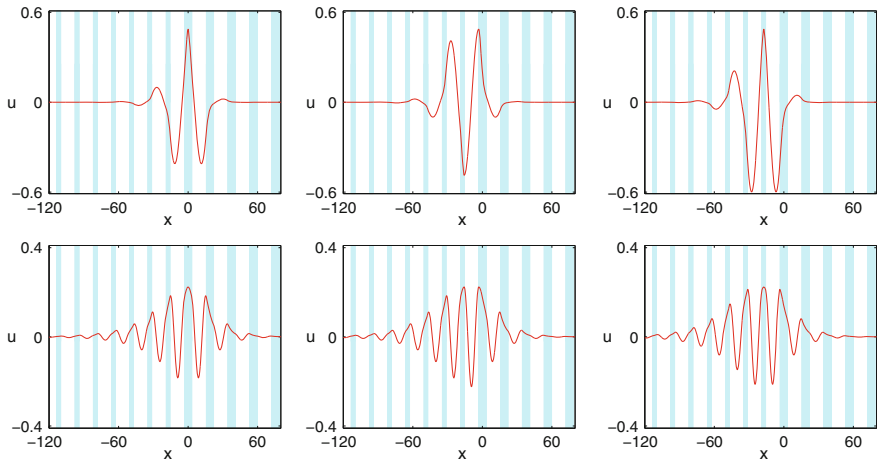

Fig. 20 Profiles of stationary surface lattice solutions for the case of the interface between two dissimilar nonlinear waveguide arrays, for $n = 1, 2$ (*top to bottom*), and $x_0 = 0, -\pi, -3\pi/2$ (*left to right*). The solutions depicted in the *first* (*second*) *row* are unstable (stable) as shown in Fig. 21

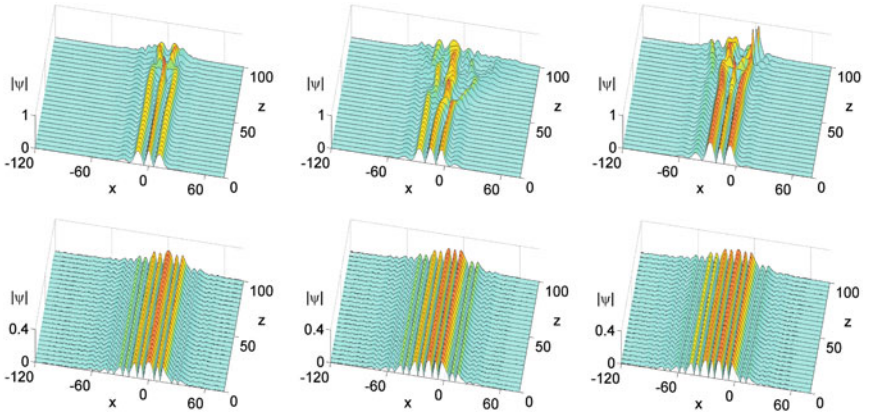

Fig. 21 Propagation of the stationary solutions shown in Fig. 20

to design photonic structures having desirable features and properties. The latter are expected to provide optical devices for "all-optical circuitry" for switching, routing, information processing and computing beyond the limitations of electronics-based systems. It is also worth noting that the aforementioned concepts are directly connected to other domains of nonlinear physics such as the formation of spin waves in magnetic films and the rapidly developing field of coherent matter waves and nonlinear atom optics. Theoretical studies in these fields proceed in parallel due to similarities between the underlying models allowing for transfer of intuition and novel ideas between them.

Spatial inhomogeneity and nonlinearity result, in general, in nonintegrability of the underlying models and lack of knowledge for analytical solutions. In this work we have considered a class of systems consisting of interlaced linear and nonlinear parts. Periodic waveguide arrays as well as structures consisting of semi-infinite waveguide arrays and their interfaces have been studied, while the method presented here can be applied to even larger classes of systems including combinations of parts of waveguide arrays, homogeneous parts and defects as well as different types of nonlinearities. The method utilizes the phase space description of the system for the construction of analytical solutions. Such solutions can serve as starting points for the exploration of even larger classes of solutions and systems with the utilization of perturbation methods. Moreover, the method provides physical intuition for the formation of solitary waves in such structures.

Acknowledgments Y. Kominis would like to thank Professor T. Bountis for valuable comments and discussions on phase space analysis of complex dynamical systems. The preparation of this article has been partially supported by the Project NWDCCPS (Y.K.) and the THALES Project ANEMOS (K.H.), co-financed by the European Union (European Social Fund - ESF) and Greek national funds through the Operational Program "Education and Lifelong Learning" of the National Strategic Reference Framework (NSRF) "Investing in knowledge society through the European Social Fund".

References

1. S. Trillo, W. Torruellas W (eds), *Spatial Solitons* (Springer, Berlin, 2001)
2. D.N. Christodoulides, F. Lederer, Y. Silberberg, Discretizing light behaviour in linear and nonlinear waveguide lattices. Nature **424**, 817–823 (2003)
3. A.A. Sukhorukov, Y.S. Kivshar, H.S. Eisenberg, Y. Silberberg, Spatial optical solitons in waveguide arrays. IEEE J. Quantum Electron. **39**, 31–50 (2003)
4. F. Lederer, G.I. Stegeman, D.N. Christodoulides et al., Discrete solitons in optics. Phys. Rep. **463**, 1–126 (2008)
5. Y.V. Kartashov, V.A. Vysloukh, L. Torner, Soliton shape and mobility control in optical lattices. Prog. Optics **52**, 63–148 (2009)
6. Y.V. Kartashov, B.A. Malomed, L. Torner, Solitons in nonlinear lattices. Rev. Mod. Phys. **83**, 247–306 (2011)
7. Y. Kominis, K. Hizanidis, Power dependent soliton location and stability in complex photonic structures. Opt. Express **16**, 12124–12138 (2008)
8. K. Hizanidis, Y. Kominis, N.K. Efremidis, Interlaced linear-nonlinear optical waveguide arrays. Opt. Express **16**, 18296–18311 (2008)
9. R.Y. Hao, R.C. Yang, L. Li, G.S. Zhou, Solutions for the propagation of light in nonlinear optical media with spatially inhomogeneous nonlinearities. Opt. Commun. **281**, 1256–1262 (2008)
10. Y. Kominis, K. Hizanidis, Power-dependent reflection, transmission and trapping dynamics of lattice solitons at interfaces. Phys. Rev. Lett. **102**, 133903 (2009)
11. A. Szameit, H. Trompeter, M. Heinrich, F. Dreisow, U. Peschel, T. Pertsch, S. Nolte, F. Lederer, A. Tunnermann, Fresnel's laws in discrete optical media. New J. Phys. **10**, 103020 (2008)
12. Y.J. He, D. Mihalache, B.B. Hu, Soliton drift, rebound, penetration, and trapping at the interface between media with uniform and spatially modulated nonlinearities. Opt. Express **35**, 1716–1718 (2010)

13. P. Papagiannis, Y. Kominis, K. Hizanidis, Power- and momentum-dependent soliton dynamics in lattices with longitudinal modulation. Phys. Rev. A **84**, 013820 (2011)
14. D.N. Christodoulides, R.I. Joseph, Discrete self-focusing in nonlinear arrays of coupled wave-guides. Opt. Lett. **13**, 794–796 (1988)
15. H.G. Winful, Pulse-compression in optical fiber filters. Appl. Phys. Lett. **46**, 527–529 (1985)
16. N.K. Efremidis, D.N. Christodoulides, Lattice solitons in Bose-Einstein condensates. Phys. Rev. A **67**, 063608 (2003)
17. S. Theodorakis, E. Leontidis, Bound states in a nonlinear Kronig-Penney model. J. Phys. A Math. Gen. **30**, 4835–4849 (1997)
18. W. Li, A. Smerzi, Nonlinear Kronig-Penney model. Phys. Rev. E **70**, 016605 (2004)
19. B.T. Seaman, L.D. Carr, M.J. Holland, Period doubling, two-color lattices, and the growth of swallowtails in Bose-Einstein condensates. Phys. Rev. A **71**, 033622 (2005)
20. D. Witthaut, K. Rapedius, H.J. Korsch, The nonlinear Schrodinger equation for the delta-comb potential: quasi-classical chaos and bifurcations of periodic stationary solutions. J. Nonlinear Math. Phys. **16**, 207–233 (2009)
21. A.A. Sukhorukov, Y.S. Kivshar, Spatial optical solitons in nonlinear photonic crystals. Phys. Rev. E **65**, 036609 (2002)
22. I.M. Merhasin, B.V. Gisin, R. Driben, B.A. Malomed, Finite-band solitons in the Kronig-Penney model with the cubic-quintic nonlinearity. Phys. Rev. E **71**, 016613 (2005)
23. Y. Kominis, Analytical solitary wave solutions of the nonlinear Kronig-Penney model in photonic structures. Phys. Rev. E **73**, 066619 (2006)
24. Y. Kominis, K. Hizanidis, Lattice solitons in self-defocusing optical media: analytical solutions of the nonlinear Kronig-Penney model. Opt. Lett. **31**, 2888–2890 (2006)
25. Y. Kominis, A. Papadopoulos, K. Hizanidis, Surface solitons in waveguide arrays: analytical solutions. Opt. Express **15**, 10041–10051 (2007)
26. A.S. Rodrigues, P.G. Kevrekidis, M.A. Porter, D.J. Frantzeskakis, P. Schmelcher, A.R. Bishop, Matter-wave solitons with a periodic, piecewise-constant scattering length. Phys. Rev. A **78**, 013611 (2008)
27. H. Sakaguchi, B.A. Malomed, Solitons in combined linear and nonlinear lattice potentials. Phys. Rev. A **81**, 013624 (2010)
28. R. Marangell, C.K.R.T. Jones, H. Susanto, Localized standing waves in inhomogeneous Schrodinger equations. Nonlinearity **23**, 2059–2080 (2010)
29. Y. Li, B.A. Malomed, M. Feng, J. Zhou, Arrayed and checkerboard optical waveguides controlled by the electromagnetically induced transparency. Phys. Rev. A **82**, 063813 (2010)
30. A. Shapira, N. Voloch-Bloch, B.A. Malomed, A. Arie, Spatial quadratic solitons guided by narrow layers of a nonlinear material. J. Opt Soc. Am. B **28**, 1481–1489 (2011)
31. R. de L. Kronig, W.G. Penney, Quantum mechanics of electrons in crystal lattices. Proc. R. Soc. London **130**, 499–513 (1930)
32. F.K.H. Abdullaev, B.B. Baizakov, S.A. Darmanyan, V.V. Konotop, M. Salerno, Nonlinear excitations in arrays of Bose-Einstein condensates. Phys. Rev. A **64**, 043606 (2001)
33. E.A. Ostrovskaya, Y.S. Kinshar, Matter-wave gap solitons in atomic band-gap structures. Phys. Rev. Lett. **90**, 160407 (2003)
34. V.A. Brazhnyi, V.V. Konotop, Theory of nonlinear matter waves in optical lattices. Mod. Phys. Lett. B **18**, 627–651 (2004)
35. J. Guckenheimer, P. Holmes, *Nonlinear oscillations dynamical systems and bifurcations of vector fields* (Springer, Berlin, 1983)
36. Y. Kominis, T. Bountis, Analytical solutions of systems with piecewise linear dynamics. Int. J. Bifurc. Chaos **20**, 509–518 (2010)
37. Y.S. Kivshar, D.E. Pelinovsky, T. Cretegny, M. Peyrard, Internal modes of solitary waves. Phys. Rev. Lett. **80**, 5032–5035 (1998)
38. N. Akhmediev, A. Ankiewicz, R. Grimshaw, Hamiltonian-versus-energy diagrams in soliton theory. Phys. Rev. E **59**, 6088 (1999)
39. E. Smirnov, C.E. Ruter, D. Kip, Y.V. Kartashov, L. Torner, Observation of higher-order solitons in defocusing waveguide arrays. Opt. Lett. **32**, 1950–1952 (2007)

40. J. Belmonte-Beitia, J. Cuevas, Existence of dark solitons in a class of stationary nonlinear Schrödinger equations with periodically modulated nonlinearity and periodic asymptotics. J. Math. Phys. **52**, 032702 (2011)
41. A. Zangwill, *Physics at surfaces* (Cambridge University Press, Cambridge, 1988)
42. I. Tamm, Phys. Z. Sowjetunion **1**, 733–746 (1932)
43. W. Shockley, On the surface states associated with a periodic potential. Phys. Rev. **56**, 317–323 (1939)
44. P. Yeh, A. Yariv, A.Y. Cho, Optical surface waves in periodic layered media. Appl. Phys. Lett. **32**, 104–105 (1978)
45. K.G. Makris, S. Suntsov, D.N. Christodoulides, G.I. Stegeman, A. Hache, Discrete surface solitons. Opt. Lett. **30**, 2466–2468 (2005)
46. S. Suntsov, K.G. Makris, D.N. Christodoulides, G.I. Stegeman, A. Hache, R. Morandotti, H. Yang, G. Salamo, M. Sorel, Observation of discrete surface solitons. Phys. Rev. Lett. **96**, 063901 (2005)
47. M.I. Molina, I.L. Garanovich, A.A. Sukhorukov, Y.S. Kivshar, Discrete surface solitons in semi-infinite binary waveguide arrays. Opt. Lett. **31**, 2332–2334 (2006)
48. M.I. Molina, R.A. Vicencio, Y.S. Kivshar, Discrete solitons and nonlinear surface modes in semi-infinite waveguide arrays. Opt. Lett. **31**, 1693–1695 (2006)
49. D. Mihalache, D. Mazilu, F. Lederer, Y.S. Kivshar, Stable discrete surface light bullets. Opt. Express **15**, 589–595 (2007)
50. M. Stepic, E. Smirnov, C.E. Ruter, D. Kip, A. Maluckov, L. Hadzievski, Tamm oscillations in semi-infinite nonlinear waveguide arrays. Opt. Lett. **32**, 823–825 (2007)
51. D. Mihalache, D. Mazilu, F. Lederer, Y.S. Kivshar, Collisions between discrete surface spatiotemporal solitons in nonlinear waveguide arrays. Phys. Rev. A **79**, 013811 (2009)
52. Y.V. Kartashov, V.A. Vysloukh, L. Torner, Surface gap solitons. Phys. Rev. Lett. **96**, 073901 (2006)
53. C.R. Rosberg, D.N. Neshev, W. Krolikowski, A. Mitchell, R.A. Vicencio, M.I. Molina, Y.S. Kivshar, Observation of surface gap solitons in semi-infinite waveguide arrays. Phys. Rev. Lett. **97**, 083901 (2006)
54. E. Smirnov, M. Stepic, C.E. Ruter, D. Kip, V. Shandarov, Observation of staggered surface solitary waves in one-dimensional waveguide arrays. Opt. Lett. **31**, 2338–2340 (2006)
55. K.G. Makris, J. Hudock, D.N. Christodoulides, G.I. Stegeman, O. Manela, M. Segev, Surface lattice solitons. Opt. Lett. **31**, 2774–2776 (2006)
56. M.I. Molina, Y.S. Kivshar, Interface localized modes and hybrid lattice solitons in waveguide arrays. Phys. Let. A **362**, 280–282 (2007)
57. M. Heinrich, Y.V. Kartashov, L.P.R. Ramirez, A. Szameit, F. Dreisow, R. Keil, S. Nolte, A. Tünnermann, V.A. Vysloukh, L. Torner, Two-dimensional solitons at interfaces between binary superlattices and homogeneous lattices. Phys. Rev. A **80**, 063832 (2009)
58. Y.V. Kartashov, V.A. Vysloukh, D. Mihalache, L. Torner, Generation of surface soliton arrays. Opt. Lett. **31**, 2329–2331 (2006)

Trapping Polarization of Light in Nonlinear Optical Fibers: An Ideal Raman Polarizer

Victor V. Kozlov, Javier Nuño, Juan Diego Ania-Castañón and Stefan Wabnitz

Abstract The main subject of this contribution is the all-optical control over the state of polarization (SOP) of light, understood as the control over the SOP of a signal beam by the SOP of a pump beam. We will show how the possibility of such control arises naturally from a vectorial study of pump-probe Raman interactions in optical fibers. Most studies on the Raman effect in optical fibers assume a scalar model, which is only valid for high-PMD fibers (here, PMD stands for the polarization-mode dispersion). Modern technology enables manufacturing of low-PMD fibers, the description of which requires a full vectorial model. Within this model we gain full control over the SOP of the signal beam. In particular we show how the signal SOP is pulled towards and trapped by the pump SOP. The isotropic symmetry of the fiber is broken by the presence of the polarized pump. This trapping effect is used in experiments for the design of new nonlinear optical devices named Raman polarizers. Along with the property of improved signal amplification, these devices transform an arbitrary input SOP of the signal beam into one and the same SOP towards the output end. This output SOP is fully controlled by the SOP of the pump beam. We overview the state-of-the-art of the subject and introduce the notion of an "ideal Raman polarizer."

V. V. Kozlov (✉) · S. Wabnitz
Department of Information Engineering, Università di Brescia,
Via Branze 38, 25123, Brescia, Italy
e-mail: victor.kozlov@email.com

V. V. Kozlov
Department of Physics, St.-Petersburg State University,
Petrodvoretz, 198504, St.-Petersburg, Russia

J. Nuño · J. D. Ania-Castañón
Instituto de Optica, Consejo Superior de Investigaciones Cientificas (CSIC),
28006, Madrid, Spain

Progress Optical Sci., Photonics (2013): 227–246
DOI: 10.1007/10091_2012_8

Published Online: 19 June 2012

1 Introduction

Over the past few years, the possibility of utilizing the Raman effect in optical waveguides as the basis for the development of non-linear polarizers has opened the way to an interesting range of potential applications, such as multi-channel repolarization in optical fibers, enhanced amplification and even the possibility of developing silicon-based Raman polarizers [1–5].

Raman-based polarization attraction falls into a broad class of potentially game-changing effects related to light-by-light control in optical waveguides. Models for such control are essentially nonlinear and usually imply the use of a high-intensity beam to modify the properties of the medium (for instance its refractive index or absorption coefficient) such that propagation of a weaker probe beam through the nonlinearly modified medium is affected in a substantial and controllable way. The possibility of achieving nonlinear polarization control is rooted in soliton theory, namely in conservative structures such as the polarization domain wall solitons [6–11]. However conclusions extracted from soliton theories involving a medium of infinite extension can be misleading for counterpropagating waves in a medium of finite length. In this case the presence of boundary conditions may lead to solitons with a finite lifetime [12]. In such situation, other so-called polarization attractors representing the unique distribution of SOPs of the two beams inside the medium play a key role in the process of trapping polarization of light [12, 13].

Different mechanisms such as photorefractive two-beam coupling [14] or Kerr nonlinearity [10, 15] have, over the years, proven to be capable of producing nonlinear polarization attraction. In their initial demonstrations, all of these methods were subject to limitations in their application in telecommunication links: their response time, in the case of photorefractive materials, or the requirement of extremely high beam powers. Only recently results of practical relevance have emerged, with non-conservative schemes based on stimulated Raman [16] or Brillouin scattering [17], as well as the first low-power lossless polarizer, consisting of a 20 km randomly weakly birefringent fiber pumped by an incoherent counter-propagating beam [18].

As mentioned above, here we will focus on the particular and very promising case of Raman polarizers, in which the pump and signal beam propagate through a Raman-active medium. By way of interacting with this medium, the pump beam induces a phonon-mediated gain for a frequency down-shifted (Stokes) signal beam. The signal beam, co- or counter-propagating with the pump beam, is then gradually amplified. This amplification mechanism lies at the heart of Raman amplifiers. One degree of control exerted by the pump beam over the signal beam is the total gain experienced by the signal from input to the output. This degree of control is well studied in literature and widely used in practice. Much less known is another degree of control—over the state of polarization (SOP) of the signal beam. The main subject of this study are *polarization-sensitive* Raman amplifiers, in which polarization-dependent gain (PDG), an intrinsic characteristic of the Raman effect which is usually considered an undesirable feature in amplification

applications, can be turned into an advantage by selectively amplifying only one polarization mode of the input beam.

Signal and pump fields considered in this study are continuous waves (CW) or relatively long pulses, such that the response of the Raman-active medium is virtually instantaneous, and as such it is described by the instantaneous dissipative cubic nonlinearity. Mostly, our theoretical study is developed for silica single-mode fibers, though extensions to other Raman-active media, such as silicon are also possible [5]. We shall demonstrate how polarization-sensitive Raman amplifiers operate in the regime of Raman polarizers. These Raman polarizers are devices that along with the function of amplification of light, also re-polarize the beam: the SOP of the outcoming signal beam is defined by the SOP of the pump beam, independently of what SOP the signal beam had at the input. In other words, the signal SOP is attracted (trapped) by the pump SOP. By changing the polarization of the pump we thereby change the signal SOP. In this way we exercise an all-optical control over the signal SOP.

In this chapter we will present the theory of Raman polarizers with an emphasis on randomly birefringent fibers, such as the ones used in the telecom industry. We shall identify the conditions that are necessary for a traditional Raman amplifier to function as Raman polarizer, and characterize its performance.

2 Model

In short, we shall consider the simultaneous propagation of two beams in a Raman-active medium. In our case the Raman active medium is a few kilometers long span of a telecom fiber. The fiber is linearly birefringent, and also characterized by both conservative and dissipative cubic nonlinearities. The main feature that makes our theory different from most previous studies on fiber-optic Raman amplifiers is its vectorial nature. Thus, we carefully consider the propagation dynamics of two polarization components of each of the two beams. In total, the number of field components is four, and they all interact with each other via cubic nonlinearity. The first vectorial theory of Raman effect in randomly birefringent optical fibers was developed by Lin and Agrawal in Ref. [19] and applied to the regime of interaction characteristic to what we call here "standard Raman amplifiers." Here we are interested in a totally different regime, namely the regime of Raman polarizer. The difference between the two regimes is explained below, in the beginning of Sect. 2.

We start from the equation of motion for the signal field, written for the two-component field vector $U_s = (u_{sx}, u_{sy})^T$, where u_{sx} and u_{sy} are the amplitudes of the normal polarization modes $\mathbf{e}_x$ and $\mathbf{e}_y$ of the fiber: $\mathbf{U}_s = u_{sx}\mathbf{e}_x + u_{sy}\mathbf{e}_y$. This equation is derived under the (as usual for nonlinear optics) unidirectional and slowly varying approximations, see for instance [19, 20], and reads

$$
\begin{aligned}
& i\partial_z U_s + i\beta'(\omega_p)\partial_t U_s + \Delta B(\omega_s) U_s \\
& \quad + \gamma_{ss}\left[\frac{2}{3}(U_s^* \cdot U_s)U_s + \frac{1}{3}(U_s \cdot U_s)U_s^*\right] \\
& \quad + \frac{2}{3}\gamma_{sp}\left[(U_p^* \cdot U_p)U_s + (U_p \cdot U_s)U_p^* + (U_s \cdot U_p^*)U_p\right] \\
& \quad + i\epsilon_s g (U_p^* \cdot U_s)U_p = 0.
\end{aligned}
\tag{1}
$$

A similar equation (with indices p and s interchanged) arises for the pump beam, which is characterized by the field vector U_p. Here γ_{ss} and γ_{sp} are self- and cross-modulation coefficients, whose values depend on frequency, and therefore in principle are different for the signal and pump beams. They are equal to the frequency-dependent Kerr coefficient of the fiber. For simplicity we assume $\gamma_{ss} = \gamma_{pp} = \gamma_{ps} \equiv \gamma$, $\beta'(\omega_{p,s})$ is the inverse group velocity of the pump/signal beam. $\epsilon_s = 1, \epsilon_p = -\omega_s/\omega_p, \Delta B(\omega_{p,s})$ is the birefringence tensor. For a linearly birefringent fiber it takes the form $\Delta B(\omega_{p,s}) = \Delta\beta(\omega_{p,s})(\cos\theta\sigma_3 + \sin\theta\sigma_1)$, where $\Delta\beta(\omega_{p,s})$ is the value of birefringence at frequency $\omega_{p,s}$, and θ the angle of orientation of the axis of the birefringence with respect to the reference frame defined by polarization modes $\mathbf{e}_x$ and $\mathbf{e}_y$. σ_3 and σ_1 are the usual Pauli matrices.

The orientation angle θ is randomly varying in fibers. In principle, the magnitude of the birefringence $\Delta\beta$ also varies stochastically. However, as noticed in Ref. [21], the two approaches, one in which θ is the only stochastic variable, and the second, where both θ and $\Delta\beta$ are stochastic variables, produce nearly identical results. Thus, here we shall develop our theory by assuming the single stochastic variable θ. Our theory can be seen as a generalization of the one beam linearly birefringent theory of Wai and Menyuk from Ref. [21] to the case of two beams interacting via the Kerr and Raman nonlinearity in a fiber. The angle θ is driven by a white noise process $\partial_z\theta = g_\theta(z)$, where $\langle g_\theta(z)\rangle = 0$ and $\langle g_\theta(z) g_\theta(z')\rangle = 2L_c^{-1}\delta(z - z')$. Here L_c is the correlation length, that characterizes the typical distance at which θ changes randomly.

Details of the theory are presented in Refs. [2, 3]. Here we quickly drive through the major steps of this theory and show how to obtain the final result—a set of four coupled first-order ordinary differential equations, one equation for each polarization component of two beams. It is instructive to present these four equations as two vectorial equations for the Stokes vectors of the pump and signal beams. Each Stokes vector has three components. Namely, the pump Stokes vector $\mathbf{S}^{(p)} = \left(S_1^{(p)}, S_2^{(p)}, S_3^{(p)}\right)$ has components $S_1^{(p)} = \Psi_{p1}^*\Psi_{p2} + \Psi_{p1}\Psi_{p2}^*, S_2^{(p)} = i\left(\Psi_{p1}^*\Psi_{p2} - \Psi_{p1}\Psi_{p2}^*\right), S_3^{(p)} = |\Psi_{p1}|^2 - |\Psi_{p2}|^2$, and power $S_0^{(p)} = |\mathbf{S}^{(p)}|$. Similar expressions define the signal Stokes vector $\mathbf{S}^{(s)}$. Here the field vector Ψ is related to the original Jones field vector U by the relation $\Psi_{p,s} = T_{p,s}U_{p,s}$, where the 2×2 matrices $T_{p,s}$ with elements

$$T_p(z) = \begin{pmatrix} a_1 & a_2 \\ -a_2^* & a_1^* \end{pmatrix}, \tag{2}$$

$$T_s(z) = \begin{pmatrix} b_1 & b_2 \\ -b_2^* & b_1^* \end{pmatrix}. \tag{3}$$

obey the stochastic differential equations

$$\pm i\partial_z T_p + \Delta B(\omega_p) T_p = 0, \tag{4}$$

$$i\partial_z T_s + \Delta B(\omega_s) T_s = 0, \tag{5}$$

where plus (minus) sign stands for the co- (counter-) propagating regime of propagation of the two beams, and

$$\Delta B(\omega_p) = \begin{pmatrix} \Delta\beta(\omega_p) & \mp\frac{i}{2}\theta_z \\ \pm\frac{i}{2}\theta_z & -\Delta\beta(\omega_p) \end{pmatrix}, \tag{6}$$

$$\Delta B(\omega_s) = \begin{pmatrix} \Delta\beta(\omega_s) & -\frac{i}{2}\theta_z \\ \frac{i}{2}\theta_z & -\Delta\beta(\omega_s) \end{pmatrix}. \tag{7}$$

Here, θ_z is the derivative of θ with respect to z. It is different from zero owing to the random changes of orientation of the birefringence axes. Now the polarization components of each beam appear to be defined with respect to the local birefringence axes, while these axes rotate stochastically along the fiber length driven by the noise source $g_\theta(z)$.

These transformations eliminate the birefringence terms from the equations of motion of Ψ_p and Ψ_s and bring about a vast number of cubic terms composed of different combinations of $\Psi_{p1}, \Psi_{p2}, \Psi_{s1}, \Psi_{s2}$ and their complex conjugates. Factors in front of these terms are products of two coefficients of the form $u_m u_n$, or $u_m^* u_n$, or $u_m^* u_n^*$, where $m, n = 1, \ldots, 14$. Products with $m = n$ we shall call self-products, while with $m \neq n$ cross-products. Here, $u_1 = |a_1|^2 - |a_2|^2, u_2 = -(a_1 a_2 + a_1^* a_2^*)$, $u_3 = i(a_1 a_2 - a_1^* a_2^*), u_4 = 2a_1 a_2^*, u_5 = a_1^2 - a_2^{*2}, u_6 = -i(a_1^2 + a_2^{*2})$, $u_7 = a_1^* b_1 - a_2 b_2^*$, $u_8 = -(b_1 a_2 + b_2^* a_1^*)$, $u_9 = i(b_1 a_2 - a_1^* b_2^*), u_{10} = -i(a_1^* b_1 + a_2 b_2^*), u_{11} = a_1 b_2^* + b_1 a_2^*$, $u_{12} = a_1 b_1 - a_2^* b_2^*, u_{13} = -i(a_1 b_1 + a_2^* b_2^*), u_{14} = i(a_1 b_2^* - a_2^* b_1)$.

In the thus obtained equations of motion for Ψ_p and Ψ_s we perform the ensemble average (over different realizations of the random process which describes linear birefringence). Thus, we write $\langle u_m u_n \rangle$ instead of $u_m u_n$. This change holds true only in the limit when the stochastic variations are faster than the nonlinear beam evolution. This is exactly the place in the derivation where our single approximation comes into play. At this point we also need to apply the ergodic theorem

$$\langle f \rangle = \lim_{z\to\infty} \frac{1}{z} \int_0^z dz' f(z'). \tag{8}$$

Our goal is to calculate ensemble averages of all necessary self- and cross-products: in this way we may complete the derivation of the differential equations for Ψ_p and Ψ_s.

The equations of motion for u_n with $n = 1, \ldots, 14$ can be easily formulated basing ourselves on Eqs. (4) and (5). As these equations are linear, in order to find an ensemble average of any function of these coefficients (in our case pair products) we need to construct a generator. We refer to the Appendix in Ref. [21] for details of this procedure, and only give here the final result. With this generator we are able to formulate the equations of motion for the ensemble averages of the products of the coefficients. Thus the solutions to the equations of motion

$$\partial_z G_1 = -2L_c^{-1}(G_1 - G_2), \tag{9}$$

$$\partial_z G_2 = 2L_c^{-1}(G_1 - G_2) \mp 4\Delta\beta(\omega_p)G_4, \tag{10}$$

$$\partial_z G_3 = \pm 4\Delta\beta(\omega_p)G_4, \tag{11}$$

$$\partial_z G_4 = -L_c^{-1}G_4 \pm 2\Delta\beta(\omega_p)(G_2 - G_3) \tag{12}$$

yield the result for the self-products $\{\langle u_1^2\rangle, \langle u_2^2\rangle, \langle u_3^2\rangle\}$, $\{\langle \mathrm{Re}^2(u_4)\rangle, \langle \mathrm{Re}^2(u_5)\rangle, \langle \mathrm{Re}^2(u_6)\rangle\}$, and $\{\langle \mathrm{Im}^2(u_4)\rangle, \langle \mathrm{Im}^2(u_5)\rangle, \langle \mathrm{Im}^2(u_6)\rangle\}$, if we associate them with $\{G_1, G_2, G_3\}$ with initial conditions given as $(1,0,0)$, $(0,1,0)$, and $(0,0,1)$, respectively.

The remaining self-products $\{\langle \mathrm{Re}^2(u_7)\rangle, \langle \mathrm{Re}^2(u_8)\rangle, \langle \mathrm{Re}^2(u_9), \langle \mathrm{Re}^2(u_{10})\rangle\}$, $\{\langle \mathrm{Im}^2(u_7)\rangle, \langle \mathrm{Im}^2(u_8)\rangle, \langle \mathrm{Im}^2(u_9), \langle \mathrm{Im}^2(u_{10})\rangle\}$, $\{\langle \mathrm{Re}^2(u_{11})\rangle, \langle \mathrm{Re}^2(u_{12})\rangle, \langle \mathrm{Re}^2(u_{13}),$ $\langle \mathrm{Re}^2(u_{14})\rangle\}$, and $\{\langle \mathrm{Im}^2(u_{11})\rangle, \langle \mathrm{Im}^2(u_{12})\rangle, \langle \mathrm{Im}^2(u_{13}), \langle \mathrm{Im}^2(u_{14})\rangle\}$, can be found from the equations

$$\partial_z G_1 = -2L_c^{-1}(G_1 - G_2) + 2\Delta_{\pm}G_5, \tag{13}$$

$$\partial_z G_2 = 2L_c^{-1}(G_1 - G_2) - 2\Delta_{\pm}G_6, \tag{14}$$

$$\partial_z G_3 = 2\Delta_{\pm}G_6, \tag{15}$$

$$\partial_z G_4 = -2\Delta_{\pm}G_5, \tag{16}$$

$$\partial_z G_5 = \Delta_{\pm}(G_4 - G_1) - L_c^{-1}G_5, \tag{17}$$

$$\partial_z G_6 = \Delta_{\pm}(G_2 - G_3) - L_c^{-1}G_6, \tag{18}$$

when we associate them with $\{G_1, G_2, G_3, G_4\}$, with initial conditions as $(1,0,0,0)$, $(0,0,0,1)$, $(0,1,0,0)$, and $(0,0,1,0)$, respectively. Here $\Delta_{\pm} \equiv [\pm\Delta\beta(\omega_p) - \Delta\beta(\omega_s)]$.

In order to find the cross-products we constructed appropriate generators and found that all the cross-products that are of interest to us turn out to be equal to zero. Similarly, terms of the form $\mathrm{Re}(u_n)\mathrm{Im}(u_n)$ also vanish. Thus, many SPM,

XPM, and Raman terms in the final equations of motion disappear. The thus found equations of motion for the fields are conveniently formulated in Stokes space. They read as

$$\begin{aligned}\left(\pm\partial_z + \beta'(\omega_p)\partial_t\right)\mathbf{S}^{(p)} = \gamma\Big(&\mathbf{S}^{(p)} \times J_s^{(p)}(z)\mathbf{S}^{(p)} + \mathbf{S}^{(p)} \times J_x(z)\mathbf{S}^{(s)}\Big) \\ &+ \epsilon_p(g/2)\Big(S_0^{(s)} J_{R0}\mathbf{S}^{(p)} + S_0^{(p)} J_R(z)\mathbf{S}^{(s)}\Big),\end{aligned} \tag{19}$$

$$\begin{aligned}\left(\partial_z + \beta'(\omega_s)\partial_t\right)\mathbf{S}^{(s)} = \gamma\Big(&\mathbf{S}^{(s)} \times J_s^{(s)}(z)\mathbf{S}^{(s)} + \mathbf{S}^{(s)} \times J_x(z)\mathbf{S}^{(p)}\Big) \\ &+ (g/2)\Big(S_0^{(p)} J_{R0}\mathbf{S}^{(s)} + S_0^{(s)} J_R(z)\mathbf{S}^{(p)}\Big).\end{aligned} \tag{20}$$

Matrices in Eqs. (19) and (20) are all diagonal with elements $J_R = \mathrm{diag}(J_{R1}, J_{R2}, J_{R3}), J_x = \mathrm{diag}(J_{x1}, J_{x2}, J_{x3}), J_s = \mathrm{diag}(J_{s1}, J_{s2}, J_{s3})$. These elements are different for the counter-propagating and the co-propagating interaction geometries.

In order to complete our theory, we need to express all elements in these matrices in terms of ensemble averages of self-products:

$$J_{R1} = \langle \mathrm{Re}(u_{14}^2 - u_{10}^2)\rangle, \tag{21}$$

$$J_{R2} = -\langle \mathrm{Re}(u_{14}^2 + u_{10}^2)\rangle, \tag{22}$$

$$J_{R3} = -\langle |u_{14}|^2 - |u_{10}|^2\rangle, \tag{23}$$

$$J_{x1} = \frac{2}{3}\langle \mathrm{Re}(u_{10}^2 + u_{13}^2 - u_9^2 - u_{14}^2)\rangle, \tag{24}$$

$$J_{x2} = \frac{2}{3}\langle \mathrm{Re}(u_{10}^2 + u_{14}^2 - u_9^2 - u_{13}^2)\rangle, \tag{25}$$

$$J_{x3} = \frac{2}{3}\langle |u_9|^2 + |u_{14}|^2 - |u_{13}|^2 - |u_{10}|^2\rangle, \tag{26}$$

$$J_{s1} = \frac{1}{3}\langle \mathrm{Re}(u_6^2)\rangle, \tag{27}$$

$$J_{s2} = -\frac{1}{3}\langle \mathrm{Re}(u_6^2)\rangle, \tag{28}$$

$$J_{s3} = \frac{1}{3}\left[3\langle u_3^2\rangle - 1\right], \tag{29}$$

and also $J_{R0} = \langle |u_{10}|^2 + |u_{14}|^2\rangle$. Note that our model reduces to the one-beam theory of Wai and Menyuk when the coefficients u_7 through u_{14} are set to zero.

The Stokes representation is particularly appealing in the context of the problem that we are considering. As we are interested in the polarization properties of the outcoming signal beam, the Stokes vector quite clearly presents the

polarization vector on the Poincaré sphere. The evolution of the Stokes vector draws a trajectory of its tip on the sphere. Another quantity of interest is the degree of polarization (DOP). In those cases where we are dealing with an ensemble of beams, the DOP characterizes the length of the average Stokes vector. Here again the Stokes representation appears to be rather useful.

Thus, the equation of motion for the Stokes vector of a CW signal beam is

$$\begin{aligned}\partial_z \mathbf{S}^{(s)} = &\gamma \mathbf{S}^{(s)} \times J_s(z)\mathbf{S}^{(s)} + \gamma \mathbf{S}^{(s)} \times J_x(z)\mathbf{S}^{(p)} \\ &+ \epsilon_p (g/2)\left[S_0^{(p)}\mathbf{S}^{(s)} + S_0^{(s)} J_R(z)\mathbf{S}^{(p)}\right].\end{aligned} \tag{30}$$

(With $J_{R0} = 1$, which is the case for all situations considered below). Here J_s is the self-polarization modulation (SPolM) tensor, J_x—cross-polarization (XPolM) modulation tensor, J_R—Raman tensor. All they are diagonal. Elements of these tensors are dependent on the magnitude of the birefringence both at signal and pump carrier frequencies, that is on the beat lengths $L_B(\omega_s)$ and $L_B(\omega_p)$, and also on the correlation length L_c. All these three lengths do not exceed 100 m in conventional telecom fibers. The physical meaning of each tensor follows from its definition. Thus, the SPolM tensor defines how two polarization components belonging to the same beam interact in the Kerr medium, and thereby rotate the Stokes vector. The XPolM tensor has similar meaning, but now the rotation is due to the interaction of polarization components belonging to different beams. Finally, the Raman tensor defines polarization-sensitive amplification of amplifier. This tensor is of particular importance to us. For instance, when all elements of this tensor vanish, the Raman amplifier becomes insensitive to the SOP of the pump beam, so that we are dealing essentially with a *scalar* model. Conversely, when the diagonal elements of the Raman tensor have appreciable values, then the theory must be necessary *vectorial*.

Certainly, the evolution of the Stokes vector sensitively depends on how the elements of these tensors evolve with distance. In order to find their dynamics it is necessary to solve the set of linear ordinary differential equations which is given above, see also Refs. [2, 3]. Instead of writing them down here, we present their approximate analytical solutions. Figure 1a, b, c shows how well these analytical solutions reproduce the exact situation. Figure 1a shows that the elements of the SPolM tensor drop very fast and already vanish within the first 10 m of the fiber. Given, that the length of the Raman amplifier exceeds $1 \div 2$ km, we can safely set

$$J_s = \mathrm{diag}(0, 0, 0). \tag{31}$$

The elements of the other two tensors also deceases with distance, however much slower, namely as

$$J_x = -\frac{8}{9}\mathrm{diag}(1, 1, 1)\exp(-z/L_d), \tag{32}$$

$$J_R = \mathrm{diag}(1, 1, 1)\exp(-z/L_d). \tag{33}$$

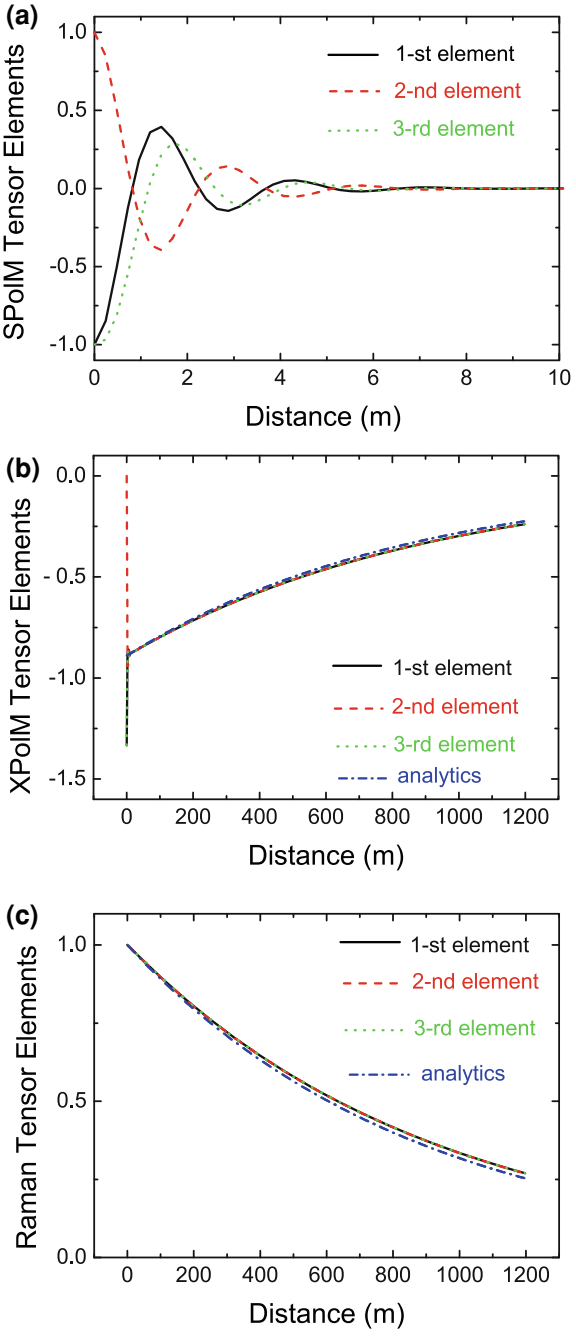

Fig. 1 Three diagonal elements of the **a** (1/3) SPolM, **b** XPolM, and **c** Raman tensors. In **b**, **c** all three curves visually coincide; the *blue curve* is the analytical result showing the exponential decay: $\propto \exp(-z/L_d)$. Parameters are: $L_c = 1\,\text{m}$, $L_B(\omega_s) = 10\,\text{m}$, $\omega_p - \omega_s = 13.2\,\text{THz}$, $\lambda_s = 1.55\,\mu\text{m}$, and $\lambda_p = 1.45\,\mu\text{m}$. The PMD diffusion length is $L_d = 870\,\text{m}$. Note that a brief transient in **b** is not resolved on the chosen scale

As demonstrated in Fig. 1b, c the decay distance is indeed determined by the characteristic length L_d, which is called the PMD diffusion length: $L_d^{-1} = \frac{1}{3}(D_p\Delta\omega)^2$, where $D_p = 2\sqrt{2}\pi\sqrt{L_c}/(L_B\omega_p)$ is the PMD coefficient, [21], and throughout the paper $\Delta\omega = \omega_p - \omega_s$ is taken to be equal to the Raman shift $\Delta\omega_R$ in the germanium-doped silica fibers, that is 13.2 THz. The theory that we are developing here is strictly valid only in two limits – the limit which we call here Manakov limit ($L_{NL}, L_R \ll L_d$) and diffusion limit ($L_{NL}, L_R \gg L_d$), where L_{NL} is nonlinear length, and L_R characteristic amplification length.

3 Raman Amplifiers Versus Raman Polarizers

Raman amplifiers, which we call here standard Raman amplifiers, operate in the diffusion limit, as they are based on fibers with large PMD coefficients. Thus, for $D_p = 0.2\,\mathrm{ps}/\sqrt{\mathrm{km}}$ and $\Delta\omega = \Delta\omega_R = 13.2\,\mathrm{THz}$, the PMD diffusion length L_d is less than 10 m. Taking into account that standard Raman amplifiers are 10 or more kilometers long, the contribution of the polarization-dependent gain [second term in brackets in Eq. (30)] to the total gain [both terms in brackets in Eq. (30) taken together] is totally negligible. The model equation for the signal beam is then

$$\partial_z \mathbf{S}^{(s)} = (g/2) S_0^{(p)} \mathbf{S}^{(s)}. \tag{34}$$

Thus, each component of the Stokes vector is amplified independently and equally with the other components. For such Raman amplifier there is no preferentially amplified polarization mode. The model is essentially a *scalar* one.

A different situation arises in the Manakov limit. For PMD coefficients less than $0.02\,\mathrm{ps}/\sqrt{\mathrm{km}}$, the PMD diffusion length becomes greater than 1 km. In this case we can write the model equation for the signal Stokes vector in the form

$$\begin{aligned} \partial_z \mathbf{S}^{(s)} = & -\bar{\gamma}\mathbf{S}^{(s)} \times \mathbf{S}^{(p)} \\ & + (g/2)\left[S_0^{(p)}\mathbf{S}^{(s)} + S_0^{(s)}\mathbf{S}^{(p)}\right], \end{aligned} \tag{35}$$

with $\bar{\gamma} = \frac{8}{9}\gamma$. In this limit ($L_d \to \infty$) we deal with an ideal Raman polarizer. The equation above includes two contributions. The XPolM contribution is a cross-phase modulation (XPM) part of the Manakov equation, in which the factor of $\frac{8}{9}$ appears as the result of averaging of fast stochastic polarization dynamics of each Stokes vector. Quite to the contrary, the Raman contribution appears exactly as in the case of isotropic fibers (i.e. in absence of the birefringence, and its stochasticity), because the mutual polarization scrambling of the relative orientations of the pump and Stokes vectors is very inefficient when the PMD diffusion length L_d is long. In other words, Raman amplification is insensitive to the absolute orientation of the individual SOPs of the signal and pump beams in the laboratory

frame. It is however sensitive to their *mutual* orientation. In the case of standard Raman amplifiers, the signal Stokes vector rotates rapidly around the pump Stokes vector, and therefore on average "feels" no polarization dependence. In the case of Raman polarizers, still the two vectors stochastically rotate in the laboratory frame, but they do it now in unison, so that their mutual orientation is almost "frozen."

4 An Ideal Raman Polarizer

As characteristic to isotropic fibers, the signal experiences maximal gain when its Stokes vector is aligned along the pump Stokes vector. To show this we can choose (without loss of generality) the pump Stokes vector be aligned along its first component: $\mathbf{S}^{(p)} = S_0^{(p)}(1,0,0)$. Then, we may write for the signal first Stokes component:

$$\partial_z S_1^{(s)} = (g/2) S_0^{(p)} \left[S_0^{(s)} + S_1^{(s)} \right]. \tag{36}$$

If initially the signal Stokes vector is also aligned with its first component, then the signal amplification coefficient is g. This value should be contrasted to the value of $g/2$, which is characteristic to standard Raman amplifiers, see Eq. (34).

The other two components of the signal Stokes vector are amplified less efficiently than the first component. Indeed, their equations of motion are:

$$\partial_z S_2^{(s)} = -\bar{\gamma} S_0^{(p)} S_3^{(s)} + (g/2) S_0^{(p)} S_2^{(s)}, \tag{37}$$

$$\partial_z S_3^{(s)} = \bar{\gamma} S_0^{(p)} S_2^{(s)} + (g/2) S_0^{(p)} S_3^{(s)}. \tag{38}$$

Here, the gain is only $g/2$.

The observations derived from Eqs. (36–38) explain the ability of a Raman polarizer to re-polarize light. They demonstrate that only the Stokes component of the signal aligned with the pump Stokes vector is dominantly amplified. In a high-gain Raman amplifier, the difference in gain for polarization components may become so large that the polarization of the outcoming beam is almost perfectly aligned with the pump SOP. This effect of alignment is called polarization attraction, or polarization trapping. Shortly, we shall quantify effect of the polarization attraction in terms of the DOP, the so-called alignment parameter, and some other parameters, while now we comment on the output SOP of the outcoming signal beam measured with respect of the laboratory frame.

As we have seen, the Raman tensor decays as the distance grows larger, see Eq. (33). Therefore, it is preferable to decrease the total fiber length at the price of increasing the pump power. Indeed, the first proof-of-principle experiment reported in Ref. Martinelli et. al. [16], was carried out with a dispersion-shifted fiber of only $2,1$ km and an average pump power as high as 2.2 W.

Most theories of Raman polarizers reported so far, see Refs. [2, 3, 16, 22, 23], are based on numerical simulations of the stochastic equations which properly take into account the randomness of the fiber birefringence (the total fiber span is divided into short segments, with each segment extended over one correlation length; the orientation of the birefringence axes is fixed within each segment, while it varies randomly when going from one segment to the next one). Such an approach is indeed necessary when the PMD diffusion length is comparable with the amplification length, a case which is in the middle between the Manakov limit and the diffusion limit. In this case, the Raman polarizer has non-optimal performances, yielding a DOP which is significantly below unity. So, this case is not advantageous in practice. In order to realize a "good" Raman polarizer, one should choose to work in the Manakov limit. As we have indicated above, working in this limit allows us to get analytical and physically transparent results. In the next section we shall continue to work with ideal Raman polarizers and provide an even deeper analytical insight.

5 Evaluation of the Performance of a Raman Polarizer

Equations (36–38) can be solved analytically. We shall limit ourselves to the undepleted pump approximation, so that the pump power $P \equiv S_0^{(p)}(z) = \text{const}$. Our model does not include linear losses in the fiber, because we have chosen to work with relatively short fiber spans, for which losses are relatively small. If necessary, the losses can be included, though analytics will become less transparent. Solutions to Eqs. (36–38) are:

$$S_0^{(s)}(z) = \frac{1}{2}\left[S_0^{(s)}(0) - S_1^{(s)}(0)\right] + \frac{1}{2}\left[S_0^{(s)}(0) + S_1^{(s)}(0)\right] e^{gPz}, \tag{39}$$

$$S_1^{(s)}(z) = -\frac{1}{2}\left[S_0^{(s)}(0) - S_1^{(s)}(0)\right] + \frac{1}{2}\left[S_0^{(s)}(0) + S_1^{(s)}(0)\right] e^{gPz}, \tag{40}$$

$$S_2^{(s)}(z) = \left[S_2^{(s)}(0)\cos(\bar{\gamma}Pz) - S_3^{(s)}(0)\sin(\bar{\gamma}Pz)\right] e^{\frac{1}{2}gPz}, \tag{41}$$

$$S_3^{(s)}(z) = \left[S_2^{(s)}(0)\sin(\bar{\gamma}Pz) + S_3^{(s)}(0)\cos(\bar{\gamma}Pz)\right] e^{\frac{1}{2}gPz}. \tag{42}$$

We are interested in the statistical properties of a Raman polarizer. All quantities of interest can be derived from the above-written solutions. First of all, we shall calculate the mean quantities. The immediate questions are—what is the SOP of the outcoming signal beam and how well the beam is polarized? In order to find an answer to the first question we need to simply get an average of Eqs. (39–42) given the statistics of the incoming light. We assume that the signal is initially unpolarized, so that $\langle S_1^{(s)}(0)\rangle = \langle S_2^{(s)}(0)\rangle = \langle S_3^{(s)}(0)\rangle = 0$. Then, at $z = L$, where L is the total length of the fiber, we get

$$\langle S_0^{(s)}(L)\rangle = \frac{1}{2}S_0^{(s)}(0)[1 + \exp(gPL)], \tag{43}$$

$$\langle S_1^{(s)}(L)\rangle = \frac{1}{2}S_0^{(s)}(0)[-1 + \exp(gPL)], \tag{44}$$

$$\langle S_2^{(s)}(L)\rangle = 0, \tag{45}$$

$$\langle S_3^{(s)}(L)\rangle = 0. \tag{46}$$

So, the signal SOP at the output is aligned with the pump SOP. The degree of alignment is characterized by the DOP, which is calculated as

$$\mathrm{DOP}(z) = \frac{\sqrt{\langle S_1^{(s)}(z)\rangle^2 + \langle S_2^{(s)}(z)\rangle^2 + \langle S_3^{(s)}(z)\rangle^2}}{\langle S_0^{(s)}(z)\rangle}. \tag{47}$$

As usual, a DOP equal to unity means that light if perfectly polarized, a DOP equal to zero indicates that the light beam is unpolarized, while intermediate values stand for a partially polarized beam. We say that the Raman polarizer perfoms its function properly when DOP becomes close to unity. Introducing gain G as $G \equiv \langle S_0^{(s)}(L)\rangle / S_0^{(s)}(0)$ we get $G = \frac{1}{2}[1 + \exp(gPL)]$ and for the DOP:

$$\mathrm{DOP} = 1 - G^{-1}. \tag{48}$$

The higher the gain, the larger the DOP. Already 20 dB gain is enough to get a DOP as high as 0.99.

A short comment is in order on how one should interpret the averaging procedure, expressed by $\langle \ldots \rangle$. There are two possible situations. On the one hand, we can vary the SOP of the signal beam in time, then $\langle \ldots \rangle = \langle \ldots \rangle_T = T^{-1}\int_0^T \ldots dt$, where T is the period of time, sufficiently long to get correct statistical averaging. $\langle S_1^{(s)}\rangle_T = \langle S_2^{(s)}\rangle_T = \langle S_3^{(s)}\rangle_T = 0$ means that we are dealing with unpolarized light. On the other hand, we can imagine an experiment with an ensemble of beams. Then, $\langle \ldots \rangle = \langle \ldots \rangle_e$ means ensemble average over all these beams. If the SOPs of all beams from the ensemble randomly or uniformly cover the Poincaré sphere, then, similarly to the time average, we get $\langle S_1^{(s)}\rangle_e = \langle S_2^{(s)}\rangle_e = \langle S_3^{(s)}\rangle_e = 0$. In this

situation we say that we are dealing with an ensemble of scrambled beams. In a case where the time average gives the same statistical information as the ensemble average, we refer to such system as an ergodic one. The Raman polarizers considered here are obviously ergodic systems, simply because time does not enter the equations of motion explicitely. Therefore, our analysis is valid for the scrambled beams approach as well as for time averaging.

Another important quantity which characterizes a Raman polarizer is the alignment parameter $A_{\uparrow\uparrow}$, defined as the cosine of the angle between the output signal SOP and the output pump SOP:

$$A_{\uparrow\uparrow} = \frac{\langle S_1^{(s)} S_1^{(p)} + S_2^{(s)} S_2^{(p)} + S_3^{(s)} S_3^{(p)} \rangle}{\langle S_0^{(s)} \rangle S_0^{(p)}}. \tag{49}$$

The closer the alignment parameter to unity, the better the alignment of the output signal and pump Stokes vectors. Using solutions in Eqs. (43–46) we get

$$A_{\uparrow\uparrow} = \frac{\langle S_1^{(s)}(L) \rangle}{\langle S_0^{(s)} \rangle} = 1 - G^{-1} \tag{50}$$

for the value of the alignment parameter at the fiber output. Although this value coincides with the value of DOP, see Eq. (48), these two quantities have different physical meanings. For a statistical ensemble of beams, the alignment parameter shows the average direction of the signal Stokes vector on the Poincaré sphere, while the DOP measures the breadth of the spot traced by the tips of the signal Stokes vectors around this average direction.

Yet another quantity of interest is the measure of the polarization-dependent gain (PDG). It is exactly the PDG which is at the heart of a Raman polarizer. Different SOPs of the signal beam experience different amplifications. The signal beam with a SOP parallel to the pump Stokes vector is amplified most efficiently, while the orthogonal polarization experiences no gain. Indeed, as it follows from the solution in Eq. (40), $G_{\max} = \exp(gPL)$ and $G_{\min} = 1$. We introduce the PDG parameter Δ as $\Delta = G_{\max} - G_{\min}$, and get for the ideal Raman polarizer $\Delta = 2(G - 1)$. The PDG parameter aquires high values for a high-gain Raman polarizer. Note that for an "ideal Raman amplifier" (an amplifier, which is perfectly described by the *scalar* theory, or in other words, the amplifier, which works deeply in the diffusion limit) $\Delta = 0$.

The high value of the PDG parameter points out that along with the desirable property of strong re-polarization of the signal beam, this device is characterized by a high level of unwanted relative intensity noise (RIN). By varying the signal SOP at the input we get pronounced variations of the intensity at the output, even if the incoming beam had a steady intensity in time. In order to characterize the output power fluctuations, let us calculate the variance

$$\sigma_s^2 = \frac{\langle S_0^2(L) \rangle}{\langle S_0(L) \rangle^2} - 1. \tag{51}$$

Using solution in Eq. (39) we get

$$\sigma_s^2 = (1 - G^{-1})^2/3. \tag{52}$$

For large $G, \sigma_s \approx 3^{-1/2} \approx 58\,\%$. This level of RIN may be detrimental for some optical devices, particularly nonlinear ones. Note that an ideal Raman amplifier is characterized by $\sigma_s = 0$, i.e., by zero RIN, thanks to the efficient polarization scrambling which is provided by PMD. The price to be paid is the totally stochastic signal SOP at the output fiber end.

A reasonable question to ask is whether it is possible for a Raman polarizer to keep the useful property of re-polarization and at the same time to suppress RIN down to an acceptable level. The answer is positive. One possible way to combat the RIN and at the same time keep the property of re-polarization is to use the Raman polarizer in the depleted-pump regime, Ref. [24]. In this saturation regime all input SOPs are amplified to approximately the same level of intensity, actually up to $S_0^{(s)}(L) \approx P$. Strictly speaking, only one signal SOP (the one which is perfectly orthogonal to the pump SOP) is not amplified at all. However, the numerous imperfections of any practical realization of a Raman polarizer, including residual PMD, may prevent the observation of such a singular behaviour.

So far we have analyzed the main statistical properties of an ideal Raman polarizer operating in the undepleted-pump regime. If necessary, any other statistical quantity of interest can be obtained from the exact analytical solutions given in Eqs. (39–42). In a similar manner, one can characterize the re-polarization of partially polarized beams. The final quantity which we would like to comment on is the mean gain of an ideal Raman polarizer. It is well known, that the gain of an ideal Raman amplifier is equal to $g/2$. The reason is that in the course of propagation the signal SOP rotates quickly around the pump SOP, and on average "feels" the arithmetic mean of the maximal gain (g) when it is parallel to the pump SOP, and minimal gain (0) when it is orthogonal, yielding $g/2$ on average. In terms of available gain, an ideal Raman polarizer performs much better. As can be seen from Eq. (43), for large values of $G, G \approx \exp(gPL - \ln 2)$, so that the gain coefficient is almost twice larger. This property makes Raman polarizers very efficient Raman amplifiers as well.

6 Counter-Propagating Raman Polarizers

So far, we have been dealing only with the co-propagating geometry. In this geometry, the pump SOP stochastically changes along the fiber, and its output SOP depends on the particular realization of the birefringence stochasticity in the chosen fiber span. Moreover, the stochasticity changes with time, as a result of variation of the environmental conditions. Therefore the trapping of signal's SOP to pump's SOP does not garantee the absence of fluctuations of signal's SOP at the output, even though these fluctuatons closely follow the time-varying pump SOP.

In other words, the co-propagating Raman polarizer provides the trapping effect in the stochastic frame, but does not garantee the SOP stabilization in the laborotary frame.

The desirable stabilization in the laboratory frame can be achieved by implementing a counter-propagating geometry, Refs. [3, 23]. Since the signal's SOP is attracted toward the instantaneous position of pump's Stokes vector, this alignment holds also at the output end of the fiber. The output pump SOP is defined solely by the source, and as such it is supposed to be well defined and deterministic. In this respect the counter-propagating geometry is preferrable. As regarding the theory, one can repeat derivations with the opposite sign of z-derivative in the equation governing evolution of the pump beam. As shown in Ref. [3], this reversing of the sign brings some changes in the components of the XPolM and Raman tensors. They become

$$J_x^{counter} = -\frac{8}{9}\mathrm{diag}(1,-1,1)\exp(-z/L_d), \tag{53}$$

$$J_R^{counter} = \frac{1}{3}\mathrm{diag}(1,-1,1)\exp(-z/L_d). \tag{54}$$

The presence of the factor $\frac{1}{3}$ in front of the Raman tensor immediately leads us to the conclusion that the counter-propagating Raman polarizer is significantly less effective in re-polarization than its co-propagating analog. In order to get similar performances we need either to increase the pump power or lengthen the fiber, or both. Let us evaluate the performance of this device.

First of all, we start with the solving the equation of motion (35) in the undepleted-pump regime. We get

$$\begin{aligned} S_0^{(s)}(z) =& \frac{1}{2}\left[S_0^{(s)}(0) - S_1^{(s)}(0)\right]\mathrm{e}^{\frac{1}{3}gPz} \\ &+ \frac{1}{2}\left[S_0^{(s)}(0) + S_1^{(s)}(0)\right]\mathrm{e}^{\frac{2}{3}gPz}, \end{aligned} \tag{55}$$

$$\begin{aligned} S_1^{(s)}(z) =& -\frac{1}{2}\left[S_0^{(s)}(0) - S_1^{(s)}(0)\right]\mathrm{e}^{\frac{1}{3}gPz} \\ &+ \frac{1}{2}\left[S_0^{(s)}(0) + S_1^{(s)}(0)\right]\mathrm{e}^{\frac{2}{3}gPz}, \end{aligned} \tag{56}$$

$$\begin{aligned} S_2^{(s)}(z) =& \left[S_2^{(s)}(0)\cos(\bar{\gamma}Pz)\right. \\ &\left. - S_3^{(s)}(0)\sin(\bar{\gamma}Pz)\right]\mathrm{e}^{\frac{1}{2}gPz}, \end{aligned} \tag{57}$$

$$\begin{aligned} S_3^{(s)}(z) =& \left[S_2^{(s)}(0)\sin(\bar{\gamma}Pz)\right. \\ &\left. + S_3^{(s)}(0)\cos(\bar{\gamma}Pz)\right]\mathrm{e}^{\frac{1}{2}gPz}. \end{aligned} \tag{58}$$

We immediately observe that the difference in amplification coefficients of the first Stokes component and the second (and third) Stokes component is given by $\frac{2}{3}g - \frac{1}{2}g$. The contrast is much weaker than for the co-propagating case, where we had $g - \frac{1}{2}g$. The average gain of the counter-propagating Raman polarizer is

$$G = \frac{1}{2}\left(e^{\frac{2}{3}gPL} + e^{\frac{1}{3}gPL}\right), \tag{59}$$

which is significantly smaller than for a Raman polarizer operating in the co-propagating configuration, although it is still larger than for an ideal Raman amplifier. For the same value of the product PL, the DOP for the counter-propagating configuration is also smaller:

$$\begin{aligned} \mathrm{DOP} &= 1 - 2\left(e^{\frac{1}{3}gPL} + 1\right)^{-1} \\ &\approx 1 - 2e^{-\frac{1}{3}gPL} (\text{for } gPL \gg 1) \\ &\approx 1 - \sqrt{2}G^{-1/2}. \end{aligned} \tag{60}$$

For $G = 20\,\mathrm{dB}$ in the co-propagating case the DOP was as high as 99 %, while in the counter-propagating configuration it is only 86 %.

It is instructive to compare our model of ideal Raman polarizer with full-scale numerical simulations of the underlying stochastic equations presented in [23], where the empirical formula:

$$\mathrm{DOP} = 1 - e^{-G_{dB}/\Gamma}, \tag{61}$$

connecting the DOP with the gain was suggested and tested numerically. Here $G_{dB} = 10\log_{10} G$ and $\Gamma \approx 10.2$ for the considered range of PMD coefficients. The graphical comparison of the results obtained with formula (60) on one hand, and the results plotted according to the empirical formula (61) on the other hand, is shown in Fig. 2a. The fit is good. On the same plot we have also shown the results based on the direct numerical solution of Eq. (30) with XPolM and Raman tensors in the form of Eqs. (53, 54). Note that we did not use any fitting parameter in this cross-comparison.

The alignment parameter for the counter-propagating geometry is different from the co-propagating case. Because of the change of the sign in front of the second element of the Raman tensor, see Eq. (54), the alignment parameter is now

$$A_{\uparrow\downarrow} = \frac{\langle S_1^{(s)} S_1^{(p)} - S_2^{(s)} S_2^{(p)} + S_3^{(s)} S_3^{(p)} \rangle}{\langle S_0^{(s)} \rangle S_0^{(p)}}. \tag{62}$$

For input unpolarized light, the alignment parameter coincides with the DOP, namely,

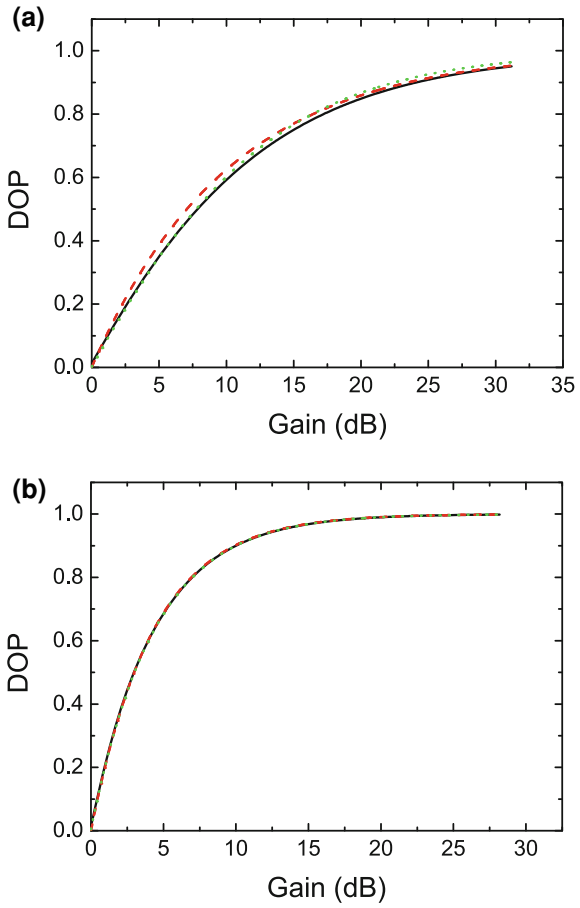

Fig. 2 DOP versus gain G. Graphical comparison of the results obtained with formulae (60) (*black solid*); results obtained with empirical formulae (61) (*green dotted*); and results based on the direct numerical solution of Eq. (30) with XPolM and Raman tensors in the form of Eqs. (53, 54) (*red dashed*). Parameters are: **a** $L_c = 1\,\mathrm{m}$, $L_B = 45\,\mathrm{m}$, $P = 8\,\mathrm{W}$, $D_p = 0.005\,\mathrm{ps}/\sqrt{\mathrm{km}}$, and $L_d = 17.5\,\mathrm{km}$, L varies from 0 to 2.5 km, and $\Gamma = 10.2$; **b** $L_c = 10\,\mathrm{m}$, $L_B = 3500\,\mathrm{m}$, $P = 8\,\mathrm{W}$, $D_p = 0.0002\,\mathrm{ps}/\sqrt{\mathrm{km}}$, and $L_d = 10914\,\mathrm{km}$, L varies from 0 to 1.5 km, and $\Gamma = 4.3$

$$\begin{aligned} A_{\uparrow\downarrow} &= 1 - 2\left(\mathrm{e}^{\frac{1}{3}gPL} + 1\right)^{-1} \\ &\approx 1 - 2\mathrm{e}^{-\frac{1}{3}gPL} (\text{for } gPL \gg 1) \\ &\approx 1 - \sqrt{2}G^{-1/2}. \end{aligned} \tag{63}$$

The PDG parameter $\Delta = G_{\max} - G_{\min}$ is easily calculated, resulting in

$$\Delta = \frac{1}{2}\left(\mathrm{e}^{\frac{2}{3}gPL} - \mathrm{e}^{\frac{1}{3}gPL}\right) = \frac{1}{2}\left(1 + 2G - \sqrt{1 + 8G}\right). \tag{64}$$

Its value is considerably less in the co-propagating configuration, particularly for moderate values of gain. This observation again points to the relatively poorer performances of the counter-propagating Raman polarizer. At the same time, the RIN is expected to have a lower level. In order to demonstrate this, let us evaluate the variance of the signal intensity. Formula (51) and solution (55) yield

$$\sigma_s^2 = \frac{1}{3}\left[1 - 2\left(e^{\frac{1}{3}gPL} + 1\right)^{-1}\right]^2. \tag{65}$$

Before concluding this section, one remark is in order about the applicability domain of these results. SPolM, XPolM and Raman tensors given by Eqs. (31–33, 53), and (54) were calculated in the limit

$$L \gg L_{bire} \equiv \frac{L_B^2(\omega_p)}{8\pi^2 L_c}. \tag{66}$$

This inequality holds for all practical situations. Thus, for L_c as small as 1 m and L_B as large as 100 m we get L_{bire} as short as 127 m. Fiber-optic Raman amplifiers are always longer than 1 km, and therefore inequality (66) is not violated. However, if for some reason inequality (66) is violated, for instance for extremely low birefringent fibers, the analysis given above must be corrected. Thus, in the limit $L_B(\omega_p) \to \infty$, the tensors of interest take the following form:

$$J_s^{counter} = \frac{1}{3}\mathrm{diag}(-1, 1, -1), \tag{67}$$

$$J_x^{counter} = \frac{4}{3}\mathrm{diag}(-1, 0, -1), \tag{68}$$

$$J_R^{counter} = \mathrm{diag}(1, 1, 1). \tag{69}$$

Figure 2b shows the dependence of DOP on Raman polarizer gain for this case. Although the performance of the Raman polarizer in this limit is very good, we will not evaluate it here explicitely because of its little practical interest.

7 Conclusion

We have studied the effect of trapping of the state of polarization of a signal beam by a pump beam in the model of a Raman polarizer. We have introduced the notion of the ideal Raman polarizer and quantified its performance it terms of gain, degree of polarization, polarization-dependent gain parameter, alignment parameter, and RIN characteristics. We have studied two different geometries: co- and counter-propagating configurations, and identified their pros and contras. Possible applications of Raman polarizers include their potential use in telecom-related signal processing, where the need of transforming an unpolarized light to a polarized one is necessary in order to provide an interface between the telecom link and post-processing polarization-sensitive devices (based, for instance, on nonlinear crystals).

References

1. V.V. Kozlov, J. Nuño, J.D. Ania-Castañón, S. Wabnitz, Multi-channel Raman polarizer with suppressed relative intensity noise for WDM transmission lines. Opt. Lett. **37** (in press, 2012)
2. V.V. Kozlov, J. Nuño, J.D. Ania-Castañón, S. Wabnitz, Theory of fiber optic Raman polarizers. Opt. Lett. **35**(23), 3970–3972 (2010)
3. V.V. Kozlov, J. Nuño, J.D. Ania-Castañón, S. Wabnitz, Theoretical study of optical fiber Raman polarizers with counterpropagating beams. J. Lightwave Techn. **29**(23), 341–347 (2011)
4. S. Sergeyev, S. Popov, Two-section fiber optic Raman polarizer. IEEE J. Quantum Electron. **48**, 56–60 (2012)
5. V.V. Kozlov, S. Wabnitz, Silicon Raman polarizer. Opt. Lett. **37**(4), 737–739 (2012)
6. V.E. Zakharov, A.V Mikhailov, Polarization domains in nonlinear optics. JETP Lett. **45**, 349–352 (1987)
7. B. Daino, S. Wabnitz, Polarization domains and instabilities in nonlinear optical fibers. Phys. Lett. A **182**, 289–293 (1993)
8. B.A. Malomed, Optical domain walls. Phys. Rev. E **50**, 1565–1571 (1994)
9. S. Pitois, G. Millot, S. Wabnitz, Polarization domain wall solitons with counterpropagating laser beams. Phys. Rev. Lett. **81**, 1409–1412 (1998)
10. S. Pitois, G. Millot, S. Wabnitz, Nonlinear polarization dynamics of counterpropagating waves in an isotropic optical fiber: theory and experiments. J. Opt. Soc. Am. B **18**, 432–443 (2001)
11. S. Wabnitz, Chiral polarization solitons in elliptically birefringent spun optical fibers. Opt. Lett. **34**, 908–910 (2009)
12. V.V. Kozlov, S. Wabnitz, Instability of optical solitons in the boundary value problem for a medium of finite extension. Lett. Math. Phys. **96**, 405–413 (2011)
13. E. Assemat, A. Picozzi, H.R. Jauslin, D. Sugny, Hamiltonian tools for the analysis of optical polarization control. J. Opt. Soc. Am. B **29**, 559–571 (2012)
14. J.E. Heebner, R.S. Bennink, R.W. Boyd, R.A. Fisher, Conversionof unpolarized light to polarized light with greater than 50 % efficiency by photorefractive two-beam coupling. Opt. Lett. **25**, 257–259 (2000)
15. S. Pitois, J. Fatome, G. Millot, Polarization attraction using counter-propagating waves in optical fiber at telecommunication wavelengths. Opt. Express **16**, 6646–6651 (2008)
16. M. Martinelli, M. Cirigliano, M. Ferrario, L. Marazzi, P. Martelli, Evidence of Raman-induced polarization pulling. Opt. Exp. **17**, 947–955 (2009)
17. A. Zadok, E. Zilka, A. Eyal, L. Thvenaz, M. Tur, Vector analysis of stimulated Brillouin scattering amplification in standard single-mode fibers. Opt. Express **16**, 21692–21707 (2008)
18. J. Fatome, S. Pitois, P. Morin, G. Millot, Observation of light-by-light polarization control and stabilization in optical fibre for telecommunication applications. Opt. Express **18**, 15311–15317 (2010)
19. Q. Lin, G.P. Agrawal, Vector theory of stimulated Raman scattering and its application to fiber-based Raman amplifiers. J. Opt. Soc. Am. B **20**, 1616–1631 (2003)
20. C.R. Menyuk, B.S. Marks, Interaction of polarization mode dispersion and nonlinearity in optical fiber transmission systems. J. Lightwave Techn. **24**, 2806–2826 (2006)
21. P.K.A. Wai, C.R. Menyuk, Polarization mode dispersion, decorrelation, and diffusion in optical fibers with randomly varying birefringence. J. Lightwave Technol. **14**, 148 (1996)
22. L. Ursini, M. Santagiustina, L. Palmieri, Raman nonlinear polarization pulling in the pump depleted regime in randomly birefringent fibers. IEEE Photon. Techn. Lett. **23**(24), 254–256 (2011)
23. F. Chiarello, L. Ursini, L. Palmieri, M. Santagiustina, Polarization attraction in counterpropagating fiber Raman amplifiers. IEEE Photon. Techn. Lett. **23**(20), 1457–1459 (2011)
24. V.V. Kozlov, S. Wabnitz, Suppression of relative intensity noise in fiber-optic Raman polarizers. IEEE Photon. Techn. Lett. **23**(20), 1088–1090 (2011)

Studies of Existence and Stability of Circularly Polarized Few-Cycle Solitons Beyond the Slowly-Varying Envelope Approximation

Hervé Leblond, Dumitru Mihalache and Houria Triki

Abstract In this chapter, we provide an overview of recent studies of theoretical models which adequately describe the temporal dynamics of circularly polarized few-cycle optical solitons in both long-wave- and short-wave-approximation regimes, beyond the framework of slowly varying envelope approximation. In the long-wave-approximation regime, i.e., when the frequency of the transition is far above the characteristic wave frequency, by using the multiscale analysis (reductive perturbation method), we show that propagation of circularly polarized (vectorial) few-cycle pulses, is described by the nonintegrable complex modified Korteweg–de Vries equation. In the short-wave-approximation regime, i.e., when the frequency of the transition is far below the characteristic wave frequency, by using the multiscale analysis, we derive from the Maxwell-Bloch equations the governing nonlinear evolution equations for the two polarization components of the electric field, in the first order of the perturbation approach. In this latter case we show that propagation of circularly-polarized few-optical-cycle solitons is described by a system of coupled nonlinear evolution equations, which reduces, for the particular case of scalar solitons, to the completely integrable sine-Gordon equation describing the dynamics of linearly polarized few-cycle pulses in the short-wave-approximation regime. It is seen that, from the slowly varying envelope approximation down to a few cycles, circularly polarized solitons are very robust, according to rotation symmetry and conservation of the angular momentum. However, in the sub-cycle regime, they become unstable, showing a spontaneous breaking of the rotation symmetry.

H. Leblond (✉)
Laboratoire de Photonique d'Angers, EA 4464 2 Bd Lavoisier 49000 Angers, France
e-mail: herve.leblond@univ-angers.fr

D. Mihalache
Horia Hulubei National Institute for Physics and Nuclear Engineering,
077125 Magurele-Bucharest, Romania

H. Triki
Radiation Physics Laboratory, Faculty of Sciences, Department of Physics,
Badji Mokhtar University, 12 23000 Annaba, Algeria

Progress Optical Sci., Photonics (2013): 247–275
DOI: 10.1007/10091_2012_28

Published Online: 30 January 2013

1 Introduction

A series of seminal papers on experimental generation and characterization of two-cycle and even sub-two-cycle pulses from Kerr-lens mode-locked Ti: sapphire lasers were published by several groups more than one decade ago [1–4]. Since then interest in intense ultrashort light pulses containing only a few optical cycles has grown steadily in recent years. This fast growing research area has considerable potential for applications in metrology of ultrafast phenomena, in systems performing laser ablation (micromachining, etching, microsurgery), etc. It still presents many exciting open problems from both a fundamental and an applied point of view. The ultrashort pulses possess extensive applications to the field of light-matter interactions, high-order harmonic generation, extreme [5] and single-cycle [6] nonlinear optics, and attosecond physics [7, 8]; see Ref. [9] for a review of earlier works in this exciting research area. We note that such ultrashort laser pulses with duration of only a few optical cycles are currently used to study chemical reactions, molecular vibration, electron in atoms and molecules, etc. The availability of ultrashort and ultraintense laser pulses generated by the powerful technique of *chirped pulse amplification* along with the development of high-fluence laser materials has opened up the field of optics in the relativistic regime [10]. Recent activity in the area of realization of future large laser facilities, namely exawatt-class lasers was overviewed by Mourou and Tajima [11]. Note that such huge power levels will be obtained by releasing a few kilojoules of energy into an ultrashort pulse with a duration of only 10 fs.

It is well known that light beams carrying a singularity with a screw-type phase distribution are associated with optical vortices characterized by a topological charge (vorticity number) corresponding to the phase dislocation. In fact, the corresponding momentum flow leads to an orbital angular momentum of the light field. Recently, strong-field physical phenomena with singular light beams have been put forward [12] and it was demonstrated that optical vortices can be generated in extreme ultraviolet domain of the spectrum using high-harmonic generation techniques; see Ref. [12]. Ultrashort optical-vortex pulse generation in the few-cycle regime was recently reported by Yamane et al. [13]. It was demonstrated the generation of a 5.9-fs (2.3-cycle) ultrashort optical-vortex pulse (ranging from 650 to 950 nm), by using optical parametric amplification. Also, few-cycle high-contrast vortex beams with pulse durations around 8 fs were generated from a Ti:sapphire laser oscillator with a single diffractive-refractive component by Bock et al. [14]. Other recent works on few-cycle pulses (FCPs) deal with few-cycle light bullets created by femtosecond filaments [15], the study of ultrashort spatiotemporal optical solitons in quadratic nonlinear media [16, 17], the ultrashort spatiotemporal optical pulse propagation in cubic (Kerr-like) media without the use of the slowly varying envelope approximation (SVEA) [18, 19], single-cycle gap solitons generated in resonant two-level dense media with a subwavelength structure [20], observation of few-cycle propagating surface plasmon polariton wavepackets [21], and the possibility of generating few-cycle

dissipative optical solitons [22–24]. Kozlov et al. [23] numerically demonstrated how to use the coherent mode locking technique for the generation of single-cycle pulses directly from a laser. Recent theoretical studies deal with the ultrafast pulse propagation in mode-locked laser cavities in the few femtosecond pulse regime and the derivation of a master mode-locking equation for ultrashort pulses [25]. Another relevant recent theoretical work presents a class of few-cycle elliptically polarized solitary waves in isotropic Kerr media, proposes a method of producing multisolitons with different polarization states, and studies their binary-collision dynamics [26].

In the experimental arena we also mention the comprehensive study of intrinsic chirp of single-cycle pulses [27]. A proposal of a method to generate extremely short unipolar half-cycle pulses based on resonant propagation of a few-cycle pulse through asymmetrical media with periodic subwavelength structure was advanced by Song et al. [28]. Other relevant recent works report the demonstration of high quality sub-two-cycle pulses (with duration of about 5 fs) from compression of broadband supercontinuum generated in all-normal dispersion photonic crystal fibers [29], the realization of essentially dispersion-free and diffraction-limited focusing of few-cycle pulses (with duration of about 6 fs) through all-reflective microscope objectives [30], generation of unipolar pulses from non-unipolar optical pulses in a quadratic nonlinear medium [31], in which case the phase invariance of the electromagnetic wave is broken due to the non-centro-symmetry of the material, and the existence of guided optical solitons of femto-second duration and nanoscopic mode area, that is, femtosecond nanometer-sized optical solitons [32]. In recent comprehensive numerical simulations performed by Li et al. [33] it was put forward an efficient and realizable scheme for the generation of ultrashort isolated attosecond (as) pulses by the optimization of three-color laser fields. As a result, an isolated 23 as pulse can be obtained directly by superimposing the supercontinuum harmonics near the cutoff region [33]. This very short attosecond pulse (23 as) is a bit less than one atomic unit of time (the time scale of electron motion in atoms), which is about 24 as.

The continuing experimental progress in the study of the wave dynamics of FCPs in nonlinear optical media has paved the way for the development of new theoretical approaches to model their propagation in physical systems. Three classes of main dynamical models for FCPs have been put forward: (i) the quantum approach [34, 35], (ii) the refinements within the framework of SVEA of the nonlinear Schrödinger-type envelope equations [36–39], and (iii) the non-SVEA models [40–48]. Extremely short pulses can be described by solving directly the Maxwell-Bloch equations for a two-level system; soliton (sech-type) solutions have been derived by Maimistov and Caputo [49]. The propagation of FCPs in Kerr media can be described beyond the SVEA by using the modified Korteweg–de Vries (mKdV) [41, 42], sine-Gordon (sG) [43, 44], or mKdV-sG equations [45–47]. A reduced Maxwell-Duffing model, very close to the mKdV equation, for the description of extremely short pulses in nonresonant media was introduced by Kazantseva et al. [50]. Note that the mKdV and sG equations are completely integrable by means of the inverse scattering transform method

[51, 52], whereas the mKdV-sG equation is completely integrable only if some condition between its coefficients is satisfied [53, 54].

To the best of our knowledge, the necessity of using the non-SVEA approach for the adequate description of FCPs was put forward in the early seminal work by Akhmediev, Mel'nikov and Nazarkin published in 1989 [55]. In a subsequent paper, Belenov and Nazarkin [40] obtained exact solutions of nonlinear optics equations outside the approximation of slowly varying amplitudes and phases for light pulses a few wavelengths long and with power densities of the order of $10^9 - 10^{18}\,\mathrm{W/cm^2}$, clearly stating that traditional SVEA methods "*are becoming ineffective in describing wave processes at such small spatial and temporal scales and at such high fields*". We also mention that in a recent study of ultrafast pulse propagation in a mode-locked laser cavity in the few femtosecond pulse it was clearly stated that the standard NLS-based approach of ultrafast pulse propagation, though has been shown "*to work quantitatively beyond its expected breakdown, into the tens of femtoseconds regime, and has been used extensively for modeling supercontinuum generation ... when pushed to the extreme of a few femtosecond pulses, the NLS description becomes suspect ...*" [25]. However, we would like to point out that, to the best of our knowledge, the necessity of using models beyond the traditional SVEA in describing the phenomenon of *self-induced transparency* for ultrashort pulses propagating in optical media was advanced by Kujawski [56, 57]; see also the subsequent works by Andreev [58] and by Parkhomenko and Sazonov [59].

In this chapter, we overview some recent studies of theoretical models which adequately describe the temporal dynamics of circularly polarized (vector) few-cycle optical solitons beyond the framework of slowly varying envelope approximation, see also two recent extensive reviews [46, 47]. In the next section we consider in detail the polarization effects in Kerr media in the long wave approximation regime and we derive the basic evolution equations for both an amorphous optical medium and for a crystal-like optical medium. The obtained complex modified Korteweg–de Vries equation (cmKdV) is analyzed in detail and robust circularly-polarized few-optical-cycle solitons are put forward. Then, in Sect. 3, we study the circularly-polarized few-optical-cycle solitons in the short wave approximation regime. We identify their stability domains in the relevant parameter space, and typical instability scenarios of such vector few-cycle solitons. Finally, the main results and conclusions are briefly summarized in Sect. 4.

2 Polarization Effects in Kerr Media: Circularly Polarized Few-Optical-Cycle Solitons in the Long Wave Approximation Regime

In this section we consider the propagation of circularly polarized few-cycle pulses in Kerr media beyond the slowly varying envelope approximation, see [62, 63]. We work in the long-wave-approximation regime. Thus, assuming that the

frequency of the transition is far above the characteristic wave frequency, we show that propagation of FCPs, taking into account the wave polarization, is described by the non-integrable complex mKdV equation, which is solved by direct numerical simulations. We get robust localized solutions to the complex mKdV equation, which describe circularly polarized few-cycle optical solitons. Note that such ultrashort solitons strongly differ from the breather soliton solutions of the mKdV equation, which adequately describes linearly polarized FCP solitons. We show that the circularly polarized FCP soliton becomes unstable when the angular frequency is less than 1.5 times the inverse of the pulse length, which is about 0.42 cycles per pulse. The unstable sub-cycle pulse decays into a linearly polarized half-cycle pulse, whose polarization direction slowly rotates around the propagation axis, see [62, 63].

2.1 Basic Equations for an Amorphous Optical Medium

As a simple model for a glass system we consider a set of two-level atoms with Hamiltonian H_0; $\Omega = \omega_b - \omega_a > 0$ is the frequency of the transition. The atoms may present some induced dipolar electric momentum $\vec{\mu}$, which is oriented randomly in space. Assuming a propagation along the z-axis, we can omit the component of $\vec{\mu}$ along the propagation direction z, and thus $\vec{\mu} = \mu(\cos\theta\vec{e}_x + \sin\theta\vec{e}_y)$, $\vec{e}_x$ and $\vec{e}_y$ being the unitary vectors along the x- and y-axis, respectively, and μ is a 2×2 matrix

$$\mu = \begin{pmatrix} 0 & \mu \\ \mu^* & 0 \end{pmatrix}. \tag{1}$$

The evolution of the electric field $\vec{E}$ is governed by the Maxwell equations which, in the absence of magnetic effects, and assuming a plane wave propagating along the z axis, reduce to

$$\partial_z^2 \vec{E} = \frac{1}{c^2}\partial_t^2(\vec{E} + 4\pi\vec{P}), \tag{2}$$

where $\vec{P}$ is the polarization density. It is given by $\vec{P} = N\langle \mathrm{Tr}(\rho\vec{\mu})\rangle$, where N is the number of atoms per unit volume, ρ is the density matrix, and $\langle\cdot\rangle$ denotes the averaging over all directions in the $x - y$ plane.

The evolution of the density-matrix is governed by the Schrödinger equation as written for the density matrix in the quantum statistical mechanics formalism, also known as the von Neumann equation (it will be referred to below as the Schrödinger-von Neumann equation), i.e., $i\hbar\partial_t\rho = [H, \rho]$, where $H = H_0 - \vec{\mu}\cdot\vec{E}$ describes the coupling between the atoms and the electric field. The relaxation effects can be neglected here as in the scalar approximation, see [43]. Note that the

physical values of the relaxation times are in the picosecond range, or even slower, thus very large with regard to the pulse duration, which allows us to neglect them.

The typical frequency ω_w of the wave must be far away from the resonance frequency Ω because the transparency of the medium is required for soliton propagation. We therefore consider $\omega_w \ll \Omega$ (the long-wave approximation regime). The typical length of the wave, say $t_w = 1/\omega_w$, is very large with respect to the characteristic time $t_r = 1/\Omega$ associated to the transition. Thus we are working in the long-wave approximation regime, as defined in the framework of the reductive perturbation method [60, 61]. Next we introduce a small parameter $\varepsilon = 1/(\Omega t_w)$, and the slow variables $\tau = \varepsilon(t - z/V), \quad \zeta = \varepsilon^3 z$. The retarded time variable τ describes the pulse shape, propagating at speed V in a first approximation. Its order of magnitude ε gives an account of the long-wave approximation, so that the corresponding values of retarded time have the same order of magnitude as $t_r/\varepsilon = t_w \gg t_r$ if τ is of the order of unity. The propagation distance is assumed to be very long with regard to the pulse length ct_w; therefore it will have the same order of magnitude as ct_r/ε^n, where $n \geqslant 2$. The value of n is determined by the distance at which dispersion effects occur. According to the general theory of the derivation of KdV-type equations [60], it is $n = 3$. The ζ variable of order ε^3 describes thus long-distance propagation, according to the same general theory.

The electric field $\vec{E}$, the polarization density $\vec{P}$, and the density matrix ρ are expanded in power series of ε as $\vec{E} = \sum_{n\geqslant 1} \varepsilon^n (u_n, v_n, 0)$, $\vec{P} = \sum_{n\geqslant 1} \varepsilon^n (P_n, Q_n, 0)$, $\rho = \sum_{n\geqslant 0} \varepsilon^n \rho_n$, in which the triplets of coordinates are given in the (x, y, z) frame, and the profiles u_1, v_1, etc., are functions of the slow variables τ and ζ. The components of ρ are denoted by

$$\rho = \begin{pmatrix} \rho_a & \rho_t \\ \rho_t^* & \rho_b \end{pmatrix}. \tag{3}$$

We assume that, in the absence of wave, all atoms are in the fundamental state (a), and hence all elements of ρ_0 are zero except $\rho_{0a} = 1$.

At lowest order ε^1, the Schrödinger-von Neumann equation yields

$$\rho_{1t} = \frac{\mu}{\hbar\Omega}(u_1 \cos\theta + v_1 \sin\theta). \tag{4}$$

The polarization density is $\vec{P} = (P, Q)$ with

$$P = N\langle \rho_t \mu^* \cos\theta + cc \rangle, \; Q = N\langle \rho_t \mu^* \sin\theta + cc \rangle \tag{5}$$

where cc denotes the complex conjugate. We get

$$(P_1, Q_1) = \frac{N|\mu|^2}{\hbar\Omega}(u_1, v_1). \tag{6}$$

The wave equation at leading order ε^3 gives the value of the velocity, $V = c/n$, with the refractive index $n = \sqrt{1 + 4\pi N|\mu|^2/(\hbar\Omega)}$. The expression of n coincides with that obtained in the scalar model (cf. Ref. [43] and Eq. (24) above) if we take into account the fact that, for a linear polarization in the present framework, only one half of the dipoles would be active, being roughly aligned with the electric field. At the order ε^2, the Schrödinger-von Neumann equation yields $\rho_{1a} = \rho_{1b} = 0$ and $\rho_{2t} = \mu/(\hbar\Omega)(u_2 \cos\theta + v_2 \sin\theta) - i\mu/\left(\hbar\Omega^2\right)\partial_\tau(u_1 \cos\theta + v_1 \sin\theta)$. Consequently, we get similar expressions for P_2 and Q_2 as those for P_1 and Q_1, with the only difference that u_1 and v_1 are replaced by u_2 and u_2. The wave equation at order ε^4 is automatically satisfied.

At order ε^3, the Schrödinger-von Neumann equation gives rise to

$$\rho_{2b} - \rho_{2a} = \frac{2|\mu|^2}{\hbar^2\Omega^2}(u_1 \cos\theta + v_1 \sin\theta)^2, \tag{7}$$

and a corresponding much longer expression for ρ_{3t}. By using

$$\langle \cos^4\theta \rangle = \frac{3}{8}, \langle \cos^2\theta \sin^2\theta \rangle = \frac{1}{8}, \tag{8}$$

the expression for the polarization density component P_3 is

$$P_3 = \frac{N|\mu|^2}{\hbar\Omega}u_3 - \frac{N|\mu|^2}{\hbar\Omega^3}\partial_\tau^2 u_1 - \frac{3N|\mu|^4}{2\hbar^3\Omega^3}\left(u_1^2 + v_1^2\right)u_1, \tag{9}$$

and we get an analogue expression for Q_3. Next, the wave equation at order ε^5 yields the following pair of coupled equations:

$$\partial_\zeta u_1 = A\partial_\tau^3 u_1 + B\partial_\tau\left[\left(u_1^2 + v_1^2\right)u_1\right], \tag{10}$$

$$\partial_\zeta v_1 = A\partial_\tau^3 v_1 + B\partial_\tau\left[\left(u_1^2 + v_1^2\right)v_1\right], \tag{11}$$

in which we have set $A = 2\pi N|\mu|^2/\left(nc\hbar\Omega^3\right), B = 3\pi N|\mu|^4/\left(nc\hbar^3\Omega^3\right)$. The dispersion coefficient A has the same expression as derived within the scalar model [43], if we consider that only one half of the dipoles are contributing. Regarding the nonlinear coefficient B, the ratio between the corresponding nonlinear coefficients is a bit smaller, $3/8$, which is due to the averaging over θ.

Equations (10, 11) can be written in the normalized form as

$$U_Z = U_{TTT} + \left[\left(U^2 + V^2\right)U\right]_T, \tag{12}$$

$$V_Z = V_{TTT} + \left[\left(U^2 + V^2\right)V\right]_T, \tag{13}$$

where the subscripts Z and T denote the derivatives, and the functions and variables are defined as $U = u_1/\mathcal{E}, V = v_1/\mathcal{E}, Z = z/\mathcal{L}, T = (t - z/V)/t_w$, with $\mathcal{L} = 2ct_w^3/n''$, and $\mathcal{E} = (1/2t_w)\sqrt{nn''/(-3\pi\chi^{(3)})}$.

Equations (12, 13) are a set of coupled mKdV equations describing the propagation of optical FCPs in an amorphous medium presenting cubic nonlinearity and dispersion. They can be also seen as describing the interaction of two linearly polarized FCPs, U and V.

2.2 Basic Equations for a Crystal-Like Optical Medium

A system of two coupled mKdV equations was derived above from a model of a glass (an amorphous medium). This model involved some induced dipolar electric momentum $\vec{\mu}$, oriented randomly in the transverse plane (x, y), the polarization density $\vec{P}$ being averaged over all directions in this plane. In the following we will show that the same governing equations (12, 13) can be derived from another model, which would rather correspond to a crystalline structure [62].

We also consider a two-level medium, in which the excited level is twice degenerated, with the induced dipole oriented either in the x or in the y direction. The corresponding Hamiltonian is given by

$$H_0 = \hbar \begin{pmatrix} \omega_a & 0 & 0 \\ 0 & \omega_b & 0 \\ 0 & 0 & \omega_b \end{pmatrix}, \tag{14}$$

with $\Omega = \omega_b - \omega_a > 0$. The dipolar momentum becomes

$$\vec{\mu} = \mu_x \vec{e}_x + \mu_y \vec{e}_y, \tag{15}$$

where $\vec{e}_x$ and $\vec{e}_y$ are the unitary vectors along the x axis and y axis, respectively, and

$$\mu_x = \begin{pmatrix} 0 & \mu & 0 \\ \mu^* & 0 & 0 \\ 0 & 0 & 0 \end{pmatrix}, \tag{16}$$

$$\mu_y = \begin{pmatrix} 0 & 0 & \mu \\ 0 & 0 & 0 \\ \mu^* & 0 & 0 \end{pmatrix}. \tag{17}$$

The evolution of the electric field $\vec{E}$ is governed by the Maxwell equations which, in the absence of magnetic effects, and assuming a plane wave propagating along the z axis, reduce to $\partial_z^2 \vec{E} = (1/c^2)\partial_t^2 \left(\vec{E} + 4\pi \vec{P}\right)$, where $\vec{P} = N\mathrm{Tr}(\rho\vec{\mu})$ is the polarization density, N is the number of atoms per unit volume, and ρ is the density matrix. There is no averaging over the transverse orientation of the dipolar momentum any more.

The evolution of the density-matrix is governed by the equation $i\hbar\partial_t \rho = [H, \rho]$, where $H = H_0 - \vec{\mu} \cdot \vec{E}$ describes the coupling between the atoms and the electric

field. The relaxation effects can be neglected here as in the scalar approximation; see Ref. [43]. Notice that the physical values of the relaxation times are indeed in the picosecond range, or even slower (nanoseconds), thus very large with regard to the pulse duration, which allows us to neglect them.

As above, we assume that the typical frequency ω_w of the wave is much lower than the resonance frequency Ω, $\omega_w \ll \Omega$. Recall that, if ω_w is in the visible range, it means that the transition frequency is in the ultraviolet, and that the typical length of the wave, say $t_w = 1/\omega_w$, is very large with respect to the characteristic time $t_r = 1/\Omega$ associated to the transition. It is thus a long wave approximation, as defined in the framework of the reductive perturbation method [60, 61]. Still as above, we introduce a small parameter ε, which can be here $\varepsilon = 1/(\Omega t_w) \ll 1$, and the slow variables $\tau = \varepsilon\left(t - \frac{z}{V}\right)$, $\quad \zeta = \varepsilon^3 z$. The retarded time variable τ describes the pulse shape, propagating at speed V in a first approximation, and the ζ variable describes long-distance propagation.

The electric field $\vec{E}$, the polarization density $\vec{P}$, and the density matrix ρ are expanded in power series of ε as

$$\vec{E} = \sum_{n \geqslant 1} \varepsilon^n \vec{E}_n = \sum_{n \geqslant 1} \varepsilon^n (u_n, v_n, 0), \tag{18}$$

$$\vec{P} = \sum_{n \geqslant 1} \varepsilon^n (P_n, Q_n, 0), \tag{19}$$

$$\rho = \sum_{n \geqslant 0} \varepsilon^n \rho_n, \tag{20}$$

in which the triplets of coordinates are given in the (x, y, z) frame, and the profiles u_1, v_1, etc., are functions of the slow variables τ and ζ. The components of ρ_n are denoted by ρ_{ij}^n.

At lowest order ε^1, the Schrödinger-von Neumann equation yields

$$\rho_{12}^1 = \frac{\mu}{\hbar\Omega} u_1, \quad \rho_{13}^1 = \frac{\mu}{\hbar\Omega} v_1, \tag{21}$$

and consequently

$$P_1 = \frac{2N|\mu|^2}{\hbar\Omega} u_1, \tag{22}$$

$$Q_1 = \frac{2N|\mu|^2}{\hbar\Omega} v_1, \tag{23}$$

which are the same expressions as in the glass model (Eq. (6) and [63]), except that N is replaced with $2N$.

At order ε^3 in the wave equation, we get an expression of the refractive index with the same slight change:

$$n = \left(1 + \frac{8\pi N|\mu|^2}{\hbar\Omega}\right)^{\frac{1}{2}}, \tag{24}$$

which exactly coincides with the index found in the scalar model [43].

At order ε^2 in the Schrödinger-von Neumann equation, we first notice that $\partial_\tau \rho_{23}^1 = 0$ and consequently $\rho_{23}^1 = 0$. In the same way, $\rho_{11}^1 = \rho_{22}^1 = \rho_{33}^1 = 0$. Then we get

$$\rho_{12}^2 = \frac{\mu}{\hbar\Omega} u_2 - \frac{i\mu}{\hbar\Omega^2} \partial_\tau u_1, \tag{25}$$

$$\rho_{13}^2 = \frac{\mu}{\hbar\Omega} v_2 - \frac{i\mu}{\hbar\Omega^2} \partial_\tau v_1, \tag{26}$$

which are the same expressions as in the case of the glass model [63], with the orientation angle of the dipolar momentum $\theta = 0$ for ρ_{12}^2 and $\theta = \pi/2$ for ρ_{13}^2. Consequently, we get

$$P_2 = \frac{2N|\mu|^2}{\hbar\Omega} u_2, \tag{27}$$

$$Q_2 = \frac{2N|\mu|^2}{\hbar\Omega} v_2, \tag{28}$$

and the wave equation at order ε^4 is automatically satisfied.

At order ε^3 in the Schrödinger-von Neumann equation, the populations are computed as

$$\rho_{11}^2 = \frac{-|\mu|^2}{\hbar^2\Omega^2}\left(u_1^2 + v_1^2\right), \tag{29}$$

$$\rho_{22}^2 = \frac{|\mu|^2}{\hbar^2\Omega^2} u_1^2, \tag{30}$$

$$\rho_{33}^2 = \frac{|\mu|^2}{\hbar^2\Omega^2} v_1^2. \tag{31}$$

Notice that a nonzero coherence term between the two excited states appears, it is

$$\rho_{23}^2 = \frac{|\mu|^2}{\hbar^2\Omega^2} u_1 v_1. \tag{32}$$

Consequently, the coherence between the fundamental state and the state excited in the x direction at next order is

$$\rho_{12}^{3} = \frac{\mu}{\hbar\Omega} u_3 - \frac{i\mu}{\hbar\Omega^2} \partial_\tau u_2 - \frac{\mu}{\hbar\Omega^3} \partial_\tau^2 u_1 - \frac{2\mu|\mu|^2}{\hbar^3\Omega^3} \left(u_1^2 + v_1^2\right) u_1. \tag{33}$$

The analogous expression, permuting u_1 and v_1, is obtained for the component ρ_{13}^{3}.

The expressions for the polarization density components P_3 and Q_3 are obtained, as

$$P_3 = \frac{2N|\mu|^2}{\hbar\Omega} u_3 - \frac{2N|\mu|^2}{\hbar\Omega^3} \partial_\tau^2 u_1 - \frac{4N|\mu|^4}{\hbar^3\Omega^3} \left(u_1^2 + v_1^2\right) u_1, \tag{34}$$

and analogously for Q_3. Apart from the change from N to $2N$ already noticed, the only discrepancy with respect to the corresponding equations in the glass model (Eq. (9) and [63]) is a coefficient value 4 instead of 3 in the nonlinear term in Eq. (34).

The wave equation at order ε^5 yields the following pair of coupled equations:

$$\partial_\zeta u_1 = A\partial_\tau^3 u_1 + B\partial_\tau \left[\left(u_1^2 + v_1^2\right) u_1\right], \tag{35}$$

$$\partial_\zeta v_1 = A\partial_\tau^3 v_1 + B\partial_\tau \left[\left(u_1^2 + v_1^2\right) v_1\right], \tag{36}$$

in which we have set

$$A = \frac{4\pi N|\mu|^2}{nc\hbar\Omega^3}, \tag{37}$$

$$B = \frac{8\pi N|\mu|^4}{nc\hbar^3\Omega^3}. \tag{38}$$

Notice that the structure of the set of Eqs. (35, 36) is the same as in the glass model (Eqs. (10, 11) and [63]), with very slightly modified coefficients. The expressions of the two dispersion coefficients coincide (the ratio between the corresponding dispersion coefficients is therefore 1) if we consider that in the case of the glass model, only one half of the dipoles are contributing, while all of them are involved in the crystal model. The same feature is observed in the case of the refractive index. Regarding the value (Eq. 38) of the coefficient B, the ratio between the corresponding nonlinear coefficients is a bit smaller, $3/8$, which is nothing else but the average value $\langle \cos^4\theta \rangle$ of $\cos^4\theta$, which is involved in the averaging of the nonlinear polarization density over all orientations θ of $\vec{\mu}$ in the glass model (Eqs. (10, 11) and [63]). In fact, the coefficients A and B have here exactly the same expressions as in the scalar model [43]. It was shown in [43] that the nonlinear coefficient can be expressed as

$$B = \frac{-1}{2n_0 c}\chi^{(3)}, \tag{39}$$

where $\chi^{(3)}$ is the third order susceptibility, while the dispersion coefficient is

$$A = \frac{1}{6}\frac{d^3k}{d\omega^3}\bigg|_{\omega=0}, \tag{40}$$

$k(\omega)$ holding for the dispersion relation. Recently we proved that the scalar mKdV model, with expressions (39) and (40) of the coefficients, is valid for a general Hamiltonian, with an arbitrary number of energy levels, within the long-wave approximation [64].

It is worthy to mention that Eqs. (35, 36) in their normalized form coincide to Eqs. (12, 13) where now the functions and variables are defined as

$$U = \frac{u_1}{\mathcal{E}}, \quad V = \frac{v_1}{\mathcal{E}}, \quad Z = \frac{z}{\mathcal{L}}, \quad T = \frac{t - z/V}{t_w}, \tag{41}$$

with

$$\mathcal{L} = \frac{n\hbar c\Omega^3 t_w^3}{2\pi N|\mu|^2}, \tag{42}$$

$$\mathcal{E} = \sqrt{\frac{2}{3}}\frac{\hbar}{|\mu|t_w}. \tag{43}$$

2.3 The Analysis of the cmKdV Equation

Looking for soliton solutions we assume that U and V vanish at infinity, the mKdV system of coupled partial differential equations (12, 13) has four conserved quantities [65]:

$$I_1 = \int_{-\infty}^{+\infty} U dT, \quad I_2 = \int_{-\infty}^{+\infty} V dT, \tag{44}$$

the momentum of the system

$$I_3 = \int_{-\infty}^{+\infty} \left(U^2 + V^2\right) dT, \tag{45}$$

and its Hamiltonian

$$I_4 = \frac{1}{2}\int_{-\infty}^{+\infty} \left\{ \left(U^2+V^2\right)^2 - 2\left[\left(\partial_T U\right)^2 + \left(\partial_T V\right)^2 \right] \right\} dT, \tag{46}$$

which remain constant with Z.

Setting

$$f = U + iV, \tag{47}$$

Eqs. (12) and (13) reduce to

$$\partial_Z f = \partial_T^3 f + \partial_T \left(|f|^2 f \right), \tag{48}$$

which is known as the complex modified Korteweg–de Vries (cmKdV) equation. Confusion must be avoided between Eq. (48) and the other cmKdV equation

$$\partial_Z f = \partial_T^3 f + |f|^2 \partial_T f. \tag{49}$$

Indeed, Eq. (49) is completely integrable [66] while Eq. (48) is not. Equations (48) and (49) are sometimes referred to as cmKdV I and cmKdV II equations, respectively. The integrable equation (49) has been extensively studied (see e.g. [66–69]), while less studies have been devoted to the non-integrable equation (48) [70, 71]. In Ref. [70], using the Painlevé analysis, it is proved that Eq. (48) is not integrable, and an exhaustive list of analytical solutions is given. In the frame of the optics of FCPs, the field f must vanish at infinity. With this condition, there is no exact analytical solution to Eq. (48) but the solutions of the real mKdV equation. Indeed, setting $f = ue^{i\varphi}$, with $u = u(Z,T)$ and φ a constant, reduces the complex mKdV equation (48) to the real one. The latter describes FCP solitons in the scalar model [43]. It is indeed well knwon that the real mKdV equation admits breather solutions. Recall that the two-soliton solution u_{two} of the mKdV equation has the expression [73]

$$u_{\text{two}} = \frac{e^{\eta_1} + e^{\eta_2} + \left(\frac{p_1-p_2}{p_1+p_2}\right)^2 \left(\frac{e^{\eta_1}}{4p_1^2} + \frac{e^{\eta_2}}{4p_2^2}\right) e^{\eta_1+\eta_2}}{1 + \frac{e^{2\eta_1}}{4p_1^2} + \frac{2e^{\eta_1+\eta_2}}{(p_1+p_2)^2} + \frac{e^{2\eta_2}}{4p_2^2} + \left(\frac{p_1-p_2}{p_1+p_2}\right)^4 \frac{e^{2\eta_1+2\eta_2}}{16p_1^2p_2^2}}, \tag{50}$$

with $\eta_j = p_j\tau - p_j^3\zeta - \gamma_j$, for $j = 1, 2$, and becomes a breather soliton if $p_2 = p_1^*$. Here $\mathrm{Re}(p_1)$ is the inverse of the pulse length, and $\mathrm{Im}(p_1)$ is the angular frequency, as are b and ω respectively in Eq. (57) below. The real part of the constant $\gamma_1 = \gamma_2^*$ determines the position of the center of the pulse, while its imaginary part is a phase. The breather solution to mKdV adequately describes a FCP, and all linearly polarized FCP solitons are retrieved in this way. Their stability to a random perturbation of the polarization can be tested numerically. Thus if we add to the constant φ a random (white) noise (we used an amplitude of $0.1 \times 2\pi$), it is obtained that the pulse is not destroyed, and that its polarization remains linear.

However, the direction of the linear polarization slowly rotates around the propagation direction.

However, we are here mainly interested in *circularly polarized solitons*. The latter would be expected to have the form

$$f = u(T - wZ)e^{i(\omega T - kZ)}. \tag{51}$$

However, no exact, even numerical, steady state solution of this type do exist. To be ensured of this, just plug f given by the expression (51) in Eq. (48); separating real and imaginary parts and integrating once yields

$$\begin{aligned} \left(3\omega^2 - w\right)u &= \partial_T^2 u + u^3, \\ \left(\omega^2 - \frac{k}{\omega}\right)u &= 3\partial_T^2 u + u^3, \end{aligned} \tag{52}$$

which are not compatible. Note that solutions having approximately the form (51) do exist and are very robust. Such solutions are studied in detail in the next subsection.

2.4 Robust Circularly Polarized Few-Optical-Cycle Solitons

We will next compute an approximate analytic solution to the cmKdV equation (48), valid for long pulses, i.e. in the SVEA. Next we introduce again a small parameter ε and the slow variables

$$\xi = \varepsilon^2 Z, \quad \eta = \varepsilon(T - wZ), \tag{53}$$

and expand f as

$$f = \varepsilon(f_0(\eta, \xi) + \varepsilon f_1(\eta, \xi) + \cdots)e^{i(\omega T - kZ)}, \tag{54}$$

and run the perturbative reduction procedure [60].

At leading order ε, we get $k = \omega^3$; at second order, we find the inverse velocity $w = 3\omega^2$, and at order ε^3 we get a nonlinear Schrödinger equation for f_0:

$$i\partial_\xi f_0 + 3\omega\partial_\eta^2 f_0 + \omega f_0 |f_0|^2 = 0. \tag{55}$$

Let us consider the fundamental soliton solution of the above written NLS equation:

$$f_0 = p\sqrt{6}\ \mathrm{sech}(p\eta)e^{i3p^2\omega\xi}. \tag{56}$$

Coming back to the initial variables, we obtain

$$f = b\sqrt{6}\ \mathrm{sech}\left[b\left(T - 3\omega^2 Z\right)\right]e^{i\omega\left[T - \left(\omega^2 - 3b^2\right)Z\right]}. \tag{57}$$

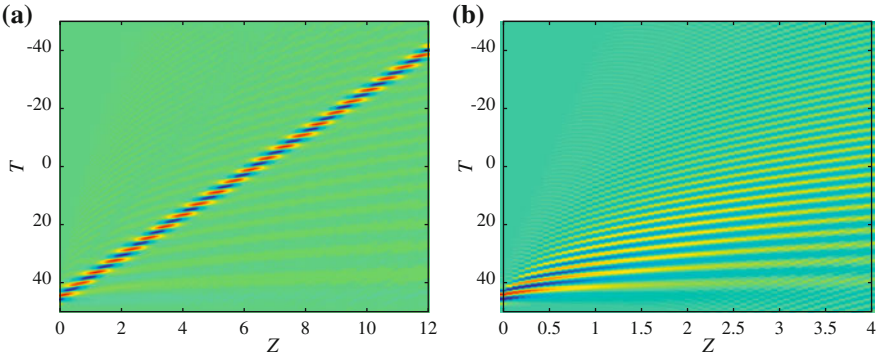

Fig. 1 (Color online) Propagation of a circularly polarized few-cycle pulse. The *left panel* shows the nonlinear propagation of the x-polarized component U. Initial data is given by Eq. (57) with $b = 1$ and $\omega = 2$. The *right panel* shows the propagation of the linearly dispersive few-cycle pulse having the same initial profile but with very small amplitude. **a** Nonlinear, **b** Linear (after Ref. [62])

Thus Eq. (57) gives an approximate solution to the cmKdV equation (48), which is valid for long pulses ($b \ll \omega$).

The numerical solution of the cmKdV equation was obtained by using the exponential time differencing second order Runge-Kutta method [72]. Note that the numerical scheme does not conserve exactly the $\mathcal{L}_2$-norm (or energy W) of the solution, however the error remains small (typically $\Delta W/W \sim 10^{-4}$ for $Z = 10000$). Due to the scale invariance of the cmKdV equation, only the ratio b/ω may modify the stability properties of the solution. Note that there is only one free parameter, which is the number of cycles in the pulse (the ratio ω/b being proportional to the number of optical cycles contained in the ultrashort pulse). For numerical calculations we fix $b = 1$ and decrease the frequency ω.

Figures 1 and 2 shows the evolution of a FCP of this form, with $b = 1$ and $\omega = 2$. The propagation of the linearly dispersive FCP is also shown for the sake of comparison.

Note that the FCP propagates without change in width and maximum amplitude over at least $z = 10000$ dimensionless units, however, its shape is somehow distorted after propagation. The propagation speed is also quite different from the result of the above analytical approximate solution. In fact, since no steady state with linear phase exists, the pulse is not a true steady state, and consequently its velocity varies in a quite erratic way; nevertheless, it is a very robust FCP.

In the following we show by numerical simulations that we get quite robust circularly polarized FCP solitons, see [62]. Notice that the approximate solution (57) has not a zero mean value, except at the SVEA limit $b \ll \omega$. However the mean value of the field is conserved. It is likely that the circularly polarized FCP soliton would have a zero mean value, and hence this would explain the discrepancy between the approximate analytical solution (57) and the direct numerical computation shown on Figs. 1 and 2. In order to check this interpretation, let

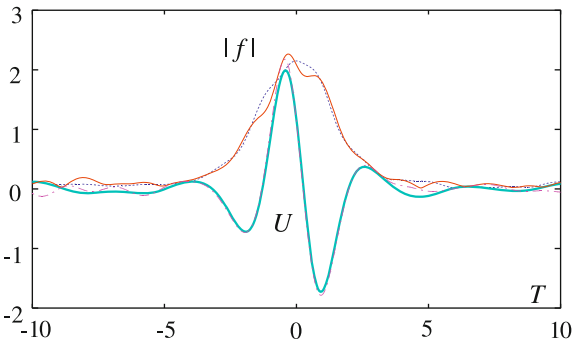

Fig. 2 (Color online) Initial ($Z = 100$) and final ($Z = 10000$) profiles of the few-cycle pulse *plotted* on Fig. 1 for the input given by Eq. (57). *Blue* (*dotted*): initial $|f|$, *light blue* (*thick gray*): initial U, *red* (*thin solid*): final $|f|$, *pink* (*dash-dotted*): final U (after Ref. [62])

us consider an input having zero mean value. Such an alternative expression is found from the breather (or two-soliton) solution of the real mKdV equation, given by Eq. (50) above. Taking for one polarization component, say U, the breather solution with $\gamma_{1U} = 0$, and for the second polarization component V the same expression, but with a $\pi/2$ dephasing, i.e. with $\gamma_{1V} = i\pi/2$, we get some expression which can be used as an input data for solving numerically the cmKdV equation. This pulse is very close to the approximate analytical solution (57), but has a zero mean value. Numerical resolution shows that the pulse, apart from small apparently chaotic oscillations, keeps its shape and characteristics during the propagation.

2.5 *Instability of Circularly Polarized Pulses in the Sub-Cycle Regime and Spontaneous Symmetry Breaking*

In what follows we will study the decay of the unstable circularly polarized FCP and the corresponding transition to a half-cycle soliton. The value $\omega/b \simeq 1.5$ appears to be the lower limit for the stability of the circularly polarized FCP soliton. Note that the ratio ω/b is proportional to the number of cycles contained in the pulse. More precisely, the number of optical cycles N_c is the ratio of the pulse duration (FWHM $= 2\ln\left(1+\sqrt{2}\right)/b$) divided by the optical period $2\pi/\omega$, i.e. $N_c \simeq 0.28\omega/b$. The stability limit of the circularly polarized FCP soliton is thus about $N_c = 0.42$. Hence circularly polarized FCP are stable down to the sub-cycle range. For smaller values of the ratio ω/b, the FCP becomes unstable, and decays into a linearly polarized single-humped (half-cycle) pulse, in the form of a fundamental soliton of the real mKdV, thus breaking the rotation symmetry of the wave.

The transition occurs, for $\omega/b = 1.4$, between $Z = 19100$ and 19200, for $\omega/b = 1.3$, between $Z = 9300$ and 9400, but for $\omega/b = 1$, between between

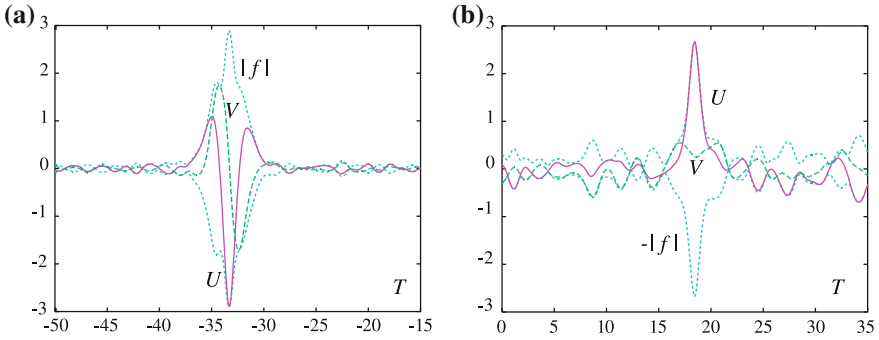

Fig. 3 (Color online) Normalized profiles of an unstable circularly polarized few-cycle pulse. Initial data is defined by the breather soliton with $p_1 = 1 + i$, i.e. both pulse width and angular frequency equal to 1, for the polarization component U, and the same with a $\pi/2$ dephasing for V. *Light blue* (*dotted*): $|f|$ and $-|f|$, *pink* (*solid*): $U = \mathrm{Re}(f)$, *green* (*dashed*): $V = \mathrm{Im}(f)$. **a** Initial (at $Z = 100$), **b** Final (at $Z = 1300$) (after Ref. [62])

$Z = 400$ and 500. Further, it occurs very abruptly, and involves a strong modification of the spectrum; see Ref. [62, 63] for more details.

The transition to a half-cycle soliton is shown in Figs. 3 and 4. It is a single pulse, whose profile accurately coincides with that of the fundamental soliton solution to the real mKdV equation

$$U = \sqrt{2}b\ \mathrm{sech}\left(bT - b^3 Z\right), \tag{58}$$

but which slowly rotates around the propagation axis.

It is worthy to mention that half-cycle optical solitons were also put forward in quadratic nonlinear media; thus a few-cycle pulse launched in a quadratic medium may result in a half-cycle soliton in the form of a single hump, with no oscillating tails [74]. However, in that case the symmetry breaking was not spontaneous as in the present one, but induced by the non-centrosymmetry of the material.

Concluding this section, we point out that the multiscale perturbation analysis was used in Refs. [62, 63] to derive approximate evolution equations governing the propagation of circularly polarized femtosecond optical solitons in cubic (Kerr-like) media beyond the slowly varying envelope approximation. Thus we took into account the vectorial nature of the electric field and therefore we properly considered the wave polarization effects. In the long-wave-approximation regime we have found that the two interacting waveforms corresponding to such vector few-optical-cycle solitons are adequately described by a coupled pair of cmKdV equations at the third-order approximation of the perturbation approach. In the sub-cycle regime instability occurs, which corresponds to a breaking of the axial symmetry of the FCP soliton.

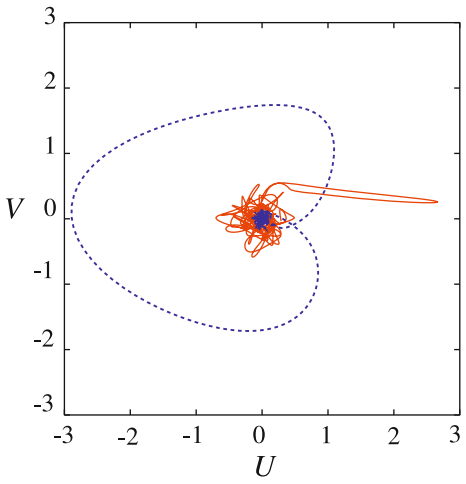

Fig. 4 (Color online) Evolution of the polarization of the unstable circularly polarized few-cycle pulse with both angular frequency and pulse length 1. *Blue* (*dotted*): initial circularly polarized pulse (at $Z = 100$), *red* (*solid*): final linearly polarized pulse (at $Z = 1300$) (after Ref. [62])

3 Circularly Polarized Few-Optical-Cycle Solitons: Short-Wave-Approximation Regime

In this section we consider the propagation of few-cycle pulses beyond the slowly varying envelope approximation and in the short-wave-approximation regime, in media in which the dynamics of constituent atoms is described by a two-level Hamiltonian, by taking into account the wave polarization, see [75]. Therefore we assume that the resonance frequency of the two-level atoms is well below the inverse of the characteristic duration of the optical pulse, it should thus belong to the infrared range if the latter is in the visible range. By using the reductive perturbation method (multiscale analysis) we then derive from the Maxwell-Bloch-Schrödinger equations the governing evolution equations for the two polarization components of the electric field in the first order of the perturbation approach. We show that propagation of circularly polarized few-optical-cycle solitons is described by a rather complicated system of coupled nonlinear equations [75], which reduces in the scalar case to the standard sine-Gordon equation describing the dynamics of linearly polarized FCPs in the short-wave-approximation regime. We then calculate the lifetime of circularly-polarized FCPs by using adequate numerical methods and we study the transition to two orthogonally polarized single-humped pulses as a generic route of their instability; for a comprehensive study of this issue see Ref. [75]. It is worthy to notice that other vectorial non-SVEA models have been also proposed [76, 77], however they were only built from a direct analogy with common SVEA models. We recall that circularly polarized short pulse propagation in a system of two-level atoms has been studied more than two decades ago in the framework of the self-induced transparency [78] and the existence of localized solutions of Maxwell-Bloch type systems beyond the SVEA has been considered too [79, 80]. However, not all the coupling mechanisms between the polarization components were taken into

account in these earlier studies. However, the authors of Ref. [80] took an essential coupling term into account through the out-of-phase polarization, which allowed them to show that the pulse solution valid within the SVEA could not be generalized beyond it by means of some corrections terms.

3.1 Governing Equations in the Short-Wave Approximation Regime

We consider a two level model, in which the excited state is degenerated twice, corresponding to oscillations along the x and y axes. The free Hamiltonian is thus given by Eq. (14). The resonance angular frequency is $\Omega = \omega_b - \omega_a > 0$. The electric field $\vec{E}$ is coupled with the atoms by the Hamiltonian $H = H_0 - \vec{\mu} \cdot \vec{E}$, in which the dipolar momentum operator is $\vec{\mu} = \mu_x \vec{e}_x + \mu_y \vec{e}_y$; μ_x and μ_x are given by Eqs. (16) and (17).

Then the evolution of the atoms is governed by the Schrödinger-von Neumann equation $i\hbar \partial_t \rho = [H, \rho]$, in which ρ is the density matrix, and the evolution of the electric field $\vec{E}$ is governed by the electromagnetic wave equation $\partial_z^2 \vec{E} = (1/c^2)\partial_t^2 \left(\vec{E} + 4\pi \vec{P}\right)$, where c is the speed of light in vacuum and the polarization density $\vec{P}$ is given by $\vec{P} = N\mathrm{Tr}(\rho \vec{\mu})$.

The short-wave-approximation is performed according to the general theory developed in Refs. [43, 81, 82]. We denote by $(u, v, 0)$ the components of the electric field $\vec{E}$ in the (xyz) frame, by $(P, Q, 0)$ the ones of $\vec{P}$, and by $\rho_{ij}, i, j = 1, 2, 3$, the elements of the Hermitian matrix ρ. All these quantities are expanded in power series of a small parameter ε as $\vec{E} = \vec{E}^0 + \varepsilon \vec{E}^1 + \varepsilon^2 \vec{E}^2 + \cdots$, and so on. We introduce fast and slow variables $\tau = \left(t - \frac{z}{V}\right)$ and $\zeta = \varepsilon z$, so that $\partial_t = \partial_\tau$ and $\partial_z = -V^{-1}\partial_\tau + \varepsilon \partial_\zeta$. The above series expansions and fast and slow variables are reported into the Maxwell and Schrödinger-von Neumann equations and the perturbative scheme is solved order by order.

The Schrödinger-von Neumann equation at order ε^0 yields $i\hbar \partial_\tau \rho^0 = -\left[\vec{\mu} \cdot \vec{E}_0, \rho^0\right]$, that is,

$$i\hbar \partial_\tau \rho_{11}^0 = -\left(\mu \rho_{12}^{0*} - \rho_{12}^0 \mu^*\right) u_0 - \left(\mu \rho_{13}^{0*} - \rho_{13}^0 \mu^*\right) v_0, \tag{59}$$

$$i\hbar \partial_\tau \rho_{22}^0 = -\left(\mu^* \rho_{12}^0 - \rho_{12}^{0*} \mu\right) u_0, \tag{60}$$

$$i\hbar \partial_\tau \rho_{33}^0 = -\left(\mu^* \rho_{13}^0 - \rho_{13}^{0*} \mu\right) v_0, \tag{61}$$

$$i\hbar \partial_\tau \rho_{12}^0 = -\mu\left(\rho_{22}^0 - \rho_{11}^0\right) u_0 - \mu \rho_{23}^{0*} v_0, \tag{62}$$

$$i\hbar \partial_\tau \rho_{13}^0 = -\mu \rho_{23}^0 u_0 - \mu\left(\rho_{33}^0 - \rho_{11}^0\right) v_0, \tag{63}$$

$$i\hbar \partial_\tau \rho_{23}^0 = -\mu^* \rho_{13}^0 u_0 + \rho_{12}^{0*} \mu v_0. \tag{64}$$

It is easy to check that Eqs. (59–61) satisfy the normalization condition for the density matrix, i.e. $\partial_\tau \mathrm{Tr}\rho^0 = 0$.

Assuming that the electric field components u and v vanish as τ tends to $-\infty$, integrating Eqs. (62) and (63), and incorporating them into Eq. (59) we get

$$\partial_\tau \rho_{11}^0 = \frac{2|\mu|^2}{\hbar^2}\left[u_0 \int_{-\infty}^{\tau} \{w_1 u_0 + \sigma v_0\} + v_0 \int_{-\infty}^{\tau} \{\sigma u_0 + w_2 v_0\}\right], \tag{65}$$

where we have defined the population differences as $w_1 = \rho_{22}^0 - \rho_{11}^0, w_2 = \rho_{33}^0 - \rho_{11}^0$, and we set $\sigma = \mathrm{Re}\rho_{23}^0$.

Then by incorporating Eq. (62) into Eq. (60), we get

$$\partial_\tau \rho_{22}^0 = -\frac{2|\mu|^2}{\hbar^2} u_0 \int_{-\infty}^{\tau} (w_1 u_0 + \sigma v_0). \tag{66}$$

Integrating Eq. (63) and incorporating it into Eq. (61) yield

$$\partial_\tau \rho_{33}^0 = -\frac{2|\mu|^2}{\hbar^2} v_0 \int_{-\infty}^{\tau} (\sigma u_0 + w_2 v_0). \tag{67}$$

The x and y components P_0 and Q_0 of the zero order polarization density $\vec{P}_0$ are given by $P_0 = N\left(\rho_{12}^0 \mu^* + \rho_{12}^{0*}\mu\right), Q_0 = N\left(\rho_{13}^0 \mu^* + \rho_{13}^{0*}\mu\right)$. By integrating Eqs. (62) and (63), incorporating them into the expressions of P_0, and Q_0 and setting $\kappa = \mathrm{Im}\left(\rho_{23}^0\right)$ we get

$$P_0 = \frac{2|\mu|^2 N}{\hbar} \int_{-\infty}^{\tau} \kappa v_0, \tag{68}$$

$$Q_0 = -\frac{2|\mu|^2 N}{\hbar} \int_{-\infty}^{\tau} \kappa u_0. \tag{69}$$

By integrating Eqs. (62) and (63), incorporating them into Eq. (64), and separating real and imaginary parts, we obtain evolution equations for $\sigma = \mathrm{Re}\rho_{23}^0$ and $\kappa = \mathrm{Im}\rho_{23}^0$, as

$$\partial_\tau \sigma = -u_0 P_y - v_0 P_x, \tag{70}$$

where we have set

$$P_x = \frac{|\mu|^2}{\hbar^2} \int_{-\infty}^{\tau} (w_1 u_0 + \sigma v_0), \tag{71}$$

$$P_y = \frac{|\mu|^2}{\hbar^2} \int_{-\infty}^{\tau} (w_2 v_0 + \sigma u_0), \tag{72}$$

and

$$\partial_\tau \kappa = -\frac{|\mu|^2}{\hbar^2} \left(u_0 \int_{-\infty}^{\tau} \kappa u_0 + v_0 \int_{-\infty}^{\tau} \kappa v_0 \right). \tag{73}$$

Then a simple analysis shows that $\kappa = 0$ and consequently, ρ_{23}^0 is a real quantity. Thus we find out that $\vec{P}_0 = \vec{0}$ and incorporating this value into the Maxwell wave equation at order ε^0, we get that the wave velocity is $V = c$ at the zero order of the series expansion in the small parameter ε.

We next get the polarization density at order ε^1 from the Schrödinger-von Neumann equation at order ε^1. The polarization density components P_1 and Q_1 involve the density matrix elements ρ_{12}^1 and ρ_{13}^1, respectively and are given by $P_1 = N\left(\rho_{12}^1 \mu^* + \rho_{12}^{1*} \mu\right)$ and $Q_1 = N\left(\rho_{13}^1 \mu^* + \rho_{13}^{1*} \mu\right)$. If we set $\hat{\kappa} = \mathrm{Im}\left(\rho_{23}^1\right)$ we get the following expressions for P_1 and Q_1:

$$P_1 = -\frac{2|\mu|^2 \Omega N}{\hbar} \int_{-\infty}^{\tau} \int_{-\infty}^{\tau} (w_1 u_0 + \sigma v_0) + \frac{2|\mu|^2 N}{\hbar} \int_{-\infty}^{\tau} \hat{\kappa} v_0, \tag{74}$$

$$Q_1 = -\frac{2|\mu|^2 \Omega N}{\hbar} \int_{-\infty}^{\tau} \int_{-\infty}^{\tau} (\sigma u_0 + w_2 v_0) - \frac{2|\mu|^2 N}{\hbar} \int_{-\infty}^{\tau} \hat{\kappa} u_0. \tag{75}$$

From the wave equation at order ε^1 we get the evolution equations for the fields u_0 and v_0 as $\partial_\zeta u_0 = (-2\pi/c)\partial_\tau P_1$ and $\partial_\zeta v_0 = (-2\pi/c)\partial_\tau Q_1$. The equations for w_1, w_2 are deduced straightforwardly from the equations for the diagonal elements of ρ^0, as $\partial_\tau w_1 = -4u_0 P_x - 2v_0 P_y$ and $\partial_\tau w_2 = -2u_0 P_x - 4v_0 P_y$. Then we get the equation for $\hat{\kappa}$:

$$\partial_\tau \hat{\kappa} = -\Omega \left(u_0 \int_{-\infty}^{\tau} P_y - v_0 \int_{-\infty}^{\tau} P_x \right). \tag{76}$$

Summarizing the analysis of Maxwell-Schrödinger-von Neumann equations, we are left with a coupled system of ten nonlinear integro-differential equations for the dependent variables $u_0,\ v_0, P_1, Q_1, P_x, P_y\ \hat{\kappa}, w_1, w_2,$ and σ; see Ref. [75] for details.

The coupled system of ten nonlinear integro-differential equations can be written in its normalized (dimensionless) form by introducing the following dimensionless functions and variables; see Ref. [75]: $(u, v) = (u_0, v_0)/E_0, T = \tau/T_0, \quad Z = \zeta/D$, where the reference electric field E_0, the reference propagation

distance D and the reference time T_0 are related through $T_0 = \hbar/(|\mu|E_0), D = E_0 c/(4\pi N\Omega|\mu|), (m,n) = (\hbar/\mu)(P_x, P_y)$ and $(p,q) = [E_0/(2N\hbar\Omega)](P_1, Q_1)$. We note that the short-wave assumption mainly expresses in the fact that the reference propagation distance D is large. If we set $w = (w_1 + w_2)/2, r = (w_2 - w_1)/2$, the system of ten nonlinear integro-differential equations reduces to the dimensionless form:

$$\partial_Z u = -\partial_T p, \tag{77}$$

$$\partial_Z v = -\partial_T q, \tag{78}$$

$$\partial_T p = -m + vK, \tag{79}$$

$$\partial_T q = -n - uK, \tag{80}$$

$$\partial_T m = (w - r)u + Sv, \tag{81}$$

$$\partial_T n = (w + r)v + Su, \tag{82}$$

$$\partial_T K = uq - vp, \tag{83}$$

$$\partial_T w = -3(um + vn), \tag{84}$$

$$\partial_T r = um - vn, \tag{85}$$

$$\partial_T S = -un - vm. \tag{86}$$

By defining four new complex quantities $P = p + iq, M = m + in, U = u + iv$ and $s = r - iS$, the nonlinear system (77–86) of ten coupled equations reduces to a more compact system of only six coupled nonlinear equations:

$$\partial_Z U = -P_T \tag{87}$$

$$\partial_T P = -M - iUK \tag{88}$$

$$\partial_T M = wU - sU^* \tag{89}$$

$$\partial_T K = \mathrm{Im}(U^* P) \tag{90}$$

$$\partial_T s = UM \tag{91}$$

$$\partial_T w = -3\mathrm{Re}(U^* M) \tag{92}$$

The above nonlinear system of coupled partial differential equations in its normalized form describing vectorial ultrashort solitons in the short-wave propagation regime can be considered as the natural generalization of the sine-Gordon equation. We will indeed show below that it reduces to the usual sine-Gordon equation in the scalar case when the second component $v = v_0/E_0$ of the electric field is equal to zero.

Now we write down two conservation laws for the above physical system. First, denoting by $I = u^2 + v^2$ the normalized intensity we straightforwardly get $\partial_Z I = -(2/3)\partial_T w$, that is, when the homogeneous population difference w has its value corresponding to the thermal equilibrium both before and after the pulse $\partial_T w = 0$, the power $\int_{-\infty}^{+\infty} I dt$ is conserved during propagation. This equation for the evolution of intensity I also shows that the energy transfer inside the pulse is entirely governed by the homogeneous population difference w. Second, we show that there is an additional conservation law which can be obtained by mimicking the obtaining of a second conservation law in the scalar case, when a sine-Gordon equation is obtained from the above complicated system of ten coupled nonlinear equations. To this aim let us consider the scalar case $v = 0$. It is seen that K, S, n, q are equal to 0 and $w = -3r$. Then the system (77–86) reduces to

$$\partial_Z u = -\partial_T p, \tag{93}$$

$$\partial_T p = -m, \tag{94}$$

$$\partial_T m = -4ru, \tag{95}$$

$$\partial_T r = um. \tag{96}$$

The nonlinear system of coupled equations (93–96) reduces to the sine-Gordon equation as follows [83]. If we set $m = A \sin\theta$ and $r = (-A/2)\cos\theta$, then a direct computation shows that $\partial_T A = 0$, hence A is a constant. From Eqs. (93–95) it is seen that $\partial_Z u = A \sin\theta$. On the other hand, $\partial_Z \partial_T u$ can be computed, either by taking the T-derivative of $\partial_Z u$, which yields $\partial_Z \partial_T u = -2r\partial_T \theta$, or by combining Eq. (93) and Eq. (95) which yields $\partial_Z \partial_T u = -4ru$. Comparison between both expressions shows that $u = \partial_T \theta/2$ and we get the sine-Gordon equation

$$\partial_Z \partial_T \theta = 2A \sin\theta. \tag{97}$$

From this derivation, it is seen that the reduction of system (93–96) to a sine-Gordon equation is based on the conservation law $\partial_T A^2 = \partial_T (m^2 + 4r^2) = 0$. This conservation law can be straightforwardly generalized to the vectorial case as follows: $\mathcal{A} = m^2 + n^2 + \frac{1}{3}w^2 + r^2 + S^2$ in terms of the normalized real variables, or equivalently, $\mathcal{A} = |M|^2 + \frac{1}{3}w^2 + |s|^2$ in terms of the normalized complex ones.

As the mKdV equation, the sine-Gordon equation (97) is completely integrable [52] and admits breather solutions. A N-soliton solution can be found using either the inverse scattering transform or the Hirota method. The 2-soliton solution writes as [52]

$$u = 2i \ln\left(\frac{f^*}{f}\right), \tag{98}$$

with

$$f = 1 + ie^{\eta_1} + ie^{\eta_2} - \frac{(k_1 - k_2)^2}{(k_1 + k_2)^2} e^{\eta_1 + \eta_2}, \tag{99}$$

where

$$\eta_j = k_j T - \frac{2AZ}{k_j} + \gamma_j \tag{100}$$

for $j = 1, 2$, while k_1, k_2, γ_1 and γ_2 are arbitrary parameters. As in the case of the mKdV equation, using complex conjugate values of the soliton parameters k_1 and k_2 yields a second-order soliton or breather, which is able to describe a FCP soliton.

The general vectorial model introduced above allows thus to retrieve the linear polarization model as a particular case of it. In what follows we look for an approximate expression of circularly polarized pulses. To this aim we note that a circularly polarized FCP is described by means of the complex system of nonlinear equations (87–92). An expression of the form $U = F\left(T - Z/v_g\right)e^{i(kZ-\omega T)}$ might be a solution of this system. However, a direct substitution of this expression into the system (87–92) shows, that no exact solution of this form exist. It is worthy to notice that the non-existence of exact non-SVEA circularly polarized pulse solutions to the Maxwell-Bloch equations was already pointed out in [79], although in the framework of a slightly different model. However, in the following we seek for an approximate solution of circularly polarized pulses in the limit of large ω, i.e., in the SVEA limit, by means of a multiscale expansion very similar to the standard one for deriving a NLS equation model in the SVEA limit [60]. To this aim we consider some small parameter ε, so that $1/\varepsilon$ is of the order of magnitude of the number of optical cycles in the pulse, which is assumed to be large in the SVEA limit. We expand U in power series $U = \sum_{r,n} \varepsilon^n e^{ir\varphi} U_{r,n}$, with $\varphi = kZ - \omega T$, and introduce slow variables $\tau = \varepsilon\left(t - z/v_g\right)$, and $\zeta = \varepsilon^2 Z$. At leading order (ε^1), we assume that $U_{1,1} = F$ is the only nonzero term in this expansion. After a standard procedure, we are left with a NLS equation for the variable F, from which we finally get the approximate expression for the circularly polarized soliton, as

$$U = be^{i\left[\left(k - \frac{b^2 k}{\omega^2}\right)Z - \omega T\right]} \operatorname{sech}\left[b\left(T + \frac{k}{\omega}Z\right)\right], \tag{101}$$

in which the soliton parameter b is assumed to be small. As concerning the stability of the circularly polarized soliton (Eq. 101) within the SVEA, it can be addressed analytically; see Ref. [75]. A direct consequence of the known properties of nonlinear Schrödinger solitons implies that the circularly polarized pulses are stable within the SVEA.

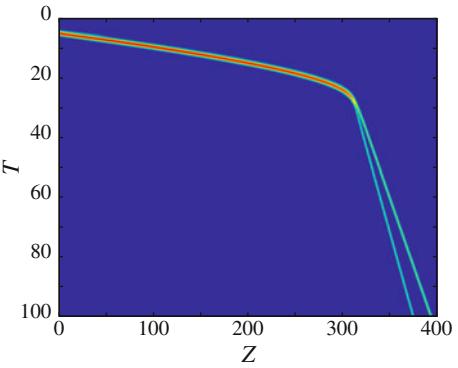

Fig. 5 (Color online) The circularly polarized few-cycle pulse and its decay into orthogonally polarized single-humped pulses. Parameters: $\omega = 5$ and $b = 2$. Here $Z_{disp} = 37$ (after Ref. [75])

3.2 *Lifetime of Circularly Polarized Few-Cycle Pulses and Spontaneous Symmetry Breaking*

Note that the existence and stability of the circularly polarized FCP within SVEA does not ensure either its stability or even its existence beyond SVEA [79]. In the following we study numerically the stability of circularly polarized few-cycle pulses beyond the SVEA. The Z evolution of u and v is computed by means of a standard fourth-order Runge-Kutta algorithm, at each step and substep of the scheme, the eight other components are computed using the same algorithm but relative to the T variable. We assume that all atoms are initially in the fundamental state, that is, $w = -1$ at $T = 0$. We use the approximate circularly polarized pulse (Eq. 101) as an input, with $\omega = 5$, and vary the pulse duration b. Extensive numerical simulations show that the input FCP decays into two linearly polarized single-humped pulses, breaking the rotation symmetry as was observed for the sub-cycle pulses within the long-wave approximation. In general, two orthogonally polarized pulses with different amplitudes are obtained (see Figs. 5, 6, and 7). For the shortest sub-cycle pulses, the instability occurs very fast, the amplitudes of the two single humped pulses strongly differ, and the angle between their polarization directions is not close to $\pi/2$. In fact, the single-humped pulses are fundamental solitons of the sine-Gordon equation (97) to which the system reduces in the case of linear polarization, i.e., the scalar case. However, no stability threshold for the circularly polarized FCPs can be evidenced by these numerical calculations. The lifetime of circularly-polarized FCPs becomes very large when the number N_c of optical cycles in the pulse is greater than one; see Ref. [75] for a detailed study of this issue.

We conclude this section devoted to circularly polarized few-cycle solitons in the short-wave regime by stressing that we took into account the vectorial nature of the electric field, and therefore we properly considered the wave polarization effects [75]. We have found that the two interacting waveforms corresponding to such vector few-optical-cycle solitons are adequately described by a coupled

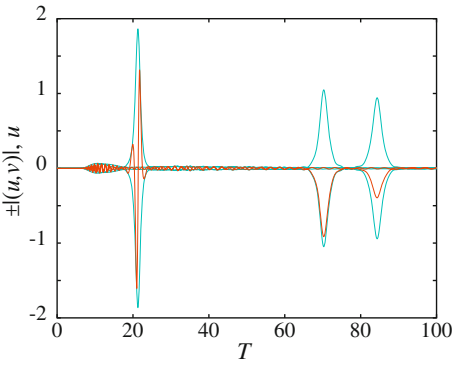

Fig. 6 (Color online) The circularly polarized few-cycle pulse and its decay into two orthogonally polarized single-humped pulses. The shape of the few-cycle pulse at $Z = 280$ (*left*) and $Z = 360$ (*right*). *Light blue* (*gray*): the amplitude $|U| = \sqrt{u^2 + v^2}$ (and $-|U|$), *red* (*black*): $u = \mathrm{Re}(U)$ (After Ref. [75])

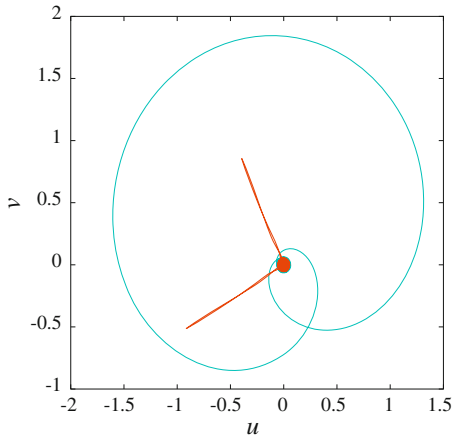

Fig. 7 (Color online) The circularly polarized few-cycle pulse and its decay into two orthogonally polarized single-humped pulses. The trajectories of the tip of the normalized electric field vector (u, v) in the transverse plane, for two values of Z, showing the polarization. *Light blue* (*gray*): at $Z = 280$, *red* (*black*): at $Z = 360$ (after Ref. [75])

system of nonlinear equations at the first-order approximation of the perturbation approach. By direct numerical simulations we calculated the lifetime of circularly polarized few-optical-cycle solitons and we studied their decay into two orthogonally polarized single-humped pulses as a generic route of their instability [75]. A challenging extension suggested by these studies is to consider the case of two transitions, one below and one above the range of propagated wavelengths. Another interesting open problem is the generalization of this study to one or even to two spatial transverse dimensions, in addition to time and spatial longitudinal coordinates, that is, the issue of formation and robustness of vector few-optical-cycle *spatiotemporal solitons*, alias ultrashort vector light bullets, beyond the slowly varying envelope approximation, in both the long- and short-wave regimes; for recent overviews of a lot of theoretical and experimental studies of spatiotemporal optical solitons in several relevant physical settings, see [84–86].

4 Conclusions

Given the rapid growth of theoretical and experimental studies in the past decade in the area of few-optical-cycle pulses and high field physics and extreme nonlinear optics, one can expect many new and exciting developments over the next years. No doubt, soon one can expect a maturity of these fast growing research areas, leading to new and interesting physical phenomena and to the utilization of their huge technological potential. We focused in this chapter on the vectorial properties of few-optical-cycle solitons, showing the existence of robust circularly polarized few-cycle solitons, while in the sub-cycle regime these circularly polarized pulses are unstable and decay into either one or two linearly polarized pulses, breaking the rotation symmetry. We conclude with the hope that this overview on some recent developments in the area of few-optical-cycle solitons will inspire further theoretical and experimental investigations.

Acknowledgments The work of DM was supported in part by a Senior Chair Grant from the Région Pays de Loire, France.

References

1. L. Gallmann, D.H. Sutter, N. Matuschek, G. Steinmeyer, U. Keller, C. Iaconis, I.A. Walmsley, Opt. Lett. **24**, 1314 (1999)
2. U. Morgner, F.X. Kärtner, S.H. Cho, Y. Chen, H.A. Haus, J.G. Fujimoto, E.P. Ippen, V. Scheuer, G. Angelow, T. Tschudi, Opt. Lett. **24**, 411 (1999)
3. D.H. Sutter, G. Steinmeyer, L. Gallmann, N. Matuschek, F. Morier-Genoud, U. Keller, V. Scheuer, G. Angelow, T. Tschudi, Opt. Lett. **24**, 631 (1999)
4. A. Shirakawa, I. Sakane, M. Takasaka, T. Kobayashi, Appl. Phys. Lett. **74**, 2268 (1999)
5. M. Wegener, *Extreme Nonlinear Optics* (Springer, Berlin, 2005)
6. E. Goulielmakis, M. Schultze, M. Hofstetter, V.S. Yakovlev, J. Gagnon, M. Uiberacker, A.L. Aquila, E.M. Gullikson, D.T. Attwood, R. Kienberger, F. Krausz, U. Kleineberg, Science **320**, 1614 (2008)
7. A. Scrinzi, M.Y. Ivanov, R. Kienberger, D.M. Villeneuve, J. Phys. B **39**, R1 (2006)
8. F. Krausz, M.Y. Ivanov, Rev. Mod. Phys. **81**, 163 (2009)
9. T. Brabek, F. Krausz, Rev. Mod. Phys. **72**, 545 (2000)
10. G.A. Mourou, T. Tajima, S.V. Bulanov, Rev. Mod. Phys. **78**, 309 (2006)
11. G.A. Mourou, T. Tajima, Science **331**, 41 (2011)
12. M. Zürch, C. Kern, P. Hansinger, A. Dreischuh, Ch. Spielmann, Nat. Phys. **8**, 743 (2012)
13. K. Yamane, Y. Toda, R. Morita, Opt. Express **20**, 18986 (2012)
14. M. Bock, J. Jahns, R. Grunwald, Opt. Lett. **37**, 3804 (2012)
15. L. Bergé, S. Skupin, Phys. Rev. Lett. **100**, 113902 (2008)
16. E.V. Kazantseva, A.I. Maimistov, B.A. Malomed, Opt. Commun. **188**, 195 (2001)
17. H. Leblond, D. Kremer, D. Mihalache, Phys. Rev. A **80**, 053812 (2009)
18. H. Leblond, D. Kremer, D. Mihalache, Phys. Rev. A **81**, 033824 (2010)
19. H. Leblond, D. Mihalache, Phys. Rev. A **81**, 063815 (2010)
20. X.-T. Xie, M.A. Macovei, Phys. Rev. Lett. **104**, 073902 (2010)
21. P. Dombi, S.E. Irvine, P. Rácz, M. Lenner, N. Kroó, G. Farkas, A. Mitrofanov, A. Baltuska, T. Fuji, F. Krausz, A.Y. Elezzabi, Opt. Express **18**, 24206 (2010)

22. N.N. Rosanov, V.V. Kozlov, S. Wabnitz, Phys. Rev. A **81**, 043815 (2010)
23. V.V. Kozlov, N.N. Rosanov, S. Wabnitz, Phys. Rev. A **84**, 053810 (2011)
24. H. Leblond, D. Mihalache, J. Phys. A: Math. Theor. **43**, 375205 (2010)
25. E.D. Farnum, J. Nathan Kutz, Opt. Lett. **35**, 3033 (2010)
26. A.V. Kim, S.A. Skobolev, Phys. Rev. A **83**, 063832 (2011)
27. Q. Lin, J. Zheng, J. Dai, I.-C. Ho, X.-C. Zhang, Phys. Rev. A **81**, 043821 (2010)
28. X. Song, W. Yang, Z. Zeng, R. Li, Z. Xu, Phys. Rev. A **82**, 053821 (2010)
29. A.M. Heidt, J. Rothhardt, A. Hartung, H. Bartelt, E.G. Rohwer, J. Limpert, A. Tünnermann, Opt. Express **19**, 13873 (2011)
30. B. Piglosiewicz, D. Sadiq, M. Mascheck, S. Schmidt, M. Silies, P. Vasa, C. Lienau, Opt. Express **19**, 14451 (2011)
31. V.V. Kozlov, N.N. Rosanov, C. De Angelis, S. Wabnitz, Phys. Rev. A **84**, 023818 (2011)
32. A. Pusch, J.M. Hamm, O. Hess, Phys. Rev. A **84**, 023827 (2011)
33. P.-C. Li, I.-L. Liu, S.-I. Chu, Opt. Express **19**, 23857 (2011)
34. X. Tan, X. Fan, Y. Yang, D.J. Tong, Mod. Opt. **55**, 2439 (2008)
35. A.I. Maimistov, Quantum Electron. **40**, 756 (2010)
36. T. Brabec, F. Krausz, Phys. Rev. Lett. **78**, 3282 (1997)
37. A.V. Husakou, J. Herrmann, Phys. Rev. Lett. **87**, 203901 (2001)
38. A. Kumar, V. Mishra, Phys. Rev. A **79**, 063807 (2009)
39. J.K. Ranka, A.L. Gaeta, Opt. Lett. **23**, 534 (1998)
40. E.M. Belenov, A.V. Nazarkin, JETP Lett. **51**, 288 (1990)
41. I.V. Mel'nikov, D. Mihalache, F. Moldoveanu, N.C. Panoiu, Phys. Rev. A **56**, 1569 (1997)
42. I.V. Mel'nikov, D. Mihalache, N.C. Panoiu, Opt. Commun. **181**, 345 (2000)
43. H. Leblond, F. Sanchez, Phys. Rev. A **67**, 013804 (2003)
44. H. Leblond, F. Sanchez, I.V. Mel'nikov, D. Mihalache, Math. Comput. Simul. **69**, 378 (2005)
45. H. Leblond, S.V. Sazonov, I.V. Mel'nikov, D. Mihalache, F. Sanchez, Phys. Rev. A **74**, 063815 (2006)
46. H. Leblond, D. Mihalache, Rom. Rep. Phys. **63**, 1254 (2011)
47. H. Leblond, D. Mihalache, Phys. Reports. doi:10.1016/j.physrep.2012.10.006
48. S. Amiranashvili, A.G. Vladimirov, U. Bandelow, Phys. Rev. A **77**, 063821 (2008)
49. A.I. Maĭmistov, J.G. Caputo, Opt. Spectrosc. **94**, 245 (2003) [Optika i Spektroskopiya **94**, 275 (2003)]
50. E.V. Kazantseva, A.I. Maimistov, J.G. Caputo, Phys. Rev. E **71**, 056622 (2005)
51. R.K. Dodd, J.C. Eilbeck, J.D. Gibbon, H.C. Morris, *Solitons and Nonlinear Wave Equations* (Academic Press, London, 1982)
52. M.J. Ablowitz, H. Segur, *Solitons and the Inverse Scattering* (Transform SIAM, Philadelphia, 1981)
53. K. Konno, W. Kameyama, H. Sanuki, J. Phys. Soc. Jpn. **37**, 171 (1974)
54. A.M. Kosevich, A.S. Kovalev, Solid State Commun. **12**, 763 (1973)
55. N.N. Akhmediev, I.V. Mel'nikov, A.V. Nazarkin, Sov. Phys. Lebedev. Inst. Rep. **2**, 66 (1989) [Kratk. Soobshch. Fiz. FIAN **2**, 49 (1989)]
56. A. Kujawski, Z. Phys. **66**, 271 (1987)
57. A. Kujawski, Z. Phys. **85**, 129 (1991)
58. A.V. Andreev, Zh. Éksp. Teor. Phys. **108**, 796 (1995) [JETP **81**, 434 (1995)]
59. A.Y. Parkhomenko, S.V. Sazonov, Zh. Éksp. Teor. Phys. **114**, 1595 (1998) [JETP **87**, 864 (1998)]
60. H. Leblond, J. Phys. B: At. Mol. Opt. Phys. **41**, 043001 (2008)
61. T. Taniuti, C.C. Wei, J. Phys. Soc. Jpn. **24**, 941 (1968)
62. H. Leblond, H. Triki, F. Sanchez, D. Mihalache, Opt. Commun. **285**, 356 (2012)
63. H. Leblond, H. Triki, F. Sanchez, D. Mihalache, Phys. Rev. A **83**, 063802 (2011)
64. H. Triki, H. Leblond, D. Mihalache, Opt. Commun. **285**, 3179 (2012)
65. H. Triki, M.S. Ismail, Appl. Math. Comput. **217**, 1540 (2010)
66. M.V. Foursov, J. Math. Phys. **41**, 6173 (2000)
67. A. Biswas, E. Zerrad, A. Ranasinghe, Appl. Math. Comput. **217**, 1491 (2010)

68. Ö. Akin, E. Özugurlu, Math. Probl. Eng. **2009**, 935030 (2009)
69. B.A. Malomed, J. Fujioka, A. Espinosa-Ceron, R.F. Rodriguez, S. González, Chaos **16**, 013112 (2006)
70. A.A. Mohammad, M. Can, J. Phys. A Math. Gen. **28**, 3223 (1995)
71. H. Zhang, Commun. Nonl. Sci. Numer. Simul. **13**, 1776 (2008)
72. S.M. Cox, P.C. Matthews, J. Comput. Phys. **176**, 430 (2002)
73. R. Hirota, Lect. Notes Math. **515**, 40 (1976)
74. H. Leblond, Phys. Rev. A **78**, 013807 (2008)
75. H. Leblond, H. Triki, D. Mihalache, Phys. Rev. A **84**, 023833 (2011)
76. V.G. Bespalov, S.A. Kozlov, Yu.A. Shpolyanskiy, I.A. Walmsley, Phys. Rev. A **66**, 013811 (2002)
77. M. Pietrzyk, I. Kanattšikov, U. Bandelow, J. Nonlin. Math. Phys. **15**, 162 (2008)
78. L. Allen, J.H. Eberly, *Optical Resonance and Two-Level Atoms* (Dover, New York, 1987)
79. S.V. Branis, O. Martin, J.L. Birman, Phys. Rev. A **43**, 1549 (1991)
80. A.V. Andreev, Sov. Phys. JETP **81**, 434 (1995) [Zh. Éksp. Teor. Fiz. **108**, 796 (1995)
81. M.A. Manna, V. Merle, Phys. Rev. E **57**, 6206 (1998)
82. M.A. Manna, J. Phys. A: Math. Gen. **34**, 4475 (2001)
83. R.A. Kraenkel, M.A. Manna, V. Merle, Phys. Rev. E **61**, 976 (2000)
84. B.A. Malomed, D. Mihalache, F. Wise, L. Torner, J. Opt. B **7**, R53 (2005)
85. D. Mihalache, J. Optoelectron. Adv. Mater. **12**, 12 (2010)
86. D. Mihalache, Rom. J. Phys. **57**, 352 (2012)

Defect Modes, Fano Resonances and Embedded States in Magnetic Metamaterials

M. I. Molina

Abstract We consider a simplified model of a nonlinear magnetic metamaterial, consisting of a weakly-coupled, periodic split-ring resonator (SRR) array capable of nonlinear capacitive response. We analyze three related problems: (a) The calculation of localized modes around simple magnetoinductive impurities located at the surface or at the bulk of the array, in closed form for both, linear and nonlinear cases. (b) The scattering of magnetoinductive waves across internal (external) capacitive (inductive) defects coupled to the SRR array and the occurrence of Fano resonances, and how to tune them by changing the external parameters of the system. (c) Description of a method for building a stable localized magnetoinductive mode embedded in the linear band of extended states.

1 Introduction

Metamaterials (MMs) are novel artificial materials characterized for having negative dielectric permittivity and negative magnetic permeability over a finite frequency range, endowing them with unusual electromagnetic wave propagation properties [1, 2]. One of the most studied MMs is a metallic composite structure consisting of arrays of wires and split-ring resonators (SRRs). The theoretical treatment of such structures relies mainly on the effective-medium approximation where the composite is treated as a homogeneous and isotropic medium, characterized by effective macroscopic parameters. The approach is valid, as long as the wavelength of the electromagnetic field is much larger than the linear dimensions of the MM

M. I. Molina (✉)
Departamento de Física, MSI-Nucleus on Advanced Optics, Center for Optics and Photonics (CEFOP), Facultad de Ciencias, Universidad de Chile, Santiago, Chile
e-mail: mmolina@uchile.cl; molina.mi@gmail.com

Progress Optical Sci., Photonics (2013): 277–307
DOI: 10.1007/10091_2012_15

Published Online: 14 August 2012

constituents. The magnetic properties of SRR arrays have been explored in a number of works [3–11].

Among the numerous aspects to explore with a new and promising electromagnetic material such as MMs, are its optical transport properties. For a SRR periodic array, it is only natural to explore the propagation of long-wavelength excitations, in the presence of one or few "impurities" that break its translational invariance. In the absence of any defects, the eigenmodes of a linear periodic SRR array are termed "magnetoinductive waves". The presence of judiciously placed defects make possible interesting phenomena such as localized linear and/or nonlinear defect modes, or resonance phenomena, such as Fano resonances (FR), where there is total reflection of plane waves through the impurity region, in an otherwise periodic potential. In a typical FR system, the wave propagation in the presence of a periodic scattering potential is characterized by open and closed channels. The open channel guides the propagating waves as long as the eigenfrequencies of closed channels do not match the spectrum of linear waves. The total reflection of waves in the open channel occurs when a localized state originating from one of the closed channels resonates with the open channel spectrum [12]. The FR effect can be used to control the optical response in novel, man-made materials, such as magnetic metamaterials. On the other hand, a judiciously chosen modulation of the resonant frequency of each resonator in an SRR array, can lead to the creation of a localized bound state of the SRR array that is embedded in the band of extended states. An explicit method for building this kind of state in general periodic discrete systems has been found recently [13], and we will apply it to the SRR array.

2 Simplified Model

Let us consider a one-dimensional, periodic array of split-ring resonators (SRRs), in the absence of nonlinearity, driving and dissipation. The most simple form of a split-ring resonator is that of a small, conducting ring with a slit. In general, each SRR unit in the array can be mapped to a resistor-inductor-capacitor (RLC) circuit featuring self-inductance L, ohmic resistance R, and capacitance C built across the slit. In our case, we will consider the case of negligible resistance R. Thus, each SRR unit possesses a resonant frequency $\omega_0 \approx 1/\sqrt{LC}$. In the array, each SRR is coupled to their nearest neighbor via mutual induction [3, 4]. A more accurate model can be found Ref. [14].

In the absence of driving and dissipation, the evolution equation for the charge Q_n residing on the nth ring is

$$\frac{d^2}{dt^2}\left(LQ_n + \sum_{m\neq n} M_{nm}Q_m\right) + \frac{Q_n}{C} = 0, \tag{1}$$

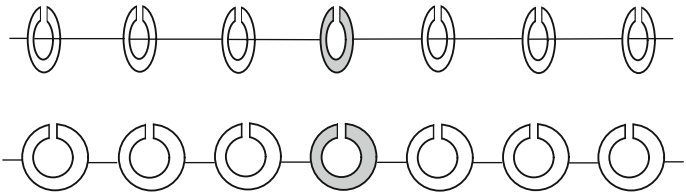

Fig. 1 Two typical configurations for the SRR array, containing a single bulk impurity

where L is the self-inductance of the nth-ring, and M_{nm} is the mutual induction between rings n and m. We cast this equation in dimensionless form by defining $\tau \equiv \omega_0 t$, $q_n \equiv Q_n/CU_0$, $\lambda_{nm} \equiv M_{nm}/L$, where U_0 is a characteristic voltage across the slits.

The dimensionless evolution equation for the charge q_n residing on the nth ring reads now

$$\frac{d^2}{d\tau^2}\left(q_n + \sum_{m\neq n} \lambda_{nm} q_m\right) + q_n = 0, \tag{2}$$

where λ_{nm} denotes the ratio of the mutual inductances between the nth and the mth ring to the self inductance of the rings, and decreases as the inverse cube of the ring-to-ring distance, $\lambda_{nm} \propto |n-m|^{-3}$ $(m \neq n)$. In the limit of weak coupling (large distance between SRR units), it is customary to take $\lambda_{nm} = \lambda\, \delta_{n,m}$.

The two most simple SRR configurations are shown in Fig. 1. In one of them (top), all couplings are positive, while for the second (bottom), they are all negative, as a result of Lenz's law.

The stationary modes of Eq. (2) are obtained by posing a solution in the form $q_n(\tau) = q_n \exp(i\Omega\tau)$. This leads to the stationary equations,

$$-\Omega^2\left(q_n + \sum_{m\neq n} \lambda_{nm} q_m\right) + q_n = 0. \tag{3}$$

Magnetoinductive plane waves of the form $q_n = A\exp(ikn)$, lead to the dispersion relation

$$\Omega^2 = \frac{1}{1 + 2\sum_{m\,>\,0} \lambda_{0m}\cos(km)}, \tag{4}$$

where the physical condition $\Omega^2 > 0$ must be imposed. Using that λ_{0m} has the form $\lambda_{0m} = \lambda/m^3$, one obtains:

$$-\frac{1}{2\zeta(3)} < \lambda < \frac{2}{3\zeta(3)}, \tag{5}$$

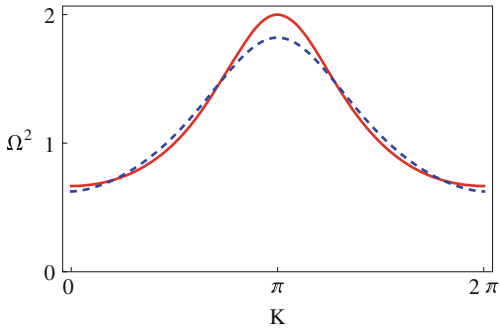

Fig. 2 Dispersion relation for magnetoinductive waves for dipolar interaction (*dashed*) and nearest-neighbor approximation (*solid*)

or, $-0.41595 < \lambda < 0.554605$, where $\zeta(s)$ is the Riemann Zeta function $\zeta(s) = \sum_{k=1}^{\infty} k^{-s}$. The limits in condition (5) change a bit when one assumes a weak coupling limit where few or even only one of the λ_{0m} is retained. Figure 2 shows the dispersion relation of the magnetoinductive waves for both, the nearest-neighbor approximation and the full dipolar-like interaction. As we can see, there are small differences between them. However, the presence of absence of interaction beyond nearest-neighbor interactions will prove important later (Sect. 4) when considering scattering of plane waves through capacitive defects and Fano resonances.

3 Localized Modes Around Magnetoinductive Defects

In general, when the discrete translational invariance of a periodic lattice is broken by the presence of a defect, it usually gives rise to a localized mode that detaches from the continuous band. The details depend on things such as the dimensionality of the array, presence or absence of nonlinear effects, type of nonlinearity, etc. It is commonly observed that in 1D, a localized state is formed for any defect strength, while at higher dimensions, a minimum defect strength is needed. Simple defects for a SRR include the capacitive defect, created when the capacitance of one of the rings is changed by either altering the slit width, or by inserting a (linear) dielectric in the slit. Another simple defect is the inductive defect, caused by altering the distance between a single ring and its closest neighbors. A third type of defect is the nonlinear capacitive defect formed when one inserts a nonlinear (e.g., Kerr) dielectric inside the ring slit. Other types of defects are, of course, possible, but they are harder to treat. For instance, if one alters the geometry of a single ring, that will change the capacitance, self-inductance, and mutual inductance the ring.

Let us consider a one-dimensional, periodic array of linear split-ring resonators (SRRs), in the absence of driving and dissipation, containing a single, capacitive impurity, located at $n = n'$. (The case of few, linear inductive bulk impurities

embedded in a SRR array, has already been treated in Ref. [15].) As mentioned above, in the linear regime, the impurity is due to a change in the slit width of the $n = n'$ SRR which causes a change in its capacitance. In the nonlinear impurity case, all the slit widths are the same, but the $n = n'$ SRR slit is filled with a nonlinear dielectric, causing a localized nonlinear capacitive response. In this work we will consider the linear and nonlinear capacitive impurity cases separately, for both, bulk impurity ($n' \gg 0$) and surface impurity ($n' = 0$).

In the presence of a single defect, Eq. (2) becomes [16, 17]

$$\frac{d^2}{d\tau^2}(\lambda q_{n-1} + q_n + \lambda q_{n+1}) + (1 + \delta_{n,n'}\Delta)q_n = 0, \tag{6}$$

where $\Delta = (\omega'/\omega)^2 - 1$, or $-\chi q_{n'}^2$ for the linear and nonlinear capacitive defect, respectively. Parameter λ denotes the ratio of the mutual inductances between two nearest-neighbor rings to the self inductance of the rings, ω'/ω is the ratio of the resonant frequency at the impurity ring to that of the background rings, and χ is the nonlinear parameter of the impurity ring, originating in the nonlinear capacitive response at the impurity ring site. Positive (negative) χ values denote the case of a soft (hard) nonlinearity. Figure 1 shows the most typical two SRRs configurations containing a single bulk defect.

3.1 Green Functions

A formal approach to solving impurity problems defined on a periodic lattice, such as (6), is by means of lattice Green functions [18]. In this formalism, the lattice Green function is defined by the operator $G(z) \equiv 1/(z - H)$, where H is the Hamiltonian of the system. The poles of G give information concerning the eigenenergies of the system while the residues of G at the poles give information about the spatial distribution of the eigenstates. In general is not possible to know G exactly, except in few, special cases. These include the case when we can decompose $H = H_0 + H_1$, where H_0 is the "unperturbed" part whose eigenvalues and eigenstates are known to us, while H_1 is the "perturbation". After inserting this into G, one obtains the formal expansion:

$$G = G^{(0)} + G^{(0)}H_1G'^{(0)} + G^{(0)}H_1G^{(0)}H_1G^{(0)} + \cdots, \tag{7}$$

where $G^{(0)}$ is the unperturbed Green function. For our impurity case, Eq. (6), we obtain the equation for the stationary modes by setting $q_n(\tau) = q_n \exp(i\Omega\tau + \phi)$:

$$-\Omega^2(\lambda q_{n-1} + q_n + \lambda q_{n+1}) + (1 + \delta_{n,n'}\Delta)q_n = 0. \tag{8}$$

After rearranging this equation we can express it as

$$\lambda(q_{n+1}+q_{n-1})-\frac{\Delta}{\Omega^2}\delta_{n,n'}q_n=\left(\frac{1}{\Omega^2}-1\right)q_n. \tag{9}$$

Thus, the system is equivalent to a simple one-band tight-binding model, with eigenvalue $\beta\equiv((1/\Omega^2)-1)$, containing a single renormalized impurity Δ/Ω^2. For this type of system, we can express H_1 in the Wannier representation as $H_1=-(\Delta/\Omega^2)|n'><n'|$, and series Eq. (7) can be resummed in closed form to yield

$$G_{mn}(\beta)=G^{(0)}_{mn}(\beta)-\frac{(\Delta/\Omega^2)G^{(0)}_{mn'}(\beta)G^{(0)}_{n'n}(\beta)}{1+(\Delta/\Omega^2)G^{(0)}_{n'n'}(\beta)}. \tag{10}$$

The poles of G are given by solving $1=(\Delta/\Omega^2)G^{(0)}_{n'n'}(\beta)$.

For instance, for the linear capacitive defect case, we obtain after solving for Ω^2:

$$\Omega^2=\frac{1-\Delta^2}{1-\mathrm{sign}(\Delta)\sqrt{4\lambda^2+\Delta^2(1-4\lambda^2)}}. \tag{11}$$

The method can also be applied to isolated, nonlinear defects [19–22]. In this case, the equation for the pole(s) at the impurity must be combined with the equation giving the amplitude profile around the defect, to obtain a nonlinear equation for the localized mode energy (frequency). From this, one or more localized states might be found, although usually only one of them is stable.

Besides bulk impurities, the Green function method can also be applied to surface defects, or defects that are at a finite distance from a boundary. The trick here is the use of the "method of images" [23–25]. For continuous systems with localized impurities, the reader might want to look at Ref. [26].

Having introduced the Green function method, we will dispense from this approach from now on and use a more simple heuristic approach that have proven useful in many (but not all) cases involving impurities. Also, for simplicity, we will confine ourselves to the simple cases of a linear and nonlinear capacitive impurity.

3.2 Bulk Impurity

Linear Case. We consider a long lattice, $-M<n<M$, where $M\gg 1$. As long as the defect is placed far away from the sample boundaries, we speak of a bulk impurity. Without loss of generality, we place the defect at $n'=0$. For $\chi=0$, Eq. (6) reads:

$$\frac{d^2}{d\tau^2}(\lambda q_{n-1}+q_n+\lambda q_{n+1})+q_n+\delta_{n,0}(\omega'^2-1)q_n=0, \tag{12}$$

where, we have scaled $\omega_n^2 = 1$. When the slit width of the defect ring tends to zero, the local capacitance goes to infinity, which means $\omega'^2 \to 0$ in (12). On the other hand, when the slit width is large, the local capacitance goes to zero, implying that $\omega'^2 \to \infty$ in (62). Therefore, the physical range of ω'^2 is $0 < \omega'^2 < \infty$.

We look for a stationary mode solution of the form $q_n(\tau) = \xi^{|n|}\cos(\Omega\tau + \phi)$, with $|\xi| < 1$. After replacing this *ansatz* into (12), one obtains, after some algebra

$$\xi = \frac{\omega'^2 - 1 + \text{sign}(\omega'^2 - 1)\sqrt{(\omega'^2 - 1)^2(1 - 4\lambda^2) + 4\lambda^2}}{2\lambda(2 - \omega'^2)}, \tag{13}$$

and

$$\Omega^2 = [1 + \lambda(\xi + (1/\xi))]^{-1}. \tag{14}$$

A quick examination of (63) reveals:

(a) If $\lambda \to -\lambda, \xi \to -\xi$ ('staggered–unstaggered' transformation).
(b) If $\omega'^2 \to 0, \xi^2 \to 0$. If $\omega'^2 \to 1, \xi^2 \to 1$.
(c) If $\omega'^2 \to \infty$, then

$$\xi = \frac{-1}{2\lambda} + \sqrt{\left(\frac{1}{2\lambda}\right)^2 - 1}. \tag{15}$$

(d) If $\omega'^2 \to 2$, then $\xi \to -2\lambda$.

From (c) and (d), and the condition $|\xi| < 1$ we see that we must impose $|\lambda| < 1/2$. Figure 3 shows that, for $\omega'^2 < 1$, the mode is unstaggered, while for ω'^2 the mode is staggered. The above holds for $\lambda > 0$. For $\lambda < 0$, the opposite behavior is obtained, as can be seen from the staggered–unstaggered symmetry. Note that for $\omega'^2 > 1$, the mode has a minimum width, given by (15). Figure 3 also shows the frequency of the localized mode, which is bounded from below, and some localized modes for different values of defect frequency and inductive coupling. Perhaps the most important feature of this mode is that it exists for any nonzero frequency mismatch value ω', as in many other 1D systems with a single defect. The mode suffers a discontinuous unstaggered–staggered symmetry transition at $\omega' = 1$.

Nonlinear case. In this case, all the SRRs are identical, but one of them (at $n' = 0$) has the space between its slits filled with a nonlinear dielectric of the Kerr type, causing it to have a nonlinear capacitive response. Now, the resonant frequency of the impurity ring depends on how much magnetic energy is residing on the ring. Equation (6) reads now:

$$\frac{d^2}{d\tau^2}(\lambda q_{n-1} + q_n + \lambda q_{n+1}) + (1 - \chi\delta_{n,0}q_n^2)q_n = 0, \tag{16}$$

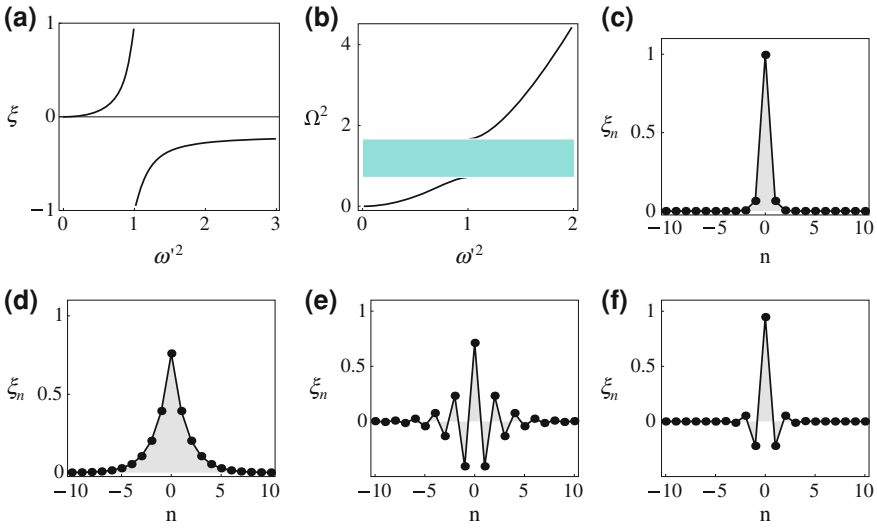

Fig. 3 Linear bulk impurity. **a** Localized mode amplitude versus defect frequency; **b** frequency of localized mode versus defect frequency; **c**–**f** spatial profiles of impurity mode for (**c**) $\omega'^2 = 0.5$, (**d**) $\omega'^2 = 0.9$, (**e**) $\omega'^2 = 1.2$, and (**f**) $\omega'^2 = 3$. In all cases, $\lambda = 0.2$

for $-\infty < n < \infty$. We look for stationary modes of the form $q_n(\tau) = q_n \cos(\Omega\tau + \phi)$, and use the rotating-wave approximation (RWA) $\cos(x)^3 \approx (3/4)\cos(x)$. The rigorous procedure involves finding the nonlinear mode (breather) by numerical techniques [27]. However, we have found that, in practice, the RWA results agree quite well with the exact numerical ones in a variety of nonlinear problems involving arrays of coupled nonlinear SRRs [28–30]. For the case of single impurity, it allows for a closed form solution. We obtain,

$$-\Omega^2(\lambda q_{n-1} + q_n + \lambda q_{n+1}) + q_n - (3/4)\chi\delta_{n0}q_n^3 = 0. \tag{17}$$

We look for a localized solution of the form $q_n = A\xi^{|n|}$, where $0 < |\xi| < 1$. After inserting this *ansatz* into Eq. (17), one obtains the equations

$$\Omega^2 = \frac{1 - (3/4)\chi A^2}{1 + 2\lambda\xi}, \tag{18}$$

and

$$\Omega^2 = \frac{1}{1 + \lambda(\xi + (1/\xi))}. \tag{19}$$

From Eq. (19), the physical condition that $\Omega^2 > 0$ together with the constraint $|\xi| < 1$ imply $|\lambda| < 1/2$. This, in turn implies, from Eq. (18), the restriction $|A| < A_c$,

where $A_c \equiv 1/\sqrt{(3/4)\chi}$ for $\chi > 0$. For $\chi < 0$ no such restriction is necessary. After equating (18) and (19), we obtain a quadratic equation for ξ:

$$\xi^2 + B(\lambda, A)\xi - C(\lambda, \xi) = 0 \tag{20}$$

with

$$B(\lambda, \xi) = \frac{(3/4)\chi A^2}{\lambda(1 + (3/4)\chi A^2)}, \tag{21}$$

and

$$C(\lambda, \xi) = \frac{1 - (3/4)\chi A^2}{1 + (3/4)\chi A^2}. \tag{22}$$

We note that, in the limit of small A, $B \to 0$ and $C \to 1$, implying $\xi^2 \to 1$, converging to an extended mode as expected. On the other hand, for $\chi > 0$ and A approaching A_c, the equation becomes $\xi(\xi + (1/2\lambda)) = 0$, which implies that $\xi \to 0$ since $|\lambda| < 1/2$. The mode becomes infinitely localized at the impurity site. Finally, in the limit of large A (relevant for $\chi < 0$ only), Eq. (20) reduces to

$$\xi^2 + \frac{1}{\lambda} + 1 = 0 \tag{23}$$

with solution

$$\xi = -\frac{1}{2\lambda} + \text{sign}(\lambda)\sqrt{\frac{1}{4\lambda^2} - 1}. \tag{24}$$

In this case, the width of the mode converges to a constant value.

On the other hand, from Eq. (19), and the unstaggered–staggered symmetry: $\lambda \to -\lambda \Longleftrightarrow \xi \to -\xi$, we see that Ω^2 is invariant under a change in sign of the inductive coupling.

The relevant solution of Eq. (20) is given by

$$\xi = \frac{1}{2}\left\{-B(\lambda, A) + \sigma\sqrt{B(\lambda, A)^2 + 4C(\lambda, A)}\right\}, \tag{25}$$

where $\sigma = \text{sign}(B(\lambda, A))$.

Figure 4 shows results for nonlinear localized modes for the soft and hard nonlinearity cases. Note that for the soft nonlinearity case, the maximum amplitude at the impurity site is restricted to the interval $A \in [0, 1\sqrt{(3/4)\chi}]$. The frequency of the mode is bounded from above ($\Omega^2 = 1/(1 - 2\lambda)$) and from below ($\Omega^2 = 0$). For the hard nonlinearity case, however, the frequency is only bounded from below ($\Omega^2 = 1/(1 - 2\lambda)$), but the magnitude of the decay rate $|\xi|$ has a minimum value given by Eq. (24). Figure 5 also shows examples of the spatial profile of nonlinear localized modes for different parameter values.

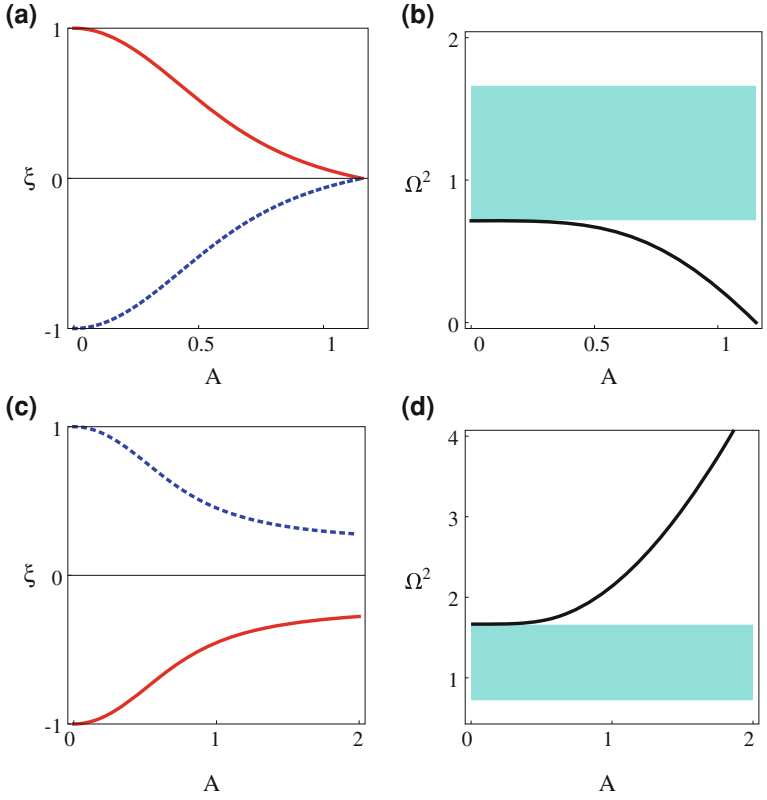

Fig. 4 Nonlinear bulk impurity. *Top* (*bottom*) *rows* correspond to $\chi = 1(-1)$. In **a** and **c** we show the decay rate ξ as a function of maximum amplitude A, for $\lambda = 0.2$ (*solid curve*) and $\lambda = -0.2$ (*dashed curve*). In **b** and **d** we show the frequency of the localized mode as a function of maximum mode amplitude for $\lambda = \pm 0.2$

3.3 Surface Impurity

Linear case. In this case, the array extends from $n = 0$ to $n \to \infty$, and the capacitive defect is placed at the very boundary, $n' = 0$. Previous experience with tight-binding models suggests that a minimum defect strength will needed to place a localized mode at the edge of the system. The evolution equations have the form

$$\begin{aligned} \frac{d^2}{d\tau^2}(q_0 + \lambda q_1) + \omega'^2 q_0 = 0 \quad n = 0, \\ \frac{d^2}{d\tau^2}(\lambda q_{n-1} + q_n + \lambda q_{n+1}) + q_n = 0 \quad n > 0. \end{aligned} \tag{26}$$

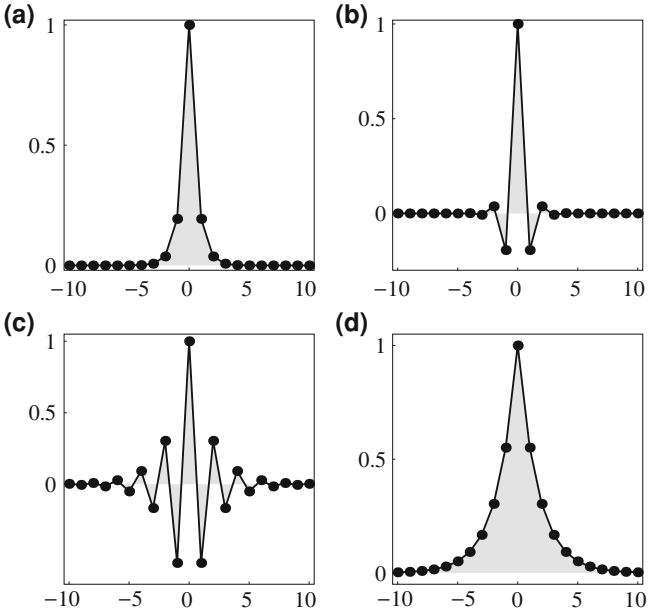

Fig. 5 Nonlinear bulk impurity. Examples of localized mode spatial profile for nonlinearity $\chi = 1$ for $\lambda = 0.2$ and $\lambda = -0.2$ (*curves* **a** and **b**), and $\chi = -1$ for $\lambda = 0.2$ and $\lambda = -0.2$ (*curves* **c** and **d**)

Linear and nonlinear (Kerr) defects can also be treated by means of the Green function technique, and the use of the image method [31, 32]. for simplicity we use here the same procedure as in Sect. 2, we pose a mode of the form $q(\tau) = \xi^n \cos(\Omega\tau + \phi)$, with $|\xi| < 1$, and $n = 0, 1, 2, \ldots$. After replacing this *ansatz* in Eq. (26), we obtain,

$$\xi = -\frac{1}{2\lambda} + sign(\lambda)\sqrt{\frac{1}{4\lambda^2} - \frac{\omega'^2}{\omega'^2 - 1}}, \tag{27}$$

and

$$\Omega^2 = \frac{1}{1 + \lambda(\xi + (1/\xi))}. \tag{28}$$

Examination of Eq. (27) under the constraints $\xi \in R$ and $|\xi| < 1$, implies the condition $|\lambda| < 1/2$, along with $(\lambda - 1)/(2\lambda - 1) < \omega'^2 < (\lambda + 1)/(2\lambda + 1)$. Figure 6 shows examples of the localized mode amplitude and the frequency of localized surface modes as a function of the impurity capacitive mismatch, as well as some representative mode profiles.

The major difference with the linear bulk case, is the presence of a window of 'forbidden' resonant frequency values, below and above the background resonant

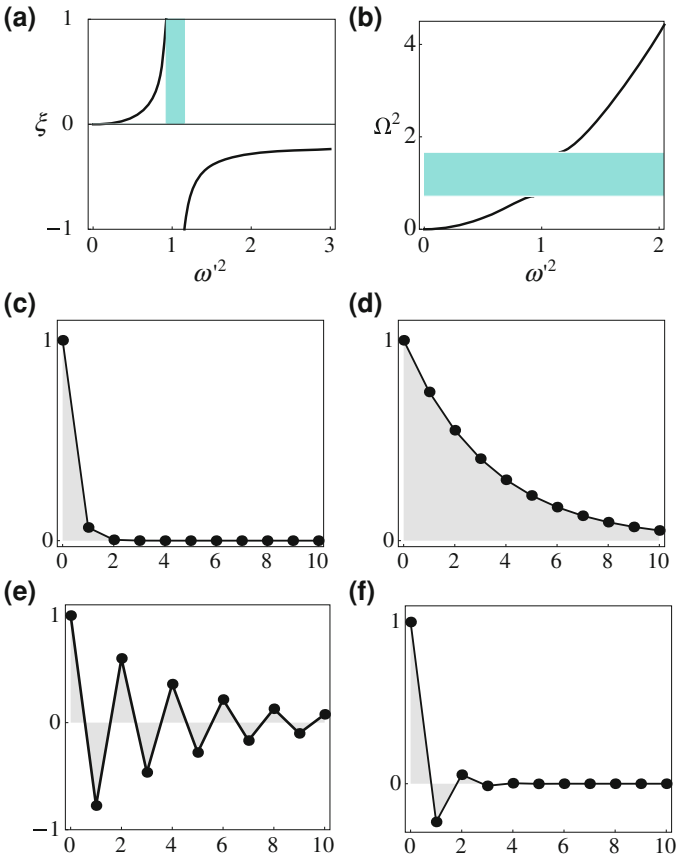

Fig. 6 Linear surface impurity. **a** Localized mode amplitude versus defect frequency; **b** frequency of localized mode versus defect frequency; **c–f** spatial profiles of impurity mode for (**c**) $\omega'^2 = 0.5$, (**d**) $\omega'^2 = 0.9$, (**e**) $\omega'^2 = 1.2$, and (**f**) $\omega'^2 = 3$. In all cases, $\lambda = 0.2$

frequency, where a localized surface mode cannot be sustained. Modes below the (allowed) band are unstaggered, while those above it are staggered.

Nonlinear case. Now, the evolution equations have the form

$$\begin{aligned} \frac{d^2}{d\tau^2}(q_0 + \lambda q_1) + q_0 - \chi q_0^3 = 0 \quad n = 0, \\ \frac{d^2}{d\tau^2}(\lambda q_{n-1} + q_n + \lambda q_{n+1}) + q_n = 0 \quad n > 0. \end{aligned} \tag{29}$$

We look for stationary modes of the form $q_n(\tau) = q_n \cos(\Omega\tau + \phi)$, and use the rotating-wave approximation (RWA) $\cos(x)^3 \approx (3/4)\cos(x)$. Equation (29) becomes

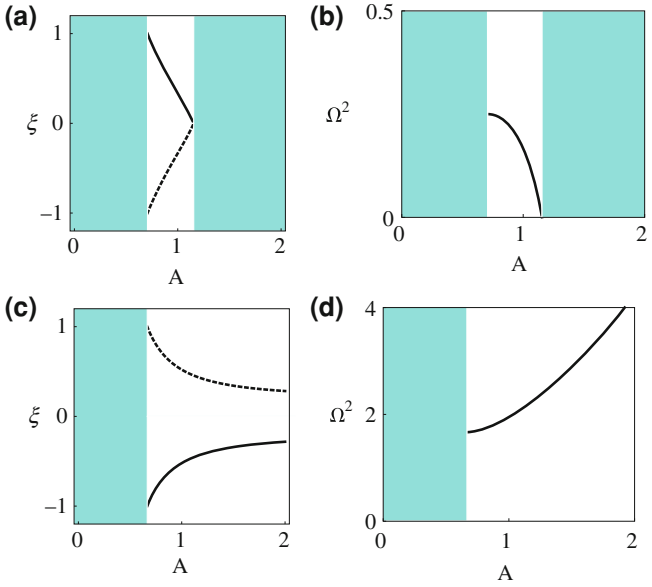

Fig. 7 Nonlinear surface impurity. *Top* (*bottom*) *rows* correspond to $\chi = 1(-1)$. In **a** and **c** we show the decay rate ξ as a function of maximum amplitude A. *Solid* (*dashed*) *curves* refer to λ positive (negative), with $\lambda = 1.5$ (**a**) and $\lambda = 0.2$ (**c**). In **b** and **d** we show the frequency of the localized mode as a function of maximum mode amplitude for $\lambda = \pm 1.5$ (**b**) and $\lambda = 0.2$ (**d**)

$$\begin{aligned} -\Omega^2(q_0 + \lambda q_1) + q_0 - (3/4)\chi q_0^3 = 0 \quad n = 0, \\ -\Omega^2(\lambda q_{n-1} + q_n + \lambda q_{n+1}) + q_n = 0 \quad n > 0. \end{aligned} \tag{30}$$

Next, we pose a mode of the form $q_n = A\xi^n$, with $|\xi| < 1$, and $n = 0, 1, 2, \ldots$. After replacing this *ansatz* in Eq. (29), we obtain,

$$\xi = -\frac{1}{2\lambda} + sign(\lambda)\sqrt{\frac{1}{4\lambda^2} - 1 + \frac{(4/3)}{\chi A^2}}, \tag{31}$$

and

$$\Omega^2 = \frac{1 - (3/4)\chi A^2}{1 + \lambda\xi}. \tag{32}$$

Since the system obeys the symmetry, $\lambda \to -\lambda \Longleftrightarrow \xi \to -\xi$, it is enough to consider $\lambda > 0$, and deal with the two possible signs of χ. In order to have $\Omega^2 > 0$ and $|\xi|^2 < 1$, one must impose the constraint $A_1 < A < A_2$, for $\chi > 0$. For $\chi < 0$, one needs $A > A_3$ and, in addition, $|\lambda| < 1/2$, where

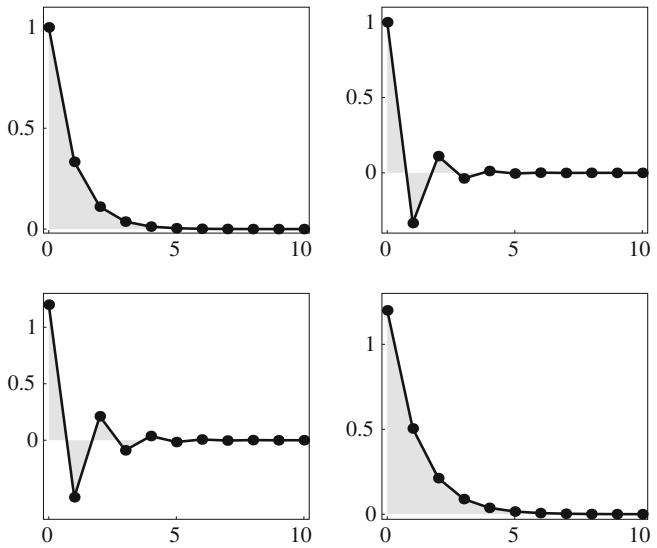

Fig. 8 Nonlinear surface impurity. Examples of localized mode spatial profile for nonlinearity $\chi = 1$ for $A = 1$ and $\lambda = 1.5$ and $\lambda = -1.5$ (*curves* **a** and **b**), and $\chi = -1$ and $A = 1.2$ for $\lambda = 0.2$ and $\lambda = -0.2$ (*curves* **c** and **d**)

$$A_1 \equiv \left(\frac{\lambda}{1+2\lambda}\frac{1}{(3/4)\chi}\right)^{1/2}, \tag{33}$$

$$A_2 \equiv \frac{1}{(3/4)\chi}, \tag{34}$$

$$A_3 \equiv \left(\frac{\lambda}{1-2\lambda}\frac{(4/3)}{|\chi|}\right)^{1/2}. \tag{35}$$

Finally, in Fig. 8 we show some examples of nonlinear localized surface modes for different values of maximum amplitude and inductive coupling. (Fig. 7)

4 Transmission Across Magnetoinductive Defects and Fano Resonances

In addition to studying the creation of localized magnetoinductive modes induced by the presence of single defects, another important issue if the study of the transport of magnetic energy across simple defects configurations. Some simple, yet interesting cases, consists on coupling the SRR array to an external defect(s) consisting of a ring(s) placed outside the SRR array. This affects the value of the

coupling between the SRR and the external ring(s) only. This external type (inductive) of defect gives rise to a more interesting scattering behavior than a single embedded (capacitive) defect, unless we allow for interactions beyond next-nearest neighbors, as we will see below. Perhaps one of the most interesting scattering effects are Fano resonances (FR). In the FR phenomenon, the eigen-frequency of a state belonging to the open channel (band of extended states) resonates with a closed channel state.

4.1 Single Capacitance Impurity

The first case we study is a single capacitance impurity embedded in the array (Fig. 2), which without loss of generality we place at $n = 0$. This impurity is created by changing the slit width of the ring at $n = 0$. The stationary equation for this case is

$$-\Omega^2\left(q_n + \sum_{m\neq n}\lambda_{nm}q_m\right) + (1 + \delta_{n,0}\Delta)q_n = 0, \tag{36}$$

where Δ is the change in the (dimensionless) resonance frequency at the defect position. When the slit width tends to zero, its capacitance diverges, making the resonant frequency approach zero. This implies $\Delta \to -1$. On the other hand, when the slit width is large, the local capacitance goes to zero, and the resonant frequency diverges, implying that $\Delta \to \infty$. Thus, $-1 < \Delta < \infty$.

Usually, embedded defects coupled locally do not lead to Fano Resonance phenomena (perfect plane-wave reflection). In the SRR array however, the couplings are dipolar and therefore, long-range, and non-local effects have to be considered. For computational simplicity we will work with couplings to first-and second nearest neighbors only. The idea is that interference between the path through nearest neighbors and the one through next-nearest neighbors will give rise to Fano resonance. Equation (36) becomes:

$$-\Omega^2[q_n + \lambda(q_{n+1} + q_{n-1}) + \lambda'(q_{n+2} + q_{n-2})] + (1 + \Delta_{n0})q_n = 0. \tag{37}$$

where λ' is the coupling among next-nearest neighbors. We pose a plane wave solution of the form

$$q_n = \begin{cases} I\,e^{ikn} + R\,e^{-ikn} & n < -1, \\ T\,e^{ikn} & n > 1. \end{cases} \tag{38}$$

After replacing this *ansatz* into (37), one obtains after a little algebra:

$$\Omega^2 = \frac{1}{1 + 2\lambda\cos(k) + 2\lambda'\cos(2k)} \tag{39}$$

and

$$t \equiv |T/I|^2 = \left|\frac{A + \Delta B}{A + \Delta C}\right|^2, \tag{40}$$

where

$$\begin{aligned} A = & -2i\sin(k)[2\lambda'^3\cos(3k) + 6\lambda\lambda'(\lambda\cos(k) + \lambda'\cos(2k)) \\ & + \lambda(\lambda^2 + 3\lambda'^2)], \\ B = & -2i\sin(k)[2\lambda\lambda'(\lambda\cos(k) + \lambda'\cos(2k)) + \lambda\lambda'], \\ C = & [(1 + 2\lambda\cos(k) + 2\lambda'\cos(2k))(\lambda^2 + 2\lambda\lambda' e^{-ik} \\ & - \lambda'^2 + 2\lambda'^3\cos(2k))]. \end{aligned} \tag{41}$$

Now, for the SRR case where dipolar interactions fall with the inverse cube of the distance between SRR units, we have $\lambda' = (1/8)\lambda$. After inserting this into Eqs. (39) and (40) and after imposing $\Omega^2 > 0$, we conclude that $-(4/9) < \lambda < (4/7)$ is the relevant coupling regime for this SRR configuration. Inside this regime it is possible to have a relatively weak Fano resonance, as shown in Fig. 9a. As expected, when coupling to second nearest neighbors is neglected ($\lambda' = 0$), there is no FR at all, since in that case the transmission becomes

$$t = \frac{(2\lambda\sin(k))^2}{(2\lambda\sin(k))^2 + \Delta^2(1 + 2\lambda\cos(k))^2}, \tag{42}$$

which can only be zero at $k = 0, \pi$. For more general λ, λ' values, it is possible to have zero, one, and even two different strong Fano resonances, as shown in Fig. 9b–d, respectively.

4.2 Single Inductive Impurity

Another simple case is a single inductive impurity embedded in the array. This is achieved by placing a SRR unit at different distances from the left and right portions of the array, leading to asymmetrical couplings λ_L and λ_R. Only couplings between nearest-neighbors are assumed. This case was already considered in Ref. [15]. In this case, it can be proven (not shown) that there is no FR for any choice of λ_L, λ_R; the transmission versus wavevector curve shows a single maximum at $k = \pi/2$. For the special symmetric case $\lambda_L = \lambda_R$, there is a single transmission resonance ($t = 1$) at $k = \pi/2$.

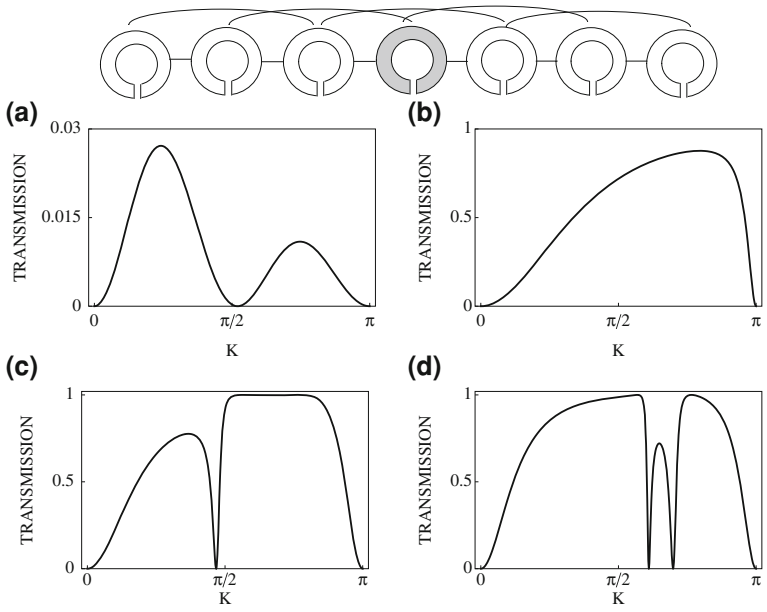

Fig. 9 *Top* Capacitive defect embedded in SSR array, with couplings to first-and second nearest neighbors. *Bottom* **a–d** show transmission coefficient versus wavevector, for several parameter values: $\lambda = -0.1, \lambda' = (1/8)\lambda, \Delta = 0.7$ (**a**), $\lambda = 0.4, \lambda' = 0.21, \Delta = -0.5$ (**b**), $\lambda = 0.4$, $\lambda' = 0.21, \Delta = 0.5$ (**c**), $\lambda = 0.4, \lambda' = 0.21, \Delta = 1.0$ (**d**)

We move now to simple cases where the defect(s) lie(s) outside the SRR array, and thus, their coupling can be tuned by changing their distance to the array.

4.3 Single External Inductive Defect: First Case

The first case of this type is that of a single external inductive defect coupled to the SRR at $n = 0$ *via* coupling to first and second nearest neighbors via coupling parameters λ_1 and λ_2, respectively (Fig. 10). From the geometry of the configuration, it is easy to obtain the relationship

$$\frac{\lambda_2}{\lambda} = \left[1 + \left(\frac{\lambda}{\lambda_1}\right)^{2/3}\right]^{-3/2}. \tag{43}$$

For simplicity, we assume only nearest neighbor coupling among the SRR units. For this approximation to be consistent, one must impose $\lambda_1 > (1/8)\lambda$ and also $\lambda_2 > (1/8)\lambda$. From Eq. (43), this implies $\lambda_1/\lambda > \text{Max}\{(1/8), 3^{-3/2}\} = 3^{-3/2} = 0.192$.

The stationary equations for this case are

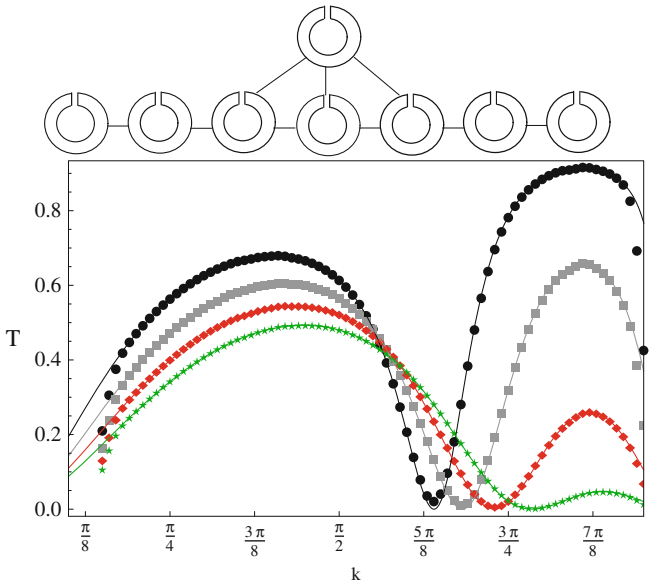

Fig. 10 *Top* SRR array with external inductive defect. *Bottom* Transmission coefficient versus wavevector, for different values of the relative coupling defect: $\lambda_1/\lambda = 1.25$ (*circles*), 1.5 (*squares*), 1.75 (*rhombi*) and 2.0 (*stars*)

$$\begin{aligned} &-\Omega^2[\lambda(q_{n+1}+q_{n-1})+q_n \\ &+q_e(\lambda_1\delta_{n,0}+\lambda_2\delta_{n,\pm1})]+q_n=0 \\ &-\Omega^2(\lambda_1 q_0+\lambda_2 q_{\pm1}+q_e)+q_e=0, \end{aligned} \tag{44}$$

where q_e is the charge residing on the external defect ring. We assume a plane wave solution of the form

$$q_n=\begin{cases} I\,e^{ikn}+R\,e^{-ikn} & n\le 0, \\ T\,e^{ikn} & n\ge 1. \end{cases} \tag{45}$$

The transmission coefficient $t\equiv|T/I|^2$ for this configuration is

$$\left|\frac{4\left(\left(\frac{\lambda_1}{\lambda}\right)\left(\frac{\lambda_2}{\lambda}\right)+\left(1+\left(\frac{\lambda_2}{\lambda}\right)^2\right)\cos(k)\right)\sin(k))}{\left(\frac{\lambda_1}{\lambda}\right)^2+4e^{ik}\left(\frac{\lambda_1}{\lambda}\right)\left(\frac{\lambda_2}{\lambda}\right)+(1+e^{2ik})\left(\frac{\lambda_2}{\lambda}\right)^2+2i\sin(2k)}\right|^2, \tag{46}$$

where, λ_2 is given by Eq. (43) for the SRR system. The most interesting feature of this transmission coefficient is the presence of a Fano resonance, whose position varies with the value of λ_1/λ. The FR occurs when $\lambda_1\lambda_2+(\lambda^2+\lambda_2^2)\cos(k)=0$, which is possible from Eq. (43), for all $0<|\lambda_1/\lambda|<2.449$. Therefore, the relevant interval where FR exists in our model is given by $0.192<\lambda_1/\lambda<2.449$. This can be achieved by simply changing the distance between the SRR array and the

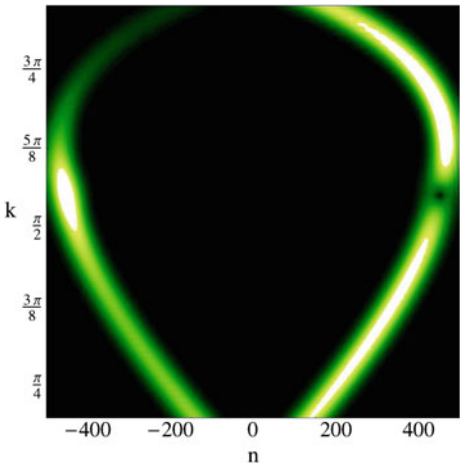

Fig. 11 SRR array with external inductive defect: output profile after $t = 1500$ as a function of wavevector and ring site, for $\lambda_1/\lambda = 1$. Impurity site is located at $n = 0$

external defect. Note from Eq. (46) that, if we neglect the effect of λ_2, the position of the FR remains locked at $k = \pi/2$.

To get a better feeling as to what would be expected to see in an actual experiment for this system, we perform a numerical simulation of a wide pulse impinging on the inductive impurity region. We used an array of 10^3 rings and resort to a symplectic algorithm to trace the time evolution of an initial broad gaussian pulse $u_n(0) = A\exp(-\alpha(n-n_0)^2)\exp(ik(n-n_0))$, where $n_0 = -300$, $A = 0.1$ and $\alpha = 0.001$ which means a width of about 120 sites, in order to simulate a plane wave with a well-defined k. The rings coupled to the inductive defect are placed at $n = 0, \pm 1$. Figure 10 shows numerical simulation results for the transmission coefficient versus wavevector for several λ'/λ values, with $\lambda = 0.4$. The agreement between analytics (Eq. (46)) and numerics is excellent, and the Fano resonances are clearly shown. The numerical discrepancies at wavevectors close to $k = 0, \pi$ are due to the long integration times needed since the pulse is quite slow at these k values. In Fig. 11 we show the output profile of the gaussian pulse for different k-values, after an integration time $t = 1500$. The transmission increases monotonically up to $k \approx 0.389\pi(0.868\pi)$ from the left (right), then decreases steadily until it vanishes completely at $k \approx 0.601\pi$.

4.4 Single External Inductive Defect: Second Case

The next case we consider is a variation of the previous case, where the external defect is now located halfway between two SRR units (Fig. 12). Without loss of generality, we take the external defect coupled symmetrically to the units at $n = 0$ and $n = 1$, with coupling λ'. As before, the units in the array interact through nearest-neighbor couplings λ only. In order for this approximation to be consistent,

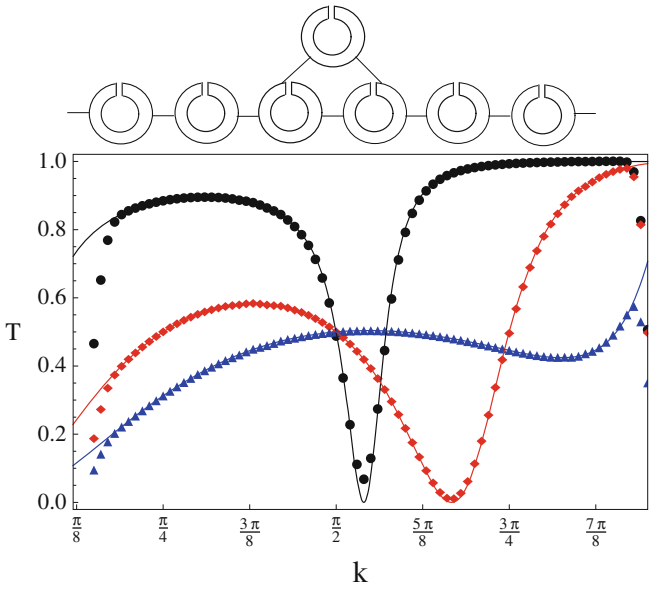

Fig. 12 *Top* External defect coupled symmetrically to the SSR array. Only couplings to first nearest neighbors are considered. *Bottom* Transmission versus wavevector for several λ'/λ values: 0.5 (*circles*), 1.0 (*rhombi*) and 1.5 (*triangles*)

and taken into account the dipolar nature of the inductive couplings, we need $|\lambda'| > (1/8)\lambda$.

The stationary equations read

$$\begin{aligned} -\Omega^2(\lambda(q_{n+1}+q_{n-1})+q_n+\lambda' q_e(\delta_{n,0}+\delta_{n,1}))+q_n=0 \\ -\Omega^2(\lambda'(q_0+q_1))+q_e=0, \end{aligned} \tag{47}$$

where q_e is the charge on the external defect ring. We pose a plane wave solution of the type

$$q_n = \begin{cases} I\,e^{ikn}+R\,e^{-ikn} & n\leq -1 \\ T\,e^{ikn} & n\geq 2 \end{cases} \tag{48}$$

leading to a transmission coefficient:

$$t \equiv \left|\frac{T}{I}\right|^2 = \left|\frac{(e^{ik}-1)(\lambda'^2+2\lambda^2\cos(k))}{2(\lambda'^2+\lambda^2\cos(k)(1-e^{ik}))}\right|^2. \tag{49}$$

Fano resonances are possible when $\lambda'^2+2\lambda^2\cos(k)=0$. This implies, $k_F=-(1/2)(\lambda'/\lambda)^2$, which is possible only if $|\lambda'/\lambda|<\sqrt{2}$. This constraint plus the consistency condition, give us the relevant coupling parameter window for this SRR configuration:

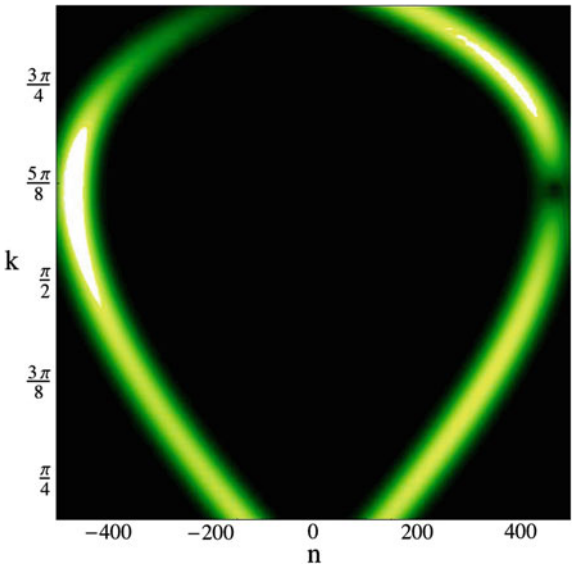

Fig. 13 Fano resonance: external defect coupled symmetrically to two array units: output profile after $t = 1500$ as a function of wavevector and ring site, for $\lambda_1/\lambda = 1$

$$(1/8) < \left|\frac{\lambda'}{\lambda}\right| < \sqrt{2}. \tag{50}$$

Figure 12 shows some transmission curves for parameter values inside and outside this window. The position and width of the Fano resonance depend on the ratio $|\lambda'/\lambda|$, which can be externally tuned by changing the distance between the defect and the array.

Figure 13 shows output intensity profile after propagation of $t = 1500$ as a function of wavevector and site position.

4.5 Two External Inductive Defects

The final array we consider consists of two external defects, each coupled to a single unit of a SRR array. The units of the array are coupled to first neighbors only via coupling λ. Between both defects, there are L units (Fig. 14). Without loss of generality we assume the defects to be coupled to units at $n = 0$ and $n = L$, with couplings λ_0 and λ_L, respectively. The stationary equations read

$$\begin{aligned} &-\Omega^2[\lambda(q_{n+1}+q_{n-1})+q_n+\lambda_0 Q_0\delta_{n,0} \\ &\qquad +\lambda_L Q_L\delta_{n,L}]+q_n=0 \\ &-\Omega^2(\lambda_0 q_0+Q_0)+Q_0=0 \\ &-\Omega^2(\lambda_L q_L+Q_L)+Q_L=0, \end{aligned} \tag{51}$$

where Q_0 and Q_L are the charges residing at the external rings coupled to units $n=0$ and $n=L$ of the array. As before, we pose a plane wave solution

$$q_n=\begin{cases} I\,e^{ikn}+R\,e^{-ikn} & n\leq 0, \\ T\,e^{ikn} & n\geq L. \end{cases} \tag{52}$$

The transmission coefficient is given in this case by

$$\left|\frac{\lambda^4(e^{4ik}-1)}{e^{4ik}[\lambda_0^2+2i\lambda^2\sin(2k)][\lambda_L^2+2i\lambda^2\sin(2k)]-\lambda_0^2\lambda_L^2 e^{2ik(L+2)}}\right|^2, \tag{53}$$

which is symmetric under the exchange between the external rings, depending only on $|\lambda_0/\lambda|$, $|\lambda_L/\lambda|$ and L. We see from Eq. (53) that, regardless of the separation L between the external defects, there is only a single Fano resonance located at $k=\pi/2$. Figure 14 shows examples of transmission versus wavevector plots for different defects separation. However, it should be noted that, in a more realistic setting that considers the presence of dissipation effects, one would expect to observe some broadening of the resonances, as well as a decrease in their heights, as the separation between defects increases. For SRRs coupled to nearest-neighbors only, this effect is more pronounced at the band edges, and minimized at mid-band [15]. For couplings beyond nearest-neighbors, the situation is more complex.[1]

Let's make a little digression here. In the case $\lambda_0=\lambda_L\equiv\lambda'$, we have two symmetrically-coupled external defects, and one natural question to ask in this case is whether we can have an asymmetrical localized mode, in addition to the usual symmetrical and antisymmetrical ones. The answer is no, at least in the absence of nonlinear effects, and will be exemplified with the case $L=1$.

The stationary equations are

$$\begin{aligned} &-\Omega^2[\lambda(q_{n+1}+q_{n-1})+q_n+\lambda' Q_0\delta_{n,0} \\ &\qquad +\lambda' Q_1\delta_{n,1}]+q_n=0 \\ &-\Omega^2(\lambda' q_0+Q_0)+Q_0=0 \\ &-\Omega^2(\lambda' q_1+Q_1)+Q_1=0. \end{aligned} \tag{54}$$

[1] In the presence of dissipation, a term of the form $i\gamma\Omega$ enters Eq. (3). For a complex wavevector $k=k_r-ik_i$, with $|k_i|\ll|k_r|$, one obtains $\Omega^2\approx(1+\sum_{nm}\lambda_{nm}\cos(mk_r))^{-1}$ and $k_i\approx\gamma(1+\sum_{nm}\lambda_{nm}\cos(mk_r))^{1/2}/\sum_m\lambda_{nm}\sin(mk_r)$. Neglect of dissipation effects is valid provided $|k_i|L\ll 1$.

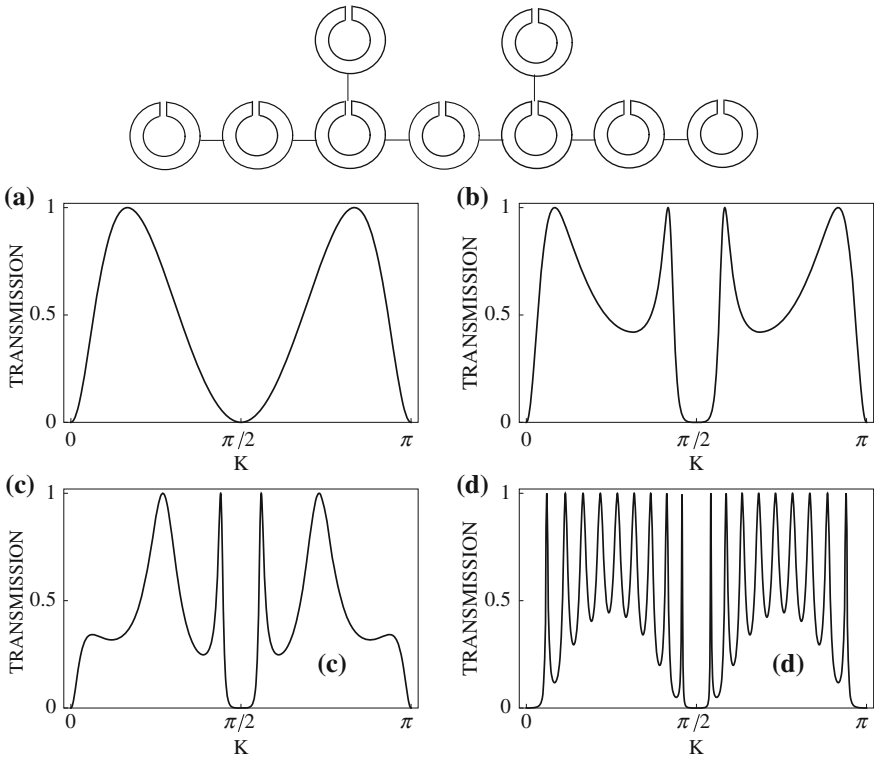

Fig. 14 Two external defects separated by L units and coupled to the SSR array. Transmission versus wavevector for several separations L: $L = 2$ (**a**), $L = 3$ (**b**), $L = 5$ (**c**) and $L = 20$ (**d**) (in all cases $\lambda = \lambda_1 = \lambda_2 = 0.4$)

From these two last equations, one obtains

$$Q_0 = \left(\frac{\lambda' \Omega^2}{1 - \Omega^2}\right) q_0 \quad Q_1 = \left(\frac{\lambda' \Omega^2}{1 - \Omega^2}\right) q_1. \tag{55}$$

We pose a localized mode of the form

$$q_n = \begin{cases} A\xi^{|n|} & n \leq 0, \\ B\chi^{n-1} & n \geq 1. \end{cases} \tag{56}$$

From Eq. (54) evaluated at $n \neq 0, 1$ one obtains

$$\Omega^2 = \left\{1 + \lambda\left(\xi + \frac{1}{\xi}\right)\right\}, \tag{57}$$

and $\xi = \chi$.

The evaluation at $n = 0$ and $n = 1$ leads to

$$(-\Omega^2(1 + \lambda\xi + \lambda'^2(\Omega^2/(1 - \Omega^2)) + 1)A - \lambda\Omega^2 B = 0, \tag{58}$$

and

$$-\lambda\Omega^2 A + (-\Omega^2(1 + \lambda\xi + (\lambda'^2\Omega^2/(1 - \Omega^2))) + 1)B = 0. \tag{59}$$

Existence of a nontrivial solution demands

$$(-\Omega^2(1 + \lambda\xi + \lambda'^2(\Omega^2/(1 - \Omega^2)) + 1)) = \pm\lambda\Omega^2. \tag{60}$$

But, from Eq. (58) one has

$$\frac{B}{A} = \frac{(-\Omega^2(1 + \lambda\xi + \lambda'^2(\Omega^2/(1 - \Omega^2)) + 1))}{\lambda\Omega^2} = \pm 1. \tag{61}$$

Therefore, the possible localized modes are symmetric or antisymmetric only. This is probably due to the purely linear character of the defects. Nonlinear effects like a nonlinear capacitance, or nonlinear inductive coupling at each of the two external defects could bring about the possibility of a stable, asymmetric state that bifurcates from the symmetrical one, similar to what happens in the nonlinear dimer [33].

To summarize this section: the possibility of achieving some degree of control over the propagation of a wave across an impurity region has always been a topic of interest. Resonance phenomena, and Fano resonances (FR) in particular, have attracted great attention. We have shown that, by judiciously placing one or few magnetic impurities, either embedded or external to the SRR array, it is possible to achieve complete reflection (FR) of a given magnetoinductive wave, inside a frequency window. Sometimes, more than one FR is possible.

5 Surface Bound States in the Continuum in SRR Arrays

A long time has elapsed since the original work of Von Neumann and Wigner [34], where they claimed that the single-particle Schrödinger equation could possess localized eigenstate solutions, whose eigenvalues lie inside the band of extended states. Their claim was based on a building recipe to generate a normalizable localized state by means of a judicious modulation of a plane wave solution, generated by a carefully chosen local potential. One problem that is common in this type of construction is that both, the potential and the wavefunction of the embedded mode decrease as power law, rendering the wavefunction un-normalizable. Since then, a number of works have been dedicated to the subject of embedded modes from both, the theoretical and experimental angles [35–44], in condensed matter, atomic physics, and optics contexts. A recent experiment proving the existence of an embedded mode in an optical waveguide array was carried out by Plotnik et al. [44].

In their work they decoupled an optical mode from the band by using a symmetrical configuration.

In a very recent work [13], we have extended Wigner's original proposal to a semi-infinite discrete system in the form of an weakly-nonlinear (Kerr) optical waveguide array, governed by the discrete nonlinear Schrödinger equation, and showed how to build a structurally stable embedded surface mode, and its associated discrete local potential (i.e., a distribution of refractive indices). Moreover, it was shown that the position of the imbedded eigenvalue inside the band could be tuned by increasing or decreasing the nonlinearity of the system. Our method can in principle be applied to any discrete periodic system of interest, where waves can propagate. In particular, it can be applied to a periodic SRR array, where magnetoinductive waves propagate. Instead of a distribution of refractive indices, we have a distribution of resonant frequencies, whose values depend on a number of factors, such as the nature of the dielectric inside the ring slits, the radius of the ring, or the slit width of the SRRs. To keep things simple, we will assume that the resonant frequency of the rings can be tuned by changing the slit widths. We look for stationary solutions of the form $q_n(\tau) = q_n \cos(\Omega\tau + \phi)$, which leads to the system

$$\begin{aligned} -\Omega^2\{\lambda q_1 + q_0\} + \omega_0^2 q_0 &= 0 \\ -\Omega^2\{\lambda(q_{n+1} + q_{n-1}) + q_n\} + \omega_n^2 q_n &= 0. \end{aligned} \tag{62}$$

One can formally solve for ω_n^2 as

$$\begin{aligned} \omega_0^2 &= \Omega^2\left[1 + \lambda\left(\frac{q_1}{q_0}\right)\right] \\ \omega_n^2 &= \Omega^2\left[1 + \lambda\left(\frac{q_{n+1}}{q_n} + \frac{q_{n-1}}{q_n}\right)\right]. \end{aligned} \tag{63}$$

In the absence of any modulation, $\omega_n^2 = \text{constant} \equiv 1$, and $q_n = \sin(nk)$, with $\Omega^2 = 1/(1 + 2\lambda\cos(k))$.

For a weak modulation, let us pose a solution of the form

$$q_n = \sin(kn) f_n, \tag{64}$$

where f_n is a modulating envelope function that must obey $f_n \to 0$ when $n \to \infty$, in order to have a *bona fide* localized surface mode. After inserting this *ansatz* into Eq. (63), we obtain

$$\omega_n^2 = \begin{cases} \Omega^2(1 + 2\lambda\cos(k)(f_1/f_0)), & n = 0 \\ \Omega^2\{1 + \lambda[(f_{n+1}/f_n)(\cos(k) + \sin(k)\cot(kn)) \\ +(f_{n-1}/f_n)(\cos(k) - \sin(k)\cot(kn))], & n \geq 1. \end{cases} \tag{65}$$

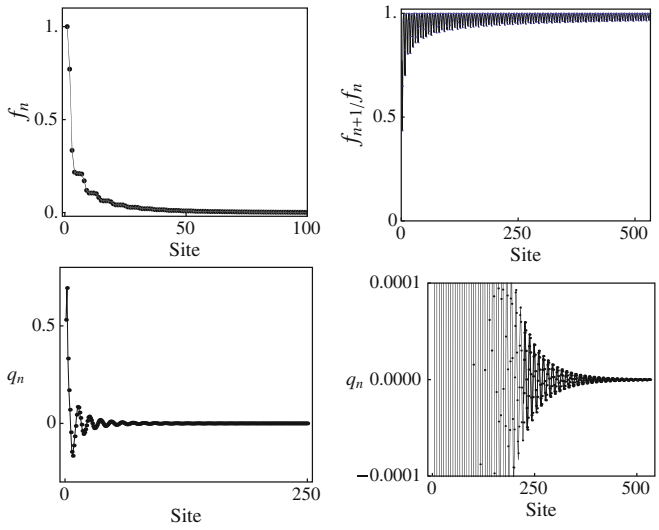

Fig. 15 Example of embedded surface mode, Eqs. (64)–(70), for $k = 0.56$. *Top left* Modulated envelope, *top right* ratio of nearby envelope values, *bottom left* spatial profile of embedded mode, *bottom right* zoom of embedded mode near the axis

As $n \to \infty$, $\omega_n^2 \to \Omega^2[1 + 2\lambda\cos(k)] = 1$, provided $\lim_{n\to\infty}(f_{n+1}/f_n) = 1$.

Let us take

$$\frac{f_{n+1}}{f_n} = (1 - \delta_n), \tag{66}$$

where $\delta_n < 1$. From this, we can solve formally for f_n:

$$f_n = \prod_{m=1}^{n-1}(1 - \delta_m), \tag{67}$$

which can be rewritten as

$$f_n = \exp\left\{\sum_{m=1}^{n-1}\log(1 - \delta_m)\right\}. \tag{68}$$

In the limit $n \to \infty$, and using that $\delta_m < 1$, we can approximate this by

$$f_\infty \approx \exp\left\{-\sum_{m=1}^{\infty}\delta_m\right\}. \tag{69}$$

since we want $f_\infty \to 0$, we need $\sum_{m=1}^{\infty}\delta_m = \infty$. A good trial function for δ_n that satisfies the above requirements is

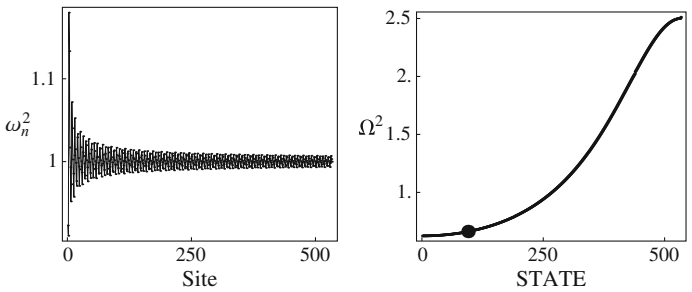

Fig. 16 Example of embedded surface mode, Eqs. (64)–(70) for $k = 0.56$. *Left* Site energy distribution (65) that gives rise to embedded mode. *Right* Linear band for a $N = 533$ sites. The *dark solid circle* shows the position of the embedded mode inside the band

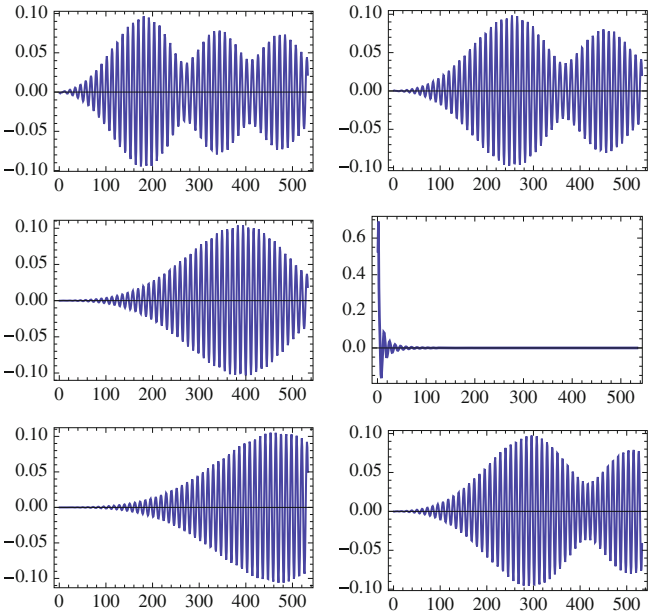

Fig. 17 Eigenstates in the immediate neighborhood of the embedded state (*middle right*) ($N = 533, \lambda = 0.3$)

$$\delta_n = \frac{1}{\sqrt{n}} \sin^2(nk) \sin^2((n+1)k). \tag{70}$$

The presence of the sine terms is not accidental; we need them to counteract the presence of the two $\cot(nk)$ terms in (65) that may otherwise lead to possible divergences. In this way, we get a smoother site energy distribution.

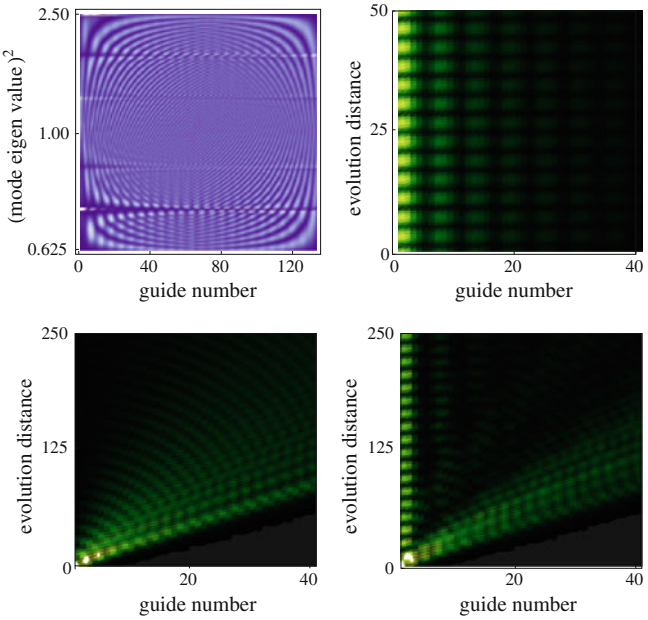

Fig. 18 *Top left* Intensity distribution of all eigenmodes of the SRR array. The localized SRR embedded mode can be seen at the lower left sector. *Top right* Dynamical evolution of SRR embedded mode. Only a portion of the SRR array is shown. *Bottom left* Intensity profile of an initially localized excitation, in a completely periodic array, after a given evolution distance. *Bottom Right* Intensity profile of an initially localized excitation, in the modulated array, after a given evolution distance. ($N = 133, \lambda = 0.3$)

Figure 15 shows results for the modulating envelope f_n, ratio f_{n+1}/f_n, and the spatial profile q_n, obtained from trial function based on Eq. (70). As we can see, the proposed embedded mode does converge to zero at large n values. Using the Euler–Maclaurin expansion, one can estimate the decay of the envelope function away from the surface as $f_n \sim \exp(-|\int_0^\infty \log(1-\delta(x))|)$, where $\delta(x)$ is the continuous version of δ_n. For the choice (70), one obtains $f_n \sim \exp(-a(k)\sqrt{n})$, with $a(k) = (1/4)(2+\cos(2k))$.

In Fig. 16 we show the local 'site energy potential' ω_n^2 that gives rise to our embedded mode. It corresponds to a distribution of resonant frequencies in the SRR array, obtained by, for instance, a distribution of slit widths of the SRRs. After we find the ω_n^2 distribution, we compute next all the eigenvalues and eigenvector of the system, to ascertain that they are all extended, with the exception of our embedded mode. With the definitions $\epsilon_n \equiv 1/\omega_n^2$, $\lambda_n \equiv \lambda/\omega_n^2$, and $\beta \equiv 1/\Omega^2$, the eigenvalue equation can be written in the standard form

$$\epsilon_n q_n + \lambda_n (q_{n+1} + q_{n-1}) = \beta q_n. \tag{71}$$

The corresponding matrix is a real tridiagonal matrix A that satisfies $A_{k,k+1}A_{k+1,k} \geq 0$. Thus, it is similar to a Hermitian matrix and, therefore all of its eigenvalues are real [45]. The band obtained is shown in Fig. 16, with the position of the embedded mode eigenvalue clearly marked. In Fig. 17 we show the eigenstates of the SRR array in the immediate neighborhood of the embedded state. They are all clearly extended. A bird's eye view of all eigenstates is shown in Fig. 18a. It is apparent that all of them are extended, save for the embedded mode (lower left sector) that stands alone as a localized mode.

Next, we examine the dynamical evolution of the embedded mode. For that purpose, we integrate Eq. (6) for a long evolution distance using a symplectic integrator, assuming no currents initially ($(dq_n/dt)_{t=0} = 0$). The result is shown in Fig. 18b, for a portion of the SRR array for ease in visualization. As expected, the mode is stable and oscillates in time with frequency $\Omega^2 = 0.663$.

Finally, we consider the issue of the dynamical excitation of the embedded mode. Since this mode is highly localized at the edge, the simplest thing is to place a highly-localized portion of magnetic energy at the edge (via an antenna). Numerical results of this procedure are shown on the bottom part of Fig. 18. In the absence of the ω_n^2 modulation, all of the energy diffracts away from the boundary; however, in the presence of the modulation, a portion of the magnetic energy does remain at the boundary.

6 Conclusions

In this work we have considered a rather simplified model of a magnetic metamaterial consisting of a weakly-coupled, periodic split-ring resonator (SRR) array capable of nonlinear capacitive response. The simplifications incurred in the model allow us to obtain closed-form results that reflect the main physical features of the model. We focused on three, different but related problems: (1) The closed-form computation of localized modes around single linear/nonlinear impurities located at the surface of the bulk of the array. (2) The scattering of magnetoinductive waves by internal (external) capacitive (inductive) defects coupled to the SRR array, and the occurrence of Fano resonance phenomena. (3) Description of an explicit method for building a localized magnetoinductive mode embedded in the linear band of extended states. The closed-form results for all of these three problems suggest that the response of this model system to various stimuli can in principle be tuned by manipulation of a few system parameters. Thus, the ability to trap magnetic energy, or to reflect a portion or the whole of an incoming magnetoinductive wave, and the capacity to create at will a localized magnetic mode living in the band, are but some examples of robust behavior of this model that can hopefully survive in a more realistic model, and thus be of technological relevance for this rapidly-evolving field.

Acknowledgments This work was supported by Fondecyt (Grant 1080374), Programa ICM P10-030-F, and Programa de Financiamiento Basal de Conicyt (Grant FB0824/2008).

References

1. D.R. smith, W.J. Padilla, D.C. Wier, S.C.N. Nasser, S. Schultz, Phys. Rev. Lett. **84**, 4184 (2000)
2. J.B Pendry, Phys. Rev. Lett. **85**, 3966 (2000)
3. S. Linden, C. Enkrich, G. Dolling, M.W. Klein, J. Zhou, T. Koschny, C.M. Soukoulis, S. Burger, F. Schmidt, M. Wegener, IEEE J. Sel. Top. Quantum Electron. **12**, 1097 (2006)
4. T.J. Yen, W.J. Padilla, N. Fang, D.C. Vier, D.R. Smith, J.B. Pendry, D.N. Basov, X. Zhang, Science **303**, 1494 (2004)
5. M. Gorkunov, M. Lapine, E. Shamonina, K.H. Ringhofer, Eur. Phys. J. B **28**, 263 (2002)
6. M.C.K. Wiltshire, E. Shamonina, I.R. Young, L. Solymar, Electron. Lett. **39**, 215 (2003)
7. R.R.A. Syms, E. Shamonina, V. Kalinin, L. Solymar, J. Appl. Phys. **97**, 64909 (2005)
8. E. Shamonina, V.A. Kalinin, K.H. Ringhofer, L. Solymar, J. Appl. Phys. **92**, 6252 (2002)
9. E. Shamonina, L. Solymar, J. Phys. D Appl. Phys. **37**, 362 (2004)
10. M.J. Freire, R. Marques, F. Medina, M.A.G. Laso, F. Martin, Appl. Phys. Lett. **85**, 4439 (2004)
11. I.V. Shadrivov, A.N. Reznik, Y.S. Kivshar, Physics B **394**, 180 (2007)
12. For a recent review see, for instance, A.E. Miroschnichenko, S. Flach, Y.S. Kivshar, Rev. Mod. Phys. **82**, 2257 (2010)
13. M.I. Molina, A.E. Miroshnichenko, Y.S. Kivshar, Phys. Rev. Lett. **108**, 070401 (2012)
14. N.N. Rosanov, N.V. Vysotina, A.N. Shatsev, I.V. Shadrivov, D.A. Powell, Y.S. Kivshar, Opt. Express **19**, 26500 (2011)
15. R.R.A. Syms, E. Shamonina, L. Solymar, IEE Proc. Microw. Antennas Propag. **153**, 111 (2006)
16. N. Lazarides, G.P. Tsironis, Y.S. Kivshar, Phys. Rev. E **77**, 065601 (2008)
17. M.I. Molina, N. Lazarides, G.P. Tsironis, Phys. Rev. E **80**, 046605 (2009)
18. E.N. Economou, *Greens Functions in Quantum Physics* (Springer, Berlin, 1979)
19. M.I. Molina, G.P. Tsironis, Phys. Rev. B (Rap. Comm.) **47**, 15330 (1993)
20. M.I. Molina, Phys. Rev. B **60**, 2276 (1999)
21. C.A. Bustamante, M.I. Molina, Phys. Rev. B **62**, 15287 (2000)
22. M.I. Molina, Phys. Rev. B **73**, 014204 (2006)
23. M.I. Molina, Phys. Rev. B **71**, 035404 (2005)
24. M.I. Molina, Phys. Rev. B **73**, 014204 (2006)
25. M.I. Molina, Phys. Rev. B **74**, 045412 (2006)
26. B.A. Malomed, M.Y. Azbel, Phys. Rev. B. **47**, 10402 (1993)
27. D. Chen, S. Aubry, G.P. Tsironis, Phys. Rev. Lett. **77**, 4776 (1996)
28. M.I. Molina, N. Lazarides, G.P. Tsironis, Phys. Rev. E **80**, 046605 (2009)
29. M.I. Molina, G.P. Tsironis, Acta Phys. Polon. A **116**, 635 (2009)
30. N. Lazarides, M.I. Molina, G.P. Tsironis, Physica B **405**, 3007 (2010)
31. M.I. Molina, Phys. Rev. B **71**, 035404 (2005)
32. M.I. Molina, Phys. Rev. B **74**, 045412 (2006)
33. J.C. Eilbeck, P.S. Lomdahl, A.C. Scott, Physics D **16**, 318 (1985)
34. von J. Neumann, E. Wigner, Phys. Z. **30**, 465 (1929)
35. F.H. Stillinger, D.R. Herrick, Phys. Rev. A **11**, 446 (1975)
36. F.H. Stillinger, T.A. Weber, Phys. Rev. A **10**, 1122 (1974)
37. F.H. Stillinger, J. Chem, Phys. **45**, 3623 (1966)
38. F.H. Stillinger, D.E. Stillinger, Phys. Rev. A **10**, 1109 (1974)

39. A.K. Jain, C.S. Shastry, Phys. Rev. A **12**, 2237 (1975)
40. F. Capasso, C. Sirtori, J. Faist, D.L. Sivco, S-N.G. Chu, A.Y. Cho, Nature **358**, 565 (1992)
41. S. Gonzlez-Prez-Sandi, J. Fujioka, B.A. Malomed, Physica D **197**, 86 (2004)
42. K. Yagasaki, A.R. Champneys, B.A. Malomed, Nonlinearity **18**, 2591 (2005)
43. B.A. Malomed, J. Fujioka, A. Espinosa-Ceron, R.F. Rodriguez, S. Gonzalez, Chaos **16**, 013112 (2006)
44. Y. Plotnik, O. Peleg, F. Dreisow, M. Heinrich, S. Nolte, A. Szameit, M. Segev, Phys. Rev. Lett. **107**, 183901 (2011)
45. R.A. Horn, C.R. Johnson, *Matrix Analysis* (Cambridge University Press, Cambridge, 1985)

Pattern Formation Under a Localized Gain

Alexander A. Nepomnyashchy

Abstract The onset of patterns due to a localized gain is studied analytically in the framework of a real or complex amplitude equation. The instability modes are found, and the bifurcation of small localized solutions is analyzed. Some exact solutions are also found.

1 Introduction

A spatial inhomogeneity can strongly influence the stability and pattern formation. Examples spread from nonlinear optics and hydrodynamics to autocatalytic reactions and biological processes. A generic model, which describes the pattern dynamics near the instability threshold in a spatially inhomogeneous extended system, is the complex Ginzburg-Landau equation with an advective term and spatially modulated linear growth rate [1]. That equation has been used for studying the pattern formation in different physical contexts [1–4] in the case where the growth rate and wave frequency are smoothly modulated with the spatial scale characteristic for the Ginzburg-Landau equation. Recall that this scale is large near the instability threshold, where that equation is valid. The investigation of the opposite case where the spatial size of the inhomogeneity is small with respect to the scale of the Ginzburg-Landau equation, was started by Lam et al. [5]. The analysis has shown a significant difference between the generic case of a nonzero diffusion coefficient and the specific case of a vanishing diffusion coefficient typical for

A. A. Nepomnyashchy (✉)
Department of Mathematics, Technion—Israel Institute of Technology, 32000 Haifa, Israel
e-mail: nepom@math.technion.ac.il

A. A. Nepomnyashchy
Minerva Center for Nonlinear Physics of Complex Systems, Technion—Israel Institute of Technology, 32000 Haifa, Israel

Progress Optical Sci., Photonics (2013): 309–320
DOI: 10.1007/10091_2012_26

Published Online: 31 January 2013

optical models. The latter case has been extensively studied by Kartashov and collaborators [6–13] and by Malomed and collaborators [14, 15].

In the present paper, we investigate the influence of localized growth rate inhomogeneities using a mathematical model similar to that suggested in [5].

In Sect. 2, we formulate the basic model which describes the action of an active spot on a system near the instability threshold. The case of a monotonic instability is considered in Sect. 3, the case of an oscillatory instability is studied in Sect. 4. Section 5 contains some concluding remarks.

2 Basic Model

The basic model used in the present paper is as follows:

$$u_t + vu_x = \gamma(x)u - \kappa|u|^2u + Du_{xx}, \tag{1}$$

where v is the group velocity of waves, $\gamma(x) = \gamma_r(x) + i\gamma_i(x)$ describes the spatially inhomogeneous growth rate and wave frequency, $\kappa = \kappa_r + i\kappa_i$ determines the nonlinear saturation of the instability and nonlinear frequency shift ($\kappa_r > 0$), and $D = d + i\alpha$ characterizes the diffusion and dispersion of waves ($d \geq 0$). By means of a scale transformation, $u \to u\kappa_r^{-1/2}$, we obtain:

$$u_t + vu_x = \gamma(x)u - (1 + i\beta)|u|^2u + Du_{xx}, \tag{2}$$

where $\beta = \kappa_i/\kappa_r$. Actually, one can scale out the real parameters v and d as well by rescaling the variables x and t. However, it is instructive to trace the influence of parameters v and d on the solutions in an explicit way, thus we retain them. Later on, we assume that the inhomogeneity of the complex growth rate $\gamma(x)$ has a spatial scale small with respect to that characteristic for the Ginzburg-Landau equation, thus assuming

$$\gamma(x) = -\lambda + \Gamma\delta(x), \tag{3}$$

where λ is a real constant (its imaginary part λ_i can be eliminated by the transformation $u \to u\exp(-i\lambda_i t)$). Below we consider also some modifications of model (2).

3 Real Amplitude Equation

3.1 Linear Stability Theory

3.1.1 Single Inhomogeneity

We will start our analysis with the simplest case of a nonlinear advection-diffusion equation with a *real* variable $u(x, t)$

$$u_t + vu_x = -\lambda u + \Gamma\delta(x)u + du_{xx} + f(u), \tag{4}$$

where $f(u)$ is a function satisfying conditions $f(0) = f'(0) = 0$, e.g., $f(u) = -u^2$ or $f(u) = -u^3$ (the latter case corresponds to a reduction of Eq. (1) in the case of a real amplitude function). The physical meaning of the variable $u(x,t)$ is a disturbance of a concentration on the background of a certain base state described by the solution $u = 0$. Without loss of generality, below we assume $v \geq 0$.

First, let us consider the evolution of infinitesimal disturbances $\tilde{u}(x)$ on the background of the base state $u = 0$. Taking $\tilde{u}(x) = U(x)\exp(\sigma t)$, we obtain the following equation governing the shape and the growth rate of the disturbance:

$$\sigma U + vU' = [-\lambda + \Gamma\delta(x)]U + dU''. \tag{5}$$

It is natural to impose the physical condition of the boundedness of the solution at the infinity,

$$\lim_{x\to\pm\infty} |U(x)| < \infty. \tag{6}$$

The eigenvalue problem (5)–(6) has two kinds of solutions. The eigenfunctions that do not decay at infinity have the form:

$$U = U_-(x) = ae^{ikx} + be^{v/d-ik}x,\ x < 0$$

$$U = U_-(x) = e^{ikx},\ x > 0,$$

where

$$b = \frac{\Gamma}{v - 2ikd},\ a = 1 - b.$$

The corresponding continuous spectrum of eigenvalues

$$\sigma(k) = -\lambda - ivk - dk^2 \tag{7}$$

is not affected by the localized inhomogeneity. However, a sufficiently strong inhomogeneity can create a *localized* eigenmode decaying at infinity, which has an eigenvalue depending on Γ. Consider solutions in the form

$$U = e^{k_- x},\ x < 0;\ U = e^{k_+ x},\ x > 0, \tag{8}$$

where $k_\pm$ satisfy the following conditions:

$$\sigma + vk_\pm = -\lambda + dk_\pm^2, \tag{9}$$

$$\Gamma + d(k_+ - k_-) = 0. \tag{10}$$

A localized mode exists if the real parts $Re(k_-) > 0, Re(k_+) < 0$. From (9), one finds that

$$k_+ - k_- = -\sqrt{v^2 + 4d(\sigma + \lambda)}\, sign\Gamma/d, \tag{11}$$

hence from (10) one concludes that

$$\sqrt{v^2 + 4d(\sigma + \lambda)} = |\Gamma|, \tag{12}$$

thus

$$\sigma = -\lambda + \frac{\Gamma^2 - v^2}{4d}, \tag{13}$$

$$k_\pm = \frac{1}{2d}(v \mp \Gamma). \tag{14}$$

Note that $k_\pm$ are real, hence a localized mode exists if $k_- > 0, k_+ < 0$. Obviously, that is possible in the case $\Gamma > v$. In a contradistinction to the continuous spectrum (7), the eigenvalue of a localized mode (13) is always real, and it is higher than the real part of any non-localized disturbances.

In the case $\lambda > 0$ (where the background is stable), the localized mode decays in time if $v < \Gamma < \sqrt{v^2 + 4\lambda d}$ and grows if $\Gamma > \sqrt{v^2 + 4\lambda d}$. In the case $\lambda < 0$ (where the background is unstable), the localized mode grows in the whole region of its existence (faster than any non-localized disturbances).

Thus, in the case of a real amplitude equation a nonzero group velocity breaks the reflection symmetry of the normal disturbance ($k_+ \neq -k_-$, see (14)) and increases the instability threshold, $\Gamma_c = \sqrt{v^2 + 4\lambda d}$.

Note that expressions (13) and (14) diverge in the limit $d \to 0$. However, for arbitrary small but nonzero d the localized solutions exist and are obtained from each other by a simple scaling transformation. Because the influence of d in the case under consideration is rather obvious, we put $d = 1$ below in this section.

3.1.2 Periodic Chain of Inhomogeneities

Let us consider now a system under the action of a periodic chain of inhomogeneities governed by the equation

$$u_t + vu_x = -\lambda u + \Gamma \sum_{n=-\infty}^{\infty} \delta(x - nl)u + u_{xx} + f(u). \tag{15}$$

The normal disturbance $\tilde{u}(x) = U(x)\exp(\sigma t)$ is governed by the equation

$$\sigma U + vU_x = -\lambda U + \Gamma \sum_{n=-\infty}^{\infty} \delta(x - nl)U + U_{xx}. \tag{16}$$

Inside each interval $nl < x < (n + 1)l$ the solution of the equation is

$$U(x) = U_n(x) = A_{+,n}e^{k_+(x-nl)} + A_{-,n}e^{k_-(x-nl)}, \tag{17}$$

where

$$k_\pm = \frac{v \mp \sqrt{v^2 + 4(\sigma + \lambda)}}{2}. \tag{18}$$

The relations on the boundaries of those intervals,

$$U_n((n+1)l) = U_{n+1}((n+1)l)$$

and

$$\Gamma U_n((n+1)l) + U'_{n+1}((n+1)l) - U'_n((n+1)l) = 0,$$

determine the linear mapping

$$(A_{+,n}, A_{-,n}) \to (A_{+,n+1}, A_{-,n+1}),$$

$$A_{+,n+1} = \frac{(S+\Gamma)e^{k_+ l}A_{+,n} + \Gamma e^{k_- l}A_{-,n}}{S},$$

$$A_{-,n+1} = \frac{-\Gamma e^{k_+ l}A_{+,n} + (S-\Gamma)e^{k_- l}A_{-,n}}{S},$$

where

$$S = \sqrt{v^2 + 4(\sigma + \lambda)}.$$

The determinant of the transition matrix M,

$$det(M) = e^{vl} \geq 1,$$

the trace

$$tr(M) = \left(1 + \frac{\Gamma}{S}\right)e^{k_+ l} + \left(1 - \frac{\Gamma}{S}\right)e^{k_- l}.$$

The eigenvalues of the matrix Q are determined by the formula

$$Q = \frac{tr(M)}{2} \pm \sqrt{\frac{(tr(M))^2}{4} - det(M)}.$$

Spatially bounded solutions forming the Brillouin zone are determined by the condition

$$Q = \exp(i\tilde{k}l),$$

where $\tilde{k}$ is the quasi-wavenumber of the disturbance, $|\tilde{k}| \le \pi/l$.

The most important disturbance is that with $\tilde{k} = 0$. It is periodic with the period of the chain of inhomogeneities, l, i.e., $(A_{+,n+1}, A_{-,n+1}) = (A_{+,n}, A_{-,n})$. In the case $\lambda > 0$, the corresponding eigenvalue is real, and it changes its sign when the amplitude of the inhomogeneity reaches the critical value

$$\Gamma_c(l) = \frac{R[\cosh(Rl/2) - \cosh(vl/2)]}{\sinh(Rl/2)}, \tag{19}$$

where $R = \sqrt{v^2 + 4\lambda}$. In the limit of large $l, \cosh(Rl/2) \gg \cosh(vl/2)$, hence

$$\Gamma_c(l) \sim R \coth(Rl/2), \tag{20}$$

which matches the value $\Gamma_c(\infty) = R$ found in the previous section. Other characteristic limits are (λ is assumed to be $O(1)$): (i) when $v \ll 1/l$, $\Gamma_c \sim 2\sqrt{\lambda}\tanh(\sqrt{\lambda}l/2)$; (ii) when $v = O(l) \gg 1, \Gamma_c \sim U[1 - \exp(-\lambda l/2v)]$; (iii) when $v \gg l, \Gamma_c \to \lambda l$ (that limit does not depend on v).

Let us present also the result for $\tilde{k} = \pi/l$ (the mode with the double period), $(A_{+,n+1}, A_{-,n+1}) = -(A_{+,n}, A_{-,n})$). The critical value of Γ in that case is

$$\tilde{\Gamma}_c(l) = \frac{R(\cosh(Rl/2) + \cosh(vl/2)}{\sinh(Rl/2)}. \tag{21}$$

Obviously, $\tilde{\Gamma}_c(l) > \Gamma_c(l)$. The limit cases are: (i) when $v \ll 1/l, \tilde{\Gamma}_c \sim 2\lambda \coth(\sqrt{\lambda}l/2)$; (ii) when $v \gg 1, \tilde{\Gamma}_c \sim U[1 + \exp(-\lambda l/2v)]$.

3.2 Nonlinear Localized Structures

Return to the case of a single inhomogeneity governed by Eq. (4).

3.2.1 The Case $v = 0$

In the case $v = 0$, the stationary localized structure created by the monotonic instability of the base state with respect to the localized mode is governed by the equation

$$-\lambda u + \Gamma\delta(x)u + u'' + f(u) = 0 \tag{22}$$

with boundary conditions

$$u(\pm\infty) = 0. \tag{23}$$

Because of the symmetry of the solution, $u(-x) = u(x)$, it is sufficient to solve the equation

$$-\lambda u + u'' + f(u) = 0 \tag{24}$$

in the region $0 < x < \infty$ with boundary conditions

$$\Gamma u(0) + 2u'(0) = 0,\ u(\infty) = 0. \tag{25}$$

Recall that $f(0) = f'(0) = 0$. First of all, in the case $\lambda < 0$ (unstable background) Eq. (24) has no non-trivial solutions decaying at the infinity, thus the boundary value problem (24), (25) has no non-trivial solutions. Later on, we will consider the case $\lambda \geq 0$.

The calculation of the solutions to (24), (25) is tedious but straightforward. Below we present results of the calculation in the cases $f(u) = -u^2$ and $f(u) = -u^3$.

In the case of a quadratic nonlinearity, $f(u) = -u^2$, the stationary solution in the region $x > 0$ for $\lambda > 0$ is

$$u(x) = \frac{3}{2}\lambda \frac{\Gamma^2 - 4\lambda}{\left[\Gamma \sinh\left(\sqrt{\lambda/2}x\right) + 2\sqrt{\gamma}\cosh\left(\sqrt{\lambda/2}x\right)\right]^2}. \tag{26}$$

In the region $x < 0, u(x) = u(-x)$. At the critical value of $\Gamma, \Gamma_c = 2\sqrt{\lambda}$, a two-sided bifurcation takes place. The nontrivial solution is $u(x)$ is positive and stable for $\Gamma > \Gamma_c$, and it is negative and unstable for $\Gamma < \Gamma_c$.

It is interesting that a localized solution exists also in the case of a neutrally stable background, $\lambda = 0$. In that case, the solution in the region $x > 0$ is

$$u(x) = \frac{6}{(x + 4/\Gamma)^2},$$

thus the decay at infinity is algebraic rather than exponential.

In the case of a cubic nonlinearity, the solution is

$$u(x) = \pm \frac{\sqrt{2\lambda(\Gamma^2 - 4\lambda)}}{\Gamma \sinh(\sqrt{\lambda}x) + 2\sqrt{\lambda}\cosh(\sqrt{\lambda}x)},\ x > 0. \tag{27}$$

A supercritical pitchfork bifurcation takes place. Note that the solution (27) belongs to the family of localized solutions obtained in [5]. For $\lambda = 0$, the localized solution is

$$u(x) = \frac{\sqrt{2}}{|x| + 2/\Gamma}$$

(see [14]).

3.2.2 The Case $v \neq 0$

In the case $v \neq 0$, the stationary localized structure created by the localized mode is governed by the boundary value problem

$$-\lambda u - vu' + \Gamma\delta(x)u + u'' + f(u) = 0 \tag{28}$$

with boundary conditions

$$u(\pm\infty) = 0. \tag{29}$$

No solutions are possible in the case $\lambda < 0$, because in that case the point $u = 0$ is a repeller in the framework of Eq. (28) (recall that $v > 0$). In the case $\lambda > 0$ the solution is possible but its analytical computation is a formidable task. Here we present only the result of the bifurcation analysis in the case $f(u) = -u^3$.

In the vicinity of the critical value $\Gamma_c = \sqrt{v^2 + 4\lambda}$,

$$\Gamma = \Gamma_c + \epsilon^2\gamma,\ \epsilon^2 \ll 1,$$

one can construct an asymptotic expansion in the form

$$u(x) = \epsilon u_1(x) + \epsilon^3 u_3(x) + \ldots,$$

which describes the bifurcation of a nontrivial localized solution of Eq. (28) from the trivial solution $u(x) = 0$. The leading order equation is linear, and its solution can be found analytically:

$$u_1(x) = Ae^{k_- x},\ x < 0;\ u(x) = Ae^{k_+ x},\ x > 0, \tag{30}$$

where

$$k_\pm = \frac{v \mp \sqrt{v^2 + 4\lambda}}{2}. \tag{31}$$

The solvability condition of the equation for $u_3(x)$ obtained in order $O(\epsilon^3)$ determines the amplitude A:

$$\left(\frac{1}{4k_- - v} - \frac{1}{4k_+ - v}\right)A^2 = \gamma. \tag{32}$$

Because

$$4k_- - v = v + 2\sqrt{v^2 + 4\lambda} > 0,\ 4k_+ - v = v - 2\sqrt{v^2 + 4\lambda} < 0,$$

the solution exists only for $\gamma \geq 0$, i.e., there is a supercritical pitchfork bifurcation of two branches of localized solutions (with positive and negative A) from the trivial solution $u = 0$. In the case $v = 0$,

$$A^2 = 2\sqrt{\lambda}\gamma, \tag{33}$$

which is compatible with (27).

4 Complex Ginzburg-Landau Equation

The results of the previous section can be easily extended to the case of the Ginzburg-Landau equation with the real coefficients,

$$u_t + vu_x = -\lambda u + \Gamma\delta(x)u + du_{xx} - |u|^2 u. \tag{34}$$

In the present section, we consider the full complex Ginzburg-Landau equation,

$$u_t + vu_x = [-\lambda + (\Gamma_r + i\Gamma_i)\delta(x)]u + (d + i\alpha)u_{xx} - (1 + i\beta)|u|^2 u. \tag{35}$$

4.1 Linear Stability Theory

Let us linearize Eq. (35) and search the solution in the form $u(x,t) = U(x)\exp(\sigma t)$. We find:

$$\sigma U + vU' = [-\lambda + (\Gamma_r + i\Gamma_i)\delta(x)]U + (d + i\alpha)U''. \tag{36}$$

In the case $v = 0$, this problem has been solved in [5]. Using ansatz (8) for localized solutions of that equation, we find the following expression for the growth rate of disturbances:

$$\sigma = -\lambda + \frac{(\Gamma_r + i\Gamma_i)^2 - v^2}{4(d + i\alpha)}, \tag{37}$$

(cf. (13)). The threshold value of $\Gamma_{r,c}$ is determined by the relation

$$Re(\sigma) = \frac{(\Gamma_{r,c}^2 - \Gamma_i^2 - v^2)d + 2\alpha\Gamma_{r,c}\Gamma_i}{4(d^2 + \alpha^2)} - \lambda = 0. \tag{38}$$

Note that the obtained expression resembles that of the *absolute* instability threshold in the absence of the inhomogeneity,

$$\lambda = -\frac{v^2 d}{4(d^2 + \alpha^2)}.$$

The instability boundary is a hyperbola in the plane (Γ_c, Γ_i) with the asymptotes

$$\Gamma_i/\Gamma_r = (\alpha \pm \sqrt{\alpha^2 + d^2})/d.$$

The explicit formula for the threshold value is

$$\Gamma_{r,c} = \frac{-\alpha\Gamma_i + \sqrt{(4\lambda + \Gamma_i^2)(d^2 + \alpha^2) + d^2 v^2}}{d}. \tag{39}$$

The values of $k_\pm$ in the expression (8) are:

$$k_\pm = \frac{v \mp \sqrt{v^2 + 4(d + i\alpha)\lambda}}{2(d + i\alpha)}. \tag{40}$$

Note that conditions of the boundedness of the eigenfunctions on the infinity, $Re(k_-) > 0, Re(k_+) < 0$, are satisfied. Indeed,

$$Re(k_\pm) = \frac{(v \mp \Gamma_r)d \mp \Gamma_i \alpha}{2(d^2 + \alpha^2)}. \tag{41}$$

Substituting the critical value of Γ_r, (39), we find that at $\Gamma_r = \Gamma_{r,c}$,

$$Re(k_\pm) = \frac{v \mp \sqrt{v^2 + (1 + \alpha^2/d^2)(\Gamma_i^2 + 4\lambda)}}{d},$$

hence the boundedness conditions are satisfied. Obviously, they are satisfied for $\Gamma_r > \Gamma_{r,c}$, because $Re(k_+)$ ($Re(k_-)$) decreases (grows) with the growth of Γ_r.

In the limit $d \ll \alpha$ the instability condition becomes $\Gamma_r \Gamma_i > 2\lambda\alpha$ (see [14]). Note that it does not depend on v. However, the velocity v influences the critical value of frequency,

$$\omega_0 = -Im\sigma = \frac{\Gamma_r^2 - \Gamma_i^2 - v^2}{4\alpha} = \frac{4\alpha^2\lambda^2 - v^2\Gamma_i^2 - \Gamma_i^4}{4\alpha\Gamma_i^2}. \tag{42}$$

Thus, in the case of a complex amplitude equation, the nonzero group velocity breaks the reflection symmetry of solutions ($k_+ \neq -k_-$, see Eq. (40)), typically enhances the instability threshold (see Eq. (39)), and influences the frequency of the oscillatory instability (see Eq. (42)).

4.2 Nonlinear Localized Structures

Let us consider the bifurcation of solutions in the framework of Eq. (35). In the vicinity of the threshold value of Γ_r,

$$\Gamma_r = \Gamma_{r,c} + \epsilon^2\gamma, \ \epsilon^2 \ll 1,$$

a nontrivial solution of (35) can be constructed in the form

$$u = \epsilon u_1(x, t_0, t_2) + \epsilon^3 u_3(x, t_0, t_2) + \ldots,$$

where $t_0 = t, t_2 = \epsilon^2 t$. At the leading order $O(\epsilon)$, the linear problem considered in the previous section is reproduced, hence

$$u_1(x, t_0, t_2) = U(x)e^{-i(\omega_0 t_0 + \omega_2 t_2)}, \tag{43}$$

where $U(x)$ is defined by (8). At the order $O(\epsilon^3)$, we obtain the following equation,

$$\begin{aligned} &u_{3,t_0} + v u_{3,x} + [\lambda - (\Gamma_{r,c} + i\Gamma_i)\delta(x)]u_3 - (d + i\alpha)u_{3,xx} \\ &\quad = -u_{1,t_2} + \gamma\delta(x)u_1 - (1 + i\beta)|u_1|^2 u_1. \end{aligned} \tag{44}$$

Assuming

$$u_3(x, t_0, t_2) = U_3^{\pm} e^{-i(\omega_0 t_0 + \omega_2 t_2)} \tag{45}$$

(the upper and lower signs corresponds to regions $x > 0$ and $x < 0$), we obtain

$$vU_{3,x}^{\pm} + (\lambda - i\omega_0)U_3^{\pm} - (d + i\alpha)U_{3,xx}^{\pm}$$

$$= i\omega_2 A e^{k_{\pm}x} - (1 + i\beta)|A|^2 A e^{\tilde{k}_{\pm}x},$$

where $\tilde{k}_{\pm} = 3Rek_{\pm} + iImk_{\pm}$, and hence

$$U_{3,x}^{\pm} = A_3^{\pm} e^{k_{\pm}x} + \frac{i\omega_2 A}{v - 2k_{\pm}(d + i\alpha)} x e^{k_{\pm}x} - \frac{(1 + i\beta)|A|^2 A}{\lambda - i\omega_0 + v\tilde{k}_{\pm} - (d + i\alpha)v\tilde{k}_{\pm}^2} e^{\tilde{k}_{\pm}x},$$

where $A_3^{\pm}$ are constants. The condition of the continuity of U_3 in the point $x = 0$ and the condition

$$-(d + i\alpha)(U_{3,x}^{+} - U_{3,x}^{-})|_{x=0} - (\Gamma_{r,c} + i\Gamma_i)U_3(0) = \gamma,$$

which is obtained by the integration of (44) in the interval $-\delta \le x \le \delta$ and by taking the limit $\delta \to 0$, give a system of two algebraic linear equations for $A_3^{\pm}$ with a zero determinant. The solvability condition of this system gives the following relation,

$$-(1 + i\beta)|A|^2 \left[\frac{1}{v - 2q_{+}(d + i\alpha)} - \frac{1}{v - 2q_{-}(d + i\alpha)}\right] + \frac{\gamma + i\omega_2}{d + i\alpha} = 0, \tag{46}$$

where $q_{\pm} = k_{\pm} + Rek_{\pm}$. Multiplying relation (46) by $d + i\alpha$ and taking the real part, we find the bifurcation equation,

$$|A|^2 Re\left\{(d + i\alpha)(1 + i\beta)\left[\frac{1}{v - 2q_{+}(d + i\alpha)} - \frac{1}{v - 2q_{-}(d + i\alpha)}\right]\right\} = \gamma, \tag{47}$$

which is the generalization of Eq. (32) in the case of the complex amplitude function.

5 Conclusions

We have considered the onset of patterns under the action of a localized inhomogeneity of the linear growth rate. The linear instability threshold has been found, and the bifurcation of a nonlinear solution near the threshold has been considered. Similarly to the threshold of the absolute instability in the absence of an inhomogeneity, the threshold of the inhomogeneity-induced instability is influenced by the group velocity of waves. An exception is the case of vanishing diffusion coefficient where the threshold is determined solely by the decay rate of waves outside the inhomogeneity and by the dispersion of waves. The instability threshold can be diminished by using a periodic chain of inhomogeneities.

References

1. B.A. Malomed, Phys. Rev. E **47**, R2257 (1993)
2. B.A. Malomed, Phys. Rev. E **50**, 4249 (1994)
3. S.I. Abarzhi, O. Desjardins, A. Nepomnyashchy, H. Pitsch, Phys. Rev. E **75**, 046208 (2007)
4. A. Nepomnyashchy, S.I. Abarzhi, Phys. Rev. E **81**, 037202 (2010)
5. C.-.K. Lam, B.A. Malomed, K.W. Chow, P.K.A. Wai, Eur. Phys. J. Special Topics **173**, 233 (2009)
6. Y.V. Kartashov, V.V. Konotop, V.A. Vysloukh, Europhys. Lett. **91**, 34003 (2010)
7. Y.V. Kartashov, V.V. Konotop, V.A. Vysloukh, L. Torner, Opt. Lett. **35**, 1638 (2010)
8. Y.V. Kartashov, V.V. Konotop, V.A. Vysloukh, L. Torner, Opt. Lett. **35**, 3177 (2010)
9. Y.V. Kartashov, V.V. Konotop, V.A. Vysloukh, Opt. Lett. **36**, 82 (2011)
10. V.E. Lobanov, Y.V. Kartashov, V.A. Vysloukh, L. Torner, Opt. Lett. **36**, 85 (2011)
11. D.A. Zezyulin, Y.V. Kartashov, V.V. Konotop, Opt. Lett. **36**, 1200 (2011)
12. O.V. Borovkova, V.E. Lobanov, Y.V. Kartashov, L. Torner, Opt. Lett. **36**, 1936 (2011)
13. Y.V. Kartashov, V.V. Konotop, V.A. Vysloukh, Opt. Lett. **83**, 041806(R) (2011)
14. C.H. Tsang, B.A. Malomed, C.K. Lam, K.W. Chow, Eur. Phys. J. D **59**, 81 (2010)
15. O.V. Borovkova, V.E. Lobanov, B.A. Malomed, Europhys. Lett. **97**, 44003 (2012)

Spontaneous Formation and Switching of Optical Patterns in Semiconductor Microcavities

Jacob Scheuer and Meir Orenstein

Abstract We study spontaneous pattern formation and symmetry breaking in broad area and pre-patterned (spatially modulated) semiconductor microcavities under lasing conditions. In broad area VCSELs, we observe the spontaneous formation of regular arrays consisting of charge "±1" optical vortices. The formation of these patterns stems from transverse mode locking of almost wavelength degenerated Gauss-Laguerre (GL) modes. The observed patterns in Gain modulated broad area VCSELs and their dynamical behavior depends dramatically on the modulation strength. In ring shaped VCSELs lasers we observe necklace-like pattern formation and switching as a function of the injection current. The formation of the patterns and, in particular, their switching is shown to stem from stability loss of the lasing pattern to perturbations of more complex pattern which, in turn, is stable under similar pumping conditions. Having the advantage of a strong, saturating nonlinear response with an inherent loss compensation mechanism, such lasers are potentially the best microlabortories for studying nonlinear phenomena and for the generation and employment of complex optical fields. Applications can be found in optical data storage, information distribution and processing, laser cooling and more.

1 Introduction

Spontaneous pattern formation and switching in nonlinear optics is a well-established research field that has been in the focus of numerous studies, both theoretical and experimental [1–4]. A fundamental hurdle in experimental studies

J. Scheuer (✉)
School of Electrical Engineering, Tel-Aviv University, Tel Aviv, Israel
e-mail: Jacob.scheuer@northwestern.edu; kobys@eng.tau.ac.il

M. Orenstein
Department of Electrical Engineering, Technion—Israel Institute of Technology, Haifa, Israel

Progress Optical Sci., Photonics (2013): 321–356
DOI: 10.1007/10091_2012_25

Published Online: 26 January 2013

involving nonlinear optics is loss. Nonlinear phenomena are affected by the intensity of the field and are, therefore, very sensitive to losses. These drawbacks characterize, in principle, all passive nonlinear media.

The nonlinear medium of semiconductor laser has several advantages for exploring spontaneous pattern formation. The main advantage is that under lasing conditions, the losses of the evolving pattern are automatically compensated by the gain mechanism of the laser. In addition, the semiconductor lasers have a relatively large nonlinear response to the electrical field (comparing to passive media such as silica) that includes both real and imaginary terms.

One of the well-known properties of lasing patterns in lasers is that they exhibiting an evident increase of their spatial frequency as the pumping is increased [5–7]. Related phenomena are beam filamentation in broad area edge emitters [8], as well as the on-switching of higher order lasing modes.

The on-switching of higher order patterns in broad area lasers was frequently explained by the modification of the gain-loss balance between the modal (diffraction) losses, and the modal gain (the intensity profile overlap with the gain profile) due to the spatial hole burning effect [9–12]. A major drawback of this argument is its failure to explain the unidirectional evolution of higher spatial frequencies in the laser as the current is increased, i.e. the preference of switching to higher order modes against switching back to lower order modes when pumping is increased. This drawback indicates that the static gain-loss mode-discrimination mechanism is not the fundamental reason for the pattern evolution.

In this chapter, the spontaneous transversal patterns that evolve in nonlinear gain medium are explored. The study was focused on two-dimensional structures realized by vertical cavity semiconductor lasers (VCSELs). The formation of the patterns was analyzed theoretically and experimentally demonstrated in broad area gain guided VCSELs.

We choose to focus on the vertical cavity configuration (VCSEL) because it possesses several inherent advantages. VCSELs are miniature devices and simple to operate, and they have the two key features for the potential formation of complex patterns: very high Fresnel number and two-dimensional emission, both are lacking from edge emitting semiconductor lasers. In addition, patterning the top mirrors of VCSELs allows for extending of nonlinear pattern formation studies to diverse geometries as well to modulated nonlinear media—a field that has received much attention because it facilitates stable patterns. These advantages make the VCSEL an excellent micro-laboratory for the generation and study of complex patterns. Another reason to explore the broad area VCSELs in this context is their application in short range optical links as low coherency sources for reduced modal noise in multimode fiber links [13, 14].

In Sect. 2 the patterns emitted by square and circular broad area VCSELs are examined. It is shown that these patterns are comprised of regular arrays of optical vortices and stem from nonlinear transverse locking of Gauss-Laguerre modes. The role of the thermal lensing effect in the pattern formation is also examined and is found to be important.

In Sect. 3 the patterns emitted by ring shaped VCSELs are examined. We choose to focus on this relatively simple geometry because it constitutes a convenient platform for studying not only the stable patterns but also the dynamical transitions between them. The patterns that were observed consisted of intensity lobes that switch to higher numbers of lobes as the injection current is increased. The pattern switching is found to stem from the mechanism of nonlinear related instability—the modulation instability which results in a sequential stability loss of lower complexity patterns to excite higher complexity patterns as the current is increased. The switching thresholds are studied theoretically and demonstrated experimentally.

2 Pattern Formation in Broad Area VCSELs

The formation of stable transverse field patterns in nonlinear optical devices was studied in recent years. Much work (mainly numerical analysis) has been exerted to the study of transverse pattern formation in cavities incorporating nonlinear medium [1, 2, 15, 16]. These studies focused mainly on externally driven cavities and exhibited the formation of ordered patterns of bright or dark spots with hexagonal symmetry. Other patterns, such as rolls had been observed as well [1]. Experimental observations of the formation of stable transverse patterns in nonlinear cavities containing Sodium vapor [17] and transition between rolls and hexagons in a system consisting of a liquid crystal light valve (LCLV) in a ring cavity [18] were reported.

Lasers are incorporating a built-in nonlinearity and cavity, thus are expected to exhibit these complex field patterns spontaneously. However, only few observations of such patterns were reported, e.g. in a Sodium vapor based laser [17] and in VCSELs [7].

In this section the formation of these complex spatial patterns in broad area VCSELs is discussed in details. The transverse patterns emitted by the VCSELs are shown to stem from transverse mode locking of wavelength degenerated Gauss-Laguerre modes. It is also shown that the temperature profile of the VCSEL has a significant role in the determination of these patterns (thermal lensing effect).

The pattern that evolves in broad area VCSELs were calculated using a rate-equations based model and compared to experimentally observed patterns.

2.1 The Thermal Lensing Effect

One of the most important linear effects in the determination of the transverse modes of the device (which in this case is found to be dominant) is the thermally induced modification of the refractive index. The injected current generates heat inside the device. The heat flows from the laser outwards and causes a non-

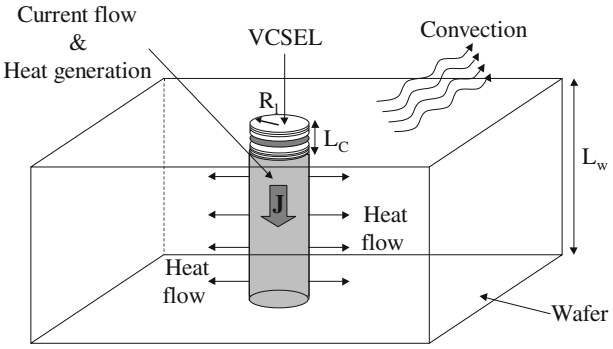

Fig. 1 Thermal model for VCSEL

uniformly heating which creates a temperature gradient over the device. This temperature profile induces changes in the refractive index profile of the laser—$\Delta n(r) = \frac{\partial n}{\partial T} \cdot \Delta T$. In semiconductor laser materials the induced index increases with the temperature and as a result, an effective lens (parabolic index) is formed (thermal lensing).

A comprehensive analysis of VCSELs including thermal effects was conducted by Hadley et al. [19], Scott et al. [20] and by Chen [21]. These studies were primarily based on numerical solutions of coupled carriers transport and heat transfer equations. Here, a relatively simple analytic thermal model is used, yielding a qualitatively good approximation for the temperature profile which was found to be parabolic within the laser area.

The heat is assumed to be uniformly generated inside a perfect cylinder with radius R_l and height L_w. R_l is the laser's radius and L_w is the width of the wafer (see Fig. 1). The heat is generated because of the ohmic resistance mainly of the top Bragg (p-doped) section. The medium is assumed to be homogeneous and isotropic. The heat generated inside the cylinder is transferred to the rest of the wafer via thermal conductance within the semiconductor material and to the air surrounding the wafer via convection from the wafer surfaces. It is assumed that the device temperature approaches room temperature as r approaches infinity and that it is limited in $r = 0$. The steady state temperature profile of the device is the solution of the heat transfer equation [22]:

$$\frac{d^2\tilde{T}}{dr^2} + \frac{1}{r}\frac{d\tilde{T}}{dr} - \frac{2k_A}{k \cdot L_W}\tilde{T} + \frac{h(r)}{k} = 0 \quad \text{where } h(r) = \begin{cases} h_0 & r \le R_l \\ 0 & r > R_l \end{cases} \tag{1}$$

$\tilde{T} = T - T_A$ is the temperature difference between the device and room temperatures, r is the radial coordinate, k and k_A are the heat conductance and convection coefficients respectively. $h(r)$ is the heat generation density which is zero outside the laser and assumed to be constant inside—$h_0 = V \cdot I / \pi R_l^2 L_w$ where V and I are the voltage and current driving the laser.

The solution of (1) is expressed by modified Bessel functions:

Table 1 Voltages and heat generation in a VCSEL for different driving currents

V (Volt)	I (mA)
4.86	20
5.12	25
5.35	30
5.56	35

$I \approx I_L \exp(V/V_L)$
$I_L = 0.377$ mA
$V_L = 0.841$ V
$I_{th} = 7$ mA
$V_{th} = 2.45$ V

$$\tilde{T} = \begin{cases} \frac{T_0 \cdot K_0'(\alpha R_l) \cdot I_0(\alpha \cdot r)}{I_0'(\alpha R_l) \cdot K_0(\alpha R_l) - I_0(\alpha R_l) \cdot K_0'(\alpha R_l)} + T_0 & r < R_l \\ \frac{T_0 \cdot I_0'(\alpha R_l) \cdot K_0(\alpha \cdot r)}{I_0'(\alpha R_l) \cdot K_0(\alpha R_l) - I_0(\alpha R_l) \cdot K_0'(\alpha R_l)} & r > R_l \end{cases} \quad (2)$$

where I_0 and K_0 are the zero order modified Bessel functions of the first and second kind, the primes denote derivatives, $\alpha^2 = 2k_A/kL_w$ and $T_0 = h_0 L_w/2k_A$. By measuring the V–I curve of the VCSEL, the diode electrical parameters—$I \approx I_L \exp(V/V_L)$ can be estimated and used to calculate h_0 and the corresponding temperature profile for each current. These parameters are, obviously, specific for the examined devices. Table 1 summarizes experimental measurements of the voltage, current and calculated I_L, V_L for a circular 20 μm diameter VCSEL (for detailed description of the devices see Sect. 2.6). These values were used to calculate the temperature profiles for each of the currents.

As the injected current increases, the temperature rises and the induced index change becomes larger and more significant (see Fig. 2). The induced index changes the guidance configuration in the VCSEL from primarily gain-guidance to index-guidance, so the thermally induced waveguide becomes the dominant ingredient in the determination of the VCSEL transverse modes.

For small argument, a parabolic approximation can be used for the zero order modified Bessel function of the first kind, $I_0(r) \underset{r \to 0}{\to} 1 + r^2/4$ and the approximated temperature profile inside the laser is $\tilde{T}(r) \approx \tilde{T}_{\max} - \alpha^2 T_0 \cdot r^2/4$.

As shown in Fig. 3, the approximated thermally induced refractive index (for I = 35 mA) is in excellent agreement with the exact solution (based on (2)) for radii smaller than the laser radius R_l (the induced index was calculated by assuming $\partial n/\partial T = 4 \cdot 10^{-4}\,^{\circ}C^{-1}$ [23]—yielding index changes of $\Delta n \sim 0.02$). Thus, the heating of the laser induces approximately an effective waveguide with a parabolic profile.

This simple and analytic thermal model has some limitations that should be considered. First, the heat transfer problem is essentially a 3D problem because the thermal and electrical characteristics of the different layers in the laser (Bragg reflectors, QWs, wafer etc.) may differ significantly. As a result, the heat generated

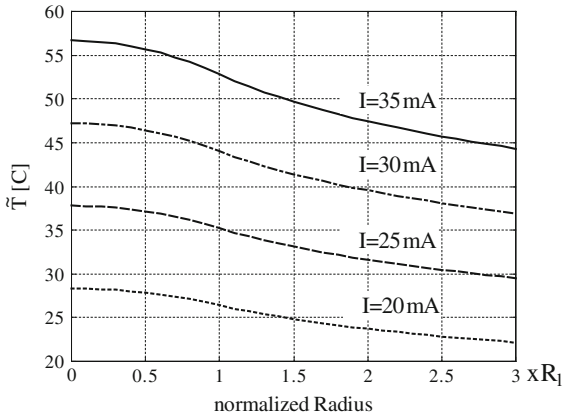

Fig. 2 Temperature profile for different injection currents

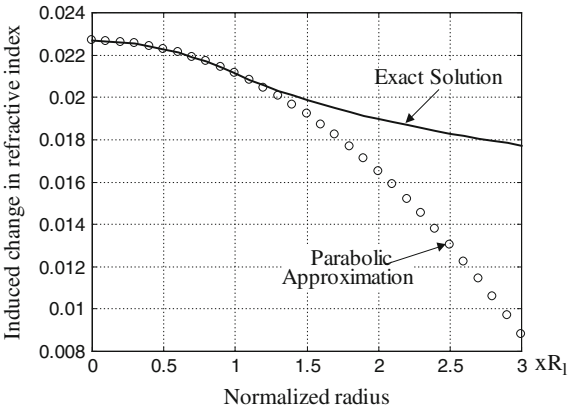

Fig. 3 Thermally induced waveguide—exact (*solid line*) and approximated (*circles*) solutions

in the laser is not distributed uniformly in the z direction. In addition, the current is not confined to a cylinder under the contact but rather spreads outwards as it flows toward the ground contact and causes the heat generation to have radial dependence as well. Despite these limitations, the model provides reasonable results which correspond to more comprehensive thermal models [19–21] and to experimental observation [21].

It should be noted, that the induced waveguide is current dependent—increasing the current results in stronger guiding and more confined modes. This causes a continuous decrease in the size of the modal waste as the current is increased. The injection profile, on the other hand, remains unchanged. As a result, the lasing pattern would also change as the current is increased.

It should be emphasized that the thermal lensing in a *linear* effect that determines a set of orthogonal function (Gauss-Laguerre modes) that can evolve in the cavity. The *nonlinear* mechanisms of the VCSEL would select the specific combinations of modes that would actually evolve in the laser.

In the next section, the guided modes of the parabolic index waveguide—the Gauss-Laguerre modes are presented and discussed.

2.2 The Gauss-Laguerre Modes

The transverse modes of the parabolic index profile waveguide are the well-known Gauss-Laguerre functions [24]. The Gauss-Laguerre set is:

$$\begin{aligned}\Psi_{p0}(r,\varphi) &= \frac{2}{\sqrt{2\pi}} L_p^0\left(2r^2\right)\cdot e^{-r^2}\Psi_{plj}(r,\varphi)\\ &= \frac{2}{\sqrt{2\pi}}\left(\sqrt{2r^2}\right)^l\cdot\left(\frac{p!}{(p+l)!}\right)^{1/2}\cdot L_p^l\left(2r^2\right)\cdot e^{-r^2}\times\begin{cases} e^{+il\varphi} & j=1\\ e^{-il\varphi} & j=2\end{cases}\end{aligned} \tag{3}$$

where $p = 0,1,\ldots$ is the radial index and $l = 0,1,\ldots$ is the angular index, r denotes the radial coordinate normalized by the beam waste, and L_p^l are the Laguerre polynomials of the indicated arguments. The functions Ψ_{plj} form an orthonormal set—$\iint \Psi_{plj}\cdot\Psi^*_{p'l'j'}\cdot da = \delta_{pp'}\delta_{ll'}\delta_{jj'}$. The lowest-order function—Ψ_{00}, is the Gaussian beam and the higher order functions are connected to the Gauss-Hermite function by simple algebraic relations.

An important property of Gauss-Laguerre modes is their wave number dependence on the transverse indices (p, l). Modes satisfying the condition $2p + l = \text{const}$, are wave number degenerated. Within a cavity, this degeneracy causes these modes to be wavelength degenerate. The Gauss-Laguerre modes can be, therefore, arranged in wavelength degenerate "families".

This degeneracy is easily understood by examining the equivalent quantum mechanical problem which is the eigen-functions of the two dimensional harmonic oscillator [25]. In the quantum analogy, the z-derivative of the electrical field is equivalent to the time-derivative of the wavefunction and the propagation factor is equivalent to the energy. Therefore, the wave number (wavelength) degenerated families of the electrical field correspond to energy-level degenerated solutions of the 2D harmonic oscillator.

An immediate conclusion from the classification of the Gauss-Laguerre modes to wavelength degenerated families is that the emitted pattern in each wavelength must be a superposition of modes belonging to a specific family. In addition, since the VCSEL supports predominantly a single longitudinal mode, all families that are lasing simultaneously (multi-mode operation) should have the same longitudinal wave-number (k_z). Since higher order families have higher transversal wave-number (larger k_t) and should, therefor, lase in shorter wavelength (higher effective wave-number). As a result, when the VCSEL is lasing in multi-mode, higher order families would have shorter wavelength (see for example Fig. 14).

It should be noted, that the thermally induced waveguide is not exactly parabolic and therefore the modes of a single family are not completely wavelength

degenerated. The nonlinearity of the laser locks the wavelengths of the almost degenerated modes to a single wavelength via the mechanism of cooperative frequency locking [26] and thus the wavelength degeneracy is regained.

Another interesting property of the Gauss-Laguerre modes is that they may include field patterns with phase singularities (optical vortices) in their center. The significance and properties of these vortices is reviewed in the next section.

2.3 What is an Optical Vortex?

Let us consider a monochromatic wave of the form:

$$U(\vec{r},t) = u(r,\varphi)\exp[i(kz - wt)] \tag{4}$$

where w is the angular frequency and k is the wave-number. Consider, for example, a transversal field profile $u(r,\varphi)$ of the form:

$$u(r,\varphi) = f(r)\exp(in\varphi) \tag{5}$$

where n is an integer. Equation (5) represents a wave that rotates around its axis as it propagates, forming a helical wave (see Fig. 4). For a given z, the electrical field rotates around the beam center similar to a fluid in a vortex. The Gauss-Laguerre modes (3) are solutions of the wave equation that encompasses also the form of (5).

An important property of the solutions that have the form (5) for $n \neq 0$ is that they have a phase singularity at $r = 0$. This singularity can be easily observed when one tries to evaluate the phase in the center by approaching it radially starting at different angles φ. For each angle of approach, a different value is found for the phase in the center—indicating that the phase is not well defined there. Because the solutions of the wave equation must be differentiable, the amplitude of the electrical field must vanish at the location of the phase singularity—as clearly seen from (3).

A more formal way to define an optical vortex is examining the phase change in a closed contour around it. A vortex exists inside a closed contour C if the circulation of the argument of $u(r,\varphi)$ along that contour is an integer multiple of 2π:

$$\oint_C \nabla \arg[u(r,\varphi)] \cdot dl = 2\pi m \quad m = \pm 1,\ \pm 2, \ldots \tag{6}$$

The integer m is called the topological charge of the phase singularity.

It should be noted that a vortex might rotate clockwise or counterclockwise—according to the sign of the topological charge n. These opposite vortices have essentially the same intensity pattern but are actually orthogonal functions.

The rotation of the wave (either clockwise or counterclockwise) indicates that the beam has angular momentum. Unlike the angular momentum of a circularly polarized beam (which is associated with the spin of the photon), the angular momentum of a vortex beam is of orbital type.

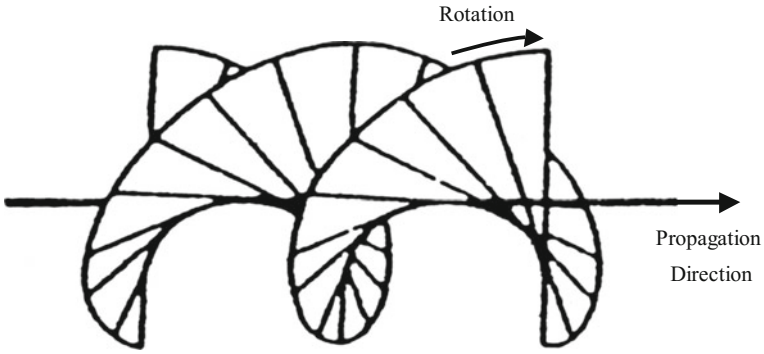

Fig. 4 Schematic representation of the wave-front of a helical wave

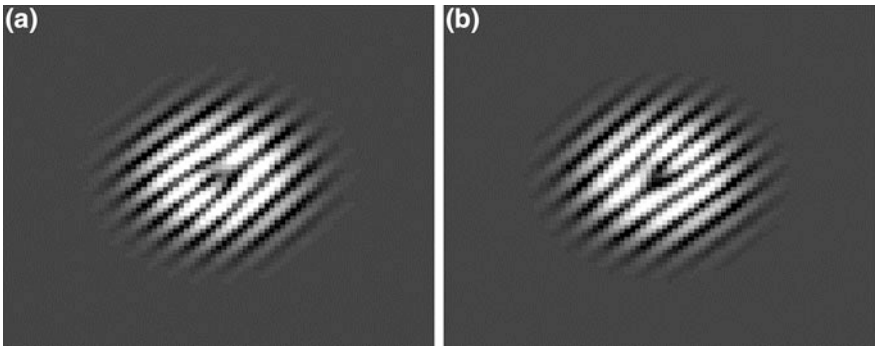

Fig. 5 Interference patterns of charge +1 vortex (**a**) and charge –1 vortex (**b**) with an oblique plane wave

Several methods were developed [27] to identify the rotation direction of a vortex, one of them is interfering between the vortex beam and an oblique plane wave. The existence of the vortex is indicated in the interference pattern by the appearance or disappearance of interference fringes. The number of the fringes indicates the magnitude of the topological charge and the direction of appearance/disappearance indicates its sign. Figure 5 shows the interference pattern of a charge +1 (a) and a charge –1 (b) vortices with an oblique plane wave. In the interference pattern of the charge +1 vortex (a) there is a fringe in the upper half of the plane that "disappears" in the lower half. On the other hand, in the interference pattern of the charge –1 vortex (b) the fringe exists in the lower half plane but disappears in the upper half.

2.4 Derivation of the Modal Rate Equations

As was shown in Sect. 2.1 the thermally induced index is the dominant ingredient in the determination of the transverse modes of the VCSEL. A key point in the analysis shown here is the representation of the transverse distribution of the electric field as a combination of the modes of the induced index—the Gauss-Laguerre modes (3). It is important to note that the induced waveguide is current dependent—increasing the current results in stronger guiding and higher mode confinement. This causes a continuous decrease in the size of the modal waste as the current is increased while the injection profile remains unchanged. As a result, the lasing pattern would also change as the current is increased.

The model is based on the semiconductor laser rate equations for the electrical field and the carrier density. The rate equations for a monochromatic wave in steady-state ($\partial_t = 0$) are [5]:

$$\frac{\partial E_F}{\partial z} = \frac{i}{2k}\nabla^2 E_F + \frac{1}{2}(g - \alpha_{\text{tot}})E_F - \frac{i}{2}R \cdot g \cdot E_F \tag{7a}$$

$$-\frac{\partial E_B}{\partial z} = \frac{i}{2k}\nabla^2 E_B + \frac{1}{2}(g - \alpha_{\text{tot}})E_B - \frac{i}{2}R \cdot g \cdot E_B \tag{7b}$$

$$D\nabla^2 N + \frac{J}{ed} - \frac{N}{T_1} - \frac{g}{\hbar w} \cdot |\varepsilon|^2 = 0 \tag{7c}$$

$$g = \frac{\alpha(N - N_{\text{tr}})}{1 + \varepsilon' \cdot |\varepsilon|^2} \tag{7d}$$

where E_F and E_B are the forward and backward propagating waves, ε is the total electric field in the active area, N is the carrier density, N_{tr} is the transparency carrier density, J the current density, d the VCSEL's cavity length, g the gain, α_{tot} the losses, k the effective propagation constant and e the electron charge. α is the confinement factor and differential gain respectively, D is the diffusion coefficient T_1 is the carriers lifetime, ε' is the non-linear gain saturation parameter, R is the anti-guiding factor representing the refractive index dependence on the free carriers distributions, and ω is the electric field frequency.

The assertion is that the transverse field distribution of any single lasing mode of the VCSEL cavity can be represented as a combination of the Gauss-Laguerre functions belonging to a specific family:

$$E_A = \sum_{\text{n}} E_A^{\text{n}}(z) \cdot \Psi_{\text{n}}(r, \varphi) \tag{8}$$

where Ψ_{n} is the nth function of the family (n runs over all the family modes), E_A^{n} is the corresponding complex coefficient where $A = F, B$. Substituting the decomposed E_F, E_B into (7a) (7b) and integrating over the whole transverse plain (taking advantage of the modes orthogonality) yields a set of equations for the coefficient E_A^{n}:

$$\frac{\partial \dot{E}_A^{\mathrm{n}}}{\partial z} = \frac{1}{2}\left(-\alpha_{tot} E_A^{\mathrm{n}} + (1 - iR)\sum_m E_A^{\mathrm{m}} \cdot \iint g \cdot \Psi_{\mathrm{m}} \cdot \Psi_{\mathrm{n}}^* \cdot da\right) \tag{9}$$

The gain of the active medium (g) in the right hand term of (9) depends also on the electrical field profile via the equation for the carrier density (7c). If the diffusion coefficient D is negligible, the carrier density, N, can be easily extracted from (7c) and be substituted to yield an expression for the gain:

$$g = \frac{\alpha\left(\frac{JT_1}{ed} - N_{\mathrm{tr}}\right)}{1 + \left(\varepsilon' + \frac{\alpha T_1}{\hbar w}\right) \cdot |\varepsilon|^2} \tag{10}$$

If the diffusion is not negligible, the extraction of the carrier density and the gain as a function of the electrical field is not simple and, in principle, requires simultaneous numerical solution of field and diffusion equations. However, if the effect of the diffusion is relatively small, an approximated expression to the gain could be derived.

Substituting (7d) into (7c) yields the following equation for the carrier density:

$$\left(1 + |\xi|^2 - DT_1\nabla^2\right)\tilde{N} = N_0 \tag{11}$$

where $\tilde{N} = N - N_{\mathrm{tr}}$, $N_0 = JT_1/ed - N_{\mathrm{tr}}$ and $|\xi|^2 = \frac{\alpha T_1}{\hbar w} \cdot |\varepsilon|^2 \Big/ \left(1 + \varepsilon' |\varepsilon|^2\right)$. A formal solution for Eq. (11) is [28]:

$$\tilde{N} = \left(1 - \frac{DT_1}{1 + |\xi|^2}\nabla^2\right)^{-1}\left(\frac{N_0}{1 + |\xi|^2}\right) \tag{12}$$

Assuming the diffusion coefficient is relatively small, the first operator on the right hand term of (12) could be approximated by a first order Taylor expansion:

$$\begin{aligned}\tilde{N} &\approx \left(1 + \frac{DT_1}{1 + |\xi|^2}\nabla^2\right) \cdot \left(\frac{N_0}{1 + |\xi|^2}\right) \\ &= \frac{N_0}{1 + |\xi|^2} + \frac{DT_1\nabla^2 N_0}{\left(1 + |\xi|^2\right)^2} + \frac{2DT_1(\nabla N_0) \cdot \nabla\left(1 + |\xi|^2\right)^{-1}}{1 + |\xi|^2} + \frac{DT_1 N_0}{1 + |\xi|^2} \cdot \nabla^2\left(\frac{1}{1 + |\xi|^2}\right)\end{aligned} \tag{13}$$

Expression (13) can be substituted into (7d) to get an approximated expression for the saturating gain of VCSEL. The gain is then substituted into (9) to get the rate equations for the modal coefficients of the Gauss-Laguerre modes.

It should be mentioned that the gain is also a function of the longitudinal coordinate—z. In the active layer the gain is given by (7d) but in the other layers (DBR mirrors etc.) there is no gain and the amplitude of the field decays according to the internal losses of the medium.

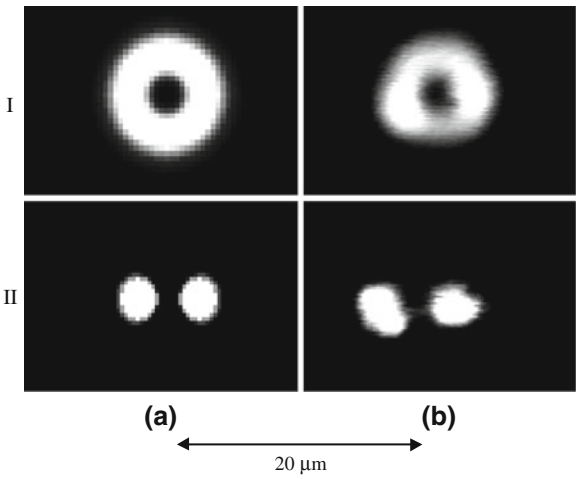

Fig. 6 Transverse pattern for $2p + l = 1$, theoretical (**a**) I $J_0 \sim 15{\cdot}10^{-18}$; II $J_0 > 20{\cdot}10^{-18}$ and experimental (**b**) I 11.3 mA, II 13.3 mA (J_0 units A/μm^2)

2.5 Steady-State Solutions

The steady state solutions for (9) were obtained numerically using the parameters of Ref. [29]. A steady state solution, obtained as a specific mode combination, was a transverse mode-locked solution supported by the nonlinearities of the VCSEL. The control parameter for the model was the injection current density (J). As the current density J was changed, a different mode locked combination of the family modes evolved as the steady state solution. The details of the evolved patterns matched the experimental results perfectly in the sense that whenever a solution was found—a corresponding experimental field distribution was observed and vice versa (see also Sect. 2.6).

Equation (9) where solved for the first non-trivial wavelength degenerated families ($2p + l = 1, 2, 3, 4$). The $2p + l = 0$ family includes a single function and is, therefore, less interesting from the complex pattern formation point of view.

The first family ($2p + l = 1$), exhibited two steady state patterns. The first one (lowest current) to evolve was one of the family basic modes (Ψ_{011} or Ψ_{012}—see Fig. 6aI). This pattern includes a charge "1" phase singularity in the middle (see also Fig. 15). Despite the similarity to the well-known "doughnut mode" the Ψ_{011} is a completely different pattern. The doughnut mode is an incoherent superposition of the Gauss-Hermite modes H_{10} and H_{01} [24], each one with different polarization while the pattern observed here has a single polarization and wavelength. Moreover, in contrast to the optical vortex pattern, the conventional doughnut mode does not have a phase singularity at all. The second pattern (Fig. 6aII) included two intensity lobes. This pattern is a superposition of the two modes of the family and is identical to the H_{10} or H_{01} Gauss-Hermite mode. This pattern was rarely observed (also experimentally) and only in rectangular VCSELs. The reason is that, unlike the vortex pattern, the H_{10} mode is less stable (according

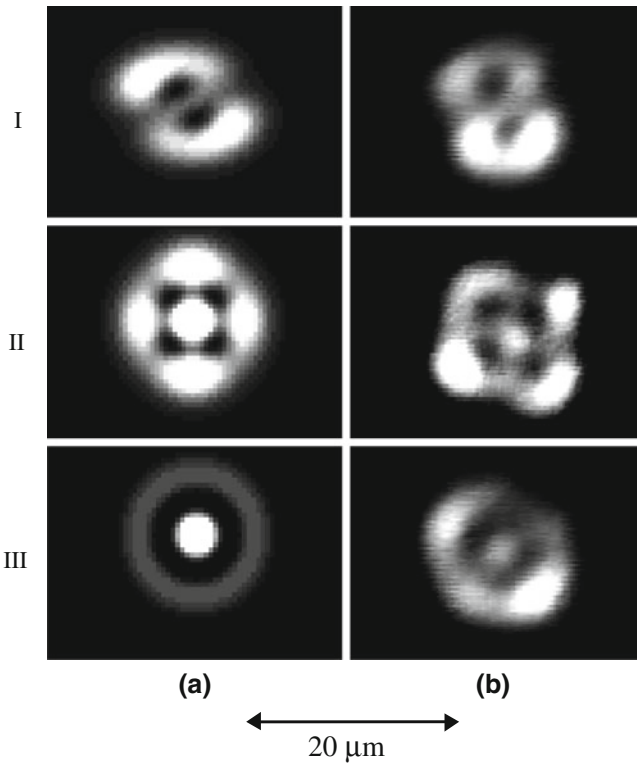

Fig. 7 Transverse pattern for $2p + l = 2$, theoretical (**a**) I $J_0 < 74{\cdot}10^{-18}$; II $J_0 > 74{\cdot}10^{-18}$; III $J_0 > 95{\cdot}10^{-18}$ and experimental (**b**) I 16 mA; II 17.2 mA, III 20 mA. (J_0 units A/μm^2)

to the numerical simulations) in circularly symmetric structure and even a small difference between the amplitudes of the vortex modes would cause the weaker mode to decay—leaving a single vortex pattern. Even in rectangular VCSELs the H_{10} pattern was hardly observed because of the thermal lensing that induces a circularly symmetric waveguide.

For the second family ($2p + l = 2$), three stable mode-locked combinations were obtained under the VCSEL lasing conditions (Fig. 7a). The first pattern to evolve (lowest current) was the "8" shaped pattern (I). The second pattern was the –"4-hole" pattern (II) and the last (III) was the Ψ_{10} basic Gauss-Laguerre (GL) mode. The first two patterns are a specific combination of the Gauss-Laguerre modes that were selected by the nonlinearities of the VCSEL. The values of the current density for each mode-locked combination are detailed in the caption of Fig. 7.

An important feature of the first two patterns is the existence of the dark peaks (two peaks in the "8" shaped pattern and four in the other pattern). These dark peaks were confirmed theoretically and later experimentally (see Fig. 15) to be optical vortices. The "8" shaped pattern (Fig. 7aI) has two charge "1" vortices

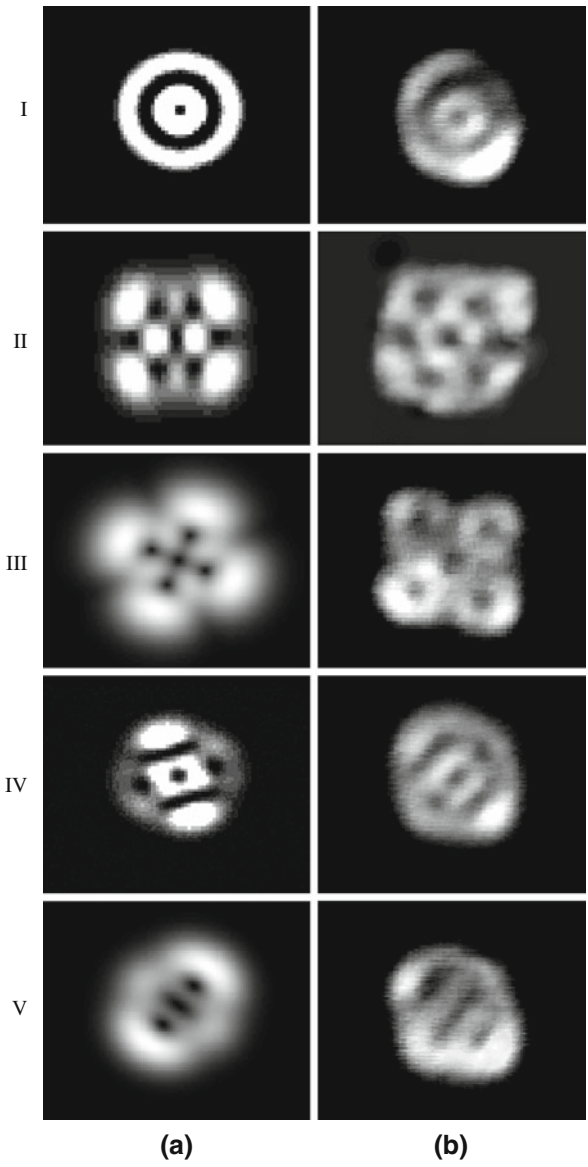

Fig. 8 Transverse pattern for $2p + l = 3$, theoretical (**a**) I $J_0 < 20{\cdot}10^{-18}$; II $28{\cdot}10^{-18} < J_0 < 52{\cdot}10^{-18}$; III $J_0 < 26{\cdot}10^{-18}$; IV $J_0 > 52{\cdot}10^{-18}$; V $20{\cdot}10^{-18} < J_0 < 64{\cdot}10^{-18}$ and experimental (**b**) I 25 mA, II 26.3 mA, III 27.8 mA, IV 28.2 mA, V 28.6 mA. (J_0 units A/μm^2)

(see also Fig. 15) and the "4-hole" pattern consists of four charge "1" vortices with alternating signs giving rise to a total phase singularity of "0". The last pattern belonging to this family, the Ψ_{10} Gauss-laguerre mode (Fig. 7aIII), has no phase singularities. The values of the current densiny for each mode-locked combination are detailed in the caption of Fig. 7.

The patterns of the third family *($2p + l = 3$)* are shown in Fig. 8a. Five stable lasing patterns of this family were obtained—one is a basic GL mode and the

others are specific combinations of all the four modes. As for the previous families, the patterns belonging to the third family are characterized by regular arrays of dark peaks.

The first pattern to appear (lowest current) was the Ψ_{111} or Ψ_{112} Gauss-Laguerre mode (Fig. 8aI) (both modes have an identical intensity pattern). The second pattern (II) was a circular pattern with seven dark peaks and the third (III) exhibited five dark peaks. The forth pattern (Fig. 8aIV) exhibited two dark peaks and two dark stripes and the last pattern (Fig. 8aV) included three dark stripes.

The patterns of the third family can be divided into two groups. The first one is characterized by overall charge "1" singularity and includes the $\Psi_{111/2}$ mode with a charge "1" vortex (Fig. 8aI) and a pattern with seven alternating charge "1" vortices (Fig. 8aII). The second group is characterized by singularities of charge "3". The patterns belonging to this group are shown in Figs. 6aIII, 8aIV and 8aV. The current densities levels are detailed in the caption of Fig. 8. The vortex configuration of these patterns is depicted in Fig. 15.

The patterns of the fourth family $(2p + l = 4)$ are shown in Fig. 9a. Five stable patterns where found numerically, none of them is a basic Gauss-Laguerre mode. The first pattern to evolve (Fig. 9aI) exhibited an array of four charge "1" vortices with identical signs. The second pattern (Fig. 9aII) included ten charge "1" vortices with alternating sign. Increasing the pump rate further resulted in the evolution of one of the patterns depicted in Figs. 9aIII–aV, depending on the initial conditions. Figure 9aIII depicts a wheel-like pattern with eight charge "1" vortices with alternating signs. Figure 9aIV depicts a pattern with four identical charge "1" vortices. The vortex configuration is similar to the one exhibited by the pattern shown in Fig. 9aI but the structure of the pattern is different. Figure 9aV depicts a pattern with ten vortices with alternating signs—two of them in the middle of the pattern the rest are in the periphery. This pattern has similar vortex configuration to the one depicted in Fig. 9aII but different overall structure.

The dependence of the evolving pattern on the initial conditions indicates that under these conditions the VCSEL exhibits multi-stability and the actual lasing pattern selected according to local elements such as defects and inhomogeneously.

It is notable, that some of the theoretically obtained patterns were not observed experimentally, in particular pattern belonging to the $2p + l = 4$ family (Fig. 9). The numerical approach which was used for the theoretical analysis utilized the complete rate equations model. Thus we can exclude stability as a possible reason for that, in particular because such patterns have been observed experimentally in other laser systems incorporating a parabolic index profile [30, 31]. We attribute the fact that some of the patterns were not observed in our experiments to the linkage between the thermal lensing (i.e. the thermally induced parabolic index profile) and the pump level. The index distribution is not fixed but rather change as the pump is increased, reducing the characteristic radius of the GL modes. This is in contrast to other laser system [17] where the index profile is not affected by the pump level. This correlation between the induced index profile and the pump level excludes part of the available parameter space which may explain the fact that some of the predicted patterns were not observed experimentally.

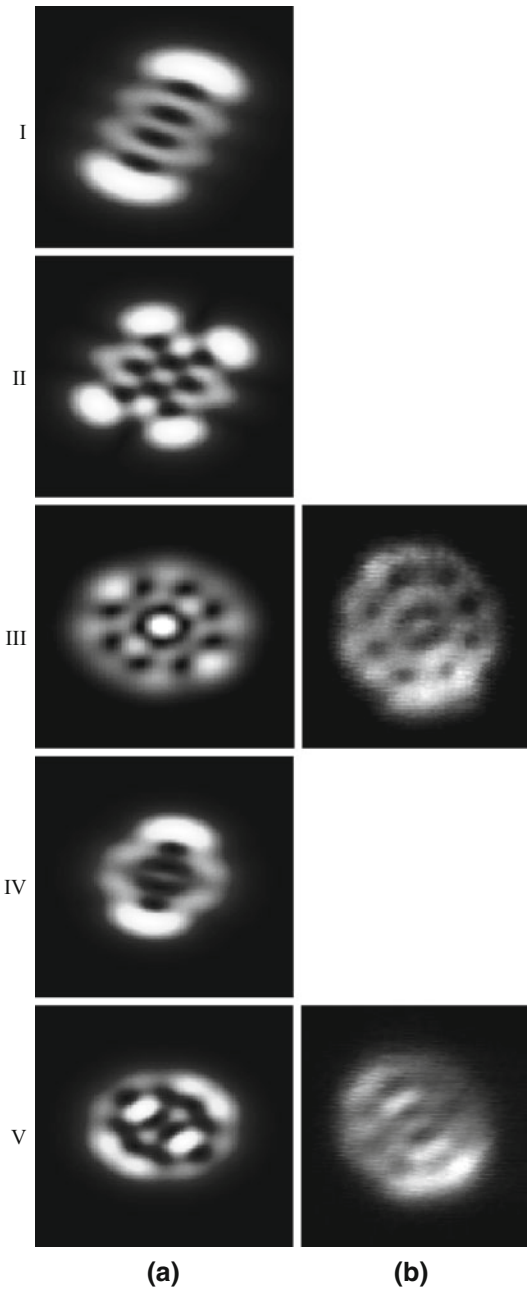

Fig. 9 Transverse pattern for $2p + l = 4$, theoretical (**a**) I $J_0 < 30{\cdot}10^{-18}$; II $32{\cdot}10^{-18} < J_0 < 42{\cdot}10^{-18}$; III $J_0 > 34{\cdot}10^{-18}$; IV $J_0 > 34{\cdot}10^{-18}$; V $J_0 > 52{\cdot}10^{-18}$ and experimental (**b**) I > 30 mA

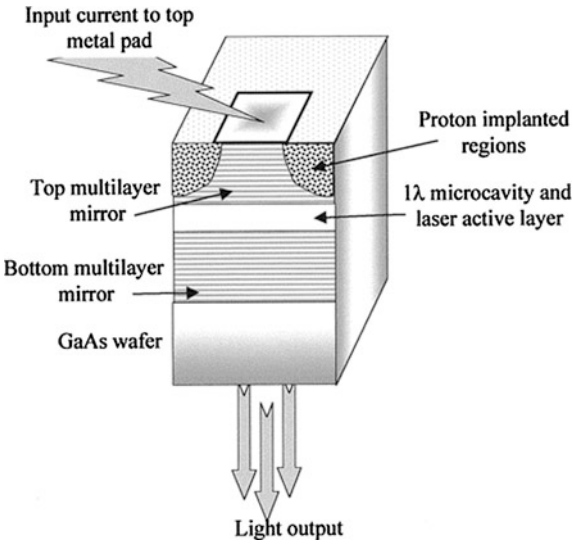

Fig. 10 Schematics of a VCSEL structure

2.6 Experimental Results

The experiments were performed using broad area round (D = 20 μm) and rectangular (20 μm × 20 μm) VCSELs. The laser devices were molecular beam epitaxy grown VCSELs with three 8 nm $In_{0.2}Ga_{0.8}As$ quantum wells (QW), laterally defined by ion implantation [5, 32] (see Fig. 10). The VCSEL is divided into three substructures. The lower includes 20 pairs of GaAs/AlAs $\lambda/4$ Si n-doped layers, creating a DBR mirror with reflection coefficient of 99.87 %. The middle is an intrinsic GaAs layer, one λ in thickness (wavelength in the material) that acts as the cavity of the laser. In the middle of this layer there are three QWs which are the active layers of the VCSEL. The upper is the top DBR mirror that includes 12 Be p-doped pairs of GaAs/AlAs $\lambda/4$ layers. The upper DBR mirror is covered by p + layer which is used both as an optical matching layer to the upper gold mirror and as an electrical contact layer. A proton implantation was used to define the area into which the current is injected (see Fig. 10). This procedure practically defines the laser area and enables the usage of wide gold contact.

The lasers were examined under CW conditions using current levels in the range of 5–43 mA. Under these conditions the lasers wavelength was ∼950 nm. The experimental setup is depicted in Fig. 11. The near-field intensity pattern was imaged (using an objective lens) through the thinned wafer and a linear polarizer on a CCD camera to observe the near-field intensity pattern. Part of the light was imaged through a spectrometer to get the spectrally resolved near-field intensity patterns. The Mirror M1 could be inserted into the optical path in order to conduct an interference experiment. The beam reflected from M1 was spatially filtered and collimated, and was used as a reference beam for interference.

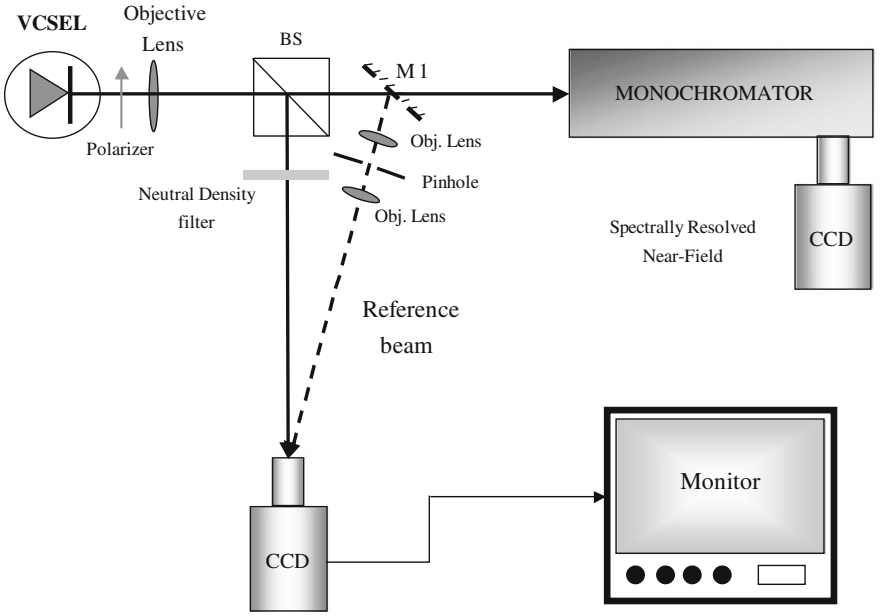

Fig. 11 The experimental setup. *BS* Beam Splitter, *M1* Mirror

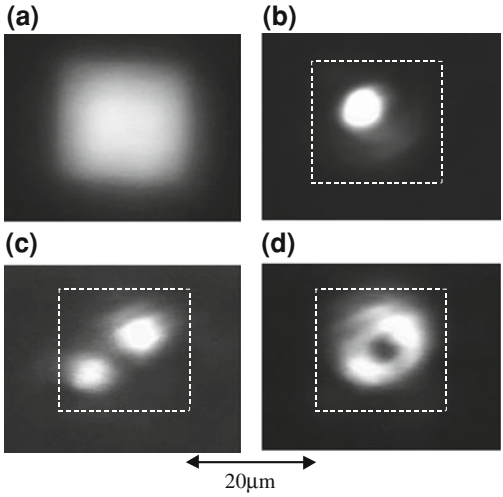

Fig. 12 Emitted patterns close to threshold (**a**) Spontaneous emission; (**b**) Bright filament; (**c**) H_{10} mode; (**d**) An optical vortex

Figure 12 depicts the intensity patterns emitted by the VCSELs at low injection current (below 15 mA). These patterns included narrow bright light filaments and modes belonging to the $2p + l = 1$ family (a vortex an the H_{10} mode) which are considered "conventional modes".

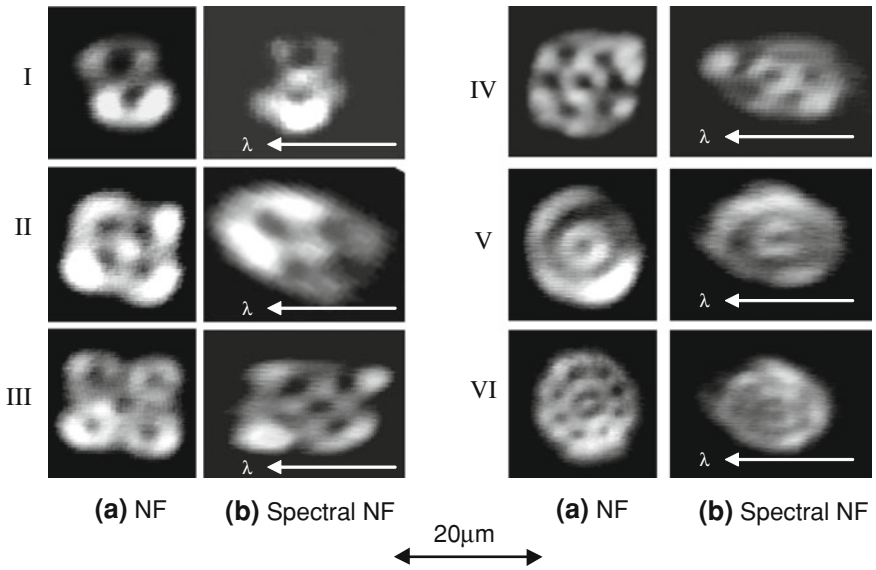

Fig. 13 Imaging through spectrometer, direct Near-Field imaging (**a**) and through the spectrometer (**b**); *I* 8-like pattern; *II* 4-hole pattern; *III* 5-hole pattern; *IV* 7-hole pattern; *V* Ψ_{111}; *VI* wheel shaped pattern. The distortion in (**b**) is due to the complex optics path of the spectrally resolved near-field scheme

As the injection current was increased above 15 mA, the near-field (NF) lasing pattern switched from these "conventional" to complex field patterns, characterized by arrays of "dark peaks" which were very similar to the theoretically predicted patterns.

The first complex patterns to emerge were (Fig. 7b) an "8" like pattern (at 16 mA), the basic Ψ_{10} Gauss-Laguerre mode (at 17.2 mA) and the pattern with 4 dark peaks (at 20 mA). As seen in Fig. 7 the experimentally observed near field patterns are extremely similar to the theoretically calculated patterns.

Increasing the current further (above 25 mA), resulted in the evolution of increasingly complex patterns, depicted in Fig. 8b and exhibiting 3, 5 and 7 dark peaks. As for the previous family, an excellent match was found between the calculated and the experimentally observed patterns.

Higher injection currents gave rise to the emission of patterns belonging to the fourth family and multi wavelength patterns. Only two of the theoretically calculated patterns where observed, probably due to the tendency of the VCSELs to emit multi wavelength patterns in these high currents.

The patterns were imaged through a spectrometer to get the spectrally resolved near-field (see examples in Fig. 13). The spectrally resolved NF revealed a single wavelength operation for each of these patterns, indicating that they indeed a coherently locked combination of wavelength degenerated modes.

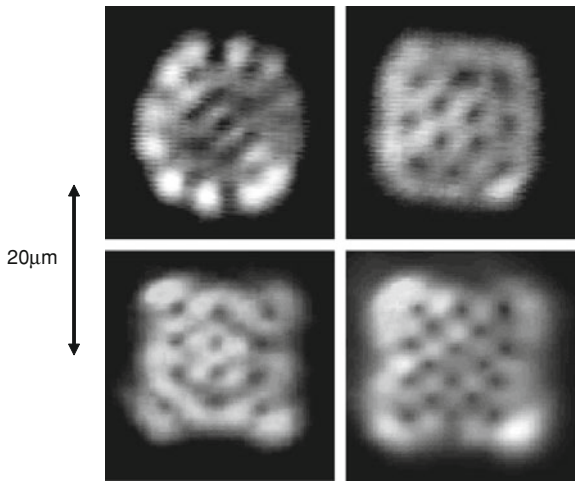

Fig. 14 Experimental near field lasing patterns of higher families and multi-mode, I > 30 mA

Injecting even higher current levels caused the complexity of the patterns to increase—exhibiting large regular arrays of optical vortices. Although multi wavelength patterns emerged eventually, the overall near-field intensity pattern preserved its highly regular "crystal-like" structure (Fig. 14), e.g. patterns with ordered arrays of dark hexagons, which were composed of 2–4 distinct patterns, each with a different wavelength.

The vortex array patterns emitted by the VCSELs were generated primarily by a single wavelength degenerated family or by a small number of families (2–3) that lase together. When lasing in multi-mode configuration, higher order families lased with shorter wavelength than the lower order families as predicted by the theoretical analysis (Sect. 2.2). Figure 16 depicts the spectrally resolved near filed of a multi-mode lasing configuration, exhibiting lower order families in longer wavelengths (left) and higher order families in shorter wavelengths (right). The spectral shift between the families is approximately 0.25 nm.

2.7 Discussion

Although the symmetry of the physical problem is essentially circular (even for the rectangular lasers because the thermally induced index is primarily circularly symmetric), the emitted patterns are not circularly symmetric. Clearly, this spontaneous symmetry breaking stems from the interaction between the GL modes belonging to a certain family through the nonlinear gain saturation mechanism (Figs. 15, 16).

The symmetries of the patterns which evolve in the VCSELS essentially reflect the symmetries of the relevant GL modes. In contrast to the well-studied problem of MI in 1D with periodic boundary conditions supporting two counter-propagating

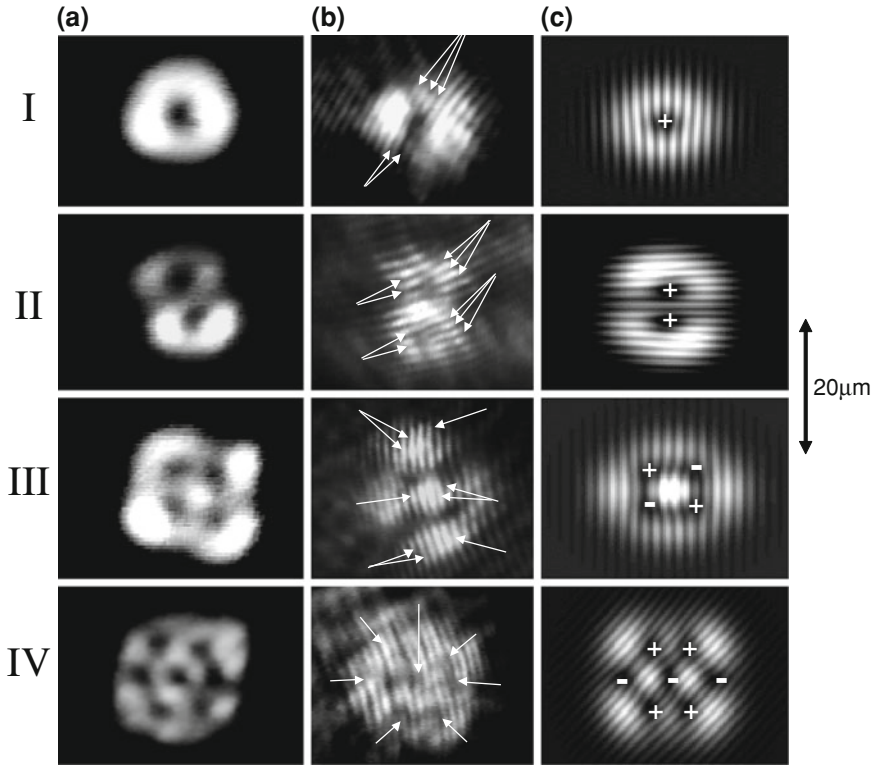

Fig. 15 Interference patterns. (**a**) The original experimental near-field patterns; (**b**) the experimental interference (**c**) the calculated interference. *I* single vortex; *II* "8"-like pattern; *III* "4-hole" pattern; *IV* "7-hole" pattern

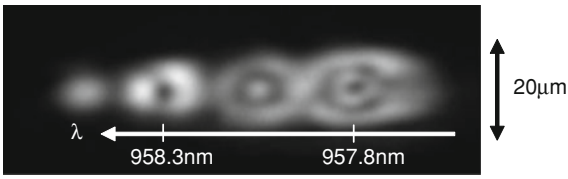

Fig. 16 Spectrally resolved near field in multi-mode lasing configuration

waves where MI tends to completely extinguish one of the solutions, here the stable patterns that evolve are specific superposition of several solutions. This is clearly an impact of the 2D geometry and the existence of more than two degenerate solutions.

It is worth noting the similarity of the observed arrays of vortices to the so-called "supervortices" patterns which were theoretically predicted in complex Ginzburg–Landau equation models with lattice trapping potentials [33, 34]. Despite the similarity, the origin of the formation of the vortex array is inherently different. While supervortices clearly exhibit the symmetry of the trapping

potential which serve as a perturbation, giving advantage to an appropriate symmetry, the vortex array observed in broad area VCSELs are self-inflicted in the sense that no external perturbation is required for their generation.

3 Pattern Formation in Ring Shaped VCSELs

Broad area VCSELs exhibit reach and interesting patterns but are complicated to analyze because of the diverse mechanisms which are involved in the pattern generation. This complexity necessitates the employment of numerical analysis approaches and makes it difficult to obtain clear understanding of the mechanisms which are responsible to the stability/instability of the lasing patterns.

In this section we study the dynamics of patterns formation in a ring shaped laser, which is basically a one-dimensional structure with no "hard" boundary conditions. These properties render the ring shaped laser an attractive configuration for investigating the basic evolution of nonlinear field patterns both experimentally and theoretically. We find that the mode switching of spatial patterns in lasers is related to an intrinsic nonlinear dynamical effect—the Modulation Instability (MI) [35, 36] and we derive the threshold conditions for the formation of the patterns. We also show how the MI mechanism explains the unidirectional evolution in the complexity of the observed patterns (increased complexity with larger pump level)—a property which is not explained completely by gain-loss considerations.

3.1 The Field Propagation Equation

Schematics of a ring shaped VCSEL is shown in Fig. 17. The structure of this VCSEL is very similar to the structure of the broad area VCSEL described in Sect. 2.6 except that its mirror is ring shaped.

The coordinates and geometry are defined in Fig. 18—z is the propagation coordinate, r is the radial coordinate and $x = \varphi \cdot \bar{r}$ is a linear coordinate along the perimeter of a circle with an average radius $\bar{r} = (r_1 + r_2)/2$. r_1 and r_2 are the internal and external radii of the ring and φ is the angular coordinate.

Under the assumption that the ring width is significantly smaller than its average perimeter, the radial and angular dependencies of the electrical field in the scalar approximation can be separated:

$$\hat{E}(x, r, z, t) = \mathrm{Re}\left[E(x, z) \cdot \bar{R}(r) \cdot e^{i(\beta z - \omega t)}\right] \tag{14}$$

where $\hat{E}$ is the total field, $\bar{R}$—the radial part of the field, $E(x,z)$—the azimuthal part, β—the propagation constant and ω is the angular frequency. In this model the

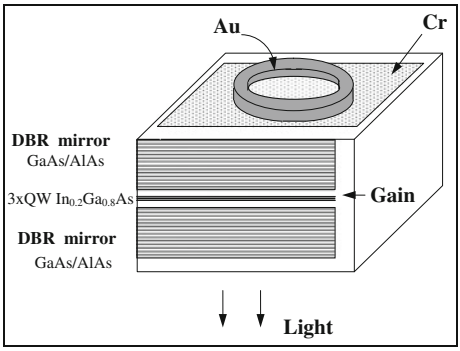

Fig. 17 Schematics of the structure of the VCSEL

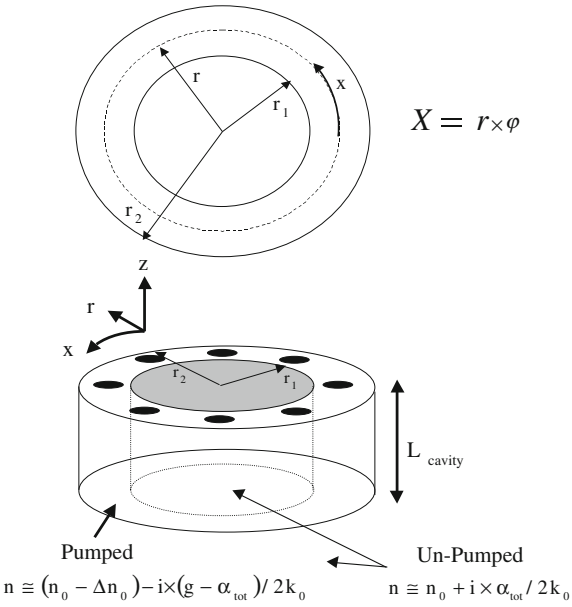

Fig. 18 The VCSEL geometry. The *black* spot schematically represent the lasing pattern (see also Fig. 23)

scalar approximation is used because the experimental observations indicated that the emission in both polarizations is identical and would merely change the effective saturation power of the medium but would not change the qualitative behavior of the model. Other effects that were neglected here such as diffusion, Bragg mirror bandwidth etc. may change the details of the analysis but yet a core of pattern switching mechanism is revealed here. Specifically, the impact of diffusion is highly important because it modifies the nature of the nonlinearity from local (negligible diffusion) to non-local (non-negligible diffusion). Essentially, diffusion causes the medium and a certain point to react to the whole field distribution in its vicinity (depending on the diffusion coefficient) and not only to the local intensity of the field at that point. Diffusion also eliminates (to some extent) the spatial-hole burning effect because it allows carrier transport to regimes where their concentration is low.

The electrical field *E(x, z)* is a periodical function—$E(x + 2\pi\bar{r}) = E(x)$. The evolution of the field inside the cavity is governed by the paraxial wave equation:

$$\frac{\partial^2 E(x,z)}{\partial x^2} + 2i\beta \cdot \frac{\partial E(x,z)}{\partial z} + \left[k_0^2 \cdot n_{\text{eff}}^2(x) - \beta^2\right] \cdot E(x,z) = 0 \tag{15}$$

The nonlinear effects within the laser medium—saturated gain and carrier induced index change, are expressed by the refractive index, n_{eff}:

$$n_{\text{eff}}^2(x) = n_0^2 + 2n_0\Gamma \cdot \Delta n(x,N) + i \cdot \frac{n_0}{k_0} \cdot (\alpha_{\text{tot}} - \Gamma \cdot g(x,N)) \tag{16}$$

where n_0 is the linear refractive index of the transparently pumped material, k_0 the wave number, Γ the confinement factor, α_{tot} the losses, g the gain and N is the carrier density. Δn is the change of the refractive index induced by the changes in the carrier density:

$$\Delta n(x,N) = -\frac{R}{2k_0} \cdot g(x,N) \tag{17}$$

where R is the anti-guiding factor. Substituting (16) and (17) into (15) yields:

$$\begin{aligned}\frac{\partial^2 E(x,z)}{\partial x^2} + 2i\beta \cdot \frac{\partial E(x,z)}{\partial z} - ik_0 n_0[\Gamma g(x,N) \cdot (1 - iR) - \alpha_{\text{tot}}] \cdot E(x,z) + \\ \left[k_0^2 \cdot n_0^2(x) - \beta^2\right] \cdot E(x,z) = 0\end{aligned} \tag{18}$$

In the paraxial limit: $\beta_r^2, \beta_x^2 \ll \beta^2 \Rightarrow \beta^2 = n_0^2 k_0^2 - \beta_r^2 - \beta_x^2 \approx n_0^2 k_0^2$ and therefore Eq. (18) can be simplified:

$$\frac{\partial E(x,z)}{\partial z} - \frac{i}{2k_0 n_0}\frac{\partial^2 E(x,z)}{\partial x^2} - \frac{1}{2}[\Gamma g(x,N) \cdot (1 - iR) - \alpha_{\text{tot}}] \cdot E(x,z) = 0 \tag{19}$$

Since the carrier lifetime ($\sim$1 ns) is much longer than the photons lifetime inside the cavity ($\sim$1 ps), the carrier dynamics can be adiabatically eliminated. Neglecting the diffusion, the equilibrium expression for the carrier density and the gain are:

$$\begin{aligned} N(x) - N_{tr} &= \frac{N_p - N_{\text{tr}}}{1 + |E|^2 \Big/ I_{\text{sat}}} \\ g(N,x) &= \frac{\Gamma\alpha \cdot (N_p - N_{\text{tr}})}{1 + |E|^2 \Big/ I_{\text{sat}}} = \frac{g_0(N_p)}{1 + |E|^2 \Big/ I_{\text{sat}}} \end{aligned} \tag{20}$$

where N_p/τ_{sp} is the pump rate, α the differential gain and $I_{\text{sat}} = h\nu/(\Gamma\alpha\tau_{\text{sp}})$ is the gain saturation intensity. By inserting n_{eff} into (19) we get an equation for the electrical field:

$$\frac{\partial E}{\partial z} - \frac{i}{2k_0 n_0}\frac{\partial^2 E}{\partial x^2} - \frac{1}{2}\left[\frac{g_0(1-iR)}{1+|E|^2\Big/I_{\text{sat}}} - \alpha_{\text{tot}}\right]E = 0 \tag{21}$$

Equation (21) is a complex Ginzburg–Landau (CGL) type nonlinear equation, but with a saturable nonlinearity rather than the conventional polynomial one. For simplicity, the following variables are introduced—$x' = k_0 x$, $z' = k_0 z/2n_0$ and $E(x,z) = E'(x',z') \cdot \sqrt{I_{\text{sat}}}$. Substituting them into (21) and dropping the primes yields a normalized equation for the field:

$$\frac{\partial E}{\partial z} - i\frac{\partial^2 E}{\partial x^2} - \frac{n_0}{k_0}\left[\frac{g_0(1-iR)}{1+|E|^2} - \alpha_{\text{tot}}\right]E = 0 \tag{22}$$

Equation (22) describes the propagation of a beam in a nonlinear medium that includes losses, saturating gain and saturating nonlinear refractive index. In the next section, the longitudinal steady-state solutions of (22) are presented and discussed.

3.2 Steady State Helical and Standing Wave Solutions

Finding analytical solutions to Eq. (22) is rather complicated and Due to the cyclic boundary condition in the angular coordinate the solution of (22) is quantized. A possible discrete set of solutions of the cyclic CGL equation is the right- and left-hand helical wave set $E = E_0 \exp[i(\pm k_m x - \eta z)]$ where:

$$E_0^2 = \frac{g_0}{\alpha_{tot}} - 1; \quad \eta = \frac{n_0 g_0 R}{k_0\left(1+E_0^2\right)} + k_m^2; \quad k_m = m \cdot 2\pi/(k_0 \cdot L) \quad m = 0, 1, 2\ldots \tag{23}$$

where L is the normalized ring perimeter. As these waves propagate along the cavity axis (z), they also rotate around the axis, resulting in a helical motion of the wave vector (see Fig. 4). The $m = 0$ case corresponds to a uniformly distributed field with no angular momentum. These solutions seem similar in structure to the solutions of a linear ring shaped waveguide, however the signature of the nonlinearity is the determination of the field amplitude for each pattern and the dependence of the propagation constant on the amplitude. Additional nonlinear effect—the coupling between counter propagating modes will be discussed.

Although the helical waves are exact solutions of the nonlinear wave Eq. (22) they are not the solutions that evolve spontaneously in ring shaped VCSELs. Both the experimental observations and the theoretical analysis of the following sections indicate that standing azimuthal wave patterns evolve in actual devices (see also Fig. 23). Since no closed form standing wave solutions to Eq. (22) are known (to the best of our knowledge) a superposition of two counter-propagating helical waves of the same order m was taken as an approximation:

$$E = A_0 \cos(2\pi m/L' \cdot x)\ ; \quad L' = k_0 L; \quad m = 1, 2, \ldots \tag{24}$$

Because Eq. (22) is nonlinear, the superposition of Eq. (24) is not a solution of (22) and thus the amplitude of the wave, A_0, cannot be extracted directly. This problem can be overtaken by arguing that in steady state the total energy of the wave is constant. $\Rightarrow \partial_z \oint_L |E|^2 dx = 0$. This condition imposes restrictions on the azimuthal profile of the field:

$$\frac{\partial}{\partial z}\int_0^{L'} |E|^2 dx = \int_0^{L'} \frac{g_0}{1+|E|^2}|E|^2 dx - \alpha_{tot}\int_0^{L'} |E|^2 dx = 0 \tag{25}$$

Inserting the ansatz (24) into (25) yields an equation for A_0. For low saturation levels the amplitude of the standing wave is given by: $A_0^2 \approx \frac{4}{3}\left(1 - \frac{\alpha_{tot}}{g_0}\right)$. The validity of this approximation was verified by comparing between the approximation and a numerically calculated transverse profile at two different gain levels (see Fig. 18 in the next section). An excellent match between the approximation and the exact solutions was found, indicating that the (24) is a good approximation to the exact solution of (22).

As mentioned in the introduction, the ring configuration is an excellent example for the failure of the "conventional" mode-switching criterion (modal gain-loss consideration). To exhibit the insignificant role of the modal gain-losses the overlap between the gain and the field intensity profiles for each mode were calculated. Eq. (24) was used to calculate the modal gain of each of the possible modes while the nth mode was lasing. The modal gain of the mth mode is given by:

$$g_m = \int_0^{L'} \frac{g_0}{1+|E_n|^2}|E_m|^2 dx = g_0 \int_0^{L'} \frac{\cos^2\left(\frac{2\pi}{L'}mx+\varphi\right)dx}{1+A_0^2\cos^2\left(\frac{2\pi}{L'}nx\right)} = \frac{g_0 L'}{2}\cdot\left[1+\sum_{q=1}^{\infty}(-1)^q \frac{A_0^{2q}}{2^{2q}}\binom{2q}{q}\right] +$$
$$g_0 L' \cdot \begin{cases} L\cdot\cos(2\varphi)\sum_{q=1}^{\infty}(-1)^{p+q}\frac{A_0^{2(p+q)}}{2^{2(p+q)}}\binom{2(p+q)}{q} & \mathrm{m=p\cdot n} \\ 0 & \text{else} \end{cases} \tag{26}$$

φ indicates a possible relative angular shift between the lasing mode, n, and the evolving mode, m. The resulting modal gain is independent on the lasing mode and is identical for all other possible modes that may evolve in the ring (with the exception of higher harmonics of the currently lasing mode—$m = n \cdot p$). The ring structure thus eliminates the influence of the gain-loss balance and enables the exposure of the fundamental mechanism for the spontaneous switching of the lasing pattern.

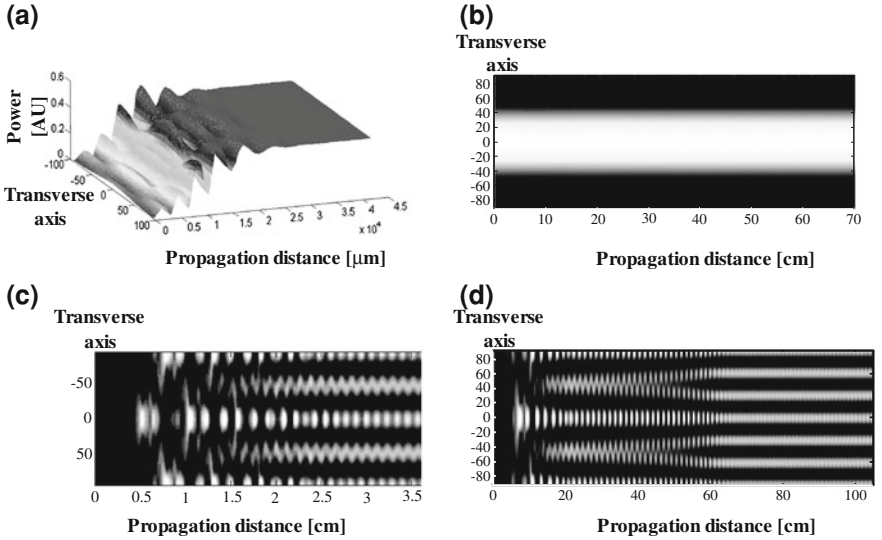

Fig. 19 Evolution of the electrical field at different pump rates—(**a**) $g_0 = 0.01004$ (**b**) $g_0 = 0.01005$ (**c**) $g_0 = 0.01008$ (**d**) $g_0 = 0.01012$. The VCSEL parameters are $R = 2$, $I_{sat} = 20$, $\alpha_{tot} = 0.01$, $n_0 = 1.45$ $L = 185\mu$ and $\lambda = 1\mu$

3.3 Numerical simulations

Equation (22) was also studied numerically to get the "exact" steady-state patterns that evolve in a ring shaped laser. The main objective of the numerical study was to examine the dynamical behavior of Eq. (22) and to verify that it exhibits the phenomenon under study (i.e. the on switching of higher modes). Another objective was to verify the validity of the approximations used in the analytical study.

The numerical study utilized 1 + 1 Dimension split-step Fourier Beam Propagation Method (BPM) [37] with 512 points for the transverse axis. Typical parameters of VCSELs were used for the simulations: $R = 2$, $I_{sat} = 20$, $\alpha_{tot} = 0.01$, $n_0 = 1.45$, $L = 185\mu$ and $\lambda = 1\mu$. The steady-state patterns were found by setting an initial transverse pattern and letting it propagate through the medium until a steady state was reached.

Figure 19 depicts the evolution of the electrical field for different pump rates ($g_0 = 0.01004$ to $g_0 = 0.01012$). In all cases, the initial conditions were identical. Figure 19a shows the evolution of a uniform field distribution ($m = 0$), Fig. 19b—a combination of uniform field and double lobed mode ($m = 0 + m = 1$), Fig. 19c—4 intensity lobes ($m = 2$) and Fig. 19d—6 intensity lobes ($m = 3$). The numerical results show that the solutions of Eq. (22) exhibit a consistent behavior with the experimentally observed patterns—higher spatial frequencies develop as the current is increased.

Figure 20 depicts comparison between the standing wave approximation (24) and the numerically calculated transverse profile at two different gain levels. There is an apparent excellent match between the approximation and the exact solutions, which indicates that the approximation describes well the patterns that evolve in the VCSEL.

3.4 Stability Analysis

Equation (26) indicates that simple modal gain-loss considerations cannot explain the unidirectional evolution of patterns with higher spatial frequencies in a ring shaped laser. In order to identify the mechanism responsible for this pattern switching, the stability characteristics of each helical wave solution were analyzed.

A small harmonic perturbation, with a spatial frequency Ω, is introduced to the mth solution which is assumed to be lasing:

$$E(x,z) = E_0 \cdot \exp[i(k_m x - \eta z)] \cdot \{1 + \mu(z) \cdot \exp[i(\Omega - k_m)\, x]\} \tag{27}$$

where μ is the amplitude of the perturbation, $\mu \ll 1$.

After perturbed solution (27) is substituted into the field Eq. (22), the equation is linearized in the perturbation μ. Most of the derivation of the evolution equation for the perturbation is straightforward except for the approximation of the nonlinearity:

$$\begin{aligned}\frac{1}{1+|E|^2} \approx \frac{1}{1+|E_0|^2 \cdot (\mu \exp[i\Omega x] + \mu^* \exp[-i\Omega x])} \approx \frac{1}{1+|E_0|^2} + \\ - \frac{|E_0|^2}{\left(1+|E_0|^2\right)^2} \cdot (\mu \exp[i\Omega x] + \mu^* \exp[-i\Omega x])\end{aligned} \tag{28}$$

Defining $\mu' = \mu \exp(i\Omega x)$ and $\gamma = n_0 \cdot \alpha_{\text{tot}}(1 - \alpha_{\text{tot}}/g_0)/k_0$ yields the following evolution equation for the perturbation (after dropping the primes):

$$\mu_z + i\mu\left[(\Omega - k_m)^2 + 2k_m(\Omega - k_m)\right] + \gamma(1 - iR) \cdot (\mu + \mu^*) = 0 \tag{29}$$

Separating the real and imaginary parts of (29) yields two real equations for $\mathrm{Re}(\mu)$ and for $\mathrm{Im}(\mu)$:

$$\begin{aligned}\mu_z^r - \left[(\Omega - k_m)^2 + 2k_m(\Omega - k_m)\right] \mu^i + 2\gamma\mu^r = 0 \\ \mu_z^i + \left[(\Omega - k_m)^2 + 2k_m(\Omega - k_m)\right] \mu^r - 2R\gamma\mu^i = 0\end{aligned} \tag{30}$$

where $\mu^r = \mathrm{Re}(\mu)$ and $\mu^i = \mathrm{Im}(\mu)$. Equations (30) are ODEs with constant coefficients which means that their solutions are either real or complex exponents—$\mu^A = \mu_0^A \exp(\xi z)$ where $A = r$ or i. The coefficient ξ can be either imaginary or

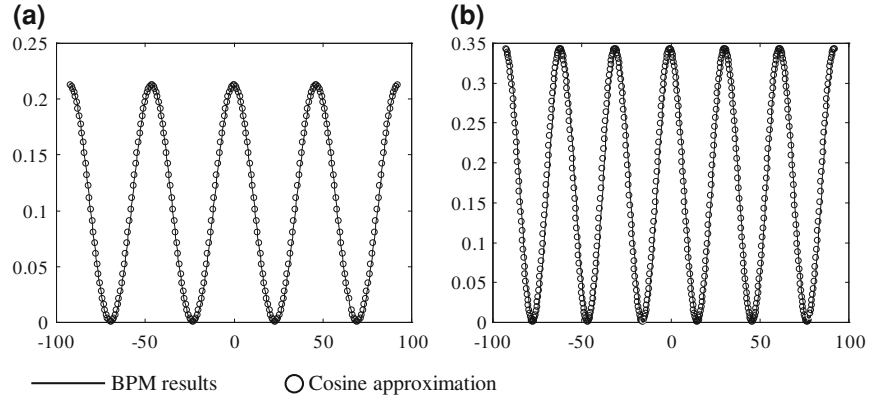

Fig. 20 Comparison between numerical results (solid *line*) and the standing wave approximation (*circles*). (**a**) $g_0 = 0.01008$ and (**b**) $g_0 = 0.01012$. The other parameters are as in Fig. 19

real. If ξ is imaginary or negative real, the perturbation μ does not increase as the field propagates and the lasing solution is, therefore, stable. If, however, ξ is positive and real, the perturbation increases exponentially as the field propagates and the lasing mode is not stable to harmonic perturbation with the spatial frequency Ω. Substituting μ^A into (30) yields a set of two homogeneous algebraic equations. In order for these equations to have non-trivial solutions, the determinant of the system must be zero, giving rise the following expressions for ξ:

$$\xi_{1,2} = -\gamma \pm \sqrt{\gamma^2 - \left(\Omega^2 - k_m^2\right)\left(\Omega^2 - k_m^2 - 2\gamma R\right)} \tag{31}$$

The growth coefficient ξ (denominated also as the MI gain), will be positive (indicating instability of the lasing solution) if the second term under the square root is negative i.e.:

$$k_m < \Omega < \sqrt{k_m^2 + 2\gamma R} \tag{32}$$

Perturbation with spatial frequencies Ω that are in the instability region (32) would grow exponentially and "destroy" the lasing mode.

It should be noted that the instability region of a lasing mode includes only spatial frequencies that are higher than k_m and that the region becomes wider for higher pumping levels. Figure 21 depicts the exponential growth rate (MI gain) of each spatial frequency while the first order mode ($m = 1$) is lasing. The instability region (blue solid line) is the frequency range where small perturbations will grow exponentially. However, because of the cyclic BC, only a discrete set of spatial frequencies can evolve in the ring (black arrows in Fig. 21). Spatial frequencies that are not part of this discrete set are suppressed and thus in the case of Fig. 21 the lasing mode is actually stable. For a higher pumping level, the instability region becomes wider and overlap with the spatial frequency characteristic of the

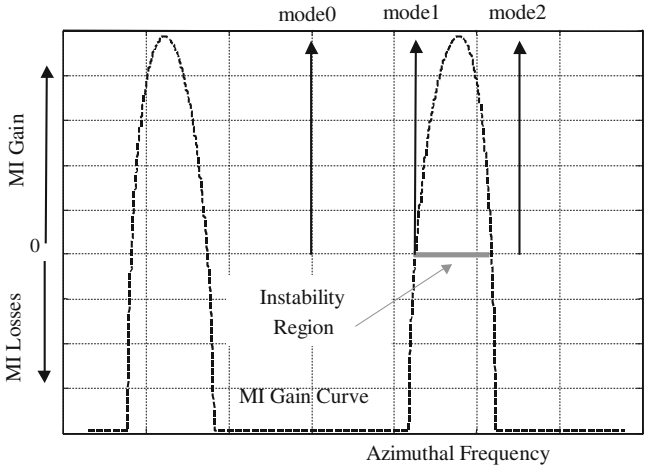

Fig. 21 MI gain curve for the $m = 1$ mode with L = 1, R = 2 and $\gamma = 2\pi^2$

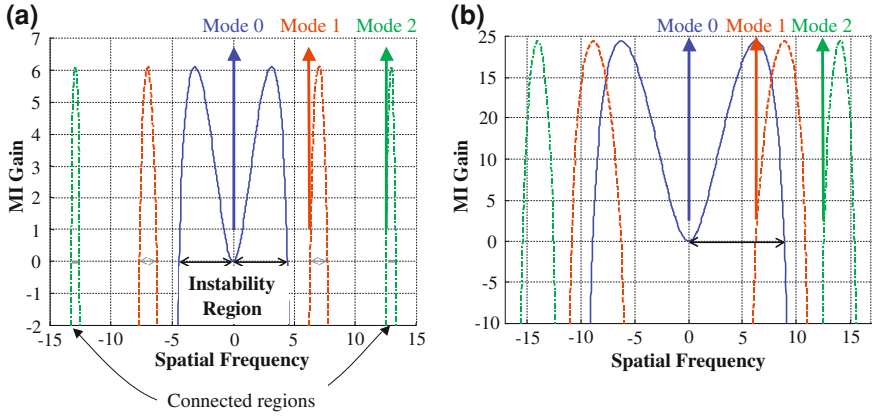

Fig. 22 Excitation of the first order mode while the fundamental mode is lasing. $L = 1$, $R = 2$ (**a**) $\gamma = \pi^2/2$; (**b**) $\gamma = 2\pi^2$

second order mode ($m = 2$). This results in the instability of the first order mode and the excitation of the second order mode.

The on switching of the first pattern ($m = 1$) from the azimutally constant emission ($m = 0$) lasing is depicted in Fig. 22. At low pumping level (Fig. 22a) the zero order mode is stable, but as the pumping level is increased (Fig. 22b), the first order mode is excited and starts to lase. For the same pumping conditions this first order mode is stable (see Fig. 22b) and would, therefore, continue to lase and would not excite other modes.

Another important phenomenon shown in Fig. 22 is the nonlinear coupling between counter propagating helical waves of the same order. The instability

region of each helical wave also includes its complex conjugated wave (Fig. 22b). As a result, when a helical wave is excited, its counter propagating wave is also excited and a standing wave evolves which matches the above discussion.

The stability analysis has identified the modulation instability (MI) as the fundamental mechanism that seeds the spontaneous pattern switching in ring shaped lasers. The analysis also yields closed form threshold conditions for the lasing of each mode—the excitation of a higher mode occurs when the instability region of the lasing mode overlaps with the frequency of the higher mode. The small signal gain level required for the lasing of the $m + 1$ mode is straightforwardly derived from (32):

$$g_0^{(m+1)} = \frac{\alpha_{\text{tot}}}{1 - \frac{2\pi^2 \cdot (2m+1)}{n_0 k_0 R L^2 \alpha_{\text{tot}}}} \tag{33}$$

For low injection level the relation between the spatial frequency of the mode (the value of m) and the modal threshold current is linear:

$$\frac{\mathrm{I}_{\text{th}}^{(m)}}{\mathrm{I}_{\text{th}}^{(0)}} = 1 + \frac{2\pi^2}{n_0 k_0 R L^2 G_{\text{th}}} \cdot (2m - 1) \tag{34}$$

where $\mathrm{I}_{\text{th}}^{(m)}$ is the threshold current of the mth mode, $\mathrm{I}_{\text{th}}^{(0)}$ is the conventional threshold current and G_{th} is the threshold gain level. Equation (34) was derived by first order Taylor expansion of the right hand term in (33) and expressing the small signal gain as a function of the injection current (20):

$$g_0 - \alpha_{\text{tot}} = \Gamma\alpha(N_P - N_{\text{th}}) = G_{\text{th}}\left(\frac{N_P}{N_{\text{th}}} - 1\right) = G_{\text{th}}\left(\frac{\mathrm{I}}{\mathrm{I}_{\text{th}}^{(0)}} - 1\right) \tag{35}$$

where N_{th} is the threshold carrier density.

However, as the current is increased and much higher order modes are excited, another interesting phenomenon comes into effect. For high modal index m, the right term of the denominator of (33) approaches unity and the required gain level, $g_0^{(m)}$, approaches infinity. This effect imposes a limit on the maximal modal index (or intensity lobes) that can evolve in the cavity, so for high pumping levels the number of intensity lobes saturates. This limit on the number of intensity lobes is given by:

$$N_{\max} = \frac{\mathrm{n}_0 k_0 \mathrm{R} \mathrm{L}^2 \alpha_{\text{tot}}}{2\pi^2} - 1 \tag{36}$$

The limit of the intensity lobe number is brought by the combined effect of MI and gain saturation (there is no limit on the lobe number when only the cubic approximation is taken, unless additional effect such as a limited spatial frequency span of the cavity mirrors is added). Note that the amplitude of the standing wave pattern according to (25) cannot exceed 4/3, due to the gain saturation. This draws

an upper limit on the width of the instability regions associated with each mode. In particular, since the instability region shrinks for higher order modes, there will be a mode that its instability region does not overlap with the consecutive higher mode. This mode will be therefore unconditionally stable upon current increase. It should be emphasized that patterns with even higher angular frequencies are in principle stable, but they would not evolve spontaneously as the current is increased.

In should be noted that the stability of the CGL solutions to perturbation has been studied extensively both for Kerr-like nonlinearity as wells as higher order polynomial terms, representing saturable nonlinearities [38–40]. Such nonlinearities can approximate the saturable nonlinearity of Eq. (21) for low pump levels and in general exhibit similar behavior in terms of increased pattern complexity with higher pump levels. However, these polynomial approximations do not exhibit the complexity saturation effect (36)—a phenomenon that was also observed experimentally as detailed in Sect. 3.5 below.

3.5 Experimental Results

Experiments were conducted on ring shaped VCSELs (28–40 μm in diameter) with similar structure to the lasers described in Sect. 2.6 but with ring shaped contact. The near-field patterns were examined at room temperature under pulsed operation.

The near field intensity patterns emitted from the VCSELs were imaged on a CCD camera (see Fig. 11) for various currents starting from threshold. A quasi uniform near field pattern was registered until the injected current was increased to $\sim$1.5 times the threshold current. Then the pattern switched to higher order modes characterized by multiple light lobes.

The first multi-lobe pattern that evolved in the 28 μm diameter ring VCSEL had eight lobes and in the 40 mm diameter VCSEL—16 lobes. As the current was increased, the number of lobes was increased but not continuously. At higher currents, however, a monotonic increase of the number of intensity lobes was observed. At the highest current levels the saturation effects was observed. Figure 23 depicts the near-field intensity pattern of 40 and 28 μm diameter lasers at various currents, from threshold up to three times threshold current.

Unlike the theoretical predictions, the first non-uniform patterns to appear had multiple intensity peaks rather than two ($m = 4$ for the 28 μm laser and $m = 8$ for the 40 μm laser). This was caused by the linear coupling between the radial and angular coordinates—patterns with higher azimuthal frequencies are narrower in the radial direction and have a better overlap with the radial gain profile. Patterns with low azimuthal frequencies have higher modal losses and are, therefore, not expected to lase.

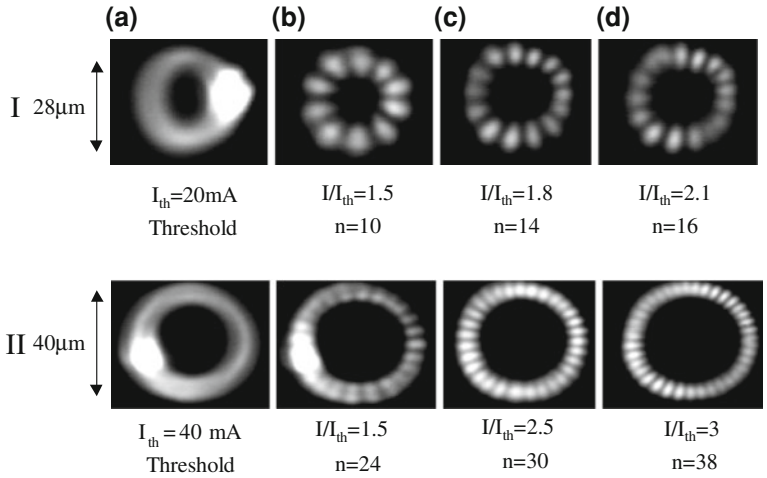

Fig. 23 Measured near field patterns of ring shaped VCSELs. *I* diameter of 28 μm, $I_{th} = 20$ mA (**a**) quasi-uniform distribution (**b**) 10 lobes (**c**) 14 lobes (**d**) 16 lobes; II –diameter of 40 μm, $I_{th} = 40$ mA (**a**) uniform distribution (**b**) 24 lobes (**c**) 30 lobes (**d**) 38 lobes

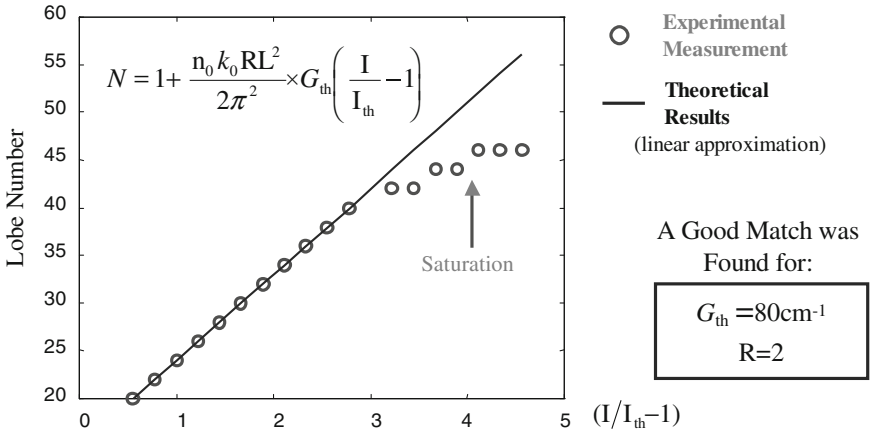

Fig. 24 Number of intensity lobes as a function of the injection current—experimental (*stars*) and theory (*solid line*)

Figure 24 shows a plot of the number of intensity lobes against the current for a 40 μm diameter ring. As predicted by the theory, at low injection levels the relation is linear but at higher pumping levels the number of intensity lobes saturates. The plot can be used to extract some of the parameters of the laser. For the tested device, a good match between the theory and the experiments was found for $G_{th}\text{cm}^{-1}$ assuming anti-guiding factor (R) of 2.

4 Summary and Conclusions

In this chapter, the evolution of the complex emission patterns in two-dimensional VCSELs was studied theoretically and experimentally.

We saw that broad area VCSELs emit complex patterns that are composed of regular arrays optical vortices that can be explained by transverse modes locking. The locking was possible due to the relatively small frequency spacing between specific modes of the cavity (almost wavelength degenerated). The theoretical results revealed that the only combinations obtainable by the model for the VCSEL nonlinear cavity were the same specific mode combinations that were observed experimentally. The similar patterns obtained previously for a completely different laser medium and laser size and geometry [17], reconfirm that the specific modal selection is a generic phenomenon rather than a specific one.

The on-switching of patterns in ring shaped semiconductor lasers were also studied. As for the broad area VCSELs, a unidirectional evolution of higher spatial frequencies was observed as the current is increased. This phenomenon was shown to stems from the dynamic effect of modulation instability and not merely by modal gain-loss considerations. It was shown both theoretically and experimentally that the number of intensity lobes increases linearly for low injection current level but saturates at high pumping levels.

Although the analysis shown here was performed for ring shaped VCSELs, the theory can explain pattern switching in various configurations of semiconductor lasers. However, in different kinds of geometries, additional linear/nonlinear mechanisms may be involved as well.

References

1. W.J. Firth, A.J. Scroggie, Spontaneous pattern formation in an absorptive system. Europhys. Lett. **26**, 521–526 (1994)
2. G. D'Alessandro, W.J. Firth, Hexagonal spatial patterns for a Kerr slice with a feedback mirror. Phys. Rev. A **46**, 537–548 (1992)
3. E. Pampaloni, S. Residori, F.T. Arecchi, Roll-hexagon transition in a Kerr-like experiment. Europhys. Lett. **24**, 647–652 (1993)
4. M. Orenstein, N.G. Stoffel, A.C. Von Lehmen, J.P. Harbison, L.T. Florez, Vertical-cavity surface-emitting InGaAs/GaAs lasers with planar lateral definition. Appl. Phys. Lett. **56**, 2384–2386 (1990)
5. J.R. Marciante, G.P. Agrawal, Nonlinear mechanisms of filamentation in broad-area semiconductor lasers. IEEE J. Quantum Electron. **32**, 590–596 (1996)
6. L. Djaloshinski, M. Orenstein, Coupling of concentric semiconductor microring lasers. Opt. Lett. **23**, 364–366 (1998)
7. J. Scheuer, M. Orenstein, Optical vortices crystals—spontaneous generation in nonlinear semiconductor microcavities. Science **285**, 230–233 (1999)
8. H. Adachihara, O. Hess, E. Abraham, P. Ru, J.V. Moloney, Spatiotemporal chaos in broad-area semiconductor lasers. J. Opt. Soc. Am B. **10**, 658–665 (1993)

9. R.J. Lang, D. Mehuys, A. Hardy, K.D. Dzurko, D.F. Welch, Spatial evolution of filaments in broad area diode laser amplifiers. Appl. Phys. Lett. **62**, 1209–1211 (1993)
10. V.N. Morozov, J.A. Neff, H. Zhou, Analysis of vertical-cavity surface-emitting laser multimode behavior. IEEE J. Quantum Electron. **33**, 980–988 (1997)
11. A. Valle, L. Pesquera, P. Rees and A. Shore, Transverse mode selection and light-current characteristics in index-guided VCSELs, Digest of the LEOS Summer Topical Meetings, pp. III 53–54 (1999)
12. B.J. Flanigan, J.E. Carroll, Mode selection in complex-coupled semiconductor DFB lasers. Electron. Lett. **31**, 977–979 (1995)
13. K.H. Hahn, M.R. Tan, Y.M. Houng, S.Y. Wang, Large area multitransverse-mode VCSELs for modal noise reduction in multimode fibre systems. Electron. Lett. **29**, 1482–1483 (1993)
14. K. Petermann, Nonlinear distortions and noise in optical communication systems due to fiber connectors. IEEE J. Quantum Electron. **16**, 761–770 (1980)
15. D. Michaelis, U. Peschel, F. Lederer, Multistable localized structures and superlattices in semiconductor optical resonators. Phys. Rev. A **56**, R3366–R3369 (1997)
16. W.J. Firth, A.J. Scroggie, G.S. McDonald, Hexagonal patterns in optical bistability. Phys. Rev. A **46**, R3609–R3612 (1992)
17. M. Brambilla, F. Battipede, L.A. Lugiato, V. Penna, F. Prati, C. Tamm, C.O. Weiss, Transverse laser patterns. I. Phase singularity crystals. Phys. Rev. A **43**, 5090–5113 (1991)
18. E. Pampaloni, S. Residori, F.T. Arecchi, Roll-hexagon transition in a Kerr-like experiment. Europhys. Lett. **24**, 647–652 (1993)
19. G.R. Hadley, K.L. Lear, M.E. Warren, K.D. Choquette, J.W. Scott, S.W. Corzine, Comprehensive numerical modeling of vertical-cavity surface-emitting lasers. IEEE J. Quantum Electron. **32**, 607–616 (1996)
20. J.W. Scott, R.S. Geels, S.W. Corzine, L.A. Coldern, Modeling temperature effects and spatial hole burning to optimize vertical-cavity surface-emitting laser performance. IEEE J. Quantum Electron. **29**, 1295 (1993)
21. G. Chen, A comparative study on the thermal characteristics of vertical-cavity surface-emitting lasers. J. Appl. Phys. **77**, 4251–4258 (1995)
22. D. T. Haar, H. Wergeland, Elements of thermodynamics. (Addison-Wesley Press, Reading)
23. N.K. Duta, W. Tu, G. Hasnain, G. Zydzik, Y.H. Wang, A.Y. Cho, Anomalous temporal response of gain guided surface emitting lasers. Electron. Lett. **27**, 208–210 (1991)
24. A.E. Siegman, *Lasers* (University Science Books, California, 1986)
25. C. Cohen-Tannoudji, B. Diu, F. Laloe, *Quantum mechanics* (Wiley-Interscience, New-York, 1977)
26. L.A. Lugiato, C. Oldano, L.M. Narducci, Cooperative frequency locking and stationary spatial structures in lasers. J. Opt. Soc. Am. B. **5**, 879–888 (1988)
27. E. Abramochkin, V. Volostnikov, Beam transformations and nontransformed beams. Opt. Comm. **83**, 123–135 (1991)
28. K. Staliunas, Stabilization of spatial solitons by gain diffusion. Phys. Rev. A., **61**, 053813-1–053813-6 (2000)
29. L.A. Coldern, S.W. Corzine, *Diode lasers and photonic integrated circuits* (Wiley-Interscience, New-York, 1995)
30. H. Yu, H. Zhang, Z. Wang, J. Wang, Z. Pan, S. Zhuang, D. Tang, Experimental observation of optical vortex in self-frequency-doubling generation. Appl. Phys. Lett. **99**, 241102 (2011)
31. K. Otsuka1, S. Chu, Generation of vortex array beams from a thin-slice solid-state laser with shaped wide-aperture laser-diode pumping. Opt. Lett. **34**, 10 (2009)
32. P. Coulet, L. Gil, F. Rocca, Optical vortices. Optics Commun. **73**, 403–408 (1989)
33. H. Sakaguchi1, B. A. Malomed, Higher-order vortex solitons, multipoles, and supervortices on a square optical lattice. Europhys. Lett. **72**, 698 (2005)
34. R. Driben, B.A. Malomed, Stabilization of two-dimensional solitons and vortices against supercritical collapse by lattice potentials. Eur. Phys. J. D **50**, 317–323 (2008)
35. T.S. Misirpashaev, C.W.J. Beenakker, Lasing threshold and mode competition in chaotic cavities. Phys. Rev. A **57**, 2041–2045 (1998)

36. J. Scheuer and M. Orenstein, Nonlinear switching and modulation instability of wave patterns in ring shaped VCSELs. J. Opt. Soc. Am. B, **19**. 2384 (2002)
37. G.P. Agrawal, *Nonlinear fiber optics* (Academic Press Inc., San Diego, 1989)
38. A. Mohamadou1, B. E. Ayissi, T. C. Kofané, Instability criteria and pattern formation in the complex Ginzburg-Landau equation with higher-order terms, Phys. Rev. E. **74**, 046604 (2006)
39. G.H.M. van Tartwijk, G.P. Agrawa, Maxwell–Bloch dynamics and modulation instabilities in fiber lasers and amplifiers. J. Opt. Soc. Am. B. **14**, 2618 (1997)
40. Y.J. He, H.H. Fan, J.W. Dong, H.Z. Wang, Self-trapped spatiotemporal necklace-ring solitons in the Ginzburg-Landau equation. Phys. Rev. E **74**, 016611 (2006)

Sub-Wavelength Plasmonic Solitons in 1D and 2D Arrays of Coupled Metallic Nanowires

F. Ye, D. Mihalache and N. C. Panoiu

Abstract In this chapter, we describe a very promising approach to achieve deep sub-wavelength confinement of the optical field guided by plasmonic nanostructures. In the plasmonic nanostructures investigated in our review, namely, one-dimensional (1D) and two-dimensional (2D) arrays of closely spaced parallel metallic nanowires embedded in an optical medium with Kerr nonlinearity, the optical nonlinearity induced by the evanescent component of the guided modes of the nanowires exactly balances the discrete diffraction due to the optical coupling among neighboring metallic nanowires. As a result, nonlinear optical modes, called plasmonic lattice solitons (PLSs), are formed in the plasmonic array. Because the radius of the nanowires and their separation distance could be much smaller than the operating wavelength the size of the PLSs can be deep in the subwavelength regime. We present fundamental (vorticityless) PLSs in both 1D and 2D plasmonic arrays, and also vortical PLSs in 2D arrays, in both focusing and defocusing nonlinear media. We demonstrate that the spatial extent of fundamental and vortical PLSs could be in the deep-subwavelength regime under experimental accessible conditions. Moreover, their existence, stability, and spatial confinement are studied in detail. Our analysis employs a model based on the coupled-mode theory as well as the full set of Maxwell equations, and shows that the predictions

F. Ye (✉)
Department of Physics, The State Key Laboratory on Fiber Optic Local Area Communication Networks and Advanced Optical Communication Systems, Shanghai Jiao Tong University, 200240 Shanghai, China
e-mail: fangweiye@sjtu.edu.cn

D. Mihalache
Department of Theoretical Physics, "Horia Hulubei" National Institute for Physics and Nuclear Engineering, 077125 Magurele-Bucharest, Romania

N. C. Panoiu
Department of Electronic and Electrical Engineering, University College London, Torrington Place, London, WC1E 7JE, UK

Progress Optical Sci., Photonics (2013): 357–375
DOI: 10.1007/10091_2012_5

Published Online: 22 August 2012

of the two models are in excellent agreement for relatively large nanowires separations. We expect that these nonlinear plasmonic modes have important applications to subwavelength nanophotonics. In particular, we demonstrate that the subwavelength PLSs can be used to optically manipulate with nanometer accuracy the power flow in ultra-compact photonic devices.

1 Introduction

The downscaling of photonic devices for confining and manipulating optical energy at the nanoscale is one of the major challenges of nanophotonics [1]. When the size of conventional optical circuits is reduced to nanoscale, the spatial confinement of light is inherently limited by diffraction. One recently proposed approach to overcome this limitation is to use surface plasmon polaritons (SPPs) [2, 3]. In particular, by using SPP modes of metallic nanowires [4], chains of resonantly coupled metallic nanoparticles [5, 6], tapered plasmonic waveguides [7, 8], or cylindrical metallic gratings [9, 10] one can spatially confine and guide optical energy over distances much smaller than the wavelength. Also, in a recent work [11] a perturbative theory for modeling of nonlinear propagation in rod waveguides with subwavelength core radii was developed and surface-induced nonlinearity enhancement in metalic, dielectric and semiconductor subwavelength rod waveguides was investigated in detail. These basic guiding nanostructures can be assembled in more complex plasmonic systems, such as Y-splitters, Mach-Zehnder interferometers, and waveguide-ring resonators [12]. Despite these promising developments, there remains a basic challenge that one has yet to overcome in order to fully exploit the technological potential of plasmonic devices: they must provide the critical functionality of all-optic active control of light at nanoscale. Because of the strong enhancement of the field induced by the excitation of SPPs, and consequently the increased optical nonlinearity, SPPs are particularly suited for providing this functionality. While basic nonlinear optical processes have been demonstrated in a variety of plasmonic nanostructures, *e.g.*, optical limiting and self-phase modulation in chains of structured nanoparticles [13] or second-harmonic generation in nanostructured metallic films [14, 15], the physical constraints imposed by large in-plane extent of the optical field and out-of-plane operation of some of these devices preclude their integration in ultra-compact plasmonic systems.

In this Chapter, we review the results of our recent work pertaining to a very promising approach to achieve subwavelength confinement of the optical field guided by plasmonic nanostructures, an approach based on a new type of nonlinear optical modes, which we called *plasmonic lattice solitons* (PLSs). In the proposed plasmonic nanostructures, which consist of one- or two-dimensional (1D, 2D) arrays of closely spaced parallel metallic nanowires embedded in a nonlinear optical medium, the optical nonlinearity induced by the field of the guiding modes

of the nanowires compensates the discrete diffraction due to the optical coupling among the nanowires. As a result, nonlinear collective modes, also called plasmonic lattice solitons, are formed in the plasmonic arrays. Because the radius of the nanowires and their separation distance are much smaller than the operating wavelength, the spatial width of the PLSs can be significantly smaller than the wavelength. Importantly, this remarkable property of PLSs cannot be achieved by using dielectric waveguide arrays, which also support discrete solitons [16–20], as the transverse size of such waveguides is comparable or larger than the wavelength.

The Chapter is organized as follows. In the next section we derive the theoretical model which describes the dynamics of the plasmonic field in 1D and 2D arrays of metallic nanowires. This general model is used then in Sects. 3 and 4 to investigate the physical properties of PLSs that are formed in 1D and 2D plasmonic arrays, respectively. Then, in Sect. 5, we compare the results obtained by using to alternative methods that can be employed to described the light propagation in plasmonic arrays, namely, the coupled-mode theory (CMT) and the full set of three-dimensional (3D) Maxwell equations (ME). Finally, the main results and conclusions are summarized in Sect. 6.

2 Theoretical Model for Light Propagation in Plasmonic Arrays

Our analysis of the dynamics of PLSs is based on an extension to the nonlinear case of a coupled-mode theory, which captures the full vectorial character of the interacting modes of the metallic nanowires [21]. This fully vectorial approach to the description of the PLSs, first introduced in Ref. [22], is essential for a rigorous analysis of their physical properties since the electric field of the modes of metallic nanowires has a large longitudinal component and therefore the optical modes cannot be described by scalar functions. Moreover, this vectorial analysis of the PLSs applies to the general case of optical systems with complex dielectric constant and as such it fully accounts for the losses in the nanowires. In particular, we use the Drude model for the dielectric constant of the metal,

$$\epsilon_m(\omega) = 1 - \frac{\omega_p^2}{\omega(\omega + i\nu)}, \tag{1}$$

where ω is the frequency, ω_p is the plasma frequency and ν is the damping frequency. Note that this assumption does not restrict the generality of our analysis as in order to describe the PLSs one only requires the value of the dielectric constant of the metal at the operating frequency. In our calculations we considered that the metallic nanowires are made of Ag, for which $\omega_p = 13.7 \times 10^{15}$ rad/s and $\nu = 2.7 \times 10^{13}$ rad/s [23].

We consider first the nonlinear propagation of the plasmonic field in a 1D array of metallic nanowires, as it is schematically illustrated in Fig. 1. We start our analysis of the PLSs by expanding the total electric field $\mathbf{E}(\mathbf{r})$ and magnetic field $\mathbf{H}(\mathbf{r})$ in a superposition of the modes of a single nanowire, a standard approach within the CMT

$$\mathbf{E}_{\perp}(\mathbf{r}_{\perp}, z) = \sum_{n} \frac{a_n(z)}{\sqrt{P_n}} \mathbf{e}_{\perp}^{(n)}(\mathbf{r}_{\perp}), \tag{2a}$$

$$E_z(\mathbf{r}_{\perp}, z) = \sum_{n} \frac{a_n(z)\epsilon^{(n)}(\mathbf{r}_{\perp})}{\sqrt{P_n}\epsilon(\mathbf{r}_{\perp})} e_z^{(n)}(\mathbf{r}_{\perp}), \tag{2b}$$

$$\mathbf{H}(\mathbf{r}_{\perp}, z) = \sum_{n} \frac{a_n(z)}{\sqrt{P_n}} \mathbf{h}_{\perp}^{(n)}(\mathbf{r}_{\perp}), \tag{2c}$$

where $a_n(z)$ is the mode amplitude in the n-th nanowire (normalized so as it is measured in $\sqrt{\mathrm{W}}$) and depends only on the longitudinal coordinate, z, $\epsilon(\mathbf{r}_{\perp})$ and $\epsilon^{(n)}(\mathbf{r}_{\perp})$ are the dielectric constant of the plasmonic array and that of an isolated nanowire, respectively, and $\mathbf{e}^{(n)}(\mathbf{r}_{\perp})$ and $\mathbf{h}^{(n)}(\mathbf{r}_{\perp})$ are the electric and magnetic field components of the optical mode, respectively. Note that due to the longitudinal translational invariance of the plasmonic nanowires the electromagnetic field of the modes depends only on the transverse coordinate, $\mathbf{r}_{\perp}$. The optical modes are normalized such that

$$\frac{1}{4}\int_S [\mathbf{e}^{(n)} \times \mathbf{h}^{(m)*} + \mathbf{e}^{(m)*} \times \mathbf{h}^{(n)}] \cdot \hat{\mathbf{z}} dS = P_n \delta_{nm}, \tag{3}$$

where P_n is the optical power carried by the mode n. For simplicity, we assumed in the expansion (2) that the nanowires have only the fundamental TM mode ($h_z = 0$), whose non-vanishing field components, $e_r, e_z,$ and h_{ϕ}, depend only on the magnitude of the radial coordinate, $r_{\perp}$. These field components can be found analytically by solving the Maxwell equations, while the dispersion relation, given by the dependence of the complex propagation constant $\beta = \beta_r + i\beta_i$ on ω, can be determined by imposing continuity conditions on the tangent fields at the metal-dielectric interface. As illustrated in Fig. 1a, the large dielectric constant of metals, combined with the subwavelength transverse size of the nanowire, leads to a strong dependence of β on the wavelength, λ. This dependence also suggests that the propagation losses, which are proportional to β_i, can be significantly reduced by increasing λ.

To find the mode amplitudes, we start from the unconjugated form of the Lorentz reciprocity theorem [24],

$$\begin{aligned} &\frac{\partial}{\partial z}\int_S [\mathbf{E}_1(\mathbf{r}, \omega) \times \mathbf{H}_2(\mathbf{r}, \omega) - \mathbf{E}_2(\mathbf{r}, \omega) \times \mathbf{H}_1(\mathbf{r}, \omega)] \cdot \hat{\mathbf{z}} dS \\ &= i\omega \int_S [\epsilon_2(\mathbf{r}) - \epsilon_1(\mathbf{r})] \mathbf{E}_1(\mathbf{r}, \omega) \cdot \mathbf{E}_2(\mathbf{r}, \omega) dS, \end{aligned} \tag{4}$$

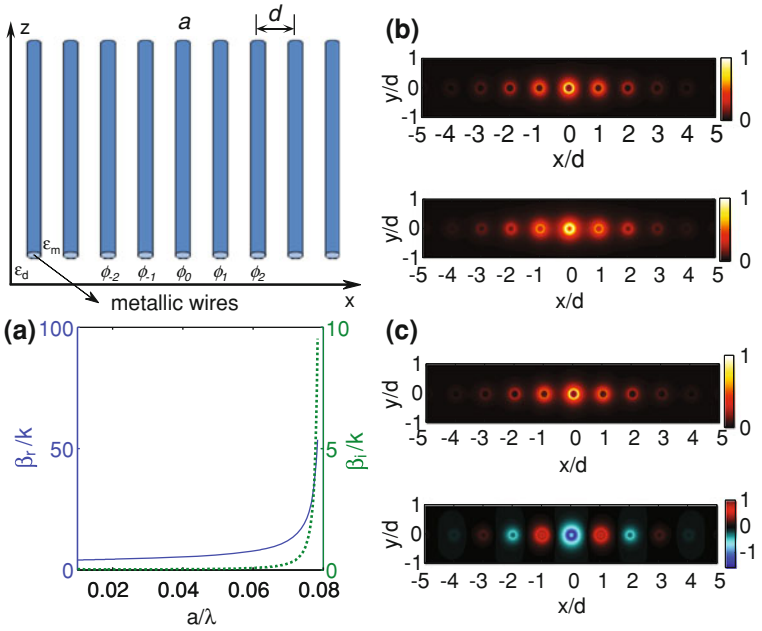

Fig. 1 Schematics of a 1D array of metallic nanowires with radius a and separation distance d (*top left panel*). **a** Real and imaginary parts of the propagation constant of the fundamental TM mode, β_r and β_i, respectively. Panels **b** and **c** show the transverse profile of the amplitude (*top*) and longitudinal component (*bottom*) of the electric field of unstaggered and staggered PLSs, respectively, for $\lambda = 1550$ nm and background index of refraction $n_b = 3.5$. In panels **b** and **c**, $\delta n_{\rm nl} = -0.05$ ($n_2 = -4 \times 10^{-18}\,{\rm m}^2/{\rm W}$) and $\delta n_{\rm nl} = 0.05$ ($n_2 = 4 \times 10^{-18}\,{\rm m}^2/{\rm W}$), respectively. The metallic nanowires have $a = 40$ nm and $d = 8a$.

where $(\mathbf{E}_1, \mathbf{H}_1)$ and $(\mathbf{E}_2, \mathbf{H}_2)$ are solutions of the Maxwell equations in the frequency domain, corresponding to the dielectric constants $\epsilon_1(\mathbf{r})$ and $\epsilon_2(\mathbf{r})$, respectively. As fields $(\mathbf{E}_1, \mathbf{H}_1)$ we choose the fields propagating in the plasmonic array, fields given by Eq. (2), whereas for the fields $(\mathbf{E}_2, \mathbf{H}_2)$ we choose a backward $(-z)$ propagating mode in the n-th nanowire. With this choice, the dielectric constants in the two cases are $\epsilon_1(\mathbf{r}) = \epsilon(\mathbf{r}_\perp) + \delta\epsilon_{\rm nl}(\mathbf{r})$ and $\epsilon_2(\mathbf{r}) = \epsilon^{(n)}(\mathbf{r}_\perp)$, where $\delta\epsilon_{\rm nl}(\mathbf{r})$ is the nonlinearly induced change in the dielectric constant of the background medium. Inserting these fields in Eq. (4) and performing some simple algebraic manipulations leads to the following system of coupled equations describing the mode amplitudes $a_n(z)$:

$$\left(i\frac{d}{dz} + \beta\right)\left(a_n + \frac{c_{n,n-1} + c_{n-1,n}}{2c_{nn}}a_{n-1} + \frac{c_{n,n+1} + c_{n+1,n}}{2c_{nn}}a_{n+1}\right) = \frac{1}{c_{nn}}\left(K_{nn}a_n + K_{n,n-1}a_{n-1} + K_{n,n+1}a_{n+1}\right) + \frac{\Gamma_{nn}}{c_{nn}}|a_n|^2 a_n. \tag{5}$$

In these equations the coupling constants are given by

$$c_{nm} = \frac{1}{2\sqrt{P_n P_m}} \int_S [\mathbf{e}^{(n)}(\mathbf{r}_\perp) \times \mathbf{h}^{(m)}(\mathbf{r}_\perp)] \cdot \hat{\mathbf{z}} dS, \tag{6a}$$

$$K_{nm} = \frac{\omega}{4\sqrt{P_n P_m}} \int_S \Delta\epsilon^{(n)}(\mathbf{r}_\perp) F_{nm}(\mathbf{r}_\perp) dS, \tag{6b}$$

where $\Delta\epsilon^{(n)}(\mathbf{r}_\perp) = \epsilon^{(n)}(\mathbf{r}_\perp) - \epsilon(\mathbf{r}_\perp)$ and $F_{nm}(\mathbf{r}_\perp) = \mathbf{e}_\perp^{(n)}(\mathbf{r}_\perp) \cdot \mathbf{e}_\perp^{(m)}(\mathbf{r}_\perp) - \frac{\epsilon^{(m)}}{\epsilon} e_z^{(n)}(\mathbf{r}_\perp) e_z^{(m)}(\mathbf{r}_\perp)$. Furthermore, the nonlinear coefficient that describes the nonlinear self-focusing or defocusing effects can be written as

$$\Gamma_{nn} = -\frac{\epsilon_0 n_b \omega n_2}{2P_n^2} \int_S F_{nn}(\mathbf{r}_\perp) \left[|\mathbf{e}_\perp^{(n)}(\mathbf{r}_\perp)|^2 + \left| \frac{\epsilon^{(n)}(\mathbf{r}_\perp)}{\epsilon(\mathbf{r}_\perp)} e_z^{(n)}(\mathbf{r}_\perp) \right|^2 \right] dS, \tag{7}$$

where n_b is the refractive index of the background and n_2 is the Kerr coefficient. Note that in deriving Eq. (5) we have neglected the nonlinear interaction among the nanowires, *i.e.*, we have considered that

$$\delta\epsilon_{\mathrm{nl}}(\mathbf{r}) = \frac{2\epsilon_0 n_b n_2}{P_n} \sum_n |a_n(z)|^2 \left[|\mathbf{e}_\perp^{(n)}(\mathbf{r}_\perp)|^2 + \left| \frac{\epsilon^{(n)}(\mathbf{r}_\perp)}{\epsilon(\mathbf{r}_\perp)} e_z^{(n)}(\mathbf{r}_\perp) \right|^2 \right]. \tag{8}$$

It should be noted that our derivation of the mathematical model describing the plasmonic field takes into account the 3D nature of the electromagnetic field, as our linear expansion of the total field is performed in terms of the full 3D optical modes of the nanowires. An alternative analysis of the propagation of the plasmonic field in a single nanowire, which accounted for the evolution of all six field components of the modes, has been performed recently [11] and led to an expression for the nonlinearity coefficient Γ_{nn} similar to that given in Eq. (11). Furthermore, in the derivation of the Eq. (5), the next-neighbor-coupling terms and the higher-order nonlinear effects have been omitted. However, the electromagnetic coupling effects between nanowires located at arbitrary positions in the array can be introduced by simply summing over all nanowire pairs in Eq. (5) and using the appropriate indices in Eq. (2), which define the coupling coefficients. As we will discuss in what follows, these considerations apply to the 2D case, too, namely, the nearest-neighbor interactions provide a good description for the dynamics of the plasmonic field in the nanowire array. The higher-order nonlinear mutual interactions between nanowires, on the other hand, can be safely neglected due to the exponential decay of the optical modes away from the nanowires. Further, our calculations show that if the distance between adjacent nanowires, d, is of the order of a few hundred nanometers $(c_{n,n\pm1} + c_{n\pm1,n})/c_{nn} < 1\%$ and thus the corresponding terms in Eq. (5) can be neglected. This conclusion is valid for both 1D and 2D plasmonic arrays.

If one now rescales the mode amplitudes, $a_n(z) = \sqrt{P_0}\phi_n(z) \exp[i(\beta - K_{nn}/c_{nn})z]$, with P_0 the power in the zeroth nanowire, the system (5) can be simplified as

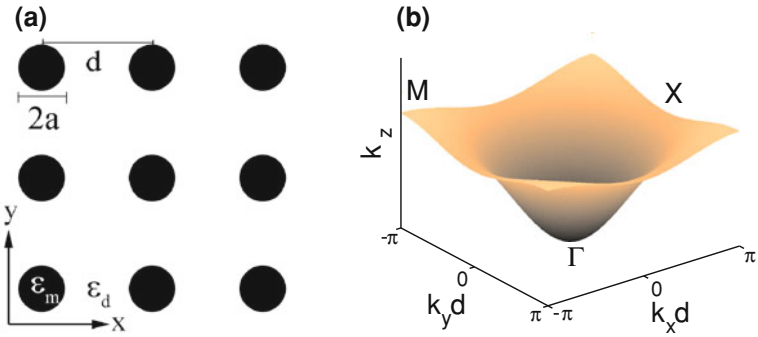

Fig. 2 **a** Schematic of a 2D square array ofmetallic nanowires. **b** The band structure predicted by the coupled mode theory. The radius of the nanowires is $a = 40\ nm$

$$i\frac{d\phi_n}{dz} + \kappa(\phi_{n-1} + \phi_{n+1}) + \gamma|\phi_n|^2\phi_n = 0, \tag{9}$$

where $\kappa = -K_{n,n\pm1}/c_{nn}$ and $\gamma = -P_0\Gamma_{nn}/c_{nn}$. Note that, the normalized nonlinearity coefficient, $\gamma > 0$ ($\gamma < 0$) for a medium with self-focusing (self-defocusing) Kerr response. The model (9) is the discrete nonlinear Schrödinger equation, which is known to have soliton solutions [16]. We emphasize that for our plasmonic array $\kappa < 0$, so that the linear dispersion relation, $k_z = 2\kappa\cos(k_x d)$, implies that anomalous (normal) diffraction occurs at $k_x = 0$ ($k_x = \pi/d$), which is opposite to the case of dielectric waveguide arrays. We note that a negative coupling coefficient also arises in all-dielectric Bragg waveguides [25–28] where the coupling mechanism is a radiative one; this is in contrast to the plasmonic arrays [22, 29–31] where the mode coupling is a purely evanescent one.

For the sake of simplicity of the presentation, we have discussed in detail the theoretical model that applies to the 1D plasmonic arrays. However, it should be noted that unlike the plasmonic crystals consisting of layered metallo-dielectric structures [29, 32], which can also supports PLSs, the plasmonic structures described here can readily be extended to 2D geometries [see Fig. 2a]. Importantly, in this case new types of nonlinear plasmonic modes, such as discrete plasmonic vortex solitons, should exist. Note that the generalization of the model to 2D arrays is straightforward. The 2D version of Eq. (9) is written as

$$\begin{aligned} &i\frac{d\phi_{m,n}}{dz} + \kappa(\phi_{m,n+1} + \phi_{m,n-1} + \phi_{m+1,n} + \phi_{m-1,n}) \\ &+ \mu(\phi_{m+1,n+1} + \phi_{m+1,n-1} + \phi_{m-1,n+1} + \phi_{m-1,n-1}) + \gamma|\phi_{m,n}|^2\phi_{m,n} = 0, \end{aligned} \tag{10}$$

where $\phi_{m,n}$ is the normalized mode amplitude in the nanowire indexed by the integers (m, n), κ and μ are the coupling coefficients between neighboring and next-neighboring nanowires, respectively. Similarly to the 1D case, $\kappa < 0$ and $\mu < 0$, so that the linear dispersion relation, $k_z = 2\kappa[\cos(k_x d) + \cos(k_y d)] +$

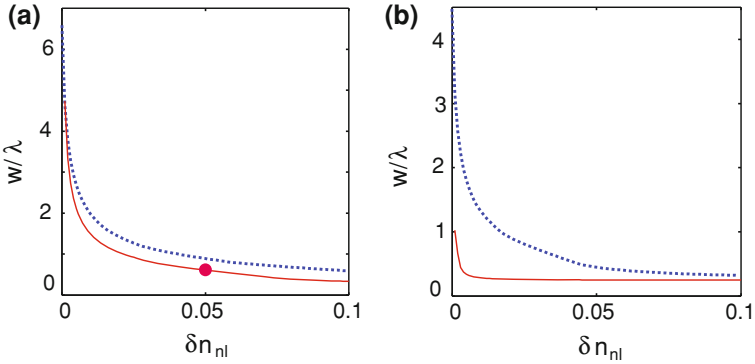

Fig. 3 Soliton width w versus the nonlinear index change δn_{nl}, calculated for plasmonic nanowires with radius $a = 40\,\mathrm{nm}$ and **a** $\lambda = 1550\,\mathrm{nm}, d = 8a$, and **b** $\lambda = 632\,\mathrm{nm}, d = 4a$. The solid and dotted curves correspond to $n_b = 3.5, n_2 = 4 \times 10^{-18}\,\mathrm{m}^2/\mathrm{W}$ and $n_b = 2.8$, $n_2 = 1.4 \times 10^{-18}\,\mathrm{m}^2/\mathrm{W}$, respectively.The red dot in **a** corresponds to the soliton in Fig. 1c

$4\mu\cos(k_x d)\cos(k_y d)$, forms a concave surface with anomalous diffraction occurring at the Γ symmetry point $(k_x = k_y = 0)$, while normal diffraction occurs at the M symmetry points $(k_x = k_y = \pm\pi/d)$ [see Fig. 2b]. In order to compare the strength of the coupling between neighboring nanowires with that of the coupling between next-neighboring nanowires, we give some typical values of the coupling coefficients, namely, $\kappa = (-9.02 - 0.52i) \times 10^4\,\mathrm{m}^{-1}$ and $\mu = (-1.48 - 0.12i) \times 10^4\,\mathrm{m}^{-1}$. These values correspond to nanowires with radius $a = 40\mathrm{nm}$ and separation distance $d = 8a$. Note that $|\kappa|$ is almost an order of magnitude larger than $|\mu|$, which illustrates the steep decrease of the field away from the nanowires. We also note that all the coefficients in Eq. (9) and Eq. (10) are complex, with the imaginary parts amounting for the Ohmic loss-induced dissipation. For the sake of completeness, in addition to the coupling coefficients given above, we also give the typical value of the effective nonlinear coefficient, $\gamma = (1.9 - 0.04i) \times 10^3\,\mathrm{m}^{-1}$, for a nonlinear material with $n_2 = 4 \times 10^{-18}\,\mathrm{m}^2/\mathrm{W}$. One can see that the imaginary parts are typically almost two orders of magnitude smaller than their real counterparts. From a mathematical point of view, the imaginary part of the nonlinearity has the same form as that of the two-photon absorption in semiconductor waveguides.

3 Plasmonic Lattice Solitons in 1D Arrays of Metallic Nanowires

We consider first the case of 1D plasmonic arrays. For this geometry, the soliton solutions of Eq. (9) are sought in the form $\phi_n(z) = u_n \exp(i\rho z)$, where the amplitudes u_n are independent of the coordinate z and ρ is the soliton wave number. In order to

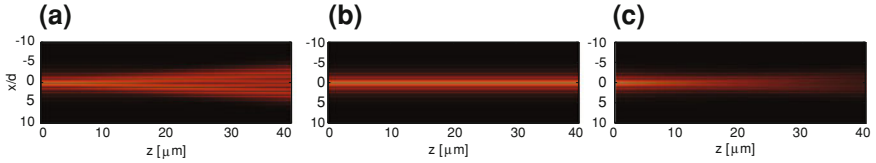

Fig. 4 **a** Linear and **b** nonlinear propagation of the plasmonic soliton in Fig. 1c in the lossless plasmonicarray with $n_b = 3.5, n_2 = 4 \times 10^{-18}\,\mathrm{m}^2/\mathrm{W}, \lambda = 1550\,\mathrm{nm}, a = 40\,\mathrm{nm}$, and $d = 8a$. **c** Propagation of the same plasmonic soliton in the lossy plasmonic array

determine the plasmonic solitons, this *ansatz* is inserted in Eq. (9) and the resulting system of equations is solved numerically by using a standard relaxation method. The corresponding amplitudes are then used to compute the fields of the PLSs. Following this procedure based on the CMT, we found that our plasmonic array supports two types of PLSs, *unstaggered* and *staggered* solitons. In the case of unstaggered PLSs the phase difference of the mode amplitudes in adjacent nanowires is equal to zero whereas in the case of staggered ones it is equal to π. The spatial profile of the field amplitude and longitudinal component of the field of unstaggered (staggered) PLSs corresponding to a nonlinear index change of $\delta n_{\mathrm{nl}} = -0.05$ $(\delta n_{\mathrm{nl}} = 0.05)$, with $\delta n_{\mathrm{nl}} = 2\delta\epsilon_{\mathrm{nl}}/(\epsilon_0 n_b)$, are shown in Fig. 1b and c. Note that due to the inverted linear dispersion relation, staggered solitons are formed in self-focusing media, whereas the unstaggered ones correspond to self-defocusing nonlinearity. This situation is opposite to the case of dielectric waveguide arrays [20]. Importantly, the calculated soliton full width at half maximum is $w \approx 0.6\lambda$, *i.e.*, the soliton has subwavelength extent. The dependence of the soliton width on δn_{nl} is presented in Fig. 3. As expected, this figure shows that the soliton width decreases with the strength of the induced nonlinearity and increases with the wavelength.

Figure 4 shows the propagation of a staggered PLS in the plasmonic array. It can be seen that in the lossless $(v = 0)$ linear propagation regime $(n_2 = 0)$, the plasmon field experiences significant discrete diffraction (see Fig. 4a). However, when the optical nonlinearity is taken into account, the plasmon field maintains its shape during propagation, which means that a PLS is formed. When the optical losses are included in our analysis, the absorption coefficient is $2\Im\mathrm{m}(\rho) = 910\,\mathrm{cm}^{-1}$, which corresponds to a decay length of 11μm. On the other hand, Fig. 4c illustrates that when both optical losses and the nonlinearity are included, the plasmon field of the PLS retains its initial width over a propagation distance of $\sim 20\mu$m. Thus, these calculations show that an experimental observation of subwavelength PLSs can be realized even without incorporating optical gain in the plasmonic nanostructure. On the other hand, a soliton-like propagation requires a gain of $g = 910\,\mathrm{cm}^{-1}$, which can be easily achieved in a practical experimental setting [33, 34].

As it is well known from soliton theory, the existence of optical solitons does not necessarily imply that they can be excited and observed in realistic experimental conditions. To be more specific, in a common experimental setting, solitons are excited from input Gaussian optical beams, which do not have the same spatial

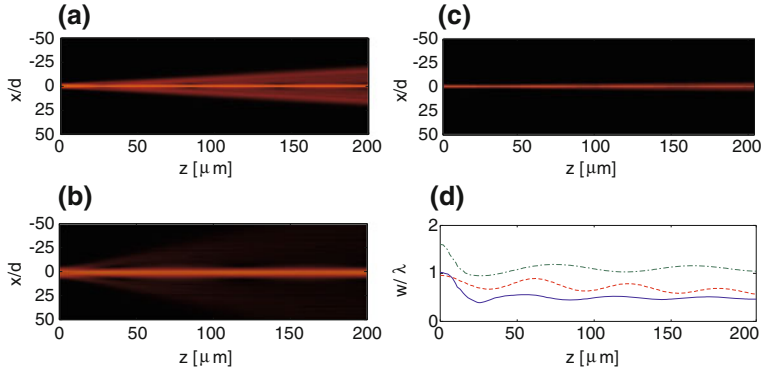

Fig. 5 Propagation of a Gaussian beam with $\lambda = 1550$ nm in a plasmonic array with: **a** $d = 6a$ **b** $d = 4a$ and **c** $d = 8a$. **d** The beamwidth versus the propagation distance z: the solid, dash-dotted, and dashed curves correspond to panels **a**, **b**, and **c**, respectively

profile of the actual soliton. We therefore investigate the excitation of PLSs from Gaussian beams whose width and amplitude are optimized so as to lead to the shortest *soliton formation length*, which is defined as the characteristic distance required for a beam to reshape itself into a soliton. The generic scenario of soliton formation is illustrated in Fig. 5. It shows that during a propagation distance of just a few tens of micrometers the input beam sheds off part of its energy as radiative waves, the remaining plasmon field evolving into a plasmonic soliton. During this latter transient stage the width of the beam presents a damped oscillatory evolution (see Fig. 5d). Importantly, Fig. 5d also shows that the soliton formation length is strongly dependent on the specific geometry of the plasmonic array. For example, for $a = 40$ nm and $\lambda = 1550$ nm, the shortest soliton formation length, of about 50 μm, is achieved for $d = 6a$.

In order to illustrate the technological potential of plasmonic solitons, *e.g.*, to subwavelength chip-level active nanodevices, we show that the dynamics of PLSs in the plasmonic array can be easily and accurately controlled *via* optical means. To this end, we launched into the plasmonic array a staggered PLS with an initial phase tilt, $\phi_n(0) = u_n \exp(ik_0 x)$, with k_0 being the transverse wave number. Figure 6 presents the power dependence of the dynamics of the PLS in the plasmonic array. Thus, as expected, at low input power, P_{in}, the PLS moves across the array, the transverse shift increasing with k_0. However, as P_{in} increases, the transverse shift of the plasmon field decreases, and, finally, for P_{in} exceeding a certain threshold value, the PLS is trapped at its initial location. Although a similar soliton dynamics have been observed in dielectric waveguide arrays [20], PLSs provide the critical functionality of all-optical control *with subwavelength precision* of the spatial confinement of the optical field (note that $d < \lambda/4$ for the plasmonic array in Fig. 6.

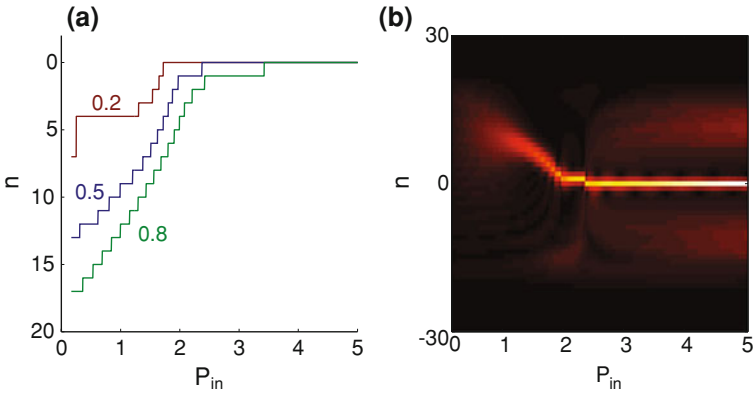

Fig. 6 **a** The location of the soliton peak amplitude at the output facet of a plasmonic array with length of 150 μm, $a = 0.03\lambda$, and $d = 8a$ versus the soliton power P_{in}, determined for different phase tilt $k_0(\lambda = 1550\,\text{nm})$. **b** The amplitude distribution of the output plasmon field versus P_{in}, calculated for $k_0 = 0.5$.The Kerr coefficient is $n_2 = 4 \times 10^{-18}\,\text{m}^2/\text{W}$

4 Plasmonic Lattice Solitons in 2D Arrays of Metallic Nanowires

By increasing the number of dimensions of plasmonic arrays from 1D to 2D, the complexity of PLSs increases, and as a result these higher-dimension plasmonic arrays support new species of plasmonic solitons that have no counterpart in lower-dimensional systems. These include, in addition to the fundamental 2D solitons, multipole PLSs and vortical PLSs, the latter ones being solitons with a topological phase of $m \times 2\pi$, along a closed trajectory around the phase singularity of the vortex soliton, m being a non-zero integer. These vortex solitons are important not only because they represent basic objects for study in nonlinear science, but also for their potential practical applications in quantum optics and optical trapping. Although vortex solitons have been studied in various nonlinear systems [35, 36], in all these cases their spatial extent was diffraction-limited, which distinguishes them from the plasmonic vortices studied in this section.

To study the plasmonic solitons formed in 2D arrays of metallic nanowires we follow an approach similar to that used in Sect. 3 to analyze the 1D PLSs. Thus, the soliton solutions to Eq. (10) are sought in the form $\phi_{m,n}(z) = u_{m,n}\exp(i\beta\kappa z)$, where again the amplitudes $u_{m,n}$ are independent of z and β is the soliton wave number (normalized by the coupling coefficient κ). The soliton is characterized by its power $P = \sum_{m,n}|\phi_{m,n}|^2$. This *ansatz* is inserted into Eq. (10) and the resulting system of equations is solved numerically by a standard relaxation method. The corresponding amplitudes are then used to reconstruct the fields of the PLSs. To quantify the transverse size of solitons we use the effective radius,

$$R = \left\{ \frac{\int_{-\infty}^{\infty}\int_{-\infty}^{\infty}\left[(x-x_0)^2+(y-y_0)^2\right]|\mathbf{E}|^2 dxdy}{\int_{-\infty}^{\infty}\int_{-\infty}^{\infty}|\mathbf{E}|^2 dxdy} \right\}^{\frac{1}{2}}, \tag{11}$$

where $x_0 = \iint_{-\infty}^{\infty} x|\mathbf{E}|^2 dxdy / \iint_{-\infty}^{\infty}|\mathbf{E}|^2 dxdy$ and $y_0 = \iint_{-\infty}^{\infty} y|\mathbf{E}|^2 dxdy / \iint_{-\infty}^{\infty}|\mathbf{E}|^2 dxdy$ are the coordinates of the center of the soliton.

We first search for fundamental solitons. As in the case of the 1D PLSs [22], we also find two types of 2D PLSs, *i.e.*, staggered and unstaggered solitons. The spatial profile of the amplitude and longitudinal field of unstaggered (staggered) PLSs corresponding to a nonlinear change of $\delta n_{\mathrm{nl}} = -0.05 (\delta n_{\mathrm{nl}} = 0.05)$ are shown in Fig. 7a, b, c and d. Similar to the case of PLSs formed in 1D plasmonic arrays, due to the inverted linear dispersion relation, staggered (unstaggered) solitons are formed in self-focusing (self-defocusing) media, which is opposite to the case of dielectric waveguide arrays. Note also that the 2D fundamental solitons have subwavelength size, the radius being $R = 0.35\,\lambda$ for the solitons shown in Fig. 7a, b and $R = 0.50\,\lambda$ for those in Fig. 7c, d. The dependence of soliton radius on the propagation constant β is presented in Fig. 7e. The plot shows that both staggered and unstaggered PLSs shrink monotonically as their wave number moves away from the band edges. This is because staggered and unstaggered PLSs originate from the extended Bloch modes at the symmetry points M and Γ, respectively, and thus when their wave number is close to the band edge, solitons have a large width. A larger change of nonlinear refractive index tunes the soliton mode deeper into the gap (see inset of Fig. 7e) and thus PLSs are increasingly smaller than the wavelength. Importantly, our calculations show that the power carried by such PLSs cannot be smaller than a threshold value, as can be seen from Fig. 7f. The nonmonotonic relationship $P = P(\beta)$ has important implications on soliton stability, as it will be shown below.

In addition to the fundamental PLSs, 2D plasmonic arrays also support a new type of PLSs, which has no counterpart in 1D systems, *i.e.*, vortex PLSs; these nonlinear modes belong to the class of *discrete vortices* [35]. Here we focus on off-site vortices, *i.e.*, compact vortex states whose singularity is located between lattice sites. Similarly to fundamental PLSs, vortex PLSs exist both in self-focusing (Fig. 8a, b) and self-defocusing media (Fig. 8c, d). As can be easily inferred from the phase profiles, the vortex has a topological charge equal to 1 (2D PLSs with topological charge 2 also exist, although they are not discussed here). Interestingly, the phase profile for PLSs in focusing media features a "staggered" pattern at the sites far away from the soliton center, which is a typical feature of "gap" vortices [36]. However, one should mention that the staggered vortex PLS resides at the semi-infinite gap (above the band) and thus is not a "gap" vortex. This is again a consequence of the inverted linear dispersion relation. The properties of vortex PLSs are summarized in Fig. 8e, f. Several differences from fundamental PLSs are observed. First, unlike the fundamental PLSs where their value of β can be very close to the band edges, vortex soliton can only exist in the gaps at a finite distance from the band edges. This is due to the fact that the vortex

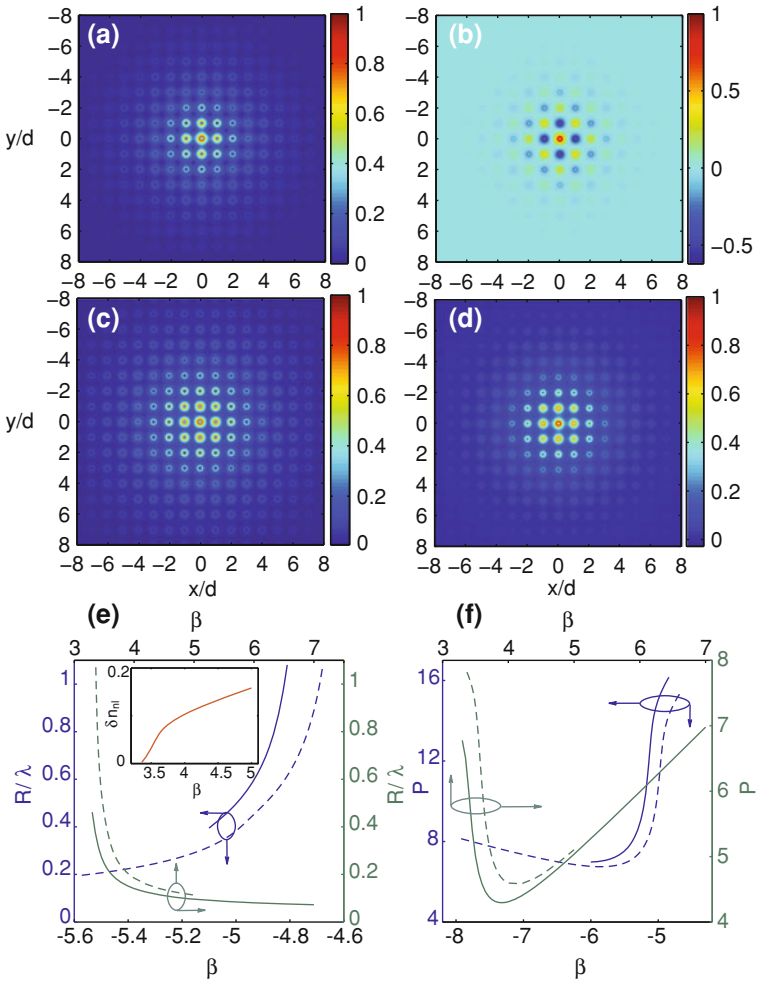

Fig. 7 2D fundamental plasmonic solitons. Panels **a** and **c** show the normalized electric field amplitude whereas the panels **b** and **d** show the longitudinal component,corresponding to focusing (*top panels*) and defocusing (*middle panels*) media. $\lambda = 1550\,\text{nm}, a = 40\,\text{nm}, d = 8a$. In **a** and **b** $\beta = 3.58, \delta n_{\text{nl}} = 0.05$ whereas in **c** and **d** $\beta = -4.89, \delta n_{\text{nl}} = -0.05$. In **e** and **f**, the radius R and power P, respectively, versus the normalized eigenvalue β. The solid and dashed lines stand for $d = 7a$ and $d = 8a$, respectively. In inset, δn_{nl} versus β for $d = 8a$, in a focusing medium. In all plots $a = 40\,\text{nm}$ and $\lambda = 1550\,\text{nm}$

mode is structurally very different from a Bloch mode of the linear plasmonic array. Secondly, as vortex PLSs possess four intensity maxima, vortex solitons always have a larger width as compared to that of the fundamental ones (under the same change of nonlinear refractive index). Therefore, forming a subwavelength vortex generally requires stronger nonlinearity. Nevertheless, we find that subwavelength vortex PLSs can be achieved under experimentally accessible

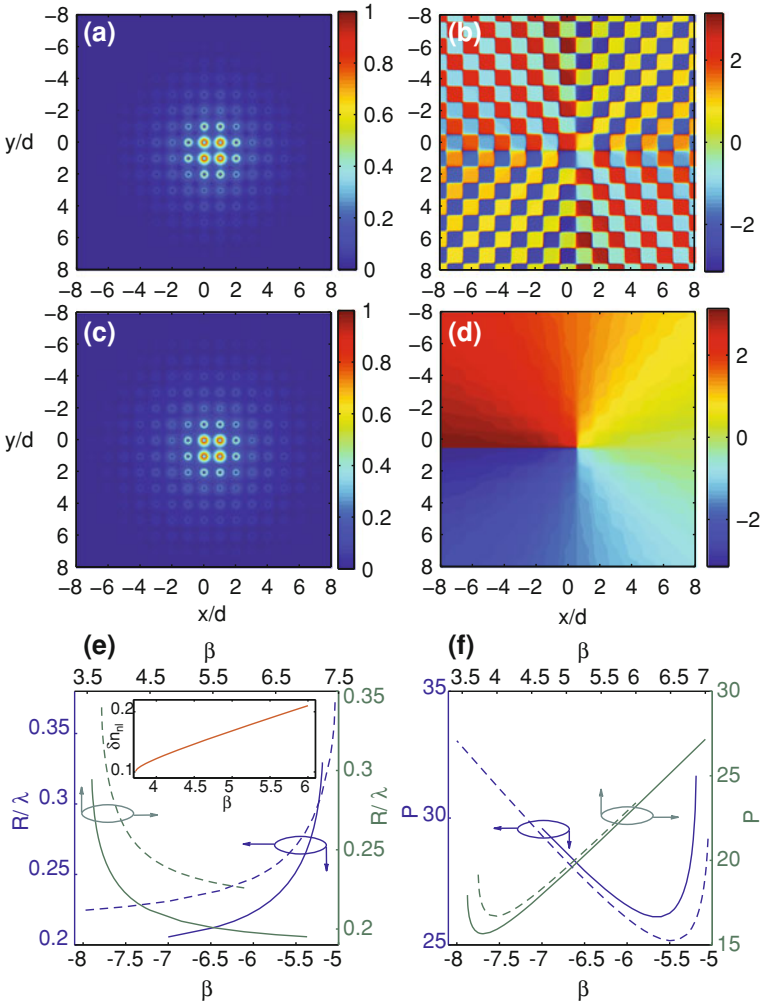

Fig. 8 2D vortex plasmonic solitons. Panels **a** and **c** show the normalized electric field amplitude whereas the panels **b** and **d** show the phase, corresponding to focusing (*top* panels) and defocusing (*middle* panels) nonlinear media. In **a** and **b** $\beta = 3.82, \delta n_{\mathrm{nl}} = 0.11$ whereas in **c** and **d** $\beta = -5.2, \delta n_{\mathrm{nl}} = -0.18$. In **e** and **f**, the radius R and power P, respectively, versus normalized eigenvalue β. The solid and dashed lines stand for $d = 7a$ and $d = 8a$, respectively. In inset, δn_{nl} versus β for $d = 8a$, in focusing medium. In all plots $a = 40\,\mathrm{nm}$ and $\lambda = 1550\,\mathrm{nm}$.

conditions. For example, the vortex presented in Fig. 8a, b has radius $R = 0.3\,\lambda$ requiring a nonlinear change of refractive index $\delta n_{\mathrm{nl}} = 0.11$. Note that an index change of ~ 0.14 was reported in Ref. [37]. Further, the size of PLSs can be significantly reduced if the operating wavelength is scaled down, thus the requirement for a strong nonlinear change of the refractive index can be relaxed.

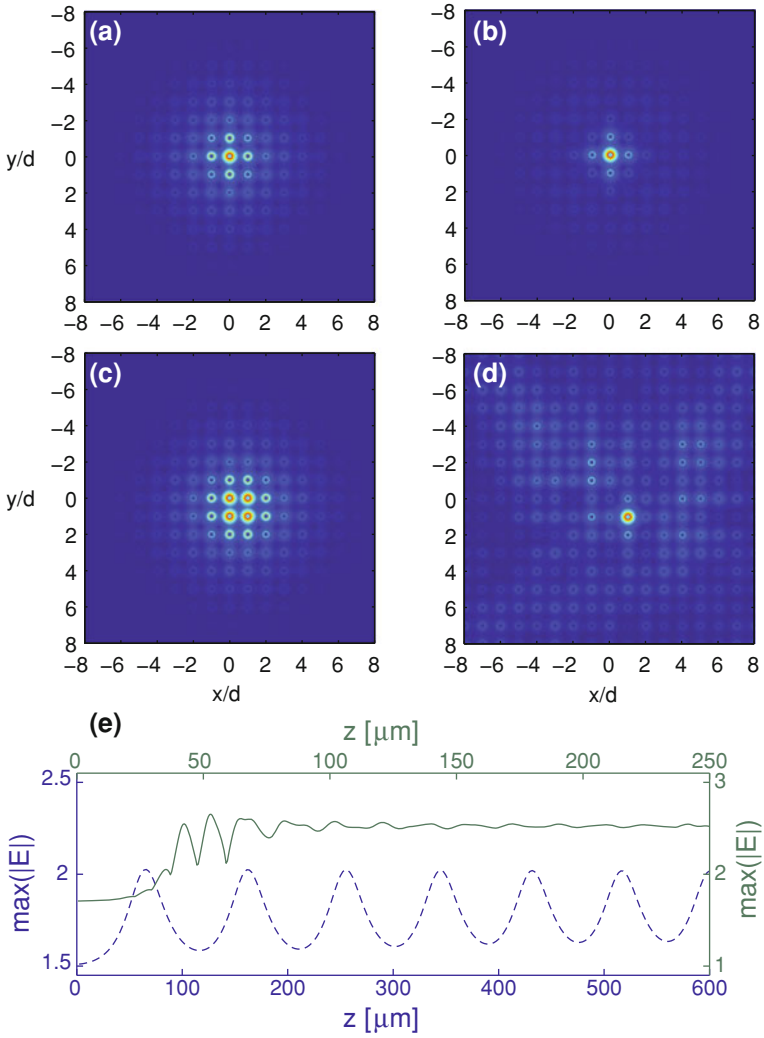

Fig. 9 Top and middle panels show the unstable propagation of a fundamental soliton with $\beta = 3.8$ and that of a vortex soliton with $\beta = 3.82$, respectively. The intensity profiles are calculated at $z = 0$(**a**, **c**), $z = 60\,\mu$m **b**, and $z = 90\,\mu$m **d**. **e** Variation of the maximum field amplitude versus propagation distance for the fundamental (dashed line) and vortex(solid line) solitons

Finally, we mention that as in the case of 2D fundamental solitons, vortex PLSs also feature power thresholds for their formation.

A relevant issue associated with the 2D PLSs is their stability. To address this issue, we integrate Eq. (10) by using a fourth-order Runge-Kutta method with the input condition being the stationary soliton solution plus a certain amount of

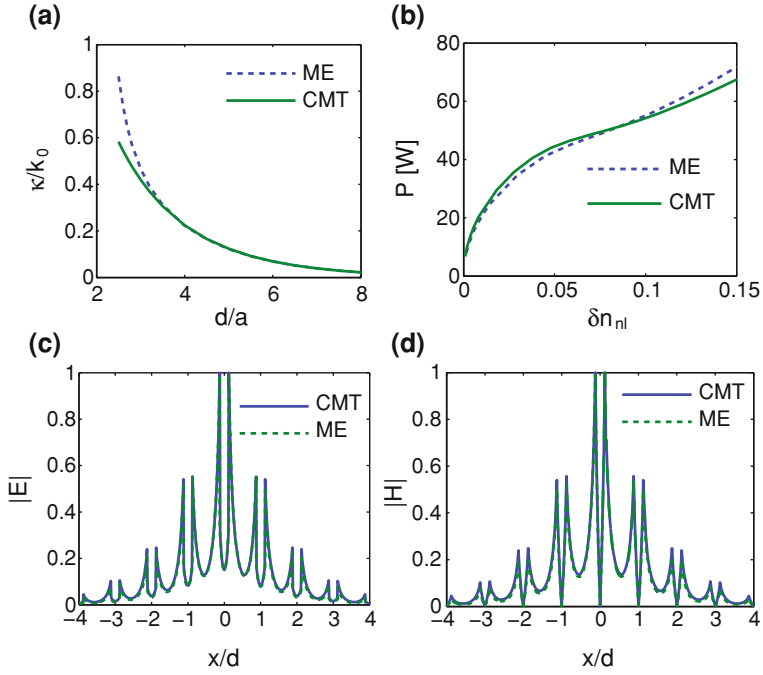

Fig. 10 Comparison between the results obtained by using the coupled mode theory (CMT) and full 3D Maxwell equations (ME). **a** The normalized coupling constant versus separation distance. **b** Soliton power versus the nonlinear change of the index of refraction. In **c** and **d**, normalized electric and magnetic field amplitudes, respectively, for soliton with $\delta n_{\mathrm{nl}} = 0.05$. In panels **b** through **d** $d = 8a$. In all plots, $a = 40\,\mathrm{nm}$ and $\lambda = 1550\,\mathrm{nm}$.

random noise. Our extensive numerical simulations show that the fundamental PLSs obey the Vakhitov-Kolokolov stability criterion, namely, the staggered (unstaggered) PLSs are stable when $dP/d\beta > 0 (dP/d\beta < 0)$ and are unstable otherwise. In the stability region, the soliton maintains its original shape over a sufficiently long distance while the initially added noise is rapidly eliminated as radiative waves. In contrast, unstable solitons tend to relax to stable ones with the same power and large oscillations are observed during propagation (Fig. 9a, b, e). The vortex can be also stable, although its stability region is more limited. An unstable propagation of vortex PLS is shown in Fig. 9c, d. The vortex quickly loses its screwed phase structure and decays into a fundamental PLS. Note that the stability domain of vortex PLSs increases at a shorter operating wavelength.

In addition to the fundamental and vortical PLSs discussed in this section, 2D plasmonic arrays also support a variety of multipole PLSs. These include dipoles, quadrupoles, and necklaces, which exist in both self-focusing and self-defocusing media. Such multipole states feature complex internal structure of the field amplitude and phase and represent basic constituents of the higher-order solitons. Equally important, they could also be of deep-subwavelengh nature and be

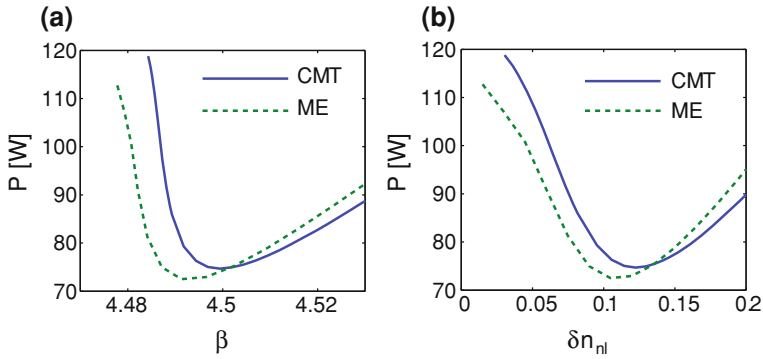

Fig. 11 Panels **a** and **b** show the soliton power versus the effective mode index and the nonlinear change of refractive index, respectively, for 2D fundamental solitons in a plasmonic array embedded in a focusing nonlinear material. Physical parameters are $a = 40\,\text{nm}, d = 8a, \lambda = 1550\,\text{nm}$, $n_b = 3.34,$ and $n_2 = 6.4 \times 10^{-20}\,\text{m}^2/\text{W}$

achievable in not too complex experimental settings. For a detailed discussion of their physical properties, stability domains as well as their dynamics, the reader is referred to [38].

5 Comparison Between Two Models: CMT Versus Maxwell Equations

All results presented here have been inferred from the models (9) and (10), which have been derived by using the CMT. Due to the strong field confinement in plasmonic nanostructures, one must determine the parameter range in which the CMT is valid as the conclusions established in the case of arrays of dielectric waveguides cannot be simply extrapolated to the case of plasmonic arrays. Therefore, in order to validate the predictions based on the CMT, we have used an alternative approach that amounted to solving the full set of 3D Maxwell equations. For this, we have used a commercially available software tool, COMSOL, which solves the ME that incorporate all the effects relevant to our problem, namely optical losses in the metallic regions of the plasmonic structures and optical Kerr nonlinearity of the background medium.

The results corresponding to the 1D case are summarized in Fig. 10. Thus, Fig. 10a presents a comparison of the coupling coefficients calculated by using the two alternative methods. It shows that the CMT provides an excellent description of the mode coupling for separation distance as small as $d \simeq 3.5a$. Equally important, Fig. 10b, which presents the soliton power dependence on the nonlinear change of the index of refraction, illustrates that the nonlinear optical effects are equally well described by the CMT as the linear ones. Thus, the two theoretical

models predict similar values for the soliton power, even for remarkably large values of the optical nonlinearity. These conclusions are further validated by the spatial profiles electromagnetic field of the 1D solitons. Thus, as illustrated in Fig. 10c, d, the two methods lead to almost identical results.

A good agreement between the predictions of the two methods is also observed in the case of PLSs in 2D arrays of metallic nanowires, although in this case the corresponding differences are larger than in the 1D case. Figure 11 plots the dependence of soliton power on the effective mode propagation constant and on the nonlinearly induced change of the index of refraction, as predicted by both theories. The observed agreement proves that our CMT provides an excellent theoretical framework for studying the light coupling and formation of nonlinear localized modes at nanoscale.

6 Conclusion

Before concluding, we note that the existence of subwavelength PLSs is not limited to arrays of metallic nanowires. They can be excited in any system of coupled plasmonic waveguides, as long as the transverse dimension of the waveguides is much smaller than the wavelength. Thus, one can consider arrays made of coupled wedge waveguides [12] or coupled chains of interacting metallic nanoparticles [13]. Moreover, the size of the plasmonic array, and implicitly the size of the PLSs, can be significantly reduced if one uses deeply scaled down nanostructures, such as metallic carbon nanotubes [39, 40], although in this case the theoretical model must be modified so as to incorporate the carriers dynamics.

In summary, we have demonstrated theoretically that subwavelength PLSs are formed in 1D and 2D arrays of metallic nanowires embedded into a host dielectric medium with Kerr nonlinearity. The excitation of PLSs from Gaussian beams has also been investigated and their potential use to all-optical nanodevices has been discussed. Our analysis employs a model based on the coupled-mode theory as well as full Maxwell equations, and shows that the predictions of the two models are in excellent agreement for relatively large regions of the parameter space. Importantly, the analysis presented here can be easily extended to other types of solitions, including spatio-temporal solitons, multi-color solitons, non-local solitons, and surface solitons. We expect, therefore, that these results will facilitate exciting new developments in nanophotonics and subwavelength optics.

Acknowledgments The work of F. Ye has been supprted by the National Natural Science Foundation of China, Grant No. 11104181. The work of N. C. Panoiu has been supported by the EPSRC, Grant No. EP/G030502/1.

References

1. W.L. Barnes, A. Dereux, T.W. Ebbesen, Nature (London) **424**, 824 (2003)
2. H. Raether, *Surface Plasmons on Smooth and Rough Surface and on Gratings* (Springer, Berlin, 1988)
3. A.V. Zayats, I.I. Smolyaninov, A.A. Maradudin, Phys. Rep. **408**, 131 (2005)
4. J. Takahara, S. Yamagishi, H. Taki, A. Morimoto, T. Kobayashi, Opt. Lett. **22**, 475 (1997)
5. M. Quinten, A. Leitner, J.R. Krenn, F.R. Aussenegg, Opt. Lett. **23**, 1331 (1998)
6. K. Li, M.I. Stockman, D.J. Bergman, Phys. Rev. Lett. **91**, 227402 (2003)
7. M.I. Stockman, Phys. Rev. Lett. **93**, 137404 (2004).
8. I.S. Maksymov, A.R. Davoyan, Y. S. Kivshar, Appl. Phys. Lettt. **99**, 083304 (2011)
9. S.A. Maier, S.R. Andrews, L. Martin-Moreno, F.J. Garcia-Vidal, Phys. Rev. Lett. **97**, 176805 (2006)
10. J.Y. Yan, L. Li, J. Xiao, Opt Express **20**, 1945 (2012)
11. A. Marini, R. Hartley, A.V. Gorbach, D.V. Skryabin, Phys. Rev. A**84**, 063839 (2011)
12. S.I. Bozhevolnyi, V.S. Volkov, E. Devaux, J.-Y. Laluet, T.W. Ebbesen, Nature (London) **440**, 508 (2006)
13. N. C. Panoiu, R. M. Osgood, Nano Lett. **4**, 2427 (2004)
14. W. Fan, S. Zhang, N.-C. Panoiu, A. Abdenour, S. Krishna, R. M. Osgood, K. J. Malloy, S. R. J. Brueck, Nano Lett. **6**, 1027 (2006)
15. J.A.H. van Nieuwstadt, M. Sandtke, R.H. Harmsen, F.B. Segerink, J.C. Prangsma, S. Enoch, Kuipers, Phys. Rev. Lett. **97**, 146102 (2006)
16. D. Christodoulides, R. Joseph, Opt. Lett. **13**, 794 (1988)
17. T. Peschel, U. Peschel, F. Lederer, Phys. Rev. E **57**, 1127 (1998)
18. N.C. Panoiu, R.M. Osgood, B.A. Malomed, Opt. Lett. **31**, 1097 (2006)
19. H.S. Eisenberg, Y. Silberberg, R. Morandotti, A.R. Boyd, J.S. Aitchison, Phys. Rev. Lett. **81**, 3383 (1998)
20. D.N. Christodoulides, F. Lederer, Y. Silberberg, Nature (London) **424**, 817 (2003).
21. S.L. Chuang, J Lightw. Technol. **LT-5**, 174 (1987)
22. F. Ye, D. Mihalache, B. Hu, N.C. Panoiu, Phys. Rev. Lett. **104**, 106802 (2010)
23. M.A. Ordal, R.J. Bell, R.W. Alexander, L.L. Long, M.R. Querry, Appl. Opt. **24**, 4493 (1985)
24. A.W. Snyder, J.D. Love, *Optical Waveguide Theory* (Chapman and Hall, London, 1983)
25. A. Szameit, T. Pertsch, S. Nolte, A. Tunnermann, F. Lederer, Phys. Rev. A**77**, 043804 (2008)
26. N.K. Efremidis, K. Hizanidis, Opt. Express **13**, 10571 (2005)
27. N.K. Efremidis, P. Zhang, Z. Chen, D.N. Christodoulides, C.E. Ruter, D. Kip, Phys. Rev. A**81**, 053817 (2010)
28. R. Iliew, C. Etrich, M. Augustin, E.B. Kley, S. Nolte, A. Tunnermann, F. Lederer, Phys. Status Sol. A **204**, 3689 (2007)
29. Y. Liu, G. Bartal, D.A. Genov, X. Zhang, Phys. Rev. Lett. **99**, 153901 (2007)
30. X. Fan, G.P. Wang, J.C.W. Lee, C.T. Chan, Phys. Rev. Lett. **97**, 073901 (2006)
31. F. Ye, D. Mihalache, B. Hu, N.C. Panoiu, Opt. Lett. **36**, 1179 (2010)
32. E. Feigenbaum, M. Orenstein, Opt. Lett. **32**, 674 (2007)
33. M.A. Noginov, V.A. Podolskiy, G. Zhu, M. Mayy, M. Bahoura, J.A. Adegoke, B.A. Ritzo, K. Reynolds, Opt. Express **16**, 1385 (2008)
34. S.M. Xiao, V. P. Drachev, A.V. Kildishev, X.J. Ni, U.K. Chettiar, H.K. Yuan, V.M. Shalaev, Nature (London) **466**, 735–738 (2010)
35. B.A. Malomed, P.G. Kevrekidis, Phys. Rev. E **64**, 026601 (2001)
36. E.A. Ostrovskaya, Y.S. Kivshar, Phys. Rev. Lett. **93**, 160405 (2004)
37. L. Brzozowski, E.H. Sargent, A.S. Thorpe, M. Extavour, Appl. Phys. Lett. **82**, 4429 (2003)
38. Y. Kou, F. Ye, X. Chen, Phys. Rev. A**84**, 033855 (2011).
39. G. Ya. Slepyan, S.A. Maksimenko, A. Lakhtakia, O. Yevtushenko, A.V. Gusakov, Phys. Rev. B**60**, 17136 (1999).
40. M.Y. Sfeir, F. Wang, L. Huang, C.-C. Chuang, J. Hone, S.P. O'Brien, T.F. Heinz, L.E. Brus, Science **306**, 1540 (2004)

From Coherent Modes to Turbulence and Granulation of Trapped Gases

V. S. Bagnato and V. I. Yukalov

Abstract The process of exciting the gas of trapped bosons from an equilibrium initial state to strongly nonequilibrium states is described as a procedure of symmetry restoration caused by external perturbations. Initially, the trapped gas is cooled down to such low temperatures, when practically all atoms are in Bose–Einstein condensed state, which implies the broken global gauge symmetry. Excitations are realized either by imposing external alternating fields, modulating the trapping potential and shaking the cloud of trapped atoms, or it can be done by varying atomic interactions by means of Feshbach resonance techniques. Gradually increasing the amount of energy pumped into the system, which is realized either by strengthening the modulation amplitude or by increasing the excitation time, produces a series of nonequilibrium states, with the growing fraction of atoms for which the gauge symmetry is restored. In this way, the initial equilibrium system, with the broken gauge symmetry and all atoms condensed, can be excited to the state, where all atoms are in the normal state, with completely restored gauge symmetry. In this process, the system, starting from the regular superfluid state, passes through the states of vortex superfluid, turbulent superfluid, heterophase granular fluid, to the state of normal chaotic fluid in turbulent regime. Both theoretical and experimental studies are presented.

V. S. Bagnato · V. I. Yukalov
Instituto de Fisica de São Calros, Universidade de São Paulo, CP 369, São Carlos, São Paulo 13560-970, Brazil

V. I. Yukalov (✉)
Bogolubov Laboratory of Theoretical Physics, Joint Institute for Nuclear Research, Dubna, Russia 141980
e-mail: yukalov@theor.jinr.ru

Progress Optical Sci., Photonics (2013): 377–401
DOI: 10.1007/10091_2012_14

Published Online: 17 August 2012

1 Introduction

Different thermodynamic phases are usually characterized by different symmetries. At the point of a phase transition, there occurs the change of system symmetry [1–3]. The observation of phase transitions can be done by slowly varying the system parameters, e.g., temperature, pressure, density, or some stationary external fields, so that the system practically always is in equilibrium.

Another possibility of observing phase transitions is to prepare a system in a nonequilibrium phase under the values of parameters favoring a different phase. Then the system, starting from one phase with a given symmetry, relaxes to the equilibrium phase with another symmetry, dynamically passing through the phase-transition line [4].

In the present paper, we suggest and study the third way of realizing phase transitions accompanied by symmetry changes. This way is opposite to the relaxation procedure. We can start from an equilibrium phase, with one type of symmetry, and then pump into the system energy by means of external alternating fields, so that to transfer the system into another state, with another symmetry type. We illustrate this idea by considering the system of trapped bosons. This system can be cooled down to very low temperatures below the Bose–Einstein condensation point, when all atoms pile down to the condensed state. The properties of these condensed atoms have been intensively studied both theoretically and experimentally, as can be inferred from the books [5–8] and reviews [9–20].

The Bose-condensed state is characterized by the global gauge symmetry breaking. Moreover, the latter is the necessary and sufficient condition for Bose–Einstein condensation [6, 15]. Acting on the system of trapped atoms by external alternating fields increases the system energy, which is similar to increasing the system temperature. The energy, pumped into the system, destroys the condensate, transferring atoms into uncondensed states. When the injected energy is very large, one should expect that the state can be reached where all condensate has been depleted, and the whole system is in the normal phase, with the restored gauge symmetry. This latter state will, of course, be nonequilibrium, being reached by subjecting the system with time-dependent alternating fields. The investigation of such a procedure of nonequilibrium transitions, going through several stages, is the aim of the present paper. We shall describe both theoretical as well as experimental peculiarities of this method. The main part of the paper summarizes the results of previous publications, while some experimental results, related to the granular state, are new.

2 Broken Gauge Symmetry

We consider a system of spinless bosons characterized by the field operators $\hat{\psi}(\mathbf{r}, t)$ satisfying Bose commutation relations. Here $\mathbf{r}$ is spatial variable and t is

time. In the equations below, for the compactness of notation, we often omit the time variable, assuming it but writing the field operator as $\hat{\psi}(\mathbf{r})$, when this does not lead to confusion. We keep in mind dilute Bose gas confined in a trap modelled by an external trapping potential $U = U(\mathbf{r}, t)$. Atomic interactions are described by the local potential

$$\Phi(\mathbf{r}) = \Phi_0 \delta(\mathbf{r}), \quad \Phi_0 \equiv 4\pi \frac{a_s}{m}, \tag{1}$$

where a_s is scattering length and m, atomic mass. The scattering length, for concreteness, is assumed to be positive. Generally, it could be negative, but then the number of atoms should be such that to avoid the collapse occurring for atoms with attractive interactions.

Here and in what follows, we shall use in the majority of equations, the system of units with the Planck and Boltzmann constants set to one ($\hbar = 1, k_B = 1$).

The external potential consists of two terms,

$$U(\mathbf{r}, t) = U(\mathbf{r}) + V(\mathbf{r}, t), \tag{2}$$

the first term being the trapping potential and the second term describing additional modulation potential pumping energy into the trap.

The energy operator is given by the standard Hamiltonian

$$\hat{\psi} = \int \hat{\psi}(\mathbf{r}) \left(-\frac{\nabla^2}{2m} + U \right) \hat{\psi}(\mathbf{r}) \, d\mathbf{r} + \frac{\Phi_0}{2} \int \hat{\psi}^\dagger(\mathbf{r}) \hat{\psi}^\dagger(\mathbf{r}) \hat{\psi}(\mathbf{r}) \hat{\psi}(\mathbf{r}) \, d\mathbf{r}, \tag{3}$$

where U is the total external potential (2). In the presence of Bose–Einstein condensate, the system global gauge symmetry is necessarily broken [6, 15]. The most convenient way of breaking the gauge symmetry is by employing the Bogolubov shift [21, 22] of the field operator:

$$\hat{\psi}(\mathbf{r}) = \eta(\mathbf{r}) + \psi_1(\mathbf{r}), \tag{4}$$

in which $\eta(\mathbf{r})$ is the condensate wave function normalized to the number of condensed atoms

$$N_0 = \int |\eta(\mathbf{r})|^2 d\mathbf{r}, \tag{5}$$

and $\psi_1(\mathbf{r})$ is the operator of uncondensed atoms defining their number

$$N_1 = \langle \hat{N}_1 \rangle, \quad \hat{N}_1 \equiv \int \psi_1^\dagger(\mathbf{r}) \psi_1(\mathbf{r}) \, d\mathbf{r}, \tag{6}$$

with the angle brackets implying statistical averaging. By this definition, the field operator of uncondensed atoms satisfies the Bose commutation relations.

The condensate function and the field operator of uncondensed atoms characterize different degrees of freedom, orthogonal to each other,

$$\int \eta^*(\mathbf{r})\psi_1(\mathbf{r})\, d\mathbf{r} = 0.$$

The condensate function plays the role of the system order parameter, such that

$$\langle\hat{\psi}(\mathbf{r})\rangle = \eta(\mathbf{r}), \quad \langle\psi_1(\mathbf{r})\rangle = 0. \tag{7}$$

This definition can also be written in the form of the statistical average

$$\langle\hat{\Lambda}\rangle = 0 \tag{8}$$

of the operator

$$\hat{\Lambda} \equiv \int \left[\lambda(\mathbf{r})\psi_1^\dagger(\mathbf{r}) + \lambda^*(\mathbf{r})\psi_1(\mathbf{r})\right] d\mathbf{r}, \tag{9}$$

in which $\lambda(\mathbf{r})$ is a Lagrange multiplier guaranteeing the validity of condition (7).

The correct description of any statistical system presupposes the use of the representative ensemble uniquely defining the system [20, 23–25]. This requires to take into account all imposed constraints that, in the present case, are given by Eqs. (5), (6), and (8). In turn, taking account of these constraints makes it necessary to introduce the grand Hamiltonian

$$H = \hat{H} - \mu_0 N_0 - \mu_1 \hat{N}_1 - \hat{\Lambda}, \tag{10}$$

with the Lagrange multipliers μ_0 and μ_1. Only employing this grand Hamiltonian allows one to correctly describe the Bose-condensed system. When one uses an ensemble that is not representative, that is, when not all constraints are taken into account, this leads to various inconsistencies in thermodynamic and dynamic characteristics, such as the arising gap in the spectrum of elementary excitations and instability of the system.

3 Nonequilibrium Bose System

In the presence of an external time-dependent potential, we have to study a nonequilibrium Bose system. The equations of motion for the system variables can be written through the variational derivatives, which is equivalent to the Heisenberg equations of motion [20, 26]. The condensate function satisfies the equation

$$i\,\frac{\partial}{\partial t}\,\eta(\mathbf{r},t) = \left\langle \frac{\delta H}{\delta\eta^*(\mathbf{r},t)} \right\rangle. \tag{11}$$

While for the field operator of uncondensed atoms, one has

$$i\,\frac{\partial}{\partial t}\,\psi_1(\mathbf{r},t)=\frac{\delta H}{\delta\psi_1^\dagger(\mathbf{r},t)}\,. \tag{12}$$

To represent the resulting evolution equations in a convenient form, let us introduce several notations. The condensate density is

$$\rho_0(\mathbf{r})\equiv|\eta(\mathbf{r})|^2. \tag{13}$$

The density of uncondensed atoms reads as

$$\rho_1(\mathbf{r})\equiv\langle\psi_1^\dagger(\mathbf{r})\psi_1(\mathbf{r})\rangle. \tag{14}$$

When the gauge symmetry is broken, there appear the anomalous averages, such as the pair anomalous average

$$\sigma_1(\mathbf{r})\equiv\langle\psi_1(\mathbf{r})\psi_1(\mathbf{r})\rangle \tag{15}$$

and the triple anomalous averages

$$\xi(\mathbf{r})\equiv\langle\psi_1^\dagger(\mathbf{r})\psi_1(\mathbf{r})\psi_1(\mathbf{r})\rangle,\quad \xi_1(\mathbf{r})\equiv\langle\psi_1(\mathbf{r})\psi_1(\mathbf{r})\psi_1(\mathbf{r})\rangle. \tag{16}$$

The total atomic density is the sum

$$\rho(\mathbf{r})=\rho_0(\mathbf{r})+\rho_1(\mathbf{r}). \tag{17}$$

Equation (11) yields the equation for the condensate function

$$\begin{aligned} i\,\frac{\partial}{\partial t}\,\eta(\mathbf{r}) &= \left(-\frac{\nabla^2}{2m}+U-\mu_0\right)\eta(\mathbf{r}) \\ &+\Phi_0[\rho_0(\mathbf{r})\eta(\mathbf{r})+2\rho_1(\mathbf{r})\eta(\mathbf{r})+\sigma_1(\mathbf{r})\eta^*(\mathbf{r})+\xi(\mathbf{r})]. \end{aligned} \tag{18}$$

And using Eq. (12), we find the continuity equation for the density of uncondensed atoms,

$$\frac{\partial}{\partial t}\,\rho_1(\mathbf{r})+\nabla\cdot\mathbf{j}_1(\mathbf{r})=-\Gamma(\mathbf{r}), \tag{19}$$

with the atomic current

$$\mathbf{j}_1(\mathbf{r})\equiv-\frac{i}{2m}\left\langle\psi_1^\dagger(\mathbf{r})\nabla\psi_1(\mathbf{r})-\left[\nabla\psi_1^\dagger(\mathbf{r})\right]\psi_1(\mathbf{r})\right\rangle \tag{20}$$

and the source term given by the expression

$$\Gamma(\mathbf{r})=i\Phi_0[\Xi^*(\mathbf{r})-\Xi(\mathbf{r})], \tag{21}$$

in which

$$\Xi(\mathbf{r})\equiv\eta^*(\mathbf{r})[\eta^*(\mathbf{r})\sigma_1(\mathbf{r})+\xi(\mathbf{r})]. \tag{22}$$

In addition, it is necessary to consider the equations for the anomalous averages. Writing down the equation for the pair average (15), we can use the Hartree-Fock-Bogolubov approximation for the four-operator correlator

$$\langle \psi_1^\dagger(\mathbf{r})\psi_1(\mathbf{r})\psi_1(\mathbf{r})\psi_1(\mathbf{r})\rangle = 3\rho_1(\mathbf{r})\sigma_1(\mathbf{r}). \tag{23}$$

Also, we define the anomalous kinetic term

$$\begin{aligned} K(\mathbf{r}) \equiv & -\frac{1}{2}\left\langle \frac{\nabla^2\psi_1(\mathbf{r})}{2m}\,\psi_1(\mathbf{r}) + \psi_1(\mathbf{r})\,\frac{\nabla^2\psi_1(\mathbf{r})}{2m}\right\rangle \\ = & \frac{1}{2m}\left\{\left\langle [\nabla\psi_1(\mathbf{r})^2]\right\rangle - \frac{1}{2}\,\nabla^2\sigma_1(\mathbf{r})\right\}. \end{aligned} \tag{24}$$

Then the evolution equation for the anomalous average (15) is

$$\begin{aligned} i\,\frac{\partial}{\partial t}\,\sigma_1(\mathbf{r}) &= 2K(\mathbf{r}) + 2(U-\mu_1)\sigma_1(\mathbf{r}) \\ &+ 2\phi_0\left[\eta^2(\mathbf{r})\rho_1(\mathbf{r}) + 2\rho_0(\mathbf{r})\sigma_1(\mathbf{r}) + 3\rho_1(\mathbf{r})\sigma_1(\mathbf{r}) + 2\eta(\mathbf{r})\xi(\mathbf{r}) + \eta^*(\mathbf{r})\xi_1(\mathbf{r})\right]. \end{aligned} \tag{25}$$

Equations (18) to (25) describe the nonequilibrium system with Bose–Einstein condensate [20].

4 Topological Coherent Modes

Strongly nonlinear time-dependent equations, such as the condensate-function equation (18), can display different nonequilibrium solutions. One usually considers a particular case of this equation corresponding to asymptotically weak interactions, when one can neglect the terms containing ρ_1 and σ_1. In that case, Eq. (18) reduces to the nonlinear Schrödinger equation, also called the Gross–Pitaevskii equation [27–31]. Such a nonlinear equation possesses a variety of soliton solutions [32, 33]. Here we shall consider a special class of nonequilibrium solutions that can exist being supported by the action of external alternating fields.

First, let us define the set of stationary solutions to the condensate-function equation (18). These solutions are obtained by considering the situation without the time-dependent perturbation $V(\mathbf{r}, t)$ and substituting into Eq. (18) the form

$$\eta_n(\mathbf{r}, t) = \eta_n(\mathbf{r})e^{-i\omega_n t}, \tag{26}$$

which results in the eigenvalue problem

$$\left[-\frac{\nabla^2}{2m} + U(\mathbf{r}) \right] \eta_n(\mathbf{r}) + \Phi_0 \left[|\eta_n(\mathbf{r})|^2 \eta_n(\mathbf{r}) + 2\rho_1(\mathbf{r})\eta_n(\mathbf{r}) + \sigma_1(\mathbf{r})\eta_n^*(\mathbf{r}) + \xi(\mathbf{r}) \right] = E_n \eta_n(\mathbf{r}), \tag{27}$$

where n is a multi-index labelling the eigenstates and

$$E_n \equiv \omega_n + \mu_0. \tag{28}$$

The related stationary solutions for ρ_1 and σ_1 are assumed to enter Eq. (27), or they are neglected in the simple case of the Gross–Pitaevskii equation. The lowest eigenvalue E_n corresponds to the equilibrium case, when

$$\mu_0 = \min_n E_n \quad (\min_n \omega_n = 0). \tag{29}$$

The solutions to Eq. (27) are termed *coherent topological modes*. They are coherent, since the condensate function corresponds to the coherent state, in agreement with the general definition of such states [34]. And they are called topological because the solutions with different indices n possess different spatial topology, having different number of zeroes. Respectively, the related densities of condensed atoms $|\eta_n(\mathbf{r})|^2$, with differing indices n, have different spatial shapes. The coherent topological modes for the Gross–Pitaevskii equation were introduced in Ref. [35]; and their properties were studied in many articles [36–61]. A dipole topological mode was excited in experiment [62]. The general case of Eq. (27) has also been considered [20, 63].

As an illustration of typical solutions, representing such coherent modes, let us consider the case of zero temperature and weak atomic interactions, when the Gross–Pitaevskii equation is applicable. The atoms are trapped in a harmonic cylindrical trapping potential. The corresponding solution can be represented [9, 35, 36, 43, 46] in the form

$$\psi_{nmj}(r,\varphi,z) = \left[\frac{2n!u^{|m|+1}}{(n+|m|)!} \right]^{1/2} r^{|m|} \exp\left(-\frac{u}{2} r^2 \right) L_n^{|m|}(ur^2) \times \frac{e^{im\varphi}}{\sqrt{2\pi}} \left(\frac{v}{\pi} \right)^{1/4} \frac{1}{\sqrt{2^j j!}} \exp\left(-\frac{v}{2} z^2 \right) H_j(\sqrt{v}\, z),$$

in which L_n^m is a Laguerre polynomial, H_j, a Hermite polynomial, $n = 0, 1, 2, \ldots$ is the radial quantum number, $m = 0, \pm 1, \pm 2, \ldots$ is the azimuthal quantum number, and $j = 0, 1, 2, \ldots$ is the axial quantum number. The variables r, φ, z are cylindrical coordinates. And the quantities u, v are the so-called control functions, depending on all system parameters and defined so that to guarantee the convergence of optimized perturbation theory [64–67]. As is clear, the solutions with nonzero azimuthal quantum number m correspond to vortices.

When there is no external perturbation, the system tends to its equilibrium state corresponding to the lowest energy level (29). But if the system is subject to an

external time-dependent perturbation, then we have to consider the evolution equation (18). It is admissible to look for the solution of this equation in the form of the expansion over the coherent modes:

$$\eta(\mathbf{r},t) = \sum_n c_n(t)\eta_n(\mathbf{r})e^{-i\omega_n t}. \tag{30}$$

Defining the number of condensed atoms at the initial time,

$$N_0 \equiv \int |\eta(\mathbf{r},0)|^2 d\mathbf{r}, \tag{31}$$

we use the notation

$$\eta_n(\mathbf{r}) = \sqrt{N_0}\,\varphi_n(\mathbf{r}), \tag{32}$$

introducing the functions φ_n normalized to one:

$$\int |\varphi_n(\mathbf{r})|^2 d\mathbf{r} = 1.$$

Note that these functions φ_n, being defined by a nonlinear equation, are not necessarily orthogonal.

We impose, in addition to the stationary trapping potential $U(\mathbf{r})$, the external potential modulating the trapping potential in the form

$$V(\mathbf{r},t) = V_1(\mathbf{r})\cos(\omega t) + V_2(\mathbf{r})\sin(\omega t), \tag{33}$$

with the total potential given by Eq. (2). Also, we require that this alternating potential be in resonance with one of the transition frequencies ω_n, so that the resonance condition

$$\left|\frac{\Delta\omega}{\omega}\right| \ll 1 \quad (\Delta\omega \equiv \omega - \omega_n) \tag{34}$$

be valid for the fixed n. Substituting expansion (30) into Eq. (18) and employing the averaging techniques [68–70], we come to the equations

$$\begin{aligned} i\,\frac{dc_0}{dt} &= \alpha_{0n}|c_n|^2 c_0 + \frac{1}{2}\,\beta_{0n}c_n e^{i\Delta\omega\cdot t}, \\ i\,\frac{dc_n}{dt} &= \alpha_{n0}|c_0|^2 c_n + \frac{1}{2}\,\beta_{0n}^* c_0 e^{-i\Delta\omega\cdot t}, \end{aligned} \tag{35}$$

in which

$$\alpha_{mn} \equiv \Phi_0 N_0 \int |\varphi_m(\mathbf{r})|^2 \left[2|\varphi_n(\mathbf{r})|^2 - |\varphi_m(\mathbf{r})|^2\right] d\mathbf{r},$$

$$\beta_{mn} \equiv \int \varphi_m^*(\mathbf{r})[V_1(\mathbf{r}) - iV_2(\mathbf{r})]\varphi_n(\mathbf{r})\,d\mathbf{r}.$$

Solving these equations gives us the fractional mode populations

$$p_n(t) = |c_n(t)|^2, \quad \sum_n p_n(t) = 1. \tag{36}$$

It is worth noting that the mathematical structure of these equations is the same as that of equations describing atomic motion in a double-well potential. Therefore solutions to these equations exhibit many properties that are analogous to the properties of solutions in the case of a double-well potential. For instance, the effect of mode locking [35, 46], occurring for Eqs. (35), is mathematically identical to the effect of self-trapping for the double well potential [71].

Among other interesting effects, exhibited by the system with the generated coherent topological modes, we can mention the interference patterns and interference current [42, 43, 46], dynamical phase transitions and critical phenomena [39, 42, 43, 46], chaotic motion under the action of several alternating fields [53, 54], atomic squeezing [46, 48, 49], Ramsey fringes [57–59], and entanglement production [72–75].

The coherent topological modes can also be generated by modulating the atomic scattering length by means of the Feshbach resonance techniques [20, 60, 61], so that the interaction strength be varying in time as

$$\Phi(t) = \Phi_0 + \Phi_1 \cos(\omega t) + \Phi_2 \sin(\omega t), \tag{37}$$

provided that the alternating frequency ω is tuned close to one of the transition frequencies ω_n.

In the case of resonance $\omega = \omega_n$, coherent modes can be generated by an external modulation of rather weak strength. But increasing the amplitude of the pumping field simplifies this generation, making the strict resonance $\omega = \omega_n$ not necessary [53, 54]. Then several other conditions come into play allowing for the mode generation. Thus, the modes can be created when the external frequency is close to the condition of *harmonic generation*

$$k\omega = \omega_n \quad (k = 1, 2, \ldots). \tag{38}$$

If there are two alternating fields, with the frequencies ω_1 and ω_2, then the modes can be produced [53, 54] by *parametric conversion*, when the frequencies satisfy (at least approximately) the relation

$$\omega_1 \pm \omega_2 = \omega_n. \tag{39}$$

This effect is similar to parametric resonance [76].

Generally, for several alternating fields, with frequencies ω_i, the condition of the *generalized resonance*

$$\sum_i k_i \omega_i = \omega_n \quad (k_i = \pm 1, \pm 2, \ldots) \tag{40}$$

is sufficient for generating coherent modes.

In this way, increasing the amplitude of the pumping field produces in the trapped Bose gas a variety of different topological coherent modes. The same multiple mode creation happens when the action of the alternating perturbing potential lasts sufficiently long, during the time after which the effect of power broadening comes into play [35, 46, 54, 63].

5 Creation of Trapped Vortices

One type of the coherent topological modes is of special interest. These are the quantum vortices. Such vortices have been observed in superfluid helium [77] and in trapped Bose–Einstein condensate [78–80]. In the dynamical picture, the appearance of vortices is caused by a dynamical instability arising in a nonequilibrium moving fluid [81–88].

The first vortex appears, when the atomic cloud is rotated with the frequency reaching the critical value ω_{vor}. Let us consider a cloud of Bose-condensed atoms in a cylindrical trap with a transverse, $\omega_\perp$, and longitudinal, ω_z, trap frequencies, and with the aspect ratio

$$\alpha \equiv \frac{\omega_z}{\omega_\perp} = \left(\frac{l_\perp}{l_z} \right)^2 , \tag{41}$$

in which the effective trap lengths are

$$l_\perp \equiv \frac{1}{\sqrt{m\omega_\perp}} , \quad l_z \equiv \frac{1}{\sqrt{m\omega_z}} .$$

The critical rotation frequency for this trap [8] can be written as

$$\omega_{vor} = \frac{5}{2mR_{TF}^2} \ln\left(0.7 \, \frac{R_{TF}}{\xi} \right), \tag{42}$$

where the notations are used for the Thomas–Fermi radius

$$R_{TF} = l_\perp \left(\frac{15}{4\pi} \, \alpha g \right)^{1/5} , \tag{43}$$

dimensionless coupling parameter

$$g \equiv 4\pi N \, \frac{a_s}{l_\perp} , \tag{44}$$

and the healing length

$$\xi \equiv \frac{1}{\sqrt{2m\rho(0)\Phi_0}} . \tag{45}$$

The vortex with vorticity one is energetically more stable than the vortices with higher vorticities. Because of this, the latter decay into several basic vortices with vorticity one. Moreover, for large coupling parameter (44) the basic vortex is the most stable among all coherent modes [9, 20]. This follows from the fact that the basic vortex energy, that can be represented by Eq. (42), can be rewritten as

$$\omega_{vor} = \frac{0.9\omega_\perp}{(\alpha g)^{2/5}} \ln(0.8\alpha g), \tag{46}$$

which shows that this energy diminishes with g. While the energies of other coherent modes increase with g as

$$\omega_n \propto (\alpha g)^{2/5} \quad (g \gg 1). \tag{47}$$

Increasing the velocity of rotation produces many basic vortices that form arrays arranged into Abrikosov lattices [79, 89].

However, if we modulate the trapping potential by alternating fields without a fixed rotation axis, as is described above for generating coherent modes, then we shall generate vortices and antivortices. Such a type of vortex creation was demonstrated in experiments [90, 91], where the harmonic trapping potential

$$U(\mathbf{r}) = \frac{m}{2}\,\omega_\perp^2\left(x^2 + y^2\right) + \frac{m}{2}\,\omega_z^2 z^2, \tag{48}$$

with $\omega_\perp = 2\pi \times 210\,\mathrm{Hz}$ and $\omega_z = 2\pi \times 23\,\mathrm{Hz}$, was modulated with the alternating potential

$$V(\mathbf{r}, t) = \frac{m}{2}\,\Omega_x^2(t)(x - x_0)^2 + \frac{m}{2}\,\Omega_y^2(t)(y' - y_0')^2 + \frac{m}{2}\Omega_z^2(t)(z' - z_0')^2. \tag{49}$$

Here the oscillation centers are defined by the equation

$$\begin{bmatrix} y' - y_0' \\ z' - z_0' \end{bmatrix} = \begin{bmatrix} \sin\vartheta_0 & \cos\vartheta_0 \\ \cos\vartheta_0 & -\sin\vartheta_0 \end{bmatrix} \begin{bmatrix} y - y_0 \\ z - z_0 \end{bmatrix},$$

and the oscillation frequencies are

$$\Omega_\alpha(t) = \omega_\alpha \delta_\alpha [1 - 1\cos(\omega t)], \tag{50}$$

with $\alpha = x, y, z$, and $x_0, y_0, z_0, \vartheta_0, \delta_\alpha, \omega$ being fixed parameters [92].

6 Trapped Turbulent Superfluid

Strong rotation creates a vortex lattice [8]. But when the trapped atomic cloud is subject to the action of an alternating modulation potential without a fixed rotation axis and this pumping injects into the system the amount of energy sufficient for creating many vortices and antivortices, then the latter are randomly distributed

inside the trap, forming a chaotic tangle. Such a random tangle of vortices is associated with turbulence, similar to the spatially tangled vortices in superfluid helium [93].

Turbulence is a phenomenon that has been studied for classical liquids for many years [94]. Vortices in a classical fluid can be of different vorticities, while the vortex circulation in a quantum fluid is quantized, which distinguishes the classical turbulence from the *quantum turbulence* [95].

One of important characteristics of turbulent motion is the mean kinetic energy that can be represented as the integral

$$K = \int_0^\infty E(k)\, dk \tag{51}$$

over the wave-number values k. In classical fluids, there exists a diapason of wave numbers, called *inertial range*, where the spectrum $E(k)$, is given by the Kolmogorov [96, 97] law for isotropic turbulence

$$E(k) = C\varepsilon^{2/3}k^{-5/3}, \tag{52}$$

with $C \approx 1.5$ and ϵ being energy transfer rate. The Kolmogorov law is universal for classical fluids [98].

Quantum turbulence was, first, studied for superfluid helium [99, 100]. It was found in experiments [101, 102] that there also exists an inertial range of wave numbers, where the Kolmogorov law (52) is valid, independently of temperature. In superfluids, the energy is dissipated through the interaction of the normal and superfluid components and, at low temperature, through vortex reconnection, Kelvin wave excitations, and phonon emission [103, 104]. More details can be found in Refs. [105–108].

Numerical simulation of quantum turbulence in Bose–Einstein condensate is usually done by solving the Gross–Pitaevskii equation. Atoms are assumed to be trapped in a stationary trap and subject to the action of an external alternating perturbation with more than one rotation axes. The kinetic energy, when all atoms are condensed, is given by the integral

$$K = \int \eta^*(\mathbf{r}, t)\left(-\frac{\nabla^2}{2m}\right)\eta(\mathbf{r}, t)\, d\mathbf{r}. \tag{53}$$

It was found [109, 110] that there again exists an inertial range, where the Kolmogorov law is applied. Thus, for atoms in a harmonic trap, the inertial range is

$$\frac{2\pi}{R_{TF}} < k < \frac{2\pi}{\xi} \quad (C \approx 0.25), \tag{54}$$

where R_{TF} is the Thomas–Fermi radius and ξ, healing length. For atoms in a box of linear size L, the inertial range is

$$\frac{2\pi}{L} < k < \frac{2\pi}{\xi} \quad (C \approx 0.55). \tag{55}$$

Experimental generation of trapped quantum turbulence was realized [111–114] for ^{87}Rb Bose–Einstein condensate. It was trapped in the harmonic potential (48) and subject to the action of the alternating potential (49).

7 Heterophase Granular Fluid

If we continue pumping energy into the system, turbulence is getting stronger and stronger. The core of each vortex can be treated as a nucleus of normal (uncondensed) phase. Producing more and more vortices increases the amount of the uncondensed component. What then happens, when the number of vortices in the strongly turbulent liquid is so large that the amount of the uncondensed fraction becomes comparable or greater than the fraction of condensed atoms? The answer to this question cannot be done being based solely on the Gross–Pitaevskii equation that describes only the condensed fraction. To take into account both the condensed as well as uncondensed fractions, it is necessary to consider the full evolution equations (18) to (25).

A simple way of understanding what happens in a strongly nonequilibrium system under the action of a time-dependent perturbation is as follows. It is possible to prove [20, 107, 115] that the system with the time-dependent perturbation can be mapped onto the system subject to the action of a random spatial potential, provided that the modulation period is larger than the local equilibration time. The behavior of the weakly interacting Bose-condensed system in a weak spatially random potential has been studied in several articles (see, e.g., [116, 117]). A theory for Bose systems with arbitrarily strong interactions and random potentials of arbitrary strength has also been developed [115, 118, 119].

Using the analogy between the spatially random and temporally perturbed Bose gas [20, 115] we can evaluate the *localization length* defining the scale at which Bose gas can be condensed. This length for a trapped Bose gas is

$$l_{loc} = \frac{1}{m^2 E_{inj}^2 l_0^3} = \left(\frac{\omega_0}{E_{inj}}\right)^2 l_0, \tag{56}$$

where the effective trap size and effective frequency are

$$l_0 \equiv \left(l_\perp^2 l_z\right)^{1/3} = \frac{1}{\sqrt{m\omega_0}}, \quad \omega_0 \equiv \left(\omega_\perp^2 \omega_z\right)^{1/3} = \frac{1}{ml_0^2}, \tag{57}$$

and the energy per atom, injected into the trap, can be evaluated as

$$E_{inj} \approx \frac{1}{N} \int \rho(\mathbf{r}, t) \left| \frac{\partial V(\mathbf{r}, t)}{\partial t} \right| d\mathbf{r} dt. \tag{58}$$

If the pumping potential is alternating, as is usual, with an amplitude A and frequency ω, then the energy, injected in the time interval $[t, t']$, is approximately

$$E_{inj} \approx A\omega(t - t'). \tag{59}$$

This expression for the injected energy is certainly approximate, since a part of the pumped energy is dispersed, but not transferred to atoms.

If the localization length (56) is larger or of order of the trap size, given in Eq. (57), then all atoms in the trap are in the Bose-condensed state. But when this length becomes shorter than the trap size, though yet larger than the mean interatomic distance a, then the atomic cloud breaks into pieces. Then the system consists of grains, composed of Bose-condensed phase, immersed into the cloud, consisting of normal phase, without gauge symmetry breaking. The sizes of the condensate grains are of order of the localization length. Thus, the condition for the occurrence of this heterophase granular state is

$$a < l_{loc} < l_0. \tag{60}$$

Such a heterophase state is similar to heterophase states arising in many condensed-matter systems [23, 120] and that can happen in optical lattices [18, 121].

The state of the heterophase granular fluid has been observed in experiment [114] with a cloud of strongly modulated ^{87}Rb atoms.

8 Normal Chaotic Fluid

What happens, if we continue pumping energy into the trapped atomic cloud? Again, following the analogy with other heterophase systems [18, 23, 120, 121], we should expect that the fraction of the Bose-condensed phase, concentrated in the grains, will diminish, and, finally, the whole system will be transferred into the normal state, with the restored gauge symmetry. Being subject to strong external perturbation, the system will, of course, be essentially nonequilibrium, experiencing chaotic fluctuations. So, this will be a normal chaotic fluid, with completely restored global gauge symmetry, without any remnants of Bose–Einstein condensate,

The normal chaotic fluid could, probably, be characterized by the approach called weak-turbulence theory, or wave-turbulence theory [122–127]. In this approach one assumes that turbulence in a weakly nonlinear system can be represented by an ensemble of weakly interacting waves. However, the nonlinearity in the system can be rather strong. And the normal chaotic state, with no condensate, cannot be described by the Gross–Pitaevskii equation appropriate only for pure condensate. More probably, the normal chaotic state is just a strongly turbulent state of a normal fluid and could be described as classical turbulence.

This state has not yet been reached in experiments [113, 114] and remains to be investigated.

9 Amplitude-Time Phase Diagram

The whole procedure of exciting the system of trapped atoms by applying an external alternating perturbation potential passes through several stages. We start with an almost completely Bose-condensed gas, where the global gauge symmetry is broken. Very weak perturbation can do not more than to produce elementary collective excitations that do not change the overall system properties. This state can be called the *regular superfluid*.

When the energy, injected into the trap, becomes comparable with the energy of a vortex, a single vortex is created. This happens when $E_{inj} \sim \omega_{vor}$. With equality (59), this gives the relation

$$A_{vor} \sim \frac{\omega_{vor}}{\omega(t - t_0)} \tag{61}$$

between the amplitude A of the alternating perturbing potential and the time t of its action, describing the effective transition line of vortex creation. Above this line, we have the state of *vortex superfluid*. Of course, the transition from the regular superfluid to vortex superfluid is not a sharp phase transition, but it is a crossover. However, the crossover line (61) serves as an approximate separation line between these two qualitatively different regimes. Similarly, the dividing lines between other qualitatively different regions are also crossover lines.

Increasing the injected energy, pumped into the trap, by either a stronger alternating field or by its longer action, leads to the generation of a variety of coherent topological modes that decay into basic vortices and antivortices. To create N_{vor} vortices (and antivortices), it is necessary to inject the energy $E_{inj} \sim N_{vor}\omega_{vor}$. When the number of vortices becomes large, of order

$$N_{vor} \sim \frac{l_0}{\xi}, \tag{62}$$

they form a random tangle, which signifies the appearance of turbulent state. Hence, the crossover line between the vortex superfluid and the *turbulent superfluid* is given by

$$A_{tur} \sim \frac{l_0\omega_{vor}}{\xi\omega(t - t_1)}. \tag{63}$$

The random vortex tangle is formed due to the property of the imposed perturbing potential that does not prescribe a single rotation axis.

As soon as the injected energy reaches the value $E_{inj} \sim \omega_0$, the condensate localization length (56) becomes of order of the trap size l_0. As is explained in Sect. 7, in the region of the localization lengths (60), the heterophase granular state arises. This *granular fluid* consists of the grains of Bose-condensed gas immersed into the cloud of normal fluid without gauge symmetry breaking. The corresponding crossover line writes as

$$A_{het} \sim \frac{\omega_0}{\omega(t - t_2)} . \tag{64}$$

The cloud of normal atoms, surrounding the Bose-condensed droplets, is characterized by the restored gauge symmetry.

When the localization length (56) becomes as small as the mean interatomic distance, no condensed droplets can be formed. That is, on the boundary, where

$$l_{loc} \sim a, \quad E_{inj} \sim \omega_0 \sqrt{\frac{l_0}{a}},$$

all condensate is completely destroyed. This defines the crossover line

$$A_{nor} \sim \frac{\omega_0}{\omega(t - t_3)} \sqrt{\frac{l_0}{a}} \tag{65}$$

between the granular fluid and the normal fluid with no gauge symmetry breaking. Since the latter is in a strongly nonequilibrium state with chaotic motion, it can be termed *chaotic fluid*. This regime, presumably, can be characterized by classical turbulent state.

Summarizing the sequence of these crossover transitions, we have:

$$\begin{array}{cc} 0 < A < A_{vor} & (regular\ superfluid) \\ A_{vor} < A < A_{tur} & (vortex\ superfluid) \\ A_{tur} < A < A_{het} & (turbulent\ superfluid) \\ A_{het} < A < A_{nor} & (granular\ fluid) \\ A > A_{nor} & (chaotic\ fluid) \end{array} .$$

The first four of these regimes have been observed in experiments, as described above. The last state of chaotic fluid has not yet been reached for trapped atoms.

10 Experiments with Strongly Nonequilibrium Trapped Bose Gas

While classical turbulence can be observed quite easily with visualization techniques, for traditional superfluids that is not the case. The high density in superfluid liquid-He makes the vortex line core of order of atomic scale dimensions, and therefore, turning the visualization techniques hard to be applied. On the other hand, in trapped atomic superfluids the low density makes possible the observation of vortex arrangement with unaided eye. We therefore use the observations of irregular arrangement of vortices as one of the macroscopic indications of Quantum Turbulence (QT). After the regime of QT is reached, the studies of many aspects, revealing the similarities and differences with the classical counterpart, become of great interest.

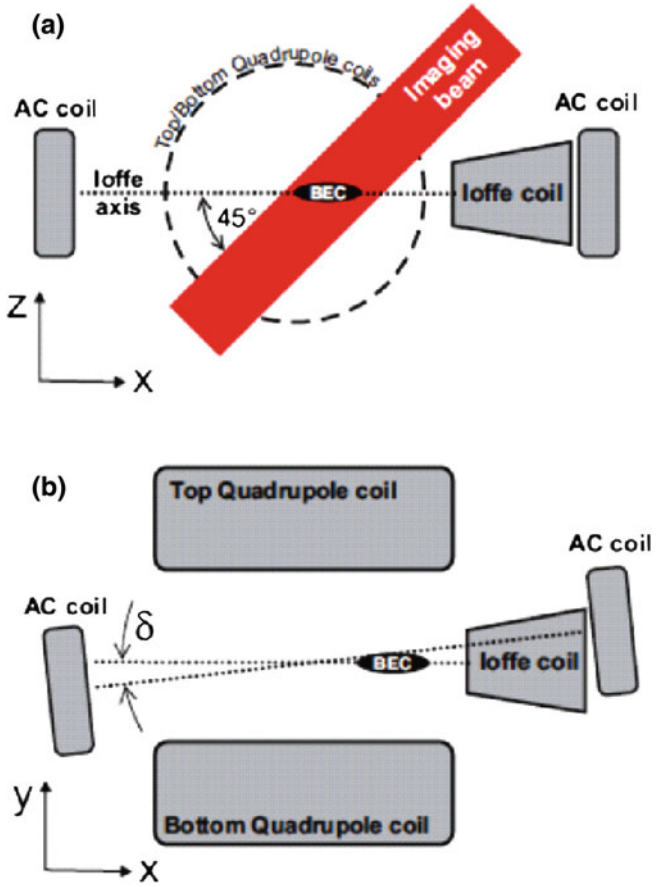

Fig. 1 Scheme of the main components composing the magnetic trap and the additional extra coils producing the necessary oscillatory fields generating trapped quantum turbulence

The first important aspect on the experimental observation of QT is the production of vortex lines. The standard way of producing quantized vortices in a trapped condensate is by stirring [128, 129]. Laser beams or rotation of an asymmetric trapping potential are the alternatives to achieve a rotating cloud of atoms. In these cases, the nucleation of vortices takes place in a specific direction (along the rotation axis), and therefore the final result is a lattice of vortices instead of a tangle configuration. To achieve a tangle configuration, we have developed a new technique [90], where a combination of oscillations in the cloud results in the nucleation of vortices in many directions, which is a necessary ingredient for the final production of a tangle configuration of vortices.

In brief, we start with a BEC of Rb atoms confined in a harmonic trapping potential with the frequencies $\omega_x = \omega_y = 9\,\omega_z$ and $\omega_z = 2\pi \times 23$ Hz. The typically produced BEC contains 2×10^5 atoms. A pair of coils (as in Fig. 1) forms a

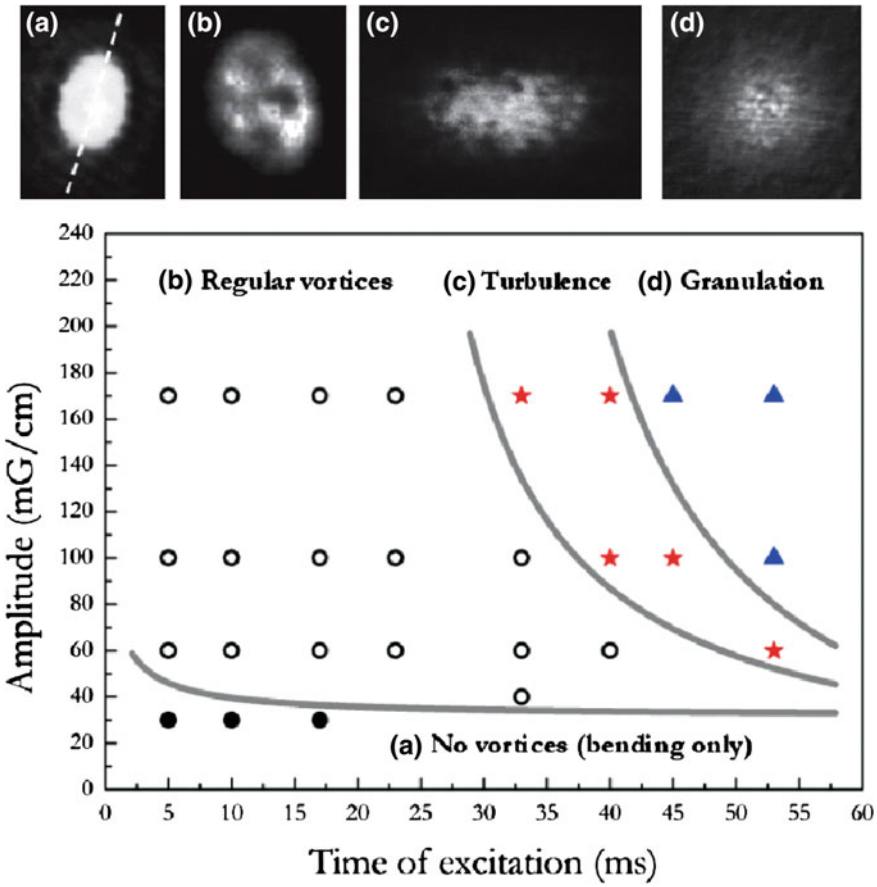

Fig. 2 Diagram, on the excitation amplitude-time plane, showing the observed characteristic regions of four different identifiable structures, from the simple bending of the superfluid axis, to the creation of vortices, vortex tangle, and to granulation

magnetic field that mechanically excites the trapped condensate. The notation of axes in this figure corresponds to that used in the text with the interchange of x and z. The excitation is achieved by applying an oscillatory current in the extra coils. The produced distortions of the trapping potential cause a combination of translations and rotations of the cloud. The result of such an excitation is a combination of the effects, going from a simple bending of the symmetry axis of the cloud up to the generation of vortices in many directions with a final granulation of the cloud. We have characterized the overall behavior of the system in a diagram presenting the regions of observations in Fig. 2 [114].

Small amplitudes of oscillation can only produce a bending mode intrinsically connected to the scissor mode [130] present in atomic trapped superfluids. Larger amplitudes of oscillation, combined with longer excitation times, can produce

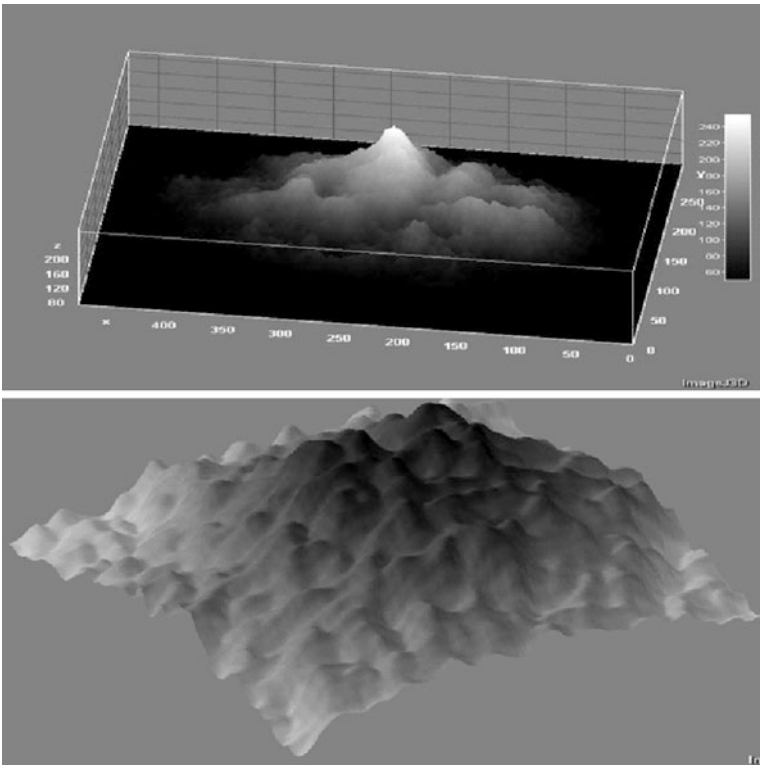

Fig. 3 The difference between a turbulent and a granulated cloud. While in the first case the landscape is made of vortex filaments distributed in space, the granulated state corresponds to a collection of grains characterizing strong density fluctuations

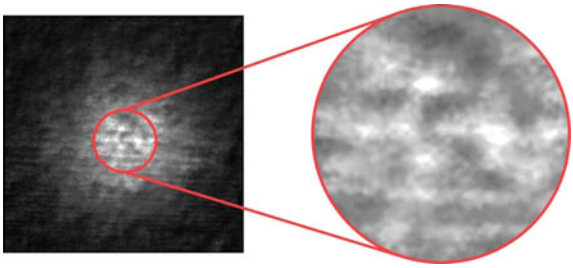

Fig. 4 Absorption by the granulated cloud showing the domains of the grains

vortices with a characteristic array of QT. As is shown in Fig. 2 , in a range of the excitation parameters, there arise vortices directed along the cloud axis, but still not yet showing a fully tangled configuration. Quantum turbulence takes place in the region of parameters with a clear separation of behavior between the regions.

The generation of vortices takes place because the oscillation of the atomic superfluid cloud produces collective modes [112] leading to the generation of

coherent modes [35]. In a more recent observation, it has been verified [131] that the excitation, through a combination of oscillations produces, together with collective modes, the excitation of the second sound mode coupled to the dipole mode. This excitation corresponds to the counterflow between condensate and thermal cloud, with the possible generation of vortices in the regions of the maximal relative motion. At low temperatures, when the normal fraction is negligible, dynamic instability appears due to the counterflow between different parts of the condensate [81–88].

Being generated, vortices can be distributed in many directions, first, without actually forming a tangled configuration. When the finite size of the cloud is saturated with the vortices, any further pumped energy forces a fast evolution of the vortices, promoting their reactions by reconnections [132], eventually yielding a turbulent cloud. At this stage, not only the distribution of the vortices is an indication for the occurrence of turbulence, but also a change in the hydrodynamic behavior, during the free expansion of the cloud, works as the indicator of turbulence. While a non-turbulent cloud of an atomic superfluid demonstrates the inversion of aspect ratio during free expansion, the turbulent cloud preserves the original aspect ratio [111, 133].

It has been observed that the existence of a boundary, between the regular and turbulent superfluids, on the amplitude-time diagram of Fig. 2 is the consequence of the finite size of the cloud, as explained in Ref. [113].

For the extreme case of excitation (high amplitude and longer excitation times), the turbulent condensate evolves into a granulated state, when the original condensate cloud breaks into many grains. The transition from the turbulent to fragmented cloud is presented by the density profile of Fig. 3.

The experimental observation of the atomic cloud inside the trap is not easy. This is because the produced condensate has the size of just a few microns. To perform an absorption measurement in situ, we would be severely limited by diffraction. We therefore, first, allow a free expansion of the cloud, and then perform absorption measurements. For the observed states, discussed above, the time of flight before absorption was of 15 ms. In this case, the size of the cloud is many times larger than the actual size in situ. As far as, during the time of flight, the density is greatly reduced, the interactions are also reduced, freezing the existent structure, that now evolves much slower in time. It is a general consensus that the free expansion preserves the in situ structure of the atomic cloud.

Figure 4 demonstrates the absorption image of the granulated cloud and the details showing the domains of the grains after free expansion of 15 ms. We observe an isotropic expansion and the details of the figure allow us to identify the grains arising in the originally homogeneous superfluid. Applying the reversibility analysis, we find that, in situ, the grains have the average size of about 0.25 μm. They are clearly not regular either in shape or in size and do not form any structure that could be observed through the absorption.

For convenience, let us summarize the data characteristic of our experiments with ^{87}Rb atoms. The mass of a Rb atom is $m = 1.445 \times 10^{-22}$ g. The scattering

length is $a_s = 0.577 \times 10^{-6}$ cm. The radial frequency is $\omega_\perp = 1.32 \times 10^3\ \mathrm{s}^{-1}$ and longitudinal frequency is $\omega_z = 1.445 \times 10^2\ \mathrm{s}^{-1}$. The corresponding oscillator lengths are $l_\perp = 0.744 \times 10^{-4}$ cm and $l_z = 2.248 \times 10^{-4}$ cm. The average oscillator frequency and length are $\omega_0 = 0.631 \times 10^3\ \mathrm{s}^{-1}$ and $l_0 = 1.076 \times 10^{-4}$ cm. The effective condensate volume is $V_{eff} = 0.783 \times 10^{-11}\ \mathrm{cm}^3$. The average condensate density is $\rho \sim 2.554 \times 10^{15}\ \mathrm{cm}^{-3}$. The mean interatomic distance is $a = 0.732 \times 10^{-5}$ cm, which is much larger than the scattering length. Hence, the gas is rarified. The gas parameters are small, $\rho a_s^3 = 0.491 \times 10^{-3}$ and $\rho^{1/3} a_s = 0.079$. This implies that atomic interactions are weak. However, the effective coupling parameter (44) is large, $g = 1.95 \times 10^4$. Therefore the corresponding nonlinearity is very large.

The trap is subject to an external field modulation during the time $t_{ext} = 0.02$–0.06 s, with an alternating potential of frequency $\omega = 1.257 \times 10^3\ \mathrm{s}^{-1}$. The related modulation period is $t_{mod} \equiv 2\pi/\omega = 5 \times 10^{-3}$ s. The local equilibration time is $t_{loc} = m/(\hbar \rho a_s) = 0.929 \times 10^{-4}$ s. This is much shorter than the modulation period, because of which the system is always in local equilibrium.

With the average grain size $l_g \sim 2.5 \times 10^{-5}$ cm, the number of atoms inside a grain is $(l_g/a)^3 \sim 40$. And the number of grains in the trap is of order $(l_0/l_g)^3 \sim 400$.

The majority of experimental observations can be explained by the models of Sects. 4–7. But, certainly, other experiments for cross-checking the measured and theoretical dependencies are needed. Recent measurements of the momentum distribution of a turbulent cloud show the existence of a power-law type dependence $n(k) \propto k^{-\delta}$, which also requires confirmation and analysis with respect to its relation to the Kolmogorov-type behavior.

11 Conclusion

We have described the procedure of exciting a system of trapped Bose-condensed atoms by an external alternating potential, forcing the system to pass through several qualitatively different stages. Initially, the system is almost completely condensed, which is characterized by the broken global gauge symmetry. Applying sufficiently strong external perturbation transfers the system into a nonequilibrium state. First, there appear separate vortices and antivortices, which marks the transfer from the regular superfluid to vortex superfluid. Increasing perturbations is realized by either strengthening the amplitude of the applied alternating field or by its longer action on the system. Sufficiently strong perturbation generates a variety of coherent topological modes that decay into basic vortices with vorticity one. Thus, a multiplicity of vortices and antivortices is effectively generated. The location of these vortices inside the trap and their directions are random, which is caused by the absence of a unique rotation axis of

the applied alternating potential. Because of this, the increasing perturbation creates not a vortex lattice, as it would be in the case of a uniaxial rotation, but forms en ensemble of randomly directed vortices. When the number of vortices becomes large, they form a random vortex tangle typical of quantum turbulence. Increasing further the amount of energy, injected into the trap, breaks the system into pieces. Then Bose-condensed grains, or droplets, are surrounded by uncondensed gas in the normal state. Pumping more energy into the trap reduces the fraction of condensed atoms. Finally, the system should transfer into the normal state, where the global gauge symmetry is restored.

Thus, starting with a regular superfluid, we pass through the states of vortex superfluid, turbulent superfluid, granular fluid, and should finish with chaotic fluid that is in a state of classical turbulence. In that way, the initial state with global gauge symmetry breaking is transformed, through a sequence of qualitatively different regimes, to a state with the restored global gauge symmetry. Transitions between different regimes are classified as crossovers, though they are sufficiently sharp for allowing us to define the corresponding crossover lines. All these transitions, except that to chaotic fluid, are illustrated by experiments with trapped ^{87}Rb atoms.

Acknowledgments We are grateful to all our co-authors for collaboration. One of the authors (V.I.Y.) acknowledges financial support from the Russian Foundation for Basic Research.

References

1. L.D. Landau, E.M. Lifshitz, *Statistical Physics* (Pergamon, Oxford, 1980)
2. V.I. Yukalov, A.S. Shumovsky, *Lectures on Phase Transitions* (World Scientific, Singapore, 1990)
3. D. Sornette, *Critical Phenomena in Natural Sciences* (Springer, Berlin, 2006)
4. A. Polkovnikov, K. Sengupta, A. Silva, M. Vengalatore, Rev. Mod. Phys. **83**, 863 (2011)
5. L. Pitaevskii, S. Stringari, *Bose–Einstein Condensation* (Clarendon, Oxford, 2003)
6. E.H. Lieb, R. Seiringer, J.P. Solovej, J. Yngvason, *The Mathematics of the Bose Gas and Its Condensation* (Birkhauser, Basel, 2005)
7. V. Letokhov, *Laser Control of Atoms and Molecules* (Oxford University, New York, 2007)
8. C.J. Pethik, H. Smith, *Bose–Einstein Condensation in Dilute Gases* (Cambridge University, Cambridge, 2008)
9. P.W. Courteille, V.S. Bagnato, V.I. Yukalov, Laser Phys. **11**, 659 (2001)
10. J.O. Andersen, Rev. Mod. Phys. **76**, 599 (2004)
11. V.I. Yukalov, Laser Phys. Lett. **1**, 435 (2004)
12. K. Bongs, K. Sengstock, Rep. Prog. Phys. **67**, 907 (2004)
13. V.I. Yukalov, M.D. Girardeau, Laser Phys. Lett. **2**, 375 (2005)
14. A. Posazhennikova, Rev. Mod. Phys. **78**, 1111 (2006)
15. V.I. Yukalov, Laser Phys. Lett. **4**, 632 (2007)
16. N.P. Proukakis, B. Jackson, J. Phys. B **41**, 203002 (2008)
17. V.A. Yurovsky, M. Olshanii, D.S. Weiss, Adv. At. Mol. Opt. Phys. **55**, 61 (2008)
18. V.I. Yukalov, Laser Phys. **19**, 1 (2009)
19. A.L. Fetter, Rev. Mod. Phys. **81**, 647 (2009)
20. V.I. Yukalov, Phys. Part. Nucl. **42**, 460 (2011)

21. N.N. Bogolubov, *Lectures on Quantum Statistics*, vol. 1 (Gordon and Breach, New York, 1967)
22. N.N. Bogolubov, *Lectures on Quantum Statistics*, vol. 2 (Gordon and Breach, New York, 1970)
23. V.I. Yukalov, Phys. Rep. **208**, 395 (1991)
24. V.I. Yukalov, Int. J. Mod. Phys. **21**, 69 (2007)
25. V.I. Yukalov, Ann. Phys. (N.Y.) **323**, 461 (2008)
26. V.I. Yukalov, Phys. Lett. A **375**, 2797 (2011)
27. E.P. Gross, Phys. Rev. **106**, 161 (1957)
28. E.P. Gross, Ann. Phys. (N.Y.) **4**, 57 (1958)
29. V.L. Ginzburg, L.P. Pitaevskii, J. Exp. Theor. Phys. **7**, 858 (1958)
30. E.P. Gross, Nuovo Cimento **20**, 454 (1961)
31. L.P. Pitaevskii, J. Exp. Theor. Phys. **13**, 451 (1961)
32. B.A. Malomed, *Soliton Management in Periodic Systems* (Springer, New York, 2006)
33. Y.V. Kartashov, B.A. Malomed, L. Torner, Rev. Mod. Phys. **83**, 247 (2011)
34. J.R. Klauder, B.S. Skagerstam, *Coherent States* (World Scientific, Singapore, 1985)
35. V.I. Yukalov, E.P. Yukalova, V.S. Bagnato, Phys. Rev. A **56**, 4845 (1997)
36. V.I. Yukalov, E.P. Yukalova, V.S. Bagnato, Laser Phys. **10**, 26 (2000)
37. E.A. Ostrovskaya, Y.S. Kivshar, M. Lisak, B. Hall, F. Cattani, D. Anderson, Phys. Rev. A **61**, 031601 (2000)
38. D.L. Feder, M.S. Pindzola, L.A. Collins, B.I. Schneider, C.W. Clark, Phys. Rev. A **62**, 053606 (2000)
39. V.I. Yukalov, E.P. Yukalova, V.S. Bagnato, Laser Phys. **11**, 455 (2001)
40. Y.S. Kivshar, T.J. Alexander, S.K. Turitsin, Phys. Lett. A **278**, 225 (2001)
41. R. D'Agosta, B.A. Malomed, C. Presilla, Laser Phys. **12**, 37 (2002)
42. V.I. Yukalov, E.P. Yukalova, V.S. Bagnato, Laser Phys. **12**, 231 (2002)
43. V.I. Yukalov, E.P. Yukalova, V.S. Bagnato, Laser Phys. **12**, 1325 (2002)
44. B. Damski, Z.P. Karkuszewski, K. Sasha, J. Zakrzewski, Phys. Rev. A **65**, 013604 (2002)
45. R. D'Agosta, C. Presilla, Phys. Rev. A **65**, 043609 (2002)
46. V.I. Yukalov, E.P. Yukalova, V.S. Bagnato, Phys. Rev. A **66**, 043602 (2002)
47. N.P. Proukakis, P. Lambropoulos, Eur. Phys. J. D **19**, 355 (2002)
48. V.I. Yukalov, E.P. Yukalova, V.S. Bagnato, Laser Phys. **13**, 551 (2003)
49. V.I. Yukalov, E.P. Yukalova, V.S. Bagnato, Laser Phys. **13**, 861 (2003)
50. S.K. Adhikari, Phys. Lett. A **308**, 302 (2003)
51. S.K. Adhikari, J. Phys. B **36**, 1109 (2003)
52. P. Muruganandam, S.K. Adhikari, J. Phys. B **36**, 2501 (2003)
53. V.I. Yukalov, K.P. Marzlin, E.P. Yukalova, Laser Phys. **14**, 565 (2004)
54. V.I. Yukalov, K.P. Marzlin, E.P. Yukalova, Phys. Rev. A **69**, 023620 (2004)
55. S.K. Adhikari, Phys. Rev. A **69**, 063613 (2004)
56. V.S. Filho, L. Tomio, A. Gammal, T. Frederico, Phys. Lett. A **325**, 420 (2004)
57. E.R. Ramos, L. Sanz, V.I. Yukalov, V.S. Bagnato, Phys. Lett. A **365**, 126 (2007)
58. E.R. Ramos, L. Sanz, V.I. Yukalov, V.S. Bagnato, Phys. Rev. A **76**, 033608 (2007)
59. E.R. Ramos, L. Sanz, V.I. Yukalov, V.S. Bagnato, Nucl. Phys. **790**, 776 (2007)
60. E.R. Ramos, E.A. Henn, J.A. Seman, M.A. Caracanhas, K.M. Magalhães, K. Helmerson, V.I. Yukalov, V.S. Bagnato, Phys. Rev. A **78**, 063412 (2008)
61. V.I. Yukalov, V.S. Bagnato, Laser Phys. Lett. **6**, 399 (2009)
62. J. Williams, R. Walser, J. Cooper, E.A. Cornell, M. Holland, Phys. Rev. A **61**, 063612 (2000)
63. V.I. Yukalov, Laser Phys. Lett. **3**, 406 (2006)
64. V.I. Yukalov, Moscow Univ. Phys. Bull. **31**, 10 (1976)
65. V.I. Yukalov, J. Math. Phys. **32**, 1235 (1991)
66. V.I. Yukalov, E.P. Yukalova, Ann. Phys. (N.Y.) **277**, 219 (1999)
67. V.I. Yukalov, E.P. Yukalova, Chaos. Solit. Fract. **14**, 839 (2002)
68. N.N. Bogolubov, Y.A. Mitroposlky, *Asymptotic Methods in the Theory of Nonlinear Oscillations* (Gordon and Breach, New York, 1961)
69. V.I. Yukalov, E.P. Yukalova, Phys. Part. Nucl. **31**, 561 (2000)
70. V.I. Yukalov, E.P. Yukalova, Phys. Part. Nucl. **35**, 348 (2004)

71. A. Smerzi, S. Fantoni, S. Giovanazzi, S.R. Shenoy, Phys. Rev. Lett. **79**, 4950 (1997)
72. V.I. Yukalov, Mod. Phys. Lett. B **17**, 95 (2003)
73. V.I. Yukalov, E.P. Yukalova, Laser Phys. **16**, 354 (2006)
74. V.I. Yukalov, E.P. Yukalova, Phys. Rev. A **73**, 022335 (2006)
75. V.I. Yukalov, E.P. Yukalova, J. Phys. Conf. Ser. **104**, 012003 (2008)
76. B. Baizakov, G. Filatrella, B. Malomed, M. Salerno, Phys. Rev. E **71**, 036619 (2005)
77. E.J. Yarmchuk, M.J. Gordon, R.E. Packard, Phys. Rev. Lett. **43**, 214 (1979)
78. M.R. Matthews, B.P. Anderson, P.C. Haljan, D.S. Hall, C.E. Wieman, E.A. Cornell, Phys. Rev. Lett. **83**, 2498 (1999)
79. K.W. Madison, F. Chevy, W. Wohlleben, J. Dalibard, Phys. Rev. Lett. **84**, 806 (2000)
80. P. Rosenbusch, V. Bretin, J. Dalibard, Phys. Rev. Lett. **89**, 200403 (2002)
81. V.I. Yukalov, Acta Phys. Pol. A **57**, 295 (1980)
82. Z. Dutton, M. Budde, C. Slowe, L.V. Hau, Science **293**, 663 (2001)
83. V.I. Yukalov, E.P. Yukalova, Laser Phys. Lett. **1**, 50 (2004)
84. J. Ruostekoski, Z. Dutton, Phys. Rev. A **72**, 063626 (2005)
85. I. Shomroni, E. Lahoud, S. Levy, J. Steinhauer, Nat. Phys. **5**, 193 (2009)
86. M. Ma, R. Carretero-Gonzalez, P.G. Kevrekidis, D.J. Frantzeskakis, B.A. Malomed, Phys. Rev. A **82**, 023621 (2010)
87. S. Ishiro, M. Tsubota, H. Takeuchi, Phys. Rev. A **83**, 063602 (2011)
88. T.P. Simula, Phys. Rev. A **84**, 021603 (2011)
89. J.R. Abo-Shaeer, C. Raman, J.M. Vogels, W. Ketterle, Science **292**, 476 (2001)
90. E.A.L. Henn, J.A. Seman, E.R.F. Ramos, M. Caracanhas, P. Castilho, E.P. Olimpio, G. Roati, D.V. Magalhães, K.M.F. Magalhães, V.S. Bagnato, Phys. Rev. A **79**, 043618 (2009)
91. J.A. Seman, E.A.L. Henn, M. Haque, R.F. Shiozaki, E.R.F. Ramos, M. Caracanhas, P. Castilho, C. Castelo Branco, P.E.S. Tavares, F.J. Poveda-Cuevas, G. Roati, K.M.F. Magalhães, V.S. Bagnato, Phys. Rev. A **82**, 033616 (2010)
92. J.A. Seman, *Thesis* (University of São Paulo, São Carlos, 2011)
93. R.P. Feynman, Prog. Low Temp. Phys. **1**, 17 (1955)
94. P.A. Davidson, *Turbulence: Introduction for Scientists and Engineers* (Oxford University, Oxford, 2004)
95. R. Donnelly, C. Swanson, J. Fluid Mech. **173**, 387 (1986)
96. A.N. Kolmogorov, Proc. USSR Acad. Sci. **30**, 299 (1941)
97. A.N. Kolmogorov, Proc. USSR Acad. Sci. **32**, 16 (1941)
98. K. Sreenivasan, Phys. Fluids **7**, 2778 (1995)
99. H.E. Hall, W.F. Vinen, Proc. R. Soc. Lond. A **238**, 204 (1956)
100. W.F. Vinen, Proc. R. Soc. Lond. A **243**, 400 (1958)
101. J. Maurer, P. Tabeling, Eur. Phys. Lett. **43**, 29 (1998)
102. S.R. Stalp, L. Skrbek, R.J. Donnelly, Phys. Rev. Lett. **82**, 4831 (1999)
103. B.V. Svistunov, Phys. Rev. B **52**, 3647 (1995)
104. M. Kobayashi, M. Tsubota, J. Phys. Soc. Jpn **74**, 3248 (2005)
105. C.F. Barenghi, R.J. Donnelly, W.F. Vinen, *Quantized Vortex Dynamics and Superfluid Turbulence* (Springer, New York, 2001)
106. W.F. Vinen, J.J. Niemela, J. Low Temp. Phys. **128**, 167 (2002)
107. V.I. Yukalov, Laser Phys. Lett. **7**, 467 (2010)
108. B. Nowak, J. Schole, D. Sexty, T. Gasenzer, Phys. Rev. A **85**, 043627 (2012)
109. M. Kobayashi, M. Tsubota, Phys. Rev. A **76**, 045603 (2007)
110. M. Tsubota, J. Phys. Condens. Matt. **21**, 164207 (2009)
111. E.A.L. Henn, J.A. Seman, G. Roati, K.M.F. Magalhães, V.S. Bagnato, Phys. Rev. Lett. **103**, 045301 (2009)
112. J.A. Seman, R.F. Shiozaki, F.J. Poveda-Cuevas, E.A.L. Henn, K.M.F. Magalhães, G. Roati, G.D. Telles, V.S. Bagnato, J. Phys. Conf. Ser. **264**, 012004 (2011)
113. R.F. Shiozaki, G.D. Telles, V.I. Yukalov, V.S. Bagnato, Laser Phys. Lett. **8**, 393 (2011)

114. J.A. Seman, E.A.L. Henn, R.F. Shiozaki, G. Roati, F.J. Poveda-Cuevas, K.M.F. Magalhães, V.I. Yukalov, M. Tsubota, M. Kobayashi, K. Kasamatsu, V.S. Bagnato, Laser Phys. Lett. **8**, 691 (2011)
115. V.I. Yukalov, E.P. Yukalova, V.S. Bagnato, Laser Phys. **19**, 686 (2009)
116. R. Graham, A. Pelster, Int. J. Bifurc. Chaos. **19**, 2745 (2009)
117. C. Gaul, C.A. Müller, Phys. Rev. A **83**, 063629 (2011)
118. V.I. Yukalov, R. Graham, Phys. Rev. A **75**, 023619 (2007)
119. V.I. Yukalov, E.P. Yukalova, K.V. Krutitsky, R. Graham, Phys. Rev. A **76**, 053623 (2007)
120. V.I. Yukalov, Int. J. Mod. Phys. **17**, 2333 (2003)
121. V.I. Yukalov, E.P. Yukalova, Laser Phys. **21**, 1448 (2011)
122. V.N. Tsytovich, *Theory of Turbulent Plasma* (Consultant Bureau, New York, 1977)
123. S. Dyachenko, A.C. Newell, A. Pushkarev, V.E. Zakharov, Physica D **57**, 96 (1992)
124. S. Galtier, S.N. Nazarenko, A.C. Newell, A. Pouquet, J. Plasma Phys. **63**, 447 (2000)
125. N.G. Berloff, B.V. Svistunov, Phys. Rev. A **66**, 013603 (2002)
126. Y. Lvov, S. Nazarenko, R. West, Physica D **184**, 333 (2003)
127. V. Zakharov, F. Dias, A. Pushkarev, Phys. Rep. **398**, 1 (2004)
128. C. Raman, Phys. Rev. Lett. **87**, 210402 (2001)
129. K.W. Madison, F. Chevy, W. Wohlleben, J. Dalibard, J. Mod. Opt. **47**, 2715 (2000)
130. O.M. Marago, S.A. Hopkins, J. Arlt, E. Hodby, G. Hechenblaikner, C.J. Foot, Phys. Rev. Lett. **84**, 2056 (2000)
131. P.E.S. Tavares, Thesis (University of São Paulo, São Carlos, 2011)
132. M. Tsubota, S.I. Ogawa, Y. Hattori, J. Low Temp. Phys. **121**, 435 (2000)
133. M. Caracanhas, A.L. Fetter, S.R. Muniz, K.M.F. Magalhães, G. Roati, G. Bagnato, V.S. Bagnato, J. Low Temp. Phys. **166**, 49 (2012)

Bright Solitary Matter Waves: Formation, Stability and Interactions

T. P. Billam, A. L. Marchant, S. L. Cornish, S. A. Gardiner and N. G. Parker

Abstract In recent years, bright soliton-like structures composed of gaseous Bose–Einstein condensates have been generated at ultracold temperature. The experimental capacity to precisely engineer the nonlinearity and potential landscape experienced by these solitary waves offers an attractive platform for fundamental study of solitonic structures. The presence of three spatial dimensions and trapping implies that these are strictly distinct objects to the true soliton solutions. Working within the zero-temperature mean-field description, we explore the solutions and stability of bright solitary waves, as well as their interactions. Emphasis is placed on elucidating their similarities and differences to the true bright soliton. The rich behaviour introduced in the bright solitary waves includes the collapse instability and asymmetric collisions. We review the experimental formation and observation of bright solitary matter waves to date, and compare

T. P. Billam
Department of Physics, Jack Dodd Centre for Quantum Technology,
University of Otago, Dunedin, New Zealand
e-mail: thomas.billam@otago.ac.nz

A. L. Marchant · S. L. Cornish · S. A. Gardiner
Department of Physics, Joint Quantum Centre (JQC) Durham-Newcastle,
Durham University, Durham, UK
e-mail: a.l.marchant@durham.ac.uk

S. L. Cornish
e-mail: s.l.cornish@durham.ac.uk

S. A. Gardiner
e-mail: s.a.gardiner@durham.ac.uk

N. G. Parker (✉)
School of Mathematics and Statistics, Joint Quantum Centre (JQC) Durham-Newcastle,
Newcastle University, Newcastle upon Tyne, UK
e-mail: nick.parker@newcastle.ac.uk

Progress Optical Sci., Photonics (2013): 403–455
DOI: 10.1007/10091_2012_20

Published Online: 30 November 2012

to theoretical predictions. Finally we discuss some topical aspects, including beyond-mean-field descriptions, symmetry breaking, exotic bright solitary waves, and proposals to exploit bright solitary waves in interferometry and as surface probes.

1 Introduction

1.1 Gaseous Bose–Einstein Condensates

In 1925 Einstein predicted that an ideal and uniform gas of bosons, under conditions of sufficiently high density and/or low temperature, would begin to "condense" into the single particle quantum state of zero energy [1]. This phenomenon of Bose–Einstein condensation is now known to extend beyond gases into liquids and solids, being the underlying mechanism responsible for superfluidity in Helium and superconductivity [2]. But it is the gaseous form of this phenomenon that offers the purest and most controllable realization of this state of matter [3–5].

Since 1995, gaseous atomic Bose–Einstein condensates (BECs) have been generated in laboratories world-wide. These gases are extremely dilute, with typical number densities of 10^{18}–10^{21} m^{-3}, and the onset of Bose–Einstein condensation occurs at ultracold temperatures of around 100 nK [3]. Typically, experiments are run sufficiently far below this critical temperature that practically all the atoms enter the Bose–Einstein condensate, and the remaining thermal gas component becomes negligible. Within the Bose–Einstein condensate, the individual de Broglie wavelengths of the atoms overlap, forming a single coherent matter wave that extends across the system. From a theoretical perspective, this enables the description of the many-body system via a single mean-field wave equation.

Although these gases are dilute, the atom–atom interactions play a significant role and introduce a nonlinearity into the system. At such low temperatures and densities, the interactions arise predominantly via elastic *s*-wave collisions, which are short-range and introduce a local cubic nonlinearity into the mean-field wave equation. Furthermore, these interactions are usually repulsive.

The gases are formed and held within confining potentials produced via magnetic or optical fields. These make the condensate finite in size and introduce an inhomogeneity across the system, both of which have major implications for the static properties and dynamics of the gases, not least for the bright solitary waves considered herein. Furthermore, these configurable traps allow for the dimensionality of the system to be engineered to produce "quasi-one-dimensional" and "quasi-two-dimensional" systems.

1.2 Solitons and Bright Solitary Matter Waves

Solitons are non-dispersive waves that arise across nonlinear systems, such as shallow water, plasmas and optical fibres [6, 7]. Although solitons are defined formally as mathematical solutions of nonlinear wave equations, a physical, "working" definition is that a soliton [7]:

- Retains its initial shape for all time
- Is localized
- Can pass through other solitons and retain its size and shape.

The mean-field wave equation of a BEC is of the form of the $(3 + 1)$D cubic nonlinear Schrödinger equation, with an additional inhomogeneous term arising from the trapping potential. In the theoretical limit of 1D and in the absence of trapping in the remaining direction, this reduces to the 1D nonlinear Schrödinger equation, for which bright and dark soliton solutions are known to exist. Bright solitons are localized humps in the field amplitude, bound together by a focussing nonlinearity. Dark solitons appear as localized reductions in an otherwise uniform field amplitude, preserved instead by a defocussing nonlinearity. While analogs of dark solitons have been observed in BECs (see [8] for a review), we here focus on the case of bright solitons.

Bright soliton-like [9–11] structures have been observed in BECs, with the required focussing nonlinearity arising from the attractive atomic interactions. Of course, the physical reality introduces three dimensions and trapping potentials/finite-sized systems, and so these are strictly distinct objects from the true bright solitons. As such we will henceforth refer to this wider family of structures as bright solitary waves. Following the definition of Morgan et al. [12] we regard a solitary wave as a wavepacket that propagates without change of shape. This relaxed definition will allow for the inclusion of solutions which feature trapping potentials and three dimensions, as we shall see. Of course, one should not assume that a solitary wave will mimic the wider properties of the classic bright soliton and it is a key focus of this chapter to elucidate this intimate relationship.

Bose–Einstein condensates are an attractive system in which to study solitonic waves, with some key features summarized below:

- A sophisticated toolbox based on atomic physics allows almost arbitrary shapes of confining potentials to be constructed, for example, waveguides to steer the wavepackets, systems of reduced dimensionality, and disordered and periodic potential landscapes.
- This toolbox also enables the interactions (i.e. the nonlinearity) to be changed effectively from infinitely attractive, through zero, to infinitely repulsive via the exploitation of Feshbach resonances. Moreover, one can employ atoms such as ^{52}Cr which feature permanent magnetic dipole moments; this introduces long-range atom–atom interactions, i.e. nonlocal nonlinearity, into the system [13].

- The condensate density can be imaged directly with high contrast. While this is most commonly performed via destructive techniques based on optical absorption, non-destructive imaging techniques are also possible, e.g. phase-contrast imaging [3]. The phase of the condensate can also be mapped out in space and time via interferometric techniques [14].
- Bright solitary waves, which typically exist as small BECs, are mesoscopic quantum systems. This scale allows interfacing of the robust and well-established mean-field description of BECs with more sophisticated models that incorporate thermal and quantum effects [4].
- The precision and control offered by BECs makes them an attractive system in general for application in ultra-precise force detection and quantum information. For these applications, bright solitary waves offer further merits through their self-trapped, highly-localized form.

1.3 The Mean-Field Gross–Pitaevskii Equation

Our theoretical analysis will be based upon the well-established Gross–Pitaevskii equation, which is a wave equation for the classical field of the many-body wave-function [3–5]. This equation is a valid description for a gaseous BEC providing:

- The condensate is macroscopically-populated, i.e. $N \gg 1$, where N is the number of atoms in the condensate.
- The temperature of the gas satisfies $T \ll T_{\mathrm{c}}$, where T_{c} is the critical temperature for Bose–Einstein condensation, such that approximately all the particles are within the BEC phase.
- The dominant inter-atomic interactions are two-body, short-range elastic s-wave collisions, parameterized by the s-wave scattering length a_{s}.
- The condition of length scales $|a_s| \ll d$, where d the average interparticle distance, is satisfied. Then, the detailed shape of the inter-atomic potential $U(\mathbf{r}-\mathbf{r}')$ becomes unimportant and it can be approximated by the contact potential.,

$$U(\mathbf{r}-\mathbf{r}') = \frac{4\pi\hbar^2 a_s}{m}\,\delta(\mathbf{r}-\mathbf{r}'), \tag{1}$$

where m is the atomic mass.

- The interactions are weak, parameterized by the condition $n|a_{\mathrm{s}}|^3 \ll 1$, such that fluctuations out of the single-particle state are negligible.

Subject to these criteria, the condensate can be parameterized in time and space by a mean-field order parameter $\psi(\mathbf{r},t)$, often termed the *macroscopic wave-function*. For convenience we take $\psi(\mathbf{r},t)$ to be normalized to unity, i.e.,

$$\int |\psi(\mathbf{r},t)|^2\,\mathrm{d}^3\mathbf{r} = 1. \tag{2}$$

According to the Madelung transform, $\psi(\mathbf{r},t)$, which is complex, can be related to the atom number density $n(\mathbf{r},t)$ and a phase function $\theta(\mathbf{r},t)$ via,

$$\psi(\mathbf{r},t) = \sqrt{\frac{n(\mathbf{r},t)}{N}}\exp[i\theta(\mathbf{r},t)], \tag{3}$$

where N is the number of atoms in the condensate (introduced here to account for the normalization of ψ to unity).

The field ψ evolves in space and time according to the Gross–Pitaevskii equation [3–5],

$$i\hbar\frac{\partial\psi(\mathbf{r},t)}{\partial t} = \left[-\frac{\hbar^2}{2m}\nabla^2 + V(\mathbf{r}) + \frac{4\pi\hbar^2 N a_s}{m}|\psi(\mathbf{r},t)|^2\right]\psi(\mathbf{r},t), \tag{4}$$

where $V(\mathbf{r})$ specifies the external potential acting on the condensate (taken, for simplicity, to be time-independent) and m is the atomic mass.

The time-independent eigenstate solutions of Eq. (4) obey the GPE in its stationary form,

$$\left[-\frac{\hbar^2}{2m}\nabla^2 + V(\mathbf{r}) + \frac{4\pi\hbar^2 N a_s}{m}|\psi(\mathbf{r})|^2 - \mu\right]\psi(\mathbf{r}) = 0, \tag{5}$$

where μ is a (real) eigenvalue. The lowest energy solution to this equation represents the mean-field ground state of the BEC.

The Gross–Pitaevskii equation has proven an excellent description of a vast spectrum of static and dynamical properties of BECs [3–5]. The present work will be based primarily on this mean-field description, although we will briefly discuss beyond-mean-field descriptions in Sect. 7.1.

As is most commonly used to confine a BEC, we will assume a trapping potential that is harmonic in shape. For simplicity, we will further assume the trap to be cylindrically symmetric. This restriction sacrifices only a little generality for significant gains in clarity. We write this potential as,

$$V(\mathbf{r}) = \frac{1}{2}m\left[\omega_x^2 x^2 + \omega_r^2(y^2+z^2)\right], \tag{6}$$

where ω_x is the trap frequency in the axial (long) direction and ω_r is the trap frequency in the transverse directions. When dealing with such three-dimensional (3D) systems we introduce the trap anisotropy $\lambda = \omega_x/\omega_r$, with $\lambda < 1 (> 1)$ corresponding to a prolate (oblate) trap.

It is useful to parameterise the interaction strength of the condensate via,

$$k \equiv \frac{|a_s|N}{a_r}, \tag{7}$$

where $a_r = \sqrt{\hbar/m\omega_r}$ is the harmonic oscillator length in the radial direction.[1]

[1] Note that in works that focus specifically on fully trapped condensates, k is more commonly defined in terms of a geometric average of trap frequencies (e.g. Refs. [11, 15–24]). The radial harmonic oscillator length here is advantageous as it allows us to readily consider the case of zero axial trapping ($\lambda = 0$).

1.4 Chapter Overview

The bright solitary waves generated experimentally are related, but strictly different, entities to the true bright solitons (which apply only in 1D and for a uniform, infinite system). It is the focus of this chapter to explore this relationship in detail, highlighting the similarities and differences. In essence, we wish to shed light on how "soliton-like" these solitary waves are. We will consider how the waves look, how they move and how they interact with each other. The deviation of the bright solitary wave from the true bright soliton is a consequence of two factors: the inclusion of an inhomogeneous trapping potential and the extension to three-dimensions, and we will consider these two factors separately so as to elucidate their independent contributions to the identity of bright solitary waves. We first begin in Sect. 2 by outlining the experimental generation and observation of bright solitary matter waves to date. Following this we begin our theoretical analysis of bright solitary waves. Sections 3 and 4 explore the static solutions of bright solitary waves. In Sect. 3 this is conducted within an effective 1D model of the condensate, and the role of axial trapping considered. Then in Sect. 4 we extend our analysis of the static solutions to 3D, where the collapse instability comes into play. In Sects. 5 and 6 we turn to the dynamics of bright solitary waves in 1D and 3D, respectively. There we consider the solitary wave dynamics resulting from the presence of axial trapping and the interaction with another solitary wave. In Sect. 7 we turn our attention to some current hot topics in bright solitary wave research, discussing beyond-mean-field descriptions and the current anomalies with mean-field predictions, examples of spontaneous symmetry breaking with solitary waves, predictions of exotic bright solitary waves, and proposals for controllable generation of bright solitary waves and exploiting them as ultra-precise atom-optical sensors. Finally, in Sect. 8, we draw some general conclusions.

2 Bright Solitary Matter Wave Experiments

In order to experimentally realise bright solitary matter waves precise control over the *s*-wave scattering properties of an atomic sample is of paramount importance. In the following section we discuss the application of magnetic Feshbach resonances as a means of establishing this control and review bright solitary matter wave experiments to date.

2.1 Tuning Atomic Interactions: Feshbach Resonances

The use of magnetically tunable Feshbach resonances [25] to control the interaction between atoms is now commonplace in many ultracold atomic gas experiments. Feshbach resonances arise when a resonant coupling occurs between the

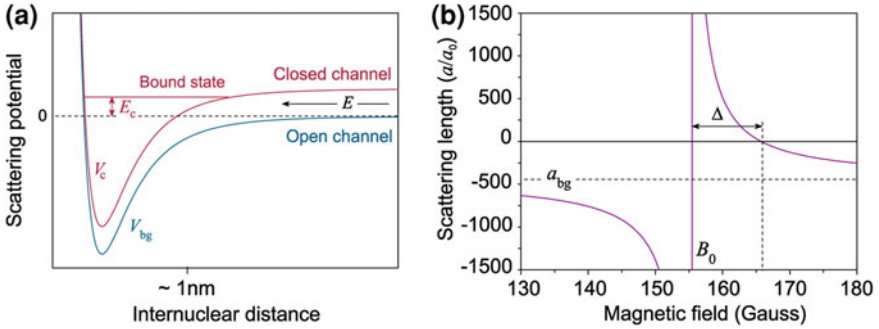

Fig. 1 Feshbach resonances: **a** A two channel model of a Feshbach resonance. A resonance occurs when two atoms colliding with energy E resonantly couple to a bound state of the closed channel. **b** The Feshbach resonance present in the $F = 2, m_F = -2$ state of ^{85}Rb

collisional open and closed channels of an atomic system, as illustrated in Fig. 1a. For large internuclear distances, the interaction between two atoms can be described by the background potential, $V_{\rm bg}$. If two free atoms approach, colliding with low energy, E, this potential represents the open or entrance channel for the collision. In contrast, closed channels (described by $V_{\rm c}$) are able to support molecular bound states. A Feshbach resonances occurs when the energy of a quasi-bound molecular state in the closed channel, $E_{\rm c}$, approaches that of the open channel. In this instance a strong mixing between the two channels can occur even in the presence of only weak coupling. By changing the magnetic field applied this energy difference can be tuned if the magnetic moments of the two channels differ thus the scattering properties of the atomic sample can be modified.

These resonances allow the value of the s-wave scattering length, a_s, to be changed over many orders of magnitude in both the positive and negative domain by simply changing the magnetic field,

$$a_s(B) = a_{\rm bg}\left(1 - \frac{\Delta}{B - B_0}\right). \tag{8}$$

Here a_s is the scattering length at the field of interest, B, $a_{\rm bg}$ is the background scattering length away from the resonance, Δ is the width of the resonance and B_0 is the resonance position. In the limit $B \to B_0$, the scattering length diverges $a_s \to \pm\infty$. Then the gas is no longer weakly-interacting (the condition $n|a_s|^3 \ll 1$ is not satisfied) and the Gross–Pitaevskii equation ceases to be an adequate model.

In the case of broad resonances, where $\Delta \gtrsim 1$ G, there is a smooth variation of the scattering length through zero from positive to negative with a slope of $da_s/dB = a_s/\Delta$. For Bose–Einstein condensation of some species (e.g. ^{85}Rb, ^{7}Li) this is of particular importance as it allows the creation of stable condensates with repulsive interactions $(a_s > 0)$ despite a negative background scattering length away from the resonance. As an illustration, Fig. 1b shows the Feshbach resonance

in the $F = 2, m_F = -2$ state of ^{85}Rb. This broad resonance, of width 10.7 G, at ~ 155 G gives tuning of the scattering length on the order $40a_0/\mathrm{G}$ close to the zero crossing.

In all of the experiments described in the following sections a Feshbach resonance is the key atomic tool without which the controlled creation of bright solitary matter waves would not be possible.

2.2 Collapse of an Attractive Bose–Einstein Condensate

A BEC (in three-dimensions) with attractive interactions is inherently unstable to collapse when its interaction parameter $k = N|a_s|/a_r$ exceeds a critical value k_c. This leads to the typical notion of a critical atom number N_c (for fixed a_s and a_r) or critical scattering length a_c (for fixed N and a_r) at which instability becomes induced. The origin of the collapse instability will be outlined theoretically in Sect. 4.1. The ensuing collapse of the condensate has been dubbed the 'Bosenova' in analogy to the astronomical phenomena of stellar explosion.

The first experimental insights into BECs with attractive interactions were made using ^{7}Li [26]. Here the negative scattering length of $a_s = (-27.4 \pm 0.8)\, a_0$, where $a_0 = 5.29 \times 10^{-11}$ m is the Bohr radius, means that the condensate atom number N grows until it reaches N_c and the condensate collapses. During the collapse the density of the cloud rises thus increasing both the elastic and inelastic collision rates. This causes atoms to be ejected from the condensate with high energy in a violent explosion. Following this, the condensate begins to reform, fed by the surrounding bath of thermal atoms also present in the trap. If observed for an extended period the system exhibits a saw-tooth dynamic of growth and collapse [27] until equilibrium is eventually reached. Throughout, the maximum condensate number is strictly limited to the critical number for an attractive BEC. It is important to note that a three-dimensional attractive condensate with $N < N_\mathrm{c}$ is a metastable state of the system, with the true ground state being the collapse state (as we shall explore theoretically later in this chapter). As such, quantum tunneling and thermal fluctuations may also enable a transition from the metastable to the collapse state, even for $N < N_\mathrm{c}$ [28–31].

Further insight into the collapse phenomena came from the group at JILA (Boulder, US) in 2001 [15, 32], carrying out a controlled collapse using a pure ^{85}Rb condensate. Tuning the scattering length from positive to negative using the broad Feshbach resonance illustrated in Fig. 1b not only enabled the collapse process to be precisely initiated but also allowed the condition $k > k_\mathrm{c}$ to be fulfilled, unlike systems using fixed negative scattering lengths. Along with control of the initial condensate number, control over scattering length made the testing of critical number models possible, finding the exact scattering length necessary to collapse the cloud, a_c. Early work examining the point of collapse using slow field ramps confirmed the relationship between critical number and scattering length,

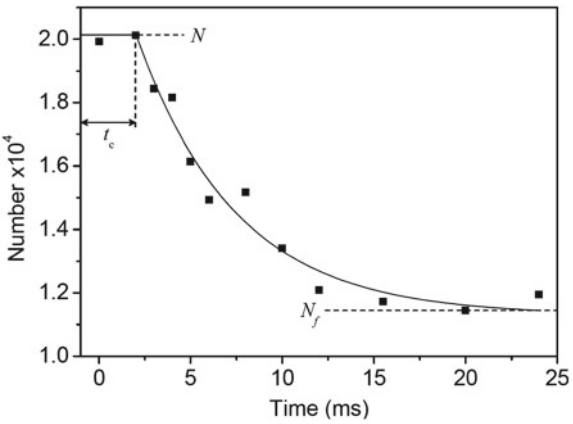

Fig. 2 Controlled collapse: The collapse of a stable Bose–Einstein condensate can be triggered by a sudden change of the scattering length from positive to negative. After some time at the new attractive scattering length a_f the condensate begins to collapse and atoms are lost. Eventually the collapse process ceases, leaving a stable remnant in the trap containing N_f atoms (Data from Durham ^{85}Rb experiment)

determining the critical interaction parameter for k_c. Later improvements to the calibration of the Feshbach resonance, enhancing precision, found k_c to be in excellent agreement with mean-field models [33].

Following this, the JILA experiments were then extended to study the dynamics of the collapse, measuring the evolution of the condensate number following a 'sudden' change in the scattering length to some value, denoted a_f. This value satisfied the criteria $a_f < a_c$ such that the condensate suddenly entered a regime where it was unstable to collapse. Measurements of atom number as a function of time showed a sudden yet delayed loss of atoms, as shown in Fig. 2. As the interactions are made attractive the condensate begins to shrink in size, thus increasing its density. This contraction tends to accelerate with time eventually leading to collapse of the condensate. The time for the collapse to begin t_c was found to be shorter for larger $|a_s|$ as the stronger attraction between atoms in the condensate results in a more rapid contraction of the cloud. Following the collapse, a stable remnant component was formed in the trap. Notably, the number of atoms maintained in this remnant, N_f, was found to depend strongly on N and a_s and in many cases exceeded N_c. This remnant was observed to persist in the trap for more than 1 s, oscillating in a highly excited state.

In addition, a number of more qualitative features were observed about the collapse process in the ^{85}Rb experiment. The first of these features was a burst of atoms being ejected from the condensate during collapse. The energy of the burst varied with the value of a_f. The burst would then focus at multiples of $T_x/2$ and $T_r/2$, where $T_{x,r} = 2\pi/\omega_{x,r}$ is the trap period in the axial (x) and radial (r) dimensions. In all experiments only full, never partial, collapse was observed.

However, if interrupted (by jumping the scattering length away from the collapse point), jets of atoms were also formed. Unlike the burst, these streams of atoms were found to have highly anisotropic velocities and were interpreted as indicating the local pinching of the wavefunction during the collapse.

The collapse process has since been revisited by the group at the Australian National University (Canberra, Australia) [34]. Again using ^{85}Rb, measurements of the collapse time have been shown to be in good agreement with mean-field models describing the process which take into account three-body loss mechanisms.

2.3 Observation of Bright Solitary Matter Waves

The advent of optical trapping led to the realisation of experimental geometries closer to the ideal 1D limit. This, in combination with control of the atomic scattering length via Feshbach resonances, led to the first observations of bright solitary matter waves by groups at Rice University (Houston, US) [9] and Ecole Normale Supérieure (Paris, France) [10] in 2002 using ^{7}Li. Despite two inherently similar experiments, the ENS group succeeded in producing a single solitary wave whereas the Rice experiment resulted in trains of multiple solitary waves.

In both experiments initial cooling of the atomic sample was carried out in a magnetic trap using the $F = 2, m_F = 2$ state. The atoms were subsequently transferred into an optical dipole trap [35] and a microwave field was used to transfer the atoms to the $F = 1, m_F = 1$ state. This state is the absolute internal ground state in a magnetic field and consequently two-body inelastic losses are completely suppressed, aiding the creation of condensates. Moreover, collisions between atoms in this state exhibit a broad Feshbach resonance suitable for the precise control of the atomic interactions necessary for the realisation of solitary waves.

In the ENS experiment optical confinement was realised using a red-detuned crossed dipole trap. Here condensates of 2×10^4 atoms were produced with $a_s = +39.7a_0$ in an approximately isotropic harmonic trap. After the creation of the BEC the scattering length was tuned close to $a_s = 0$ before adiabatically reducing the power in one of the beams, producing a highly elongated cylindrical harmonic trap with $\omega_x = 2\pi \times 50$ Hz and $\omega_r = 2\pi \times 710$ Hz. The bias field, and hence scattering length, was then ramped to its final value before the vertical beam was switched off, releasing the cloud into a 1D waveguide. In this trap, the atoms experience a slightly expulsive potential due to the magnetic coils used to produce the bias field. As a typical example, at $B = 520$ G, the trap frequency along the waveguide can be considered imaginary, around $\omega_x = 2i\pi \times 78$ Hz. Tuning the scattering length to a small negative value, $a_s = -3.97\, a_0$, resulted in a soliton of 6×10^3 atoms able to propagate without dispersion for over 1.1 mm.

In contrast to the crossed ENS trap, the Rice experiment used a single red-detuned dipole beam to provide radial confinement. Two additional blue detuned

beams were applied to cap the ends of the trap in the axial direction. After forming a condensate of 3×10^5 atoms with $a_s \approx 200a_0$ the magnetic field controlling the scattering length was ramped exponentially to the final value and the laser end caps switched off thus setting the resulting solitary waves in motion.

In this experiment multiple solitary waves were observed. The number of these wavepackets, N_s, was found to be insensitive to the time constant of the exponential magnetic field ramp. However, N_s increased linearly with Δt, the time delay between the switch off of the end caps and the time of the scattering length change to $a_s < 0$. For the Rice experiment four solitary waves were observed for $\Delta t = 0$ with this number increasing to 10 for $\Delta t = 35$ ms. The wavepackets were observed to propagate for ~ 3 s, this being limited by atom loss rather than dispersion effects.

With many solitary waves confined in a single trap it becomes possible to explore the dynamical interactions of the wavepackets. Observation of the solitary wave motion showed evidence of a short range repulsive interaction between neighbouring wavepackets raising many questions regarding their formation and collisional dynamics. A possible explanation for the formation of multiple solitary waves was the presence of a modulational instability [36]. Here, phase fluctuations of the condensate lead to a local increase in density at wavelengths approximately equal to the healing length. The attractive nonlinearity leads to the growth of these density fluctuations and the emergence of solitary waves.

The spacing between neighbouring solitary waves observed at Rice increased near the centre of the oscillation and decreased near the turning points. This result implied a repulsive interaction between solitary waves. This interaction was attributed to the existence of π-phase differences between neighbouring solitary waves, somehow imprinted during their formation. The phase-dependence of the solitary wave interaction will be discussed in Sects. 5.1 and 6, and the origin of the π-phase difference in Sect. 7.1.

It was not until 2006 that solitary waves were again investigated experimentally, this time at JILA [11] using the same ^{85}Rb experiment that has first observed tunable atomic interactions [37] and controlled collapse [15]. This new work concluded that the stable remnant observed previously in the collapse experiments divided into similar solitary wave structures as seen at Rice. Intriguingly, these observations persisted despite the fact that the JILA trap remained almost isotropic (with radial and axial trap frequencies of 17.3 Hz and 6.8 Hz, respectively), far from the highly elongated geometries employed at ENS and Rice. The somewhat surprising capacity of bright solitary waves to be supported in almost isotropic trap geometries will be discussed in Sect. 4.3.

Unlike the ENS and Rice experiments, the JILA apparatus used a purely magnetic trap. However, the method of creating solitary waves by modifying the scattering length can be considered an inherently similar process. After producing condensates of up to 15,000 atoms at $a_s > 0$ the magnetic field was adiabatically ramped to decrease the scattering length to $a_s = 9a_0$. To initiate the collapse, the magnetic field was changed so as to rapidly (0.1) ms jump the scattering length

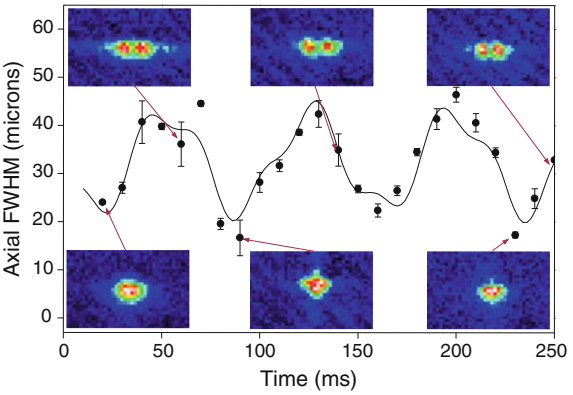

Fig. 3 Solitary wave oscillation in a weak magnetic trap [11]: Following the collapse process used in the JILA experiment a stable remnant is formed. The variation in the remnant's width with time can be explained by the creation of multiple bright solitary matter waves oscillating in the trap, which are visible in the 2D plots of atomic density (*insets*)

from a positive initial value to a negative final value of a_{f}. Following some time at the final scattering length, t_{evolve}, the atoms were destructively imaged. Investigating the collapse process as a function of a_{f} and the initial condensate number it was clear that the number of condensate atoms surviving the collapse could greatly exceed N_{c}. Furthermore, the lifetime of the stable remnant could be as long as several seconds. As we will review in Sect. 6.2, this observation is consistent with the presence of several repulsively-interacting bright solitary waves.

Observations of the condensate size in the trap as a function of time suggested a highly excited state had been produced during the collapse, with the remnant cloud's width doubling during its oscillation in the trap. However, further analysis revealed that, as in the Rice experiment, multiple solitary waves were being created which oscillated back and forth along the weak axial direction of the trap, shown in Fig. 3. The wavepackets were observed to persist in the trap for $\sim 3\,\mathrm{s}$, undergoing as many as 40 collisions in this time. This provided additional experimental data to accompany the Rice experiments and the growing body of theoretical work on the stability of three-dimensional bright solitary waves (which we will review in Sects. 4 and 6). The number of solitary waves created in the ^{85}Rb collapse experiment was found to be controllable, to a degree, depending on a_{f} and N_0. As expected, N_s increased with $|a_{\mathrm{f}}|$. Importantly, the number of atoms observed in any one solitary wave was never found to exceed N_{c}.

2.4 Current Developments

In order to further explore the results from both previous experiments and theoretical simulations, an experiment has been constructed at Durham University (Durham, UK). As in the JILA experiment, this apparatus uses ^{85}Rb in the $F = 2, m_F = -2$ state allowing access to the 10.7 G wide Feshbach resonance giving control over the scattering length of order $40\,a_0/\mathrm{G}$ close to $a_s = 0$. However, the trapping geometry, a crossed dipole trap and additional waveguide beam

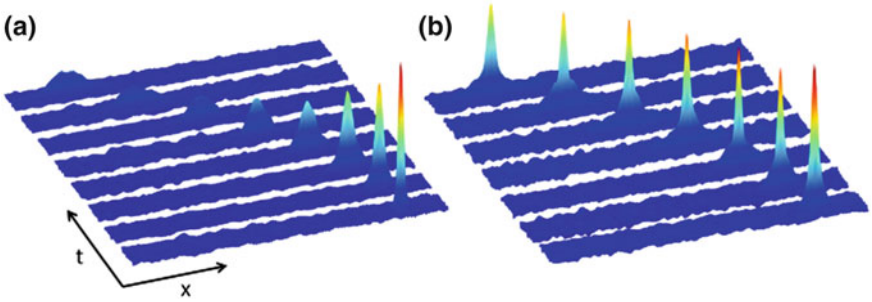

Fig. 4 Propagation in the waveguide: **a** As a repulsive BEC travels along the waveguide the interactions in the condensate cause it to spread out. **b** In contrast, the attractive interactions present in a bright solitary matter wave cause the wavepacket to hold together as it propagates, maintaining its shape with time (Data from Durham ^{85}Rb experiment)

to produce a quasi 1D geometry, allows entirely independent control of the trap frequencies and *s*-wave scattering properties (due to an independent magnetic bias field).

Here BECs are first created in the crossed dipole trap (at 300--400 a_0 by careful tuning of the atomic scattering properties. Once condensed, the scattering length is ramped close to $a_s = 0$ before the BEC is loaded into the waveguide by synchronously switching the cross beams off and the waveguide beam on. The scattering length is then jumped to a small, negative value ($\sim -6.5\, a_0$) and the BEC is allowed to propagate along the waveguide as shown in Fig. 4. Weak axial confinement along the beam is realised with the addition of a magnetic quadrupole gradient. Typically this results in trap frequencies of $\omega_x = 2\pi \times 1$ Hz and $\omega_r = 2\pi \times 27$ Hz. Using this method a single soliton can be produced containing $\sim$3,000 atoms observed to propagate a distance of $\sim$1 mm in 150 ms.

In addition to experiments aimed at investigating soliton splitting and binary collisions (the theory of which will be detailed in Sect. 7.3.1), the Durham experiment has the potential to be extended to the study of atom–surface interactions. Contained within the experimental apparatus is a super polished Dove prism (surface roughness <1 Å) designed to allow the study of both classical and quantum reflection from a surface. The self-stabilizing, localized nature of the wave packets means bright solitary matter waves show great potential as surface probes for the study of short-range atom–surface interactions in the future. This idea will be explored in more detail in Sect. 7.4.

The Rice group have reported further experimental activity on bright solitary matter waves [38]. Here they "kick" a bright solitary wave towards a thin potential barrier, formed by a near-resonant focussed laser beam. The wave-barrier interaction is observed to result in either reflection, transmission and splitting of the solitary wave, depending on the kinetic energy of the solitary wave, the potential strength and the nonlinearity (*s*-wave interaction strength). Moreover, for the case of a split solitary wave, they have applied a phase imprinting to one of the solitary waves and thereby studied phase-dependent interaction of solitary waves [39].

3 Bright Solitary Waves in 1D: Static Properties

Having reviewed the experimental formation and observation of bright solitary matter waves to date, we will now review our theoretical understanding of these wavepackets. Within a quasi-one-dimensional (quasi-1D) system, bright solitary matter waves become completely analogous—within the mean-field, Gross–Pitaevskii equation (GPE) treatment—to classical bright solitons of the 1D nonlinear Schrödinger equation (NLSE) [40]. In this section we examine the quasi-1D limit in which this occurs. In Sect. 3.1 we describe the conventional factorization to reduce the 3D GPE to an effective 1D form, and some approaches to include higher-order terms. In Sect. 3.2 we demonstrate the link to bright solitons and explore the static properties of bright soliton solutions of the NLSE. Then, in Sect. 3.3, we consider the bright solitary matter waves which occur as the ground state of an axially trapped BEC, elucidating how their form depends on the strength of the axial trap, and how they compare to the bright solitons of the 1D NLSE.

3.1 Effective One-Dimensional Descriptions

We begin by considering an attractively-interacting (s-wave scattering length $a_s < 0$) three-dimensional BEC confined by the cylindrically-symmetric harmonic trap of Eq. (6) and described by the 3D Gross–Pitaevskii equation, Eq. (4).

3.1.1 Quasi-One-Dimensional GPE

The quasi-1D limit is associated with highly elongated ($\omega_r \gg \omega_x$) traps. The reduction from the full 3D to an effective 1D description typically proceeds by assuming that the radial confinement is sufficiently strong,[2] that the radial modes of the condensate become essentially "frozen" into the ground harmonic oscillator ground state (i.e. a Gaussian wavefunction). This approximation then allows the factorization,

$$\psi(\mathbf{r}) = \sqrt{\frac{m\omega_r}{\pi\hbar}} \exp\left[\frac{-m\omega_r(y^2+z^2)}{2\hbar}\right] \psi(x) \tag{9}$$

where it is implied that both the Gaussian radial wavefunction and the axial wavefunction are both normalized to unity. Integrating over the y- and z-directions then yields the quasi-1D GPE for $\psi(x)$,

[2] Specifically, the criteria $\hbar\omega_r \gg \mu$ and $\hbar\omega_r \gg k_B T$ are required to ensure that the condensate and thermal energy scales are insufficient to excite the radial modes.

$$i\hbar\frac{\partial\psi(x,t)}{\partial t}=\left[-\frac{\hbar^2}{2m}\frac{\partial^2}{\partial x^2}+\frac{m\omega_x^2x^2}{2}-2\hbar\omega_rN|a_s||\psi(x,t)|^2\right]\psi(x,t). \tag{10}$$

In the static case, one obtains the stationary quasi-1D GPE,

$$\left[-\frac{\hbar^2}{2m}\frac{\partial^2}{\partial x^2}+\frac{m\omega_x^2x^2}{2}-2\hbar\omega_rN|a_s||\psi(x)|^2-\mu\right]\psi(x)=0. \tag{11}$$

This factorization has often been applied in the study of attractively-interacting condensates (in both dynamic and static situations) [41–46]. However, the regime in which this factorization is valid is significantly restricted for attractively-interacting condensates [47]; this issue is revisited using a full 3D analysis in Sect. 4.

3.1.2 One-Dimensional Equations with 3D Effects

Alternatives to the factorization presented above exist, which yield 1D equations retaining more 3D character by choosing to incorporate the coupling between axial and radial modes, and time-dependent dynamics of the radial modes [48–53]. These effects are manifest in the effective 1D equation through the appearance of higher-order terms. Consequently, the resulting equations have a wider range of validity than the bare 1D GPE (10), but are no longer isomorphous to the NLSE (for $\omega_x=0$).

For example, Salasnich et al. [48, 49] chose to factorize the 3D GPE wave-function into a slowly-varying axial function, multiplied by a rapidly varying radial function. The radial function was also given a dependence on the axial function itself; this incorporates the effect unique to attractive interactions in a cigar-shaped trap, where an increase in axial density leads to an associated increase in radial density. A variational calculation then yields the non-polynomial Schrödinger equation [48],

$$\begin{aligned}i\hbar\frac{\partial\psi(x,t)}{\partial t}=&-\frac{\hbar^2}{2m}\frac{\partial^2\psi(x,t)}{\partial x^2}+\frac{m\omega_x^2x^2}{2}\psi(x,t)+\frac{2\hbar^2|a_s|N|\psi(x,t)|^2\psi(x,t)}{ma_r\sqrt{1-2|a_s|N|\psi(x,t)|^2}}\\&+\frac{\hbar\omega_x}{2}\left(\frac{1}{\sqrt{1-2|a_s|N|\psi(x)|^2}}+\sqrt{1-2|a_s|N|\psi(x,t)|^2}\right)\psi(x,t).\end{aligned} \tag{12}$$

When $|a_s|N|\psi(x)|^2\ll1$ for all x this reduces first to an effective 1D equation with both cubic and quintic nonlinearities [51], and then to the bare 1D GPE (10) itself. These equations can be applied to both positive and negative a_s, although a modified equation for the case of positive a_s offers improved accuracy [52]. An

even more general approach can be taken, incorporating even fewer assumptions about the form of the ground state, but leading to a coupled system of effective 1D equations [50, 53].

3.2 Bright Soliton Solutions

Consider the 1D GPE (10) in the homogeneous regime $\omega_x = 0$. With the removal of the quadratic potential term, this becomes a 1D nonlinear Schrödinger equation (NLSE) with a focusing nonlinearity [40]. The 1D NLSE is a classical field equation which is integrable, in the sense that solutions possess an infinite and complete set of conserved quantities [6, 40, 54]. This is analogous to a discrete (Liouville-integrable) system which possesses as many conserved quantities as it does degrees of freedom [55]. This integrability leads to a spectrum of true soliton solutions [6, 54]. In the case of the 1D NLSE with focusing nonlinearity, these bright-soliton solutions were first discovered in Refs. [56, 57] using the inverse scattering technique (see Refs. [6, 54] for an overview).

The classical bright soliton solutions of this equation have been extensively studied in the context of optical solitons [56–62]. The same equation appears in many other fields, including biophysics, astrophysics and particle physics [40], and in the study of deep ocean waves [63]. The single-bright-soliton solution of the homogeneous 1D GPE is given by,

$$\psi(x,t) = \frac{a}{2\sqrt{b_x}}\operatorname{sech}\left[\frac{a(x-x_0-vt)}{2b_x}\right] \times \exp\left[i\left\{\frac{m}{\hbar}\left(v(x-x_0)+\frac{v^2t}{2}+\frac{\omega_r^2|a_s|^2N^2a^2t}{2}\right)+\Phi\right\}\right]. \tag{13}$$

This solution describes a single bright soliton with amplitude and norm[3] a, velocity v, displacement x_0, and phase Φ. The parameter $b_x \equiv \hbar/2m\omega_r|a_s|N$ is a length scale characterizing the soliton's spatial extent. Dynamical solutions composed of multiple bright solitons also exist; in these solutions each soliton has a similar form to Eq. (13) when well-separated from the others. These multiple-soliton solutions contain additional, dynamic phase and position shifts to account for the nonlinear interactions between solitons; these dynamical solutions are discussed further in Sect. 5.

The single-soliton ground state of the static 1D GPE (11) in its homogeneous ($\omega_x = 0$) form is given exactly by Eq. (13) with $a = 1$, $v = 0$, and arbitrary Φ and x_0. The quantity Φ can be chosen arbitrarily because it corresponds to a global

[3] In contrast to our definition here, a common convention in the literature is to define an amplitude A such that the norm is $2A$ [59].

phase of the wavefunction, and Eq. (11) possesses a $U(1)$ global phase symmetry. Similarly, the displacement x_0 may be chosen arbitrarily because the assumption of homogeneity $(\omega_x = 0)$ ensures the 1D GPE to be translationally symmetric. However, the choice of displacement x_0 in Eq. (13) for the ground state breaks this symmetry; in the context of atomic BECs, this symmetry-breaking is a feature of the mean-field description. This feature is at odds with a fully quantum-mechanical treatment; in the latter, the ground state of the system retains the translational symmetry of the equation, leading to a delocalized ground state [64, 65].

3.3 *Effect of Axial Trapping*

The addition of an axial harmonic trap $(\omega_x > 0)$ removes the integrability of the system and prevents the appearance of true solitons. While the new ground state is no longer a soliton, it remains a solitary wave in the sense of being capable of propagation without emission of radiation (see Sect. 5 and Refs. [12, 45, 46]). In this section we elucidate the form of the ground state under axial trapping and compare the form of this ground state to the NLSE bright soliton.

3.3.1 Variational Analysis

A great deal of insight into the form of the bright soliton state can be gained using the variational approach, first applied to bright solitons in the context of nonlinear optics [66, 67]. More recently, the variational approach has proved useful for treating a variety of problems involving bright solitary matter waves [47–51, 68–73] and will be used extensively in Sect. 4. Note that here we present the variational approach to analyse stationary solutions of the Gross–Pitaevskii equation. However, it can be extended to a non-stationary form to analyse dynamics, e.g., centre-of-mass motions [42] and excitation frequencies [71].

The ground state solution of Eq. (11) can be alternatively defined as the function $\psi(x)$ which minimizes the value of the classical field Hamiltonian,

$$H_{1D}[\psi(x)] = \int dx \left[\frac{\hbar^2}{2m} \left| \frac{\partial}{\partial x} \psi(x) \right|^2 + \frac{m\omega_x^2 x^2}{2} |\psi(x)|^2 - \hbar\omega_r N |a_s| |\psi(x)|^4 \right]. \quad (14)$$

This functional represents the energy per particle, and generates the 1D GPE (10) through the functional derivative $\delta H_{1D}[\psi]/\delta\psi^* = i\partial\psi/\partial t$.

In the homogeneous limit $(\omega_x = 0)$ the ground state is given by Eq. (13) with $a = 1$ and $v = 0$. In the trap-dominated limit $(\omega_x \to \infty)$ the ground state tends to the harmonic oscillator eigenstate $\psi(x) = (m\omega_x/\pi\hbar)^{1/4} e^{-m\omega_x x^2/2\hbar}$. These limits motivate our use of a normalized Gaussian ansatz,

$$\psi(x) = \left(\frac{m\omega_x}{\pi\hbar\ell_{x,\mathrm{G}}^2}\right)^{1/4} \exp\left(-\frac{m\omega_x x^2}{2\hbar\ell_{x,\mathrm{G}}^2}\right), \tag{15}$$

or a normalized sech ansatz,

$$\psi(x) = \frac{1}{2\sqrt{b_x\ell_{x,\mathrm{S}}}} \operatorname{sech}\left(\frac{x}{2b_x\ell_{x,\mathrm{S}}}\right), \tag{16}$$

to describe the intermediate regime $\omega_x > 0$. Substituting theses ansatz into Eq. (14) we obtain an energy functional in terms of the dimensionless length ℓ_x. Note that the sech ansatz length $\ell_{x,\mathrm{S}}$ is defined so that $\ell_{x,\mathrm{S}} \to 1$ as $\omega_x \to 0$, while the Gaussian ansatz length $\ell_{x,\mathrm{G}}$ is defined such that $\ell_{x,\mathrm{G}} \to 1$ as $\omega_x \to \infty$.

In the Gaussian case, one obtains the energy functional,

$$H_{1\mathrm{D}}(\ell_{x,\mathrm{G}}) = \hbar\omega_x\left(\frac{1}{4\ell_{x,\mathrm{G}}^2} + \frac{\ell_{x,\mathrm{G}}^2}{4} - \frac{a_x|a_s|N}{\sqrt{2\pi}a_r^2\ell_{x,\mathrm{G}}}\right), \tag{17}$$

where $a_x = \sqrt{\hbar/m\omega_x}$ and $a_r = \sqrt{\hbar/m\omega_r}$ are the axial and radial harmonic oscillator lengths. In the sech case, one instead obtains,

$$H_{1\mathrm{D}}(\ell_{x,\mathrm{S}}) = m\omega_r^2 a_s^2 N^2\left(\frac{1}{6\ell_{x,\mathrm{S}}^2} - \frac{1}{3\ell_{x,\mathrm{S}}} + \frac{\pi b_x^4\ell_{x,\mathrm{S}}^2}{24a_x^4}\right). \tag{18}$$

Either of these energy functionals can be analytically (or numerically) minimized to give the corresponding, variational-energy-minimizing, axial length ℓ_x [47]. The axial lengths ℓ_x for both variational solutions are shown in Fig. 5a as a function of the axial trap frequency ω_x.

3.3.2 Comparison to Bright Soliton Solution

The variational solutions can be compared with a full numerical solution of the 1D GPE [Eq. (10)] to give an idea of how the axial trapping affects the ground state [47]. The results of such an analysis are shown in Fig. 5b, which shows the maximum difference in shape between the lowest-energy (and hence, most accurate) variational solution and the numerically exact ground state. As one would expect, the sech ansatz converges to the exact solution in the axially free limit $\omega_x \to 0$ and it is in this regime, where this ansatz approximates the exact solution well, that the ground state can be regarded as soliton-like. In the opposite, trap-dominated limit $\omega_x \to \infty$, the Gaussian ansatz converges to the exact solution, which is no longer soliton-like in appearance. Convergence is also somewhat slower for the Gaussian ansatz as $\omega_x \to \infty$ than for the sech ansatz as $\omega_x \to 0$ due to the density-dependent nature of the nonlinearity [47]. In intermediate regimes, one or other ansatz provides a good approximation to the solution over a wide

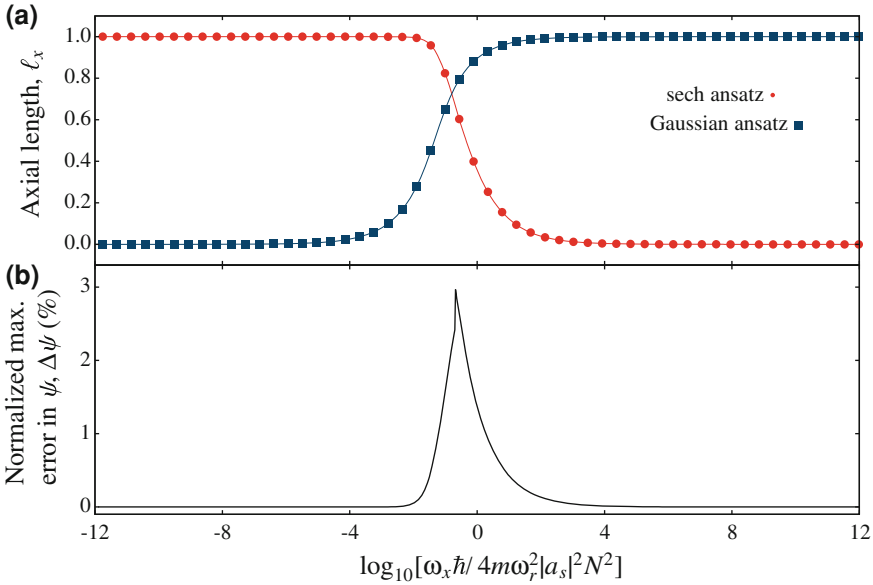

Fig. 5 Gaussian-ansatz [Eq. (15)] and sech-ansatz [Eq. (16)] solutions of the 1D GPE [Eq. (10)], as found in Ref. [47]. In **a**, the energy-minimizing axial length for each ansatz is shown, as a function of ω_x. In **b** the maximum absolute difference between the best-fitting ansatz, ψ_{Ansatz}, and the exact numerical solution, ψ_0, is shown as a percentage of the peak value of ψ_0. This can be expressed mathematically as $\Delta\psi = 100\text{max}(|\psi_{\text{Ansatz}} - \psi_0|)/\text{max}(\psi_0)$. Our deliberate definition of the ansatz such that $\ell_{x,\text{S}} \to 1$ as $\omega_x \to 0$ and $\ell_{x,\text{G}} \to 1$ as $\omega_x \to \infty$ results in the potentially confusing trend that $\ell_{x,\text{G}} \to 0$ as $\omega_x \to 0$ despite the fact that the *physical* length of the Gaussian ansatz tends to a non-zero constant in this limit

range of trap strengths, with only a small gap in which neither ansatz is particularly accurate. Consequently, one can usefully think of the ground state being deformed from sech-shaped to Gaussian-shaped as ω_x is increased.

However, the preceding analysis assumes the validity of the quasi-1D approximation. To obtain a complete picture of the ground state, and its relationship to the NLSE bright soliton, a full treatment of the 3D GPE is required. We undertake such a treatment in Sect. 4.

4 Bright Solitary Waves in 3D: Static Properties

The 3D GPE [Eq. (4)] is non-integrable and does not support true bright solitons. Nonetheless, bright solitary matter waves can be observed [9–11] which continue to exhibit soliton-like behaviour for a wide range of parameters. They are particularly soliton-like in their dynamical properties—especially when considering their mutual interactions and collisions. In this section, however, we focus on the static regime by considering the solitary wave stationary states of the 3D GPE.

The existence and form of bright solitary wave states of the 3D GPE is intricately linked to the instability of attractive condensates to collapse. In this section we review the properties of stationary 3D bright solitary matter waves in detail. In Sect. 4.1 we discuss the collapse phenomena. In Sect. 4.2 we present variational and numerical approaches to the problem. In Sect. 4.3 we review the properties of bright solitary waves as elucidated by the variational and numerical methods, and compare the 3D results to the predictions of the 1D approach considered in Sect. 3.

4.1 Collapse and the Critical Parameter

An attractively-interacting BEC in 3D is prone to a collapse instability. Indeed, in the absence of trapping, the system will undergo collapse. Importantly, the presence of trapping can support metastable, non-collapsing states, although the existence of the metastable state depends on the atom number, interaction strength and shape and strength of the trapping potential. The collapse instability has been investigated experimentally [15, 26, 27, 32]. Numerous theoretical studies have focused on identifying the parameters associated with the onset of collapse in condensates of various geometries, using variational [47, 48, 69, 70, 72], perturbative [24], and numerical [16, 17, 23, 47, 69, 70, 74] methods. The condensate dynamics during collapse are the subject of continuing theoretical study [34, 75–78].

Recall, we parameterise the interaction strength of the condensate via $k = N|a_s|/a_r$. The relevance of k is that, when it exceeds a critical value k_c, the metastable states cease to exist and the collapse phenomenon kicks in. The value of k_c is dependent on the trap geometry.

4.2 Variational and Numerical Approaches to the Static Solutions

The parameter regime of metastable solutions of the 3D GPE with $a_s < 0$ is most accurately determined by numerically solving the 3D GPE. However, as shown in Sect. 3.3 in 1D, a variational approach can give insightful and accurate results, especially into the threshold for collapse, and we will begin here with this approach. Note that the variational approach was first used to study collapse of bright solitons in the context of nonlinear optics [79]. We begin with this approach using two variational ansatz: an ansatz with Gaussian radial and axial profiles, and an ansatz with a Gaussian radial profile and a sech axial profile.

4.2.1 Variational Analysis: Gaussian Ansatz

The solution of the 3D GPE under cylindrically symmetric trapping can be approximated by a normalized Gaussian ansatz of the form,

$$\left(\frac{1}{\pi^{3/2}a_r^3\ell_{r,\mathrm{G}}^2\ell_{x,\mathrm{G}}}\right)^{1/2}\exp\left(-\frac{1}{2a_r^2}\left[\frac{x^2}{\ell_{x,\mathrm{G}}^2}+\frac{r^2}{\ell_{r,\mathrm{G}}^2}\right]\right), \tag{19}$$

where $\ell_{x,\mathrm{G}}$ and $\ell_{r,\mathrm{G}}$ are, respectively, axial and radial variational length parameters associated with the Gaussian ansatz. (Of course, this becomes the exact solution in the noninteracting regime $(a_\mathrm{s}=0)$.) Such an ansatz has been considered for bright solitary waves in [47, 70, 72], and is most appropriate in parameter regimes where the strength of the trap potential dominates over the strength of interactions in all directions. Substituting this Gaussian ansatz [Eq. (19)] into the classical field Hamiltonian for Eq. (4),

$$H_{3\mathrm{D}}[\psi]=\int d\mathbf{r}\left[\frac{\hbar^2}{2m}|\nabla\psi(\mathbf{r})|^2+V(\mathbf{r})|\psi(\mathbf{r})|^2-\frac{2\pi N|a_s|\hbar^2}{m}|\psi(\mathbf{r})|^4\right], \tag{20}$$

where $V(\mathbf{r})=m\omega_r^2(\lambda^2x^2+r^2)/2$, yields

$$H_{3\mathrm{D}}[\psi]=\hbar\omega_r\left(\frac{1}{4\ell_{x,\mathrm{G}}^2}+\frac{1}{2\ell_{r,\mathrm{G}}^2}+\frac{\lambda^2\ell_{x,\mathrm{G}}^2}{4}+\frac{\ell_{r,\mathrm{G}}^2}{2}-\frac{k}{\sqrt{2\pi}\ell_{r,\mathrm{G}}^2\ell_{x,\mathrm{G}}}\right). \tag{21}$$

This defines an "energy landscape" in terms of the variational lengthscales $\ell_{x,\mathrm{G}}$ and $\ell_{r,\mathrm{G}}$, in which the variational solution corresponds to an energy minimum. Typical energy landscapes for this Gaussian variational ansatz are shown in Fig. 6. We seek the lengthscales that minimize this variational energy. Differentiating with respect to each of the lengthscale variables produces, respectively, two coupled conditions for the variational energy-minimizing lengths,

$$\lambda^2\ell_{x,\mathrm{G}}^4+\frac{2k\ell_{x,\mathrm{G}}}{\sqrt{2\pi}\ell_{r,\mathrm{G}}^2}-1=0, \tag{22}$$

and

$$\ell_{r,\mathrm{G}}^4+\frac{2k}{\sqrt{2\pi}\ell_{x,\mathrm{G}}}-1=0. \tag{23}$$

In the case of prolate and oblate trap potentials these equations can be solved via straightforward iterative procedures [47], while for the axially free case an analytic solution can be found [47, 69].

4.2.2 Variational Analysis: Sech Ansatz

One can take the same variational approach but with a normalized sech ansatz of the form

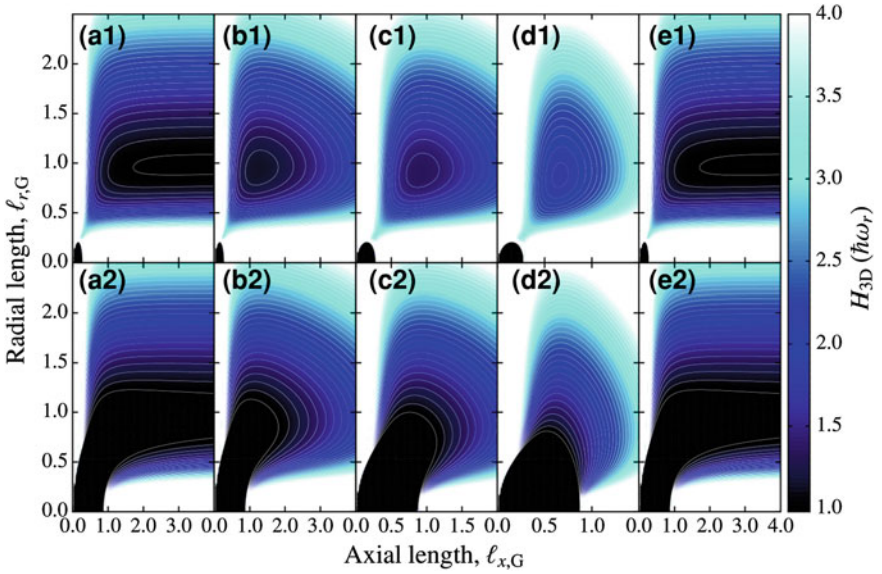

Fig. 6 Per-particle energy functional, $H_{3\mathrm{D}}$, determined using a Gaussian ansatz [Eq. (19)] for a BEC in a cylindrically symmetric, harmonic trap. Trap anisotropies shown are: **a** $\lambda = 0$, **b** $\lambda = 1/2$, **c** $\lambda = 1$, **d** $\lambda = 2$, **e** $\lambda^2 = -4 \times 10^{-4}$ (expulsive axial potential). The *top row* [sub-label (i)] shows the case $k = 0.35$, for which all the trap geometries are stable to collapse. In this case there is a stable local minimum in the variational energy, which corresponds to the (metastable) bright solitary matter wave state. The *bottom row* [sub-label (ii)] shows the case $k = 1.1$, for which all the trap geometries are unstable to collapse

$$\left(\frac{1}{4\pi a_r^3 \ell_{r,\mathrm{S}}^2 \ell_{x,\mathrm{S}}}\right)^{1/2} \mathrm{sech}\left(\frac{x}{2a_r \ell_{x,\mathrm{S}}}\right) \exp\left(-\frac{r^2}{2a_r^2 \ell_{r,\mathrm{S}}^2}\right), \tag{24}$$

where $\ell_{x,\mathrm{S}}$ and $\ell_{r,\mathrm{S}}$ are, respectively, axial and radial variational length parameters. Such an ansatz has been considered in [47, 69, 70], and is most appropriate in parameter regimes where the strength of the *radial* trap potential dominates over the strength of interactions, but the strength of interactions dominates over the strength of the *axial* trap potential. Following the above procedure, the variational energy expression now becomes,

$$H_{3\mathrm{D}}[\psi] = \hbar\omega_r \left(\frac{1}{6\ell_{x,\mathrm{S}}^2} + \frac{1}{2\ell_{r,\mathrm{S}}^2} + \frac{\pi^2\lambda^2\ell_{x,\mathrm{S}}^2}{24} + \frac{\ell_{r,\mathrm{S}}^2}{2} - \frac{k}{3\ell_{r,\mathrm{S}}^2 \ell_{x,\mathrm{S}}}\right), \tag{25}$$

yielding the two conditions for the energy-minimizing lengthscales,

$$\lambda^2 \ell_{x,\mathrm{S}}^4 + \frac{4k\ell_{x,\mathrm{S}}}{\pi^2 \ell_{r,\mathrm{S}}^2} - \frac{4}{\pi^2} = 0, \tag{26}$$

and

$$\ell_{r,\mathrm{S}}^4 + \frac{2k}{3\ell_{x,\mathrm{S}}} - 1 = 0. \tag{27}$$

The sech ansatz yields variational energy landscapes which are qualitatively very similar to those yielded by the Gaussian ansatz [69, 70].

4.2.3 Numerical Approaches

A variational approach to the stability of bright solitary matter waves in 3D yields considerable qualitative insight, particularly with regard to the collapse phenomenon. However, the approach is not particularly accurate in its prediction of the critical parameter k_c; the imposition of a certain shape on the wavefunction via the variational ansatz causes variational methods to consistently over-estimate k_c. Consequently, a great deal of work in the field of attractively-interacting BECs has focused on accurately identifying k_c, for various trap configurations, via numerical solution of the 3D GPE. The main approaches to solving the GPE numerically are reviewed in Ref. [80]. As in Sect. 3, the numerical and variational results can also be compared in order to investigate how bright-soliton-like the bright solitary matter wave states are in terms of their shape; such a comparison is, however, only meaningful in cases which approach the quasi-1D limit [47].

Studies have investigated traps with spherical [23, 74] and cylindrical [16] symmetry, cylindrically symmetric waveguides without axial trapping [70], and the case of a generally asymmetric trap [17]. Several works also investigated the configurations of specific experiments in detail [69, 81]. The parameter space of bright solitary wave solutions, under cylindrically-symmetric trapping, is summarized in Fig. 7.

4.3 Static Solutions in 3D and the Role of Trapping

Here we discuss the predicted bright solitary matter wave solutions (in cylindrically symmetric traps) according to the variational method and the full numerical solution. The structure of the energy surfaces described by the Gaussian [Eq. (21)] is illustrated for a selection of trap geometries and interaction strengths in Fig. 6. The collapse instability is manifest as an unbounded decrease of $H_{3\mathrm{D}}$ as the variational lengths ℓ_x and ℓ_r tend to zero. In cases where a bright solitary wave state exists (upper rows in figures) it is stabilized against collapse by an energy barrier (forming a local energy minimum in the energy surface); in cases where such an energy barrier is not present (lower rows in figures), no bright solitary matter wave state exists. The parameter space of metastable state solutions as predicted by the variational methods is compared to numerical solutions of the cylindrically

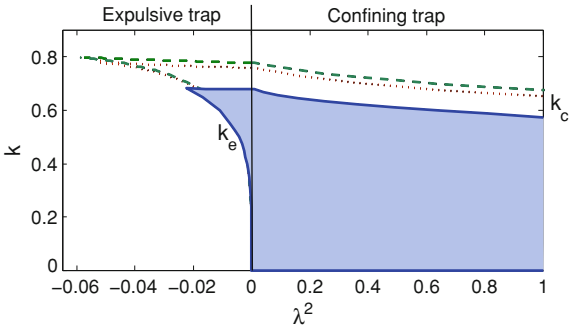

Fig. 7 Existence and properties of bright solitary matter wave stationary states in cylindrically symmetric traps as a function of trap geometry, parameterized by λ^2. The presence of metastable states is indicated by the various regions, according to the 3D GPE (*blue/grey* region), the Gaussian ansatz (region bound by the *green dashed line*) and the sech ansatz (region bound by the *red dotted line*). The *uppermost lines* represent the critical parameter for collapse k_c; under an expulsive trap $\lambda^2 < 0$ there exists a lower bounding line representing the critical parameter for expansion k_e. Note the difference in scale on the abscissa either side of $\lambda^2 = 0$ axis (Colour figure online)

symmetric 3D GPE in Fig. 7. In this plot we use the parameter λ^2 to specify the trap geometry; this is because that, as well as considering the conventional case of *confining* axial potentials ($\lambda^2 > 0$) we will also consider the case of *expulsive* axial potentials ($\lambda^2 < 0$). We will discuss the results of these figures below by separately discussing four key trapping regimes (specified in terms of λ^2).

Zero axial potential ($\lambda^2 = 0$)

The case of a zero axial potential (which is equivalent, more generally, to any constant uniform potential in the axial direction), results in a waveguide-like trap. It leads to some algebraic simplification in the variational equations and, in the case of the sech ansatz, the variational energy-minimizing lengths ℓ_x and ℓ_r and the critical parameter $k_c = 3^{-1/4}$ can be found analytically [47, 69].

More insight into the physical situation can be gleaned from the corresponding variational energy surfaces, shown in Fig. 6a. The energy surface forms a relatively flat "plain" for larger ℓ_x and ℓ_r, with sharply rising "ridges" occurring when either length becomes small. However, the (negative) interaction term in the energy functional leads to a distinct "chute" [69] at the meeting point of these two ridges (when both ℓ_x and ℓ_r are small). For low k a raised saddle point separates the chute from the plain, thus forming the local energy minimum of the metastable solution; as k increases this saddle lowers, until at $k = k_c$ it disappears and the entire parameter regime of the plain becomes unstable. For the sech ansatz, this transition at $k_c = 1/3^{1/4} \approx 0.76$ [47, 69]. For the Gaussian ansatz the critical value is $k_c \approx 0.778$ [72]. For comparison, the non-polynomial Schrödinger equation (an extended quasi-1D approach) predicts $k_c = 2/3$, through a simpler calculation [49].

The true mean-field result, obtained by numerical solution of the 3D GPE, is $k_c = 0.675$ [70].

Within the regime of metastable solutions, the solitary wave lengthscales vary with the interaction strengths. For $k = 0$ the axial lengthscale is effectively infinite. As k is increased the axial lengthscale reduces monotonically, until the point of collapse. The radial lengthscale stays close to the radial harmonic oscillator length $a_r = \sqrt{\hbar/m\omega_r}$ throughout. Interestingly, the solution approaches being spherical as the collapse point is reached [69].

In regimes where a bright solitary wave stationary state does exist, the energy of the saddle point relative to that of the local energy minimum on the plain sets an energy scale at which the bright solitary wave state will be unstable to collapse when excited. Excitations with sufficient energy could allow the condensate to overcome the barrier formed by the saddle point and lead to a dynamical collapse in which ℓ_x decreases to zero [69, 70, 82]. A second channel of instability also arises; because the lack of an axial trap results in a finite-valued energy as $\ell_x \to \infty$, there exists a "dispersive channel" in which excitations of the metastable state above a certain energy threshold can lead to dynamics where ℓ_x increases without bound [69, 70].

In Ref. [47] the 3D solitary wave state in the waveguide-like trap was compared to the NLSE bright soliton. It was found in Ref. [47] that, while it is possible to reach a highly soliton-like state in a waveguide-like trap, it lies in an experimentally challenging regime. Nonetheless, as we review in Sects. 5 and 6, the dynamics of 3D bright solitary waves can be highly soliton-like even when their static shape does not closely resemble the NLSE soliton.

Prolate and isotropic traps $(0 < \lambda^2 \leq 1)$

For $0 < \lambda^2 < 1$ the trap is prolate, i.e. elongated in x, while for $\lambda = 1$ it is spherically symmetric. In such cases the variational solutions must be obtained numerically [47].

The energy landscape under these potentials (with examples shown in Fig. 6b, c) is similar to that for the waveguide trap $\lambda = 0$ in and around the region of the collapse instability. Indeed, the critical point for removal of the metastable state depends quite weakly on λ, as evident from Fig. 7. The only qualitative difference introduced into the variational energy by axial trapping arises in the high-ℓ_x limit, where the potential energy of the trap leads to an infinite total energy in the limit $\ell_x \to \infty$, eliminating the dispersive channel altogether.

In Ref. [47] the solitary wave state in a prolate trap was also compared to the NLSE bright soliton and similarly to above, the achievement of a soliton-like state was found to be highly experimentally challenging.

Oblate trap $(\lambda^2 > 1)$

Such a trapping geometry, in which $\omega_x > \omega_r$, is not typical for the study of bright solitary matter waves, as in this geometry no clear analogy can be drawn with an integrable NLSE.

Nonetheless, when an oblate trap possesses a metastable state it is indeed a solitary wave under the definition used by [12]. These stationary states have been

studied using the 3D GPE [70], and 2D reductions with 3D effects [83]. The variational energy surface (Fig. 6d) is similar to the prolate/isotropic case.

Expulsive axial potential $(\lambda^2 < 0)$

The self-trapped nature of bright solitary matter waves means they can withstand being placed in a trap with a weakly expulsive harmonic axial potential $(\lambda^2 < 0)$ without dispersing. This was the case in the experiment of Ref. [10], and considered theoretically in [69, 70].

The ensuing variational energy surfaces, shown in Fig. 6e, again (i) permit metastable states [Fig. 6e(i)] and (ii) fully collapsed scenarios for $k > k_c$. However, the expulsive potential leads to a second instability via an "expansive channel" [70]. This corresponds to axial spreading of the solutions $\ell_x \to \infty$. In contrast to the dispersive channel—which never completely prevents the existence of a metastable ground state, but renders it unstable to (potentially very small) excitations—the expansive channel can destabilize the state; like the collapse channel's "chute", the expansive channel is separated from the solitary wave state by a saddle point, which disappears for sufficiently low k, or high $|\lambda|$. This introduces a critical expansion parameter k_e, such that one must have $k_e < k < k_c$ in order to observe a metastable state. The structure of k_c and k_e is illustrated in Fig. 7; it is immediately apparent that the regime of metastable ground state solutions with an expulsive axial potential is severely restricted compared to the other cases. In particular, $|\lambda|$ must be relatively close to zero to avoid passing the cusp point $(k_c = k_e)$, beyond which metastable solutions are no longer found.

4.3.1 Asymmetric Trap Potentials

Removing the restriction to cylindrically symmetric trap geometries which we have enforced up to now leads to a considerably enlarged parameter space to explore. The critical parameter in such traps has been numerically determined by Gammal et al. [17]. The existence and form of the bright solitary wave ground state in anisotropic traps shows no qualitative differences from the cylindrically symmetric case.

5 Bright Solitary Waves in 1D: Dynamics

When analysing the dynamics of bright solitary matter waves, it is naturally of interest to compare their dynamics to the well-known and rich dynamics of bright solitons. The natural regime for such comparison is the case in which the axial potential is weak compared to the radial trap potential. As discussed in Sects. 3 and 4, this regime is where stationary bright solitary matter waves bear the greatest resemblance to bright solitons, and experiments to date have focused on this regime.

Under a quasi-1D geometry, the condensate dynamics are described by the 1D GPE [Eq. (10)]. In the case of zero axial trapping this reduces further to the focusing NLSE, admitting exact bright solitons. With a weak trapping or expulsive axial potential, as realized in experiments, integrability is lost and the dynamics are no longer those of true solitons. Nonetheless, as we illustrate in this section, the dynamics remain highly soliton-like under the assumption that a 1D description is accurate. We shall later relax this 1D assumption in Sect. 6.

In this section, we begin by reviewing the dynamics of single and multiple NLSE bright solitons (Sect. 5.1), and introduce a particle-like model for their motion and interactions. Introducing axial trapping, we then explore the dynamics of bright solitary waves in the quasi-1D approximation (Sect. 5.2.1); these dynamics are highly soliton-like and can be easily understood using a straightforward modification of the particle model.

5.1 Dynamics and Collisions of the Classic Bright Soliton

In the absence of axial trapping, an attractively-interacting BEC in a quasi-1D trap is described by the focusing 1D NLSE, which supports bright soliton solutions [56, 57]. The single- and many-soliton solutions to this equation have been extensively explored in the context of optical solitons [56–61]. We review the results pertinent to soliton dynamics in this section.

5.1.1 Dynamic Bright Soliton Solutions

Eliminating the axial trapping in the 1D GPE [Eq. (10)] yields the focusing NLSE,

$$i\hbar\frac{\partial\psi(x,t)}{\partial t} = -\frac{\hbar^2}{2m}\frac{\partial^2\psi(x,t)}{\partial x^2} - 2\hbar\omega_r N|a_s||\psi(x,t)|^2\psi(x,t). \tag{28}$$

Despite its nonlinear nature, the integrability of Eq. (28) means solutions can be found using the inverse scattering method [56, 57]. In summary, a scattering transform of $\psi(x,t)$ yields, at any time t, a spectral decomposition of $\psi(x,t)$ into solitons and radiation. The radiation part of the spectrum is continuous, and has in general a non-trivial time-dependence. However, the soliton part of the spectrum is discrete and *time-independent*, and is completely described by four real quantities for each soliton. Consequently, the spectrum of an N-soliton solution with no radiation component can be completely described by $4N$ real quantities, from which the complete solution $\psi(x,t)$ can be recovered using the inverse scattering transform.

The most general N-soliton solution to Eq. (28), containing no radiation, can be written as [59],

$$\psi(x,t) = \sum_{j=1}^{N}\psi_j(x,t), \tag{29}$$

where,

$$\sum_{j=1}^{N} \frac{\gamma_i^{-1} + \gamma_j^*}{\lambda_i + \lambda_j^*} \psi_j(x,t) = \frac{1}{\sqrt{b_x}}. \tag{30}$$

Here we have defined the quantities,

$$\lambda_j = \frac{a_j}{2} + \frac{iv_j}{2\omega_r |a_s| N}, \tag{31}$$

and,

$$\gamma_j = \exp\left[\lambda_j \left(\frac{x - x_j}{b_x}\right) + i\lambda_j^2 \frac{2m\omega_r^2 a_s^2 N^2}{\hbar} t + i\Phi_j\right], \tag{32}$$

in addition to the characteristic soliton length $b_x = \hbar/2m\omega_r|a_s|N$. Each soliton is described by a real amplitude a_j, velocity v_j, position offset x_j, and phase Φ_j. In the case that the jth soliton is well-separated from the other $N-1$ solitons, the linear system defined by Eq. (30) can be approximately solved to give [59],

$$\begin{aligned}\psi(x,t) = \frac{a_j}{2\sqrt{b_x}} \operatorname{sech}\left(\frac{a_j(x - x_j - v_j t)}{2b_x} + q_j\right) \\ \times \exp\left(i\left\{\frac{m}{\hbar}\left(v_j(x - x_j) + \frac{v_j^2 t}{2} + \frac{\omega_r^2 a_s^2 N^2 a_j^2 t}{2}\right) + \Phi_j + \Psi_j\right\}\right).\end{aligned} \tag{33}$$

Here, q_j and Ψ_j are time-dependent position- and phase-shifts which appear as a result of collisions with the other $N-1$ solitons. They are given by,

$$q_j + i\Psi_j = \sum_{k \neq j} \pm \log\left(\frac{a_j + a_k + i(v_j - v_k)/2\omega_r|a_s|N}{a_j - a_k + i(v_j - v_k)/2\omega_r|a_s|N}\right), \tag{34}$$

where the sign is positive (negative) when the jth soliton is to the left (right) of the kth [59]. While the jth soliton is well-separated these shifts remain approximately constant, and only change significantly during collisions.

5.1.2 Bright Soliton Dynamics and Collisions

The dynamics of a single bright soliton in the NLSE are determined entirely by their nonlinear interactions with the remainder of the solution. It is convenient to divide the remainder of the solution into soliton and radiation components, and consider the influence of these components on the dynamics separately. We review soliton dynamics due to soliton interactions in this section. The majority of these dynamics can be understood on the basis of a simple particle model. The interaction of solitons with radiation is more mathematically involved [58, 61, 84] and no similarly general picture is available.

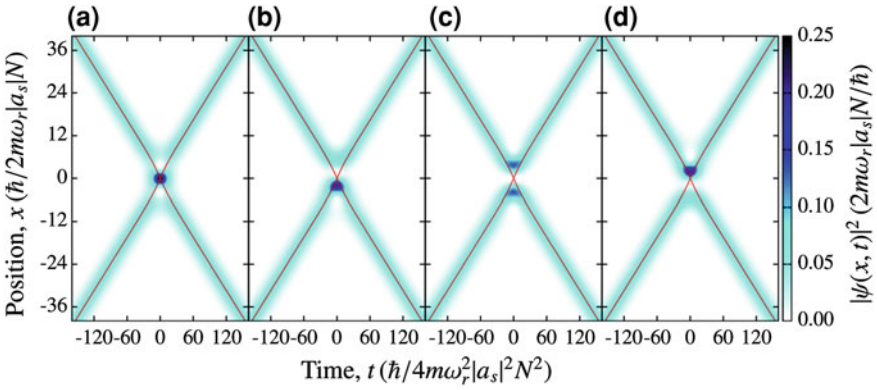

Fig. 8 Bright soliton collisions in the nonlinear Schrödinger equation, for solitons with equal amplitude and relative phase $\Delta\Phi = 0$ (**a**), $\pi/2$ (**b**), π (**c**), and $3\pi/2$ (**d**). In each case the density profile of the solution is superimposed with the soliton trajectories predicted by a particle model [45, 46]. This phase-independent model fails to describe the dynamics of the collision in detail, but correctly incorporates the asymptotic position shift of the solitons

In the absence of radiation, the dynamics of multiple bright solitons are dominated by the interactions and collisions between solitons. One of the defining characteristics of true solitons, associated with the integrability of the system, is that they survive mutual collisions entirely unchanged in form. The only observable effects of the collision are the asymptotic position and phase shifts discussed in Sect. 5.1.1.

The main characteristics of soliton interactions can be illustrated by the collisions of two equal-amplitude solitons. This is shown, for various relative phases $\Delta\Phi = \Phi_1 - \Phi_2$, in Fig. 8. As expected, the solitons survive such a collision completely unchanged in form. The position shifts q_j are clearly visible as the deviation of both solitons from their initial linear trajectories. Although the dynamics of the collision itself differ with the relative phase $\Delta\Phi$, the position shift q_j is unchanged. Note that, due to the phase symmetry of the collision, the 0-relative phase case leads to a central density anti-node, whereas for π-relative phase a density node is preserved at the origin.

The independence of the position shifts q_j from the solitons' relative phase $\Delta\Phi$ allows one, in principle, to predict their asymptotic trajectories independently of their phase. Disregarding the phase information in this way leaves each soliton described by a position, velocity, and amplitude. One can then treat the solitons as classical particles with an effective mass proportional to their amplitude and some appropriate inter-particle potential. This approach was developed for optical NLSE solitons [85–88], using the inter-particle potential,

$$V(x_j - x_k) = -2\eta_j\eta_k(\eta_j + \eta_k)\mathrm{sech}^2\left(\frac{2\eta_j\eta_k(x_j - x_k)}{b_x(\eta_j + \eta_k)}\right), \tag{35}$$

where the solitons are treated as classical particles of effective mass $\eta_j = a_j/4$. This potential reproduces the correct asymptotic position shifts provided the velocities and effective masses satisfy the condition $|\eta_j - \eta_k| \ll |v_j - v_k|/4\omega_r|a_s|N$ [46]. The particle model therefore reproduces the asymptotic shift exactly for the equal-effective-mass solitons in Fig. 8. For collisions of solitons with non-equal effective mass, the asymptotic shift predicted by the particle model approaches the correct value for weak soliton interactions (small density or *s*-wave scattering length) or short interaction times (high-velocity collisions).

5.2 Dynamics and Collisions Under Axial Trapping

Despite the lack of integrability in the 1D GPE with an inhomogeneous axial potential, and the resulting absence of true solitons, one may still observe solitary waves if the stationary, eigenstate solutions of the equation can propagate without changing shape [12]. While they do not satisfy the strict mathematical requirements to be solitons [6, 54], these non-dispersive solitary waves can nonetheless, under certain conditions, behave and interact in a soliton-like way.

5.2.1 Dynamic Bright Solitary Matter Wave Solutions

The possibility to observe solitary waves of this type was examined in considerable generality in Ref. [12]. In this work the authors considered, in 1, 2 and 3D, how static eigenstate solutions of nonlinear Schrödinger equations with a general nonlinearity and an arbitrary external potential behaved when used as initial conditions in a nonlinear Schrodinger equation with the same nonlinearity and a new, possibly time-dependent, external potential. Two conditions were found to be necessary for the original eigenstates behave as solitary waves under the influence of the new potential: firstly, the nonlinearity must be decoupled from the absolute position, a requirement immediately satisfied by the conventional cubic form of the nonlinearity appearing in the GPE. Secondly, the new potential must differ no more than linearly in any spatial coordinate from the original potential [12]. We note that this second condition implies that one can use a time-dependent linear potential as a way to control bright solitary waves in experiments without causing them to lose their solitary-wave character; experimental control techniques such as this are discussed further in Sect. 7.

We shall restrict our attention to the case where the eigenstates are the bright solitary wave stationary states considered in Sect. 2,[4] and the "new" potential is a harmonic one of identical frequency to the original, but with a displaced center;

[4] It is also possible to consider solitary waves having the form of higher-energy nonlinear eigenstates; such eigenstates were considered in Ref. [89].

this is equivalent to the case of the original potential acting on a displaced bright solitary wave stationary state. In this case, the solitary wave has the same spatial profile as the stationary state, but its centre of mass moves as a classical particle in the static harmonic potential. If free from the influence of other solitary waves or other components of the solution, it thus undergoes simple harmonic motion like a classical particle [12, 45, 46]. This feature of the GPE stationary state is analogous to the Kohn theorem for the many-body ground state. The latter guarantees that the true quantum mechanical ground state of N bosons in a harmonic trap can be expressed as a separable tensor product of a single-body wavefunction in the centre of mass coordinate with a general $(N-1)$-body wavefunction in the remaining inter-particle coordinates.

5.2.2 Bright Solitary Matter Wave Collisions Under Axial Trapping

If the bright solitary wave is not well-separated from other components of the solution, its dynamics are influenced by the nonlinear interaction with the other components. As in the case of bright solitons, we concentrate on the interactions between solitary wave components only. For bright solitons the asymptotic effects of the interactions were entirely described by phase and position shifts (Sect. 5.1.2). For bright solitary waves this is no longer strictly true; however, this can be considered a satisfactory approximation in the limit that the external potential is approximately constant over the region of the collision and provided that the solitary waves are approximately bright-soliton-shaped. Making these approximations, one can combine the particle model of soliton collisions (Sect. 5.1.2) with the behaviour of a particle in a harmonic trap [45, 46]. This leads to a combined particle model for multiple bright solitary waves in a harmonic trap, which is most accurate for (a) weak harmonic traps, (b) fast solitary wave collisions, and (c) in-phase solitary wave collisions.

The collisional dynamics of two, identical bright solitary waves according to the 1D GPE are illustrated in Fig. 9 for relative phases of 0 and π. As anticipated by the particle model, the dynamics are dominated by harmonic particle-like motion when the waves are well-separated; however, when the waves collide, periodically, at the trap centre, a soliton-like collision results in a position shift. There is no overall phase shift between collisions, however [46]. During the collision, we obtain qualitatively the same phase-dependent density structure as for the bright soliton collisions. The particle model predicts these trajectories well over the short times shown here. However, over longer times deviations do build up, arising from the variation of the harmonic axial potential over the characteristic length scale of the collision [45, 46].

The complex dynamics of three or more solitary waves oscillating and colliding in a harmonic trap can be effectively predicted using the particle model; interestingly, the model is itself non-integrable for three or more solitary waves, leading to chaotic particle-like dynamics [45, 46].

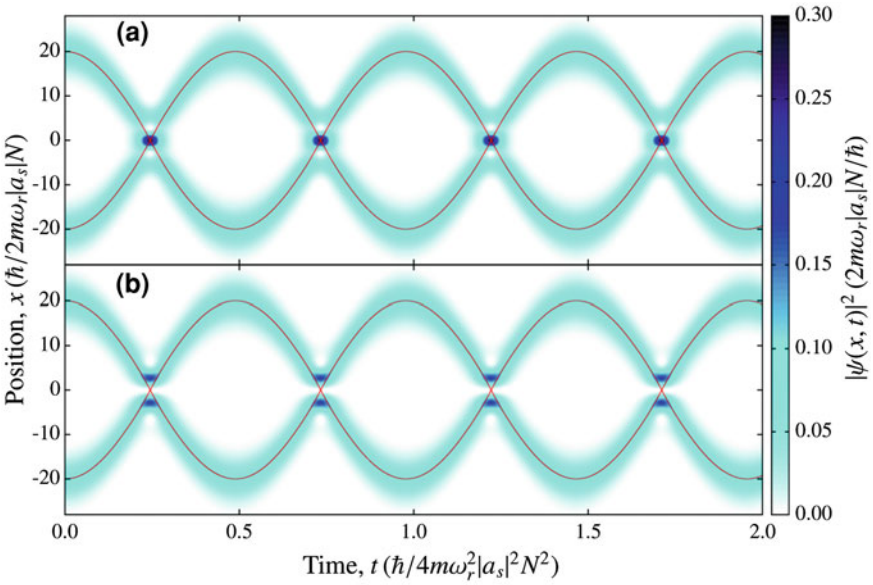

Fig. 9 Bright solitary wave collisions in the 1D GPE with harmonic axial trapping. The initial solitary waves, each with $N/2$ atoms, are ground states of the trap displaced by $\pm \approx 10.35$ in x and with zero initial velocity and relative phase $\Delta\Phi = 0$ (**a**), and π (**b**). In each case the density profile of the solution is superimposed with the soliton trajectories predicted by the particle model

6 Bright Solitary Waves in 3D: Dynamics

The solitary waves of the 1D GPE explored in the previous section are in many respects similar to NLSE bright solitons despite the addition of a trap potential. However, in real experiments it is not only the addition of trapping which leads to deviation from the NLSE, but also three-dimensional effects. While the 3D stationary state is still a solitary wave [12], residual 3D effects can lead to large deviations from soliton-like behaviour, although there are regimes where highly soliton-like dynamics can still be observed.

Although the absence of an axial trap potential does not lead to exact soliton solutions in 3D, we nonetheless begin by considering the axially free case in Sect. 6.1. We then consider the additional effects of an axial trap in Sect. 6.2. In broad parallel to the previous section, we focus on the dynamics and interactions of solitary waves only. However, this distinction is blurred due to the 3D effects during collisions, which can lead to non-soliton-like behaviour and eventual destruction of solitary waves. This behaviour is fundamentally linked to the collapse instability in 3D, explored in Sect. 4.

6.1 Dynamics and Collisions in a Waveguide

In this section we consider a waveguide-like trap, with harmonic radial and zero axial trapping potential. In such a trap the solitary wave profile is the stationary state, in the parameter regimes that are stable against collapse (Sect. 4). With uniform axial potential this solitary wave is self-trapped in the x-direction, and the dynamics of multiple such solitary waves is consequently dominated by their interactions, as for NLSE bright solitons.

6.1.1 Stability of Solitary Wave Collisions

In the absence of analytic solutions for binary solitary wave collisions in a waveguide trap, such collisions must be simulated numerically. This can be done from an initial condition composed of two copies of the (numerically obtained) stationary state, displaced from each other by some distance and given some velocity toward each other.[5] For equal-sized solitary waves the resulting collisions can be studied within the parameter space of incident velocity v, interaction strength parameter k, and relative phase $\Delta\Phi$ [81].

As for the stationary state itself, the key parameter determining the stability of collisions of this type is the interaction strength parameter k; this must remain below some threshold k_c in order to avoid a dynamically-induced collapse when the waves meet. However, k_c itself is dependent on the other collision parameters. In particular, k_c is larger for faster collisions, and for collisions with a relative phase closer to π. This is evident from the simulated results in Fig. 10a, b. The latter effect is most noticeable for low velocities, with the phase-dependence of k_c disappearing in the high-velocity limit.[6] At low velocity, this phase-dependence can be understood from the collision profiles illustrated for the NLSE in Fig. 8; in the case $\Delta\Phi = \pi$ the density profile of the collision itself resembles two solitons interacting *repulsively* [59] and never overlapping, whereas in the case $\Delta\Phi = 0$ the solitons overlap, leading to a strong density peak. While this peak is of no consequence in the NLSE or the 1D GPE, in the 3D GPE this peak in the atomic density can trigger the collapse instability. The full dependence of the collisional stability on k and incident speed v is shown in Fig. 10 for the cases of $\Delta\Phi = 0$ and $\Delta\Phi = \pi$. Note that the phase dependence of the collisional stability is also predicted by effective 1D equations retaining more 3D character than the 1D GPE [51].

---

[5] Such a velocity is imparted numerically by applying a spatially varying phase of $e^{\pm imvx/\hbar}$. Experimentally, this could be achieved by applying a linear external potential to each solitary wave for a short time.

[6] The GPE is based on the assumption of atomic scattering at low energy and momentum and so by "high velocity" here we refer to a scale relative to the condensate's natural speed scale of the speed of sound $c = \sqrt{4\pi\hbar a_s n/m^2}$ [3].

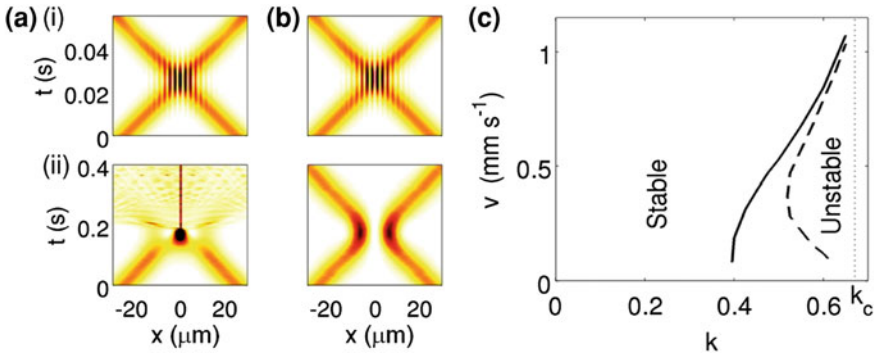

Fig. 10 Stability of solitary wave collisions in an axially homogeneous waveguide potential. **a** Space-time plots of atom density during collision between two identical solitary waves, each with $k = 0.4$ and featuring $\Delta\Phi = 0$, for (i) high incident speed and (ii) low incident speed. **b** The same but for $\Delta\Phi = \pi$. **c** Stability diagram of the solitary wave collisions as a function of incident speed v_i and interaction parameter k, where the *solid* (*dashed*) *line* marks the boundary between stable and unstable collisions for $\Delta\Phi = 0\,(\pi)$. The *vertical line* denoted k_c indicates the critical interaction strength for collapse of a single, isolated bright solitary wave. The figure and parameters are from [81]

The dependence of k_c on the incident velocity v can be understood in terms of the relationship between the characteristic time for collapse of the condensate, t_c, and the characteristic time for the collision-interaction to take place, t_{int}. In Ref. [81] it was illustrated that the critical collision velocity, below which collapse occurred in numerical simulations of collisions, for the parameters of the JILA solitary wave experiment [11], corresponds to a collision-interaction time t_{int} approximately equal to the experimentally measured collapse time, t_c. Theoretical investigation of the role of the two timescales has not proceeded further to date, in part because the GPE has not been generally considered an accurate predictor of t_c. However, recent results suggesting that the GPE can accurately predict t_c when a three-body loss term is included [34] offer the possibility of further progress in this area.

6.1.2 Population Transfer in Solitary Wave Collisions

Another effect occurring as a result of the 3D nature of the system is that of population transfer between bright solitary waves. In both the 1D NLSE, and the 3D GPE for a waveguide trap, collisions between solitons or solitary waves with relative phases $\Delta\Phi = 0$ and π have a density profile which remains completely symmetric in x after the collision; in this respect the 1D NLSE and 3D GPE are analogous. The two descriptions, however, lead to very different dynamics for intermediate phases $0 < \Delta\Phi < \pi$ and $\pi < \Delta\Phi < 2\pi$. In the 1D NLSE the density profile, which is initially symmetric in x, loses its symmetry during the collision and regains it afterwards. In the 3D GPE for a waveguide trap, the initially-symmetric

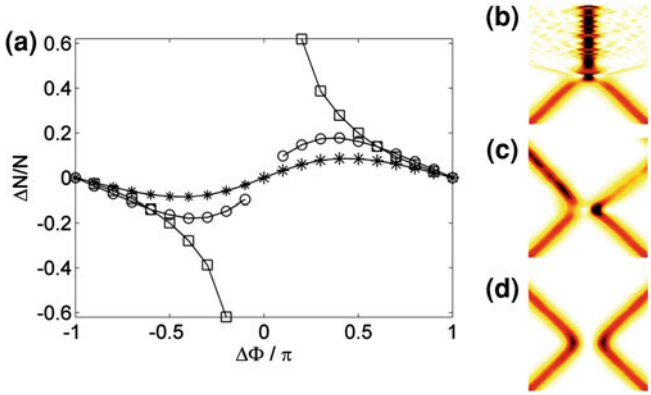

Fig. 11 **a** Population transfer ΔN during bright solitary wave collisions within a homogeneous waveguide, as a function of the relative phase between the waves $\Delta\Phi$. At high incident speed (*stars*) the transfer is sinusoidal. For reduced speed (*circles*) the transfer becomes larger and skewed towards $\Delta\Phi = 0$. For low speed (*squares*) the population transfer diverges as $\Delta\Phi \to 0$, due to runaway nonlinear effects and collapse. The results are taken from [81]. **b–d** Wave dynamics for the low speed case with **b** $\Delta\Phi = 0$, **c** $\pi/2$ and **d** π

density profile loses its symmetry during the collision, and this loss of symmetry leads to population transfer between the two waves: the first solitary wave grows in amplitude and slows down, while the second wave loses amplitude and speeds up. Example dynamics are shown in Fig. 11b–d. In addition to the 3D GPE, this effect can also be seen in effective-1D approaches retaining extra 3D character [51].

The amount of population transferred shows interesting dependencies on the relative phase and velocity of the solitary waves (Fig. 11) [81]. For fast collisions the amount of population transfer depends sinusoidally on the relative phase, with the maximum transfer occurring at $\Delta\Phi = \pi/2$ and $\Delta\Phi = 3\pi/2$, and the magnitude of this transfer decreasing with velocity. At lower velocities, however, this dependence becomes heavily skewed, with the maximum transfer occurring closer to $\Delta\Phi = 0$ and the collapse instability occurring in extreme cases. This deviation from sinusoidal transfer is a result of strong transient nonlinear effects during the collision [81].

6.2 Dynamics and Collisions Under Axial Trapping

We now introduce an axial harmonic trap, in addition to the waveguide-like trap of the previous sections. In analogy to transition from the NLSE to the 1D GPE, such a system supports solitary wave excitations which have the shape of the stationary state of the system and move like classical particles in the axial harmonic trap when well-separated from other solitary waves. When these solitary waves do

interact and collide, two key questions arise: (a) how soliton-like, and (b) how stable are these collisions? Both these questions are particularly pertinent to the interpretation of bright solitary wave experiments to date, and to unresolved issues regarding the role of relative phase (as will be discussed in Sect. 7). We address each question in turn in the following sections.

6.2.1 Soliton-Like Dynamics

Again, the trapping is assumed to be cylindrically symmetric with a shape specified by the trap anisotropy $\lambda = \omega_x/\omega_r$. As was discussed in Sect. 4, the static bright solitary wave solutions in such traps have the most soliton-like shape in the low-λ limit (provided the collapse threshold is not exceeded), and least soliton-like in the opposite case. One naturally expects a similar trend in the soliton-like-ness of the solitary wave dynamics, but is faced with the issue of how to quantify the soliton-like-ness of the dynamics.

When considering repeated collisions between two solitary waves at the centre of a harmonic trap, as shown in Fig. 9, soliton-likeness can be defined in relation to the characteristic tendency for true solitons to emerge from mutual collisions unscathed. In Ref. [90] a metric was defined as the number of binary collisions for which the solitary waves subsequently reach their turning point in the harmonic trap while still having amplitudes and displacements from the origin above 75 % of their original value. Since 1D collisions satisfy this criteria almost indefinitely,[7] this metric is termed the "number of 1D collisions", C_{1D}. While more sophisticated definitions could also be employed, this simple metric for the soliton-likeness of the dynamics is enough to reveal a rich variation in the dynamics of collisions in the parameter space of incident velocity v, trap anisotropy λ and relative phase $\Delta\Phi$ [90]. Figure 12 illustrates the variation of C_{1D} in the v-λ-$\Delta\Phi$ parameter space, for interaction strength $k = \sqrt{\lambda/0.08}$; this choice of k ensures that the effective 1D trap strength used in Ref. [90] is fixed to $\omega = 0.02$, for which value a solitary-wave state exists for N atoms. Rather than being set in motion by an initial displacement, the solitary waves in Fig. 12 are set in motion using an interference protocol providing arbitrary control over the relative phase and velocity (see Sect. 7 and Ref. [90]).

As would be expected from the analysis of collisional stability in the waveguide trap, how soliton-like the solitary wave collisions are is strongly dependent on the relative phase $\Delta\Phi$ at low velocity, with C_{1D} being significantly higher for $\Delta\Phi = \pi$ than for $\Delta\Phi = 0$. This phase-dependence weakens for faster collisions, which become more soliton-like as the velocity is increased. However, the dependence of C_{1D} on λ is oscillatory in character. This is quite distinct from the case when

[7] Eventually, the effects of the variation in the external trap potential across the collisions could lead to the break-up of solitary waves in the 1D GPE. However, this does not seem to occur on timescales easily accessible to numerical simulation; instead the numerical errors grow faster than the deviation from the soliton-like behaviour.

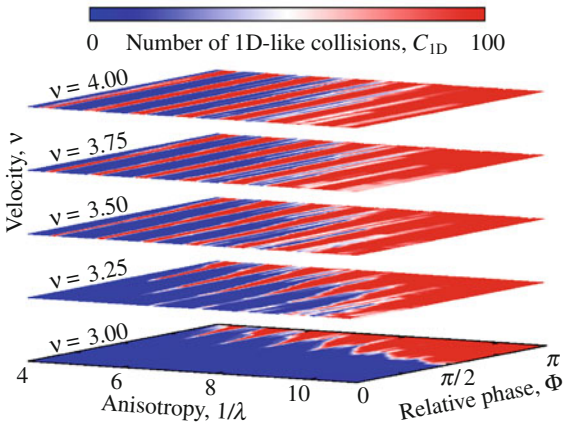

Fig. 12 Stability of bright solitary wave collisions in a cylindrically symmetric 3D trap, as established in Ref. [90]. The number of 1D-like bright solitary wave collisions, C_{1D}, is shown as a function of the incident velocity v, relative phase Φ, and trap anisotropy λ. Here, C_{1D} is defined as the number of collisions for which the solitary waves return to within 75 % of their original peak amplitude and position at their maximum distance from the origin. Higher C_{1D} indicates greater stability. The interaction strength parameter k varies with anisotropy as $k(\lambda) = \sqrt{\lambda/0.08}$; this ensures that the effective quasi-1D trap frequency $\omega = \lambda/4k^2$ remains equal to 0.02 [90]. Rather than being released from displaced positions in the trap, the solitary waves are launched with a controlled velocity and relative phase using the interference method described in Ref. [90]. The computation takes advantage of the radial symmetry of the problem, using a pseudospectral split-step method in 2D cylindrical coordinates

considering the *static* solitary wave states (Sect. 4), where the solitary wave shape varied smoothly with λ. These oscillations represent the entirely dynamical effect of radial breathing oscillations of the solitary waves being excited during the collision. Depending on the trap anisotropy λ the transfer of energy to these radial breathing oscillations can be either enhanced or suppressed, possibly providing an experimental "knob" with which to enhance the stability of bright solitary waves [90].

6.2.2 Stability of Solitary Wave Collisions

While the analysis of the previous section gives a comprehensive account of the soliton-likeness of collisions for varying velocity, anisotropy and relative phase, the interaction parameter k in Fig. 12 is fixed (as a function of λ). Other theoretical work has explored the k-dependence of solitary-wave collision dynamics, for fixed λ [81, 91]. It was found, for example, that even in the presence of axial trapping, the stability diagrams in v-k space were qualitatively the same as for the axially-homogeneous case (Fig. 10). The population transfer for $\Delta\Phi \neq 0, \pi$ also occurs within an axially-trapped system, but with an additional consequence: the repetition of collisions under axial trapping leads to the continued growth of asymmetric

populations between the two colliding waves, which terminates only when collapse instability occurs in one of the waves. As such even a small deviation from $\Delta\Phi = 0$ or π can, over repeated collisions in a trap, leads to significant changes in the long term state of the system [91].

These studies also performed modelling of the JILA experiment [11] using the 3D GPE. Excellent agreement with the experiment data was achieved assuming the bright solitary waves to have a relative phase very close to $\Delta\Phi = \pi$, i.e. locally repulsive interactions. In this manner, the solitary waves are predicted to be able to survive many collisions without collapse, as were observed in the JILA experiment. This is in general agreement with other work predicting that the multiple soliton-trains seen in experiment [9, 11] are consistent with neighbouring solitary waves having a relative phase close to π [22, 42–44, 81, 91]. The origin, and even the true existence, of these π-phase differences is an open question, and will be discussed in Sect. 7.

7 Hot Topics in Bright Solitary Matter Waves

The degree of control over the potential landscape and nonlinearity of BECs offers unique opportunities to study the fundamental properties of solitary waves, as well as nonlinear systems and quantum many-body physics in general. Furthermore, the properties of bright solitary matter waves makes them promising candidates for a variety of future applications. Areas of current research towards future applications include the development of soliton atom-lasers [92–94], the stabilization and manipulation of bright solitary matter waves using spatially and temporally varying traps and inter-atomic *s*-wave scattering lengths [95, 96], and manipulation of bright solitary matter waves in periodic potentials [97, 98], with the potential for applications in quantum information [99].

In this section we focus on four areas of current research: the description of bright solitary matter waves beyond the mean-field approximation (including open questions over their relative phase), spontaneous symmetry breaking, the exploitation of bright solitary matter waves in interferometry, the application of solitary waves as surface probes, and more exotic forms of bright solitary matter wave.

7.1 Beyond-Mean-field Treatments and Relative Phase

The results presented in this chapter have focussed on the mean-field, zero temperature description of a Bose–Einstein condensate provided by the Gross–Pitaevskii equation. However, Bose–Einstein condensates are in fact many-body quantum mechanical systems at finite temperature. To incorporate these general and important additional effects, more sophisticated models must be employed. Such effects become particularly relevant in tightly confined geometries, e.g. a

quasi-1D system, or close to the transition to Bose–Einstein condensation. The most common family of methods to describe beyond-mean-field effects (quantum and/or thermal effects) are the various embodiments of the stochastic GPE [4]. A more fundamental quantum mechanical approach is to describe the many-body dynamics via the multiconfigurational time-dependent Hartree method for interacting bosons [100].

There have been limited beyond-mean-field studies of bright solitary matter waves to date, although what studies have been performed have raised intriguing differences from the mean-field predictions.

In the two experiments to date that have generated multiple bright solitary waves [9, 11], the observed wave dynamics (post-formation of the waves) could be well described by the mean-field GPE under the assumption that the waves featured phase differences close to π [42, 81, 91]. This pattern of relative phases can potentially be explained by a process of solitary wave formation through modulational instability, followed by collapse of neighbouring solitons with relative phases close to zero [22, 42–44]. However, the mean-field GPE, even when supplemented with phenomenological three-body loss terms, cannot provide a quantitatively accurate description of solitary wave formation out of a condensate collapse [75, 77, 101]. More sophisticated simulations of the condensate quantum field during collapse recover the formation of multiple solitary waves but without π-phase differences [78]. The origin of the π-phase differences (if they truly exist) remains an open question.

In Ref. [78] it was also observed that, under 1D quantum field simulations, that the solitary wave collisions behaved repulsively, i.e. akin to mean-field collision with π-phase difference, but independent of the initial relative phase. Although these 1D results were not supported by the corresponding 3D quantum field simulations, uncertainty remains over whether π-phase differences do indeed appear in the experimental systems, and indeed whether relative phase as defined by the GPE is a well-defined quantity for experimental bright solitary waves. Potentially, the relative phase and velocity dependencies predicted by the GPE could be verified in experiment using the controlled generation method of Ref. [90], providing a test of the mean-field description.

More recently, Cederbaum et al. used the time-dependent Hartree method [100] to describe the collisions between two initially-formed bright solitary waves [102]. While the GPE assumes that all atoms occupy a single quantum state, this method relaxes this condition and allows occupation of an arbitrary number of states. It was observed that the freely evolving solitary waves rapidly lost their coherence, evolving into fragmented condensates distributed over multiple states. These are fundamentally different objects to the original solitary waves, which within the GPE are assumed to perpetuate. These final states can be distinguished in experiment via their signatures in the first-order correlation functions.

Recent work has also considered the quantum dynamics of bright solitons in the presence of a disordered potential, showing that quantum bright solitons are able to undergo Anderson localization [103]. This analysis was performed through an effective potential approximation, later confirmed through full many-body simulations

[104]. Furthermore, for a *pair* of bright solitons in a disordered potential it was shown that the localization effect is sensitive to soliton interactions, and becomes destroyed when the soliton interactions become too strong [105].

7.2 Spontaneous Symmetry Breaking

Symmetry breaking plays a central role in the formation of bright solitons from an initially broad condensate. The exact many-body ground state of a one-dimensional system with translational symmetry and attractive interactions is fragile and prone to localization into a bright soliton state, thereby spontaneously breaking the translational symmetry of the system [106]. This localization is achieved via a superposition of low-lying many-body eigenstates of the system. This scenario can be realized experimentally within a ring-shaped trapping potential, as considered in Ref [106]. Although the bright soliton state is well described within the mean-field Gross–Pitaevskii equation, in a mesoscopic system it was predicted that there exists a cross-over from the translationally symmetric state to the soliton state as a function of the interaction strength.

Experimentally it is possible to rotate the trapping potential which confines the condensate. For a 3D bright solitary wave confined in an axi-symmetric waveguide of trap frequency ω_r and rotated about its untrapped axis at a frequency $\Omega < \omega_r$, the stationary states are bright solitary waves which are elliptically deformed in the transverse plane [107, 108]. However, the orientation of the ellipticity has no preferred direction and one can expect a spontaneous breaking of axi-symmetry. Meanwhile, at higher rotation frequencies, the favoured state is believed to be for the wave centre-of-mass to be off-axis and undergo precessional motion, also associated with spontaneous breaking of axi-symmetry [109, 110]. Interestingly, one may add quintic trapping in the transverse plane, for which the effective potential experienced by the rotating solitary wave takes the form of the classic Mexican hat potential.

7.3 Bright Solitary Wave Interferometry

Over the last two decades the advent of atom interferometry [111] has led to significant improvements in metrological precision for real-world measurements of, e.g., rotation [112] and the acceleration due to gravity [113]. The development of atomic BECs has enabled a new form of atom interferometry in which a *trapped* BEC is coherently split and recombined after a period of differential evolution. Following a pioneering early experiment [114], many BEC interferometers have been constructed based around the principle of a raised, and subsequently lowered, double-well potential [115–119]. This scheme allows long interaction times [120] and the small spatial scale potentially permits accurate measurements of, e.g., the

Casimir–Polder potential of a surface [119]. Provided the raising of the barrier is sufficiently fast, the GPE can provide a good description of the dynamics, in the sense that nearly all atoms remain in a single mode, which is coherent across the barrier [121]. However, interactions also cause undesirable phase diffusion during the interaction time, and for this reason experiments have typically chosen to reduce or eliminate them where possible [118, 120, 122].

The properties of bright solitary waves offer a novel solution to the problem of inter-atomic interactions; one can envisage an analogue to the optical Mach–Zender interferometer in which a BEC is split into two coherent, non-dispersive, spatially-localized bright solitary waves, which are manipulated and eventually recombined using a time-dependent external potential. In the following sections we briefly review two proposals for the necessary coherent beam-splitting of solitary waves, using an internal-state interference protocol [90] (Sect. 7.3.1) and potential barriers [123–126] (Sect. 7.3.2). Note that bright solitons may also be split by imposing a spatially-dependent chirp on the soliton, which may be realized by an appropriately profiled laser beam [127]. In Sect. 7.4 we outline proposals to use interferometry devices based on bright solitary waves for improved sensitivity in the measurement of atom–surface interactions [128].

7.3.1 Splitting Solitary Waves Using Interference Methods

In this section we consider using a magnetic Feshbach resonance to quasi-instantaneously change the (negative) s-wave scattering length from an initial value a_s^0, related to the new value a_s by $a_s^0 = \alpha^2 a_s$. If the BEC is initially in the bright solitary wave stationary state at scattering length a_s^0, it remains so immediately after the change to scattering length a_s. Assuming a 1D description and negligible axial trapping ($\omega_x = 0$), the subsequent dynamics are described by the NLSE [Eq. (28)] with initial condition,

$$\psi_0(x) = \frac{1}{2\alpha\sqrt{b_x}}\,\mathrm{sech}\left(\frac{x}{2\alpha^2 b_x}\right), \tag{36}$$

where the original soliton is assumed to be centered on the origin for convenience. Solutions of the NLSE for this initial condition are well-known in the context of nonlinear optics [58]: for integer $\alpha = J$, Eq. (36) consists of a bound state, or multi-soliton pulse, of J solitons with unequal amplitudes a_j and zero velocity ($v_j = 0$). For non-integer $\alpha = J + \beta$, where $0 < \beta < 1$, it consists of J solitons plus radiation [58].

Subjecting such a pulse to a sinusoidal density modulation, such that,

$$\psi_0'(x) = \frac{1}{2\alpha\sqrt{b_x}}\,\mathrm{sech}\left(\frac{x}{2\alpha^2 b_x}\right)\cos\left(\frac{Kx}{2\alpha^2 b_x} + \frac{\Delta\Phi}{2}\right), \tag{37}$$

is the new initial condition, alters the character of the multi-soliton pulse. For the case of most interest, $\alpha \gtrsim 2$, this modulation was explored in Refs. [60, 61] using

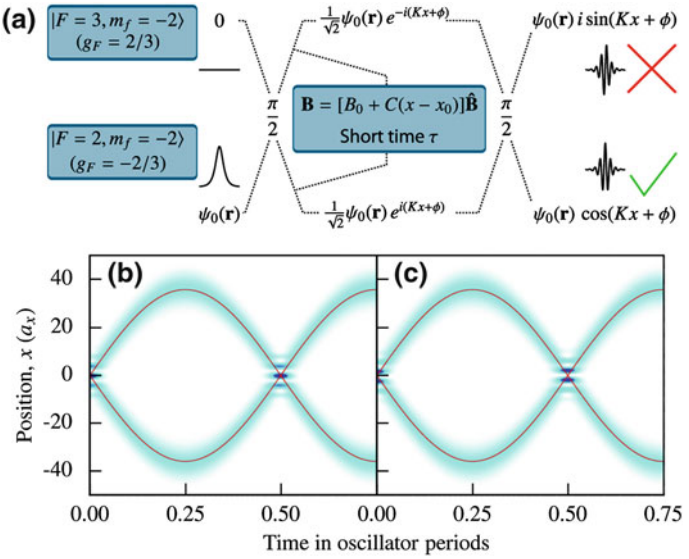

Fig. 13 Interferometric scheme to phase-coherently split a single bright solitary wave into two bright solitary waves with controlled velocity and phase [90]: **a** interferometric protocol illustrated for ^{85}Rb and magnetic field **B**, which is applied for a short time τ between two quasi-instantaneous $\pi/2$-pulses. The component in $|3, -2\rangle$ is not trapped, and escapes. **b** Splitting and re-collision with relative phase $\phi = 0$, and **c** $\phi = \pi$. *Red lines* indicate the trajectories predicted by the particle-like model discussed in Sect. 5 [45] (Colour figure online)

perturbative and numerical methods. In this case, beyond a (relatively low) threshold value of the modulation wavevector K the multi-soliton pulse is split into two solitons and a (generally negligible) radiation component. The two solitons have equal amplitudes, oppositely directed velocities approximately proportional to K [60], and relative phase $\Delta\Phi$. Consequently such a modulation can be used to to control the velocity and relative phase of a pair of bright solitons.

In Ref. [90], a theoretical scheme was developed to implement such a modulation, and hence controllably generate a pair of bright solitons, using an internal state interference protocol; this protocol is illustrated schematically in Fig. 13a. In this protocol, the application of a linear perturbing potential for a short time is used to impart momentum on the solitons; the waves continue to behave as solitary waves under such a potential as shown in Ref. [12]. Numerical simulations verified that the same protocol is effective for bright solitary matter waves both in the presence of an axial trap (Fig. 13b, c) and outside the quasi-1D limit. If such a technique can be experimentally implemented, the possibility to carefully engineer the relative phase between two solitary waves would represent a crucial first step towards a general bright solitary wave interferometer.

7.3.2 Splitting Solitary Waves at a Potential Barrier

Compared to the interference method discussed in the previous section, a simpler method to split bright solitary waves is afforded by collisions with a potential barrier. In return for experimental simplicity, however, this method lacks the same fine-grained control over the relative phase.

Within the mean field description, the dynamics of NLSE bright soliton collisions with potential barriers and wells has been widely explored (see, e.g., [73, 129–132] and references therein). The behaviour of solitary waves is similar in soliton-like regimes; in particular, fast solitary wave collisions with a narrow barrier lead to smooth splitting of an incoming solitary wave into transmitted and reflected solitary waves [125, 126, 132–134]. This behaviour is analogous to bright solitons in the NLSE scattering from a δ-function potential: it can be analytically demonstrated in such a situation that the incoming bright soliton is split into transmitted and reflected components, each of which consist mainly of a bright soliton, plus a small amount of radiation [132]. Bright solitary waves interacting with barriers much narrower than their width largely follow this prediction [125, 133, 134]. Within the mean-field description, potential barrier collisions of this nature have been proposed as another means to realize solitary wave interferometers, potentially based on solitary wave molecules [133], oscillating bright solitary waves in a harmonic trap [134] and bright solitary waves in a toroidal trap [125].

In understanding the operation of such an interferometer one must be careful in interpreting the predictions of the GPE. This mean-field description is most often thought of as describing a system with a wavefunction of Hartree product form (that is, a single macroscopically occupied single particle mode). Such a state is free of many-body correlations [124]. At face value, this seems to be at odds with many-body descriptions of the scattering of a bright solitary wave on a potential: it was demonstrated in Ref. [123], using an effective potential approximation, that a condensate bright soliton of 100 atoms could be placed in a coherent macroscopic superposition between reflected and transmitted solitons via a slow collision with a wide Gaussian barrier—a state entirely dominated by many-body correlations rather than free of them. Similar collisions were investigated in Ref. [124] using the MCTDHB many-body computational method [100, 135]. In this work, the condensate was found to fragment, leaving two macroscopically occupied orbitals. One of these orbitals corresponded to a transmitted, and the other to a reflected, bright soliton, implying creation of a macroscopic coherent superposition between spatially distinct states.

This apparent disagreement with the GPE prediction is, however, only a disagreement with the Hartree-product interpretation of the GPE; in classical-field methods one commonly uses the GPE to describe *all* macroscopically occupied modes of a system [136], and in this interpretation there is no general disagreement with the many-body description. Importantly, in the proposed solitary wave interferometers [125, 134] the actual interferometric measurement consists of

measuring the average fraction of atoms ending up on a particular side of a potential barrier. Such a measurement is independent of the underlying occupations of single particle modes, suggesting the mean-field GPE may still give a useful description of a bright solitary wave interferometer.

Nonetheless, the realization of macroscopic quantum effects using bright solitary waves offers exciting potential for future interferometric devices, for example in exploiting the macroscopic quantum superposition to achieve quantum enhancement of the measurement precision [120, 122] and using pairs of entangled quantum solitons [137]. A bright solitary wave interferometer therefore offers the intriguing possibility of observing the effects of macroscopic quantum superposition [138, 139] through the formation of a fragmented state [123, 124] and hence enhancing measurement sensitivities [138, 140].

7.4 Soliton Surface Probes and Quantum Reflection

There is growing interest in the use of ultracold atoms to measure short range forces close to a surface motivated by the possibility of probing short range corrections to gravity which extend beyond the Standard model [141–143]. Traditional experiments, following the pioneering measurements of Cavendish in 1798 [144], now use a variety of approaches from superconducting gravity gradiometers [145] and microcantilevers [146] to planar oscillators [147] and torsion balance experiments [148]. However, in scaling down experiments to probe ever decreasing length scales a new, fundamental problem arises. Quantum electrodynamics predicts a macroscopic force between conductors, known as the Casimir force [149]. This force vastly overwhelms the much weaker gravitational attraction between the test masses, such that experiments are forced to search for deviations between the theoretical and experimental Casimir forces. Precisely calculating such Casimir forces for a specific macroscopic test mass near a surface is generally difficult [150]. In contrast, the interaction between a single neutral atom and a plane surface is well understood [151, 152] being characterised by the attractive Casimir–Polder potential,

$$U_{\mathrm{vdW}} = -\frac{C_3}{z^3} \quad \text{for} \quad z < \lambda_{\mathrm{opt}}/2\pi, \tag{38}$$

$$U_{\mathrm{ret}} = -\frac{C_4}{z^4} \quad \text{for} \quad \lambda_{\mathrm{opt}}/2\pi < z < \lambda_{\mathrm{T}}, \tag{39}$$

where for longer length scales the $1/z^3$ form of the van der Waals potential, characterised by C_3, becomes $1/z^4$ due to retardation effects. This new regime is characterised by C_4 with the transition point between the two regimes determined by the wavelength corresponding to the dominant excitation energy of the interacting atoms, λ_{opt} [153]. Further from the surface (larger than the thermal

wavelength of photons, λ_T) the interaction becomes dominated by the thermal fluctuation of the electromagnetic field [154].

The inherent advantage of directly probing the atom–surface interaction has prompted the recent proposal of a new generation of experiments which aim to exploit the precision and control offered by atomic physics and ultracold quantum gases to push the measurement of short-range forces into a new regime [155–158]. Indeed a number of proof-of-principle experiments have already utilised ultracold atomic gases to explore the short range van der Waals and Casimir–Polder potentials [159–162]. Nevertheless such experiments are in their infancy and considerable refinement is required before they become competitive with the classical 'Cavendish style' experiments as a test of short-range gravitational forces.

The attractive Casimir–Polder potential described above can also be investigated through the study of *quantum reflection*. The term quantum reflection refers to the process where a particle reflects from a potential without reaching a classical turning point and is a direct consequence of the wave nature of the particle. Significant reflection occurs when the local wave vector of the particle $k = \sqrt{(k_\infty^2 - 2mU(z)/\hbar^2)}$ changes by more than k over a distance of $1/k$, where k_∞ is the wave vector of the particle of mass m far from the potential $U(z)$. This requires an abrupt variation in the potential $U(z)$, exactly as is found for an atom in the vicinity of a solid surface. The demonstration of quantum reflection from solid surfaces is typically performed at grazing incidence in order to reduce the wave vector normal to the surface [163, 164]. The advent of ultracold and quantum degenerate atomic samples with large de Broglie wavelengths opens up new possibilities to study quantum reflection at normal incidence with unprecedented control over the atomic motion. Reflection probabilities as high as 20 % have been demonstrated for ^{23}Na condensates incident on a solid silicon surface [165].

The use of bright matter wave solitons has been proposed to study quantum reflection from a solid surface. In Ref. [128] the authors show that the use of solitons presents a number of unique advantages resulting from the presence of attractive interactions. Crucially the robust, self-trapped and highly localised nature of bright solitons can result in a clean reflection from the surface, with very limited disruption to the density profile as compared to condensates with repulsive interactions [165]. Moreover, previous numerical studies of quantum reflection from purely attractive potential wells revealed that in certain regimes the whole soliton reflects with very little loss, leading to a significant enhancement of the reflection probability as compared to the single particle case [130]. The presence of attractive interactions has also been shown to be advantageous in the performance of traps for cold atoms based upon quantum reflection [166]. The absence of dispersion as the soliton propagates permits the precise control of the velocity normal to the surface and allows much lower velocities to be achieved.

Current experiments in Durham [167, 168] aim to exploit this combination of advantages and promise to deliver accurate measurements of the quantum

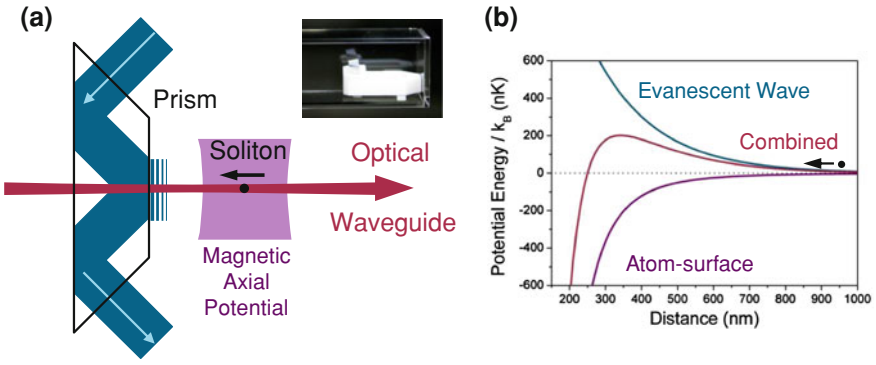

Fig. 14 **a** Schematic of the proposed experimental configuration for the study of quantum reflection of bright matter wave solitons from a solid surface. The soliton propagates towards the surface in an optical waveguide formed by a focussed 1,064 nm laser beam. Motion of the soliton along the waveguide is controlled through the manipulation of a weak magnetic potential along the waveguide. An optional repulsive evanescent field can be added through the total internal reflection of a 532 nm laser beam in the prism. The *inset* shows a photograph of the super-polished Dove prism mounted in a UHV glass cell in the Durham experiment. **b** The total potential (*red*) experienced by the atoms in the vicinity of the surface is the sum of the Casimir–Polder potential (*purple*) and the evanescent field (*blue*) (Colour figure online)

reflection probability. The proposed experimental scenario for the study of quantum reflection is depicted in Fig. 14.

Bright matter wave solitons are formed in an optical waveguide from an ^{85}Rb condensate with attractive interactions. For rubidium and a room temperature surface, the lengthscales relating to the Casimir–Polder potential are $\lambda_{\mathrm{opt}}/2\pi \approx 0.12\,\mu\mathrm{m}$ and $\lambda_{\mathrm{T}} \approx 7.6\,\mu\mathrm{m}$. The velocity of the soliton towards the surface can be controlled by manipulating a weak (~ 1 Hz) magnetic potential along the axis of the waveguide. The experimental configuration also allows for the addition of a repulsive (or attractive) evanescent field in the vicinity of the surface formed by the total internal reflection of a blue (or red) detuned laser field within the glass prism. This produces a potential which decays exponentially with distance from the surface; the decay length being determined by the laser wavelength, the refractive index of the prism and the angle of incidence of the laser beam. When combined with the atom–surface potential, the repulsive evanescent field leads to a repulsive barrier of finite height, in close proximity to the surface (see Fig. 14b). Studies of classical reflection from such a barrier can be used to probe the atom–surface potential [159]. Moreover, the addition of both repulsive and attractive evanescent fields can be used to engineer a potential in the vicinity of the surface that significantly enhances the quantum reflection probability [169].

7.5 Exotic Bright Solitary Waves

We have focussed in this chapter on bright solitary waves of a single-species condensate with *s*-wave interactions. However, part of the beauty of these atomic gases is that it is possible to precisely introduce additional complexity into the system, e.g. additional condensate components or long-range interactions. In certain such scenarios, distinct bright soliton-like structures can arise, with even richer properties than their *s*-wave counterparts. We will briefly summarise these exotic bright solitary waves below.

Bright-dark solitons

Condensate systems which involve two co-existing condensates, composed of either different atomic species or the same atomic species but in two different magnetic states, have been the topic of much experimental and theoretical study [4]. As well as the local intra-species interactions within each component, there exists a local inter-species interaction. When all interactions are repulsive, and the inter-species interaction is sufficiently strong, phase separation of the condensates becomes favourable [3]. Then, the system can enter a state where one component adopts a bright soliton-like structure, about which the other component forms a dark soliton-like density notch. These hybrid structures, termed dark-bright solitons, have analogs in nonlinear optics [170] and were first predicted to exist in inhomogeneous BECs by Busch and Anglin [171]. Since then they have been generated and observed in several experiments [172–174]. Possessing only repulsive interactions, they are free from the collapse instability and behave more akin to dark solitary waves (see Ref. [8] for a review) than bright solitary waves.

Bose–Fermi solitons

Similar to above, it is possible to create a system in which a Bose–Einstein condensate co-exists with a degenerate gas of fermions. For identical fermions, the Pauli exclusion principle prevents *s*-wave interactions, and so the predominant interactions in this ultracold mixture are the *s*-wave boson–boson interactions and the boson–fermion interactions. Here, an attractive boson–fermion interaction can support a soliton structure in which localized wavepacket of each gas, overlapping in space, is self-trapped by their mutual interaction. These structures, termed Bose–Fermi solitons, have been predicted via numerical and variational approaches [175–179], and have been simulated to propagate without dispersion [175, 180]. The boson–fermion interaction must be sufficiently strong to overcome the internal repulsion within the BEC component but not so large as to induce collapse. As such, in 3D, they exist as metastable states of the system. Interestingly, under the inclusion of higher order *p*-wave interactions with repulsive sign, the collapse instability can be completely eradicated, suggesting a greatly enhanced stability [179]. Related bright solitary wave structures are also predicted to arise in Bose–Fermi mixtures in the presence of optical lattice potential [181–183].

Non-local bright solitons

In recent years, BECs have been produced in which the atomic species have a large natural magnetic dipole moment [13]. In contrast to *s*-wave interactions which are short-range and isotropic, these interactions are long-range and anisotropic. By polarizing the dipoles in a common direction, the whole condensate takes on a dipolar nature, which can be accounted for within the GPE by the inclusion of a non-local term [13]. The attractive component of the dipolar interactions lends itself to support self-trapped solitary wave states, but it also makes the collapse instability a general feature of dipolar BECs.

Within a quasi-1D waveguide, solitary waves of dipolar BECs are predicted to be supported [184, 185]. In general, dipolar interactions also co-exist with *s*-wave interactions, and the capacity for self-trapping was shown to occur for various regimes of the dipolar interaction and the *s*-wave interaction. Collisions between two such dipolar solitary waves were found to exhibit more complicated dynamics including regimes where the colliding waves form a bound state [184] and sensitivity to the polarization direction [185]. More strikingly, in Refs. [186, 187] it was shown that a dipolar BEC within a quasi-two-dimensional trap can form a bright solitary wave that is self-trapped in two-dimensions and free to move within the untrapped plane of the system.

Distinct non-local effects can be introduced by coupling of a BEC to highly excited Rydberg states [188], excited atomic states with high principal quantum number. These excited states become coherently shared throughout the condensate, inducing a strong collective interaction via van der Waals forces. Using a GPE which incorporated an appropriate non-local term, it was predicted in [189] that bright solitary waves could form which are not only free from the collapse instability, but are self-trapped in all three dimensions. These wavepackets are predicted to remain stable for hundreds of milliseconds and raise the prospect of the first realization of 3D bright solitary matter waves.

8 Conclusions

We have reviewed bright solitary waves composed of gaseous Bose–Einstein condensates, from their experimental formation and observation, through to a theoretical exposition of their static and dynamical mean-field properties. Emphasis is placed on how the harmonic trapping potential and three-dimensional setting leads to departures in behaviour from the classic bright soliton. Soliton-like states remain supported, in the sense that they are capable of self-trapping and retaining their static form as they propagate. The most marked deviation is introduced by the extension from 1D to 3D, which introduces an instability to collapse for sufficiently large interaction parameter and a population transfer during collisions. These deviant behaviours can be greatly reduced in appropriate regimes but may be exploited in their own right, e.g. by using population transfer as a means to infer relative phase.

The properties of these bright solitary matter waves are now, generally speaking, well understood at the mean-field level. Emphasis is now turning to developing a full quantum mechanical understanding of these excitations and much work remains to be done in this direction. The experimental capacity to engineer additional atomic components and interactions into the system promises new families of bright solitary waves, which are, for instance, self-trapped in higher dimensions and stable to collapse. Furthermore, we believe that bright solitary waves hold strong potential as atomic vehicles for applications in matter wave interferometry and surface force detection.

References

1. A. Einstein, Sitzungsber. Preuss. Akad. Wiss. **1**, 3 (1925)
2. D.R. Tilley, J. Tilley, *Superfluidity and Superconductivity* (Institute of Physics, London, 1990)
3. C. Pethick, H. Smith, *Bose–Einstein Condensation in Dilute Gases* (Cambridge University Press, Cambridge, 2002)
4. P.G. Kevrekidis, D.J. Frantzeskakis, R. Carretero-González, *Emergent Nonlinear Phenomena in Bose–Einstein Condensates*. Springer Series on Atomic, Optical and Plasma Physics (Springer, Berlin, 2008)
5. L. Pitaevskii, S. Stringari, *Bose–Einstein Condensation* (Clarendon Press, Oxford, 2003)
6. M.J. Ablowitz, H. Segur, *Solitons and the Inverse Scattering Transform* (SIAM, Philadelphia, 1981)
7. P.G. Drazin, R.S. Johnson, *Solitons: an Introduction*, 2nd edn. (Cambridge University Press, Cambridge, 1989)
8. D.J. Frantzeskakis, J. Phys. A: Math. Theor. **43**, 213001 (2010)
9. K.E. Strecker, G.B. Partridge, A.G. Truscott, R.G. Hulet, Nature **417**, 150 (2002)
10. L. Khaykovich, F. Schreck, G. Ferrari, T. Bourdel, J. Cubizolles, L.D. Carr, Y. Castin, C. Salomon, Science **296**, 1290 (2002)
11. S.L. Cornish, S.T. Thompson, C.E. Wieman, Phys. Rev. Lett. **96**, 170401 (2006)
12. S.A. Morgan, R.J. Ballagh, K. Burnett, Phys. Rev. A **55**, 4338 (1997)
13. T. Lahaye, C. Menotti, L. Santos, M. Lewenstein, T. Pfau, Rep. Prog. Phys. **72**(12), 126401 (2009)
14. J.E. Simsarian, J. Denschlag, M. Edwards, C.W. Clark, L. Deng, E.W. Hagley, K. Helmerson, S.L. Rolston, W.D. Phillips, Phys. Rev. Lett. **85**, 2040 (2000)
15. J.L. Roberts, N.R. Claussen, S.L. Cornish, E.A. Donley, E.A. Cornell, C.E. Wieman, Phys. Rev. Lett. **86**, 4211 (2001)
16. A. Gammal, T. Frederico, L. Tomio, Phys. Rev. A **64**, 055602 (2001)
17. A. Gammal, L. Tomio, T. Frederico, Phys. Rev. A **66**, 043619 (2002)
18. C. Huepe, S. Métens, G. Dewel, P. Borckmans, M.E. Brachet, Phys. Rev. Lett. **82**, 1616 (1999)
19. L. Bergé, T.J. Alexander, Y.S. Kivshar, Phys. Rev. A **62**, 023607 (2000)
20. N. Akhmediev, M.P. Das, A.V. Vagov, Int. J. Mod. Phys. B **13**, 625 (1999)
21. M. Houbiers, H.T.C. Stoof, Phys. Rev. A **54**, 5055 (1996)
22. S.K. Adhikari, New J. Phys. **5**, 137 (2003)
23. R.J. Dodd, M. Edwards, C.J. Williams, C.W. Clark, M.J. Holland, P.A. Ruprecht, K. Burnett, Phys. Rev. A **54**, 661 (1996)
24. V.I. Yukalov, E.P. Yukalova, Phys. Rev. A **72**, 063611 (2005)
25. C. Chin, R. Grimm, P. Julienne, E. Tiesinga, Rev. Mod. Phys. **82**, 1225 (2010)
26. C.C. Bradley, C.A. Sackett, R.G. Hulet, Phys. Rev. Lett. **78**, 985 (1997)
27. J.M. Gerton, D. Strekalov, I. Prodan, R.G. Hulet, Nature **408**, 692 (2000)
28. Y. Kagan, G.V. Shlyapnikov, J.T.M. Walraven, Phys. Rev. Lett. **76**, 2670 (1996)

29. E. Shuryak, Phys. Rev. A **54**, 3151 (1996)
30. H.T.C. Stoof, J. Stat. Phys. **87**, 1353 (1997)
31. M. Ueda, A.J. Leggett, Phys. Rev. Lett. **80**, 1576 (1998)
32. E.A. Donley, N.R. Claussen, S.L. Cornish, J.L. Roberts, E.A. Cornell, C.E. Wieman, Nature **412**, 295 (2001)
33. N.R. Claussen, S.J.J.M.F. Kokkelmans, S.T. Thompson, E.A. Donley, E. Hodby, C.E. Wieman, Phys. Rev. A **67**, 060701 (2003)
34. P.A. Altin, G.R. Dennis, G.D. McDonald, D. Döring, J.E. Debs, J.D. Close, C.M. Savage, N.P. Robins, Phys. Rev. A **84**, 033632 (2011)
35. R. Grimm, M. Weidemuller, Y.B. Ovchinnikov, (Academic Press, 2000), pp. 95–170
36. K. Tai, A. Hasegawa, A. Tomita, Phys. Rev. Lett. **56**, 135 (1986)
37. S.L. Cornish, N.R. Claussen, J.L. Roberts, E.A. Cornell, C.E. Wieman, Phys. Rev. Lett. **85**, 1795 (2000)
38. P. Dyke, L. Sidong, S. Pollack, D. Dries, R. Hulet, in *42nd Annual Meeting of the APS Division of Atomic, Molecular and Optical Physics*, vol. 56, No. 5 (2011), http://meetings.aps.org/link/BAPS.2011.DAMOP.E1.124
39. P. Dyke, L. Sidong, R. Hulet, in *43rd Annual Meeting of the APS Division of Atomic, Molecular and Optical Physics*, vol. 57, No. 5 (2012), http://meetings.aps.org/link/BAPS.2012.DAMOP.U6.1
40. T. Dauxois, M. Peyrard, *Physics of Solitons* (Cambridge University Press, Cambridge, 2006)
41. V.M. Pérez-García, H. Michinel, H. Herrero, Phys. Rev. A **57**, 3837 (1998)
42. U. Al Khawaja, H.T.C. Stoof, R.G. Hulet, K.E. Strecker, G.B. Partridge, Phys. Rev. Lett. **89**, 200404 (2002)
43. L.D. Carr, J. Brand, Phys. Rev. Lett. **92**, 040401 (2004)
44. V.Y.F. Leung, A.G. Truscott, K.G.H. Baldwin, Phys. Rev. A **66**, 061602 (2002)
45. A.D. Martin, C.S. Adams, S.A. Gardiner, Phys. Rev. Lett. **98**, 020402 (2007)
46. A.D. Martin, C.S. Adams, S.A. Gardiner, Phys. Rev. A **77**, 013620 (2008)
47. T.P. Billam, S.A. Wrathmall, S.A. Gardiner, Phys. Rev. A **85**, 013627 (2012)
48. L. Salasnich, A. Parola, L. Reatto, Phys. Rev. A **66**, 043603 (2002)
49. L. Salasnich, A. Parola, L. Reatto, Phys. Rev. A **65**, 043614 (2002)
50. A.M. Kamchatnov, V.S. Shchesnovich, Phys. Rev. A **70**, 023604 (2004)
51. L. Khaykovich, B.A. Malomed, Phys. Rev. A **74**, 023607 (2006)
52. A. Mũnoz Mateo, V. Delgado, Phys. Rev. A **77**, 013617 (2008)
53. L. Salasnich, B.A. Malomed, Phys. Rev. A **74**, 053610 (2006)
54. L.D. Fadeev, L.A. Takhtajan, *Hamiltonian Methods in the Theory of Solitons* (Springer, Berlin, 1987)
55. L.N. Hand, J.D. Finch, *Analytical Mechanics* (Cambridge University Press, Cambridge, 1998)
56. V. Zakharov, A. Shabat, Sov. Phys. JETP **34**, 62 (1972)
57. V. Zakharov, A. Shabat, Zh. Eksp. Teor. Fiz. **61**, 118 (1971)
58. J. Satsuma, N. Yajima, Prog. Theor. Phys. Suppl. **55**, 284 (1974)
59. J.P. Gordon, Opt. Lett. **8**, 596 (1983)
60. Y. Kodama, A. Hasegawa, Opt. Lett. **16**, 208 (1991)
61. V.V. Afanasjev, V.A. Vysloukh, J. Opt. Soc. Am. B **11**, 2385 (1994)
62. H.A. Haus, W.S. Wong, Rev. Mod. Phys. **68**, 423 (1996)
63. N. Akhmediev, A. Ankiewicz, M. Taki, Phys. Lett. A **373**, 675 (2009)
64. J.B. McGuire, J. Math. Phys. **5**, 622 (1964)
65. D.I.H. Holdaway, C. Weiss, S.A. Gardiner, Phys. Rev. A **85**, 053618 (2011)
66. D. Anderson, Phys. Rev. A **27**, 3135 (1983)
67. D. Anderson, M. Lisak, T. Reichel, J. Opt. Soc. Am. B **5**, 207 (1988)
68. B.A. Malomed, Chapter 2: Variational methods in nonlinear fiber optics and related fields, in *Progress in Optics*, vol. 43, ed. by E. Wolf (Elsevier, Berlin, 2002), pp. 71–193
69. L.D. Carr, Y. Castin, Phys. Rev. A **66**, 063602 (2002)
70. N.G. Parker, S.L. Cornish, C.S. Adams, A.M. Martin, J. Phys. B **40**, 3127 (2007)

71. V.M. Pérez-García, H. Michinel, J.I. Cirac, M. Lewenstein, P. Zoller, Phys. Rev. Lett. **77**, 5320 (1996)
72. V.M. Pérez-García, H. Michinel, J.I. Cirac, M. Lewenstein, P. Zoller, Phys. Rev. A **56**, 1424 (1997)
73. T. Ernst, J. Brand, Phys. Rev. A **81**, 033614 (2010)
74. P.A. Ruprecht, M.J. Holland, K. Burnett, M. Edwards, Phys. Rev. A **51**, 4704 (1995)
75. C.M. Savage, N.P. Robins, J.J. Hope, Phys. Rev. A **67**, 014304 (2003)
76. H. Saito, M. Ueda, Phys. Rev. Lett. **86**, 1406 (2001)
77. S. Wüster, J.J. Hope, C.M. Savage, Phys. Rev. A **71**, 033604 (2005)
78. B.J. Dąbrowska-Wüster, S. Wüster, M.J. Davis, New J. Phys. **11**, 053017 (2009)
79. M. Desaix, D. Anderson, M. Lisak, J. Opt. Soc. Am. B **8**, 2082 (1991)
80. A. Minguzzi, S. Succi, F. Toschi, M.P. Tosi, P. Vignolo, Phys. Rep. **395**, 223 (2004)
81. N.G. Parker, A.M. Martin, S.L. Cornish, C.S. Adams, J. Phys. B **41**, 045303 (2008)
82. L.P. Pitaevskii, Phys. Lett. A **221**, 14 (1996)
83. L. Salasnich, B.A. Malomed, Phys. Rev. A **79**, 053620 (2009)
84. G. Boffetta, A.R. Osborne, J. Comp. Phys. **102**, 252 (1992)
85. J.N. Maki, T. Kodama, Phys. Rev. Lett. **57**, 2097 (1986)
86. R. Scharf, A.R. Bishop, Phys. Rev. A **46**, R2973 (1992)
87. R. Scharf, A.R. Bishop, Phys. Rev. E **47**, 1375 (1993)
88. R. Scharf, Chaos Soliton. Fract. **5**, 2527 (1995)
89. Y.S. Kivshar, T.J. Alexander, S.K. Turitsyn, Phys. Lett. A **278**, 225 (2001)
90. T.P. Billam, S.L. Cornish, S.A. Gardiner, Phys. Rev. A **83**, 041602(R) (2011)
91. N.G. Parker, A.M. Martin, C.S. Adams, S.L. Cornish, Physica D **238**, 1456 (2009)
92. M.I. Rodas-Verde, H. Michinel, V.M. Pérez-García, Phys. Rev. Lett. **95**, 153903 (2005)
93. A.V. Carpentier, H. Michinel, M.I. Rodas-Verde, V.M. Pérez-García, Phys. Rev. A **74**, 013619 (2006)
94. P.Y.P. Chen, B.A. Malomed, J. Phys. B **38**(23), 4221 (2005)
95. H. Saito, M. Ueda, Phys. Rev. Lett. **90**, 040403 (2003)
96. B. Malomed, *Soliton Management in Periodic Systems* (Springer, Berlin, 2006)
97. D. Poletti, T.J. Alexander, E.A. Ostrovskaya, B. Li, Y.S. Kivshar, Phys. Rev. Lett. **101**, 150403 (2008)
98. D. Poletti, E.A. Ostrovskaya, T.J. Alexander, B. Li, Y.S. Kivshar, Physica D **238**, 1338 (2009)
99. V. Ahufinger, A. Mebrahtu, R. Corbaln, A. Sanpera, New J. Phys. **9**, 4 (2007)
100. O.E. Alon, A.I. Streltsov, L.S. Cederbaum, Phys. Rev. A **77**, 033613 (2008)
101. S. Wüster, B.J. Dabrowska-Wüster, A.S. Bradley, M.J. Davis, P.B. Blakie, J.J. Hope, C.M. Savage, Phys. Rev. A **75**, 043611 (2007)
102. A.I. Streltsov, O.E. Alon, L.S. Cederbaum, Phys. Rev. Lett. **106**, 240401 (2011)
103. K. Sacha, C.A. Müller, D. Delande, J. Zakrzewski, Phys. Rev. Lett. **103**, 210402 (2009)
104. D. Delande, K. Sacha, M. Plodzien, S.K. Avazbaev, J. Zakrzewski, arxiv:1207.2001
105. M. Plodzień, K. Sacha, Phys. Rev. A **86**, 033617 (2012)
106. R. Kanamoto, H. Saito, M. Ueda, Phys. Rev. A **73**, 033611 (2006)
107. N.A. Jamaludin, N.G. Parker, A.M. Martin, Phys. Rev. A **77**, 051603(R) (2008)
108. N.A. Jamaludin, N.G. Parker, A.M. Martin, Phys. Rev. A **83**, 059910(E) (2011)
109. A. Collin, E. Lundh, K.-A. Suominen, Phys. Rev. A **71**, 023613 (2005)
110. A. Collin, Phys. Rev. A **73**, 013611 (2006)
111. A.D. Cronin, J. Schmiedmayer, D.E. Pritchard, Rev. Mod. Phys. **81**, 1051 (2009)
112. T.L. Gustavson, P. Bouyer, M.A. Kasevich, Phys. Rev. Lett. **78**, 2046 (1997)
113. A. Peters, K.Y. Chung, S. Chu, Nature **400**, 849 (1999)
114. M.R. Andrews, C.G. Townsend, H.J. Miesner, D.S. Durfee, D.M. Kurn, W. Ketterle, Science **275**, 637 (1997)
115. Y. Shin, M. Saba, T.A. Pasquini, W. Ketterle, D.E. Pritchard, A.E. Leanhardt, Phys. Rev. Lett. **92**, 050405 (2004)

116. T. Schumm, S. Hofferberth, L.M. Andersson, S. Wildermuth, S. Groth, I. Bar-Joseph, J. Schmiedmayer, P. Krüger, Nat. Phys. **1**, 57 (2005)
117. Y.J. Wang, D.Z. Anderson, V.M. Bright, E.A. Cornell, Q. Diot, T. Kishimoto, M. Prentiss, R.A. Saravanan, S.R. Segal, S. Wu, Phys. Rev. Lett. **94**, 090405 (2005)
118. M. Fattori, C. D'Errico, G. Roati, M. Zaccanti, M. Jona-Lasinio, M. Modugno, M. Inguscio, G. Modugno, Phys. Rev. Lett. **100**, 080405 (2008)
119. F. Baumgärtner, R.J. Sewell, S. Eriksson, I. Llorente-Garcia, J. Dingjan, J.P. Cotter, E.A. Hinds, Phys. Rev. Lett. **105**, 243003 (2010)
120. J. Grond, U. Hohenester, I. Mazets, J. Schmiedmayer, New J. Phys. **12**, 065036 (2010)
121. D.K. Faust, W.P. Reinhardt, Phys. Rev. Lett. **105**, 240404 (2010)
122. K. Maussang, G.E. Marti, T. Schneider, P. Treutlein, Y. Li, A. Sinatra, R. Long, J. Estève, J. Reichel, Phys. Rev. Lett. **105**, 080403 (2010)
123. C. Weiss, Y. Castin, Phys. Rev. Lett. **102**, 010403 (2009)
124. A.I. Streltsov, O.E. Alon, L.S. Cederbaum, Phys. Rev. A **80**, 043616 (2009)
125. J.L. Helm, T.P. Billam, S.A. Gardiner, Phys. Rev. A **85**, 053621 (2012)
126. B. Gertjerenken, T. Billam, L. Khaykovich, C. Weiss, Phys. Rev. A **86**, 033608 (2012)
127. D.J. Kaup, J. El-Reedy, B.A. Malomed, Phys. Rev. E **50**, 1635 (1994)
128. S.L. Cornish, N.G. Parker, A.M. Martin, T.E. Judd, R.G. Scott, T.M. Fromhold, C.S. Adams, Physica D **238**, 1299 (2009)
129. Y.S. Kivshar, B.A. Malomed, Rev. Mod. Phys. **61**, 763 (1989)
130. C. Lee, J. Brand, Europhys. Lett. **73**, 321 (2006)
131. X.D. Cao, B.A. Malomed, Phys. Lett. A **206**, 177 (1995)
132. J. Holmer, J. Marzuola, M. Zworski, Commun. Math. Phys. **274**, 187 (2007)
133. U. Al Khawaja, H.T.C. Stoof, New J. Phys. **13**, 085003 (2011)
134. A.D. Martin, J. Ruostekoski, New J. Phys. **14**, 043040 (2012)
135. A.I. Streltsov, O.E. Alon, L.S. Cederbaum, Phys. Rev. Lett. **99**, 030402 (2007)
136. P.B. Blakie, A.S. Bradley, M.J. Davis, R.J. Ballagh, C.W. Gardiner, Adv. Phys. **57**, 363 (2008)
137. M. Lewenstein, B.A. Malomed, New J. Phys. **11**, 113014 (2009)
138. J.A. Dunningham, K. Burnett, Phys. Rev. A **70**, 033601 (2004)
139. J.J. Cooper, D.W. Hallwood, J.A. Dunningham, Phys. Rev. A **81**, 043624 (2010)
140. J.A. Dunningham, Contemp. Phys. **47**, 257 (2006)
141. S. Dimopoulos, G.F. Giudice, Phys. Lett. B **379**, 105 (1996)
142. N. Arkani-Hamed, S. Dimopoulos, G. Dvalic, Phys. Lett. B **429**, 263 (1998)
143. I. Antoniadis, N. Arkani-Hamed, S. Dimopoulos, G. Dvali, Phys. Lett. B **436**, 257 (1998)
144. H. Cavendish, Roy. Soc. Phil. Trans. **88**, 469 (1798)
145. M.V. Moody, H.J. Paik, Phys. Rev. Lett. **70**(9), 1195 (1993)
146. J. Chiaverini, S.J. Smullin, A.A. Geraci, D.M. Weld, A. Kapitulnik, Phys. Rev. Lett. **90**(15), 151101 (2003)
147. J.C. Long, H.W. Chan, A.B. Churnside, E.A. Gulbis, M.C.M. Varney, J.C. Price, Nature **421**, 922 (2003)
148. D.J. Kapner, T.S. Cook, E.G. Adelberger, J.H. Gundlach, B.R. Heckel, C.D. Hoyle, H.E. Swanson, Phys. Rev. Lett. **98**(2), 021101 (2007)
149. H. Casimir, Proc. K. Ned. Akad. Wet. **51**, 793 (1948)
150. A. Lambrecht, P.A.M. Neto, S. Reynaud, New J. Phys. **8**(10), 243 (2006)
151. H.B.G. Casimir, D. Polder, Phys. Rev. **73**(4), 360 (1948)
152. A. McLachlan, Mol. Phys. **7**, 381 (1963–1964)
153. H.B.G. Casimir, D. Polder, Nature **158**, 787 (1946)
154. M. Antezza, L.P. Pitaevskii, S. Stringari, Phys. Rev. A **70**(5), 053619 (2004)
155. S. Dimopoulos, A.A. Geraci, Phys. Rev. D **68**(12), 124021 (2003)
156. P. Wolf, P. Lemonde, A. Lambrecht, S. Bize, A. Landragin, A. Clairon, Phys. Rev. A **75**(6), 063608 (2007)
157. V. Sandoghdar, C.I. Sukenik, E.A. Hinds, S. Haroche, Phys. Rev. Lett. **68**(23), 3432 (1992)
158. R. Onofrio, New J. Phys. **8**, 237 (2006)

159. A. Landragin, J.Y. Courtois, G. Labeyrie, N. Vansteenkiste, C.I. Westbrook, A. Aspect, Phys. Rev. Lett. **77**(8), 1464 (1996)
160. C.I. Sukenik, M.G. Boshier, D. Cho, V. Sandoghdar, E.A. Hinds, Phys. Rev. Lett. **70**(5), 560 (1993)
161. H. Bender, P.W. Courteille, C. Marzok, C. Zimmermann, S. Slama, Phys. Rev. Lett. **104**(8), 083201 (2010)
162. D.M. Harber, J.M. Obrecht, J.M. McGuirk, E.A. Cornell, Phys. Rev. A **72**(3), 033610 (2005)
163. A. Anderson, S. Haroche, E.A. Hinds, W. Jhe, D. Meschede, L. Moi, Phys. Rev. A **34**, 3513 (1986)
164. F. Shimizu, Phys. Rev. Lett. **86**, 987 (2001)
165. T.A. Pasquini, Y. Shin, C. Sanner, M. Saba, A. Schirotzek, D.E. Pritchard, W. Ketterle, Phys. Rev. Lett. **93**, 223201 (2004)
166. A. Jurisch, J.M. Rost, Phys. Rev. A **77**, 043603 (2008)
167. S. Händel, A.L. Marchant, T.P. Wiles, S.A. Hopkins, S.L. Cornish, Rev. Sci. Instr. **83**, 013105 (2012)
168. A.L. Marchant, S. Händel, T.P. Wiles, S.A. Hopkins, S.L. Cornish, New J. Phys. **13**(12), 125003 (2011)
169. R. Côté, B. Segev, Phys. Rev. A **67**, 041604 (2003)
170. Y.S. Kivshar, B. Luther-Davies, Phys. Rep. **298**(23), 81 (1998)
171. T. Busch, J.R. Anglin, Phys. Rev. Lett. **87**, 010401 (2001)
172. B.P. Anderson, P.C. Haljan, C.A. Regal, D.L. Feder, L.A. Collins, C.W. Clark, E.A. Cornell, Phys. Rev. Lett. **86**, 2926 (2001)
173. C. Becker, S. Stellmer, P. Soltan-Panahi, S. Doerscher, M. Baumert, E.M. Richter, J. Kronjaeger, K. Bongs, K. Sengstock, Nat. Phys. **4**(6), 496 (2008)
174. C. Hamner, J.J. Chang, P. Engels, M.A. Hoefer, Phys. Rev. Lett. **106**, 065302 (2011)
175. T. Karpiuk, M. Brewczyk, S. Ospelkaus-Schwarzer, K. Bongs, M. Gajda, K. Rzazewski, Phys. Rev. Lett. **93**, 100401 (2004)
176. S.K. Adhikari, Phys. Rev. A **72**, 053608 (2005)
177. S.K. Adhikari, L. Salasnich, Phys. Rev. A **76**, 023612 (2007)
178. L. Salasnich, S.K. Adhikari, F. Toigo, Phys. Rev. A **75**, 023616 (2007)
179. N.G. Parker, D.A. Smith, Phys. Rev. A **85**, 013604 (2012)
180. T. Karpiuk, M. Brewczyk, K. Rzazewski, Phys. Rev. A **73**, 053602 (2006)
181. M. Salerno, Phys. Rev. A **72**, 063602 (2005)
182. Y.V. Bludov, J. Santhanam, V.M. Kenkre, V.V. Konotop, Phys. Rev. A **74**, 043620 (2006)
183. S.K. Adhikari, B.A. Malomed, Phys. Rev. A **76**, 043626 (2007)
184. J. Cuevas, B.A. Malomed, P.G. Kevrekidis, D.J. Frantzeskakis, Phys. Rev. A **79**, 053608 (2009)
185. L.E. Young-S, P. Muruganandam, S.K. Adhikari, J. Phys. B **44**(10), 101001 (2011)
186. P. Pedri, L. Santos, Phys. Rev. Lett. **95**, 200404 (2005)
187. I. Tikhonenkov, B.A. Malomed, A. Vardi, Phys. Rev. Lett. **100**, 090406 (2008)
188. G. Pupillo, A. Micheli, M. Boninsegni, I. Lesanovsky, P. Zoller, Phys. Rev. Lett. **104**, 223002 (2010)
189. F. Maucher, N. Henkel, M. Saffman, W. Królikowski, S. Skupin, T. Pohl, Phys. Rev. Lett. **106**, 170401 (2011)

Temporal Quantum Fluctuations in the Fringe-Visibility of Atom Interferometers with Interacting Bose-Einstein Condensate

Doron Cohen and Amichay Vardi

Abstract We formulate a semiclassical approach to study the dynamics of coherence loss and revival in a Bose-Josephson dimer. The phase-space structure of the bi-modal system in the Rabi, Josephson, and Fock interaction regimes, is reviewed and the prescription for its WKB quantization is specified. The local density of states (LDOS) is then deduced for any given preparation from its semiclassical projection onto the WKB eigenstates. The LDOS and the non-linear variation of its level-spacing are employed to construct the time evolution of the initial preparation and study the temporal fluctuations of interferometric fringe visibility. The qualitative behavior and characteristic timescales of these fluctuations are set by the pertinent participation number, quantifying the spectral content of the preparation. We employ this methodology to study the Josephson-regime coherence dynamics of several initial state preparations, including a Twin-Fock state and three different coherent states that we denote as 'Zero', 'Pi', and 'Edge' (the latter two are both on-separatrix preparations, while the Zero is the standard ground sate preparation). We find a remarkable agreement between the semiclassical predictions and numerical simulations of the full quantum dynamics. Consequently, a characteristic distinct behavior is implied for each of the different preparations.

D. Cohen
Departments of Physics, Ben-Gurion University of the Negev,
P.O. Box 653 84105 Beer-Sheva, Israel

A. Vardi (✉)
Departments of Chemistry, Ben-Gurion University of the Negev,
P.O. Box 653 84105 Beer-Sheva, Israel
e-mail: avardi@bgu.ac.il

Progress Optical Sci., Photonics (2013): 457–472
DOI: 10.1007/10091_2012_2

Published Online: 18 February 2012

1 Introduction

Atom interferometry [1–4] with Bose-condensed atoms offers the possibility of constructing compact and highly precise measurement tools. Recent experiments [5–20] demonstrate that bi-modal Bose-Einstein condensates (BECs) have the necessary phase-coherence and controllability of coupling and interaction parameters, to operate atom interferometers at the best sensitivity allowed by quantum mechanics.

A typical atom interferometer follows the Mach-Zehnder scheme consisting of a preparation stage, in which the bimodal input state is mixed by a (usually 50:50) beam-splitter, a waiting time t during which the system evolves and the two modes acquire a relative phase difference φ, and a measurement stage where the two condensates are either released and allowed to interfere or are mixed again by a second beamsplitter. In the former case, the accumulated relative phase φ correlates with the location of interference fringes, whereas in the latter it is reflected in the final atom number difference.

The single-particle coherence of the split BEC is characterized by the many-realizations fringe-visibility function $g_{12}^{(1)}(t)$. The useful timescale of an interferometric measurement is set by decoherence. For trapped BEC interferometers, an important source for the loss of single-particle coherence, is the phase-diffusion induced by nonlinear inter-particle interactions [9, 21–29]. For uncoupled condensates starting from a coherent preparation, this process amounts to a simple Gaussian decay of $g_{12}^{(1)}(t)$ on a time scale $t \sim (U\sqrt{N})^{-1}$, where U is the interaction strength and N is the number of particles. However, most current atom-interferometer setups with trapped BECs operate in the Josephson interaction regime, where coupling while small, still affects the dynamics and generates richer coherence evolution which includes oscillations, fluctuations, and recurrences of $g_{12}^{(1)}(t)$ due to quantum collapse and revival [30–32]. The evolution of fringe visibility in the Josephson regime, thus offers a unique opportunity for the controlled study of strong correlation dynamics, beyond the usual focus on ground state properties.

Our objective here is to characterize the quantum dynamics of single-particle coherence and explore the dependence of its fluctuations on the initial preparation [32–35]. For this purpose we employ a semiclassical picture of the quantum two-mode Bose-Hubbard model normally used to describe BEC atom interferometers. In Sect. 2 We introduce the model Hamiltonian for N bosons in a dimer system. In Sect. 3 we provide the prescription for the WKB quantization of the associated spherical phase space. Several experimentally viable preparations are introduced in Sect. 4, and their local density of states (LDOS) is characterized using a participation number M, with marked differences in the dependence of M on the particle number N, and on the interaction U. Consequently we are able to analyze the observed temporal fluctuations in Sect. 5 and determine their long time average and their characteristic variance. We show that the RMS of the fluctuations scales differently with N, depending on the nature of the prepared state.

2 Model Hamiltonian and Phase-Space Structure

Matter-wave interferometers can be realized using double-well spatial confinement [5–14] or internal spin states [15–19]. In both cases, the bimodal system of interacting atoms is described to good accuracy [36] by the tight-binding Bose-Hubbard Hamiltonian (BHH) [27–29, 37–39]. Here we refer to N particles in a two-site (bi-modal) system, also known as a 'dimer':

$$\mathcal{H} = \sum_{i=1,2}\left[\mathcal{E}_i\hat{n}_i + \frac{U}{2}\hat{n}_i(\hat{n}_i - 1)\right] - \frac{K}{2}(\hat{a}_2^\dagger\hat{a}_1 + \hat{a}_1^\dagger\hat{a}_2), \tag{1}$$

where K is the hopping amplitude, U is the interaction, and $\mathcal{E}_i$ are the on-site energies. One may define an SU(2) algebra, where

$$J_z \equiv \frac{1}{2}(\boldsymbol{n}_1 - \boldsymbol{n}_2) \equiv \boldsymbol{n}, \tag{2}$$

$$J_+ \equiv \hat{a}_1^\dagger\hat{a}_2, \tag{3}$$

and $J_- = [J_+]^\dagger$. Hence $J_x = (J_+ + J_-)/2$ and $J_y = (J_+ - J_-)/2i$. Rewriting the Hamiltonian (1) in terms of these SU (2) generators, we see it is formally the same as that of a spin $j = N/2$ system,

$$\mathcal{H} = -\mathcal{E}\hat{J}_z + U\hat{J}_z^2 - K\hat{J}_x + \text{const}, \tag{4}$$

where $\mathcal{E} = \mathcal{E}_2 - \mathcal{E}_1$ is the bias in the on-site potentials. It is thus clear that the characteristic dimensionless parameters which determine both stationary and dynamic properties, are

$$u \equiv NU/K \tag{5}$$

$$\varepsilon \equiv \mathcal{E}/K \tag{6}$$

The two-site BHH can be regarded as the quantized version of the top Hamiltonian, whose *spherical* phase space is described by the conjugate non-canonical coordinates $(\boldsymbol{\theta}, \boldsymbol{\varphi})$ that are defined through

$$\hat{J}_z = [(j{+}1)j]^{1/2}\cos(\boldsymbol{\theta}), \tag{7}$$

$$\hat{J}_x = [(j{+}1)j]^{1/2}\sin(\boldsymbol{\theta})\cos(\boldsymbol{\varphi}), \tag{8}$$

The Hamiltonian (4) is thus transformed into the top Hamiltonian,

$$\mathcal{H}(\boldsymbol{\theta}, \boldsymbol{\varphi}) = \frac{NK}{2}\left[\frac{1}{2}u(\cos\boldsymbol{\theta})^2 - \varepsilon\cos\boldsymbol{\theta} - \sin\boldsymbol{\theta}\cos\boldsymbol{\varphi}\right]. \tag{9}$$

which is closely related to the Josephson Hamiltonian. The *cylindrical* phase space of the latter is described by the canonical coordinate $\boldsymbol{n}$ of (2), and its conjugate

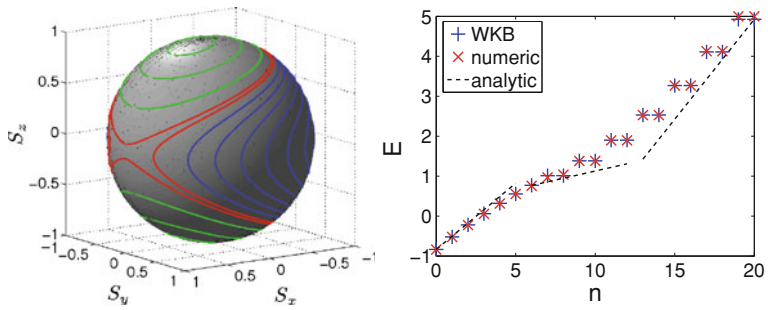

Fig. 1 Contour lines for $u > 2$. Sea levels are colored *blue*, Island levels are colored *green*, and the Separatrix is colored *red* (*left panel*). Energy spectrum for $N = 20$ and $u = 10$. WKB energies (*red x*) are compared with exact eigenvalues (*blue +*). *Dashed lines* indicate slopes ω_J for low energies, ω_x for near-separatrix energies, and ω_+ for high energies (*right panel*)

angle $\boldsymbol{\varphi}$. In the absence of bias, in the vicinity of the Equator, it is just the pendulum Hamiltonian:

$$\mathcal{H}(\boldsymbol{n}, \boldsymbol{\varphi}) \approx U\boldsymbol{n}^2 - \frac{1}{2}KN\cos\boldsymbol{\varphi}\,. \tag{10}$$

In Fig. 1 we draw the constant energy contours $\mathcal{H}(\theta, \varphi) = \text{const}$ of the top Hamiltonian (9) for $u = 10$ and $\varepsilon = 0$. Generally, the qualitative features of the phase-space structure [23, 40], change drastically with the interaction strength. For $u > 1$ a separatrix appears provided $|\varepsilon| < \varepsilon_c$, where

$$\varepsilon_c = \left(u^{2/3} - 1\right)^{3/2}. \tag{11}$$

This separatrix divides the spherical phase space into "sea" and two "islands" as shown in Fig. 1. In what follows, we focus on the case of zero bias. Accordingly we distinguish between three regimes depending on the strength of the interaction [41]:

$$\text{Rabi regime}: \quad u < 1, \tag{12}$$

$$\text{Josephson regime}: 1 < u < N^2, \tag{13}$$

$$\text{Fock regime}: u > N^2. \tag{14}$$

In the Rabi regime the separatrix disappears and the entire phase-space consists of the nearly linear "sea". By contrast, in the Fock regimes the "sea" has area less than $1/N$, and therefore it cannot accommodate quantum states. Thus in the Fock regime phase space is composed entirely of two nonlinear components: the "islands" occupy the entire upper and lower hemispheres. Our main interest below is in the intermediate Josephson regime where linear and non-linear regions coexist and the dynamics is least trivial. This is the regime of interest to most current BEC interferometers and luckily, precisely where semiclassical methods are expected to be most effective.

3 WKB Quantization and Associated Frequencies

Due to the simplicity of the two mode BHH (9), it is possible to carry out its semiclassical quantization analytically [32–34, 42–46] and acquire great insight on the ensuing dynamics of the corresponding Wigner distribution [47, 50]. We begin by accurately determining the quantum energy levels in the Josephson regime, using the WKB prescription. Having a phase-space area of 4π spherical angle supporting $N+1$ quantum states, the Planck cell area is,

$$h = \text{Planck cell area in steradians} = \frac{4\pi}{N+1}, \tag{15}$$

and the WKB quantization condition thus reads,

$$A(E_v) = \left(\frac{1}{2} + v\right)h, \quad v = 0, 1, 2, 3, ..., \tag{16}$$

where $A(E)$ is the phase space area which is enclosed by the energy contour. Note that it does not matter which area, of which "side" of the contour, is selected. Away from the separatrix the levels spacing equals approximately to the classical oscillation frequency:

$$\omega(E) \equiv \frac{dE}{dv} = \left[\frac{1}{h}A'(E)\right]^{-1} \tag{17}$$

In particular in the absence of interaction this is the Rabi frequency

$$\omega_K \approx K \tag{18}$$

For strong interaction, in the bottom of the sea, it is the Josephson frequency

$$\omega_J \approx \sqrt{NUK} = \sqrt{u}\,\omega_K \tag{19}$$

while in the top of the islands it is

$$\omega_+ \approx NU = u\,\omega_K \tag{20}$$

Finally, in the vicinity of the separatrix a more careful analysis is required, leading to the h dependent result

$$\omega_x \approx \left[\log\left(\frac{N^2}{u}\right)\right]^{-1} \omega_J \tag{21}$$

Comparing Eq. (21) to Eqs. (19) and (20) we realize that only in the vicinity of the separatrix does the number of particles N become an essential parameter in the spectral analysis of the dynamics at fixed u.

4 The Preparations

Current experiments in matter-wave interferometry enable the preparation of nearly coherent states of the $SU(2)$ algebra, by fast splitting of the condensate [12]. Alternatively, number-squeezed states, approaching relative-number Fock states for large separation, can be prepared by slow, adiabatic splitting [14]. So far, the main focus of study in the Josephson regime, has been on coherent population dynamics, contrasting coherent preparations located near the bottom of the linear sea which exhibit Josephson oscillations around the ground state [8, 51–54] , with coherent preparations located near the top of the nonlinear islands, which result in self-trapped phase-oscillations around the 'poles' [8, 55]. Our focus here, is on the interesting effects incurred in the *fringe-visibility dynamics* of coherent preparations located *on the separatrix* and contrasting them with the more common ground-state, north-pole, and number-squeezed preparations.

4.1 Wigner Distributions

In order to gain semiclassical insight, it is convenient to represent each eigenstates $|E_v\rangle$ by a proper spin Wigner function [47, 50], which is a quasi-distribution that dwells on the spherical phase space. In this representation these eigenstates corresponds to strips along the contour lines of $\mathcal{H}$. In the same representation Coherent states $|\theta\varphi\rangle$ are like a minimal Gaussian wavepackets, while Fock states $|n\rangle$ are like equi-latitude annulus. Note that the coherent state $\theta = 0$ is also a Fock state with all the particles occupying one site, while $|n = 0\rangle$ is the Twin Fock state with equal number of particles in both sites.

In Fig. 2 we plot the Wigner functions corresponding to the five preparations under study. These include the NorthPole self-trapped state, the TwinFock state, two equal-population coherent states that we call Zero ($\varphi = 0$) and Pi ($\varphi = \pi$,) and a third coherent state preparation that we call Edge. The two latter states (Pi and Edge) are both on-separatrix preparations. Note that in the Zero state all the particles occupy the symmetric orbital, while in the highly excited Pi state all the particles occupy the antisymmetric orbital.

Some of these preparations were experimentally realized and studied [8]. While in the experimental work the emphasis was on contrasting Josephson-Oscillation and Self-Trapping, with regard to near-Zero and near-NorthPole preparations, here our main interest is in contrasting the Zero preparation with the on-separatrix preparations Pi and Edge.

4.2 Local Density of States

In order to analyze the dynamics ensuing from the said preparations, we expand the initial state as a superposition of the eigenstates $|E_v\rangle$. The probability of the vth

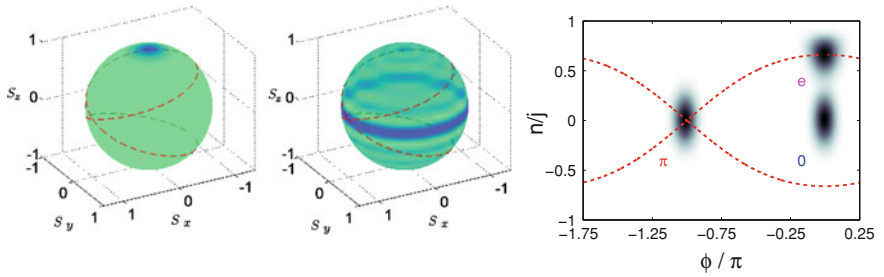

Fig. 2 An illustration of the NorthPole ($\theta = 0$) coherent state preparation (*left*), the TwinFock ($n = 0$) preparation (*middle*), and of Pi ("π"), Zero ("0") and Edge ("e") preparations (*right*) using Wigner plots on a sphere. The *left* and *middle* panels are a 3D plots, while the *right panel* is a Mercator projection of the sphere using $(\boldsymbol{\varphi}, \boldsymbol{n})$ coordinates

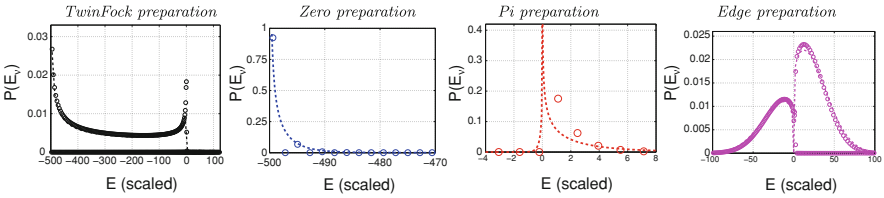

Fig. 3 The LDOS of $N = 500$ bosons with $u = 4$, for TwinFock, Zero, Pi, and Edge preparations (*left* to *right*). The horizontal axes are $E - E_x$ and ω/ω_J. The *lines* in the LDOS figures are based on a semiclassical analysis, while the *circles* are from the exact quantum calculation. Note the outstanding difference between the spectral support of Zero and Pi preparations compared with continuous-like support in the case of Edge and Fock preparations

eigenstate in the superposition is denoted $P(E_v)$, and is known as the local density of states (LDOS) with respect to the pertinent preparation. The LDOS of the various preparations is illustrated in Fig. 3 and the line shape can be determined analytically via a semiclassical calculation [32, 35]. Schematically the results can be summarized as follows:

$$P(E)\Big|_{\text{TwinFock}} \sim \left[1 - \left(\frac{2E}{NK}\right)^2\right]^{-1/2} \tag{22}$$

$$P(E)\Big|_{\text{Zero}} \sim \mathbf{I}\left[\frac{E - E_-}{NU}\right] \tag{23}$$

$$P(E)\Big|_{\text{Pi}} \sim \mathbf{K}\left[\frac{E - E_x}{NU}\right] \tag{24}$$

$$P(E)\Big|_{\text{Edge}} \sim \exp\left[-\frac{1}{N}\left(\frac{E - E_x}{\omega_J}\right)^2\right] \tag{25}$$

where **I** and **K** are Bessel functions. It is important to observe that the classical energy scales are NK and N^2U. Accordingly only the line shape of the TwinFock LDOS has a purely classical interpretation. In contrast to that, the width of the coherent preparations is determined by the quantum uncertainty.

4.3 Participation Number

The qualitative features of the fringe-visibility dynamics, given some initial preparation, are determined by its *participation number* defined as:

$$M \equiv \left[\sum_v P(E_v)^2\right]^{-1} = \text{number of participating levels in the LDOS} \tag{26}$$

In the case of a TwinFock preparation, the Wigner function is spread all over the equator of the spherical phase-space and thus overlaps with all the states in the sea up to the separatrix level (the equator intersects with all sea trajectories in Fig. 2 but with no island trajectory). Therefore we expect M to be of order N, with classical (N independent) prefactor that reflects the relative size of the sea:

$$M = \text{ClassicalPrefactor} \times N, \quad [\text{TwinFock preparation}] \tag{27}$$

In the case of a coherent preparation, the Wigner function is a minimal wavepacket that has width $\sigma_n = (N/2)^{1/2}$. If the Fock states $|n\rangle$ were the eigenstates of the Hamiltonian, as they are in the Fock regime, we would get

$$M = (2\pi N)^{1/2}, \quad [\text{Coherent preparation, } n \text{ basis}], \tag{28}$$

for all three coherent preparations. However in the Josephson regime the eigenstates are $|E_v\rangle$, and therefore the differences between the LDOS of the three coherent states Zero, Pi, and Edge, are set by the ratio between σ_n and the width of the separatrix ($\Delta n = NK/U$). The ratio $\sigma_n/\Delta n$ equals the dimensionless semiclassical parameter $(u/N)^{1/2}$. If this ratio is larger than unity the distinction between the Zero, the Pi and the Edge preparations is blurred, and we expect to have the same participation number. Indeed plotting the participation number of these three initial states (Fig. 4), we see that at the strong interaction limit $M \approx (3/2)N^{1/2}$. This is roughly half compared with Eq. (28), and reflects the odd-even selection rule that removes half of the overlaps (the semiclassical states do not have a well-defined parity with respect to site substitution, whereas the actual quantum eigenstates are constructed from their odd and even superpositions. The participating constituents are those that have the same parity as that of the preparation).

For weaker interaction, when the semiclassical parameter $(u/N)^{1/2}$ is smaller than unity the different nature of the Zero, the Pi and the Edge preparations expresses itself. Now we have to account for both the width of LDOS line shape and the mean level spacing. This leads to the following results:

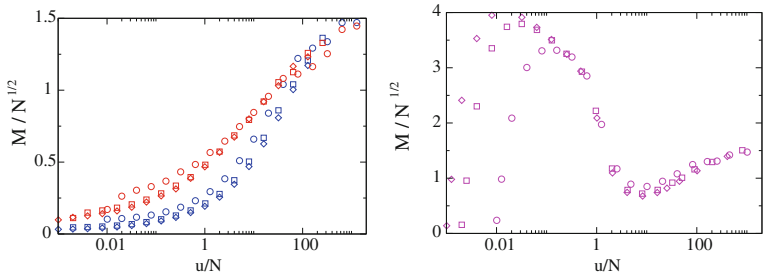

Fig. 4 The participation number M as determined from the LDOS for $N = 100$(*Circle*), 500(*Square*), and 1000(*Diamond*) particles. The *left panel* contains the Zero (*lower set* in *blue*) and Pi (*upper set* in *red*) preparations, while the Edge preparation is presented in the *right panel*. Note the different vertical scale. In the crudest approximation we expect in the Edge case $M \sim N^{1/2}$, while in the Pi case $M \ll N^{1/2}$ as long as $(u/N) \ll 1$

$$M \approx \sqrt{u}, \quad \text{[Zero preparation]} \tag{29}$$

$$M \approx \left[\log\left(\frac{N}{u}\right)\right]\sqrt{u}, \quad \text{[Pi preparation]} \tag{30}$$

$$M \approx \left[\log\left(\frac{N}{u}\right)\right]\sqrt{N}, \quad \text{[Edge preparation]} \tag{31}$$

The striking point here is that the Pi preparation resembles the Zero preparation, rather than its sister separatrix Edge state. This seems at first sight in contradiction with semiclassical intuition: one would naively expect that wavepackets that have the same energy and reside in the same phase space region (separatrix) would behave similarly. This is not the case, as we see here, and later in the dynamical analysis. The Pi state is actually closer to the Zero preparation, as both have a small participation value. The resemblance of the Pi and Edge preparations is only detectable in the formal limit $N \to \infty$. In other words, because of the N dependence of M it is "easier" to approach the "classical limit" in the case of an Edge preparation.

5 Coherence Dynamics

5.1 Classical, Semiclassical, and Quantum Dynamics of the Bloch Vector

In this section, we describe the dynamics of single-particle coherence for the preparations of Sect. 4. The lowest-order approximation is the *mean field* dynamics. It is generated by replacing the operators in the Hamiltonians of

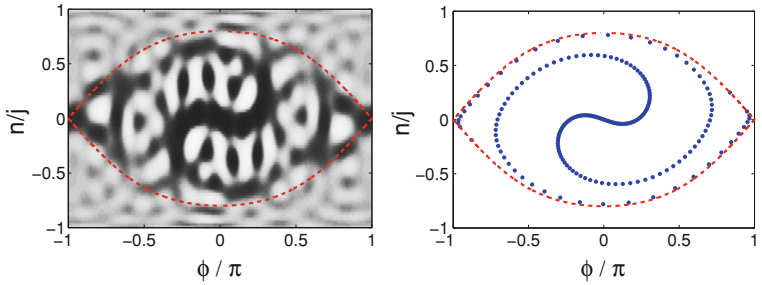

Fig. 5 The evolving quantum state of $N = 40$ bosons with $u = 5$ for TwinFock ($n = 0$) preparation. The units are such that $K = 1$ and the time is $t = 4$. On the *left*—the Wigner function of the evolved quantum state. On the *right*— the corresponding classical evolution

Eqs. (1), (4), or (9) by c-numbers, thus obtaining a set of classical equations of motion for them. For example, in the spin representation,

$$\begin{aligned} \dot{J}_x &= (\mathcal{E} - 2UJ_z)J_y, \\ \dot{J}_y &= KJz - (\mathcal{E} - 2UJ_z)J_x, \\ \dot{J}_z &= -KJ_y. \end{aligned} \tag{32}$$

These Gross-Pitaevskii equations (GPE) describe the *classical* evolution of a *point* in phase space, which is a single trajectory. The classical evolution assumes that the state of the system is coherent at all times, so that the single-particle coherence is fixed to unity and the Wigner distribution always resembles a minimal Gaussian (the center of which is the traced point). By contrast, the *semi-classical* theory describes the classical evolution and subsequent deformation of a *distribution* in phase space, according to the GPE equations (34). Finally the *Quantum theory* is obtained by direct solution of the Schrödinger or Heisenberg equations with the Hamiltonians (1), (4), or (9). This full quantum solution adds recurrences and fluctuations which are absent from the classical and semiclassical pictures and result from the discreteness of the energy spectrum. The dimer system is integrable, and therefore the WKB method provides a very good basis for the analysis. Fig. 5 illustrates the agreement between the quantum evolution of the Wigner function, starting from the TwinFock state [33, 35] and the semiclassical evolution of a corresponding distribution. It should be emphasized that in the Wigner-Wyle formalism any operator $\hat{A}$ is presented by the phase-space function $A_W(\Omega)$, and the calculation of an expectation value can be done in a classical-like formulation:

$$\langle \hat{A} \rangle = \mathrm{trace}[\hat{\rho}\hat{A}] = \int \frac{d\Omega}{h} \rho_W(\Omega) A_W(\Omega)\,. \tag{33}$$

The single-particle density matrix of the two-mode system can be presented using the Bloch vector,

$$\vec{\boldsymbol{S}} = \langle \vec{\boldsymbol{J}} \rangle / (N/2) = (S_x, S_y, S_z), \tag{34}$$

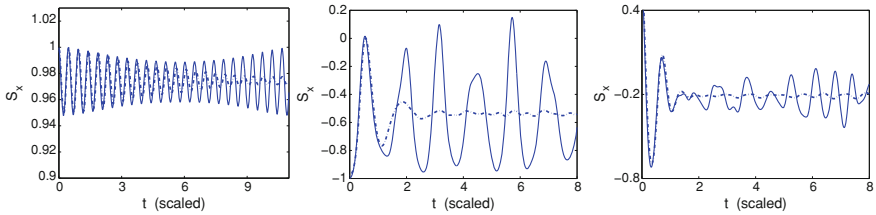

Fig. 6 The variation of $S_x(t)$ with time for $N = 40$ particles with $u = 5$, for Zero (*left*), Pi (*middle*), and Edge (*right*) preparations. Note the different vertical scale. The *dashed-dotted* lines are based on semiclassical simulation

Whereas previous work [8] has focused on the mean-field dynamics of the occupation difference $(N/2)\langle S_z\rangle$, here we study the *single-particle coherence* manifested in the one body purity,

$$\text{OneBodyPurity} = (1/2)\left[1 + \langle S_x\rangle^2 + \langle S_y\rangle^2 + \langle S_z\rangle^2\right], \tag{35}$$

and the transverse component of the Bloch vector, the fringe visibility,

$$g_{12}^{(1)} = \left[\langle S_x\rangle^2 + \langle S_y\rangle^2\right]^{1/2}. \tag{36}$$

This quantity reflects the fringe-contrast over multiple runs of an experiment in which the particles from the two confined modes are released and allowed to interfere. In Fig. 6 we plot examples for the evolution of the Bloch vector, and observe significant differences in the dynamical behavior of the Zero, Pi, and Edge preparations. Our objective is to understand how the dynamics depends on the dimensional parameters: the "classical" parameter u and the "quantum" parameter N.

In accordance with the opening paragraph of this section, we see in Fig. 6 that in the semiclassical simulation the fluctuations always die after a transient. This should be contrasted with both the *classical* (single trajectory) behavior, and the *quantum* behavior. In the latter quantum case the wavepacket is a superposition of $M > 1$ eigenstates, and consequently there are persistent fluctuations that depend on the "quantum" parameter N. In what follows, we will quantitatively analyze the characteristic features of the quantum dynamics resulting from the three coherent preparations, including the frequency of oscillation, its mean long-time value, and its RMS amplitude, and compare the analytic predictions to the numerical results at various values of the characteristic parameter u/N.

5.2 Characteristic Frequencies

The typical frequency of the fluctuations is the simplest characteristic that differentiate the three panels of Fig. 6. The numerically-obtained frequency ω_{osc} as a function of the interaction parameter u/N is displayed in Fig. 7. In the

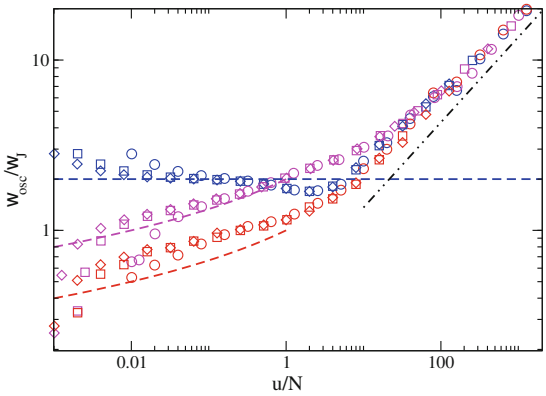

Fig. 7 The mean frequency of the $S_x(t)$ oscillations versus u/N for , and 1000(*diamond*) particles. The preparations are (*upper* to *lower* sets of data points): Zero (*blue*), Edge (*magenta*), and Pi (*red*). The weaker-interaction theoretical predictions (37–39), which are doubled due to mirror symmetry, are represented by *blue*, *red*, and *magentadashed lines*, while the strong interaction prediction (40) is represented by a *black dash-double-dotted line*

classical picture $\omega_{\rm osc}$ should be related to the Josephson frequency ω_J at the bottom of the sea, while quantum mechanically it reflects the level spacings of the participating levels. A straightforward analysis leads to the followings estimates:

$$\omega_{\rm osc} \approx 2\omega_J \quad [\text{Zero}] \tag{37}$$

$$\omega_{\rm osc} \approx 1\times\left[\log\left(\frac{N}{u}\right)\right]^{-1} 2\omega_J \quad [\text{Pi}] \tag{38}$$

$$\omega_{\rm osc} \approx 2\times\left[\log\left(\frac{N}{u}\right)\right]^{-1} 2\omega_J \quad [\text{Edge}] \tag{39}$$

$$\omega_{\rm osc} \approx \left(\frac{u}{N}\right)^{1/2} 2\omega_J \quad [u \gg N] \tag{40}$$

The first three expressions apply for $(u/N)<1$, where the differences between the preparations is distinct. The last expression refers to the regime $(u/N) > 1$ where the differences are blurred and the three preparations become equivalent equatorial states (as clearly evident from Fig. 7). Note that due to the mirror symmetry of the Zero preparation the expected frequency should approach $2\omega_J$, while for the Pi preparation it is bound from below by $2\omega_x$. Both frequencies are indicated in Fig. 7 by dashed lines.

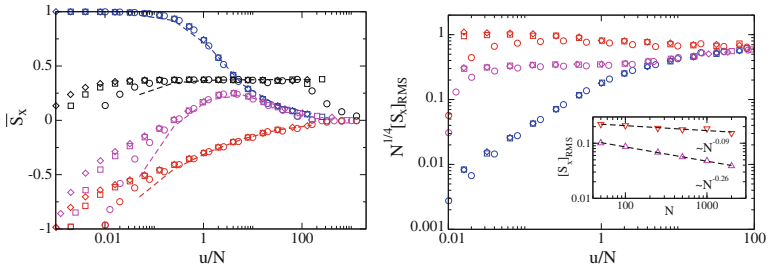

Fig. 8 *Left:* The long-time average of $S_x(t)$ versus u/N for , and 1000(*diamond*) particles. The preparations are (*upper* to *lower* sets of data points): Zero (*blue*), TwinFock (*black*), Edge (*magenta*), and Pi (*red*). The symbols are used for the quantum results and the *dashed lines* are the semiclassical prediction for 40 particles. Note that the scaling holds only in the Josephson regime $1 \ll u \ll N^2$, and therefore, for a given u/N range, becomes better for large N. *Right:* The long time RMS of $S_x(t)$ for the three coherent preparations (*lower* to *upper* sets): Zero (*blue*), Edge (*magenta*), and Pi (*red*). In the *inset*, the RMS of $S_x(t)$ for Edge (*triangle*) and Pi (*down-pointing triangle*) preparations is plotted versus N while $u = 4$ is fixed

5.3 Long Time Average

Next we examine the long time average, plotted in Fig. 8 as a function of the characteristic parameter. Unlike the fluctuations around it, this average value does not reflect the quantization of energy and therefore a purely semi-classical analysis is adequate. The naive expectation might be that coherence would be diminished due to phase spreading (aka "phase diffusion"). This is indeed the case in the Fock regime, leading to $\langle S_x \rangle_\infty \approx 0$. However, the situation is rather more complicated in the Josephson regime, where $\langle S_x \rangle_\infty$ is determined by u/N. The semi-classical phase space picture allows to calculate the phase distribution $P(\varphi)$ that pertains to the long time ergodic-like distribution (see for example Fig. 5). This distribution is determined by the LDOS. Then we use the integral

$$\overline{S_x} \approx \int \cos(\varphi) \mathrm{P}(\varphi) d\varphi, \tag{41}$$

to evaluate the residual coherence. This procedure results in the following predictions:

$$\overline{S_x} \approx 1/3 \quad [\text{TwinFock}] \tag{42}$$

$$\overline{S_x} \approx \exp[-(u/N)] \quad [\text{Zero}] \tag{43}$$

$$\overline{S_x} \approx -1 - 4/\log\left[\frac{1}{32}(u/N)\right] \quad [\text{Pi}] \tag{44}$$

Thus, the coherence of the Zero preparation is robustly maintained as long as $u/N < 1$, corresponding to the $\varphi = 0$ phase locking of the two condensates due to

the weak coupling. By contrast, the Pi and Edge coherence is far more fragile throughout the Josephson regime [32]. Note that the phase locking of the Pi state take place only in the Rabi-regime (no separatrix). As evident from the Twin-Fock self-induced coherence (46), one-particle coherence should not necessarily be lost due to interactions, but could actually be *built* [33]. This course of events is somewhat similar to the coherent relaxation of a system to its ground state at low temperatures: the ground state has higher purity compared with the initial preparation.

5.4 RMS of the Fluctuations

Finally, we turn to discuss the RMS of the fluctuations, which constitute a fingerprint of energy quantization. General reasoning implies that the *classical* fluctuations are suppressed by factor M:

$$\mathrm{RMS}\left[\langle A\rangle_t\right] = \left[\frac{1}{M}\int \tilde{C}_{\mathrm{cl}}(\omega)d\omega\right]^{1/2}. \tag{45}$$

In this formula $\tilde{C}cl(\omega)$ is the *classical* power spectrum of an ergodic trajectory. What we want to highlight is the *quantum* N dependence. It is important to clarify that in the *semi-classical* limit $M \to \infty$, and therefore the fluctuations are suppressed. We emphasize again that the quantum behavior is intermediate between the coherence-preserving *classical* (single trajectory) dynamics and the strong coherence-attenuation of the *semi-classical* (infinite M) dynamics.

The dependence of M on N is remarkably different for the various preparations. In the case of the TwinFock preparation $M \sim N$ and therefore the RMS is inversely proportional to $N^{1/2}$. This should be contrasted with the case of the Pi and the Edge preparations:

$$\mathrm{RMS}[S_x(t)] \sim N^{-1/2} \quad [\mathrm{TwinFock}] \tag{46}$$

$$\mathrm{RMS}[S_x(t)] \sim N^{-1/4} \quad [\mathrm{Edge}] \tag{47}$$

$$\mathrm{RMS}[S_x(t)] \sim (\log(N))^{-1/2} \quad [\mathrm{Pi}] \tag{48}$$

We further note that in the Pi case the leading dependence of the participation number is on the classical parameter ($M \sim u^{1/2}$), unlike the case of the Edge preparation where the leading dependence in on the quantum parameter ($M \sim N^{1/2}$). The results of the RMS analysis are presented in Fig. 8. The implied $N^{1/4}$ scaling based on Eq. (45) is confirmed. The dashed lines in the inset are power-law fits that nicely agree with the predictions of Eq. (46).

6 Summary

Using semiclassical machinery, we have analyzed the temporal fluctuation of the single-particle coherence, and of the fringe-visibility, in the Bose Josephson model. While recent experiments in the Josephson regime have essentially focused on mean-field population dynamics [8], with coherent preparations at the spectral extremes (self trapping versus Josephson oscillations), here we highlight intricate effects that can be found by studying the coherence-dynamics in the intermediate separatrix regime. We predict significant differences in the transverse relaxation of seemingly similar coherent initial states, differing by the initial relative-phase or by their location along the separatrix, as well as the interaction-induced phase-locking of two initially separated BECs due to the combined effect of interaction and coupling. The semiclassical WKB quantization facilitates the calculation of the LDOS for the pertinent preparations, and thus the estimation of the number of participating eigenstates. This allows for a detailed quantitative analysis of the time evolution of the fringe visibility function. The obtained analytic expressions are found to be in a very good agreement with the results of numerical calculations.

Acknowledgments The current manuscript summarizes the approach taken in a series of recent publications [32–35]. We acknowledge contributions to these works by Maya Chuchem, Erez Boukobza, Katrina Smith-Mannschott, Moritz Hiller, and Tsampikos Kottos. This research was supported by the Israel Science Foundation (grant nos. 29/11 and 346/11) and by Grant No. 2008141 from the United States-Israel Binational Science Foundation (BSF).

References

1. N. F. Ramsey, Phys. Rev. **78**, 695 (1950)
2. C. Bordé, Phys. Lett. A **140**, 10 (1989)
3. P.R. Berman, *Atom Interferometry* (Academic Press, San Diego, 1997)
4. D. Cronin, J. Schmiedmayer, D.E . Pritchard, Rev. Mod. Phys. **81**, 1051 (2009)
5. M.R. Andrews, C.G. Townsend, H.-J. Miesner, D.S. Durfee, D.M. Kurn, W. Ketterle, Science **275**, 637 (1997)
6. Y. Shin, M. Saba, T.A. Pasquini, W. Ketterle, D.E. Pritchard, A.E. Leanhardt, Phys. Rev. Lett. **92**, 050405 (2004)
7. Y.-J. Wang, D.J. Anderson, V.M. Bright, E.A. Cornell, Q. Diot, T. Kishimoto, M. Prentiss, R.A. Saravanan, S.R. Segal, S. Wu, Phys. Rev. Lett. **94**, 090405 (2005)
8. M. Albiez, R. Gati, J. Folling, S. Hunsmann, M. Cristiani, M.K. Oberthaler, Phys. Rev. Lett. **95**, 010402 (2005)
9. G.-B. Jo, Y. Shin, S. Will, T.A. Pasquini, M. Saba, W. Ketterle, D.E. Pritchard, M. Vengalattore, M. Prentiss, Phys. Rev. Lett. **98**, 030407 (2007)
10. G.-B. Jo, J.-H. Choi, C.A. Christensen, T.A. Pasquini, Y.-R. Lee, W. Ketterle, D.E. Pritchard, Phys. Rev. Lett. **98**, 180401 (2007)
11. G.-B. Jo, J.-H. Choi, C.A. Christensen, Y.-R. Lee, T.A. Pasquini, W. Ketterle, D.E. Pritchard, Phys. Rev. Lett. **99**, 240406 (2007)
12. T. Schumm, S. Hofferberth, L.M. Andersson, S. Wildermuth, S. Groth, I. Bar-Joseph, J. Schmiedmayer, P. Krüger, Nat. Phys. **1**, 57 (2005)

13. S. Hofferberth, I. Lesanovsky, B. Fischer, T. Schumm, J. Schmiedmayer, Nature (London) **449**, 324 (2007)
14. J. Esteve, C. Gross, A. Weller, S. Giovanazzi, M.K. Oberthaler, Nature **455**, 1216 (2008)
15. P. Böhi, M.F. Riedel, J. Hoffrogge, J. Reichel, T.W. Hänsch, P. Treutlein, Nat. Phys. **5**, 592 (2009)
16. C. Gross, T. Zibold, E. Nicklas, J. Esteve, M.K. Oberthaler, Nature **464**, 1165 (2010)
17. M.F. Riedel, P. Böhi, Y. Li, T.W. Hänsch, A. Sinatra, P. Treutlein, Nature **464**, 1170 (2010)
18. Z. Chen, J.G. Bohnet, S.R. Sankar, J. Dai, J.K. Thompson, Phys. Rev. Lett. **106**, 133601 (2011)
19. B. Lüke, M. Scherer, J. Kruse, L. Pezze, F. Deuretzbacher, P. Hyllus, O. Topic, J. Peise, W. Ertmer, J. Arlt, L. Santos, A. Smerzi, C. Klempt, Science **334**, 773 (2011)
20. R. Bücker et al., Nat. Phys. **7**, 608 (2011)
21. J. Javanainen, M. Wilkens, Phys. Rev. Lett. **78**, 4675 (1997)
22. J. Javanainen, M. Wilkens, Phys. Rev. Lett. Phys. Rev. Lett. **81**, 1345 (1998)
23. A. Vardi , J.R. Anglin, Phys. Rev. Lett. **86**, 568 (2001)
24. J.R. Anglin, A. Vardi, Phys. Rev. A **64**, 013605 (2001)
25. M. Greiner, O. Mandel, T.W. Hänsch, I. Bloch, Nature **419**, 51 (2002)
26. A. Widera, S. Trotzky, P. Cheinet, S. Fölling, F. Gerbier, I. Bloch, V. Gritsev, M.D. Lukin, E. Demler, Phys. Rev. Lett. **100**, 140401 (2008)
27. J. Grond, U. Hohenester, I. Mazets, J. Schmiedmayer, New J. Phys. **12**, 065036 (2010)
28. I. Tikhonenkov, M.G. Moore, A. Vardi, Phys. Rev. A **82**, 043624 (2010)
29. J. Grond, U. Hohenester, J. Schmiedmayer, A. Smerzi, Phys. Rev. A **84**, 023619 (2011)
30. E.M. Wright, D.F. Walls, J.C. Garrison, Phys. Rev. Lett. **77**, 2158 (1996)
31. S. Will, T. Best, U. Schneider, L. Hackermüller, D.S. Lühmann, I. Bloch, Nature **465**, 197 (2010)
32. E. Boukobza, M. Chuchem, D. Cohen, A. Vardi, Phys. Rev. Lett. **102**, 180403 (2009)
33. E. Boukobza, D. Cohen, A. Vardi, Phys. Rev. A **80**, 053619 (2009)
34. K. Smith-Mannschott, M. Chuchem, M. Hiller, T. Kottos, D. Cohen, Phys. Rev. Lett. **102**, 230401 (2009)
35. M. Chuchem, K. Smith-Mannschott, M. Hiller, T. Kottos, A.Vardi, D. Cohen, Phys. Rev. A **82**, 053617. Optionally arXiv:1001.2120, which includes extra appendices
36. Y. Li, P. Treutlein, J. Reichel, A. Sinatra, Eur. Phys. J. B **68**, 365 (2009)
37. M. Kitagawa, M. Ueda, Phys. Rev. A **47**, 5138 (1993)
38. M.J. Holland, K. Burnett, Phys. Rev. Lett. **71**, 1355 (1993)
39. L. Pezze, A. Smerzi, Phys. Rev. Lett. **102**, 100401 (2009)
40. K.W. Mahmud, H. Perry, W.P. Reinhardt, Phys. Rev. (A) **71**, 023615 (2005)
41. R. Gati, M.K. Oberthaler, J. Phys. B **40**, R(61) (2007)
42. Franzosi et al., Int. J. Mod. Phys. B (14), 943 (2000)
43. E.M. Graefe, H.J. Korsch, Phys. Rev. A **76**, 032116 (2007)
44. D. Witthaut, E.M. Graefe, H.J. Korsch, Phys. Rev. A **73**, 063609 (2006)
45. E.M. Graefe, H.J. Korsch, A. E. Niederle, Phys. Rev. A **82**, 063628 (2010)
46. F. Nissen, J. Keeling, Phys. Rev. A **81**, 063628 (2010)
47. J.C. Varilly, J.M. Gracia-Bondia, Ann. Phys. **190**, 107 (1989)
48. C. Brif, A. Mann, J. Phys. A **31**, L(9) (1998)
49. G.S. Agarwal, Phys. Rev. A. **24**, 2889 (1981)
50. J.P. Dowling, G.S. Agarwal, W.P. Schleich, Phys. Rev. A **49**, 4101 (1994)
51. S. Giovanazzi, A. Smerzi, S. Fantoni, Phys. Rev. Lett. **84**, 4521 (2000)
52. F.S. Cataliotti, S. Burger, C. Fort, P. Maddaloni, F. Minardi, A. Trombettoni, A. Smerzi, M. Inguscio, Science **293**, 843 (2001)
53. S. Levy, E. Lahoud, I. Shomroni, J. Steinhauer, Nature **449**, 579 (2007)
54. C. A Sackett, Nature **449**, 546 (2007)
55. A. Smerzi, S. Fantoni, S. Giovanazzi, R.S. Shenoy, Phys. Rev. Lett. **79**, 4950 (1997)

Temperature Effects on the Quantum Coherence of Bosonic Josephson Junctions

B. Juliá-Díaz, J. Martorell and A. Polls

Abstract We analyze the effects of temperature on the properties of a system of ultracold atoms confined by a double-well potential. We consider the case of repulsive interactions and review the different approximations to the exact many-body results.

1 Introduction

Our experimental control on trapped ultracold atomic systems is constantly improving, allowing an impressive degree of control on both the microscopic, e.g. atom–atom scattering length, and macroscopic, e.g. external traps [1, 2], parameters. A conceptually simple but rich configuration which has been already engineered is that of condensing a bosonic atomic cloud on a double-well external potential [3–5]. This has allowed to explore the effect of atom–atom interactions on the tunneling dynamics of the atomic cloud, as predicted by [6, 7]. The

Useful discussions with M. K. Oberthaler are gratefully acknowledged. This work has been supported by FIS2008-01661, and 2009-SGR1289. B. Juliá-Díaz is supported by the Ramón y Cajal program.

B. Juliá-Díaz (✉)
ICFO-Institut de Ciències Fotòniques, Parc Mediterrani de la Tecnologia,
08860 Barcelona, Spain
e-mail: bruno.julia@icfo.es

J. Martorell · A. Polls
Departament d'Estructura i Constituents de la Matèria, Facultat de Física,
U. Barcelona, 08028 Barcelona, Spain

Progress Optical Sci., Photonics (2013): 473–484
DOI: 10.1007/10091_2012_17

Published Online: 6 October 2012

properties of this coherent tunneling dynamics can be predicted by means of semiclassical approximations to the two-site Bose-Hubbard (BH) model. Several bosonic aggregates have been found to be well described by the BH Hamiltonian, in particular condensates confined by external double-well potentials [8] or condensates with two internal degrees of freedom confined by harmonic traps [9].

During the last years the interest has shifted towards preparing experimental set-ups exhibiting quantum properties beyond the semiclassical ones: cat-like states, and squeezed states [8]. In simple terms, a cat-like state corresponds to a many-body quantum state where the system is described by a macroscopic superposition of two states each of them mostly localized on one well. The most extreme case is the so-called NOON state, in which the state of the system is an equal weight superposition of two many-body states, each of which consisting on all particles populating a single well. Cat-like states appear in systems with finite number of atoms N as quasidegenerate ground states in the case of attractive atom–atom interactions [10]. The energy difference between the ground state and the first excited state decreases as $1/N!$, thus producing an almost exact two-fold degenerate ground state manifold as N is increased.

Recently it has also been noted that the existence of strongly correlated cat-like many-body ground states in the systems at finite N is directly linked to the presence of a degenerate ground state in the semiclassical/large N description of the system. In the $N \to \infty$ limit the system exhibits a quantum phase transition, which can be identified by the dependence of the imbalance of population between both wells, which shows a characteristic bifurcation, as a function of the interaction between the atoms [11]. In this limit, by increasing the atom–atom interaction strength, the system exhibits a spontaneous symmetry breaking in which the ground state of the system evolves from having an equal population on both sites to being mostly localized on one of the two sites of the double well.

In this chapter we review the thermal effects, both in the exact BH and by means of approximate expressions, on the quantum coherence of the system for the case of repulsive interactions. Exact numerical solution of the BH are compared to previously derived approximate expressions [12, 13] and to expressions derived within the large-N model of Refs. [14, 15]. First, we describe the theoretical framework in Sect. 2. Then, in Sect. 3 we discuss thermal effects first in the exactly-solvable non-interacting case, and finally in the interacting case, comparing semiclassical results with the $1/N$ model described in Sect. 2 and with the exact BH results. Finally, in Sect. 4 a summary and conclusions are provided.

2 Two Site Bose-Hubbard Hamiltonian

We will consider a many-body system of bosons described by a two-site Bose-Hubbard Hamiltonian, $\hat{H}$, of the form,

$$\hat{H} = -J(\hat{a}_1^\dagger \hat{a}_2 + \hat{a}_2^\dagger \hat{a}_1) + \frac{U}{2}(\hat{n}_1(\hat{n}_1 - 1) + \hat{n}_2(\hat{n}_2 - 1)), \tag{1}$$

where J is the hopping strength, taken positive, and U is the atom–atom interaction strength. $U > 0$ ($U < 0$) corresponds to repulsive (attractive) atom–atom interaction. $\hat{a}_i^\dagger$ creates a particle in site i, the number operator of particles on site i is defined as $\hat{n}_i = \hat{a}_i^\dagger \hat{a}_i$. It is customary to define three operators [16, 17],

$$\begin{aligned} \hat{J}_x &= \frac{1}{2}(\hat{a}_1^\dagger \hat{a}_2 + \hat{a}_2^\dagger \hat{a}_1) \\ \hat{J}_y &= \frac{1}{2i}(\hat{a}_1^\dagger \hat{a}_2 - \hat{a}_2^\dagger \hat{a}_1) \\ \hat{J}_z &= \frac{1}{2}(\hat{a}_1^\dagger \hat{a}_1 - \hat{a}_2^\dagger \hat{a}_2), \end{aligned} \tag{2}$$

which satisfy angular momentum commutation relations, provided $[\hat{a}_i, \hat{a}_j^\dagger] = \delta_{i,j}$. Using these operators the Hamiltonian reads,

$$\hat{H} = -2J\hat{J}_x + U\hat{J}_z^2 + U\left(\frac{N^2}{4} - \frac{N}{2}\right). \tag{3}$$

The corresponding time dependent Schrödinger equation is written as,

$$i\partial_t|\Psi\rangle = \hat{H}|\Psi\rangle. \tag{4}$$

An appropriate many-body basis for this bosonic system is the Fock basis [16], $\{|N_1, N_2\rangle\}$, with $N_1 + N_2 = N$, being N_i the number of atoms in site i. The total number of atoms, N, is taken to be constant. A general many-body state, $|\Psi\rangle$, can be written in this basis as,

$$|\Psi\rangle = \sum_{k=0}^{N} c_k |k, N-k\rangle. \tag{5}$$

The phase coherence of a many-body quantum state is defined as,

$$\alpha = \langle\hat{\alpha}\rangle, \qquad \text{where } \hat{\alpha} = \frac{1}{N}(\hat{a}_1^\dagger \hat{a}_2 + \hat{a}_2^\dagger \hat{a}_1) = 2\frac{\hat{J}_x}{N}, \tag{6}$$

and can be experimentally measured [4]. The phase coherence takes values from -1 to 1. The two extreme values correspond to the two coherent states $\Psi^{(+)} \equiv \Psi_{\pi/2,0} = \left[\frac{1}{\sqrt{2}}(|1\rangle + |2\rangle)\right]^{\otimes N}$ and $\Psi^{(-)} \equiv \Psi_{\pi/2,\pi} = \left[\frac{1}{\sqrt{2}}(|1\rangle - |2\rangle)\right]^{\otimes N}$, where $|1\rangle \equiv \hat{a}_1^\dagger|\text{vac}\rangle$ and $|2\rangle \equiv \hat{a}_2^\dagger|\text{vac}\rangle$. A coherent state is defined as a state in which all atoms populate the same single particle state.

In real experiments the temperature of the cloud is not absolute zero. In this case, the quantum mechanical description of the system is given by a mixed state where the different energy levels are populated according to a thermal distribution. In the canonical ensemble the thermal average of an operator $\hat{A}$, is

$$\langle \hat{A} \rangle_T = \mathcal{Z}^{-1} \operatorname{Tr} e^{-\beta \hat{H}} \hat{A}, \tag{7}$$

where the partition function, $\mathcal{Z}$, is

$$\mathcal{Z} = \operatorname{Tr} e^{-\beta \hat{H}} \tag{8}$$

and $\beta = 1/(k_B T)$.

2.1 1/N Expansion of the Bose-Hubbard Model

In Refs. [14, 15], $1/N$ approximations to the Bose-Hubbard Hamiltonian have been presented. They rely on using a systematic expansion on $h \equiv 1/N$ of the relevant expectation values. For states in the neighborhood of the ground state the variation with k of the c_k coefficients is smooth. That is, $c_k \sim c_{k\pm1}$. For the topmost excited states the opposite is true: the signs of the c_k alternate with k and $c_k \sim (-)^k c_{k\pm1}$. As explained in Refs. [14, 15] two different semiclassical Hamiltonians emerge depending on the regime considered. The two extreme cases correspond, in the non-interacting case, to states close to the coherent states $\Psi^{(+)}$ and $\Psi^{(-)}$ defined in the previous section.

The equations that govern the dynamics of states close to these two extremes are,

$$ih\partial_t \psi(z) = \left(\mp 2h^2 \partial_z \sqrt{1-z^2}\partial_z + \mathcal{V}_\pm(z) \right) \psi(z) \equiv \mathcal{H}_N \psi(z) \tag{9}$$

with either $\psi(x = k/N) = \sqrt{N} c_k$ or $\psi(x = k/N) = \sqrt{N}(-)^k c_k$, and

$$\mathcal{V}_\pm(z) = (1/2)\gamma z^2 \mp \sqrt{1-z^2}\left(1 + \frac{h}{1-z^2}\right), \tag{10}$$

where x is a continuous variable which interpolates k/N, and $z = 2x - 1$ is the population imbalance. $h = 1/N$ is the expansion parameter, $\gamma \equiv NU/(2J)$, and t is the time measured in units of J. See Fig. 1 for two representative examples of $\mathcal{V}_\pm(z)$. The wave function $\psi(z)$ is re-normalized as,

$$\int_{-1}^{1} |\psi(z)|^2 \, \mathrm{d}z = 1. \tag{11}$$

The expression for $\mathcal{V}_\pm$ contains only terms up to first power in the small parameter h, as explicitly given in Eq. (9) of Ref. [15]. The linear term in h will play a significant role when studying the coherence of the system, which for a broad range of γ values is fairly close to 1.

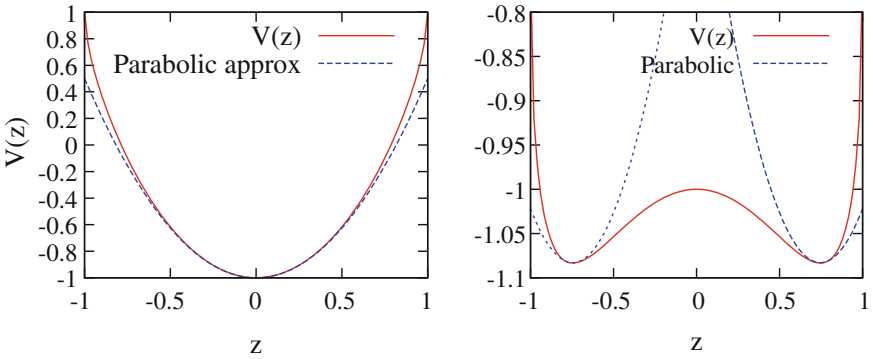

Fig. 1 (*left*) Potential $\mathcal{V}_+(z)$ for $\gamma = 1.5$ (*solid*). (*right*) Potential $-\mathcal{V}_-(z)$ for $\gamma = -1.5$ (*solid*). The *dashed lines* correspond to the parabolic approximation to the potential described in the text (Color figure online)

Equation (9) can be regarded as a Schrödinger-like equation defined on the closed interval, $z \in [-1, 1]$. The equation provides an important insight into the quantum behavior of the system, essentially builds on the usual semiclassical Hamiltonian, which is equal to $\mathcal{V}(z)$, and quantizes it, through the kinetic term, $-2h^2\partial_z\sqrt{1-z^2}\partial_z$. An important feature of this approximation is that it maps the many-body problem onto that of a single fictitious particle whose dynamics is governed by this Schrödinger-like equation.

In this approximation the coherence of a state can be computed as [18],

$$\langle\hat{\alpha}\rangle = -E^s + \frac{1}{2}\gamma \int_{-1}^{1} dz\, z^2\, |\psi(z)|^2 \tag{12}$$

which relates the energy of the system E^s, its coherence α, and the dispersion of the population imbalance.

The semiclassical $1/N$ models corresponding to $\mathcal{V}_+$ and $\mathcal{V}_-$, provide very accurate descriptions of the lowest part and of the highest part of the spectrum, respectively. See for instance Fig. 2, where two important features of the ground state: its coherence and the dispersion of the population imbalance obtained with the $1/N$ model are compared to the exact values.

As can be seen in Fig. 1, the potential $\mathcal{V}_+$ which enters when considering the lower part of the spectrum is almost a parabolic-like potential. Thus, the low part of the spectrum is expected to be harmonic-oscillator-like. In contrast, $\mathcal{V}_-$ exhibits a clear double-well structure, predicting the existence of quasidegenerate states in the higher part of the spectrum. These two effective potentials capture properly both limiting cases and agree well with the known spectral properties of the BH Hamiltonian, see for instance [11, 17, 19]. It is linear for the lower excitations and quasi-double degenerate for the higher part of the spectrum. It should be noted however, that each of the semiclassical models predicts correctly only a different

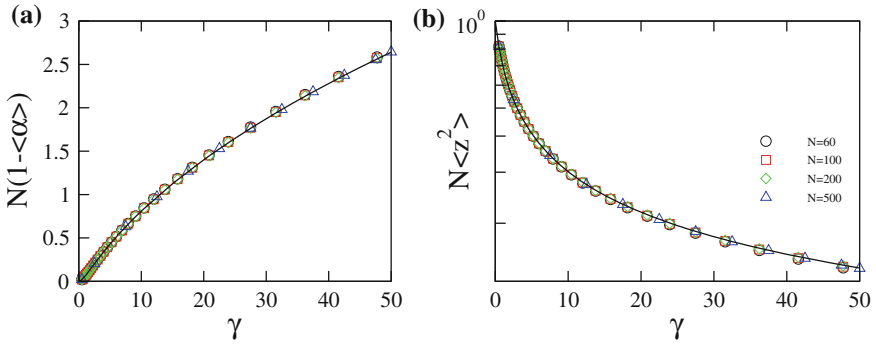

Fig. 2 Deviation of the coherence of the ground state of the system $N(1-\langle\hat{\alpha}\rangle)$, (**a**), and dispersion of the population imbalance $N\langle z^2\rangle$, (**b**) as a function of γ for $N = 60, 100, 200$ and 500 obtained by means of the Bose-Hubbard model, symbols. The *lines* are the predictions of the $1/N$ model, see Ref. [18] for explicit analytical expressions (Color figure online)

part of the spectrum. Therefore they will fail to capture properties in which the full spectrum is proved, as will be the case when high temperatures are considered.

3 Finite Temperature Effects

In this section we will consider the effect of temperature on the coherence of the system. Our aim is to compare different approximations [4, 12, 13, 20], which are expected to be valid in different regimes, e.g. non-interacting, low temperature, large atom–atom interactions, high N, etc.

3.1 The Exactly Solvable Non-Interacting System

The non-interacting case provides an important limiting scenario and can be solved exactly for any N.

In this case, $\hat{H} = -2J\hat{J}_x$ and the eigenstates are those of $\hat{J}_x$: $\hat{J}_x|q\rangle = q|q\rangle$, with $q = -N/2, \ldots, N/2$, which can also be represented in the basis defined in Eq. (5). The eigenenergies are $E_q = -2Jq$. Since $J > 0$ the ground state corresponds to $q = N/2$, whereas the most excited state has $q = -N/2$. The partition function is given by

$$\mathcal{Z} = \sum_{q=N/2}^{-N/2} e^{-\beta E_q} = \frac{\sinh(\beta J(N+1))}{\sinh \beta J}. \tag{13}$$

For the state $|q\rangle$, it is immediate that $\langle\hat{\alpha}\rangle_q = 2q/N$. Therefore it is easy to show that the thermal average can be exactly computed,

$$\langle\hat{\alpha}\rangle_T = \frac{1}{\mathcal{Z}}\sum_q \frac{2}{N} q\, e^{2\beta J q} = \frac{N+1}{N\tanh(\beta J(N+1))} - \frac{1}{N\tanh(\beta J)}. \tag{14}$$

Two relevant limits can be easily identified: (a) $\lim_{T\to 0}\langle\hat{\alpha}\rangle_T = 1$. (b) when $T \to \infty$:

$$\langle\hat{\alpha}\rangle_T \simeq \frac{1}{3}(N+2)\beta J + \mathcal{O}(\beta^3) \to 0, \tag{15}$$

as expected, as T increases the coherence decreases, making the system more classical.

For large N it is possible to derive very simple expressions. Assuming that $N \gg 1$, one can replace sums by integrals. For instance, in Eq. (13):

$$\mathcal{Z} \simeq \int_{-N/2}^{N/2} dq\, e^{2\beta J q} = \frac{N}{\beta E_J}\sinh(\beta E_J), \tag{16}$$

where $E_J \equiv NJ$. For the coherence factor we now have:

$$\langle\hat{\alpha}\rangle_T = \frac{1}{NJ}\frac{\partial}{\partial\beta}\ln\mathcal{Z} = -\frac{1}{\beta E_J} + \frac{1}{\tanh\beta E_J}. \tag{17}$$

The latter expression agrees with the semi-classical expression given in Ref. [13] for the non-interacting case.

It is easy to check that $\partial\langle\hat{\alpha}\rangle_T/\partial\beta > 0$ for all $\beta > 0$. And thus that $\langle\hat{\alpha}\rangle_T$ decreases smoothly when T increases. It is also immediate that $\langle\hat{\alpha}\rangle_T$ starts with zero slope at $T = 0$ ($\beta \to \infty$). These features are clearly reflected in Fig. 3.

As seen above the spectrum runs only from $q = N/2$ (ground state) to $q = -N/2$ (highest excited state). Let us consider the differences that arise when the spectrum is extended to $q = -\infty$. As expected these differences appear when the temperature is increased above a certain limit that we will quantify. The partition function for a semiinfinite equally spaced spectrum is:

$$\mathcal{Z}^{(\infty)} = \sum_{q=-\infty}^{N/2} e^{2\beta J q} = \frac{2\,\exp(\beta J(N-1))}{\sinh\beta J} \tag{18}$$

which should be compared to Eq. (13). Similarly:

$$\langle\hat{\alpha}\rangle_T^{(\infty)} = \frac{1}{NJ}\frac{\partial}{\partial\beta}\left(\ln\mathcal{Z}^{(\infty)}\right) = \frac{N+1}{N} - \frac{1}{N\tanh\beta J}, \tag{19}$$

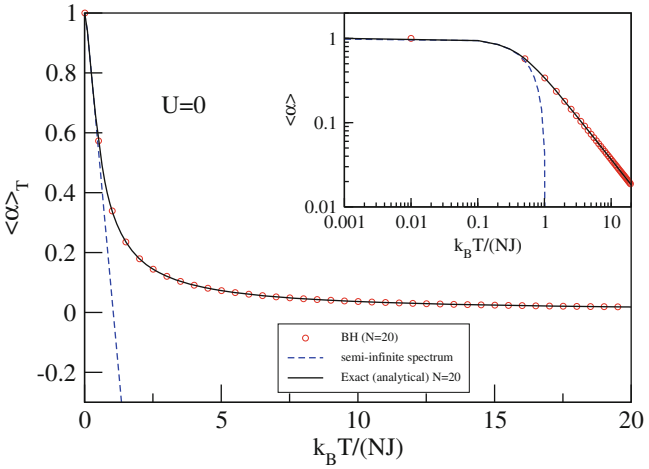

Fig. 3 Coherence as a function of temperature for the non-interacting case. We compare the numerical BH results (symbols), the exact analytical formula (14), *solid line*, and the prediction for a spectrum of infinite equally spaced levels, Eq. (19), *dashed-line*

instead of Eq. (14). Then, when $T \to \infty$, $\langle\hat{\alpha}\rangle_T^{(\infty)} \simeq ((N+1)/N - 1/(\beta E_J)) \neq 0$, in strong disagreement with Eq. (15) above. Figure 3 shows that, as expected, extending the spectrum to infinity is only a good approximation at small temperatures. Note that $1/(\beta[E(q=-N/2) - E(q=N/2)]) = 1/(2\beta E_J)$, which is roughly the value at which the two sets of curves in Fig. 3 begin to disagree.

3.2 Thermal Effects in the Interacting Case

Now lets consider the case of non-zero interaction between the atoms.

3.2.1 Results from the 1/N Model

We consider the case $\gamma > -1$ for which the potential in the semiclassical Hamiltonian, Eq. (10), is well approximated by a parabolic function. The stationary states and energies are written in this approximation as: $H_s\psi_v(z) = E_v\psi_v(z)$, $v = 0, 1, 2, \ldots$, so that

$$E_v = \langle H_s\rangle_v = -\langle\hat{\alpha}\rangle_v^{(s)} + \frac{1}{2}\gamma\langle z^2\rangle_v. \tag{20}$$

When $\gamma > -1$ it is a good approximation to set $\sqrt{1-z^2} \simeq 1$ in the kinetic energy term, and to expand the potential:

$$\mathcal{V}(z) = \frac{1}{2}\gamma z^2 - \sqrt{1-z^2} - \frac{h}{\sqrt{1-z^2}} \simeq -1 - h + \frac{1}{2}(\gamma + 1 - h)z^2. \tag{21}$$

This leads to a parabolic approximation in which we have a harmonic-oscillator-like Hamiltonian with $m^* = 1/4$, $\omega = 2\sqrt{1+\gamma-h}$ and $b = \sqrt{2h}/(1+\gamma-h)^{1/4}$. Therefore

$$E_v = 1 + h + h\frac{-\gamma/2 - 1 + h}{\sqrt{\gamma + 1 - h}}(2v+1). \tag{22}$$

We introduce auxiliary constants:

$$E_v \equiv E_0 + 2Fv \quad \text{and} \qquad \langle\hat{\alpha}\rangle_v^{(s)} \equiv \mathcal{A} + \mathcal{B}v. \tag{23}$$

where,
$E_0 = -1 - h + h\sqrt{\gamma+1-h}$, $F = h\sqrt{\gamma+1-h}$, $\mathcal{A} = 1 + h + h\frac{-\gamma/2-1+h}{\sqrt{\gamma+1-h}}$, and $\mathcal{B} = 2h\frac{-\gamma/2-1+h}{\sqrt{\gamma+1-h}}$. Using the parabolic approximation we calculate the partition function following a similar procedure as for the $\gamma = 0$ case,

$$\mathcal{Z} = e^{-\beta(E_0+FN)}\frac{\sinh(\beta F(N+1))}{\sinh \beta F} \tag{24}$$

and the thermal average of the coherence,

$$\langle\hat{\alpha}\rangle_T^{(s)} = \mathcal{A} - \frac{\mathcal{B}}{2}\left(\frac{N+1}{\tanh \beta F(N+1)} - \frac{1}{\tanh \beta F} - N\right). \tag{25}$$

One can also derive expressions similar to Eqs. (16) and (17) for the large N limit.[1]

In Fig. 4 exact Bose-Hubbard results for the coherence of the system are compared to the predictions of Eq. (25). The analytic expression captures very well the $T \to 0$ limit, with a good prediction of the initial curvature and its dependence on γ. Also, the validity of the analytic expression extends to higher T as the number of atoms is increased. As noted by comparing results at $N = 100$ (left) and $N = 200$ (right).

Taking the $\gamma \gg 1$ limit the above results lead to the Bogoliubov approximation presented in Ref. [20], where the Bogoliubov excitations around the ground state are considered.

[1] Although the physics is of course different, the mathematical approach followed here is the familiar one in the theory of paramagnetism. See e.g. the textbooks of Ashcroft and Mermin [21] or Kittel [22]. In particular Eqs. (14), and (25) involve the same Brillouin function that plays a central role in the study of paramagnetic ions.

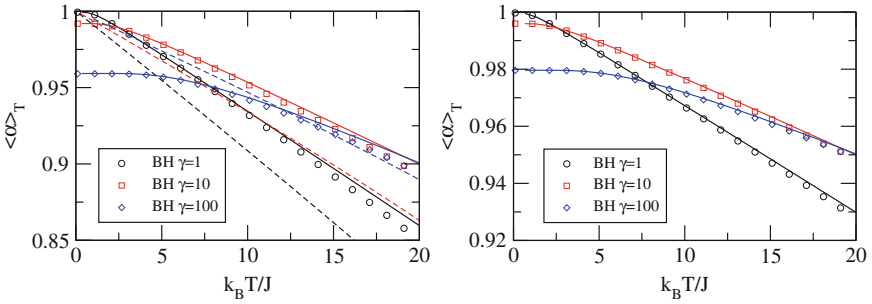

Fig. 4 Low temperature behavior of the coherence for different values of γ for $N = 100$ (*left*) and $N = 200$ (*right*). The comparison includes: BH results, symbols, and $1/N$ results in the parabolic approximation, Eq. (25), *solid lines*. For $N = 100$ we also compare the results of Eq. (27) [13], *dashed lines*

3.2.2 Previous Approximations

In Ref. [12] the authors provide an expression for the coherence as a function of temperature valid in the limit in which the interaction energy is much larger than the thermal energy, $k_B T$.[2] They find,

$$\alpha_{\text{S.P.}}(T) = \frac{\mathrm{I}_1[NJ/(k_B T)]}{\mathrm{I}_0[NJ/k_B T)]} \tag{26}$$

where $\mathrm{I}_j(x)$ are the spherical Bessel functions. More recently, Ref. [13] presented an approximate expression of $\langle\alpha\rangle_T$,

$$\alpha_{\text{G.S.}}(T) = \frac{\int_{-1}^{1} dx\, x\, \mathrm{I}_0[\epsilon(1-x^2)/4] e^{\delta x + \epsilon x^2/4}}{\int_{-1}^{1} dx\, \mathrm{I}_0[\epsilon(1-x^2)/4] e^{\delta x + \epsilon x^2/4}} \tag{27}$$

where $\epsilon = N^2 U/(2k_B T)$ and $\delta = NJ/(k_B T)$. This approximation is justified when $\delta, \epsilon \ll N$, and N is large. As limit cases, Eq. (27) reproduces the semiclassical expression, Eq. (26) when $\epsilon \gg 1$, and Eq (16) when $\epsilon = 0$.

In Fig. 5 we compare the results from Eq. (27) to the exact Bose-Hubbard results and to the results obtained from the harmonic oscillator approximation, valid for low temperatures. Equation (27) predicts accurately the large temperature behavior when $\gamma = 10$ and $N = 100$.

In contrast it fails to reproduce the low temperature behavior, which involves the thermal population of a few number of states, as seen in the comparison in Fig. 4.

[2] Note that in Refs. [23, 24] experimental data are measured for $E_C = 0.016\,\text{nK}$, $E_J = 0.43\,\text{nK}$ and $N = 3000$ atoms. Thus $E_J/(E_C N^2) = 2.986 \cdot 10^{-4} \ll 1$. In our notations: $E_J/(E_C N^2) = (JN)/(2UN^2) = 1/(4\gamma)$, and indeed this implies that $\gamma \gg 1$ in their experiment.

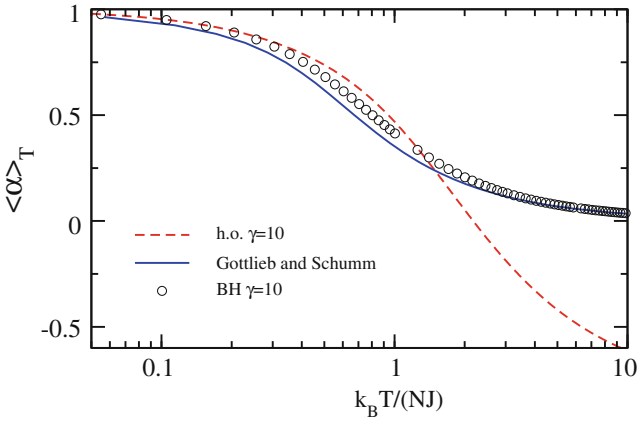

Fig. 5 High temperature behaviour of the coherence for $\gamma = 10$ and $N = 100$. Numerical BH results, symbols, are compared to Eq. (27), *solid lines*, and Eq. (25), *dashed lines*

4 Summary and Conclusions

We have presented a brief rendition of the thermal effects on the coherence of Bose-Einstein condensates trapped in double-well potentials. The aim has been to compare the exact quantum results, obtained diagonalizing the two-site Bose-Hubbard Hamiltonian, with previous approximate expressions present in the literature and with the semiclassical $1/N$ expansion, which correctly predicts the quantum properties of the ground state of the system. We have shown that the approximate models developed in Refs. [12, 13] describe very well the loss of coherence due to thermal effects in the bosonic Josephson junction. In contrast, the $1/N$ provides an accurate description of the low-temperature regime in which few levels of the Hamiltonian are thermally populated, and therefore the quantum many-body effects are more important. In the large γ limit, this model recovers the previously derived Bogoliubov description presented in Ref. [20].

References

1. M. Lewenstein, A. Sanpera, V. Ahufinger, B. Damski, A. De Sen, U. Sen, Adv. Phys. **56**, 243 (2007)
2. I. Bloch, J. Dalibard, W. Zwerger, Rev. Mod. Phys. **80**, 885 (2008)
3. M. Albiez, R. Gati, J. Fölling, S. Hunsmann, M. Cristiani, M.K. Oberthaler, Phys. Rev. Lett. **95**, 010402 (2005)
4. R. Gati, M.K. Oberthaler, J. Phys. B.: At. Mol. Opt. Phys. **40**, R61–R89 (2007)
5. S. Levy, E. Lahoud, I. Shomroni, J. Steinhauer, Nature **449**, 579 (2007)
6. A. Smerzi, S. Fantoni, S. Giovanazzi, S.R. Shenoy, Phys. Rev. Lett. **79**, 4950 (1997)
7. G.J. Milburn, J. Corney, E.M. Wright, D.F. Walls, Phys. Rev. A **55**, 4318 (1997)
8. J. Esteve, C. Gross, A. Weller, S. Giovanazzi, M.K. Oberthaler, Nature **455**, 1216 (2008)

9. T. Zibold, E. Nicklas, C. Gross, M.K. Oberthaler, Phys. Rev. Lett. **105**, 204101 (2010)
10. J.I. Cirac, M. Lewenstein, K. Mølmer, P. Zoller, Phys. Rev. A **57**, 1208 (1998)
11. B. Juliá-Díaz, D. Dagnino, M. Lewenstein, J. Martorell, A. Polls, Phys. Rev. A **81**, 023615 (2010)
12. L. Pitaevskii, S. Stringari, Phys. Rev. Lett. **87**, 180402 (2001)
13. A.D. Gottlieb, T. Schumm, Phys. Rev. A **79**, 063601 (2009)
14. V.S. Shchesnovich, M. Trippenbach, Phys. Rev. A **78**, 023611 (2008)
15. B. Juliá-Díaz, J. Martorell, A. Polls, Phys. Rev. A **81**, 063625 (2010)
16. A.J. Leggett, Rev. Mod. Phys. **73**, 307 (2001)
17. M. Holtaus, S. Stenholm, Eur. Phys. J. B **20**, 451 (2001)
18. B. Juliá-Díaz, T. Zibold, M.K. Oberthaler, M. Melé-Messeguer, J. Martorell, A. Polls, Phys. Rev. A **86**, 023615 (2012)
19. E. Boukobza, M. Chuchem, D. Cohen, A. Vardi, Phys. Rev. Lett. **102**, 180403 (2009)
20. R. Gati, J. Esteve, B. Hemmerling, T.B. Ottenstein, J. Appmeier, A. Weller, M.K. Oberthaler, New. J. Phys. **8**, 189 (2006)
21. N.W. Ashcroft, N.D. Mermin, *Solid State Physics* (Holt Saunders International Editions, Philadelphia, 1976), pp. 655–656
22. C. Kittel, *Introduction to Solid State Physics*, 7th edn. (Wiley, New York, 2004), pp. 420–422
23. R. Gati, B. Hemmerling, J. Fölling, M. Albiez, M.K. Oberthaler, Phys. Rev. Lett. **96**, 130404 (2006)
24. R. Gati, J. Esteve, B. Hemmerling, T.B. Ottenstein, J. Appmeier, A. Weller, M.K. Oberthaler, arXiv:cond-mat/0606281v2

Multiple Fluxon Analogues and Dark Solitons in Linearly Coupled Bose–Einstein Condensates

M. I. Qadir, H. Susanto and P. C. Matthews

Abstract Two effectively one-dimensional parallel coupled Bose–Einstein condensates in the presence of external potentials are studied. The system is modelled by linearly coupled Gross–Pitaevskii equations. In particular, the interactions of grey-soliton-like solutions representing analogues of superconducting Josephson fluxons as well as coupled dark solitons are discussed. A theoretical approximation based on variational formulations to calculate the oscillation frequency of the grey-soliton-like solution is derived and a qualitatively good agreement with numerics is obtained.

1 Introduction

The concept of electron tunnelling between two superconductors separated by a thin insulating barrier predicted by Josephson [1] has been extended relatively recently to tunnelling of Bose–Einstein condensates (BECs) across a potential barrier by Smerzi et al. [2–4]. Such tunnelling has been observed experimentally where a single [5, 6] and an array [7] of *short* Bose–Josephson junctions (BJJs)

M. I. Qadir · H. Susanto (✉) · P. C. Matthews
School of Mathematical Sciences, University of Nottingham,
University Park, Nottingham NG7 2RD, UK
e-mail: hadi.susanto@nottingham.ac.uk

M. I. Qadir
e-mail: mirfan@uet.edu.pk

M. I. Qadir
Department of Mathematics, University of Engineering and Technology,
Lahore, Pakistan

Progress Optical Sci., Photonics (2013): 485–508
DOI: 10.1007/10091_2012_18

Published Online: 19 October 2012

were realized. The dynamics of the phase difference between the wavefunctions of the condensates [2–4, 8–11] resembles that of point-like Josephson junctions [12].

Recently a proposal for the realization of a *long* BJJ has been presented by Kaurov and Kuklov [13, 14]. Similarly to superconducting long Josephson junctions, one may also look for an analogue of Josephson fluxons [15] in this case. It was shown in [13, 14] that fluxon analogues are given by coupled dark-soliton-like solutions, as the relative phase of the solutions has a kink shape with the topological phase difference equal to 2π. Moreover, it was emphasized that fluxon analogues (FAs) can be spontaneously formed from coupled dark solitons due to the presence of a critical coupling at which the two solitonic structures exchange their stability. The idea of FAs in tunnel-coupled BECs is then extended to rotational FAs in the ground state of rotating annular BECs confined in double-ring traps [16]. The work in [13, 14] was extended in [17] where the existence and the stability of both FAs and the coupled dark solitons were investigated in the presence of a magnetic trap.

In this chapter, we consider the existence and the stability of multiple FAs and dark solitons in two coupled cigar-shaped condensates in the presence of a magnetic trap along the elongated direction. The system is modelled by the normalized coupled Gross–Pitaevskii equations

$$i\psi_{j_t} = -\frac{1}{2}\psi_{j_{xx}} + |\psi_j|^2\psi_j - \rho_0\psi_j - k\psi_{3-j} + V\psi_j, \tag{1}$$

where $\psi_j, j = 1, 2$, is the bosonic field, and t and x are the time and axial coordinate, respectively. Here, we assume that the parallel quasi one-dimensional BECs are linked effectively by a weak coupling k. Note that herein $k > 0$. The case $k < 0$ corresponds to an excited state in which there is a π-phase difference between the condensates. ρ_0 is the chemical potential which is considered to be the same in both waveguides and V is the magnetic trap with strength Ω, i.e.

$$V(x) = \frac{1}{2}\Omega^2 x^2. \tag{2}$$

Different works have been done in similar settings as (1), such as the spontaneous symmetry breaking were analyzed in [18] when BECs are loaded in two parallel quasi-one-dimensional traps fitted with optical lattices, the study of stable defects in nonlinear patterns known as optical domain walls [19], and the investigation of the separation of two far separated domain walls along with their stability limits were considered in [20]. Recently, the studies were extended for the case when two components of BECs are coupled by both linear and nonlinear terms [21].

When $\Omega = 0$, writing $\psi_j = |\psi_j| \exp(i\varphi_j)$, it was shown that the relative phase $\phi = \pm(\varphi_2 - \varphi_1)$ will satisfy a modified sine-Gordon equation [13]. An FA of (1) in that case is given by the solution $\psi_1 = \psi_2^* = \psi$, with

$$\psi = \pm\sqrt{\rho_0 + k}\tanh(2\sqrt{k}x) \pm i\sqrt{\rho_0 - 3k}\,\mathrm{sech}(2\sqrt{k}x), \tag{3}$$

where the asterisk denotes complex conjugation. The soliton (3) can be regarded as an analogue of Josephson fluxons [13, 14] as the phase difference ϕ between the phases of ψ_1 and ψ_2 forms a spatial kink connecting $\phi = 0$ and $\phi = \pm 2\pi$. In the following, solution (3) (and its continuations) will be referred to as FAs. The case of $k < 0$ can be obtained accordingly as there is a symmetry transformation $k \to -k$ and $\psi_j \to i\psi_j$. From the expression, it is clear that an FA exists only for $0 < k < \rho_0/3$. The amplitude of the imaginary part of FA decreases with k and tends to zero as $k \to \rho_0/3$. For $k = \rho_0/3$, the solution in (3) transforms into a dark soliton [13, 14]

$$\psi_{1,2} = \pm\sqrt{\rho_0 + k}\tanh(\sqrt{\rho_0 + k}x), \tag{4}$$

which exists for $k > -\rho_0$. Thus, solutions in (3) and (4) coexist for $0 < k < \rho_0/3$. Hence, $k = \rho_0/3$ is a bifurcation point along the family of (4). The bifurcation in this case is a pitchfork bifurcation. When there is no trap, it is found in [13] that the FA solution (3) is stable for all values of k where it exists, while the coupled dark soliton (4) remains unstable for $k < \rho_0/3$ and becomes stable for $k \geq \rho_0/3$.

It is shown in [17] that the presence of a magnetic trap destabilizes the FA solution. However, stabilization is possible by controlling the effective linear coupling k between the condensates. The critical coupling above which FA does not exist is almost independent of the trapping strength. Moreover, the existence and stability regions for coupled dark soliton remain unaffected by the presence of the trap. The transition between FA and dark soliton in the presence of the trap can be realized as a pitchfork bifurcation. In the limiting case, when $\Omega \to 0$, the critical value of stability k_{cs} of FA goes to zero whereas the critical value of existence k_{ce} remains unaffected.

When the two condensates are uncoupled or the same, i.e. $k = 0$ or $\psi_1 = \psi_2$ with $\rho_0 + k \to \rho_0$, respectively, (1) reduces to

$$i\psi_t = -\frac{1}{2}\psi_{xx} + |\psi|^2\psi - \rho_0\psi + V\psi. \tag{5}$$

In the absence of the external potential, i.e. $V = 0$, a single dark soliton on top of a background with constant density ρ_0 has the form of [22, 23] (cf. (4))

$$\psi(x,t) = \sqrt{\rho_0}[A\tanh(\sqrt{\rho_0}A(x - \sqrt{\rho_0}x_0)) + iv], \tag{6}$$

where the parameters A and v determine the soliton depth and velocity, respectively, and are in general functions of time t with $A^2 + v^2 = 1$. When $v = 0$, the dark soliton becomes a stationary kink also called a black soliton and has unit depth (see (4)). When $v = 1$, the depth of the solution vanishes and the dark soliton becomes the background solution. Since $|\psi|^2$ represents the density of the dark soliton, its minimum value ρ_{min} can be obtained by differentiating $|\psi|^2$ partially with respect to x and equating it to zero, i.e.

$$\frac{\partial|\psi|^2}{\partial x} = 0. \tag{7}$$

Here,

$$|\psi|^2 = \rho_0[A^2 \tanh^2(\sqrt{\rho_0}A(x - \sqrt{\rho_0}x_0)) + v^2]. \tag{8}$$

Using Eq. (7), the critical point we obtain is $x = \sqrt{\rho_0}x_0$. Substituting this value back in Eq. (8) yields $\rho_{min} = \rho_0 v^2$.

Multiple dark soliton solutions of Eq. (5) in the absence of a magnetic trap are also available. The wavefunction for the simplest case of two dark solitons moving with velocities $v_1 = -v_2 = v$ can be expressed as [24]

$$\psi(x,t) = \frac{(2\rho_0 - 4\rho_{min})\cosh(qt) - 2\sqrt{\rho_0\rho_{min}}\cosh(px) - 2iq\sinh(qt)}{2\sqrt{\rho_0}\cosh(qt) + 2\sqrt{\rho_{min}}\cosh(px)}, \tag{9}$$

where $q = 2\sqrt{\rho_{min}(\rho_0 - \rho_{min})}$ and $p = 2\sqrt{\rho_0 - \rho_{min}}$.

The dynamics of a dark soliton in BECs in the uncoupled system with magnetic trap has been considered before theoretically [25, 26] (see also [27] and references therein) and experimentally [28–32]. Interesting phenomena on the collective behavior of a quantum degenerate bosonic gas, such as soliton oscillations [28, 29, 31] and frequency shifts due to soliton collisions [32] were observed. A theoretical analysis based on variational formulation was developed in [23, 33] that is in good agreement with numerics as well as with experiments (see, e.g. [34, 35]). A similar variational method was derived in [17] to explain the dynamics of FAs in (1). It was shown that the equation of motion for the core of the FA solution is

$$\frac{d^2x_0}{dt^2} = \frac{(1-5k)\Omega^2}{1+k}x_0. \tag{10}$$

Note that when $k = 1/3$, i.e. the critical coupling for a pitchfork bifurcation between dark solitons and FAs, the oscillation frequency of dark solitons in a harmonic trap is recovered [36] (see also [26, 28, 34]). When the FAs are moving with the velocity v, the critical value of the coupling constant is [17]

$$k = -\frac{1}{3}v^2 - \frac{1}{21} + \frac{4}{21}\sqrt{7v^4 - 7v^2 + 4}. \tag{11}$$

In a similar fashion as the case when $v = 0$, travelling FA solutions are found to be stable in their existing domain. Travelling coupled dark solitons are stable beyond the critical value and unstable otherwise.

Here, we will consider the interaction of multiple FAs as well as dark solitons in (1) both in the absence and presence of a magnetic trap. Depending on the symmetry of the imaginary parts of the solutions, multiple FAs can be categorized into $(+-)$-configuration and $(++)$-configuration. Note that for dark solitons, we have a single configuration for both $(+-)$ and $(++)$-configurations as the

imaginary part is zero. In the context of a parametrically driven nonlinear Schrödinger (NLS) equation, the bound states of FA correspond to Bloch–Bloch states and were discussed in [37, 38].

The chapter is outlined as follows. In Sect. 2, we will derive a variational formulation for the oscillation frequency of the $(+-)$-configuration of FA solution. In Sect. 3, we will consider the interactions of FAs and dark solitons in (1) in the absence and presence of a trap. We conclude the work in Sect. 4.

2 Variational Approximations

In this section, we shall first derive the interaction potential of two dark solitons given by (5) in the absence of the magnetic trap, which was discussed rather briefly in [23, 28]. We shall then generalize the concept for the interaction of n solitons. The interaction potential will then be used to approximate the oscillation frequency of multiple FAs in the presence of the trap.

2.1 Determining the Interaction Potential

When $k = 0$, the system (1) is decoupled and we are left with the one-dimensional NLS equation (5). We consider the interaction of two dark solitons in (5) where one of the solitons is located at $x = x_0$ while the other is at $x = -x_0$. Both solitons are moving with velocities equal in magnitude but opposite in signs, i.e. $v_1 = -v_2 = v$. Then in the weak interacting limit and in the absence of external potential, one can find the equation of the trajectory of the dip of the soliton x_0 as a function of time t. To do this, we identify the soliton dip x_0 as the point of minimum density (cf. Eq. (7)). In this case, $|\psi|^2$ can be obtained from Eq. (9) and is given by

$$|\psi|^2 = \frac{\left[(2\rho_0 - 4\rho_{min})\cosh(qt) - 2\sqrt{\rho_0\rho_{min}}\cosh(px)\right]^2 + 4q^2\sinh^2(qt)}{\left[2\sqrt{\rho_0}\cosh(qt) + 2\sqrt{\rho_{min}}\cosh(px)\right]^2}. \quad (12)$$

Differentiating $|\psi|^2$ partially with respect to x and equating the resulting equation to zero yields

$$\begin{aligned}(8\rho_0^2 - 8\rho_0^2v^2 + 16\rho_0^2v^4 - 16\rho_0^2v^2)\cosh^2(qt) + 4q^2\sinh^2(qt)\\ + (8\rho_0^2v^3 - 8\rho_0^2v)\cosh(px)\cosh(qt) = 0.\end{aligned}$$

Using $A^2 = 1 - v^2$, the above equation can be written as

$$(8\rho_0^2A^2 - 16\rho_0^2v^2A^2)\cosh^2(qt) + 4q^2\sinh^2(qt) - 8\rho_0^2vA^2\cosh(px)\cosh(qt) = 0.$$

Since $q = 2\sqrt{\rho_{min}(\rho_0 - \rho_{min})}$ or $q^2 = 4\rho_0^2 v^2 A^2$, substituting the value of q^2 in the above equation and using the identity $\cosh^2(qt) - \sinh^2(qt) = 1$, we obtain

$$8\rho_0^2 A^2 \cosh^2(qt) - 16\rho_0^2 v^2 A^2 - 8\rho_0^2 v A^2 \cosh(px)\cosh(qt) = 0.$$

Dividing throughout by $8\rho_0^2 v A^2 \cosh(qt)$, the equation simplifies to

$$x = \frac{1}{p}\cosh^{-1}\left(\frac{\cosh(qt)}{v} - \frac{2v}{\cosh(qt)}\right). \tag{13}$$

Then the minimum distance $2x_0^*$ between the two dark solitons corresponding to $t = 0$ can be obtained from the last equation as

$$2x_0^* = \frac{2}{p}\cosh^{-1}\left(\frac{1}{v} - 2v\right). \tag{14}$$

When the solitons are moving slowly, they remain well separated for every value of time. This suggests that the distance $2x_0^*$ should be large. This can be justified if the second term on the right hand side of Eq. (13) is much smaller than the first term and hence can be neglected. Then, the resulting equation at $x = x_0$ can be written as

$$x_0 = \frac{1}{p}\cosh^{-1}\left(\frac{\cosh(qt)}{v}\right). \tag{15}$$

Note that differentiating Eq. (15) twice with respect to time yields

$$\frac{d^2x_0}{dt^2} = \frac{A^2q^2v^{-3}\cosh(qt)}{p[v^{-2}\cosh^2(qt) - 1]^{3/2}}.$$

From Eq. (15), we have $v^{-1}\cosh(qt) = \cosh(px_0)$. Substituting this value and using the identity $\cosh^2(px_0) - 1 = \sinh^2(px_0)$ in the second derivative above yields

$$\frac{d^2x_0}{dt^2} = \frac{A^2q^2\cosh(px_0)}{pv^2\sinh^3(px_0)} = -\frac{\partial}{\partial x_0}\left(\frac{A^2q^2}{2p^2v^2\sinh^2(px_0)}\right). \tag{16}$$

Equation (16) is the equation of motion of the dip of soliton from which we acquire the repulsive potential W to be

$$W = \frac{A^2q^2}{2p^2v^2\sinh^2(px_0)}.$$

Substituting the values of p and q, we obtain

$$W = \frac{\rho_0 A^2}{2\sinh^2(2\sqrt{\rho_0}Ax_0)}. \tag{17}$$

It is clear that this potential is velocity dependent as $A^2 = 1 - v^2$. Even though the potential W is relevant to the symmetric interactions, however it can be applied to the asymmetric interactions as well, provided that the average depth of the two solitons is used.

The effective repulsive potential (17) can be used to construct an approximate potential for the interaction of n solitons. In this case the position of the dip of the ith soliton (where $i = 1, 2, \ldots, n$) is at x_i and is moving with velocity v_i and having depth $A_i = \sqrt{1 - v_i^2}$. We may define, respectively, the average depth and the relative position of the dip for the ith and jth solitons as $A_{ij} = (1/2)(A_i + A_j)$ and $x_{ij} = (1/2)(x_i - x_j)$. Then the repulsive potential W_i can be expressed as

$$W_i = \sum_{i \neq j}^{n} \frac{\rho_0 A_{ij}^2}{2 \sinh^2[\sqrt{\rho_0} A_{ij}(x_i - x_j)]}. \tag{18}$$

The kinetic energy E and the potential energy V of a structure of n interacting solitons are given by $E = \sum_{i=1}^{n} (1/2)\dot{x}_i^2$ and $V = \sum_{i=1}^{n} W_i$. Here dot represents the derivative with respect to time t. The Lagrangian $\mathcal{L}$, which is the difference of kinetic and potential energies, is $\mathcal{L} = E - V$. To find the equations of motion we use the Euler–Lagrange equations

$$\frac{\partial}{\partial t}\left(\frac{\partial \mathcal{L}}{\partial \dot{x}_i}\right) - \frac{\partial \mathcal{L}}{\partial x_i} = 0, \quad i = 1, 2, \ldots, n. \tag{19}$$

Hence the following n coupled dynamical equations for the trajectories $x_i(t)$ of n interacting solitons are obtained as

$$\ddot{x}_i - \sum_{k=1}^{n}\left(\frac{\partial^2 V}{\partial x_k \partial \dot{x}_i}\dot{x}_k + \frac{\partial^2 V}{\partial \dot{x}_k \partial \dot{x}_i}\ddot{x}_k\right) + \frac{\partial V}{\partial x_i} = 0. \tag{20}$$

2.2 Variational Approximation for Multiple FAs

We can now use a Lagrangian approach to find the oscillation frequency Ω of multiple FA solution, in the presence of a magnetic trap. Here, we assume that the FAs are well separated. Then in the limiting case when k is close to the critical coupling for a pitchfork bifurcation, the Lagrangian can be written as

$$\mathcal{L} = \frac{1}{2}(\dot{x}_1^2 + \dot{x}_2^2) + \left(\frac{1 - 5k}{1 + k}\right)\Omega^2(x_1^2 + x_2^2) - \frac{\rho_0}{\sinh^2[\sqrt{\rho_0}(x_2 - x_1)]}. \tag{21}$$

Note that we have used (10) to describe the potential due to a magnetic trap to an FA. Since we assume that the FAs are well separated, i.e. $|x_2 - x_1| \gg 0$, this implies that $e^{-\sqrt{\rho_0}(x_2 - x_1)}$ approaches zero. Hence (21) can be approximated by

$$\mathcal{L} = \frac{1}{2}(\dot{x}_1^2 + \dot{x}_2^2) + \left(\frac{1-5k}{1+k}\right)\Omega^2(x_1^2 + x_2^2) - 4\rho_0 e^{-2\sqrt{\rho_0}(x_2 - x_1)}.$$

Using Eq. (19), we then have the following system of governing equations

$$\ddot{x}_1 = -8\rho_0^{\frac{3}{2}} e^{-2\sqrt{\rho_0}(x_2 - x_1)} + 2\left(\frac{1-5k}{1+k}\right)\Omega^2 x_1, \tag{22}$$

$$\ddot{x}_2 = 8\rho_0^{\frac{3}{2}} e^{-2\sqrt{\rho_0}(x_2 - x_1)} + 2\left(\frac{1-5k}{1+k}\right)\Omega^2 x_2. \tag{23}$$

In order to find the fixed points of this system, we set $\ddot{x}_1 = 0 = \ddot{x}_2$. On adding the resulting equations one can easily see that both fixed points x_1 and x_2 are additive inverse of each other i.e. $x_1 = -x_2 = \tilde{x}$ (say), from which we obtain a single nonlinear algebraic equation which is

$$8\rho_0^{\frac{3}{2}} e^{4\sqrt{\rho_0}\tilde{x}} - 2\left(\frac{1-5k}{1+k}\right)\Omega^2\tilde{x} = 0. \tag{24}$$

We solve this equation numerically to find the values of $\tilde{x}$ corresponding to different values of k.

Now let δ_1 and δ_2 be small perturbations in x_1 and x_2 and $X_1 = x_1 + \delta_1(x_1, t)$, $X_2 = x_2 + \delta_2(x_2, t)$ be the solutions of Eqs. (22) and (23), respectively. Substituting these solutions into Eq. (22) with $X_1 = -X_2$, we obtain

$$\ddot{\delta}_1 = -8\rho_0^{\frac{3}{2}} e^{4\sqrt{\rho_0}\tilde{x}} e^{-2\sqrt{\rho_0}(\delta_2 - \delta_1)} + 2\left(\frac{1-5k}{1+k}\right)\Omega^2(\tilde{x} + \delta_1).$$

Using Taylor series expansion of $e^{-2\sqrt{\rho_0}(\delta_2 - \delta_1)}$ in the first term on the right hand side yields

$$\ddot{\delta}_1 = -8\rho_0^{\frac{3}{2}} e^{4\sqrt{\rho_0}\tilde{x}}[1 - 2\sqrt{\rho_0}(\delta_2 - \delta_1)] + 2\left(\frac{1-5k}{1+k}\right)\Omega^2(\tilde{x} + \delta_1).$$

Since $\tilde{x}$ is a fixed solution, the terms $-8\rho_0^{\frac{3}{2}} e^{4\sqrt{\rho_0}\tilde{x}}$ and $2(\frac{1-5k}{1+k})\Omega^2\tilde{x}$ provide only the vertical shift in the solution δ_1, but do not affect the oscillation frequency and hence can be neglected. So, we have

$$\ddot{\delta}_1 = 16\rho_0^2 e^{4\sqrt{\rho_0}\tilde{x}}(\delta_2 - \delta_1) + 2\left(\frac{1-5k}{1+k}\right)\Omega^2\delta_1. \tag{25}$$

Similarly from Eq. (23) we obtain

$$\ddot{\delta}_2 = -16\rho_0^2 e^{4\sqrt{\rho_0}\tilde{x}}(\delta_2 - \delta_1) + 2\left(\frac{1-5k}{1+k}\right)\Omega^2\delta_2. \tag{26}$$

Now let ω is the common oscillation frequency of FA solutions, then we can write $\delta_1 = \gamma_1 e^{i\omega t}$ and $\delta_2 = \gamma_2 e^{i\omega t}$. Substituting these values into Eqs. (25) and (26), we obtain

$$-\omega^2\gamma_1 = 16\rho_0^2 e^{4\sqrt{\rho_0}\tilde{x}}(\gamma_2 - \gamma_1) + 2\left(\frac{1-5k}{1+k}\right)\Omega^2\gamma_1, \tag{27}$$

$$-\omega^2\gamma_2 = -16\rho_0^2 e^{4\sqrt{\rho_0}\tilde{x}}(\gamma_2 - \gamma_1) + 2\left(\frac{1-5k}{1+k}\right)\Omega^2\gamma_2. \tag{28}$$

This system of equations represents an eigenvalue problem and can be written in matrix form as $AY = \lambda Y$, where

$$A = \begin{bmatrix} 2\left(\frac{1-5k}{1+k}\right)\Omega^2 - 16\rho_0^2 e^{4\sqrt{\rho_0}\tilde{x}} & 16\rho_0^2 e^{4\sqrt{\rho_0}\tilde{x}} \\ 16\rho_0^2 e^{4\sqrt{\rho_0}\tilde{x}} & 2\left(\frac{1-5k}{1+k}\right)\Omega^2 - 16\rho_0^2 e^{4\sqrt{\rho_0}\tilde{x}} \end{bmatrix},$$

$Y = [\gamma_1, \gamma_2]^T$ (T represents the transpose) and $\lambda = -\omega^2$. The characteristic frequency which corresponds to in-phase oscillations (i.e. $\delta_1 = \delta_2$) of FA solutions is

$$\omega = \sqrt{2\left(\frac{5k-1}{k+1}\right)}\Omega, \tag{29}$$

while the frequency corresponding to out-of-phase oscillations (i.e. $\delta_1 = -\delta_2$) is

$$\omega = \sqrt{2\left(\frac{5k-1}{k+1}\right)\Omega^2 + 32\rho_0^2 e^{4\sqrt{\rho_0}\tilde{x}}}. \tag{30}$$

It is important to note that in the above calculations we did not distinguish between FAs with $(+-)$ and $(++)$-configurations. It is because the imaginary part of the solution is treated as a passive component. Later through comparisons with numerical results we will see that the theoretical results above are only valid for the $(+-)$-configuration.

3 Numerical Simulations and Computations

3.1 Interactions of Uncoupled Dark Solitons Without Trap

Let us reconsider the interaction of two dark solitons in (5), i.e. (1) with $k = 0$, which are located at $x = \pm x_0$ and are moving with velocities $v_1 = -v_2 = v$. This problem has been considered in details in [28]. Since the domain of inverse hyperbolic cosine is $[1, \infty]$, Eq. (14) holds for $1/v - 2v > 1$ or $v^2 < 1/4$, otherwise

it gives a complex value for x_0. This means that there exists a critical value of velocity $v_{cr} = 1/2$ which separates two scenarios.

In the first scenario, two dark solitons having velocities $v_1 = -v_2 = v < v_{cr}$ start coming close to each other and at the point of their closest proximity, they repel and continuously go away from each other. In this case, before and after the interaction, both dark solitons can be described by two individual density minimum equal to zero. This shows that dark solitons moving with velocity $v < v_{cr}$ are well separated and can be regarded as low speed solitons. Physically this means that well-separated low speed solitons repel each other and their low kinetic energy could not overcome the interparticle repulsion. A direct numerical integration of (5) is performed and shown in Fig. 1a. Numerical simulations have also been done to check the validity of Eq. (20). The trajectories obtained through Eq. (20) are then plotted in Fig. 1a and indicated by white solid curves. The approximation shows excellent agreement quantitatively with the results obtained through direct numerical integration of Eq. (5).

In the second scenario, dark solitons approaching each other with velocity greater than the critical velocity will collide and after collision transmit through each other. Unlike low speed solitons, at the collision point they overlap entirely and are indistinguishable. Physically this means that due to the high velocity, their kinetic energy defeats the interparticle repulsion. This situation is shown in Fig. 1b. Even though this case is beyond the particle-like approximation, we show in Fig. 1b that Eq. (20) can still provide an approximate trajectory of the soliton collision.

In the above discussion, we only considered the symmetric case where solitons collide with the same absolute velocity. Let us now consider the asymmetric case. In this case, a dark soliton moving with velocity v will interact with a static dark soliton. At the interaction point, the static soliton is repelled by the travelling soliton. The energy possessed by the moving soliton is used to push the static soliton away from the original position. The travelling soliton transfers all its kinetic energy to the static soliton and becomes stationary after collision as shown in Fig. 1c. The white solid lines in this figure depict the trajectories obtained through the numerical integration of Eq. (20).

3.2 *Interaction of Dark Solitons in Coupled NLS Equations Without Trap*

Next, we consider the case $k \neq 0$. Let us first consider the symmetric case in which a pair of coupled dark solitons interact with each other. The interaction scenarios for coupled dark solitons are almost similar to the scenarios for the uncoupled dark solitons in the previous section. The scenario for slow moving solitons is presented in Fig. 2a, where we can see that both coupled solitons are repelling each other and remain well separated for all time t. The only difference from the uncoupled case is

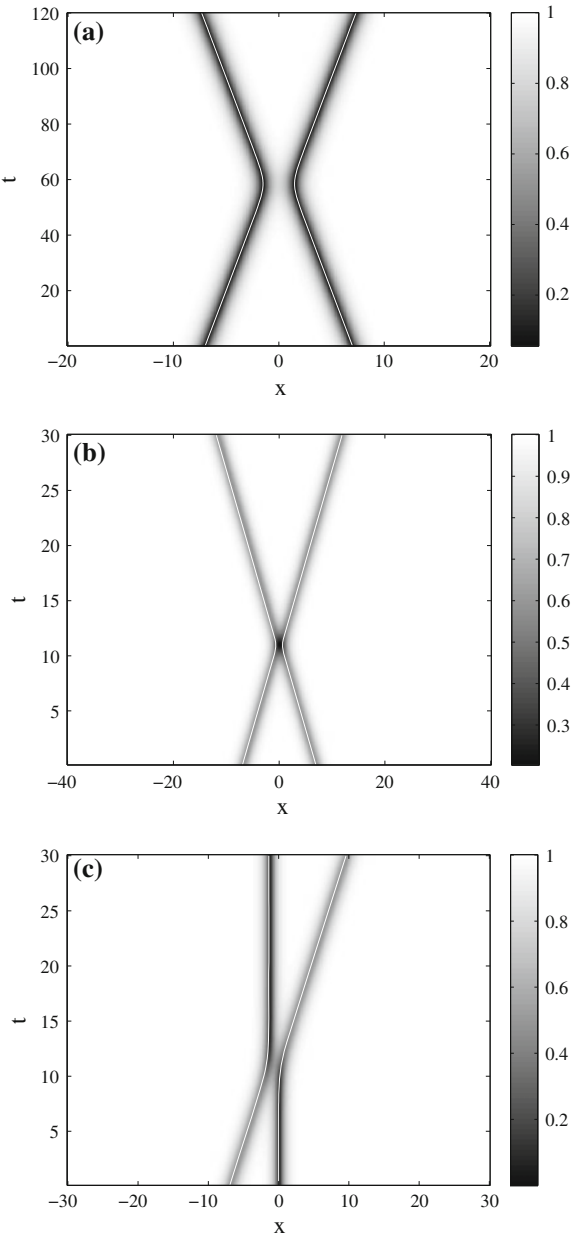

Fig. 1 Numerical evolutions of interaction of two dark solitons. **a** The solitons are moving with velocities $v_1 = -v_2 = 0.1$. The interparticle repulsion is dominant over the kinetic energies of solitons and solitons are going away from each other after interaction. **b** The solitons are moving with velocities $v_1 = -v_2 = 0.6$. The interparticle repulsion is suppressed by the kinetic energies of the solitons and they transmit through each other at the interacting point. **c** One of the solitons is static and the other is moving with velocity $v = 0.5$. After interaction, the travelling soliton becomes stationary and the static soliton starts moving with the velocity of the other soliton. In *all panels*, the *white solid curves* are simulations of trajectories of solutions obtained through Eq. (20). Note that solutions in *upper and middle panels* have an exact analytic solution given by (9)

that there is radiation emerging after interaction which was not seen in the uncoupled case. The reason for the emergence of this radiation is because the system is non-integrable. Also after a particular time the coupled dark solitons break up because they are unstable for the parameter values used for the

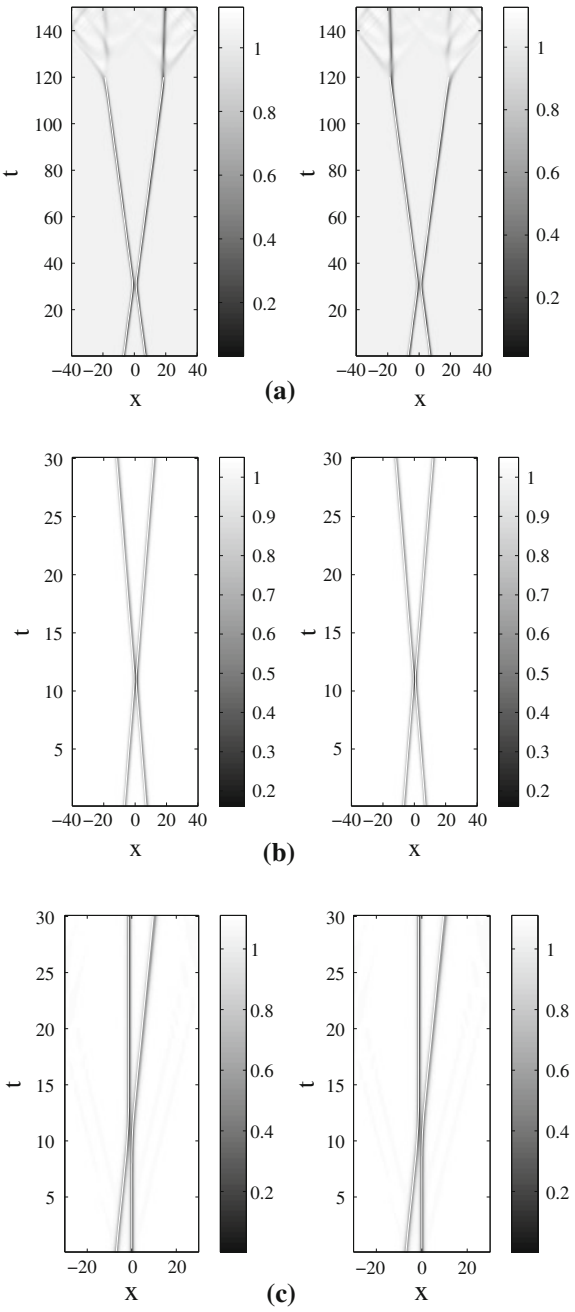

Fig. 2 As Fig. 1, but for coupled dark solitons. In **a** the solitons are moving with velocities $v_1 = -v_2 = 0.2$. The interparticle repulsion is dominant over the kinetic energies and the solitons are going away from each other after interaction. Due to an instability, they break down at approximately $t = 120$. For **b** the coupled dark solitons are moving with velocities $v_1 = -v_2 = 0.6$. The interparticle repulsion is suppressed by the kinetic energies of the solitons and they transmit through each other at the interacting point. In **c** one of the coupled solitons is static and the other is moving with velocity $v = 0.5$. In all the cases $k = 0.1$

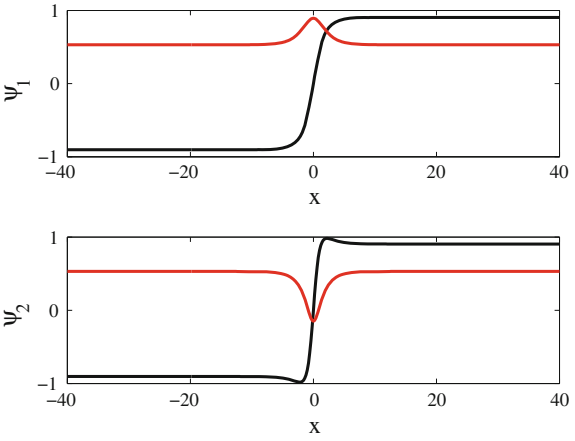

Fig. 3 Numerically obtained FAs travelling with velocity $v = 0.2$ corresponding to $k = 0.1$. The *black curves* represent the real parts while the *red curves* are the imaginary parts of ψ_1 and ψ_2, respectively (Color figure online)

interaction. Since a travelling uncoupled dark soliton is stable for all values of velocity, no radiation or break up could be seen. In the interaction scenario of the fast moving coupled solitons, they transmit through each other. Like the uncoupled case, their high kinetic energy overcomes the interparticle repulsion as shown in Fig. 2b. In an asymmetric interaction when one of the coupled dark solitons is static while the other is moving with some non-zero velocity v, the interaction scenario is similar to that of the uncoupled case and is shown in Fig. 2c. The trajectories of dips obtained by doing numerical simulations of Eq. (20) are compared with the trajectories found through direct numerical integration of Eq. (1). The white solid curves in Fig. 2 are the approximations obtained through Eq. (20) showing excellent agreement.

3.3 Interaction of FAs in the Absence of a Magnetic Trap

In this section, we will consider symmetric as well as asymmetric interactions of two FAs. An FA solution moving with velocity v corresponding to a particular value of k is shown in Fig. 3. We use a numerically obtained FA solution to construct a collision of two FAs. Since FAs are coupled solutions which consist of ψ_1 and ψ_2, there are two possibilities to connect two FA solutions. In the first possibility, ψ_1 and ψ_2 of the first FA are connected, respectively, to ψ_1 and ψ_2 of the second FA solution. In the second possibility, ψ_1 and ψ_2 of the first FA are connected, respectively, to ψ_2 and ψ_1 of the second FA solution. The combined pictures for both possibilities are shown in Fig. 4. From the symmetry of the imaginary parts, we refer to the first possibility as an odd symmetric interaction or $(+-)$-configuration and the second possibility as an even symmetric interaction or $(++)$-configuration.

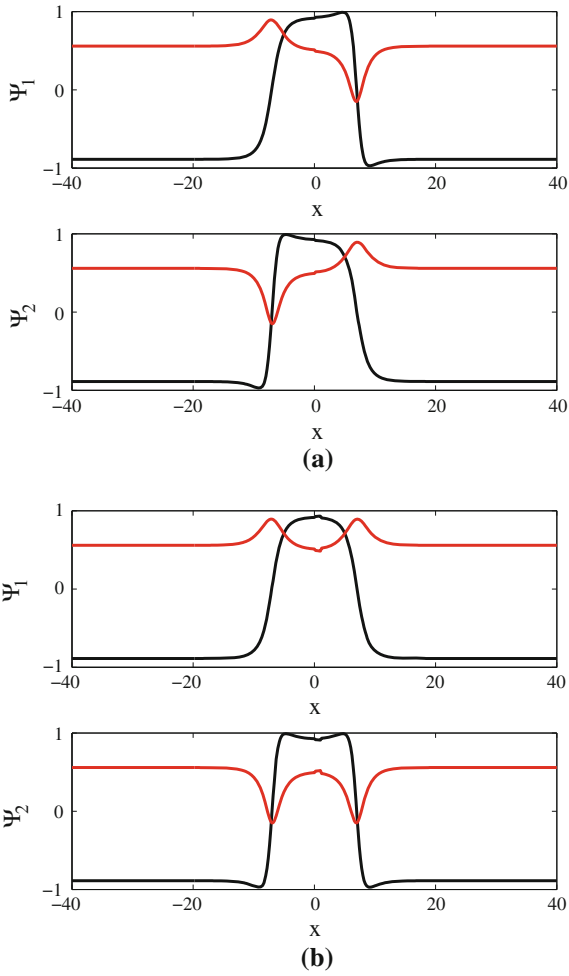

Fig. 4 Profiles of an initial condition representing two coupled FAs travelling with velocities $v_1 = -v_2 = 0.2$ corresponding to $k = 0.1$. The figure in the *upper panel* represents the odd interaction, while figure in the *lower panel* is the even interaction

First, we discuss the odd symmetric interaction. In this case, two FA solutions initially localized at $x = \pm x_0$ move with opposite velocities. Shown in Fig. 5a is the interaction of relatively slow moving FAs. Both FAs can be characterized by an individual density minimum before and after collision while at the interacting point they exhibit a single nonzero density minima. Both FAs show attraction towards each other at the interacting point which results in the deflection of positions of dips of both solutions. Radiation emerges and phase shift is induced due to collision. Figure 5b depicts an interaction of relatively high speed FA solutions. Neither of the FAs show any resistance during collision. Due to their high kinetic energies, both FAs pass through each other without shifting the phase and without showing any deflection in the trajectories of their dips.

Next, we consider the even symmetric interaction. An interaction of extremely slow moving FA solutions is displayed in Fig. 6a. The FAs come close to each

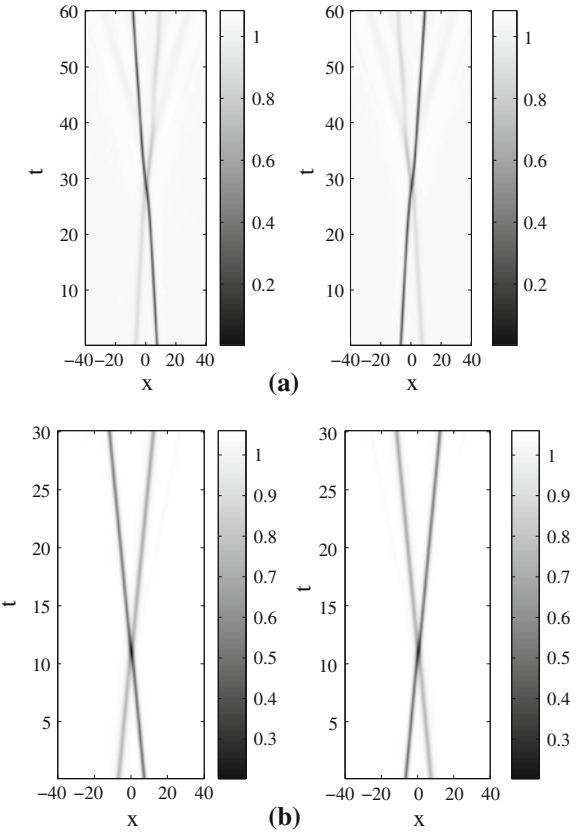

Fig. 5 As Fig. 1, but for the odd symmetric collision of FAs for (**a**) $v = 0.2$ and (**b**) $v = 0.6$. In *both panels* $k = 0.1$

other, but at the point of their closest proximity, they repel each other. Both the solutions can be identified by two individual density minima before and after the interaction as well as at the point of interaction. Another output from the interaction of two FAs moving with relatively slow velocities is shown in Fig. 6b. In this scenario, the solitons merge and form a breather similar to that reported in [37] in a parametrically driven Schrödinger equation. Radiation emerging after the collision is clear. Shown in Fig. 6c is the collision of FA solution moving with relatively high velocities. The FA solutions collide with each other and become indistinguishable at the interacting point.

Finally, we consider asymmetric interactions of two FAs. We show in Fig. 7a an odd interaction of a relatively slow moving FA with a static FA. The travelling FA pushes the static FA away from the interacting point. This mean that the travelling FA transfers all its kinetic energy to the static FA. Due to collision, radiation appears. In Fig. 7b we show an interaction of a relatively fast moving FA solution with a static FA solution, where we obtain a similar behavior as before. Even interactions of a slow and a fast moving FA with a static FA are shown in Fig. 8a, b, respectively. From Figs. 7 and 8, one can conclude that the collisions of

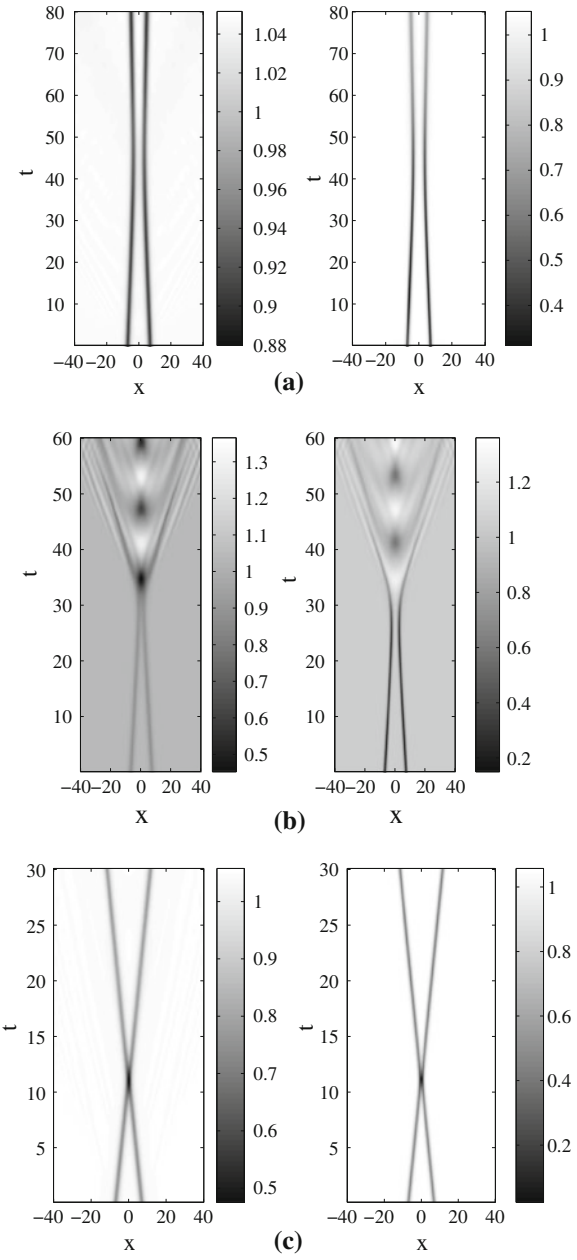

Fig. 6 As Fig. 1, but the even symmetric collision of FAs for (**a**) $v = 0.1$, (**b**) $v = 0.2$ and (**c**) $v = 0.6$. In *all panels* $k = 0.1$

two slowly moving FAs or a moving and a static FA are strongly inelastic. The radiation after the collision is so pronounce that it can be difficult to identify the outputs of the collisions.

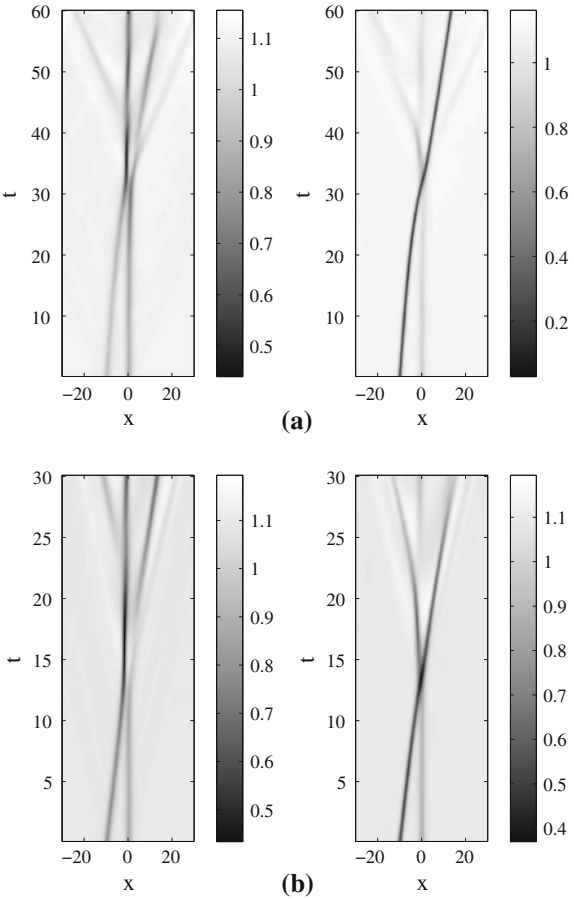

Fig. 7 Numerical evolutions of the odd symmetric collisions of two FAs when one of them is static while the other is moving with velocity (**a**) $v = 0.2$ and (**b**) $v = 0.6$. In *both panels* $k = 0.1$

3.4 Stationary Multiple FAs and Dark Solitons in the Presence of Magnetic Trap

In this section, we will consider the existence, stability and time-dynamics of multiple FAs and dark solitons in the coupled NLS equations (1) in the presence of a magnetic trap. In particular, we consider stationary solutions of the governing equations.

To seek for static solutions in the time-independent framework of (1), we use a Newton–Raphson continuation method. The spatial second order derivative is approximated using central finite differences with three-point or five-point stencils. At the computational boundaries, we use Neumann boundary conditions. In all the calculations, the grid spacing $\Delta x = 0.2$ or smaller. Numerical linear stability analysis of a solution $\psi_j^{(0)}(x)$ is then performed by looking for perturbed solutions of the form

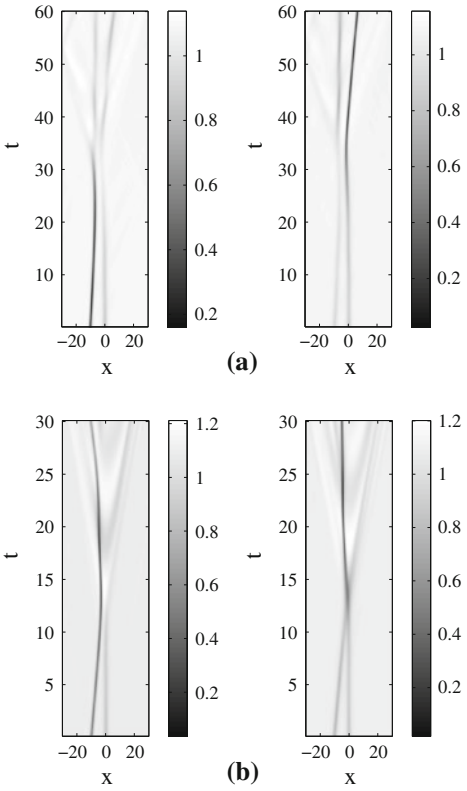

Fig. 8 As Fig. 7, but the even symmetric collision of FAs for (**a**) $v = 0.2$ and (**b**) $v = 0.6$. In *both panels* $k = 0.1$

$$\psi_j = \psi_j^{(0)}(x) + \epsilon[a_j(x)e^{i\lambda t} + b_j^*(x)e^{-i\lambda^* t}], \quad j = 1, 2.$$

Substituting the ansatz into the governing equation (1) and keeping the linear terms in ϵ, one will obtain a linear eigenvalue problem for the stability of $\psi_j^{(0)}$. The ensuing eigenvalue problem is then discretized using a similar finite difference scheme as above and solved numerically for the eigenfrequency λ and corresponding eigenfunctions a_j and b_j. It is then clear that $\psi_j^{(0)}(x)$ is a stable solution if the imaginary parts of all the eigenvalues vanish, i.e. $\mathrm{Im}(\lambda) = 0$.

3.4.1 $(+-)$-Configuration of FAs

First, we consider the $(+-)$-configuration of FA solutions of (1), which is shown in Fig. 9. The amplitude of the imaginary parts of the solution reduces with k and ultimately become zero at a critical value k_{ce}, when we obtain coupled dark solitons. The imaginary parts remain zero for all values of k greater than or equal to k_{ce}.

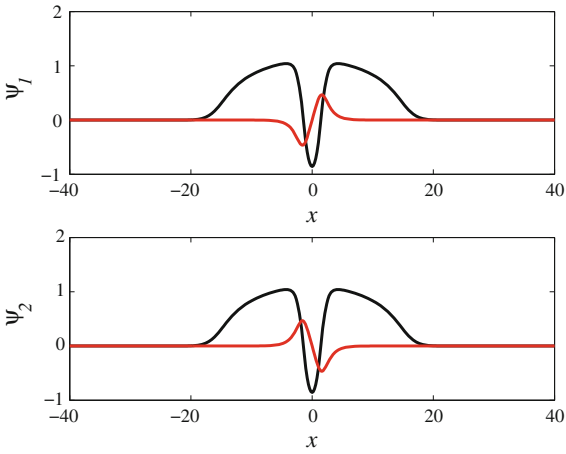

Fig. 9 Numerically obtained multiple FAs with a $(+-)$-configuration for $\Omega = 0.1$, $\rho_0 = 1$, $k = 0.2$

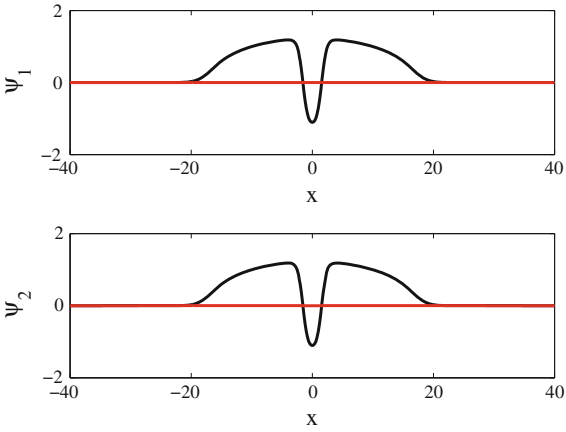

Fig. 10 Coupled dark soliton solutions for $\Omega = 0.1$, $\rho_0 = 1$, $k = 0.5$

We have calculated the existence and stability of FA solutions for different non-zero values of trapping parameter Ω. The critical value k_{ce} for which this FA solution changes into dark soliton decreases with the increment of Ω. The conversion of FAs into coupled dark solitons for $\Omega = 0.1$ is shown in Fig. 10. The variation in the value of Ω also affects the stability of the solution. The critical coupling k_{cs} where the solution becomes stable increases with Ω. In this case, the value of k_{cs} always remains greater than its corresponding value of k_{ce}. This shows that the $(+-)$-configuration of FA solution is completely unstable for all values of k where it exists. We note that the value of k_{cs} corresponding to a specific value of Ω is actually the critical value for dark soliton at which it attains stability. The eigenvalue structure of FAs for a specific value of Ω is displayed in Fig. 11 showing that most of the eigenvalues are real as they are lying on the horizontal

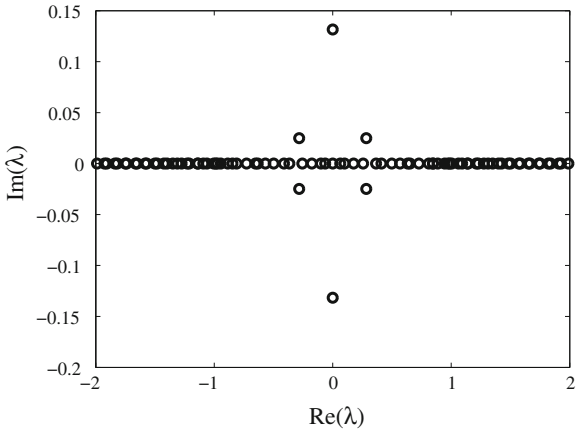

Fig. 11 The eigenvalue structure of the soliton in Fig. 9 in the complex plane

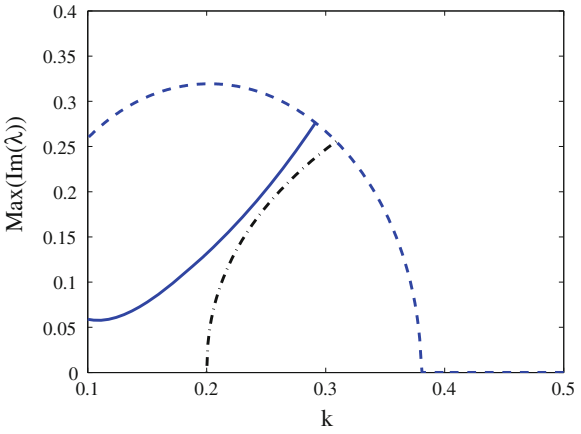

Fig. 12 The graph of k and the maximum imaginary parts of eigenvalues for $\Omega = 0.1$. The *solid* and *dashed curves* represent the trajectory of the most unstable eigenvalue for FAs and dark soliton as a function of k, respectively. The *dash-dotted curve* represents the approximation (30) for the oscillation frequency of the $(+-)$-configuration of FAs

axis, while few of them are complex. The most unstable eigenvalues are purely imaginary. The magnitude of the most unstable pair of eigenvalues increases for all $k \leq k_{ce}$ and then decreases with k and ultimately becomes zero at $k = k_{cs}$. The stability curve is shown in Fig. 12 by a solid curve. In the figure, we also present the stability curve of coupled dark solitons in dashed line. At $k = k_{ce}$ the solid and dashed curves meet. This corresponds to the situation when FAs turn into dark solitons, i.e. $k = k_{ce}$ is a pitchfork bifurcation point. The dark soliton becomes stable for $k \geq k_{cs}$. The dashed dotted curve shows the approximation (30) obtained through a variational approach for $\Omega = 0.1$, where one can see that a qualitatively good agreement is obtained.

In order to verify our results, we solve the time-dependent system (1) numerically for the configuration of FA solutions above. For $\Omega = 0.1$ and $k = 0.2$, the numerical evolution of the unstable FA solutions represented by ψ_1 and ψ_2 is shown in Fig. 13. Different from the collisions of two moving FAs with $(+-)$-

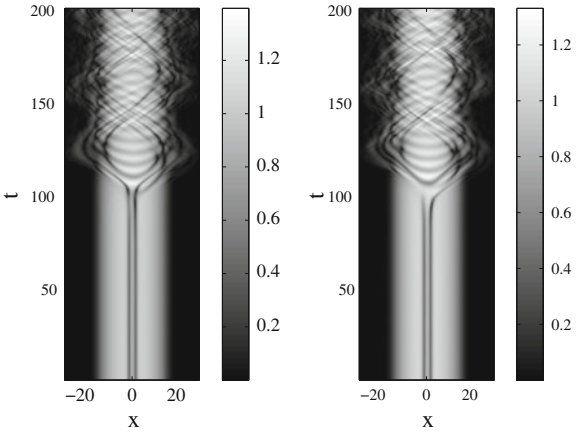

Fig. 13 Numerical evolution of the solution shown in Fig. 9 for $\Omega = 0.1$ and $k = 0.2$

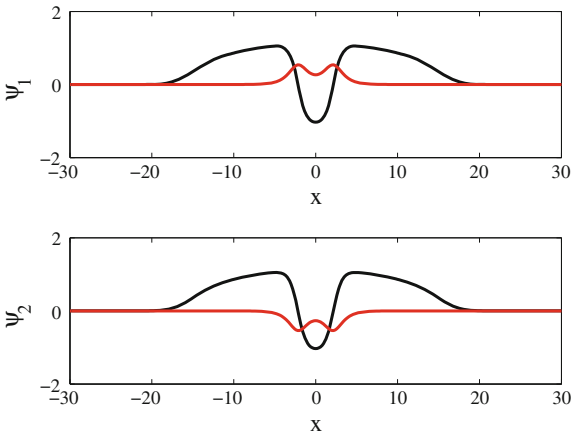

Fig. 14 Numerically obtained FAs for a $(++)$-configuration with $\Omega = 0.1$, $\rho_0 = 1$, $k = 0.25$

configuration that are attractive (see Fig. 5), the dynamics of unstable stationary FAs in here is rather repulsive. This can be seen in Fig. 13 where at $t \approx 100$ the FAs are moving away from each other.

3.4.2 $(++)$-Configuration of FAs

Finally, we consider FA solutions of (1) with $(++)$-configuration as shown in Fig. 14. Similarly to the $(+-)$-configuration, the imaginary parts of the solution reduces to zero with k and at the critical value $k = k_{ce}$ coupled dark solitons are obtained. The critical value k_{ce} increases with Ω. The change in the value of Ω also changes the critical value k_{cs} for the stability of this solution. For $\Omega = 0.1$, the $(++)$-configuration of FA solution is unstable for $k < 0.16$ due to two pairs of purely imaginary eigenvalues. The solution remains stable up to $k = 0.21$, at which two pairs of unstable eigenvalues emerge from the spectrum. The imaginary

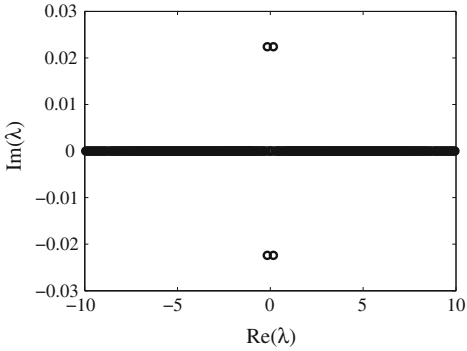

Fig. 15 The eigenvalue structure of the soliton in Fig. 14. All eigenvalues are real except two pairs of eigenvalues, which are complex, indicating the instability of the solution

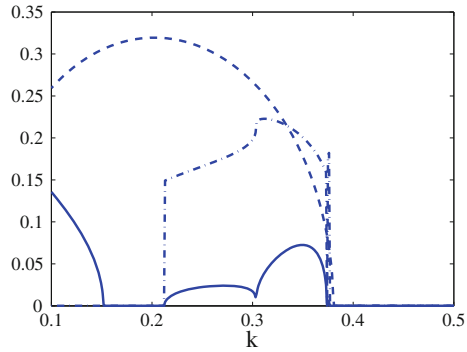

Fig. 16 The trajectory of the most unstable eigenvalue λ_{max} corresponding to $\Omega = 0.1$ for FAs solution with the $(++)$-configuration. The imaginary part of λ_{max} is represented by the *solid curve*. The *dashed line* is the eigenvalue of coupled dark solitons (see Fig. 12). The *dash-dotted curve* shows the real part of λ_{max} indicating an oscillatory instability when it is nonzero

part of the unstable eigenvalues becomes zero at $k = 0.38$ showing that the solution is stable for $k \geq 0.38$. The eigenvalues structure for $\Omega = 0.1$ and $k = 0.25$ is shown in Fig. 15. Since this solution changes into a dark soliton at $k = 0.38$, so the dark soliton is unstable for $k < 0.38$ but becomes stable for $k \geq 0.38$. The stability curve for $\Omega = 0.1$ is shown in Fig. 16 by solid line. The real part of the most unstable eigenvalue as a function of k is displayed in the same figure by dashed line. At $k = k_{ce}$, the $(++)$-configuration in FA solutions merges with dark solitons, similarly to the case of $(+-)$-configuration in a pitchfork bifurcation. Note that our analytical result (30) cannot be used to approximate the instability of the $(++)$-configuration. It is because (30) only yields purely imaginary eigenvalues while the instability of the solution here is oscillatory.

The results obtained for the $(++)$-configuration of FA solutions above are also verified by direct numerical integration of the time-dependent system (1). A typical evolution of unstable FA solutions is shown in Fig. 17 for $\Omega = 0.1$ and $k = 0.1$. In a similar fashion as the $(+-)$-configuration (see Fig. 13), the FAs repel each other. One difference between Figs. 13 and 17 is that in the latter case the break up is preceded by oscillations of the soliton pair. This is caused by the fact that the instability is oscillatory.

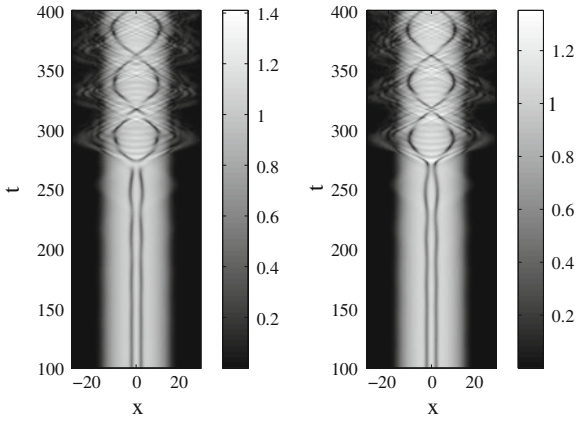

Fig. 17 Numerical evolution of the solution shown in Fig. 14

4 Conclusion

We have studied the existence and stability of multiple FAs and coupled dark solitons in linearly coupled Bose–Einstein condensates. In the absence of a harmonic trap, we have shown numerically that the interactions of the solitary waves are strongly inelastic, especially in the case of slow incoming velocities. Symmetric and asymmetric interactions of coupled dark solitons as well as FA solutions for different values of velocity were discussed. Interesting outcomes, such as breathers that do not exist in the uncoupled case, due to the inelastic collisions of FAs were observed. In the presence of a magnetic trap, bound states of solitons were shown to exist. The effects of variation of the trapping strength on the existence and stability of the multiple solitary waves were investigated numerically. It is found that for FAs with the $(+-)$-configuration, the critical coupling for existence k_{ce} decreases while the critical value for stability k_{cs} increases with the magnetic strength Ω. For the $(++)$-configuration, both k_{ce} and k_{cs} increase with Ω. An analytical approximation was derived based on variational formulations to calculate the oscillation frequency of FA solutions with the $(+-)$-configuration, where a qualitatively good agreement was obtained.

References

1. B.D. Josephson, Phys. Lett. **1**, 251 (1962)
2. A. Smerzi, S. Fantoni, S. Giovanazzi, S.R. Shenoy, Phys. Rev. Lett. **79**, 4950 (1997)
3. S. Raghavan, A. Smerzi, S. Fantoni, S.R. Shenoy, Phys. Rev. A **59**, 620–633 (1999)
4. S. Giovanazzi, A. Smerzi, S. Fantoni, Phys. Rev. Lett. **84**, 4521 (2000)
5. M. Albiez, R. Gati, J. Folling, S. Hunsmann, M. Cristiani, M.K. Oberthaler, Phys. Rev. Lett. **95**, 010402 (2005)
6. S. Levy, E. Lahoud, I. Shomroni, J. Steinhauer, Nature **449**, 579 (2007)

7. F.S. Cataliotti, S. Burger, C. Fort, P. Maddaloni, F. Minardi, A. Trombettoni, A. Smerzi, M. Inguscio, Science **293**, 843 (2001)
8. E.A. Ostrovskaya, Yu.S. Kivshar, M. Lisak, B. Hall, F. Cattani, D. Anderson, Phys. Rev. A **61**, 031601-4 (2000)
9. D. Ananikian, T. Bergeman, Phys. Rev. A **73**, 013604 (2006)
10. D. Ananikian, T. Bergeman, Phys. Rev. A **74**, 039905(E) (2006)
11. X.Y. Jia, WD. Li, J.Q. Liang, Phys. Rev. A **78**, 023613 (2008)
12. A. Barone, G. Paterno, *Physics and Applications of the Josephson Effect* (Wiley, New York, 1982)
13. V.M. Kaurov, A.B. Kuklov, Phys. Rev. A **71**, 011601 (2005)
14. V.M. Kaurov, A.B. Kuklov, Phys. Rev. A **73**, 013627 (2006)
15. A.V. Ustinov, Physica D **123**, 315 (1998)
16. J. Brand, T.J. Haigh, U. Zülicke, Phys. Rev. A **80**, 011602(R) (2009)
17. M.I. Qadir, H. Susanto, P.C. Matthews, J. Phys. B: At. Mol. Opt. Phys. **45**, 035004 (2012)
18. A. Gubeskys, B.A. Malomed, Phys. Rev. A **75**, 063602 (2007)
19. B.A. Malomed, Phys. Rev. E **50**, 1565 (1994)
20. B.A. Malomed, A.A. Nepomnyashchy, Europhys. Lett. **27**, 649 (1994)
21. N. Dror, B.A. Malomed, J. Zeng, Phys. Rev. E **84**, 046602 (2011)
22. V.E. Zakharov, A.B. Shabat, Sov. J. Exp. Theor. Phys. **37**, 823 (1973)
23. Y.S. Kivshar, W. Krolikowski, Opt. Commun. **114**, 353–362 (1995)
24. N. Akhmediev, A. Ankiewicz, Phys. Rev. A **77**, 3213 (1993)
25. V.V. Konotop, in *Emergent Nonlinear Phenomena in Bose–Einstein Condensates Theory and Experiment*, ed. by P.G. Kevrekidis, D.J. Frantzeskakis, R. Carretero-González (Springer, Berlin, 2008), pp. 65–97
26. D.J. Frantzeskakis, J. Phys. A: Math. Theor. **43**, 213001 (2010)
27. D.E. Pelinovsky, D.J. Frantzeskakis, P.G. Kevrekidis, Phys. Rev. E **72**, 016615 (2005)
28. G. Theocharis, A. Weller, J.P. Ronzheimer, C. Gross, M.K. Oberthaler, P.G. Kevrekidis, D.J. Frantzeskakis, Phys. Rev. A **81**, 063604 (2010)
29. A. Weller, J.P. Ronzheimer, C. Gross, J. Esteve, M.K. Oberthaler, D.J. Frantzeskakis, G. Theocharis, P.G. Kevrekidis, Phys. Rev. Lett. **101**, 130401 (2008)
30. S. Burger, K. Bongs, S. Dettmer, W. Ertmer, K. Sengstock, A. Sanpera, G.V. Shlyapnikov, M. Lewenstein, Phys. Rev. Lett. **83**, 5198 (1999)
31. C. Becker, S. Stellmer, P. Soltan-Panahi, S. Dörscher, M. Baumert, E.-M. Richter, J. Kronjäger, K. Bongs, K. Sengstock, Nat. Phys. **4**, 496 (2008)
32. S. Stellmer, C. Becker, P. Soltan-Panahi, E.-M. Richter, S. Dörscher, M. Baumert, J. Kronjäger, K. Bongs, K. Sengstock, Phys. Rev. Lett. **101**, 120406 (2008)
33. Yu.S. Kivshar, B. Luther-Davies, Phys. Rep. **298**, 81–197 (1998)
34. D.J. Frantzeskakis, G. Theocharis, F.K. Diakonos, P. Schmelcher, Yu.S. Kivshar, Phys. Rev. A **66**, 053608 (2002)
35. L. Hong, W. Dong-Ning, Chin. Phys. B **18**, 2659 (2009)
36. Th. Busch, J.R. Anglin, Phys. Rev. Lett. **84**, 2298–2301 (2000)
37. I.V. Barashenkov, S.R. Woodford, E.V. Zemlyanaya, Phys. Rev. Lett. **90**, 054103 (2003)
38. I.V. Barashenkov, S.R. Woodford, E.V. Zemlyanaya, Phys. Rev. E **75**, 026604 (2007)

Symmetry-Breaking Effects for Polariton Condensates in Double-Well Potentials

A. S. Rodrigues, P. G. Kevrekidis, J. Cuevas, R. Carretero-González and D. J. Frantzeskakis

Abstract We study the existence, stability, and dynamics of symmetric and anti-symmetric states of quasi-one-dimensional polariton condensates in double-well potentials, in the presence of nonresonant pumping and nonlinear damping. Some prototypical features of the system, such as the bifurcation of asymmetric solutions, are similar to the Hamiltonian analog of the double-well system considered in the realm of atomic condensates. Nevertheless, there are also some nontrivial differences including, e.g., the unstable nature of both the parent and the daughter branch emerging in the relevant pitchfork bifurcation for slightly larger values of atom numbers. Another interesting feature that does not appear in the atomic condensate case is that the bifurcation for attractive interactions is slightly sub-critical instead of supercritical. These conclusions of the bifurcation analysis

A. S. Rodrigues
Departamento de Física/CFP, Faculdade de Ciências, Universidade do Porto,
R. Campo Alegre, 687, 4169-007 Porto, Portugal

P. G. Kevrekidis
Department of Mathematics and Statistics, University of Massachusetts,
Amherst, MA 01003-4515, USA

J. Cuevas
Grupo de Física No Lineal, Departamento de Física Aplicada I, Escuela Politécnica
Superior, Universidad de Sevilla, C/ Virgen de África, 7, 41011 Sevilla, Spain

R. Carretero-González (✉)
Nonlinear Dynamical Systems Group, Department of Mathematics and Statistics,
Computational Science Research Center, San Diego State University,
San Diego, CA 92182-7720, USA
e-mail: carreter@sciences.sdsu.edu
URL: http://nlds.sdsu.edu

D. J. Frantzeskakis
Department of Physics, University of Athens, Panepistimiopolis,
Zografos, 157 84 Athens, Greece

Progress Optical Sci., Photonics (2013): 509–529
DOI: 10.1007/10091_2012_13

Published Online: 28 July 2012

are corroborated by direct numerical simulations examining the dynamics of the system in the unstable regime.

1 Introduction

Over the past few years, a novel direction in the study of Bose–Einstein condensation has captured a considerable amount of attention. This concerns the observation of exciton–polariton Bose–Einstein condensates (BECs) in semiconductor microcavities [1–4]. A fundamental feature of these exciton–polariton BECs is that, upon confinement, the excitons (bound pairs of electrons and holes) couple strongly to the incident light creating the polariton quasi-particles [5, 6]. The resulting exciton–polariton BEC possesses a number of remarkable properties that we briefly touch upon below.

The radiative lifetime of the polaritons is the shorter relaxation time scale of the system being of the order of 1–10 ps [7]. On the other hand, the light mass of the exciton–polaritons provides this system with a significantly higher condensation temperature. The photonic component of the exciton–polaritons is responsible for their short lifetime which, in turn, does not allow thermalization; instead, it produces a non-equilibrium condensate, wherein the presence of external pumping from an exciton reservoir is critical towards a counter-balance of the polariton loss. In such genuinely non-equilibrium condensates, numerous remarkable features have been not only theoretically predicted but also experimentally established; these include the flow without scattering (analog of the flow without friction) [8], the existence of vortices [9] (see also Ref. [10] for vortex dipole dynamics and Ref. [11] for observations thereof), the collective dynamics [12], as well as remarkable applications such as spin switches [13] and light emitting diodes [14] operating even near room temperatures.

Perhaps the most customary approach to modeling exciton–polariton BECs involves the coupling of the evolution of the polaritons to that of the exciton reservoir which enables their production (and which features diffusive spatial dynamics of the excitons); this way, the model takes the form of two coupled complex Ginzburg–Landau (cGL) equations describing the evolution of exciton and photon wavefunctions [15–17]. Nevertheless, it has been proposed in Refs. [18–20] that a single cGL equation for the macroscopically occupied polariton state can also be used in a way consistent with experimental observations [21]. A similar approach was followed in Ref. [22] where a BEC of magnon quasi-particles, incorporating a source term rather than an amplification of the field, was shown to be phenomenologically described by a system two nonlinearly coupled cGL-type equations. In the context of the single cGL model for the polaritons, there exists a localized (pumping) region of gain and a nonlinear saturating loss term, in addition to all the standard terms (quantum pressure, external parabolic trapping and repulsive interatomic interaction) that one encounters in atomic BECs [23–25].

Furthermore, it should be pointed out that the prototypical setting where experiments have been conducted is two-dimensional in nature. Yet, highly anisotropic traps (similar to what has been done in atomic BECs [23–25]) can be envisioned which reduce the effective dynamics to a quasi one-dimensional (1D) setting [26–31]. Moreover, recent experimental advances have enabled the use of thin microwires in order to guide the condensates along the direction of the wire [32]. In this setting, the recent analysis of Ref. [33] presented a number of striking characteristics due to the interplay of gain and loss terms with the standard ones of atomic BECs. Prominent examples included the destabilization of the nodeless state of the system and the creation of stability inversions (where states with nodes would be more robust), as well as the existence of bubble-like and sawtooth-like solutions in the system.

A very interesting research direction in the physics of atomic and polariton BECs concerns the dynamics of the condensates in a double-well potential. The latter can be created in atomic BEC experiments through the combination of a parabolic trap and a periodic (so-called optical lattice) potential generated through the interference of laser beams illuminating the BEC [34]. Relevant experiments in atomic BECs [35, 36] have paved the way towards the exploration of numerous features such as tunneling and Josephson oscillations for small numbers of atoms in the condensate, and macroscopic quantum self-trapped states, as well as symmetry-breaking effects for large atom numbers. On the other hand, double-well potentials can also be created in polariton BEC experiments in microcavities by applying stress [2, 37], by employing photolithographic techniques [26, 27], or allowing natural formation during the sample growth [38]. Importantly, the latter technique was used for the study of a "polariton Josephson junction" [38], in the spirit of earlier studies on "bosonic Josephson junctions" [39] in the context of atomic BECs. Importantly, a large volume of theoretical studies has accompanied these developments, first in the context of atomic BECs, through investigations related to finite-mode reductions and symmetry-breaking bifurcations [40–49], quantum effects [50], and nonlinear variants of the double-well potential [51], and more recently in the context of polariton condensates, especially as concerns Josephson oscillations therein [52–55]. It should be mentioned in passing that similar (spontaneous symmetry breaking) effects have been monitored in the realm of nonlinear optics: in this context, formation of asymmetric states in dual-core fibers [56–62], self-guided laser beams in Kerr media [63], and optically-induced dual-core waveguiding structures in photorefractive crystals [64] have been reported.

It is the aim of the present work to combine these two themes, namely the focus on the exciton–polariton BEC with pumping and loss and the fundamental interest in the understanding of double-well trapping potentials in a spirit similar to the proposal of Ref. [15]. In particular, we will consider the single-component model of Refs. [18–20] combined with a double-well potential in a quasi-1D (e.g., microwire) setting. We will attempt a systematic (Galerkin) finite-dimensional reduction of the system via projection to the two principal eigenstates of the potential, and will derive a damped-driven system of ordinary differential

equations (ODEs) that have been shown in the Hamiltonian case to capture the essence of the statics [65] and dynamics [66] of double-well potentials. We will then examine the bifurcation structure of the resulting ODEs and compare it to that of the original partial differential equation (PDE) model. This already provides us with a number of interesting features that distinguish this system from its Hamiltonian analog. For instance, in the case of attractive interatomic interactions (which is studied together with that of repulsive interactions) the relevant symmetry-breaking pitchfork bifurcation is subcritical instead of supercritical as in the Hamiltonian case. Furthermore, both branches that emerge from the pitchfork bifurcations, the stable asymmetric one and the (now) unstable "parent" branch, both appear to become destabilized in this polariton BEC setting for slightly larger nonlinearities, posing the natural question of what is the stable dynamics for larger values of the nonlinearity. These questions will in part be addressed via direct numerical simulations.

Our presentation will be structured as follows. First, in Sect. 2, we will present the model and its theoretical study via the Galerkin analysis. In Sect. 3, we will study the model numerically and compare the results of the numerical bifurcation analysis with the prediction of the Galerkin approximation. We will also complement these results with direct numerical simulations of the original model. Finally, in Sect. 4 we summarize our results and present our conclusions.

2 Model Setup and Analytical Predictions

In our analysis below, we adopt the model of Refs. [18–20]. It has been argued in these works that the original exciton–polariton system given by a set of two coupled equations can be effectively reduced to a single cGL equation with a nonlinear saturating loss term. This reduction can be used when the reservoir mean-field potential is negligible and the spot size is large compared with the condensate size (i.e., if we can consider that the spot width is the same as the spatial extent of the system). In particular, the amplification of the existing field introduces a gain and hence acts as a generator of polaritons. Then the loss term saturates this gain beyond a certain threshold. These two terms are analogous to the pumping of polaritons from the excitons and to the natural decay of the polaritons. This reduced model can be expressed in dimensionless form as follows:

$$i\partial_t u = -\partial_x^2 u + s|u|^2 u + V(x)u - \mu u + i\left[\chi(x) - \sigma|u|^2\right]u. \tag{1}$$

The above model is actually a complex Ginzburg–Landau equation [67] for the complex order parameter $u(x,t)$, which is assumed to evolve in the presence of the effectively-1D double-well potential $V(x)$. Equation (1) can be applied to both the contexts of atomic and polariton BECs: in the first case, the two last terms in the right-hand side of Eq. (1) are absent, and the model—known as the

Gross-Pitaevskii equation [23–25]—describes the evolution of the macroscopic wavefunction for the cold atoms and μ is the chemical potential; in the second case, $u(x,t)$ denotes the polariton wavefunction, and the last two terms in the right-hand side are included in the model. More specifically, in the context of polariton condensates, Eq. (1) incorporates (a) the spatially dependent gain term of the form

$$\chi(x) = \alpha\Theta(x_m - |x|), \tag{2}$$

where Θ is the step function generating a symmetric pumping spot of "radius" x_m and strength α for the gain, and (b) a nonlinear saturation loss term, characterized by its strength σ. As concerns the parameter $s \equiv \pm 1$, it sets the type of nonlinearity (i.e., the type of interactions between atoms or polaritons): for $s = +1$ the nonlinearity is defocusing (i.e., the interactions are repulsive), while for $s = -1$ the nonlinearity is focusing (i.e., the interactions are attractive). In the context of atomic BECs, the value of s depends on the atom species (e.g., $s = +1$ for ^{87}Rb or ^{23}Na, while $s = -1$ for ^{7}Li or ^{85}Rb atoms). On the other hand, in the context of polariton condensates, the sign of the effective mass of polaritons [i.e., the sign of the first term in the right-hand side of Eq. (1)] may become either positive or negative, depending on the values of transverse momentum: in fact, the transition from positive to negative mass is associated with the inflection point of the energy-momentum diagram [68, 69]. Here, we will consider both cases of $s = \pm 1$ to take into regard that the effective polariton mass may be positive or negative, respectively. We finally note that the relevant physical time and space scales, as well as physically relevant parameter values associated with Eq. (1), can be found in Ref. [18].

In what follows, we will use the Galerkin (few mode truncation) approach of Ref. [49]. A similar approach, in the absence of external confining potential, has been used in Ref. [70] for a polariton laser. We start by considering the corresponding linear eigenproblem which reads:

$$Hu \equiv -\partial_x^2 u + V(x)u = \omega u, \tag{3}$$

whose spectrum consists of a ground state, $u_0(x)$, and excited states, $u_i(x)$ (with $i \geq 1$). Then, in the weakly nonlinear regime, we consider a superposition of the two lowest linear eigenmodes,

$$u(x,t) = c_0(t)u_0(x) + c_1(t)u_1(x), \tag{4}$$

where $c_{0,1}(t)$ are unknown time-dependent complex prefactors; obviously, the above ansatz is relevant for values of the chemical potential μ such that higher order modes can be safely ignored. Substituting this ansatz into Eq. (1) we obtain:

$$\begin{aligned} i(\dot{c_0}u_0 + \dot{c_1}u_1) = {} & (\omega_0 - \mu)u_0c_0 + (\omega_1 - \mu)u_1c_1 + s|u|^2(c_0u_0 + c_1u_1) \\ & + i\left[\chi(x) - \sigma|u|^2\right](c_0u_0 + c_1u_1), \end{aligned} \tag{5}$$

where the $|u|^2$ has not been expanded only for reasons of compactness but should actually be thought as expanded according to Eq. (4). Next, projecting on u_0 and u_1 (i.e., multiplying the above equation by u_0 and u_1 and integrating over x), and using the orthogonality of the states u_i, we respectively derive the following equations:

$$\begin{aligned} i\dot{c_0} &= (\omega_0 - \mu + i\alpha_0)c_0 \\ &+ (s - i\sigma)\Big\{A_0|c_0|^2c_0 + \Big(c_0^2c_1^* + 2|c_0|^2c_1\Big)\Gamma_0 + \Big(2|c_1|^2c_0 + c_1^2c_0^*\Big)B + |c_1|^2c_1\Gamma_1\Big\}, \end{aligned} \tag{6}$$

and

$$\begin{aligned} i\dot{c_1} &= (\omega_1 - \mu + i\alpha_1)c_1 \\ &+ (s - i\sigma)\Big\{\Gamma_0|c_0|^2c_0 + \Big(c_0^2c_1^* + 2|c_0|^2c_1\Big)B + \Big(2|c_1|^2c_0 + c_1^2c_0^*\Big)\Gamma_1 + |c_1|^2c_1A_1\Big\}. \end{aligned} \tag{7}$$

In the above equations, overdots denote time derivatives, the involved constants (depending on the eigenbasis $\{u_i\}$) take the values $A_0 = \int u_0^4 dx$, $A_1 = \int u_1^4 dx$, $B = \int u_0^2 u_1^2 dx$, $\Gamma_0 = \int u_1 u_0^3 dx$, and $\Gamma_1 = \int u_0 u_1^3 dx$, while the effective gain coefficients read: $\alpha_0 = \int \chi(x) u_0^2 dx$ and $\alpha_1 = \int \chi(x) u_1^2 dx$. We now use amplitude and phase variables for the time-dependent prefactors, i.e., $c_i = \rho_i e^{i\phi_i}$ (with the amplitudes ρ_i and phases ϕ_i being real functions), to derive a set of four equations for the unknown functions $\rho_{0,1}$ and $\phi_{0,1}$. Introducing the relative phase of the first two modes as $\varphi \equiv \phi_1 - \phi_0$, the above mentioned set of equations takes the following form:

$$\begin{aligned} \dot{\rho}_0 &= \alpha_0\rho_0 - \sigma\big(A_0\rho_0^3 + 2B\rho_1^2\rho_0\big) + s\big(\Gamma_1\rho_1^3 + \Gamma_0\rho_0^2\rho_1\big)\sin\varphi \\ &+ sB\rho_1^2\rho_0 \sin 2\varphi - \sigma\big(\Gamma_1\rho_1^3 + 3\Gamma_0\rho_0^2\rho_1\big)\cos\varphi - \sigma B\rho_1^2\rho_0\cos 2\varphi, \end{aligned} \tag{8}$$

$$\begin{aligned} \dot{\phi}_0 &= -(\omega_0 - \mu) - s\big(A_0\rho_0^2 + 2B\rho_1^2\big) - \sigma\big(\Gamma_0\rho_0\rho_1 + \Gamma_1\rho_1^3/\rho_0\big)\sin\varphi \\ &- \sigma B\rho_1^2 \sin 2\varphi - s\big(3\Gamma_0\rho_0\rho_1 + \Gamma_1\rho_1^3/\rho_0\big)\cos\varphi - sB\rho_1^2\cos 2\varphi, \end{aligned} \tag{9}$$

$$\begin{aligned} \dot{\rho}_1 &= \alpha_1\rho_1 - \sigma\big(A_1\rho_1^3 + 2B\rho_0^2\rho_1\big) - s\big(\Gamma_0\rho_0^3 + \Gamma_1\rho_1^2\rho_0\big)\sin\varphi \\ &- sB\rho_0^2\rho_1 \sin 2\varphi - \sigma\big(\Gamma_0\rho_0^3 + 3\Gamma_1\rho_1^2\rho_0\big)\cos\varphi - \sigma B\rho_0^2\rho_1\cos 2\varphi, \end{aligned} \tag{10}$$

and

$$\begin{aligned} \dot{\phi}_1 &= -(\omega_1 - \mu) - s\big(A_1\rho_1^2 + 2B\rho_0^2\big) + \sigma\big(\Gamma_1\rho_1\rho_0 + \Gamma_0\rho_0^3/\rho_1\big)\sin\varphi \\ &+ \sigma B\rho_0^2 \sin 2\varphi - s\big(3\Gamma_1\rho_1\rho_0 + \Gamma_0\rho_0^3/\rho_1\big)\cos\varphi - sB\rho_0^2\cos 2\varphi. \end{aligned} \tag{11}$$

Subtracting Eq. (9) from Eq. (11), we can readily obtain an equation for φ, namely:

$$\begin{aligned}\dot{\varphi} = &-\Delta\omega - s\left(A_1\rho_1^2 - A_0\rho_0^2\right) - sB[2+\cos 2\varphi]\left(\rho_0^2-\rho_1^2\right)\\ &- s\frac{\cos\varphi}{\rho_0\rho_1}\left(\Gamma_0\rho_0^2(\rho_0^2-3\rho_1^2)+\Gamma_1\rho_1^2(3\rho_0^2-\rho_1^2)\right)\\ &+\sigma\frac{\sin\varphi}{\rho_0\rho_1}\left(\Gamma_0\rho_0^2(\rho_0^2+\rho_1^2)+\Gamma_1\rho_1^2(\rho_0^2+\rho_1^2)\right)+\sigma B\sin 2\varphi(\rho_0^2+\rho_1^2),\end{aligned} \tag{12}$$

where $\Delta\omega \equiv \omega_1 - \omega_2$. This way, we have arrived to a system of three equations [cf. Eqs. (8), (10) and (12)] for the unknown functions $\rho_{0,1}$ and φ. These equations are subject to an additional constraint stemming from the balance condition $dN/dt = 0$, where $N \equiv \int_{-\infty}^{+\infty}|u|^2dx$ is the number of polaritons (mathematically the squared L^2 norm). The evolution of the latter, can readily be found by multiplying Eq. (1) by u^*, the complex conjugate of Eq. (1) by u, and then adding and integrating the resulting equations. It is straightforward to find that the condition for equilibrium is:

$$\int_{-\infty}^{+\infty}\left(\chi(x)-\sigma|u|^2\right)|u|^2dx = 0. \tag{13}$$

Substituting Eq. (4) into Eq. (13), also using the polar decomposition for $c_i(t)$ [and assuming a definite—even in our considerations—parity for the function $\chi(x)$], we find that the balance condition (13) takes the form:

$$\begin{aligned}\left(\alpha_0\rho_0^2+\alpha_1\rho_1^2\right) - \sigma\left(A_0\rho_0^4+\rho_1^4A_1+4\rho_0^2\rho_1^2B\right) - 4\sigma\left(\rho_0^3\rho_1\Gamma_0+\rho_1^3\rho_0\Gamma_1\right)\cos\varphi\\ - 2\sigma\rho_0^2\rho_1^2B\cos 2\varphi = 0,\end{aligned} \tag{14}$$

which essentially fixes ρ_1 once ρ_0 and φ are found and thus reducing the effective number of degrees of freedom for our approximations to only two (ρ_0 and φ).

Below, we will consider the case of a symmetric double-well potential, for which $\Gamma_1 = \Gamma_0 = 0$. In this case, Eqs. (8), (10) and (12) are reduced to the following simpler form,

$$\dot{\rho}_0 = \alpha_0\rho_0 - \sigma\left(A_0\rho_0^3+2B\rho_1^2\rho_0\right) + sB\rho_1^2\rho_0\sin 2\varphi - \sigma B\rho_1^2\rho_0\cos 2\varphi, \tag{15}$$

$$\dot{\rho}_1 = \alpha_1\rho_1 - \sigma\left(A_1\rho_1^3+2B\rho_0^2\rho_1\right) - sB\rho_0^2\rho_1\sin 2\varphi - \sigma B\rho_0^2\rho_1\cos 2\varphi, \tag{16}$$

$$\dot{\varphi} = -\Delta\omega - s\left(A_1\rho_1^2 - A_0\rho_0^2\right) - sB[2+\cos 2\varphi]\left(\rho_0^2-\rho_1^2\right) + \sigma B\sin 2\varphi(\rho_0^2+\rho_1^2), \tag{17}$$

while the equilibrium condition is accordingly simplified as:

$$\left(\alpha_0\rho_0^2+\alpha_1\rho_1^2\right) - \sigma\left(A_0\rho_0^4+\rho_1^4A_1+4\rho_0^2\rho_1^2B\right) - 2\sigma\rho_0^2\rho_1^2B\cos 2\varphi = 0. \tag{18}$$

We can now turn to the study of stationary solutions (i.e., $\dot{\rho}_0 = \dot{\rho}_1 = \dot{\varphi} = 0$) resulting from the Galerkin truncation analysis. Particularly, from Eq. (15) we obtain two possible solutions:

$$\begin{cases} (i) & \rho_0 = 0, \\ (ii) & \alpha_0 - \sigma\left(A_0\rho_0^2 + 2B\rho_1^2\right) + sB\rho_1^2 \sin 2\varphi - \sigma B\rho_1^2 \cos 2\varphi = 0, \end{cases} \tag{19}$$

while from Eq. (16) we obtain:

$$\begin{cases} (i) & \rho_1 = 0 \\ (ii) & \alpha_1 - \sigma\left(A_1\rho_1^2 + 2B\rho_0^2\right) - sB\rho_0^2 \sin 2\varphi - \sigma B\rho_0^2 \cos 2\varphi = 0. \end{cases} \tag{20}$$

Next, multiplying the nontrivial equilibria of Eq. (19) by ρ_0^2, the one from Eq. (20) by ρ_1^2, and adding the resulting equations, we obtain:

$$\cos 2\varphi = \frac{(\alpha_0\rho_0^2 + \alpha_1\rho_1^2) - \sigma\left(A_0\rho_0^4 + A_1\rho_1^4 + 4B\rho_0^2\rho_1^2\right)}{2\sigma B\rho_0^2\rho_1^2}, \tag{21}$$

while subtracting Eq. (20) from Eq. (19) yields:

$$\sigma\left(A_1\rho_1^4 - A_0\rho_0^4 + 2B(\rho_0^2 - \rho_1^2) + B(\rho_0^2 - \rho_1^2)\cos 2\varphi\right) + sB(\rho_0^2 + \rho_1^2)\sin 2\varphi + (\alpha_0 - \alpha_1) = 0. \tag{22}$$

Combining now Eq. (22) with Eq. (17) we finally obtain the result:

$$(\rho_0^2 + \rho_1^2)\sin 2\varphi = \frac{\sigma\Delta\omega - s(\alpha_0 - \alpha_1)}{B(\sigma^2 + s^2)}. \tag{23}$$

Let us now focus again on Eqs. (15) and (16): it is clear that if Eq. (16) is satisfied for $\rho_1 = 0$ then $\rho_0^2 = \frac{\alpha_0}{\sigma A_0}$, and if Eq. (15) is satisfied with $\rho_0 = 0$ then $\rho_1^2 = \frac{\alpha_1}{\sigma A_1}$. Aside from these trivial symmetric and anti-symmetric solutions, past the critical point for the symmetry breaking bifurcation, an asymmetric solution is expected to exist which possesses non-vanishing ρ_0 and ρ_1 (as well as a non-zero relative phase between them), which can be computed from Eq. (21). It is anticipated that the presence of loss and gain will not (generically) modify the nature of the bifurcations in comparison to the Hamiltonian case [49]. Namely, an asymmetric solution will bifurcate from the symmetric one in the focusing nonlinearity case of $s = -1$, due to a non-vanishing contribution of the anti-symmetric part in the solution, while on the contrary, an asymmetric mode will emanate from the anti-symmetric one in the defocusing nonlinearity setting of $s = 1$ (due to a symmetric contribution within the solution). These results are detailed for a particular case example potential in what follows and compared to full numerical results.

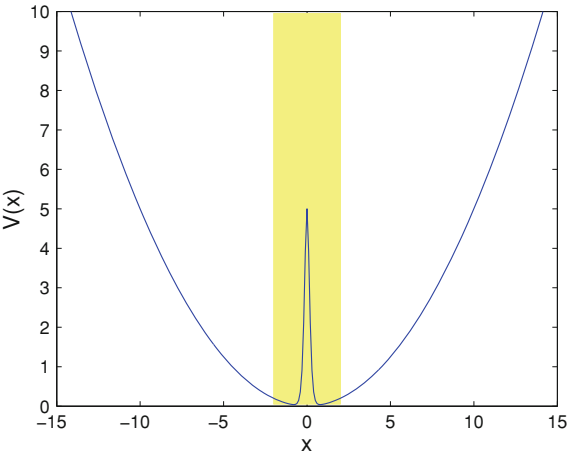

Fig. 1 The parabolic trapping potential and the localized barrier creating the double-well potential configuration. The parameter values used are: $\Omega^2 = 0.1$, $w = 0.2$, and $V_0 = 5$; the *shaded area* corresponds to the region where the pumping acts, i.e., $|x| < x_m = 2$ (Color online)

3 Numerical Results

In our theoretical approximations, the double-well potential is constructed by placing a localized barrier at the center of the parabolic trap potential of strength Ω. Particularly, the double-well potential is assumed to be of the form:

$$V(x) = \frac{1}{2}\Omega^2 x^2 + V_0 \mathrm{sech}\left(\frac{x}{w}\right), \tag{24}$$

where w is the width of the barrier and V_0 its height. The results presented below are for the potential parameters $\Omega^2 = 0.1$, $V_0 = 5$, and $w = 0.2$; we have checked that other parameter values lead to qualitatively similar results. For the gain we consider a strength $\alpha = 0.2$ and a spot size of $x_m = 2.0$. The damping parameter σ is used to vary the number of atoms, N, in order to do the continuation. For the above double-well potential, the values of the linear eigen-energies are $\omega_0 = 0.515729$ and $\omega_1 = 0.677697$. The potential setting under consideration is depicted in Fig. 1.

We have performed a continuation of symmetric, anti-symmetric and asymmetric states in both cases of repulsive and attractive interactions. The continuations have been performed by increasing the damping parameter σ, which is tantamount to decreasing the norm or chemical potential. It is important to note that the chemical potential is no longer a free parameter in the present setting in sharp contrast to what is the case in the Hamiltonian regime of atomic BECs (see also the discussion of Refs. [18, 33]). Similar results can be obtained by decreasing the pumping parameter α. However, a crucial realization that emerges from considering variations of the different parameters is that the spot size x_m must be chosen in a very limited range in order for the three above mentioned nonlinear modes to co-exist and be potentially stable; outside this range, instabilities lead to

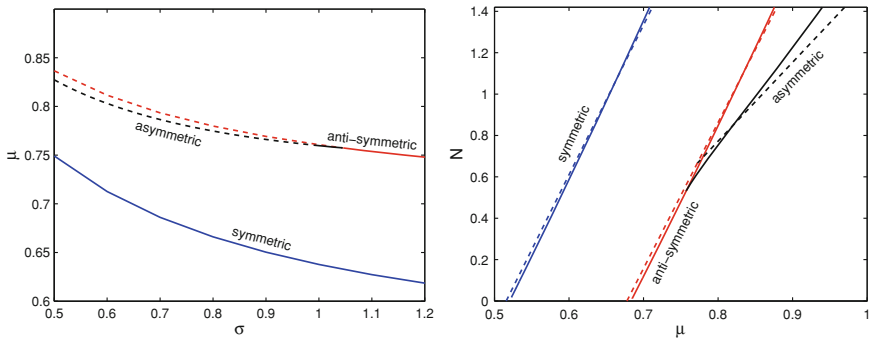

Fig. 2 Bifurcation diagrams for the symmetric, anti-symmetric and asymmetric branches for defocusing (repulsive) nonlinearity ($s = 1$). *Left* Dependence of the chemical potential on the damping parameter. *Right* Dependence of the (normalized) number of polaritons on the chemical potential. Unstable solutions are depicted by *dashed lines* on the *left panel*. On the *right solid lines* display numerical results obtained by a nonlinear (Newton-Raphson) solver of the steady state equations of the model of Eq. (1), while *dashed lines* display analytical results of our Galerkin approach. The linear modes are located at $\mu = 0.5157$ and 0.6667 (Color online)

breathing multi-bump coherent structures. In what follows, the values of $x_m = 2$ and $\alpha = 0.2$ have been used unless explicitly indicated otherwise.

3.1 Repulsive Case

We start by considering the case of the repulsive interaction with $s = +1$ (and vary σ as mentioned above). The family of symmetric solutions is found to be always stable. As expected, on the other hand, and in agreement to our expectation from the realm of atomic BECs, the anti-symmetric solutions are exponentially unstable for small σ, which is tantamount to large polariton population numbers N. They become stable after the symmetry-breaking pitchfork bifurcation occurring at $\sigma = 1.045$ (i.e., for $\mu < \mu_{cr} = 0.7574$ and for $N < N_{cr} = 0.5333$). The asymmetric branch that emerges through this bifurcation is stable for $\mu < 0.7603$ and $N < 0.5509$, i.e., for a narrow parametric interval past the bifurcation critical point. However, past this secondary critical point, the asymmetric solutions are prone towards an oscillatory instability emerging through a Hopf bifurcation (the critical loss strength in this case is $\sigma = 0.989$). The relevant bifurcation diagrams are presented in Fig. 2, which shows the dependence of μ on σ, as well as the dependence of N on μ (note that the latter form of the bifurcation diagram is more commonly used in relevant studies). The latter graph also contains the results of the theoretical analysis for the symmetric branch of Eq. (20) and for the anti-symmetric one of Eq. (19), as well as for the asymmetric branch which is theoretically predicted for the parameters of our double-well potential to bifurcate from the anti-symmetric solution for $\mu > 0.7722$ and

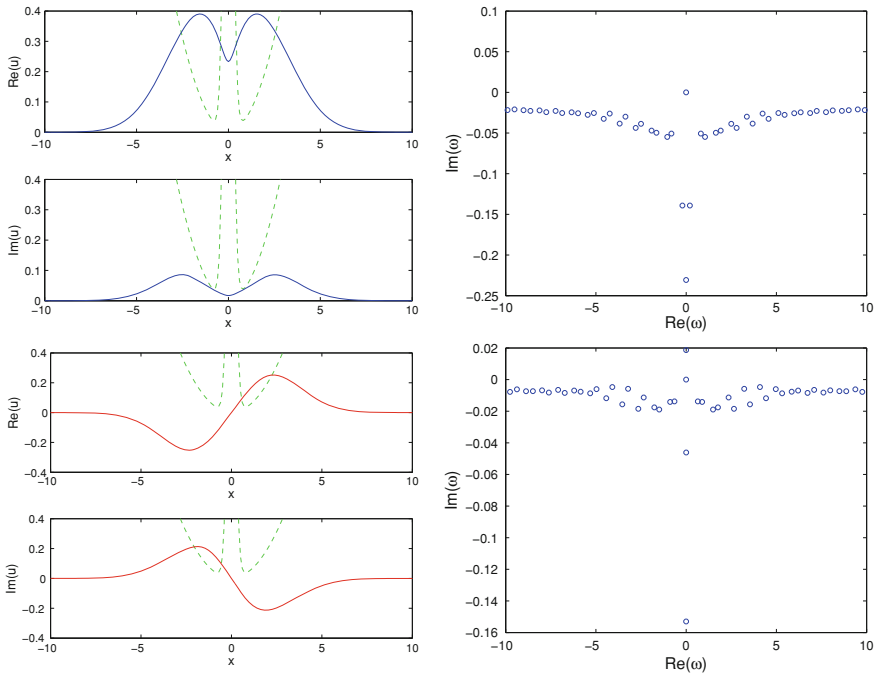

Fig. 3 *Left* Real and imaginary part of the wavefunction profile for a symmetric (*top*) and anti-symmetric (*bottom*) solution. *Right* Their corresponding stability eigenvalues. In all cases $\sigma = 1$ and the interactions are repulsive $(s = +1)$ (Color online)

$N > 0.6661$. As can be seen (also from Fig. 2), there is good agreement between theoretical predictions and numerical findings.

Some case examples of solution profiles for the different branches, together with the results of their corresponding linear stability analysis as performed by means of the Bogolyubov-de Gennes (BdG) ansatz [23–25] are shown in Figs. 3 and 4. The BdG analysis is represented by the spectral plane of the linearization eigenfrequencies $\omega = \mathrm{Re}(\omega) + i\mathrm{Im}(\omega)$. Contrary to what is the case in the Hamiltonian setting of Ref. [49] (where the spectrum is chiefly on the imaginary axis), here the spectrum contains predominantly decaying modes with $\mathrm{Im}(\omega) < 0$. For the stable symmetric ground state in Fig. 3, all modes are decaying except for the symmetry mode associated with $\omega = 0$, while for the unstable anti-symmetric mode of the bottom panel the eigenfrequency associated with the growth is purely imaginary with $\mathrm{Im}(\omega) > 0$. On the other hand, for the asymmetric modes of Fig. 4, it is evident that shortly past the critical point for their emergence, a genuine (now that the system is dissipative, in nature) Hopf bifurcation arises through the crossing of a complex conjugate pair through the axis of $\mathrm{Im}(\omega) = 0$. Additional Hopf bifurcations happen for smaller values of σ (larger values of N), a case example of which is evident in the bottom panel of Fig. 4. The dependence of

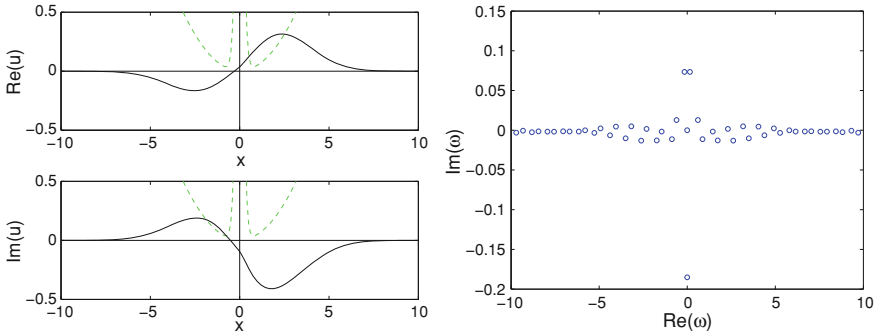

Fig. 4 *Left* Real and imaginary part of the wavefunction profile for an asymmetric solution with $\sigma = 0.5$. *Right* Their corresponding stability eigenvalues. All cases correspond to the repulsive interaction case $(s = +1)$ (Color online)

the imaginary part of the relevant eigenvalues for the anti-symmetric and asymmetric solutions with respect to σ is shown in Fig. 5, illustrating, respectively, the relevant pitchfork (left panel) and multiple Hopf bifurcations (right panel). Naturally, the Hopf bifurcation of the asymmetric branch is anticipated to give rise to a limit cycle attractor within the dynamics [the relevant solution is expected to be periodic in the squared modulus of the wavefunction, hence quasi-periodic in the original field $u(x,t)$].

Two examples of the dynamics of unstable anti-symmetric solutions are illustrated in Fig. 6. It is observed that the unstable solutions generically tend to the stable attractors. However, interestingly, in the $\sigma = 1$ case, the attractor of relevance consists of an asymmetric steady state, while in the $\sigma = 0.8$ case it consists of a symmetric one (the ground state of the system). The symmetry and asymmetry of the configurations can be easily seen from the time series of the densities $|u|_-^2$ and $|u|_+^2$ measured, respectively, at the bottom of the left and right wells. These time series are depicted in the lower panels of the figure. The relevance of the asymmetric attractor, especially for larger values of N (smaller values of σ, where the only stable steady state is the symmetric one) is confirmed by the simulation shown in the left panel of Fig. 7, where the dynamics of an unstable asymmetric solution is traced, leading indeed to the same attractor. The right panel of Fig. 7 shows the evolution of a perturbed asymmetric state close to the Hopf bifurcation; in that case, it is observed that the soliton relaxes to a quasi-periodic asymmetric solution. [Recall that these solutions have a quasi-periodic evolution for the wavefunction (due to the periodic evolution of the phase through $e^{-i\mu t}$) but the evolution in density is *periodic* as the panels show]. We have observed that perturbations of the asymmetric solution lead to quasi-periodic dynamics for $\sigma \in [0.970, 0.990]$.

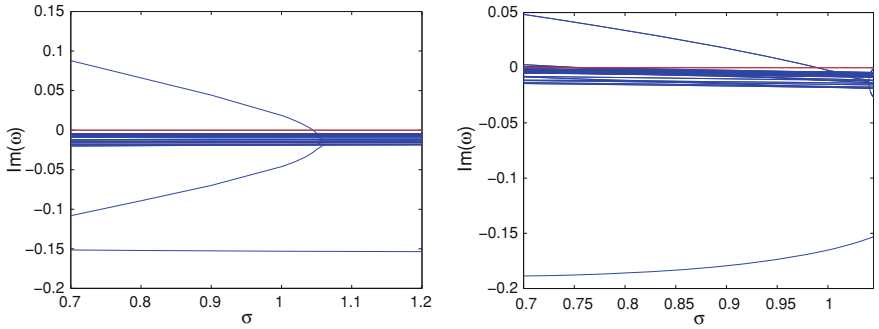

Fig. 5 Dependence of the imaginary part of the stability eigenvalues with respect to σ for the anti-symmetric (*left*) and asymmetric solutions (*right*) in the repulsive interaction case $(s = +1)$ (Color online)

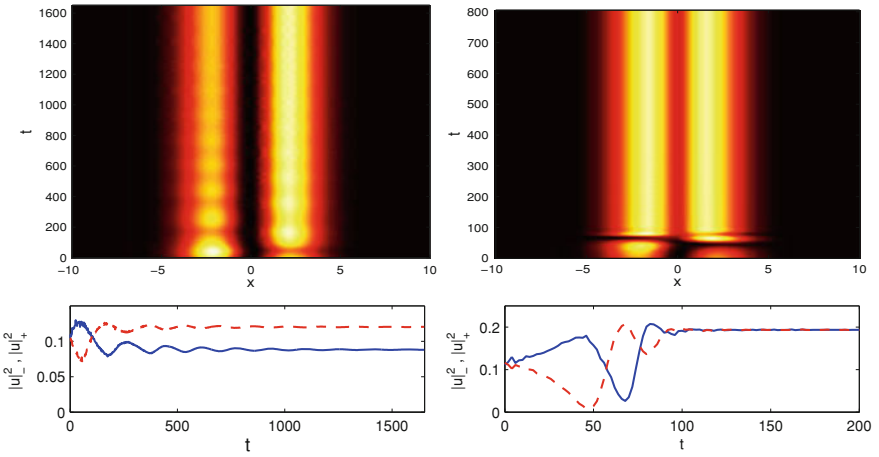

Fig. 6 *Top* Evolution of a perturbed anti-symmetric soliton for $\sigma = 1$ (*left*) and $\sigma = 0.8$ (*right*) in the repulsive case $(s = +1)$. The former case relaxes to the asymmetric stationary state, while the latter to the symmetric ground state. *Bottom* Respective time series for the density at the *bottom* of the *left* (*solid blue line*) and *right* (*dashed red line*) wells (Color online)

3.2 Attractive Case

In the case of attractive interactions $(s = -1)$, the scenario is similar in nature, except for the origin of the symmetry breaking bifurcation. More specifically, now, the asymmetric solution branch, which stabilizes at $\sigma = 0.923$ ($\mu = 0.4182$ and $N = 0.7199$), bifurcates from the symmetric solutions branch at $\sigma = 1.118$ ($\mu = 0.4101$ and $N = 0.7741$). Figures 8 and 11 are the equivalent to Figs. 2 and 5, respectively, but for $s = -1$. Nevertheless, we observe that both the dependence of the chemical potential μ on the nonlinear saturation parameter σ and that of N on μ is,

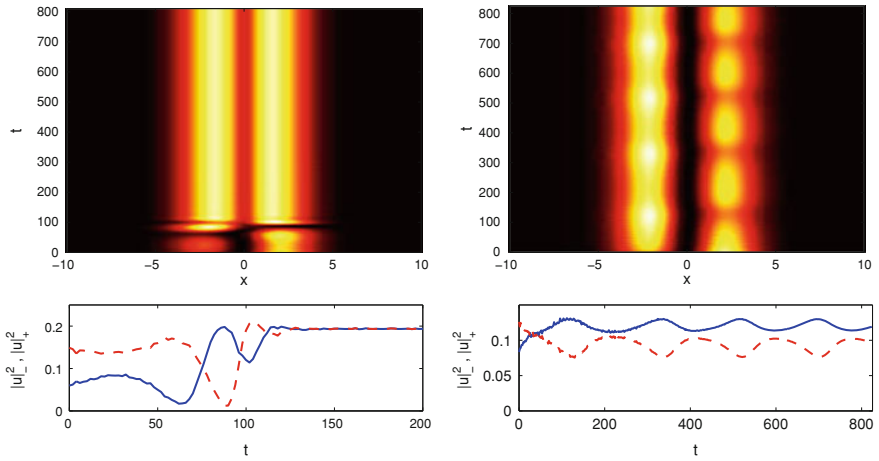

Fig. 7 *Top* Evolution of a perturbed asymmetric soliton with $\sigma = 0.8$ (*left*) and $\sigma = 0.98$ (*right*) in the repulsive case $(s = +1)$. In the former case, perturbation leads to the symmetric ground state attractor, while in the latter case, it relaxes to a non-stationary (quasi-periodic) solution. *Bottom* Respective time series for the density at the *bottom* of the *left* (*solid blue line*) and *right* (*dashed red line*) wells (Color online)

in fact, non-monotonic for this example in the case of the bifurcating asymmetric branch. This clearly indicates (see the right panel of Fig. 8) that the relevant bifurcation is *subcritical*
(as the chemical potential μ is decreased, which is the natural direction of variation off of the linear limit). This is contrary to the corresponding supercritical expectation of its Hamiltonian analog [49, 65]. It should be noticed, however, that other examples where such subcritical bifurcations have been previously reported in Refs. [71, 72] although in neither case was the nonlinearity purely cubic as was the case here (and they did not contain driving/damping effects). Importantly, it should also be pointed out that the analytical prediction of the Galerkin approach suggests a supercritical scenario for $\mu < 0.4247$ and $N > 0.6590$. Despite the inability of the approximation to capture the short subcritical segment of the bifurcating branch, we nevertheless see that the Galerkin method is a useful tool for obtaining an estimate of the relevant critical point.

An additional feature worth pointing out concerns the nature of the instabilities of the different branches as detailed in Figs. 9 and 10. While the symmetric branch becomes unstable at the relevant critical point by developing an imaginary eigenfrequency with $\mathrm{Im}(\omega) > 0$ (the rest of the spectrum has $\mathrm{Im}(\omega) < 0$), the antisymmetric state remains dynamically robust. On the other hand, the asymmetric branch emerges as stable at the critical point of the symmetry breaking but shortly thereafter (for $\sigma < 0.923$), it becomes subject to a Hopf bifurcation through the crossing of the axis with $\mathrm{Im}(\omega) = 0$ of a complex eigenvalue pair. In fact, for $\sigma < 0.74$, a secondary Hopf bifurcation has occurred and is mirrored in the two complex pairs with $\mathrm{Im}(\omega) > 0$ shown in Fig. 10. This phenomenology is enforced

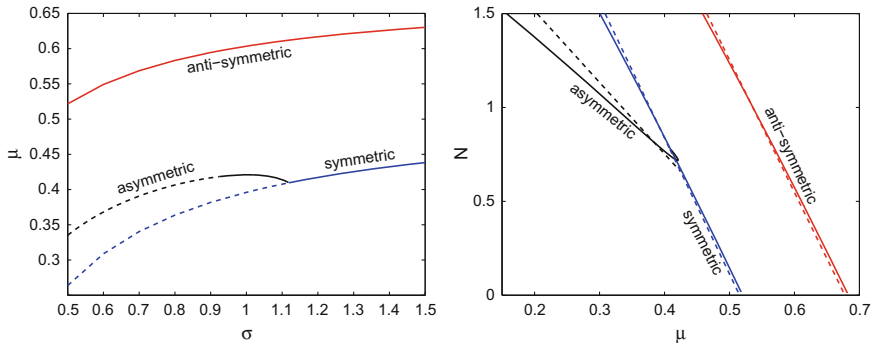

Fig. 8 Bifurcation diagrams for the symmetric, anti-symmetric and asymmetric branches for focusing (attractive) nonlinearity ($s = -1$). *Left* Dependence of the chemical potential on the damping parameter. *Right* Dependence of the (normalized) number of polaritons on the chemical potential. Unstable solutions are depicted by *dashed lines* on the *left panel*. On the *right panel solid lines* display numerical (Newton-Raphson) results, while *dashed lines* display analytical (Galerkin) results (Color online)

by Fig. 11 which illustrates the dependence of the relevant stability eigenvalues on the nonlinear loss parameter σ (see the right panel for the sequence of Hopf bifurcations, while the left panel highlights the symmetry-breaking induced crossing of a single eigenfrequency pair for the symmetric branch). As in the repulsive case, the Hopf bifurcation of the asymmetric branch is anticipated to give rise to a limit cycle attractor within the dynamics.

The dynamics of Figs. 12 and 13 naturally reflects the above conclusions. In particular, the evolution of the symmetric state in the double-well potential of the left panel of Fig. 12 gives rise to the asymmetric state as the latter is stable and indeed an attractor for the value of $\sigma = 1$. The right panel of the figure displays the evolution of a perturbed symmetric solution tending to an anti-symmetric one; in that case, the asymmetric solution is unstable and no longer a dynamical attractor.

On the other hand, Fig. 13 shows different case examples of the (unstable via the Hopf) asymmetric branch for different values of σ. In those cases, the asymmetric branch is no longer a stable stationary state and as a result the dynamics becomes periodic in the modulus (quasi-periodic in the original field) for $\sigma \in [0.74, 0.92]$. It is interesting to follow the changes in the dynamics for these periodic states as σ is decreased below the bifurcating point from the asymmetric branch. In particular, close to bifurcation point, the periodic evolution remains proximal to the state from which it emanates, namely the asymmetric state as it can be seen in the left panels of Fig. 13. However, as σ is decreased further from the bifurcation point, the instability of the asymmetric state is stronger and the departure from the asymmetric solution is more significant. In particular, it is interesting to notice that for smaller values of σ, the solution tends to display strong oscillations of the densities resembling the *symmetric* tunneling of matter from one well to the other. An example of this evolution for $\sigma = 0.8$ is depicted in the right panels of Fig. 13 where it is evident that the oscillations in the two wells become similar to each other

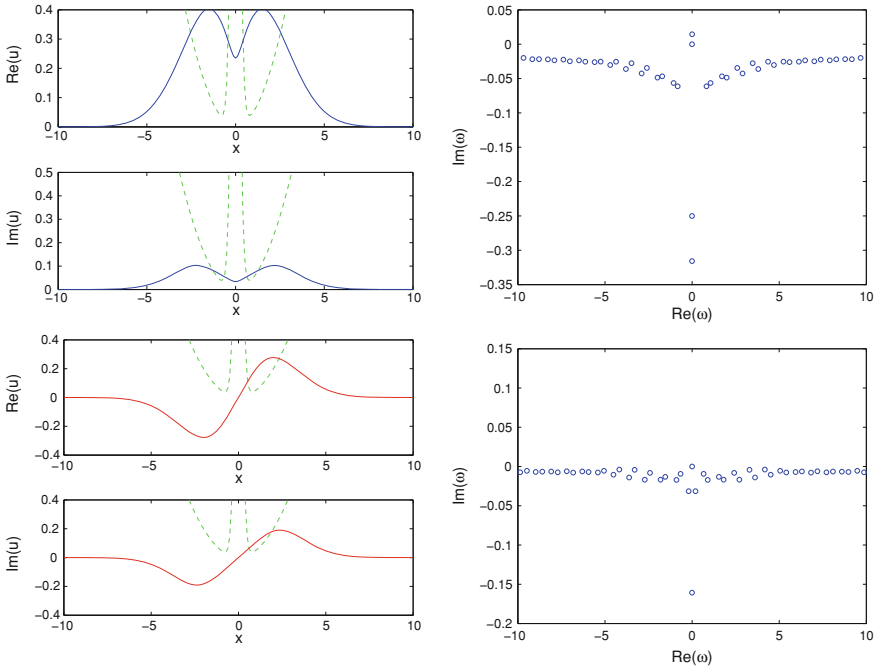

Fig. 9 *Left* Real and imaginary part of the wavefunction profile for a symmetric (*top*) and anti-symmetric (*bottom*) solution. *Right* Their corresponding stability eigenvalues. In all cases $\sigma = 1$ and the nonlinearity is attractive $(s = -1)$ (Color online)

but with a phase shift between them, leading to an effective re-symmetrization of the dynamics.

It is also interesting to highlight here the difference between the repulsive case of Figs. 6 and 7 and the attractive case of Figs. 12 and 13. In the former case, when the emerging asymmetric branch is unstable the dynamics typically is found to lead to the stable ground state of the system (the symmetric one). On the other hand, for the attractive case, when both the symmetric and the asymmetric branch are destabilized, the dynamics does not resort to the excited (yet stable) anti-symmetric state. Instead, it leads to periodic oscillations in the density between the two wells.

Finally, we have considered the effect of varying the spot size fixing $\sigma = 1$. In the repulsive case, the symmetric branch is stable for $x_m \in [0.9, 5.7]$; out of this range, the instabilities are caused by a Hopf bifurcation cascade and develop into non-stationary multi-dark soliton waveforms, similar to the states that were previously reported in Ref. [33] (but for a purely parabolic trap). The anti-symmetric branch, which is unstable for every x_m (for this value of σ), experiences a Hopf bifurcation cascade for $x_m \leq 2.0$ and $x_m \geq 5.3$. The instabilities for $x_m \in (2.0, 5.3)$ are the exponential ones previously explored. However, considering higher values of σ, a stability range appears which is enlarged for growing σ.

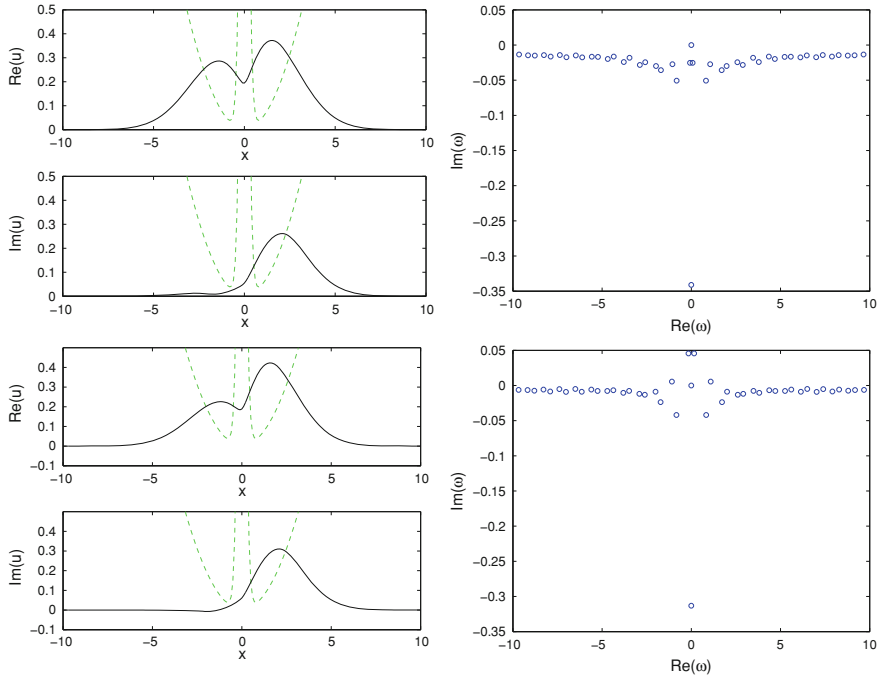

Fig. 10 *Left* Real and imaginary part of the wavefunction profile for an asymmetric solution with $\sigma = 1$ (*top*) and $\sigma = 0.7$ (*bottom*). *Right* Their corresponding stability eigenvalues. Notice the Hopf bifurcations and the associated oscillatory instabilities through two complex pairs which have occurred in the latter case. Here, the nonlinearity is attractive $(s = -1)$ (Color online)

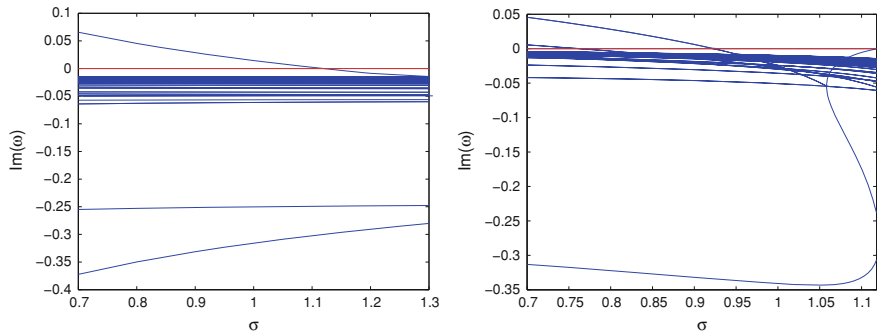

Fig. 11 Dependence of the imaginary part of the stability eigenvalues with respect to σ for symmetric (*left*) and asymmetric solutions (*right*). Here, again, the nonlinearity is attractive $(s = -1)$ (Color online)

A similar effect is observed for the asymmetric branch, i.e., there is a small stability interval $x_m \in [1.9, 2.0]$ that is enlarged when σ is decreased. Outside this range, the branch experiences Hopf bifurcation cascades.

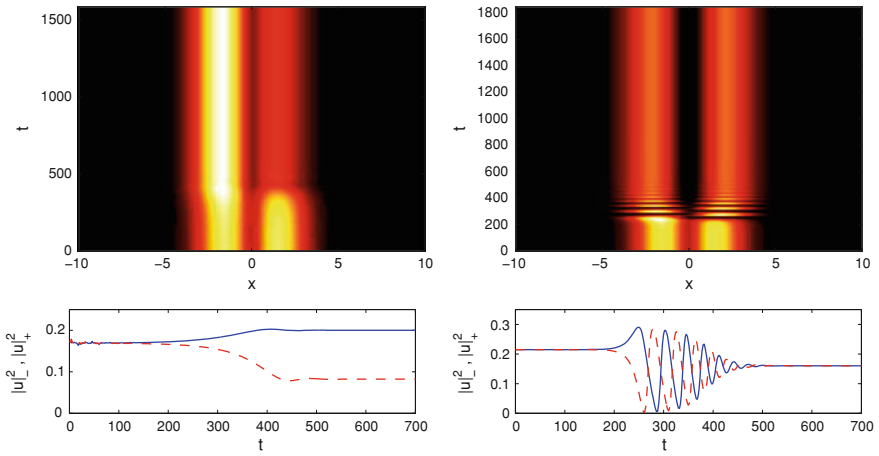

Fig. 12 *Top* Evolution of perturbed symmetric solitons with $\sigma = 1$ (*left*) and $\sigma = 0.82$ (*right*) for attractive nonlinearity $(s = -1)$. *Bottom* Respective time series for the density at the *bottom* of the *left* (*solid blue line*) and *right* (*dashed red line*) wells (Color online)

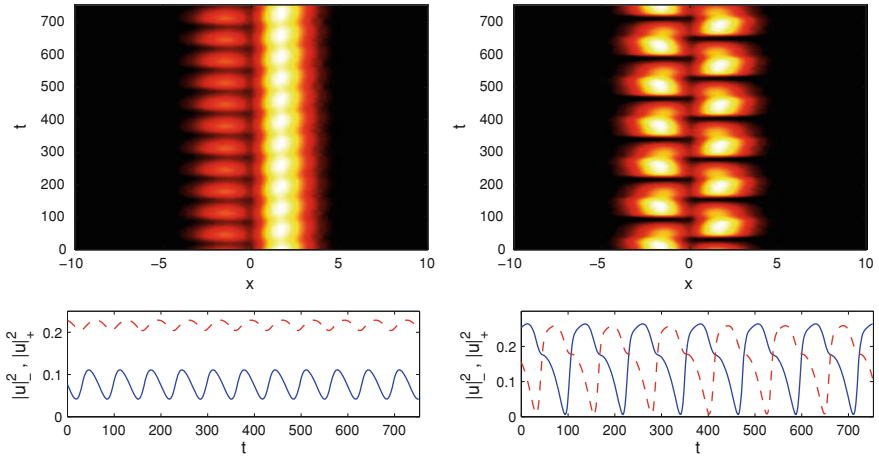

Fig. 13 *Top* Dynamical evolution of the density of the non-stationary asymmetric solution branch found for attractive nonlinearity $(s = -1)$ in two cases: $\sigma = 0.9$ (*left*) and $\sigma = 0.8$ (*right*). *Bottom* Respective time series for the density at the *bottom* of the *left* (*solid blue line*) and *right* (*dashed red line*) wells (Color online)

The above mentioned scenario is almost equivalent for the attractive case, except that the symmetric and anti-symmetric branches are interchanged. In that case, the anti-symmetric branch is stable for $x_m \in [2.0, 4.8]$; the symmetric branch is now stable for $x_m \in [1.0, 1.9]$, starting the Hopf cascade at $x_m = 4.5$. The asymmetric branch is stable for $x_m \in [1.0, 2.0]$, while being oscillatorily unstable for other values of x_m.

4 Conclusions and Future Challenges

In the present work, we studied the existence of solutions, their spectral stability and nonlinear dynamics for the case of a polariton condensate confined in a quasi-1D double well potential. Motivated by recent developments for the study of polaritons in such settings [26–32, 52–55], and by the work of Ref. [15] which proposed a two-well model, we presented a systematic Galerkin analysis for the model with the gain over a localized spot and nonlinear saturation loss formulated in Refs. [18–20]. It was theoretically predicted that nonlinear states emanate from the corresponding linear ones of the potential and that bifurcations are expected to arise, similarly to the Hamiltonian analog of this setting studied earlier in the context of atomic BECs. Such symmetry breaking pitchfork events emerge from the anti-symmetric, first excited state in the case of the repulsive interactions, while they arise from the symmetric ground state branch in the case of attractive ones. Despite the similarities with the atomic BEC case, nontrivial differences exist as well. One of them concerns the nature of the bifurcation, which in the attractive case was found to be weakly subcritical (instead of supercritical) upon decrease of the chemical potential. Importantly also, the resulting asymmetric branches aside from narrow intervals of stability are generically found to be unstable due to genuine Hopf bifurcations, which, in turn, give rise to periodic orbits (in the density). While in the repulsive case, the dynamics of anti-symmetric and asymmetric branches is found to be attracted to the ground state when both of them are unstable, the periodic orbits are essential to the evolution in the case of attractive interactions as they seem to constitute the robust dynamical attractor.

This is merely the first step in the examination of the similarities (but also the differences) of the polariton BECs and their atomic counterparts within a setting that contains the interplay of a double-well potential and nonlinear interactions. Yet, our study paves the way for a number of potential future avenues. On the one hand, one can consider the more detailed model of Refs. [15–17] and examine whether the inclusion of the diffusive dynamics of the exciton population induces any qualitative differences in the features reported herein. On the other hand, and bearing in mind the predominantly two-dimensional nature of the polariton dynamics, one can envision generalizations of the potential considered herein in a 2D realm. Relevant possibilities may include not only the straightforward generalization of a double well encompassing two quasi-one-dimensional tracks, but also that of a genuinely two-dimensional four well potential that has recently been examined in detail in atomic BECs [73]. Even in the context of the present model, there are further possibilities to explore, including the systematic investigation of the emergent periodic orbits and their Floquet spectral stability analysis. Such studies are currently in progress and will be reported in future publications.

Acknowledgments J.C. acknowledges financial support from the MICINN project FIS2008-04848. P.G.K. and R.C.G. gratefully acknowledge support from the National Science Foundation under grant DMS-0806762. P.G.K. also acknowledges support the Alexander von Humboldt and Binational Science Foundations. The work of D.J.F. was partially supported by the Special Account for Research Grants of the University of Athens.

References

1. J. Kasprzak, M. Richard, S. Kundermann, A. Baas, P. Jeambrun, J. Keeling, F.M. Marchetti, M.H. Szymańska, R. André, J.L. Staehli, V. Savona, P.B. Littlewood, B. Deveaud, L.S. Dang, Nature **443**, 409 (2006)
2. R. Balili, V. Hartwell, D. Snoke, L. Pfeiffer, K. West, Science **316**, 1007 (2007)
3. W. Lai, N.Y. Kim, S. Utsunomiya, G. Roumpos, H. Deng, M.D. Fraser, T. Byrnes, P. Recher, N. Kumada, T. Fujisawa, Y. Yamamoto, Nature **450**, 529 (2007)
4. H. Deng, G.S. Solomon, R. Hey, K.H. Ploog, Y. Yamamoto, Phys. Rev. Lett. **99**, 126403 (2007)
5. G. Björk, S. Machida, Y. Yamamoto, K. Igeta, Phys. Rev. A **44**, 669 (1991)
6. C. Weisbuch, M. Nishioka, A. Ishikawa, Y. Arakawa, Phys. Rev. Lett. **69**, 3314 (1992)
7. B. Deveaud (eds), *The Physics of Semiconductor Microcavities* (Wiley-VCH, Weinheim, 2007)
8. A. Amo, J. Lefrère, S. Pigeon, C. Abrados, C. Ciuti, I. Carusotto, R. Houdré, E. Giacobino, A. Bramati, Nat. Phys. **5**, 805 (2009)
9. K.G. Lagoudakis, M. Wouters, M. Richard, A. Baas, I. Carusotto, R. André, L.S. Dang, B. Deveaud-Plédran, Nat. Phys. **4**, 706 (2008)
10. M.D. Fraser, G. Roumpos, Y. Yamamoto, New J. Phys. **11**, 113048 (2009)
11. G. Roumpos, M.D. Fraser, A. Loffler, S. Höffling, A. Forchel, Y. Yamamoto, Nat. Phys. **7**, 129 (2011)
12. A. Amo, D. Sanvitto, F.P. Laussy, D. Ballarini, E. del Valle, M.D. Martin, A. Lemaitre, J. Bloch, D.N. Krizhanovskii, M.S. Skolnick, C. Tejedor, L. Viña, Nature **457**, 291 (2009)
13. A. Amo, T.C.H. Liew, C. Adrados, R. Houdré, E. Giacobino, A.V. Kavokin, A. Bramati, Nat. Photonics **4**, 361 (2010)
14. S.I. Tsintzos, N.T. Pelekanos, G. Konstantinidis, Z. Hatzopoulos, P.G. Savvidis, Nature **453**, 372 (2008)
15. M. Wouters, I. Carusotto, Phys. Rev. Lett. **99**, 140402 (2007)
16. M. Wouters, I. Carusotto, C. Ciuti, Phys. Rev. B **77**, 115340 (2008)
17. C. Ciuti, I. Carusotto, Phys. Stat. Sol. (b) **242**, 2224 (2005)
18. J. Keeling, N.G. Berloff, Phys. Rev. Lett. **100**, 250401 (2008)
19. M.O. Borgh, J. Keeling, N.G. Berloff, Phys. Rev. B **81**, 235302 (2010)
20. J. Keeling, N.G. Berloff, Contemp. Phys. **52**, 131 (2011)
21. G. Tosi, G. Christmann, N.G. Berloff, P. Tsotsis, T. Gao, Z. Hatzopoulos, P.G. Savvidis, J.J. Baumberg, Nat. Phys. **8**, 190 (2012)
22. B.A. Malomed, O. Dzyapko, V.E. Demidov, S.O. Demokritov, Phys. Rev. B **81**, 024418 (2010)
23. C.J. Pethick, H. Smith, *Bose–Einstein Condensation in Dilute Gases* (Cambridge University Press, Cambridge, 2002)
24. L.P. Pitaevskii, S. Stringari, *Bose–Einstein Condensation* (Oxford University Press, Oxford, 2003)
25. P.G. Kevrekidis, D.J. Frantzeskakis, R. Carretero-González (eds), *Emergent Nonlinear Phenomena in Bose–Einstein Condensates: Theory and Experiment* (Springer, Heidelberg, 2008)
26. R. Idrissi Kaitouni, O. El Daïf, A. Baas, M. Richard, T. Paraïso, P. Lugan, T. Guillet, F. Morier-Genoud, J.D. Ganière, J.L. Staehli, V. Savona, B. Deveaud, Phys. Rev. B **74**, 155311 (2006)
27. O. El Daïf, A. Baas, T. Guillet, J.-P. Brantut, R.I. Kaitouni, J.L. Staehli, F. Morier-Genoud, B. Deveaud, Appl. Phys. Lett. **88**, 061105 (2006)
28. D. Bajoni, E. Peter, P. Senellart, J.L. Smirr, I. Sagnes, A. Lemaître, J. Bloch, Appl. Phys. Lett. **90**, 051107 (2007)
29. D. Bajoni, P. Senellart, E. Wertz, I. Sagnes, A. Miard, A. Lemaître, J. Bloch, Phys. Rev. Lett. **100**, 047401 (2008)
30. R. Cerna, D. Sarchi, T.K. Paraïso, G. Nardin, Y. Léger, M. Richard, B. Pietka, O. El Daïf, F. Morier-Genoud, V. Savona, M.T. Portella-Oberli, B. Deveaud-Plédran, Phys. Rev. B **80**, 121309(R) (2009)
31. M. Wouters, T.C.H. Liew, V. Savona, Phys. Rev. B **82**, 245315 (2010)

32. E. Wertz, L. Ferrier, D.D. Solnyshkov, R. Johne, D. Sanvitto, A. Lemaître, I. Sagnes, R. Grousson, A.V. Kavokin, P. Senellart, G. Malpuech, J. Bloch, Nat. Phys. **6**, 860 (2010)
33. J. Cuevas, A.S. Rodrigues, R. Carretero-González, P.G. Kevrekidis, D.J. Frantzeskakis, Phys. Rev. B **83**, 245140 (2011)
34. O. Morsch, M.K. Oberthaler, Rev. Mod. Phys. **78**, 179 (2006)
35. M. Albiez, R. Gati, J. Fölling, S. Hunsmann, M. Cristiani, M.K. Oberthaler, Phys. Rev. Lett. **95**, 010402 (2005)
36. T. Zibold, E. Nicklas, C. Gross, M.K. Oberthaler, Phys. Rev. Lett. **105**, 204101 (2010)
37. R.B. Balili, D.W. Snoke, L. Pfeiffer, K. West, Appl. Phys. Lett. **88**, 031110 (2006)
38. K.G. Lagoudakis, B. Pietka, M. Wouters, R. André, B. Deveaud-Plédran, Phys. Rev. Lett. **105**, 120403 (2010)
39. R. Gati, M.K. Oberthaler, J. Phys. B Atomic Mol. Opt. Phys. **40**, R61 (2007)
40. S. Raghavan, A. Smerzi, S. Fantoni, S.R. Shenoy, Phys. Rev. A **59**, 620 (1999)
41. S. Raghavan, A. Smerzi, V.M. Kenkre, Phys. Rev. A **60**, R1787 (1999)
42. A. Smerzi, S. Raghavan, Phys. Rev. A **61**, 063601 (2000)
43. E.A. Ostrovskaya, Yu.S. Kivshar, M. Lisak, B. Hall, F. Cattani, D. Anderson, Phys. Rev. A **61**, 031601(R) (2000)
44. K.W. Mahmud, J.N. Kutz, W.P. Reinhardt, Phys. Rev. A **66**, 063607 (2002)
45. V.S. Shchesnovich, B.A. Malomed, R.A. Kraenkel, Physica D **188**, 213 (2004)
46. D. Ananikian, T. Bergeman, Phys. Rev. A **73**, 013604 (2006)
47. P. Ziń, E. Infeld, M. Matuszewski, G. Rowlands, M. Trippenbach, Phys. Rev. A **73**, 022105 (2006)
48. T. Kapitula, P.G. Kevrekidis, Nonlinearity **18**, 2491 (2005)
49. G. Theocharis, P.G. Kevrekidis, D.J. Frantzeskakis, P. Schmelcher, Phys. Rev. E **74**, 056608 (2006)
50. D.R. Dounas-Frazer, A.M. Hermundstad, L.D. Carr, Phys. Rev. Lett. **99**, 200402 (2007)
51. T. Mayteevarunyoo, B.A. Malomed, G. Dong, Phys. Rev. A **78**, 053601 (2008)
52. I.A. Shelykh, D.D. Solnyshkov, G. Pavlovi, G. Malpuech, Phys. Rev. B **78**, 041302 (2008)
53. D.D. Solnyshkov, R. Johne, G. Malpuech, Phys. Rev. B **80**, 235303 (2009)
54. C. Zhang, G. Jin, Phys. Rev. B **84**, 115324 (2011)
55. W.L. Zhang, Y.J. Rao, Chaos Solitons Fractals **45**, 373 (2012)
56. A. Sigler, B.A. Malomed, Physica D **212**, 305 (2005)
57. C. Paré, M. Florjańczyk, Phys. Rev. A **41**, 6287 (1990)
58. A.I. Maimistov, Kvant. Elektron. **18**, 758 (1991) [In Russian; English translation: Sov. J. Quantum Electron. **21**, 687]
59. W. Snyder, D.J. Mitchell, L. Poladian, D.R. Rowland, Y. Chen, J. Opt. Soc. Am. B **8**, 2102 (1991)
60. P.L. Chu, B.A. Malomed, G.D. Peng, J. Opt. Soc. Am. B **10**, 1379 (1993)
61. N. Akhmediev, A. Ankiewicz, Phys. Rev. Lett. **70**, 2395 (1993)
62. B.A. Malomed, I. Skinner, P.L. Chu, G.D. Peng, Phys. Rev. E **53**, 4084 (1996)
63. C. Cambournac, T. Sylvestre, H. Maillotte, B. Vanderlinden, P. Kockaert, Ph. Emplit, M. Haelterman, Phys. Rev. Lett. **89**, 083901 (2002)
64. P.G. Kevrekidis, Z. Chen, B.A. Malomed, D.J. Frantzeskakis, M.I. Weinstein, Phys. Lett. A **340**, 275 (2005)
65. E. Kirr, P.G. Kevrekidis, E. Shlizerman, M.I. Weinstein, SIAM J. Math. Anal. **40**, 566 (2008)
66. J.L. Marzuola, M.I. Weinstein, Discret. Control Dyn. Syst. **28**, 1505 (2010)
67. I.S. Aranson, L. Kramers, Rev. Mod. Phys. **74**, 99 (2002)
68. H.M. Gibbs, G. Khitrova, S.W. Koch, Nat. Photonics **5**, 273 (2011)
69. M. Sich, D.N. Krizhanovskii, M.S. Skolnick, A.V. Gorbach, R. Hartley, D.V. Skryabin, E.A. Cerda-Mèndez, K. Biermann, R. Hey, P.V. Santos, Nat. Photonics **6**, 50 (2012)
70. P.R. Eastham, Phys. Rev. B **78**, 035319 (2008)
71. A. Sacchetti, Phys. Rev. Lett. **103**, 194101 (2009)
72. E. Kirr, P.G. Kevrekidis, D.E. Pelinovsky, Commun. Math. Phys. **308**, 795 (2011)
73. C. Wang, G. Theocharis, P.G. Kevrekidis, N. Whitaker, K.J.H. Law, D.J. Frantzeskakis, B.A. Malomed, Phys. Rev. E **80**, 046611 (2009)

Classical Dynamics of a Two-species Bose-Einstein Condensate in the Presence of Nonlinear Maser Processes

B. M. Rodríguez-Lara and R.-K. Lee

1 Introduction

A great deal of attention has been granted to research about unifying concepts in classical and quantum physics through experimental demonstrations involving Bose-Einstein Condensates (BECs) at a macroscopic scale [1]. For example, by considering BECs loaded in a double-well potential, the quantum tunnelling between two trapped condensates provides a possibility to study and understand symmetry-breaking, self-trapping, and Josephson oscillation; all of them are fundamental problems in quantum physics. Macroscopic quantum self-trapping [2] and bosonic Josephson junction [3] have been demonstrated recently, and successfully described by a mean-field approach. The realization of these macroscopic quantum self-trapped modes opens up new avenues for research; e.g., generation of squeezed atomic states [4] and atomic interferometry [5].

By using the symmetric and asymmetric stationary eigenstates of the Gross–Pitaevskii equation for a macroscopic condensate trapped in a symmetric double-well potential (SDW), the nonlinear Hamiltonian (in units of $\hbar$) describing coherent atomic tunnelling between two zero-temperature BECs is equivalent to that of a nonrigid pendulum [6, 7], i.e.,

$$H_{SDW} = \frac{\Lambda}{2} z^2 - \sqrt{1 - z^2} \cos \Phi, \tag{1}$$

B. M. Rodríguez-Lara (✉)
Centre for Quantum Technologies, National University of Singapore,
117542 Singapore, Singapore
e-mail: bmlara@nus.edu.sg

R.-K. Lee
Department of Physics, Institute of Photonics Technologies,
National Tsing-Hua University, Hsinchu 300, Taiwan
e-mail: rklee@ee.nthu.edu.tw

Progress Optical Sci., Photonics (2013): 531–542
DOI: 10.1007/10091_2012_7

Published Online: 22 May 2012

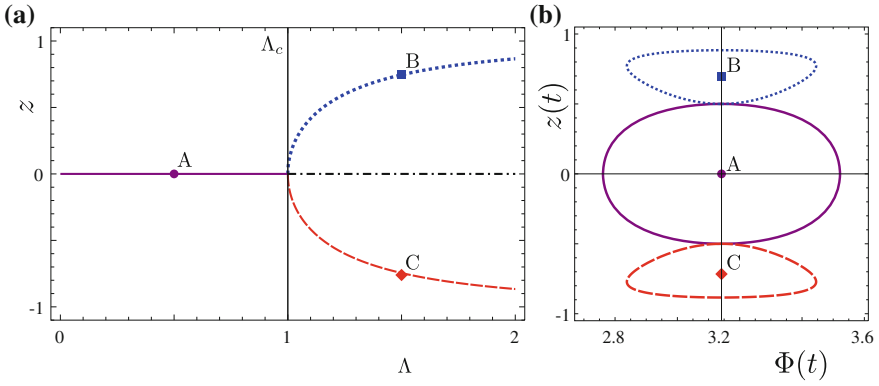

Fig. 1 **a** Fixed points for the equations of motion of a BEC in a double-well potential, described by Eqs. (2 and 3), at $\Phi = \pi$. The bifurcation of a single stable fixed point in the Rabi regime (*solid purple*) split into two fixed points in the Josephson regime (*dotted blue* and *dashed red*) is shown at the critical value, $\Lambda_c = 1$. The unstable fixed point, or separatrix, in the Josephson regime (*dash-dotted black*) is also shown. **b** Examples of trajectories for identical Rabi oscillations (*solid purple*) around the fixed point A ($\Lambda = 0.5$) and localized Josephson oscillations around the fixed points B (*dotted blue*) and C (*dashed red*) ($\Lambda = 1.5$) are demonstrated with symmetrical initial conditions $\{z_\pm = \pm 0.5, \Phi = \pi\}$ (Color online)

where the length of pendulum decreases with the angular momentum z, which denotes the fractional relative population between the condensates in the two wells. The ratio of the on-site interaction energy and the coupling matrix element is characterized by the parameter Λ, while the tilt angle Φ shows the phase difference between the two condensates.

This nonlinear system allows for macroscopic quantum self-trapping (i.e., localized oscillations of the fractional population difference z), which can be easily deduced from the equations of motion of the system,

$$\dot{z} = -\sqrt{1 - z^2} \sin \Phi, \tag{2}$$

$$\dot{\Phi} = \Lambda z + \frac{z}{\sqrt{1 - z^2}} \cos \Phi. \tag{3}$$

The fixed points of such equations of motion present a pitchfork bifurcation at the critical point $\Lambda_c = 1$; i.e., $\{z_\pi = 0, \Phi = \pi\}$ for $\Lambda < 1$ and $\{z_\pi = \pm\sqrt{\Lambda^2 - 1}/\Lambda, \Phi = \pi\}$ for $\Lambda > 1$. This bifurcation signals a symmetry-breaking in the dynamics of the system from Rabi to Josephson dynamics; such that for symmetric initial conditions, $\{z_\pm = \pm z_0, \Phi = \pi\}$, the trajectories will be identical in the Rabi regime, $\Lambda < 1$, but localize in opposite hemispheres of phase space in the Josephson regime, $\Lambda > 1$. Figure 1 shows an example of such symmetry-breaking phenomena. The transition from Rabi to Josephson dynamics due to the pitchfork bifurcation of the fixed points has been confirmed experimentally in an equivalent model consisting of two hyperfine states of a single atomic specie BEC coupled by a classical two-photon transition in the semi-classical limit [8].

Recently, strong coupling between a BEC and the quantized field mode of an ultrahigh-finesse optical cavity has been demonstrated [9–11]. The spectra of these strongly-coupled systems shows a level splitting attributed to different hyperfine structures of the given atomic species. Motivated by these experiments, here, we consider a gaseous BEC, composed of bosonic atoms populating two hyperfine levels, coupled to a quantized field cavity mode, including nonlinear interactions among the ultracold atoms. Instead of two trapped BECs interacting through quantum tunnelling in a double-well potential, the hyperfine levels of the two-species condensate are driven by the quantized cavity field. It will be demonstrated later that the Hamiltonian describing this system consisting of a BEC in a cavity can be reduced into a nonlinear Dicke model with an additional atom-atom quadratic interaction term; in the semi-classical limit, this system can be thought of as a pendulum with changeable mass. In order to study a general model, we consider second and third order nonlinear processes for the field. Our goal is to present a steady-state analysis of the equations of motion in the large-ensemble-size limit for the collective dynamics of this system. In Sect. 2, the model and possible physical realizations are presented and discussed. In order to present analytical results, a weak regime is defined in Sect. 3 for weak coupling and nonlinearities (compared to the frequency of the driving field). The symmetry of Josephson dynamics is shown to break by the driving quantum field. Finally, Sect. 4 closes with a summary.

2 Model

The proposed model Hamiltonian describing the interaction of a single electromagnetic cavity mode $\hat{a}$ coupled to a BEC with two internal hyperfine structure levels $\hat{b}_\downarrow$ and $\hat{b}_\uparrow$ can be obtained from the Gross–Pitaevskii equation describing a two-species BEC interacting with a quantum field [12] and is written as,

$$\begin{aligned}\hat{H}_0 =&\omega_f \hat{a}^\dagger \hat{a} + \sum_{j=\uparrow,\downarrow}\left(E_j \hat{b}_j^\dagger \hat{b}_j + \frac{1}{2}G_{jj}\hat{b}_j^\dagger \hat{b}_j^\dagger \hat{b}_j \hat{b}_j\right)\\ &+ \frac{g}{\sqrt{N}}(\hat{a}+\hat{a}^\dagger)\left(\hat{b}_\uparrow^\dagger \hat{b}_\downarrow + \hat{b}_\downarrow^\dagger \hat{b}_\uparrow\right) + G_{\uparrow\downarrow}\hat{b}_\uparrow^\dagger \hat{b}_\downarrow^\dagger \hat{b}_\downarrow \hat{b}_\uparrow,\end{aligned} \tag{4}$$

where the frequency ω_f is the cavity mode frequency, the parameter g is the coupling strength between the cavity mode and condensed atoms, and N is the number of atoms in the condensate. The energies of two internal hyperfine levels are labelled as $E_\downarrow$ and $E_\uparrow$ with an intra-atomic transition frequency $\omega_a \equiv E_\uparrow - E_\downarrow$. Here, we suppose the interaction Hamiltonian as a coupled two-component BEC [13], by introducing $G_{jj}(j = \uparrow$ and $\downarrow)$ and $G_{\uparrow\downarrow}$ for the inter-atomic and intra-atomic interactions, respectively.

The Hamiltonian in Eq. (4) can be further reduced by regarding all atoms as spin $1/2$ particles and defining collective angular momentum operators via

Schwinger transformation, $\hat{J}_x = \left(\hat{b}_\uparrow^+ \hat{b}_\downarrow + \hat{b}_\uparrow \hat{b}_\downarrow^+\right)/2, \hat{J}_y = \left(\hat{b}_\uparrow^+ \hat{b}_\downarrow - \hat{b}_\uparrow \hat{b}_\downarrow^+\right)/2i$, and $\hat{J}_z = \left(\hat{b}_\uparrow^+ \hat{b}_\uparrow - \hat{b}_\downarrow^+ \hat{b}_\downarrow\right)/2$, alongside the raising and lowering operators $\hat{J}_+ = \hat{b}_\uparrow^+ \hat{b}_\downarrow$ and $\hat{J}_- = \hat{b}_\uparrow \hat{b}_\downarrow^+$. The reduced Hamiltonian is given by the expression,

$$\hat{H}_{DLMG} = \Delta \hat{J}_z + \frac{g}{\sqrt{N}}\left(\hat{a} + \hat{a}^\dagger\right)\hat{J}_x + \frac{\xi}{N}\hat{J}_z^2, \tag{5}$$

where we have dropped the constant energy term $\frac{N}{2}\left[E_\uparrow + E_\downarrow - \frac{1}{2}\left(G_{\uparrow\uparrow} + G_{\downarrow\downarrow}\right)\right] + \frac{N^2}{8}\left(G_{\uparrow\uparrow} + G_{\downarrow\downarrow} + 2G_{\uparrow\downarrow}\right)$. The average interaction energy of each atom is defined as $\xi/N = \frac{1}{2}\left(G_{\uparrow\uparrow} + G_{\downarrow\downarrow} - 2G_{\uparrow\downarrow}\right)$ to account for the collective interaction among the condensates. The frequency detuning between cavity field and hyperfine transition is given by $\Delta = \omega_a - \omega_f$. In the following analysis, only positive values of ξ are considered (repulsive interaction) for the case of inter-species interaction, $G_{\uparrow\uparrow}$ or $G_{\downarrow\downarrow}$, larger than the intra-species interaction, $G_{\uparrow\downarrow}$.

Equation (5), the starting Hamiltonian for our analysis, corresponds to a generalized Dicke Hamiltonian without the rotating wave approximation and an additional atom–atom quadratic nonlinear interaction. It is well known that the Dicke Hamiltonian describes the collective dynamics for an ensemble of two-level systems driven by a quantum field cavity mode within a quantum electrodynamics (QED) configuration [14]. From many-body physics, the Hamiltonian in Eq. (5) is also equivalent to the Lipkin–Meshkov–Glick (LMG) model in the limit $g = 0$ [15]. Through the interaction among ensemble atoms, the LMG model, originally for N fermions distributed in two N-fold degenerate levels and interacting via a monopole-monopole force, was used to describe the Josephson effect in a two-species BEC and found to produce a maximal pairwise entanglement of formation at the phase transition of its ground state [16, 17]. Schemes proposed to implement a dissipative LMG model in optical cavity-QED [18] and in circuit-QED [19] have been discussed. The Hamiltonian in Eq. (5) hereby will be called the Dicke-LMG (DLMG) Hamiltonian. Recently, it has been theorized that the ground state of the DLMG model supports phase transitions [20]. In the semi-classical limit, both pitchfork and asymmetric bifurcations of the stable fixed points were found for this model [21]. Also, the full quantum analysis of such a system showed a highly entangled ground state near the values of the semi-classical critical parameters [22].

Now, we extend the DLMG Hamiltonian to include a Kerr medium [23, 24] and degenerate parametric amplification [25] with nonlinear parameters κ and χ, respectively. The model Hamiltonian for such a system is given by the expression:

$$\hat{H} = \omega_0 \hat{a}^\dagger \hat{a} + \kappa(\hat{a}^\dagger \hat{a})^2 + \chi\left(\hat{a}^2 + \hat{a}^{\dagger 2}\right) + \omega_a \hat{J}_z + \frac{\xi}{N}\hat{J}_z^2 + \frac{g}{\sqrt{N}}\left(\hat{a} + \hat{a}^\dagger\right)\hat{J}_x, \tag{6}$$

where the modified field frequency $\omega_0 = \omega_f - \kappa + 2\chi$ involves the modifications arising from the original Kerr and parametric amplifier terms, $\hat{a}^{\dagger 2}\hat{a}^2$ and $\left(\hat{a} + \hat{a}^\dagger\right)^2$. Experimental realizations providing an assorted range of tunable parameters for

the DLMG model may include a two-hyperfine-structure-defined-modes BEC coupled to a quantum cavity field mode through a one microwave photon process; e.g., trapped hyperfine ground states of a Sodium BEC inside a microwave cavity [26]. Arrays of interacting superconducting qubits coupled to the quantum field mode of a coplanar waveguide resonator may be considered as a physical realization limited by small ensemble sizes [27].

In the literature, similar model Hamiltonians have been considered without the feedback from the BEC on the electromagnetic field; e.g., a second-order phase transition from immiscibility to miscibility is revealed in such a two-species system by considering a linear mixing between the binary components [28]. Stable domain-wall solutions, on top of flat continuous wave asymmetric bimodal states, can also be found near the point of the symmetry-breaking bifurcations [29]. The relative phase of domain-walls and breather-like dynamics for these dressed two-species BECs has also been studied by considering a classical external driving field [30, 31]. Our results with a driven quantum field differs considerably from earlier studies: It is found that even in the semi-classical limit, the quantum field drive manifests in the excitation ratio parameter. When this excitation parameter is small or close to one, a discrete total excitation strongly modifies the classical dynamics of the system, producing localized asymmetric dynamics where some of the phase space trajectories present a running phase; e.g., Fig. 3a, b.

The proposed Hamiltonian in Eq. (6) may be experimentally realized by a two-species BEC, where the species are defined by two hyperfine-structure levels. The condensate is confined and coupled to a quantum cavity field mode through a one-microwave-photon process in the presence of a Kerr and a $\chi^{(2)}$ medium. In general, the model described by Hamiltonian (6) has complex dynamics that deserve a study on their own. In order to give a clear interpretation, here, we limit ourselves to an analytical approach in the weak regime where intra-ensemble and ensemble-field couplings, as well as nonlinearities, are small compared to the field and hyperfine transition frequencies.

3 Weak Regime

The full Hamiltonian in Eq. (6) does not conserve the total number of excitations, $\hat{\mathcal{N}} = \hat{a}^\dagger \hat{a} + \hat{J}_z$, i.e., $[\hat{H}, \hat{\mathcal{N}}] \neq 0$. This fact prevents a simple approach like those given in the literature [8, 21]. This inconvenience may be bridged in the regime where nonlinearities and couplings are weak compared to the field and transition frequencies. In this weak regime it is possible to define a couple of unitary transformations [32]

$$\hat{T} = e^{\eta\left(\hat{a}^2 - \hat{a}^{\dagger 2}\right)}, \tag{7}$$

$$\hat{U} = e^{-iv\left(\hat{a} + \hat{a}^\dagger\right)\hat{J}_y}. \tag{8}$$

The first of these transformations is equivalent to consider a squeezed basis; while the second one is similar to a polariton transformation and provides an effective rotating wave approximation, with the introduction of the small parameters $\eta = \chi/\omega_0 \ll 1$ and $v = g(1-2\eta)/(\omega_a + \omega_0 - 4\chi\eta) \ll 1$, respectively. The following effective Hamiltonian, up to a constant and in units of $\hbar$, is obtained by neglecting all the products of couplings with nonlinearities (i.e., $\kappa, \xi, \chi, \lambda, \eta$ and v are all at least a couple orders of magnitude smaller than the field and atom frequencies) and moving into the frame defined by the total excitation number rotating at frequency $\omega = \omega_0 - 4\chi\eta$,

$$\hat{H}_{eff} = \delta\hat{J}_z + \kappa\left(\hat{a}^\dagger\hat{a}\right)^2 + \frac{\xi}{N}\hat{J}_z^2 + \frac{\lambda}{\sqrt{N}}\left(\hat{a}\hat{J}_+ + \hat{a}^\dagger\hat{J}_-\right). \tag{9}$$

Here, the frequency detuning is given by $\delta = \omega_a - \omega$ and the effective ensemble-field coupling is $\lambda = \omega v$. This effective Hamiltonian in the weak regime is nothing else than the extended Dicke model studied in reference [22] plus a Kerr term. The Hamiltonian in Eq. (9) conserves the total number of excitations, $[\hat{H}_{eff}, \hat{\mathcal{N}}] = 0$. Note that the exact dynamics defined by Hamiltonian Eq. (9) can be calculated by quantum inverse methods [33].

3.1 Semi-Classical Limit

In order to link our proposed configuration to a generalized pendulum problem, we apply the mean-field approach to study the semi-classical dynamics of this two-species BEC coupled to an optical cavity mode. It is possible to approximate the expectation values by considering the system in a separable state composed of a coherent photon state [34, 35], $|\sqrt{n}e^{\imath\Phi}\rangle$, and a coherent spin $1/2$ state [36, 37], $|z, \theta\rangle$, respectively. The expectation values for the field with the photon number n and optical phase ϕ are:

$$\langle\hat{a}\rangle \equiv \alpha = \sqrt{n}e^{i\phi}, \tag{10}$$

$$\langle\hat{a}^\dagger\rangle \equiv \alpha^* = \sqrt{n}e^{-i\phi}, \tag{11}$$

$$\langle\hat{a}^\dagger\hat{a}\rangle \equiv |\alpha|^2 = n. \tag{12}$$

If the ensemble is large enough, such that $N \gg 1$ but less than the restriction brought by the two-mode approximation [12, 38], the expectation values for the ensemble operators may be approximated by those in the thermodynamic limit,

$$\langle\hat{J}_z\rangle \equiv J_z \approx \frac{N}{2}z, \tag{13}$$

$$\langle \hat{J}_{\pm} \rangle \equiv J_{\pm} \approx \frac{N}{2}\sqrt{1-z^2}e^{\pm i\theta}, \tag{14}$$

where the fractional population difference is defined by the rotating angle in the corresponding atomic Bloch sphere, i.e., $z = cos\theta$. The conserved quantity in our system is the mean total excitation number, which is given by the expression:

$$\langle \hat{\mathcal{N}} \rangle \equiv \mathcal{N} = n + \frac{N}{2}z. \tag{15}$$

This mean-field approximation plus the definition of a total phase variable, $\Phi = \phi + \theta$, and an excitation ratio, $k = 2\mathcal{N}/N$, allow us to write the weak regime effective Hamiltonian in units of $\hbar N\lambda/2$ and up to a constant as:

$$H = \left(\Delta + \frac{\Lambda}{2}z\right)z + \sqrt{2(k-z)(1-z^2)}\cos\Phi, \tag{16}$$

where the re-scaled transition detuning is now shifted by the self-phase modulation from the Kerr nonlinearity, $\Delta = (\delta + \kappa)/\lambda$. Moreover, the re-scaled coupling ratio is defined as $\Lambda = \xi/\lambda$. This mean-field Hamiltonian is equivalent with that of the DLMG model in [22], with the difference that in this case the Kerr and $\chi^{(2)}$ nonlinearities play important roles in the frequency detuning Δ and the characteristic interaction ratio Λ, respectively.

Equation (16) may be viewed as a more general pendulum with nonlinear pendulum length and changeable pendulum mass described by the excitation ratio, k. This distinguishes our system from the double-well configuration which is equivalent to a pendulum with just nonlinear pendulum length. Also, note the restriction $k - z > 0$ induced by the model Hamiltonian. Our system is equivalent to the case of a BEC in an asymmetric double-well (ADW) via a phase π-shift and a restriction given by $k - z = 1/2$,

$$H_{ADW} = \left(\Delta + \frac{\Lambda}{2}z\right)z - \sqrt{1-z^2}\cos\Phi, \tag{17}$$

3.2 Fixed Points of the System

The dynamics of the semi-classical system is given by the equations of motion for the dimensionless fractional population difference and total phase variable,

$$\dot{z} = \sqrt{2(1-z^2)(k-z)}\sin\Phi, \tag{18}$$

$$\dot{\Phi} = \Delta + \Lambda z - \frac{1 + 2kz + 3z^2}{\sqrt{2(1-z^2)(k-z)}}\cos\Phi. \tag{19}$$

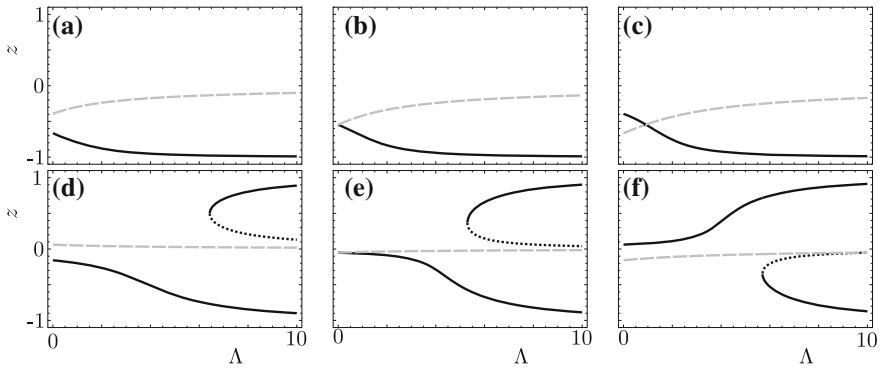

Fig. 2 Example of fixed points in the weak regime, described by Eqs. (18 and 19), for excitation ratios (**a**–**c**) $k = 0.1$ and (**d**–**f**) $k = 10$, respectively. Different tunning ratios, $\Delta = (\delta + \kappa)/\lambda$, are shown: (**a**, **d**) $\Delta = -0.5$, (**b**, **e**) $\Delta = 0$, (**c**, **f**) $\Delta = 0.5$. *Solid* and *dotted black lines* correspond to stable and unstable fixed points for $\pi-$oscillations; while *dashed grey lines* correspond to fixed points for plasma oscillations

Stationary states are found at the total phase variables values of $\Phi = 0$ and π. Due to the π phase difference with Eq. (1), here the plasma and π oscillations will exchange places appearing at $\Phi = \pi$ and $\Phi = 0$, respectively.

The fixed points of this Hamiltonian coincide with the critical points as $\dot{z} \equiv -\partial H/\partial \Phi$ and $\dot{\Phi} \equiv \partial H/\partial z$ [21]. Stationary states are found for the phase variable values $\Phi = 0, \pi$ and the excitation parameter value

$$k = \frac{3z^2 - 1}{2z} + \frac{(1 - z^2)|(\Delta + \Lambda z)|}{4z^2} \times \left\{ |\Delta + \Lambda z| \pm \left[(\Delta + \Lambda z)^2 - 4z \right]^{1/2} \right\}. \quad (20)$$

Notice that, in order to obtain a real excitation ratio, k, the allowed fractional population difference is bounded to the range $z \in [-1, z_-] \cup [z_+, 1]$, where $z_\pm = [2 - \Delta\Lambda \pm 2(1 - \Delta\Lambda)^{1/2}]/\Lambda^2$ sets the condition $\Delta \leq 1/\Lambda$.

An example of fixed points in the weak regime is shown in Fig. 2. When the value of the excitation ratio k is less than or within the order of the magnitude of one, we have a quantum drive compared to a classical one ($k \gg 1$). It is the introduction of the quantum drive and nonlinear processes that brings a peculiar breaking of the symmetry, different from the pitchfork bifurcation of the classical driving. It is possible to numerically sample the parameter space, $\{\Delta, \Lambda, k\}$, and see that for any given excitation ratio, k, the fixed points satisfy mirror inversion at $\Lambda = 0$; i.e., $z(\Lambda, |\Delta|) = z(-\Lambda, -|\Delta|)$. Also, if the frequency detuning, δ, is set to compensate the Kerr nonlinearity, $\delta = -\kappa$, it is possible to recover results that have been studied in the past; e.g., Fig. 2b, e correspond to Fig. 2 in [21].

From the mean-field Hamiltonian in Eq. (16), it is straightforward to see that the quantum drive restricts the phase space accessible to Rabi oscillations for low excitation ratio, $k < 1$, in order to keep the mean effective energy real, as shown in

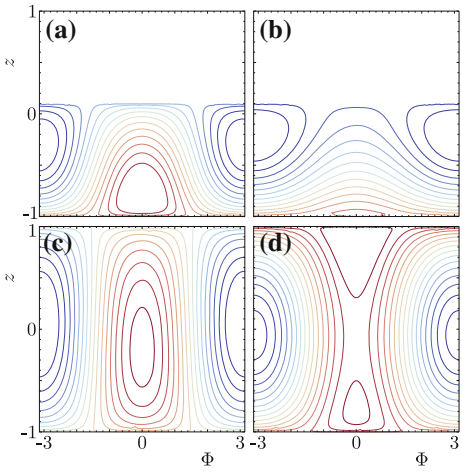

Fig. 3 Normalized mean value of the effective Hamiltonian energy in Eq. (16), where a compression of the available phase space is shown for parameter sets $\{\Delta, \Lambda, k\} =$ (**a**) $\{-0.5, 1, 0.1\}$ and (**b**) $\{0.5, 8, 0.1\}$. Also, the existence of asymmetric trajectories for symmetric initial parameters is intuited from the lack of symmetry with respect to the horizontal axis of the normalized mean value effective energy for parameter sets in the Rabi and Josephson regimes, $\{\Delta, \Lambda, k\} =$ (**c**) $\{-0.5, 1, 10\}$ and (**d**) $\{0.5, 8, 10\}$, in that order (Color figure online)

Fig. 3a, b. Figure 3c, d allow us to see that the quantum drive also breaks the symmetry of symmetric initial conditions as isoenergetic lines are not symmetric with respect to the horizontal axis even when the whole phase space is accessible.

Figure 4 shows an example of asymmetric Rabi and Josephson oscillations brought by the quantum driving field. A parameter set $\{\Delta = 0.5, k = 10\}$ is taken and the fixed points found in Fig. 4a. From the fixed points, two coupling ratios are chosen in the Rabi, $\Lambda = 1$, and Josephson, $\Lambda = 8$, regimes; this procedure delivers one stable fixed point, $\{A\}$, in the Rabi regime and two stable, $\{B, C\}$, and one unstable, $\{D\}$, fixed points in the Josephson regime. Figure 4b shows typical trajectories in these two regimes, where it is possible to see that symmetric initial conditions, i.e., $\{z_{\pm}(t = 0) = \pm z_0, \Phi(t = 0) = 0\}$, do not deliver symmetric trajectories. The latter can be seen straightforward from the position of the unstable fixed point, also called separatrix, and trajectories starting close to it.

In the limit where the couplings ratio is large, $\Lambda \to \infty$, it is possible to see a pitchfork bifurcations depending on the excitation ratio; an approximate critical excitation ratio can be calculated as $k_c \approx \Lambda^2/2$. At this critical value, a stable fixed point bifurcates into two new stable fixed points and the original fixed point becomes an unstable fixed point acting as a separatrix in phase space. There is a symmetry breaking in the dynamics due to the bifurcation, a transition from Rabi to Josephson oscillations; i.e., two initial symmetric states share identical dynamics in the Rabi regime, while in the Josephson regime they localize in different regions of phase space. Figure 5 shows an example of this symmetry

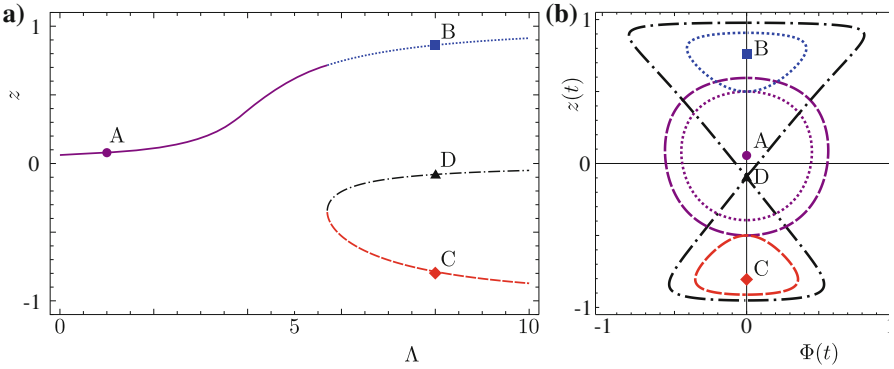

Fig. 4 Fixed points and typical trajectories for parameter set $\{\Delta = -0.5, \Lambda = 1 \text{ and } 8, k = 10\}$. **a** Fixed points for the equations of motion in the weak regime, described by Eqs. (18 and 19) at $\varphi = 0$, showing the splitting of a single stable fixed point in the Rabi regime (*solid purple*) into two fixed points in the Josephson regime (*dotted blue* and *dashed red*). The unstable fixed point, or separatrix, in the Josephson regime (*dash-dotted black*) is also shown. **b** Examples of trajectories with symmetrical initial conditions $\{z_\pm = \pm 0.5, \Phi = 0\}$, leading to asymmetrical Rabi oscillations (*purple dotted* for z_+ and *dashed for* z_-) around the fixed point A; and asymmetrically localized Josephson oscillations around the fixed point B (*blue dotted* for z_+) and C (*red dashed* for z_+). Two trajectories starting slightly above and below the separatrix D are also shown (*dash-dotted black*) (Color figure online)

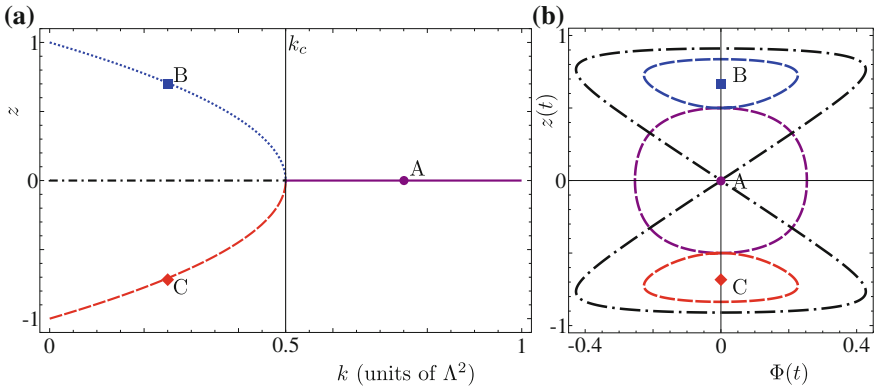

Fig. 5 Off resonance, $\delta \neq 0$, with $\Delta = (\delta + \kappa)/\lambda = 0$, i.e., $\delta = -\kappa$. **a** Fixed points for the equations of motion in the weak regime, described by Eqs. (18 and 19) at $\Phi = 0$, in the large couplings ratio limit, $\Lambda = \xi/\lambda \to \infty$ (numerical value $\Lambda = 1{,}000$), showing the bifurcation of a single stable fixed point in the Rabi regime (*solid purple*) into two fixed points in the Josephson regime (*dotted blue* and *dashed red*). The unstable fixed point, or separatrix, in the Josephson regime (*dash-dotted black*) is also shown. **b** Examples of trajectories with symmetrical initial conditions $\{z_\pm = \pm 0.5, \Phi = 0\}$, identical Rabi oscillations (*purple solid*) around the fixed point A (numerical value $k = 75{,}0000$), and symmetrically localized Josephson oscillations around the fixed point B (*blue dotted*) and C (*red dashed*). Two trajectories starting slightly above and below the separatrix D are also shown (*dash-dotted black*) (numerical value $k = 25{,}0000$) (Color figure online)

breaking in the dynamics, in which for large coupling ratios, $\Lambda \gg 1$, i.e., $\eta \gg \lambda$, it is possible to locate a pitchfork bifurcation point, $k_{c+} \approx \Lambda^2/2$ even for the off-resonance condition, $\delta \neq 0$. Now the transition between the two-level system and the field δ is different from zero but balances off the nonlinearity, i.e., $\Delta = 0$. This condition, $\eta \gg \lambda$, relates to the phase space region where maximal shared bipartite concurrence in the atomic ensemble may be obtained in the quantum treatment of this model [22]. The difference comes from the large excitation parameter ratio arising in this semi-classical analysis, $k_{c+} \gg 1$, i.e., $N_q \ll n$ as $z_c \approx 3/\Lambda^2 \ll 1$.

4 Conclusion

In summary, we have presented an analysis of the classical dynamics of a two-species BEC large in size driven by a quantized field in the presence of nonlinear processes. In the weak regime, we find that the nonlinear phase from the Kerr nonlinearity, κ, shifts the transition detuning of the effective Hamiltonian of a generalized Dicke model; while the $\chi^{(2)}$ nonlinear coefficient re-scales the coupling ratio. This mean-field Hamiltonian is equivalent to a nonrigid, nonlinear pendulum, for which a transition from Rabi to Josephson dynamics is identified depending on both the intra-BEC interactions to field-ensemble coupling ratio and the ratio between the total excitation number and the ensemble size. Moreover, we find that the symmetry of Josephson dynamics is broken by the quantum field, and an actual pitchfork bifurcation point is found in the regime where the intra-ensemble interaction is larger than the field-ensemble coupling. Furthermore, It is known that symmetry-breaking in the classical dynamics of BEC may herald entangled quantum states [39, 40]. Our results may provide a deeper understanding about the collective dynamics of interacting BECs and give another example in favour of the aforementioned conjecture relating classical and quantum regimes for nonlinear systems.

Acknowledgments B.M.R.L. is grateful for the hospitality and camaraderie of the Theoretical Optics Group at National Tsing Hua University, Taiwan.

References

1. C.J. Pethick, H. Smith, *Bose-Einstein Condensation in Dilute Gases* (Cambridge University Press, Cambridge, 2002)
2. M. Albiez, R. Gati, J. Fölling, S. Hunsmann, M. Cristiani, M. K. Oberthaler, Phys. Rev. Lett. **95**, 010402 (2005)
3. S. Levy, E. Lahoud, I. Shomroni, J. Steinhauer, Nature **449**, 579 (2007)
4. J.A. Dunningham, K. Burnett, M. Edwards, Phys. Rev. A **64**, 015601 (2001)

5. E. Andersson, T. Calarco, R. Folman, M. Andersson, B. Hessmo, J. Schmiedmayer, Phys. Rev. Lett. **88**, 100401 (2002)
6. A. Smerzi, S. Fantoni, S. Giovanazzi, S. R. Shenoy, Phys. Rev. Lett. **79**, 4950 (1997)
7. S. Raghavan, A. Smerzi, S. Fantoni, S.R. Shenoy, Phys. Rev. A **59**, 620 (1999)
8. T. Zibold, E. Nicklas, C. Gross, M.K. Oberthaler, Phys. Rev. Lett. **105**, 204101 (2010)
9. F. Brennecke, T. Donner, S. Ritter, T. Bourdel, M. Kohl, T. Esslinger, Nature **450**, 268 (2007)
10. Y. Colombe, T. Steinmetz, G. Dubois, F. Linke, D. Hunger, J. Reichel, Nature **450**, 272 (2007)
11. K. Baumann, C. Guerlin, F. Brennecke, T. Esslinger, Nature **464**, 1301 (2010)
12. G. Chen, Z. Chen, J.-Q. Liang, EuroPhys. Lett. **80**, 40004 (2007)
13. C. Lee, Phys. Rev. Lett. **102**, 070401 (2009)
14. R.H. Dicke, Phys. Rev. **93**, 99 (1954)
15. H.J. Lipkin, N. Meshkov, A.J. Glick, Nucl. Phys. **62**, 188 (1965)
16. J. Vidal, G. Palacios, R. Mosseri, Phys. Rev. A **69**, 022107 (2004)
17. J. Vidal, G. Palacios, C. Aslangul, Phys. Rev. A **70**, 062304 (2004)
18. S. Morrison, A.S. Parkins, Phys. Rev. Lett. **100**, 040403 (2008)
19. J. Larson, Europhys. Lett. **90**, 54001 (2010)
20. Q.-H. Chen, T. Liu, Y.-Y. Zhang, K.-L. Wang, Phys. Rev. A **82**, 053841 (2010)
21. B. M. Rodríguez-Lara, R.-K. Lee, Phys. Rev. E **84**, 016225 (2011)
22. B.M. Rodríguez-Lara and R.-K. Lee, arXiv: 1008.2572v1 (2010)
23. S. Chi, T.Y. Wang, S. Wen, Phys. Rev. A **47**, 3371 (1993)
24. B. Deb, D.S. Ray, Phys. Rev. A **48**, 3191 (1993)
25. M.J. Collett, C.W. Gardiner, Phys. Rev. A **30**, 1386 (1984)
26. A. Görlitz, T.L. Gustavson, A.E. Leanhardt, R. Low, A.P. Chikkatur, S. Gupta, S. Inouye, D.E. Pritchard, W. Ketterle, Phys. Rev. Lett. **90**, 090401 (2003)
27. D.I. Tsomokos, S. Ashhab, F. Nori, Phys. Rev. A **82**, 052311 (2010)
28. I.M. Merhasin, B.A. Malomed, R. Driben, J. Phys. B: At. Mol. Opt. Phys. **38**, 877 (2005)
29. N. Dror, B.A. Malomed, J. Zeng, Phys. Rev. E **84**, 046602 (2011)
30. D.T. Son, M.A. Stephanov, Phys. Rev. A **65**, 063621 (2002)
31. S.D. Jenkins, T.A.B. Kennedy, Phys. Rev. A **68**, 053607 (2003)
32. B.M. Rodríguez-Lara, R.-K. Lee, J. Opt. Soc. Am. B **27**, 2443 (2010)
33. N.M. Bogoliubov, R.K. Bullough, J. Timonen, J. Phys. A: Math. Gen. **29**, 6305 (1996)
34. E.C.G. Sudarshan, Phys. Rev. Lett. **10**, 277 (1963)
35. R.J. Glauber, Phys. Rev. **131**, 2766 (1963)
36. G. Nienhuis, van S.J. Enk, Phys. Scr. T **48**, 87–93 (1993)
37. F.T. Arecchi, E. Courtens, R. Gilmore, H. Thomas, Phys. Rev. A **6**, 2211 (1972)
38. G.J. Milburn, J. Corney, E.M. Wright, D.F. Walls, Phys. Rev. A **55**, 4318 (1997)
39. A. Micheli, D. Jacksch, J. I. Cirac, P. Zoller, Phys. Rev. A **67**, 013607 (2003)
40. A. P. Hines, R. H. McKenzie, G.J. Milburn, Phys. Rev. A. **71**, 042303 (2005)

Existence, Stability and Nonlinear Dynamics of Vortices and Vortex Clusters in Anisotropic Bose-Einstein Condensates

J. Stockhofe, P. G. Kevrekidis and P. Schmelcher

Abstract This chapter is devoted to the study of vortex excitations in one-component Bose-Einstein condensates, with a special emphasis on the impact of anisotropic confinement on the existence, stability and dynamical properties of vortices and particularly few-vortex clusters. Symmetry breaking features are pervasive within this system even in its isotropic installment, where cascades of symmetry breaking bifurcations give rise to the multi-vortex clusters, but also within the anisotropic realm which naturally breaks the rotational symmetry of the multi-vortex states. Our first main tool for analyzing the system consists of a weakly nonlinear (bifurcation) approach which starts from the linear states of the problem and examines their continuation and bifurcation into novel symmetry-broken configurations in the nonlinear case. This is first done in the isotropic limit and the modifications introduced by the anisotropy are subsequently presented. The second main tool concerns the highly nonlinear regime where the vortices can be considered as individual topologically charged "particles" which precess within the parabolic trap and interact with each other, similarly to fluid vortices. The conclusions stemming from both the bifurcation and the interacting particle picture are corroborated by numerical computations which are also used to bridge the gap between these two opposite-end regimes.

J. Stockhofe · P. Schmelcher (✉)
Zentrum für Optische Quantentechnologien, Universität Hamburg,
Luruper Chaussee 149, 22761 Hamburg, Germany
e-mail: pschmelc@physnet.uni-hamburg.de

J. Stockhofe
e-mail: jstockho@physnet.uni-hamburg.de

P. G. Kevrekidis
Department of Mathematics and Statistics, University of Massachusetts,
Amherst, 01003-4515 MA, USA
e-mail: kevrekid@math.umass.edu

Progress Optical Sci., Photonics (2013): 543–581
DOI: 10.1007/10091_2012_10

Published Online: 3 July 2012

1 Introduction

The study of topologically charged vortex states is a theme of wide appeal in numerous fields such as superfluid helium [1], type-II superconductors [2], nonlinear optics [3, 4] and atomic Bose-Einstein condensates (BECs) [5–7], among many others [8]. Admittedly, BECs constitute one of the most pristine settings where structural and dynamical properties of single- and multi-vortex (both of the same and of opposite charge) and multi-charged-vortex states can be investigated not only theoretically and computationally but also by means of a wide array of experimental techniques.

The main focus of study within this theme of vortex dynamics over the past decade has been the examination of single- and multi-charge vortices, as well as of highly structured vortex lattices [7]. On the other hand, far less attention has been paid to the dynamics of small clusters of (few) vortices. In this context, it is particularly relevant to understand both the potential existence of stationary or periodic orbits in such systems, and their dynamical stability, as well as the motion near such "equilibria", but also the generic motion of the vortices in these clusters far from their equilibrium configurations. Questions concerning also the integrable or non-integrable structure of the vortex trajectories and the existence of chaotic dynamics therein constitute a fascinating topic for further investigation. Much of the relevant literature has been reserved to the fundamental (beyond the single vortex) building block of the vortex dipole [9–17]. Recently, this state has also received considerable experimental attention [18–20] but other configurations have been considered theoretically as well [12, 13, 16, 21] and are becoming amenable to experiments [22]. Let us remark that from the theoretical side small vortex clusters have also been studied in the presence of periodic lattice potentials [23], and it was demonstrated how introducing different lattice parameters along the different axes can significantly affect their stability properties. In the presence of a periodic lattice potential, also more complex entities such as super-vortices have been constructed [24]. Recently, there has also been an increase in interest in so-called azimuthon excitations, i.e. vortices accompanied by azimuthal density modulations around their cores [25, 26]. Clusters of these have been studied in [27].

Our aim here, in considerable extension of the recent discussion of [28], is to examine the context where vortex clusters become subject to anisotropy in the harmonic trapping potential. Although some effort has been invested in such investigations in the context of co-rotating vortex systems by the works of [29–31], very little attention has been paid to this subject in the case of counter-rotating vortices. In that light, we offer a perspective encompassing two complementary approaches: close to the linear limit, we develop a weakly nonlinear (bifurcation) approach which examines the continuation of various states and their bifurcation into novel symmetry-broken states in the nonlinear regime; far from the linear regime (in fact, in the highly nonlinear regime), the vortices can be considered as individual topologically charged "particles" for which (ordinary differential) equations of motion describing their precessions and interactions are devised and

analyzed. Our numerical analysis of the system corroborates these limits and bridges them by means of detailed computations[1].

The presentation of this chapter will be structured as follows. In Sect. 2, we present the model and its theoretical setup. Upon a discussion of the highly nonlinear particle-type description of vortex dynamics in anisotropic traps in Sect. 3, we focus on aligned vortex clusters in Sects. 4 and 5 from the particle and bifurcation perspectives, respectively. In Sect. 6, we address non-aligned vortex clusters, which are examined in the presence of anisotropy in Sect. 7. Finally, in Sect. 8, we summarize our findings and present our conclusions.

2 Model and Theoretical Setup

Our prototypical model for the pancake-shaped Bose-Einstein condensates under consideration is the 2D Gross-Pitaevskii equation (GPE) for the condensate wavefunction $\psi(x, y, t)$ which can be cast into a convenient dimensionless form by measuring length, time, energy and density $|\psi|^2$ in units of a_z (harmonic oscillator length in the z-direction), ω_z^{-1} (inverse trap strength in the z-direction), $\hbar\omega_z$ and $(2\sqrt{2\pi}|a|a_z)^{-1}$, respectively. Here, a denotes the s-wave scattering length, encoding the low-energy limit of the interaction between the bosons [6]. In the rescaled variables the model of interest is given by:

$$\mathrm{i}\partial_t\psi(x, y, t) = \left[-\frac{1}{2}\nabla_\perp{}^2 + V(x, y) + \sigma|\psi(x, y, t)|^2\right]\psi(x, y, t), \tag{1}$$

where σ denotes the sign of the s-wave scattering length a. In the following we will exclusively discuss the case of repulsive interaction, $\sigma = +1$, which ensures stability of the condensate against collapse.

In Eq. 1, the harmonic (parabolic trap) potential that will be considered in this work is given by $V(x, y) = (\omega_x^2 x^2 + \omega_y^2 y^2)/2$, where the trapping frequencies in the plane have already been rescaled by the trap strength in the z-direction. All equations will be presented in dimensionless units for simplicity.

Below, we will analyze the existence and linear stability of the stationary modes of Eq. 1. These are obtained in the form $\psi(x, y, t) = \phi(x, y)\exp(-\mathrm{i}\mu t)$, where μ denotes the chemical potential. Substituting into Eq. 1 yields the stationary 2D Gross-Pitaevskii equation for $\phi(x, y)$. Numerically the relevant

[1] The connection provided through the numerical results is often essential as some configurations may e.g. be stable in the above two limits but possess instabilities in finite intermediate ranges of parameter values that would not be observable by restricting our view to the analytically tractable limits. A notable example of this type is offered by the vortex quadrupole configuration (see e.g. Fig. 8 of [16] and equivalently the isotropic limit of both Fig. 10d and e below). Such a state is found to be linearly stable in both of the above quasi-analytical limits and its intermediate range of instability parameter values is only detected by the bridging numerical continuation.

nonlinear stationary states will be identified as a function of the chemical potential μ and often as a function of the anisotropy by means of a Newton-Krylov scheme over a rectangular two-dimensional domain with suitably small spacing. Linear stability will be explored by means of the Bogoliubov-de Gennes (BdG) analysis. This involves the derivation of the BdG equations, which stem from a linearization of the GPE Eq. 1 around the stationary solution $\phi(x,y)$ by using the ansatz [7]

$$\psi(x,y,t) = \left[\phi(x,y) + a(x,y)e^{-\mathrm{i}\omega t} + b^*(x,y)e^{+\mathrm{i}\omega^* t}\right]e^{-\mathrm{i}\mu t}, \tag{2}$$

where $*$ indicates complex conjugation, and expanding to first order in a, b. The solution of the ensuing BdG eigenvalue problem yields the eigenvectors $(a(x,y), b(x,y))$ and eigenfrequencies ω. As concerns the latter, we note that due to the Hamiltonian nature of the system, if ω is an eigenfrequency of the Bogoliubov-de Gennes spectrum, so are $-\omega$, ω^* and $-\omega^*$. Notice that a linearly stable configuration is tantamount to $\mathrm{Im}(\omega) = 0$, i.e., all eigenfrequencies being real.

An important quantity resulting from the BdG analysis is the energy carried by the normal mode with eigenfrequency ω, namely,

$$E = \omega \int \mathrm{d}x\mathrm{d}y(|a|^2 - |b|^2). \tag{3}$$

The sign of this quantity, known as *Krein sign* [32], is a topological property of each eigenmode. Let us remark that for a real mode ω, both (ω, a, b) and $(-\omega, b^*, a^*)$ solve the BdG equations, such that both modes of this pair have the same E and the same Krein signature according to Eq. 3. For eigenfrequencies with a nonvanishing imaginary part, one can show that $E = 0$ [7].

A BdG mode for which the sign of E is negative is called *anomalous mode* [5], or *negative energy mode* [33], or mode with *negative Krein signature* [32]. If in the course of tuning one of the system's parameters such a mode becomes resonant with a mode with positive Krein signature then, typically, complex frequencies appear in the excitation spectrum, i.e., a dynamical instability arises [34].

3 A Vortex Particle Picture in Anisotropic Traps

Let us in the following consider a harmonic trapping potential $V(x,y) = (\omega_x^2 x^2 + \omega_y^2 y^2)/2$, where the two dimensionless trapping frequencies ω_x, ω_y can be different. The parameter $\alpha = \omega_y/\omega_x$ will be used to quantify the anisotropy of the trap. For simplicity, we restrict the discussion to singly-charged vortices with charge $s \in \{\pm 1\}$, although generalizations to multiply-quantized vortices are available [35]. In [35, 36] a set of vortex precession ODEs is derived within the full three-dimensional Gross-Pitaevskii framework which also holds in the anisotropic regime of $\omega_x \neq \omega_y$. Matching this result to the expressions obtained in

[37] for the two-dimensional GPE in the isotropic limit, we find the following set of ordinary differential equations governing the precessional dynamics of a single vortex of charge s:

$$\dot{x} = -s\omega_y^2 Q y, \qquad \dot{y} = s\omega_x^2 Q x. \tag{4}$$

where $Q(\mu, \omega_x, \omega_y) = \ln(A\mu/\omega_{\text{eff}})/(2\mu)$, $\omega_{\text{eff}} = \sqrt{(\omega_x^2 + \omega_y^2)/2}$, and the numerical constant $A \approx 8.88$.

It is straightforward to check that $(x^2/\omega_y^2 + y^2/\omega_x^2)$ is a constant of motion for this dynamical system. Thus, these equations describe elliptical vortex orbits in the anisotropic trap, where the precession frequency at which both the x and y coordinates perform harmonic oscillations is given by $\omega_{\text{pr}} = \omega_x \omega_y Q$. We note that in isotropic traps the precession frequency is known to increase as a function of displacement from the trap center [35], but this correction is small for vortices close to the center and we will neglect it here for simplicity. Additionally, we point out that the above mentioned elliptical orbits of a single vortex inside the parabolic trap naturally degenerate into circular ones in the isotropic limit of $\omega_x = \omega_y$.

In the presence of more than one vortex, there is an additional interaction contribution to the equations of motion: Each vortex moves with the local velocity field created by all the other vortices [38, 39]. Neglecting modifications of the velocity field profiles due to the inhomogeneous condensate background in the presence of the trap, we can employ the interaction term that has also been used in [16, 20], yielding

$$\dot{x}_k = -s_k\omega_y^2 Q y_k + B\sum_{j\neq k} s_j \frac{y_j - y_k}{2\rho_{jk}^2}, \quad \dot{y}_k = s_k\omega_x^2 Q x_k - B\sum_{j\neq k} s_j \frac{x_j - x_k}{2\rho_{jk}^2}, \tag{5}$$

where $\rho_{jk}^2 = (x_j - x_k)^2 + (y_j - y_k)^2$. B is a numerical constant, which in earlier works for isotropically trapped quasi two-dimensional condensates of aspect ratio $\omega_r/\omega_z = 0.2$ (which coincides with the isotropic limit in our simulations) has been found to be $B \approx 1.35$ from fits of the dipole's equilibrium position [16, 20]. We will use this value of B whenever numerically evaluating results from the above ODE system.

The "particle picture" of Eq. 5 will be used throughout this work to study equilibrium positions, linearization frequencies and dynamics of few-vortex arrangements in anisotropic traps.

Before concluding this section, let us remark that the above equations of motion for the vortices can also be obtained from a suitable Hamiltonian with a logarithmic interaction potential [39]. A similar type of interaction term has also been used in the study of mesoscopic systems, in particular to model electrostatically interacting charged balls of millimetre size free to move on a plane conductor [40, 41].

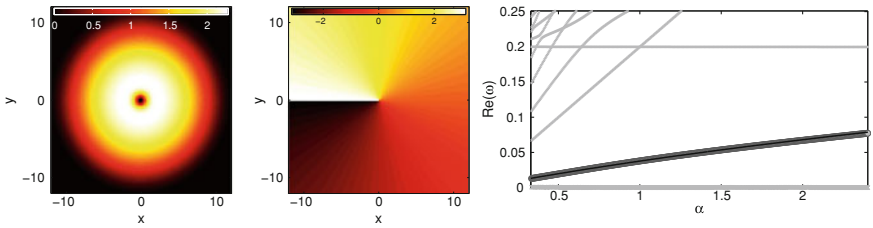

Fig. 1 Profiles (density in the left panel and phase in the middle panel) and BdG spectrum (right panel) of the single vortex state, precession frequency from the particle picture in black, coinciding with the anomalous BdG mode (dark gray line made up of circular markers). Chemical potential fixed at $\mu = 2.5$

4 Aligned Vortex States in the Particle Picture

One particular class of stationary vortex clusters in Bose-Einstein condensates has received considerable attention in the past years, namely configurations where a number of singly-charged vortices is located along one of the symmetry axes of the trap, and the sign of the vortex charges is alternating between adjacent vortices, see e.g. [12, 13, 16]. We will refer to these solutions of the Gross-Pitaevskii equation as "aligned vortex states". In the following, we will apply the particle picture ODEs to determine equilibrium positions and linearization frequencies of the aligned vortex cluster states. In contrast to numerous previous works on the theme of counter-rotating vortices (see [16] for a recent discussion of the relevant literature), we will not restrict the analysis to isotropic traps, but allow for different trapping frequencies in the x- and y-direction. This will turn out to have important consequences for the stability of the vortex clusters. It should be noted again, on the other hand, that the subject of co-rotating vortices in the presence of anisotropy has been considered in some detail in the series of works [29–31].

4.1 Single Vortex

To start out, we numerically determine the stationary single vortex solution to the full Gross-Pitaevskii equation for different values of $\alpha = \omega_y/\omega_x$ by representing the Laplacian in terms of finite differences on a spatial grid and employing a Newton-Krylov method as described in [42]. Technically, to scan α, we fix $\omega_x = 0.2$ throughout this work and vary ω_y. The chemical potential is held fixed at $\mu = 2.5$, high enough for the Thomas-Fermi (TF) large-density approximation to be applicable. As expected, and predicted by the particle picture, the stationary single vortex is located at the trap center $x = y = 0$ for any value of α. A typical profile of the state's density and phase structure is shown in the left and middle panel of Fig. 1. Let us remark that these profiles do not show the full size of the grid used in our numerical simulations.

Having numerically identified the vortex solution in various anisotropic settings, we calculate its BdG spectrum as a function of α by diagonalizing the ensuing BdG matrix. The resulting spectrum is shown in Fig. 1, together with the linearization frequency calculated from the particle picture (black line). The spectrum contains one anomalous (negative Krein) mode indicated by the gray circles. This anomalous mode in the BdG spectrum is connected to the precessional motion of the vortex [43]. Exciting it slightly shifts the vortex from its equilibrium position and makes it precess around the trap center. Obviously, this mode's numerically found dependence on α is very well described by the precession frequency of the particle picture, both in the isotropic limit and in anisotropic settings. Finally, we stress that the BdG spectrum contains no eigenfrequencies with non-zero imaginary part, indicating that the single vortex state is dynamically stable in arbitrary anisotropic traps.

Apart from the anomalous mode responsible for vortex precession, the full BdG spectrum exhibits a large number of "background modes" which are not captured by the vortex particle picture. The $\omega = 0$ mode present for any value of α can be identified as the Goldstone mode related to the $U(1)$ invariance of the Gross-Pitaevskii equation. In addition, there is always a so-called Kohn or dipolar mode with frequency ω_x (which assumes the value 0.2 independent of α in Fig. 1). Similarly there is a dipolar mode (linear in α in Fig. 1) with frequency ω_y. These modes involve a collective oscillation of the entire cloud around the center of the trap in each of these two directions.

4.2 Vortex Dipole

Let us perform the same analysis for the so-called vortex "dipole", i.e. two vortices with opposite charges, say $s_1 = +1$, $s_2 = -1$. The existence of stationary configurations of such a vortex-antivortex pair (as it is sometimes called) was first demonstrated in [10], followed by more detailed discussions [12, 13, 15]. Stability properties of the dipole have been studied in a number of works, but the results were partially incoherent, in particular when anisotropic trapping was taken into account [13, 16]. Recently, interest in the vortex dipole has been renewed by experimental progress in the field, allowing to controllably create and observe such structures with unprecedented precision [18, 19, 14, 20].

The particle picture predicts two equilibrium positions of the vortices along each of the trap's main axes. Fixing the dipole along the y-axis, these read $x_1 = 0,\ y_1 = \pm\sqrt{B/(4\omega_y^2 Q)},\ x_2 = 0,\ y_2 = \mp\sqrt{B/(4\omega_y^2 Q)}$. Naturally, the solutions associated with the two different signs can be transformed into each other by simply interchanging the positive- and the negative-charge vortex.

The middle panel of Fig. 2 compares the numerically found equilibrium positions of the vortices forming the stationary dipole to this prediction. Technically, from the numerically calculated wavefunctions the vortex locations are extracted by

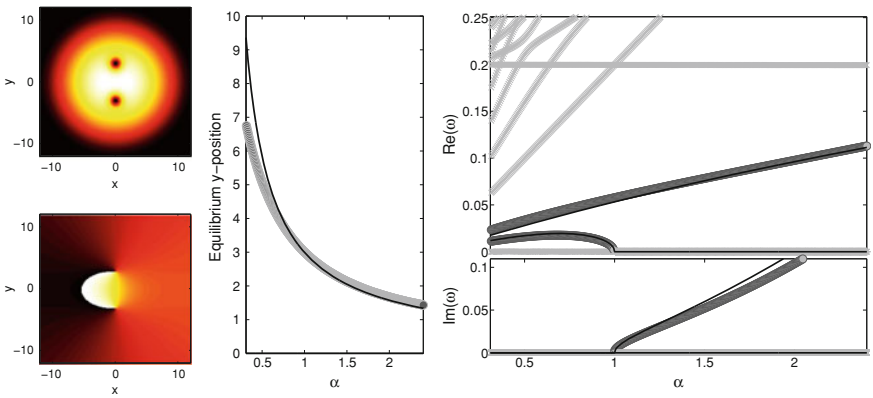

Fig. 2 The left panels show a typical example of the density and phase of a vortex dipole for an equilibrium position of the vortices within the PDE. The middle panel shows the equilibrium position of the dipole configuration as a function of the 2D aspect ratio: Numerical data (line of gray circles) and ODE prediction (black line). The right panel shows the results of the linearization around such a dipole as a function of α. For the anomalous (internal) modes of the two vortices the prediction from the particle equation theory is given again by the solid black lines, while the numerical findings are given by lines of dark gray circles. Purely imaginary modes are also denoted by gray circles. Notice the instability emerging for $\alpha > 1$. The chemical potential is fixed at $\mu = 2.5$ throughout

evaluating the z-component of the superfluid vorticity. The vortices then show up as sharp, well localized extrema. It can be observed that the agreement between the numerical data and the ODE prediction is better in the $\alpha > 1$ regime, and for small α the errors become larger. Partially, this inaccuracy of the particle picture in the low α regime can presumably be attributed to the radial dependence of the vortex precession frequency which we do not take into account. Another factor that should be taken into consideration here and accounts for the observed discrepancy is the modification of the vortex-vortex interaction due to the non-homogeneous, modulated TF density, especially near the condensate boundaries. The latter effect has been implicitly included in the equations through a shift of the B factor away from its background value. However, the deviations in the middle panel of Fig. 2 suggest that including effects due to the presence of the trap (and the ensuing non-homogeneous condensate background) on the vortex-vortex interaction by using an effective B is not sufficiently accurate for full quantitative agreement. A refined description of vortex interaction in the trapped condensate, taking into account not only the vortices' positions but also the non-trivial shape of the background density distribution and the ensuing deformation of the velocity fields around the vortices, would be an interesting direction for further studies and could presumably, when included into our particle picture equations, significantly improve their quantitative predictions.

The dipole's linearization frequencies are found to be $\omega_{1,2} = \pm\sqrt{2}\omega_{\rm pr}$, $\omega_{3,4} = \pm\omega_{\rm pr}\sqrt{1-\alpha^2}$. A key consequence of this prediction is that for $\alpha > 1$, the spectrum of the vortex dipole exhibits a purely imaginary mode, indicating instability in this

regime. On the other hand, for $\alpha \leq 1$ the dipole is stable. In this stable interval, the spectrum contains two anomalous modes (indicated by the gray line made up of circular markers in the right panel of Fig. 2) whose functional dependence is well described by the linearization frequencies predicted in the particle picture. At $\alpha = 1$, one of these two anomalous modes vanishes. The existence of such a zero mode in the isotropic limit is a general feature that will be found for all subsequent aligned vortex states: One can think of the presence of the aligned vortex configuration breaking the rotational symmetry of the $\alpha = 1$ system, which leads to the emergence of a corresponding Goldstone mode. For $\alpha > 1$, this former Goldstone mode in the dipole's spectrum becomes a purely imaginary eigenfrequency, which again is predicted correctly by the particle picture. Intuitively, in the isotropic setting of $\alpha = 1$ the dipole as a whole can be arbitrarily rotated. This neutrality is represented by the zero mode in the BdG spectrum. When $\alpha > 1$, in our current setup, the vortex pair is compressed along the axis of the vortex dipole, which favours "buckling" of the axial structure and leads to instability, while $\alpha < 1$ has the opposite effect. A typical example of the dipole's decay at $\alpha > 1$ is shown below, in Fig. 5.

4.3 Vortex Tripole

Let us now turn to the next aligned vortex state, consisting of three vortices of alternating charge, i.e. $s_1 = \pm 1,\ s_2 = \mp 1,\ s_3 = \pm 1$. As for the vortex dipole, we take the stationary vortices to be aligned along the y-axis, i.e. $x_{1,2,3} = 0$, and for their equilibrium y-coordinates we consider the symmetric ansatz $y_2 = 0,\ y_1 = -y_3 = y$. Inserting this into the particle picture ODEs yields a fixed point for $y = \sqrt{B/(4\omega_y^2 Q)}$. Thus, the particle picture predicts a stationary "vortex tripole" state, where two vortices of the same charge are placed along one of the trap's main axes, while the oppositely charged third vortex rests between them, at the trap center. Previous theoretical discussions of this tripole configuration can be found in [12, 13, 21], while a recent experimental observation has been reported in [22].

Again, we can compare the fixed point coordinates calculated from the vortex particle picture to the vortex positions obtained from numerically identifying the vortex tripole solution of the stationary GPE. The results are shown in Fig. 3.

Interestingly, we observe that while choosing $B = 1.35$ led to good agreement for the dipole configuration, this is no longer fully the case for the tripole. Here, better quantitative agreement is achieved if the interaction constant B is taken at its background value $B = 1.95$, valid for vortex interaction in a homogeneous condensate [16] (data not shown). This discrepancy may again be regarded as a warning sign that accounting for condensate inhomogeneities due to the trap by rescaling B is insufficient in the general case and it is certainly desirable to take into account the effects of the nonhomogeneous background discussed above.

Next, we calculate the linearization frequencies around the tripole equilibrium. From the particle picture ODEs we obtain $\omega_{1,2} = \pm\sqrt{2}\omega_{\mathrm{pr}}\sqrt{1-\alpha^2}$, $\omega_{3,4,5,6}$

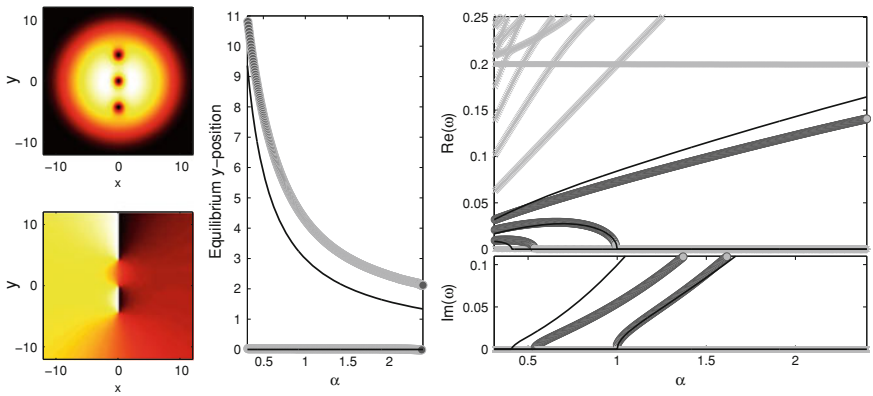

Fig. 3 The left panels show a typical example of the density and phase of an equilibrium vortex tripole. The position of the vortices in the tripole configuration as a function of the 2D aspect ratio is shown in the middle panel with numerical data shown as line of gray circles and the ODE prediction shown in black solid line. The right panel shows the eigenmodes of linearization around the tripole: ODE theoretical predictions represented by solid lines and anomalous modes and purely imaginary modes by lines of gray circles. Chemical potential $\mu = 2.5$

$= \pm\omega_{\mathrm{pr}}\sqrt{4 - 5\alpha^2 \pm \sqrt{9 + 2\alpha^2 + 25\alpha^4}}$. In the isotropic limit of $\alpha = 1$, these equations reproduce the result of [16]. Concerning stability, the most important conclusion to be drawn is that below the critical anisotropy $\alpha_{\mathrm{cr}} = 1/\sqrt{6} \approx 0.408$, all linearization frequencies become real, i.e., the tripole can be completely stabilized by means of strong enough transversal confinement. Comparing with the numerically found BdG spectrum of the tripole essentially confirms this prediction. The particle picture still captures the overall behaviour of the relevant vortex modes. In detail, however, the predictions are less exact than for the vortex dipole. In particular, while stabilization in general is correctly predicted by the particle picture, the critical value of α for which it occurs is found to be $\alpha_{\mathrm{cr}} \approx 0.53$. It should also be stressed that similarly to the dipole case, the neutral mode present for $\alpha = 1$ (due to isotropic rotation of the tripole) can be tipped towards stability (for $\alpha < 1$) or instability (for $a > 1$) depending on the direction of anisotropic compression of the condensate with respect to the axis of the multi-vortex state (perpendicular, or parallel, respectively). A typical example of the dynamics following the tripole's decay in an isotropic trap, triggered by the imaginary linearization modes, will be shown in Fig. 5 below.

Concerning the three vortex case, one more remark is in order here. For more than two vortices, we found it impossible to determine all fixed points of the vortex equations of motion analytically. This is why we had to make an ansatz motivated by the expected symmetry properties to find the tripole fixed point of the ODE system. One result that can still be proved in full generality is that for any fixed point $(x_1, y_1, , x_K, y_K)$ of a K vortex system, the x- and y-coordinates have to sum up to zero independently. Of course, this by itself does not rule out other equilibrium positions than the aligned tripole for the three vortex system. Thus, we checked numerically that no other stationary vortex solutions are predicted by the

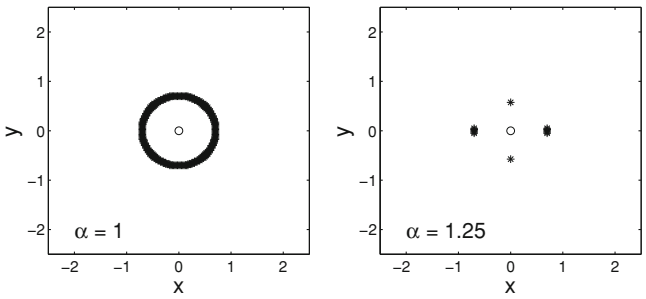

Fig. 4 Numerically calculated fixed points of the three vortex ($s_1 = s_3 = -s_2$) ODE system. Coordinates $x_1,\ y_1,\ x_2,\ y_2$ were each scanned in the interval $[-2.5, 2.5]$ (divided into 200 steps). The plots show positions of the three vortices for configurations at which $\max\{|\dot{x}_j|, |\dot{y}_j|\} < 0.03$ for each $j \in \{1, 2, 3\}$. Vortex 1 and 3 denoted by $\times$ and $+$ symbol, respectively, vortex 2 by an open circle. Note that, as anticipated, an exchange of vortices 1 and 3 does not lead to a different configuration, so symbols $\times$ and $+$ appear on top of each other. Position variables are scaled by a factor of $\sqrt{2\omega_x^2 Q/B}$

particle picture. To do so, we evaluated the functions $\dot{x}_j,\ \dot{y}_j,\ j \in \{1, 2, 3\}$, within a large region of configuration space, i.e. for a large number of test coordinates $(x_1, y_1, x_2, y_2, x_3 = -x_1 - x_2, y_3 = -y_1 - y_2)$ and identified their roots. The results are shown in Fig. 4, confirming that the tripole along one of the trap's main axes really is the only equilibrium solution predicted by the particle picture ODE system. It should be mentioned in passing that this result is only true if the precession frequency is identical for all vortices; if it depends on the distance of the vortex from the center of the trap, then the above result no longer holds.

Having discussed both the vortex dipole and the vortex tripole case should render evident the fact that anisotropy presents a remarkable handle for controlling the stability and dynamics of multi-vortex clusters at will away from the isotropic limit. In particular, it is evident that configurations such as the vortex dipole which are structurally robust in the isotropic limit can be immediately rendered unstable when departing from that limit for values of $\alpha > 1$. On the flip side, any configuration which is more highly excited and unstable in the isotropic limit, can instead be stabilized when operating in a sufficiently anisotropic regime for $\alpha < 1$. Examples of all four of these scenaria: perturbed but stable isotropic dipole, perturbed unstable anisotropic dipole for $\alpha > 1$, perturbed unstable isotropic tripole and finally, perturbed but stable sufficiently anisotropic tripole for $\alpha \ll 1$ are shown systematically in Fig. 5.

We would like to point out that a systematic study of vortex dynamics far from equilibrium in the presence of the anisotropic trap, similar to the work of [17], promises to be a very interesting direction for further investigations. At first sight, the dynamics triggered by the decay of the vortex dipole at $\alpha > 1$ seem to be periodic, i.e., continuing the propagation we observe a regular sequence of revivals and decays of the dipole (Fig. 5 only shows part of the first half period). For the decaying tripole, on the other hand, no such periodicity seems to be present. A general investigation of these dynamics far away from the fixed points, and the

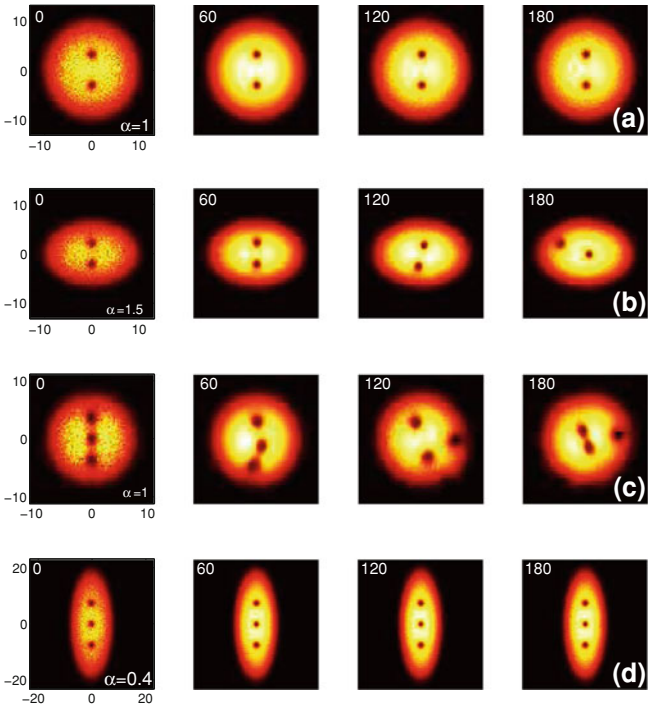

Fig. 5 Dynamical evolution of aligned vortex states perturbed by white noise for different values of α: (a) $\alpha = 1$ dipole, (b) $\alpha = 1.5$ dipole, (c) $\alpha = 1$ tripole, (d) $\alpha = 0.4$ tripole. All plots show $|\psi|^2$, and the elapsed dimensionless time is given in the upper left corners. Reprinted with permission from [28]

potentially different types of dynamics triggered by the different imaginary BdG modes, is beyond the scope of this work where our main aim is to identify and understand the parameter regimes of linear (in)stability for the equilibrium vortex clusters. Nevertheless, we should add that the dynamical evolution results of Fig. 5 afford the more general expectation that the instability of the vortex clusters will evolve towards smaller, more stable "building blocks" of the configuration. In this sense, the anisotropic dipole can only break up towards a stable single vortex (and one in the periphery of the cloud). Following the decay of larger vortex clusters we particularly often observe the formation of transient vortex dipoles, i.e. pairs of vortices of opposite charge moving together over comparably long timescales and only unbinding to pair with other vortices. This resembles observations made in studies of large-scale superfluid turbulence in Bose gases, see e.g. [44]. The occurence of such transient dipoles can be observed e.g. in the isotropic tripole's decay in Fig. 5c and has also been checked numerically for more complex states such as the aligned vortex quadrupole discussed below in Fig. 6. The same feature is also present in the vortex dynamics triggered by the decay of non-aligned clusters, see Fig. 20 in Sect. 7.

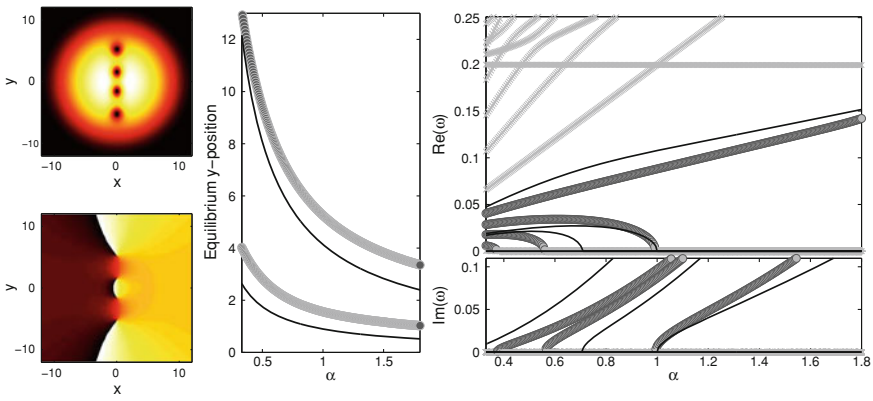

Fig. 6 Same as Figs. 2 and 3 but now for the aligned vortex quadrupole

4.4 Aligned Vortex Quadrupole

As a final example, let us consider the case of four vortices with $s_1 = s_3 = \pm 1$, $s_2 = s_4 = \mp 1$. An ansatz where these four vortices are aligned along the y-axis, symmetrically with respect to the origin, allows us to determine the following equilibrium positions of the aligned vortex quadrupole along the y-axis:

$$y_1 = -y_4 = \sqrt{\frac{B}{4\omega_y^2 Q}} \cdot \sqrt{1 + \sqrt{2\sqrt{2} - 2}},$$

$$y_2 = -y_3 = \sqrt{\frac{B}{4\omega_y^2 Q}} \cdot \sqrt{1 - \sqrt{2\sqrt{2} - 2}}.$$

The central panel of Fig. 6 compares these predictions to the numerically calculated equilibrium positions. Again, qualitative (and to some extent also quantitative) agreement is very good.

The linearization frequencies from the particle equations of motion could not be obtained analytically in this case. The results calculated by numerical diagonalization of the ODE system's Jacobian at the aligned quadrupole fixed point, together with the full BdG spectrum, are shown in Fig. 6.

Once again, we observe the onset of stabilization for small enough values of α. This feature is contained in the particle picture predictions as well, but the critical value α_{cr} theoretically identified is below the corresponding numerical one. From the BdG spectrum we obtain $\alpha_{\mathrm{cr}} \approx 0.37$. In summary, quantitative agreement between our particle picture predictions and the BdG modes calculated from the full Gross-Pitaevskii theory somewhat deteriorates the more vortices are considered. We assume that mainly two effects are responsible for this: On the one hand, the more vortices are present, the further the vortex

cluster stretches out into the condensate and the off-center correction term to the precession frequency which we neglect becomes increasingly important. On the other hand, our simple, semiclassically justified modeling of vortex interaction is not fully accurate in that it does not adequately account for density inhomogeneities due to the trap i.e., the background-induced effect mentioned above. The higher the number of vortices, the further outward the vortex cluster extends and hence the more the density variation at the rims of the cloud affects the result. Nevertheless, for all the cases considered the qualitative agreement between the conclusions of the particle picture and those of the full PDE has been excellent.

As an aside, it should be mentioned at this point that for four vortices of alternating charge, the aligned quadrupole does not form the only possible equilibrium position. Other quadrupole configurations, where the vortices are located at the vertices of a non-degenerate parallelogram, will be discussed in Sect. 6.

5 Aligned Vortex States: Bifurcations

In this section, we will show that valuable insight into aligned vortex states, and in particular into their stability, can be obtained from the point of view of bifurcation theory. In particular, solutions to the stationary GPE depend non-trivially on their norm, or on the total particle number $N = \int \mathrm{d}x\mathrm{d}y|\psi|^2$, physically speaking. In the following, we study branches of vortex cluster (and solitonic) solutions to the stationary GPE, varying the chemical potential μ. This amounts to examining a state's parametric dependence on the particle number N, as μ is a strictly increasing function of N and vice versa. Relevant bifurcations are identified and related to the stability properties of the different branches. This will prove to be a useful complementary tool to better understand the changes in stability induced by anisotropy that we observed for the vortex states of Sect. 4.

In a sense, the above presented perspective of "particle theory" is the one of the highly nonlinear limit where the individual coherent structures (the vortices) can be clearly identified as distinct, highly localized objects which form an effective interacting particle system. On the other hand, the discussion of the present section will focus on the opposite limit, namely that of the weakly nonlinear regime. In the latter, the states bifurcate from the eigenstates of underlying linear operators which constitute the canonical starting point for the relevant bifurcation analysis that will be presented below. Lastly, the aim of the overall program is to connect this weakly nonlinear analysis with the strongly nonlinear particle regime by means of numerical computations that bridge the two limits.

5.1 Bifurcation Approach in the Isotropic Case

In this section, we review the bifurcation analysis put forward in [16] to study aligned vortex states within an isotropic trap for which $\omega_x = \omega_y \equiv \omega_r$. In that work, it was argued that aligned vortex clusters are intimately related to the dark soliton stripe solution of the two-dimensional Gross-Pitaevskii equation. For reference, density and phase profiles of a dark soliton state (in an anisotropic setting) are presented below, in Fig. 9. In an isotropic trap, following the soliton stripe branch of solutions as the chemical potential μ is increased, one finds that subsequently new branches of fixed points bifurcate from it. These emerging branches are identified as the aligned vortex solutions, with the dipole branch bifurcating first, then the tripole branch and so on. Similar observations, concerning the dipole branch only, had previously been made in [10, 15].

It has been argued in [16] that the bifurcations leading from the soliton branch to the aligned vortex branches are of the supercritical pitchfork type. Such pitchfork bifurcations generically occur in systems with some internal symmetry. The transfer of stability from a symmetric (parental) branch of fixed points to two non-symmetric branches can then be thought of as a symmetry-breaking process: beyond the bifurcation point, the stable equilibra do not exhibit the system's full symmetry anymore.

Let us apply these statements to the dipole's bifurcation from the dark soliton stripe branch. For small values of μ, the soliton is linearly stable. One can check that its BdG spectrum exhibits no imaginary mode. Increasing the chemical potential, for our choice of $\omega_r = 0.2$ at a critical value of $\mu \approx 0.68$ the vortex dipole branch bifurcates from the soliton branch. More precisely, there are two different dipole branches coming into existence at this critical μ: These two can be transformed into each other by interchanging the roles of the vortex and antivortex, i.e. by globally flipping the vorticity. This should be thought of as a time-reversal transformation: As known from (linear) quantum mechanics, applying the antiunitary time-reversal operator is essentially tantamount to complex conjugation. Thus, under a time-reversal transformation, the wavefunction phase changes its sign, which in turn means that the velocity field $\mathbf{v}(\vec{r})$, proportional to the gradient of the phase, changes its sign, too. The same goes for the vorticity field $\nabla \times \mathbf{v}$. Physically speaking, the superfluid flow changes its direction. Note now that the soliton stripe state is purely real, i.e. it is invariant with respect to time-reversal. The vortex dipoles, on the other hand, are described by complex wavefunctions. Thus, they are not invariant under the action of time-reversal, instead they are transformed into each other. This is the characteristic symmetry-breaking feature expected in a supercritical pitchfork bifurcation. Furthermore, one can observe that the two dipole branches "inherit" the soliton's stability, while in the soliton's BdG spectrum an imaginary mode occurs. The corresponding decay mechanism is well-known as the transversal (or "snaking") instability of the soliton stripe in two dimensions, see e.g. the recent review [45] and references therein.

Having outlined the close connection between bifurcation theory and stability analysis, a natural question to ask is whether one can understand why certain bifurcations occur, and at which particular critical value of μ or N. This problem has been addressed in the slightly different context of a condensate trapped in a 1D double-well potential in [46]. In [16], the same technique has been demonstrated to be of use for the study of vortex states in isotropic traps as well.

Lying at the heart of this approach to bifurcations in the Gross-Pitaevskii equation is the observation that in the limit of $N \to 0$ the nonlinear interaction term can be neglected, and the stationary GPE reduces to the familiar (linear) Schrödinger equation (with the chemical potential μ playing the role of energy). In the presence of a harmonic trap, the solutions of this equation are the well-known 2D harmonic oscillator eigenfunctions $\gamma_{mn}(x, y) = \gamma_m(x)\gamma_n(y)$, where the quantum numbers m, n are non-negative integers and the energy eigenvalue of state γ_{mn} is given by $E_{mn} = (m + n + 1)\omega_r$.

Thus, in the limit of $N \to 0$, the stationary solutions of the GPE have to reduce to harmonic oscillator eigenstates asymptotically. For the soliton stripe branch and the single vortex branch, which both exist in the linear limit of infinitesimally small particle numbers, these linear counterparts are readily identified. Taking the direction of its density minimum along the y-axis, the soliton stripe can be traced back to the eigenstate γ_{10}, which is purely real and has a nodal line at $x = 0$. The vortex, on the other hand, approaches the complex linear combination $\gamma_{10} \pm \mathrm{i}\gamma_{01}$, which in polar coordinates (r, θ) leads to the characteristic $\exp(\pm \mathrm{i}\theta)$ phase profile. Due to the isotropic trap, γ_{01} and γ_{10} are degenerate, and thus their superposition is also a solution of the linear Schrödinger equation. Let us remark that a continuation of this linear solution into the vortex state for the case of an *attractive* cubic nonlinearity has been performed in [47], where also the doubly charged vortex we will encounter in the next section was studied.

We now turn to branches of states which do not exist in the limit of vanishing N, but bifurcate close to it, such as the vortex dipole. While these states cannot be expected to reduce to a single eigenfunction of the Schrödinger equation, it has been demonstrated that they can be approximated as linear combinations of non-degenerate harmonic oscillator functions [9, 10, 16]. One can think of this as a Galerkin-type method, where the nonlinear GPE problem is approximately discretized by projecting onto suitable eigenspaces of the Schrödinger Hamiltonian. From the point of view of such a few-mode expansion, the dipole is described as a superposition of γ_{10} and γ_{02}, with a constant relative phase of $\pm\pi/2$. In other words, as μ and N are increased away from the linear limit, the soliton stripe branch is still approximated by γ_{10}, and the dipole's bifurcation is then attributed to an admixture of $\pm \mathrm{i}\gamma_{02}$ that sets in at a critical particle number (or chemical potential, equivalently).

In such a setting, considering a linear combination of the two relevant linear modes φ_0, φ_1 and requiring that it be stationary can be shown to lead to a prediction for the critical values where the bifurcation from the branch starting as φ_0 due to an admixture of φ_1 at a relative phase of $\pm\pi/2$ occurs [46, 16]

$$N_{\mathrm{cr}} = \frac{E_1 - E_0}{A_{0000} - A_{0011}}, \tag{6}$$

$$\mu_{\mathrm{cr}} = E_0 + A_{0000} N_{\mathrm{cr}}. \tag{7}$$

Here, $A_{0000} = \int \mathrm{d}x\mathrm{d}y\varphi_0^4$, $A_{0011} = \int \mathrm{d}x\mathrm{d}y\varphi_0^2\varphi_1^2$ and $A_{1111} = \int \mathrm{d}x\mathrm{d}y\varphi_1^4$ denote the two modes' nonlinear overlap integrals, E_0, E_1 their energies. Several generic assumptions are made in the derivation of Eqs. 6, 7. The linear modes are taken to be real, "mixed" overlap integrals $A_{0001} = \int \mathrm{d}x\mathrm{d}y\varphi_0^3\varphi_1$, $A_{0111} = \int \mathrm{d}x\mathrm{d}y\varphi_0\varphi_1^3$ are assumed to vanish, and use of the inequalities $A_{0000} > A_{0011}$, $A_{1111} > A_{0011}$ is made.

Let us now return to the aligned vortex states bifurcating from the soliton branch. Generally, the bifurcation of the aligned vortex state with n vortices $(n \geq 2)$ can be attributed to an admixture of $\pm\mathrm{i}\gamma_{0n}$ to the soliton's γ_{10} mode. With this two-mode picture in mind, one can apply the Galerkin approach to predict critical particle numbers and chemical potentials for the bifurcations. In [16], it has been demonstrated that excellent agreement with the numerical data is obtained for the lowest-lying bifurcations, leading to the dipole and tripole. For higher numbers of vortices, the Galerkin predictions tend to be less exact. This is understandable, as the corresponding bifurcations happen at comparably large values of N, far away from the linear limit, which impairs the applicability of the near-linear few-mode expansion.

5.2 Modified Bifurcation Approach in Anisotropic Settings

Extending this analysis to the anisotropic regime is essentially straightforward. Let us in the following explain how insight into qualitative changes in the bifurcation diagram due to $\alpha \neq 1$ (and the ensuing implications for stability) can be gained using the Galerkin approach. Linear eigenfunctions in the anisotropic trap still factorize according to $\gamma_{mn}(x, y) = \gamma_m(x)\gamma_n(y)$, where the one-dimensional modes now read

$$\gamma_m(x) \propto H_m(\sqrt{\omega_x}x)\exp(-\omega_x x^2/2),$$
$$\gamma_n(y) \propto H_n(\sqrt{\omega_y}y)\exp(-\omega_y y^2/2),$$

where normalization constants have been omitted and H_n denotes the n-th Hermite polynomial. The energy eigenvalue of state γ_{mn} is given by

$$E_{mn} = (m + 1/2 + \alpha(n + 1/2))\omega_x.$$

Thus, for the two linear modes used to predict the bifurcation of aligned vortex clusters, γ_{10} and γ_{0n}, the difference between the eigenenergies is found to be $E_{0n} - E_{10} = (n\alpha - 1)\omega_x$. This energy difference crucially enters the expression for the critical particle number of the bifurcation predicted by the Galerkin approach,

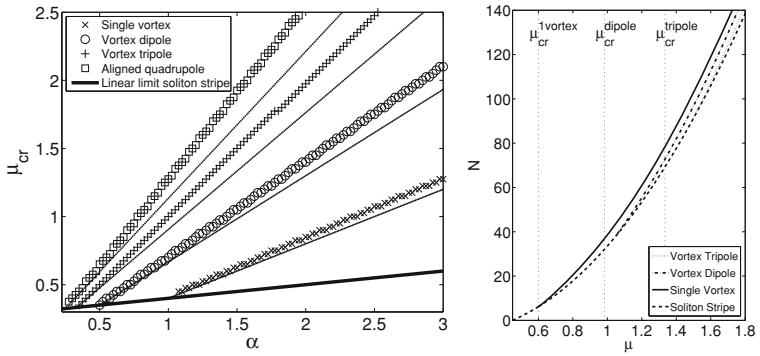

Fig. 7 (Left) Critical values of μ at which bifurcations leading to aligned vortex states occur, as a function of the anisotropy parameter α: predictions of the Galerkin approach (thin dotted lines) and numerically found values (symbols as shown in legend). (Right) Example of an $N(\mu)$ bifurcation diagram, $\alpha = 1.5$, predicted critical values indicated by dotted vertical lines. Reprinted with permission from [28]

Eq. 6, and in turn the position of the critical point is controlled by the anisotropy parameter α.

The theoretical predictions for μ_{cr} are shown in Fig. 7, together with the bifurcation points obtained from our numerical simulations. We find that for any of the bifurcations considered the Galerkin approach gives correct results as long as the bifurcation happens sufficiently close to the linear limit. As α is increased, the bifurcation points are shifted to higher values of the particle number N, and the Galerkin approximation is less accurate.

Intuitively, for $\alpha > 1$, that is $\omega_y > \omega_x$, the energy of the γ_{0n} $(n \geq 1)$ states is higher than in the isotropic limit, while the energy of the γ_{10} state is only weakly affected. In particular, the degeneracy of γ_{10} and γ_{01} (that constitute the one-vortex state) is lifted: In contrast to the isotropic case, the admixture of a γ_{01} component to the γ_{10} soliton state is suppressed, and thus the bifurcation of the single vortex is shifted away from the linear limit to a nonzero value of N. By the same reasoning, all the other aligned vortex states bifurcate further away from the linear limit, too. We note that this has implications also for the stability of the higher aligned multi-vortex states, since the only stable bifurcating state will be the single charge vortex inheriting the soliton's initial stability and the remaining aligned states will, by necessity, be more unstable (by one eigenmode) than before, a feature corroborated in the previous section by the particle picture for $\alpha > 1$.

On the other hand, for $\alpha < 1$ the energy of the γ_{0n} states is lower than in the isotropic case, that is their admixture to the γ_{10} soliton state is favored. For values of α just below 1, the consequences are most drastic for the single vortex state. As the energy of the γ_{01} state is now lower than that of the γ_{10} soliton state, it is no longer the case that the vortex emerges by an admixture of $\pm \mathrm{i}\gamma_{01}$ to γ_{10}. Rather, this picture is reversed, with the vortex emerging by an admixture of $\pm \mathrm{i}\gamma_{10}$ to the

(energetically favourable) γ_{01} state. In other words, the vortex branch now bifurcates from the soliton stripe oriented along the x-axis. Similar arguments apply to the other aligned vortex states if the value of α is further decreased. For $\alpha = 1/2$, the energies of the γ_{10} soliton state and the γ_{02} state (whose admixture leads to the vortex dipole) are the same, and thus the vortex dipole emerges from the linear limit. For even smaller values of α, the vortex dipole no longer bifurcates from the single soliton, but rather from the two soliton state γ_{02} parallel to the x-axis (through an admixture of $\pm i\gamma_{10}$). Obviously, this goes for any aligned vortex state: For $\alpha = 1/n$, the states γ_{10} and γ_{0n} are degenerate and the vortex state emerges from the linear limit. For smaller values than this, the bifurcation picture is reversed and the vortex state no longer bifurcates from the single soliton stripe along the y-axis, but rather γ_{0n} becomes the lower energy state to which $\pm i\gamma_{10}$ gets admixed.

Now that we have understood the structural dependence of the bifurcation diagram on α, let us summarize the conclusions on the stability properties of aligned vortex states in the presence of anisotropy.

We consider the regime of $\alpha > 1$ first. As in the isotropic case, the soliton stripe is stable when it emerges from the linear limit. The first bifurcation (which now leads to the single vortex state) renders it unstable, with the vortex inheriting the soliton's stability. The vortex dipole then bifurcates from this already unstable soliton stripe and is thus unstable as well (in contrast to the isotropic case). The higher aligned vortex states (tripole, quadrupole...) are all more unstable by the same reasoning. Remember that, as stated above, (further) destabilization of the dipole, tripole and aligned quadrupole for $\alpha > 1$ is also predicted by the particle picture and confirmed by our numerical computations.

We can also draw some conclusions on the stability of the soliton stripe itself. For $\alpha > 1$, we find that the length of the interval between the emergence of the soliton from the linear limit and the first bifurcation point increases as a function of α, see Fig. 7. The Galerkin approach predicts a linear increase. This corresponds to a growing range of values of the chemical potential for which the soliton stripe is stable. This, in turn, reflects the fact that for $\alpha \gg 1$ we progressively approach the 1D regime where the soliton stripe—ultimately, the 1D dark soliton—is stable for all values of μ for which it exists (which is consonant with the prediction of the 1D Gross-Pitaevskii theory).

On the other hand, for $\alpha < 1$ the aligned vortex clusters with the vortices located along the y-axis tend to get stabilized. In the interval $1/2 \leq \alpha \leq 1$ the vortex dipole is the first state bifurcating from the soliton and is thus stable, while the soliton stripe gets destabilized. For $1/3 \leq \alpha \leq 1/2$ the vortex dipole no longer bifurcates from the soliton and the tripole takes its place (and its stability properties) as the first emerging state. So for $\alpha \leq 1/2$ the vortex tripole (which is unstable in isotropic traps) is expected to be stabilized. By the same reasoning, the aligned quadrupole gets stabilized for $\alpha \leq 1/3$, the vortex quintupole for $\alpha \leq 1/4$, and so on. It can further be argued that the aligned vortex states are still stable when α is so small that they no longer bifurcate from the soliton stripe along the y-axis. In this case (as discussed above) the state with n vortices aligned bifurcates from the

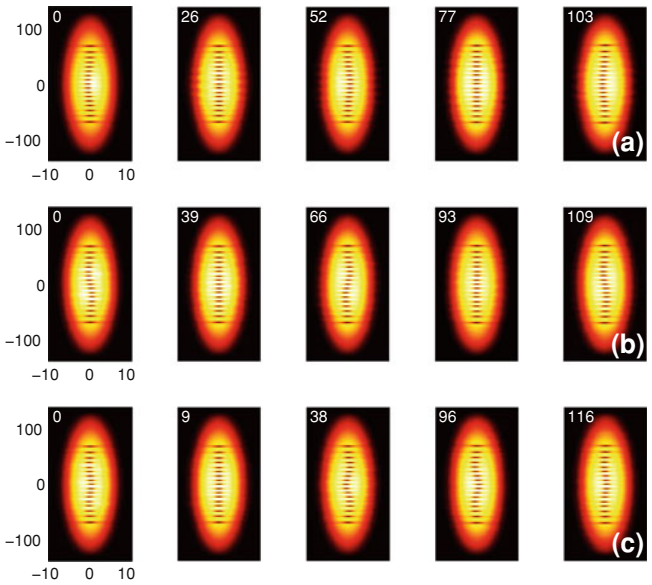

Fig. 8 Anomalous modes of a stabilized 17-vortex cluster, resembling the fundamental and first harmonic modes of a classical string. Note the different scaling in the x- and y-axes. Reprinted with permission from [28]

γ_{0n} branch through an admixture of $\pm i\gamma_{10}$. Similarly to the γ_{01} soliton stripe branch, the general γ_{0n} solitonic branch can be expected to be stable when it emerges from the linear limit, and the admixture of $\pm i\gamma_{10}$ will induce the first bifurcation from it, thus leading to a stable vortex cluster state (while the n soliton state gets destabilized). Thus, in total, the states with n vortices aligned along the y-axis are expected to be stable for any $\alpha \leq 1/(n-1)$, which is in very good agreement with our numerical results for the single vortex, vortex dipole, tripole and quadrupole shown above. It has been demonstrated numerically in [28] that even large aligned vortex clusters of up to $n = 17$ vortices can be stabilized by strong enough transversal confinement, and that the anomalous BdG eigenmodes of such a linear cluster are reminiscent of standing waves on a classical string, see Fig. 8. Interestingly, in such a vortex string, there will be n (i.e., in the above example 17) internal (anomalous) modes of vibration in its spectrum, which will, in turn, correspond to the n normal modes of such a vortex lattice.

At this point, a remark is in order. We have demonstrated in this section how on the one hand insight into the stability of vortex clusters can be gained by identifying the relevant bifurcations from the solitonic branch. Tuning the anisotropy parameter α can lead to qualitative changes in the bifurcation diagram, which carry over to changes in the stability properties of vortex clusters close to their emergence from the soliton. From this, one can learn about the stability of vortex clusters in the limit of small values of N or μ. On the other hand, in the limit of large chemical potentials we have the results from the particle picture ODEs and

the corresponding stability analysis. In the preceding section it has been shown that predictions concerning the stability obtained from these two opposite end regimes agree very well. However, it is not to be taken for granted that in the course of tuning the chemical potential μ from small values to larger ones the stability properties of each state have to be preserved. In fact, the BdG spectra, of course, do not only depend on α but in general also on μ. We have performed extensive numerical scans to cover the whole parameter space and make sure that no essential dependence of the stability on μ is missed. Indeed, we find that in almost all cases tuning the chemical potential at fixed α only weakly affects the BdG spectrum and does not lead to the appearance or vanishing of purely imaginary modes (which are the ones that the bifurcation approach can tell us about). However, in numerous cases we observe collisions between modes of positive and negative Krein signature, resulting in the emergence of complex mode quartets that persist for a limited range of values of μ and then split again into two real, stable modes (see also the relevant footnote at the end of the Introduction). For the vortex dipole in isotropic traps, e.g., the presence of these complex "bubbles" at intermediate μ is well-known [16], and it is no surprise that such intervals of weak oscillatory instability can also be found in anisotropic settings. Let us note that in general neither the near-linear bifurcation approach nor the highly nonlinear particle picture can provide information about these complex quartets at intermediate chemical potentials, and these are only captured by the detailed numerical continuations discussed (wherever relevant) herein.

Finally, let us point out that our findings presented in this section are consistent with previous results on the stability of the one soliton state in anisotropic settings [11]. In this work it was found (employing box boundary conditions and keeping the particle density fixed) that in the regime corresponding to our $\alpha \gg 1$ relaxing the confinement in the y-direction (i.e. approaching $\alpha = 1$) opens up an increasing number of decay channels for the soliton, with the first one leading to a single vortex, the second one leading to a vortex dipole and so on: In our analysis, these "decay channels" correspond to the imaginary modes in the soliton's BdG spectrum, induced by supercritical pitchfork bifurcations from the soliton branch having happened at lower values of N (or μ) than the one under consideration.

Furthermore, the authors of [11] report the numerical observation of a "solitonic vortex" solution to the GPE in anisotropic settings, i.e. a stationary state with its density and phase properties in between those of a soliton stripe and a single vortex. This is reported to bifurcate from the dark soliton stripe as the anisotropy of the confinement is varied. Even though different boundary conditions are employed, this agrees well with our findings: If $\alpha \neq 1$, the single vortex state bifurcates from the soliton stripe at a finite particle number (due to the non-degeneracy of γ_{01} and γ_{10}). This, in turn, necessarily means that close to the bifurcation point the vortex state will still show some similarity to the soliton solution from which it just bifurcated. Figure 9 shows an example of the single vortex state close to its bifurcation from the soliton stripe. Clearly, the density shows remnants of the soliton stripe. The phase runs from $-\pi$ to $+\pi$ continuously, a characteristic of the singly charged vortex, however the azimuthal phase gradient

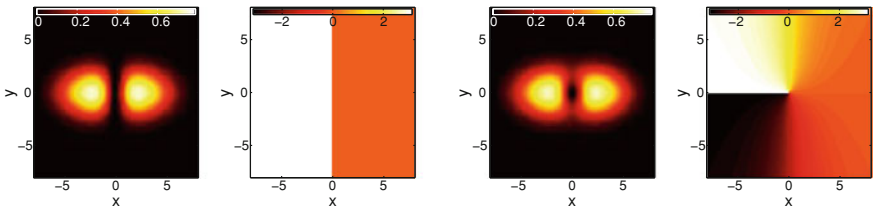

Fig. 9 Soliton stripe (left panels) and single vortex state (right panels) profiles at $\mu = 1,\ \alpha = 2.1$ ("solitonic vortex")

is not constant (as it is for the known vortex solution in isotropic settings). Rather, the phase changes very sharply in the region around the y-axis, again owing to the state's former solitonic properties.

6 Non-Aligned Vortex Clusters: The Isotropic Limit

Let us now apply the methods developed so far to stationary clusters of vortices that are not necessarily aligned along one axis. Having extensively discussed aligned vortex states bifurcating from the one soliton stripe branch (which reduces to γ_{01} or γ_{10} in the linear limit), the natural next step is to turn to the next higher excited harmonic oscillator states, namely $\gamma_{20},\ \gamma_{02}$ and γ_{11}, and study solitonic and vortex-type branches of states that reduce to linear combinations of these modes in the linear limit. Again, the strategy is to gain insight into the stability properties of vortex clusters under the influence of anisotropy by locating their bifurcations from solitonic branches. Subsequently, calculations within the particle picture ODE system and full dynamical simulations will be employed in Sect. 7 to access the problem from different directions and to provide a unifying picture.

Before entering the discussion of bifurcation diagrams in anisotropic settings, in this section we will first take a detailed look at the isotropic case where $\omega_x = \omega_y \equiv \omega_r$. Figure 10 collects density and phase profiles of the different branches of states which emerge from the linear limit at a chemical potential of $\mu = 3\omega_r$, i.e. which reduce to superpositions of harmonic oscillator states $\gamma_{20},\ \gamma_{11},\ \gamma_{02}$ as $N \to 0$. $N(\mu)$ bifurcation diagrams including a number of these plus some additional branches (which emerge further away from the linear limit and are therefore not relevant for our present discussion) can be found in [21].

For $\alpha = 1$ there are three different (apart from trivial rotations) solitonic branches emerging from the linear limit at $\mu = 3\omega_r$: The first of these is a state with two parallel soliton stripes, see Fig. 10a. It can be traced back to the harmonic oscillator eigenstate γ_{20} as $N \to 0$, where again we fix the y-axis parallel to the density minima of the soliton stripes. The other two are the dark ring soliton, Fig. 10c, and the two diagonally crossed dark solitons, Fig. 10b, which can asymptotically (for small N) be decomposed as $\gamma_{20} + \gamma_{02}$ and $\gamma_{20} - \gamma_{02}$,

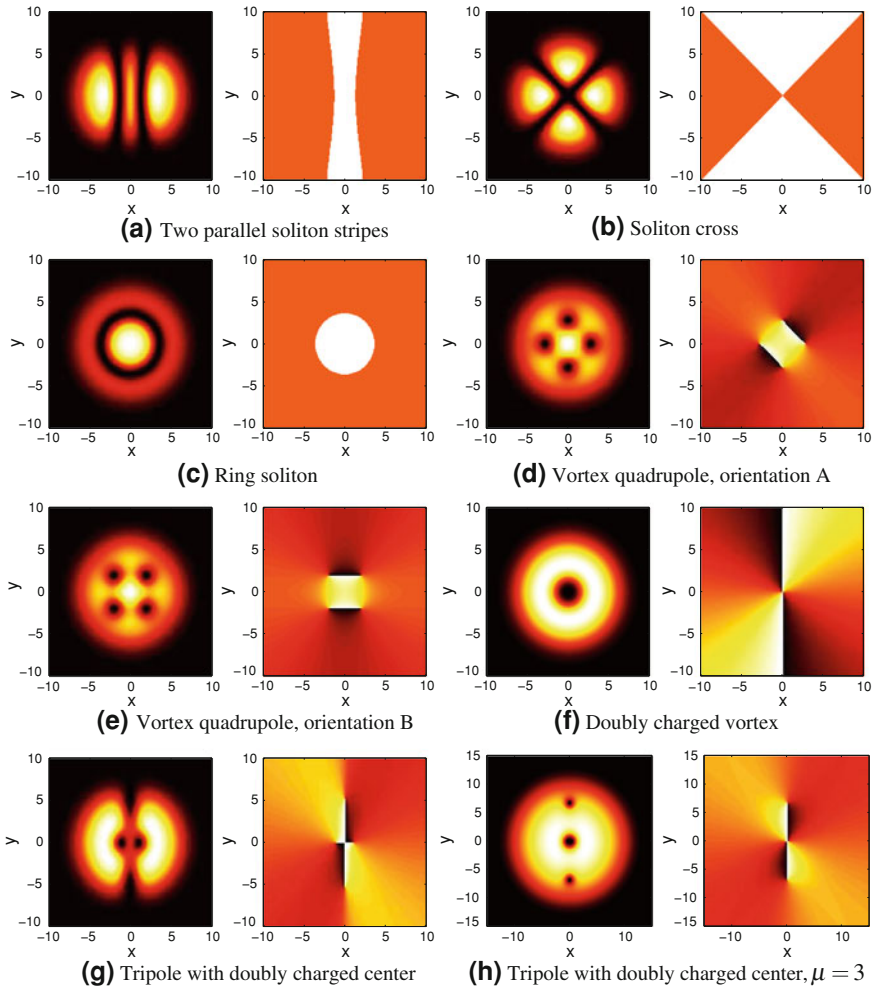

Fig. 10 Density and phase profiles of states emerging from the linear limit at $\mu = 3\omega_r$. Chemical potential is chosen to be $\mu = 1.2$ except where stated otherwise. **a** Two parallel soliton stripes **b** Soliton cross **c** Ring soliton **d** Vortex quadrupole, orientation A **e** Vortex quadrupole, orientation B **f** Doubly charged vortex **g** Tripole with doubly charged center **h** Tripole with doubly charged center, $\mu = 3$

respectively (where again overall normalization constants are omitted). Of the three solitonic states, two (namely, the ring and the cross) are unstable right from the linear limit, while the two soliton stripe state is stable for small μ. As μ is increased, vortex states bifurcate from all the solitonic branches leading to (further) destabilization.

Additionally, there is a number of vortex states that also emerge from the linear limit at $\mu = 3\omega_r$: The most prominent cluster state of these is probably the (nonaligned) vortex quadrupole, consisting of four singly charged vortices of

alternating vorticity which in the isotropic trap are located at the vertices of a square, and opposite vortices have the same charge. This state has been identified and discussed in [12, 13, 16, 48]. Having in mind the extension to anisotropic settings, we already distinguish two different orientations of this vortex quadrupole, even if at $\alpha = 1$ they can be transformed into each other by a trivial rotation. We speak of orientation A if the four vortices sit at the trap's x- and y-axes as in Fig. 10d. In this case, the state's linear decomposition as $N \to 0$ is identified to be $\gamma_{20} + \gamma_{02} \pm \mathrm{i}\sqrt{2}\gamma_{11}$, where we take the linear modes to be normalized to unity and omit the overall normalization constant. On the other hand, if the vortices are located along the diagonals of the coordinate system as in Fig. 10e, we call this orientation B. The corresponding linear limit reads $\gamma_{20} \pm \mathrm{i}\gamma_{02}$. For $\alpha = 1$, the quadrupole state (in any orientation) is stable for arbitrary chemical potentials (apart from an oscillatory instability window, see also [16]), and no other stationary states are found that bifurcate from it.

Next, we turn to a branch of states that to our knowledge has not been described before, see Figs. 10g and 10h. Our findings indicate that it starts as $\gamma_{20} \pm \mathrm{i}\gamma_{11}$ in the linear limit, and for small N it shows some similarity to the vortex quadrupole in orientation A: There are four singly charged vortices situated at the trap's axes. In contrast to the quadrupole configuration, these four vortices do not form a square, however. Instead, two of them (which have the same charge) are located closer to each other near the center of the trap, while the other two are further away from the trap center, in regions of low density. Increasing the chemical potential, we find that the two central vortices finally merge to form one vortex of charge 2. The whole configuration then has a tripole-like structure, where the charges of the three vortices in the tripole are given by $\mp 1, \pm 2, \mp 1$. Fig. 10h illustrates this tripole profile at larger chemical potentials. Concerning stability, we find that in an isotropic setting this branch only suffers from relatively weak oscillatory instabilities when emerging from the linear limit, before at $\mu \approx 1.4$ one small purely imaginary mode arises in its BdG spectrum. This destabilization is again due to a pair of symmetry-broken states bifurcating from the tripole with the doubly charged center, but in contrast to the prototypical bifurcations of vortex clusters from dark solitonic branches encountered so far, the symmetry that is broken is of a different kind: while the density of the tripole with the doubly charged center is symmetric with respect to reflections about both the x- and y-axes, the clusters of six vortices that bifurcate from it break the axial symmetry with respect to the y-direction, see Fig. 11. To be more precise, the tripole state itself (not just its density) is invariant with respect to a combined reflection about y and time-reversal transformation, and this symmetry is not shared by the vortex branches emerging in the bifurcation. As can be seen in Fig. 11, the newly found symmetry-broken clusters are made up of six singly charged vortices, three of each sign. One vortex is located in the trap center, surrounded by a triangular configuration of three oppositely charged vortices. The remaining two vortices are of the same charge as the central one and they are located close to the edge of the cloud near the y-axis equilibrating the whole structure. As μ is decreased towards the bifurcation point, the cluster

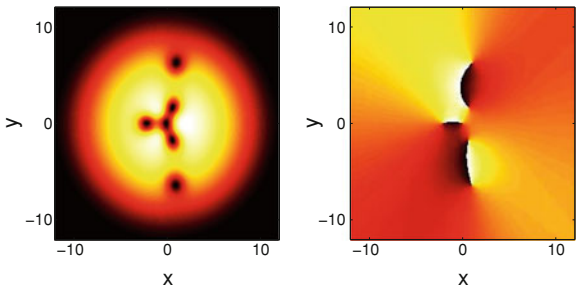

Fig. 11 Density and phase profiles at $\alpha = 1, \mu = 2.5$ of one of the symmetry-broken six vortex clusters that bifurcate from the tripole with the doubly charged center, destabilizing it

straightens along the y-axis and a vortex-antivortex pair in the center vanishes in the zero density core of a third vortex, until at the critical value the precursor of the tripole with the doubly charged center as shown in Fig. 10g is recovered. As one would expect in this type of supercritical pitchfork bifurcation, the symmetry-broken six vortex clusters are stable in the sense that their BdG spectra do not exhibit purely imaginary modes as we have checked. Let us remark, however, that their spectra exhibit weak oscillatory instabilities to which our theoretical bifurcation analysis cannot provide access, but which can only be tracked numerically, see also the remark at the end of the preceding section.

The next (and final) branch emerging from the linear limit at $\mu = 3\omega_r$ is again well-known: It is the charge 2-vortex branch, see Fig. 10f. In the linear limit, this vortex state consists of $\gamma_{20} - \gamma_{02} \pm \mathrm{i}\sqrt{2}\gamma_{11}$, which in polar coordinates (r, θ) leads to the expected azimuthal variable dependence $\propto \exp(\pm \mathrm{i}2\theta)$ characteristic of a doubly charged vortex. Apart from small oscillatory instability "bubbles" that arise due to subsequent collisions of positive and negative Krein signature modes, and then disappear and reappear again as μ is increased, we find the doubly charged vortex to be stable. This agrees with the results obtained in [49]. It should be noted here that the instability of such a higher charged vortex is towards splitting into lower charge vortices, a feature which by now has been observed experimentally, see e.g. [50].

Having commented on all branches that emerge from the linear limit, let us now turn to the first bifurcations from them. Increasing the chemical potential, we find bifurcations leading to vortex states for all three solitonic states.

For the two soliton stripe state, these bifurcations lead to pairs of aligned vortex configurations, analogous to those discussed in the one soliton case. Their emergence can be explained by subsequent admixtures of $\pm \mathrm{i}\gamma_{0n}$, where $n \geq 2$. In a degenerate sense, the vortex quadrupole in orientation B is the first example in this line of double aligned vortex states. The lowest-lying bifurcation happening at finite N leads to a double tripole (2 x 3). The numerically found critical chemical potential is $\mu_{\mathrm{cr}} \approx 0.87$, while the Galerkin approach predicts $\mu_{\mathrm{cr}} = \frac{283}{67}\omega_r \approx 0.84$. At this bifurcation, the two soliton stripe state is rendered unstable, while the 2 x 3 vortex state inherits its stability (that is, its BdG spectrum shows no purely imaginary mode). All the higher double aligned vortex states then bifurcate from the destabilized two soliton branch and are thus unstable. None of them will be touched upon in this work.

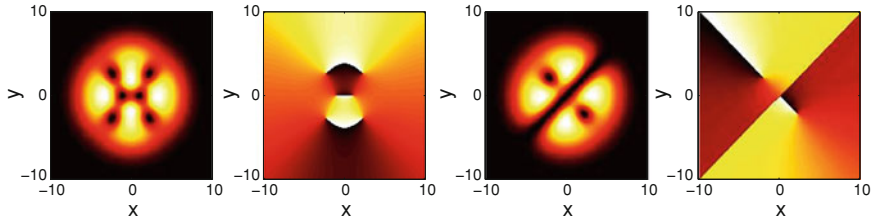

Fig. 12 Density and phase profiles of states bifurcating from the soliton cross branch, $\mu = 1.3$. **a** 2 x 3 crossed vortex cluster **b** Hybrid one soliton/two vortex state

The same goes for the vortex states bifurcating from the ring soliton branch. These are known as "vortex necklace" states [51], and they are characterized by an even number (4, 6, ...) of alternately charged vortices, hence resulting into to net topological charge, located at the vertices of a regular polygon. One can also consider the vortex quadrupole as the first, again degenerate, example of such a necklace state, followed by a vortex hexagon, octagon, and so on. Theoretically, the bifurcations of the necklace states have been studied in great detail in [48]. In this work, we will omit a detailed analysis of the unstable necklace states.

Concerning the first bifurcations from the soliton cross, there are two branches of stationary states emerging from it at essentially the same critical value of μ. On the one hand, we find a six vortex state, similar to the double tripole bifurcating from the parallel soliton stripes, but with the vortices located along the former soliton cross, see Fig. 12a. Numerically, we find that this bifurcation happens at $\mu_{\mathrm{cr}} \approx 0.92$. In the linear picture, it is convenient to analyze this bifurcation in the rotated coordinate frame, where the soliton cross branch reduces to γ_{11} in the linear limit. Numerical decomposition of the numerically obtained branch of solutions into its harmonic oscillator components indicates that the emergence of the 2 x 3 crossed vortex state is then explained by an admixture of $\pm\mathrm{i}(\gamma_{30} \pm \gamma_{03})$, where the relative sign between γ_{03} and γ_{30} decides along which direction the two central vortices in the cross configuration are located. With these linear modes, the Galerkin equations yield $\mu_{\mathrm{cr}} = \frac{111}{25}\omega_r \approx 0.89$. Finally, a second branch (which also has not been identified before, to our knowledge) emerges from the soliton cross at the same critical chemical potential as the crossed 2 x 3 vortex branch. This new branch is characterized by one of the soliton stripes formerly forming the cross staying intact while the other is replaced by two vortices, i.e., this is a "hybrid" state containing both solitonic stripes and vortex waveforms as shown in Fig. 12b. As in the symmetry-breaking bifurcation either of the soliton stripes can stay intact, there are actually again two different branches here, which can be transformed into each other by a rotation. The numerically found critical chemical potential is $\mu_{\mathrm{cr}} \approx 0.92$. The bifurcation leading to this hybrid one soliton/two vortex state is also easier to understand if the axes are rotated by $\pi/4$, in which case the cross state coincides with γ_{11} in the linear limit. Our numerical data indicates that the linear admixture causing the bifurcation is then given by $\pm\mathrm{i}\gamma_{03}$ or

$\pm i\gamma_{30}$, depending on which of the soliton stripes is preserved and which is replaced by vortices. In this rotated frame, evaluating the Galerkin equations is straightforward and again leads to $\mu_{cr} = \frac{111}{25}\omega_r \approx 0.89$, the same result as for the crossed 2 x 3 vortex branch. Thus, the near-linear picture confirms that both branches should emerge at the same critical chemical potential, in agreement with our numerical findings. As the soliton cross is unstable from the linear limit on, the bifurcating crossed 2 x 3 vortex branch and the one soliton/two vortex branch inherit this instability, and consequently their BdG spectra exhibit imaginary modes, a feature that has been numerically checked. It is worth noting that as μ is increased further, the 2 x 3 vortex states bifurcating from the parallel soliton stripes and the soliton cross, respectively, become more and more similar, and finally identical. At a critical value of $\mu \approx 1.35$ a saddle-node bifurcation occurs and the two stationary states annihilate, as has also been observed in [21].

7 Non-Aligned Vortex Quadrupoles in the Presence of Anisotropy

We now leave the isotropic limit and turn to cases where $\alpha \neq 1$. Our primary (although not sole) focus will be on the vortex quadrupole state in its different orientations, as this state has received the most theoretical attention [12, 13] and with its comparably small number of vortices also seems experimentally more accessible than other, more complex non-aligned clusters. In the first part of this section, we will therefore focus on the branches of states which are relevant for the emergence and stability of the quadrupole in its different orientations.

The first observation we make is that as soon as the rotational invariance is broken, the vortex quadrupole can no longer exist in arbitrary orientations. In the presence of anisotropy, the four vortices can either be located at the trap's main axes, forming a rhombus centered at $x = y = 0$ (this is the anisotropic generalization of orientation A), or alternatively, the four vortices can form a rectangle centered at $x = y = 0$ whose edges are parallel to the trap's main axes (this is the orientation B).

Let us now try to get insight into the bifurcation diagram including the two quadrupole branches. First, it is useful to note that, due to their symmetry, studying the quadrupoles in the $\alpha > 1$ regime is in principle sufficient: the way we scan α (by keeping ω_x fixed and varying ω_y), going from α to $1/\alpha$ for the quadrupoles merely corresponds to a rotation of the coordinate frame by $\pi/2$, followed by complex conjugation of the order parameter (flipping the signs of the vortex charges) and a rescaling of the overall trapping frequency (which, in turn, sets the scale for the chemical potential μ). Thus, all properties of the quadrupole solutions in the $\alpha < 1$ regime can be inferred from the results of the $\alpha > 1$ regime by accurately rescaling μ and N. The BdG spectra of the quadrupoles shown below illustrate this symmetry property.

Having this in mind, we can restrict the discussion of the relevant bifurcations to $\alpha > 1$. In the opposite regime of anisotropy, the topology of the bifurcation diagram (with all states rotated by $\pi/2$) is identical, even if the critical values where bifurcations occur are rescaled due to the different overall trapping.

In contrast to the isotropic case, for $\alpha \neq 1$ the harmonic oscillator states γ_{02}, γ_{20} and γ_{11} are no longer degenerate which leads to numerous modifications of the bifurcation diagram. Specifically, for $\alpha > 1$, γ_{20} is energetically most favourable and thus exists for the smallest value of μ. Continuing this linear eigenstate to finite particle numbers, we find that the ensuing nonlinear mode progressively increasingly resembles a dark soliton ring. The additional two branches which become the two parallel dark soliton stripes and the diagonal ("cross") configuration in the isotropic limit emerge in a saddle-node bifurcation detached from the above dark soliton ring branch. The critical particle number at which this saddle-node bifurcation occurs increases very rapidly as a function of α, and both states emerging in it tend to be highly unstable for $\alpha > 1$.

Let us therefore in the following concentrate on the γ_{20} branch, that near the linear limit is reminiscent of two dark solitons but as μ is increased progressively acquires a ring-shaped profile. The first vortex cluster bifurcating from this initially stable solitonic branch is the quadrupole in configuration A. In linear terms, this bifurcation can be approximately understood by an admixture of $\pm i\gamma_{11}$, as for any $\alpha > 1$ this mode is lower in energy than γ_{02} and can be expected to dominate the quadrupole's bifurcation, while the quadrupole's characteristic γ_{02} component smoothly arises only well above the critical point. We remind the reader that the pure $\pm i\gamma_{11}$ admixture previously (i.e., in the isotropic case) led to the modified tripole with the doubly charged vortex in the center of Fig. 10g, while the anisotropy changes this scenario and our results indicate that only one pitchfork bifurcation from the γ_{20} soliton branch involving the $\pm i\gamma_{11}$ admixture remains at $\alpha > 1$, namely the one leading to the quadrupole A. The role of the tripole with the doubly charged center in the $\alpha > 1$ regime will be addressed below.

Again, the first supercritical pitchfork bifurcation renders the soliton branch unstable, while the quadrupole A inherits its stability. The second bifurcation, then, leads to the quadrupole B, through a dominant admixture of $\pm i\gamma_{02}$, and this quadrupole configuration inherits the solitonic instability. From this analysis, we expect the quadrupole in configuration B to be unstable for any $\alpha > 1$, while configuration A should remain stable when leaving the isotropic limit.

Let us at this point also address the other two vortex clusters shown in Fig. 10, namely the doubly charged vortex and the tripole with the doubly charged center. Our findings indicate that these two branches also detach from the others as soon as $\alpha > 1$, and when lowering the particle number at some point they collide and vanish in a saddle-node bifurcation (with the doubly charged vortex playing the role of the more stable branch). Due to the different net topological charge of the doubly charged vortex and the tripole with the doubly charged center, it is interesting to study how these branches can become identical and annihilate. In fact, we observe that close to the bifurcation point both branches exhibit four vortex-type phase singularities, two of each sign, reminiscent of the profile shown

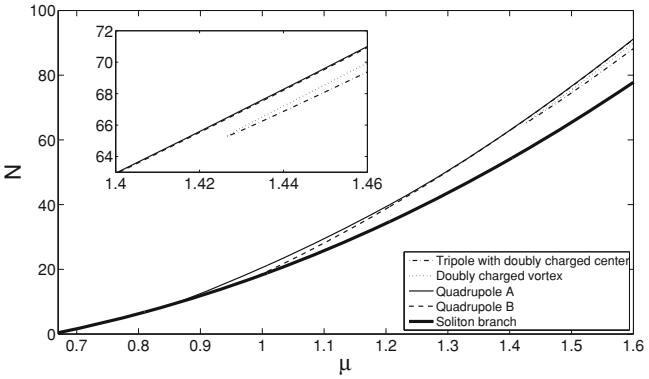

Fig. 13 $N(\mu)$ bifurcation diagram at $\alpha = 1.6$ including the two non-aligned quadrupoles (which for large μ can hardly be distinguished by their $N(\mu)$ dependence) and the additional two branches emerging from a nearby saddle-node bifurcation as seen in the blown up inset

in Fig. 10g. In the tripole branch as μ is increased two of these merge to form the doubly charged center while the other two remain located at the y-axis. In the doubly charged vortex branch, on the other hand, the central singularities merge to form the $s = 2$ vortex, while the other two phase singularities are pushed out to regions of zero density and vanish there as μ is increased away from the bifurcation point. In the immediate vicinity of the isotropic limit this bifurcation scenario is hard to clearly confirm by numerical simulations (as the expected saddle-node bifurcation still happens very close to the quadrupole branch), but for $\alpha = 1.6$ the detaching of the two branches is clearly observable, see Fig. 13.

A major change in the bifurcation diagram occurs when α reaches the value 2. As discussed in the section on aligned clusters, above this critical value of the anisotropy the vortex dipole along the x-axis no longer bifurcates from the single soliton branch starting at γ_{01}, but instead from the γ_{20} two soliton branch considered here. This dipole branch is now the first to bifurcate from this solitonic branch, rendering it unstable and inheriting its stability. From this observation one would expect the quadrupole A branch to be unstable for $\alpha > 2$, as in this regime it bifurcates from the destabilized solitonic branch. By the same reasoning, the quadrupole B should have two imaginary eigenfrequencies in the $\alpha > 2$ regime (i.e., one more than in the $1 < \alpha < 2$ regime), as it is the third state to bifurcate from the γ_{20} solitonic branch. We will discuss these predictions in more detail below.

Numerically continuing the relevant branches of states in the parameters μ and α, we can track the dependence on the anisotropy parameter α of the critical chemical potentials at which bifurcations from the γ_{20} branch occur. Figure 14 shows the numerically found critical values, together with the theoretical predictions from the Galerkin approach. In addition to the vortex branches discussed above, it also depicts the bifurcation points of the 2 x 3 double tripole branch, which for $\alpha < 1$ is the first to bifurcate from the γ_{20} solitonic branch.

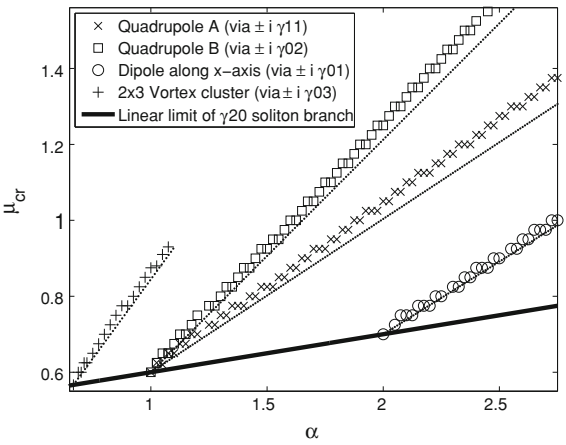

Fig. 14 Critical values of the chemical potential μ at which bifurcations from the γ_{20} soliton state occur, as a function of the anisotropy parameter α: predictions of the Galerkin approach (thin dotted lines) and numerically found values (symbols as shown in legend). The fundamental change of stability properties of the quadrupole states due to the (prior) bifurcation of the vortex dipole along the x-axis for $\alpha > 2$ is evident

The numerical data shown in Fig. 14 is obtained by stepwise continuations of the vortex quadrupole states, the 2 x 3 vortex state and the vortex dipole, respectively, from high values of μ to lower ones, until eventually the parental solitonic branch is reached. These scans over the parameter μ were repeated at different values of the anisotropy parameter α. Next, we employed two different methods for numerically identifying the critical chemical potentials. On the one hand, we compared the particle number of the branch under consideration with the particle number of the γ_{20} soliton branch and identified the bifurcation point as the parameter value of μ at which the difference in N becomes nonzero. On the other hand, we also made use of an indirect method, tracking down the emergence of the expected linear admixtures in the linear decomposition of the investigated branch. Both approaches lead to consistent results. Altogether, the data shown in Fig. 14 supports our interpretation of the linear combinations underlying the bifurcating vortex states. In general, the numerically found bifurcation points agree well with the theoretical predictions, especially when the bifurcations happen close to the linear limit. For increasing critical chemical potential (and thus increasing critical particle number) the Galerkin approach is no longer exact and the deviations get larger.

As an interesting aside, let us comment on the two different 2 x 3-type vortex clusters that we discussed in the isotropic case, the one bifurcating from the γ_{20} branch included in Fig. 14, and the one shown in Fig. 12a which bifurcates from the cross-like solitonic branch. As stated above, in the isotropic case an increase in μ eventually leads to a saddle-node bifurcation in which these two states collide and vanish. Going to $\alpha > 1$, we find that the critical values of μ where these two vortex clusters bifurcate from their respective solitonic parents increases. At the same time, the value of μ where they collide and annihilate in the saddle-node bifurcation decreases. Thus, the range of chemical potentials for which these two vortex branches exist becomes smaller as α is increased away from 1, and eventually for $\alpha \gtrsim 1.1$ they do not exist for any value of μ.

Finally, we discuss in a bit more detail whether the Galerkin approach can be expected to be applicable to the bifurcations encountered here. To this end, remember that in deriving the expressions for N_{cr} and μ_{cr}, it is assumed that the integrals $A_{0001} = \int \varphi_0^3 \varphi_1 \mathrm{d}x\mathrm{d}y$ and $A_{0111} = \int \varphi_0 \varphi_1^3 \mathrm{d}x\mathrm{d}y$ vanish. As the harmonic oscillator states are parity eigenstates and one typically integrates over a product of an odd and an even function, this is valid in most of the cases we discuss here. For example, for the $\gamma_{10} \pm \mathrm{i}\gamma_{0n}$ combinations discussed in the context of aligned vortex states, the integrals are zero due to the different parity of $\gamma_1(x)$ and $\gamma_0(x)$. Now we encounter the first case where this assumption is not true, namely the quadrupole B composed of $\gamma_{20} \pm \mathrm{i}\gamma_{02}$. Explicitly, with $\varphi_0 = \gamma_{20},\ \varphi_1 = \gamma_{02}$, the overlap integrals are calculated to be $A_{0000} = A_{1111} = \frac{41\sqrt{\alpha}}{128\pi}\omega_x$, $A_{0011} = \frac{9\sqrt{\alpha}}{128\pi}\omega_x$, $A_{0001} = A_{0111} = -\frac{\sqrt{\alpha}}{128\pi}\omega_x$. Note that the "mixed" integrals A_{0001} and A_{0111} do not vanish, yet are considerably smaller than the decisive integrals A_{0000} and A_{0011}, which one may take as a hint that the results from the Galerkin equations can still be of use. In fact, as Fig. 14 shows, this is justified, as the predictions from the Galerkin approach for the quadrupole B are in good agreement with the numerically found bifurcation points.

7.1 Non-aligned Quadrupoles in the Particle Picture

Let us now employ the particle picture ODEs to obtain the equilibrium positions and linearization frequencies of the non-aligned quadrupoles. Making an ansatz with rhombic symmetry, we find the vortices' equilibrium positions in orientation A to be given by

$$\begin{aligned} x_{1,3} &= y_{2,4} = 0, \\ x_2 &= -x_4 = \sqrt{\frac{B}{\omega_x^2 Q}} \cdot \frac{1}{\sqrt{3\alpha^2 - 1 + \sqrt{9\alpha^4 - 14\alpha^2 + 9}}}, \\ y_1 &= -y_3 = \sqrt{\frac{B}{\omega_x^2 Q}} \cdot \frac{1}{\sqrt{3 - \alpha^2 + \sqrt{9\alpha^4 - 14\alpha^2 + 9}}}, \end{aligned}$$

where the charges were taken to be $s_1 = s_3 = -s_2 = -s_4$. We were not able to give analytical solutions for the linearization frequencies as a function of α for this state (although they can be straightforwardly computed numerically).

On the other hand, the rectangular configuration of orientation B is captured by a fixed point of the particle picture system with

$$y_{1,2} = -y_{3,4} = \sqrt{\frac{B}{4\omega_x^2 Q}} \cdot \frac{1}{\sqrt{\alpha + \alpha^2}}, \quad x_{2,3} = -x_{1,4} = \sqrt{\frac{B}{4\omega_x^2 Q}} \cdot \frac{1}{\sqrt{1 + \alpha}}.$$

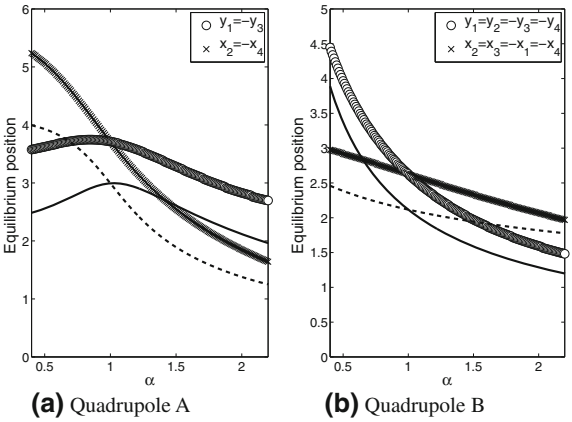

Fig. 15 Equilibrium position of vortices in the non-aligned quadrupole configurations as a function of the 2D aspect ratio: numerical data (crosses/open circles) and ODE predictions (solid lines for the y-coordinates, dashed lines for x). The chemical potential is chosen as $\mu = 2.5$.
a Quadrupole A
b Quadrupole B

Here, we can give analytical expressions for the linearization frequencies around this equilibrium position, namely $\omega_{1,2} = \pm 2\sqrt{2}\omega_{\mathrm{pr}}$, $\omega_{3,4} = \pm\omega_{\mathrm{pr}}\sqrt{2-\alpha^{-2}}$, $\omega_{5,6} = \pm\omega_{\mathrm{pr}}\sqrt{2-\alpha^2}$, $\omega_{7,8} = \pm \mathrm{i}\omega_{\mathrm{pr}}\sqrt{(1-1/\alpha)^2(1+4\alpha+\alpha^2)}$. While the first mode $\omega_{1,2}$ stays real over the whole range of α, $\omega_{7,8}$ (forming the zero mode due to rotational invariance in isotropic settings) becomes imaginary as soon as $\alpha \neq 1$. The remaining modes $\omega_{3,4}$ and $\omega_{5,6}$ become purely imaginary for $\alpha < 1/\sqrt{2}$ and $\alpha > \sqrt{2}$, respectively.

We now compare these predictions to the numerical results, obtained by solving the full GPE. Fig. 15a and b show the numerically found equilibria positions of the vortices in the quadrupole states for different values of the anisotropy parameter α, together with the fixed points of the ODE system calculated above. Generally, both quadrupole configurations are qualitatively, and to a large extent also quantitatively, accurately described by the particle picture. As an aside, we remark that the quantitative agreement becomes better if the non-modified value of $B = 1.95$, valid for vortex interaction on a homogeneous condensate background, is used for the particle picture interaction constant (data not shown), again indicating that the vortex-vortex interaction on the inhomogeneous background is not fully accurately modeled by our ODEs.

Let us now turn to the BdG spectra. Figure 16 shows the numerically obtained spectrum of the quadrupole in orientation B as a function of α. The chemical potential μ is fixed to $\mu = 2.5$. The particle picture again captures the main features: For any $\alpha \neq 1$, the existence of a purely imaginary mode is correctly predicted. Furthermore, there are additional imaginary BdG modes arising in regimes of larger anisotropy. While the particle picture predicts these to occur at $\alpha > \sqrt{2}$ and $\alpha < 1/\sqrt{2}$, respectively, numerically they are found even further away from the linear limit, at $\alpha \gtrsim 2$ and $\alpha \lesssim 1/2$. Finally, there is one purely real anomalous mode eigenfrequency whose general functional dependence on α is correctly captured by the ODE description. In the spectrum shown here, this anomalous mode collides

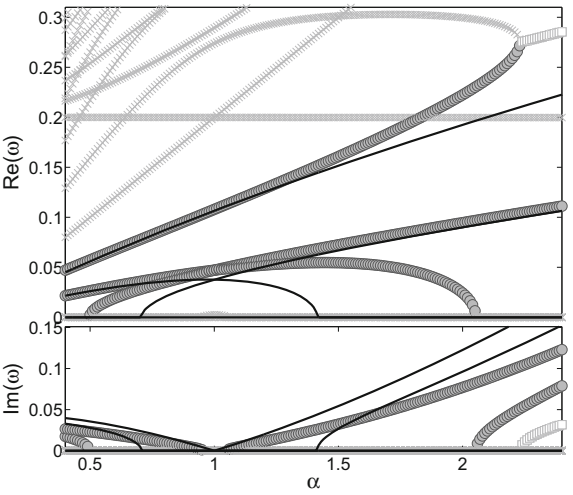

Fig. 16 BdG spectra of the vortex quadrupole B as a function of α. The predictions for the anomalous and purely imaginary modes given by the particle picture are shown in black

with a background mode at $\alpha \approx 2.2$, resulting in the emergence of a complex quartet (represented by open square symbols). This process is not contained in the particle picture predictions, and it cannot be expected to be: in fact, this oscillatory instability in the quadrupole's spectrum at large α is only present for comparably small values of the chemical potential, and the fact that it shows up at large α here merely indicates that for the particle picture to hold in the $\alpha \gtrsim 2$ regime, one has to study the spectrum at a higher value of μ (remember that the particle picture ODEs are derived under the assumption of the large μ Thomas-Fermi limit, where the highly localized vortex structures can be identified as individual particles).

We decided to still show the spectrum containing the oscillatory mode here because it illustrates our introductory remarks on the quadrupole's symmetry with respect to $\alpha \to 1/\alpha$. In general, this transformation is an exact symmetry if it is accompanied by an appropriate rescaling of the other variables, in particular of the particle number and the chemical potential. In the special case encountered here, the spectrum's symmetry around $\alpha = 1$ (up to an overall scaling of the modes' numerical values) is clearly visible. However, as we keep μ fixed while scanning, the underlying symmetry is not obvious in our numerical data: Increasing α effectively increases the trapping frequency, and consequently the effective chemical potential (measured in units of the trapping frequency) becomes smaller. Eventually, the oscillatory instabilities appear, which are not captured by the particle picture as they vanish when further approaching the appropriate Thomas-Fermi limit.

Before turning to the other quadrupole configuration, let us recall the bifurcation picture discussed above. In the $\alpha > 1$ regime we have seen there that for $1 < \alpha < 2$ the quadrupole B is the second branch to bifurcate from the γ_{20} soliton branch, thus inheriting one unstable mode. For $\alpha \geq 2$ there is also the vortex dipole along the x-axis which bifurcates from the γ_{20} soliton branch, thus inducing a

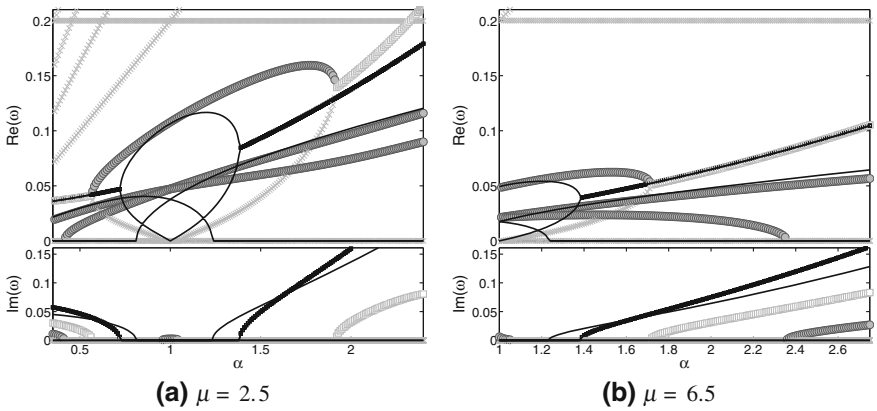

Fig. 17 BdG spectra of the vortex quadrupole A as a function of α, predictions from the particle picture in black. **a** $\mu = 2.5$ **b** $\mu = 6.5$

second instability which is passed on to the quadrupole B. By symmetry of the quadrupole, the same effects must occur in the $\alpha < 1$ regime: For $1/2 < \alpha < 1$, the quadrupole A branch is the first to bifurcate from the γ_{02} soliton branch, before the quadrupole B, and for $\alpha \leq 1/2$ additionally the vortex dipole along the y-axis becomes relevant. Thus, the discussion of the bifurcation diagram (and its approximate analytical description in terms of the Galerkin approach) correctly describes the imaginary modes arising in the spectrum of the quadrupole B in different regimes of anisotropy.

Next, let us discuss the spectrum of the quadrupole A branch of Fig. 17. Interestingly, for this configuration (where we had to find the roots of the characteristic polynomial numerically) the particle picture predicts not only the onset of purely imaginary modes, but also the existence of oscillatory instabilities in anisotropic regimes, namely for $\alpha \gtrsim 1.4$, $\alpha \lesssim 0.7$ in our case. In Fig. 17 the modes predicted by the ODEs are shown as black solid lines, with the oscillatorily unstable modes distinguished by small additional square markers. In the numerically found BdG spectrum such oscillatory instabilies emerge at $\alpha \approx 1.9$ and $\alpha \approx 0.58$, respectively, where a positive energy mode (which forms the Goldstone mode associated with the rotational invariance at $\alpha = 1$) and an anomalous mode collide as qualitatively correctly predicted by the particle picture. As a final feature, the ODEs predict purely imaginary modes for $\alpha \gtrsim 1.22$, $\alpha \lesssim 0.8$. Indeed we observe the presence of such an imaginary mode in the full BdG spectrum below $\alpha \approx 0.4$, in qualitative agreement with, but quantitatively quite far away from the particle picture prediction. In the $\alpha > 1$ part of the spectrum, a corresponding imaginary mode at $\mu = 2.5$ cannot be found, which can again be attributed to the effective rescaling of the chemical potential due to our way of scanning α: Scanning the $\alpha > 1$ regime at $\mu = 6.5$, the imaginary mode is present, and furthermore the agreement between the numerical data and the other predicted modes is better than at $\mu = 2.5$, which is expected when approaching the Thomas-Fermi

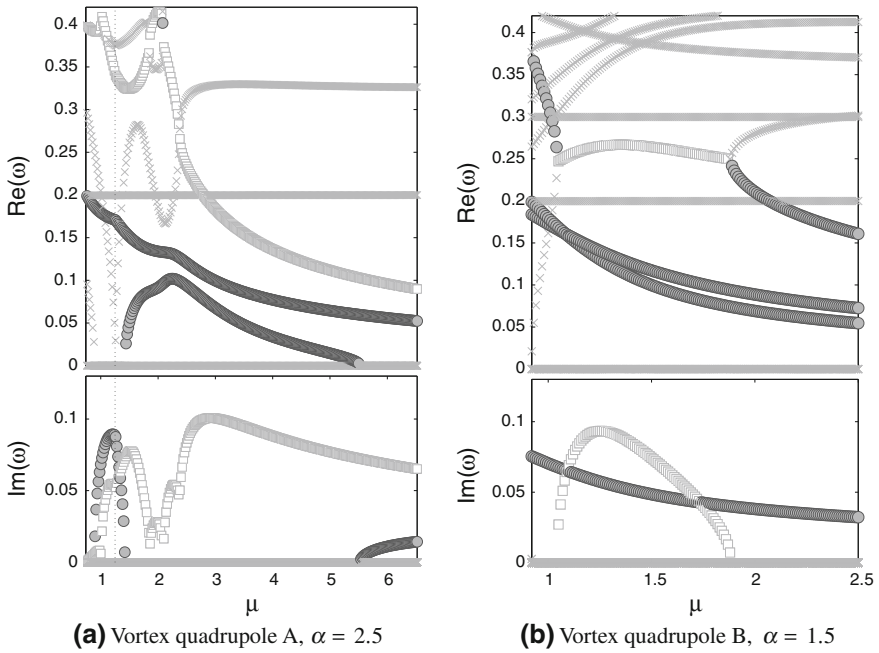

Fig. 18 BdG spectra of the vortex quadrupoles as a function of μ at fixed α. The quadrupole A branch is continued down to its solitonic origin at small μ: The dipole's bifurcation from the branch at $\mu_{cr} \approx 0.9$ induces an imaginary mode in the spectrum. At $\mu_{cr} \approx 1.25$ (indicated by the dotted vertical lines) the quadrupole A itself arises, inheriting this unstable mode which however becomes real again very quickly as μ is further increased. Only for large chemical potentials it turns imaginary again as is correctly predicted by the particle picture ODEs. In contrast, for quadrupole B (where the solitonic lower part of the branch is not shown) the imaginary mode induced by the first bifurcation from the two soliton branch is present for all values of μ that we scanned. **a** Vortex quadrupole A, $\alpha = 2.5$ **b** Vortex quadrupole B, $\alpha = 1.5$

limit, see Fig. 17b. Finally, let us remark that the very small purely imaginary mode that seems to be present in the above spectra near $\alpha = 1$ is only due to the finite resolution of our numerical grid, we have observed that it diminishes the smaller the grid spacing is chosen.

Generally, we can conclude from the above that the particle picture still gives qualitatively and, to some extent, also quantitatively accurate results when applied to the non-aligned quadrupole configurations. In comparison to the aligned vortex states, the predictions are less exact, which can be attributed to a number of possible sources of error. On the one hand, in the quadrupole A and B all four vortices are located off-center which leads to an effective change in their precession frequency that we do not take into account. Furthermore, in these regions of relatively low and inhomogeneous densities, the assumption of an undisturbed velocity field around the individual vortices that implicitly underlies our modeling of the vortex-vortex interaction is no longer justified. Both effects must be

expected to lead to a modification of the effective vortex dynamics, which our simple ODE system does not appropriately correct for. Amending these aspects of the model would be a natural direction for future work that could improve the quantitative agreement with the full model of the Gross-Pitaevskii equation.

We have already made a remark concerning the imaginary mode in the $\alpha > 1$ regime of quadrupole A which indicates that our previous strategy of explaining the emergence of instabilities at different values of α from the bifurcation diagram will not be straightforward to apply here. The bifurcation analysis allows statements about the number of unstable modes in a state's spectrum right after its bifurcation from the parental branch. No predictions can be made on what happens to these modes as μ is increased, away from the critical value. In the case of quadrupole A, the fact that at $\mu = 6.5$ an imaginary mode is present at $\alpha = 2.5$ which cannot be observed at $\mu = 2.5$ implies that there is a substantial dependence of the number of imaginary modes on the chemical potential in this branch. Indeed, we found direct numerical proof for this shifting of the imaginary modes as a function of μ at fixed anisotropy: For the quadrupole A at $\alpha = 2.5$, Fig. 18a, we expect one imaginary mode at low μ, caused by the dipole's bifurcation from the γ_{20} branch and then passed on to the quadrupole. Indeed, such a mode is present, but as μ is increased, it quickly crosses to the real axis again. Only at large μ an imaginary mode reappears, which is the one that we have seen in the spectrum as a function of α, Fig. 17b, and which is contained in the particle picture's predictions. In contrast, for the quadrupole B at $\alpha = 1.5$, Fig. 18b, the imaginary mode that is present for small μ and explained by the previous bifurcations stays present over the whole range of chemical potentials.

Finally, we have probed the stability of vortex quadrupoles in different regimes of anisotropy by simulating their time-evolution according to the full Gross-Pitaevskii equation. The results are as expected: For $\alpha = 0.75$, the quadrupole in orientation A is fully stable, while the quadrupole in orientation B is weakly unstable and starts to rotate if initially disturbed, see Fig. 19. For much larger values of α, the quadrupole A is unstable as well, and adding a noise signal leads to the onset of vortex dynamics. As can be seen in Fig. 20, when moving through the condensate the four vortices have a tendency to form dipole-like vortex-antivortex pairs.

8 Conclusions and Outlook

In this chapter, we illustrated how dramatically the dynamics of vortices may be affected by the presence of anisotropy in Bose-Einstein condensates. Although the single vortex remains dynamically robust under the effect of anisotropic trapping, all other encountered configurations are subject to fundamental changes in their stability and nonlinear dynamics through the critical handle of distinct trapping strengths in the different axial directions. More specifically, it was found that compressions parallel to the axis of an aligned vortex cluster always destabilize it

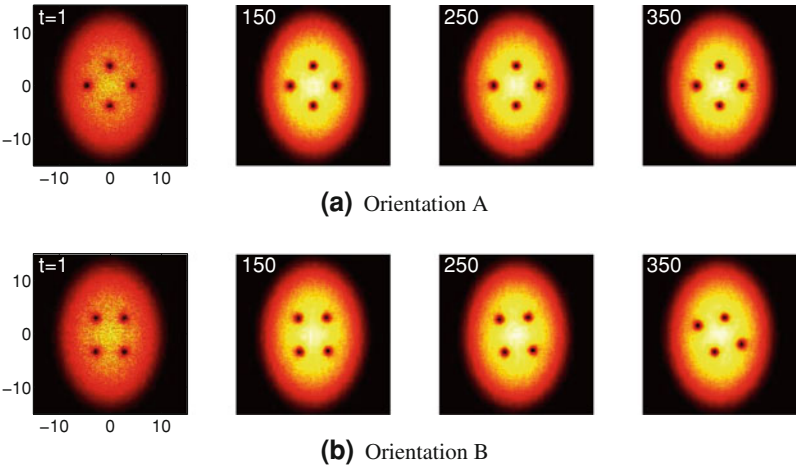

Fig. 19 Time propagation of the vortex quadrupoles, seeded with white noise at $\alpha = 0.75$, initial $\mu = 2.5$. While configuration A is stable, configuration B is dynamically unstable and starts to rotate. **a** Orientation A **b** Orientation B

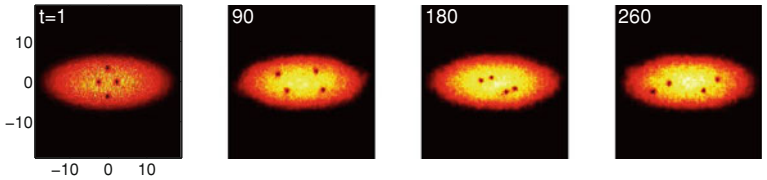

Fig. 20 Time propagation of vortex quadrupole A, seeded with white noise at $\alpha = 2.5$, initial $\mu = 6.5$. The strong anisotropy of the trap renders orientation A unstable as well

by breaking its symmetry of rotational invariance, while compressions perpendicular to the axis of the cluster may eventually stabilize even highly unstable vortex clusters. It was demonstrated how these aligned vortex states arise from nonlinear variants of linear states of the system through symmetry breaking bifurcations, and that an analysis of these bifurcations can shed light on their observed (de)stabilization due to anisotropy. The phenomenology is even more complex for the multitude of non-aligned multi-vortex solutions identified (many of which are generically unstable). However, the critical role of the anisotropy in improving or completely eliminating the stability of such states was confirmed in this case as well.

This investigation indicates a high level of experimental control that can be achieved in the coherent multi-vortex states of BECs. This control could be used for transport, manipulation, dynamical localization and numerous other similar scopes both in this more pristine context but also in other related fields, e.g. in nonlinear optics. A natural direction for extending these investigations is the context of multi-component condensates. There, novel states including vortex-

bright solitary waves can be seen to arise [52] and understanding the dynamics and interactions of multiple ones of these structures is far more complex (due to the "dual" character—soliton and vortical—of the interactions). On the other hand, another natural extension consists of the three-dimensional generalizations of the present states, namely of vortex rings which have already been experimentally observed [53, 54]. Yet, it would be of particular interest to devise a description of both their near linear as well as especially of their highly nonlinear phenomenology analogous to the one presented herein, both in isotropic and in anisotropic settings. Such themes are presently under investigation and will be reported in future publications.

References

1. R.J. Donnelly, *Quantized Vortices in Helium II* (Cambridge University Press, Cambridge, 2005)
2. G. Blatter, M.V. Feigel'man, V.B. Geshkenbein, A.I. Larkin, V.M. Vinokur, Rev. Mod. Phys. **66**, 1125 (1994)
3. Y.S. Kivshar, B. Luther-Davies, Phys. Rep. **298**, 81 (1998)
4. A. Desyatnikov, Y. Kivshar, L. Torner, Prog. Opt. **47**, 291 (2005)
5. L. Pitaevskii, S. Stringari, *Bose-Einstein Condensation* (Clarendon Press, Oxford, 2003)
6. C.J. Pethick, H. Smith, *Bose-Einstein Condensation in Dilute Gases* (Cambridge University Press, Cambridge, 2008)
7. P.G. Kevrekidis, D.J. Frantzeskakis, R. Carretero-González, *Emergent Nonlinear Phenomena in Bose-Einstein Condensates* (Springer, Berlin, 2008)
8. L.M. Pismen, *Vortices in Nonlinear Fields* (Clarendon Press, Oxford, 1999)
9. L.C. Crasovan, G. Molina-Terriza, J.P. Torres, L. Torner, V.M. Pérez-García, D. Mihalache, Phys. Rev. E **66**, 036612 (2002)
10. L.C. Crasovan, V. Vekslerchik, V.M. Pérez-García, J.P. Torres, D. Mihalache, L. Torner, Phys. Rev. A **68**, 063609 (2003)
11. J. Brand, W.P. Reinhardt, Phys. Rev. A **65**, 043612 (2002)
12. M. Möttönen, S.M.M. Virtanen, T. Isoshima, M.M. Salomaa, Phys. Rev. A **71**, 033626 (2005)
13. V. Pietilä, M. Möttönen, T. Isoshima, J.A.M. Huhtamäki, S.M.M. Virtanen, Phys. Rev. A **74**, 023603 (2006)
14. P. Kuopanportti, J.A.M. Huhtamäki, M. Möttönen, Phys. Rev. A **83**, 011603 (2011)
15. W. Li, M. Haque, S. Komineas, Phys. Rev. A **77**, 053610 (2008)
16. S. Middelkamp, P.G. Kevrekidis, D.J. Frantzeskakis, R. Carretero-González, P. Schmelcher, Phys. Rev. A **82**, 013646 (2010)
17. P. Torres, P. Kevrekidis, D. Frantzeskakis, R. Carretero-González, P. Schmelcher, D. Hall, Phys. Lett. A **375**, 3044 (2011)
18. T.W. Neely, E.C. Samson, A.S. Bradley, M.J. Davis, B.P. Anderson, Phys. Rev. Lett. **104**, 160401 (2010)
19. D.V. Freilich, D.M. Bianchi, A.M. Kaufman, T.K. Langin, D.S. Hall, Science **329**, 1182 (2010)
20. S. Middelkamp, P.J. Torres, P.G. Kevrekidis, D.J. Frantzeskakis, R. Carretero-González, P. Schmelcher, D.V. Freilich, D.S. Hall, Phys. Rev. A **84**, 011605 (2011)
21. S. Middelkamp, P. Kevrekidis, D. Frantzeskakis, R. Carretero-González, P. Schmelcher, Physica D **240**, 1449 (2011)
22. J.A. Seman, E.A.L. Henn, M. Haque, R.F. Shiozaki, E.R.F. Ramos, M. Caracanhas, P. Castilho, C. Castelo Branco, P.E.S. Tavares, F.J. Poveda-Cuevas, G. Roati, K.M.F. Magalhães, V.S. Bagnato, Phys. Rev. A **82**, 033616 (2010)
23. T. Mayteevarunyoo, B.A. Malomed, B.B. Baizakov, M. Salerno, Physica D **238**, 1439 (2009)

24. H. Sakaguchi, B. Malomed, Europhys. Lett. **72**, 698 (2005)
25. A.S. Desyatnikov, A.A. Sukhorukov, Y.S. Kivshar, Phys. Rev. Lett. **95**, 203904 (2005)
26. V.M. Lashkin, Phys. Rev. A **77**, 025602 (2008)
27. V.M. Lashkin, A.S. Desyatnikov, E.A. Ostrovskaya, Y.S. Kivshar, Phys. Rev. A **85**, 013620 (2012)
28. J. Stockhofe, S. Middelkamp, P.G. Kevrekidis, P. Schmelcher, Europhys. Lett. **93**, 20008 (2011)
29. S. McEndoo, T. Busch, Phys. Rev. A **79**, 053616 (2009)
30. S. McEndoo, T. Busch, Phys. Rev. A **82**, 013628 (2010)
31. N. Lo Gullo, T. Busch, M. Paternostro, Phys. Rev. A **83**, 053612 (2011)
32. T. Kapitula, P.G. Kevrekidis, B. Sandstede, Physica D **195**, 263 (2004)
33. D.V. Skryabin, Phys. Rev. A **63**, 013602 (2000)
34. R.S. MacKay, J. Meiss, *Hamiltonian Dynamical Systems* (Hilger, Bristol, 1987)
35. A.L. Fetter, A.A. Svidzinsky, J. Phys.: Cond. Matt. **13**, R135 (2001)
36. A.A. Svidzinsky, A.L. Fetter, Phys. Rev. Lett. **84**, 5919 (2000)
37. S. Middelkamp, P.G. Kevrekidis, D.J. Frantzeskakis, R. Carretero-González, P. Schmelcher, J. Phys. B **43**, 155303 (2010)
38. P.G. Kevrekidis, R. Carretero-González, D.J. Frantzeskakis, I.G. Kevrekidis, Mod. Phys. B **18**, 1481 (2004)
39. P.K. Newton, G. Chamoun, Siam Review **51**, 501 (2009)
40. M.S. Jean, C. Even, C. Guthmann, Europhys. Lett. **55**, 45 (2001)
41. S.W.S. Apolinario, B. Partoens, F.M. Peeters, Phys. Rev. E **72**, 046122 (2005)
42. C.T. Kelley, *Solving Nonlinear Equations with Newton's Method* (Society for Industrial and Applied Mathematics, Philadelphia, 2003)
43. D.L. Feder, A.A. Svidzinsky, A.L. Fetter, C.W. Clark, Phys. Rev. Lett. **86**, 564 (2001)
44. B. Nowak, J. Schole, D. Sexty, T. Gasenzer, Phys. Rev. A **85**, 043627 (2012)
45. D.J. Frantzeskakis, J. Phys. A **43**, 213001 (2010)
46. G. Theocharis, P.G. Kevrekidis, D.J. Frantzeskakis, P. Schmelcher, Phys. Rev. E **74**, 056608 (2006)
47. D. Mihalache, D. Mazilu, B.A. Malomed, F. Lederer, Phys. Rev. A **73**, 043615 (2006)
48. T. Kapitula, P. Kevrekidis, R. Carretero-González, Physica D **233**, 112 (2007)
49. H. Pu, C.K. Law, J.H. Eberly, N.P. Bigelow, Phys. Rev. A **59**, 1533 (1999)
50. Y. Shin, M. Saba, M. Vengalattore, T.A. Pasquini, C. Sanner, A.E. Leanhardt, M. Prentiss, D.E. Pritchard, W. Ketterle, Phys. Rev. Lett. **93**, 160406 (2004)
51. G. Theocharis, D.J. Frantzeskakis, P.G. Kevrekidis, B.A. Malomed, Y.S. Kivshar, Phys. Rev. Lett. **90**, 120403 (2003)
52. K.J.H. Law, P.G. Kevrekidis, L.S. Tuckerman, Phys. Rev. Lett. **105**, 160405 (2010)
53. B.P. Anderson, P.C. Haljan, C.A. Regal, D.L. Feder, L.A. Collins, C.W. Clark, E.A. Cornell, Phys. Rev. Lett. **86**, 2926 (2001)
54. N.S. Ginsberg, J. Brand, L.V. Hau, Phys. Rev. Lett. **94**, 040403 (2005)

Josephson Tunneling of Excited States in a Double-Well Potential

H. Susanto and J. Cuevas

Abstract We study the dynamics of matter waves in an effectively one-dimensional Bose–Einstein condensate in a double well potential. We consider in particular the case when one of the double wells confines excited states. Similarly to the known ground state oscillations, the states can tunnel between the wells experiencing the physics known for electrons in a Josephson junction, or be self-trapped. Numerical existence and stability analysis based on the full equation is performed, where it is shown that such tunneling can be stable. Through a numerical path following method, unstable tunneling is also obtained in different parameter regions. A coupled-mode system is derived and compared to the numerical observations. The validity regions of the two-mode approximation are discussed.

1 Introduction

One fundamental physical phenomenon observable on a macroscopic scale is the Josephson tunneling of electrons between two superconductors connected by a weak link, predicted by Josephson in 1962 [1]. It is due to the macroscopic wave

H. Susanto (✉)
School of Mathematical Sciences, University of Nottingham,
University Park, Nottingham, NG7 2RD, UK
e-mail: Hadi.Susanto@nottingham.ac.uk

J. Cuevas
Grupo de Física No Lineal, Departamento de Física Aplicada I,
Escuela Politénica Superior, Universidad de Sevilla,
C/ Virgen de Africa, 7, 41011 Sevilla, Spain

Progress Optical Sci., Photonics (2013): 583–599
DOI: 10.1007/10091_2012_11

Published Online: 2 August 2012

functions with global phase coherence that have a small spatial overlap. The first observation of this effect was reported by Anderson et al. [2].

Since the only requirement for the occurrence of Josephson tunneling is a weak coupling, [3] other weakly connected macroscopic quantum samples were also expected to admit such tunneling. For neutral superfluids, Josephson tunneling has been observed in liquid ^{3}He [4] and ^{4}He [5]. In the context of Bose–Einstein condensates (BECs) [6–12], the prediction was made by Smerzi et al. [13–15], followed by the experimental observation where a single [16, 17] and an array [18] of short Bose–Josephson junctions (BJJs) were realized. The idea of BJJs has also been extended to a long BJJ [19, 20], which mimics long superconducting Josephson junctions. Such a junction can be formed between two parallel quasi one-dimensional BECs linked by a weak coupling. Atomic Bose–Josephson vortices (BJVs) have also been proposed in [19, 20]. The solutions are akin to Josephson fluxons in superconducting long Josephson junctions [21] due to the relative phase of the solitons that has a kink shape with the topological phase difference equal to 2π. Moreover, it was emphasized that a BJV can transform from and to a dark soliton, due to the presence of a critical coupling at which the two solitonic structures exchange their stability [22]. In addition to BJVs that can be considered as domain-walls in the phase field, recently it is shown in [23] that a similar linearly coupled system may also admit solutions whose density difference forms a kink shape, i.e. the solutions are domain walls in the density field.

The study of Josephson tunneling in BECs considers the tunneling of the Thomas-Fermi cloud, i.e. a continuation of the ground state. The tunneling dynamics has been explained using a two-mode approximation [13, 15]. The validity of the approximation has been shown in [24, 25]. To improve the applicability regime of such an approximation, modified coupled-mode equations have been presented in, e.g., [26–30].

It is important to note that in addition to the ground state, nonlinear excitations, such as dark matter waves, can also be created in BECs. Dark soliton dynamics in BECs with single well potentials has been studied theoretically (see reviews [31, 32]) and experimentally [33–35, 37]. Interesting phenomena on the collective behavior of a quantum degenerate bosonic gas, such as soliton oscillations [34–36] and frequency shifts due to soliton collisions [37] were observed. The evolution of solitons is of particular interest as the extent to which their behavior can be described in a particle picture is an open question and merits further experimental and theoretical investigation. A combination of soliton physics with the dynamics at weak links within double well potentials will shed light on the collective behavior of excited Bose–Einstein condensates in non-trivial potentials. In this paper, we present an analysis of the dynamics of dark matter waves in a double well potential. Static properties of such a configuration have been recently studied in [38, 39]. Here, we show that dark matter waves can also experience stable quantum tunneling between the wells. This implies that localized excitations in higher dimensions, such as vortices, may also experience Josephson tunneling. The (in)stability is obtained using numerical Floquet analysis. The numerical calculations are necessary as the stability of the observed tunneling is not immediately obvious. This is especially

the case because dark solitons are higher-order excited states. The possibility that modes with lower energy will be excited is not ruled out by a coupled-mode approximation.

The present paper is outlined as follows. In Sect. 2, we discuss the governing equation used in the current study. We then solve the equation numerically, where we obtain stable and unstable Josephson tunneling through a numerical path following method. The stability analysis is performed through calculating the Floquet multipliers of the solutions. In Sect. 3, we derive a coupled-mode approximation describing the tunneling dynamics. Good agreement between the numerics and the approximation is obtained and shown. We also discuss the failure of the coupled-mode approximation in capturing unstable Josephson tunneling. Finally we conclude the work in Sect. 4.

2 Josephson Tunnelings

2.1 Mathematical Model

We consider the normalized nonlinear Schrödinger (NLS) equation modelling the BECs (see, e.g., [40] for the scaling)

$$i\psi_t + \psi_{xx} + s|\psi|^2\psi - V(x)\psi = 0, \tag{1}$$

where ψ is the bosonic field, and t and x is the time and position coordinate, respectively. The parameter $s = \pm 1$ characterizes the attractive and repulsive nonlinear interaction, respectively, and $V(x)$ is the external double well potential, which for simplicity is taken as

$$V = \frac{1}{2}\Omega^2(|x| - a)^2, \tag{2}$$

with the parameters Ω and a controlling steepness and position of the two minima. The total number of atoms N in the trap is conserved with

$$N = \int_{-\infty}^{+\infty} |\psi|^2 dx. \tag{3}$$

Throughout the present paper, we set $s = -1$, i.e. we consider repulsive interactions between particles.

For non-interacting particles $(s = 0)$ in a single well potential $(a = 0)$, the governing equation (1) can be solved analytically to yield $\psi_n = e^{-iE_n t}\phi_n(x)$, where ϕ_n satisfies

$$\phi_{n+1} = \left(\frac{\Omega}{\sqrt[4]{2}}x - \frac{\sqrt[4]{2}}{\Omega}\partial_x\right)\phi_n, \quad n = 0, 1, 2, \ldots, \tag{4}$$

with

$$\phi_0 = e^{-\frac{\Omega}{2\sqrt{2}}x^2},$$

and the chemical potential E_n is given by

$$E_n = \frac{1}{2}\sqrt{2}(2n+1)\Omega.$$

The excitations ϕ_n can be continued to nonzero s, which has been considered in, e.g., [41–51] (see also [52] for discussions on stationary solutions of the NLS equation with a multi-well potential that do not reduce to any of the eigenfunctions of the linear Schrödinger problem). Similar numerical continuations for localized modes in two-dimensional settings have been presented in, e.g., [53, 54]. The existence and the stability analysis of continuations of ϕ_n in a double-well potential has been discussed in [55], where it was shown that there is a symmetry breaking of the corresponding solutions, i.e. a change of stability from a symmetric to an asymmetric state. One typical manifestation of the instability is a periodic transfer of atoms between the wells, i.e. Josephson tunneling.

As most of Josephson tunneling studied in BECs considers the tunneling of a ground state cloud, which is a continuation of ϕ_0, here we consider in particular the tunneling of dark solitons as continuations excited states ϕ_1.

2.2 Numerical Periodic Solutions

To look for time-periodic solutions describing Josephson tunneling, we seek solutions that fulfills the relation $\psi(x,T) = \psi(x,0)$, with T being the period of the Josephson oscillations. Such solutions posses double periodicity, i.e. one due to the solitonic nature with a period $2\pi/E$, where E is the chemical potential (intra-well oscillations) and the other one caused by the Josephson effect (inter-well oscillations). Consequently, we can express the solutions in terms of a Fourier series multiplied by a factor related to the stationary character of dark solitons

$$\psi(x,t) = \exp(-iEt)\sum_{k=-\infty}^{\infty} z_k(x)\exp(ik\omega t), \tag{5}$$

where $\omega = 2\pi/T$ is the Josephson oscillation frequency. These solutions are denoted as commensurate if the commensurability condition $E = (q/p)\omega = (2q\pi)/(pT)$ is fulfilled, with $\{q,p\} \in \mathbb{N}$. In what follows, we fix $p = 1$.

Commensurate solutions are consequently fixed points of the map $\psi(x,0) \to \psi(x,T)$ and can be found either by using shooting methods in real space or algebraic methods in Fourier space. In order to do that, we will transform the problem into a discrete one by means of a finite difference discretization with spatial step $\Delta x = 0.2$ and apply the techniques developed for discrete breathers in Klein–Gordon lattices [56, 57]. If a shooting method were used, a time step $\Delta t = 0.02$ would be necessary. As the considered oscillations herein have periods about 1,500 time units, this

method would imply many integration steps. In addition to that, the lack of an analytical Jacobian would also imply the necessity of the numerical determination of this matrix. These facts suggest the suitability of the proposed Fourier space method, which, apart from transforming the set of differential equations into an algebraic one, provides an analytical expression for the Jacobian.

Truncating the Fourier series at k_m, i.e. the maximum value of $|k|$, which has been chosen to be 9 in most of the calculations due to computational reasons, Eq. (1) yields a set of nonlinear equations with the kth component of the dynamical equation set given by

$$F_k(x) \equiv (E - \omega k) z_k + \partial_x^2 z_k - V(x) z_k - s \sum_{m=-k_m}^{k_m} \sum_{n=-k_m}^{k_m} z_m z_n z_{k-m+n} = 0. \tag{6}$$

We then obtain the following expression for each component of the Jacobian

$$\begin{aligned} \frac{\partial F_k(x)}{\partial z_n(x')} = & \left\{ [E - \omega k - V(x)] \delta(x - x') + \partial_{xx}^2 \right\} \delta_{k,n} \\ & - s \delta(x - x') \sum_m \left[z_m^* z_{k-n+m} + z_m (z_{k-m+n} + z_{n+m-k}^*) \right], \end{aligned} \tag{7}$$

where we have written $z_k \equiv z_k(x)$ in both equations.

Once a periodic solution, say $\Psi(x,t)$, is obtained, to study its (linear) orbital stability one needs to analyze the time evolution of a small perturbation $\xi(x,t)$ to $\Psi(x,t)$. The equation satisfied to leading order by $\xi(x,t)$ is

$$i\xi_t + \xi_{xx} - s(2|\Psi|^2 \xi + \Psi^2 \xi^*) - V(x)\xi = 0. \tag{8}$$

Then, the stability properties of commensurate solutions can be determined by means of a Floquet analysis. It is performed by diagonalizing the monodromy matrix $\mathcal{M}$ which is defined as

$$\begin{bmatrix} \mathrm{Re}(\xi(x,T)) \\ \mathrm{Im}(\xi(x,T)) \end{bmatrix} = \mathcal{M} \begin{bmatrix} \mathrm{Re}(\xi(x,0)) \\ \mathrm{Im}(\xi(x,0)) \end{bmatrix}. \tag{9}$$

The linear stability of the solutions requires that the monodromy eigenvalues (also called Floquet multipliers) must be at the unit circle (see, e.g., [56, 58, 59] for details). In order to get the monodromy with enough accuracy, the simulations must be performed using a time step around $\Delta t = 0.001$.

We have calculated commensurate solitons for $\Omega = 0.1$ and $a = 10$ using the method described above and analysed the stability of those solutions. Presented in the top panels of Fig. 1 are two periodic solutions that we obtained in a double well potential. The left and right panel respectively corresponds to Josephson tunneling and a transition to macroscopic quantum self-trapping, similarly to the dynamics of the ground state oscillations [13, 15].

In the middle panels of Fig. 1, we present the distribution of the Floquet multipliers of the two solutions depicted in the top panels in the complex plane. It

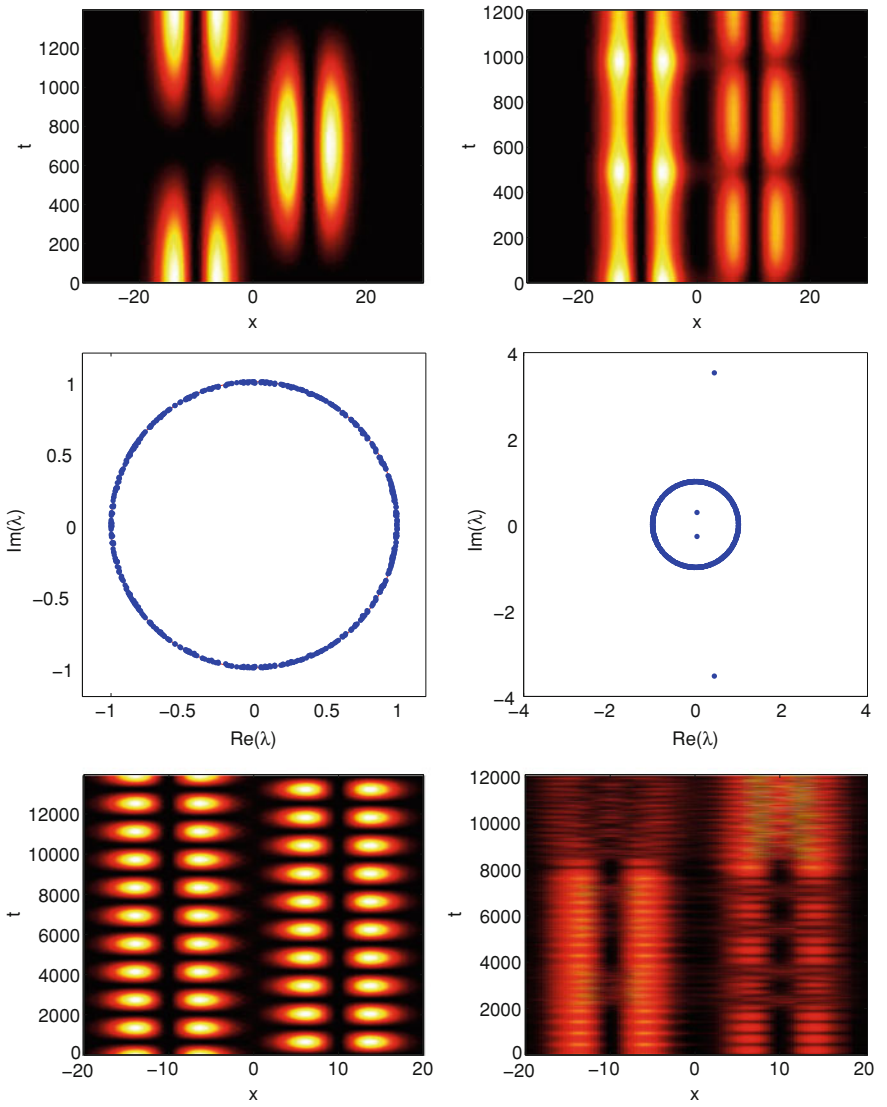

Fig. 1 (*Top*) The first few oscillations of the atom density $|\psi(x,t)|^2$ for dark solitons in a double well potential with $\Omega = 0.1$, $a = 10$, and (*left*) $\omega = 0.00450$ and (*right*) $\omega = 0.00520$, which respectively corresponds to $N = 0.0340$ and $N = 0.7677$. In both cases, the initial conditions are obtained from a numerical continuation with $q = 47$ (see the text). (*Middle*) Floquet multiplier distributions corresponding to solutions in the *top left and right panel*, respectively. (*Bottom*) Longer time evolutions of the *top panels* where one can see that the solution in the *top right panel* is indeed unstable

is worth noting that as there is a quartet of multipliers that do not lie on the unit circle, one can conclude that the solution in the top right panel is unstable.

We show in the bottom panels of Fig. 1 a longer time evolution of the solutions in the top panels, where one can see that the solution in the top right panel is indeed unstable. The instability we reported here is a clear evidence that the nonlinearity term in the governing equation (1) plays an important role, as all the solutions would have been stable otherwise. A typical instability dynamics is a repulsive interaction between the dark solitons in different wells so that they start to oscillate about the minimum of the wells as shown in the bottom right panel of Fig. 1. This is a typical dynamics due to the presence of complex eigenvalues, i.e. oscillatory instabilities.

We have also obtained periodic solutions for various parameter values. In the top left panel of Fig. 2 we show the dependence of the norm (number of atoms) N of tunneling dark solitons when the inter-well oscillation frequency is varied. In the panel, several representative values of q are considered. Note that the possible values of q are not limited to those shown in the graph. As ω is increased further, there is a critical value above which solutions are unstable. Unstable solutions are indicated as dashed lines in the top left panel. The solutions can also be continued for decreasing frequencies ω down to a critical value. Below this critical value, the only existing solutions are non-oscillating ones. In the top right panel of Fig. 2 we show the dependence of the growth rate (the logarithm of the maximum modulus of the Floquet multipliers) with respect to ω for $q = 47$. We also present the growth rate of Josephson tunneling for a fixed ω and q and variable separation distance between the two wells a in the bottom panels of the same figure, i.e. $\omega = 0.0049$ and $q = 47$. For small a, the solutions tend to a non-oscillating one with one dark soliton in each well, analogously to what occurs for small ω and fixed a.

3 Coupled-Mode Approximations and Their Validity

To describe dark soliton dynamics reported in the previous section, we will readily use a two-mode approximation derived in [27, 28]. Following [27, 28], we write

$$\psi = \sqrt{N}(b_2(t)\Phi_2(x) + b_3(t)\Phi_3(x)), \quad \Phi_{2,3} = \frac{\Phi_+(x) \pm \Phi_-(x)}{\sqrt{2}}, \tag{10}$$

where $\Phi_\pm(x)$ is a continuation of $\phi_{2,3}$ (4) for nonzero a satisfying

$$\partial_{xx}\Phi_\pm + \beta_\pm\Phi_\pm - V(x)\Phi_\pm + sN\Phi_\pm^3 = 0, \tag{11}$$

with the constraint $\int_{-\infty}^{+\infty} \Phi_j\Phi_k dx = \delta_{j,k},\ i,j = +,-$. Two examples of Φ_j, which corresponds to the norm N in the Fig. 1 are presented in Fig. 3. We obtained $\Phi_j(x)$ numerically by solving (11) using a fixed point algorithm, i.e. in this case a Newton–Raphson method.

Next, for simplicity we write $b_j(t) = |b_j(t)|e^{i\theta_j(t)}$. Equations (3) and (10) imply that $|b_2(t)|^2 + |b_3(t)|^2 = 1$. Defining

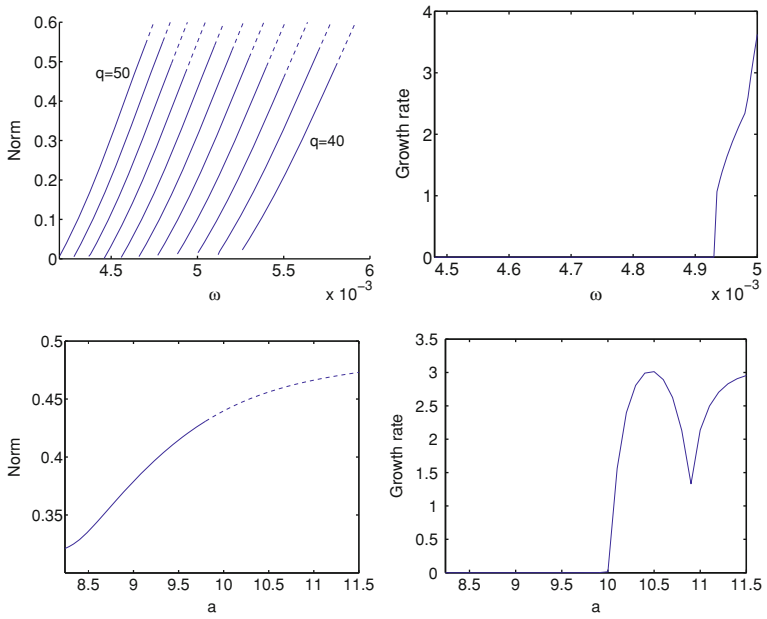

Fig. 2 The *top left panel* presents the dependence of the norm with respect to ω for dark solitons with $a = 10$. *Central panel* shows the minimum transmission coefficient for those solutions. *Dashed lines* indicate unstable solutions. Here, q sweeps the values between 40 and 50. The *top right panel* shows the dependence of the growth rate with respect to ω for $q = 47$. *Bottom panels* depict the norm and the growth mode of tunneling dark solitons with fixed $\omega = 0.0049$ and $q = 47$ for varying a

$$z(t) = |b_2(t)|^2 - |b_3(t)|^2, \quad \Delta\theta(t) = \theta_3(t) - \theta_2(t), \tag{12}$$

one can obtain the equations satisfied by z and $\Delta\theta$ [27, 28]

$$\frac{dz}{dt} = -\frac{\partial H}{\partial \Delta\theta}, \quad \frac{d\Delta\theta}{dt} = \frac{\partial H}{\partial z}, \tag{13}$$

where

$$H = \frac{1}{2}Az^2 - B\sqrt{1-z^2}\cos\Delta\theta + \frac{1}{2}C(1-z^2)\cos 2\Delta\theta, \tag{14}$$

$$A = \frac{10\gamma_{+-} - \gamma_{++} - \gamma_{--}}{4}, \quad B = \beta_- - \beta_+ + \frac{\gamma_{++} - \gamma_{--}}{2}, \tag{15}$$

$$C = \frac{-2\gamma_{+-} + \gamma_{++} + \gamma_{--}}{4}, \tag{16}$$

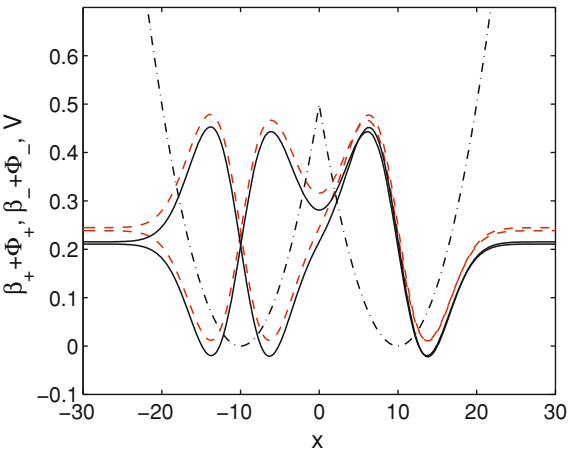

Fig. 3 The second and third collective modes of the confining potential $V(x)$ (*dash-dotted*) for (*solid*) $N = 0.034$ and (*dashed*) $N = 0.7677$, with $s = -1$

$$\gamma_{jk} = -sN \int_{-\infty}^{\infty} \Phi_j^2(x)\Phi_k^2(x)dx, \tag{17}$$

with $j, k = +, -$. In the $(\Delta\theta, z)$-plane, Φ_+ and Φ_- correspond to the equilibrium point $(0, 0)$ and $(\pm\pi, 0)$, respectively.

We plot the phase-portrait of (13) in Fig. 4 for the two values of N in Fig. 1. To compare the two-mode approximation with the top panels of Fig. 1, we calculate the variable z from the numerics of the full equation (1) as [27, 28]

$$z = \frac{\int_{-\infty}^{0} |\psi(x,t)|^2 dx - N/2}{NS}, \quad S = \left| \int_{-\infty}^{0} \Phi_+\Phi_- dx \right|,$$

where in the present case $S \approx 0.5$. As $\Delta\theta$ can be calculated immediately, one can compare the numerics and the approximation right away. Shown in Fig. 4 are the comparisons, where satisfactory agreement is obtained. The bold trajectory in the right panel is obtained from the top right panel of Fig. 1, i.e. only the first few oscillations are used such that the instability has not developed yet.

The phase portrait in the left panel of Fig. 4 has two families of periodic oscillations, i.e. one centred at $\Delta\theta = 0$ and the other at $\pm\pi$. The latter is known as π-oscillations [14]. The stable solution in the top left panel of Fig. 2 with $q = 50$ and the same norm belongs to this family. As for the phase portrait in the right panel of Fig. 4, one can also observe that there are two types of solutions, i.e. Josephson oscillations and running states. The latter type is also referred to as macroscopically quantum self-trapped states.

As for the instability of the solution in the top right panel that develops at a later time, it is clearly beyond the validity of the two-mode approximation presented herein. One would need a better ansatz for the approximation to capture the stability of the periodic solutions. We conjecture that the invalidity of the

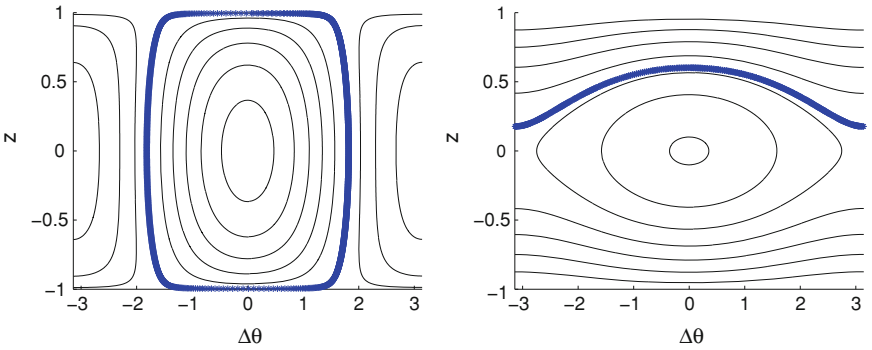

Fig. 4 The phase-portraits of (13) for the two values of N in Fig. 1, i.e. (*left*) $N = 0.0340$ and (*right*) $N = 0.7677$. *Thick symbols* correspond to the periodic solutions shown in the *top panels* of Fig. 1

approximation is caused by the assumption that the basis functions Φ_2 and Φ_3 are thought to be stable (time-independent), which are not necessarily the case. Note that the validity issue mentioned here is completely different from that in [27, 28]. In [27, 28], the issue is related to the fact that the approximation does not capture the Josephson oscillation of the full equation directly from the beginning, which typically occurs when $|sN| \gg 1$, while in our case $|sN| < 1$ and the approximation does capture the existence, but not the stability.

To analyse further the above conjecture, we have calculated the stability of the bases $\Phi_\pm$. The linear stability of Φ_j is determined by solving for the eigenvalues λ and eigenvectors $a(x)$ and $b(x)$ of the eigenvalue problem

$$\begin{aligned}\lambda a &= \left(\beta_j + d_{xx} - V(x) + 2sN{\Phi_j}^2\right)a + sN{\Phi_j}^2 b,\\ -\lambda b &= \left(\beta_j + d_{xx} - V(x) + 2sN{\Phi_j}^2\right)b + sN{\Phi_j}^2 a,\end{aligned}$$

obtained by the substitution of

$$\psi(x,t) = \left[\sqrt{N}\Phi_j(x) + \epsilon\left(a(x)e^{i\lambda t} + b^*(x)e^{-i\lambda^* t}\right)\right]e^{-i\beta_j t}$$

into (1) and linearization in the formal small parameter ϵ. As the eigenvalues are generally complex, i.e. $\lambda = \lambda_r + i\lambda_i$, instability corresponds to $\lambda_i \neq 0$ due to the Hamiltonian structure of the equation. The stability analysis of the bases $\Phi_\pm$ as a function the norm N is summarized in Fig. 5.

From our numerical analysis, Φ_- becomes unstable at $N \approx 0.056$. At this point, a pair of eigenvalues bifurcates from the zero eigenvalues into the imaginary axis, i.e. an exponential instability. This change of stability is due to a symmetry-breaking (pitchfork) bifurcation with an asymmetric solution, which is accurately predicted by the two-mode approximation above (see, e.g., [38]). Note that the equilibrium $(\Delta\theta, z) = (\pm\pi, 0)$ in the left and right panel of Fig. 4 has different stability. The stability does change at the critical norm above. The typical outcome

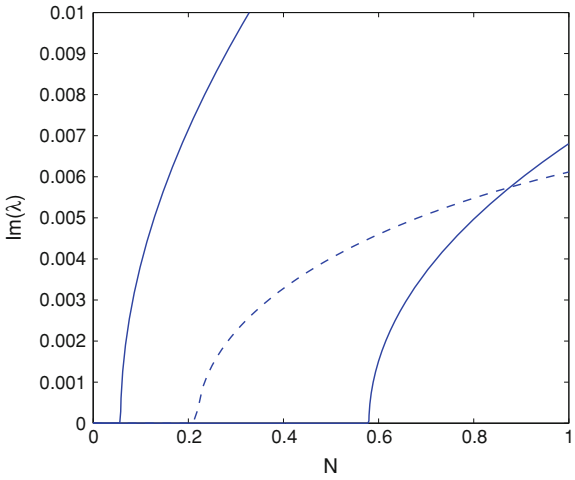

Fig. 5 The imaginary part of the unstable eigenvalues of Φ_+ (*dashed*) and Φ_- (*solid*) as a function of the norm N

of the instability is a stable time-periodic solution, which is in agreement with the two-mode approximation.

When N is increased further, there is a critical norm $N \approx 0.21$ above which Φ_+ becomes unstable. It is important to note that in this case the critical eigenvalue is complex, i.e. the solution suffers from an oscillatory instability, as shown in the top panel of Fig. 6 for $N = 0.3$. From the middle panel, it can be seen that the unstable mode creates out-of-phase oscillations of the dark soliton pairs in the wells. Computing the atom imbalance $z(t)$ and the phase-difference $\Delta\theta(t)$ between atoms in the wells, interestingly we obtain that the unstable dynamics still yields the equilibrium point $(\Delta\theta, z) = (0, 0)$. Another interesting observation is that superposing Φ_+ with Φ_- may suppress the instability provided that the coefficient of Φ_- is sufficiently large. As shown in the bottom panel of Fig. 6, even a coefficient as small as $\sqrt{0.1} \approx 0.32$ already reduces the instability of Φ_+. These may likely be related to the numerical results in Fig. 2, where we still obtained stable periodic solutions with norms slightly larger than $N = 0.3$.

Next, we increased N further and observed that for the stability of Φ_- there is a pair of complex eigenvalues that bifurcates in the complex plane at $N \approx 0.58$. The eigenvalue structure of the solution for $N = 0.7677$ is shown in the top panel of Fig. 7. Hence, in addition to an exponential instability, now Φ_- also suffers from an oscillatory instability. The typical dynamics of the state is presented in the middle panel, where initially the exponential instability creates partial tunneling of atoms from one well to the other followed by in-phase oscillations of the dark soliton pairs. As opposed to stabilization of Φ_+ due to a superposition of $\Phi_\pm$ when it becomes unstable, in the present case we did not observe any instability suppression. It may be because both $\Phi+$ and Φ_- are already unstable due to complex eigenvalues. This is also in agreement with the numerics in Fig. 2 where all the numerically obtained periodic solutions are unstable above $N \approx 0.58$ due to complex eigenvalues (see the middle, right panel of Fig. 1).

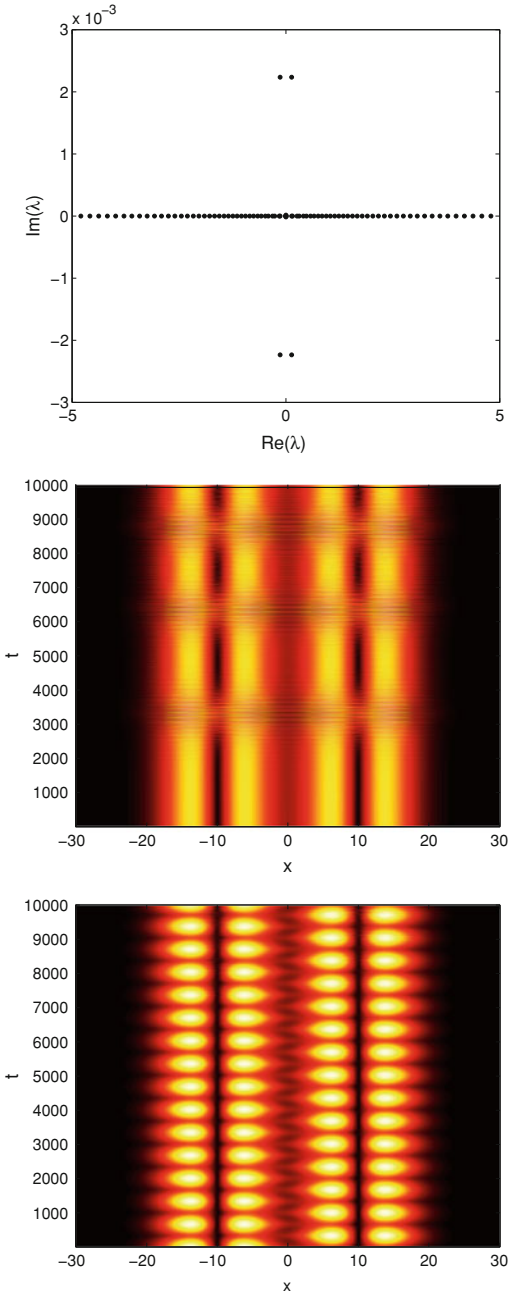

Fig. 6 (*Top*) The eigenvalue structure of Φ_+ for $N = 0.3$. (*Middle*) The dynamics of an unstable Φ_+ for the same norm. (*Bottom*) The dynamics of an initial condition $\psi(x,0) = \sqrt{0.9}\Phi_+ + \sqrt{0.1}\Phi_-$

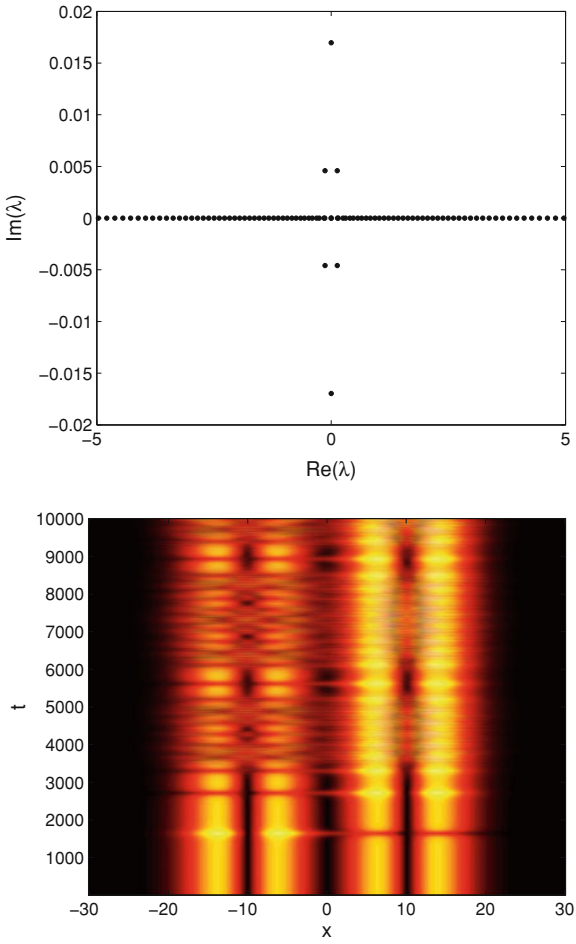

Fig. 7 The same as Fig. 6, but for Φ_- with $N = 0.7677$

4 Conclusion and Future Work

We have studied dynamics of excited states in a double well potential, where it has been shown that such states can experience tunnelings between the wells. Numerical stability analysis based on the full governing equation has been performed to show that the time-periodic solutions can be stable. Through path following methods, unstable solutions were also obtained. The instability is because of complex eigenvalues, i.e. oscillatory instability. A coupled-mode approximation has been derived to explain the numerical results. The break-down of the approximation has been discussed as well, where it was shown through a hand-wavy argument that two-mode approximations are not able to capture instability due to complex eigenvalues. Nevertheless, it was also shown trough numerical simulations that an instability caused by a quartet of complex eigenvalues can be

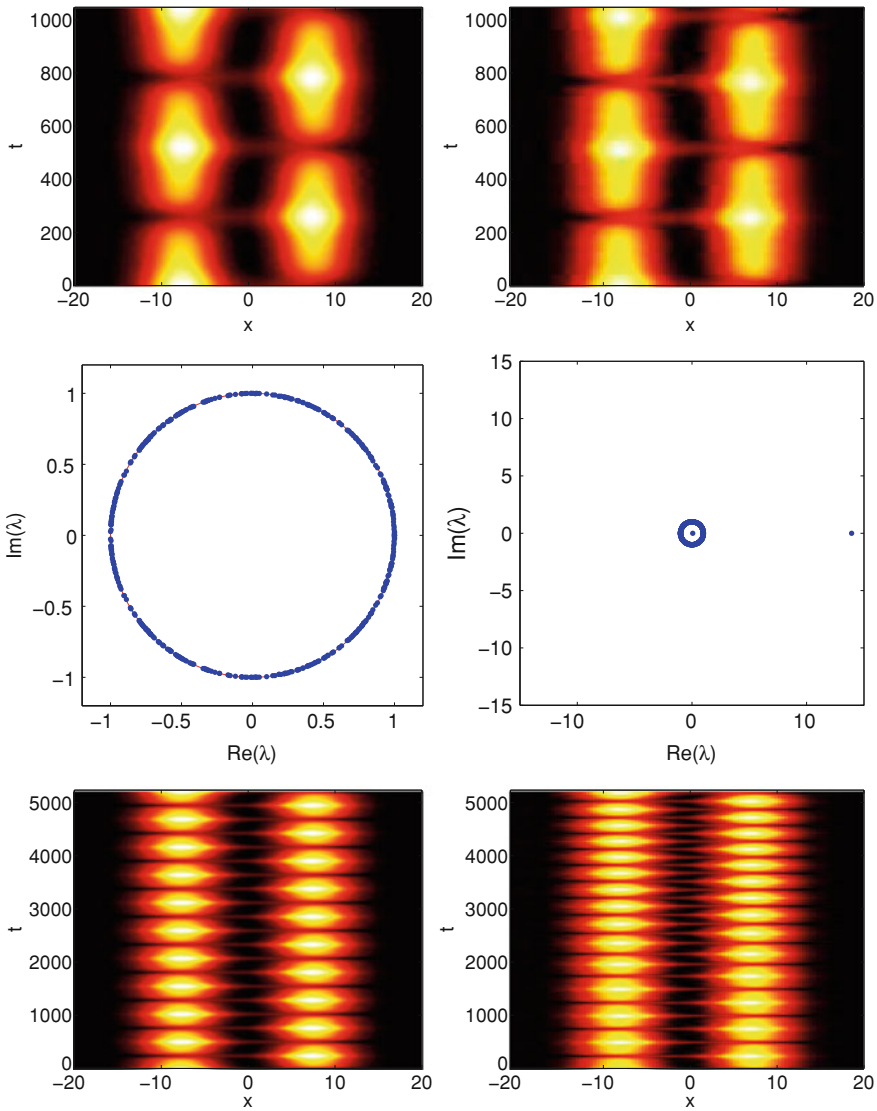

Fig. 8 (*Top*) The first two oscillations of the atom density $|\psi(x,t)|^2$ for a Thomas-Fermi cloud in a double well potential with $\Omega = 0.1$, $a = 7.5$, (*left*) $q = 10$ and (*right*) $q = 13$. In both cases, the initial conditions are obtained from a numerical continuation with $\omega = 0.01$. (*Middle*) Floquet multiplier distributions corresponding to solutions in the *top left and right panel*, respectively. (*Bottom*) Longer time evolutions of the *top panels* corresponding to 10 oscillation periods; clearly, the unstable solution develops oscillations with a period different from the initial one

suppressed by Josephson tunneling. In that regard, it is interesting to mention that the lifetime of purely black stationary solitons can be short due to quantum depletion [60], as atoms tunnel in to fill up the notch at the soliton center. In a

double-well potential, because the soliton dip can effectively tunnel from one well to the other and hence a periodic transfer of atoms in each well, Josephson tunneling may provide an alternative way to obtain a long-lived dark soliton by suppressing the depletion-induced decay of the soliton.

A natural problem to follow the analysis reported herein is the existence and stability of time-periodic solutions of the ground states (Thomas-Fermi cloud). A two-mode approximation for this case has been derived and discussed in, e.g., [27, 28]. Using the approximation, periodic solutions should be stable. We have performed preliminary computations presented in Fig. 8 where we also obtained unstable periodic solutions due to multipliers leaving at 1, i.e. exponentially unstable. Different from the dark soliton case, the instabilities here do not lead to the destruction of the periodicity of the solutions, but to a change in the oscillation period of the tunneling. Hence, again a coupled-mode approximation breaks down here. Nevertheless, our analysis presented above cannot be used in this case as the bases, which are continuations of ϕ_0 and ϕ_1 (see (4) and (11)), do not experience any oscillatory instability [55]. This is an ongoing work and will be reported elsewhere.

Several other directions that currently we work on include, on the one hand, the extension of the dark soliton tunneling to non-commensurate solutions using the technique developed in [61], and, on the other hand, an analysis of Josephson tunneling of excitations in polaritonic Bose–Einstein condensates [62] whose description includes gain and damping terms in the Gross–Pitaevskii equation [63].

Acknowledgments JC acknowledges financial support from the MICINN project FIS2008-04848

References

1. B.D. Josephson, Phys.Lett. **1**, 251 (1962)
2. P.L. Anderson, J.W. Rowell, Phys.Rev.Lett. **10**, 230 (1963)
3. A. Barone, G. Paterno, *Physics and Applications of the Josephson Effect* (Wiley, New York, 1982)
4. S.V. Pereverzev, A. Loshak, S. Backhaus, J.C. Davis, R.E. Packard, Nature **388**, 449 (1997)
5. K. Sukhatme, Y. Mukharsky, T. Chui, D. Pearson, Nature **411**, 280 (2001)
6. S.N. Bose, Zeit. Phys. **26**, 178 (1924)
7. A. Einstein, Sber. Preuss. Akad. Wiss. **22**, 261–267 (1924)
8. A. Einstein, Sber. Preuss. Akad. Wiss. **1**, 3–14 (1925)
9. M.H. Anderson, J.R. Ensher, M.R. Matthews, C.E. Wieman, E.A. Cornell, Science **269**, 198–201 (1995)
10. K.B. Davis, M.-O. Mewes, M.R. Andrews, van N.J. Druten, D.S. Durfee, D.M. Kurn, W. Ketterle, Phys. Rev. Lett. **75**, 3969–3973 (1995)
11. C.C. Bradley, C.A. Sackett, R.G. Hulet, Phys. Rev. Lett. **75**, 1687–1690 (1995)
12. F. Dalfovo et al., Rev. Mod. Phys. **71**, 463–512 (1999)
13. A. Smerzi, S. Fantoni, S. Giovanazzi, S.R. Shenoy, Phys. Rev. Lett. **79**, 4950 (1997)
14. S. Raghavan, A. Smerzi, S. Fantoni, S.R. Shenoy, Phys. Rev. A **59**, 620–633 (1999)
15. S. Giovanazzi, A. Smerzi, S. Fantoni, Phys. Rev. Lett. **84**, 4521 (2000)
16. M. Albiez, R. Gati, J. Folling, S. Hunsmann, M. Cristiani, M.K. Oberthaler, Phys. Rev. Lett. **95**, 010402 (2005)

17. S. Levy, E. Lahoud, I. Shomroni, J. Steinhauer, Nature **449**, 579 (2007)
18. F.S. Cataliotti, S. Burger, C. Fort, P. Maddaloni, F. Minardi, A. Trombettoni, A. Smerzi, M. Inguscio, Science **293**, 843 (2001)
19. V.M. Kaurov, A.B. Kuklov, Phys. Rev. A **71**, 011601 (2005)
20. V.M. Kaurov, A.B. Kuklov, Phys. Rev. A **73**, 013627 (2006)
21. A.V. Ustinov, Physica D **123**, 315 (1998)
22. M.I. Qadir, H. Susanto, P.C. Matthews, J. Phys. B: At. Mol. Opt. Phys. **45**, 035004 (2012)
23. N. Dror, B.A. Malomed, J. Zeng, Phys. Rev. E **84**, 046602 (2011)
24. A. Sacchetti, SIAM J. Math. Anal. **35**, 1160–1176 (2003)
25. A. Sacchetti, J. Evol. Eq. **4**, 345–369 (2004)
26. E.A. Ostrovskaya, Y.S. Kivshar, M. Lisak, B. Hall, F. Cattani, D. Anderson, Phys. Rev. A **61**, 031601–4 (2000)
27. D. Ananikian, T. Bergeman, Phys. Rev. A **73**, 013604 (2006)
28. D. Ananikian, T. Bergeman, Phys. Rev. A **74**, 039905(E) (2006)
29. X.Y. Jia, W.D. Li, J.Q. Liang, Phys. Rev. A **78**, 023613 (2008)
30. B. Juliá-Díaz, J. Martorell, M. Melé-Messeguer, A. Polls, Phys. Rev. A **82**, 063626 (2010)
31. V.V. Konotop, in *Emergent Nonlinear Phenomena in Bose–Einstein Condensates Theory and Experiment*, ed. by P.G. Kevrekidis, D.J. Frantzeskakis, R. Carretero-González (Springer, Berlin, 2008), pp. 65–97
32. D.J. Frantzeskakis, J. Phys. A: Math. Theor. **43**, 213001 (2010)
33. S. Burger, K. Bongs, S. Dettmer, W. Ertmer, K. Sengstock, A. Sanpera, G.V. Shlyapnikov, M. Lewenstein, Phys. Rev. Lett. **83**, 5198 (1999)
34. C. Becker, S. Stellmer, P. Soltan-Panahi, S. Dörscher, M. Baumert, E-M. Richter, J. Kronjäger, K. Bongs, K. Sengstock, Nature Phys. **4**, 496 (2008)
35. A. Weller, J.P. Ronzheimer, C. Gross, J. Esteve, M.K. Oberthaler, D.J. Frantzeskakis, G. Theocharis, P.G. Kevrekidis, Phys. Rev. Lett. **101**, 130401 (2008)
36. G. Theocharis, A. Weller, J.P. Ronzheimer, C. Gross, M.K. Oberthaler, P.G. Kevrekidis, D.J. Frantzeskakis, Phys. Rev. A **81**, 063604 (2010)
37. S. Stellmer, C. Becker, P. Soltan-Panahi, E.-M. Richter, S. Dörscher, M. Baumert, J. Kronjäger, K. Bongs, K. Sengstock, Phys. Rev. Lett. **101**, 120406 (2008)
38. S. Middelkamp, G. Theocharis, P.G. Kevrekidis, D.J. Frantzeskakis, P. Schmelcher, Phys. Rev. A **81**, 053618 (2010)
39. R. Ichihara, I. Danshita, T. Nikuni, Phys. Rev. A **78**, 063604 (2008)
40. R. Carretero-González, D.J. Frantzeskakis, P.G. Kevrekidis, Nonlinearity **21**, R139 (2008)
41. J.A. Vaccaro, O. Steuernagel, B. Lorimer, ArXiv:cond-mat/0007233v1
42. M.P. Coles, D.E. Pelinovsky, P.G. Kevrekidis, Nonlinearity **23**, 1753–1770 (2010)
43. R.J. Dodd, J. Res. Natl. Inst. Stand. Technol. **101**, 545 (1996)
44. Yu.S. Kivshar, T.J. Alexander, S.K. Turitsyn, Phys. Lett. A **278**, 225 (2001)
45. V.I. Yukalov, E.P. Yukalov, V.S. Bagnato, Phys. Rev. A **56**, 4845 (1997)
46. C. Trallero-Giner, J.C. Drake-Perez, V. López-Richard, J.L. Birman, Physica D **237**, 2342 (2008)
47. P.G. Kevrekidis, V.V. Konotop, A. Rodrigues, D.J. Frantzeskakis, J. Phys. B: At. Mol. Opt. Phys. **38**, 1173 (2005)
48. G.L. Alfimov, D.A. Zezyulin, Nonlinearity **20**, 2075 (2007)
49. D.A. Zezyulin, G.L. Alfimov, V.V. Konotop, V.M. Pérez-García, Phys. Rev. A **78**, 013606 (2008)
50. R. D'Agosta, B.A. Malomed, C. Presilla, Laser Phys. **12**, 37–42 (2002)
51. R. D'Agosta, B.A. Malomed, C. Presilla, Phys. Lett. A **275**, 424–434 (2000)
52. R. D'Agosta, C. Presilla, Phys. Rev. A **65**, 043609 (2002)
53. D. Mihalache, D. Mazilu, B.A. Malomed, F. Lederer, Phys. Rev. A **73**, 043615 (2006)
54. G. Herring, L.D. Carr, R. Carretero-González, P.G. Kevrekidis, D.J. Frantzeskakis, Phys. Rev. A **77**, 023625 (2008)
55. G. Theocharis, P.G. Kevrekidis, D.J. Frantzeskakis, P. Schmelcher, Phys. Rev. E **74**, 056608 (2006)

56. J.L. Marín, S. Aubry, Nonlinearity **9**, 1501 (1996)
57. J. Cuevas, J.F.R. Archilla, F.R. Romero, J. Phys. A: Math. and Theor. **44**, 035102 (2011)
58. T.R.O. Melvin, A.R. Champneys, P.G. Kevrekidis, J. Cuevas, Physica D **237**, 551 (2008)
59. S. Aubry, Physica D **103**, 201 (1997)
60. J. Dziarmaga, K. Sacha, Phys. Rev. A, **66**, 043620 (2002)
61. D. Yan, J.J. Chang, C. Hamner, M. Hoefer, P.G. Kevrekidis, P. Engels, V. Achilleos, D.J. Frantzeskakis, J. Cuevas, J. Phys. B: At. Mol. Opt. Phys. **45**, 115301 (2012)
62. A.S. Rodrigues, P.G. Kevrekidis, J. Cuevas, R. Carretero-Gonzlez, D.J. Frantzeskakis, in the present book
63. J. Cuevas, A.S. Rodrigues, R. Carretero-González, P.G. Kevrekidis, D.J. Frantzeskakis, Phys. Rev. B **83**, 245140 (2011)

Solitons in a Parametrically Driven Damped Discrete Nonlinear Schrödinger Equation

M. Syafwan, H. Susanto and S. M. Cox

Abstract We consider a parametrically driven damped discrete nonlinear Schrödinger (PDDNLS) equation. Analytical and numerical calculations are performed to determine the existence and stability of fundamental discrete bright solitons. We show that there are two types of onsite discrete soliton, namely onsite type I and II. We also show that there are four types of intersite discrete soliton, called intersite type I, II, III, and IV, where the last two types are essentially the same, due to symmetry. Onsite and intersite type I solitons, which can be unstable in the case of no dissipation, are found to be stabilized by the damping, whereas the other types are always unstable. Our further analysis demonstrates that saddle-node and pitchfork (symmetry-breaking) bifurcations can occur. More interestingly, the onsite type I, intersite type I, and intersite type III–IV admit Hopf bifurcations from which emerge periodic solitons (limit cycles). The continuation of the limit cycles as well as the stability of the periodic solitons are computed through the numerical continuation software Matcont. We observe subcritical Hopf bifurcations along the existence curve of the onsite type I and intersite type III–IV. Along the existence curve of the intersite type I we observe both supercritical and subcritical Hopf bifurcations.

M. Syafwan · H. Susanto (✉) · S. M. Cox
School of Mathematical Sciences, University of Nottingham,
University Park, Nottingham, NG7 2RD, UK
e-mail: Hadi.Susanto@nottingham.ac.uk

M. Syafwan
Department of Mathematics, Andalas University, Limau Manis,
Padang 25163, Indonesia

Progress Optical Sci., Photonics (2013): 601–638
DOI: 10.1007/10091_2012_12

Published Online: 17 July 2012

1 Introduction

In this chapter, we consider a lattice model governed by a parametrically driven damped discrete nonlinear Schrödinger (PDDNLS) equation

$$i\dot{\phi}_n = -\varepsilon \Delta_2 \phi_n + \Lambda \phi_n + \gamma \overline{\phi}_n - i\alpha \phi_n - \sigma |\phi_n|^2 \phi_n. \tag{1}$$

In the above equation, $\phi_n \equiv \phi_n(t)$ is a complex-valued wave function at site n, the overdot and the overline indicate, respectively, the time derivative and complex conjugation, ε represents the coupling constant between two adjacent sites, $\Delta_2 \phi_n = \phi_{n+1} - 2\phi_n + \phi_{n-1}$ is the one-dimensional (1D) discrete Laplacian, γ is the parametric driving coefficient with frequency Λ, α is the damping constant, and σ is the nonlinearity coefficient. Here we confine our study to the case of focusing nonlinearity, i.e., by setting positive valued σ which then can be scaled, without loss of generality, to $\sigma = +1$.

In the absence of parametric driving and damping, i.e., for $\gamma = 0$ and $\alpha = 0$, Eq. (1) reduces to the standard discrete nonlinear Schrödinger (DNLS) equation which appears in a wide range of important applications [1]. It is known that the DNLS equation admits bright and dark solitons with focusing and defocusing nonlinearities, respectively. The stability of discrete bright solitons in the DNLS system has been discussed, e.g., in Refs. [2–4], where it was shown that one-excited-site (onsite) solitons are stable and two-excited-site (intersite) solitons are unstable, for any coupling constant ε. Moreover, the discrete dark solitons in such a system have also been examined [5–9]; it is known that intersite dark solitons are always unstable, for any ε, and onsite solitons are stable only in a small window of coupling constant ε.

Furthermore, the parametrically driven discrete nonlinear Schrödinger (PDNLS) equation, i.e, Eq. (1) with no damping ($\alpha = 0$), has been studied in [10] for the case of focusing nonlinearity, where it was reported that an onsite bright discrete soliton can be destabilized by a parametric driving. The study of the same equation was extended for the other variants of discrete solitons in [11], showing that a parametric driving can not only destabilize onsite bright solitons, but also stabilize intersite bright discrete solitons as well as onsite and intersite dark discrete solitons. In the latter, the PDNLS model was particularly derived, using a multiscale expansion reduction, from a parametrically driven Klein-Gordon system describing coupled arrays of nonlinear resonators in micro- and nano-electromechanical systems (MEMS and NEMS).

The discrete nonlinear Schrödinger equation with the inclusion of parametric driving and damping terms as written in Eq. (1) was studied for the first time, to the best of our knowledge, by Hennig [12] focusing on the existence and stability of localized solutions using a nonlinear map approach. He demonstrated that, depending upon the strength of the parametric driving, various types of localized lattice states emerge from the model, namely periodic, quasiperiodic, and chaotic breathers. The impact of damping constant and driving (but external) in the integrable version of the DNLS system, i.e., the discrete Ablowitz-Ladik equation,

has also been studied [13] which confirmed the existence of breathers and multibreathers. In deriving Eq. (1), one can follow, e.g., the method of reduction performed in [11] by including a damping term in the MEMS and NEMS resonators model.

On the other hand, the continuous version of the PDDNLS (1), i.e., when $\phi_n \approx \phi$ and $\varepsilon \Delta_2 \phi_n \approx \partial_x^2 \phi$, was numerically discussed earlier in [14] resulting in a single-soliton attractor chart on the (γ, α)-plane from which one may determine the regions of existence of stable stationary solitons as well as stable time-periodic solitons (with period-1 and higher). Instead of using direct numerical integration as performed in the latter reference, Barashenkov et al. [15] recently proposed obtaining the time-periodic one-soliton and two-soliton [16] solutions as solutions of a two-dimensional boundary-value problem.

Our objective in the present chapter is to examine the existence and stability of the fundamental onsite and intersite excitations of bright solitons in the focusing PDDNLS (1). The analysis of this model is performed through a perturbation theory for small ε which is then corroborated by numerical calculations. Such analysis is based on the concept of the so-called *anticontinuum* (*AC*) *limit approach* which was introduced initially by MacKay and Aubry [17]. In this approach, the trivial localized solutions in the uncoupled limit $\varepsilon = 0$ are continued for weak coupling constant. Moreover, our study here is also devoted to exploring the relevant bifurcations which occur in both stationary onsite and intersite discrete solitons, including time-periodic solitons emerging from Hopf bifurcations. For the latter scheme, we employ the numerical continuation software Matcont to path-follow limit cycles bifurcating from the Hopf points.

The presentation of this chapter is organized as follows. In Sect. 2, we firstly present our analytical setup for the considered model. In Sect. 3, we perform the existence and stability analysis of the discrete solitons through a perturbation method. Next, in Sect. 4, we compare our analytical results with the corresponding numerical calculations and discuss bifurcations experienced by the fundamental solitons. The time-periodic solitons appearing from the Hopf bifurcation points of the corresponding stationary solitons are furthermore investigated in Sect. 5. Finally, we conclude our results in Sect. 6.

2 Analytical Formulation

Static localized solutions of the focusing system (1) in the form of $\phi_n = u_n$, where u_n is complex valued and time-independent, satisfy the stationary equation

$$-\varepsilon \Delta_2 u_n + \Lambda u_n + \gamma \overline{u}_n - i\alpha u_n - |u_n|^2 u_n = 0, \tag{2}$$

with spatial localization condition $u_n \to 0$ as $n \to \pm\infty$. We should notice that Eq. (2) (and accordingly Eq. (1)) admits the reflection symmetry under the transformation

$$u_n \rightarrow -u_n. \tag{3}$$

Following [14–16], we assume that both the damping coefficient α and the driving strength γ are positive. For the coupling constant ε, we also set it to be positive (the case $\varepsilon<0$ can be obtained accordingly by the so-called staggering transformation $u_n \rightarrow (-1)^n u_n$ and $\Lambda \rightarrow (\Lambda - 4\varepsilon)$). The range of the parameter Λ is left to be determined later in the following discussion.

In the undriven and undamped cases, the localized solutions of Eq. (2) can be chosen, without lack of generality, to be real-valued (with $\Lambda > 0$) [2]. This is no longer the case for non-zero γ and α in the stationary PDDNLS (2), therefore we should always take into account complex-valued u_n. By writing $u_n = a_n + ib_n$, where $a_n, b_n \in \mathbb{R}$, and decomposing the equation into real and imaginary parts, we obtain from Eq. (2) the following system of equations:

$$-\varepsilon\Delta_2 a_n + (\Lambda + \gamma)a_n + \alpha b_n - (a_n^2 + b_n^2)a_n = 0, \tag{4a}$$

$$-\varepsilon\Delta_2 b_n + (\Lambda - \gamma)b_n - \alpha a_n - (a_n^2 + b_n^2)b_n = 0. \tag{4b}$$

Thus, the solutions of Eq. (2) can be sought through solving the above system for a_n and b_n.

Next, to examine the stability of the obtained solutions, let us introduce the linearization ansatz $\phi_n = u_n + \delta\epsilon_n$, where $\delta \ll 1$. Substituting this ansatz into Eq. (1) yields the following linearized equation at $\mathcal{O}(\delta)$:

$$i\dot{\epsilon}_n = -\varepsilon\Delta_2\epsilon_n + \Lambda\epsilon_n + \gamma\overline{\epsilon}_n - i\alpha\epsilon_n - 2|u_n|^2\epsilon_n - u_n^2\overline{\epsilon}_n. \tag{5}$$

By writing $\epsilon_n = \eta_n e^{i\omega t} + \overline{\xi}_n e^{-i\overline{\omega}t}$, Eq. (5) can be transformed into the eigenvalue problem (EVP)

$$\begin{bmatrix} \varepsilon\Delta_2 - \Lambda + i\alpha + 2|u_n|^2 & u_n^2 - \gamma \\ \gamma - \overline{u}_n^2 & -\varepsilon\Delta_2 + \Lambda - i\alpha - 2|u_n|^2 \end{bmatrix} \begin{bmatrix} \eta_n \\ \xi_n \end{bmatrix} = \omega \begin{bmatrix} \eta_n \\ \xi_n \end{bmatrix}. \tag{6}$$

The stability of the solution u_n is then determined by the eigenvalues ω, i.e., u_n is stable only when $\mathrm{Im}(\omega) \geq 0$ for all eigenvalues ω.

As the EVP (6) is linear, we can eliminate one of the eigenvectors, for instance ξ_n, so that we obtain the simplified form

$$\left[\mathcal{L}_+(\varepsilon)\mathcal{L}_-(\varepsilon) - 4(a_n b_n)^2\right]\eta_n = (\omega - i\alpha)^2\eta_n, \tag{7}$$

where the operators $\mathcal{L}_+(\varepsilon)$ and $\mathcal{L}_-(\varepsilon)$ are given by

$$\mathcal{L}_+(\varepsilon) \equiv -\varepsilon\Delta_2 - (a_n^2 + 3b_n^2 - \Lambda + \gamma),$$
$$\mathcal{L}_-(\varepsilon) \equiv -\varepsilon\Delta_2 - (3a_n^2 + b_n^2 - \Lambda - \gamma).$$

3 Perturbation Analysis

Solutions of Eq. (2) for small coupling constant ε can be calculated analytically through a perturbative analysis, i.e., by expanding u_n in powers of ε as

$$u_n = u_n^{(0)} + \varepsilon u_n^{(1)} + \varepsilon^2 u_n^{(2)} + \cdots. \tag{8}$$

Solutions $u_n = u_n^{(0)}$ correspond to the case of the uncoupled limit $\varepsilon = 0$. For this case, Eq. (2) permits the exact solutions $u_n^{(0)} = a_n^{(0)} + ib_n^{(0)}$ in which $\left(a_n^{(0)}, b_n^{(0)}\right)$ can take one of the following values

$$(0,0), \quad (sA_+, -sB_-), \quad (sA_-, -sB_+), \tag{9}$$

where

$$A_\pm = \sqrt{\frac{(\gamma \pm \sqrt{\gamma^2 - \alpha^2})(\Lambda \pm \sqrt{\gamma^2 - \alpha^2})}{2\gamma}},$$
$$B_\pm = \sqrt{\frac{(\gamma \pm \sqrt{\gamma^2 - \alpha^2})(\Lambda \mp \sqrt{\gamma^2 - \alpha^2})}{2\gamma}},$$

and $s = \pm 1$. Due to the reflection symmetry (3), we are allowed to restrict consideration to the case $s = +1$.

Following the assumption $\gamma, \alpha > 0$, we can easily confirm that nonzero $(A_+, -B_-)$ and $(A_-, -B_+)$ are together defined in the following range of parameters

$$\Lambda > \gamma \geq \alpha > 0. \tag{10}$$

In particular, when $\gamma = \alpha$, the values of $(A_+, -B_-)$ are exactly the same as $(A_-, -B_+)$.

Once a configuration for $u_n^{(0)}$ is determined, its continuation for small ε can be sought by substituting expansion (8) into Eq. (2). In this chapter, we only focus on two fundamental localized solutions, i.e., one-excited site (onsite) and in-phase two-excited site (intersite) bright solitons. Out-of-phase two-excited site modes also referred to as twisted discrete solitons (see, e.g., [18]), which exist in the model considered herein, are left as a topic of future research.

Next, to study the stability of the solitons, we also expand the eigenvector having component η_n and the eigenvalue ω in powers of ε as

$$\eta_n = \eta_n^{(0)} + \varepsilon \eta_n^{(1)} + \mathcal{O}(\varepsilon^2), \quad \omega = \omega^{(0)} + \varepsilon \omega^{(1)} + \mathcal{O}(\varepsilon^2). \tag{11}$$

Substituting these expansions into Eq. (7) and collecting coefficients at successive powers of ε yield the $\mathcal{O}(1)$ and $\mathcal{O}(\varepsilon)$ equations which are respectively given by

$$L\eta_n^{(0)} = 0, \tag{12}$$

$$L\eta_n^{(1)} = f_n, \tag{13}$$

where

$$L = \mathcal{L}_+(0)\mathcal{L}_-(0) - 4(a_n^{(0)}b_n^{(0)})^2 - (\omega^{(0)} - i\alpha)^2, \tag{14}$$

$$f_n = \Big[\mathcal{L}_-(0)(\Lambda_2 + 2a_n^{(0)}a_n^{(1)} + 6b_n^{(0)}b_n^{(1)}) + \mathcal{L}_+(0)(\Lambda_2 + 2b_n^{(0)}b_n^{(1)} + 6a_n^{(0)}a_n^{(1)}) + 8a_n^{(0)}b_n^{(0)}(a_n^{(0)}b_n^{(1)} + a_n^{(1)}b_n^{(0)}) + 2\omega^{(0)}\omega^{(1)} - 2i\alpha\omega^{(1)}\Big]\eta_n^{(0)}. \tag{15}$$

One can check that the operator L is self-adjoint and thus the eigenvector $h = \mathrm{col}(\ldots, \eta_{-1}^{(0)}, \eta_0^{(0)}, \eta_1^{(0)}, \ldots)$ is in the null-space of the adjoint of L.

From Eq. (12), we obtain that the eigenvalues in the uncoupled limit $\varepsilon = 0$ are

$$\omega_C^{(0)} = \pm\sqrt{\Lambda^2 - \gamma^2} + i\alpha, \tag{16}$$

and

$$\omega_E^{(0)} = \pm\sqrt{\mathcal{L}_+(0)\mathcal{L}_-(0) - 4(a_n^{(0)}b_n^{(0)})^2} + i\alpha, \tag{17}$$

which correspond, respectively, to the solutions $u_n^{(0)} = 0$ (for all n) and $u_n^{(0)} = a_n^{(0)} + ib_n^{(0)} \neq 0$ (for all n). For bright soliton solutions having boundary condition $u_n \to 0$ as $n \to \pm\infty$, the eigenvalues $\omega_E^{(0)}$ and $\omega_C^{(0)}$ have, respectively, finite and infinite multiplicities which then generate a corresponding discrete and continuous spectrum as ε is turned on.

Let us first investigate the significance of the continuous spectrum. By introducing a plane-wave expansion $\eta_n = \mu e^{i\kappa n} + \nu e^{-i\kappa n}$, one can obtain the dispersion relation

$$\omega = \pm\sqrt{(2\varepsilon(\cos\kappa - 1) - \Lambda)^2 - \gamma^2} + i\alpha, \tag{18}$$

from which we conclude that the continuous band lies between

$$\omega_L = \pm\sqrt{\Lambda^2 - \gamma^2} + i\alpha, \quad \text{when } \kappa = 0, \tag{19}$$

and

$$\omega_U = \pm\sqrt{\Lambda^2 - \gamma^2 + 8\varepsilon(\Lambda + 2\varepsilon)} + i\alpha, \quad \text{when } \kappa = \pi, \tag{20}$$

From the condition (10), one can check that all the eigenvalues $\omega \in \pm[\omega_L, \omega_U]$ always lie on the axis $\mathrm{Im}(\omega) = \alpha > 0$ for all ε, which means that the continuous spectrum does not give contribution to the instability of the soliton. Therefore, the

analysis of stability is only devoted to the discrete eigenvalues. Discrete eigenvalues that potentially lead to instability are also referred to as critical eigenvalues.

3.1 Onsite Bright Solitons

When $\varepsilon = 0$, the configuration of an onsite bright soliton is of the form

$$u_n^{(0)} = 0 \quad \text{for} \quad n \neq 0, \quad u_0^{(0)} = A + iB, \tag{21}$$

where $(A, B) \neq (0, 0)$. From the combination of nonzero solutions (9), we can classify the onsite bright solitons, indicated by the different values of (A, B), as follows:

(i) Type I, which has $(A, B) = (A_+, -B_-)$,
(ii) Type II, which has $(A, B) = (A_-, -B_+)$,

which we denote hereinafter by $u_{n\{\pm\}}$ and $u_{n\{\mp\}}$, respectively.

The continuation of the above solutions for small ε can be calculated from the expansion (8), from which one can show that an onsite soliton type I and type II, up to $\mathcal{O}(\varepsilon^2)$, are respectively given by

$$u_{n\{\pm\}} = \begin{cases} (A_+ - iB_-) + \frac{(A_+ - iB_-)\varepsilon}{\Lambda + \sqrt{\gamma^2 - \alpha^2}}, & n = 0, \\ \frac{(A_+ - iB_-)\varepsilon}{\Lambda + \sqrt{\gamma^2 - \alpha^2}}, & n = -1, 1, \\ 0, & \text{otherwise}, \end{cases} \tag{22}$$

and

$$u_{n\{\mp\}} = \begin{cases} (A_- - iB_+) + \frac{(A_- - iB_+)\varepsilon}{\Lambda - \sqrt{\gamma^2 - \alpha^2}}, & n = 0, \\ \frac{(A_- - iB_+)\varepsilon}{\Lambda - \sqrt{\gamma^2 - \alpha^2}}, & n = -1, 1, \\ 0, & \text{otherwise}. \end{cases} \tag{23}$$

In particular, when $\alpha = \gamma$, the onsite type I and type II become exactly the same.

To examine the stability of the solitons, we need to calculate the corresponding discrete eigenvalues for each of type I and type II, which we elaborate successively.

3.1.1 Onsite Type I

One can show from Eq. (12) that at $\varepsilon = 0$, an onsite bright soliton type I has a leading-order discrete eigenvalue which comes as the pair

$$\omega_{\{\pm\}}^{(0)} = \pm\sqrt{\mathcal{P}} + i\alpha, \tag{24}$$

where

$$\mathcal{P} = 4\Lambda\sqrt{\gamma^2 - \alpha^2} + 4\gamma^2 - 5\alpha^2. \tag{25}$$

The eigenvector corresponding to the above eigenvalue has components $\eta_n^{(0)} = 0$ for $n \neq 0$ and $\eta_0^{(0)} = 1$.

We notice that $\mathcal{P}$ can be either positive or negative depending on whether $\alpha \lessgtr \alpha_{\text{th}}$, where

$$\alpha_{\text{th}} = \frac{2}{5}\sqrt{5\gamma^2 - 2\Lambda^2 + \Lambda\sqrt{4\Lambda^2 + 5\gamma^2}}. \tag{26}$$

Therefore, the eigenvalue $\omega_{\{\pm\}}^{(0)}$ can be either

$$\omega_{1\{\pm\}}^{(0)} = \pm\sqrt{4\Lambda\sqrt{\gamma^2 - \alpha^2} + 4\gamma^2 - 5\alpha^2} + i\alpha, \tag{27}$$

for the case $\alpha < \alpha_{\text{th}}$, or

$$\omega_{2\{\pm\}}^{(0)} = i\left(\alpha \pm \sqrt{5\alpha^2 - 4\Lambda\sqrt{\gamma^2 - \alpha^2} - 4\gamma^2}\right), \tag{28}$$

for the case $\alpha_{\text{th}} < \alpha \leq \gamma$.

The continuation of the eigenvalues (27) and (28) for nonzero ε can be evaluated from Eq. (13) by applying a Fredholm solvability condition. As the corresponding eigenvector has zero components except at site $n = 0$, we only need to require $f_0 = 0$, from which we obtain the discrete eigenvalue of $u_{n\{\pm\}}$ for small ε, up to $\mathcal{O}(\varepsilon^2)$, as follows.

(i) For the case $\alpha < \alpha_{\text{th}}$:

$$\omega_{1\{\pm\}} = \pm\sqrt{4\Lambda\sqrt{\gamma^2 - \alpha^2} + 4\gamma^2 - 5\alpha^2} \pm \frac{(4\sqrt{\gamma^2 - \alpha^2})\varepsilon}{\sqrt{4\Lambda\sqrt{\gamma^2 - \alpha^2} + 4\gamma^2 - 5\alpha^2}} + i\alpha. \tag{29}$$

(ii) For the case $\alpha_{\text{th}} < \alpha \leq \gamma$:

$$\omega_{2\{\pm\}} = i\left(\alpha \pm \sqrt{5\alpha^2 - 4\Lambda\sqrt{\gamma^2 - \alpha^2} - 4\gamma^2} \mp \frac{(4\sqrt{\gamma^2 - \alpha^2})\varepsilon}{\sqrt{5\alpha^2 - 4\Lambda\sqrt{\gamma^2 - \alpha^2} - 4\gamma^2}}\right). \tag{30}$$

We should note here that the above expansions remain valid if $\pm\mathcal{P}$ are $\mathcal{O}(1)$.

Let us now investigate the behavior of the above eigenvalue in each case. In case (i), the imaginary part of $\omega_{1\{\pm\}}^{(0)}$ (i.e., when $\varepsilon = 0$) is α, which is positive. We also note that $|\omega_{1\{\pm\}}^{(0)}| \gtrless |\omega_C^{(0)}|$ when $\alpha \lessgtr \alpha_{\text{cp}}$, where

$$\alpha_{\text{cp}} = \frac{1}{5}\sqrt{25\gamma^2 - \Lambda^2}. \tag{31}$$

As ε increases, the value of $|\omega_{1\{\pm\}}|$ also increases. As a result, the eigenvalues $\omega_{1\{\pm\}}$ will collide either with the upper band (ω_U) of the continuous spectrum for $\alpha < \alpha_{\text{cp}}$, or with the lower band (ω_L) for $\alpha_{\text{cp}} < \alpha < \alpha_{\text{th}}$. These collisions then create a corresponding pair of eigenvalues bifurcating from the axis $\text{Im}(\omega_{1\{\pm\}}) = \alpha$. This collision, however, does not immediately lead to the instability of the soliton as it does for $\alpha = 0$ [10, 11]. In addition, the distance between $\omega_{1\{\pm\}}^{(0)}$ and $\omega_C^{(0)}$ increases as α tends to 0, which means that the corresponding collisions for smaller α happen at larger ε. From the above analysis we hence argue that for $\alpha < \alpha_{\text{th}}$ and for relatively small ε, the onsite soliton type I is stable.

In case (ii), it is clear that $\sqrt{5\alpha^2 - 4\Lambda\sqrt{\gamma^2 - \alpha^2} - 4\gamma^2} \leq \alpha$ which implies $0 \leq \min(\text{Im}(\omega_{2\{\pm\}}^{(0)})) < \alpha$; the latter indicates the soliton is stable at $\varepsilon = 0$. As ε increases, both $\max(\text{Im}(\omega_{2\{\pm\}}))$ and $\min(\text{Im}(\omega_{2\{\pm\}}))$ tend to α at which they finally collide. From this fact, we conclude that for small ε and for $\alpha_{\text{th}} < \alpha \leq \gamma$, the soliton remains stable. In particular, when $\alpha = \gamma$, we have $\min(\text{Im}(\omega_{2\{\pm\}})) = 0$ for all ε, which then implies that the soliton is always stable.

3.1.2 Onsite Type II

Performing the calculations as before, we obtain that the discrete eigenvalue (in pairs) of an onsite bright soliton type II is given, up to $\mathcal{O}(\varepsilon^2)$, by

$$\omega_{\{\mp\}} = i\left(\alpha \pm \sqrt{4\Lambda\sqrt{\gamma^2 - \alpha^2} - 4\gamma^2 + 5\alpha^2} \pm \frac{(4\sqrt{\gamma^2 - \alpha^2})\varepsilon}{\sqrt{4\Lambda\sqrt{\gamma^2 - \alpha^2} - 4\gamma^2 + 5\alpha^2}}\right). \tag{32}$$

Again, we should assume that the term $(4\Lambda\sqrt{\gamma^2 - \alpha^2} - 4\gamma^2 + 5\alpha^2)$ in the above expansion is $\mathcal{O}(1)$.

When $\alpha < \gamma$, we simply have $\sqrt{4\Lambda\sqrt{\gamma^2 - \alpha^2} - 4\gamma^2 + 5\alpha^2} > \alpha$, from which we deduce $\min(\text{Im}(\omega_{\{\mp\}}^{(0)})) < 0$, meaning that at $\varepsilon = 0$ the soliton is unstable. In fact, as ε increases, the value of $\min(\text{Im}(\omega_{\{\mp\}}))$ decreases. Therefore, in this case we infer that the soliton is unstable for all ε.

When $\alpha = \gamma$, by contrast, the value of $\min(\mathrm{Im}(\omega_{\{\mp\}}))$ is zero for all ε, which indicates that the soliton is always stable. In fact, the stability of an onsite type II in this case is exactly the same as in type I. This is understandable as the onsite type I and type II possess the same profile when $\alpha = \gamma$.

3.2 Intersite Bright Solitons

Another natural fundamental solution to be studied is a two-excited site (intersite) bright soliton whose mode structure in the uncoupled limit is of the form

$$u_n^{(0)} = \begin{cases} A_0 + iB_0, & n = 0, \\ A_1 + iB_1, & n = 1, \\ 0, & \text{otherwise}, \end{cases} \tag{33}$$

where $(A_0, B_0) \neq (0, 0)$ and $(A_1, B_1) \neq (0, 0)$. The combination of the nonzero solutions (9) gives the classification for the intersite bright solitons, indicated by different values of (A_0, B_0) and (A_1, B_1), as follows:

(i) Type I, which has $(A_0, B_0) = (A_1, B_1) = (A_+, -B_-)$,
(ii) Type II, which has $(A_0, B_0) = (A_1, B_1) = (A_-, -B_+)$,
(iii) Type III, which has $(A_0, B_0) = (A_+, -B_-)$ and $(A_1, B_1) = (A_-, -B_+)$,
(iv) Type IV, which has $(A_0, B_0) = (A_-, -B_+)$ and $(A_1, B_1) = (A_+, -B_-)$.

Let us henceforth denote the respective types by $u_{n\{\pm\pm\}}$, $u_{n\{\mp\mp\}}$, $u_{n\{\pm\mp\}}$, and $u_{n\{\mp\pm\}}$.

From the expansion (8), we obtain the continuation of each type of solution for small ε, which are given, up to order ε^2, by

$$u_{n\{\pm\pm\}} = \begin{cases} (A_+ - iB_-) + \frac{1}{2}\frac{(A_+ - iB_-)\varepsilon}{\Lambda + \sqrt{\gamma^2 - \alpha^2}}, & n = 0, \\ (A_+ - iB_-) + \frac{1}{2}\frac{(A_+ - iB_-)\varepsilon}{\Lambda + \sqrt{\gamma^2 - \alpha^2}}, & n = 1, \\ \frac{(A_+ - iB_-)\varepsilon}{\Lambda + \sqrt{\gamma^2 - \alpha^2}}, & n = -1, 2, \\ 0, & \text{otherwise}, \end{cases} \tag{34}$$

$$u_{n\{\mp\mp\}} = \begin{cases} (A_- - iB_+) + \frac{1}{2}\frac{(A_- - iB_+)\varepsilon}{\Lambda - \sqrt{\gamma^2 - \alpha^2}}, & n = 0, \\ (A_- - iB_+) + \frac{1}{2}\frac{(A_- - iB_+)\varepsilon}{\Lambda - \sqrt{\gamma^2 - \alpha^2}}, & n = 1, \\ \frac{(A_- - iB_+)\varepsilon}{\Lambda - \sqrt{\gamma^2 - \alpha^2}}, & n = -1, 2, \\ 0, & \text{otherwise}, \end{cases} \tag{35}$$

$$u_{n\{\pm\mp\}} = \begin{cases} \frac{(A_+ - iB_+)\varepsilon}{\Lambda + \sqrt{\gamma^2 - \alpha^2}}, & n = -1, \\ (A_+ - iB_-) + \frac{1}{2}\frac{(\mathcal{A}_+ - i\mathcal{B}_-)\varepsilon}{\gamma(\Lambda + \sqrt{\gamma^2 - \alpha^2})}, & n = 0, \\ (A_- - iB_+) + \frac{1}{2}\frac{(\mathcal{A}_- - i\mathcal{B}_+)\varepsilon}{\gamma(\Lambda - \sqrt{\gamma^2 - \alpha^2})}, & n = 1, \\ \frac{(A_- - iB_-)\varepsilon}{\Lambda - \sqrt{\gamma^2 - \alpha^2}}, & n = 2, \\ 0, & \text{otherwise}, \end{cases} \tag{36}$$

$$u_{n\{\mp\pm\}} = \begin{cases} \frac{(A_- - iB_-)\varepsilon}{\Lambda - \sqrt{\gamma^2 - \alpha^2}}, & n = -1, \\ (A_- - iB_+) + \frac{1}{2}\frac{(\mathcal{A}_- - i\mathcal{B}_+)\varepsilon}{\gamma(\Lambda - \sqrt{\gamma^2 - \alpha^2})}, & n = 0, \\ (A_+ - iB_-) + \frac{1}{2}\frac{(\mathcal{A}_+ - i\mathcal{B}_-)\varepsilon}{\gamma(\Lambda + \sqrt{\gamma^2 - \alpha^2})}, & n = 1, \\ \frac{(A_+ - iB_+)\varepsilon}{\Lambda + \sqrt{\gamma^2 - \alpha^2}}, & n = 2, \\ 0, & \text{otherwise}, \end{cases} \tag{37}$$

where

$$\mathcal{A}_\pm = 2\gamma A_\pm + (\Lambda \pm \sqrt{\gamma^2 - \alpha^2})A_\mp, \tag{38}$$

$$\mathcal{B}_\pm = 2\gamma B_\mp - (\Lambda \pm \sqrt{\gamma^2 - \alpha^2})B_\pm. \tag{39}$$

All solutions above are defined on the region (10) and exhibit the same profiles when $\alpha = \gamma$. One can check that intersite type III and IV are symmetric, thus they should really be considered as one solution. However, we write them here as two 'different' solutions because, as shown later in the next section, they form two different branches in a pitchfork bifurcation (together with intersite type I).

Let us now examine the stability of each solution by investigating their corresponding discrete eigenvalues.

3.2.1 Intersite Type I

By considering Eq. (12) and carrying out the same analysis as in onsite type I, we obtain that the intersite type I has the double leading-order discrete eigenvalue

$$\omega_{1\{\pm\pm\}}^{(0)} = \pm\sqrt{4\Lambda\sqrt{\gamma^2 - \alpha^2} + 4\gamma^2 - 5\alpha^2} + i\alpha, \tag{40}$$

for $\alpha < \alpha_{\text{th}}$, and

$$\omega_{2\{\pm\pm\}}^{(0)} = i\left(\alpha \pm \sqrt{5\alpha^2 - 4\Lambda\sqrt{\gamma^2 - \alpha^2} - 4\gamma^2}\right), \tag{41}$$

for $\alpha_{\text{th}} < \alpha \leq \gamma$. The corresponding eigenvector for the above eigenvalues has components $\eta_n^{(0)} = 0$ for $n \neq 0, 1$, $\eta_0^{(0)} \neq 0$, and $\eta_1^{(0)} \neq 0$.

One can check, as in onsite type I, that the position of $\omega_{1\{\pm\pm\}}^{(0)}$ relative to $\omega_C^{(0)}$ depends on whether $\alpha \lessgtr \alpha_{\rm cp} = \frac{1}{5}\sqrt{25\gamma^2 - \Lambda^2}$, i.e., the value of $|\omega_{1\{\pm\pm\}}^{(0)}|$ is greater (less) than $|\omega_C^{(0)}|$ when α is less (greater) than $\alpha_{\rm cp}$.

The next correction for the discrete eigenvalues of an intersite type II can be calculated from Eq. (13), for which we need a solvability condition. Due to the presence of two non-zero components of the corresponding eigenvector at $n = 0, 1$, we only require $f_0 = 0$ and $f_1 = 0$. Our simple analysis then shows $\eta_0^{(0)} = \pm\eta_1^{(0)}$ from which we obtain that each of double eigenvalues (40) and (41) bifurcates into two distinct eigenvalues, which are given, up to order ε^2, as follows.

(i) For the case $\alpha < \alpha_{\rm th}$:

$$\omega_{11\{\pm\pm\}} = \pm\sqrt{4\Lambda\sqrt{\gamma^2-\alpha^2} + 4\gamma^2 - 5\alpha^2} \pm \frac{(2\sqrt{\gamma^2-\alpha^2})\varepsilon}{\sqrt{4\Lambda\sqrt{\gamma^2-\alpha^2} + 4\gamma^2 - 5\alpha^2}} + i\alpha, \tag{42}$$

$$\omega_{12\{\pm\pm\}} = \pm\sqrt{4\Lambda\sqrt{\gamma^2-\alpha^2} + 4\gamma^2 - 5\alpha^2} \mp \frac{2(\Lambda + \sqrt{\gamma^2-\alpha^2})\varepsilon}{\sqrt{4\Lambda\sqrt{\gamma^2-\alpha^2} + 4\gamma^2 - 5\alpha^2}} + i\alpha. \tag{43}$$

(ii) For the case $\alpha_{\rm th} < \alpha \leq \gamma$:

$$\omega_{21\{\pm\pm\}} = i\left(\alpha \pm \sqrt{5\alpha^2 - 4\Lambda\sqrt{\gamma^2-\alpha^2} - 4\gamma^2} \mp \frac{(2\sqrt{\gamma^2-\alpha^2})\varepsilon}{\sqrt{5\alpha^2 - 4\Lambda\sqrt{\gamma^2-\alpha^2} - 4\gamma^2}}\right), \tag{44}$$

$$\omega_{22\{\pm\pm\}} = i\left(\alpha \pm \sqrt{5\alpha^2 - 4\Lambda\sqrt{\gamma^2-\alpha^2} - 4\gamma^2} \pm \frac{2(\Lambda + \sqrt{\gamma^2-\alpha^2})\varepsilon}{\sqrt{5\alpha^2 - 4\Lambda\sqrt{\gamma^2-\alpha^2} - 4\gamma^2}}\right). \tag{45}$$

As before, we assume here that the terms $\pm(4\Lambda\sqrt{\gamma^2-\alpha^2} + 4\gamma^2 - 5\alpha^2)$ are $\mathcal{O}(1)$ so that the above expansions remain valid.

Let us first observe the behavior of the eigenvalues in case (i). In the uncoupled limit $\varepsilon = 0$, the imaginary part of $\omega_{11\{\pm\pm\}}^{(0)} = \omega_{12\{\pm\pm\}}^{(0)}$ is $\alpha > 0$ which indicates that the soliton is initially stable. When ε is turned on, the value of $|\omega_{11\{\pm\pm\}}|$ increases but $|\omega_{12\{\pm\pm\}}|$ decreases. Therefore, we can determine the mechanism of collision

of these two eigenvalues with the inner or outer boundary of continuous spectrum (ω_L or ω_U) as follows.

- For $\alpha < \alpha_{\rm cp}$, the first collision is between $\omega_{12\{\pm\pm\}}$ and ω_U. Because ω_U moves faster (as ε is varied) than $\omega_{11\{\pm\pm\}}$, the next collision is between these two aforementioned eigenvalues.
- For $\alpha > \alpha_{\rm cp}$, the mechanism of collision can be either between $\omega_{11\{\pm\pm\}}$ and ω_L, or between $\omega_{12\{\pm\pm\}}$ and itself.

All of the mechanisms of collision above generate new corresponding pairs of eigenvalues bifurcating from their original imaginary parts, which is α. Yet these collisions do not immediately cause an instability, because $\alpha > 0$. Therefore, we may conclude that for sufficiently small ε and for $\alpha < \alpha_{\rm th}$, an intersite bright soliton type I is stable.

Next, we describe the analysis for the eigenvalues in case (ii). When $\varepsilon = 0$, we have $0 \leq \min(\mathrm{Im}(\omega_{21}^{(0)}_{\{\pm\pm\}})) = \min(\mathrm{Im}(\omega_{22}^{(0)}_{\{\pm\pm\}})) < \alpha$. As ε is increased, $\min(\mathrm{Im}(\omega_{21\{\pm\pm\}}))$ increases but $\min(\mathrm{Im}(\omega_{22\{\pm\pm\}}))$ decreases. The latter then becomes negative, leading to the instability of the soliton. By taking $\min(\mathrm{Im}(\omega_{22\{\pm\pm\}})) = 0$, one obtains

$$\varepsilon_{\rm cr} = \frac{\alpha\sqrt{5\alpha^2 - 4\Lambda\sqrt{\gamma^2-\alpha^2} - 4\gamma^2}}{2(\Lambda + \sqrt{\gamma^2-\alpha^2})} - \frac{5\alpha^2 - 4\Lambda\sqrt{\gamma^2-\alpha^2} - 4\gamma^2}{2(\Lambda + \sqrt{\gamma^2-\alpha^2})}, \tag{46}$$

which yields an approximate boundary for the onset of instability, e.g., in the (ε, α)-plane for fixed Λ and γ.

3.2.2 Intersite Type II

From our analysis of Eqs. (12) and (13), we obtain the discrete eigenvalues for an intersite bright soliton type II, which are given, with errors of order ε^2, by

$$\omega_{1\{\mp\mp\}} = i\left(\alpha \pm \sqrt{4\Lambda\sqrt{\gamma^2-\alpha^2} - 4\gamma^2 + 5\alpha^2} \pm \frac{(2\sqrt{\gamma^2-\alpha^2})\varepsilon}{\sqrt{4\Lambda\sqrt{\gamma^2-\alpha^2} - 4\gamma^2 + 5\alpha^2}}\right), \tag{47}$$

$$\omega_{2\{\mp\mp\}} = i\left(\alpha \pm \sqrt{4\Lambda\sqrt{\gamma^2-\alpha^2} - 4\gamma^2 + 5\alpha^2} \pm \frac{2(\Lambda - \sqrt{\gamma^2-\alpha^2})\varepsilon}{\sqrt{4\Lambda\sqrt{\gamma^2-\alpha^2} - 4\gamma^2 + 5\alpha^2}}\right), \tag{48}$$

assuming the term $(4\Lambda\sqrt{\gamma^2-\alpha^2} - 4\gamma^2 + 5\alpha^2)$ is $\mathcal{O}(1)$. Notice that $\omega_{1\{\mp\mp\}}$ and $\omega_{2\{\mp\mp\}}$ are equal when $\alpha = \sqrt{4\gamma^2 - \Lambda^2}/2$.

When $\alpha<\gamma$, both $\min(\mathrm{Im}(\omega_{1\{\mp\mp\}}))$ and $\min(\mathrm{Im}(\omega_{2\{\mp\mp\}}))$ are negative at $\varepsilon=0$ and always decrease as ε is increased; the decrement of $\min(\mathrm{Im}(\omega_{2\{\mp\mp\}}))$ is greater than $\min(\mathrm{Im}(\omega_{1\{\mp\mp\}}))$ for $\alpha>\sqrt{4\gamma^2-\Lambda^2}/2$. When $\alpha=\gamma$, $\min(\mathrm{Im}(\omega_{1\{\mp\mp\}}))$ and $\min(\mathrm{Im}(\omega_{2\{\mp\mp\}}))$ are zero at $\varepsilon=0$. At nonzero ε, the former remains zero, but the latter becomes negative and decreases as ε increases. These facts allow us to conclude that an intersite bright soliton type II is always unstable, except at $\alpha=\gamma$ and $\varepsilon=0$. One can check that when $\alpha=\gamma$, the eigenvalues of intersite type II are the same as in intersite type I.

3.2.3 Intersite Type III and IV

As intersite type III and IV are symmetric, their eigenvalues are exactly the same. Our calculation shows the following.

(i) For the case $\alpha<\alpha_{\mathrm{th}}$, the eigenvalues of the intersite type III and IV, up to $\mathcal{O}(\varepsilon^2)$, are

$$\omega_{11\{\pm\mp\}}=\omega_{11\{\mp\pm\}}=i\alpha\pm\sqrt{4\Lambda\sqrt{\gamma^2-\alpha^2}+4\gamma^2-5\alpha^2}\pm\frac{(2\gamma\sqrt{\gamma^2-\alpha^2}-\Lambda\gamma+\alpha\sqrt{\Lambda^2-\gamma^2+\alpha^2})\varepsilon}{\gamma\sqrt{4\Lambda\sqrt{\gamma^2-\alpha^2}+4\gamma^2-5\alpha^2}}, \tag{49}$$

$$\omega_{12\{\pm\mp\}}=\omega_{12\{\mp\pm\}}=i\left(\alpha\pm\sqrt{4\Lambda\sqrt{\gamma^2-\alpha^2}-4\gamma^2+5\alpha^2}\pm\frac{(2\gamma\sqrt{\gamma^2-\alpha^2}+\Lambda\gamma-\alpha\sqrt{\Lambda^2-\gamma^2+\alpha^2})\varepsilon}{\gamma\sqrt{4\Lambda\sqrt{\gamma^2-\alpha^2}-4\gamma^2+5\alpha^2}}\right). \tag{50}$$

(ii) For the case $\alpha_{\mathrm{th}}<\alpha\leq\gamma$, the eigenvalues, up to order ε^2, are

$$\omega_{21\{\pm\mp\}}=\omega_{21\{\mp\pm\}}=i\left(\alpha\pm\sqrt{5\alpha^2-4\Lambda\sqrt{\gamma^2-\alpha^2}-4\gamma^2}\mp\frac{(2\gamma\sqrt{\gamma^2-\alpha^2}-\Lambda\gamma+\alpha\sqrt{\Lambda^2-\gamma^2+\alpha^2})\varepsilon}{\gamma\sqrt{5\alpha^2-4\Lambda\sqrt{\gamma^2-\alpha^2}-4\gamma^2}}\right), \tag{51}$$

$$\omega_{22\{\pm\mp\}} = \omega_{22\{\mp\pm\}} = i\left(\alpha \pm \sqrt{4\Lambda\sqrt{\gamma^2-\alpha^2}-4\gamma^2+5\alpha^2}\right.$$
$$\left. \pm \frac{(2\gamma\sqrt{\gamma^2-\alpha^2}+\Lambda\gamma-\alpha\sqrt{\Lambda^2-\gamma^2+\alpha^2})\varepsilon}{\gamma\sqrt{4\Lambda\sqrt{\gamma^2-\alpha^2}-4\gamma^2+5\alpha^2}}\right). \tag{52}$$

We should assume again that the terms $\pm(4\Lambda\sqrt{\gamma^2-\alpha^2}+4\gamma^2-5\alpha^2)$ and $(4\Lambda\sqrt{\gamma^2-\alpha^2}-4\gamma^2+5\alpha^2)$ in the above expansions are of $\mathcal{O}(1)$.

In the first case, the eigenvalues (50) are apparently pure imaginary, with an imaginary part whose minimum value is negative for all ε. In the second case, it is clear that for $\alpha<\gamma$ the minimum value of the imaginary part of the eigenvalues (51) is positive (less than α) initially at $\varepsilon = 0$ and then increases as ε increases. However, for this case ($\alpha<\gamma$), the minimum value of the imaginary part of the eigenvalues (52), which are exactly the same as the eigenvalues (50), is negative at $\varepsilon = 0$ and then decreases as ε is turned on. In contrast, for $\alpha = \gamma$ the minimum value of the imaginary part of the eigenvalues (51) and (52) remains zero for all ε. The above fact shows that both intersite soliton type III and IV are always unstable, except at $\alpha = \gamma$. In fact, as shown in the numerical calculation later, the intersite type III and IV are no longer defined along this line, due to a pitchfork bifurcation with intersite type I.

4 Comparisons with Numerical Results, and Bifurcations

In order to find the numerical solutions for each soliton discussed in the previous section, we solve the stationary equation (2) [cf. Eqs. (4a), (4b)] using a Newton-Raphson (NR) method. The evaluation is performed in domain $n \in [-N, N]$, i.e., for a lattice of $2N + 1$ sites, with periodic boundary conditions $u_{\pm(N+1)} = u_{\mp N}$. As an initial guess, we use the corresponding exact soliton solutions in the uncoupled limit $\varepsilon = 0$ from which we then numerically continue for nonzero ε. As an illustrative example, the numerical solutions for each type of onsite and intersite bright soliton with parameter values $(\varepsilon, \Lambda, \gamma, \alpha) = (0.1, 1, 0.5, 0.1)$ are depicted in Fig. 1. The corresponding analytical approximations are also plotted therein showing good agreement with the numerical results.

To examine the stability of each soliton, we solve the eigenvalue problem (6) numerically and then compare the results with the analytical calculations. Moreover, we show later that the relevant solitons experience saddle-node and/or pitchfork bifurcations. To depict the diagram of these bifurcations, we use a pseudo-arclength method which allows us to continue the solution past turning points (by varying one parameter). In addition, our analysis of the eigenvalues for

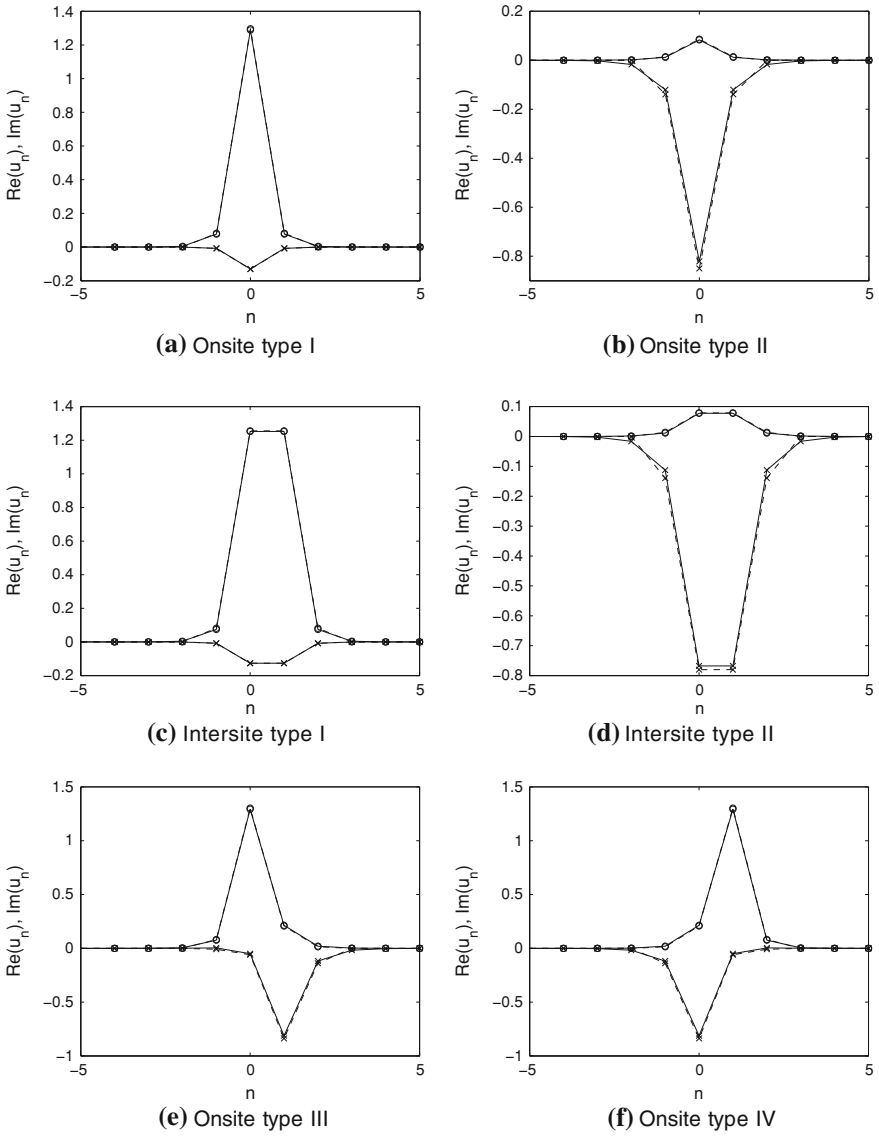

Fig. 1 Profiles of onsite (**a**, **b**) and intersite (**c**–**f**) bright solitons of different types, as indicated in the caption of each panel, for parameter values $(\varepsilon, \Lambda, \gamma, \alpha) = (0.1, 1, 0.5, 0.1)$. *Solid lines* show the numerical results while *dashed lines* indicate the analytical approximations given by Eqs. (22) and (23) for the onsite type I and II, respectively, and by Eqs. (34), (35), (36) and (37) for the intersite type I, II, III, and IV, respectively. The *circle and cross markers* correspond to the real and imaginary part of the solutions, respectively

some particular solutions leads to the fact of the presence of Hopf bifurcations. We will determine the nature of Hopf bifurcation points and perform continuation

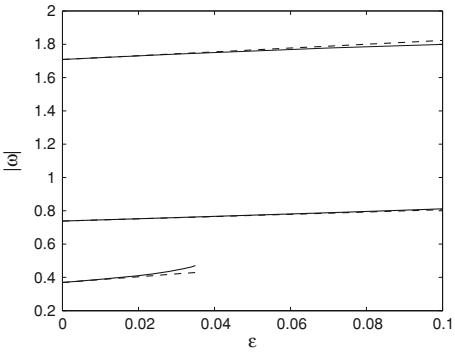

Fig. 2 Comparisons between the critical eigenvalues of an onsite bright soliton type I obtained numerically (*solid lines*) and analytically (*dashed lines*). The *upper and middle curves* correspond, respectively, to $\alpha = 0.1$ and $\alpha = 0.485$, which are approximated by Eq. (29), whereas the *lower* corresponds to $\alpha = 0.497$, which is approximated by Eq. (30)

of the bifurcating limit cycles in the next section by employing the numerical continuation package Matcont.

In all illustrative examples below, we use $N = 50$ which is large enough to capture the behavior of the soliton in an infinite domain but not too costly in numerical computations. In addition, for the sake of simplicity, we set $\Lambda = 1$ and $\gamma = 0.5$.

4.1 Onsite Bright Solitons

4.1.1 Onsite Type I

We start by testing the validity of our analytical approximation for the critical eigenvalues given by Eqs. (29) and (30). We present in Fig. 2 comparisons between the analytical and numerical results for the critical eigenvalues as functions of ε. We plot comparisons for three values $\alpha = 0.1, 0.485, 0.497$ to represent the cases $\alpha < \alpha_{cp}$, $\alpha_{cp} < \alpha < \alpha_{th}$, and $\alpha_{th} < \alpha < \gamma$, respectively (see again the relevant discussion in the previous section). From the figure, we conclude that our prediction for small ε is relatively close to the numerics.

For the three values of α given above, we now present in Fig. 3 the eigenvalue structure of the soliton and the corresponding diagram for the imaginary part of the critical eigenvalues as functions of ε. Let us now describe the results in more detail.

First, we notice that at $\varepsilon = 0$ the critical eigenvalues for $\alpha = 0.1$ lie beyond the outer band of the continuous spectrum, while for $\alpha = 0.485$ they are trapped between the two inner bands of the continuous spectrum. As ε is turned on, the corresponding critical eigenvalues for $\alpha = 0.1$ and $\alpha = 0.485$ collide with, respectively, the outer and the inner bands, leading to the bifurcation of the corresponding eigenvalues. The minimum imaginary part of these bifurcating eigenvalues, however, does not immediately become negative. Hence, for relatively small ε we conclude that the soliton is always stable; this in accordance with our analytical prediction of the previous section. The critical values of ε at which $\min(\mathrm{Im}(\omega)) = 0$ indicating the onset of the instability are depicted by the star

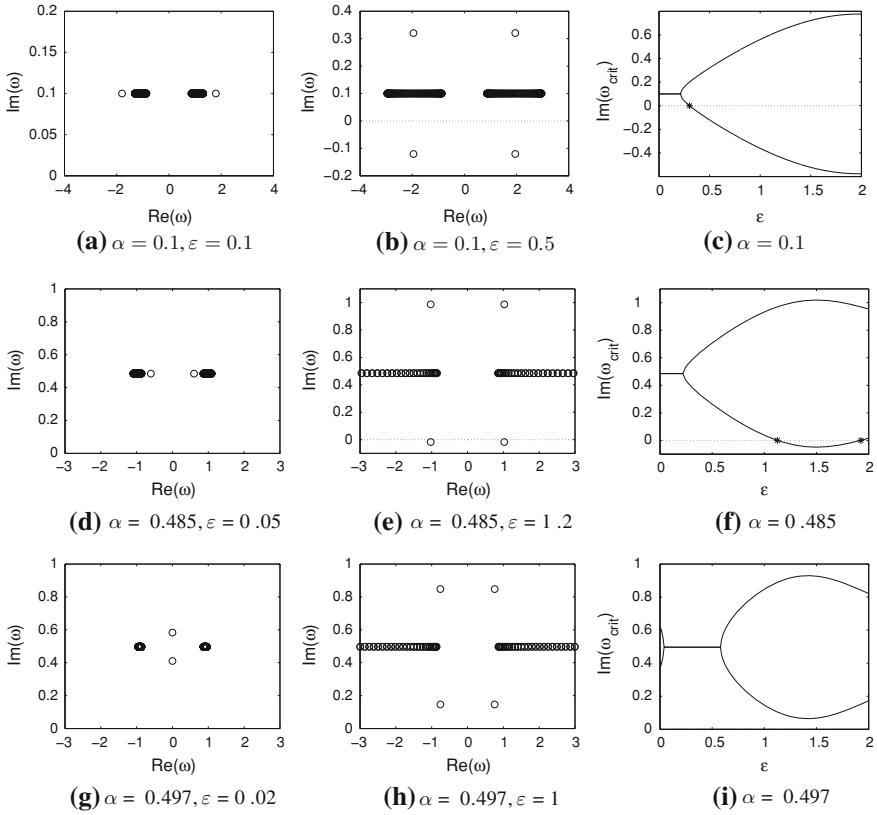

Fig. 3 The first (**a**, **d**, **g**) and second (**b**, **e**, **h**) columns of panels show the $(\mathrm{Re}(\omega), \mathrm{Im}(\omega))$-plane of the eigenvalues of onsite bright solitons type I for several values of α and ε, as indicated in the caption of each panel (each row of panels depicts three different values of α). For $\alpha = 0.1$ and $\alpha = 0.485$, the corresponding *left and middle panels* illustrate the eigenvalues of stable and unstable solitons. The third column (**c**, **f**, **i**) shows the path of the imaginary part of the critical eigenvalues ω_{crit} as functions of ε for the corresponding α. The locations of ε at which $\mathrm{Im}(\omega_{\mathrm{crit}}) = 0$ are indicated by the *star markers*

markers in Fig. 3c, f. Interestingly, for $\alpha = 0.485$ there is a re-stabilization of the soliton as shown by the larger ε star marker in panel (f).

Next, for $\alpha = 0.497$ the discrete eigenvalues initially (at $\varepsilon = 0$) lie on the imaginary axis; they come in pairs and are symmetric about the line $\mathrm{Im}(\omega) = \alpha = 0.497$, furthermore the minimum one is above the real axis. When ε increases, both eigenvalues approach one another and finally collide at the point $(0, \alpha = 0.497)$ creating a new pair of discrete eigenvalues along the line $\mathrm{Im}(\omega) = \alpha = 0.497$. Each pair of the eigenvalues then again bifurcates after hitting the inner edge of the continuous spectrum. However, the minimum imaginary part of these bifurcating eigenvalues is always greater than zero even for larger ε [see panel (i)]. From this fact, we therefore conclude that the soliton in this case is always stable. This conclusion agrees with our analytical investigation.

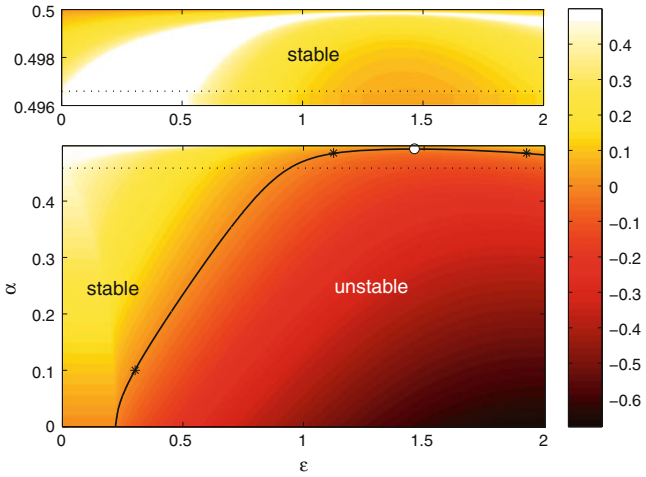

Fig. 4 The (in)stability region of onsite bright solitons type I in the (ε, α)-plane. The corresponding color represents the minimum value of $\mathrm{Im}(\omega)$ (for all eigenvalues ω) for each ε and α. Thus, the region in which $\min(\mathrm{Im}(\omega)) \geq 0$ indicates the region of stable soliton, otherwise unstable. The boundary of stable–unstable regions, i.e., when $\min(\mathrm{Im}(\omega)) = 0$, is given by the *solid line* (three representative points (*star markers*) on this line correspond to those points in Fig. 3c, f). The *boundary curve* also indicates the occurrence of Hopf bifurcations with one degenerate point, i.e. a double-Hopf bifurcation, at $\varepsilon \approx 1.46$ as indicated by the *white-filled circle*. The *lower and upper horizontal dotted lines* correspond to Eqs. (31) and (26), respectively (see text) (Color figure online)

The minimum value of $\mathrm{Im}(\omega)$ (in color representation) of the onsite bright soliton type I for a relatively large range of ε and α gives the (in)stability region in the (ε, α)-plane as presented in Fig. 4. The stable region is indeed determined whenever $\min(\mathrm{Im}(\omega)) \geq 0$ for each ε and α. The lower and upper dotted horizontal lines in this figure, i.e., respectively, $\alpha = \alpha_{\mathrm{cp}} \approx 0.4583$ and $\alpha = \alpha_{\mathrm{th}} \approx 0.49659$, represent the boundaries of the regions which distinguish the description of the eigenvalue structure of the soliton. The solid line in this figure indicates the (in)stability boundary, i.e., when $\min(\mathrm{Im}(\omega)) = 0$. Three representative points (star markers) lying on this line reconfirm the corresponding points in Fig. 3c, f. As shown in the figure, there is an interval of α in which the soliton is stable for all ε. This is interesting as the onsite soliton, which was shown [10, 11] to be destabilized by a parametric driving, now can be re-stabilized by a damping constant.

Let us revisit Fig. 3 for $\alpha = 0.1$ and $\alpha = 0.485$. We notice that at zero-crossing points ε_c (shown by the star markers in panels (c) and (f)), the following conditions hold:

(i) There is a pair (equal and opposite) of non-zero real eigenvalues, and
(ii) The ε-derivative of the imaginary part of the pair of eigenvalues mentioned in (i) is non-zero at ε_c.

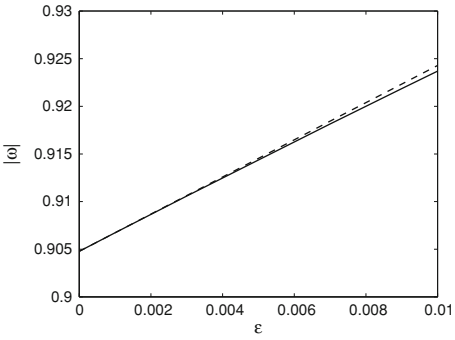

Fig. 5 Comparison between the critical eigenvalues of onsite bright solitons type II for $\alpha = 0.1$ produced by numerics (*solid line*) and by analytical approximation (32) (*dashed line*)

The second condition is also called the transversality condition. We assume that the so-called *first Lyapunov coefficient* of the zero-crossing points is nonzero, i.e. the genericity condition. According to the Hopf bifurcation theorem (see, e.g., Ref. [19], keeping in mind that our eigenvalue is denoted by $i\omega$), the above conditions imply that at $\varepsilon = \varepsilon_c$, Eq. (1) has time-periodic (limit cycle) solutions bifurcating from a (steady-state) onsite bright soliton type I. We then call such a critical point ε_c a Hopf point. By applying the centre manifold theorem, for example, we can generally determine the nature of a Hopf point ε_c through its first Lyapunov coefficient $l_1(\varepsilon_c)$ (see, e.g., Ref. [19]); the Hopf bifurcation is subcritical iff $l_1(\varepsilon_c) > 0$ and supercritical iff $l_1(\varepsilon_c) < 0$.

Because the occurrence of Hopf bifurcation in the onsite type I also indicates the onset of (in)stability, the collection of Hopf bifurcation points in the (ε, α)-plane therefore lies precisely on the (in)stability boundary line (see again Fig. 4). However, at the stationary point $\varepsilon \approx 1.46$ the condition (ii) for the occurrence of a (non-degenerate) Hopf bifurcation does not hold. At this special point, we have a saddle-node bifurcation of Hopf points, i.e. a double-Hopf (Hopf-Hopf) bifurcation. Due to the violation of the transversality condition, there may be no periodic solution or even multiple periodic solutions at the degenerate point. We will examine this point later in Sect. 5, where it will be shown through numerical continuations of limit cycles near the degenerate point that the former possibility occurs.

4.1.2 Onsite Type II

For this type of solution, a comparison between the critical eigenvalues obtained by analytical calculation, which is given by Eq. (32), and by numerics, is presented in Fig. 5. We conclude that our analytical prediction for small ε is quite accurate.

The eigenvalue structure of onsite solitons type II for $\alpha = 0.1$ and the two values $\varepsilon = 0.1, 1$ and the corresponding curve of imaginary part of the critical eigenvalues are given in Fig. 6. This figure shows that the soliton is always unstable even for a large ε. This fact is consistent with the analytical prediction. We notice in the figure that there is a new pair of discrete eigenvalues bifurcating from the inner edge of continuous spectrum at relatively large ε [see panel (b)].

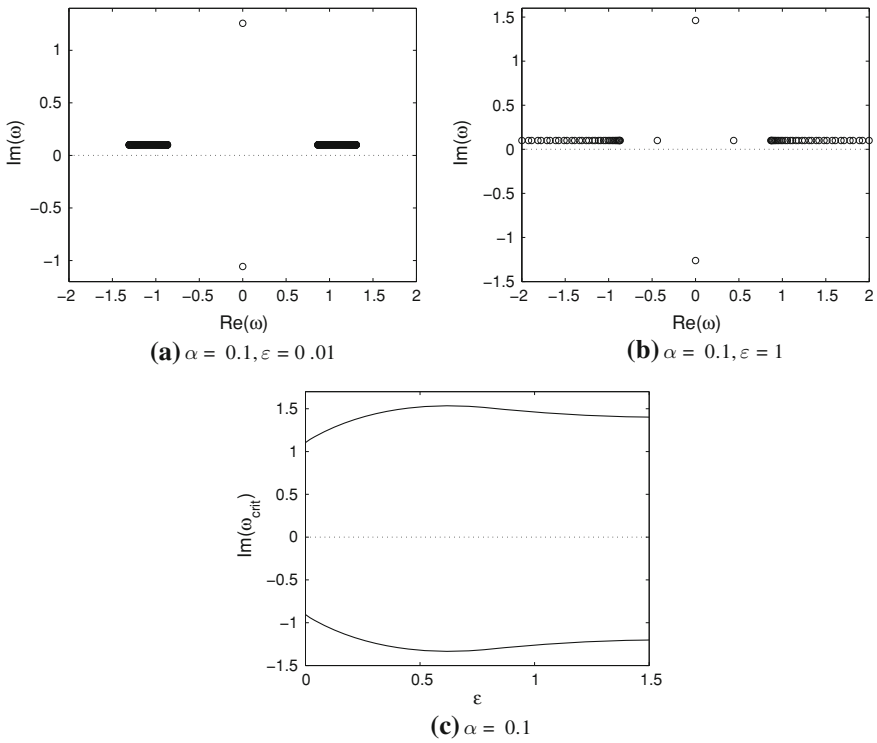

Fig. 6 The *top panels* (**a**, **b**) show the eigenvalue structure of onsite bright solitons type II for $\alpha = 0.1$ and two values of ε as indicated in the caption. The *bottom panel* (**c**) depicts the imaginary part of the critical eigenvalues as a function of ε

By evaluating the minimum value of $\mathrm{Im}(\omega)$ for a relatively large ε and α, we obtain that the soliton is always unstable for $\alpha < \gamma = 0.5$ and, contrastingly, stable for $\alpha = \gamma$. In the latter case, the eigenvalues of the onsite type II are exactly the same as in the onsite type I; the minimum value of the imaginary part remains zero for all ε.

4.1.3 Saddle-Node Bifurcation of Onsite Bright Solitons

We observed from numerics and analytics that when approaching $\alpha = \gamma$, the onsite bright soliton type I and type II possess the same profile as well as the same stability, consistent with the saddle-node bifurcation experienced by the two solitons. A diagram of this bifurcation can be produced, e.g., by plotting the norm of the numerical solution of these two solitons as a function of α for fixed $\varepsilon = 0.1$. To do so, we apply a pseudo-arc-length method to perform the numerical continuation, starting from the onsite type I at $\alpha = 0$. The obtained diagram is presented in Fig. 7 and the corresponding analytical approximation is also depicted therein. As

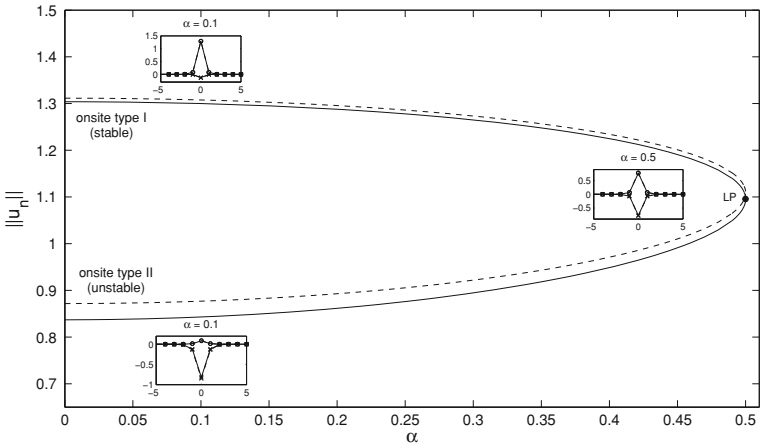

Fig. 7 A saddle-node bifurcation of onsite bright solitons for $\varepsilon = 0.1$. The onsite type I (stable) merges with the onsite type II (unstable) at a limit point (LP) $\alpha = \gamma = 0.5$. The *solid and dashed lines* represent the norm of the solutions obtained by numerical calculation and analytical approximation, respectively. The *insets* depict the profile of the corresponding solutions at the two values $\alpha = 0.1, 0.5$

shown in the figure, the onsite type I, which is stable, turns into the onsite type II, which is unstable. Both numerics and analytics give the same turning point [or so-called limit point (LP)] at $\alpha = \gamma = 0.5$. We also conclude that the analytical approximation for the norm is quite close to the numerics, with the accuracy for the onsite type I better than type II. Indeed, their accuracy could be improved if one uses smaller ε.

4.2 Intersite Bright Solitons

4.2.1 Intersite Type I

Let us first compare our analytical prediction for the critical eigenvalues, given by Eqs. (42)–(43) and (44)–(45), with the corresponding numerical results. We present the comparisons in Fig. 8 by considering three values of $\alpha = 0.1, 0.465, 0.497$ as representative points for the three cases discussed in the previous section. From the figure we see that the double eigenvalues which coincide originally at $\varepsilon = 0$ then split into two distinct eigenvalues as ε increases. We conclude that our approximation for small ε is generally quite accurate.

Next, we move on to the description of the eigenvalue structure of the intersite bright solitons type I and the corresponding imaginary part of the two critical eigenvalues as functions of ε; these are depicted in Fig. 9 for the three values of α used before. The first and second columns in the figure represent conditions of

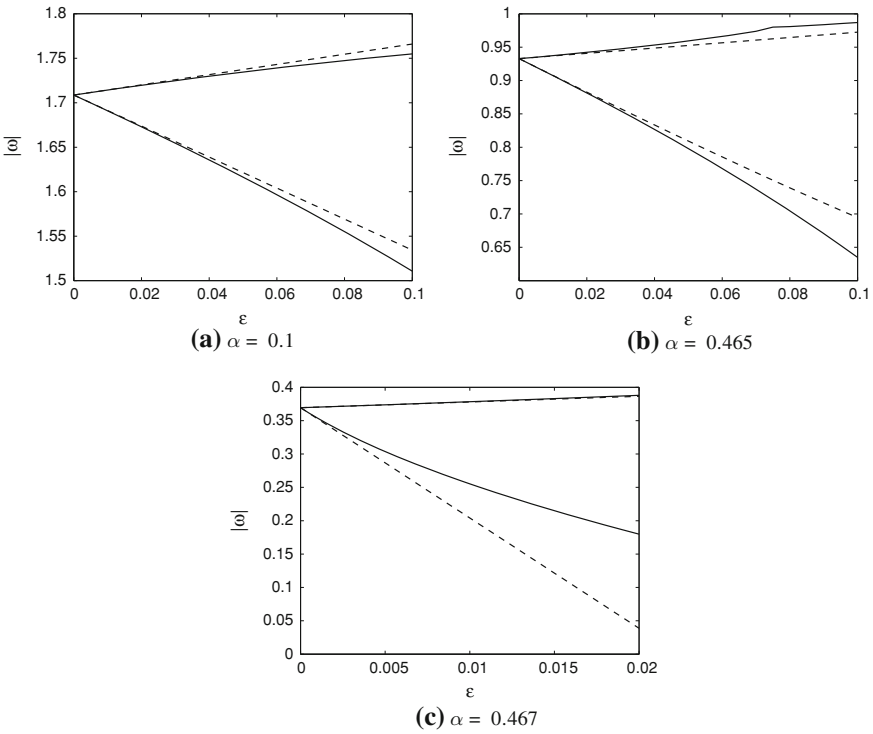

Fig. 8 Comparisons of the two distinct critical eigenvalues of intersite bright solitons type I obtained numerically (*solid lines*) and analytically (*dashed lines*) for three values of α as indicated in the caption of each panel. The *upper and lower curves* in **a** and **b** are plotted from, respectively, Eqs. (42) and (43), while in **c** from Eqs. (45) and (44)

stability and instability, respectively. For $\alpha = 0.1$, the two critical eigenvalues successively collide with the outer band of the continuous spectrum and the corresponding bifurcating eigenvalues coming from the first collision contribute to the instability. For $\alpha = 0.465$, the first collision is between one of the critical eigenvalues with the inner edge of the continuous spectrum. The second collision is between the other critical eigenvalue with its pair. In contrast to the previous case, the instability in this case is caused by the bifurcating eigenvalues coming from the second collision. Moreover, for $\alpha = 0.497$, contribution to the instability is given by one of the critical eigenvalues moving down along the imaginary axis. All the numerical results described above are in accordance with our analytical observations in Sect. 3.

Let us now focus our attention on the right panels of Fig. 9 by particularly discussing the properties of the critical points of ε at which the curve of the minimum imaginary part of the critical eigenvalues crosses the real axis (these are shown by the star markers). The first and third points (from left to right) in panel (c) as well as the points in panels (f) and (i) indicate the onset of stable-to-unstable

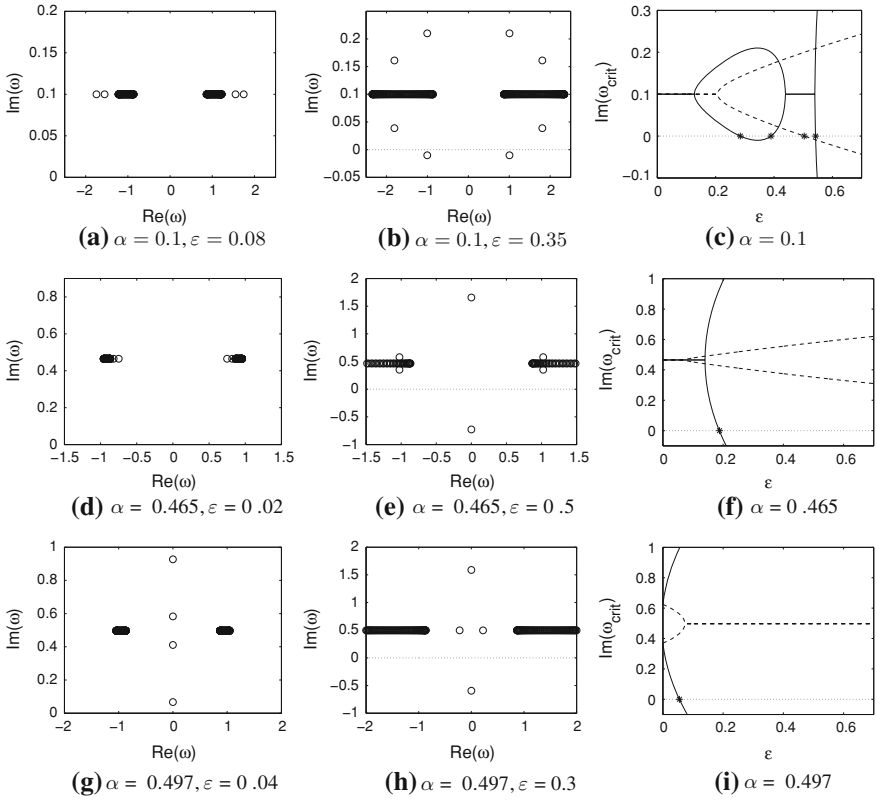

Fig. 9 The first (**a**, **d**, **g**) and second (**b**, **e**, **h**) columns of panels show the structure of eigenvalues of intersite bright solitons type I in the complex plane, for three values of α, each of which uses two different values of ε, to depict the condition of stability (*left panel*) and instability (*middle panel*). The third column (**c**, **f**, **i**) shows the imaginary part of the two distinct critical eigenvalues as functions of ε for the corresponding α. The locations of zero-crossings in these panels are indicated by the *star markers*

transition. Contrastingly, the second point in panel (c) illustrates the beginning of the re-stabilization of solitons. In fact, the first three points in panel (c) mentioned above admit all conditions for the occurrence of a Hopf bifurcation (see again the relevant explanation about these conditions in our discussion of onsite type I); therefore, they also correspond to Hopf points. In addition, the fourth point of zero crossing in panel (c), which comes from one of the purely imaginary eigenvalues, indicates the branch point of a pitchfork bifurcation experienced by the solutions of intersite type I, III, and IV. We will discuss this type of bifurcation in more detail in the next section.

The (in)stability region of intersite bright solitons type I in the (ε, α)-plane is given in Fig. 10. In the figure, we also depict the two distinguishable (solid and dashed) lines representing the two distinct critical eigenvalues whose imaginary

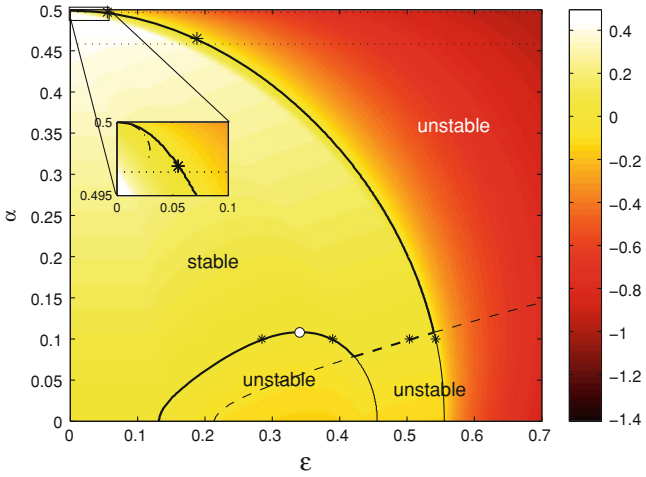

Fig. 10 As Fig. 4 but for intersite bright solitons type I. The boundary between stable and unstable regions is given by the bold (*solid and dashed*) lines. The *dashed-dotted line* in the inset is our analytical approximation given by Eq. (46). The Hopf bifurcation lines are depicted by the *solid* (not the rightmost) and *dashed lines*. The *white-filled circle* indicates a degenerate Hopf point. The branch points of pitchfork bifurcation are shown by the *rightmost solid lines* (Color figure online)

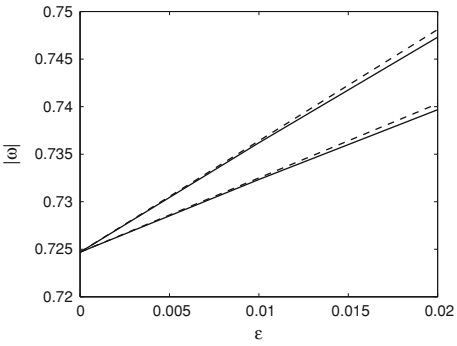

Fig. 11 Comparison of two critical eigenvalues of intersite bright solitons type II for $\alpha = 0.3$ between numerics (*solid lines*) and analytics (*dashed lines*). The analytical approximation is given by Eqs. (47) (*lower curve*) and (48) (*upper curve*)

parts become zero. The star points on the lines correspond to those points in the right panels of Fig. 9. The boundary line which separates the stable and unstable regions in the figure is shown by the bold (solid and dashed) lines. The lower and upper dotted horizontal lines in the figure represent, respectively, $\alpha = \alpha_{\rm cp} \approx 0.4583$ and $\alpha = \alpha_{\rm th} \approx 0.49659$ which divide the region into three different descriptions of the eigenvalue structure. Interestingly, for $\alpha_{\rm th} < \alpha$, we can make an approximation for the numerically obtained stability boundary (see the inset). This approximation is given by Eq. (46) which is quite close to the numerics for small ε.

We notice in Fig. 10 that the solid line (not the rightmost) and dashed line also represent Hopf bifurcations, with one special point (the white-filled circle) which does not meet the second condition for the occurrence of a (non-degenerate) Hopf

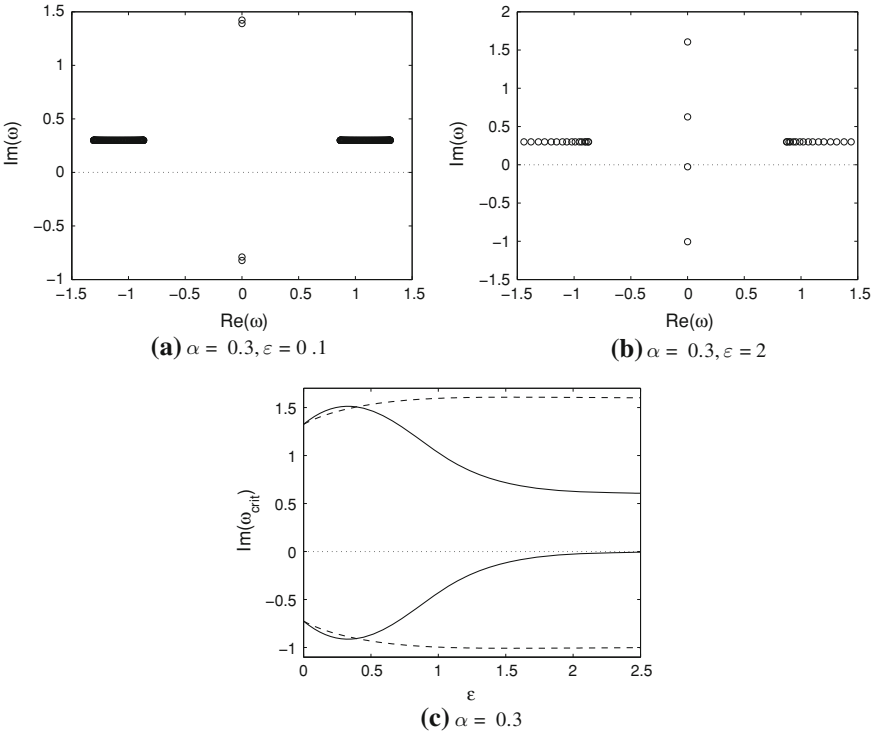

Fig. 12 **a**–**b** The eigenvalue structure of intersite bright solitons type II for two values (α, ε) as indicated in the caption; **c** the imaginary part of two discrete eigenvalues in varied ε

bifurcation mentioned above. We will analyze the special point in the next section. We see from the figure that the bold parts of the Hopf lines coincide with the (in)stability boundary, while the nonbold ones exist in the unstable region. In addition, we also observe that the rightmost solid line in Fig. 10 indicates the collection of branch points of pitchfork bifurcation experienced by the intersite type I, III, and IV; the bold part of this line also indicates the (in)stability boundary.

4.2.2 Intersite Type II

For intersite bright solitons type II, we present in Fig. 11 a comparison of two critical eigenvalues between the numerics and the analytical calculation given by Eqs. (47) and (48). We see from the figure that our approximation for relatively small ε is quite close to the numerics. The snapshot of the eigenvalue structure of this type of solution for two points (α, ε) and the path of the imaginary part of corresponding two discrete eigenvalues are depicted in Fig. 12. We conclude that the intersite soliton type II is unstable even for large ε.

Moreover, the evaluation of the minimum value of $\mathrm{Im}(\omega)$ of the intersite bright solitons type II in the (ε, α)-plane gives the (in)stability window (not shown here).

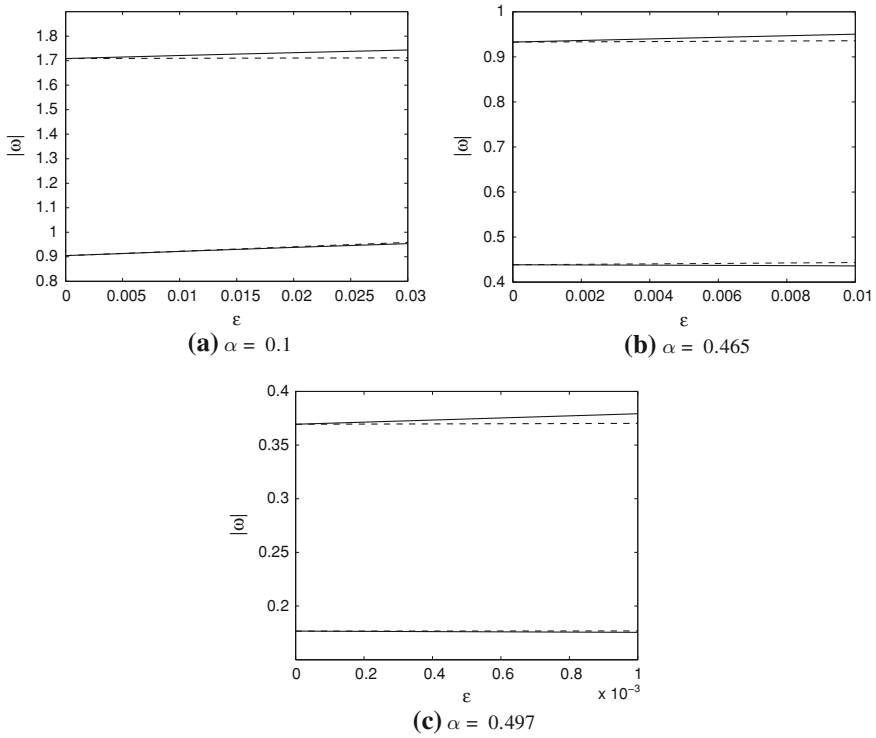

Fig. 13 Comparisons between two critical eigenvalues of intersite bright solitons III and IV obtained numerically (*solid lines*) and analytically (*dashed lines*) for values of α as shown in the caption. In **a** and **b**, the *upper and lower dashed curves* correspond, respectively, to Eqs. (49) and (50), whereas in **c** they correspond to Eqs. (51) and (52)

It is shown that the soliton, except at the point $\alpha = \gamma = 0.5$ and $\varepsilon = 0$, is always unstable. This result agrees with our analytical prediction.

4.2.3 Intersite Type III and IV

Now we examine the intersite bright soliton type III which, due to symmetry, has exactly the same eigenvalues as type IV. Shown in Fig. 13 is the analytical approximation for two critical eigenvalues given by Eqs. (49)–(50) or (51)–(52), which are compared with the corresponding numerical results. We conclude that the approximation is quite accurate for small ε and that the range of accuracy is wider for smaller value of α.

The structure of the eigenvalues of this type of solution and the curves of the imaginary part of the corresponding two critical eigenvalues are given in Fig. 14 for the three values of α used in Fig. 13. The figure reveals the condition of instability of solitons up to the limit points of ε at which the minimum imaginary

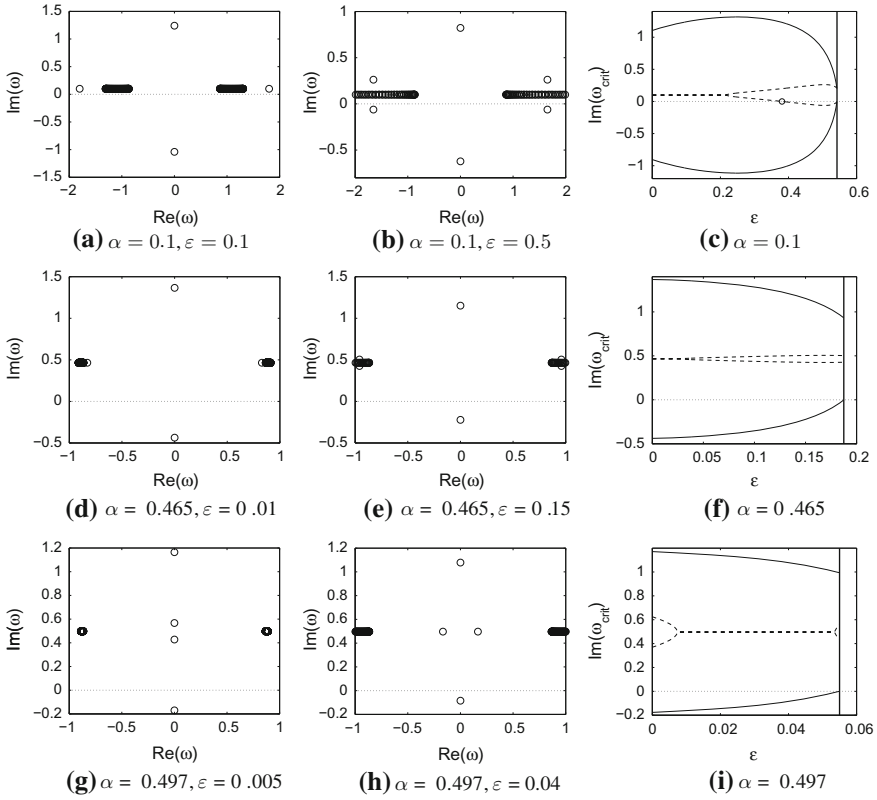

Fig. 14 (First and second columns) The structure of eigenvalues of intersite bright solitons type III and IV for parameter values (α, ε) as indicated in the caption. (Third column) The imaginary part of two critical eigenvalues obtained by varying ε. The *vertical lines* indicate the limit points of ε up to which the soliton exists, i.e., when the minimum imaginary part of the eigenvalues becomes zero

part of the eigenvalues becomes zero; these conditions are indicated by the corresponding vertical lines in the third column. In fact, these limit points indicate the branch points of pitchfork bifurcation experienced by the intersite solitons type I, III, and IV (we will discuss this bifurcation in more detail in the next section).

The first and second columns of Fig. 14 respectively present the condition just before and after a collision of one of the discrete eigenvalues which does not contribute to the instability of solitons. Interestingly, as shown in panel (c), such an eigenvalue also crosses the real axis at some critical ε as indicated by the empty circle. The latter condition, in fact, indicates a Hopf bifurcation, which occurs when the soliton is already in unstable mode. This is different from the previous discussions where the Hopf bifurcations also indicate the change of stability of solitons.

Presented in Fig. 15 is the (in)stability window for intersite bright solitons type III and IV which is defined as the area to the left of the solid line; this line represents the set of the branch points of pitchfork bifurcation in the (ε, α)-plane.

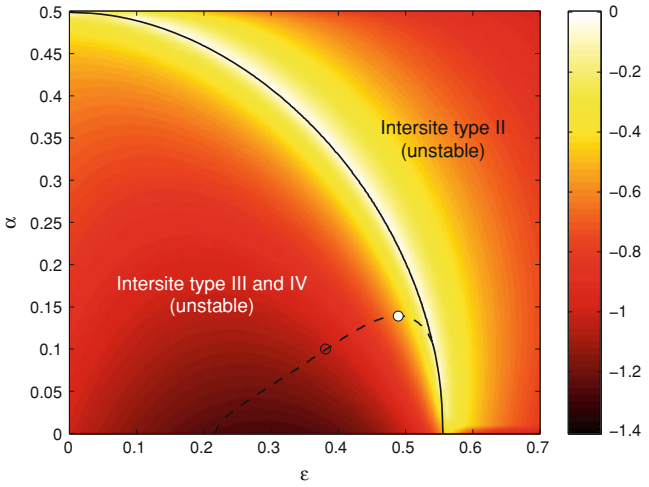

Fig. 15 The (in)stability region of intersite bright solitons type III and IV in (ε, α)-space. The *solid line* indicates the branch-point line of pitchfork bifurcation. The *dashed line* represents the occurrence of Hopf bifurcations (with one degenerate point at the *white-filled circle*), which arises from one of the critical eigenvalues which does not contribute to the instability of solitons. The *empty circle* lying on the *dashed line* corresponds to that point depicted in Fig. 14c

From the figure, we conclude that the intersite type III and IV are always unstable. The area to the right of the solid line belongs to the unstable region of intersite type I. One can check that this line is exactly the same as the rightmost solid line in Fig. 10. In addition, the dashed line appearing in Fig. 15 depicts the occurrence of Hopf bifurcations. However, there is one special point indicated by the white-filled circle, at which the ε-derivative of the imaginary part of the corresponding critical eigenvalue is zero; this degenerate point will be discussed further in Sect. 5. The empty circle lying on the Hopf line reconfirms the corresponding point in Fig. 14c.

4.2.4 Saddle-Node and Pitchfork Bifurcation of Intersite Bright Solitons

From both numerical and analytical results discussed above, we observed that the intersite type I and type II have the same profile and stability when approaching $\alpha = \gamma$. This fact indicates the appearance of a saddle-node bifurcation undergone by the two solitons. Moreover, there also exists a pitchfork bifurcation experienced by the intersite type I, III, and IV.

One can check that the norm of the intersite type III and IV is exactly the same for all parameter values so that this quantity can no longer be used for depicting a clear bifurcation diagram. Therefore, we now simply plot the value of $|u_0|^2$ for each solution, e.g., as a function of α and fixed $\varepsilon = 0.1$; this is shown in Fig. 16 where the numerics (solid lines) is obtained by a pseudo-arc-length method. As seen in the figure, the intersite type I, III, and IV meet at a (pitchfork) branch point

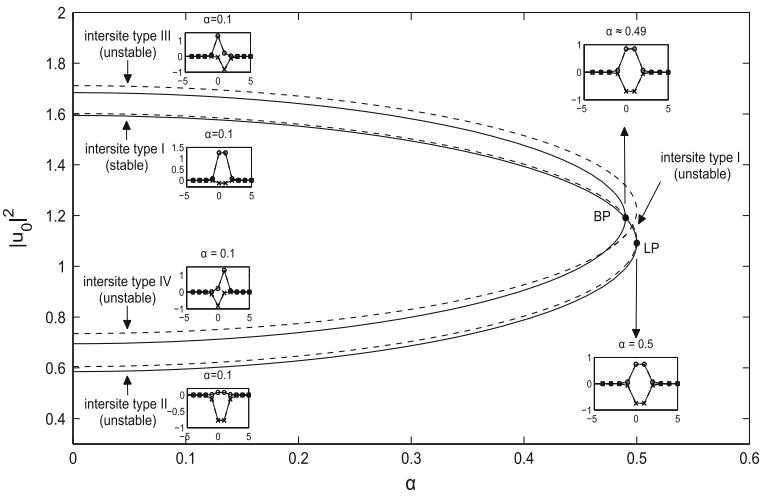

Fig. 16 Saddle-node and pitchfork bifurcations of intersite bright solitons by varying α and fixing $\varepsilon = 0.1$. *The curves* depict the value of $|u_0|^2$ of each solutions obtained numerically (*solid lines*) and analytically (*dashed lines*). The profiles of the corresponding solutions at some values of α are shown in the relevant *insets*. The intersite type I, III, and IV merge at a branch point (BP) $\alpha \approx 0.49$ and the intersite type I and II meet at a limit point (LP) $\alpha = \gamma = 0.5$

(BP) $\alpha \approx 0.49$. At this point, the stability of the intersite type I is switched. Furthermore, the intersite type I and II also experience a saddle-node bifurcation where they merge at a limit point (LP) $\alpha = \gamma = 0.5$. Just before this point, the intersite type I possesses one unstable eigenvalue, while the type II has two unstable eigenvalues. The two critical eigenvalues for the intersite type I and II then coincide at LP. We confirm that our analytical approximation for the value of $|u_0|^2$ is relatively close to the corresponding numerical counterpart.

Next, let us plot the value of $|u_0|^2$ for each soliton by fixing $\alpha = 0.1$ and varying ε (presented in Fig. 17). The pitchfork bifurcation experienced by the intersite type I (solid line), type III (upper dashed line), and type IV (lower dashed line) is clearly shown in the figure. The three solitons meet together at a branch point BP. We also depict in the figure the points at which Hopf bifurcations emerge (labelled by indexed H). For the shake of completeness, we also plot the relevant curve for the intersite type II (dotted line).

5 Nature of Hopf Bifurcations and Continuation of Limit Cycles

If there is only one pair of non-zero real eigenvalues and the other eigenvalues have strictly positive imaginary parts, a Hopf bifurcation also indicates the change of stability of the steady state solution. In this case, the periodic solutions

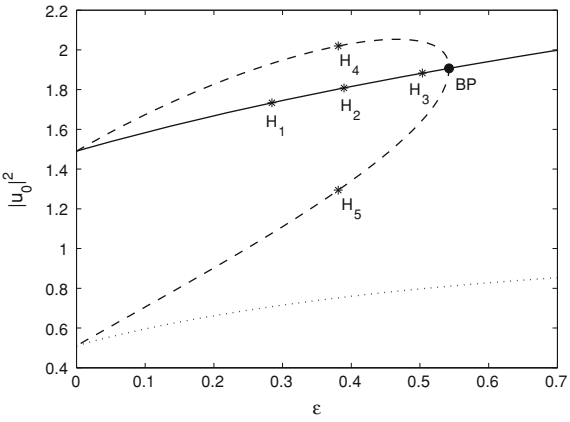

Fig. 17 A pitchfork bifurcation of intersite bright solitons for fixed $\alpha = 0.1$ and varied ε. The *curves* represent the numerical value of $|u_0|^2$ for the corresponding solutions as a function of ε. The intersite type I (*solid line*), type III (*upper dashed line*), and type IV (*lower dashed line*) merge at a branch point (BP). The occurrence of Hopf bifurcation (H_i) is detected in intersite type I, III, and IV. The *dotted line* corresponds to the intersite type II

bifurcating from the Hopf point coexist with either the stable or unstable mode of the steady state solution. If the periodic solutions coexist with the unstable steady state solution, they are stable and the Hopf bifurcation is called *supercritical*. On the other hand, if the periodic solutions coexist with the stable steady state solution, they are unstable and the Hopf bifurcation is called *subcritical*.

To numerically calculate the first Lyapunov coefficient for a Hopf point and perform a continuation of the bifurcating limit cycle, we use the numerical continuation package Matcont. Due to the limitations of Matcont, we evaluate the soliton using 21 sites. In fact, this setting does not affect significantly the soliton behavior compared to that used in the previous section.

In this section, we examine the nature of Hopf points and the stability of cycle continuations in onsite type I, intersite type I, and intersite type III–IV.

5.1 Onsite Type I

For this type of solution, in particular at $\alpha = 0.1$, we have one Hopf point, which occurs at $\varepsilon_c \approx 0.3077$ (see again Fig. 3c). From Matcont, we obtain $l_1(\varepsilon_c \approx 0.3077) > 0$ which indicates that the Hopf point ε_c is subcritical and hence the limit cycle bifurcating from this point is unstable. A continuation of the corresponding limit cycle is given in Fig. 18a. As the Hopf point in this case also indicates the change of stability of the stationary soliton, one can confirm that the bifurcating periodic solitons are stable because they coexist with the stable onsite type I; this agrees with the computed first Lyapunov coefficient above.

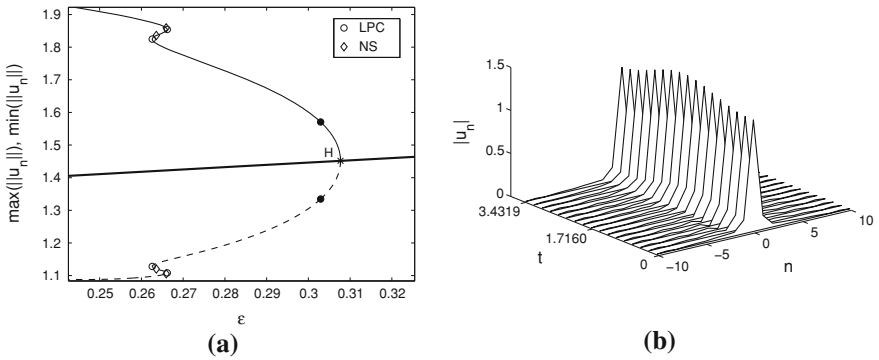

Fig. 18 **a** The continuation of the limit cycle from a Hopf point H for an onsite soliton type I with $\alpha = 0.1$. The first Lyapunov coefficient for H calculated by Matcont is positive, i.e. H is subcritical. The *bold solid line* represents the norm of the stationary soliton while the *solid and dashed lines* indicate, respectively, the maximum and minimum of the norm of the bifurcating periodic solitons; **b** the profile of an unstable periodic soliton (as H is subcritical) over one period ($T \approx 3.4319$) corresponding to the *black-filled circle* in **a**

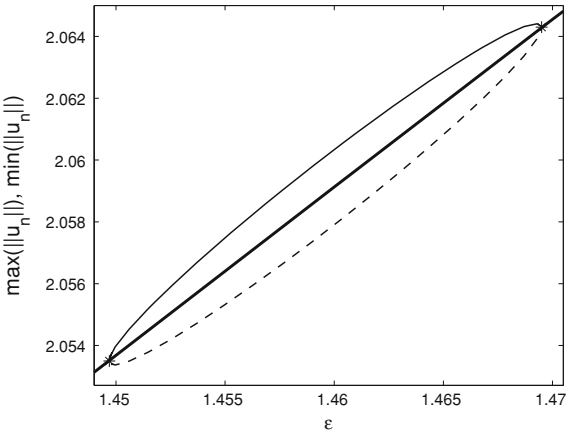

Fig. 19 As Fig. 18a, but for $\alpha = 0.492642$. Two Hopf points (*stars*) in the neighbourhood of the degenerate point (the *while-filled circle* in Fig. 4) are shown to be connected by a branch of limit cycles

Interestingly, the continuation of the limit cycle also experiences saddle-node and torus bifurcations, as indicated by the points labelled limit point cycle (LPC) and Neimark-Sacker (NS), respectively. The profile of a representative periodic soliton over one period is shown in Fig. 18b, from which we clearly see the typical oscillation in the soliton amplitude.

From the previous discussion we have mentioned that there is one degenerate point for Hopf bifurcations in onsite type I, which is indicated by the white-filled circle in Fig. 4. In Fig. 19, we depict numerical continuations of periodic orbits of two Hopf bifurcations near the degenerate point. We obtained that the limit cycle branches bifurcating from the Hopf points are connected and form a closed loop. This informs us that as α approaches the critical value for a degenerate Hopf point,

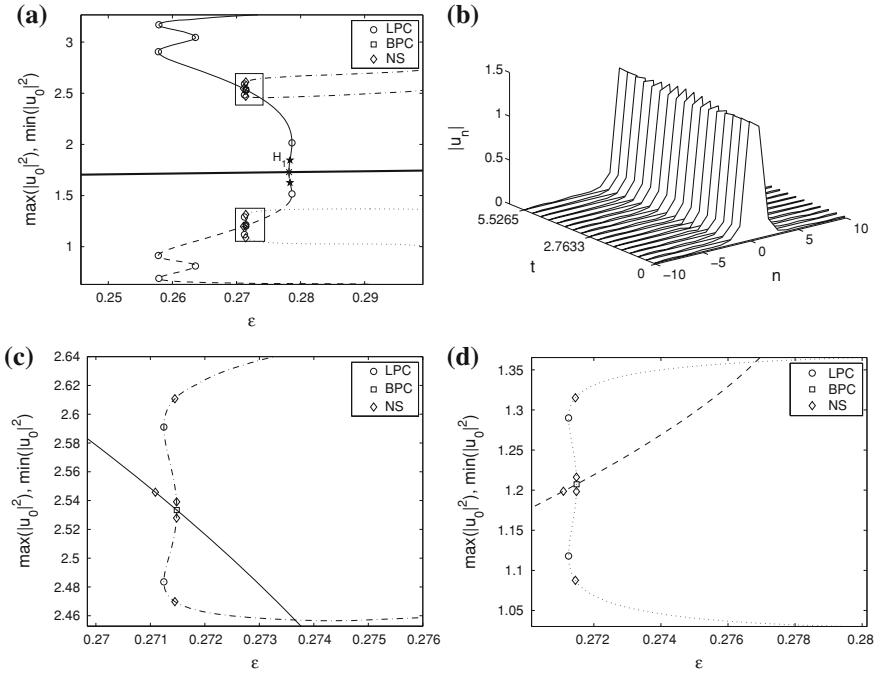

Fig. 20 **a** The cycle continuation from Hopf point H_1 for intersite bright soliton type I with $\alpha = 0.1$. In this case, H_1 is supercritical. The *bold solid line* indicates the value of $|u_0|^2$ for the stationary soliton, which is the same as that shown in Fig. 17. The *solid and dashed lines* represent, respectively, the maximum and minimum value of $|u_0|^2$ for the bifurcating periodic solitons, which also experience a pitchfork cycle bifurcation. The branches of the cycle are depicted by the *dash-dotted* (maximum $|u_0|^2$) and *dotted* (minimum $|u_0|^2$) *lines*; **b** the profile of a stable periodic soliton (as H_1 is supercritical) over one period ($T \approx 5.5265$) corresponding to the *star point* in **a**; **c**, **d** enlargements of, respectively, the *upper and the lower rectangles* in **a**

the "radius" of the loop tends to zero. Hence, one may conclude that at the double-Hopf point, there is no bifurcation of periodic orbits.

5.2 Intersite Type I

In particular for $\alpha = 0.1$, there are three Hopf points detected for the intersite type I (see again Fig. 17). For point H_1 ($\varepsilon \approx 0.2782$), Matcont gives a negative value for the first Lyapunov coefficient, which means that the bifurcating periodic soliton is stable or H_1 is supercritical. The corresponding cycle continuation is presented in Fig. 20a. As shown in the figure, the limit cycle bifurcating from H_1 coexist with the unstable mode of the (steady-state) intersite type I which confirms

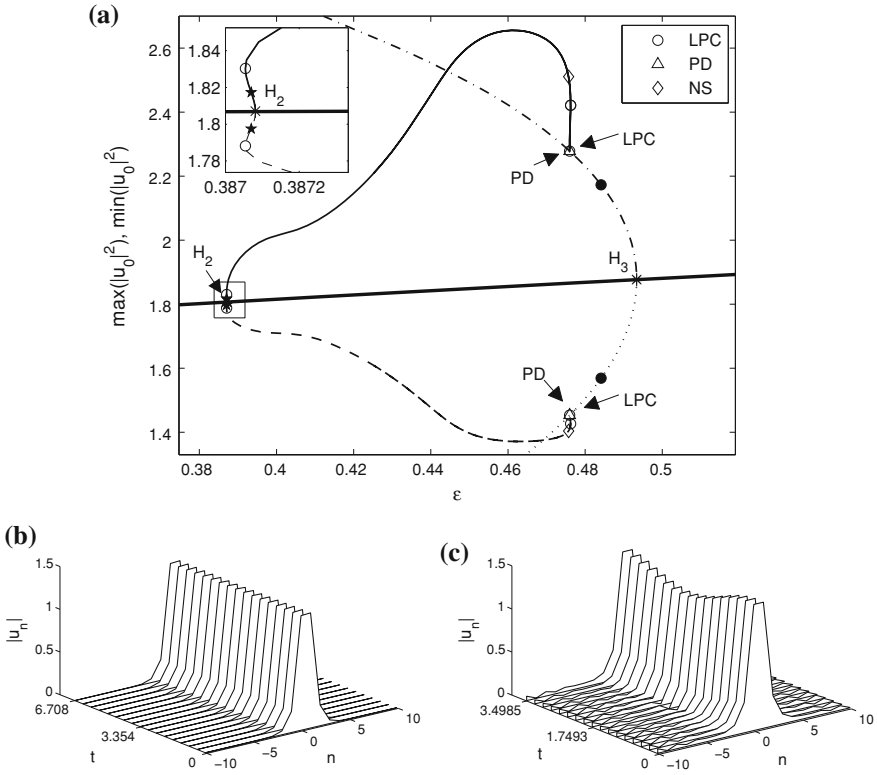

Fig. 21 **a** As Fig. 20a, but for H_2 and H_3, where the *inset* gives the zoom-in for the corresponding region showing that H_2 and H_3 are supercritical and subcritical, respectively. The *bold solid line* is the same as that shown in Fig. 17, i.e., representing the value of $|u_0|^2$ for the stationary intersite soliton. The *solid* (*dashed*) and *dash-dotted* (*dotted*) *lines* shows the maximum (minimum) value of $|u_0|^2$ for the periodic soliton which bifurcates from, respectively, H_2 and H_3; **b**, **c** the profile of periodic solitons over one period $T \approx 6.708$ and $T \approx 3.4985$ which corresponds, respectively, to the *star and the black-filled circle* in **a**. From the nature of H_2 and H_3, periodic solitons in **b** and **c** are stable and unstable, respectively

the supercritical H_1. This is valid because the Hopf bifurcation in this case also indicates the change of stability of the soliton. We also see from the figure that the cycle continuation contains NS, LPC, and branch point cycle (BPC) points which indicate the occurrence of, respectively, torus, saddle-node, and pitchfork bifurcations for limit cycle. The branches of the cycle continuation from the BPC point are shown in the figure. A representative periodic soliton (in one period) which occurs at one representative point along the cycle continuation is depicted in Fig. 20b, which shows the oscillation between the two excited sites.

Next, for H_2 ($\varepsilon \approx 0.3871$) and H_3 ($\varepsilon \approx 0.4934$), the first Lyapunov coefficients given by Matcont are negative and positive valued, respectively. Thus, H_2 is

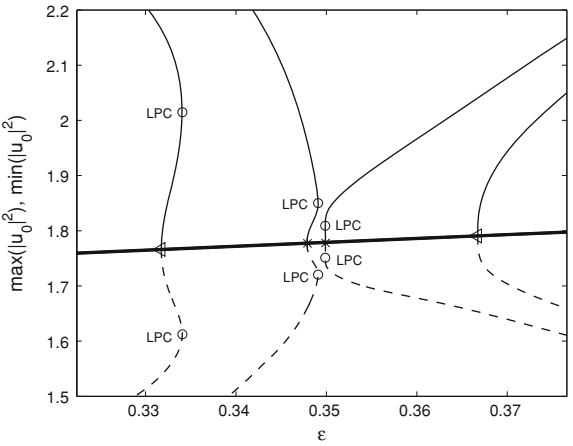

Fig. 22 As Fig. 21a, but for $\alpha = 0.108$ (*triangles*) and $\alpha = 0.11082$ (*stars*) in the proximity of the *while-filled circle* in Fig. 10

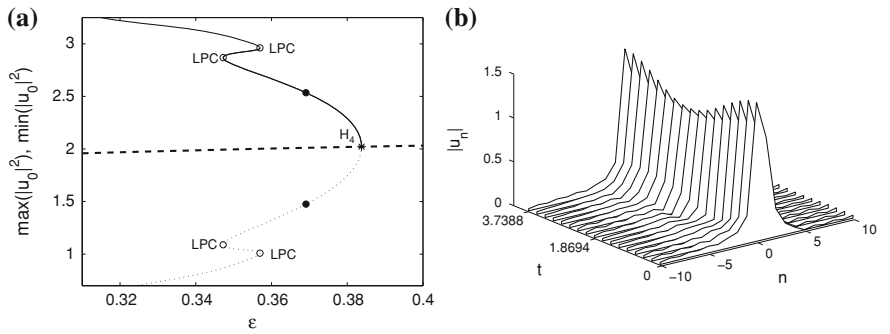

Fig. 23 **a** The cycle continuation from Hopf point H_4 for intersite bright soliton type III with $\alpha = 0.1$ showing that H_4 is subcritical. The *dashed line* shows the value of $|u_0|^2$ for the stationary soliton (the same as that shown in Fig. 17) while the *solid and dotted lines* represent, respectively, the maximum and minimum $|u_0|^2$ of the bifurcating periodic solitons; **b** the profile of an unstable periodic soliton over one period $T \approx 3.7388$ corresponding to the *black-filled circle* in **a**

supercritical while H_3 is subcritical, which implies that the limit cycle bifurcating from H_2 and H_3 are stable and unstable, respectively. The continuations of the corresponding limit cycles are shown in Fig. 21a. From the figure, we see that the limit cycles bifurcating from H_2 and H_3 respectively coexist with the unstable and stable stationary intersite soliton type I. This fact is consistent with the nature of H_2 and H_3 as given by Matcont. In addition, as shown in the figure, a period-doubling (PD) bifurcation also occurs in the cycle continuation coming from H_3. This bifurcation seems to coincide with the turning point of cycle (LPC) which appears in the cycle continuation starting from H_2. The profile of one-period periodic solitons at the two representative points near H_2 and H_3 are presented in Fig. 21b, c, respectively. We cannot see clearly the typical oscillation of the

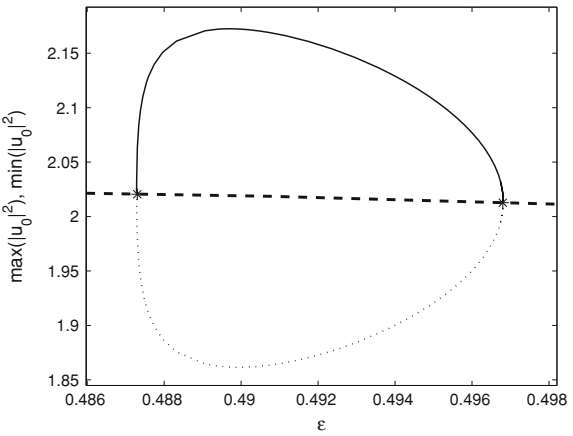

Fig. 24 As Fig. 23a, but for $\alpha = 0.1411$. The degenerate (Hopf-Hopf) point indicated as the *while-filled circle* in Fig. 15 is at $\varepsilon \approx 0.49$

periodic soliton in Fig. 12.21b as it occurs very near to H_2. By contrast, the oscillation in the soliton amplitude is clearly visible in Fig. 12.21c.

Similarly to the onsite type I, we also noticed the presence of a double-Hopf bifurcation in the intersite type I, i.e., the white-filled circle in Fig. 10. To investigate the point, we evaluate several Hopf points nearby the bifurcation point and perform numerical continuations for limit cycles, which are presented in Fig. 22. Unlike the case in the onsite type I, here the (non-degenerate) Hopf points are not connected to each other by a closed loop of a branch of limit cycles. As we observe this scenario at any Hopf point that is arbitrarily close (up to a numerical accuracy) to the degenerate (codimension 2) bifurcation, it indicates that at the double-Hopf point, there is a bifurcation of at least two branches of periodic solutions.

5.3 Intersite Type III and IV

As intersite bright soliton type III and IV possess the same eigenvalue structures, the nature of the corresponding Hopf bifurcation and the stability of the continuation of each limit cycle will be the same as well. Therefore it is sufficient to devote our discussion to intersite type III only.

As shown in Fig. 17, there is one Hopf point, namely H_4, for the intersite type III at $\alpha = 0.1$. In this type of solution, the Hopf bifurcation occurs while other eigenvalues already give rise to instability; this is different from the type of Hopf bifurcation discussed previously. Therefore we cannot perform the analysis as before in determining the stability of the bifurcating periodic soliton. In fact, according to calculation given by Matcont, the first Lyapunov coefficient for H_4 is positive (subcritical), which means that the bifurcating periodic soliton is unstable.

Figure 23a shows the continuation of the corresponding limit cycle from H_4. A representative one-period periodic soliton at ε near H_4 (indicated by the

black-filled circle) is shown in Fig. 23b, from which we can see clearly the oscillation in the amplitude of soliton.

Next, we study the double-Hopf bifurcation for the intersite type III–IV shown by the white-filled circle in Fig. 15. Presented in Fig. 24 is the continuation of the limit cycles from two Hopf points about the degenerate point, from which we see that they are connected to each other. Therefore, as for the case of the onsite type I, we argue that there is no bifurcation of periodic solutions at the degenerate point.

6 Conclusion

In this chapter, we have considered a parametrically driven damped discrete nonlinear Schrödinger (PDDNLS) equation. The existence and stability of fundamental discrete bright solitons have been examined analytically through a perturbation theory for small ε and then corroborated by numerical calculations. We showed that there are two types of onsite discrete soliton, namely onsite type I and II. For onsite type I, we found an interval in α for which the soliton is stable for any coupling constant, i.e., a damping can re-stabilize a driven onsite soliton. Contrastingly, the onsite type II was found to be always unstable for all ε. These two solitons experience a saddle-node bifurcation with the limit point $\alpha = \gamma$ for any ε.

We also showed that there are four types of intersite discrete soliton, called intersite type I, II, III, and IV. In fact, intersite type III and IV are essentially considered as one solution due to its symmetry. We obtained that intersite type I in the region of instability in the non-dissipative case can be stabilized by damping while intersite type II and III–IV are always unstable. A saddle-node bifurcation, as for the onsite soliton, was found to be undergone by intersite type I and II. Moreover, we also obtained that intersite type I, III, and IV experience a pitchfork bifurcation. The branch points of such a bifurcation in the (ε, α)-plane have been calculated numerically.

More interestingly, we observed that Hopf bifurcation also occurs in onsite type I, intersite type I, and intersite type III–IV, which confirms the existence of the corresponding periodic solitons (limit cycles) in the PDDNLS equation. The continuation of the limit cycles as well as the stability of the periodic solitons have been demonstrated numerically using the numerical continuation software Matcont. In particular, subcritical Hopf bifurcations for onsite type I and intersite type III–IV were observed. Moreover, we obtained three Hopf bifurcations for intersite type I. It was shown that two of these points generate stable periodic solitons, i.e. the bifurcations are supercritical.

Note that similar studies for the continuum limit of Eq. (1) have been put forward in, e.g., Refs. [14–16]. Hopf bifurcations and the corresponding periodic solitons were reported and discussed therein. The connection between the results presented in this work, which correspond to weakly coupled lattices, and those of [14–16] are proposed for future study.

Acknowledgments The authors thank Hill Meijer for fruitful discussions and guidance on Matcont. MS acknowledges financial support from the Ministry of National Education of the Republic of Indonesia.

References

1. P.G. Kevrekidis (ed.), *Discrete Nonlinear Schrödinger Equation: Mathematical Analysis, Numerical Computations and Physical Perspectives* (Springer, New York, 2009)
2. D. Hennig, G. Tsironis, Wave transmission in nonlinear lattices. Phys. Rep. **307**, 333 (1999)
3. G.L. Alfimov, V.A. Brazhnyi, V.V. Konotop, On classification of intrinsic localized modes for the discrete nonlinear Schrödinger equation. Phys. D **194**, 127 (2004)
4. D.E. Pelinovsky, P.G. Kevrekidis, D.J. Frantzeskakis, Stability of discrete solitons in nonlinear Schrödinger lattices. Phys. D **212**, 1 (2005)
5. E.P. Fitrakis, P.G. Kevrekidis, H. Susanto, D.J. Frantzeskakis, Dark solitons in discrete lattices: Saturable versus cubic nonlinearities. Phys. Rev. E **75**, 066608 (2007)
6. M. Johansson, S. Yuri Kivshar, Discreteness-induced oscillatory instabilities of dark solitons. Phys. Rev. Lett. **82**, 85 (1999)
7. S. Yu Kivshar, W. Królikowski, O.A. Chubykalo, Dark solitons in discrete lattices. Phys. Rev. E **50**, 5020 (1994)
8. H. Susanto, M. Johansson, Discrete dark solitons with multiple holes. Phys. Rev. E **72**, 016605 (2005)
9. D.E. Pelinovsky, P.G. Kevrekidis, Stability of discrete dark solitons in nonlinear Schrödinger lattices. J. Phys. A. **41**, 185206 (2008)
10. H. Susanto, Q.E. Hoq, P.G. Kevrekidis, Stability of discrete solitons in the presence of parametric driving. Phys. Rev. E **74**, 067601 (2006)
11. M. Syafwan, H. Susanto, S.M. Cox, Discrete solitons in electromechanical resonators. Phys. Rev. E **81**, 026207 (2010)
12. D. Hennig, Periodic, quasiperiodic, and chaotic localized solutions of a driven, damped nonlinear lattice. Phys. Rev. E **59**, 1637 (1999)
13. M. Kollmann, H.W. Capel, T. Bountis, Breathers and multibreathers in a periodically driven damped discrete nonlinear Schrödinger equation. Phys. Rev. E **60**, 1195 (1999)
14. M. Bondila, I.V. Barashenkov, M.M. Bogdan, Topography of attractors of the parametrically driven nonlinear Schrödinger equation. Phys. D **87**, 314 (1995)
15. I.V. Barashenkov, E.V. Zemlyanaya, van T.C. Heerden, Time-periodic solitons in a damped-driven nonlinear Schrödinger equation. Phys. Rev. E **83**, 056609 (2011)
16. I.V. Barashenkov, E.V. Zemlyanaya, Soliton complexity in the damped-driven nonlinear Schrödinger equation: Stationary to periodic to quasiperiodic complexes. Phys. Rev. E **83**, 056610 (2011)
17. R.S. MacKay, S. Aubry, Proof of existence of breathers for time-reversible or Hamiltonian networks of weakly coupled oscillators. Nonlinearity **7**, 1623 (1994)
18. P.G. Kevrekidis, A.R. Bishop, K.Ø. Rasmussen, Twisted localized modes. Phys. Rev. E **63**, 036603 (2001)
19. Y.A. Kuznetsov, *Elements of Applied Bifurcation Theory*. Applied Mathematical Sciences, vol. 112, 2nd edn. (Springer, New York, 1998)

Conditions and Stability Analysis for Saddle-Node Bifurcations of Solitary Waves in Generalized Nonlinear Schrödinger Equations

Jianke Yang

Saddle-node bifurcations of solitary waves in generalized nonlinear Schrödinger equations with arbitrary forms of nonlinearity and external potentials in arbitrary spatial dimensions are analyzed. First, general conditions for these bifurcations are derived. Second, it is shown analytically that the linear stability of these solitary waves does not switch at saddle-node bifurcations, which is in stark contrast with finite-dimensional dynamical systems where stability switching takes place. Third, it is shown that this absence of stability switching does not contradict the Vakhitov–Kolokolov stability criterion or the results in finite-dimensional dynamical systems. Fourth, it is shown that this absence of stability switching holds not only for real potentials but also for complex potentials. Lastly, various numerical examples will be given to confirm these analytical findings. In particular, saddle-node bifurcations with both branches of solitary waves being stable will be presented.

1 Introduction

Saddle-node bifurcation is the generic and most common bifurcation in finite-dimensional dynamical systems [1]. In this bifurcation, there are two fixed-point branches on one side of the bifurcation point and no fixed points on the other side, and the stability of these two fixed-point branches switches at the bifurcation point (one branch stable and the other branch unstable). In nonlinear partial differential equations (which can be viewed as infinite-dimensional dynamical systems),

J. Yang (✉)
Department of Mathematics and Statistics,
University of Vermont,
Burlington, VT 05401, USA
e-mail: jxyang@uvm.edu

Progress Optical Sci., Photonics (2013): 639–655
DOI: 10.1007/10091_2012_3

Published Online: 20 April 2012

this bifurcation occurs as well (it is also called fold bifurcation in the literature). For instance, solitary waves in nonlinear physical systems often exhibit this type of bifurcation. Examples include the Boussinesq equations and the fifth-order Korteweg-de Vries equation in water waves [2–4], the Swift–Hohenberg equation in pattern formation [5], the nonlinear Schrödinger (NLS) equations with localized or periodic potentials in nonlinear optics and Bose–Einstein condensates [6–9], and many others. Motivated by stability switching of saddle-node bifurcations in finite-dimensional dynamical systems, it is widely believed that in nonlinear partial differential equations, stability of solitary waves also always switches at saddle-node bifurcations (see [5–8] for examples). Even though it was claimed on numerical evidence that both branches of saddle-node bifurcations were stable for various solitons in a Kronig–Penney model with cubic-quintic nonlinearity [10], that numerical evidence was not reliable since many solitons which the authors claimed to be stable are actually unstable. Thus that work could not shake this pervasive belief of stability switching.

In this paper, we show that this belief of universal stability switching at saddle-node bifurcations in nonlinear partial differential equations is incorrect. Specifically, we show that in generalized nonlinear Schrödinger equations with arbitrary forms of nonlinearity and external real or complex potentials, stability of solitary waves actually does not switch at saddle-node bifurcations. This fact is proved analytically in two ways by using the general conditions of saddle-node bifurcations, eigenvalue-bifurcation analysis and the method of contradiction. It is also verified numerically by several examples, where both branches of solitary waves are stable at saddle-node bifurcations. In addition, we show that this absence of stability switching does not contradict the Vakhitov–Kolokolov stability criterion even though the lower and upper branches of the saddle-node bifurcation have opposite signs of power slopes. Reconciliation of our results with those in finite-dimensional dynamical systems is also provided.

2 Conditions for Saddle-Node Bifurcations

We consider generalized nonlinear Schrödinger equations with arbitrary forms of nonlinearity and external potentials in arbitrary spatial dimensions,

$$iU_t + \nabla^2 U + F(|U|^2, \mathbf{x})U = 0, \tag{1}$$

where ∇^2 is the Laplacian in the N-dimensional space $\mathbf{x} = (x_1, x_2, \cdots, x_N)$, and $F(\cdot, \cdot)$ is a general function which contains nonlinearity as well as external potentials. These equations include the Gross–Pitaevskii equation in Bose–Einstein condensates and nonlinear light-transmission equations in linear potentials and nonlinear lattices as special cases [11–14]. Below, we will first focus on the case where the function F is real-valued, which applies when the system (1) is conservative. Extension to the non-conservative case of complex functions of F will be considered in Sect. 6 later.

When the function F is real, Eq. (1) admits stationary solitary waves of the form

$$U(\mathbf{x}, t) = e^{i\mu t} u(\mathbf{x}), \tag{2}$$

where $u(\mathbf{x})$ is a localized real function satisfying

$$\nabla^2 u - \mu u + F(u^2, \mathbf{x})u = 0, \tag{3}$$

and μ is a real propagation constant which is a free parameter. Under certain conditions, these solitary waves undergo saddle-node bifurcations at special values of μ [6–9]. A signature of these bifurcations is that on one side of the bifurcation point μ_0, there are no solitary wave solutions; but on the other side of μ_0, there are two distinct solitary-wave branches which merge with each other at $\mu = \mu_0$. To derive conditions for these bifurcations, we introduce the linearization operator of Eq. (3),

$$L_1 = \nabla^2 - \mu + \partial_u [F(u^2, \mathbf{x})u]. \tag{4}$$

We also introduce the standard inner product of functions

$$\langle f, g \rangle = \int_{-\infty}^{\infty} f^*(\mathbf{x}) g(\mathbf{x}) d\mathbf{x}, \tag{5}$$

where the superscript '*' stands for complex conjugation. Our analysis starts with the basic observation that, if a bifurcation occurs at $\mu = \mu_0$, by denoting the corresponding solitary wave and the linearization operator as

$$u_0(\mathbf{x}) = u(\mathbf{x}; \mu_0), \quad L_{10} = L_1|_{\mu=\mu_0,\ u=u_0}, \tag{6}$$

then the linear operator L_{10} should have a discrete zero eigenvalue. This is a necessary condition for all types of bifurcations (not just for saddle-node bifurcations). To derive sufficient conditions for saddle-node bifurcations, let us make the following assumption.

Assumption 1 It is assumed that this zero eigenvalue of L_{10} is discrete and simple.

This assumption holds for all bifurcations in one spatial dimension since L_{10} in this case is a Sturm–Liouville operator whose discrete eigenvalues are all simple. This assumption holds for many bifurcations in higher spatial dimensions as well. Under this assumption, we denote the unique discrete (localized) eigenfunction of L_{10} at the zero eigenvalue as $\psi(\mathbf{x})$, i.e.,

$$L_{10}\psi = 0. \tag{7}$$

Since L_{10} is a real operator, we can normalize the eigenfunction ψ to be a real function and hence require ψ real below. We also denote

$$G(u; \mathbf{x}) = F(u^2; \mathbf{x})u, \quad G_k(\mathbf{x}) = \partial_u^k G|_{u=u_0}, \tag{8}$$

where $k = 1, 2, 3, \cdots$. Then the sufficient condition for saddle-node bifurcations of solitary waves is given by the following theorem.

Theorem 1 Under Assumption 1 and the above notations, if $\langle u_0, \psi \rangle \neq 0$ and $\langle G_2, \psi^3 \rangle \neq 0$, then a saddle-node bifurcation of solitary waves occurs at $\mu = \mu_0$ in Eq. (1).

Proof Solitary waves which exist near $\mu = \mu_0$ admit the following perturbation series expansions

$$u(\mathbf{x}; \mu) = \sum_{k=0}^{\infty} (\mu - \mu_0)^{k/2} u_k(\mathbf{x}). \tag{9}$$

Inserting this expansion into Eq. (3), we get the following equations for u_k at order $(\mu - \mu_0)^{k/2}$, $k = 0, 1, 2,$:

$$\nabla^2 u_0 - \mu_0 u_0 + F(u_0^2, \mathbf{x}) u_0 = 0, \tag{10}$$

$$L_{10} u_1 = 0, \tag{11}$$

$$L_{10} u_2 = u_0 - G_2 u_1^2 / 2!, \tag{12}$$

and so on. Equation (10) for u_0 is satisfied automatically since u_0 is a solitary wave at $\mu = \mu_0$. The u_1 solution to Eq. (11) is found from (7) as

$$u_1 = b_1 \psi, \tag{13}$$

where b_1 is a constant. The u_2 function satisfies the linear inhomogeneous equation (12). Due to the Fredholm Alternative Theorem and the fact that L_{10} is self-adjoint, Eq. (12) admits a localized solution for u_2 if and only if the homogeneous solution ψ is orthogonal to the inhomogeneous term, i.e.,

$$\langle \psi, u_0 - G_2 u_1^2 / 2 \rangle = 0. \tag{14}$$

Inserting the solution (13) into this orthogonality condition and recalling the conditions in Theorem 1, we find that

$$b_1 = \pm \beta, \quad \beta \equiv \sqrt{\frac{2 \langle u_0, \psi \rangle}{\langle G_2, \psi^3 \rangle}}. \tag{15}$$

Thus, we get two b_1 values $\pm\beta$ which are opposite of each other. Inserting the corresponding u_1 solutions (13) into (9), we then get two perturbation-series solutions of solitary waves $u(\mathbf{x}; \mu)$ as

$$u^{\pm}(\mathbf{x}; \mu) = u_0(\mathbf{x}) \pm \beta (\mu - \mu_0)^{1/2} \psi(\mathbf{x}) + O(\mu - \mu_0). \tag{16}$$

If $\langle u_0, \psi \rangle$ and $\langle G_2, \psi^3 \rangle$ have the same sign, then β is real. Recalling that $u_0(\mathbf{x})$ and $\psi(\mathbf{x})$ are both real as well, we see that these perturbation-series solutions (16) give

two real-valued (legitimate) solitary waves when $\mu > \mu_0$, but these solitary waves do not exist when $\mu < \mu_0$. On the other hand, if $\langle u_0, \psi \rangle$ and $\langle G_2, \psi^3 \rangle$ have the opposite sign, β is purely imaginary. In this case, the perturbation series (16) give two real-valued solitary waves when $\mu < \mu_0$ but not when $\mu > \mu_0$.

The above perturbation calculations can be continued to higher orders. We can show that the two real solitary-wave solutions (16), which exist on only one side of $\mu = \mu_0$, can be constructed to all orders of $(\mu - \mu_0)^{1/2}$. In addition, these two solitary waves $u^{\pm}(\mathbf{x}; \mu)$ merge with each other when $\mu \to \mu_0$. We can also show that except these two solitary-wave branches, there are no other solitary-wave solutions near the bifurcation point. Thus a saddle-node bifurcation occurs at $\mu = \mu_0$. This completes the proof of Theorem 1. □

Using the perturbation expansion (16) of solitary waves, we can also calculate the power function $P(\mu)$ of these waves near the saddle-node bifurcation point μ_0. The power P of a solitary wave $u(\mathbf{x})$ is defined as

$$P = \int_{-\infty}^{\infty} u^2(\mathbf{x}) d\mathbf{x}. \tag{17}$$

Using (16) and the condition in Theorem 1, we readily find that

$$P^{\pm}(\mu) = P_0 \pm (\mu - \mu_0)^{1/2} P_1 + O(\mu - \mu_0), \tag{18}$$

where coefficients P_0 and P_1 are

$$P_0 = \langle u_0, u_0 \rangle, \quad P_1 = 2\beta \langle u_0, \psi \rangle \neq 0,$$

and β is given in Eq. (15). It is seen that the power function is a horizontally-oriented parabola, which is not surprising for a saddle-node bifurcation.

3 Stability Analysis for Saddle-Node Bifurcations

Stability properties of solitary waves near saddle-node bifurcations is an important issue. In finite-dimensional dynamical systems, the stability of fixed points is known to switch at saddle-node bifurcations, and this switching is caused by a linear-stability eigenvalue of the fixed points crossing zero along the real axis [1]. For solitary waves in nonlinear partial differential equations (which can be viewed as fixed points in infinite-dimensional dynamical systems), it is widely believed that their stability also always switches at saddle-node bifurcations. We find that this belief is incorrect. Below, we show that for solitary waves (2) in the generalized NLS equations (1), there are no linear-stability eigenvalues crossing zero at a saddle-node bifurcation point, thus stability-switching does not occur.

To study the linear stability of solitary waves (2) in Eq. (1), we perturb them as [13]

$$U(\mathbf{x}, t) = e^{i\mu t} \Big\{ u(\mathbf{x}) + [v(\mathbf{x}) + w(\mathbf{x})] e^{\lambda t} + [v^*(\mathbf{x}) - w^*(\mathbf{x})] e^{\lambda^* t} \Big\}, \tag{19}$$

where $v, w \ll 1$ are normal-mode perturbations, and λ is the mode's eigenvalue. Inserting this perturbed solution into (1) and linearizing, we obtain the following linear-stability eigenvalue problem

$$\mathcal{L}\Phi = -i\lambda\Phi, \tag{20}$$

where

$$\mathcal{L} = \begin{bmatrix} 0 & L_0 \\ L_1 & 0 \end{bmatrix}, \quad \Phi = \begin{bmatrix} v \\ w \end{bmatrix}, \tag{21}$$

$$L_0 = \nabla^2 - \mu + F(u^2, \mathbf{x}), \tag{22}$$

and L_1 has been given in Eq. (4).

At a saddle-node bifurcation point $\mu = \mu_0$, we denote

$$L_{00} = L_0|_{\mu=\mu_0,\, u=u_0}, \quad \mathcal{L}_0 = \mathcal{L}_{\mu=\mu_0,\, u=u_0}. \tag{23}$$

Then in view of Eq. (3), we have

$$L_{00}u_0 = 0, \tag{24}$$

thus zero is a discrete eigenvalue of L_{00}. From this equation as well as (7), we have

$$\mathcal{L}_0 \begin{bmatrix} 0 \\ u_0 \end{bmatrix} = \mathcal{L}_0 \begin{bmatrix} \psi \\ 0 \end{bmatrix} = 0, \tag{25}$$

thus zero is also a discrete eigenvalue of $\mathcal{L}_0$.

On the bifurcation of the zero eigenvalue in $\mathcal{L}_0$ when μ moves away from μ_0, we have the following main result.

Theorem 2 Assuming that zero is a simple discrete eigenvalue of L_{00} and L_{10}, then at a saddle-node bifurcation point μ_0, no eigenvalues of the linear-stability operator $\mathcal{L}$ cross zero, thus no stability switching occurs.

Proof The idea of the proof is to show that, when μ moves away from μ_0, the algebraic multiplicity of the zero eigenvalue in $\mathcal{L}$ does not decrease, thus the zero eigenvalue in $\mathcal{L}$ cannot bifurcate out to nonzero.

At the saddle-node bifurcation point $\mu = \mu_0$, $(0, u_0)^T$ and $(\psi, 0)^T$ are two linearly independent eigenfunctions of the zero eigenvalue in $\mathcal{L}_0$ in view of Eq. (25). Here the superscript 'T' represents the transpose of a vector. Under the assumption of Theorem 2, zero is a simple discrete eigenvalue of L_{00} and L_{10}. Thus it is easy to see that $\mathcal{L}_0$ does not admit any additional eigenfunctions at the zero eigenvalue, which means that the geometric multiplicity of the zero eigenvalue in $\mathcal{L}_0$ is two. To determine the algebraic multiplicity of the zero eigenvalue in $\mathcal{L}_0$, we need to examine the number of generalized eigenfunctions of this zero eigenvalue. The lowest-order generalized eigenfunction $(f_1, g_1)^T$ to the eigenfunction $(0, u_0)^T$ of this zero eigenvalue satisfies the equation

$$\mathcal{L}_0 \begin{bmatrix} f_1 \\ g_1 \end{bmatrix} = \begin{bmatrix} 0 \\ u_0 \end{bmatrix}, \tag{26}$$

so the equation for f_1 is

$$L_{10} f_1 = u_0. \tag{27}$$

From Eq. (7), we see that this inhomogeneous equation has a homogeneous localized solution ψ. In addition, from conditions of saddle-node bifurcations in Theorem 1, $\langle u_0, \psi \rangle \neq 0$. Furthermore, L_{10} is a self-adjoint operator. Thus, from the Fredholm Alternative Theorem, the inhomogeneous equation (27) does not admit any localized solution, which means that the eigenfunction $(0, u_0)^T$ of the zero eigenvalue in $\mathcal{L}_0$ does not have any generalized eigenfunctions. Similarly, we can show that the eigenfunction $(\psi, 0)^T$ of the zero eigenvalue in $\mathcal{L}_0$ does not have any generalized eigenfunctions either. Hence the algebraic multiplicity of the zero eigenvalue in $\mathcal{L}_0$ is equal to its geometric multiplicity and is two.

Away from the bifurcation point (i.e., $\mu \neq \mu_0$,) $\mathcal{L}$ always has a zero eigenmode

$$\mathcal{L} \begin{bmatrix} 0 \\ u \end{bmatrix} = 0 \tag{28}$$

in view of Eq. (1). In addition, by differentiating Eq. (1) with respect to μ, we also get

$$\mathcal{L} \begin{bmatrix} u_\mu \\ 0 \end{bmatrix} = \begin{bmatrix} 0 \\ u \end{bmatrix}, \tag{29}$$

thus $(u_\mu, 0)^T$ is a generalized eigenfunction of the zero eigenvalue in $\mathcal{L}$. This means that the algebraic multiplicity of the zero eigenvalue in $\mathcal{L}$ is at least two when $\mu \neq \mu_0$.

If nonzero eigenvalues bifurcate out from the zero eigenvalue in $\mathcal{L}$, the algebraic multiplicity of this zero eigenvalue must decrease. Our results above show that, when μ moves away from μ_0, the algebraic multiplicity of the zero eigenvalue in $\mathcal{L}$ does not decrease, thus there cannot be nonzero eigenvalues of $\mathcal{L}$ bifurcating out from zero. Consequently, no eigenvalues of $\mathcal{L}$ cross zero at the saddle-node bifurcation point, thus no stability switching occurs. This completes the proof of Theorem 2. □

We would like to add that under the assumption of Theorem 2, we can readily show that in the neighborhood of a saddle-node bifurcation point ($0 < |\mu - \mu_0| \ll 1$), $\mathcal{L}$ does not admit any additional eigenfunctions or generalized eigenfunctions at the zero eigenvalue, thus the algebraic multiplicity of the zero eigenvalue in $\mathcal{L}$ is exactly two. This means that the algebraic multiplicity of $\mathcal{L}$'s zero eigenvalue does not change when μ moves away from the bifurcation point μ_0, thus there is no eigenvalue bifurcation out of the origin at a saddle-node bifurcation.

Alternative Proof Theorem 2 can also be proved by the following alternative method of contradiction. For the eigenvalue problem (20), i.e.,

$$L_0 w = -i\lambda v, \qquad L_1 v = -i\lambda w, \tag{30}$$

by taking the inner product of the first equation with the solitary wave $u(\mathbf{x})$ and noticing that L_0 is a self-adjoint operator, we get

$$-i\lambda\langle u, v\rangle = \langle u, L_0 w\rangle = \langle L_0 u, w\rangle = 0.$$

Thus, for any non-zero eigenvalue λ, its eigenfunction v must be orthogonal to u, i.e.,

$$\langle u, v\rangle = 0. \tag{31}$$

Similarly, by taking the inner product of the second equation in (30) with u_μ and recalling $L_1 u_\mu = u$ from (29), we get

$$-i\lambda\langle u_\mu, w\rangle = \langle u_\mu, L_1 v\rangle = \langle L_1 u_\mu, v\rangle = \langle u, v\rangle.$$

Thus for any non-zero eigenvalue λ, in view of the orthogonality (31), we see that u_μ and w must be orthogonal as well, i.e.,

$$\langle u_\mu, w\rangle = 0. \tag{32}$$

Now suppose at a saddle-node bifurcation point μ_0, non-zero eigenvalues bifurcate out from the origin. Then when μ is very close to μ_0, these non-zero eigenvalues are very small. Thus, from the eigenvalue Eq. (30) and our assumption in Theorem 2, we see that

$$(v, w) \to (c_1\psi, c_2 u_0), \quad \text{when } \mu \to \mu_0, \tag{33}$$

where c_1 and c_2 are certain constants which cannot be zero simultaneously. In addition, we see from (16) that when $\mu \to \mu_0$, $u_\mu \propto \psi$. Upon substituting these expressions into the orthogonality conditions (31) and (32) and taking the limit of $\mu \to \mu_0$, we find that

$$c_1\langle u_0, \psi\rangle = 0, \quad c_2\langle \psi, u_0\rangle = 0. \tag{34}$$

Since at a saddle-node bifurcation, $\langle u_0, \psi\rangle \neq 0$ (see Theorem 1), the above relations then give $c_1 = c_2 = 0$, which contradicts our earlier requirement that c_1 and c_2 not being zero simultaneously. Thus there cannot be eigenvalues bifurcating out from the origin at a saddle-node bifurcation. This also proves Theorem 2. □

4 Consistency with the Generalized VK Criterion for Positive Solitary Waves

The above result of no stability switching at a saddle-node bifurcation in the generalized NLS equations (1) applies to general real-valued solitary waves, certainly including positive (or equivalently sign-definite) solitary waves.

For positive solitary waves in NLS-type equations, the stability result best known in the physical community is the Vakhitov–Kolokolov (VK) stability criterion, which says that the solitary wave $u(\mathbf{x};\mu)$ is linearly stable if its power slope $P'(\mu)$ is positive and linearly unstable if $P'(\mu)$ is negative [12, 13, 15]. Near a saddle-node bifurcation, we know from Eq. (18) that the power function is a horizontally-oriented parabola. Thus the lower and upper branches always have opposite signs of power slope. Then from this VK stability criterion, one might conclude that the lower and upper branches should have opposite stability as well, which would contradict our result in Theorem 2. The error in this reasoning is that the above (original) VK criterion, which derives linear stability exclusively from the power slope, applies only when Eq. (1) has no external potentials (i.e., $F = F(|U|^2)$ only) [13]. This no-potential condition for the use of the original VK criterion is not well recognized in the physical community. Saddle-node bifurcations, however, can only occur when F depends also on $\mathbf{x}$ explicitly, i.e., Eq. (1) has external potentials such as linear or nonlinear potentials (the latter means that the coefficients of nonlinear terms are spatially modulated [14]). In this case, the original VK criterion must be generalized. The generalized VK criterion derives linear stability not only from the power slope but also from the number of positive eigenvalues in the operator L_1 [13]. Thus even though the lower and upper branches of a saddle-node bifurcation have opposite signs of power slope, if the number of positive eigenvalues in L_1 also changes between the two branches, then both branches can still have the same linear stability. Below we will show that the number of positive eigenvalues in L_1 *does* change at a saddle-node bifurcation, thus there is no contradiction between our analytical result in Theorem 2 and the generalized VK criterion. In Example 1 of the next section, we will further see explicitly that Theorem 2 and the generalized VK criterion give exactly the same stability results.

Our result on positive eigenvalues in L_1 near a saddle-node bifurcation is given in the following theorem.

Theorem 3 Assume the conditions of Theorem 1 (for a saddle-node bifurcation) hold. Then across this saddle-node bifurcation point (from the lower branch to the upper one or vise versa), a simple real eigenvalue of L_1 crosses zero, thus the number of positive eigenvalues in L_1 changes by one.

Proof The eigenvalue problem for the linear Schrödinger operator L_1 is

$$L_1\Psi = \Lambda\Psi, \tag{35}$$

where Λ is a real eigenvalue and Ψ is the associated eigenfunction. At the saddle-node bifurcation point $\mu = \mu_0$, $L_{10}\psi = 0$ (see Eq. 7), thus $\Lambda = 0$ is a discrete eigenvalue of L_1. In addition, due Assumption 1, $\Lambda = 0$ is also a simple eigenvalue of L_1. Next we calculate how this simple zero eigenvalue of L_1 bifurcates out when μ is away from the bifurcation point μ_0.

Before we start, we first expand the operator L_1 as

$$L_1 = L_{10} + (\mu - \mu_0)^{1/2}L_{11} + (\mu - \mu_0)L_{12} + \cdots. \tag{36}$$

The solitary wave $u(\mathbf{x})$ is also expanded by Eq. (9). Upon substituting these two expansions into the relation $L_1 u_\mu = u$ out of (29), at order $(\mu - \mu_0)^{-1/2}$, we get

$$L_{10} u_1 = 0. \tag{37}$$

This is consistent with our earlier formula (13) for u_1. At $O(1)$, we get

$$L_{11} u_1 = 2(u_0 - L_{10} u_2). \tag{38}$$

This relation will be needed later.

Now we expand Λ and Ψ into the following perturbation series,

$$\Lambda = (\mu - \mu_0)^{1/2} \gamma_1 + (\mu - \mu_0)\gamma_2 + \cdots, \tag{39}$$

$$\Psi = \Psi_0 + (\mu - \mu_0)^{1/2} \Psi_1 + (\mu - \mu_0)\Psi_2 + \cdots. \tag{40}$$

Substituting these expansions as well as the expansion of L_1 above into the eigenvalue equation (35), at $O(1)$ we get

$$L_{10} \Psi_0 = 0. \tag{41}$$

For convenience, instead of taking the Ψ_0 solution as ψ, we take it as

$$\Psi_0 = u_1. \tag{42}$$

Note that u_1 is related to ψ by a non-zero constant [see Eqs. (13) and (15)].

At order $(\mu - \mu_0)^{1/2}$, we get the equation for Ψ_1 as

$$L_{10} \Psi = \gamma_1 u_1 - L_{11} u_1. \tag{43}$$

Inserting (38) into this equation and imposing the Fredholm solvability condition (which says that its right hand side must be orthogonal to the homogeneous solution u_1), we find that the eigenvalue coefficient γ_1 is obtained as

$$\gamma_1 = \frac{2\langle u_1, u_0 \rangle}{\langle u_1, u_1 \rangle}. \tag{44}$$

For the two branches of the saddle-node bifurcation, the solutions u_1 are given by Eqs. (13) and (15), i.e.,

$$u_1 = \pm \beta \psi. \tag{45}$$

Inserting this u_1 into the γ_1 formula (44) and then back into the eigenvalue expansion (39), we find that the leading-order term of the eigenvalues on the two solution branches are

$$\Lambda^{\pm} = \pm(\mu - \mu_0)^{1/2} \alpha, \tag{46}$$

where

$$\alpha \equiv \frac{2\langle u_0, \psi \rangle}{\beta \langle \psi, \psi \rangle} \neq 0. \tag{47}$$

This eigenvalue formula shows that as the solution moves from the lower to the upper branches (or vise versa), this eigenvalue crosses zero and changes sign. Thus the number of positive eigenvalues in L_1 changes by one. This completes the proof of Theorem 3. □

5 Numerical Examples

In this section, we use two examples to confirm the above analytical findings.

Example 1 Consider Eq. (1) with a symmetric double-well potential and cubic-quintic nonlinearity, i.e.,

$$iU_t + U_{xx} - V(x)U + |U|^2 U - |U|^4 U = 0, \tag{48}$$

where the double-well potential

$$V(x) = -3\left[\mathrm{sech}^2(x + 1.5) + \mathrm{sech}^2(x - 1.5)\right] \tag{49}$$

is shown in Fig. 1a, and the quintic nonlinearity has the opposite sign of the cubic nonlinearity. A similar model and its various solitary waves were considered in [16]. Solitary waves in this conservative system (48) are of the form (2), where $u(x)$ is real. We have computed these solitary waves by the Newton-conjugate-gradient method [13], and their power curve is plotted in Fig. 1b. It is seen that a saddle-node bifurcation occurs at $\mu_0 \approx 2.16$. Two solitary waves at $\mu = 2.1$ on the lower and upper branches near this bifurcation point are displayed in Fig. 1c, d. To determine the linear stability of these solitary waves, we have computed their linear-stability spectra by the Fourier collocation method [13], and these spectra are shown in Fig. 1e, f respectively. It is seen that none of the spectra contains unstable eigenvalues, indicating that these solitary waves on both lower and upper branches are linearly stable. We have also performed this spectrum computation for other solitary waves on the power curve of Fig. 1b, and found that they are all linearly stable. Thus there is no stability switching at the saddle-node bifurcation point, in agreement with our analytical result. Additionally, we have found numerically that the zero eigenvalue for all these solitons has algebraic multiplicity two, again in agreement with our analytical result.

In the spectra of Fig. 1e, f, one may notice that there is a pair of purely imaginary eigenvalues $\pm\lambda$ near the origin and may wonder whether that pair of eigenvalues ever collide at the origin at the saddle-node bifurcation point. Numerically we have tracked this pair of eigenvalues as the solitary wave crosses the bifurcation point, and the eigenvalue λ (with a negative imaginary part) versus μ is shown in Fig. 1g.

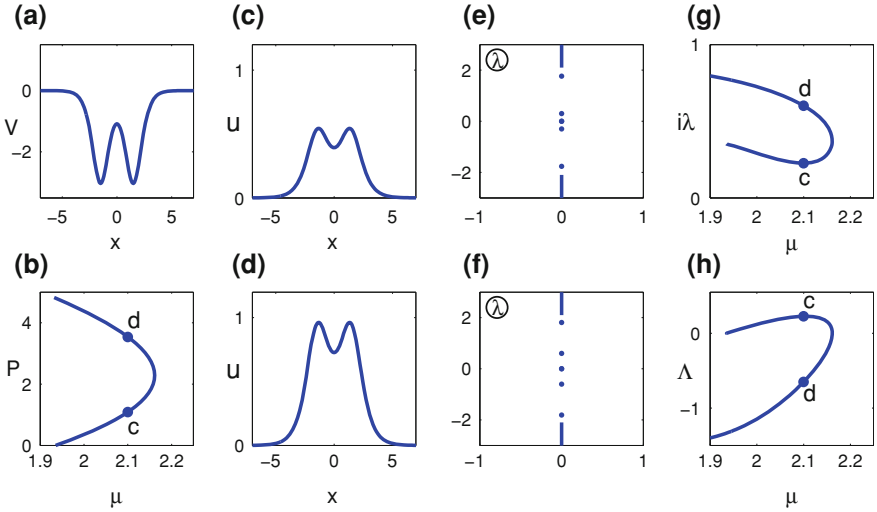

Fig. 1 Saddle-node bifurcation and linear-stability behaviors of solitary waves in Example 1. **a** Potential (49); **b** power curve of solitons; **c**, **d** soliton profiles at points marked by the same letters in (**b**); **e**, **f** stability spectra of solitons in(**c**, **d**); **g** the imaginary discrete eigenvalue λ (near the origin) versus μ ; **h** the largest real eigenvalue Λ in L_1 versus μ . The letters 'c, d' in (**g**, **h**) correspond to those on the power curve in (**b**) to show correspondence of solution branches

Here the plotted quantity is $i\lambda$, which is real positive. We find that as the solitary wave crosses the saddle-node bifurcation point, this pair of imaginary eigenvalues never collide at or cross the origin. This confirms our analytical result in Theorem 2 that no eigenvalues cross zero at the saddle-node bifurcation point.

The solitary waves in Fig. 1 are positive, thus the generalized VK stability criterion applies. Now we show that this generalized VK criterion predicts linear stability for both branches of these solitary waves as well. For this purpose, we have numerically computed the largest eigenvalue Λ in operator L_1 for each solitary wave, and this Λ versus μ is plotted in Fig. 1h. We see that this Λ crosses zero at the saddle-node bifurcation point, in agreement with Theorem 3. In addition, on the lower branch of the power curve (where the power slope is positive), $\Lambda > 0$, thus L_1 has a single positive eigenvalue; whereas on the upper branch of the power curve (where the power slope is negative), $\Lambda < 0$, thus L_1 has no positive eigenvalues. Then according to the generalized VK stability criterion [13], solitary waves on both branches of the power curve are linearly stable, in agreement with Theorem 2 and the numerical spectra in Fig. 1e, f.

Lastly, we have also checked numerically that zero is a simple discrete eigenvalue for both L_{10} and L_{00} (the zero eigenvalue being simple in L_{10} is already clear from Fig. 1h). In addition, $\langle u_0, \psi \rangle \neq 0$ and $\langle G_2, \psi^3 \rangle \neq 0$. Thus assumptions of Theorems 1–3 are all met, hence these theorems apply to this example.

In saddle-node bifurcations in Eq. (1), solitary waves sometimes possess a non-zero minimum power, and the power curve assumes a slanted U-shape [7, 13]. In some reports of such bifurcations, the two solution branches were marked with opposite stability, giving readers the impression that stability switching occurs at the saddle-node bifurcation point (see [7], Fig. 3). Those markings contradict our Theorem 2 and are incorrect. What happens is that the stability switching actually occurs at the power minimum point (see [13], Sect. 5.4). Since this power minima is often very close to the saddle-node bifurcation point, one might get the wrong impression of stability switching at the saddle-node bifurcation instead. In the next example, we will clarify this issue explicitly.

Example 2 In this example, we consider the NLS equation with an asymmetric double-well potential,

$$iU_t + U_{xx} - V(x)U + |U|^2 U = 0, \tag{50}$$

where the asymmetric potential $V(x)$ is taken as

$$V(x) = -3.5\mathrm{sech}^2(x + 1.5) - 3\mathrm{sech}^2(x - 1.5) \tag{51}$$

and is shown in Fig. 2a. Solitary waves in this conservative system are of the form (2), where $u(x)$ is a real localized function. A family of solitary waves with more of their energy located at the right (shallower) potential well exists (see Fig. 2c), and their power curve is shown in Fig. 2b. It is seen that this power curve exhibits a slanted U-shape with a non-zero minimal power, and a saddle-node bifurcation occurs. We have determined the linear stability of these solitary waves and the results are indicated on the power curve of Fig. 2b (with solid blue for stable waves and dashed red for unstable ones). From first sight, one may see that the lower branch is stable and the upper one unstable, thus stability switching seems to occur at the saddle-node bifurcation point (as Fig. 3 of [7] conveys to the reader). However, when we amplify the bifurcation region of the power curve (see Fig. 2d), we find that stability switching actually occurs at the minimum-power point (as explained in [13]) rather than the saddle-node bifurcation point. Indeed, from the spectra for solitary waves on the lower and upper branches very close to the saddle-node bifurcation point (see Fig. 2e, f), we see that both waves are linearly unstable, thus there is no stability switching at the saddle-node bifurcation, in agreement with Theorem 2.

6 Extension to Complex Potentials

In this section, we extend the above results to complex potentials, i.e., the function $F(\cdot,\cdot)$ in (1) is complex-valued. In this case, if F admits parity-time (PT) symmetry

$$F^*(|U|^2, \mathbf{x}) = F(|U|^2, -\mathbf{x}),$$

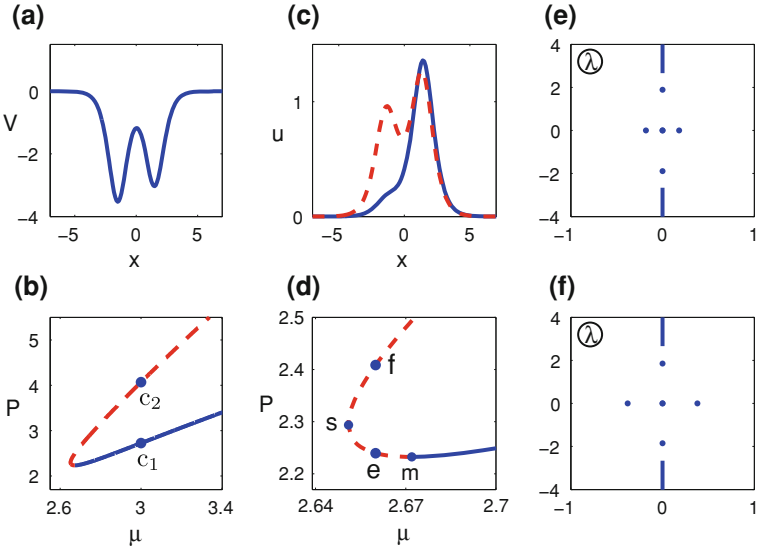

Fig. 2 Saddle-node bifurcation and linear-stability behaviors of solitary waves in Example 2. **a** Potential (51); **b** power curve of solitons (*solid blue* and *dashed red* represent stable and unstable solitons respectively); **c** profiles of solitons at points 'c_1, c_2 ' of (**b**), with *solid blue* for point c_1 and *dashed red* for point c_2; **d** amplification of the power curve in (**b**) near the bifurcation point; point 'm' is the power minimum, and point 's' is the bifurcation point; **e**, **f** stability spectra of solitons at points marked by letters 'e, f' in (**d**)

then solitary waves (2) can still exist over a continuous range of real μ values [17, 18], and saddle-node bifurcations can also occur. By slightly modifying the previous analysis, we can show that there is no stability switching at saddle-node bifurcations in these nonconservative systems either. Details of these slight modifications will not be presented here. For our purpose, it would suffice to present a numerical example.

Example 3 We still consider Eq. (48) in Example 1 but now with a complex PT-symmetric localized potential

$$\begin{aligned} V(x) = &-3\left[\operatorname{sech}^2(x+1.5)+\operatorname{sech}^2(x-1.5)\right] \\ &+0.25i\left[\operatorname{sech}^2(x+1.5)-\operatorname{sech}^2(x-1.5)\right], \end{aligned} \tag{52}$$

see Fig. 3a. This nonconservative system still admits solitary waves (2) for continuous real ranges of μ, but $u(x)$ is complex-valued now. We have numerically obtained a family of these solitons by the Newton-conjugate-gradient method applied to a normal equation [13], and the power curve of these solitons is plotted in Fig. 3b. Again a saddle-node bifurcation can be seen at $\mu_0 \approx 2.02$. For solitary waves on the lower and upper branches near this bifurcation point (see Fig. 3c, d), their stability spectra lie entirely on the imaginary axis (see Fig. 3e, f), indicating that they are all linearly stable. Hence no stability switching occurs at saddle-node

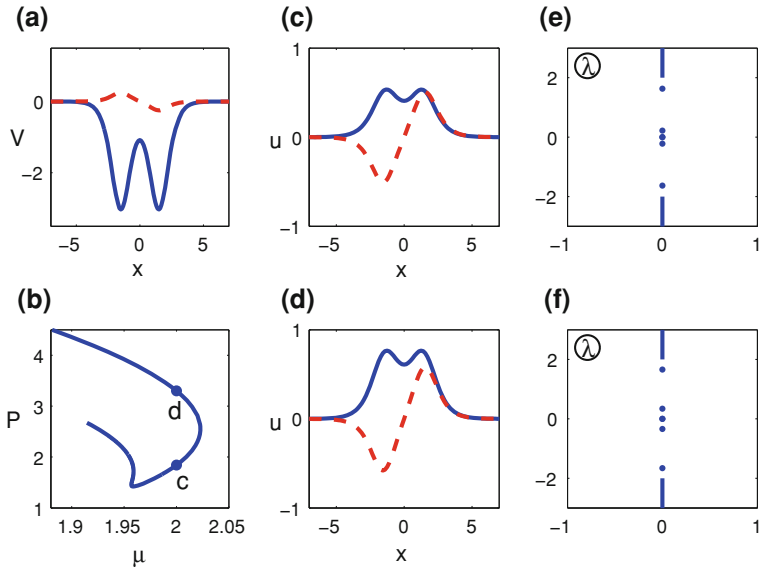

Fig. 3 Saddle-node bifurcation and linear stability of solitons in PT-symmetric potentials of Example 3. **a** PT potential (52); *solid blue* is the real part of the potential and *dashed red* is the imaginary part; **b** power curve of solitons; **c**, **d** soliton profiles at points 'c, d' in (**b**); *solid blue* is the real part of u and *dashed red* is the imaginary part; **e**, **f** stability spectra of solitons in (**c**, **d**)

bifurcations in this nonconservative system either. For this system, the zero eigenvalue of all solitons on the power curve also has algebraic multiplicity two as in the previous two examples. This explains why no zero-eigenvalue bifurcation occurs in this case either.

7 Summary and Discussion

In summary, we have derived analytical conditions for saddle-node bifurcations of solitary waves in generalized NLS equations (1) with arbitrary nonlinearities and potentials. More importantly, we have shown, both analytically and numerically, that for real as well as complex potentials, stability of solitary waves does not switch at saddle-node bifurcations. This disproves a wide-spread belief that such stability switching should always occur in nonlinear partial differential equations. We have also shown that for positive solitary waves in Eq. (1), this absence of stability switching at a saddle-node bifurcation is consistent with the generalized Vakhitov–Kolokolov stability criterion. Since the generalized NLS equations (1) arise frequently in nonlinear optics, Bose–Einstein condensates and other physical disciplines, our finding could have broad impact.

How can one reconcile our result of no-stability-switching in the generalized NLS equations (1) with the widely accepted result of stability switching in finite-

dimensional dynamical systems? One might argue that Eq. (1) is an infinite-dimensional dynamical system, thus results from finite-dimensional dynamical systems do not apply. While this explanation sounds reasonable, it is not the key reason in our opinion. We believe the key reason is that, when the result of stability switching is derived in finite-dimensional dynamical systems, it is always assumed that zero is a simple eigenvalue of the Jacobian (linearization) matrix of the system at a saddle-node bifurcation point (see Ref. [1], Theorem 3.4.1, Hypothesis SN1). For the generalized NLS equations (1), the counterpart of this Jacobian matrix is the linearization operator $\mathcal{L}_0$ defined in Eq. (23), but zero is *not* a simple eigenvalue of $\mathcal{L}_0$ in view of Eq. (25). Thus the assumption for stability switching is not met in our system, hence our result of no stability switching does not contradict that in finite-dimensional dynamical systems.

This work is supported in part by the National Science Foundation and the Air Force Office of Scientific Research.

References

1. J. Guckenheimer, P. Holmes, *Nonlinear Oscillations, Dynamical Systems, and Bifurcations of Vector Fields*. (Springer, New York, 1990)
2. B. Buffoni, A.R. Champneys, J.F. Toland, Bifurcation and coalescence of a plethora of homoclinic orbits for a Hamiltonian system, J. Dyn. Differ. Equ. **8**, 221 (1996)
3. T.S. Yang, T.R. Akylas, On asymmetric gravitycapillary solitary waves. J. Fluid Mech. **30**, 215 (1997)
4. M. Chen, Solitary-wave and multi-pulsed travelling-wave solutions of Boussinesq systems. Appl. Anal. **75**, 213 (2000)
5. J. Burke, E. Knobloch, Homoclinic snaking: Structure and stability. Chaos **17**, 037102 (2007)
6. G. Herring, P.G, Kevrekidis, R. Carretero–Gonzalez, B.A. Malomed, D.J. Frantzeskakis, A.R. Bishop. Trapped bright matter–wave solitons in the presence of localized inhomogeneities, Phys. Lett. A **345**, 144 (2005)
7. T. Kapitula, P. Kevrekidis, Z. Chen, Three is a crowd: Solitary waves in photorefractive media with three potential wells. SIAM J. Appl. Dyn. **5**, 598 (2006)
8. A. Sacchetti, Universal critical power for nonlinear Schrodinger equations with symmetric double well potential. Phys. Rev. Lett. **103**, 194101 (2009)
9. T.R. Akylas, G. Hwang, J. Yang, From nonlocal gap solitary waves to bound states in periodic media. Proc. Roy. Soc. A **468**, pp. 116–135 (2012)
10. I.M. Merhasin, B.V. Gisin, R. Driben, B.A. Malomed, Finite-band solitons in the Kronig–Penney model with the cubic-quintic nonlinearity. Phys. Rev. E **71**, 016613 (2005)
11. F. Dalfovo, S. Giorgini, L.P. Pitaevskii, S. Stringari, Theory of Bose–Einstein condensation in trapped gases. Rev. Mod. Phys. **71**, 463 (1999)
12. Y.S. Kivshar, G.P. Agrawal, *Optical Solitons: From Fibers to Photonic Crystals* (Academic Press, San Diego, 2003)
13. J. Yang, *Nonlinear Waves in Integrable and Nonintegrable Systems* (SIAM, Philadelphia, 2010)
14. Y.V. Kartashov, B.A. Malomed, L. Torner, Solitons in nonlinear lattices. Rev. Mod. Phys. **83**, 247–306 (2011)
15. N.G. Vakhitov, A.A. Kolokolov, Stationary solutions of the wave equation in a medium with nonlinearity saturation, Izv. Vyssh. Uchebn. Zaved., Radiofiz. **16**, p. 1020. [Radiophys. Quantum Electron. 16, p. 783 (1973)]

16. Z. Birnbaum, B.A. Malomed, Families of spatial solitons in a two-channel waveguide with the cubic–quintic nonlinearity. Physica D **237**, 3252 (2008)
17. C.M. Bender, S. Boettcher, Real spectra in non-Hermitian Hamiltonians having PT symmetry, Phys. Rev. Lett. **80**, 5243 (1998)
18. S. Nixon, L. Ge, J. Yang, Stability analysis for solitons in PT-symmetric optical lattices, Phys. Rev. A **85**, 023822 (2012)

Escape Time of Josephson Junctions for Signal Detection

P. Addesso, G. Filatrella and V. Pierro

Abstract In this Chapter we investigate with the methods of signal detection the response of a Josephson junction to a perturbation to decide if the perturbation contains a coherent oscillation embedded in the background noise. When a Josephson Junction is irradiated by an external noisy source, it eventually leaves the static state and reaches a steady voltage state. The appearance of a voltage step allows to measure the time spent in the metastable state before the transition to the running state, thus defining an escape time. The distribution of the escape times depends upon the characteristics of the noise and the Josephson junction. Moreover, the properties of the distribution depends on the features of the signal (amplitude, frequency and phase), which can be therefore inferred through the appropriate signal processing methods. Signal detection with JJ is interesting for practical purposes, inasmuch as the superconductive elements can be (in principle) cooled to the absolute zero and therefore can add (in practice) as little intrinsic noise as refrigeration allows. It is relevant that the escape times bear a hallmark of

An erratum to this chapter is available at 10.1007/10091_2012_21.

P. Addesso (✉)
Department of Electronic and Computer Engineering, University of Salerno, Via Ponte Don Melillo, 1, 84084, Fisciano, Italy
e-mail: paddesso@unisa.it

G. Filatrella
Department of Sciences for Biological, Geological, and Environmental Studies and Salerno unit of CNSIM, University of Sannio, Via Port'Arsa 11, 82100, Benevento, Italy
e-mail: filatrella@unisannio.it

V. Pierro
Department of Engineering, University of Sannio, Corso Garibaldi, 107, 82100, Benevento, Italy
e-mail: pierro@unisannio.it

Progress Optical Sci., Photonics (2012): 657–678
DOI: 10.1007/10091_2012_9

Published Online: 3 July 2012

the noise itself. The spectrum of the fluctuations due to the intrinsic classical (owed to thermal or environmental disturbances) or quantum (due to the tunnel across the barrier) sources are different. Therefore, a careful analysis of the escape times could also assist to discriminate the nature of the noise.

1 Introduction

The Josephson effect, early observed in superconductivity [4], essentially consists in particles tunneling between two weakly coupled systems, each described by a macroscopic wave functions. The effect is for instance observed when two superconductors are placed close enough (few nanometers) to let the bosonic waveforms of the charge carriers (Cooper's pairs) overlap. However, The effect is generic, and has been predicted [28] and observed [39] also between Bose-Einstein bosonic condensates [15]. The main features of the Josephson effect in superconductivity are the possibility of a non dissipative flow of Cooper's pairs from one superconductor to the other (the so called d.c. Josephson effect) and the appearance of a voltage proportional to the derivative of the phase difference between the superconductors' wave functions (the a.c. Josephson effect). The two effects give rise to a nonlinear device, a Josephson Junction (JJ). A Josephson Junction (JJ) can be used as a threshold detector [13, 46], i.e. as a device capable to discriminate a signal with a sharp transition from a state to another [1, 23]. Threshold detection is a suboptimal tool in signal processing, because in typical applications the optimal choice is linear matched filtering. However in some circumstances analogue devices might prove competitive, for optimal strategies cannot be efficiently implemented, when: (i) the amount of data necessary to claim a detection at very low Signal to Noise Ratio (SNR) is too high (such as all-sky all-frequency search of gravitational wave emitted by a pulsar [34, 49]); (ii) the amplitude of the signal is too low, and amplification introduces a significant additional noise; (iii) the frequency band of the signal falls in the THz range, where standard digital sampling procedures fails (e.g. THz sensing [45]).

When numerical analysis of the sampled data is impractical one should resort analogue techniques. A hysteretic JJ can be employed as signal detector, because a sinusoidal waveform corrupted by noise eventually forces the junction to switch from the zero voltage to a finite voltage state. The switch occurs when the gauge invariant phase crosses a threshold: the maximum of the potential that hooks the phase in the superconducting state. The appearance of a voltage step thus flags that the JJ phase has exceeded the threshold and makes it possible to measure how much time the JJ has been in the superconducting state before to overcome the energy barrier. The measure of the escape time in JJ is a well established technique, inasmuch it has been for more than 50 years a standard tool to characterize the properties of the metastable state [3]. For instance it has been employed to prove the existence of Macroscopic Quantum Tunneling (MQT) [17], i.e. the

possibility that the escape occurs even at zero temperature for the quantum nature of the Josephson phase [10].

The behaviour of the Josephson phase cannot be directly observed, it is just possible to detect the change of the voltage (proportional to the phase derivative) associated with the passage over the barrier. Moreover, it is not possible to recover the Josephson phase sampling the derivative (i.e. the junction voltage).In fact the measured signal is altered by the application of a very selective filtering stage to avoid that environmental noise reaches the device. Moreover, voltage oscillations fall on a frequency scale (close to the Josephson frequency) outside the band of conventional electronic devices. Thus it makes good-sense to assert that the available information is to be confined to the escape time.

From the point of view of data analysis, a further loss of information occurs when the analysis of the escape time sequence is limited to the average lifetime. Apart from the simplicity of the analysis, so much information can be depleted because the average escape time retains most of the physics of the escape from a static potential. In fact in Kramer theory [50] the average escape time is related to the most important parameter of the escape process, the ratio between the potential well and the intensity of the fluctuations. Recently, suitable statistics (e.g. variance and skewness) of the lifetime distribution have been analyzed to highlight the Poissonian nature of the process [48] or to detect the transition from the under-damped to moderately damped regime [20, 42]. Detection theory allows to take a further step and to exploit the full distribution of the escape times to improve the performances of the JJ as a detector [1]. In this Chapter after the discussion of the JJ model (Sect. 2), we will show how the analysis of the distribution of the escape times can be performed with the methods of signal processing (Sect. 3) The main features of detectors based on JJ are described in Sect. 4. In Sect. 5 we discuss about some practical issues in real experimental scenarios together with a brief discussion about the possibility of distinguishing between the quantum or classic nature of the noise. The last Sect. 6 is, as usual, devoted to the conclusions.

2 Physical Model of a JJ Detector

The dynamic variable of a JJ is the gauge invariant superconducting phase, φ, ruled by the celebrated Josephson equations [4]:

$$\begin{aligned} I &= I_c \sin(\varphi) \\ V &= \frac{\hbar}{2e}\frac{\mathrm{d}\varphi}{\mathrm{d}t} \end{aligned} \tag{1}$$

I_c denotes the Josephson critical current, or the maximum current of Cooper's pairs (whose charge is $2e$) which can tunnel without an applied voltage. However, a practical device is far more complicated than this. First, a real junction is also characterized by a resistance and a capacitance, second the JJ is dc and ac biased,

and third the environment at finite temperature disturbs the junction with noise. The resulting Langevin model equation of a JJ biased with a sinusoidal signal corrupted by additive noise $\xi(t)$ and subject to thermal fluctuations $n(t)$ reads [23]:

$$\frac{C\hbar}{2e}\frac{\mathrm{d}^2\varphi}{\mathrm{d}t^2}+\frac{\hbar}{R2e}\frac{\mathrm{d}\varphi}{\mathrm{d}t}+I_c\sin(\varphi)=I_b+S_0\sin(\Omega t+\varphi_0)+\sqrt{D}\xi(t)+\sqrt{k_BT/R}\,n(t). \tag{2}$$

Here C and R are the capacitance and the resistance of the JJ, respectively (we consider JJ in the underdamped regime, i.e. that the capacitance is not negligible). Furthermore I_b is the dc bias current, S_0 the amplitude of the ac term of frequency Ω and initial phase φ_0. In Eq. (2) two random terms appear: $\xi(t)$, with intensity $\sqrt{D}$, that represents an additive noise corrupting the external signal and $n(t)$, with intensity $\sqrt{k_BT/R}$, that represents thermal current (k_B denotes the Boltzmann constant and T the temperature). The terms $\xi(t)$ and $n(t)$ are white Gaussian noise stochastic processes, whose correlators read $<n(t)n(t')>=2\delta(t-t')$, and $<\xi(t)\xi(t')>=2\delta(t-t')$. For signal detectors it is important that in Eq. (2) thermal fluctuations $\sqrt{k_BT/R}$ can be neglected with respect to the signal noise intensity $\sqrt{D}$. In fact JJ can be cooled down at a temperature T much below the signal noise temperature viz. $T\ll DR/k_B$, an assumption that we will retain for the remaining of the Chapter.

The low temperature condition is favored when the junction resistance is high (i.e. when dissipation is low) because Eq. (2) is based on a parallel lumped circuit model (see the inset to Fig. 1).

To assume that the signal is corrupted only by an additive term is a simplification: noise can affect the signal in several ways, for instance as a multiplicative noise [40, 41] or phase and frequency fluctuations [29]. In the following we will limit our analysis to the standard additive noise case; however we expect that the results can be indicative of the behavior also for other noise sources. For instance frequency fluctuations of the JJ driving signal can be treated, in some limits, as an additive noise [22]. A special mention is deserved to the role of quantum fluctuations. Tunneling of the macroscopic phase φ has been demonstrated in early measurements [16, 18] as a saturation of the escape times at very low temperatures. The experiments are performed while decreasing the bath temperature to reduce the fluctuations; if one eventually observes a constant escape rate in spite of the change in temperature, it is concluded that the rate itself should be due to some other fluctuation source, such as MQT. It has been shown that quantum fluctuations contribute as an equivalent thermal source of temperature $\theta^*=e\omega_J/(\pi I_c)$ [2] where $\omega_J=[2eI_c/(\hbar C)]^{1/2}$ is the characteristic frequency (called the Josephson frequency). If only the average escape time is considered, quantum noise and stochastic effects are nearly equivalent, with the fundamental difference that quantum noise is unavoidable and operates also in the zero temperature limit. Further details about the differences between quantum and classical noise will be reported in Sect. 3.

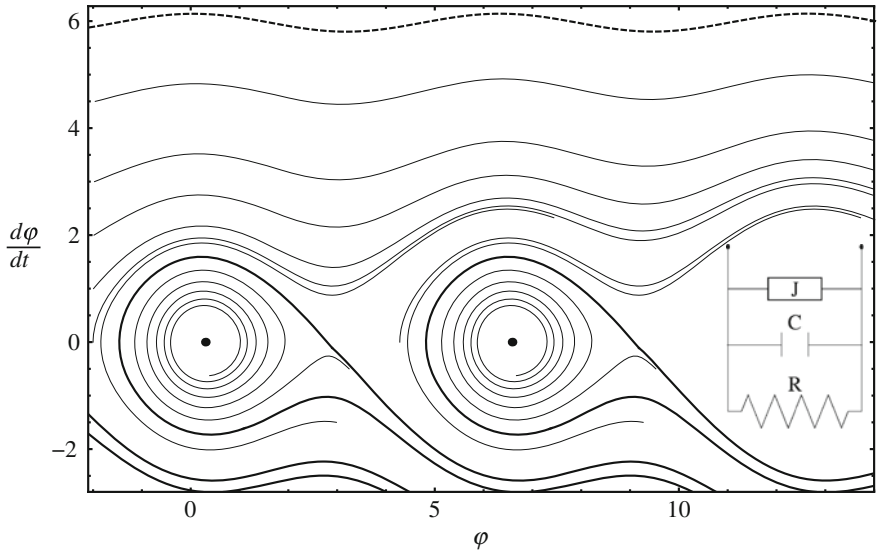

Fig. 1 Phase plane portrait of Eq. (4) for $\gamma = 0.3$, $\alpha = 0.05$, $\varepsilon = \varepsilon_n = 0$. Thin curves denote the phase lines, while the solid thick curves denote the separatrix between the asymptotic running state (dashed curve) and the static solution (thick dots). The symbol + denotes the instable fix point. The inset shows the electric circuit model of Eq. (2)

We recast Eq. (2) introducing the dimensionless time $\tau = \omega_J t$, normalized with respect to ω_J. Dividing for the critical current I_c, and rearranging the terms, Eq. (2) reads

$$\frac{\mathrm{d}^2\varphi}{\mathrm{d}\tau^2} + \frac{\omega_J}{RI_c}\frac{\hbar}{2e}\frac{\mathrm{d}\varphi}{\mathrm{d}\tau} + \sin(\varphi) = \frac{I_b}{I_c} + \frac{S_0}{I_c}\sin(\frac{\Omega}{\omega_J}\tau + \varphi_0) + \frac{\sqrt{\omega_J D}}{I_c}\tilde{\xi}(\tau), \qquad (3)$$

where the correlator reads $<\tilde{\xi}(\tau)\tilde{\xi}(\tau') > = 2\delta(\tau - \tau')$. With the definitions $\gamma = I_b/I_c$ as the normalized bias current, $\alpha = (\omega_J/RI_c)(\hbar/2e)$ as the normalized dissipation, $\varepsilon = S_0/I_c$ as the normalized signal amplitude and $\sqrt{\varepsilon_n} = \sqrt{(\omega_J D/I_c^2)}$ as the normalized noise intensity, Eq. (3) becomes:

$$\frac{\mathrm{d}^2\varphi}{\mathrm{d}\tau^2} + \alpha\frac{\mathrm{d}\varphi}{\mathrm{d}\tau} + \sin(\varphi) = \gamma + \varepsilon\sin(\omega\tau + \varphi_0) + \sqrt{\varepsilon_n}\tilde{\xi}(\tau). \qquad (4)$$

Eq. (4) is a well established framework for periodically driven stochastic systems [35]. The analysis of the asymptotic or stationary states can be performed with the analysis of the corresponding Fokker-Planck equation [50]. Unfortunately, to profitably apply the methods of signal detection it is important to accurately know the distribution of the shortest escape times, which is not easily retrieved from the analysis of the Fokker Planck equation.

The schematic of the physics of the device is depicted in Fig. 1 by the zero noise limit phase plane of Eq. (4). The thick line is the separatrix between confined

oscillations and running states. In fact a JJ is also a practical realization of the prototypal washboard potential

$$U(\varphi) = -\gamma\varphi - \cos(\varphi). \tag{5}$$

For $\gamma < 1$ Eq. 4) gives rise to a barrier [4, 7]:

$$\Delta U(\gamma) = 2[\sqrt{1-\gamma^2} - \gamma \cos^{-1}(\gamma)]. \tag{6}$$

If the oscillating current is zero ($\varepsilon = 0$) for low noise ($\varepsilon_n << \Delta U$) escape occurs at a rate r_K [50]

$$r_K \propto T_K^{-1} \exp\left(-\frac{\Delta U}{\varepsilon_n}\right). \tag{7}$$

Such a rate is related to the average escape time $\mu_0 = 1/r_K$ and T_K is the Kramer prefactor [50]. The individual escape times can be directly measured in a variety of conditions [55, 16], including high-Tc superconductors [5, 6]; in the case of underdamped JJ ($\alpha < 1$) when the system overcomes the energy barrier ΔU, it switches from the locked state to a finite voltage running state [4]:

$$\frac{< V >}{V_0} = < \frac{\mathrm{d}\varphi}{\mathrm{d}\tau} > \simeq \frac{\gamma}{\alpha}, \tag{8}$$

where $< \cdot >$ indicates the temporal moving average and the voltage is normalized with respect to $V_0 = \hbar\omega_J/2e$. The efficiency of this voltage switching is less evident for moderately damped (i.e. $0.25 < \alpha < 1$) JJ, when the Josephson phase after the passage over the barrier could be retrapped in another well by the noise (this corresponds in Fig. 1 to cross the separatrix in the reverse direction, from the running to the static state) [42].

The escape process is illustrated in Fig. 2 : The Josephson phase φ fluctuates at the bottom of the washboard potential until it is driven across the separatrix (the vertical line) and the running state is reached. The elapsed time is the escape time τ_i of the metastable state.

The acquisition of escape times is a process that should be carefully performed to retain maximal information about the presence of signal. In particular, the initial phase is a crucial parameter because the signal to noise mixture can be applied to the JJ in different ways [23, 56] to acquire the escape time sequence $\underline{\tau} = \{\tau_i\}_{i=1}^N$. Indeed, after the JJ has switched to the running state there are a variety of methods to reset the system. If the frequency of the signal is perfectly known, in principle it is possible to reapply the signal with the same initial phase φ_0. This acquisition strategy is called coherent. To apply the signal again with the same initial phase some fraction of the signal is lost waiting for the correct time to restart the process (see Fig. 2).

When the frequency cannot be easily controlled or the time measurement precision is too low, another possibility arises, i.e. incoherent acquisition. It consists in reapplying the signal with any phase it might have after the reset

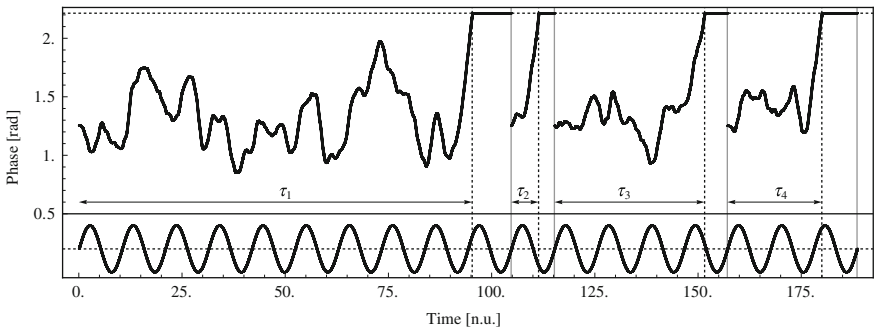

Fig. 2 Examples of the time dependent trajectories of the phase φ for the coherent acquisition strategy. The lower part of the figure shows the applied signal $\varepsilon \sin(\omega\tau + \varphi_0)$. The dotted vertical lines denote the transitions across the separatrix [the threshold is $\varphi = \pi - \sin^{-1}(\gamma)$] that determines the escape times $\tau_1, \tau_2, \ldots \tau_N$. After the switching has occurred, the JJ is restarted with static state initial condition ($\varphi = \sin^{-1}(\gamma)$, $d\varphi/d\tau = 0$) and the signal is applied with the same initial phase φ_0 (continuous vertical line). Parameters of the simulations are: $\gamma = 0.8$, $\alpha = 0.05$, $\varepsilon_N = 0.0175$. The signal parameters are: $\varepsilon = 0.05$, $\varphi_0 = 0$ and $\omega = 0.7$

procedure and therefore with an essentially random initial value of φ_0. We investigate two extreme experimental situations.

- Instantaneous signal reset: the initial phase coincides with the exit phase across the separatrix of the previous escape.
- Random signal reset: the initial phase is supposed uniformly distributed in $[0, 2\pi]$.

In both cases much of the information carried by the initial phase parameter is lost. In the next Section we analyze the escape time distributions and we use statistical decision theory to seek efficient methods for detection of noisy harmonic signals.

3 Detection Theory for Josephson Junctions Threshold Detection

Detection theory methods are aimed to discern the presence of a known waveform embedded in a random (noisy) background. In this framework the analysis of the escape times serves to discern if the time dependent bias, the right hand side of Eq. (4), consists of just the constant bias γ and the unavoidable noise $\sqrt{\varepsilon_n}\tilde{\xi}(t)$, or contains also a sinusoidal oscillation of amplitude ε, frequency ω and phase φ_0.

The system is characterized by a SNR related to the ratio $\varepsilon/\sqrt{\varepsilon_n}$, which weights the signal against the intensity of the noise correlations. In the language of signal detection one formulates two hypothesis:

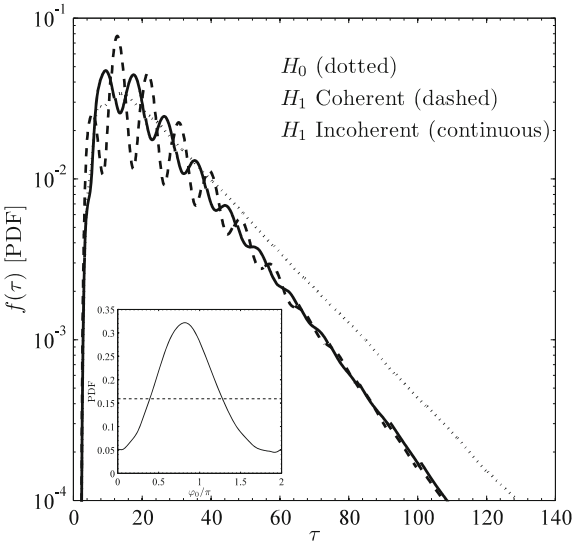

Fig. 3 PDFs of the escape times. The three curves represent: Signal absence (H_0 : dotted line); signal acquired by a coherent strategy (H_1 : dashed line); signal acquired by an incoherent strategy with instantaneous signal reset (H_1 : continuous line). The inset shows the PDFs of the signal initial phase φ_0 for the incoherent acquisition with instantaneous signal reset (continuous line), and with random signal reset (dashed line). Parameters of the simulations are: $\gamma = 0.8$, $\alpha = 0.05$, $\varepsilon_N = 0.0175$. The signal parameters are: $\varepsilon = 0.05$, $\varphi_0 = 0$ and $\omega = 0.7$

- H_0 : the JJ is uniquely driven by noise;
- H_1 : the JJ is driven by noise and a sinusoidal excitation.

If one collects the escape times, obtained with numerical simulations of Eq. (4) [43], it is possible to estimate the Probability Density Functions (PDF) as in Fig. 3 . Here we show three cases: (i) the signal is absent (H_0); (ii) the signal is present and escape times are acquired by the coherent strategy (H_1 coherent); (iii) the signal is present and escape times are acquired by the incoherent strategy with instantaneous signal reset (H_1 incoherent).

It is evident that the three curves have significantly distinct shapes, even if they share an exponential decay. In particular the PDFs related to the signal presence have approximately the same slope (i.e. the same average escape time), which differs from the slope of the H_0 hypothesis. Moreover both H_1 PDFs exhibit oscillations. The oscillations, related to the signal amplitude and frequency, are most evident for the coherent acquisition strategy. In the coherent case the oscillations also depend upon the signal initial phase φ_0. Noticeably, the incoherent acquisition with instantaneous signal reset exhibits oscillations due to a synchronization of the signal exit phase around π, as can be seen in the inset to Fig. 3 (more precisely the density is peaked around $4\pi/5$). These oscillations are

definitively smaller in the incoherent case with random signal reset (not shown in Fig. 3), which only preserves the same slope of the other two H_1 curves.

Several strategies can be designed to discriminate the presence from the absence of the sinusoidal signal. A starting point is that the PDF of the type shown in Fig. 3 are approximately exponential and exhibit a change of slope, i.e. the statistical average of escape times under the two hypotheses (say $\mu_0 = E[\tau|H_0]$ and $\mu_1 = E[\tau|H_1]$) are different. In this case, it is possible to use a detection strategy based on the Sample Mean (SM). In fact by averaging N identically distributed escape times $\underline{\tau} = \{\tau_i\}_{i\in[1,N]}$, it is possible to define a detector based on the following test:

$$\mathscr{A}(\underline{\tau}) = \frac{s}{N}\sum_{i=1}^{N}\tau_i \underset{H_0}{\overset{H_1}{\gtrless}} \zeta, \tag{9}$$

where $s = sign(\mu_1 - \mu_0)$ and ζ is a suitable threshold. The SM strategy, analyzed in detail in [23], has the great advantage of simplicity, but it is obviously suboptimal. Indeed in the coherent and the incoherent (with instantaneous signal reset) acquisition strategies escape time PDFs exhibit oscillations (see Fig. 3). Thus it is important to identify a strategy that fully exploits the information carried by the escape time statistics. the Neyman-Pearson lemma [51] indicates that an optimal strategy, based on the Likelihood Ratio Test (LRT), exists. The analysis can be performed by comparing the product of the ratio between the PDF, evaluated at the escape time samples τ_i, with and without the signal. If we denote by $f_{0,1}(\cdot)$ the PDFs of the escape times under the hypothesis $H_{0,1}$, the test can be written as:

$$\mathscr{A}(\underline{\tau}) = \frac{s}{N}\sum_{i=1}^{N}\tau_i \underset{H_0}{\overset{H_1}{\gtrless}} \zeta, \tag{10}$$

A useful transformation, by means of the log nonlinearity, leads to the statistics:

$$\Lambda(\underline{\tau}) = \frac{1}{N}\sum_{i=1}^{N}\log\left[\frac{f_1(\tau_i)}{f_0(\tau_i)}\right] \underset{H_0}{\overset{H_1}{\gtrless}} \zeta. \tag{11}$$

where the new threshold is $\zeta = \log(\zeta')/N$.

Optimality of the LRT concerns the minimization of the error rate. Two types of error assess the quality of a detector:

- the *false alarm probability* P_f, also known as Type I error probability, i.e. the probability to decide for the hypothesis H_1 when H_0 is true;
- the *miss probability* P_m, also known as Type II error probability, i.e. the probability to decide for the hypothesis H_0 when H_1 is true.

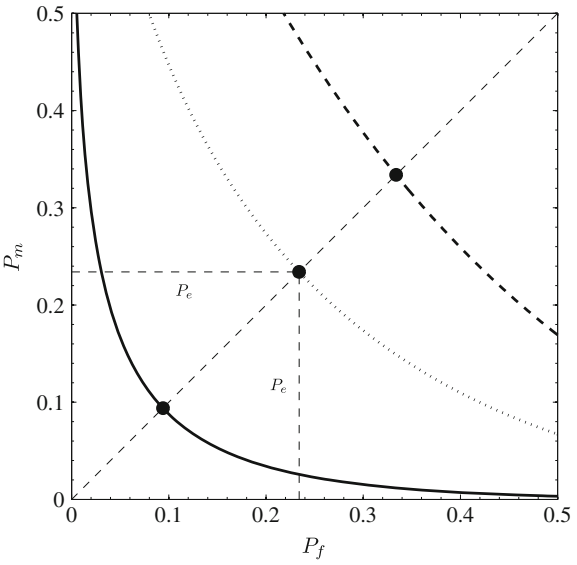

Fig. 4 Typical ROCs of a JJ based detector under the hypothesis of complete parameter knowledge. The three curves are related to: LRT Coherent(continuous line); LRT Incoherent with instantaneous signal reset (dotted line); SM Coherent (dashed line). Parameters of the simulations are: $\gamma = 0.8$, $\alpha = 0.05$, $\varepsilon_N = 0.0175$. The signal parameter are $\varepsilon = 0.05$ and $\omega = 0.7$. The simulations are performed setting the mean observation time under H_0, $E[T_{obs}|H_0] = 500$

Under the hypothesis that the JJ parameters (α and γ), the noise variance ε_n (which does not depend on the particular hypothesis in force) and the signal parameters (ε, ω and φ_0) are *perfectly known*, LRT minimizes, among all possible tests, the miss probability P_m at a fixed false alarm level P_f. In this framework, both P_f and P_m are functions of the threshold ζ. Thus a popular way to summarize the results of signal analysis is to compute the Receiver Operator Characteristic (ROC) of the test statistic, that is the plot of P_f versus P_m for different values of ζ.

A ROC example is presented in Fig. 4, in which the unavoidable trade-off between the two error probabilities is shown. The performance of the LRT strategies, especially in the case of coherent acquisition, are significantly better than the SM ones. For sake of clarity, we have shown only one SM curve (in the coherent case), because in the other cases the performances are approximately the same. Noticeably, due to the lack of oscillations, in the incoherent random signal reset case the SM detector performs as well as the LRT one. Indeed SM is the optimal strategy for exponential distributions because the sample mean is a sufficient statistic [51], and the statistics $\Lambda(\underline{\tau})$ and $\mathscr{A}(\underline{\tau})$ coincide.

To simplify the performance analysis of the detector we introduce a synthetic index. To this aim, we consider the intersection between the ROC and the bisector of the first quadrant angle, which is very close to the point of ROC curve with the minimum distance from the axis origin. At this point $P_f = P_m$, and we can unambiguously define the error rate $P_e \equiv P_f = P_m$, which is representative of the detector behavior[1].

[1] In ref. [1] it has been shown that, for large sample size N, it is possible to relate P_e with the well-known Kumar-Carrol index d_{KC} [36].

To characterize the detectors, it is necessary to specify the time T_{obs} in which the N escape times are collected. The average escape time depends upon the hypothesis in force, and so does the number of escapes collected in a fixed time interval. However, to properly use the LRT strategy in its classical formulation the sample size has to be *fixed*. We have adopted the solution to compute N with constant mean observation time under H_0 hypothesis, $E[T_{obs}|H_0]$. In the incoherent case with the instantaneous signal reset strategy, we have

$$N = \frac{E[T_{obs}|H_0]}{\mu_0}. \tag{12}$$

Equation (12) is to be changed for the coherent case because of the time lost to reset the signal with the same initial phase. This loss leads to the approximated relation [1]:

$$N \approx \begin{cases} \dfrac{E[T_{obs}|H_0]}{2\pi/\omega}, & \mu_0 \leq \dfrac{\pi}{\omega} \\ \dfrac{E[T_{obs}|H_0]}{\mu_0 + \pi/\omega}, & \mu_0 > \dfrac{\pi}{\omega} \end{cases} \tag{13}$$

In the incoherent case with random signal reset strategy, it is hard to map the mean observation time to a fixed number of escapes. To perform a fair comparison, we have supposed that no more of a signal period is lost. So the relationship is:

$$N = \frac{E[T_{obs}|H_0]}{\mu_0 + \pi/\omega}. \tag{14}$$

Another more challenging issue arises when using LRT that, as evident from the Eq. (11), improves detection by using the whole PDF. Unfortunately, the escape time distributions are not theoretically known for the system described by Eq. (4). Even in the case $S_0 = 0$ the Arrhenius law is approximately valid for rare escapes [17] (in the unperturbed oscillator time scale ω_J), while for fast escapes (that are interesting for signal analysis) only approximated analytical estimates exist [53]. When the signal is applied the knowledge of the escape time distributions is even poorer, and essentially limited to the overdamped case [9]. Thus we are compelled to numerically estimate the PDFs; however, it is possible to do better than just accumulate data with extensive simulations using a suitable non-parametric statistical technique, such as the Kernel Density Estimation (KDE) [54]. This technique generalizes the basic idea of histogram by means of a so-called Kernel function $K(\cdot)$, usually a symmetric PDF (we employ a standard normal distribution). For the random sample $\underline{X} = \{X_i\}_{i\in[1,N]}$ of size N the kernel estimator is

$$\widehat{g}(x) = \frac{1}{Nw}\sum_{i=1}^{N} K\left(\frac{x - X_i}{w}\right). \tag{15}$$

The parameter w is the *bandwidth* (also called *smoothing parameter*). The optimal choice for this parameter depends on the sample size, the kernel and the PDF which has to be estimated. In several scenarios it is computed by means of the relation

$$w = \left(\frac{4}{3}\right)^{1/5} \widehat{\sigma} N^{-1/5}, \tag{16}$$

where $\widehat{\sigma}$ is the sample standard deviation of the random sample. In applying this framework to escape times, we immediately encounter a first difficulty. Escape times are *positive*, i.e. the PDFs, under both hypothesis $H_{0,1}$, are:

$$f_j(t) = 0, \quad \forall t < 0. \tag{17}$$

On the contrary, Eq. (15) leads to an estimated PDF which does not satisfy the inequality (17). To go around this problem we can transform escape times $\underline{\tau} = \{\tau_i\}_{i\in[1,N]}$ according to

$$X = \log(\tau). \tag{18}$$

The obtained random sample $\underline{X} = \{X_i\}_{i\in[1,N]}$ can assume every value on the real axis and the PDFs $\widehat{g}_j(x)$ can be estimated with Eq. (15). Finally, the PDF $\widehat{f}_j(t)$ is obtained from $\widehat{g}_j(x)$ via

$$\widehat{f}_j(t) = \frac{\widehat{g}_j(\log(t))}{t}, \quad t > 0. \tag{19}$$

The procedure is applied to both PDFs, $\widehat{f}_0(\cdot)$ and $\widehat{f}_1(\cdot)$, with (H_1) and without (H_0) the deterministic signal. The estimates are finally inserted in the statistic, Eq. (11):

$$\widehat{\Lambda}(\underline{\tau}) = \frac{1}{N}\sum_{i=1}^{N} \log\left[\frac{\widehat{g}_1(\log(\tau_i))}{\widehat{g}_0(\log(\tau_i))}\right] \underset{H_0}{\overset{H_1}{>\atop<}} \zeta, \tag{20}$$

To obtain reliable estimations a large sample size ($\sim 5 \times 10^5$) has been used. We observe a slight over-smoothing, whose effect is some worsening of performances for LRT. Indeed the PDF oscillations, which contain most of the additional information with respect to the sample mean, are underestimated. This approach is to be considered *conservative*, because the presence of artifacts in the opposite under-smoothing case could artificially improve the LRT performances, leading to over-estimated results.

4 Josephson Junction Detector: Performance Evaluation

The application of the detection theory of Sect. 3 to JJ allows to improve the possibility of exploiting JJ to reveal signals. The quality of the detection—the parameter P_e—can greatly vary with the same noise-signal combination (or SNR) applied to JJ with different parameters (dissipation, capacitance, constant bias). Let us summarize the parameter region in which to expect the best detection performances. In discussing the basic Eq. (2), we have emphasized that JJ are characterized by four electrical quantities: the bias current I_b, the Josephson critical current I_c, the junction resistance R and capacitance C. The optimization of a JJ as a detector leads to the following results [1, 23]:

1. The dc current I_b can be assumed positive (for the symmetry of the problem) and below the critical current [to have two solutions, see Eq. (6)]: $0 \leq I_b \leq I_c$. In normalized units the interval reads $0 \leq \gamma \leq 1$. The optimal bias current I_b for the LRT strategy should be set as close as possible to $\gamma = I_b/I_c \simeq 1$ to achieve the lowest value of ΔU. For the SM strategy the currents should be set at an intermediate value that depends on the ratio between the energy barrier and the signal.
2. The critical current I_c normalizes (among the other quantities) the signal amplitude and noise, ε and ε_n, respectively. This normalization, as expected, does not change the SNR which is connected to $\varepsilon/\sqrt{\varepsilon_n}$. However it is found that, at a given level of SNR, larger normalized noise intensity favors detection. The limit for the parameter ε_n is to keep negligible the number of escapes of the system toward the higher local minima of the potential [see Eq. (5)], i.e. toward the stable points at the left in Fig. 1
3. The resistance R normalizes the dissipation parameter α. A low dissipation is beneficial because results in shorter average escape time, and therefore increases the statistic numerosity at a fixed length of the analyzed signal.
4. The capacitance C determines the normalized frequency $\omega = \Omega/\omega_J$ of the signal. The best performances occur around the geometrical resonance of Eq. (4), $\omega \simeq \omega_{res}$, for both LRT and SM. JJ are therefore best suited for signals whose frequency is in the range $10 - 1000\,GHz$.

The last property, the behavior of the JJ detector as a function of external signal frequency deserves special attention. It amounts to use the JJ as a nonlinear filter, with a peculiar resonance figure. In Fig. 5 it is displayed the error rate P_e for the coherent SM an LRT strategy, compared with the same error for the incoherent detection strategy in the instantaneous signal reset case.

Figure 5 clearly indicates that a minimum error probability occurs at the resonance frequency (e) determined through linearization of Eq. (4) for small signal amplitude ε [4]:

$$\omega_{res} \simeq \left(1 - \gamma^2\right)^{1/4}. \tag{21}$$

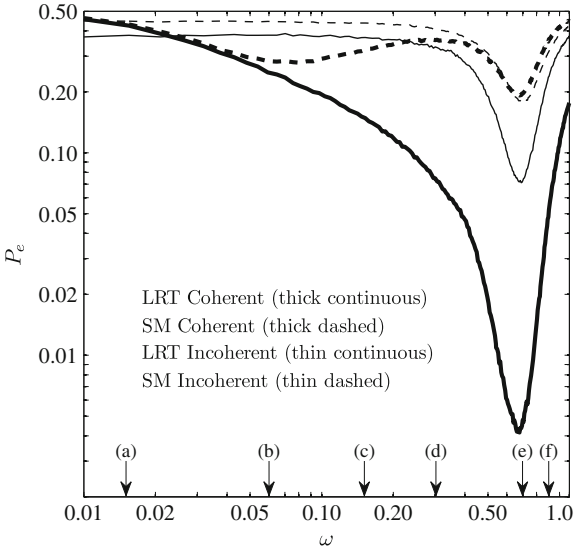

Fig. 5 The error rate P_e versus the angular velocity ω of the applied signal. The curves represent: LRT Coherent (thick continuous line); SM Coherent (thick dashed line); LRT Incoherent with instantaneous signal reset (thin continuous line); SM Incoherent with instantaneous signal reset (thin dashed line). The labeled arrows indicate the frequencies of the PDF shown in Fig. 6. Parameters of the simulations are: $\gamma = 0.8$, $\alpha = 0.05$, $\varepsilon_N = 0.0175$. The signal parameter are $\varepsilon = 0.05$ and $\varphi_0 = 0$. The mean observation time under H_0 is $E[T_{obs}|H_0] = 2000$

For non vanishing ε nonlinear corrections to the second order Taylor expansion tune the resonance: $\omega_{res} = \omega_{res}(\varepsilon)$ [32]. The analysis of JJ detectors confirms the dependence predicted by Eq. (21); there exists a suitable neighborhood of ω_{res} that is one of the best regions for detection purpose, with a small correction for the finite signal amplitude. The phenomenon is associated with a multivalued resonance curve of the non linear plasma frequency [37]. It is remarkable, to our opinion, that best detection performances (in terms of error probability P_e) are reached in the same strongly non linear distortion regime as in amplifiers [58].

Focusing on the coherent case, we note that for SM strategy a second interesting region occurs at a lower normalized signal frequency ω_{SR} (see (b) in Fig. 5), where another resonance appears at a frequency that can be also much smaller than the geometric resonance. The position of this resonance dip depends upon the phase and signal temperature [23], so it can be considered a stochastic resonance [8, 26, 27, 44] or resonant activation [19, 21, 57]. In Ref. [23] it has been found that a region of optimal detection is pinpointed if the potential well barrier (tuned by γ), the normalized signal frequency ω and the normalized noise intensity ε_n are connected by the relation ($C(\varphi_0)$ is a function of the initial phase φ_0 and μ_0 is the average escape time under the hypothesis H_0):

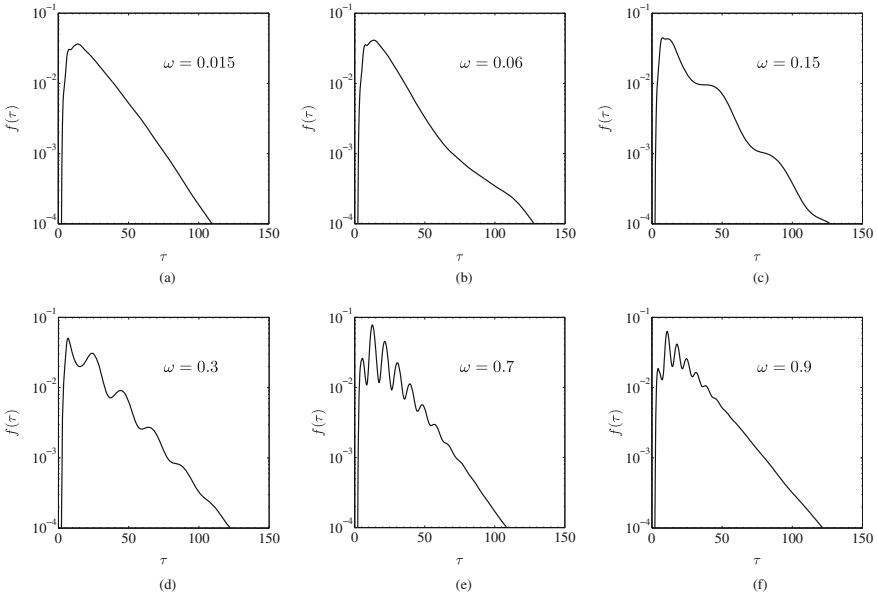

Fig. 6 PDFs of the escape times acquired by means of the coherent strategy at different applied frequency (see the arrows at the bottom of Fig. 5). **a** $\omega = 0.015$. **b** $\omega = 0.06$ (stochastic resonance). **c** $\omega = 0.15$. **d** $\omega = 0.3$. **e** $\omega = 0.7$ (geometric resonance). **f** $\omega = 0.9$. Parameters of the simulations are the same as in Fig. 5

$$\omega_{SR} = \frac{\mu_0}{2\pi C(\varphi_0)} \exp\left\{ \frac{2}{\varepsilon_n} \left[\sqrt{1-\gamma^2} - \gamma \cos^{-1}(\gamma) \right] \right\}. \tag{22}$$

Below the stochastic resonance frequency the PDFs computed under H_1 and H_0 are very similar, while above this frequency the PDFs computed under H_1 develop oscillations (see Fig. 6). This explains the disappearance of stochastic resonance of Eq. (22) in the coherent LRT detection framework, for LRT exploits the PDFs oscillations and does not deteriorate above the frequency (22). To see this, let us imagine to increase the applied frequency ω around ω_{SR}, marked by the label (b) in Fig. 5. The analysis of the PDF of Fig. 6 reveals that the curves shown in Fig. 5 have an intuitive explanation. In fact the crucial passages across the SR (Fig. 6a,b,c) and the geometric resonance (Fig. 6d,e,f) are marked by a qualitative change of the PDF. At the SR frequency ω_{SR} (Fig. 6b) the slope (and hence the average escape time) is most changed, while above ω_{SR} (Fig. 6b) the oscillations are clearly visible. This is the reason why, in the coherent case, SM and LRT methods have so different behaviors. Indeed coherent SM, that just detects the average, is most sensible to the changes of the slope and exhibits a minimum (i.e. best performances) in correspondence of this point. Conversely LRT, that takes into account "all" details of the PDF's, can improve even when the first momentum ceases to be an effective statistics for hypothesis discrimination. For completeness, let us point out that inspection of Eq. (22) reveals that ω_{SR}

decreases when the normalized noise intensity ε_n increases, and therefore a fixed value of the external applied frequency has the effect to increase the efficiency of the SM. Such paradoxical increase of the performances increasing the noise level for the SM is solved by the observation that the improvement obtained at the ω_{SR} frequency can be outperformed by the choice of a more refined detection strategy (the LRT) that takes into account the PDFs oscillations. In this sense it is not really possible to improve detectors increasing the noise. Indeed, see Fig. 5, the coherent SM detector performances are always worse than the coherent LRT performances, and this also confirms the general idea that stochastic resonance is a consequence of a suboptimal detection scheme [25]. The practical consequence is that synergetic effects leading to stochastic resonance between noise and signal in JJ devices can only be exploited in suboptimal strategies such as SM, while in optimal detection strategies noise should only be reduced as much as the experimental set up allows.

Turning to the incoherent detection strategies, it is evident that their performances are worse than the corresponding coherent ones [23]. In any case, due to the residual oscillation of the PDF under H_1 hypothesis, the LRT approach guarantees better performances than the SM for the instantaneous signal reset case. Moreover, it is remarkable that the stochastic activation phenomenon disappears for SM, as a consequence of the reshuffling of the initial phase in the reset procedure of the JJ.

Performances for the random signal reset case are not shown in Fig. 5. However the SM incoherent curve represents quite well the behavior of both SM and LRT. As expected, LRT does not significantly improve the SM, due to the absence of oscillations.

In the above performed analysis we have fixed both the average time observation window $E[T_{obs}|H_0]$ and the SNR (related to the ratio $\varepsilon/\sqrt{\varepsilon_n}$). On the other hand, they strongly affect the error rate; for large sample size N the error rate can be expressed as [1]:

$$P_e = \frac{1}{2}\mathrm{erfc}\left[B_Y\sqrt{E[T_{obs}|H_0]}\left(\frac{\varepsilon}{\sqrt{\varepsilon_n}}\right)^{\eta_Y}\right] \tag{23}$$

where B_Y and η_Y depend on the particular detection strategy ($Y = \mathscr{A}, \Lambda$, for the SM and LRT respectively). If we focus on the scaling law index η_Y, it is remarkable that, for the coherent LRT case, it exhibits the *nearly optimal* behaviour $\eta_\Lambda \approx 1$. Indeed this is also the behaviour of the *ideal* matched filter that directly analyzes the signal (and not the escape times) and that attains the optimal detection performance [33]. The proposed LRT coherent strategy never outperforms the matched filter, because the value of B_Λ is not optimal [1]. The performances of SM strategy are poorer, especially for small signals, because $\eta_{\mathscr{A}} \approx 3/2$, as shown in [23]. This type of analysis can be reformulated in more intuitive fashion as follows. By lowering the ratio $\varepsilon/\sqrt{\varepsilon_n}$, the average observation time window $E[T_{obs}|H_0]$ should be increased to preserve the same error rate according to the law

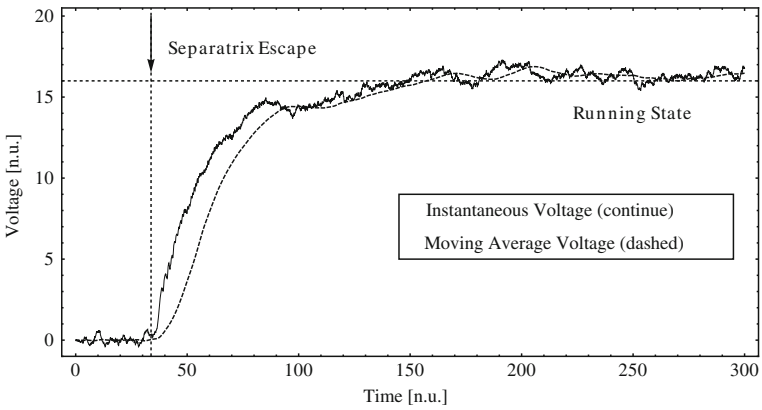

Fig. 7 Time dependence of the instantaneous and moving average voltage. The average is computed over two periods of the Josephson frequency, see Eq. (25)

$$E[T_{obs}|H_0] \propto \left(\frac{\varepsilon}{\sqrt{\varepsilon_n}}\right)^{-2\eta_Y} \tag{24}$$

Therefore for low SNR, the SM detector (characterized by $\eta_{\mathscr{A}} = 3/2$) is very inefficient with respect to the LRT detector (characterized by $\eta_\Lambda = 1$) because it requires a much longer observation time to achieve the same error rate.

5 Practical Issues for Josephson Junction Detectors

We have so far described the analysis of the escape times across the separatrix of Fig. 1. This corresponds to set a threshold of the phase at a fixed level, see Fig. 2, roughly related to the appearance of a finite voltage, Eq. (8). To transform such idea into practical realization there are several limits that further deteriorate the performances. First, the passage across the separatrix does not cause immediately the appearance of nonzero average voltage, for real voltmeter will measure the voltage average over a finite time.

In Fig. 7 we compare the instantaneous voltage (continuous line) to the voltage computed with a moving average voltage over 2 periods of the Josephson frequency (dashed line). The averaging roughly corresponds to a passing bandwidth 2 times lower than the Josephson frequency ω_J. In Fig. 7 the dashed vertical line indicates to the time when the phase crosses the separatrix and the instantaneous voltage starts increasing. The actually accessible voltage is the moving average of the instantaneous voltage of the Josephson Eq. (2):

$$< V > \; = \frac{V_0}{\Delta T} \int_{\tau - \Delta T}^{\tau} \left(\frac{d\varphi(\tau')}{d\tau'}\right) d\tau'. \tag{25}$$

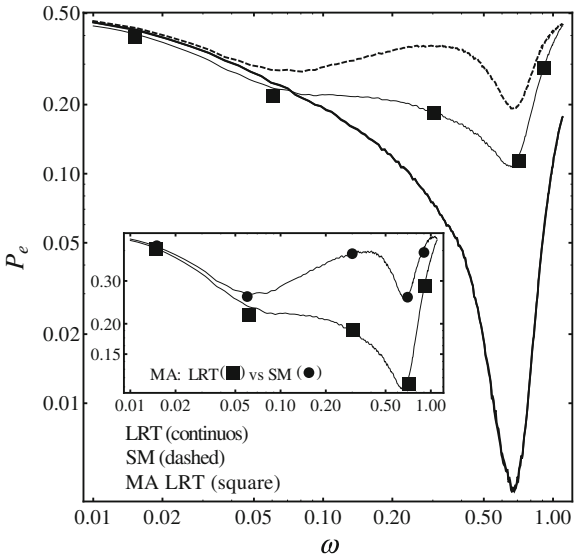

Fig. 8 Error rate P_e as a function of the applied signal frequency ω. The line with square markers is computed for the LRT coherent strategy when the escape is defined through the moving average of the voltage, Eq. (25). For sake of comparison, the LRT (continuous line) and SM (dashed line) error rates, computed in the coherent case when the escape is defined through the passage across the separatrix, are also shown. In the inset it is shown a closeup of the LRT coherent (line with square markers) and SM coherent (line with circle markers), both computed when the escape is defined through the moving average of the voltage. Parameters of the simulations are: $\gamma = 0.8$, $\alpha = 0.05$, $\varepsilon_N = 0.0175$. Moreover, when the signal is present, $\varepsilon = 0.05$ and $\varphi_0 = 0$. The simulations are performed setting the mean observation time under H_0, $E[T_{obs}|H_0] = 2000$

The detection of an escape time is established with a suitable threshold on $< V >$. A realistic averaging is particularly important when the junction is in the so called intermediate damping regime ($0.25 < \alpha < 1$) and retrapping, that lowers $< V >$, occurs [42].

The smoothing and the consequent loss of information of the device are shown in Fig. 8 by a dashed line with square symbols. It is evident that LRT methods are also in this case better than the SM approach. Moreover, it is confirmed that stochastic resonance does not occur for optimized methods.

It is experimentally convenient to slowly ramp the bias current up to the critical value I_c and to record the current at which the voltage appears. The escape time distributions $f_{0,1}(\tau)$ are related to the switching current distributions $P_{0,1}(\gamma)$. In the adiabatic approximation the relationship reads [24]:

$$P_{0,1}(\gamma) = \frac{1}{f_{0,1}(\tau)} \left(\frac{d\gamma}{d\tau}\right)^{-1} \left(1 - \int_0^{\gamma} P_{0,1}(\gamma')d\gamma'\right).$$

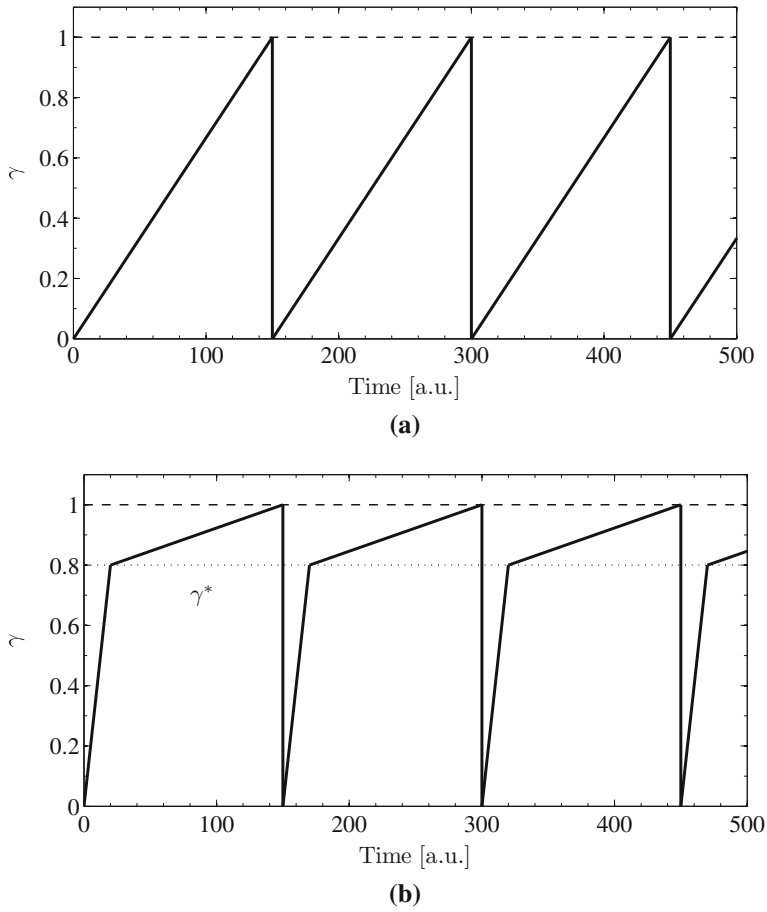

Fig. 9 Top plot (**a**): current sawtooth waveform (continuous line) of the current γ. Bottom plot (**b**): current waveform (continuous line) with the maximum normalized current γ (dashed line) and the starting point current level $\gamma^* = I_b^*/I_c$ (dotted line)

The advantage for the experiments is twofold. First, it is possible to use the ramping time as a sort of clock, and this enables an accurate timing easily available in the labs. Second, and more important, the sweeping bias method guarantees that a switch occurs during each ramp, thus fixing the time to collect the prescribed number of escapes.

In Fig. 9a the time dependent I_b follows a simple sawtooth up to the critical current. When the switching current is close to the critical current the sawtooth bias method has the disadvantage that leaves the system for most of the time in the zero voltage state, and only collects escape times in a narrow region close to I_c. To avoid the depletion of so much time, a more sophisticated method could be employed, applying a profile of the type displayed in Fig. 9. In this case the bias current is quickly increased in the region where escape is not likely to occur, marked in Fig. 9

as $\gamma^* = I_b^*/I_c$. At this point the current sweep is slowed down to carefully examine the region $I_b^* < I_b < I_c$. Indeed in the second region the switching effectively occurs, and the data are consequently recorded. Our analysis roughly corresponds to reach very quickly (in a negligible time) γ^* and to sweep much more slowly in the second region. However, apart some indications [30], a careful analysis of the consequences of the bias sweep on JJ detectors is at the moment still lacking. We remark that constant bias with an external clock allows time resolution down to nanoseconds and the range spans over six orders of magnitude [55].

Another relevant issue is related to the impossibility of perfect knowledge of the JJ and signal parameters. It is unrealistic to suppose that the initial phase φ_0 of the signal is known, while it is possible to exploit some guess, related to the particular application, about the signal amplitude ε and frequency ω. A viable solution, briefly analyzed in [1], is to use a Generalized LRT detection strategy [33] that performs a joint near—optimal signal detection and phase estimation. Unfortunately, due to the difficulties encountered in realizing perfectly reproducible JJ, also some physical parameters, such as the critical current I_c or the capacitance C, are not perfectly known. We guess that a careful analysis of the escape time could be useful to individuate some phenomena, characterized by a well known *signature*, that can be used to reduce the uncertainty.

We conclude the Section with the role of the noise sources in JJ. The distribution of the escape times has been used to reveal the non-Gaussian character of the noise due to the granularity of weak bias currents [47]. In Eq. (2) quantum noise has been neglected. To include quantum fluctuations more than a simple differential equation is required. However, quantum fluctuations can be approximated by a correlated Gaussian noise, although there is not a single approach to the solution of the full model (as shown for instance in Refs. [12, 38, 52]). The noise spectrum is therefore an hallmark of quantum behavior; we speculate that the analysis of the escape times could be employed to discriminate if the noise is correlated, and thus to go beyond the use of the simple mean escape time. Moreover, it has been argued that several phenomena that are characteristic of quantum behavior could be reproduced by a classical model such as Eq. (2) through an appropriate choice of the temperature [14, 30, 31, 11]. We suggest that even in the case when the temperature of the junction is not certainly known, for example if the thermal contact with the bath is not perfect, the analysis of the full PDF with the methods of signal theory, rather than just compare the average escape time [11], could give indications for the correct model.

6 Conclusions

We have proposed to examine the escape time dynamics of JJs from the perspective of detection. Indeed from this standpoint JJs are potentially interesting for two main reasons: speed and low intrinsic noise (temperature). To assess the effectiveness of the detector, we have chosen the error rate as performance indicator of the capability of discerning between two different conditions

(e.g. presence and absence of a sinusoidal excitation). Moreover, the real experimental set-up should be designed in view of the detection, calibrating the parameter of the junction (I_c, C, and R) and the external bias supply (I_b). Finally, the analysis of the data should be optimized to extract as much information as possible from the available measurements. In this framework it is possible to find several interesting features, for instance that low dissipation junctions are the most suitable for signal analysis, or that the bias point should be chosen to have such a low energy barrier as it is possible, compatibly with the speed of the electronics to keep trace of the escape. Also the feasible criterion to decide if an escape has actually occurred is important, because practical methods to detect a voltage change entail a loss of information that should be carefully controlled. As a concluding remark, we want to underline that signal detection is important for practical purposes as the identification of a waveform embedded in a noisy background, but the underlying theory, i.e. the statistical hypothesis testing, can also be used as a tool to distinguish between two models. Two noticeable examples are the retrapping regime for intermediate damping and the identification of the escapes due to quantum tunneling. In these circumstances, the detection theory approach allows to search for the most efficient way to distinguish which model is best corroborated by the data. The gain with respect to an analysis confined to intuitive statistics, such as the sample mean, could be considerable.

Acknowledgments We acknowledge Giacomo Rotoli for fruitful advices. We also thank Luca Galletti, Davide Massarotti and Francesco Tafuri for useful discussions. This work has been supported by the Italian Super Computing Resource Allocation ISCRA, CINECA, Italy (Grant IscrB_NDJJBS 2011).

References

1. P. Addesso, G. Filatrella, V. Pierro, to appear on Phys. Rev. E. **82**, 046712 (2010)
2. I. Affleck, Phys. Rev. Lett. **46**, 388 (1981)
3. J.T. Anderson, A.M. Goldman, Phys. Rev. Lett. **23**, 128 (1969)
4. A. Barone, G. Paternò, *Physics and Application of Josephson Effect* (John Wiley, New York, 1982)
5. A. Barone, F. Lombardi, G. Rotoli, F. Tafuri, Low Temp. Phys. **36**, 876 (2010)
6. T. Bauch, T. Lindstro, F. Tafuri, G. Rotoli, P. Delsing, T. Claeson, F. Lombardi, Science **311**, 57 (2006)
7. E. Ben-Jacob, D.J. Bergman, Phys. Rev. A **29**, 2021 (1984)
8. R. Benzi, A. Sutera, A. Vulpiani, J. Phys. A Math. Gen. **14**, L453 (1981)
9. N. Berglund, B. Guentz, Europhys. Lett. **70**, 1 (2005)
10. A.J. Berkley, H. Xu, R.C. Ramos, M.A. Gubrud, F.W. Strauch, P.R. Johnson, J.R. Anderson, A.J. Dragt, C.J. Lobb, F.C. Wellstood, Science **300**, 1548 (2003)
11. J.A. Blackburn, M. Cirillo, N. Grønbech-Jensen, Phys. Lett. A **374**, 2827 (2010)
12. F.T. Brandt, J. Frenkel, J.C. Taylor, Phys. Rev. B **82**, 014515 (2010)
13. A.R. Bulsara, A. Zador, Phys. Rev. E **54**, R2185 (1996)
14. M. Cirillo, C. Cosmelli, L.V. Filippenko, R. Russo, G. Torrioli, Phys. Rev. Lett. **93**, 107002 (2004)
15. F. Dalfovo, S. Giorgini, L.P. Pitaevskii, S. Stringari, Rev. Mod. Phys. **71**, 463 (1999)

16. M.H. Devoret, J.M. Martinis, D. Esteve, J. Clarke, Phys. Rev. Lett. **53**, 1260 (1984)
17. M.H. Devoret, J.M. Martinis, J. Clarke, Phys. Rev. Lett. **55**, 1908 (1985)
18. M.H. Devoret, D. Esteve, J.M. Martinis, A. Cleland, J. Clarke, Phys. Rev. B **36**, 58 (1987)
19. C.R. Doering, J.C. Gadoua, Phys Rev Lett. **69**, 2318 (1992)
20. J.C. Fenton, P.A. Warburton, Phys. Rev. B **78**, 054526 (2008)
21. A. Fiasconaro, B. Spagnolo, Phys. Rev. E **83**, 041122 (2011)
22. G. Filatrella, B.A. Malomed, S. Pagano, Phys. Rev. E **65**, 051116 (2002)
23. G. Filatrella, V. Pierro, Phys. Rev. E **82**, 046712 (2010)
24. T.A. Fulton, L.N. Dunkleberger, Phys. Rev. B **9**, 4760 (1974)
25. V. Galdi, V. Pierro, I.M. Pinto, Phys. Rev. E **57**, 6470 (1998)
26. L. Gammaitoni, F. Marchesoni, E. Menichella-Saetta, S. Santucci, Phys. Rev. Lett. **62**, 349 (1989)
27. L. Gammaitoni, P. Hänggi, P. Jung, F.P. Marchesoni, Rev. of Mod. Phys. **70**, 223 (1998)
28. S. Giovanazzi, A. Smerzi, S. Fantoni, Phys. rev. Lett. **84**, 4521 (2000)
29. A. Godone, D. Andreone, IEEE Trans. Instr. Meas. **46**, 246 (1997)
30. N. Grønbech-Jensen, M.G. Castellano, F. Chiarello, M. Cirillo, C. Cosmelli, L.V. Filippenko, R. Russo, G. Torrioli, Phys. Rev. Lett. **93**, 107002 (2004)
31. N. Grønbech-Jensen, J.E. Marchese, M. Cirillo, J.A. Blackburn, Phys. Rev. Lett. **105**, 010501 (2010)
32. T. Hanaguri, Y. Tsuchiya, A. Maeda, Phys. Rev. B **58**, R8929 (1998)
33. C.W. Helstrom, *Statistical Theory of Signal Detection* (Pergamon Press, Oxford, 1968)
34. P. Jaranowski, A. Krolak, B.F. Schutz, Phys. Rev. D **58**, 063001 (1998)
35. P. Jung, Phys. Rep. **234**, 175 (1993)
36. B.V.K.V. Kumar, C.W. Carroll, Opt. Eng. **23**, 732 (1984)
37. L.D. Landau, E.M. Lifshitz, *Mechanics* (Pergamon, New York, 1976)
38. Y. Levinson, Phys. Rev. B **67**, 184504 (2003)
39. S. Levy, E. lahoud, J. Steinhauer, Nature **449**, 579 (2007)
40. J.H. Li, Z.Q. Huang, Phys. Rev. E **57**, 3917 (1998)
41. J.H. Li, Phys. Rev. E **67**, 061110 (2003)
42. L. Longobardi, D. Massarotti, G. Rotoli, D. Stornaiuolo, G. Papari, A. Kawakami, G.P. Pepe, A. Barone, F. Tafuri, Phys. Rev. B **84**, 184504 (2011)
43. R. Mannella, in *Stochastic Processes in Physics, Chemistry and Biology*, ed. by J.A. Freund, T. Pöschel (Springer, Berlin, 2001), p. 353
44. B. McNamara, K. Wiesenfeld, Phys. Rev. A **39**, 4854 (1989)
45. M.D. Mittleman, *Sensing with Terahertz Radiation* (Springer, Berlin, 2003)
46. T. Novotný, J. Stat. Mech. P01050 (2009)
47. J.P. Pekola, Phys. Rev. Lett. **93**, 206601 (2004)
48. J.P. Pekola, T.E. Nieminen, M. Meschke, J.M. Kivioja, A.O. Niskanen, J.J. Vartiainen, Phys. Rev. Lett. **95**, 197004 (2005)
49. V. Pierro, LIGO Sci. coll. PRD **80**, 042003 (2009)
50. H. Risken, *The Fokker-Planck Equation: Methods of Solution and Applications* (Springer, Berlin, 1989)
51. J. Shao, *Mathematical Statistics* (Springer, New York, 2003)
52. A. Shit, S. Bhattacharya, S. Chattopadhyay, J.R. Chaudhuri, Physica A **390**, 2880 (2011)
53. P. Silvestrini, S. Pagano, R. Cristiano, O. Liengme, K.E. Gray, Phys. Rev. Lett. **60**, 844 (1988)
54. B.W. Silverman, *Density Estimation for Statistics and Data Analysis* (Chapman and Hall/CRC, London, 1998)
55. Y. Yu, Y. Zhang, W. Qiu, S. Li, S. Han, Z. Wang, Superc. Sci. Technol. **15**, 555 (2002)
56. Y. Yu, S. Han, Phys. Rev. Lett. **91**, 127003 (2003)
57. X.X. Wang, J.D. Bao, Phys. Rev. E **83**, 011127 (2011)
58. S. Wahlsten, S. Rudner, T. Claeson, J. Appl. Phys. **49**, 4248 (1978)

Symmetry Breaking Criteria in Electrostatically Loaded Bistable Curved/Prebuckled Micro Beams

Lior Medina, Rivka Gilat and Slava Krylov

Abstract The symmetric and asymmetric buckling of micro beams subjected to distributed electrostatic force is studied. The analysis is carried out for two separate cases: a case of a stress-free beam, which is initially curved by fabrication and a case of a pre-stressed beam buckled due to an axial force. The analysis is based on a reduced order (RO) model resulting from the Galerkin decomposition with vibrational or buckling modes of a straight beam used as the base functions. The criteria of symmetric, limit point, buckling and of non-symmetric bifurcation are derived in terms of the geometric parameters of the beams. While the necessary symmetry breaking criterion establishes the conditions for the appearance of bifurcation points on the unstable branch of the symmetric limit point buckling curve, the sufficient criterion assures a realistic asymmetric buckling bifurcating from the stable branches of the symmetric equilibrium path. It is shown that while the symmetry breaking conditions are affected by the nonlinearity of the electrostatic force, its influence is less pronounced than in the case of the symmetric snap-through. A comparison between the results provided by the reduced order model, and those obtained by other numerical analyses confirms the accuracy of the symmetry breaking criteria and their applicability for the analysis and design of micro beams.

L. Medina · S. Krylov (✉)
Faculty of Engineering, School of Mechanical Engineering,
Tel Aviv University, Ramat Aviv 69978 Tel Aviv, Israel
e-mail: krylov@post.tau.ac.il

R. Gilat
Faculty of Engineering, Department of Civil Engineering,
Ariel University Center, Ariel 44837, Israel

Progress Optical Sci., Photonics (2013): 679–705
DOI: 10.1007/10091_2012_19

Published Online: 14 October 2012

1 Introduction

Bi-stability, namely, the existence of two different stable configurations at the same loading, is an intrinsic feature of many mechanical structures. The transition between the two stable states is commonly refereed to as a snap-though buckling. One of the most common examples is a flexible arch (or a curved beam) loaded by a transverse uniformly distributed "mechanical" displacement-independent force (load), as demonstrated in Fig. 1. The stability of bi-stable structures, mainly arches, frames, cylindrical panels and spherical caps is a well established topic in engineering, and is largely reported in the literature [1–6]. While the initial increase of loading is accompanied by small displacements decreasing the arch's height, at a certain load level the snap-through collapse takes place and the arch suddenly shifts its position to a new (not adjacent) stable configuration. Under subsequent decreasing load, the structure remains in its post-buckling stable configuration till the snap-back (release) point is reached at which the structure returns to its initial pre-buckling state. The structure is therefore bi-stable in the interval of the force bounded between the snap-through and the snap-back values as can be seen in Fig. 1a. The snap-through and release points are thus defined as limit points. In addition, the two stable states specify two stable branches upon which the arch moves in response to the applied load. The third branch is an unstable one, which cannot be reached under static loading. The beam's response is bistable and hysteretic in nature as commonly observed in various physical systems characterized by a double well potential. It is to note, that in order to make a conclusion about the stability or instability of an equilibrium (fixed) point, dynamic analysis should be carried out. Such an analysis is out of the scope of this work. Note, however, that the stable branches of the equilibrium curves corresponds to stable nodes on a phase plane whereas the points located at the unstable branch (dashed lines in Fig. 1) are saddles. At the limit points stable and unstable fixed points annihilate through the saddle-to-node bifurcation (for details, see [5, 6]).

However, the transition between the two stable states can occur symmetrically or asymmetrically. When the ratio between the arch's elevation and its thickness is higher than a certain value, the asymmetric transition may take place. In this case the dependency between the load and the displacement includes an additional unstable branch, which emanates from the stable one prior to the symmetric limit point as shown in Fig. 1b. The intersection point of the two branches is refereed to as a bifurcation point. As schematically illustrated in Fig. 1b, the beam jumps to the post-buckling state non-symmetrically due to the increase of the inner axial force to the level of the second (associated with the asymmetric buckling) critical Euler force. This phenomenon is commonly referred to as symmetry breaking.

Recently, emerging of new applications in the realm of micro and nanoelectromechanical systems (MEMS and NEMS) stimulated a renewed interest in the mechanics of bistable beams [7–16]. Micro and nano devices incorporating bistable structural elements have functional advantages in applications such as switches [17], sensors [18] and non-volatile memories [19]. On the other hand, while being a

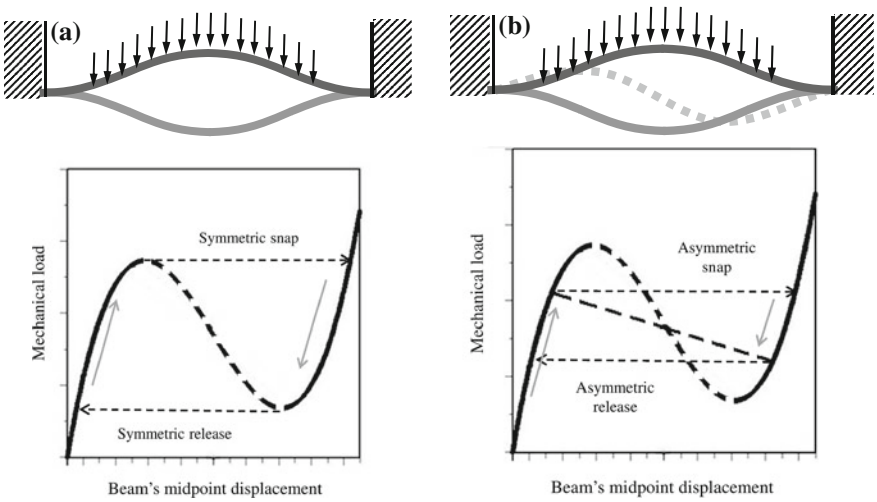

Fig. 1 "Mechanically" bi-stable structures, composed of an initially curved double-clamped beam under a uniform displacement-independent loading, and schematics of the corresponding bifurcation diagrams, which depict the dependence between the load and the midpoint displacement of the beam. *Black solid lines* represent the initial shape of the beam, *gray solid lines* represent deformed stable configurations; *dashed lines* correspond to the unstable configurations. **a** and **b** depict symmetric and asymmetric responses, respectively

relatively simple structure, double-clamped micro beam actuated by a nonlinear deflection-dependent electrostatic force, exhibits rich behavior and represents a convenient platform for analytical, numerical and experimental investigation of the nonlinear phenomena, which are abundant at the microscale (see reviews [20–22] and references therein). As an example for this kind of phenomena, one can mention intrinsic electrostatic (so-called pull-in) instability, taking place in micro beams and associated with the softening (reducing the effective stiffness of the structure) nonlinearity of the electrostatic forces as shown in Fig. 2a. In contrast to straight beams, electrostatically loaded curved beams combine both geometric mechanical nonlinearity typical for bistable structures and generic electrostatic nonlinearity. As was recently shown in [10, 13, 15, 16], these structures may exhibit sequential snap-through buckling and pull-in instability as depicted in Fig. 2b (resonant behavior of this kind of devices was analyzed in [14]).

Note that in the case of curved beams of different shapes subjected to a "mechanical" deflection-independent loading, the limit point (snap-through) and the symmetry breaking criteria are well established. These criteria are fully dictated by the geometry of the beam itself—namely the ratio between the initial elevation/curvature of the beam and its thickness—and thus, are independent on the loading [3, 6]. However, in the case of the electrostatic actuation, the snap-through behavior is affected by the nonlinearity of the electrostatic force parameterized by the initial distance between the beam and the electrode, as reflected in the symmetric (limit-point) snap-through criterion first obtained in [10] for an initially stress-free

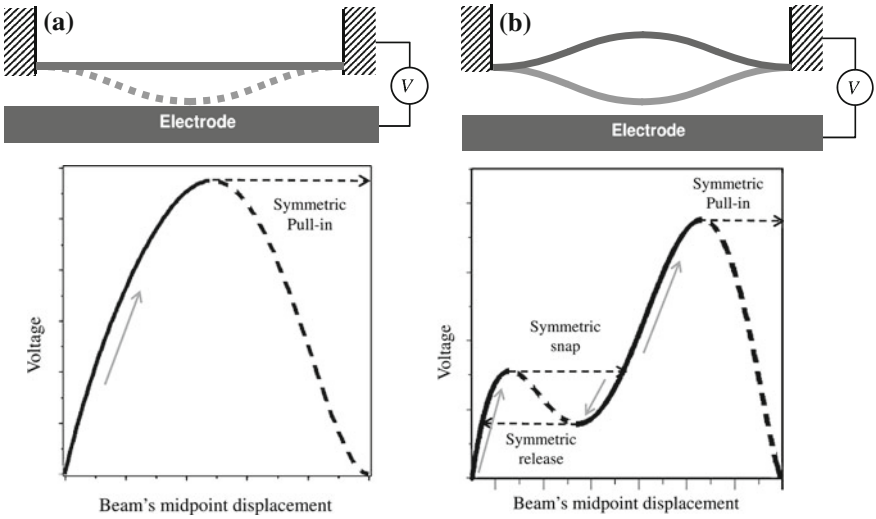

Fig. 2 **a** Initially straight double-clamped beam under a displacement-dependent electrostatic loading, and schematics of the corresponding bifurcation diagram, which depicts the dependence between the voltage and the midpoint displacement of the beam. **b** Initially curved double-clamped beam under a displacement-dependent electrostatic loading, and schematics of the corresponding bifurcation diagram, which depicts the symmetric response of the beam. *Black solid lines* represent the initial shape of the beam, *gray solid lines* represent deformed stable configurations; *dashed lines* correspond to the unstable configurations

bell-shaped beam. It was shown, that in the case of the electrostatic loading, the snap-through may take place in beams with lower initial elevation/curvature when compared to the case of "mechanical" deflection-independent loading.

In this work, we extend the stability analysis of electrostatically actuated initially curved stress-free micro beams to the case of higher initial elevations, such that non-symmetric buckling configurations appear. In addition, the case in which the initial curvature of the beam is due to a compressive axial force is considered. Our goal is to highlight the leading phenomena taking place in this type of structure, to investigate the influence of the device parameters on its stability and to establish criteria of symmetric and asymmetric buckling. These criteria are in a sense an extension of the well-documented results obtained for "mechanically" loaded curved beams (see [3, 6]) to the case of the intrinsic nonlinear electrostatic loading.

2 Formulation

We consider a flexible initially curved, axially loaded, double clamped prismatic micro beam of length L having a rectangular cross-section of width $\hat{b}$ and thickness $\hat{d}$ as shown in Fig. 3. The beam is assumed to be made of homogeneous isotropic

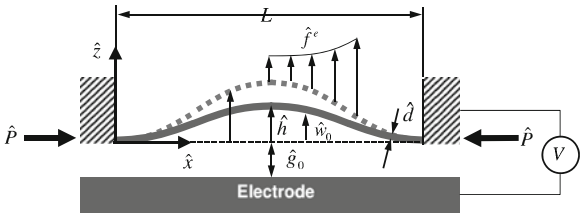

Fig. 3 Model of an initially curved axially loaded double-clamped beam actuated by distributed electrostatic force. The *dashed line* corresponds to the deformed configuration. Positive directions of the beam's deflection and of the loading are shown

linearly elastic material with Young's modulus E. Since the width $\hat{b}$ of a micro-beam is typically larger than it's thickness $\hat{d}$, an effective (plane strain) modulus of elasticity $\tilde{E} = E/(1-\nu^2)$ is used, where ν is Poisson's ratio. The initial shape of the stress-free (before the application of the axial force) beam is described by the function $\hat{w}_0(\hat{x}) = \hat{h}_0 z_0(\hat{x})$, where $\hat{h}_0$ is the initial elevation of the beam's central point above it's ends, and $z_0(\hat{x})$ is a non dimensional function such that $\max_{\hat{x}\in[0,L]}[z_0(\hat{x})] = 1$. The beam is subjected to an axial compressive force $\hat{P}$ and to a distributed electrostatic force provided by an electrode located at a distance $\hat{g}_0$ (the gap) from the beam and extended beyond it's ends (see [10] for details).

We assume that $\hat{d} \ll L, \hat{h}_0 \ll L$ and that the deflections are small with respect to the beam's length. Under these assumptions, the beam's behavior is described in the framework of the Euler–Bernoulli theory combined with the shallow arch approximation. The non-dimensional potential energy can we written in the form (e.g., see [23] for the details of the development, see [10] for the case of zero axial pre-stress $P = 0$)

$$U = \frac{1}{2}\int_0^1 \left(w_0'' - w''\right)^2 dx + \frac{1}{4\alpha}\int_0^1 \left(-P + \alpha\left(2u' + (w')^2 - \left(w_0'\right)^2\right)\right)^2 dx - \beta\int_0^1 \frac{dx}{1+w} \tag{1}$$

Here, $u(x)$ and $w(x)$ are the non-dimensional axial displacement and the beam's elevation above the x axis, respectively; α is the stretching parameter and β is the voltage parameter. Hereafter $()'$ denotes derivative with respect to the non-dimensional coordinate $0 \le x \le 1$. The non-dimensional quantities are listed in Table 1, where A and I_{yy}, are the cross-section's area and second moment of the area, respectively; $\varepsilon_0 = 8.854 \times 10^{-12}\ F/m$ is the dielectric permittivity and V is the actuation voltage. In Eq. (1), the first term is associated with bending, the second term is associated with the stretching of the beam's axis originated in a constant pre-loading force P and with a nonlinear deflection-dependent stretching; the last term is the electrostatic co-energy.

Table 1 Non-dimensional quantities

$x \triangleq \hat{x}/L$	Coordinate
$u \triangleq \hat{u}L/\hat{g}_0^2$	Axial displacement
$w \triangleq \hat{w}/\hat{g}_0,\ w_0 \triangleq \hat{w}_0/\hat{g}_0$	Elevation/initial elevation
$h \triangleq \hat{h}_0/\hat{g}_0$	Initial midpoint elevation
$d \triangleq \hat{d}/\hat{g}_0$	Thickness
$\alpha \triangleq \left(\hat{g}_0^2 A\right)/\left(2I_{yy}\right)$	Stretching parameter
$P \triangleq \left(\hat{P}L^2\right)/\left(EI_{yy}\right)$	Axial load
$\beta \triangleq \left(\epsilon_0 \hat{b} V^2 L^4\right)/\left(2\hat{g}_0^3 \tilde{E} I_{yy}\right)$	Voltage parameter

Using the principle of stationary potential energy and calculating the variation of Eq. (1), one obtains the following non-dimensional equilibrium equations (see [24, 25] for the case of "mechanical" loading)

$$\left(-P + 2\alpha\left(u' + \frac{1}{2}(w')^2 - \frac{1}{2}\left(w_0'\right)^2\right)\right)' = 0 \tag{2}$$

$$w^{IV} - w_0^{IV} + \left(P - 2\alpha\left(u' + \frac{1}{2}(w')^2 - \frac{1}{2}\left(w_0'\right)^2\right)\right)w'' = -\frac{\beta}{(1+w)^2} \tag{3}$$

completed by homogeneous boundary conditions. Note that Eq. (3) suggests that the applied electrostatic force is approximated by the simplest parallel capacitor formula. Since, in accordance with Eq. (2), the axial force is constant along the beam, Eqs. (2), (3) can be reduced to the following single non-dimensional equation (e.g., see [25])

$$w^{IV} - w_0^{IV} + \left(P - \alpha\int_0^1 \left((w')^2 - \left(w_0'\right)^2\right)dx\right)w'' = -\frac{\beta}{(1+w)^2} \tag{4}$$

In this work, Eq. (4) is used for the development of the buckling criteria while Eqs. (2), (3) serve as the basis for numerical analysis. Note, that the potential energy associated with Eq. (4) is given by the expression (see [10], see [24, 25] for the case of "mechanical" loading)

$$U = \frac{1}{2}\int_0^1 \left(w_0'' - w''\right)^2 dx - \frac{1}{2}\int_0^1 P(w')^2 dx + \frac{\alpha}{4}\int_0^1 \left(\int_0^1 \left((w')^2 - \left(w_0'\right)^2\right)dx\right)^2 dx - \beta\int_0^1 \frac{dx}{1+w} \tag{5}$$

3 Initially Curved Stress-Free Beam

We first consider the beam with zero axial force. In this case the beam is stress-free in its initial configuration and its curved shape is defined lithographically during the fabrication (see [10]). The behavior of the beam is described by Eqs. (2), (3) or (4) where $P = 0$.

3.1 Reduced Order Model

In order to analyze the snap-through and pull-in behavior of the beam, a RO model based on the Galerkin decomposition is built. The initial and deformed shapes of the beam are approximated by the series

$$w(x) \approx \sum_{i=1}^{n} q_i \varphi_i(x) \tag{6}$$

where q_i are the generalized coordinates and $\varphi_i(x)$ are the linear undamped eigenmodes of a straight stress-free double-clamped beam, which are given by the expression

$$\varphi_i(x) = C_i(J_i(\cos(\lambda_i x) - \cosh(\lambda_i x)) + \sin(\lambda_i x) - \sinh(\lambda_i x)) \tag{7}$$

Here $J_i = (\cos\lambda_i - \cosh\lambda_i)/(\sinh\lambda_i + \sin\lambda_i)$; C_i are constants, which are chosen such that $\max_{x\in[0,1]}(\varphi_i(x)) = 1$; $\lambda_i = (\omega_i)^{1/2}(\rho AL^4/EI)^{1/4}$ are the frequency parameters, which are related to the eigenfrequencies ω_i of the beam, and are found as solution's to the frequency equation $\cos\lambda_i \cosh\lambda_i = 1$.

Note that while beams of different initial shapes can be analyzed, we consider a beam of an initial shape that can be expanded into series in terms of the eigenmodes, i.e., can be represented in the form of Eq. (6) as $w_0(x) \approx \sum_{i=1}^{n} q_{0i}\varphi_i(x)$. By implementing the usual Galerkin procedure, we obtain a system of coupled nonlinear algebraic equations (see [26])

$$\mathbf{B}(\mathbf{q} - \mathbf{q}_0) + \alpha\left(\mathbf{q}^{\mathbf{T}}\mathbf{S}\mathbf{q} - \mathbf{q}_0^T\mathbf{S}\mathbf{q}_\mathbf{0}\right)\mathbf{S}\mathbf{q} = -\beta\mathbf{Q} \tag{8}$$

where $\mathbf{q} = \{q_i\}$, $\mathbf{q}_0 = \{q_{0i}\}$ and $(\ )^T$ denotes the matrix transpose. The elements of the generalized force vector $\mathbf{Q} = \{Q_i\}$ and of the matrices $\mathbf{B} = \{b_{ij}\}$ and $\mathbf{S} = \{s_{ij}\}$, associated with the bending and stretching stiffness of the beam, respectively, are given by

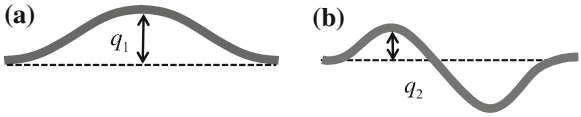

Fig. 4 The first symmetric (**a**) and the second, non-symmetric (**b**) modes of a straight double clamped beam as derived from (Eq. 7)

$$Q_i = \int_0^1 \frac{\varphi_i}{\left(1 + \sum_{j=1}^{n} q_j \varphi_j(x)\right)^2} dx \tag{9}$$

$$b_{ij} = \delta_{ij} \int_0^1 \varphi_i'' \varphi_j'' dx \qquad s_{ij} = \int_0^1 \varphi_i' \varphi_j' dx \tag{10}$$

with δ_{ij} being the Kronecker delta. Hereafter we adopt a bell-shaped initial configuration such that $q_{0i} = 0$ for $i > 1$ and denote $q_{01} = h_0$ unless stated otherwise. Note that the RO model, Eq. (8), can be also obtained from the variational principle, namely by substituting the approximation (6) into Eq. (5) and by using the Rayleigh–Ritz method.

For the investigation of the asymmetric snap-through, the RO model should include at least two terms: the first symmetric and asymmetric modes, which are shown in Fig. 4. By setting $n = 2$ in Eq. (6), the RO model, Eq. (8), is reduced to the form

$$b_{11}(q_1 - h_0) + \alpha s_{11}^2 \left(q_1^2 - h_0^2\right) q_1 + \alpha s_{11} s_{22} q_2^2 q_1 = \beta I_{11} \tag{11}$$

$$b_{22} q_2 + \alpha s_{11} s_{22} \left(q_1^2 - h_0^2\right) q_2 + \alpha s_{22}^2 q_2^3 = \beta I_{22} \tag{12}$$

where $b_{11} = 198.463, b_{22} = 1669.859, s_{11} = 4.878$, $s_{22} = 20.218$ and the integrals I_{11}, I_{22} are as follows

$$\begin{aligned} I_{11}(q_1, q_2) &= \int_0^1 \frac{\varphi_1}{(1 + q_1\varphi_1 + q_2\varphi_2)^2} dx \\ I_{22}(q_1, q_2) &= \int_0^1 \frac{\varphi_2}{(1 + q_1\varphi_1 + q_2\varphi_2)^2} dx \end{aligned} \tag{13}$$

Since Eqs. (11), (12) cannot be solved in a closed form due to the presence of the integral terms, three-dimensional bifurcation diagrams, mapping all stable and unstable equilibrium configurations in the q_1, q_2, β space were first built numerically. The result is presented in Fig. 5 and implies that several buckling criteria can be established. The first one defines the minimal initial elevation necessary for

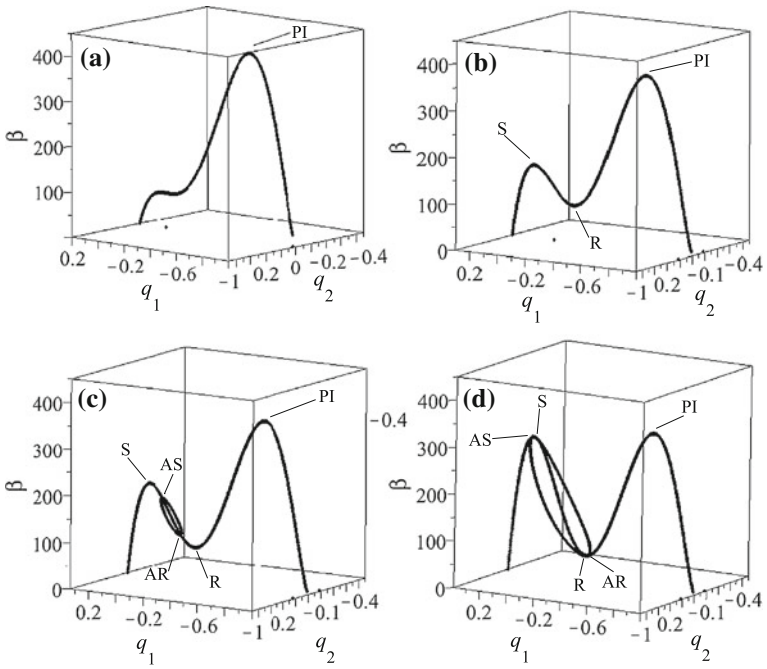

Fig. 5 Bifurcation diagram of the electrostatically loaded beam [two DOF RO model, Eqs. (11), (12)] for $d = 0.2$ and different initial elevations: **a** $h_0 = 1$, **b** $h_0 = 0.3$, **c** $h_0 = 0.332$, **d** $h_0 = 0.386$. Point S and R are snap-through and release limit points; points AS and AR are the bifurcation points corresponding to the asymmetric snap-through and release, respectively, and point PI is the pull-in point

the appearance of the limit points (symmetric snap-through). The second is associated with the non-critical asymmetric buckling emerging from the unstable symmetric branch of the equilibrium curve (the necessary condition). Finally, the third one defines the threshold criterion sufficient for the appearance of the critical symmetry breaking, when the asymmetric snap-through takes place under a loading smaller than the limit-point value (the sufficient condition).

3.2 Snap-Through Criteria

In accordance with Fig. 5, the branches of the bifurcation diagram corresponding to the non-symmetric configurations of the electrostatically loaded beam emerge from the branches representing the symmetric response. Hence, in order to find the position of the bifurcation points on the symmetric branch, we linearize Eqs. (11), (12) around the path $q_2 = 0$. Taking into account that the following integrals vanish

$$\int_0^1 \frac{\varphi_1\varphi_2}{(1+q_1\varphi_1)^3}dx = 0 \qquad \int_0^1 \frac{\varphi_2}{(1+q_1\varphi_1)^2}dx = 0 \tag{14}$$

we obtain

$$b_{11}(q_1 - h_0) + \alpha s_{11}^2\left(q_1^2 - h_0^2\right)q_1 + \beta I_1(q_1) = 0 \tag{15}$$

$$\left(b_{22} + \alpha s_{11}s_{22}\left(q_1^2 - h_0^2\right) - 2\beta I_2(q_1)\right)q_2 = 0 \tag{16}$$

where

$$I_1(q_1) = \int_0^1 \frac{\varphi_1}{(1+q_1\varphi_1)^2}dx \qquad I_2(q_1) = \int_0^1 \frac{\varphi_2^2}{(1+q_1\varphi_1)^3}dx \tag{17}$$

Equation (15) is independent on q_2, and corresponds to a single DOF model, which describes the symmetric response of the beam. By expressing β in terms of q_1 using Eq. (15), requiring that $d\beta/dq_1 = 0$ and taking into account that $I_1 > 0$ for $q_1 > -1$, we obtain the equation

$$\alpha {s_{11}}^2 {q_1}^2(I_3q_1 - 3I_1) + (I_3q_1 - I_1)(b_{11} - \alpha s_{11}^2 h_0^2) - b_{11}I_3h_0 = 0 \tag{18}$$

whose roots q_S, q_R, q_{PI} correspond to the symmetric snap-through, symmetric release and pull-in points, respectively. Here $I_3 = dI_1/dq_1$. The dependence between the location of the roots q_S, q_R, q_{PI} of Eq. (18) and the initial elevation of the beam, h_0, is shown in Fig. 6a, b for two values of d. The corresponding critical values of the voltage parameter are shown in Fig. 6c, d.

In order to obtain the symmetric snap-through criterion, we note that Eq. (18) is quadratic in h_0 and can be solved to obtain $h_0(q_1)$. For a prescribed α, the minimum of $h_0(q_1)$ is found by solving numerically $dh_0(q_1)/dq_1 = 0$. This yields the value of q_1 corresponding to the minimum of the curve $h_0 = h_0(q_1)$ on Fig. 6a, b. The snap-through criterion, namely, the minimal value of h_0 required to have the snap-through, can be obtained by substituting this value of q_1 back into the solution $h_0(q_1)$ of Eq. (18). The dependence of the ratio h_0/d on the relative thickness $d = \hat{d}/g_0$ of a beam of a rectangular cross section (when $\alpha = 6/d^2$) is shown by solid line no. 1 in Fig. 7. Figure 6a, b indicates that the minimum of the curve $h_0(q_1)$ defining the necessary condition of the symmetric snap-through is located at small q_1. Hence, we linearize the derivative dh_0/dq_1 in the vicinity of $q_1 = 0$, solve the equation $dh_0/dq_1 = 0$ in terms of q_1, substitute the result back into the dependence $h_0 = h_0(q_1)$ [obtained from Eq. (18)] and then expand it into Taylor series up to quadratic order (in terms of d). As a result, we obtain an simple approximation for the symmetric snap-through criterion

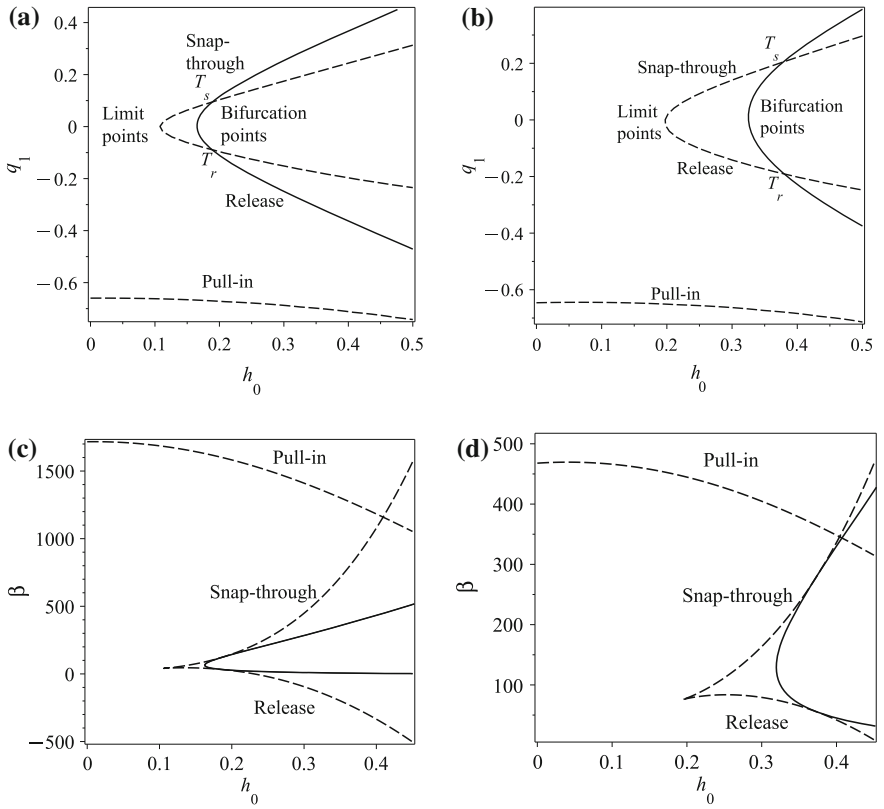

Fig. 6 **a**, **b** Location of the critical points of the electrostatically loaded beam with rectangular cross-section and **c**, **d** corresponding critical values of the voltage parameter for: **a**, **c** $d = 0.1$ and **b**, **d** $d = 0.2$ and varying h_0. The *black dashed lines* represents the limit points of the buckling diagram given by Eq. (18) and corresponding to the symmetric snap-through (point *S*), symmetric release (*R*) and pull-in (*PI*). The *solid black lines* represents bifurcation points of the asymmetric snap-through (point *AS*) and asymmetric release (point *AR*), given by Eq. (21). Points T_s and T_r represents the threshold for the critical asymmetric snap-through and release points, respectively

$$\frac{h_0}{d} > \sqrt{\frac{b_{11}}{6s_{11}^2}}\left(1 - \frac{m_{11}}{p_1}\sqrt{\frac{b_{11}}{6s_{11}^2}}d\right) \tag{19}$$

where $p_1 = \int_0^1 \varphi_1(x)dx$. For the adopted base functions,

$$\frac{h_0}{d} > 1.179 - 1.054d \tag{20}$$

Note that Eq. (20) is in excellent agreement with the approximate symmetric snap-through criterion first obtained in [10] using a different approach.

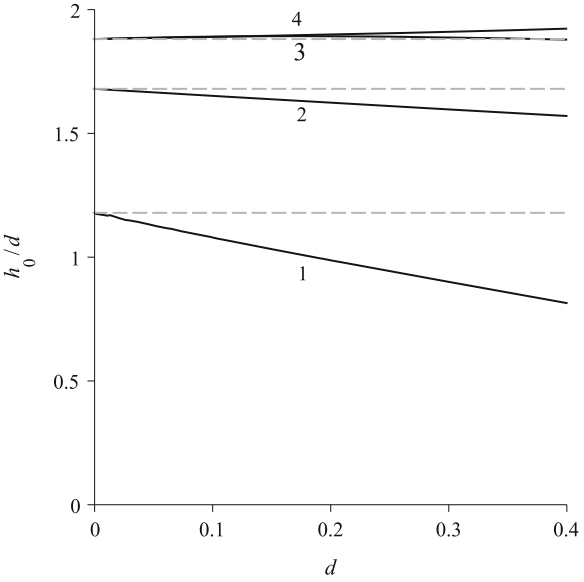

Fig. 7 Phase diagram of the symmetrical and non symmetrical snap-through criteria. The *black solid lines* represents the criteria for the electrostatically loaded beam, and the *dashed grey lines* represents the criteria for a "mechanically" loaded beam. *Solid line no. 1* is the necessary criterion given by Eq. (20) (see also [10]); *line 2* represents the necessary condition; *lines 3* and *4* corresponds to the sufficient conditions for the snap-through and release points, respectively

Consider now the criteria for the asymmetric snap-through. By expressing β in terms of q_1 using Eq. (15) and by substituting this expression into Eq. (16), we obtain an eigenvalue problem, which has a non-trivial solution when the following equation is satisfied

$$2I_2(q_1 - h_0)\big(b_{11} + \alpha s_{11}^2 q_1(q_1 + h_0)\big) + I_1\big(b_{22} - \alpha s_{11}s_{22}\big(q_1^2 - h_0^2\big)\big) = 0 \qquad (21)$$

The roots $q_1(h, \alpha)$ of Eq. (21) define the location of the bifurcation points and are shown by the solid lines in Fig. 6a, b. As was already mentioned, two asymmetric bifurcation criteria can be formulated.

The necessary condition is obtained by solving Eq. (21), which is quadratic in h_0, in terms of the initial mid span elevations. The non-critical bifurcation criterion is then obtained by finding the minimum of the curve $h_0 = h_0(q_1)$ (with α being a parameter). As a result we obtain the value of the initial elevation $h_0 = \hat{h}_0/g_0$ required for the appearance of the asymmetric bifurcation. The curve h_0/d as a function of $d = \hat{d}/g_0$ is shown by solid line no. 2 in Fig. 7.

Similarly to the approach used for the approximation of the symmetric snap-through criterion, we linearize the equation $dh_0/dq_1 = 0$ for small q_1 (in accordance with Fig. 6a, b $h_0(q_1)$ reaches minimum in the vicinity of $q_1 = 0$), solve it in terms of q_1 and obtain the following approximation

$$\frac{h_0}{d} > \sqrt{\frac{b_{22}}{6s_{11}s_{22}}}\left(1 - \frac{b_{11}m_{22}}{p_1}\sqrt{\frac{1}{6s_{11}s_{22}b_{22}}}d\right) \qquad (22)$$

or, for the adopted base functions,

$$\frac{h_0}{d} > 1.680 - 0.312d \tag{23}$$

In order to formulate the sufficient conditions for the non-symmetric snap-through and release, the points of intersection between the curve corresponding to the limit points and the curve associated with the points of bifurcation (threshold points T_s and T_r on Fig. 6) have to be found. This is achieved by solving both Eqs. (18) and (21) for $h_0(q_1)$ and equilibrating these two expressions, which results in an implicit relation corresponding to the threshold points. For a given α, the numerical solution of this equation provides two values of q_1, which, when substituted back into the solution $h_0(q_1)$ of Eqs. (18) or (21) yield the threshold values of h_0, which are sufficient for the appearance of the critical asymmetric responses. The dependence between these values of h_0 and the thickness of the beam d is shown by lines 3, 4 in Fig. 7.

It is worth noting, that the location $q_1(d)$ of the points corresponding to the critical asymmetric responses is not symmetric with respect to $q_1 = 0$. Consequently, two different sufficient criteria should be formulated: one for the critical asymmetric snap-through and another for the asymmetric release.

Since the implicit relation based on the simultaneous solution of Eqs. (18) and (21), which provides the sufficient criterion for the symmetry breaking, cannot be solved in a closed form, simple approximate expression describing the dependence between the h_0/d ratio and d were obtained by using polynomial (up to quadratic order) fits of the numerically obtained solutions

$$\frac{h_0}{d} > 1.881 + 0.154d - 0.585d^2 \quad \text{(sufficient snap-through)} \tag{24}$$

$$\frac{h_0}{d} > 1.881 + 0.089d \qquad \text{(sufficient release)} \tag{25}$$

Figure 7 indicates, that the necessary condition is a lower-bound for bifurcation. As for a certain range of d, the sufficient snap-through condition is below the sufficient release condition, suggesting that an asymmetric snap-through followed by a symmetric release can occur.

3.3 Numerical Validation

In order to validate the criteria and estimate their accuracy, Eqs. (2), (3) (where we set $P = 0$) were solved numerically. Two different tools were used for this purpose: the finite difference boundary value problem solver, which is a part of the MAPLE package [27] and a collocation-based boundary value problem solver bvp4c, which is a part of MATLAB (see [28]).

Since we are interested in the analysis of the symmetry breaking, the initial configuration of the beams was taken to incorporate a small initial imperfection.

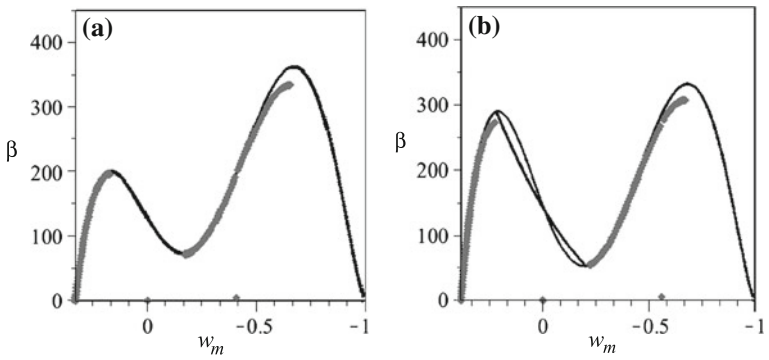

Fig. 8 Buckling diagram (w_M—midpoint elevation) for beams with $d = 0.2$ and **a** $h_0 = 0.332$ **b** $h_0 = 0.386$ where the *black* and *grey lines* represents the RO model and the force control numerical analysis, respectively

The initial shape of the beams was taken to be a combination of the first and the second modes so that $w_0(x) = h_0\varphi_1(x) + \delta\varphi_2(x)$ with δ being the amplitude of the imperfection. A value of $\delta = \hat{\delta}/g_0 = 0.001$ was used in all the calculations.

First, the accuracy of the two DOF RO model was estimated. The comparison between the RO model and the numerical solution is illustrated in Fig. 8. In the framework of the force control approach, which reflects an actual physical experiment [11, 13], the voltage applied to the electrode was increased incrementally and the deflected shape of the beam was found at each increment. Note that only stable branches of the equilibrium curve can be tracked by this approach. In order to get as close as possible to the limit or bifurcation points, smaller load increments were used in the vicinity of the critical points.

Figure 8 shows that the two DOF RO model provides a reasonable accuracy. The model accuracy slightly decreases with the increasing voltage parameter. Specifically, a relative error of 0.01 % in the critical voltage was observed at the snap-through point of a beam with $d = 0.2$ and $h_0 = 0.332$, Fig. 8a; errors of 4.1 and 8.1 % in the critical voltages were obtained at the bifurcation and pull-in points, respectively, for a beam with $d = 0.2$ and $h_0 = 0.386$, Fig. 8b. Note that errors of the same magnitude were reported in [10].

In addition, a displacement control procedure [29], was used to track both stable and unstable responses together with the corresponding shapes of the deformed beam. The midpoint deflection of the beam was prescribed (but the symmetry conditions at the midpoint were not enforced, see [11] for details) and the voltage parameter and the deformed shape of the beam were found by means of the multidomain boundary value problem solver bvp4c implemented in MATLAB. Note that while the displacement control approach adopted in this work may have a limited applicability for the analysis of beams with higher initial elevations or smaller relative gap (it is to say, larger relative thickness $\hat{d}/g_0$), where the contribution of higher modes may lead to looping behavior [16], see also [30], it is suitable for relatively shallow configurations analyzed in this work. To ensure that

the contribution of higher modes is not pronounced for the considered configurations of the beam, the results obtained by the displacement control were compared with the results of the force control analysis, which describes the actual behavior of the beam up to the first instability point. An excellent agreement between the two approaches was observed.

The results for beams of three different initial elevations are shown in Fig. 9. Note that in order to highlight the correspondence between the points on the equilibrium curve of the beam and its deformed configurations, rotated plots of the voltage-deflection dependence are shown. The initial elevations of the beams were chosen in such a way that they fall within three different regions of the phase diagram, defining the buckling behavior of the beam. A non-symmetric response is clearly observed when the parameters of the beams are within the appropriate region. We emphasize that Fig. 9 shows the results of the solution of a quasi static (rather than dynamic) problem. The snapshots of the beam's shape represent the (stable or unstable) equilibrium configurations for corresponding voltage increments and not the snapshots of the dynamic configurations, realized during the dynamic snap-through collapse.

Finally, we compare the location of the snap-through, release and pull-in points extracted from the direct numerical analysis with the values provided by the RO model, Fig. 6. The result of this comparison is shown in Fig. 10, which indicates that the approximate and numerical values are in a good agreement. One may conclude therefore, that the approximate criteria obtained in this work can be used to predict the symmetry breaking in electrostatically actuated curved micro beams.

4 Initially Straight Beam Buckled due to Prestress

In this section, the behavior of initially straight micro beams buckled due to axial load prior to the application of the electrostatic force, is studied. The behavior of the beam is governed by Eq. (4) with $w_0 = 0$.

4.1 Reduced Order Model

The deformed shape of the beam is approximated by the series $w(x) \approx \sum_{i=1}^{n} q_i \varphi_i(x)$, where for the present case φ_i represents the buckling eigenmodes of a straight double-clamped beam

$$\varphi_i(x) = C_i \left(\frac{\cos(\lambda_i) - 1}{\sin(\lambda_i) - \lambda_i} \sin(\lambda_i x) - \cos(\lambda_i x) + \lambda_i \frac{1 - \cos(\lambda_i)}{\sin(\lambda_i) - \lambda_i} x + 1 \right) \tag{26}$$

which are derived from the Sturm–Liouville problem $w^{IV} + \lambda w'' = 0$ associated with the equilibrium equation of the beam [31]. Recall that C_i are constants, which

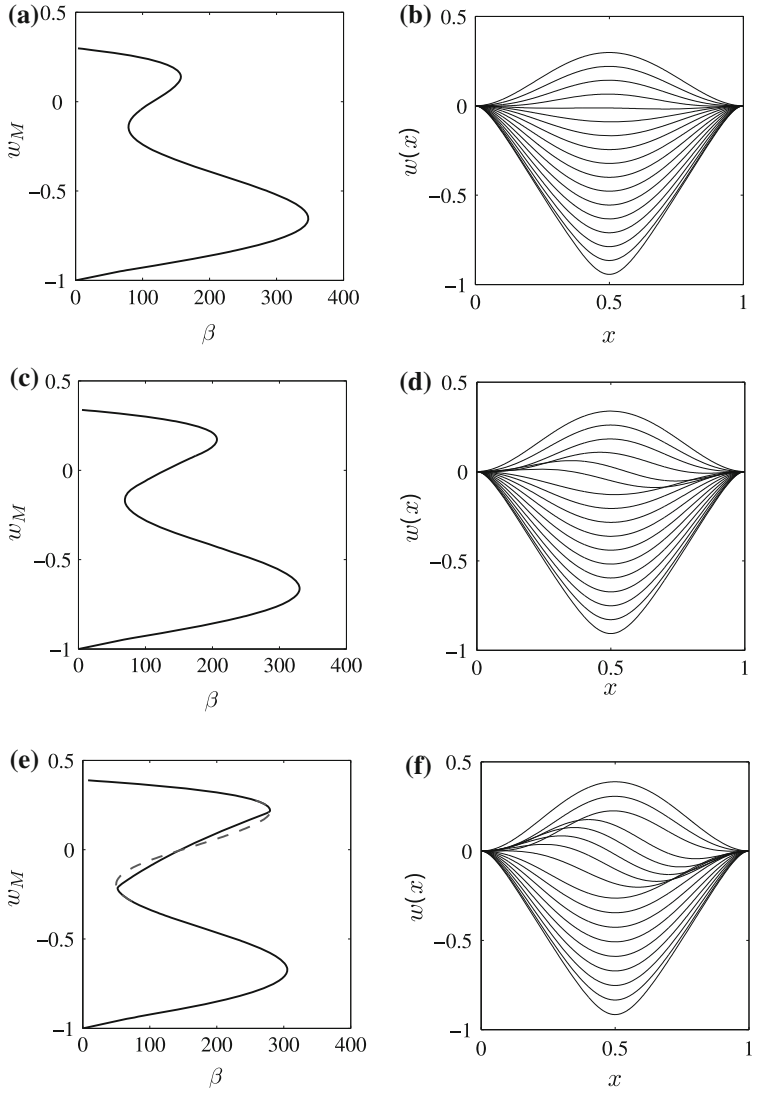

Fig. 9 **a**, **c**, **e** Bifurcation diagrams (w_M—midpoint elevation) and **b**, **d**, **f** snapshots of the shape of the beam under the corresponding level of the loading for $d = 0.2$ and different initial elevations of the beam: **a**, **b** $h_0 = 0.3$ (region 2 in Fig. 7); **c**, **d** $h_0 = 0.34$ (region 3 in Fig. 7); **e**, **f** $h_0 = 0.39$ (region 4 in Fig. 7). *Dashed line* corresponds to the solution obtained under the symmetry conditions enforced at the midpoint

are chosen such that $\max_{x\in[0,1]}[\varphi_i(x)] = 1$ and λ_i are the eigenvalues, found as a solution to the characteristic equation $\cos(\lambda_i) + (\lambda_i/2)\sin(\lambda_i) = 1$. The first two modes have the qualitative shape depicted in Fig. 4.

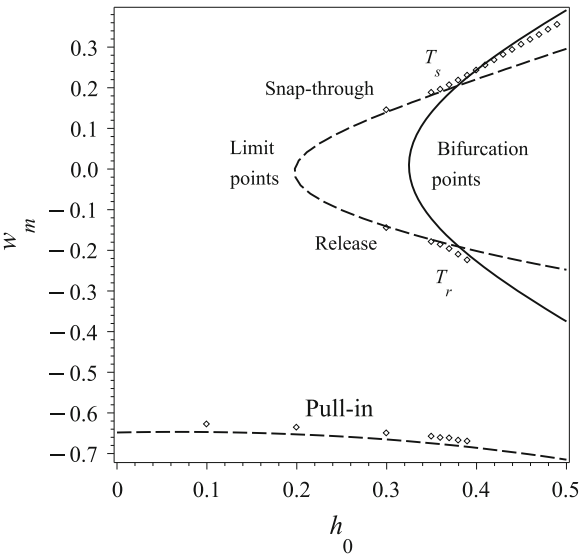

Fig. 10 Location of the beam's midpoint corresponding to the snap-through, release and pull-in points and extracted via the numerical force control analysis (*circles*) for a beam of $d = 0.2$. *Dashed* and *solid lines* depict the limit-points and the bifurcation points resulting from Eqs. (18), (21), respectively

Galerkin's procedure converts Eq. (4) (with $w_0 = 0$) to a system of coupled nonlinear algebraic equations

$$\mathbf{B}q - \left(P - \alpha \mathbf{q}^{\mathbf{T}}\mathbf{S}\mathbf{q}\right)\mathbf{S}\mathbf{q} = -\beta\mathbf{Q} \tag{27}$$

where the elements Q_i of the force vector $\mathbf{Q}$ and b_{ij}, s_{ij} of the matrices $\mathbf{B}$ and $\mathbf{S}$ are as defined by Eqs. (9) and (10), respectively. By setting $n = 2$ in the beam's shape approximation, Eq. (27) is reduced to the form of two coupled equations in terms of the generalized coordinates q_1 and q_2

$$b_{11}q_1 - \left(P - \alpha\left(s_{11}q_1^2 + s_{22}q_2^2\right)\right)s_{11}q_1 = -\beta I_{11} \tag{28}$$

$$b_{22}q_2 - \left(P - \alpha\left(s_{11}q_1^2 + s_{22}q_2^2\right)\right)s_{22}q_2 = -\beta I_{22} \tag{29}$$

where I_{11} and I_{22} are defined by Eq. (13), $b_{11} = 2\pi^4, b_{22} = 1667.962, s_{11} = \pi^2/2$ and $s_{22} = 20.653$. Note that since the exact buckling modes are used as the base functions, we have from the homogeneous ($\beta = 0$) linearized counterpart of Eq. (28) that $b_{11}/s_{11} = \lambda_1^2 = 4\pi^2 = P_c^{(1)}$ is the exact lowest non-dimensional (see Table 1) buckling force of the initially straight beam (Euler's force). Similarly, from Eq. (29), $b_{22}/s_{22} = \lambda_2^2 = 80.761 = P_c^{(2)}$ is the second buckling force, corresponding to the asymmetric buckling of the straight beam.

First, three-dimensional bifurcation diagrams, mapping all stable and unstable equilibrium configurations in the q_1, q_2, β space are built numerically in the manner described in Sect. 3.1. The results are presented in Fig. 11, which is the counterpart of Fig. 5, illustrating the response of an electrostatically loaded initially stress-free curved beam. The expected similarity between the figures implies

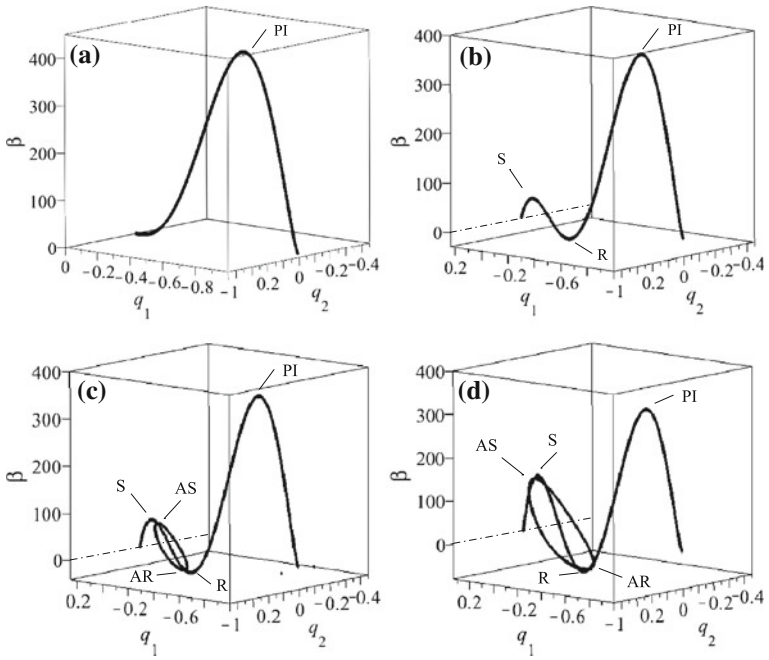

Fig. 11 Bifurcation diagram of the electrostatically loaded beam [two DOF RO model, Eqs. (28), (29)] for $d = 0.2$ and different axial loads: **a** $P/P_c^{(1)} = 1$, **b** $P/P_c^{(1)} = 2.01$, **c** $P/P_c^{(1)} = 2.27$, **d** $P/P_c^{(1)} = 3.03$. Point S and R are the snap-through and release limit points; points AS and AR are the bifurcation points of the asymmetric snap-through and release, respectively; point PI is the pull-in point

that the criteria for symmetric snap-through and for both non-critical (necessary condition) and critical (sufficient condition) bifurcations, should be defined also in the case of initially buckled beams. Note that at $\beta = 0$, the value of $q_1 \neq 0$ defines the elevation h of the beam prior to the application of the electrostatic force. This elevation is associated with the post-buckling response of the initially straight beam compressed by the axial force $P > P_c^{(1)}$ and it is given by the expression in Eq. (30), obtained from Eq. (28) where we set $\beta = 0,\ q_2 = 0$ (see [32])

$$h = 2\sqrt{\frac{2}{\alpha}\left(\frac{P}{P_c^{(1)}} - 1\right)} \tag{30}$$

One observes that the elevation becomes non-zero when P exceeds the axial buckling (Euler's) load $P_c^{(1)} = 4\pi^2$ and increases with the increase of P.

4.2 Snap-Through Criteria

In accordance with Fig. 11, and similarly to the case of an initially stress-free curved beam, the equilibrium branches corresponding to the non-symmetric configurations of the electrostatically loaded beam bifurcate from the equilibrium path representing the symmetric response. Hence, in order to find the position of the bifurcation points on the symmetric branch we linearize Eqs. (28), (29) around the path of $q_2 = 0$. Taking into account that the integrals in Eq. (14) vanish in the case of the base functions φ_i given by Eq. (26) as well, we obtain

$$b_{11}q_1 - \left(P - \alpha s_{11}q_1^2\right)s_{11}q_1 + \beta I_1 = 0 \tag{31}$$

$$\left(b_{22} - \left(P - \alpha s_{22}q_1^2\right)s_{22} - 2\beta I_2\right)q_2 = 0 \tag{32}$$

where $I_1(q_1)$ and $I_2(q_1)$ are defined in Eq. (17) with $\varphi_1,\ \varphi_2$, which are now given by Eq. (26). Note that for φ_1 given by Eq. (26) (with $i = 1$), we have

$$I_1 = \frac{1}{2\sqrt{(1+q_1)^3}} \tag{33}$$

4.2.1 Symmetric Snap-Through

Equation (31) is independent on q_2 and corresponds to a single DOF model describing the symmetric response of the beam. By expressing β in terms of q_1 using Eq. (31) and requiring $d\beta/dq_1 = 0$, while taking into account that $I_1 > 0$ for $q_1 > -1$, we obtain the equation

$$2q_1\left(\alpha s_{11}^2 q_1^2 + Ps_{11} - b_{11}\right)I_3 - \left(3\alpha s_{11}^2 q_1^2 - Ps_{11} + b_{11}\right)I_1 = 0 \tag{34}$$

where $I_3 = dI_1/dq_1 = -(3/4)(1+q_1)^{-5/2}$. The roots $q_S,\ q_R,\ q_{PI}$ of Eq. (34) correspond to the symmetric snap-through, symmetric release and pull-in limit points of the bifurcation diagram, respectively. Since $b_{11}/s_{11} = P_c^{(1)}$ and in view of Eq. (30), we obtain from Eq. (34)

$$h = q_1\sqrt{\frac{3I_1 - 2q_1I_3}{I_1 + 2q_1I_3}} \qquad \text{or} \qquad \frac{P}{P_c^{(1)}} = 1 + \frac{\alpha q_1^2(3I_1 - 2q_1I_3)}{8(I_1 + 2q_1I_3)} \tag{35}$$

The dependence between the axial force ratio, $P/P_c^{(1)}$, and the location of the limit points is shown by the dashed lines in Fig. 12a, b for two different values of d. The corresponding dependence of the limit points values of the voltage parameter on the axial force is shown in Fig. 12c, d and is obtained by substituting the solution of Eq. (35) back into Eq. (31).

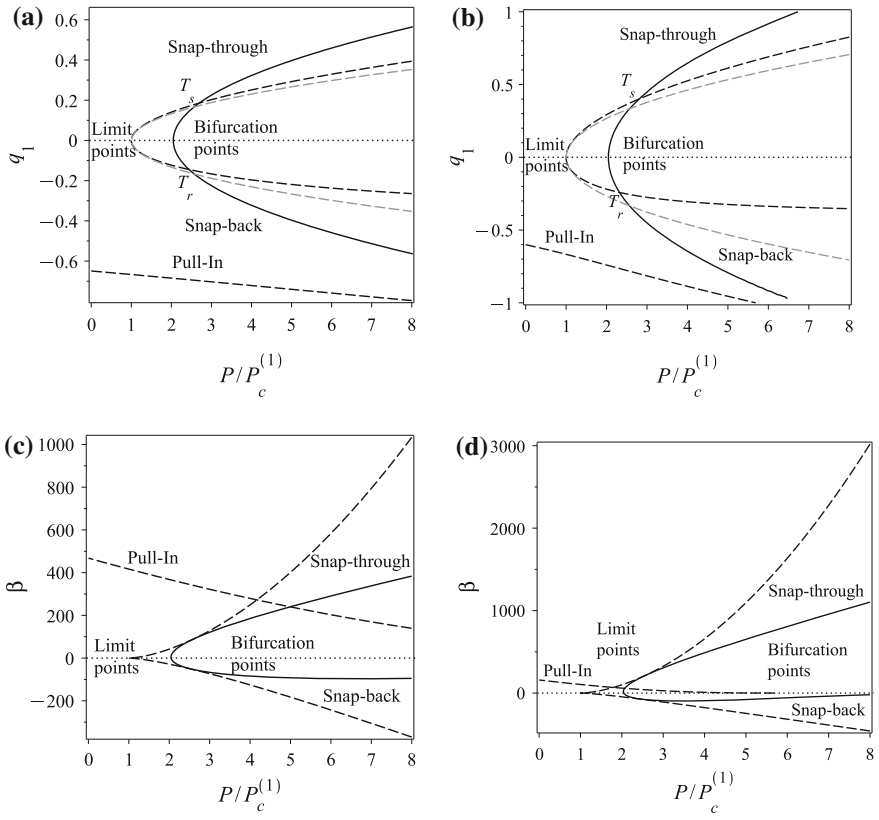

Fig. 12 **a**, **b** Location of the critical points of the electrostatically loaded beam and **c**, **d** corresponding critical values of the voltage parameter for: **a** $d = 0.2$ and **b** $d = 0.4$ and varying $P/P_c^{(1)}$. The *black dashed lines* represent the limit points of the buckling diagram given by Eq. (34) for the electrostatic model and corresponding to the symmetric snap through (point *S*), the symmetric snap back (point *R*) and the pull-in (point *PI*). The *dashed grey lines* represents the limit points of the "mechanical" model. The *solid lines* represent bifurcation points of the asymmetric snap-through (point *AS*) and release (point *AR*) given by Eq. (36). Points T_s and T_r represent the threshold of the critical asymmetric snap-through and snap-back points, respectively, where the bifurcation points coincide with the limit points. The *dotted line* represent $q_1 = 0$ in (**a**), (**b**) and $\beta = 0$ in (**c**), (**d**)

Similarly to the case of initially stress-free curved beams, the location (in terms of q_1) of the limit points corresponding to the symmetric snap-through and release is not symmetric with respect to the line $q_1 = 0$ (dotted line on Fig. 12a, b). This asymmetry is attributed to the influence of the electrostatic force and it increases with the increase of d, with the effect of the latter being more pronounced than in the case of initially stress-free curved beam. It is noted that for $d = 0.4$, and under large enough axial prestressing, the pull-in is suppressed. This is due to the fact that the elevation of the beam in the initial (prior to the application of the

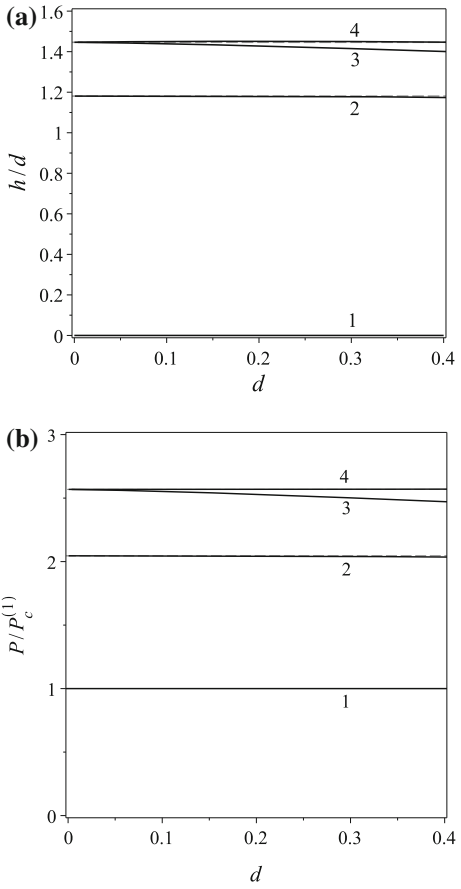

Fig. 13 Phase diagram of the symmetrical and non-symmetrical snap-through criteria. The *black solid lines* represent the criteria for the electrostatically loaded beam, and the *dashed gray lines* represent the criteria for a "mechanically" loaded beam. *Solid line no. 1* is the necessary criterion; *line 2* represents the necessary condition for the appearance of an asymmetrical snap-through; *lines 3* and *4* corresponds to the sufficient conditions for the snap-back and snap-through bifurcation points, respectively

electrostatic force) post-buckled configuration is higher than the distance between the beam's end and the electrode, i.e., $\hat{h} > g_0$ and the snap-through collapse is followed by the contact with the electrode.

Aiming at obtaining the symmetric snap-through criterion, we note through Fig. 12 and Eq. (35), that this criterion is defined by the minimum of $P = P(q_1)$ (or of $h = h(q_1)$). One observes from Eq. (35) that $dP/dq_1 = 0$ at $q_1 = 0$ and therefore the minimum value of P, above which the snap-through under "mechanical" or electrostatic force is possible, is $P_c^{(1)}$. This means that the snap-through occurs in a beam with any non-zero elevation h originated in a buckling. This situation is different from the case of the initially curved stress-free beam, where the snap-through in the electrostatically loaded beam may occur at the initial elevations, which are lower than are required for the appearance of the snap-through in "mechanically" loaded beams, but higher than a certain non-zero value. In the case of an initially straight and then buckled beam, the criteria of snap-through are identical in "mechanically" and electrostatically loaded beams, as

shown by the solid line 1 in Fig. 13a and b where the criteria for a beam with a rectangular cross section ($\alpha = 6/d^2$) are presented.

4.2.2 Asymmetric Snap-Through

Having defined the condition for the symmetric response, consider now the criteria for the asymmetric snap-through. By expressing β in terms of q_1, using Eq. (31) and substituting it into Eq. (32), one obtains that the eigenvalue problem in Eq. (32) has a non-trivial solution when the following equation is satisfied

$$2q_1\left(\alpha s_{11}^2 q_1^2 - P s_{11} + b_{11}\right)I_2 + \left(\alpha s_{11} s_{22} q_1^2 - P s_{22} + b_{22}\right)I_1 = 0 \tag{36}$$

or

$$2q_1 b_{11}\left(\frac{\alpha}{8}q_1^2 - \frac{P}{P_c^{(1)}} + 1\right)I_2 + b_{22}\left(\frac{\alpha s_{11}}{P_c^{(2)}}q_1^2 - \frac{P}{P_c^{(2)}} + 1\right)I_1 = 0 \tag{37}$$

The roots of Eq. (36) define the location of the bifurcation points on the equilibrium path which corresponds to the symmetric response. Like in the case of the initially stress-free curved beam, the location of these points given by q_1 depends on two parameters, α (and therefore d) and P [and therefore h, see Eq. (30)]. The dependence of the location of the bifurcation points [roots of Eq. (36)] and of the corresponding voltage parameter, β, on the axial force ratio, $P/P_c^{(1)}$, is shown by the solid lines in Fig. 12, for two different values of d. Figure 12 indicates, that two asymmetric bifurcation criteria can be formulated, one defining the conditions required for the appearance of a bifurcation (the necessary condition) and one defining the conditions for the appearance of the bifurcation points on the stable branch of the symmetric response (the sufficient condition). Furthermore, from Fig. 12 it is evident that due to the non linear nature of the electrostatic load, which increases as the beam is closer to the electrode, the beam snaps earlier (in relation to the deflection-independent load depicted by the gray lines). This observation was made for the stress free beam in [10] as well. However, the asymmetric response coincides with the asymmetric response of the "mechanical" model for lower d, suggesting that the necessary condition is similar to the condition of the linear model.

The necessary condition is obtained by finding the minimum of the curve $P/P_c^{(1)}$ (as a function of q_1) extracted from Eq. (37) with α (or d) considered to be a parameter. This minimum is the value of the prestressing axial load which guarantees the appearance of asymmetric bifurcations. The curves depicting the necessary condition, namely, the variation of $P/P_c^{(1)}$ and the corresponding h/d as a function of d, are shown by solid lines no. 2 in Fig. 13a and b, respectively. These lines almost coincide with the criterion defining the necessary condition for asymmetric response in an axially compressed buckled beams subjected to

transverse displacement-independent "mechanical" load (dashed lines no. 2 in Fig. 13). Thus it can be concluded, that initially straight beams buckled under axial compression which is greater than the second mode buckling load, may exhibit asymmetric response due to either deflection-independent "mechanical" or non-linear electrostatic transverse force.

In order to formulate the sufficient conditions for non-symmetric snap-through and non-symmetric snap-back, the approach introduced in Sect. 3.2 is used. By extracting from both Eqs. (35) and (37) expressions for P, and by equalizing them, one receives an implicit relation between α and the beam's midpoint elevations q_1 corresponding to the threshold points, T_s and T_r (Fig. 12). For a given α, the numerical solution of this equation provides two values of q_1. Substitution of these back into Eqs. (34) or (36) yields the threshold value of P which is sufficient for the appearance of asymmetric snap-through and snap-back bifurcation points located at the stable branches of the symmetric response. The dependence between these values of $P/P_c^{(1)}$ and the thickness of the beam d is shown by lines 3, 4 in Fig. 13 where line 3 is the condition for the snap-back and line 4 is for the snap-through. As is with the necessary condition, both sufficient conditions coincide with the "mechanical" counterpart $P > P_c^{(2)}$. The following fits (in terms of d) are given as an approximation of $P/P_c^{(1)}$ and h/d for the snap-back only

$$\frac{P}{P_c^{(1)}} > 2.569 + 0.122\, d - 0.408\, d^2 \text{ (sufficient snap-back)} \tag{38}$$

$$\frac{h}{d} > 1.446 + 0.056\, d - 0.187\, d^2 \text{ (sufficient snap-back)} \tag{39}$$

The finding that for the present case, two different criteria define the sufficient conditions for asymmetric snap-through and snap-back is similar to the finding of Sect. 3. Nevertheless, for the present case of initially bucked beams, the difference between line 3 and line 4 is more pronounced than for the case of initially stress-free curved beams (Fig. 7). This is in accordance with the previously mentioned observation that the asymmetry between the location of the snap-through and release limit points (Fig. 12) is more pronounced in the present case. Moreover, in contrast to the case of initially stress-free curved beam, for the present case the sufficient criterion for the asymmetric snap-back is lower than the asymmetric snap-through criterion. This implies that symmetric snap-through followed by asymmetric snap-back can occur.

4.3 Numerical Validation

The snap-through points and symmetry breaking criteria obtained in the previous section, were developed using an approximate two degrees of freedom RO model. In order to validate the approximation, two additional solutions were obtained

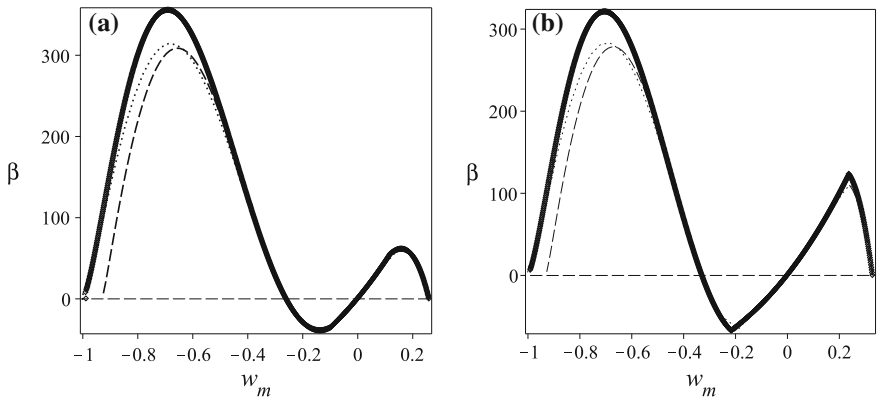

Fig. 14 Buckling diagram (w_M—midpoint elevation) for beams with $d = 0.2$ and **a** $P/P_c^{(1)} = 2.27$ **b** $P/P_c^{(1)} = 3.03$. Results are as follows: *solid line* depicts two DOF Galerkin RO model, *dashed line* represents seven DOF Galerkin RO model and the *dotted line* describes the result obtained through finite differences

numerically: the solution of the RO model including the first seven modes, and the finite differences (FD) solution of Eqs. (2), (3) for $w_0 = 0$, governing the behavior of the beam. For the latter, second order central differences with 30 intervals were used. Both approaches were implemented in conjunction with the arc-length method [33].

A comparison between the responses as predicted by the two DOF RO model, the seven DOF RO model and the FD solution is presented in Fig. 14, where variation of the midpoint deflection of the beam with the applied voltage is shown for two values of prestress. It can be seen that for the micro beam considered here, the two DOF RO model provides a reasonable accuracy. Yet, the difference between the results becomes more pronounced as the voltage parameter increases, and the distance between the beam and the electrode decreases. Under these conditions, the contribution of the terms of the RO model associated with higher symmetric and non-symmetric base functions could be significant. Specifically, relative errors of 0.7 and 11.2 % in the critical snap-through voltage are observed for beams subjected to prestresses of $P = 2.27P_c^{(1)}$ and $P = 3.03P_c^{(1)}$, respectively, while a relative error of 13.2 % in the critical pull-in voltage is observed under the two prestressing conditions. It is noted, that these errors are somewhat larger than those observed for initially curved stress-free beams.

In order to further validate the symmetry breaking criteria obtained on the basis of the two DOF RO model, the location of the snap-through, release and pull-in points predicted by the latter is compared to the location as extracted from the numerical analyzes. This comparison, for beams under various magnitudes of prestress, as shown in Fig. 15, indicates that the present approximation and the numerical results are in a good agreement. This implies that the presently obtained criteria for symmetry-breaking in electrostatically actuated prestressed micro beams are reliable.

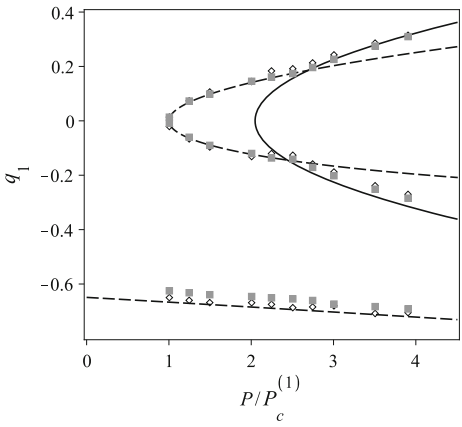

Fig. 15 Location of the beam's midpoint corresponding to the snap-through, release and pull-in points as extracted via numerical analysis: *diamond markers* represent the solution of the seven DOF Galerkin RO model; *grey boxes* represent the solution obtained by finite differences. *Dashed* and *solid lines* depict the limit-points and the bifurcation points resulting from the two DOF RO model, Eqs. (34), (36), respectively, for $d = 0.2$

5 Conclusions

In this work, the non-symmetric buckling of both an initially curved stress free beam and of a straight axially loaded beam subjected to an electrostatic force was analyzed. The approximate reduced order model of the beam was built by means of Galerkin decomposition with linear undamped eigenmodes of a straight beam as base functions for the first case and of a buckled straight beam for the latter. Then, the criteria of a non-symmetric buckling were developed for both beams using models limited to two DOF. Numerical verification of the obtained results indicates that the established criteria can be used for the prediction of the symmetry breaking in electrostatically actuated curved micro beams with satisfactory accuracy.

Since the bifurcation points associated with the non-symmetric buckling may be located on stable or unstable branches of the symmetric equilibrium curve, two symmetry breaking criteria were established for both models. The necessary criterion provides the conditions required for the appearance of non-symmetric solutions which may emerge from points located on an unstable branch of the symmetric buckling path. In contrast, the sufficient criterion establishes the condition for the critical non-symmetric buckling, when the bifurcation takes place at loading and deflection smaller than the limit-point values.

It was found that the nonlinearity of the electrostatic force has a significant influence on both buckling criteria. Specifically, the minimal values of the initial curvature of the stress-free beam required for the appearance of the instabilities are lower than in the "mechanical" case. However, for the buckled beam the criteria

for the cases of the "mechanical" and the electro-static loads are closer to each other than in the case of the initially curved stress-free beam. Note, however, that each of the criteria coincides with its "mechanical" counterpart when the distance between the beam and the electrode is large enough and the nonlinearity of the electrostatic force is less pronounced. Consequently, for practical purposes, the common "mechanical" criterion can be used for the prediction of the critical non-symmetric buckling of electrostatically actuated shallow micro beams.

It is worth noting, that the results presented in this work are obtained for shallow beams. The analysis of the behavior of deep beams is planned as a part of our future research.

Acknowledgments The authors thank Prof. J. Aboudi for fruitful discussions. The research is supported by The Israel Science Foundation (ISF, Grant No. 1426/08).

References

1. S. Timoshenko, *Theory of Elastic Stability* (McGraw-Hill, New York, 1961)
2. Z.P. Bažant, L. Cedolin, *Stability of Structures Elastic Inelastic Fracture and Damage Theories* (Dover Publications Inc, New-York, 1991)
3. C.L. Dym, *Stability Theory and Its Applications to Structural Mechanics* (Noordhoff Pub, Groningen, 1974)
4. A.P. Seyranian, I. Elishakoff, *Modern Problems of Structural Stability* (Springer, New York, 1989)
5. J. Thompson, G. Hunt, *A General Theory of Elastic Stability* (Wiley-Interscience publication, London, 1973)
6. G.J. Simitses, *Dynamic Stability of Suddenly Loaded Sturctures* (Springer, New York, 1989)
7. M.T.A. Saif, On a tunable bistable MEMS-theory and experiment. J. Microelectromech. Syst. **9**(2), 157–170 (2000)
8. S. Park, D. Hah, Pre-shaped buckled-beam actuators: theory and experiments. Sens. Actuators A Phys. **148**(1), 186–192 (2008)
9. J. Qiu, J. Lang, A.H. Slocum, A curved-beam bistable mechanism. J. Microelectromech. Syst. **13**(2), 137–146 (2004)
10. S. Krylov, B. Ilic, D. Schreiber, S. Seretensky, H. Craighead, The pull-in behavior of electrostatically actuated bistable microstructures. J. Micromech. Microeng. **18**, 055026 (2008)
11. S. Krylov, B.R. Ilic, S. Lulinsky, Bistability of curved micro beams actuated by fringing electrostatic fields. Nonlinear Dyn. **66**, 403–426 (2011)
12. I.Z. Pane, T. Asano, Investigation on bistability and fabrication of bistable prestressed curved beam. Jpn. J. Appl. Phys. **47**, 5291–5296 (2008)
13. Y. Zhang, Z. Wang, L.i. Yisongand, Y. Huang, D. Li, Snap-through and pull-in instabilities of an arch-shaped beam under an electrostatic loading. J. Microelectromech. Syst. **16**(3), 684–693 (2007)
14. H.M. Ouakad, M.I. Younis, The dynamic behavior of MEMS arch resonators actuated electrically. Int. J. Non-Linear Mech. **45**(7), 704–713 (2010)
15. K. Das, R.C. Batra, Pull-in and snap-through instabilities in transient deformations of microelectromechanical systems. J. Micromech. Microeng. **19**, 035008 (2009)
16. K. Das, R.C. Batra, Symmetry breaking, snap-through and pull-in instabilities under dynamic loading of microelectromechanical shallow arches. Smart Mater. Struct. **18**, 115008 (2009)
17. V. Intaraprasonk, S. Fan, Nonvolatile bistable all-optical switch from mechanical buckling. Appl. Phys. Lett. **98**, 241104 (2011)

18. D.R. Southworth, L.M. Bellan, Y. Linzon, H.G. Craighead, J.M. Parpia, Stress-based vapor sensing using resonant microbridges. Appl. Phys. Lett. **96**, 163503 (2010)
19. B. Charlot, W. Sun, K. Yamashita, H. Fujita, H. Toshiyoshi, Bistable nanowire for micromechanical memory. J. Micromech. Microeng. **18**, 045005 (2008)
20. A.H. Nayfeh, E.M. Abdel-Rahman, M.I. Younis, A reduced-order model for electrically actuated microbeam-based MEMS. J. Microelectromech. Syst. **12**, 672–680 (2003)
21. J.F. Rhoads, S.W. Shaw, K.L. Turner, Nonlinear dynamics and its applications in micro- and nanoresonators. in *Proceedings of DSCC2008 2008 ASME Dynamic Systems and Control Conference*, Ann Arbor, Michigan, USA, paper DSCC2008–2406, 20–22 Oct 2008
22. R.C. Batra, M. Porfiri, D. Spinello, Review of modeling electrostatically actuated microelectromechanical systems. Smart Mater. Struct. **16**, R23–R31 (2003)
23. M. Younis, *MEMS Linear and Nonlinear Statics and Dynamics*, Microsystems Series, (Springer, New York, 2011)
24. G.J. Simitses, D.H. Hodges, *Fundamentals of Structural Stability* (Butterworth-Heinemann, Burlington, 2006)
25. P. Villagio, *Mathematical Models for Elastic Structures* (Cambridge University Press, Cambridge, 1997)
26. S. Krylov, N. Dick, Dynamic stability of electrostatically actuated initially curved shallow micro beams. Continuum Mech. Thermodyn. **22**(6), 445–468 (2010)
27. Maplesoft, a division of Waterloo Maple Inc., dsolve/numeric/BVP—find numerical solution of ODE boundary value problems. http://www.maplesoft.com/support/help/Maple/view.aspx?path=dsolve/numeric/BVP, 2011. Online software support
28. L.F. Shampine, M.W. Reichelt, J. Kierzenka, Solving boundary value problems for ordinary differential equations in MATLAB with bvp4c. http://www.mathworks.com/bvp_tutorial, 2011
29. O. Bochobza-Degani, D. Elata, Y. Nemirovsky, An efficient DIPIE algorithm for CAD of electrostatically actuated MEMS devices. J. Microelectromech. Syst. **11**(5), 612–620 (2002)
30. S. Krylov, S. Seretensky, Higher order correction of electrostatic pressure and it's influence on the pull-in behavior of microstructures. J. Micromech. Microeng. **16**, 1382–1396 (2006)
31. A. Nayfeh, S. Emam, Exact solution and stability of postbuckling configurations of beams. Nonlinear Dyn. **54**(4), 395–408 (2008)
32. S. Emam, A. Nayfeh, On the nonlinear dynamics of a buckled beam subjected to a primary-resonance excitation. Nonlinear Dyn. **35**(1), 1–17 (2004)
33. A. Crisfield, *Non-linear Finite Element Analysis of Solids and Structures* (Wiley, Chichester, 1997)

Erratum to: Escape Time of Josephson Junctions for Signal Detection

P. Addesso, G. Filatrella and V. Pierro

Erratum to: Springer, Progress Optical Sci., Photonics 10091, doi:10.1007/10091_2012_9

In reference [1] of the chapter "Escape Time of Josephson Junctions for Signal Detection".

The reference: P. Addesso, G. Filatrella, V. Pierro, to appear on Phys. Rev. E. 82, 046712 (2010).

Should read as: P. Addesso, G. Filatrella, V. Pierro, Phys. Rev. E. 85, 016708 (2012).

The online version of the original chapter can be found under 10.1007/10091_2012_9.

P. Addesso (✉)
Department of Electronic and Computer Engineering, University of Salerno,
Via Ponte Don Melillo, 1 84084 Fisciano, Italy
e-mail: paddesso@unisa.it

G. Filatrella
Department of Sciences for Biological, Geological, and Environmental Studies and Salerno unit of CNSIM, University of Sannio, Via Port'Arsa 11 82100 Benevento, Italy
e-mail: filatrella@unisannio.it

V. Pierro
Department of Engineering, University of Sannio,
Corso Garibaldi, 107 82100 Benevento, Italy
e-mail: pierro@unisannio.it

Progress Optical Sci., Photonics (2013): E1
DOI: 10.1007/10091_2012_21

Published Online: 23 November 2012